

Volume 60
Number 2, 1996

International Journal of

QUANTUM CHEMISTRY

Editor-in-Chief
PER-OLOV LÖWDIN

Editors
ERKKI BRÄNDAS
YNGVE ÖHRN

Associate Editors
OSVALDO GOSCINSKI
STEN LUNELL
JOHN R. SABIN
MICHAEL C. ZERNER

DISTRIBUTION STATEMENT A

Approved for public release;
Distribution Unlimited

Proceedings of the
International Symposium on

**Atomic, Molecular, and
Condensed Matter Theory
and Computational Methods**

Held at the Ponce de Leon Resort,
St. Augustine, Florida, February 24–
March 2, 1996

Editor-in-Chief: Per-Olov Löwdin
Special Editors: Yngve Öhrn
John R. Sabin
Michael C. Zerner



A Wiley-Interscience
John Wiley

19970505 131

ISSN 0860-8842

Quantum Chemistry

Editor-in-Chief

Per-Olov Löwdin
University of Florida at Gainesville, USA
Uppsala University, Sweden

Editors

Erkki Brändas
Uppsala University, Sweden
Yngve Öhrn
University of Florida at Gainesville, USA

Associate Editors

Oswaldo Goswinski
Uppsala University, Sweden
Sten Lunell
Uppsala University, Sweden
John R. Sabin
University of Florida at Gainesville, USA
Michael C. Zerner
University of Florida at Gainesville, USA

Honorary Editors

Gerhard Herzberg
*National Research Council,
Ottawa, Ontario, Canada*
Kenichi Fukui
*Institute for Fundamental Chemistry at Kyoto,
Japan*
Rudy Marcus
*California Institute of Technology at
Pasadena, USA*

Editorial Board

Jiri Čížek
University of Waterloo, Ontario, Canada
Enrico Clementi
Université Louis Pasteur, Strasbourg, France
Raymond Daudel
*Académie Européenne de Arts, des Sciences et
des Lettres, Paris, France*
Ernest Davidson
Indiana University at Bloomington, USA
George G. Hall
University of Nottingham, UK
Laurens Jansen
Kusnacht, Switzerland
Norman H. March
University of Oxford, UK
Roy McWeeny
Università di Pisa, Italy
Saburo Nagakura
*Graduate University for Advanced Studies,
Yokohama, Japan*
Kimio Ohno
Hokkaido Information University, Japan
Josef Paldus
University of Waterloo, Ontario, Canada
Robert G. Parr
University of North Carolina at Chapel Hill, USA
Ruben Pauncz
Technion, Haifa, Israel

John A. Pople
Northwestern University at Evanston, Illinois, USA
Alberte Pullman
Institut de Biologie Physico-Chimique, Paris, France
Paul von Ragué Schleyer
*Universität Erlangen-Nürnberg,
Erlangen, Germany*
Harrison Shull
*Naval Postgraduate School,
Monterey, California, USA*
Tang Au-Chin
Jilin University, Changchun, China
Rudolf Zahradník
*Czech Academy of Sciences,
Prague, Czech Republic*

Advisory Editorial Board

Teijo Åberg
Helsinki University of Technology, Espoo, Finland
Michail V. Basilevsky
*Karpov Institute of Physical Chemistry,
Moscow, Russia*
Axel D. Becke
Queen's University, Kingston, Ontario, Canada
Gian Luigi Bendazzoli
Università di Bologna, Italy
Fernando Bernardi
Università di Bologna, Italy
Juan Bertran
*Universitat Autònoma de Barcelona,
Bellaterra, Spain*
Geza Biczó
*Hungarian Academy of Sciences,
Budapest, Hungary*
Jerzy Cioslowski
The Florida State University at Tallahassee, USA
Giorgina Corongiu
*Centro di Ricerca, Sviluppo e Studi Superiori
in Sardegna, Cagliari, Italy*
Mireille Defranceschi
*DPEL/SERGD/LMVT,
Fontenay Aux Roses, France*
Karl F. Freed
The University of Chicago, Illinois, USA
Peter Fulde
*Max-Planck-Institut für Festkörperforschung,
Stuttgart, Germany*
Odd Gropen
University of Tromsø, Norway
Aage E. Hansen
University of Copenhagen, Denmark
Trygve Helgaker
University of Oslo, Norway
Ming-Bao Huang
*Academia Sinica,
Beijing, People's Republic of China*
James T. Hynes
University of Colorado at Boulder, USA
Mu Shik Jhon
*Korea Advanced Institute of Science and
Technology, Seoul, Korea*
Uzi Kaldor
Tel Aviv University, Israel
Mati Karelson
Tartu University, Estonia
Hiroshi Kashiwagi
Kyushu Institute of Technology, Fukuoka,
Martin Klessinger
Universität Munster, Germany
Peter A. Kollman
University of California at San Francisco,
Eugene S. Kryachko
Academy of Sciences of Ukraine, Kiev, U
Sven Larsson
*Chalmers University of Technology,
Gothenburg, Sweden*
Lucas Lathouwers
Universitair Centrum (RUCA), Antwerp, B
Shyi-Long Lee
*National Chung Chang University,
Taiwan, Republic of China*
Claude Leforestier
Université Paris-Sud, Orsay, France
Jean-Paul Malrieu
Université Paul Sabatier, Toulouse, France
John D. Morgan III
University of Delaware at Newark, USA
J. Vincent Ortiz
University of New Mexico at Albuquerque
Lars Pettersson
University of Stockholm, Sweden
Leon Phillips
*University of Canterbury,
Christchurch, New Zealand*
Mark A. Ratner
Northwestern University at Evanston, Illin
William Reinhardt
University of Washington at Seattle, USA
Sten Rettrup
H. C. Ørsted Institut, Copenhagen, Denma
C. Magnus L. Rittby
Texas Christian University at Fort Worth, L
Michael Robb
King's College, London, UK
Mary Beth Ruskai
University of Massachusetts at Lowell, US
Vipin Srivastava
University of Hyderabad, India
Nicolai F. Stepanov
Moscow State University, Russia
Jiazong Sun
*Jilin University, Changchun,
People's Republic of China*
Colin Thomson
University of St. Andrews, Scotland, UK
Donald G. Truhlar
University of Minnesota at Minneapolis, U
Frank Weinhold
University of Wisconsin at Madison, USA
Harel Weinstein
*Mount Sinai School of Medicine,
New York, USA*
Robert E. Wyatt
The University of Texas at Austin, USA

REPORT DOCUMENTATION PAGE

Form Approved
OMB No. 0704-0188

Public reporting burden for this collection of information is estimated to average 1 hour per response, including the time for reviewing instructions, searching existing data sources, gathering and maintaining the data needed, and completing and reviewing the collection of information. Send comments regarding this burden estimate or any other aspect of this collection of information, including suggestions for reducing this burden to Washington Headquarters Services, Directorate for Information Operations and Reports, 1215 Jefferson Davis Highway, Suite 1204, Arlington, VA 22202-4302, and to the Office of Management and Budget, Paperwork Reduction Project (0704-0188), Washington, DC 20503.

1. AGENCY USE ONLY (Leave blank)		2. REPORT DATE 04-30-97		3. REPORT TYPE AND DATES COVERED Final 02-01-96 to 03-31-97	
4. TITLE AND SUBTITLE 1996 Sanibel Symposium on Development Tools & Methods for Computational Chemistry				5. FUNDING NUMBERS N00014-96-1-0197	
6. AUTHOR(S) Dr. Rodney Bartlett					
7. PERFORMING ORGANIZATION NAMES(S) AND ADDRESS(ES) University of Florida P.O. Box 118435 Gainesville, FL 32611-8435				8. PERFORMING ORGANIZATION REPORT NUMBER 1	
9. SPONSORING / MONITORING AGENCY NAMES(S) AND ADDRESS(ES)				10. SPONSORING / MONITORING AGENCY REPORT NUMBER	
11. SUPPLEMENTARY NOTES					
12. DISTRIBUTION / AVAILABILITY STATEMENT Approved for public release				12. DISTRIBUTION CODE N00179	
13. ABSTRACT (Maximum 200 words) The Sanibel Symposium on the Quantum Theory of Matter, embracing Quantum Chemistry, Quantum Biology and Solid-State Physics, have been held annually since their beginning in 1961. The 1996 symposium represents the 36th meeting. The Sanibel Symposia, which are uniquely influential in the field of Quantum Theory of matter, address the critical areas of research where modern quantum theoretical methods are playing key roles in the elucidation of current concepts and topics of great interest. Today the format for these symposia consists of a single eight-day meeting composed of various topical subsymposia that cover a wide range of current topics in molecular and materials sciences. This compact schedule, with no reduction in the total number of plenary and poster sessions, meets the original goals of the Sanibel Symposium, which are to stimulate the exchange of ideas on a cross disciplinary, international level and to report on the current state-of-the-art methodology for quantum theoretical computational methods. Typically, more than 300 scientists from 30-40 different nations come to this symposium. We expect a similar sized meeting for 1996.					
14. SUBJECT TERMS				15. NUMBER OF PAGES 1722	
				16. PRICE CODE	
17. SECURITY CLASSIFICATION OF REPORT	18. SECURITY CLASSIFICATION OF THIS PAGE	19. SECURITY CLASSIFICATION OF ABSTRACT	20. LIMITATION OF ABSTRACT		

International Journal of QUANTUM CHEMISTRY

Quantum Chemistry Symposium No. 30

*Proceedings of the
International Symposium on*

Atomic, Molecular, and Condensed Matter
Theory and Computational Methods

Held at Ponce de Leon Resort, St. Augustine, Florida,
February 24–March 2, 1996

Editor-in-Chief: Per-Olov Löwdin
Special Editors: Yngve Öhrn, John R. Sabin, and
Michael C. Zerner

an Interscience® Publication
published by JOHN WILEY & SONS

The *International Journal of Quantum Chemistry* (ISSN 0020-7608) is published semi-monthly with two extra issues in November by John Wiley & Sons, Inc., 605 Third Avenue, New York, New York 10158.

Copyright © 1996 John Wiley & Sons, Inc. All rights reserved. No part of this publication may be reproduced in any form or by any means, except as permitted under section 107 or 108 of the 1976 United States Copyright Act, without either the prior written permission of the publisher, or authorization through the Copyright Clearance Center, 222 Rosewood Drive, Danvers, MA 01923, (508) 750-8400, fax (508) 750-4470. Periodicals postage paid at New York, NY, and at additional mailing offices.

The code and the copyright notice appearing at the bottom of the first page of an article in this journal indicate the copyright owner's consent that copies of the article may be made for personal or internal use, or for the personal or internal use of specific clients, on the condition that the copier pay for copying beyond that permitted by Sections 107 or 108 of the US Copyright Law.

This consent does not extend to the other kinds of copying, such as copying for general distribution, for advertising or promotional purposes, for creating new collective work, or for resale. Such permission requests and other permission inquiries should be addressed to the Permissions Dept.

Subscription price (Volumes 57-60, 1996): \$3,328.00 in the US, \$3,588.00 in Canada and Mexico, \$3,731.00 outside North America. All subscriptions outside US will be sent by air. Personal rate (available only if there is an institutional subscription): \$150.00 in North America, \$306.00 outside North America. Subscriptions at the personal rate are available only to individuals. Payment must be made in US dollars drawn on a US bank. Claims for undelivered copies will be accepted only after the following issue has been received. Please enclose a copy of the mailing label. Missing copies will be supplied when losses have been sustained in transit and where reserve stock permits.

Please allow four weeks for processing a change of address. For subscription inquiries, please call (212) 850-6645; e-mail: SUBINFO@Wiley.com.

Postmaster: Send address changes to *International Journal of Quantum Chemistry*, Susan Malawski, Director, Subscription Fulfillment and Distribution, Subscription Department, John Wiley & Sons, Inc., 605 Third Avenue, New York, NY 10158.

Advertising Sales: Inquiries concerning advertising should be forwarded to Susan Levey, Advertising Sales, John Wiley & Sons, Inc., 605 Third Avenue, New York, NY 10158; (212) 850-8832. Advertising Sales, European Contact: Michael Levermore, Advertising Manager, John Wiley & Sons, Ltd., Baffins Lane, Chichester, Sussex PO 19 1UD, England.

Reprints: Reprint sales and inquiries should be directed to the customer service department, John Wiley & Sons, Inc. 605 Third Ave., New York, NY 10158. Tel: 212-850-8776.

Manuscripts should be submitted in triplicate and accompanied by an executed Copyright Transfer Form to the Editorial Office, *International Journal of Quantum Chemistry*, Quantum Chemistry Group, Uppsala University, Box 518, S-75120, Uppsala, Sweden. Authors may also submit manuscripts to the Editorial Office, *International Journal of Quantum Chemistry*, Quantum Theory Project, Williamson Hall, University of Florida, Gainesville, Florida 32611. **Information for Contributors** appears in the first and last issue of each volume. **All other correspondence** should be addressed to the *International Journal of Quantum Chemistry*, Publisher, Interscience Division, Professional, Reference, and Trade Group, John Wiley & Sons, Inc., 605 Third Avenue, New York, New York 10158, U.S.A. The contents of this journal are indexed or abstracted in *Chemical Abstracts*, *Chemical Titles*, *Chemical Database*, *Current Contents/Physical, Chemical, and Earth Sciences*, *Research Alert (ISI)*, *Science Citation Index (ISI)*, and *SCISEARCH Database (ISI)*.

**This paper meets the requirements of ANSI/NISO
Z39.48-1992 (Permanence of Paper).** ☺

Contents

List of Participants	ix
Introduction	
<i>N. Y. Öhrn, J. R. Sabin, and M. C. Zerner</i>	1213
The Chairman's Introductory Remark	
<i>G. Bergson</i>	1215
Partial Waves in the Nonspherical Case	
<i>T. Levitina and E. J. Brändas</i>	1217
Path Integral Monte Carlo Method for Ab Initio Calculation	
<i>H. Kawabe, H. Nagao, and K. Nishikawa</i>	1223
Efficient Numerical Method for Finding the Initial Response of Quantum Processes to Changes in the Potential	
<i>M. J. Hagmann</i>	1231
Direct Algorithm for the Random-Phase Approximation	
<i>V. G. Zakrzewski, O. Dolgounitcheva, and J. V. Ortiz</i>	1241
Computation of Curve-Crossing Diagrams by Approximate Valence Bond Method	
<i>L. Rincón</i>	1249
Evaluation of the Alpha-Function for Large Parameter Values	
<i>H. W. Jones and J. L. Jain</i>	1257
Nonadiabatic Treatment of Molecular Systems by the Wavepackets Method	
<i>H. Nagao, K. Kodama, Y. Shigeta, K. Nishikawa, H. Kawabe, M. Nakano, and K. Yamaguchi</i>	1261

(continued)

Calculation of Intramolecular Force Fields from Second-Derivative Tensors <i>J. M. Seminario</i>	1271
Intermolecular Perturbation Theory: Renormalized Interaction Energies <i>W. H. Adams</i>	1279
Many-Electron-Wavepackets Method <i>H. Nagao, M. Nakano, S. Yamanaka, S. Yamada, D. Yamaki, I. Shigemoto, S. Kiribayashi, K. Yamaguchi, and Y. Shigeta</i>	1291
Stochastic Path-Integral Method for Chemical Reaction Dynamics: Application to the Full 3D H ₃ System <i>M. Nagaoka</i>	1303
Sinc Collocation in Quantum Chemistry: Solving the Planar Coulomb Schrödinger Equation <i>V. G. Koures and F. E. Harris</i>	1311
On Approximating Electron Repulsion Integrals with Linear Combination of Atomic-Electron Distributions <i>S. Ten-No and S. Iwata</i>	1319
Multireference Basis-Set Reduction <i>W. Wenzel, M. M. Steiner, and K. G. Wilson</i>	1325
Basis Set and Correlation Effects on Geometry of Octahedral Second-Row Transition-Metal Complexes <i>A. Broo</i>	1331
Gaussian Fitting Function Basis Sets for Crystalline Silicon: Bond-Centered <i>s</i> -Type vs. Site-Centered <i>f</i> -Type <i>J. C. Boettger</i>	1345
Reaction Energetics of Tetrahedrane and Other Hydrocarbons: Ab Initio and Density Functional Treatments <i>J. M. Seminario, P. Politzer, H. J. Soscun M., A. G. Zacarías, and M. Castro</i>	1351

(continued)

Attempts Toward a Pair Density Functional Theory <i>P. Ziesche</i>	1361
On the Optimal Mixing of the Exchange Energy and the Electron–Electron Interaction Part of the Exchange–Correlation Energy <i>O. V. Gritsenko, R. Van Leeuwen, and E. J. Baerends</i>	1375
Resemblance Analysis of Molecular Systems on the Grounds of DFT-Evaluated Parameters. Platinum Complexes and Their Anticancer Activity <i>L. Schulz and H. Chojnacki</i>	1385
Spin-Multiplet Energies from Time-Dependent Density Functional Theory <i>M. Petersilka and E. K. U. Gross</i>	1393
Simple Modification of the Lee–Yang–Parr Correlation Functional to Satisfy Exact Nonuniform Scaling Requirements <i>S. Ivanov</i>	1403
DFT Calculations of Alternative Structures in the Allyl–Nickel Catalyzed Polymerization of Butadiene <i>H. Boegel and S. Tobisch</i>	1409
Density Functional Study of $\text{Fe}_2\text{--N}_2$ <i>A. G. Zacarías and M. Castro</i>	1419
Electronic Structure and Properties of MCO and M_5CO Carbonyls ($\text{M} = \text{Fe}, \text{Ni}, \text{Cu}$) by Density Functional Methods <i>R. M. Sosa and P. Gardiol</i>	1429
Ensemble Density Functional Theory for Inhomogeneous Fractional Quantum Hall Systems <i>O. Heinonen, M. I. Lubin, and M. D. Johnson</i>	1443
Linear Response and Quasiparticle Calculations as Probes of the Kohn–Sham Eigenvalues in Metals <i>A. G. Eguiluz</i>	1457

(continued)

Intensity and Polarization of Light Emitted in Slow Ion–Atom Collisions <i>H. F. M. DaCosta, D. A. Micha, and K. Runge</i>	1469
Hybrid Quantum/Classical Studies of Photodissociation and Recombination of $I_2(A)$ in Rare Gas Matrices: A Linear Chain Model <i>H. Guo and L. Liu</i>	1479
Fourier Space for Accurate Ab Initio RHF Band Structure Calculations on Chainlike Systems <i>I. Flamant, J. G. Fripiat, and J. Delhalle</i>	1487
Iodine-Doped Transpolyacetylene <i>G. P. Das, A. T. Yeates, and D. S. Dudis</i>	1499
Theoretical Study of the X-ray Photoionization Spectra of Polycycloalkanes <i>M. Deleuze and J. Delhalle</i>	1505
Molecular Shape Transitions in Grafted Polymers Under Geometrical Confinement <i>G. A. Arteca</i>	1515
Modification of the Local Self-Consistent Field Method for Modeling Surface Reactivity of Covalent Solids <i>L. G. Gorb, J.-L. Rivail, V. Thery, and D. Rinaldi</i>	1525
Self-Expansion and Compression of Charged Clusters of Stabilized Jellium <i>A. Vieira, C. Fiolhais, M. Brajczewska, and J. P. Perdew</i>	1537
Free Energy in Relation to Order Parameter in Magnets and Pyroelectrics <i>N. H. March, A. M. L. Nip, and J. A. Tuszyński</i>	1549
Behavior of Carriers in δ -Doped Quantum Wells Under In-Plane Magnetic Fields <i>A. T. Lino, E. K. Takahashi, L. M. R. Scolfaro, and J. R. Leite</i>	1559
Computational Studies of Less Common Fullerene-Related Species <i>S.-L. Lee, M.-L. Sun, and Z. Slanina</i>	1567

(continued)

Investigation on the Interaction on and the Rotation of C_{60} in Alkali-Doped Complexes $A_xA'_{3-x}C_{60}$ ($X = 1, 2, 3; A, A' = \text{Alkali}$) <i>J.-M. Yan, C.-B. Zhu, and Z.-J. Xu</i>	1577
Comparison of Theoretical Models of Solvation <i>K. K. Stavrev, T. Tamm, and M. C. Zerner</i>	1585
Using Theoretical Descriptors to Model Solvent Effects in the Isomerization of <i>cis</i> -Stilbene <i>R. A. McGill, J. K. Rice, A. P. Baronavski, J. C. Owrutsky, A. H. Lowrey, K. K. Stavrev, T. Tamm, and M. C. Zerner</i>	1595
Does the Proton-Transfer Reaction Take Place in the Ground State of Phenol- $(H_2O)_4$ Clusters? <i>H. Watanabe and S. Iwata</i>	1607
Generalized Conductor-like Screening Model (GCOSMO) for Solvation: An Assessment of Its Accuracy and Applicability <i>T. N. Truong, U. N. Nguyen, and E. V. Stefanovich</i>	1615
Analysis of Chemical Bonding in C_2 Using Dyson Orbitals <i>W. Tong, R. C. Morrison, and O. W. Day, Jr.</i>	1623
Polarizabilities of Heteroaromatic Molecules: Azines Revisited <i>R. J. Doerksen and A. J. Thakkar</i>	1633
Negative Hydrogen and Helium in a Variety of Debye Plasmas <i>L. Zhang and P. Winkler</i>	1643
Condensed-Phase Effects on the Conformational Equilibrium of Ethylene Glycol <i>B. J. Costa Cabral</i>	1651
The π, π^* State in Formaldehyde and Thioformaldehyde <i>F. Grein and M. R. J. Hachey</i>	1661
SCMEH-MO Calculations on Lanthanide Systems. III. $Ln(CO)_6, Ln(OC)_6$ ($Ln = Nd, Sm$) <i>E. A. Boudreaux</i>	1673
The Electronic g -Tensor of MgF : A Comparison of ROHF and MRD-CI Level Results <i>G. H. Lushington and F. Grein</i>	1679

(continued)

Wave-Function Splitting Technique for Calculating Above-Threshold Ionization Electron Spectra <i>S. Chelkowski and A. D. Bandrauk</i>	1685
Kernel Projector Matrices for Leu ¹ -Zervamicin <i>L. Huang, L. Massa, and J. Karle</i>	1691
Fission of Metal Clusters: A Comparison of Jellium Model Calculations and Shell Correction Method Calculations <i>H. Koizumi and Y. Fukumoto</i>	1701
Comparisons of the Theoretical Calculation of Nitrogen Clusters by Semiempirical MO Method <i>C. Chen and K.-C. Sun</i>	1709
Combined Effect of the Screening of a Donor Ion and the Conduction Band Nonparabolicity on the Binding Energy of a Donor at the Center of a Spherical Quantum Dot <i>A. M. Elabsy and P. Csavinszky</i>	1719
Author Index	1723
Published Symposia	I
Diskette Submission Instructions	VII

1996 Sanibel Symposia

List of Participants

WILLIAM H. ADAMS
Rutgers University
Department of Chemistry
P.O. Box 939
Piscataway, NJ 08855-0939
Phone: 908/445-3758
FAX: 908/445-5312
EMail: adams@rutchem.rutgers.edu

ARIE AIZMAN
Univ. Technica Fed. Santa Maria
Department of Chemistry
Casilla 110-V
Valparaiso
Chile
Phone: 56-32-626364
FAX: 56-32-625461
EMail: aaizman@itata.disca.utfsm.cl

DAVID ALLARA
Pennsylvania State University
185 MRI Bldg, Dept. of Chemistry
230 Innovation Blvd.
University Park, PA 16802
Phone: 814/865-2254
FAX: 814/863-0618
EMail: dla3@psu.edu

ALEJANDRO AMAYA
Univ. Nacional Autonoma de Mexico
Inst. de Fisica
AP 48-3
Cuernavaca, Morelos 62251
Mexico
Phone: 73-17-5388
FAX: 52 73 173077
EMail: jano@ce.ifisicam.unam.mx

IRIS ANTES
Universitaet Zuerich
Org.-Chem. Institut
Winterthurerstr. 190
Zuerich, CH 8044
Switzerland
Phone: 0041-1-257
EMail: antes@ocisgi14.unizh.ch

YOSSLEN ARAY
Centro de Quimica IVIC
Km. 11, Carretera Panamericana
Apartado Postal 21827
Caracas 1020A
Venezuela

GUSTAVO A. ARTECA
Laurentian University
Chimie et Biochimie
Ramsey Lake Rd
Sudbury, Ontario P3E 2C6
Canada
Phone: 705/675-1151
FAX: 705/675-4844
EMail: gustavo@nickel.laurentian.ca

RICHARD BADER
McMaster University
Department of Chemistry
128 Main St. W.
Hamilton, Ontario L8S4M1
Canada
Phone: 905/525-9140 ext. 23499
FAX: 905/522-2509

LIST OF PARTICIPANTS

KYOUNG K. BAECK
Quantum Theory Project
University of Florida
362 Williamson Hall
P.O. Box 118435
Gainesville, FL 32611-8435
Phone: 352/392-1597
FAX: 352/392-8722
EMail: baeck@knusun.kangnung.ac.kr

E. J. BAERENDS
Vrije Universiteit
Department of Chemistry
De Boelelaan 1083
Amsterdam, HV 1081
The Netherlands
Phone: 31-20-44-47621
FAX: 31-20-44-47643
EMail: baerends@chem.vu.nl

CAREY K. BAGDASSARIAN
Albert Einstein Coll. of Med.
1300 Morris Park Avenue
Dept. of Physiology and Biophys.
Bronx, NY 10461
Phone: 718/430-3332
EMail: carey@riscl.aecom.yu.edu

ANNA BALKOVA
US Naval Academy
572 Holloway Road
Chemistry Department
Annapolis, MD 21402
Phone: 410/293-6626
FAX: 410/293-2218
EMail: balkova@gold.nadn.navy.mil

ANDRE D. BANDRAUK
University of Sherbrooke
Department of Chemistry
2500 Universite
Sherbrooke, Quebec J1K 2R1
Canada
Phone: 819/821-7098
FAX: 819/821-8017
EMail: bandrauk@planck.chimie.usherb.

ROBERT N. BARNETT
Georgia Inst. of Technology
Dept. of Physics
Atlanta, GA 30332-0430
Phone: 404/894-5219
FAX: 404/894-9958
EMail: robert.barnett@physics.gatech.edu

RODNEY J. BARTLETT
Quantum Theory Project
University of Florida
381 Williamson Hall
P.O. Box 118435
Gainesville, FL 32611-8435
Phone: 352/392-1597
FAX: 352/392-8722
EMail: bartlett@qtp.ufl.edu

SULLIVAN BECK
Quantum Theory Project
University of Florida
345 Williamson Hall
P.O. Box 118435
Gainesville, FL 32611-8435
Phone: 352/392-1597
FAX: 352/392-8722
EMail: beck@qtp.ufl.edu

DARIO BEKSIC
Univ. Auto. de Barcelona
Department de Quimica
Bellaterra, Catalonia 08193
Spain
Phone: 34-3-581-2857
FAX: 34-3-581-2477
EMail: dario@klngon.uab.es

RICHARD L. BELL
University of Utah
Department of Chemistry
Salt Lake City, UT 84112-1194
Phone: 801/581-7445
FAX: 801/581-7445
EMail: rbell@chemistry.utah.edu

CHRIS BENDER
Albert Einstein Coll. of Medicine
Molecular Pharmacology
1300 Morris Park Ave.
Bronx, NY 10461
Phone: 718/430-2175
EMail: bender@spin.aecom.yu.edu

GORAN BERGSON
Uppsala University
Dept. of Chemistry
Thunbergsvagen 5
Uppsala S-75121
Sweden
Phone: 46-18-183799
FAX: 46-18-508542
EMail: gb@kemi.uu.se

LIST OF PARTICIPANTS

DAVID E. BERNHOLDT
Syracuse University
111 College Place
NE Parallel Architecture Center
Syracuse, NY 13244-4100
Phone: 315/443-3857
FAX: 315/443-1973
EMail: bernhold@npac.syr.edu

MANUEL BERRONDO
Brigham Young University
Physics Department
268 FB
Provo, UT 84602
Phone: 801/378-4635
FAX: 801/378-2265
EMail: berrondom@plasma.byu.edu

ISAAC BERSUKER
University of Texas at Austin
Department of Chemistry
Austin, TX 78712
Phone: 512/471-4671
FAX: 512/471-8696
EMail: bersuker@eeyore.cm.utexas.edu

RICARDO BICCA DE ALENCASTRO
Univ. Federal de Rio de Janeiro
Inst. de Quimica
Bloco A-CT
Sala 622, Cidade Univ.
Rio de Janeiro, RJ 21949-900
Brazil
Phone: 55-021-590-3544
FAX: 55-021-2904746
EMail: bicca@iq.ufrj.br

DAVID M. BISHOP
University of Ottawa
Department of Chemistry
10 Marie Curre
Ottawa K1N 6N5
Canada
Phone: 613/562-5181
FAX: 613/562-5170

FRANK E. BLANEY
Smithkline Beecham
Computational Chemistry
New Frontiers Science Park (N)
Third Avenue
Harlow, Essex CM19 5AW
England
Phone: 011-44-1279-622143
FAX: 011-44-1279-622348

BRETT M. BODE
Iowa State Univeristy
Department of Chemistry
Gilman Hall
Ames, IA 50011
Phone: 515/294-4604
EMail: brett@si.fi.ameslab.gov

HORST BOEGEL
University of Halle
Inst. Phys. Chem.
Geusaerstr.
Merseburg D-06217
Germany
Phone: 49-3461-46-2127
FAX: 49-3461-46-2370
EMail: boegel@chemie.uni-halle.de

JON C. BOETTGER
Los Alamos National Laboratory
Group T-1, MS B221
Los Alamos, NM 87545
Phone: 505/667-7483
FAX: 505/665-5757
EMail: jcb@kohnsham.lanl.gov

ALEXANDER I. BOLDYREV
University of Utah
Department of Chemistry
Salt Lake City, UT 84112-1194
Phone: 801/581-7445
FAX: 801/581-8433
EMail: boldyrev@chemistry.utah.edu

EDWARD A. BOUDREAUX
University of New Orleans
Department of Chemistry
Lake Front
New Orleans, LA 70148
Phone: 504/286-6311
FAX: 504/286-6860

MIRIXA BOVES
IVIC
Department of Chemistry
Apartado Postal 21827
Caracas 1020-A
Venezuela
Phone: 58-02-5011442
FAX: 58-02-5011350
EMail: mboves@quimica.ivic.ve

LIST OF PARTICIPANTS

PAUL BRACKEN
Quantum Theory Project
University of Florida
386 Williamson Hall
P.O. Box 118435
Gainesville, FL 32611-8435
Phone: 352/392-6715
FAX: 352/392-8722
EMail: bracken@qtp.ufl.edu

MARTA BRAJCZEWSKA
Universidade de Coimbra
Departamento de Fisica
Coimbra P-3000
Portugal
Phone: 351-39-410621
FAX: 351-39-29158
EMail: marta@ftedr4.fis.uc.pt

ERKKI BRÄNDAS
Uppsala University
Dept. of Quantum Chemistry
Uppsala, S-75120
Sweden
Phone: 46-18-183263
FAX: 46-18-502402
EMail: erkki@kvac.uu.se

MARCUS E. BREWSTER
University of Florida
Pharmos Corp.
Two Innovation Drive
Alachua, FL 32615
Phone: 904/462-1210
FAX: 904/462-5401
EMail: mbrews@aol.com

TORRE BRINCK
Royal Institute of Technology
Dept. of Physical Chemistry
Stockholm 10044
Sweden
Phone: 46-8-7908595
FAX: 46-8-7908207
EMail: tore@physchem.kth.se

ANDERS BROO
Chalmers University of Technology
Physical Chemistry
Goteborg 41296
Sweden
Phone: 46-31-7723051
FAX: 46-31-7723858
EMail: broo@phc.chalmers.se

BERNARD BROOKS
National Institute of Health
Building 12A, Room 2055
Bethesda, MD 20892
Phone: 301 496-0148
FAX: 301 496-2172

DOUGLAS BUSTER
IBM
1505 LBJ Freeway, 5th Floor
Dallas, TX 75234
Phone: 214/280-3960
FAX: 214/280-2779

BENEDITO CABRAL
University of Lisbon
CFMC
2, Av. Prof. Gama Pinto
Lisbon 1699
Portugal
Phone: 351-1-7973325
EMail: ben@alf1.cc.fc.ul.pt

SYLVIO CANUTO
Quantum Theory Project
University of Florida
362 Williamson Hall
P.O. Box 118435
Gainesville, FL 32611-8435
Phone: 352/392-1597
FAX: 352/392-8722
EMail: canuto@qtp.ufl.edu

GLORIA INES CARDENAS JIRON
Universidad de Chile
Dept. de Quimica
Casilla 653
Santiago
Chile
Phone: 56-2-678-7272
FAX: 56-2-271-3888
EMail: atl@abello.dic.uchile.cl

CRISTIAN CARDENAS-LAILHACAR
Quantum Theory Project
University of Florida
P.O. Box 118435
345 Williamson Hall
Gainesville, FL 32611-8435
Phone: 904/392-6365
FAX: 904/392-8722
EMail: cardenas@qtp.ufl.edu

LIST OF PARTICIPANTS

SIDONIO CASTILLO

Univ. Auto Metropolitana Azcapotzalco
Ciencias Basicas
Av. San Pablo #180
Azcapotzalco, D.F. 02200
Mexico
Phone: 525/724-4218
FAX: 525/723-5940
EMail: sca@hp9000al.uam.mx

EDUARDO A. CASTRO

Programma QUINOR
Departamento de Quimica
47 y 115, C de Correo 962
Le Plata, Buenos Aires 1900
Argentina
Phone: 021-214037
FAX: 021-259485
EMail: castro@biol.unlp.edu.ar

MIGUEL CASTRO

Univ. Nacional Autonoma de Mexico
Dept. de Fisica
Mexico, D.F. 04510
Mexico
Phone: 525/622-3783
FAX: 525/616-2010
EMail: castro@papalotl.pruim.unam.mx

LEOPOLDO CASTRO-CABALLERO

Univ. Aut. de Puebla Benemerita
Facultad de Ciencias Quimicas
AP 1694, Dept. de Computacion
Puebla, Pue 72000
Mexico
FAX: 22-44-31-06

MAURO CAUSA

University of Torino
Inorganic Chemistry
Via P. Giural 5
Torino, Italy 10034
Italy
Phone: +3911 6707833
FAX: +39116707855
EMail: causa@ch.unito.it

ANNE CHAKA

The Lubrizol Corporation
29400 Lakeland Blvd.
Research Division
Wickliffe, OH 44092-2298
Phone: 216/943-1200
FAX: 216/943-9020
EMail: chaka@lubrizol.com

MATT CHALLACOMBE

Minnesota Supercomputer Inst.
MSI
1200 Washington Ave. South
Minneapolis, MN 55414
Phone: 612/626-0763
FAX: 612/624-8861
EMail: mf10111@msi.umn.edu

JAMES CHEESEMAN

Lorentzian, Inc.
140 Washington Ave.
North Haven, CT 06473
Phone: 203/234-0618
FAX: 203/239-0846
EMail: cheese@lorentzian.com

CHENG CHEN

Chung Cheng Institute of Technology
Dept. of Applied Chemistry
Yuan-su-lin, Ta-hsi
Taoyuan, Taiwan 33509
Republic of China
Phone: 886-3-3802149
FAX: 886-3-3891519
EMail: chenc@cc02.ccit.edu.tw

HAI-PING CHENG

Quantum Theory Project
University of Florida
371 Williamson Hall
P.O. Box 118435
Gainesville, FL 32611-8435
Phone: 352/392-1597
FAX: 352/392-8722
EMail: cheng@qtp.ufl.edu

HENRYK CHOJNACKI

Institute of Physical and Theoretical Chemistry
I-30, Wyb.
Wyspiarskiego 27
Wroclaw 50-370
Poland
Phone: 48-71-203520
FAX: 48-71-203364
EMail: chojnacki@kchf.ch.pwr.wroc.pl

LIST OF PARTICIPANTS

PAUL W. CHUN
University of Florida
P.O. Box 100245, HSC
Dept. of Biochem. and Mol. Biology
Gainesville, FL 32610-0245
Phone: 904/392-3356
FAX: 904/392-2953
EMail: pwchun@pine.circa.ufl.edu

MIKAEL CIFTAN
US Army Research Office Physics Division
P.O. Box 12211
Research Triangle Park, NC 27709-2211
FAX: 919/549-4310

JIRI CIZEK
University of Waterloo
Applied Math.
Waterloo N2L 3G1
Canada
Phone: 519/885-1211
FAX: 519/746-4319
EMail: jcizek@theochem.uwaterloo.ca

TIM CLARK
University of Erlangen
Institut für Organische Chemie
Naegelschachstr. 25
Erlangen D-91052
Germany
Phone: 49-9131-852948
FAX: 49-9131-856565
EMail: clark@organik.uni-erlangen.de

JAMES COFFIN
IBM, Computational Chemistry
1505 LBJ Freeway, 5th Floor
Computational Chemistry
Dallas, TX 75234
Phone: 214/280-3960
FAX: 214/280-2779

RENATO R. CONTRERAS
Universidad de Chile
Dept. de Química
Casilla 653
Santiago
Chile
Phone: 56-2-6787261
FAX: 56-2-2713888
EMail: rcontrer@abello.dic.uchile.cl

JOAO CORDEIRO
Ilha Solteira
Fac. de Engenharia
Av. Brasil 56
Ilha Solteira, SP 15385-000
Brazil
Phone: 018-7623113
FAX: 018-7622735
EMail: cordeiro@isl000.uesp.anp.br

MARSHALL CORY
Quantum Theory Project
University of Florida
380 Williamson Hall
P.O. Box 118435
Gainesville, FL 32611-8435
Phone: 352/392-1597
FAX: 352/392-8722
EMail: cory@qtp.ufl.edu

KALINE COUTINHO
Quantum Theory Project
University of Florida
362 Williamson Hall
P.O. Box 118435
Gainesville, FL 32611-8435
Phone: 352/392-1597
FAX: 352/392-8722
EMail: kaline@if.usp.br

MAURICIO COUTINHO-NETO
Quantum Theory Project
University of Florida
343 Williamson Hall
P.O. Box 118435
Gainesville, FL 32611-8435
Phone: 352/392-1597
FAX: 352/392-8722

ATTILA CSASZAR
Eotvos University
Dept. of Theoretical Chem.
P.O. Box 32
Budapest H-1518
Hungary
Phone: 35-1-209-0600
FAX: 36-1-209-0602
EMail: csaszar@para.elte.hu

LIST OF PARTICIPANTS

JOAQUIM DA MOTTA NETO

Quantum Theory Project
University of Florida
348 Williamson Hall
P.O. Box 118435
Gainesville, FL 32611-8435
Phone: 352/392-1597
FAX: 352/392-8722
EMail: quim@qtp.ufl.edu

HERBERT DACOSTA

Quantum Theory Project
University of Florida
348 Williamson Hall
P.O. Box 118435
Gainesville, FL 32611-8435
Phone: 352/392-1597
FAX: 352/392-8722
EMail: dacosta@qtp.ufl.edu

ROBERT S. DAILEY

Indiana University
Department of Chemistry
Chemistry Building
Bloomington, IN 47405-4001
Phone: 812/855-4601
FAX: 812/855-8300
EMail: rsdailey@indiana.edu

GURU P. DAS

Wright Laboratory
MLBP
WPAFB, OH 45433
Phone: 513/255-9147
FAX: 513/476-4706
EMail: dasgp@picard.ml.wpafb.af.mil

JANET DEL BENE

Youngstown State University
Department of Chemistry
Youngstown, OH 44555
Phone: 216/742-3466
FAX: 216/742-1579
EMail: fr042008@ysub.ysu.edu

JOSEPH DELHALLE

FUNDP
Department of Chemistry
Rue de Bruxelles 61
Namur B-5000
Belgium
Phone: 32-81-724552
FAX: 32-81-724530
EMail: joseph.delhalle@fundp.ac.be

BRUCE DERBY

Sun Microsystems
Suite 840
6200 Cambell Causeway
Tampa, FL 33607

ERIK DEUMENS

Quantum Theory Project
University of Florida
359 Williamson Hall
P.O. Box 118435
Gainesville, FL 32611-8435
Phone: 352/392-1597
FAX: 352/392-8722
EMail: deumens@qtp.ufl.edu

DAVID DIXON

Pacific Northwest National Laboratory
P.O. Box 999
MS-K1-83
Richland, WA 99352
Phone: 509/372-4999
FAX: 509/375-6631
EMail: da_dixon@pnl.gov

ROBERT J. DOERKSEN

University of New Brunswick
Dept. of Chemistry
Fredericton, New Brunswick E3B 6E2
Canada
Phone: 506/454-7385
FAX: 506/453-4981
EMail: ab12@unb.ca

M. CRISTINA DONNAMARIA

IFLYSIB
Inst. Fisica Liq. y Sist. Biol.
CC 565, 59 N 789
La Plata 1900
Argentina
Phone: 54-21-254904
FAX: 54-21-257317
EMail: donna@iflysi.edu.ar

ANTHONY DRIBBEN

University of Florida
Dept. of Chemistry
P.O. Box 117200
Gainesville, FL
Phone: 352/846-0742
FAX: 352/392-8758
EMail: dribben@chem.ufl.edu

LIST OF PARTICIPANTS

JAMES DUFTY
University of Florida
Department of Physics
215 Williamson Hall
Gainesville, FL 32611
Phone: 904/392-6693
FAX: 904/392-0524
EMail: dufty@phys.ufl.edu

P. LEALIE DUTTON
University of Pennsylvania
Dept. of Biochemistry
B501 Richards Bldg.
Philadelphia, PA 19104-6089
Phone: 215/898-0991
FAX: 215/573-2235
EMail: dutton@mail.med.upenn.edu

ADOLFO EGUILUZ
University of Tennessee
Dept. of Physics and Astronomy
1408 Circle Drive
Knoxville, TN 37996-1200
Phone: 423/974-7822
FAX: 423/974-7843
EMail: aeguiluz@utkvx.utk.edu

DONALD E. ELLIS
Northwestern University
Dept. of Physics and Astronomy
Evanston, IL 60208
Phone: 708/491-3665
FAX: 708/491-9982
EMail: don-ellis@nwu.edu

RODOLFO GARCIA ESQUIVEL
Univ. Autonoma Metropolitana-Iztapalapa
Dept. de Quimica
A. P. 55-534
Mexico, D.F. 09340
Mexico
Phone: 525/724-4675
FAX: 525/724-4666
EMail: esquivel@xanum.uam.mx

JACK FAJER
Brookhaven National Laboratory
Department of Applied Sciences
Building 815
Upton, NY 11973-5000
Phone: 516/282-4521
FAX: 516/282-3137

ANTONIO FERREIRA
University of Memphis
Department of Chemistry
Memphis, TN 38152
Phone: 901/678-4429
FAX: 901/678-3447
EMail: amferreira@cc.memphis.edu

KIM F. FERRIS
Pacific Northwest National Laboratory
P.O. Box 999, MS-K2-44
Environmental & Energy Science
Richland, WA 99352
Phone: 509/375-3754
FAX: 509/375-2186
EMail: kim@darterm.pnl.gov

CARLOS FIOLHAIS
University of Coimbra
Department de Fisica
Coimbra P-3000
Portugal
Phone: 351-39-410624
FAX: 351-39-29158
EMail: mbody@gemm.ci.uc.pt

SIGHART FISCHER
Universitat Munchen
Theoretische Physik 1 38
Physik-Department
Garching b. Munchen 85747
Germany
Phone: 49-89-32092373
FAX: 49-89-32092444
EMail: jilljupiter.t30.physik.tu.muchen.de

RICHARD FRIESNER
Columbia University
Department of Chemistry
New York, NY 10027
Phone: 212/854-7606
FAX: 212/932-1289
EMail: rich@cucbs.chem.columbia.edu

JOSEPH G. FRIPIAT
Facultes Univ. de Namur
Dept. of Chimie
61 rue de Bruxelles
Namur B-5000
Belgium
Phone: 32-81-724551
FAX: 32-81-724530
EMail: joseph.fripiat@fundp.ac.be

PATRICIO P. FUENTEALBA

Universidad de Chile
Dept. Fisica, Casilla 653
Las Palmeras 3425
Santiago
Chile
Phone: 562-6787268
FAX: 562-2713882
EMail: pfuentea@bello.dic.uchile.cl

LASZLO FUSTI-MOLNAR

Eotvos Lorand University
P.O. Box 32
Dept. of Theor. Chem.
Budapest H-1518
Hungary
Phone: 36-1-209-0555
FAX: 36-1-209-0602
EMail: fusti@para.elte.hu

JIALI GAO

State University of New York at Buffalo
Department of Chemistry
Natural Sciences & Math Complex
Buffalo, NY 14260-3000
Phone: 716/645-6800
FAX: 716/645-6963
EMail: jiali@tams.chem.buffalo.edu

ANGELICA GARCIA-ZACARIAS

UNAM
Dept. de Fisica
Mexico, D.F. 04510
Mexico
Phone: 525/622-3776
FAX: 525/622-3724
EMail: zacarias@papalotl.pquim.unam.mx

JORGE GARZA

Univ. Autonoma Metropolitana-Iztapalapa
Dept. de Quimica
Michoacan y Purisima s/n
Mexico, D.F. 09340
Mexico
Phone: 525-7244675
FAX: 525-7244666
EMail: jgo@xanum.uam.mx

JURGEN GAUSS

Universitat Mainz
Inst. fur Physikalische Chemie
D-55099 Mainz
Germany
Phone: 49-6131-393736
FAX: 49-6131-393768
EMail: craps@tchibm3.chemie.uni-karlsruhe.de

JOSEPH GERRATT

University of Bristol
School of Chemistry
Cantock's Close
Bristol BS8 1TS
United Kingdom
Phone: 011-44-117-9288164
FAX: 011-44-117-9251295
EMail: j.gerratt@bristol.ac.uk

SANNE SCHRODER GLAD

Odense University
Department of Chemistry
Campusvej 55
Odense M 5230
Denmark
Phone: 4566158600-2509
FAX: 4566158780
EMail: sanne@dou.dk

LIONEL GOODMAN

Rutgers University
Chemistry Department
New Brunswick, NJ 08903
Phone: 908/445-2603
FAX: 908/445-5312
EMail: goodman@rutchem.rutgers.edu

LEONID GORB

University of Kiev-Mohyla Academy
Dept. of Chemistry
2, Skovorada str.
Kiev
Ukraine
Phone: 380-44-416-12-46
FAX: 380-44-416-51-16
EMail: glg@iccw.freenet.kiev.ua

FRITZ GREIN

University of New Brunswick
Department of Chemistry
Fredericton, New Brunswick E3B 6E2
Canada
Phone: 506/453-4776
FAX: 506/453-4981
EMail: fritz@unb.ca

E. K. U. GROSS

Institut fur Theoretische Phys
Universitat Wurzburg
Am Hubland
Wurzburg D-97074
Germany
Phone: 49-931-888-5724
FAX: 49-931-888-5141
EMail: gross@physik.uni-wuerzburg.de

LIST OF PARTICIPANTS

HUA GUO
University of Toledo
Department of Chemistry
Toledo, OH 43609
Phone: 419/530-4579
FAX: 419/530-4033
EMail: hguo@uoft02.utoledo.edu

GENNADY L. GUTSEV
Quantum Theory Project
University of Florida
370 Williamson Hall
P.O. Box 118435
Gainesville, FL 32611-8435
Phone: 352/392-1597
FAX: 352/392-8722
EMail: gutsev@qtp.ufl.edu

STEVEN GWALTNEY
Quantum Theory Project
University of Florida
345 Williamson Hall
P.O. Box 118435
Gainesville, FL 32611-8435
Phone: 352/392-1597
FAX: 352/392-8722
EMail: gwaltney@qtp.ufl.edu

MARK J. HAGMANN
University Florida International
Electrical & Comp. Eng.
Maimi, FL 33199
Phone: 305/348-3017
FAX: 305/348-3707
EMail: hagmann@eng.fiu.edu

FRANK HARRIS
University of Utah
Department of Chemistry
Salt Lake City, UT 84112
Phone: 801/581-8445
FAX: 801/585-3207
EMail: harris@dirac.chem.utah.edu

MAGNUS HEDSTROM
Quantum Theory Project
University of Florida
362 Williamson Hall
P.O. Box 118435
Gainesville, FL 32611-8435
Phone: 352/392-1597
FAX: 352/392-8722
EMail: hedstrom@qtp.ufl.edu

OLLE HEINONEN
University of Central Florida
Department of Physics
Orlando, FL 32816-2385
Phone: 407/823-5145
FAX: 407/823-5112
EMail: ogh@physics.ucf.edu

ROBERT N. HILL
University of Delaware
Dept. of Physics & Astronomy
Newark, DE 19716
Phone: 302/831-8787
FAX: 302/831-1637
EMail: hill@strauss.udel.edu

KIMIHIKO HIRAO
University of Tokyo School of Engineering
Dept. of Applied Chemistry
Bunkyo-ku Hongo
Tokyo 113
Japan
Phone: 81-3-5802-3335
FAX: 81-3-5802-3335
EMail: hirao@qcl.t.u-tokyo.ac.jp

YA-WEN HSIAO
Quantum Theory Project
University of Florida
348 Williamson Hall
P.O. Box 118435
Gainesville, FL 32611-8435
Phone: 352/392-1597
FAX: 352/392-8722
EMail: hsiao@qtp.ufl.edu

MING-JU HUANG
University of Florida
Center for Drug Discovery
Box 100497
Gainesville, FL 32610
Phone: 904/392-8186
FAX: 904/392-8589
EMail: mjhuang@pine.circa.ufl.edu

NOEL HUSH
University of Sydney
School of Chemistry
Sydney, NSW 2006
Australia
Phone: 61-2-351-4688
FAX: 61-2-351-3329

LIST OF PARTICIPANTS

HAMZA A. HUSSAIN

University of Baghdad
College of Science
Chem Department
Baghdad
Iraq

AKIRA IRINOYA

Okayama University of Science
Dept. of Electronic Engineering
Ridai-cho
Oyakama City 700
Japan
Phone: 086-252-3161

STANISLAV IVANOV

Tulane University
Chemistry Department
New Orleans, LA 70118
Phone: 504/865-5575
FAX: 504/865-5596
EMail: stan@mailhost.tsc.tulane.edu

TAKASHI IWAMI

Okayama University of Science
Dept. of Electronic Engineering
Bidaviho
Okayama City 700
Japan
Phone: 086-252-3161

SUEHIRO IWATA

Inst. for Molecular Science
Myodaiji
Okazaki 444
Japan
Phone: 81-564-55-7300
FAX: 81-564-53-4660
EMail: iwata@ims.ac.jp

SAUL JACCHIERI

Instituto Adolfo Lutz
10 Andar
Av. Dr Arnaldo 355
Sao Paulo, SP 01246-902
Phone: 55-11-8510111
FAX: 55-11-8533503
EMail: jacchier@fcrfv1.ncifcrf.gov

HERBERT W. JONES

Florida A & M University
Department of Physics
Tallahassee, FL 32307
Phone: 904/599-3470
FAX: 904/599-3577

SVANTE JONSELL

Quantum Theory Project
University of Florida
343 Williamson Hall
P.O. Box 118435
Gainesville, FL 32611-8435
Phone: 352/392-1597
FAX: 352/392-8722
EMail: jonsell@qtp.ufl.edu

DAN JONSSON

Linkoping University
Physics & Measurement Tech.
Linkoping S-58183
Sweden
Phone: 46-13-288953
FAX: 46-13-137568
EMail: dajon@ifm.liu.se

JOSHUA JORTNER

Tel Aviv University
School of Chemistry
Ramat Aviv
Tel Aviv 69978
Israel
Phone: 972-3-640-8322
FAX: 972-3-641-5054
EMail: jortner@chemsg1.tau.ac.il

SABRE KAIS

Purdue University
Department of Chemistry
1393 Brown Building
West Lafayette, IN 47907
Phone: 317/494-5965
FAX: 317/494-0239
EMail: sabre@salam.chem.purdue.edu

MATTIE KARELSON

Quantum Theory Project
University of Florida
P.O. Box 118435
Gainesville, FL 32611-8435

JEROME KARLE

Naval Research Laboratory
Laboratory for the Structure
of Matter
Washington, DC 20375-5341
Phone: 202/767-2665
FAX: 202/767-0953
EMail: williams6@lsm.nrl.navy.mil

LIST OF PARTICIPANTS

SHASHI P. KARNA
US Air Force Phillips Laboratory
PL/VTE, Space Electronics Div.
3550 Aberdeen Ave., SE
Kirtland AFB, NM 87117-5776
Phone: 505/853-3157
FAX: 505/846-2290
EMail: karnas@plk.af.mil

MICHAEL KASHA
Florida State University
Inst. of Molec. Biophys.
452 Molecular Biophysics
Tallahassee, FL 32306
Phone: 904/644-6452

HIROYUKI KAWABE
Kinjo College
Secretarial Department 1200
Matto, Ishikawa 924
Japan
Phone: 81-762-76-4411
FAX: 81-762-75-4183
EMail: kiyoshi@wriron1.s.kanazawa-v.ac.jp

SALIM M. KHALIL
University of Mosul
Department of Chemistry
College of Science
Mosul
Iraq

JAMES W. KING
Foundation for Chemistry
P.O. Box 116
Balsam, NC 28707-0116
Phone: 704/452-7570
FAX: 704/452-5432

NICHOLAS KIOUSSIS
California State University at Northridge
Dept. of Physics
Materials Theory Center
Northridge, CA 91330
FAX: 818/717-5615
EMail: nkiousi@newton.csun.edu

BERNARD KIRTMAN
University of California
Department of Chemistry
Santa Barbara, CA 93106
Phone: 805/893-2217
EMail: kirtman@sbmm1.ucsb

MIKE KLEIN
University of Pennsylvania
Department of Chemistry
3231 Walnut St.
Philadelphia, PA 19104-6202
Phone: 215/898-8317
FAX: 215/573-2112
EMail: klein@lrsm.upenn.edu

PETER J. KNOWLES
University of Birmingham
School of Chemistry
Edgbaston
Birmingham B15 2TT
United Kingdom
Phone: 44/121-414-7472
FAX: 44/121-414-7471
EMail: p.j.knowles@bham.ac.uk

K. KODAMA
Kanazwa University
Chemistry Department
Kakuma-machi
Kanazawa, Ishikawa 920-11
Japan
Phone: 81-762-64-5687
FAX: 81-762-64-5742

HIROYASU KOIZUMI
Himeji Inst. of Technology
Kamigori-cho
Material Science
Ako-gun, Kyogo 678-12
Japan
Phone: 81-7915-8-0147
FAX: 81-7915-8-0151
EMail: koizumi@sci.himeji-tech.ac.jp

JING KONG
Dalhousie University
Department of Chemistry
Halifax, Nova Scotia B3H 4J3
Canada
Phone: 902/494-7021
FAX: 902/494-1310
EMail: jkong@is.dal.ca

ANATOLI A. KORKIN
Quantum Theory Project
University of Florida
370 Williamson Hall
P.O. Box 118435
Gainesville, FL 32611-8435
Phone: 352/392-1597
FAX: 352/392-8722
EMail: korkin@qtp.ufl.edu

LIST OF PARTICIPANTS

GENRICH L. KRASKO
US Army Research Lab.
Materials Directorate
Aberdeen Proving Ground, MD 21005-5069
Phone: 302/892-6539
FAX: 302/892-6504
EMail: gkrasko@arl.mil

JEFFREY L. KRAUSE
Quantum Theory Project
University of Florida
372 Williamson Hall
P.O. Box 118435
Gainesville, FL 32611-8435
Phone: 352/392-1597
FAX: 352/392-8722
EMail: krause@qtp.ufl.edu

YURI KRUGLYAK
Odessa State University
Dept. for Molecular Elect.
Dvoryanskaya St. 2
Odessa 270100
Ukraine
Phone: 380-482-60-33-14
FAX: 380-482-63-77-85
EMail: quantum@intgt.odessa.ua

CARLOS KUBLI-GARFIAS
National Auton. Univ. of Mexico
Lab. of Hormonal Chemistry
Apdo Postal 70-469
Mexico, D.F. 04511
Mexico
Phone: 525-6-223815
FAX: 525-5-500048
EMail: kubli@servidor.unam.mx

IGOR KURNIKOV
University of Pittsburgh
Chemistry Department
Pittsburgh, PA 15260
Phone: 412/624-1217
FAX: 412/624-8552
EMail: igor@ganesh.chem.pitt.edu

HENRY A. KURTZ
University of Memphis
Department of Chemistry
Memphis, TN 38152
Phone: 901/678-4414
FAX: 901/674-3447
EMail: kurtzh@cc.memphis.edu

ZEKI KURUOGLU
Bilkent University
Associate Provost
Eng. Bldg., G-07
Bilkent, Ankara 06533
Turkey
Phone: 90-312-2664417
FAX: 90-312-2664161
EMail: kuruoglu@bilkent.edu.tr

JANOS LADIK
Nurnberg Universitat-Erlangen
Egerlandstr. 3
91058
Erlangen
Germany
Phone: 49-9131-857766
FAX: 49-9131-857736
EMail: ladik@pctc.chemie.uni-erlangen.de

WILLIAM LAIDIG
Procter & Gamble Co.
Miami Valley Laboratories
P.O. Box 538707
Cincinnati, OH 45253-8707
Phone: 513/627-2857
FAX: 513/627-1233
EMail: laidig@pg.com

UZI LANDMAN
Georgia Inst. of Technology
School of Physics
Atlanta, GA 30332-0430
Phone: 404/853-9958
FAX: 404/894-9958

SVEN LARSSON
Chalmers University of Technology
Dept. of Physical Chemistry
Goteborg S-41296
Sweden
Phone: 46-31-7723058
FAX: 46-31-7723858
EMail: larsson@phc.chalmers.se

LUCAS LATHOUWERS
University of Antwerp
Antwerp
Belgium

LIST OF PARTICIPANTS

WALTER LAUDERDALE

Wright Laboratory
WL/POS
1790 Loop Road North
Wright-Patterson AFB, OH 45433-7103
Phone: 513/255-7266
FAX: 513/255-1125
EMail: lauderdale@quantum.appl.wpafb.af.mil

FRANCISCO LAVARDA

Quantum Theory Project
University of Florida
375 Williamson Hall
P.O. Box 118435
Gainesville, FL 32611-8435
Phone: 352/392-6973
FAX: 352/392-8722
EMail: lavarda@qtp.ufl.edu

NIKOLAI LAVRIK

Institute of Chemical Kinetics and Combustion
Novosibirsk 630090
Russia
Phone: 383-2-357088
FAX: 383-2-352350
EMail: lavrik@kinetics.nsk.su

PAOLO LAZZERETTI

University of Modena
Dipartimento di Chimica
Via Campi
Modena 41100
Italy
Phone: 0039-59-378450
FAX: 0039-59-373543
EMail: lazzeret@c220.unimo.it

PIERRE LEBRETON

University of Illinois at Chicago
Department of Chemistry
845 W. Taylor Street
Chicago, IL 60607-7061
Phone: 312/996-5431
FAX: 312/996-0431
EMail: lebreton@uic.edu

SHYI-LONG LEE

Department of Chemistry
National Chung-Cheng Univ.
Chiayi 621
Taiwan
Phone: 886-5-2428177
FAX: 886-5-2721040
EMail: sllee@nas01.ccu.edu.tw

J. R. LEITE

Universidade de Sao Paulo
Inst. de Fisica
CP 66318
Sao Paulo, SP 05389-970
Brazil
Phone: 55-11-8186878
FAX: 55-11-8186984
EMail: jrleite@uspif.bitnet

MAX LEONG

University of Texas-Austin
Department of Chemistry
Welch 3.140
Austin, TX 78712
Phone: 512/471-4671
FAX: 512/471-8696
EMail: max@eeyore.cm.utexas.edu

WLODZIMERZ LEWANDOWSKI

Warsaw Agricultural Univ.
Inst. of General Chemistry
Rakowiecka 26/30
Warsaw 02-528
Poland
Phone: 49-13-93
FAX: 49-13-75

LE-MIN LI

Peking University
Department of Chemistry
Beijing 100871
China
Phone: 86-10-2502905
FAX: 86-10-2564095
EMail: lilm@pku.edu.cn

ANTONIO TADEU LINO

Univ. Fed. de Uberlandia
Dept. de Ciencias Fisicas
Campus Santa Monica
Uberlandia, Minas Gerais
Brazil
FAX: 55 34 236-0466
EMail: atlino@brufu.bitnet

GILDA LOEW

Molecular Research Institute
845 Page Mill Road
Palo Alto, CA 94304
Phone: 415/424-9924
FAX: 415/424-9501
EMail: loew@montara.molres.org

LIST OF PARTICIPANTS

PER-OLOV LOWDIN
Quantum Theory Project
University of Florida
365 Williamson Hall
P.O. Box 118435
Gainesville, FL 32611-8435
Phone: 352/392-1597
FAX: 352/392-8722
EMail: lowdin@qtp.ufl.edu

ALFRED H. LOWREY
Naval Research Laboratory
Laboratory for the
Structure of Matter
Washington, DC 20375

NING LUO
Mount Sinai School of Medicine
One Gustave Levy Lane
Dept. Physiology & Biophysics
New York, NY 10029
Phone: 212/241-1611
FAX: 212/860-3369
EMail: nluo@msvax.mssm.edu

YI LUO
Linköping University
Physics & Measurement Tech.
Linköping S-58183
Sweden
Phone: 46-13-281703
FAX: 46-13-137568
EMail: luo@ifm.liu.se

GERRY LUSHINGTON
University of New Brunswick
Department of Chemistry
Fredericton, New Brunswick E3B 6E2
Canada
Phone: 506/453-4781
FAX: 506/453-4981
EMail: s6ok@jupiter.sun.csd.unb.ca

ROBERT MACLAGAN
Rice University
Department of Chemistry
6100 Main Street
Houston, TX 77005-1892
EMail: maclagan@katzo.rice.edu

YOSHINORI MANMOTO
Okayama University of Science
Faculty of Engineering
1-1 Ridai-cho
Okayama 700
Japan
Phone: 086-252-3161
FAX: 086-255-3611
EMail: manmoto@ee.ous.ac.jp

UKO MARAN
University of Florida
Department of Chemistry
229 Chemistry Research Bldg.
Gainesville, FL 32611-7200
Phone: 352/392-0554
FAX: 352/392-9199
EMail: uko@ufark2.chem.uf.edu

NORMAN H. MARCH
University of Oxford
Inorganic Chemistry Dept.
South Parks Road
Oxford OX1 3QR
England
FAX: 441-865-275415

LOU MASSA
Hunter College
City University of New York
695 Park Avenue
New York, NY 10021
Phone: 212/772-5330
FAX: 212/772-5332
EMail: massa@mvaxgr.hunter.cuny.edu

RICHARD J. MATHAR
Quantum Theory Project
University of Florida
368 Williamson Hall
P.O. Box 118435
Gainesville, FL 32611-8435
Phone: 352/392-1597
FAX: 352/392-8722
EMail: mathar@qtp.ufl.edu

JOHN M. MCKELVEY
Eastman Kodak Co.
Computational Science Lab.
Bldg. 83
Rochester, NY 14650-2216
Phone: 716/477-3335
FAX: 716/722-2327
EMail: mckelvey@kodak.com

LIST OF PARTICIPANTS

CHANGJANG MEI
Quantum Theory Project
University of Florida
386 Williamson Hall
P.O. Box 118435
Gainesville, FL 32611-8435
Phone: 352/392-1597
FAX: 352/392-1597
EMail: mei@qtp.ufl.edu

JESUS MANDIETA-PEREZ
Benemerita Universidad
Facultad de Ciencias Quimicas
Apartado Postal 1694
Puebla, Pue 72000
Mexico
FAX: 22-44-31-06

FERNANDO MENDIZABAL
Universidad de Chile
Dept. de Quimica
Casilla 653
Santiago
Chile
Phone: 56-02-2713888
FAX: 56-02-2713888
EMail: rcontrer@abello.dic.uchile.cl

KENNETH MERZ, JR.
Pennsylvania State Univ.
Department of Chemistry
152 Davey Lab.
University Park, PA 16802
Phone: 814/865-3623
FAX: 814/863-8403
EMail: merz@retino.chem.psu.edu

MICHAEL MESSINA
University of California at San Diego
Department of Chemistry
3050 Urey Hall Addition
La Jolla, CA 92093-0339
Phone: 619/534-0290
FAX: 619/534-7654
EMail: mmessina@ucsd.edu

DAVID A. MICHA
Quantum Theory Project
University of Florida
366 Williamson Hall
P.O. Box 118435
Gainesville, FL 32611-8435
Phone: 352/392-2597
FAX: 352/392-8722
EMail: micha@qtp.ufl.edu

JOSEF MICHL
University of Colorado
Department of Chemistry
Boulder, CO 80309-0215
Phone: 303/492-6519
FAX: 303/492-0799
EMail: michl@eefus.colorado.edu

WILLIAM H. MILLER
University of California
Department of Chemistry
Berkeley, CA 94720
Phone: 510/642-0653
FAX: 510/642-6262
EMail: miller@neon.cchem.berkeley.edu

BENNY MOGENSEN
Quantum Theory Project
University of Florida
362 Williamson Hall
P.O. Box 118435
Gainesville, FL 32611-8435
Phone: 352/392-1597
FAX: 352/392-8722
EMail: benny@qtp.ufl.edu

JOSE R. MOHALLEM
Univ. Federal de Minas Gerais
Dept. de Fisica
CP 702
Belo Horizonte, MG 30161-970
Brazil
Phone: 031-4485659
FAX: 031-4485600
EMail: rachid@tapajos.fisica.ufmg.br

MICHAEL MOLLER
Hypercube, Inc.
#7-419 Phillip St.
Waterloo, Ontario N2L 3X2
Canada
Phone: 519/725-4040
FAX: 519/725-5193
EMail: info@hyper.com

LIST OF PARTICIPANTS

HENDRIK J. MONKHORST
Quantum Theory Project
University of Florida
362 Williamson Hall
P.O. Box 118435
Gainesville, FL 32611-8435
Phone: 352/392-1597
FAX: 352/392-8722
EMail: monkhorst@qtp.ufl.edu

LUIS A. MONTERO
Universidad de la Habana
Faculty of Chemistry
Lab. Computational and Theo. Chem.
Havana 10400
Cuba
Phone: 53-7-333502
FAX: 53-7-333502

JORGE A. MORALES
Quantum Theory Project
University of Florida
348 Williamson Hall
P.O. Box 118435
Gainesville, FL 32611-8435
Phone: 352/392-1597
FAX: 352/392-8722
EMail: morales@qtp.ufl.edu

JOHN D. MORGAN
University of Delaware
Dept. of Physics & Astronomy
Newark, DE 19716
Phone: 302/831-2661
FAX: 302/831-1637
EMail: 32399@udel.edu

KEIJI MOROKUMA
Emory University
Department of Chemistry
1515 Pierce Drive
Atlanta, GA 30322
Phone: 404/727-2180
FAX: 404/727-6586
EMail: morokuma@emory.edu

ROBERT MORRISON
East Carolina University
Department of Chemistry
Greenville, NC 27858
Phone: 919/328-6238
FAX: 919/328-6210
EMail: chmorrison@ecuvms.cis.ecu.edu

CHRIS MOSER
University of Pennsylvania
B501 Richards Building
Philadelphia, PA 19104
Phone: 215/898-0816
FAX: 215/573-2235
EMail: moserc@mail.med.upenn.edu

KEN MUSETH
H. C. Orsted Institute
Universitetsparken 5
Chemical Lab. 3
Copenhagen DK-2100
Denmark
Phone: 45-35320253
FAX: 45-35320259
EMail: kmu@moldyn.ki.ku.dk

MASATAKA NAGAOKA
Inst. for Fundamental Chem.
34-4 Takano Nishihiraki-cho
Sakyo-ku
Kyoto 606
Japan
Phone: 81-75-711-7708
FAX: 81-75-781-4757
EMail: nagaoka@power5.ifc.or.jp

BENGT NAGEL
Royal Inst. of Technology
Dept. of Theoretical Physics
Stockholm 10044
Sweden
Phone: 46-8-7907168
FAX: 46-8-104879
EMail: nagel@theophys.kth.se

MASAYOSKI NAKANO
Osaka University
Department of Chemistry
Machikaneyama 1-1
Osaka 560
Japan
Phone: 81-6-850-5404
FAX: 81-6-843-7744

MARSHALL NEWTON
Brookhaven National Lab.
P.O. Box 5000
Dept. of Chemistry
Upton, NY 11973
Phone: 516/282-4366
FAX: 516/282-5815
EMail: newton@quantum.chm.bnl.edu

LIST OF PARTICIPANTS

PETER AADAL NIELSEN
Odense University
Department of Chemistry
Campusvej 55
Odense M 5230
Denmark
Phone: 4566158600-2509
FAX: 4566158780
EMail: par@dou.dk

JOZEF NOGA
Institute Inorganic Chemistry
Slovak Academy of Sciences
Bratislava SK-84236
Slovakia
Phone: 42-7-375170
FAX: 42-7-373541
EMail: uachnoga@savba.sk

MARCEL NOOIJEN
Quantum Theory Project
University of Florida
343 Williamson Hall
P.O. Box 118435
Gainesville, FL 32611-8435
Phone: 352/392-1597
FAX: 352/392-8722
EMail: noojien@qtp.ufl.edu

PATRICK NORMAN
Linköping University
Computational Physics
Linköping 58183
Sweden
Phone: 46-13-281688
FAX: 46-13-137568
EMail: panor@ifm.liu.se

JAMES NORRIS
University of Chicago
Department of Chemistry
5735 S. Ellis Avenue
Chicago, IL 60637-1403
Phone: 312/702-7864
FAX: 312/702-0805
EMail: j-norris@uchicago.edu

TED O'BRIEN
Quantum Theory Project
University of Florida
CRB 201
Department of Chemistry
Gainesville, FL 32611
Phone: 352/392-9306
FAX: 352/392-8722
EMail: obrien@qtp.ufl.edu

CHRISTIAN OCHSENFELD
University of California at Berkeley
Department of Chemistry
Berkeley, CA 94720
Phone: 510/642-8265
FAX: 510/643-1255
EMail: chi@alcatraz.cchem.berkeley.ed

YNGVE OHRN
Quantum Theory Project
University of Florida
363 Williamson Hall
P.O. Box 118435
Gainesville, FL 32611-8435
Phone: 352/392-1597
FAX: 352/392-8722
EMail: ohrn@qtp.ufl.edu

ALEXANDER OKOTRUB
Inst. of Inorganic Chemistry
SB RAS
pr. Lavrnet'eva, 3
Novosibirsk 630090
Russia
Phone: 7-383-2-355243
FAX: 7-383-2-355960
EMail: spectrum@che.nsk.su

JUAN OREIRO
Quantum Theory Project
University of Florida
348 Williamson Hall
P.O. Box 118435
Gainesville, FL 32611-8435
Phone: 352/392-1597
FAX: 352/392-8722
EMail: oreiro@qtp.ufl.edu

VINCENT ORTIZ
University of New Mexico
Chemistry Department
Albuquerque, NM 87131-1096
Phone: 505/277-4313
FAX: 505/277-2609
EMail: ortiz@nestor.unm.edu

LIST OF PARTICIPANTS

VLADIMIR OSHEROV
Institute of Chemical Physics
Russian Academy of Sciences
Chernogolovka, Moscow 142 432
Russia
Phone: 7-96-517-1939
FAX: 7-96-515-3588
EMail: osherov@icph.scherna.msk.su

ROMAN OSMAN
Mt. Sinai School of Medicine
Dept. of Physiology & Biophysics
New York, NY 10029
Phone: 212/241-5609
FAX: 212/860-3369
EMail: osman@msvax.mssm.edu

NEIL S. OSTLUND
Hypercube, Inc.
2135 NW 15th Ave.
Gainesville, FL 32605
Phone: 352/378-9776
EMail: ostlund@hyper.com

LUIS PADILLA-CAMPOS
Universidad de Chile
Dept. de Chem.
Casilla 653
Las Palmeras 3425
Santiago
Chile
Phone: 56-2-6787272
FAX: 56-2-2713888
Email: at11@abello.dic.uchile.cl

JOSEPH M. PAIKEDAY
Southeast Missouri State University
Physics Department
One University Plaza
Cape Girardeau, MO 63701-4799
Phone: 314/651-2393
FAX: 314/651-2223
EMail: c314scp@semovm.semo.edu

GREG MARTIN PEARL
Quantum Theory Project
University of Florida
CRB 201
Department of Chemistry
Gainesville, FL 32611
Mars
Phone: 352/392-9306
FAX: 352/392-8722
EMail: pearl@qtp.ufl.edu

AJITH S. PERERA
Quantum Theory Project
University of Florida
343 Williamson Hall
P.O. Box 118435
Gainesville, FL 32611-8435
Phone: 352/392-1597
FAX: 352/392-8722
EMail: perera@qtp.ufl.edu

PATRICIA L. PEREZ
Universidad de Chile
Dept. de Quimica
Casilla 653
Santiago
Chile
Phone: 26-2-6787272
FAX: 56-2-2713888
EMail: rcontrer@abello.dic.uchile.cl

GEORGE PERKINS
Sun Microsystems
6200 Courtney Campbell Causeway
Suite 840
Tampa, FL 33607

WILLIS PERSON
University of Florida
Department of Chemistry
P.O. Box 117200
Gainesville, FL 32611-7200
Phone: 352/392-0528
FAX: 352/392-0872
EMail: person@pine.circa.ufl.edu

RUSSELL PITZER
Ohio State University
120 W. 18th Avenue
Dept. of Chemistry
Columbus, OH 43210
Phone: 614/292-7063
FAX: 614/292-1685
EMail: pitzer.3@osu.edu

EMIL POP
Pharmos Corporation
2 Innovation Drive
Alachua, FL 32615
Phone: 904/462-1210
FAX: 904/462-5401

LIST OF PARTICIPANTS

JOHN POPLÉ
Northwestern University
Chemistry Department
2145 Sheridan Road
Evanston, IL 60208-3113
Phone: 847/491-3403
FAX: 847/491-7713
EMail: pople@lithium.chem.nwu.edu

ENRIQUE POULAIN
Universidad Autonoma de Mexico
Tlalnepantla-Edo
Mexico
FAX: 52 5 517 24 82
EMail: sca@hp9000a1.uam.mx

SATYAM PRIYADARSHY
University of Pittsburgh
Department of Chemistry
219 Parkman Avenue
Pittsburgh, PA 15260
Phone: 412/624-8200
FAX: 412/624-8552
EMail: satyam@vms.cis.pitt.edu

MICHAEL PROBST
Innsbruck University
Dept. of Inorganic Chemistry
Innrain 520
Innsbruck A-6020
Austria
Phone: 43-512-5075153
FAX: 43-512-5072934
EMail: michael.probst@uibk.ac.at

MICHAEL RAMEK
Technische Universitat Graz
Inst. fur Phys. und Theoret. Chem.
Graz A-8010
Austria
Phone: 43-316-873-8227
FAX: 43-316-873-7699
EMail: ramek & ftug.dnet.tu-graz.ac.at

JUAN CARLOS RAMIREZ
Univ. Autonoma Metropolitana-Iztapalapa
Dept. de Quimica
AP 55-534
Mexico D.F. 09340
Mexico
Phone: 525/724-4675
FAX: 525/724-4666

MILAN RANDIC
Drake University
Dept. of Math & Computer Sci.
Des Moines, IA 50311
Phone: 515/271-2163
FAX: 515/217-3977

MARK RATNER
Northwestern University
Chemistry Department
2145 Sheridan Rd.
Evanston, IL 60208-3113
Phone: 708/491-5371
FAX: 708/491-7713
EMail: ratner@mercury.chem.nwu.edu

WILLIAM P. REINHARDT
University of Washington
Chemistry Department
P.O. Box 351700
Seattle, WA 98195
Phone: 206/543-0578
EMail: rein@chem.washington.edu

PETER REYNOLDS
Office of Naval Research
Physics Division, Code 1113
800 North Quincy Street
Arlington, VA 22217-5000

WILLIAM RHODES
Florida State University
Department of Chemistry
Tallahassee, FL 32306-3006
Phone: 904/644-1227
FAX: 904/644-8281
EMail: rhodes@chem.fsu.edu

JULIA E. RICE
IBM Almaden Research Center
K43B/D2
650 Harry Road
San Jose, CA 95120-2100
Phone: 408/927-2516
FAX: 408/927-2100
EMail: julia@almaden.ibm.com

NIGEL G. J. RICHARDS
University of Florida
Department of Chemistry
428 Leigh Hall
P.O. Box 117200
Gainesville, FL 32611
Phone: 352/392-3601
FAX: 352/392-8758
EMail: richards@qtp.ufl.edu

LIST OF PARTICIPANTS

LUIS RINCON
 Universidad de Los Andes
 Facultad de Ciencias
 Chemistry Department
 Merida 5101
 Venezuela
 Phone: 58-074-401344
 FAX: 58-074-401286
 EMail: lrincon@ciens.ula.ve

JESUS RODRIGUEZ
 IVIC Centro de Quimica
 Carretera Panamericana, Km11
 Apartado Postal 21827
 Caracas 1020A
 Venezuela
 Phone: 58-2-501-1335
 FAX: 58-2-501-1350
 EMail: jrodriguez@quimica.ivic.ve

INGE ROEGGEN
 University of Tromso
 Inst. Math. Phys. Sciences
 Tromso 9037
 Norway
 Phone: 47-77-644025
 FAX: 47-77-644765
 EMail: inge@mach.uit.no

FELIX ROSILLO
 Universidad del Zulia
 Centro de Quimica, IVIC
 Apartado Postal 21827
 Caracas 1020A
 Venezuela
 Phone: 58-2-501-1335
 FAX: 58-2-5011350
 EMail: frosillo@quimica.ivic.ve

PIOTR B. ROZYCZKO
 Quantum Theory Project
 University of Florida
 345 Williamson Hall
 P.O. Box 118435
 Gainesville, FL 32611-8435
 Phone: 352/392-1597
 FAX: 352/392-8722
 EMail: rozyczko@qtp.ufl.edu

FERNANDO RUETTE
 IVIC Centro de Quimica
 Apartado Postal 21827
 Caracas
 Venezuela
 Phone: 58-2-5011354
 FAX: 58-2-5011350
 EMail: fruette@quimica.ivic.ve

KEITH RUNGE
 Quantum Theory Project
 University of Florida
 P.O. Box 118435
 376 Williamson Hall
 Gainesville, FL 32611-8435
 Phone: 352/392-1597
 FAX: 352/392-8722
 EMail: runge@qtp.ufl.edu

NINO RUSSO
 Universita Della Calabria
 Dipartimento di Chimica
 I-87030 Arcavacata di Rende
 Italy
 Phone: 984-492105
 FAX: 984-492044
 EMail: russo@fis.unical.it

JOHN R. SABIN
 Quantum Theory Project
 University of Florida
 355 Williamson Hall
 P.O. Box 118435
 Gainesville, FL 32611-8435
 Phone: 352/392-1597
 FAX: 352/392-8722
 EMail: sabin@qtp.ufl.edu

RAYMOND SADEGHI
 Quantum Theory Project
 University of Florida
 379 Williamson Hall
 P.O. Box 118435
 Gainesville, FL 32611-8435
 Phone: 352/392-1597
 FAX: 352/392-8722
 EMail: rsadeghi@qtp.ufl.edu

ASIYA YU. SADYKOVA
 Kazan State Tech. University
 Dept. of Technology
 K. Marx 68
 Kazan 420015
 Tatarstan
 Phone: 8432-76-05-13
 EMail: sadykova@univex.kazan.su

LIST OF PARTICIPANTS

MICHAEL SALAZAR
University of Utah
Department of Chemistry
Salt Lake City, UT 84112-1194
Phone: 801/581-7445
FAX: 801/581-1194
EMail: salazar@chemistry.utah.edu

RUGGERO M. SANTILLI
Inst. per la Ricerca di Base
US Division, Box 1577
Palm Harbor, FL 34682
Phone: 813/934-9593
FAX: 813/934-9275
EMail: ibrrms@pinet.aip.org

JOACHIM SAUER
Humboldt Universitat an der
Max-Planck-Gesellschaft
Jagerstr. 10/11
Berlin 10117
Germany
Phone: 49-30-20192-300
FAX: 49-30-20192-302
EMail: js@qc.ag-berlin.mpg.de

HAROLD SCHERAGA
Cornell University
Baker Lab. of Chemistry
Ithaca, NY 14853-1307
Phone: 607/255-4034
FAX: 607/254-4900
EMail: has5@cornell.edu

MICHAEL SCHMIDT
Iowa State University
Department of Chemistry
Ames, IA 50011-3111
Phone: 515/294-9796
EMail: mike@si.fi.ameslab.gov

PETER SCHMIDT
Office of Naval Research
Chemistry Division, Code 1113
800 North Quincy Street
Bolling AFB, DC 20332-6448

VERN SCHRAMM
College of Medicine Albert Einstein
Department of Biochemistry
1300 Morris Park Avenue
The Bronx, NY 10461
Phone: 718/430-2813
FAX: 718/892-0703
EMail: vern@aecom.yu.edu

LECH SCHULZ
Institute of Physics and Theoretical Chemistry
I-30, Wyb.
Wypianskiego 27
Wroclaw 50-370
Poland
Phone: 48-71-203520
FAX: 48-61-658701
EMail: lsch@plpuam11.amu.edu.pl

ERIC SCHWEGLER
University of Minnesota
Department of Chemistry
207 Pleasant St. SE
Minneapolis, MN 55455
Phone: 612/626-0763
FAX: 612/624-8861
EMail: schwegle@chemsun.chem.umn.edu

HIDEO SEKINO
Quantum Theory Project
University of Florida
362 Williamson Hall
P.O. Box 118435
Gainesville, FL 32611-8435
Phone: 352/392-1597
FAX: 352/392-8722
EMail: sekino@qtp.ufl.edu

ALEX SEMENYAKA
Quantum Theory Project
University of Florida
343 Williamson Hall
P.O. Box 118435
Gainesville, FL 32611-8435
Phone: 352/392-1597
FAX: 352/392-8722
EMail: semenyaka@qtp.ufl.edu

JORGE M. SEMINARIO
University of New Orleans
Department of Chemistry
New Orleans, LA 70148
Phone: 504/286-7216
FAX: 504/286-6860
EMail: jsmcm@uno.edu

CATHER SIMPSON
Quantum Theory Project
University of Florida
362 Williamson Hall
Gainesville, FL 32611
Phone: 352-392-1597
FAX: 352-392-8722

LIST OF PARTICIPANTS

OKTAY SINANOGLU
Yale University
SCL
P.O. Box 6666
New Haven, CT 06511
Phone: 203/432-3957
FAX: 203/432-6144
EMail: osinano@minerva.cis.yale.edu

G. M. SIPAHI
Universidade de Sao Paulo
C.P. 66318
Inst. de Fisica
Sao Paulo, SP 05389-970
Brazil
Phone: 55-11-8187098
FAX: 55-11-8186984
EMail: gmsipahi@if.usp.br

YVES G. SMEYERS
C.S.I.C.
Dept. Quim. y Fis. Teoricas
Inst de Estruc de la materia
Madrid 28006
Spain
Phone: 34-1-5855404
FAX: 34-1-5642431
EMail: emsmeyers@roca.csic.es

ANDERS SNIS
Goteborg University
Inorganic Chemistry
Goteborg 41296
Sweden
Phone: 46-31-7722861
FAX: 46-31-7722853
EMail: snis@inoc.chalmers.se

THOMAS SOMMERFELD
Universitat Heidelberg
Physikalisch-Chemischen Inst.
INF 253, Theoret. Chemie
Heidelberg 69120
Germany
Phone: 49-6221-565209
Fax: 49-6221-565221
EMail: thomas@tc.pci.uni-heidelberg.de

RAMON M. SOSA
Institute of Physics
Avda. J. Herrera y Reissig 565
Fac. of Engineering
Montevideo 11300
Uruguay
Phone: 5982-710905
FAX: 5982-711630
EMail: rsosa@fing.edu.ug

HUMBERTO SOSCUN
Universidad de Zulia
Dept. de Quimica
AP 526, Grano de Oro
Maracaibo
Venezuela
Phone: 58-61-519795
FAX: 58-61-529432
EMail: humberto@solidos.ciens.luz.be

RICHARD H. SQUIRE
Marshall University
Department of Chemistry
901 W. DuPont Avenue
Belle, WV 25015
Phone: 304/357-1292
FAX: 304/357-1230

JOHN STANTON
University of Texas at Austin
Department of Chemistry
Welch Hall
Austin, TX 78712
Phone: 512/471-5903
EMail: stanton@jfs1.cm.utexas.edu

KRASSIMIR K. STAVREV
Quantum Theory Project
University of Florida
380 Williamson Hall
P.O. Box 118435
Gainesville, FL 32611-8435
Phone: 352/392-1597
FAX: 352/392-8722
EMail: stavrev@qtp.ufl.edu

JAMES STEWART
Stewart Computational Chemistry
15210 Paddington Circle
Colorado Springs, CO 80921-2512
Phone: 719/488-9416
EMail: jstewart@fai.com

LIST OF PARTICIPANTS

HAMISH STRUTHERS
University of Canterbury
Dept. of Chemistry
Private Bag 4800
Christchurch
New Zealand
Phone: 0064-3-3667-001
FAX: 0064-3-3642-110
EMail: chem171@csc.canterbury.ac.nz

NEIL SULLIVAN
University of Florida
Department of Physics
P.O. Box 118440
Gainesville, FL 32611
Phone: 904/392-0521
EMail: neil@phys.ufl.edu

JUN-QIANG SUN
Quantum Theory Project
University of Florida
386 Williamson Hall
P.O. Box 118435
Gainesville, FL 32611-8435
Phone: 352/392-1597
FAX: 352/392-8722
EMail: sun@qtp.ufl.edu

PETER G. SZALAY
Eotvos Loran University
P.O. Box 32
Dept. of Theor. Chem.
Budapest H-1518
Hungary
Phone: 36-1-209-0555
FAX: 36-1-209-0602
EMail: szalay@theo.elte.hu

KRYSTYNA SZCZEPANIAK
University of Florida
Department of Chemistry
Gainesville, FL 32611
Phone: 352/392-4653
EMail: ksperson@pine.circa.ufl.edu

EDUARDO K. TAKAHASHI
Univ. Federal de Uberlandia
Dept. de Ciencias Fisicas
Campus Santa Monica
Uberlandia, Minas Gerais 38400-089
Brazil
Phone: 034-2394222
FAX: 034-2360466
EMail: decifo6@crufu.bitnet

TOOMAS TAMM
Quantum Theory Project
University of Florida
378 Williamson Hall
P.O. Box 118435
Gainesville, FL 32611-8435
Phone: 352/392-1597
FAX: 352/392-8722
EMail: tamm@qtp.ufl.edu

MINARU TEI
Okayama University of Science
Electronic Engineering
1-1 Ridai-cho
Okayama 700
Japan
Phone: 086-252-3161
FAX: 086-255-3611
EMail: minaru@ee.ous.ac.jp

SHICHIRO TEN-NO
Inst. for Molecular Science
Myodaiji
Okazaki 444
Japan
Phone: 81-564-55-7260
FAX: 81-564-53-4660
EMail: tenno@ims.ac.jp

STEVEN THOMPSON
U.S. Air Force Academy
HQ, Department of Chemistry
2354 Fairchild Dr, Ste 2A21
USAF Academy, CO 80840-6230
Phone: 719/472-2601
FAX: 719/472-2947
EMail: thompsonsdfc%usafa
@dfbmail.usaffa.af.mil

SAMUEL B. TRICKEY
Quantum Theory Project
University of Florida
364 Williamson Hall
P.O. Box 118435
Gainesville, FL 32611-8435
Phone: 352/392-1597
FAX: 352/392-8722
EMail: trickey@qtp.ufl.edu

THANH N. TRUONG
University of Utah
Department of Chemistry
Salt Lake City, UT 84112
Phone: 801/581-4301
FAX: 801/581-8433
EMail: truong@chemistry.chem.utah.edu

LIST OF PARTICIPANTS

ILIA TUPITSYN
St. Petersburg University
Physics Institute
198 904 Stary Petershoff
St. Petersburg 198 904
Russia
Phone: 7-812-533-1526
FAX: 7-812-218-13-46
EMail: tup@niit.spb.su

PIET, TH. VAN DUIJNEN
University of Groningen
Chemistry Department
Nyenborgh 4
Groningen AG 9747
The Netherlands
Phone: 31-503634373
FAX: 31-503634296
EMail: ptvd@chem.rug.ne

RUBICELIA VARGAS
Univ. Auto. Metropolitana-Iztapalapa
Dept. de Quimica
Michoacan y Purisima s/n
Mexico, D.F. 09340
Mexico
Phone: 525-7-244675
FAX: 525-7-244666
EMail: jgo@xanum.uam.mx

AUREA VASCONCELLOS
Instituto de Fisica UNICAMP
CP 6165
Campinas, Sao Paulo 13083-970
Brazil
FAX: 55-192-393137

DAN VASILESCU
Laboratoire de Biophysique
Faculte des Sciences
Parc Valrose
Nice Cedex 06108
France
Phone: 33-93-52-98-51
FAX: 33-93-52-98-51
EMail: vasilescu@naxos.unice.fr

ALBERTO VELA
UAM-Iztapalapa
Av. Michoacan y Purisima s/n
Col. Vicenta, Dept. de Quimica
Mexico, CF C.P. 09340
Mexico
Phone: 525-724-4675
FAX: 525-724-4666
EMail: ava@xamvm.uam.mx

GREGORY A. VOTH
University of Pennsylvania
Department of Chemistry
231 S. 34th Street
Philadelphia, PA 19104-6323
Phone: 215/898-3048
FAX: 215/573-2112
EMail: voth@a.chem.upenn.edu

JOHN WATTS
Quantum Theory Project
University of Florida
P.O. Box 118435
367 Williamson Hall
Gainesville, FL 32611-8435
Phone: 352/392-1597
FAX: 352/392-8722
EMail: watts@qtp.ufl.edu

CHARLES WEATHERFORD
Florida A & M
Physics Dept.
Room 205 Jones Hall
Tallahassee, FL 32307

BRIAN WEINER
Penn State University
Department of Physics
College Place
DuBois, PA 15801
Phone: 814/375-4700
FAX: 814/234-4291
EMail: bqw@psu.edu

HAREL WEINSTEIN
Mt. Sinai School of Medicine
Physiology & Biophysics Dept.
One Gustave L. Levy Place
New York, NY 10029-6574
Phone: 212/241-7018
FAX: 212/860-3369
EMail: hweinstein@msvax.mssm.edu

WOLFGANG WENZEL
Dortmund University
Theoretical Physics I
Otto-Hahn-Str. 4
Dortmund 44221
Germany
Phone: 49-231-755-3551
FAX: 49-231-755-3569
EMail: wenzel@cip.physik.uni-dortmund.de

LIST OF PARTICIPANTS

BIRGITTA K. WHALEY
University of California at Berkeley
Department of Chemistry
Berkeley, CA 94720-1460
Phone: 501/643-6820
FAX: 501/643-6232
EMail: whaley@holmium.cchem.berkeley.edu

ROBERT L. WHETTEN
Georgia Inst. of Technology
Department of Physics
Atlanta, GA 30332-0430
Phone: 404/894-5201
FAX: 404/894-9958
EMail: ph289rw@prism.gatech.edu

HAYES L. WILLIAMS
Army Research Laboratory
Weapons Tech. Direct.
AMSRL-WT-PC
Aberdeen Proving Ground, MD 21005-5066
Phone: 410/278-6182
FAX: 410/278-6150
EMail: williams@arl.mil

ANGELA K. WILSON
Pacific Northwest National Lab.
K1-83, P.O. Box 999
Richland, WA 99352
Phone: 509/372-4937
FAX: 509/375-6631
EMail: ak_wilson@pnl.gov

PETER WINKLER
University of Nevada
Department of Physics/220
Reno, NV 89557-0058
Phone: 702/784-6792
FAX: 702/784-1398
EMail: winkler@rigel.physics.unr.edu

THOMAS G. WINTER
Pennsylvania State University
Department of Physics
Wilkes-Barre Campus
Lehman, PA 18627
Phone: 717/675-9221
FAX: 717/675-8308
EMail: txw2@psuadmin.psu.edu

JOSEPH WORTH
AT&T Bell Labs.
MS 4C537
101 Crawfords Corner Rd.
Holmdel, NJ 07733-3030
Phone: 908/949-3642
FAX: 908/949-3697
EMail: worth@research.att.com

SATOSHI YABUSHITA
Keio University
Department of Chemistry
3-14-1, Hiyoshi, Kohoku-ku
Yokohama 223
Japan

KIZASHI YAMAGUCHI
Osaka University
Department of Chemistry
Machikaneyama 1-1
Osaka 560
Japan
Phone: 81-6-850-5404
FAX: 81-6-843-7744
EMail: yama@chem.sci.osaka-u.ac.jp

JI-MIN YAN
Institute of Chemistry
Academia Sinica
Beijing 100080
P.R. China
FAX: 8610-2569564
EMail: huangsl@rose.cnc.ac.cn

ZHIGANG YI
Quantum Theory Project
University of Florida
348 Williamson Hall
P.O. Box 118435
Gainesville, FL 32611-8435
Phone: 352/392-1597
FAX: 352/392-8722
EMail: yi@qtp.ufl.edu

MICHAEL C. ZERNER
Quantum Theory Project
University of Florida
382 Williamson Hall
P.O. Box 118435
Gainesville, FL 32611-8435
Phone: 352/392-1597
FAX: 352/392-8722
EMail: zerner@qtp.ufl.edu

LIST OF PARTICIPANTS

XUEHE ZHENG
Quantum Theory Project
University of Florida
CRB 201
Department of Chemistry
Gainesville, FL 32611
Phone: 352/392-9306
FAX: 352/392-8722
EMail: zheng@qtp.ufl.edu

PAUL ZIESCHE
Max Planck Institute for Physics of Complex
Systems
Bayreuther Str. 40, Haus 16
Dresden D-01187
Germany
Phone: 49-351-4636203
FAX: 49-351-4637279
EMail: pz@idefix.mpipks-dresden.mpg.de

R. W. J. ZIJLSTRA
University of Groningen
Nijenborgh 4
Organic Chemistry
Groningen, AG 9747
The Netherlands
Phone: 0-50-3634258
FAX: 0-50-3634296
EMail: zijlstra@chem.rug.nl

YURI L. ZUB
University of Kiev-Mohyla
Dept. of Chemistry and Geology
2, Skovoroda Str.
Kiev 254070
Ukraine
Phone: 7-044-416-12-46
FAX: 7-044-415-50-16
EMail: vicerec@kma.courier.kiev.ua

Introduction

The 36th annual Sanibel Symposium, organized by the faculty, students, and staff of the Quantum Theory Project of the University of Florida, was held on February 24–March 2, 1996. The meeting was again held at the Ponce de Leon Conference Center in St. Augustine, Florida. About 320 participants gathered for eight days of lectures and informal discussions.

The format of the symposium adopted for the past few years was followed again this year with a compact eight-day schedule with an integrated program of quantum biology, quantum chemistry, and condensed matter physics. The topics of the sessions covered by these proceedings included Developmental Tools and Methodologies for Computational Chemical Physics, Density Functional Theory and Applications, Quantum-Classical Dynamics for Extended Systems, Simulations of Nanocrystals, Clusters and Molecules, Novel Method in Electronic Structure Theory, Potential Energy Surfaces for Excited States, Industrial Applications of Quantum Chemistry, Time-Dependent Dynamics for Many-Electron Systems, Methods for Big Molecules, Molecular Self-Assembly and Design, and Medium Effects on Embedded Molecules.

The articles have been subjected to the ordinary refereeing procedures of the *International Journal of Quantum Chemistry*. The articles presented in the sessions on quantum biology and associated poster sessions are published in a separate volume of the *International Journal of Quantum Chemistry*.

The organizers acknowledge the following sponsors for their support of the 1996 Sanibel Symposium:

- U.S. Army Research Office and U.S. Army

Edgewood RD & E Center through Grant No. DAAH04-96-1-PHCF. (The views, opinions, and/or findings contained in this report are those of the author(s) and should not be construed as an official Department of the Army position, policy, or decision, unless so designated by other documentation.)

- The Office of Naval Research through Grant No. N00014-96-1-0197. (This work relates to Department of Navy Grant No. N00014-96-1-0197 issued by the Office of Naval Research. The United States Government has a royalty-free license throughout the world in all copyrightable material contained herein.)
- IBM Corporation
- HyperCube, Inc.
- Sun Microsystems Computer Corporation
- The University of Florida

Very special thanks go to the staff of the Quantum Theory Project of the University of Florida for handling the numerous administrative, clerical, and practical details. The organizers are proud to recognize the contributions of Mrs. Judy Parker, Ms. Leann Golemo, Ms. Sandra Weakland, and Mr. Sullivan Beck. All the graduate students of the Quantum Theory Project who served as "gofers" are gratefully recognized for their contributions to the 1996 Sanibel Symposium.

N. Y. ÖHRN
J. R. SABIN
M. C. ZERNER

The Chairman's Introductory Remark

JEAN-LOUIS CALAIS

1932–1995

Before introducing our speakers, let me remind you of one of the Sanibel Pioneers, Jean-Louis Calais of Uppsala University. He died suddenly in Uppsala on May 30, 1995 at the age of 62, while still approaching the highest peaks of his scientific career.

When the first Sanibel Symposium took place at Sanibel Island, Jean-Louis was a very young scientist, but he played a major role in organizing that symposium. Jean-Louis was one of Per-Olov Löwdin's first graduate students and coworkers and thus one of the founding members of the Uppsala Quantum Chemistry Group and the Quantum Theory Project (QTP) at the University of Florida, where he became an adjunct professor.

Jean-Louis made fundamental contributions to the methods of quantum chemistry, to solid-state and polymer physics and chemistry, electron nuclear dynamics in the hydrogen molecule and extended systems, and much more.

Jean-Louis' students and coworkers came from all over the world. For many years he was instrumental in organizing and lecturing at the International Summer School in Quantum Chemistry held in Scandinavia and the corresponding Winter Institutes at Gainesville, and he was the Uppsala editor of the *International Journal of Quantum Chemistry*.

Jean-Louis was a Scholar in the true sense of the word. During the last few years, I had the privilege to witness his success in establishing—or rather reestablishing—human and scientific contacts with colleagues and students in the Baltic Countries, especially at the University of Tartu. It was no surprise that he succeeded so well. He was almost an expert in Baltic history and culture, and had started to learn the languages. Above all, he was almost unique in generosity, kindness, and friendship.

GÖRAN BERGSON

Partial Waves in the Nonspherical Case

T. LEVITINA* AND E. J. BRÄNDAS

Quantum Chemistry Group for Research in Atomic, Molecular and Solid State Physics, Uppsala University, Box 518, S-751 20 Uppsala, Sweden

Received February 28, 1996; revised manuscript received April 2, 1996; accepted May 8, 1996

ABSTRACT

Many quantum mechanical problems are separable in one or several of the standard classifications of general coordinate systems. The associated solution is most conveniently evaluated using expansions in Lamé wave functions. We give here some preliminary numerical results displaying the continuous distortion of an *s*-, *p*-, and *d*-wave spherical harmonic. The results indicate rather surprising features which may be useful in general quantum mechanical contexts. © 1996 John Wiley & Sons, Inc.

Introduction

When separating the variables in terms of ellipsoidal coordinates, particular solutions of the Helmholtz equation are formed as products of the so-called angle and radial ellipsoidal (or Lamé) wave functions. For comparison, in the case of a sphere, the angle functions are the Legendre polynomials and the associated functions, while the radial ones are the Bessel and Hankel functions.

Consider the ellipsoidal coordinate system given by $x^2/(a^2 + \eta) + y^2/(b^2 + \eta) + z^2/(c^2 + \eta) = 1$, where the basical ellipsoid has the semiaxes $a >$

$b > c$. Going over to dimensionless variables $\xi = (\eta + a^2)/(a^2 - b^2)$, one writes

$$\frac{x^2}{(a^2 - b^2)\xi} + \frac{y^2}{(a^2 - b^2)(\xi - 1)} + \frac{z^2}{(a^2 - b^2)(\xi - \rho^2)} = 1.$$

Here, we have set $\rho^2 = (a^2 - c^2)/(a^2 - b^2)$, i.e., $\rho^2 > 1$. This equation for each point (x, y, z) , $xyz \neq 0$, has exactly three different roots: $\xi_1 \in I_1 = (0; 1)$, $\xi_2 \in I_2 = (1; \rho^2)$, and $\xi_3 \in I_3 = (\rho^2; \infty)$. If $\xi = \xi_1$, the surface defined above is an ellipsoid; for $\xi = \xi_2$, it is a hyperboloid of one sheet; and for $\xi = \xi_3$, it is a hyperboloid of two sheets.

The above three families of confocal surfaces form an orthogonal curvilinear coordinate sys-

*Permanent address: Department of Numerical Methods, Computing Center of Russian Academy of Sciences, Vavilova str. 40, 117967 Moscow GSP-1, Russia.

tem related to Cartesian coordinates within each octant (e.g., $x \geq 0$, $y \geq 0$, $z \geq 0$) by one-to-one correspondence:

$$\begin{aligned}x^2 &= (a^2 - b^2)\xi_1\xi_2\xi_3/\rho^2, \\y^2 &= -(a^2 - b^2)(\xi_1 - 1)(\xi_2 - 1)(\xi_3 - 1)/ \\&\quad (\rho^2 - 1), \\z^2 &= (a^2 - b^2)(\xi_1 - \rho^2)(\xi_2 - \rho^2)(\xi_3 - \rho^2)/ \\&\quad [(\rho^2 - 1)\rho^2]. \quad (1)\end{aligned}$$

One can find the detailed consideration of the variables separation in ellipsoidal coordinates in, e.g., [1, 2].

As a result, we obtain a system of three equations known as the Lamé wave equations:

$$\begin{aligned}\sqrt{f(\xi_1)} \frac{d}{d\xi_1} \left\{ \sqrt{f(\xi_1)} \frac{d\Lambda_1}{d\xi_1} \right\} \\+ \frac{1}{4}q(\xi_1, h, l, \omega)\Lambda_1 = 0, \quad \xi_1 \in I_1, \quad (2.a)\end{aligned}$$

$$\begin{aligned}\sqrt{-f(\xi_2)} \frac{d}{d\xi_2} \left\{ \sqrt{-f(\xi_2)} \frac{d\Lambda_2}{d\xi_2} \right\} \\- \frac{1}{4}q(\xi_2, h, l, \omega)\Lambda_2 = 0, \quad \xi_2 \in I_2, \quad (2.b)\end{aligned}$$

$$\begin{aligned}\sqrt{f(\xi_3)} \frac{d}{d\xi_3} \left\{ \sqrt{f(\xi_3)} \frac{d\Lambda_3}{d\xi_3} \right\} \\+ \frac{1}{4}q(\xi_3, h, l, \omega)\Lambda_3 = 0, \quad \xi_3 \in I_3, \quad (2.c)\end{aligned}$$

where h and l are the separation constants, $f(\xi) = \xi(\xi - 1)(\xi - \rho^2)$, $q(\xi, h, l, \omega) = h\rho^2 - l\rho^2\xi + \omega^2\xi^2$, and $\omega^2 = \hat{k}^2(a^2 - b^2)$, \hat{k} standing for the wave number. Hereafter, we consider the first two equations, i.e., those determining the angular part of a particular solution to the Helmholtz equation.

Results and Discussion

Owing to the symmetry of the problem, a particular solution must be either odd or even with respect to each coordinate plane. Since coordinate planes correspond to the ends of the intervals of

ellipsoidal coordinate variations, we have

$$\begin{aligned}\lim_{\xi_1 \rightarrow +0} \Lambda_1(\xi_1) = 0 \text{ or } \lim_{\xi_1 \rightarrow +0} \left(\sqrt{f(\xi_1)} \Lambda_1'(\xi_1) \right) = 0, \\ \lim_{\xi_1 \rightarrow 1-0} \Lambda_1(\xi_1) = 0 \text{ or } \lim_{\xi_1 \rightarrow 1-0} \left(\sqrt{f(\xi_1)} \Lambda_1'(\xi_1) \right) = 0, \\ \lim_{\xi_2 \rightarrow 1+0} \Lambda_2(\xi_2) = 0 \text{ or } \\ \lim_{\xi_2 \rightarrow 1+0} \left(\sqrt{-f(\xi_2)} \Lambda_2'(\xi_2) \right) = 0, \\ \lim_{\xi_2 \rightarrow \rho^2-0} \Lambda_2(\xi_2) = 0 \text{ or } \\ \lim_{\xi_2 \rightarrow \rho^2-0} \left(\sqrt{-f(\xi_2)} \Lambda_2'(\xi_2) \right) = 0, \quad (3)\end{aligned}$$

besides the boundary conditions for $\xi_1 \rightarrow 1 - 0$ and for $\xi_2 \rightarrow 1 + 0$, which must be identical.

No reliable methods for the evaluation of ellipsoidal wave functions existed until [3, 4] appeared and, therefore, the application of these functions had been delayed. This is because the angle Lamé wave functions compose the eigenfunctions of a two-parameter self-adjoint Sturm-Liouville problem (see, e.g., [5]), i.e., on separating variables, we arrive at a couple of ODEs (2.a, b), each depending on its own argument and being subject to its own boundary conditions. The equations are linked together only by a couple of separation constants, which enter each equation. One must, hence, find such a couple of values for the separation constants such that both equations have nontrivial solutions satisfying the corresponding boundary conditions. The eigenvalue of the problem is such a couple of values, and the product of the corresponding solutions to the system gives its eigenfunction.

One can find a detailed analytical investigation of the Lamé wave functions in [6] and the articles cited therein. The Lamé wave functions depend continuously on the parameters ρ and ω , and in the case $\omega = 0$, they coincide with the well-known Lamé polynomials (see [2]). Eigenfunctions associated with different eigenvalues are orthogonal with respect to the inner product:

$$(*, *) = \iint_{\Pi} \{ * \times * \} \sigma(\xi_1, \xi_2) d\xi_1 d\xi_2,$$

where $\Pi = I_1 \times I_2$, $\sigma(\xi_1, \xi_2) = (\xi_2 - \xi_1) [-f(\xi_1)f(\xi_2)]^{-1/2}$.

The methods proposed in [3, 4] provide an efficient and economic way to calculate the Lamé wave functions at a rather wide range of param-

ter variations. This technique exploits a generalized Prüfer transformation, which has also been successfully used for solving various similar problems (see [7, 8]). The merit of the above technique can be illustrated from [9], where the solution of an acoustic wave-scattering problem by a general ellipsoid has been expanded in terms of the Lamé wave functions and multiple results of the calculations have been plotted. When expanding functions defined over a three-dimensional space, one faces the necessity to prolong the partial solutions expressed in Lamé wave functions to the whole space, since (1) defines the relations between ellipsoidal and Cartesian coordinates only within an octant. The prolongation of the partial solutions defined in one octant into the others has also been considered in [9].

Here, we present the examples of angular distribution densities which have been calculated as squared eigenfunctions of the above two-parameter Sturm–Liouville problem, normalized accord-

ing to the condition

$$\iint_{\Pi} [\Psi_n^m(\xi_1, \xi_2)]^2 \sigma(\xi_1, \xi_2) d\xi_1 d\xi_2 = 1/8$$

(here, we take into account the above comment that Π covers only a part of an ellipsoid enclosed in an octant). Each surface is plotted as a function of spherical angles θ and φ , where θ is counted off x , and the connection between the angle ellipsoidal coordinates and the spherical ones is given by

$$\begin{aligned}\xi_1 \xi_2 &= \rho^2 \cos^2 \theta, \\ (\xi_1 - 1)(\xi_2 - 1) &= -(\rho^2 - 1) \sin^2 \theta \cos^2 \varphi, \\ (\xi_1 - \rho^2)(\xi_2 - \rho^2) &= \rho^2(\rho^2 - 1) \sin^2 \theta \sin^2 \varphi\end{aligned}$$

(for more details, see [9]).

Given a set of boundary conditions (3) and an eigenvalue multi-index, i.e., a couple of integers

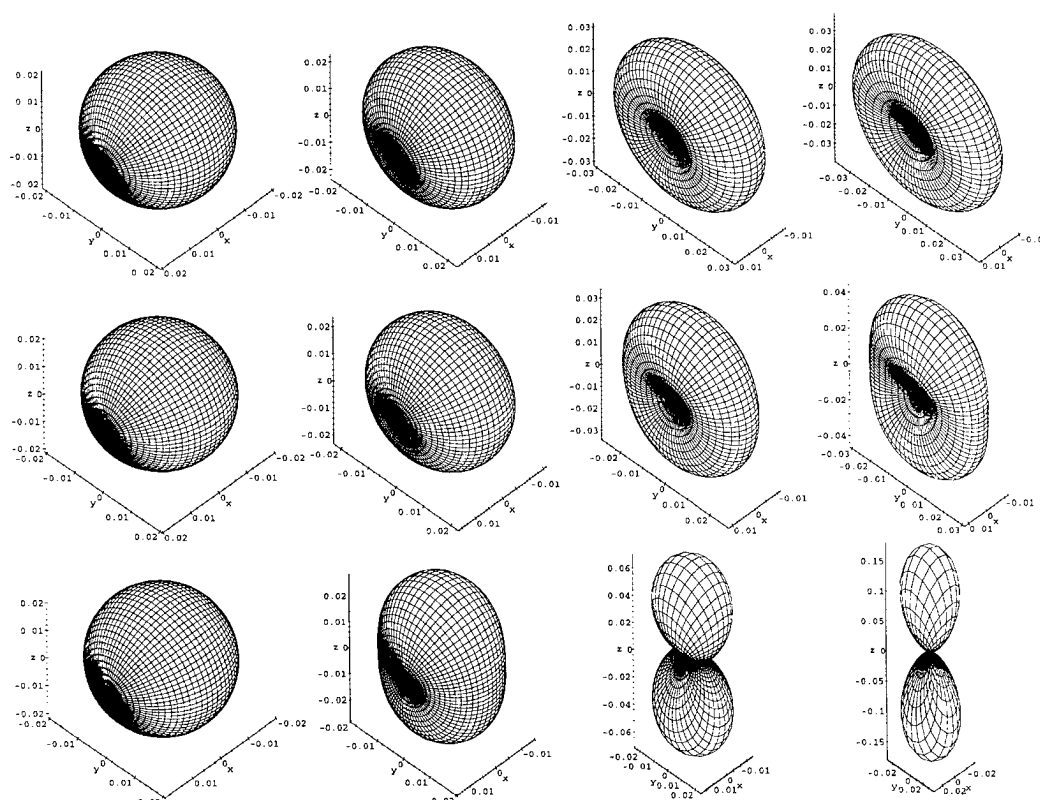


FIGURE 1. $\rho\omega$ -diagram for the s-like density. For more details, see text.

specifying the number of internal zeros of solutions to (2.a) and (2.b), the parameters ρ and ω uniquely determine the problem. Hence, we can vary the semiaxes of the basal ellipsoid and the wave number \hat{k} and obtain the same solution provided that the values of ρ and ω do not change.

In Figure 1, we give the $\rho\omega$ -diagram for the s-like state density, i.e., the dependence on the parameters ρ and ω . The value of ρ remains constant in each line ($\rho^2 = 1.01, 1.1$, and 2.0 , respectively), while the value of ω is constant in each column ($\omega^2 = 0.1, 1.0, 5.0, 10.0$). One can see that for small ω the shapes of partial angular distributions is almost independent of the geometry of the problem and the orbitals are close to the spherical case. In the case $\omega^2 = 0$, all the orbitals of the same type (i.e., both the same boundary condition set and the same multi-index) coincide regardless of the value of ρ . This fact can be easily proved for the basal state orbitals under all possible sets of boundary conditions (3); it also seems

to be true for all harmonics. Thus, the orbitals can be naturally classified according to the conventional classification in the spherical case, in spite of the fact that the higher the value of ω (or \hat{k}^2) the more is the difference among the shapes.

In Figure 2, one can see the changes in the p - and d -like orbitals, which appear as ω increases from left to right ($\omega^2 = 0.0, 5.0, 10.0, 20.0, 50.0$), with ρ remaining constant ($\rho^2 = 2.0$). The original shapes should be obvious to the reader.

In practice, much more complicated Lamé wave functions can be calculated; see, e.g., [3]. Here, we have only displayed the continuous distortion of some simple partial wave distributions, as viewed and comprehended via so-called $\rho\omega$ -diagrams. It is interesting to note, however, that the distortions occurring in Figures 1 and 2 can be obtained in several ways: For instance, a specific distributional shape in the $\rho\omega$ -diagram may be obtained for certain values of the semiaxes a , b , and c at given \hat{k}^2 . Alternatively, the same angular distribution

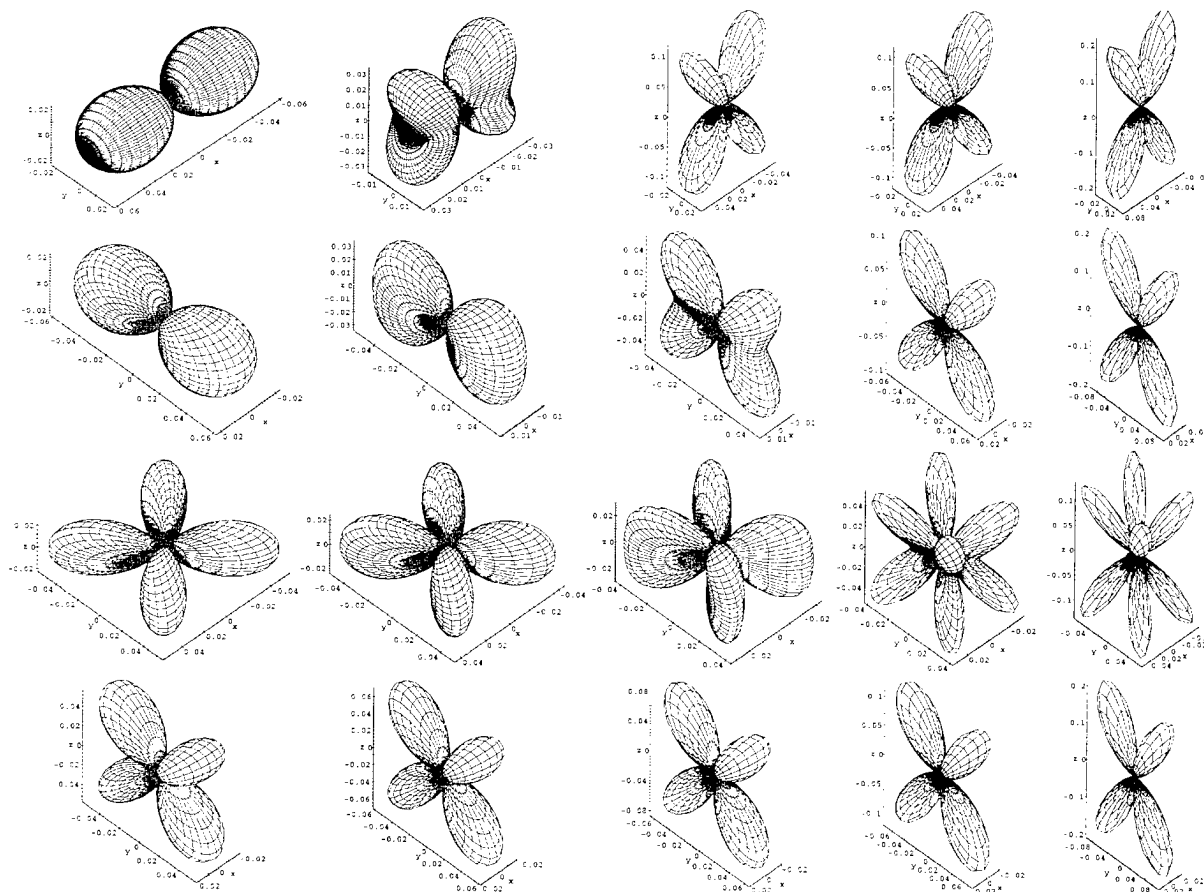


FIGURE 2. $\rho\omega$ -diagrams for the p - and d -like orbitals. Note that only ω changes here.

can also be maintained via different values of \hat{k}^2 if ρ and ω remain constant—a flexibility not given by standard choices of coordinate system. This result could be of potential interest, suggesting useful applications in a more general quantum chemical context.

ACKNOWLEDGMENTS

One of the authors (T. L.) is grateful for a support from the Russian Fond of Fundamental Research (Project 96-01-00951).

References

1. A. Erdelyi, W. Magnus, F. Oberhettinger, and F. G. Tricomi, *Higher Transcendental Functions*, Vol. 3 (McGraw-Hill, New York, Toronto, London, 1955).
2. R. T. Whittaker and G. N. Watson, *A Course of Modern Analysis* (Cambridge University Press, 1927).
3. A. A. Abramov, A. L. Dyshko, N. B. Konyukhova, and T. V. Levitina, *USSR Comput. Math. Math. Phys.* **29**(3), 119 (1989).
4. A. A. Abramov, A. L. Dyshko, N. B. Konyukhova, and T. V. Levitina, *USSR Comput. Math. Math. Phys.* **31**(2), 25 (1991).
5. B. D. Sleeman, *Multiparameter Spectral Theory in Hilbert Space* (Pitman, London, 1978).
6. M. V. Fedoryuk, *Uspekhi Matematicheskikh Nauk*, **44**(1), 123 (1989).
7. A. A. Abramov, A. L. Dyshko, N. B. Konyukhova, T. V. Pak, and B. S. Pariiskii, *USSR Comput. Math. Math. Phys.* **24**(1), 1 (1984).
8. D. I. Kitoroage, N. B. Konyukhova, and B. S. Pariiskii, *A Modified Phase Function Method for Problems Concerning Bound States of Particles*, *Soobshch. Prikl. Mat.* (Computer Center Academy of Science, USSR, Moscow, 1986) (in Russian).
9. A. A. Abramov, N. B. Konyukhova, and T. V. Levitina, in *1995 Design Engineering Technical Conferences* (ASME, 1995), DE-Vol. 84-2, 3-Part B, p. 437.

Path Integral Monte Carlo Method for Ab Initio Calculation

H. KAWABE*

Secretarial Department, Kinjo College, Matto City 924, Japan

H. NAGAO AND K. NISHIKAWA*

Department of Chemistry, Faculty of Science, Kanazawa University, Kanazawa 920-11, Japan

Received February 24, 1996; revised manuscript received June 20, 1996; accepted June 24, 1996

ABSTRACT

The Feynman path integral method is applied to the many-electron problem. We first give new closure relations in terms of ordinary complex and real numbers, which could be derived from an arbitrary complete set of state vectors. Then, in the path integral form, the partition function of the system and the ensemble average of energy are explicitly expressed in terms of these closure relations. It is impossible to evaluate the path integral by direct numerical integrations because of its huge amount of integration variables. Therefore, we develop an algorithm by the Monte Carlo method with constraints corresponding to the normalization condition of states to calculate the required integral. Finally, the ensemble average of energy for the hydrogen molecule is explicitly evaluated by the quantum Monte Carlo method and results are compared with the result obtained by the ordinary full configuration interaction (CI) method. © 1996 John Wiley & Sons, Inc.

Introduction

The path integral introduced by Feynman [1] has been applied to many problems in quantum mechanics. The quantization by the path integral is different from the usual canonical procedures, namely, the physical quantity can be handled as a commuting variable similar to a classical one. Thus the physical processes can be under-

stood more clearly than in ordinary quantum mechanics. On the other hand, almost all the studies of quantum chemistry have been done by dealing with the Schrödinger equation. The wave function of the many-electron system is usually written in terms of the Slater determinant composed of one-body functions, where the wave nature of electrons is in the orbital function and the Fermion character of electrons is represented by the anti-symmetric property of the determinant. When we apply the path integral method directly to the electron field described by the anticommuting field

* To whom correspondence should be addressed.

operator, we must deal with the corresponding anticommutable c-numbers, the Grassmann numbers. However, the properties of the Grassmann numbers are, in general, not so well known [2, 3], so that, in the field of quantum chemistry, the path integral method has not been widely applied to the many-electron problems for a long time.

Recently, the path integral method has been applied to the Hückel model [4] and the many-electron problems [5]. We have also developed the path integral method without using the Grassmann number to estimate the electron correlation in molecules [6]. In that work, we have derived the new closure relation in terms of the linear combination of atomic orbital (LCAO) coefficients of the molecular orbital and have constructed a path integral form of some physical quantities using the LCAO closure relation. In this treatment, there appears no Grassmann numbers corresponding to the electron field operator but the c-numbers corresponding to LCAO coefficients.

The essence of the path integral is a sum of histories, and the path integral is usually expressed as a multidimensional integral with a huge number of variables. Therefore, we cannot directly carry out this integration by ordinary ways and will be forced to use statistical methods, such as the Monte Carlo method. The ordinary quantum Monte Carlo method is a very powerful tool in order to estimate thermal and quantal fluctuations of interacting quantum spin systems and strongly correlated electron systems [7]. This method is based on the generalized Trotter formula, and the quantum fluctuation is expressed in the ordinary path integral form. Therefore, we can apply the Monte Carlo method to evaluate the path integral, though the path summation scheme needs a large amount of machine time even in high-speed computers.

In this study, we present the new closure relations which could be, in principle, derived from an arbitrary complete set of state vectors, and apply the closure relation to construct the partition function in the path integral form. Here, we use the closure relation corresponding to the multiconfigurational configuration interaction (CI) state and show that it is very useful in the path integral method in both theoretical treatments and practical calculations. To reduce a huge amount of integral variables, we introduce the static approximation and discuss the physical meaning of the approximation. To evaluate the required integral, we develop an algorithm by the Monte Carlo

method with the normalization condition of states. Finally, we apply this method to the hydrogen molecule, evaluate the ensemble average of the energy, and compare it with the result obtained by the ordinary full CI method.

Closure Relation

In the usual path integral method, a transition amplitude $\langle x_f, t_f | x_i, t_i \rangle$ is expressed by a summation of the action along all possible paths from $|x_i, t_i\rangle$ to $|x_f, t_f\rangle$. In the coordinate representation, all position eigenstates $|x\rangle$ can appear as intermediate states in the path from $|x_i, t_i\rangle$ to $|x_f, t_f\rangle$. Thus, the following closure relation is applied:

$$1 = \int d^3x |x\rangle \langle x|. \quad (1)$$

Even if we have a nonorthonormal but complete set, $\{|r\rangle\}$, we could generally orthonormalize them by the proper unitary transformation as follows:

$$|k\rangle = \sum_{r=1}^M U_{rk} |r\rangle, \quad (2)$$

$$\langle k | k' \rangle = \delta_{kk'}, \quad (3)$$

where M is a dimension of the vector space $\{|r\rangle\}$ and U_{rk} is an element of an unitary matrix. Hereafter, we develop our theory in terms of the orthonormal set, $\{|k\rangle\}$, for mathematical convenience.

The state $|k\rangle$ could be either the single-particle state or the many-electron configurational one. However, it is the essential point in our formulation that the basis set satisfies the following closure relations:

$$1 = \sum_{k=1}^M |k\rangle \langle k|, \quad (4)$$

that is, we assume that the orthonormal set, $\{|k\rangle\}$, spans the Hilbert space. We construct a generalized state vector by the linear combination of the above state vectors, as

$$|C\rangle = \sum_{k=1}^M C_k |k\rangle. \quad (5)$$

Here, the coefficient C_k is an arbitrary complex number. If we choose the atomic orbital as $|k\rangle$, then $|C\rangle$ corresponds to the molecular orbital, and if $|k\rangle$ is the many-electron configuration, it becomes the CI state.

Here, let us assume that C_k are variables and change these parameters arbitrarily. Then resulting $|C\rangle$ is transformed into an arbitrary state vector. It is important to notice that the space spanned by the state vector, $|C\rangle$ generated by changing C_k arbitrarily could include every state in the Hilbert space, namely, the set $\{|C\rangle\}$ is an overcomplete set. Thus, we could construct the closure relation:

$$1 = \int \prod_{k=1}^M \frac{dC_k^* dC_k}{2\pi i} \exp\left(-\sum_{k=1}^M |C_k|^2\right) |C\rangle\langle C|. \quad (6)$$

The derivation of the closure relation is given in Appendix A. Each variables covers the whole complex plane. However, the Gaussian weight function effectively restricts a region of the integration. By suitable variable transformations, we can derive another form of the closure relation:

$$1 = M! \int \prod_{k=1}^M \frac{dC_k^* dC_k}{2\pi i} \delta\left(\sum_{k=1}^M |C_k|^2 - 1\right) |C\rangle\langle C|. \quad (7)$$

The derivation of this equation from Eq. (6) is given in Appendix B. The delta function ensures the normalization condition of the state vectors. Thus, in this case, each variable varies only on the surface of the unit sphere in the complex space.

Next, we restrict C_k in Eq. (5) to be real. Then, we could get the real-number closure relation with the real Gaussian weight function,

$$1 = 2 \int \prod_{k=1}^M \frac{dC_k}{\sqrt{\pi}} \exp\left(-\sum_{k=1}^M C_k^2\right) |C\rangle\langle C|. \quad (8)$$

The real delta function closure relation can be also derived;

$$1 = 2\Gamma\left(\frac{M}{2}\right) \int \prod_{k=1}^M \frac{dC_k}{\sqrt{\pi}} \delta\left(\sum_{k=1}^M C_k^2 - 1\right) |C\rangle\langle C|. \quad (9)$$

These real closure relations are derived in Appendix C.

Path Integral Formulation

Consider a partition function, $Z = \text{Tr } e^{-\beta H}$, where Tr implies a trace operation, and $\beta = (k_B T)^{-1}$ with the Boltzmann constant k_B and a temperature T . Let us divide the temperature in-

terval, β into L infinitesimal time slices, i.e., $\beta = L\tau$, and inserting the closure relation among segments, then Z becomes

$$Z = \lim_{L \rightarrow \infty} \frac{1}{\Xi} \int d\mu[C^*, C] Z[C^*, C], \quad (10)$$

where

$$\begin{aligned} d\mu[C^*, C] &= \prod_{l=1}^L \prod_{k=1}^M \frac{dC_k^*(l) dC_k(l)}{2\pi i} \prod_{l=1}^L W[C^*(l), C(l)], \end{aligned} \quad (11)$$

$$Z[C^*, C] = \prod_{l=1}^L \langle C(l) | e^{-\beta H/L} | C(l-1) \rangle, \quad (12)$$

and

$$\Xi = \mathcal{N}^L. \quad (13)$$

$W[C^*(l), C(l)]$ is the Gaussian weight function or the delta function corresponding to Eq. (6) or (7), respectively, and \mathcal{N} is the normalization factor appearing in the denominator of the closure relation. The trace operation in the partition function imposes a periodic boundary condition upon $|C(l)\rangle$ as

$$|C(0)\rangle = |C(L)\rangle. \quad (14)$$

The ensemble average of any operator O can be calculated as

$$\begin{aligned} \langle O \rangle &= \frac{\text{Tr}(e^{-\beta H} O)}{\text{Tr } e^{-\beta H}} \\ &= \lim_{L \rightarrow \infty} \left\{ \int d\mu[C^*, C] Z[C^*, C] \right. \\ &\quad \times \frac{1}{L} \sum_{l=1}^L \frac{\langle C(l) | O | C(l-1) \rangle}{\langle C(l) | C(l-1) \rangle} \left. \right\} \\ &\quad \times \left\{ \int d\mu[C^*, C] Z[C^*, C] \right\}^{-1}. \end{aligned} \quad (15)$$

Note that, in the above expression, the normalization factor Ξ has disappeared. In general, we could express the ensemble average of any physical quantity in terms of the logarithmic derivative of the partition function with respect to suitable parameters. For example, the ensemble average of

the Hamiltonian, i.e., the average energy, $\langle H \rangle$ is given by

$$\begin{aligned}\langle H \rangle &= \frac{\text{Tr}(e^{-\beta H} H)}{\text{Tr} e^{-\beta H}} \\ &= -\frac{\partial}{\partial \beta} \log Z.\end{aligned}\quad (16)$$

Thus substituting Eq. (10) into (16), we get

$$\begin{aligned}\langle H \rangle &= \lim_{L \rightarrow \infty} \left\{ \int d\mu[C^*, C] Z[C^*, C] \right. \\ &\quad \times \frac{1}{L} \sum_{l=1}^L \frac{\langle C(l)|H|C(l-1) \rangle}{\langle C(l)|C(l-1) \rangle} \left. \right\} \\ &\quad \times \left\{ \int d\mu[C^*, C] Z[C^*, C] \right\}^{-1}.\end{aligned}\quad (17)$$

It is impossible to evaluate Eq. (17) by direct numerical integration because of its huge amount of integration variables generated by slicing β and the presence of the two-body interactions. Therefore, we should approximate the above integral or should adopt other integration methods such as the Monte Carlo method.

Now, we introduce the static approximation, where all the integral variables are independent of the temperature (the imaginary time) as,

$$\{C_k^*, C_k\} = \{C_k^*(l), C_k(l)\}.\quad (18)$$

Therefore, we have an approximate energy;

$$\begin{aligned}\langle H \rangle_{\text{static}} &= \lim_{L \rightarrow \infty} \left\{ \int d\mu_{\text{static}}[C^*, C] \right. \\ &\quad \times Z_{\text{static}}[C^*, C] \frac{\langle C|H|C \rangle}{\langle C|C \rangle} \left. \right\} \\ &\quad \times \left\{ \int d\mu_{\text{static}}[C^*, C] Z_{\text{static}}[C^*, C] \right\}^{-1},\end{aligned}\quad (19)$$

where the measure of integral and the static Boltzmann factor are given by

$$d\mu_{\text{static}}[C^*, C] = \prod_{k=1}^M \frac{dC_k^* dC_k}{2\pi i} W[C^*, C],\quad (20)$$

$$\begin{aligned}Z_{\text{static}}[C^*, C] &= (\langle C|e^{-\beta H/L}|C \rangle)^L \\ &\approx \langle C|C \rangle^L \exp\left(-\beta \frac{\langle C|H|C \rangle}{\langle C|C \rangle}\right).\end{aligned}\quad (21)$$

When we adopt the delta function as the weight function, Eq. (19) becomes

$$\begin{aligned}\langle H \rangle_{\text{static}} &= \left\{ \int \prod_{k=1}^M \frac{dC_k^* dC_k}{2\pi i} \delta\left(\sum_{k=1}^M |C_k|^2 - 1\right) \right. \\ &\quad \times e^{-\beta \langle C|H|C \rangle} \langle C|H|C \rangle \left. \right\} \left\{ \int \prod_{k=1}^M \frac{dC_k^* dC_k}{2\pi i} \right. \\ &\quad \times \delta\left(\sum_{k=1}^M |C_k|^2 - 1\right) e^{-\beta \langle C|H|C \rangle} \left. \right\}^{-1}.\end{aligned}\quad (22)$$

The approximation in Eq. (21) seems to be very rough; however, in the zero-temperature limit we can give Eq. (22) a positive meaning as shown in the following.

Now, the set $\{|k\rangle\}$ is complete, so we could, in principle, construct the eigenstates of the Hamiltonian as

$$H|C^{(n)}\rangle = E_n|C^{(n)}\rangle,\quad (23)$$

$$|C^{(n)}\rangle = \sum_{k=1}^M C_k^{(n)}|k\rangle,\quad (24)$$

where E_n is the n th energy eigenvalue. Thus, for the numerator of Eq. (22), we have an inequality as

$$\begin{aligned}\int \prod_{k=1}^M \frac{dC_k^* dC_k}{2\pi i} \delta\left(\sum_{k=1}^M |C_k|^2 - 1\right) \\ \times e^{-\beta \langle C|H|C \rangle} \langle C|H|C \rangle \geq e^{-\beta E_0} E_0.\end{aligned}\quad (25)$$

Here, the equality holds when β is infinity, i.e., in the case of the zero-temperature limit, where only the ground state contributes to the integral. We also have another inequality for the denominator of Eq. (22) as,

$$\int \prod_{k=1}^M \frac{dC_k^* dC_k}{2\pi i} \delta\left(\sum_{k=1}^M |C_k|^2 - 1\right) e^{-\beta \langle C|H|C \rangle} \geq e^{-\beta E_0}.\quad (26)$$

Therefore, we obtain a required result as,

$$\lim_{\beta \rightarrow \infty} \langle H \rangle_{\text{static}} = E_0.\quad (27)$$

For the finite temperature calculations, we must use the exact expression, Eq. (17). The approximation expression, Eq. (22), works practically for the zero-temperature calculations.

Monte Carlo Method

An estimation of Eq. (17) requires the numerical calculation of two multidimensional integrals over $M \times L$ variables with large enough L , but we cannot directly carry out this integration by ordinary ways. Therefore we apply the Monte Carlo method to do it.

We have two kinds of closure relations, Eqs. (6) and (7) with the weight functions of the Gauss-type function and the delta function, respectively;

$$\exp\left(-\sum_{k=1}^M |C_k|^2\right), \quad (28)$$

$$\delta\left(\sum_{k=1}^M |C_k|^2 - 1\right). \quad (29)$$

For the former, we must generate random numbers distributed from $-\infty$ to ∞ , and the physical meaning of the amplitude is not so clear. On the other hand, the distribution of random numbers in Eq. (29) is restricted on the surface of the unit sphere. Thus an elegant algorithm enables us to generate them under the restriction of the delta function, which ensures the normalization condition of the state. Therefore, we adopt the delta function weight in the practical calculation.

The algorithm of generating random numbers with the constraint of the delta function, which generate the set of the next generation, $\{C_k(l+1)\}$ from the original set, $\{C_k(l)\}$, is as follows:

1. Assume that $\{C_k(l)\}$ ($1 \leq l < L$) is normalized and consider it as the set of variables of the next generation, $\{C_k(l+1)\}$:

$$\{C_k(l+1)\} \leftarrow \{C_k(l)\}. \quad (30)$$

2. Choose randomly k, k' ($k \neq k'$), and θ ($0 \leq \theta < 2\pi$).
3. Generate new variables by the following orthogonal transformation of the selected variables:

$$\begin{bmatrix} C_k^*(l+1) \\ C_{k'}^*(l+1) \end{bmatrix} \leftarrow \begin{bmatrix} \cos \theta & -\sin \theta \\ \sin \theta & \cos \theta \end{bmatrix} \begin{bmatrix} C_k^*(l) \\ C_{k'}^*(l) \end{bmatrix}, \quad (31)$$

$$\begin{bmatrix} C_k(l+1) \\ C_{k'}(l+1) \end{bmatrix} \leftarrow \begin{bmatrix} \cos \theta & -\sin \theta \\ \sin \theta & \cos \theta \end{bmatrix} \begin{bmatrix} C_k(l) \\ C_{k'}(l) \end{bmatrix}. \quad (32)$$

Resulting $\{C_k(l+1)\}$ is also normalized.

4. Repeat procedures 2 and 3 a suitable number of times and finally obtain the orthonormal set of the next generation, $\{C_k(l+1)\}$.

This procedure generates the normalized variables of the further generations in succession.

Numerical Examples—Hydrogen Molecule

We calculate here the average energy, $\langle H \rangle$, of the hydrogen molecule as numerical examples. We do not intend to reproduce the experimental results but concentrate on how our method works by comparing our results with ones obtained by the ordinary full CI method.

We carry out numerical calculations under the static approximation using Eq. (22), because an

TABLE I
Energy of hydrogen molecule (a.u.): temperature vs. energy.

Temperature, β^{-1}	Energy (STO-3G)	Energy (4-31G)
0.1	$-1.8211376557 \pm 0.0000002212$	$-1.8668794694 \pm 0.0000000519$
1	$-1.8211396153 \pm 0.0000001303$	$-1.8666971526 \pm 0.0000021232$
10	$-1.8211250591 \pm 0.0000045046$	$-1.8667716435 \pm 0.0000231532$
100	$-1.8210604210 \pm 0.0000685900$	$-1.8642273943 \pm 0.0002478408$
(HF approx.)	-1.7991487410	-1.8105620770
(Full CI)	-1.8211407332	-1.8670253484

estimation of Eq. (17) requires a large amount of machine time in the Monte Carlo simulation due to two multidimensional integrals over $M \times L$ variables with large enough L . Moreover, we are interested in the electronic structure of molecules and have already a complete set of orthonormal state vectors satisfying Eq. (23), that is, the CI basis set. Therefore, even if we restrict ourselves to the static approximation, we could evaluate physical quantities in the zero-temperature limit.

The calculation is carried out with the STO-3G and 4-31G basis sets at the internuclear distance of 1.46 a.u. The Monte Carlo integration was done changing the temperature, β^{-1} , from 0.1 to 100 K. The number of samplings is 100 for each calculations. Calculations are executed on the S-4/1000 (FUJITSU Co. Ltd.). The temperature dependence of the energy is presented in Table I. Note that our calculation is based on Eq. (22) and the calculated energy tends to the full CI ground-state energy, E_0^{CI} . We might expect that results for lower temperature are more accurate than that for higher ones. However, the calculated energy does not necessarily approach to E_0^{CI} monotonously due to the sampling procedure we adopted in the Monte Carlo integration. As the temperature is lower, the energy is closer to E_0^{CI} on the calculations using the 4-31G basis set. While, the results of the STO-3G basis set shows that the energy for 1 K is closer to E_0^{CI} than that for 0.1 K. In spite of these results, we could expect that the energy for low temperature is close to E_0^{CI} .

Concluding Remarks

Fermion path integrals are usually based on the closure relation for the Fermion coherent state which is expressed in terms of the Grassmann numbers [8], auxiliary fields [9], or the bond order [5]. Since the standard computation of the quantum chemistry is based upon the LCAO-MO-CI method, it is very convenient to express the path integrals in terms of the related LCAO coefficients, which enable us to utilize conventional techniques and ideas of the molecular calculation.

We have derived the general closure relation from the complete set of state vectors and have shown that it is possible to carry out the ab initio calculation by using the complete set of the many-electron configurational state in the zero tempera-

ture. We have restricted ourselves to the zero-temperature calculation in this study, but we can, in principle, evaluate physical quantities for finite temperatures. Moreover, as we could formulate the finite temperature Green's function in the path integral form, we could calculate dynamical quantities in the finite temperature. Static and dynamic quantities at finite temperature will be calculated in separate studies.

In the path integral method, all the independent paths of particles must be taken into account, but "the classical path" is determined by optimizing the action. If we interpret particle as molecule, this image of the classical path in the path integral may correspond to the reaction path. Therefore, the path integral method of both electrons and nuclei enables us to directly investigate the chemical reaction by the ab initio calculation. In usual chemical reaction theories based on the orbital theory or the collision theory, it is very hard to take simultaneously into account the temperature and the dynamics. While, our theory could treat the dynamical processes of systems mentioned above and includes explicitly the temperature which plays an essential role in the chemical reaction. In the future, we will discuss the chemical reaction from a path integral point of view.

Now, the ab initio calculations of molecules are usually carried out by the LCAO-MO-CI method. The CI method, however, requires a huge amount of computer memory. On the other hand, for the zero-temperature calculations, the path integral Monte Carlo method described in this work, requires memories comparable to or less than the full CI method. If we use the closure relation in terms of the LCAO coefficients [6] instead of the CI relation, the memory required is much less than the full CI method, though we meet with the negative sign problem [7]. Therefore, it would be possible to calculate large molecules by the path integral Monte Carlo method.

Since, in the Monte Carlo method, the computing time is everything, we need high-speed computers rather than large-storage ones. The high-speed computing can be achieved by parallel computing, and the Monte Carlo integration can be easily executed by parallel computers. Thus, the massively parallel computers enable us to calculate large molecules in realistic computational times. Therefore, we think that the path integral Monte Carlo method is very powerful and applicable to a large area of chemistry.

Appendix A: Derivation of Closure Relation

Now we consider an operator \mathcal{O} in the following form:

$$\mathcal{O} = \frac{1}{\mathcal{N}} \int \prod_{k=1}^M \frac{dC_k^* dC_k}{2\pi i} W[C^*, C] |C\rangle \langle C|, \quad (33)$$

where $W[C^*, C]$ is an unknown weight function and \mathcal{N} the normalization factor. In order to make \mathcal{O} be the resolution of unity, we must find a suitable weight function. Substituting Eq. (5) into (33), we have

$$\begin{aligned} \mathcal{O} &= \frac{1}{\mathcal{N}} \int \prod_{k=1}^M \frac{dC_k^* dC_k}{2\pi i} W[C^*, C] \\ &\times \sum_{k_1 k_2=1}^M C_{k_1} C_{k_2}^* |k_1\rangle \langle k_2|. \end{aligned} \quad (34)$$

In this equation, if we could construct $W[C^*, C]$ satisfying the following relation:

$$\int \prod_{k=1}^M \frac{dC_k^* dC_k}{2\pi i} W[C^*, C] C_{k_1} C_{k_2}^* = A \delta_{k_1 k_2}, \quad (35)$$

where A is a real constant, then Eq. (34) is reduced to the closure relation of the set $\{|k\rangle\}$. This means that the square terms, $|C_k|^2$'s, with appropriate $W[C^*, C]$ could be integrated to give finite values, and on the other hand, the cross terms, $C_{k_1} C_{k_2}^*$'s, with $W[C^*, C]$ to vanish. Thus, we could easily show that one of the simplest forms for $W[C^*, C]$ is the Gaussian function:

$$W[C^*, C] = \exp\left(-\sum_{k=1}^M |C_k|^2\right). \quad (36)$$

Therefore, the explicit form of a novel closure relation is

$$1 = \int \prod_{k=1}^M \frac{dC_k^* dC_k}{2\pi i} \exp\left(-\sum_{k=1}^M |C_k|^2\right) |C\rangle \langle C|. \quad (37)$$

The proof is quite elementary.

Appendix B: Another Closure Relation

Here, we derive the delta function closure relation from the Gaussian one. We can rewrite the

Gaussian weight function in Eq. (6) as

$$\begin{aligned} &\exp\left(-\sum_{k=1}^M |C_k|^2\right) \\ &= \int_0^\infty dx \delta\left(x - \sum_{k=1}^M |C_k|^2\right) e^{-x} \\ &= \int_0^\infty dx x^{-1} \delta\left(1 - x^{-1} \sum_{k=1}^M |C_k|^2\right) e^{-x}. \end{aligned} \quad (38)$$

Here we have used a fact that the summation in the exponent gives a positive value. While, in the integrand of Eq. (6), we note the following relation:

$$|C\rangle = x \times |Cx^{-1}\rangle. \quad (39)$$

Then, we could derive the required relation as follows:

$$\begin{aligned} &\int \prod_{k=1}^M \frac{dC_k^* dC_k}{2\pi i} \exp\left(-\sum_{k=1}^M |C_k|^2\right) |C\rangle \langle C| \\ &= \int \prod_{k=1}^M \frac{dC_k^* dC_k}{2\pi i} \int_0^\infty dx \\ &\times \delta\left(1 - x^{-1} \sum_{k=1}^M |C_k|^2\right) e^{-x} |Cx^{-1}\rangle \langle C| \\ &= \int_0^\infty dx x^M e^{-x} \times \int \prod_{k=1}^M \frac{dC_k^* dC_k}{2\pi i} \\ &\times \delta\left(\sum_{k=1}^M |C_k|^2 - 1\right) |C\rangle \langle C| \\ &= M! \int \prod_{k=1}^M \frac{dC_k^* dC_k}{2\pi i} \delta\left(\sum_{k=1}^M |C_k|^2 - 1\right) |C\rangle \langle C|. \end{aligned} \quad (40)$$

Appendix C: Real-Number Closure Relation

By following the derivation in the Appendix A, we could easily obtain the real Gaussian weight closure relation as

$$1 = 2 \int \prod_{k=1}^M \frac{dC_k}{\sqrt{\pi}} \exp\left(-\sum_{k=1}^M C_k^2\right) |C\rangle \langle C|. \quad (41)$$

Notice here that the factor, 2, appears in the above expression. The origin of the factor is directly derived from the complex number closure relation,

Eq. (6). By separating a complex integral variable into real and imaginary parts,

$$C_k = x_k + iy_k, \quad (42)$$

we can rewrite the measure of integral as

$$\frac{dC_k^* dC_k}{2\pi i} = \frac{dx_k}{\sqrt{\pi}} \frac{dy_k}{\sqrt{\pi}}. \quad (43)$$

Thus nonvanishing integrals are calculated as

$$\int \frac{dC_k^* dC_k}{2\pi i} e^{-C_k^* C_k} = \int \frac{dx_k}{\sqrt{\pi}} \frac{dy_k}{\sqrt{\pi}} e^{-x_k^2 - y_k^2} = 1, \quad (44)$$

$$\begin{aligned} & \int \frac{dC_k^* dC_k}{2\pi i} C_k^* C_k e^{-C_k^* C_k} \\ &= 2 \int \frac{dx_k}{\sqrt{\pi}} \frac{dy_k}{\sqrt{\pi}} x_k^2 e^{-x_k^2 - y_k^2} = 1. \end{aligned} \quad (45)$$

Thus, Eq. (45) shows that the real and the imaginary parts of the integral variable equally contribute to the integral. This is the origin of the factor.

Finally, we give the real delta function closure relation. This is obtained by the same variable

transformation as in the Appendix B,

$$1 = 2\Gamma\left(\frac{M}{2}\right) \int \prod_{k=1}^M \frac{dC_k}{\sqrt{\pi}} \delta\left(\sum_{k=1}^M C_k^2 - 1\right) |C\rangle\langle C|. \quad (46)$$

References

1. R. P. Feynman and A. R. Hibbs, *Quantum Mechanics and Path Integrals* (McGraw-Hill, New York, 1965).
2. L. H. Ryder, *Quantum Field Theory* (Cambridge University Press, London, 1984).
3. F. A. Berezin, *Method in Second Quantization* (Academic, New York, 1966).
4. H. Nagao, K. Nishikawa and S. Aono, *Chem. Phys. Lett.* **190** 97 (1992); *Ibid.*, **215**, 5 (1993).
5. H. Kawabe, K. Nishikawa, and S. Aono, *Int. J. Quantum Chem.* **51**, 265 (1994).
6. H. Kawabe, H. Nagao, and K. Nishikawa, *Int. J. Quantum Chem.*, to appear.
7. M. Suzuki, Ed., *Quantum Monte Carlo Methods in Condensed Matter Physics* (World Scientific, Singapore, 1993).
8. Y. Ohnuki and T. Kashiwa, *Prog. Theor. Phys.* **60**, 548 (1978).
9. J. W. Negele and H. Orland, *Quantum Many-Particle Systems* (Addison Wesley, New York, 1987).

Efficient Numerical Method for Finding the Initial Response of Quantum Processes to Changes in the Potential

MARK J. HAGMANN

*Department of Electrical and Computer Engineering, Florida International University,
Miami, Florida 33199*

Received February 26, 1996; revised manuscript received July 31, 1996; accepted August 2, 1996

ABSTRACT

The time-dependent Schrödinger equation is solved for an electron with potentials of the form $f_1(\mathbf{r}) + f_2(\mathbf{r}, t)U(t)$, where $U(t)$ is the unit step function. We use a product formulation, solving for $F(\mathbf{r}, t)$ where the wave function $\Psi(\mathbf{r}, t) = F(\mathbf{r}, t)\Phi(\mathbf{r})e^{-iEt/\hbar}$ in which $\Phi(\mathbf{r})e^{-iEt/\hbar}$ is the solution for $t < 0$. A simple implementation of the product formulation that does not use absorbing boundary conditions and is explicit, without using split operators, is applied in two examples. The first example pertains to resonances in tunneling with square barriers when the barrier height varies sinusoidally with time. The initial response of quantum tunneling to oscillations in the barrier height shows a buildup for oscillations at the resonance frequency and an off-resonance response that diminishes to approach the steady-state solution after several cycles. The second example is the initial response of a hydrogen atom to an intense applied electric field. In both examples the response is delayed, and for tunneling particles the delay is approximately equal to the semiclassical value for the duration of barrier traversal, defined as the time for traversing the inverted barrier. © 1996 John Wiley & Sons, Inc.

Introduction

Various methods have been used to solve the time-dependent Schrödinger equation for time-varying potentials. Floquet methods have been used to determine the steady-state response to a potential varying periodically with time [1, 2].

Transient solutions have been obtained using finite differences with an alternating-direction implicit propagation scheme [3], finite differences with a split-operator propagator [4], finite differences with a fourth-order predictor-corrector [5], a split-operator spectral technique with fast Fourier transforms [6], finite-element methods [7], and quadratures with an expansion in Vokolov states [8]. It is the objective of this study to describe a product

formulation for transient solutions that is particularly simple to implement and to illustrate its use with several examples.

Analysis

We begin the present analysis with the dipole approximation [9] of the time-dependent Schrödinger equation for an electron in a static potential plus a radiation field,

$$i\hbar \frac{\partial \Psi}{\partial t} = -\frac{\hbar^2}{2m} \nabla^2 \Psi + [V_0(\mathbf{r}) - e\mathbf{r} \cdot \mathbf{E}(\mathbf{r}, t)]\Psi, \quad (1)$$

where $V_0(\mathbf{r})$ is the static potential and $\mathbf{E}(\mathbf{r}, t)$ is the electric field intensity of the radiation field. We define the function $F(\mathbf{r}, t)$ such that the wave function $\Psi(\mathbf{r}, t) = F(\mathbf{r}, t)\Phi(\mathbf{r})e^{-iEt/\hbar}$, where $\Phi(\mathbf{r})e^{-iEt/\hbar}$ is the solution without the radiation field. Substituting into Eq. (1) leads to the following:

$$\frac{\partial F}{\partial t} = \frac{i\hbar}{2m} \nabla^2 F + \frac{i\hbar}{m\Phi} \nabla \Phi \cdot \nabla F + \frac{ie\mathbf{r} \cdot \mathbf{E}(\mathbf{r}, t)F}{\hbar}. \quad (2)$$

For problems with only one spatial dimension, when the electric field $\mathbf{E}(x, t)$ is in the x direction, Eq. (2) may be written as follows:

$$\frac{\partial F}{\partial t} = \frac{i\hbar}{2m} \frac{\partial^2 F}{\partial x^2} + \frac{i\hbar}{m\Phi} \frac{d\Phi}{dx} \frac{\partial F}{\partial x} + \frac{iexE(x, t)F}{\hbar}. \quad (3)$$

We set $E(x, t) = E_1 \sin(\omega t)U(t)$, where E_1 is a constant and $U(t)$ is the unit step function (1 for $t > 0$, else 0). The following finite-difference approximation of Eq. (3) is obtained by using the midpoint method [10] to approximate the time derivative of $F(x, t)$:

$$\begin{aligned} F_{l,j+1} = & F_{l,j-1} \\ & + \frac{i\hbar \Delta t}{m(\Delta x)^2} [F_{l+1,j} - 2F_{l,j} + F_{l-1,j}] \\ & + \frac{i\hbar \Delta t}{m \Delta x} \left[\frac{1}{\Phi} \frac{d\Phi}{dx} \right]_l [F_{l+1,j} - F_{l-1,j}] \\ & + \frac{2i \Delta t l \Delta x E_1}{\hbar} \sin(\omega J \Delta t) U(J) F_{l,j}, \quad (4) \end{aligned}$$

where $F_{l,j} \equiv F(I \cdot \Delta x, J \cdot \Delta t)$. The product formulation, which was used for the examples presented in this study, consists of the following three steps: First, analytical or numerical methods are used to solve the time-independent Schrödinger equation to determine $\Phi(x)$. Next Eq. (4), or the corresponding equation for two- or three-dimensional problems, is solved by time stepping from $t = 0$ where $F_{l,0} = 1$. Finally, the wave function $\Psi(x, t)$ is determined from the definition $\Psi(x, t) \equiv F(x, t)\Phi(x)e^{-iEt/\hbar}$.

For all of the examples studied thus far, we have found that it is sufficient to limit the spatial increment so that $|k|\Delta x$ does not exceed a value of 0.2 at any point in the grid, where $|k|$ is the magnitude of the wave vector. If the radiation field is not too strong when compared with the static potential, then $F(x, t)$ varies more slowly in space than does $\Psi(x, t)$, and so it is possible to use values of Δx with the product formulation that are somewhat larger than this recommended limit. Our numerical studies have also shown that there are six criteria which are necessary (but not sufficient) conditions limiting the maximum size of the time step Δt . The first three criteria may be understood from physical considerations: (1) The ratio $\Delta x/\Delta t$ must exceed the velocities that would be anticipated under the conditions of the problem. (2) The ratio $\Delta x/\Delta t$ should exceed the semiclassical value for barrier traversal [11] at all points where tunneling occurs. (3) It is necessary that $\Delta t \ll 2\pi/\omega$ so that the time dependence of the radiation field is sampled sufficiently. The remaining three criteria for numerical stability limit the coefficients on the right-hand side of Eq. (4). (4) From the first coefficient, $\Delta t < m(\Delta x)^2/\hbar$. (5) From the second coefficient, $\Delta t < m \Delta x \Phi / (\hbar d\Phi/dx)$ for all points on the grid. (6) From the third coefficient, $\Delta t < \hbar/(2exE_1)$ for all points on the grid. While each of these six criteria must be satisfied, the fourth is especially pertinent because numerical solutions diverge sharply at the point where this criterion is violated. The sixth criterion is only relevant for extremely intense fields. While these six criteria are not claimed to be sufficient conditions, in all of the examples studied thus far we have found that when they are satisfied the solution is stable for a short interval of time (~ 1 –5 fs). A reduction in the size of the time step is generally required for stability when simulating much longer durations. We have also solved Eq. (3) using the modified midpoint method with Richardson's de-

ferred approach to extrapolate to zero step size with rational functions (Bulirsch-Stoer technique) [12]. However, the latter method was found to require considerably greater computer time, and it does not appear to provide any noticeable improvement in accuracy or stability when all of the above criteria are satisfied.

When solving directly for the wave function, others have used various absorbing boundary conditions [13] and empirically adjusted "windowing" and "gobbling" [14]. Split-operator formulations, requiring matrix methods, have been used to improve the numerical stability [3-6]. The product formulation is much simpler to implement. At each time step Eq. (4) is used to update the values of the function F at all interior points of the grid. A separate procedure must be used for the points at the ends of the grid because Eq. (4) requires values of the function F at increments of $\pm \Delta x$ from the point that is updated. We have found that for a given value of Δx , the numerical stability is greatest if (1) linear extrapolation is used ($F_{1,j+1} = 2F_{2,j+1} - F_{3,j+1}$, $F_{N,j+1} = 2F_{N-1,j+1} - F_{N-2,j+1}$) when the increment is relatively small; (2) continuity is imposed ($F_{1,j+1} = F_{2,j+1}$, $F_{N,j+1} = F_{N-1,j+1}$) for intermediate values of the increment; and (3) the end points are not updated when the increment is relatively large. Solutions obtained by using Eq. (4) in the manner described are not unconditionally stable, but they have been shown to be stable over the range of durations simulated in the examples.

Numerical Example: Sinusoidal Variation of a Square Barrier

Büttiker and Landauer [15] used analytical methods to show that when a time-dependent potential is added to a square barrier ("modulation" of the barrier) tunneling particles absorb and emit modulation quanta. We have used Floquet methods [2] and other procedures [16] to determine the steady-state solution when the barrier height varies sinusoidally with time. These solutions show that there are resonances with a marked increase in the transmission. For square barriers, these resonances occur when modulation quanta have sufficient energy to take tunneling particles above the barrier, and the length of the barrier is an integral multiple of one-half the (now real) de Broglie wavelength [2].

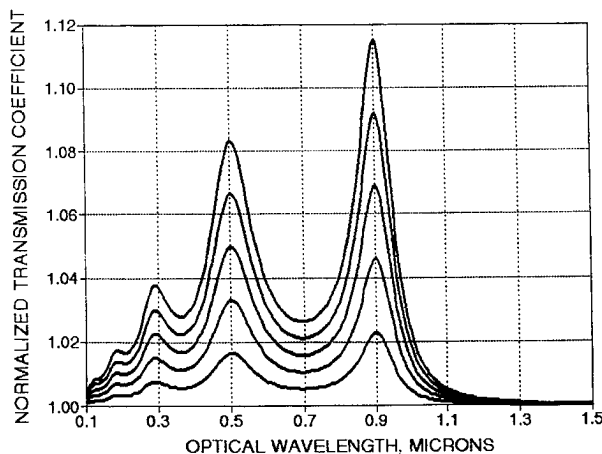


FIGURE 1. Ratio of transmission to the static value as a function of wavelength for 10-eV electrons with an 11-eV 1-nm square barrier. The radiation field has power flux densities of $0.2, 0.4, 0.6, 0.8$, and $1.0 \times 10^{12} \text{ W/m}^2$, from bottom to top curve, respectively.

Figure 1 shows the ratio of the transmission coefficient with barrier modulation to the static value as a function of the wavelength for 10-eV electrons with a square barrier having a height of 11 eV and a length of 1 nm. Floquet methods were used as previously described [2] to determine the steady-state solution of Eq. (1) for a radiation field with $E(x, t) = E_1 \sin(\omega t)$. Three resonances are evident in this figure ($\lambda = 0.905, 0.506$, and $0.296 \mu\text{m}$), for which the barrier length equals $\frac{1}{2}$, $\frac{2}{2}$, and $\frac{3}{2}$ of the de Broglie wavelength for particles absorbing one quantum. It may be seen in Figure 1 that the increase in transmission caused by the radiation field is proportional to the power flux density, which is consistent with the mechanism being the absorption of modulation quanta.

Figures 2-5 show the transient response of 10-eV electrons with an 11-eV 1-nm square barrier to a radiation field with a power flux density of 10^{12} W/m^2 . Each calculation was made using 450 points on the axis, with a prebarrier length of 0.5 nm, the 1 nm barrier, and a 1.5 nm postbarrier length. Thus, $\Delta x = 0.00667 \text{ nm}$ so that $k \Delta x = 0.108$ and $K \Delta x = 0.0342$, where $k = (2mE)^{1/2}/\hbar$ and $K = [2m(V - E)]^{1/2}/\hbar$, where V is the height of the square barrier. The calculations were repeated for other numbers of intervals, and with 225 points ($\Delta x = 0.0133 \text{ nm}$) the maximum difference between the probability density and that for 450 points is 0.68% at all grid locations for the 12-fs simulated duration. However, these errors in-

crease precipitously for $\Delta x > 0.03$ nm at which point $k\Delta x \approx \frac{1}{2}$. The calculations were made for radiation at two different wavelengths. Figures 2 and 3 are for the dominant resonance seen in Figure 1 ($\lambda = 0.905$ μm), for which the barrier

length is one-half of the de Broglie wavelength. Figures 4 and 5 are for the off-resonance wavelength of 1.50 μm , which exceeds the limit for which the absorption of a single quantum can take a tunneling electron above the barrier (1.24 μm).

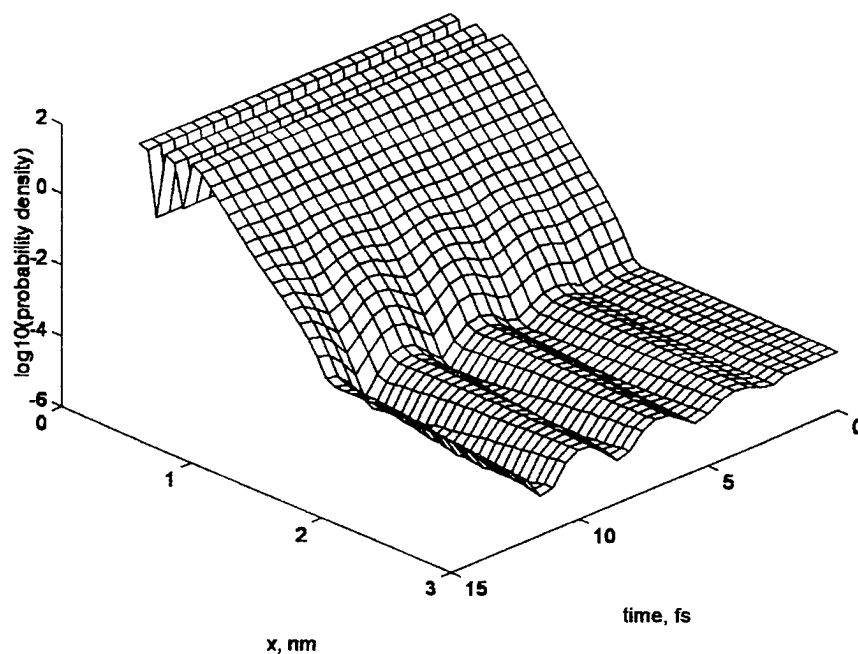


FIGURE 2. Probability density for 10-eV electrons with an 11-eV 1-nm square barrier. For time $t > 0$ the barrier height is modulated sinusoidally at $\lambda = 0.905$ μm by a radiation field with a power flux density of 10^{12} W/m^2 .

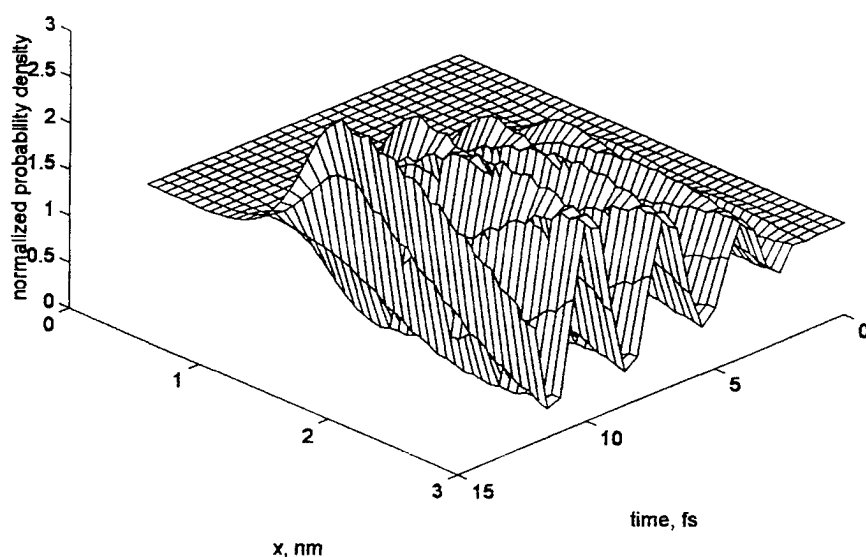


FIGURE 3. Ratio of the probability density to the static value for 10-eV electrons with an 11-eV 1-nm square barrier. For time $t > 0$ the barrier height is modulated sinusoidally at $\lambda = 0.905$ μm by a radiation field with a power flux density of 10^{12} W/m^2 .

The probability density ($\Psi\Psi^*$) is shown in Figures 2 and 4, and the ratio of the probability density to the static value (FF^*) is shown in Figures 3 and 5.

For this example, the most stringent of the six criteria for the time step is the fourth, that $\Delta t <$

$m(\Delta x)^2/\hbar$ giving a limit of 0.384 attoseconds (as). Numerical solutions converge for simulated durations of 1 fs or less when $\Delta t = 0.384$ as, and diverge sharply when the time step exceeds this value. To obtain stability for a simulated duration

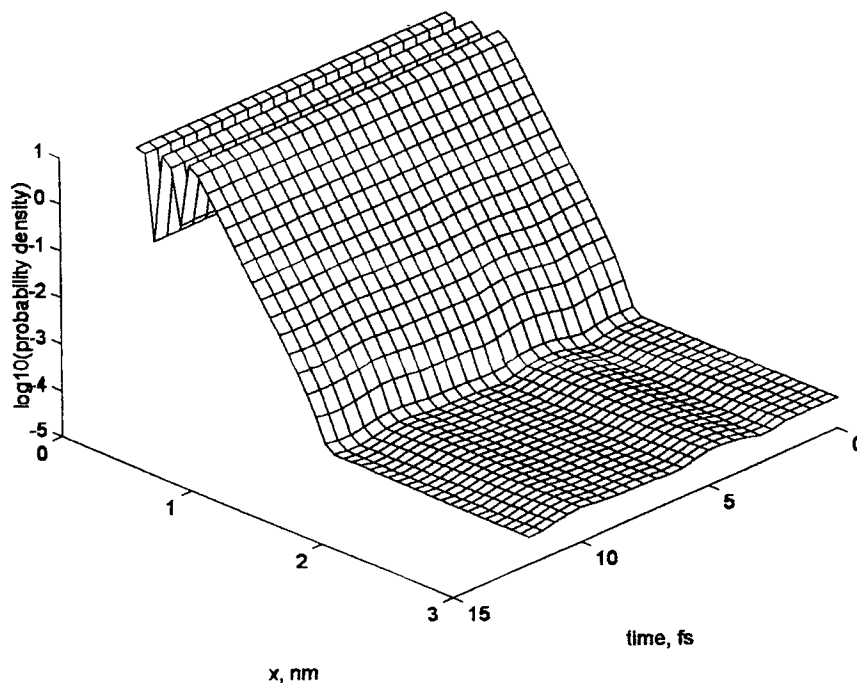


FIGURE 4. Probability density for 10-eV electrons with an 11-eV 1-nm square barrier. For time $t > 0$ the barrier height is modulated sinusoidally at $\lambda = 1.50 \mu\text{m}$ by a radiation field with a power flux density of 10^{12} W/m^2 .

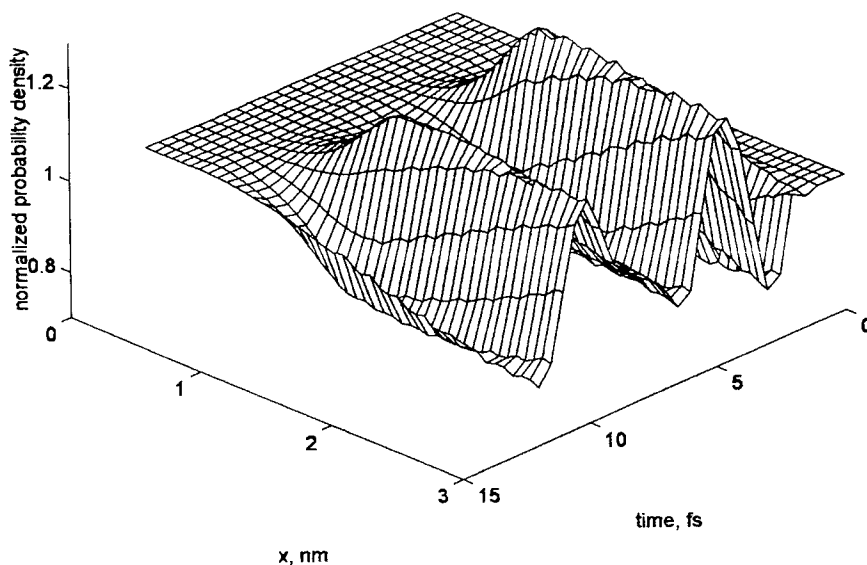


FIGURE 5. Ratio of the probability density to the static value for 10 eV electrons with an 11-eV 1-nm square barrier. For time $t > 0$, the barrier height is modulated sinusoidally at $\lambda = 1.50 \mu\text{m}$ by a radiation field with a power flux density of 10^{12} W/m^2 .

of 12 fs in Figures 2-5, it was necessary to use time steps of 0.002 as with $\lambda = 0.905 \mu\text{m}$ and 0.01 as with $\lambda = 1.50 \mu\text{m}$. When the calculations were repeated using one-tenth of these time increments, all values of probability density were found to be unchanged to within 1 part in 10^4 for the full 12 fs. In this example the end points of the grid were updated by imposing continuity ($F_{1,j+1} = F_{2,j+1}$, $F_{N,j+1} = F_{N-1,j+1}$).

The semiclassical value of the tunneling time, defined as the time for traversing the inverted barrier [11], is $T_{\text{sc}} = 1.69$ fs for the static square barrier in this example. It may be seen in Figures 2 and 3 that there is no response to the radiation field until after T_{sc} . There is a monotonic increase in the magnitude of the consecutive peaks in the transmission during the 12 fs simulation to approach the steady-state solution at resonance. At $\lambda = 0.905 \mu\text{m}$ (Figs. 2 and 3) the height of the modulated barrier is maximum at 0.75, 3.77, 6.79, and 9.81 fs and minimum at 2.26, 5.28, 8.30, and 11.32 fs. Each decrease in the barrier height causes an increase in the transmission, and each increase in the barrier height causes a decrease in the transmission. However, there is a delay of approximately $T_{\text{sc}}/2$ between each extremum in the barrier height and the corresponding extremum in the probability density at the end of the barrier.

At $\lambda = 1.50 \mu\text{m}$ (Figs. 4 and 5) the height of the modulated barrier is maximum at 1.25, 6.25, and 11.26 fs, and minimum at 3.75 and 8.76 fs. It may be seen in Figures 4 and 5 that, as with $\lambda = 0.905 \mu\text{m}$, there is no response to the radiation field until after T_{sc} . However, with $\lambda = 1.50 \mu\text{m}$ extrema in the transmission are irregularly spaced, corresponding approximately to wavelengths from 1.0 to $1.2 \mu\text{m}$. Furthermore, the response diminishes to approach the steady-state solution for this off-resonance wavelength after several periods of oscillation. It is known [17] that the steady-state response of both classical and quantum systems to a periodic perturbation is approached only for durations t such that $\omega t \gg 2\pi$, and this may be understood by noting the breadth of the spectrum for a sinusoidal pulse. We attribute the monotonic increase in the magnitude of the consecutive peaks at resonance (Figs. 2 and 3) and the decrease off resonance (Figs. 4 and 5) to increased definition of the frequency of the radiation field with elapsed time. For comparison, Figure 6 shows the square of the magnitude of the Fourier transform of a sine wave as a function of the frequency for pulses having durations of 0.5, 0.8, 1.5, and 3.0 periods.

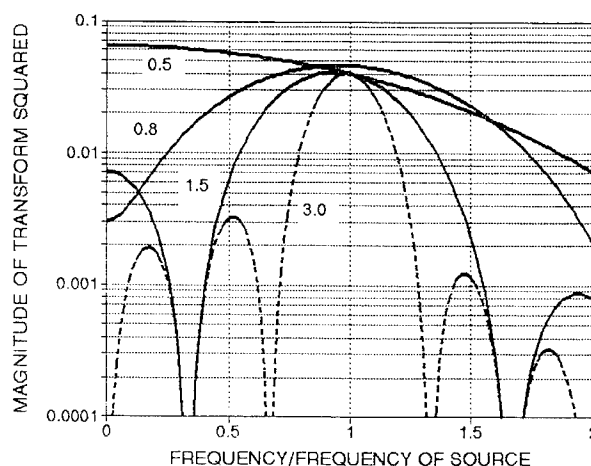


FIGURE 6. Square of the magnitude of the Fourier transform of a sine wave as a function of the frequency for durations of 0.5, 0.8, 1.5, and 3.0 periods.

Numerical Example: Response of a Hydrogen Atom to a Laser

Pulse compression for the generation of extremely short optical pulses has received considerable emphasis in laser science. High-order harmonics have been measured [18] when neon is irradiated with intense femtosecond optical pulses, and it appears this effect may lead to subfemtosecond pulses [19]. We have simulated the response of a hydrogen atom to intense fields as a preliminary to modeling these phenomena. First, the effect of a static electric field on the ground state of a hydrogen atom was determined by solving the time-independent Schrödinger equation using separation of variables in parabolic coordinates [20], with care to allow for the three turning points in the solution.

In solving the time-dependent Schrödinger equation to determine the transient response by a hydrogen atom, we use cylindrical coordinates with the z axis parallel to the applied electric field. The solution is independent of the polar angle because, due to the orientation of the applied field, the azimuthal symmetry in the ground state is not altered by the applied field. For the product formulation we define the function $F(r, z, t)$ such that the wave function $\Psi(r, z, t) = F(r, z, t)\Phi(r, z)e^{-iEt/\hbar}$, where $\Phi(r, z)e^{-iEt/\hbar}$ is the solution

without the radiation field, with

$$\Phi(r, z) = \frac{e^{\sqrt{r^2+z^2}/a_0}}{\sqrt{\pi a_0^3}} \quad (5)$$

where a_0 is the radius of the first Bohr orbit. Substituting into Eq. (2) results in the following partial differential equation for the function $F(r, z, t)$:

$$\begin{aligned} \frac{\partial F}{\partial t} = & \frac{i\hbar}{2m} \left[\frac{\partial^2 F}{\partial r^2} + \left(\frac{1}{r} - \frac{2r}{a_0\sqrt{r^2+z^2}} \right) \frac{\partial F}{\partial r} \right. \\ & \left. + \frac{\partial^2 F}{\partial z^2} - \frac{2z}{a_0\sqrt{r^2+z^2}} \frac{\partial F}{\partial z} \right] \\ & + \frac{iezE_1}{\hbar} \sin \omega t U(t) F. \end{aligned} \quad (6)$$

The following finite-difference approximation of Eq. (6) is obtained by using the midpoint method [10] to approximate the time derivative of $F(r, z, t)$:

$$\begin{aligned} F_{I,J,K+1} = & F_{I,J,K-1} \\ & + \frac{i\hbar \Delta t}{m} \left[\frac{F_{I+1,J,K} - 2F_{I,J,K} + F_{I-1,J,K}}{(\Delta r)^2} \right. \\ & + \left(\frac{1}{I \cdot \Delta r} - \frac{2I \cdot \Delta r}{a_0\sqrt{(I\Delta r)^2 + (J\Delta z)^2}} \right) \\ & \times \frac{(F_{I-1,J,K} - F_{I+1,J,K})}{2\Delta r} \\ & + \frac{F_{I,J+1,K} - 2F_{I,J,K} + F_{I,J-1,K}}{(\Delta z)^2} \\ & - \frac{2J\Delta z}{a_0\sqrt{(I\Delta r)^2 + (J\Delta z)^2}} \\ & \left. \times \frac{(F_{I,J+1,K} - F_{I,J-1,K})}{2\Delta z} \right] \\ & + \frac{2i\Delta t J \Delta z e E_1}{\hbar} \sin(\omega K \Delta t) U(K) F_{I,J,K}, \end{aligned} \quad (7)$$

where $F_{I,J,K} \equiv F(I \cdot \Delta r, J \cdot \Delta z, K \cdot \Delta t)$. For points on the z axis ($I = 0$) the equation is modified by deleting the term approximating the first derivative in respect to r . Equation (7) is used to solve

for the function F by time stepping from $t = 0$ where $F_{I,J,0} = 1$ in the same manner as Eq. (4) was used in the example with a square barrier. However, for this example the stability is greatest when the points on the boundary of the grid are updated by means of linear extrapolation.

Values of $\Delta r = \Delta z = 0.024$ nm, and $\Delta t = 1.0$ as were used in this set of simulations. Criteria limiting the maximum size of the time step Δt in Eq. (7) have been determined as they were for Eq. (4). For this example the most stringent criteria are that $\Delta t < m(\Delta r)^2/\hbar$ and $\Delta t < m(\Delta z)^2/\hbar$, which are analogous to those in the first example, giving a limit of 5.0 as. Numerical solutions diverge sharply when the time step exceeds this value, but converge to within 1 part in 10^4 for $\Delta t = 1.0$ as in the range of simulated durations for this example. Figure 7 shows the initial and steady-state response of a hydrogen atom to a step function pulse having an amplitude of 1 V/nm for $t > 0$. The ratio of the probability density to the unperturbed value is shown at 0.04, 0.08, 0.10, and 0.12 fs, and in steady state (dashed curve). Figure 8 shows the ratio of the probability density at 0.12 fs as a function of r and z . It may be seen in Figure 7 that there is a delay of approximately 0.05 fs, which may be attributed to the uncertainty principle, before the atom begins to respond to the applied field. Other simulations made using optical frequencies show that this delay is relatively insensitive to the wavelength. These results suggest that delays present in the transient response must be

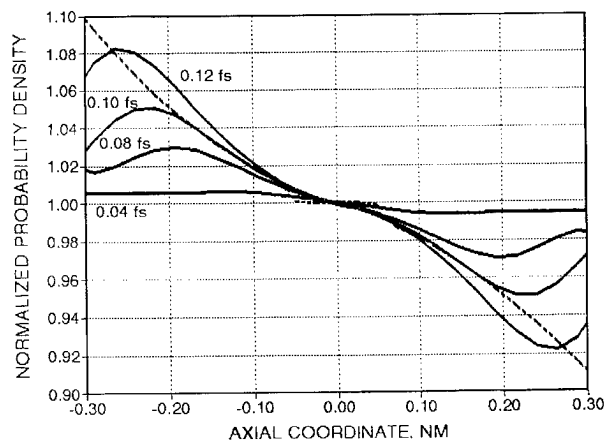


FIGURE 7. Ratio of the probability density for the electron in a hydrogen atom with an applied field of 1 V/nm to the unperturbed value as a function of the axial coordinate. The dashed curve is the static solution, and the solid curves are for a step function pulse.

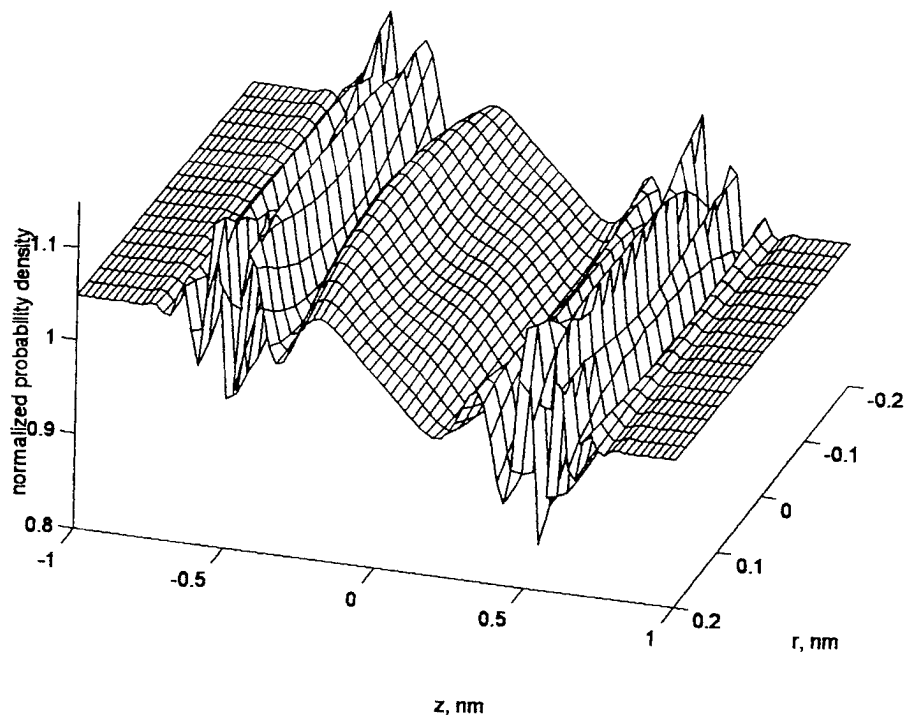


FIGURE 8. Ratio of the probability density for the electron in a hydrogen atom to the unperturbed value at 0.12 fs after the start of a step function pulse having an amplitude of 1 V/nm.

considered when modeling the response of atoms to intense fields.

Discussion

The simple implementation of the product formulation illustrated in this study does not use absorbing boundary conditions and is explicit, without using split operators. This implementation is not unconditionally stable, but the solutions are stable over the range of simulated durations used in the examples.

The first numerical example, for sinusoidal variation of the height of a square barrier, offers promise as a new approach to the unsolved problem [21] of evaluating the duration of quantum tunneling. A variety of different theoretical approaches have been used to examine tunneling times [21], but all of these are based on steady-state solutions with the exception of transient solutions for wave packets [22]. While these transient solutions show a delay between the arrival of the incident wave packet and the departure of the

transmitted packet, they have been criticized [23] because there is no valid basis for comparing any part (e.g., peak or centroid) of the two different packets. The interpretation is further complicated because the distribution of energies in a wave packet would smear the effects of tunneling times. The calculations in the first numerical example do not use such a distribution of energies. While the result is by no means unanimous [21], 12 analytical methods result in the semiclassical expression for the tunneling time [11] which is the classical time for traversing the inverted barrier. The results in the first example are consistent with the semiclassical expression for tunneling time.

ACKNOWLEDGMENT

We acknowledge the assistance of J. G. Krasnow in editing, helpful discussions with H. F. Gray and J. L. Shaw, and support with graphics software by H. Ghassemi. The Pentium PC used for the calculations was made possible by NSF research equipment grant No. 9500007.

References

1. H. P. Breuer, K. Dietz, and M. Holthaus, *J. Phys. B* **22**, 3187 (1989).
2. M. J. Hagmann, *J. Appl. Phys.* **78**, 25 (1995).
3. K. C. Kulander, *Phys. Rev. A* **35**, 445 (1987).
4. P. L. DeVries, *J. Opt. Soc. Am. B* **7**, 517 (1990).
5. K. J. LaGattuta, *J. Opt. Soc. Am. B* **7**, 639 (1990).
6. M. R. Hermann and J. A. Fleck, Jr., *Phys. Rev. A* **38**, 6000 (1988).
7. M. S. Pindzola, G. J. Bottrell, and C. Bottcher, *J. Opt. Soc. Am. B* **7**, 659 (1990).
8. L. A. Collins and A. L. Merts, *J. Opt. Soc. Am. B* **7**, 647 (1990).
9. F. H. M. Faisal, *Theory of Multiphoton Processes* (Plenum, New York, 1987), pp. 8–10.
10. D. M. Young and R. T. Gregory, *A Survey of Numerical Mathematics*, Vol. 1 (Addison-Wesley, Reading, MA, 1972), pp. 453–456.
11. M. J. Hagmann, *Int. J. Quantum Chem.* **52**, Quantum Symposium Issue No. 28, 271 (1994).
12. J. Stoer and R. Bulirsch, *Introduction to Numerical Analysis* (Springer-Verlag, New York, 1980), pp. 458–460.
13. D. Macias, S. Brouard, and J. G. Muga, *Chem. Phys. Lett.* **228**, 672 (1994).
14. J. T. Muckerman, R. V. Weaver, T. A. B. Kennedy, and T. Uzer, in *Numerical Grid Methods and their Applications to Schrödinger's Equation*, C. Cerjan, Ed. (Academic, Dordrecht, 1992).
15. M. Büttiker and R. Landauer, *Phys. Scr.* **32**, 429 (1985).
16. M. J. Hagmann, *Int. J. Quantum Chem.* **56**, Quantum Symposium Issue No. 29, 289 (1995).
17. R. Shankar, *Principles of Quantum Mechanics* (Plenum, New York, 1980), pp. 490–492.
18. J. J. Macklin, J. D. Kmetec, and C. L. Gordon III, *Phys. Rev. Lett.* **70**, 766 (1993).
19. P. B. Corkum, N. H. Burnett, and M. Y. Ivanov, *Opt. Lett.* **19**, 1870 (1994).
20. L. D. Landau and E. M. Lifshitz, *Quantum Mechanics*, 2nd ed. (Pergamon, Oxford, 1965), pp. 269–276.
21. R. Landauer and Th. Martin, *Rev. Mod. Phys.* **66**, 217 (1994).
22. C. R. Leavens and G. C. Aers, *Phys. Rev. B* **39**, 1202 (1989); S. Brouard, R. Sala, and J. G. Muga, *Europhys. Lett.* **22**, 159 (1993).
23. R. Landauer and Th. Martin, *Solid State Commun.* **84**, 115 (1992).

Direct Algorithm for the Random-Phase Approximation

V. G. ZAKRZEWSKI, O. DOLGOUNITCHEVA, AND J. V. ORTIZ*

Department of Chemistry, University of New Mexico, Albuquerque, New Mexico 87131; e-mail for J. V. O.: ortiz@nestor.unm.edu

Received February 25, 1996; revised manuscript received March 13, 1996; accepted March 18, 1996

ABSTRACT

An algorithm for calculating excitation energies and transition moments in the random-phase approximation (RPA) of the polarization propagator is presented. The algorithm includes direct solution of the RPA eigenvalue problem and direct evaluation of products of superoperator Hamiltonian matrices with excitation vectors. Given sufficient memory, only one integral evaluation step per iteration is needed. Illustrative calculations on the excitation energies and oscillator strengths of ethylene are presented. © 1996 John Wiley & Sons, Inc.

Introduction

The random-phase approximation (RPA) of the polarization propagator is a clearly defined method for calculating excitation energies and transition moments [1, 2]. It is a convenient point of reference for more ambitious models that consider electron correlation [3]. Efficient implementation of the RPA in accessible and transparent programs can facilitate comparisons with other methods that are in common use. To this end, we present the following report on algorithms, codes, and an illustrative calculation on ethylene.

RPA excitation energies and transition moments obtain from solutions of the generalized eigen-

value problem:

$$E \begin{bmatrix} \langle \mathbf{q}^\dagger | \mathbf{q}^\dagger \rangle & \langle \mathbf{q}^\dagger | \mathbf{q} \rangle \\ \langle \mathbf{q} | \mathbf{q}^\dagger \rangle & \langle \mathbf{q} | \mathbf{q} \rangle \end{bmatrix} \begin{bmatrix} \mathbf{Z} \\ \mathbf{Y} \end{bmatrix} = \begin{bmatrix} \langle \mathbf{q}^\dagger | \hat{H} \mathbf{q}^\dagger \rangle & \langle \mathbf{q}^\dagger | \hat{H} \mathbf{q} \rangle \\ \langle \mathbf{q} | \hat{H} \mathbf{q}^\dagger \rangle & \langle \mathbf{q} | \hat{H} \mathbf{q} \rangle \end{bmatrix} \times \begin{bmatrix} \mathbf{Z} \\ \mathbf{Y} \end{bmatrix}. \quad (1)$$

Single excitation operators in the Hartree-Fock orbital basis are included in the \mathbf{q}^\dagger space and their de-excitation counterparts are found in \mathbf{q} . The superoperator metric, $\langle r | s \rangle$, and the action of the superoperator Hamiltonian, \hat{H} , are defined in the usual manner [4]:

$$\langle r | s \rangle = \langle 0 | r^\dagger s - s r^\dagger | 0 \rangle \quad (2)$$

$$\hat{H}r = rH - Hr, \quad (3)$$

*To whom correspondence should be addressed.

where H is the second quantized Hamiltonian and the reference state $|0\rangle$ is the Hartree-Fock determinantal wave function.

More detailed discussions of the RPA have been presented elsewhere [2, 3]; only essential aspects need be considered here. The eigenvalue problem presented in Eq. (1) is usually written as

$$E \begin{bmatrix} 1 & 0 \\ 0 & -1 \end{bmatrix} \begin{bmatrix} Z \\ Y \end{bmatrix} = \begin{bmatrix} A & B \\ B & A \end{bmatrix} \begin{bmatrix} Z \\ Y \end{bmatrix}. \quad (4)$$

An equivalent formulation takes the form of a nonsymmetric eigenvalue equation:

$$E \begin{bmatrix} Z \\ Y \end{bmatrix} = \begin{bmatrix} A & B \\ -B & -A \end{bmatrix} \begin{bmatrix} Z \\ Y \end{bmatrix}. \quad (5)$$

For every eigenvector obtained from the last equation, there corresponds another solution with an eigenvalue equal in magnitude but opposite in sign:

$$-E \begin{bmatrix} Y \\ Z \end{bmatrix} = \begin{bmatrix} A & B \\ -B & -A \end{bmatrix} \begin{bmatrix} Y \\ Z \end{bmatrix}. \quad (6)$$

Several so-called direct algorithms have been proposed [5-11]. The term *direct* must be understood in two senses. The first refers to direct calculation of excitation energies and transition moments without actual recourse to matrix elements of \hat{H} . Instead, products of the latter matrix with trial vectors are assembled (directly) and reduced eigenvalue problems (or linear equations) are solved [12]. This approach has been applied extensively in configuration interaction calculations. The second sense of the word *direct* implies that electron repulsion integrals are not stored but are reevaluated as needed. Here, we discuss an algorithm that is direct in both senses [13].

Direct solution of eigenvalue problems and linear equations with the paired eigenvalue structure characteristic of the RPA has been discussed recently [5]. Direct treatments of electron repulsion integrals for RPA response properties [6, 7] and excitation energies [8, 9] have emphasized N^4 arithmetic scaling, where N is the number of basis functions. Two other implementations stress the formal convenience of so-called one-index-transformed integrals arising from evaluation of the $\hat{H}\mathbf{q}$ and $\hat{H}\mathbf{q}^\dagger$ commutators [10, 11]. Integral transformations necessarily scale as N^5 , however. The utility of these intermediates remains formal, rather than computational. We therefore present an alternative algorithm that retains N^4 scaling.

A Direct Algorithm

Let i, j, k (a, b, c) denote occupied (virtual) Hartree-Fock orbitals, while Greek indices stand for basis functions. X stands for Y or Z , the \mathbf{q}^\dagger and \mathbf{q} components, respectively, of the eigenvectors. C is the matrix of Hartree-Fock eigenvectors. Finally, we let D stand for matrices with the same dimensions as the A or B matrices of Eqs. (4)-(6). Primes indicate transformation to the primitive basis.

The core of a direct RPA algorithm is evaluation of products of the \hat{H} matrix with trial vectors. Such a contraction is

$$(DX)_{ia} = \sum_{jb} D_{ia,jb} X_{jb}. \quad (7)$$

In terms of basis functions,

$$(DX)_{ia} = \sum_{\mu\nu} C_{\mu i} C_{\nu a} (DX)'_{\mu\nu}, \quad (8)$$

where

$$(DX)'_{\mu\nu} = \sum_{\rho\sigma} D'_{\mu\nu\rho\sigma} X'_{\rho\sigma} \quad (9)$$

and

$$X'_{\rho\sigma} = \sum_{jb} C_{\rho j} C_{\sigma b} X_{jb}. \quad (10)$$

The contraction of Eq. (9) requires generation of primitive electron repulsion integrals only and is the most demanding step.

Spin-projected formulas facilitate separate consideration of singlet and triplet final states for a closed-shell reference state. Let the A matrix in the canonical orbital basis be decomposed into its zeroth- and first-order parts such that

$$A = A^{(0)} + A^{(1)}. \quad (11)$$

For the singlet case,

$$A_{ia,jb}^{(0)} = \delta_{ij} \delta_{ab} (\varepsilon_a - \varepsilon_i), \quad (12)$$

$$A_{ia,jb}^{(1)} = 2(ia|jb) - (ij|ab) \quad (13)$$

and

$$B_{ia,jb} = -2(ia|jb) + (ib|ja), \quad (14)$$

where electron repulsion integrals are expressed in Mulliken notation.

An examination of the permutational symmetry properties of $(\mathbf{A}^{(1)} \pm \mathbf{B})$ shows how these matrices are more suitable intermediates for direct algorithms than \mathbf{A} and \mathbf{B} . In the canonical orbital basis,

$$(\mathbf{A}^{(1)} + \mathbf{B})_{ia, jb} = -(ij|ab) + (ib|ja) \quad (15)$$

and

$$(\mathbf{A}^{(1)} - \mathbf{B})_{ia, jb} = 4(ia|jb) - [(ij|ab) + (ib|ja)]. \quad (16)$$

Analogous expressions in the primitive basis are

$$(\mathbf{A}^{(1)} + \mathbf{B})'_{\mu\nu\rho\sigma} = -(\mu\rho|\nu\sigma) + (\mu\sigma|\nu\rho) \quad (17)$$

and

$$(\mathbf{A}^{(1)} - \mathbf{B})'_{\mu\nu\rho\sigma} = 4(\mu\nu|\rho\sigma) - [(\mu\rho|\nu\sigma) + (\mu\sigma|\nu\rho)]. \quad (18)$$

$(\mathbf{A}^{(1)} + \mathbf{B})'$ is antisymmetric with respect to permutation of indices ρ and σ and $(\mathbf{A}^{(1)} - \mathbf{B})'$ is symmetric with respect to the same permutation. The same properties apply to permutations of μ and ν . While \mathbf{X}' is a square matrix that is neither symmetric nor antisymmetric, contractions with $(\mathbf{A}^{(1)} + \mathbf{B})'$ and $(\mathbf{A}^{(1)} - \mathbf{B})'$ of the type represented by Eq. (9) can be done with the antisymmetric and symmetric parts of \mathbf{X}' , respectively. Only lower triangles of these parts of \mathbf{X}' are needed. The expression for $(\mathbf{A}^{(1)} - \mathbf{B})'$ is identical to the contribution to the closed-shell Fock matrix suggested by Raffanetti [14]; the expression for $(\mathbf{A}^{(1)} + \mathbf{B})'$ corresponds to a second Raffanetti combination used for open-shell calculations. For triplet final states, $(\mathbf{A}^{(1)} + \mathbf{B})'$ remains the same, but for $(\mathbf{A}^{(1)} - \mathbf{B})'$ one finds

$$(\mathbf{A}^{(1)} - \mathbf{B})_{ia, jb} = -[(ij|ab) + (ib|ja)]. \quad (19)$$

In the primitive basis, the matrix elements are

$$(\mathbf{A}^{(1)} - \mathbf{B})'_{\mu\nu\rho\sigma} = -(\mu\rho|\nu\sigma) - (\mu\sigma|\nu\rho), \quad (20)$$

and thus correspond to the Raffanetti format required for complex Hartree-Fock calculations.

All summations pertaining to Eq. (9) can be accomplished using the Gaussian 94 [15] routine FoFDir, which performs direct contractions of various types of Raffanetti combinations with density matrices. These contractions can be executed for a set of vectors through a single call to FoFDir per iteration, provided there is enough memory to store all the necessary matrices. Singlet and triplet transitions are treated separately. Because prod-

ucts of $\mathbf{A}^{(1)} \pm \mathbf{B}$ with \mathbf{Z} may be generated in this procedure, consideration of the eigenvalue problem in the Tamm-Dancoff approximation [TDA or single excitation configuration interaction (CI)],

$$\mathbf{AZ} = \mathbf{EZ}, \quad (21)$$

is accomplished straightforwardly by addition of intermediates, i.e.,

$$\mathbf{A}^{(1)}\mathbf{Z} = \frac{1}{2}(\mathbf{A}^{(1)} + \mathbf{B})\mathbf{Z} + \frac{1}{2}(\mathbf{A}^{(1)} - \mathbf{B})\mathbf{Z}. \quad (22)$$

An alternative approach, suggested in Ref. [16], diagonalizes the product

$$\mathbf{M} = (\mathbf{A} - \mathbf{B})(\mathbf{A} + \mathbf{B}). \quad (23)$$

Two integral evaluation steps instead of one are necessary to perform the contractions

$$(\mathbf{A} + \mathbf{B})\mathbf{X} = \mathbf{F} \quad (24)$$

and

$$(\mathbf{A} - \mathbf{B})\mathbf{F} = \mathbf{M}. \quad (25)$$

This method is used in the TURBOMOLE [8, 9] RPA code.

For the present direct algorithm, intermediates from Eq. (10) must be contracted with the Raffanetti combinations according to Eq. (9). Maximum performance is achieved when as many contractions as possible (depending on memory available) are done in one call to the appropriate routine. The vectors may pertain to different irreducible representations. After performing these contractions, construction of new vectors, and orthogonalizations, errors are introduced which violate symmetry restrictions in the Hartree-Fock orbital basis. These small errors are converted to zeros and the new vectors are renormalized. Solutions of the TDA are used as initial guesses for the \mathbf{Z} components of the RPA guess vectors.

Eigenvalues and eigenvectors are obtained through a generalization of Davidson's method for symmetric eigenvalue problems [12]. This procedure consists of the following steps.

1. A set of guess vectors is chosen such that

$$[\mathbf{Z}^\dagger \quad \mathbf{Y}^\dagger]_p \begin{bmatrix} \mathbf{Z} \\ \mathbf{Y} \end{bmatrix}_q = \delta_{pq}. \quad (26)$$

For example, \mathbf{Z} components of the guess vectors may be TDA eigenvectors, while \mathbf{Y} components are zero vectors. The vectors are

then transformed to the primitive basis according to Eq. (10).

- Contractions represented by Eq. (9) generate $(\mathbf{A}^{(1)} \pm \mathbf{B})\mathbf{X}'$ in the primitive basis. These intermediates are transformed back to the Hartree-Fock basis through Eq. (8). $\mathbf{A}^{(0)}\mathbf{X}$ contributions are then added to produce \mathbf{AZ} , \mathbf{AY} , \mathbf{BZ} , and \mathbf{BY} .
- The projected $\hat{\mathbf{H}}$ matrix is assembled from the previous intermediates according to

$$\hat{H}_{iu} = Z_i^\dagger (AZ)_u + Z_i^\dagger (BY)_u - Y_i^\dagger (BZ)_u - Y_i^\dagger (AY)_u. \quad (27)$$

- Eigenvalues, e , and eigenvectors, W , of the projected $\hat{\mathbf{H}}$ matrix are obtained using routines appropriate for small matrices.
- Eigenvectors, W , having the largest overlaps with previous guesses or solutions are selected.
- Residual vectors, R , are built, such that

$$R = \begin{bmatrix} \mathbf{A} & \mathbf{B} \\ -\mathbf{B} & -\mathbf{A} \end{bmatrix} \begin{bmatrix} W_Z \\ W_Y \end{bmatrix} - e \begin{bmatrix} W_Z \\ W_Y \end{bmatrix}, \quad (28)$$

where e is the eigenvalue pertaining to W .

- Additional expansion vectors, S , are constructed such that

$$S_p = R_p / (e \pm A_{pp}), \quad (29)$$

where the $+$ sign is used for the \mathbf{Y} components of S and the $-$ sign is used for the \mathbf{Z} components.

- The new vectors are orthogonalized to the old vectors and to each other. In the absence of convergence of the eigenvectors and eigenvalues, the algorithm returns to step 2 with an enlarged vector space. These iterations may continue until a maximum number of vectors is reached, whereupon the process returns to step 1.
- After achieving convergence, the solutions are renormalized such that

$$\mathbf{Z}^\dagger \mathbf{Z} - \mathbf{Y}^\dagger \mathbf{Y} = \mathbf{1}. \quad (30)$$

Transition moments are properly normalized in this manner.

Because this procedure solves a nonsymmetric eigenvalue problem, there is always the danger of

obtaining complex solutions. In the present applications, where TDA guesses closely resemble the RPA solutions, this problem has not been in evidence. Iterations on all the vectors are performed simultaneously.

Excitation Energies of Ethylene

Excitation energies of ethylene were calculated using the algorithm presented here. In order to make the results comparable with those published previously [17, 18], we used the geometry optimized at the MP2(Full)/6-31G* level. For the RPA calculations themselves, we used the following basis sets: 6-311(2 + ,2 +)G** from Ref. [17], augmented, correlation-consistent valence double ζ (aug-cc-pVDZ) [19] and two additional basis sets derived from aug-cc-pVDZ. The latter we denote as aug2-cc-pVDZ and aug3-cc-pVDZ; these include one and two additional sets of diffuse s , p , and d atomic orbitals (AOs), respectively. Exponents of the additional diffuse functions were obtained by dividing those from aug-cc-pVDZ by 3.32. The performance of the algorithm and the code is illustrated by the timings given in Table I. In each of these calculations, 15 singlet states were computed and the convergence threshold on the norm of the residual vector was set to 10^{-6} . For the aug-cc-pVDZ basis set, direct contractions were done in one pass and the RPA CPU time is about two times that of the self-consistent field (SCF). With the larger basis sets, two passes were made to test the code, but this choice was not necessary to execute the calculations. The timings indicate that RPA calculations are no less feasible than the SCF step.

Tables II-V compare TDA and RPA excitation energies and oscillator strengths for C_2H_4 with reliable experimental data. RPA results obtained with the 6-311(2 + ,2 +)G** basis set do not differ much from TDA values for transitions assigned as Rydberg states (see entries 1, 2, 4-12, 14, and 15

TABLE I
SCF and RPA CPU time (sec).

Basis Set	Number of AOs	SCF	RPA	Iterations
aug-cc-pVDZ	82	185.6	378.0	7
aug2-cc-pVDZ	116	491.6	1231.7	5
aug3-cc-pVDZ	150	2161.8	8036.0	8

TABLE II
6-311(2 + ,2 +)G** C₂H₄ excitation energies (eV).

Transition	TDA	<i>f</i>	RPA	<i>f</i>	Expt.
1 B _{3u}	7.13	.0913	7.11	.0865	7.11 [20]
2 B _{1g}	7.71	.0000	7.70	.0000	7.80 [22]
3 B _{1u}	7.74	.5127	7.39	.4152	7.60 [20]
4 B _{2g}	7.86	.0000	7.85	.0000	
5 A _g	8.09	.0000	8.07	.0000	8.29 [20]
6 B _{3u}	8.63	.0061	8.63	.0058	8.62 [20]
7 A _u	8.77	.0000	8.77	.0000	
8 B _{3u}	8.93	.0108	8.93	.0099	8.90 [22]
9 B _{1g}	9.09	.0000	9.08	.0000	
10 B _{1u}	9.09	.0544	9.04	.0205	
11 B _{3u}	9.11	.1003	9.10	.0942	
12 B _{2g}	9.18	.0000	9.18	.0000	
13 B _{1g}	9.28	.0000	9.23	.0000	
14 B _{2g}	9.56	.0000	9.56	.0000	
15 A _u	9.65	.0000	9.65	.0000	

in Table II) [20, 21]. However, a significant red shift is observed for the valence ¹B_{1u} state. A smaller shift occurs for the valence $\pi'_{CH_2} \rightarrow \pi^*$ transition to the ¹B_{1g} state (entry 13 in Table II).

RPA vertical excitation energies obtained with the 6-311(2 + ,2 +)G** basis set agree very well with established experimental results for ¹B_{3u}, ¹B_{1u}, ¹B_{1g}, ¹A_g, and ¹B_{3u}. Every transition is described by more than one excited configuration. *D* orbitals are unimportant in describing transitions calculated with the aug-cc-pVDZ and 6-311(2 + ,2 +)G** basis sets, but they can be-

TABLE III
aug-cc-pVDZ C₂H₄ excitation energies (eV).

Transition	TDA	<i>f</i>	RPA	<i>f</i>	Expt.
1 B _{3u}	7.15	.0930	7.13	.0875	7.11 [20]
2 B _{1g}	7.75	.0000	7.74	.0000	7.80 [22]
3 B _{1u}	7.73	.5166	7.38	.4082	7.60 [20]
4 B _{2g}	7.92	.0000	7.92	.0000	
5 A _g	8.80	.0000	8.74	.0000	8.29 [20]
6 A _u	9.00	.0000	8.99	.0000	
7 B _{1g}	9.21	.0000	9.15	.0000	
8 B _{3u}	9.23	.0181	9.24	.0169	8.90 [22]
9 B _{2g}	10.28	.0000	10.17	.0000	
10 B _{1g}	10.47	.0000	10.45	.0000	
11 B _{3g}	10.48	.0000	10.47	.0000	
12 B _{2g}	10.50	.0000	10.48	.0000	
13 B _{3u}	10.52	.1729	10.50	.1711	
14 B _{1u}	10.60	.0800	10.52	.0376	
15 B _{3u}	10.87	.1511	10.83	.1171	

TABLE IV
aug2-cc-pVDZ C₂H₄ excitation energies (eV).

Transition	TDA	<i>f</i>	RPA	<i>f</i>	Expt.
1 B _{3u}	7.12	.0903	7.10	.0851	7.11 [20]
2 B _{1g}	7.70	.0000	7.69	.0000	7.80 [22]
3 B _{1u}	7.71	.4932	7.37	.3996	7.60 [20]
4 B _{2g}	7.85	.0000	7.84	.0000	
5 A _g	8.08	.0000	8.06	.0000	8.29 [20]
6 B _{3u}	8.60	.0017	8.59	.0016	8.62 [20]
7 A _u	8.76	.0000	8.76	.0000	
8 B _{3u}	8.88	.0030	8.88	.0046	8.90 [22]
9 B _{3u}	8.98	.1084	8.97	.0987	
10 B _{1g}	9.04	.0000	9.03	.0000	
11 B _{1u}	9.06	.0483	9.01	.0187	
12 B _{2g}	9.12	.0000	9.11	.0000	
13 B _{1g}	9.21	.0000	9.16	.0000	
14 B _{2u}	9.29	.0855	9.28	.0774	
15 A _u	9.55	.0000	9.55	.0000	

come significant for some states when the other basis sets are used.

The first ¹B_{3u} transition is chiefly a $\pi \rightarrow 3s$ transition.

The order of the next two states, ¹B_{1g}, and ¹B_{1u}, which were almost degenerate in the TDA calculations, is changed in RPA calculations. The gap between the states widens, in agreement with experiment. This change is due to the significant lowering of the ¹B_{1u} excitation energy in the RPA calculations. While the ¹B_{1g} state clearly has Rydberg character ($\pi \rightarrow 3p_y$), the ¹B_{1u} state seems

TABLE V
aug3-cc-pVDZ C₂H₄ excitation energies (eV).

Transition	TDA	<i>f</i>	RPA	<i>f</i>	Expt.
1 B _{3u}	7.12	.0902	7.10	.0851	7.11 [20]
2 B _{1g}	7.70	.0000	7.69	.0000	7.80 [22]
3 B _{1u}	7.71	.4929	7.37	.3996	7.60 [20]
4 B _{2g}	7.85	.0000	7.84	.0000	
5 A _g	8.08	.0000	8.06	.0000	8.29 [20]
6 B _{3u}	8.55	.0023	8.55	.0025	8.62 [20]
7 B _{3u}	8.72	.0586	8.72	.0550	
8 B _{2u}	8.74	.0334	8.74	.0306	
9 A _u	8.76	.0000	8.76	.0000	
10 B _{3u}	8.87	.0169	8.87	.0150	8.90 [22]
11 B _{1u}	9.00	.0360	8.97	.0147	
12 B _{1g}	9.01	.0000	9.00	.0000	
13 B _{2g}	9.08	.0000	9.08	.0000	
14 A _g	9.15	.0000	9.14	.0000	
15 B _{1g}	9.21	.0000	9.16	.0000	

to be a mixture of valence ($\pi \rightarrow \pi^*$) and Rydberg ($\pi \rightarrow 3p_x$) transitions, the contribution of the latter decreasing in the RPA.

There is another pair of neighboring transitions, $^1B_{1g}$ and $^1B_{1u}$ (transitions 9 and 10, Table II), the order of which changes in the RPA calculations. These transitions are described as $\pi \rightarrow np_y$ ($^1B_{1g}$) and $\pi \rightarrow np_x$ ($^1B_{1u}$).

Results obtained with aug-cc-pVDZ are less satisfactory. The first three transitions are in quite good agreement with experiment (both TDA and RPA results), while the higher TDA excitation energies are not acceptable. Augmentation of the aug-cc-pVDZ basis set with diffuse functions changes the results of TDA calculations dramatically, bringing the excitation energies into close agreement with both experimental and 6-311(2 + ,2 +)G** data. TDA energies of the first seven transitions calculated with aug2-cc-pVDZ differ only by 0.01–0.03 eV from those calculated with the 6-311(2 + ,2 +)G** basis set. Changes between aug2-cc-pVDZ and 6-311(2 + ,2 +)G** calculations begin with the ninth final state, which is $^1B_{1g}$ in the latter basis. The energy of $^1B_{1g}$ transition is somewhat lower with aug2-cc-pVDZ. A greater lowering occurs for $^1B_{3u}$ [state 11 in 6-311(2 + ,2 +)G** at 9.11 eV], the energy of which approaches that of the preceding $^1B_{3u}$ state in Table IV.

The $^1B_{2g}$ and $^1B_{1g}$ transitions (12 and 13 in Tables II and IV) have lower energies with the larger basis. The most significant feature of this range of the theoretical spectrum is that a transition of different symmetry (9.29 eV, $^2B_{2u}$) appears before 1A_u which, in its turn, occurs at lower energy (9.55 vs. 9.65 eV), thus pushing the $^1B_{2g}$ transition out of the calculated 15 states. ($^1B_{2g}$ probably would be the next one, had the number of computed states been larger.)

Continued augmentation of the aug-cc-pVDZ basis set with additional diffuse functions has no influence on the energies of the first 5 transitions (Table V). Both TDA and RPA values coincide with those of aug2-cc-pVDZ calculations. The energy of the sixth ($^1B_{3u}$) transition is 0.05 eV lower. Transitions $^1B_{3u}$ and $^1B_{2u}$ occur at 8.72 and 8.74 eV, while the 1A_u energy (8.76 eV) remains the same (see Tables II, IV, and V). The order of transitions at higher energies is changed again, however. A new 1A_g transition appears at 9.14 eV, leaving the B_{2u} (9.29 in aug2-cc-pVDZ, Table IV) and A_u (9.55 in aug2-cc-pVDZ, Table IV) states beyond the limit of 15 calculated transitions. Unlike the

6-311(2 + ,2 +)G** results, pertinent molecular orbitals obtained with aug2-cc-pVDZ and aug3-cc-pVDZ do contain appreciable contributions from d orbitals. Only diffuse d functions with exponents near 0.045 and 0.014 have nonnegligible coefficients in those virtual molecular orbitals to which transitions occur. The $^1B_{2u}$ transition, which is absent in calculations with two smaller basis sets, is described as an excitation to virtual orbitals with pure d character.

Inclusion of additional diffuse functions leads to the appearance of new transitions at lower energies, the increase in the number of configurations describing a given transition, and lower excitation energies for many transitions. The first six singlet states are treated consistently in Tables II, IV, and V and are not likely to be affected by additional diffuse functions.

Conclusions

An algorithm that is direct in both senses discussed in the Introduction has been presented. It retains N^4 arithmetic scaling and is comparable in difficulty with direct SCF methods, therefore. Intermediates dependent on electron repulsion integrals take advantage of efficient techniques for the evaluation of Raffinetti lists. Just one call to the corresponding routines for performing direct contractions with density matrices occurs in each iteration. Only the lower triangles of the symmetric and antisymmetric components of the X' intermediates in the primitive basis are needed. Consistent assignments of the ethylene excitation spectrum have been made.

ACKNOWLEDGMENTS

This work was supported by the National Science Foundation under grant CHE-9321434, the Petroleum Research Fund under grant 29848-AC6, Gaussian, Inc., and Sandia National Laboratory.

References

1. J. Lindenberg and Y. Öhrn, *Propagators in Quantum Chemistry* (Academic Press, New York, 1973).
2. J. Oddershede, *Adv. Chem. Phys.* **69** (Part II), 201 (1987).
3. J. Oddershede, P. Jorgensen, and D. L. Yeager, *Comput. Phys. Rep.* **2**, 33, (1984).

4. O. Goscinski and B. Lukman, *Chem. Phys. Lett.* **7**, 573 (1970).
5. J. Olsen, H. J. Aa. Jensen, and P. Jorgensen, *J. Comp. Phys.* **74**, 265 (1987).
6. M. Feyereisen, J. Nichols, J. Oddershede, and J. Simons, *J. Chem. Phys.* **96**, 2978 (1992).
7. S. P. Karna, *Chem. Phys. Lett.* **214**, 186 (1993).
8. H. Weiss, R. Ahlrichs, and M. Häser, *J. Chem. Phys.* **99**, 1262 (1993).
9. C. Ochsenfeld, J. Gauss, and R. Ahlrichs, *J. Chem. Phys.* **103**, 7401 (1995).
10. H. Ågren, O. Vahtras, H. Koch, P. Jorgensen, and T. Helgaker, *J. Chem. Phys.* **98**, 6417 (1993).
11. H. Koch, H. Ågren, P. Jorgensen, T. Helgaker, and H. J. Aa. Jensen, *Chem. Phys.* **172**, 13 (1993).
12. E. R. Davidson, *J. Comput. Phys.* **17**, 87 (1975).
13. There is a third sense of the word *direct* which is implicit in methods that determine energy differences, such as excitation energies, without considering individual state energies.
14. R. G. Raffanetti, *Chem. Phys. Lett.* **20**, 335 (1973).
15. M. J. Frisch, G. W. Trucks, H. B. Schlegel, P. M. W. Gill, B. G. Johnson, M. A. Robb, J. R. Cheeseman, T. A. Keith, G. A. Peterson, J. A. Montgomery, K. Raghavachari, M. A. Al-Laham, V. G. Zakrzewski, J. V. Ortiz, J. B. Foresman, J. Cioslowski, B. B. Stefanov, A. Nanayakkara, M. Challacombe, C. Y. Peng, P. Y. Ayala, W. Chen, M. W. Wong, J. L. Andres, E. S. Replogle, R. Gomperts, R. L. Martin, D. J. Fox, J. S. Binkley, D. J. Defrees, J. Baker, J. J. P. Stewart, M. Head-Gordon, C. Gonzales, and J. A. Pople, *Gaussian 94*, Gaussian, Inc., Pittsburgh PA, 1995.
16. S. Rettrup, *J. Comp. Phys.* **45**, 100 (1982); Aa. E. Hansen, B. Voigt, and S. Rettrup, *Int. J. Quant. Chem.* **23**, 595 (1983).
17. C. M. Hadad, J. B. Foresman, and K. B. Wiberg, *J. Phys. Chem.* **97**, 4293 (1993).
18. M. Head-Gordon, R. J. Rico, M. Oumi, and T. Lee, *Chem. Phys. Lett.* **219**, 21 (1994).
19. T. H. Dunning, *J. Chem. Phys.* **90**, 1007 (1989).
20. M. Robin, *Higher Excited States of Polyatomic Molecules* (Academic Press, New York, 1985).
21. K. B. Wiberg, C. M. Hadad, J. B. Foresman, and W. A. Chupka, *J. Phys. Chem.* **96**, 10756 (1992).
22. A. Gedanken, N. A. Kuebler, and M. B. Robin, *J. Chem. Phys.* **76**, 46 (1982).



605 Third Avenue
New York, NY 10158-0012
212.850.6000
FAX 212. 850.6088

John Wiley & Sons, Inc.
Publishers Since 1807

January 22, 1997

To our subscribers and authors:

We have realized that the page numbering system that was employed in Volume 60, Numbers 7 and 8, 1996, of the *International Journal of Quantum Chemistry* would lead to problems and confusion regarding citations. To alleviate these potential problems we are reprinting these issues with page numbers following the conventional page numbering system for the *Journal*.

We apologize for any inconvenience our error has caused you. Please accept the enclosed copies of the reprinted issues with our compliments and discard the copies you previously received.

Please contact Customer Service at (212) 850-6645, fax (212) 850-6021 or e-mail subinfo@wiley.com if you have any questions concerning your subscription to *International Journal of Quantum Chemistry*.

Sincerely,

Jacqueline I. Kroschwitz
Publisher

Computation of Curve-Crossing Diagrams by Approximate Valence Bond Method

LUIS RINCÓN

Departamento de Química, Facultad de Ciencias, Universidad de Los Andes, Mérida-5101, Venezuela

Received March 25, 1996; accepted July 29, 1996

ABSTRACT

Avoided crossing diagram parameters for the radical exchange reaction and the concerted exchange of two and three bonds are computed by using the approximated valence bond method, which is a nonorthogonal configuration interaction (CI) semiempirical method among the valence bond configuration functions. Here, each valence bond configuration function is a spin-adapted combination of Slater determinants constructed from the Heitler–London or Coulson–Fischer hybrid orbitals. Atomic orbitals integrals are evaluated using semiempirical philosophy, and these provide considerable saving of computer time compared with the most standard *ab initio* multistructure valence bond methods. The results indicate that the approximate valence bond method is capable of yielding reasonable results for the avoided crossing diagram parameters. These results also indicate that the diagram gap (G) is the decisive factor for the stability of symmetric clusters, X_n , although no clear correlation between the gap G and the geometric distortion is found for different values of n . © 1996 John Wiley & Sons, Inc.

Introduction

Valence bond (VB) calculations provide us with useful information about the structure and physical properties of organic and inorganic molecules. *Ab initio* VB theory has been extensively developed in the last years, representative examples are the generalized VB method (GVB) of Goddard [1], the resonating GVB method (RGVB)

of Voter and Goddard [2], the spin-coupled VB method (SCVB) of Cooper, Gerratt, and Raimondi [3], the spin-free VB method (SFVB) of McWeeny [4], the biorthogonal VB method (BVB) of McDouall [5], and the new SFVB method proposed by Li and Wu [6]. In spite of considerable advances, such methods are currently slow, and their routine application for many systems of chemical interest is still not practical. The use of a nonorthogonal set of orbital remains the major difficulty of such kinds of VB calculation. A few semiempirical VB

methods have also been proposed [7]. In all of these semiempirical methods, the zero differential overlap (ZDO) approximation has been used for the integral evaluation and for the simplification of the nonorthogonal matrix elements of the Hamiltonian. The use of the ZDO approximation is apparently contradictory with the VB philosophy, since it is well known that the use of an orthogonal set of atomic orbitals has been incapable of predicting the chemical bonding [8]. In order to overcome this contradiction, many of the semiempirical ZDO-VB calculations have been implemented using the so-called overlap-enhanced atomic orbitals (OEAO). Although the use of OEAO produce a nonorthogonal set of hybrid orbitals, the contradiction due to impose the ZDO approximation remains. Here we want to emphasize that an approximate valence bond (AVB) method, without the ZDO assumption, is more consistent with the spirit of the VB theory. It is the purpose of this communication to outline one possible AVB formalism without the ZDO approximation. In these preliminary calculations, this method will be used to compute the reactivity parameters of curve-crossing VB diagrams [9, 10] for the linear radical exchange reaction [Fig. (1a)] and the concerted exchange of two and three bonds shown in Figures 1(b) and (c). As representative test cases, we have selected three different atomic systems representing one orbital for one center, $X = \text{H}(1s)$, $\text{Li}(2s)$, and $\text{Li}(2p_\pi)$.

Some of this system has been studied by Maitre and co-workers [11] using ab initio multistructure VB method to understand the stability of small atomic clusters, a problem that is closely related to the concept of aromaticity [12].

Approximate Valence Bond Method

This communication deals with an approximate method for calculating VB wave function for valence electrons of a molecule. The molecular wave function, Φ , is expanded as a linear combination of VB configuration function, $\{\phi_i\}$,

$$\Phi = \sum_i c_i \phi_i. \quad (1)$$

Each VB configuration function can be represented as a single VB resonance structure or a linear combination of these and can be written in the form

$$\phi_i = \frac{1}{\sqrt{N!}} \mathcal{A} [\Omega_\kappa \Theta_{SM,k}^N]. \quad (2)$$

The spatial factor, Ω_κ , is a product of nonorthogonal hybrid orbitals, where the subindex κ indicates a particular configuration. For a particular configuration, $\Theta_{SM,k}^N$ is one of N -electron spin eigenfunctions of \hat{S}^2 and \hat{S}^z with eigenvalue $S(S$

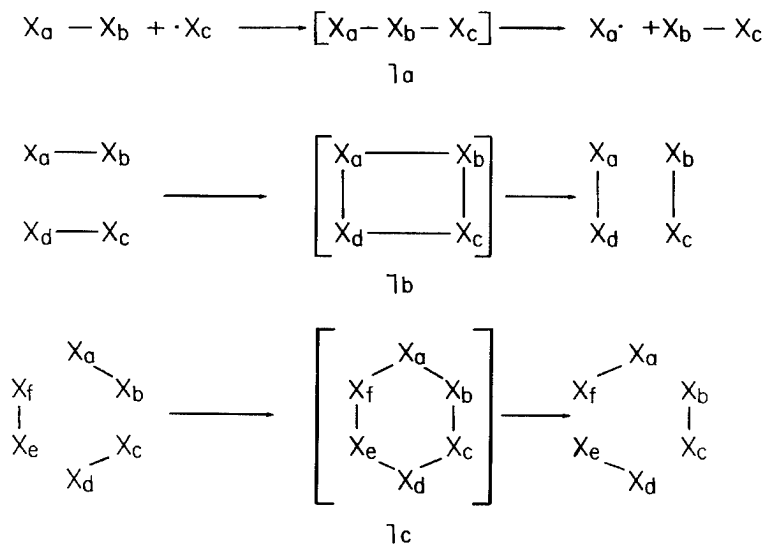


FIGURE 1. (a) Linear radical exchange reaction; (b) D_{4h} -concerted exchange of two-bond exchange; (c) D_{6h} -concerted three-bond exchange.

+ 1) and M , respectively. In order to obtain a chemical interpretation of the final wave function, the Rumer spin function is used [13]. Using the properties of the antisymmetrizer, \mathcal{A} , the term $\mathcal{A}[\Omega_\kappa \Theta_{SM,k}^N]$ will be expressed as a linear combination of 2^p Slater determinants, where p is the number of covalent bonds in the configuration κ . The VB wave function yields, after minimizing the total energy, the secular matrix equation $[H][C] = [S][C][E]$, where the elements of the $[H]$ and $[S]$ matrix are defined by $H_{KL} = \langle \phi_K | \hat{H} | \phi_L \rangle$ and $S_{KL} = \langle \phi_K | \phi_L \rangle$, respectively. The matrix elements between VB structures are given in terms of matrix elements between nonorthogonal Slater determinants.

In the computational strategy two problems must be addressed: an efficient scheme for evaluation of matrix elements between nonorthogonal Slater determinants and the optimization of the orbitals to be used in the wave function. These are the crucial problems in the implementation of the VB theory. The matrix elements between VB structures are computed by means of the Löwdin cofactor formula [14], using the factorized cofactor-driven algorithm developed by Raimondi and co-workers [15], which results in important savings in computer time. Let us now consider the choice of hybrid orbitals. We distinguish two types of hybrid orbitals. First, the atomic Heitler–London (HL) hybrids orbitals, which in the case of H and Li atoms correspond to the atomic basis. Second, the Coulson–Fischer (CF) hybrid orbitals [16]. In the CF orbitals the HL orbitals must be allowed to deform and delocalized onto other nuclear centers. This delocalization is implemented here by using a unique variational parameter that allows one to mix HL orbitals in a nucleus different from the reference one, with a weight proportional to the overlap integral. This scheme reduces the optimization problem to one parameter. As is shown in the next section, this scheme is essential for a compact representation of the curve-crossing diagrams for the reaction of Figure 1.

At this point a discussion of the semiempirical approximation is appropriated. The task now is to discuss the manner in which atomic orbital integrals can be computed, and the objective is that the approximate integrals should reproduce the atomic integrals as accurately as possible in each point of the nuclear configuration space. This method uses a basis set of Slater-type orbitals (STO). Once the configuration functions are generated, the superposition integral and the cofactor of

the Löwdin formula are evaluated without approximation. In a typical calculation, the evaluation of cofactors require about 80% of CPU time. After some manipulation, the expression for the diagonal one-electron atomic integral, H_{kk} , becomes

$$H_{kk} = U_{kk}^A - \sum_{B \neq A} V_{kk}^B, \quad (3)$$

both U_{kk}^A and V_{kk}^B are approximated as in the CNDO/1 parametrization of Pople and co-worker [17, 18]. This approximation can be justified without any introduction of the ZDO approximation. By using a modification of the standard Mulliken approximation, the one-electron nondiagonal terms, H_{kl} , are approximated as

$$H_{kl} = \beta_{kl}^0 S_{kl} + \beta_{kl}^1 w_{kl}^2 \exp(-w_{kl}), \quad (4)$$

where β_{kl}^0 and β_{kl}^1 are empirical parameters derived from the equilibrium bond length and dissociation energy of diatomic homonuclear molecules, $w_{kl} = \alpha_{kl} R_{kl}$, with $\alpha_{kl} = 0.5(\xi_k + \xi_l)$, ξ_k and ξ_l are the exponents of the orbitals k and l , R_{kl} are the bond distances between the center of orbitals k and l , and S_{kl} is the overlap integral. This approximation requires some comments. In the first version of this method, we tried to implement the standard Mulliken approximation, proportional to the overlap integral. However, with this approximation it was impossible to obtain good prediction both for the equilibrium bond length and dissociation energy for the simple case of H_2 . The H_2 molecule is very instructive, since with the exception of the nondiagonal elements, H_{kl} , the rest of the integrals are evaluated without approximation. Then, it is clear in this case that the error in the parametrization is due to H_{kl} . The exact form of H_{kl} for the H_2 molecule is

$$H_{kl} = \frac{\alpha - 4\alpha^2}{2} S_{kl} + \frac{-\alpha^2 + 2\alpha}{3} w_{kl}^2 \exp(-w_{kl}), \quad (5)$$

where α is the orbital exponent of hydrogen and the rest of the terms have the same meaning as in Eq. (4). Equation (4) is a generalization of the result for the H_2 molecule; the use of this equation is perhaps a better approximation than other semiempirical formulas for H_{kl} . All three- and four-center integrals are equal to zero, and it is assumed that the two- and one-center integrals depend only upon the nature of the atom and

not upon the nature of the orbitals involved. We only have computed one type of one-center-two-electron integral for each atom: $(AA|AA)$, and four types of two-center-two-electron integral for each diatomic pair: $(AA|BB)$, $(AA|AB)$, $(AB|BB)$, and $(AB|AB)$. Furthermore, the requirements of space invariance are fulfilled by treating all the integrals as if they only involved spherically symmetric orbitals.

Avoided Crossing Diagrams

The construction of avoided crossing diagrams (ACD) has been discussed in great detail by Shaik and Pross [9, 10], therefore only a brief description is presented here. ACD for the single-step chemical reaction $R \rightarrow P$ is shown in Figure 2. This diagram consists of two *diabatic* curves as a function of an abstract reaction coordinate, one for a reactant VB configuration, E_R , and other for the product VB configuration, E_P . The avoided crossing of these two curves generate two *adiabatic* curves, denoted by dashed lines. The crossing point corresponds in a good approximation to the transition state, i.e., the point where the formation of the new bonds compensates for the breaking of the old ones [19].

Following the Shaik-Pross theory, the activation energy can be characterized by three quanti-

ties. The first quantity is the vertical energy gap G . This parameter is the energy required for the electronic reorganization that converts the reactant configuration to the product configuration at the geometry of the reactant. The second quantity is the height of the crossing point (ΔE_c) which can be expressed as a fraction (f) of the gap G ; that is

$$\Delta E_c = fG. \quad (6)$$

The fraction f depends on the curvature of the reactant and product *diabatic* curves. The third quantity is the degree of avoided crossing B . This is the *quantum mechanical resonance energy* at the transition state. The reaction barrier can be expressed in terms of these three quantities and reads:

$$\Delta E^\# = fG - B. \quad (7)$$

The intersection point of *diabatic* states corresponds to the symmetric geometry of the X_n systems in Figure 1. The energy of the avoided curve in this point, relative to the minimum energy point of the reactant and product *diabatic* curves, is determined by two opposing factors. One is the energy to reach the cross point, which is due to the geometrical distortion of the reactant in order to achieve the crossing point. This energy depends both on the electronic gap G and the curvature factor f . The second factor is the resonance interaction. Equation (7) expresses this balance in a quantitative form. Shaik and co-workers [12] have postulated that the variation in the energy gap G dominates the other factors of Eq. (7). Thus, for a large G , the symmetric geometry of the X_n clusters is expected to be unstable as in 2 of Figure 3. In the case of a small gap, the symmetric geometry is stable as in 3 of Figure 3. We would like to note that explicit calculations of reactivity parameters,

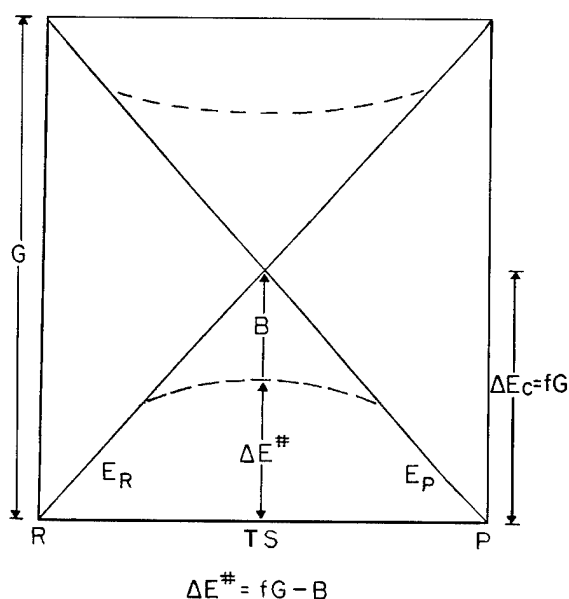


FIGURE 2. Curve-crossing diagram.

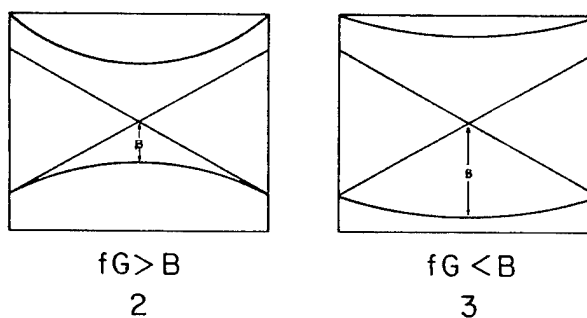


FIGURE 3. Avoided curve-crossing diagrams. The resonance interaction is B .

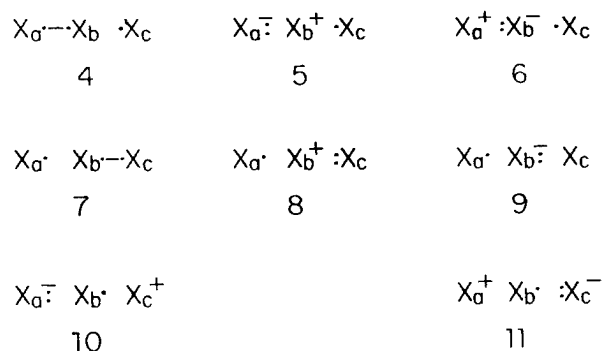


FIGURE 4. Classical VB resonance structures for three atoms / three orbitals.

f , G , and B for an ample spectrum of reactions, are scarce in the literature.

We now discuss how to construct the ACD for reactions of Figure 1. Consider the reaction **1a**. If one atomic orbital per atom is used (a , b , c), then eight classical resonance structures are obtained (Fig. 4). Three of these structures correspond to reactant (4–6), three to product (7–9), and two participate in the resonance at intermediate points in the reaction coordinate (10–11). These eight structures can be included in the ACD in a succinct form using CF hybrid orbitals described in the previous section. Using the Heitler–London spin coupling of the reactant (4) and the product (7), the wave function for the *diabatic* configuration may be constructed as:

$$\phi_R = |X_a^R \bar{X}_b^R X_c^R| - |\bar{X}_a^R X_b^R X_c^R|, \quad (8)$$

for reactant, and

$$\phi_P = |X_a^P X_b^P \bar{X}_c^P| - |X_a^P \bar{X}_b^P X_c^P|, \quad (9)$$

for the product. The electron of the reactant VB configuration function occupy the CF orbitals

$$\begin{aligned} X_a^R &= a + \epsilon \langle a|b \rangle b, \\ X_b^R &= b + \epsilon \langle a|b \rangle a, \\ X_c^R &= c, \end{aligned} \quad (10)$$

and similar orbitals for the product VB configuration function:

$$\begin{aligned} X_a^P &= a, \\ X_b^P &= b + \epsilon \langle b|c \rangle c, \\ X_c^P &= c + \epsilon \langle b|c \rangle b. \end{aligned} \quad (11)$$

Here ϵ is a unique variational parameter of the CF orbitals. If $\epsilon = 0$ the orbitals of the reactant, Eq. (10) and the product, Eq. (11) are the same, and the configuration function of Eqs. (8) and (9) is reduced to the HL configuration of reactant (4) and product (7), respectively. In the case of $\epsilon \neq 0$, the inclusion of orbitals [Eq. (10)] in the reactant configuration function only increases the ionic contribution of the reactants, (5) and (6), in the form

$$\phi_R = (1 - \epsilon^2 \langle a|b \rangle^2) 4 + \epsilon \langle a|b \rangle (5 + 6). \quad (12)$$

The CF orbitals of Eq. (11) have a similar effect on the product configuration function. As can be seen, the weight of ionic structures depend on the overlap integrals between the covalent bond of the HL structure and the variational parameter ϵ . The intermediate structures (10) and (11) of Figure 4 can be included, if the central orbital, both in the reactant and the product configuration function, is replaced by

$$X_b^R = X_b^P = b + \epsilon (\langle a|b \rangle a + \langle b|c \rangle c). \quad (13)$$

This scheme is closely related to the VB symbolism of Harcourt [20], based on the concept of *increase-valence structures*. A generalization of this method is used for calculation of the reactivity parameters in the reactions of Figure 1.

Results and Discussion

A summary of the parametrization is presented in Table I. The results of dissociation energy and geometry optimization compare well with the experimental values for the H_2 ($D_e = 109.5$ kcal/mol and $r_e = 0.746$ Å) and the Li_2 ($D_e = 24.16$ kcal/mol and $r_e = 2.67$ Å). On the other hand, our results are in moderate agreement with the full CI calculation of Shaik and Hiberty [21] for these systems: H_2 ($D_e = 128.1$ kcal/mol, $\Delta E_{ST} = 384.4$ kcal/mol and $r_e = 0.735$ Å), $Li_2(s)$ ($D_e = 11.0$ kcal/mol, $\Delta E_{ST} = 25.2$ kcal/mol and $r_e = 2.872$ Å), and $Li_2(\pi)$ ($D_e = 13.4$ kcal/mol, $\Delta E_{ST} = 47.7$ kcal/mol and $r_e = 2.193$ Å). We think that there are many refinements to make in the model, however, our main interest at this moment is to explore whether or not this crude parametrization works well.

The reactivity parameters for the reactions of Figure 1 are shown in Table II for the HL ($\epsilon = 0$) and the CF orbitals. We also report the symmetric geometry distance, R_e , and two reactivity index:

TABLE I
Summary of parametrization.^a

X_2	HO	IP (eV)	OE	β^0	β^1	r_e (Å)	D_e (kcal/mol)	ΔE_{ST} (kcal/mol)
H_2	CF	13.6	1.20	-1.68	0.32	0.75	109.4	338.22
	HL	13.6	1.20	-1.68	0.32	0.74	105.5	329.23
$Li_2(s)$	CF	5.4	0.65	-0.60	1.16	2.88	35.5	77.85
	HL	5.4	0.65	-0.60	1.16	2.66	32.9	76.11
$Li_2(\pi)$	CF	3.5	0.65	-0.60	1.16	1.88	44.3	100.82
	HL	3.5	0.65	-0.60	1.16	1.80	39.7	96.15

^aHO, type of hybrid orbital; IP, ionization potential; OE, orbital exponent. For β^0 and β^2 see text. r_e , equilibrium bond distance; D_e , dissociation energy, ΔE_{ST} ; singlet-triplet excitation energy.

(i) a distortion index, $[R_e - r_e/r_e]$, which is the relative lengthening of the diatomic bond to achieve the symmetric structure, and (ii) a resonance index, $[B/\Delta E_c]$, which is the relative importance of the quantum mechanical resonance energy in the stability of the symmetric X_n clusters.

The CF results for the collinear reaction **1a** are in reasonable agreement with the VB calculation of Maitre et al. [11] for the case of H ($\Delta E^\# = 15.3$ kcal/mol, $G = 156.6$ kcal/mol, $f = 0.37$, and $B = 42.4$ kcal/mol) and Li ($\Delta E^\# = -3.8$ kcal/mol, $G = 22.4$ kcal/mol, $f = 0.13$, and $B = 6.6$ kcal/mol). To our knowledge, no quantitative calculation of the reactivity parameters (G , f , and B) have yet been performed for the rest of the reactions in Figure 1. The estimated activation energy and optimized geometry for the three-bond exchange reaction are in general higher than the ab initio value of Shaik and Hiberty [21]: H_6 ($\Delta E^\# = 109.3$ kcal/mol, $R_e = 0.9886$ Å), $Li_6(s)$ ($\Delta E^\# = +0.04$ kcal/mol, $R_e = 3.0717$ Å) and $Li_6(\pi)$ ($\Delta E^\# = +27.4$ kcal/mol, $R_e = 2.7718$ Å). Comparison with some ab initio calculations for the two-bond exchange reaction also shows higher values for the activation energy and equilibrium geometry [22]. Considering the smallness of the atomic orbital (AO) basis set used and the neglect of the three- and four-center two-electron integrals, it is not surprising that these estimates differ considerably from the ab initio results.

Two clear correlations emerge from Table II. The first is the strong relationship between the energy gap G , the energy of the crossing point ΔE_c , and the activation energy $\Delta E^\#$. This result shows that the gap G is the factor that governs the stability of the symmetric structures; this relationship has already been derived within VB approach

by Maitre et al. [11] and Shaik et al. [12]. The second is the relationship between the curvature factor f and the geometric index $\Delta r/r$. Finally, no clear correlation with the resonance index is found, although it is apparent that the *quantum mechanical resonance energy* is underestimated in this calculation.

The results given in Table II show that G is proportional to the number of bonds broken. Then for a given atom, X , the value of the gap increase in the order, $X_6 > X_4 > X_3$. This is the same order for ΔE_c and $\Delta E^\#$. Also, the energy gap increases in the order: $H > Li(\pi) > Li(s)$. As is shown in Table I, this is the same order for the dissociation energy and the singlet-triplet excitation energy of the X_2 bond. This result agrees with the analysis of Maitre et al. [11]; they have found that G follows the relation

$$G = \left(\frac{3}{4}\right)n\Delta E_{ST}, \quad (14)$$

where n is the number of bonds broken in the process. The previous equation works relatively well both for HL and CF orbitals. In general, the deviation of this equation is greater for H than for Li due to the neglect of the AO overlap in the derivation of Eq. (14).

Table II shows a strong correlation between the curvature factor f and the geometric index. These factors increase in the order $X_4 > X_6 > X_3$. The value of f reveals a parabolic curvature of the *adiabatic* curves for the case of X_3 ($f < 0.5$), semi-linear for X_6 ($f \sim 0.5$), and exponential for X_4 ($f > 0.5$). The tendency of the symmetric X_4 cluster for higher geometric distortion is well documented in many four-member rings. Therefore, no trivial correlation exists between the geometric

Evaluation of the Alpha-Function for Large Parameter Values

H. W. JONES AND J. L. JAIN

Department of Physics, Florida A & M University, Tallahassee, Florida 32307

Received March 28, 1996; accepted April 24, 1996

ABSTRACT

In carrying out our plan for doing multicenter molecular integrals over Slater-type orbitals, it is necessary to evaluate the Löwdin α -function over a grid from the origin of the coordinate system to the displacement distance of the center of the orbital. A previous article obtained excellent results by expanding the exponentials in the α -function, for both interior and exterior regions. However, if the displacement distance multiplied by the screening constant, i.e., the ζa parameter, is larger than 16, we suggest that it may be more efficient in time and storage if we use the closed formula for the α -function for values of the radial distance r greater than 8. This remarkable rule of thumb was tested for a variety of orbitals up to $\zeta a = 64$ and one to $\zeta a = 128$. Also, in the exterior region, the formula may always be used if $\zeta a \geq 16$. This strategy necessitates using the formula in quadruple precision arithmetic. © 1996 John Wiley & Sons, Inc.

Introduction

We continue to fill in the details that will make the Löwdin α -function method capable of dealing with all the kinds of Slater-type orbitals (STOs) needed for problems in quantum chemistry. In a companion article [1], the case of small values for (ζa), namely, $\zeta a < 16$, where ζ is the screening constant of an orbital and a is its displacement from the origin of the working coordinate system, was examined. The exponentials in the α -functions were expanded and the number of terms needed for acceptable accuracy were noted for various orbital parameters. In this article, to

evaluate an α -function over a grid when $r < a$, we show that it is expedient and efficient when $\zeta a > 16$ to deal with the closed formula for the α -function. Of course, in the region of the orbital when $r \ll a$, we are compelled to again use expanded exponentials. In Table I, we tabulate this crossover point for a variety of orbitals and their harmonics. We note that the evaluation of our closed formulas always results in a loss of significant figures due to cancellation errors. Our aim was to work with numbers accurate to the 16 decimal digits (double precision) on our Silicon Graphics Power Challenge). To achieve this, we started with 32 digit numbers (quadruple precision), and to be conservative, we determined the value of r when 12 digits are sacrificed. Below this value, the α -func-

TABLE I

Switch over value of r when the closed formula is valid; $r < a$; (ζa) = 16.

Orbitals	l	r	Orbitals	l	r	Orbitals	l	r
100	0	1	411	1	1	521	1	1
	4	1		4	1		4	1
	8	2		8	2		8	2
	12	4		12	5		12	6
200	0	1	420	0	1	522	2	1
	4	1		4	1		4	1
	8	2		8	2		8	2
	12	5		12	5		12	6
210	0	1	421	1	1	530	0	1
	4	1		4	1		4	1
	8	2		8	2		8	2
	12	4		12	6		12	5
211	1	1	422	2	1	531	1	1
	4	1		4	1		4	1
	8	2		8	2		8	2
	12	4		12	5		12	7
300	0	1	430	0	1	532	2	1
	4	1		4	1		4	1
	8	2		8	2		8	2
	12	5		12	6		12	6
310	0	1	431	1	1	533	3	1
	4	1		4	1		4	1
	8	2		8	2		8	2
	12	5		12	6		12	5
311	1	1	432	2	1	540	0	1
	4	1		4	1		4	1
	8	2		8	2		8	2
	12	5		12	5		12	6
320	0	1	433	3	1	541	1	1
	4	1		4	1		4	1
	8	2		8	2		8	2
	12	5		12	6		12	7
321	1	1	500	0	1	542	2	1
	4	1		4	1		4	1
	8	2		8	2		8	2
	12	5		12	7		12	6
322	1	1	510	0	1	543	3	1
	4	1		4	1		4	1
	8	2		8	2		8	2
	12	5		12	6		12	6
400	0	1	511	1	1	544	4	1
	4	1		4	1		8	2
	8	2		8	2		12	6
	12	6		12	6			
410	0	1	520	0	1			
	4	1		4	1			
	8	2		8	2			
	12	6		12	7			

tion is evaluated by expansion; above this value, the α -function is evaluated by a closed formula.

The α -Function

A complex STO $\chi = AR^{N-1}e^{-\zeta R}Y_L^M(\Theta, \phi)$ in its local coordinate system (R, Θ, ϕ) has its origin displaced to $(0, 0, a)$ in the working coordinate system (r, θ, ϕ) . Its expansion in spherical harmonics is [2, 3]

$$\chi = \frac{A}{\zeta^{N-1}} \left[\frac{(2L+1)(L+M)!}{4\pi(L-M)!} \right]^{1/2} (-1)^M \times \sum_{l=M}^{\infty} \left[\frac{4\pi(l+M)!}{(2l+1)(l-M)!} \right]^{1/2} \times \alpha_l^{NLM}(\zeta a, \zeta r) Y_l^M(\theta, \phi). \quad (1)$$

Interior Evaluation of the α -Function

The α -function for $r < a$ is given by

$$\alpha_l^{NLM}(\zeta a, \zeta r) = \frac{(2l+1)(l-M)!}{2(l+M)!} \times \sum_{i=0}^{i\text{stop}} \sum_{j=0}^{j\text{stop}} C_l^{NLM}(i, j) \cdot H_{ij} \cdot (\zeta a)^{i-L-l-1} (\zeta r)^{j-l-1}, \quad (2)$$

with

$$H_{ij} = e^{-\zeta a} [(-1)^j e^{\zeta r} - e^{-\zeta r}].$$

and

$$i\text{stop} = N + L + l - M$$

and

$$j\text{stop} = N + l.$$

For efficiency in programming, we reduce the double sum to a single sum by the introduction of one-dimensional matrices $T_l(j)$ [4]:

$$\alpha_l^{NLM}(\zeta a, \zeta r) = \sum_{j=0}^{N+l} T_l(j) [(-1)^j e^{\zeta r} - e^{-\zeta r}] r^{j-l-1}, \quad (3)$$

with

$$T_l(j) = \frac{(2l+1)(l-M)!}{2(L+M)!} e^{-\zeta a} \cdot \zeta^{j-l-1} \times \sum_{i=0}^{i\text{stop}} C_l^{NLM}(i, j) \cdot (\zeta a)^{i-L-l-1}. \quad (4)$$

Although the C-matrix elements increase explosively with the harmonic l [5], they can be brought under control with sufficiently large values of r and (ζa) . The price is the loss of significant digits. In our aim to achieve 16-digit accuracy, we start with quadruple precision of 32 digits and, to be conservative, find the lowest value of r that will result in a loss of only 12 digits of accuracy. These switch-over values are tabulated in Table I. Hence, for r less than this value, we evaluate the α -function by the expansion method using an E-matrix. For r greater than this value, we may use the closed formula in quadruple precision.

We note that the expansion method is very reliable, having been tested for 1s orbitals ($l=0$) to $\zeta a = 128$ with $j_{\text{max}} = 238$. However, for efficiency and to minimize storage requirements for the E and F matrices, the closed formula approach should be considered. To avoid a profusion of "IF" statements in our programming implied by Table I, it was decided to just have one condition: If $r < 8$, use the expansion method, and if $r > 8$, use the formula. This is surprisingly valid at least up to $\zeta a = 64$. In all cases of $\zeta a < 16$, use the expansion method.

Exterior Evaluation of the α -Function

The situation is much clearer for the $r > a$ case in the evaluation of the α -function. We start with the exterior definition of H_{ij} :

$$H_{ij} = e^{-\zeta r} [(-1)^i e^{\zeta a} - e^{-\zeta a}].$$

Again, the double sum is changed to a single sum by the introduction of a one-dimensional matrix $X_l(j)$:

$$X_l(j) = \frac{(2l+1)(l-M)!}{2(l+M)!} \zeta^{j-l-1} \sum_{i=0}^{i\text{stop}} C_l^{NLM}(i, j) \cdot [(-1)^i e^{\zeta a} - e^{-\zeta a}] \cdot (\zeta a)^{i-L-l-1}. \quad (5)$$

Then,

$$\alpha_l(\zeta a, \zeta r) = e^{-\zeta r} \sum_{j=0}^{N+l} X_l(j) \cdot r^{j-l-1}. \quad (6)$$

We recall the definition of the $Z_l(j)$ matrix obtained by the expansion of $\exp(\zeta a)$ and $\exp(-\zeta a)$:

$$Z_l(j) = \zeta^{j-l-1} \sum_{i=i_{\text{start}}}^{i_{\text{max}}} F_l^{NLM}(i, j) \cdot (\zeta a)^i; \quad (7)$$

Then,

$$\alpha_l(\zeta a, \zeta r) = e^{-\zeta r} \sum_{j=0}^{N+l} Z_l(j) \cdot r^{j-l-1}. \quad (8)$$

As an update, we found by numerical experimentation, that $i_{\text{start}} = |l - L|$ and that only nonzero values occur in the summation at every other position starting with i_{start} , i.e., the i index starts at i_{start} and proceeds in steps of two.

The form of the α -function is the same whether $X_l(j)$ or $Z_l(j)$ is used. We have found that the closed formula at quadruple precision is adequate for all the orbitals in Table I with $(\zeta a) \geq 16$ and up to at least $\zeta a = 64$. Multicenter integrals in the exterior region may be done analytically, since all the exponentials have negative arguments.

Conclusion

We have made it plausible that the α -function can be dealt with in its closed formula form and in its expanded form; the two expressions of the α -function complement each other. Hence, we state that the α -function method can be applied to all orbitals of chemical interest.

ACKNOWLEDGMENTS

Partial support was provided by NASA (CeN-NAs), by the ONR Contract N00014-95-1-0614, and by the AHPARC Cooperative Agreement DAAH04-95-2-0003 under Contract Number DAAH04-95-C-0008.

References

1. H. W. Jones, Int. J. Quantum Chem. (in press).
2. H. W. Jones and C. A. Weatherford, Int. J. Quantum Chem. Symp. **12**, 483 (1978).
3. H. W. Jones, Phys. Rev. A **30**, 1 (1984).
4. H. W. Jones, Int. J. Quantum Chem. **42**, 779 (1992).
5. A. Bouferguene and D. Rinaldi, Int. J. Quantum Chem. **50**, 21 (1994).

Nonadiabatic Treatment of Molecular Systems by the Wavepackets Method

H. NAGAO, K. KODAMA, Y. SHIGETA, AND K. NISHIKAWA

Department of Chemistry, Faculty of Science, Kanazawa University, Kanazawa 920-11, Japan; e-mail for K.N.: kiyoshi@wiron1.s.kanazawa-u.ac.jp

H. KAWABE

Secretarial Department, Kinjo College, Matto 924, Japan

M. NAKANO AND K. YAMAGUCHI

Department of Chemistry, Faculty of Science, Osaka University, Toyonaka 560, Japan

Received February 24, 1996; revised manuscript received June 24, 1996; accepted June 25, 1996

ABSTRACT

We have already developed the many-electron wavepackets (MEWP) method in order to study the dynamics and electronic structure of molecular systems. We extended the MEWP method to study the nonadiabatic effects and formulated a nonadiabatic molecular theory, where both electron and nucleus are treated equivalently. Then we applied our method to the isotope series of hydrogen molecule i.e., H_2 , HD, and D_2 , and calculated the total energy and the average distance between nucleus-nucleus, electron-electron, and nucleus-electron in order to analyze numerically the nonadiabatic effect in the molecule. Finally we calculated the real-time evolution of the polarization by means of Chebyshev scheme; and by Fourier transforming this, we found out the excitation spectrum of the system, which corresponds to the electronic excitation and the nuclear vibrational frequency. © 1996 John Wiley & Sons, Inc.

Introduction

The time-dependent formulation is an extremely important tool in the field of molecular dynamics [1, 2]. We have already developed the many-electron wavepacket (MEWP) method and succeeded in describing the static and dynamic electronic structure of molecules. In the MEWP method, we calculate the imaginary-time evolution of the many-electron wavepacket, where this time evolution is accurately evaluated by the Chebyshev polynomial method [3]. We appropriately divide the real space of electrons into the small grid, and so we made up the discretized Hamiltonian of the molecule. We construct the Slater determinant as an initial state of system in the imaginary-time development. This relaxation method [4] directly generates the ground state, and excited states of the system could be also obtained by using the projection operator method after one gets the ground state. We could perfectly treat the electron correlation by this method, however this method is based upon the Born-Oppenheimer (BO) approximation as well as in the ordinary *ab initio* calculation.

Recent progress of experiments using the laser have revealed the detailed properties of molecular state and dynamic process in molecules, so new molecular theories beyond the BO approximation have been tried from the different point of view [5, 6]. Thus we will extend our MEWP method to include nonadiabatic BO (NBO) effects completely. We regard a molecule as a quantum mechanical collective of electrons and nuclei, and we treat electrons and nuclei equivalently by extending the MEWP method to include both electrons and nuclei. Thus the initial molecular state for electrons and nuclei is described as a product of Slater determinant corresponding to electrons and a wavepacket of nuclei, where the explicit form of the nuclear wavepacket depends on the quantum statistics of the nucleus under consideration. We would like to call our extended wavepackets method the molecular wavepackets (MWP) method.

In the following section we give the outline of the new molecular theory. Here we show how to represent the discretized Hamiltonian by expanding the field operator in terms of basis set, which discretize the real space, and how to construct the

initial wave function. In the third section, we apply our method to the isotope series of one-dimensional hydrogen molecules (H_2 , HD, and D_2). Here, we calculate the energy and the mean square root of particle distance in order to analyze the isotope effect due to the nonadiabaticity, and then evaluate the real-time development of polarization to calculate the excitation energy of molecular system. In the last section we conclude with remarks and future work, and we address the validity of our method.

Molecular Wavepacket Method

RELAXATION METHOD

We, first, summarize briefly the relaxation method, which plays an important role in the MWP method. The time-dependent Schrödinger equation and its formal solution are given by

$$i \frac{d}{dt} |\Psi(t)\rangle = H |\Psi(t)\rangle, \quad (1)$$

$$|\Psi(t)\rangle = e^{-iHt} |\Psi(0)\rangle. \quad (2)$$

The basic idea of the relaxation method [4] is as follows: First, we introduce the imaginary time $\beta = it$. The component of the excited state in the time-developed state $|\Psi(\beta)\rangle$ decreases faster than the ground state due to the exponential factor $e^{-\beta E_n}$. Namely, for a sufficiently large β , we get only the information of the ground state as follow:

$$\begin{aligned} |\Psi(\beta)\rangle &= e^{-\beta H} |\Psi(0)\rangle \\ &= \sum_{n=0} e^{-\beta E_n} |\Psi_n\rangle \langle \Psi_n | \Psi(0) \rangle \\ &\rightarrow e^{-\beta E_0} |\Psi_0\rangle \langle \Psi_0 | \Psi(0) \rangle, \quad \text{as } \beta \rightarrow \infty, \quad (3) \end{aligned}$$

where $|\Psi_n\rangle$ means the n th eigenstate of Hamiltonian and $|\Psi_0\rangle$ is the ground state. In order to evaluate the imaginary-time evolution of the system explicitly, we divide the imaginary time β into L infinitesimal time slices, i.e., $\beta = L\tau$;

$$|\Psi(\beta)\rangle = (e^{-\tau H})^L |\Psi(0)\rangle. \quad (4)$$

Therefore we consider the following recurrence formula in the infinitesimal evolution:

$$|\Psi(\tau_l)\rangle = e^{-\tau H} |\Psi(\tau_{l-1})\rangle, \quad \tau_l = l\tau. \quad (5)$$

This infinitesimal time evolution operator could be estimated by various methods. For time-independent Hamiltonian, we adopt the Chebyshev scheme, where this evolution operator is approximated by the Chebyshev polynomial as

$$e^{-\tau H} = \sum_{i=0}^{I_{\max}} \lambda_i(H). \quad (6)$$

The number of term I_{\max} is large enough to converge the sum; then this method practically gives most accurate results. Substituting Eq. (6) into Eq. (5) and using the resolution of unity, we obtain

$$\begin{aligned} \langle n|\Psi(\tau_l)\rangle &= \langle n|e^{-\tau H}|\Psi(\tau_{l-1})\rangle \\ &\equiv \sum_m C_{nm} \langle m|\Psi(\tau_{l-1})\rangle, \end{aligned} \quad (7)$$

where

$$C_{nm} = \sum_{i=0}^{I_{\max}} \langle n|\lambda_i(H)|m\rangle. \quad (8)$$

After time-developing the initial wave packet according to the above procedure, we could obtain the ground state of the system under consideration. On the other hand, the excited state could be generated by the projection method. Namely, we first remove the ground-state component from the initial wavepacket; then we apply the relaxation method to this wavepacket and get the excited state.

Finally, we note that we calculate the time development of the polarization by means of the real-time evolution, which is treated in the same way as the imaginary-time evolution method except for the complex Chebyshev polynomial. The Fourier transformation of this polarization results in the excitation spectrum of the system.

MODEL HAMILTONIAN

We here construct the discretized Hamiltonian according to following procedure. For a system composed of electrons and nuclei, the Hamiltonian is given in terms of the field operator $\psi_\sigma(\mathbf{r})$ and $\phi_{\alpha I}(\mathbf{R})$ as follows:

$$H = H_e + H_n + H_{en}, \quad (9)$$

where

$$\begin{aligned} H_e &= \sum_\sigma \int d^3\mathbf{r} \psi_\sigma^\dagger(\mathbf{r}) \left(-\frac{\hbar^2}{2m_e} \nabla^2 \right) \psi_\sigma(\mathbf{r}) \\ &\quad + \frac{1}{2} \sum_{\sigma\sigma'} \int d^3\mathbf{r} d^3\mathbf{r}' \psi_\sigma^\dagger(\mathbf{r}) \psi_{\sigma'}^\dagger(\mathbf{r}') \\ &\quad \times \frac{e^2}{|\mathbf{r} - \mathbf{r}'|} \psi_{\sigma'}(\mathbf{r}') \psi_\sigma(\mathbf{r}), \end{aligned} \quad (10)$$

$$\begin{aligned} H_n &= \sum_\alpha \sum_I \int d^3\mathbf{R} \phi_{\alpha I}^\dagger(\mathbf{R}) \left(-\frac{\hbar^2}{2M_\alpha} \nabla^2 \right) \phi_{\alpha I}(\mathbf{R}) \\ &\quad + \frac{1}{2} \sum_{\alpha\alpha'} \sum_{II'} \int d^3\mathbf{R} d^3\mathbf{R}' \phi_{\alpha I}^\dagger(\mathbf{R}) \phi_{\alpha' I'}^\dagger(\mathbf{R}') \\ &\quad \times \frac{Z_\alpha Z_{\alpha'} e^2}{|\mathbf{R} - \mathbf{R}'|} \psi_{\alpha' I'}(\mathbf{R}') \psi_{\alpha I}(\mathbf{R}), \end{aligned} \quad (11)$$

$$\begin{aligned} H_{en} &= \sum_\sigma \sum_\alpha \sum_I \int d^3\mathbf{r} d^3\mathbf{R} \psi_\sigma^\dagger(\mathbf{r}) \phi_{\alpha I}^\dagger(\mathbf{R}) \\ &\quad \times \frac{-Z_\alpha e^2}{|\mathbf{r} - \mathbf{R}|} \phi_{\alpha I}(\mathbf{R}) \psi_\sigma(\mathbf{r}), \end{aligned} \quad (12)$$

where H_e , H_n , and H_{en} represent the electron, nuclear, and interaction Hamiltonian between electrons and nuclei, respectively; m_e , M_α , and Z_α are an electron mass, a nuclear mass, and an atomic number of α th nucleus, respectively. The electron field operator with spin σ a space coordinate \mathbf{r} , $\psi_\sigma(\mathbf{r})$, and the field operator for a nucleus α with nuclear spin I at space coordinate \mathbf{R} , $\phi_{\alpha I}(\mathbf{R})$, satisfy the following commutation relations:

$$\begin{aligned} [\psi_\sigma(\mathbf{r}), \psi_{\sigma'}^\dagger(\mathbf{r}')]_{\pm} &= \delta(\mathbf{r} - \mathbf{r}') \delta_{\sigma\sigma'}, \\ [\psi_\sigma(\mathbf{r}), \psi_{\sigma'}(\mathbf{r}')]_{\pm} &= [\psi_\sigma^\dagger(\mathbf{r}), \psi_{\sigma'}^\dagger(\mathbf{r}')]_{\pm} = 0, \quad (13) \\ [\phi_{\alpha I}(\mathbf{R}), \phi_{\alpha' I'}^\dagger(\mathbf{R}')]_{\pm} &= \delta_{\alpha\alpha'} \delta(\mathbf{R} - \mathbf{R}') \delta_{II'}, \\ [\phi_{\alpha I}(\mathbf{R}), \phi_{\alpha' I'}(\mathbf{R}')]_{\pm} &= [\phi_{\alpha I}^\dagger(\mathbf{R}), \phi_{\alpha' I'}^\dagger(\mathbf{R}')]_{\pm} = 0, \quad (14) \\ [\psi_\sigma(\mathbf{r}), \phi_{\alpha I}^\dagger(\mathbf{R})]_{\pm} &= [\psi_\sigma(\mathbf{r}), \phi_{\alpha I}(\mathbf{R})]_{\pm}, \\ [\psi_\sigma^\dagger(\mathbf{r}), \phi_{\alpha I}(\mathbf{R})]_{\pm} &= [\psi_\sigma^\dagger(\mathbf{r}), \phi_{\alpha I}^\dagger(\mathbf{R})]_{\pm} = 0, \end{aligned} \quad (15)$$

where the $+$ sign refers to the anticommutation relation for Fermion and the $-$ sign means the ordinary commutation relation for Boson.

Then we expand the field operator by the basis set $\chi_q(\mathbf{r})$ ($\chi_Q(\mathbf{R})$), which vanishes everywhere except for one small grid generated by discretizing the real space and is therefore specified by the

corresponding lattice point $q(Q)$. For example,

$$\begin{aligned}\psi_{\sigma}(\mathbf{r}) &= \sum_q \chi_q(\mathbf{r}) a_{q\sigma}, \\ \phi_{\alpha I}(\mathbf{R}) &= \sum_Q \chi_Q(\mathbf{R}) b_{\alpha Q I},\end{aligned}\quad (16)$$

where $a_{q\sigma}$ ($b_{\alpha Q I}$) is the annihilation operators of electron (nucleus) at the lattice point $q(Q)$ with spin σ (α), and satisfy the anticommutation or commutation relation:

$$\begin{aligned}[a_{q\sigma}, a_{q'\sigma'}^\dagger]_{\pm} &= \delta_{qq'} \delta_{\sigma\sigma'}, \\ [b_{\alpha Q I}, b_{\alpha' Q' I'}^\dagger]_{\pm} &= \delta_{\alpha\alpha'} \delta_{QQ'} \delta_{II'}, \\ \text{others} &= 0.\end{aligned}\quad (17)$$

Then the discretized Hamiltonian is given by

$$\begin{aligned}H &= \sum_{\sigma} \sum_{qq'} t_{qq'} a_{q\sigma}^\dagger a_{q'\sigma'} \\ &+ \frac{1}{2} \sum_{\sigma\sigma'} \sum_{qq'} v_{qq'} a_{q\sigma}^\dagger a_{q'\sigma'}^\dagger a_{q'\sigma'} a_{q\sigma} \\ &+ \sum_{\alpha} \sum_I \sum_{QQ'} T_{\alpha QQ'} b_{\alpha Q I}^\dagger b_{\alpha Q' I'} \\ &+ \frac{1}{2} \sum_{\alpha\alpha'} \sum_{II'} \sum_{QQ'} V_{\alpha\alpha' QQ'} b_{\alpha Q I}^\dagger b_{\alpha' Q' I'}^\dagger b_{\alpha' Q' I'} b_{\alpha Q I} \\ &+ \sum_{\sigma q} \sum_{\alpha I Q} U_{q\alpha Q} a_{q\sigma}^\dagger b_{\alpha Q I}^\dagger b_{\alpha Q I} a_{q\sigma},\end{aligned}\quad (18)$$

where the differential operator of the kinetic part is estimated by second-order differencing. Then introducing a lattice constant ϵ , the matrix element of kinetic part is explicitly given by

$$t_{qq'} = \frac{1}{m_e \epsilon^2} \delta_{q, q'} - \frac{1}{2m_e \epsilon^2} \delta_{q, q'+1} - \frac{1}{2m_e \epsilon^2} \delta_{q+1, q'}.\quad (19)$$

The atomic unit $\hbar = m_e = e = 1$ is used throughout this article.

INITIAL MOLECULAR WAVE FUNCTION

We construct an initial many-particle wave function in terms of single-particle electron and nuclear wavepackets. The single-particle state $|\phi\rangle$ of the initial state is represented by the Gaussian

wavepacket as

$$\begin{aligned}\langle x\rho|\phi\rangle &= \frac{1}{\pi^{1/4} \sqrt{\sigma}} \\ &\times \exp\left[-\frac{(x-x_0)^2}{2\sigma^2} + ik_0(x-x_0)\right],\end{aligned}\quad (20)$$

where ρ , x_0 , k_0 , and σ is the spin coordinate, the mean position, the mean momentum, and the dispersion of the initial Gaussian wavepacket, respectively. Then we construct the Slater determinant of the initial many-electron wavepacket as

$$\begin{aligned}\langle x_1 \rho_1, \dots, x_N \rho_N | \psi_e \rangle \\ = \frac{1}{\sqrt{N!}} \begin{vmatrix} \langle x_1 \rho_1 | \phi_1 \rangle & \dots & \langle x_N \rho_N | \phi_1 \rangle \\ \vdots & \ddots & \vdots \\ \langle x_1 \rho_1 | \phi_N \rangle & \dots & \langle x_N \rho_N | \phi_N \rangle \end{vmatrix},\end{aligned}\quad (21)$$

where N is the number of electrons. We could construct the wavepacket for identical Fermion nuclei in the same way as for electrons. For identical Boson nuclei, we use the permanent instead of the determinant. Thus total initial wave function is written as the product form of the electron and nuclear part:

$$\langle x_1 \rho_1, \dots, x_N \rho_N, | \psi_e \rangle \langle X_1 \xi_1, \dots, X_M \xi_M, | \psi_n \rangle.\quad (22)$$

If a molecule consists of nonidentical nuclei, then the nuclear wave function is factorized into parts of the corresponding nuclear species.

Numerical Examples

We have applied the MWP method to the isotope series of one-dimensional hydrogen molecule for simplicity. We discretize one-dimensional molecular space by dividing its range L_c into N segments, and the hydrogen molecule is a four-particle system of two electrons and two nuclei. Thus this one-dimensional model Hamiltonian is represented by a symmetric matrix of N^4 dimension. The wave function for the hydrogen molecule is explicitly given as

$$\langle x_1 \rho_1, x_2 \rho_2; X_1 \xi_1, X_2 \xi_2 | \Psi \rangle.\quad (23)$$

In the one-dimensional systems, Javanainen, Eberly, and Su [7] showed that the Coulomb potential is approximated by the softened Coulombic

form:

$$\frac{1}{|x|} = \frac{1}{(a + x^2)^{1/2}}, \quad (24)$$

where Javanainen et al. set $a = 1$. This approximate potential retains the asymptotic form of the Coulomb potential; moreover it reduces the singularity at the origin. Thus we also adopt this softened Coulombic potential in the practical calculation.

ISOTOPE EFFECTS OF H₂, HD, AND D₂

When we construct the initial molecular wavepacket of these isotope molecules, we have to pay attention on the statistics of nucleus. Namely, the nuclear part of H₂ is given by the Slater determinant, and we use the permanent for D₂ as the nucleus D is Boson. On the other hand, we have to treat both H and D independently for the HD molecule. Moreover, for H₂ molecule, we could take into account the total nuclear spin angular momentum, i.e., we treat separately the ortho- and para-hydrogen molecule. Therefore, we could analyze the effect of the quantum statistics on the physical quantity in detail.

Table I summarizes various parameters of the initial nuclear-electron wavepackets adapted in this calculation. We assume that the range of molecular space is $L_e = 21$ a.u., and we divide L_e into $N = 21$ grids. Therefore, the grid interval dx is 1.0 a.u.. For the initial single-particle Gaussian wavepackets of nucleus, we set $x_1 = 9$, $k_1 = 0.0$,

$\sigma_1 = 1.5$ for up spin nuclei, $x_2 = 13$, $k_2 = 0.0$, $\sigma_2 = 1.5$ for downspin. While for those of electron wavepackets, we choose $x_1 = 9$, $k_1 = 0.0$, $\sigma_1 = 2.1$ for up spin, and $x_2 = 13$, $k_2 = 0.0$, $\sigma_2 = 2.1$ for down spin. Namely, the initial Gaussian wavepacket of the electrons and nuclei with up (down) spin are put in the same position, but with the different width. The width for the electron is taken to be larger than the one for the nuclei. The result does not depend on the initial value, which has an effect just on the computational time. The initial probability density is shown in Figure 1. We also set the potential parameter $a = 1.0$ [7].

Total energy by MWP method is shown in Table II. We cannot definitely find out the energy difference in the singlet ground state of ortho- and para-H₂, so that the nuclear spin yields almost no contribution to the total energy. Table III shows that average nuclear distance between protons in para-H₂ is rather larger than one in ortho-H₂, and the difference of average distance between electrons in para- and ortho-H₂ is a little bit amplified due to the mobility of electron.

The order of the total energy increases like $D_2 < HD < H_2$, which is good agreement with the Kolos et al. [8]. This indicates that the heavy nucleus moves slowly compared to the light nucleus, in other words, the amplitude of the light nucleus is larger than that of the heavy nucleus.

The average distance between nuclei in this isotope series increases like $H_2 < HD < D_2$, and the same tendency is also shown in the average distance between electrons. The order of average

TABLE I
Parameters of initial single-particle wavepacket.

Parameters of initial singlet ortho-H ₂ wave function					
Le	dx	Electron wave function		Nucleus wave function	
(1) BO-H ₂ (MEWP method)					
21	1.0	$x_{01} = 9$ $k_{01} = 0.0$ $\sigma_1 = 2.1$ Up	$x_{02} = 13$ $k_{02} = 0.0$ $\sigma_2 = 2.1$ Down	$X_{01} = 10$	$X_{02} = 12$
	(spin)				
(2) NonBO singlet ortho-H ₂ (MWP method)					
21	1.0	$x_{01} = 9$ $k_{01} = 0.0$ $\sigma_1 = 2.1$ Up	$x_{02} = 13$ $k_{02} = 0.0$ $\sigma_2 = 2.1$ Down	$X_{01} = 10$ $k_{01} = 0.0$ $\sigma_1 = 2.1$ Up	$X_{02} = 12$ $k_{02} = 0.0$ $\sigma_2 = 2.1$ Down
	(spin)				
	(mass)		1		1836

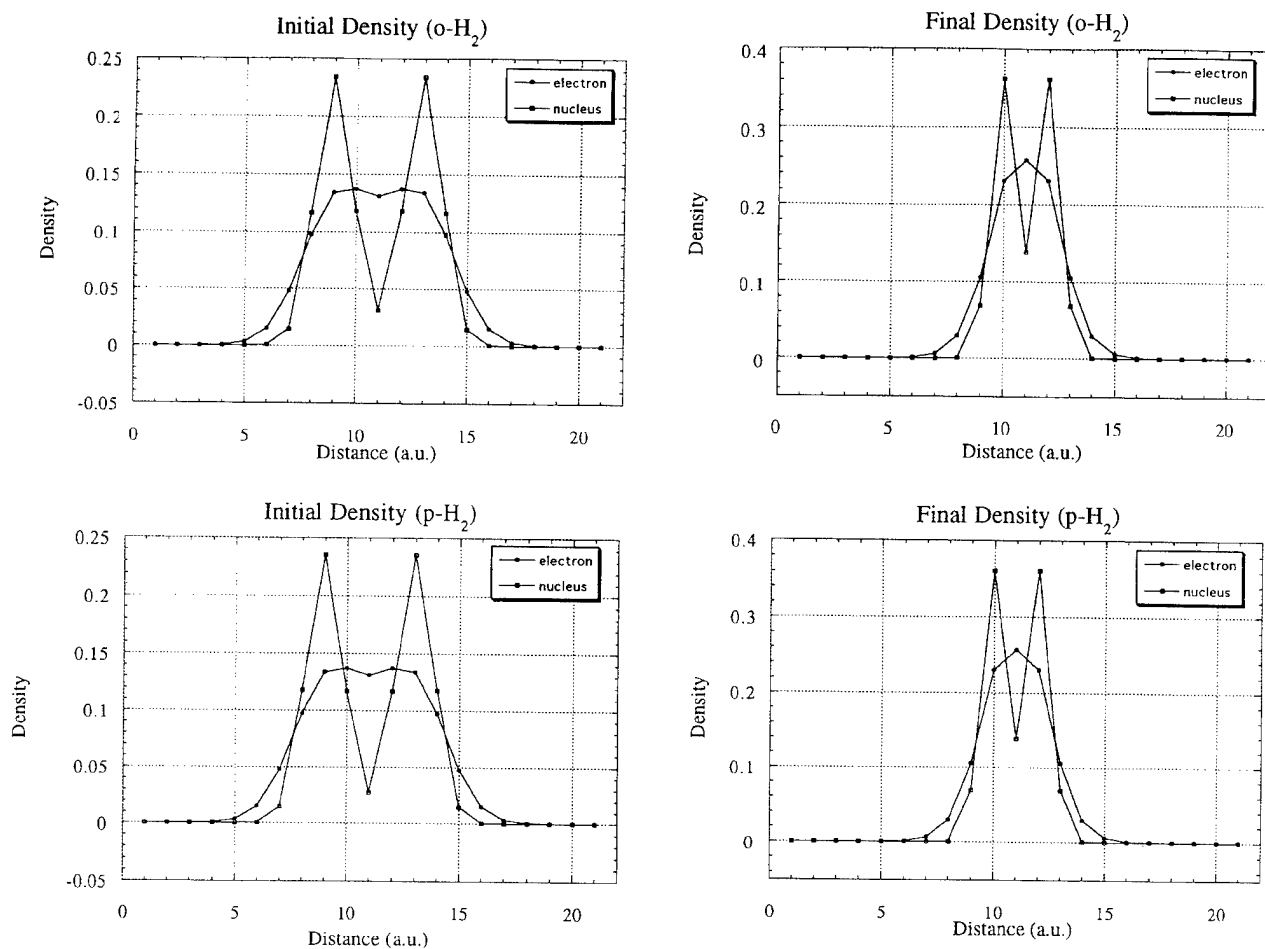


FIGURE 1. Probability density of electrons and nuclei of ortho- and para- H_2 for the initial wavepacket and the calculated ground state: (a) singlet state and (b) triplet state.

TABLE II
Total energy of H_2 , HD, and D_2 (a.u.).

Nucleus:	Ortho		Para	
	Singlet	Triplet	Singlet	Triplet
(1) H_2	-1.4588412068	-1.3644142801	-1.4588412043	-1.3644129998
Electron:	Singlet		Triplet	
(2) HD	-1.4591075654		-1.36449593229	
(3) D_2	-1.4593753100		-1.3645815086	

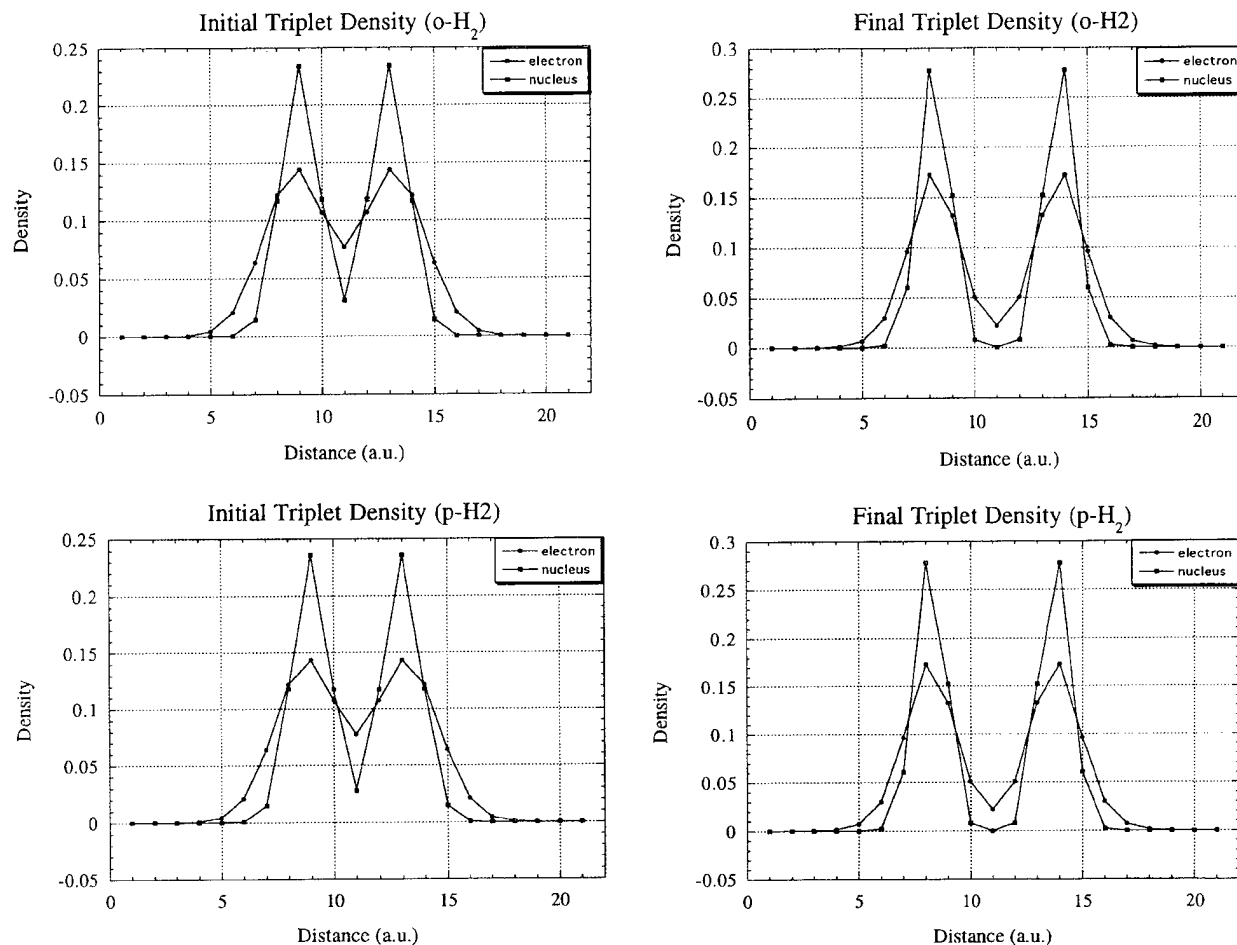


FIGURE 1. (Continued)

distance is reversed compared to the order of the total energy.

REAL-TIME EVOLUTION OF THE POLARIZATION

Finally we calculate the real-time evolution of the polarization:

$$P(t) = \langle \Psi(t) | (-x + X) | \Psi(t) \rangle. \quad (25)$$

The results for BO-H₂ and NBO-ortho-H₂ are illustrated in Figure 2. By Fourier transforming the polarization, we obtain the excitation spectra as shown in Figure 3. For the BO-H₂ molecule, we have one sharp peak at 16496 cm⁻¹ which corresponds to the electronic excitation to the first excited state. On the other hand, for the NBO-ortho-H₂ molecule, we have two sharp peaks at 4713 and 16496 cm⁻¹. In the nonadiabatic treatment, in

addition to the electronic excitation, we could obtain the nuclear vibrational frequency of 4713 cm⁻¹.

Concluding Remarks and Future Work

In this study, we have formulated the nonadiabatic molecular theory and analyzed the nonadiabatic effects and the nuclear quantum statistics effect in the isotope series of hydrogen molecule and the nuclear spin multiplicity effect of the para- and ortho-H₂ molecule.

In the imaginary-time development, we obtained the total energy and the average distance between electrons, nuclei, and electron-nucleus of ortho-H₂, para-H₂, HD, and D₂. We also calculated the real-time evolution of the polarization in BO-H₂ and NBO-ortho-H₂, and by the Fourier transform we got the excitation spectrum of the

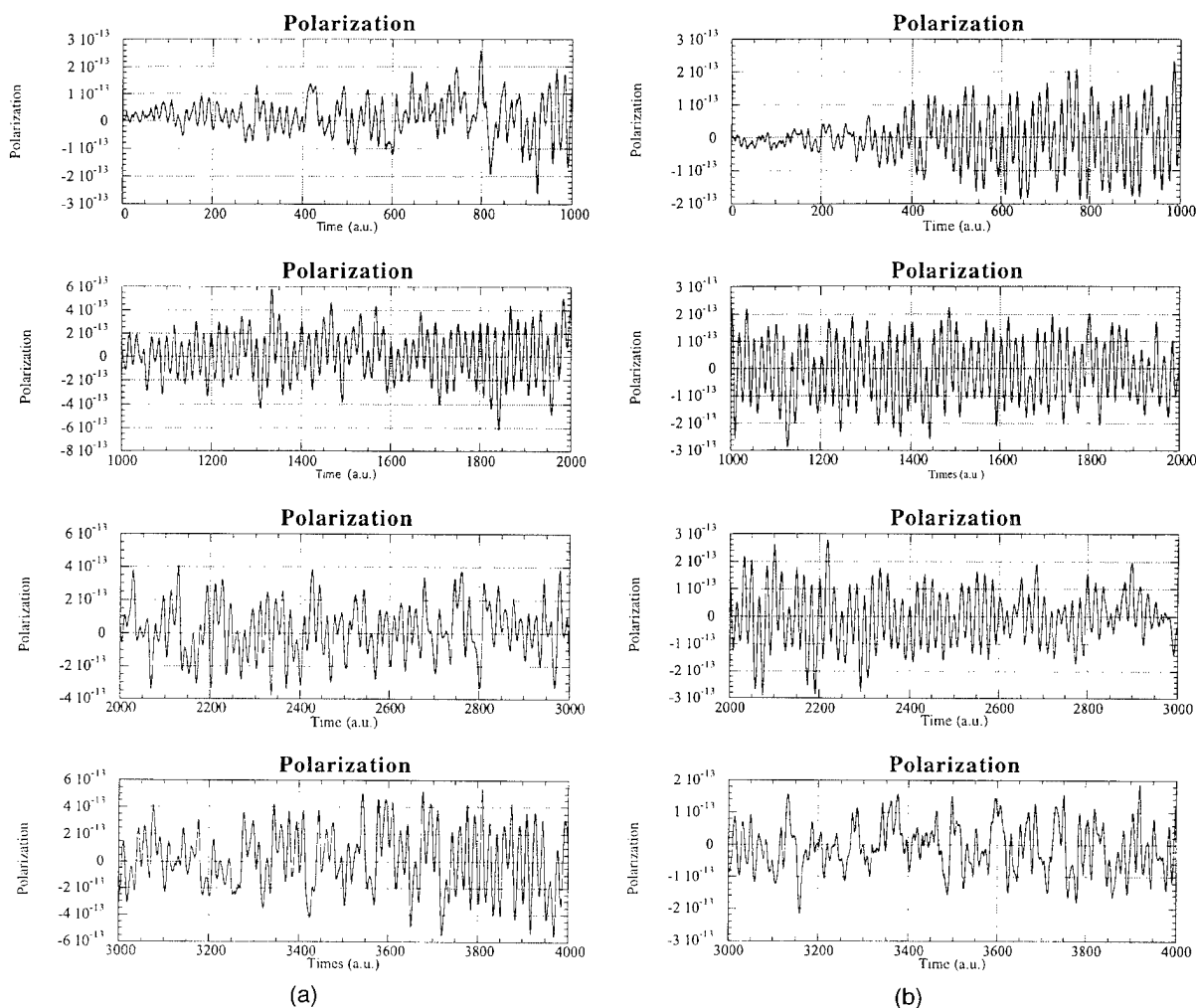


FIGURE 2. Time evolution of polarization from 0 to 4000 a.u.: (a) BO-H₂ and (b) NBO-H₂.

molecular system. BO-H₂ has only the electronic excitation; on the other hand NBO-ortho-H₂ has two peaks corresponding to the electron excitation and the nuclear vibrational frequency. From these results we are sure that our method is truly a nonadiabatic theory, which directly includes the nuclear motion.

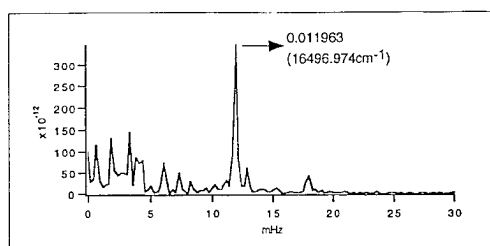
Because the MWP method is an extension of the MEWP method, the MWP method has the same merits as the MEWP method; that is, the MWP method could include the dynamical correlation of the electron-electron, nucleus-nucleus, and nucleus-electron. The relaxation technique due to the imaginary-time development yields the ground and excited states. In order to reduce the computa-

tional resources, we could introduce some approximations into our method. The mean-field approximation, for example, will drastically reduce a CPU time and core memories, which are indispensable for molecular calculations. The method could be applied to a larger system by means of the parallel processing computer.

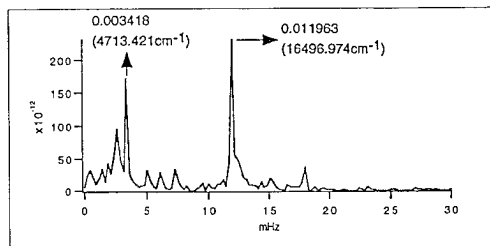
There are characteristic features in the MWP method, which originate from classical and quantum properties of nuclei. Our method fully takes into account the quantum effect of the nuclear motion and is beyond the BO approximation. The method, of course, optimizes automatically the molecular geometry and is applicable to the vibrational and rotational motion of molecule. In these

TABLE III
Mean square root of particle distances (a.u.).

Electron state:	Singlet	Triplet
<u>(1) Ortho-H₂</u>		
e-e:	2.1897892672	5.8619611057
e-H:	1.6689229382	4.1324366305
H-H:	1.9996299013	5.6360858657
<u>(2) para-H₂</u>		
e-e:	2.1897893589	5.9620001840
e-H:	1.6689230174	4.1324636646
H-H:	1.9996300363	5.6361244806
<u>(3) HD</u>		
e-e	2.1898848722	5.8457056682
e-H:	1.6690108471	4.1208203462
e-D:	1.6690070541	4.1207963036
H-D:	1.9997793058	5.6188735236
<u>(4) D₂</u>		
e-e:	2.1899598503	5.8291993119
e-D	1.6690763368	4.1089969332
D-D:	1.9998963145	5.6013881927

BO H₂

(a)

NBO o-H₂

(b)

FIGURE 3. Excitation spectra of (a) BO-H₂ and (b) NBO-ortho-H₂ obtained by Fourier transform of the polarization in Figure 2.

cases, the isotope effect due to a nuclear mass on the electronic structure is naturally described. Moreover, in our method, electrons and nuclei are treated at the same level. Therefore, our method could visualize chemical reactions and could identify the reaction path and the activated complex. As our method can easily deal with the excited state, it is applicable to the relaxation process in the excited molecule, the radiationless transition, the photo- and thermal dissociation, the intermolecular excitation, and so on. Therefore, our method could simulate in principle all the chemical processes; the simulation chemistry may be established in this framework.

Because our method fully takes the nuclear spin into consideration, we could discuss the isotope effect due to the nuclear spin and could calculate physical constants appearing in the magnetic resonance, such as the hyperfine constant, the chemical shift, the spin-spin coupling constant, and so on, from the first principle.

ACKNOWLEDGMENTS

We are grateful to the Ministry of Education, Science and Culture of Japan (Specially Promoted

Research No. 06101004) for financial support. All calculations were carried out on the IBM Powerstation models 580 and 3CT.

References

1. R. Kosloff, J. Phys. Chem. **92**, 2087 (1988).
2. D. Kosloff and R. Kosloff, J. Comput. Phys. **52**, 35 (1983).
3. H. Tal-Ezer and R. Kosloff, J. Chem. Phys. **81**, 3967 (1984).
4. B. Kosloff and H. Tal-Ezer, Chem. Phys. Lett. **127**, 223 (1986).
5. E. Deumens and Y. Öhrn, J. Phys. Chem. **92**, 3181 (1988); E. Deumens, A. Diz, R. Longo, and Y. Öhrn, Rev. Mod. Phys. **66**, 917 (1994).
6. A. D. Bandrauk and H. Shen, J. Chem. Phys. **99**, 1185 (1993).
7. J. Javanainen, J. Eberly, and Q. Su, Phys. Rev. A **38**, 3430 (1988); Q. Su and J. H. Eberly, *Ibid.* **44**, 5997 (1991).
8. W. Kolos and L. Wolniewicz, J. Chem. Phys. **41**, 3663 (1964); *Ibid.*, **41**, 3674 (1964).

Calculation of Intramolecular Force Fields from Second-Derivative Tensors

JORGE M. SEMINARIO

Department of Chemistry, University of New Orleans, New Orleans, Louisiana 70148; e-mail: jsmcm@uno.edu

Received February 24, 1996; revised manuscript received March 13, 1996; accepted March 18, 1996

ABSTRACT

A practical procedure (FUERZA) to obtain internal force constants from Cartesian second derivatives (Hessians) is presented and discussed. It allows a systematic analysis of pair atomic interactions in a molecular system, and it is fully invariant to the choice of internal coordinates of the molecule. Force constants for bonds or for any pair of atoms in general are defined by means of the eigenanalysis of their pair interaction matrix. Force constants for the angles are obtained from their corresponding two-pair interaction matrices of the two bonds or distances forming the angle, and the dihedral force constants are similarly obtained using their corresponding three-pair interaction matrices.

© 1996 John Wiley & Sons, Inc.

Introduction

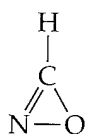
Classical molecular dynamics methods that analyze the time evolution of macroscopic systems for several thousands of time steps or conformations have become very effective tools for gaining insight into a variety of macroscopic systems and processes [1, 2]. Most of this work has involved the use of empirical force fields obtained from experimental measurements of geometries, heats of formation, vibrational frequencies, and barrier heights. However, with the increasing accuracy and availability of first-principles methods (standard *ab initio* and density functional theory), there is a growing tendency to obtain the force field data from high-level computations on the

basic molecular units [3–7]. This makes it possible to treat macroscopic systems that have not yet been investigated experimentally or that may not even exist at present.

In early molecular dynamics (MD) simulations, there was only limited use of intramolecular force fields, primarily because the time step could be increased more than twofold when molecules were constrained to having fixed bond lengths and sometimes angles (the SHAKE method [8]). However, for studying the effects of external factors, such as temperature and pressure, upon molecular properties of a fluid [9–11], e.g., shifts in vibrational spectra [12], the force field clearly must include an intramolecular component.

If the intramolecular portion of the force field is expressed in terms of force constants corresponding to molecular internal coordinates (bond lengths,

bond angles, and dihedral angles), then a significant problem that arises is that of assuring invariance of the individual internal force constants with respect to the chosen set of internals. A given molecule can be described by various sets of internal coordinates, and these may give different values for a particular internal coordinate force constant. Thus the internal force constants, and therefore their intramolecular force field, are not invariant to the choice of internal coordinates. This is due to fact that physical force constants are tensors of rank 2, but we want to use them in practical MD simulations as scalars (tensors of rank 0). An example of this problem can be visualize with the cyclic chon molecule:



A quick HF/STO-3G calculation yields a force constant for the CO bond of 0.54 a.u. if the chosen internals are the CO bond, CN bond, and NCO angle; 0.57 a.u. if we choose the CO bond, NO bond, and CON angle; and 0.26 a.u. if we choose redundant internal coordinates [13] CO, NO, CN,

CNO, NOC, and OCN (for the sake of clarity, the coordinates containing the hydrogen atom are not mentioned in this example). The choice of a value of the force constant to be used in MD calculations is therefore ambiguous. In this study, we present a procedure to compute, in an invariant fashion, the force constants corresponding to internal coordinates.

Background

The 3N component reaction force δF due to a displacement δx of the N atoms in a molecular system can be expressed exactly to second order on a Taylor series expansion as

$$\delta F = -[k]\delta x, \quad (1)$$

where $[k]$, the Hessian, is a tensor of rank 2 and dimension $3N \times 3N$ defined by

$$[k] = k_{ij} = \frac{\partial^2 E}{\partial x_i \partial x_j}. \quad (2)$$

Explicitly, Eq. (1) can be written as

$$\begin{bmatrix} \delta F_1 \\ \delta F_2 \\ \delta F_3 \\ \vdots \\ \delta F_{3N} \end{bmatrix} = - \begin{bmatrix} \frac{\partial^2 E}{\partial x_1^2} & \frac{\partial^2 E}{\partial x_1 \partial x_2} & \frac{\partial^2 E}{\partial x_1 \partial x_3} & \cdots & \frac{\partial^2 E}{\partial x_1 \partial x_{3N}} \\ \frac{\partial^2 E}{\partial x_2 \partial x_1} & \frac{\partial^2 E}{\partial x_2^2} & \frac{\partial^2 E}{\partial x_2 \partial x_3} & \cdots & \frac{\partial^2 E}{\partial x_2 \partial x_{3N}} \\ \frac{\partial^2 E}{\partial x_3 \partial x_1} & \frac{\partial^2 E}{\partial x_3 \partial x_2} & \frac{\partial^2 E}{\partial x_3^2} & \cdots & \frac{\partial^2 E}{\partial x_3 \partial x_{3N}} \\ \vdots & \vdots & \vdots & \ddots & \vdots \\ \frac{\partial^2 E}{\partial x_{3N} \partial x_1} & \frac{\partial^2 E}{\partial x_{3N} \partial x_2} & \frac{\partial^2 E}{\partial x_{3N} \partial x_3} & \cdots & \frac{\partial^2 E}{\partial x_{3N}^2} \end{bmatrix} \begin{bmatrix} \delta x_1 \\ \delta x_2 \\ \delta x_3 \\ \vdots \\ \delta x_{3N} \end{bmatrix}. \quad (3)$$

Tensor $[k]$ can be obtained by procedures available in density functional theory and ab initio programs such as deMon [14, 15] and Gaussian 94 [16].

The tensor $[k]$ represents the intramolecular force field to second order for small displacements δx . The eigenvalues λ_i of $[k]$ are the 3N force

constants corresponding to the 3 translational, 3 rotational and $3N-6$ vibrational modes of the system. The eigenvectors \hat{v}_i of the Hessian $[k]$ indicate the directions of the displacements of the normal modes corresponding to each eigenvalue. If a displacement of magnitude δr occurs in the direction of one of these eigenvectors, the reaction force acts exclusively parallel or antiparallel to that

direction:

$$F_i = -[k]\hat{v}_i\delta r = -\lambda_i\hat{v}_i\delta r. \quad (4)$$

Displacements in any other direction result, in most cases, in a reaction force that is not in the direction of the displacement vector.

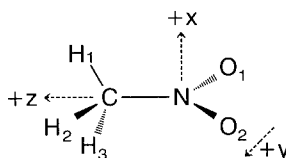
The use of the symmetric tensor $[k]$ in a molecular simulation could be cumbersome because of the large number of independent elements, $3N(3N+1)/2$. Many of these may be relatively small in magnitude, as is shown in Figure 1 for the case of nitromethane. A more practical approach is to re-

late the force field to internal coordinates, which can generally reduce the number of terms to as few as $3N-6$. The potential energy function is then

$$V = \sum_{\text{bonds}} \frac{1}{2}k_b(b-b_0)^2 + \sum_{\text{angles}} \frac{1}{2}k_\theta(\theta-\theta_0)^2 + \sum_{\text{dihedrals}} \frac{1}{2}k_\phi(\phi-\phi_0)^2 + \sum_{\text{impropers}} \frac{1}{2}k_\omega(\omega-\omega_0)^2 \quad (5)$$

	X _N	Y _N	Z _N	X _C	Y _C	Z _C	X _{H1}	Y _{H1}	Z _{H1}	X _{H2}	Y _{H2}	Z _{H2}	X _{H3}	Y _{H3}	Z _{H3}	X _{O1}	Y _{O1}	Z _{O1}	X _{O2}	Y _{O2}	Z _{O2}
X _N	489	0	-7	-201	0	-4	9	0	-84	-1	-6	38	-1	6	38	-147	8	9	-147	-8	9
Y _N	0	1934	0	0	-164	0	0	-5	0	-1	-7	-69	1	-7	69	12	-875	-372	-12	-875	372
Z _N	-7	0	1322	1	0	-231	-1	0	-39	-6	2	-25	-6	-2	-25	9	-366	-501	9	366	-501
X _C	-201	0	1	1241	0	-27	-653	0	-151	-236	237	81	-236	-237	81	43	0	8	43	0	8
Y _C	0	-164	0	0	1389	0	0	-98	0	233	-536	-131	-233	-536	131	-4	-28	-94	4	-28	94
Z _C	-4	0	-231	-27	0	788	-158	0	-138	91	-154	-150	91	154	-150	4	-51	-60	4	51	-60
X _{H1}	9	0	-1	-653	0	-158	694	0	173	-25	-4	-8	-25	4	-8	0	2	1	0	-2	1
Y _{H1}	0	-5	0	0	-98	0	0	94	0	55	5	19	-55	5	-19	3	0	-3	-3	0	3
Z _{H1}	-84	0	-39	-151	0	-138	173	0	162	22	3	10	22	-3	10	9	0	-2	9	0	-2
X _{H2}	-1	-1	-6	-236	233	91	-25	55	22	240	-254	-91	19	-27	-14	2	-2	-3	0	-3	0
Y _{H2}	-6	-7	2	237	-536	-154	-4	5	3	-254	562	164	27	-33	-17	2	5	-3	-1	4	5
Z _{H2}	38	-69	-25	81	-131	-150	-8	19	10	-91	164	171	-14	17	10	-3	-3	-19	-4	3	3
X _{H3}	-1	1	-6	-236	-233	91	-25	-55	22	19	27	-14	240	254	-91	0	3	0	2	2	-3
Y _{H3}	6	-7	-2	-237	-536	154	4	5	-3	-27	-33	17	254	562	-164	1	4	-5	-2	5	3
Z _{H3}	38	69	-25	81	131	-150	-8	-19	10	-14	-17	10	-91	-164	171	-4	-3	3	-3	3	-19
X _{O1}	-147	12	9	43	-4	4	0	3	9	2	2	-3	0	1	-4	51	-12	-13	51	-2	-2
Y _{O1}	8	-875	-366	0	-28	-51	2	0	0	-2	5	-3	3	4	-3	-12	1117	450	2	-224	-27
Z _{O1}	9	-372	-501	8	-94	-60	1	-3	-2	-3	-3	-19	0	-5	3	-13	450	475	-2	27	104
X _{O2}	-147	-12	9	43	4	4	0	-3	9	0	-1	-4	2	-2	-3	51	2	-2	51	12	-13
Y _{O2}	-8	-875	366	0	-28	51	-2	0	0	-3	4	3	2	5	3	-2	-224	27	12	1117	-450
Z _{O2}	9	372	-501	8	94	-60	1	3	-2	0	5	3	-3	3	-19	-2	-27	104	-13	-450	475

FIGURE 1. Hessian matrix (kcal / Å² mol) for the staggered conformation of CH₃NO₂.



The pair interaction matrix that gives the reaction force on the atom N due to a displacement of atom C is given by

$$\begin{bmatrix} \delta F_{x_N} \\ \delta F_{y_N} \\ \delta F_{z_N} \end{bmatrix} = \begin{bmatrix} 201 & 0 & 4 \\ 0 & 164 & 0 \\ -1 & 0 & 231 \end{bmatrix} \begin{bmatrix} \delta x_C \\ \delta y_C \\ \delta z_C \end{bmatrix}$$

in which b , θ , ϕ , and ω correspond to the bond lengths, bond angles, dihedral angles, and improper dihedrals (out-of-plane); b_o , θ_o , ϕ_o , and ω_o are their equilibrium values; and k_b , k_θ , k_ϕ , and k_ω are the respective force constants (the indexes for bonds, angles, dihedrals, and impropers are not shown). We will now show how to obtain an invariant force constant corresponding to any internal coordinate. The same procedure can be applied for force fields that contain cross terms such as

$$\sum_{\text{bonds \& angles}} \frac{1}{2} k_{b\theta} (b - b_o)(\theta - \theta_o) \quad (6)$$

Method

BOND FORCE CONSTANTS

The essential concept is to analyze the interactions between all pairs of atoms in the molecule and to determine which ones are pairwise stable, the criterion for which shall be explained. From Eq. (3), we can get the reaction force $\delta \mathbf{F}_A = (\delta F_{x_A}, \delta F_{y_A}, \delta F_{z_A})$ on atom A due to a displacement $\delta \mathbf{r}_B = (\delta x_B, \delta y_B, \delta z_B)$ of atom B:

$$\begin{bmatrix} \delta F_{x_A} \\ \delta F_{y_A} \\ \delta F_{z_A} \end{bmatrix} = - \begin{bmatrix} \frac{\partial^2 E}{\partial x_A \partial x_B} & \frac{\partial^2 E}{\partial x_A \partial y_B} & \frac{\partial^2 E}{\partial x_A \partial z_B} \\ \frac{\partial^2 E}{\partial y_A \partial x_B} & \frac{\partial^2 E}{\partial y_A \partial y_B} & \frac{\partial^2 E}{\partial y_A \partial z_B} \\ \frac{\partial^2 E}{\partial z_A \partial x_B} & \frac{\partial^2 E}{\partial z_A \partial y_B} & \frac{\partial^2 E}{\partial z_A \partial z_B} \end{bmatrix} \times \begin{bmatrix} \delta x_B \\ \delta y_B \\ \delta z_B \end{bmatrix} \quad (7)$$

or in compact notation,

$$\delta \mathbf{F}_A = [k_{AB}] \delta \mathbf{r}_B. \quad (8)$$

The interatomic force constant matrix $[k_{AB}]$, defined including the minus sign, permits an analysis of the nature of the interaction between atoms

A and B. It has three eigenvalues λ_i^{AB} and three eigenvectors \hat{v}_i^{AB} ($i = 1, 2, 3$), which we assume to have unitary norm. An example of one interatomic force constant matrix of nitromethane molecule is also shown in Figure 1.

The physical interpretation of Eqs. (7) and (8) is as follows: If a particular eigenvalue λ_i^{AB} of $[k_{AB}]$ is positive, this means that the reaction force on A due to a displacement of B in the direction of \hat{v}_i^{AB} is in the same direction. If all three eigenvalues are positive, then for any displacement of B there is always a restoring reaction force on A that seeks to maintain the original interatomic separation. The atoms A and B are then described as pairwise stable. All pairs of formally bonded atoms belong to this category, as well as some between which there is no formal bond but such a strong interaction that the atoms can be viewed as bonded. If one or more eigenvalues are negative, then A will not feel a restoring reaction force trying to maintain unchanged the AB separation. This condition is described as a pairwise unstable interaction, and we conclude that A and B are not bonded. The same conclusion is reached when two of the three eigenvalues or eigenvectors are complex.

If one of the eigenvectors, \hat{v}_i^{AB} , is in the direction from A to B, which shall be described by the unit vector \hat{u}^{AB} , and forms an orthonormal system with the other two eigenvectors, then the force constant for the interaction between A and B, whether they are bonded or not, is,

$$k_{AB} = \lambda_i^{AB}. \quad (9)$$

When the direction from A to B does not coincide with that of any of the eigenvectors, or when the eigenvectors are not orthogonal to each other, then the force constant k_{AB} may have contributions from more than one eigenvalue of $[k_{AB}]$ in proportion to the projections of the corresponding eigenvectors upon the unit vector \hat{u}^{AB} :

$$k_{AB} = \sum_{i=1}^3 \lambda_i^{AB} |\hat{u}^{AB} \cdot \hat{v}_i^{AB}|. \quad (10)$$

Equation (9) is clearly a special case of Eq. (10). The magnitude of k_{AB} , as given by these equations, is obtained directly from the eigenvalues of the matrix $[k_{AB}]$ in Cartesian coordinates, and hence is invariant to the choice of internal coordinates. This invariance is a fundamental requirement for any physical quantity.

BOND ANGLE FORCE CONSTANTS

Consider the bonds AB and CB which have unit vectors \hat{u}^{AB} and \hat{u}^{CB} . Their interatomic matrices $[k_{AB}]$ and $[k_{CB}]$ have eigenvalues λ_i^{AB} and λ_i^{CB} , and eigenvectors \hat{v}_i^{AB} and \hat{v}_i^{CB} ($i = 1, 2, 3$). Let \hat{u}_N be a unit vector perpendicular to the plane ABC:

$$\hat{u}_N = \frac{\hat{u}^{CB} \times \hat{u}^{AB}}{|\hat{u}^{CB} \times \hat{u}^{AB}|}. \quad (11)$$

Then the unit vectors perpendicular to the bonds AB and CB on the plane ABC are

$$\hat{u}^{PA} = \hat{u}_N \times \hat{u}^{AB} \quad (12)$$

and

$$\hat{u}^{PC} = \hat{u}^{CB} \times \hat{u}_N. \quad (13)$$

They are the direction of small displacements of atoms A and C that result from opening or closing the angle ABC. If R_{AB} and R_{CB} are the length of the bonds, the bond angle force constant is then given by

$$\frac{1}{k_\theta} = \frac{1}{R_{AB}^2 \sum_{i=1}^3 \lambda_i^{AB} |\hat{u}^{PA} \cdot \hat{v}_i^{AB}|} + \frac{1}{R_{CB}^2 \sum_{i=1}^3 |\hat{u}^{PC} \cdot \hat{v}_i^{CB}|}. \quad (14)$$

DIHEDRAL ANGLE FORCE CONSTANTS

Consider the dihedral angle defined by the atoms A, B, C, and D which are linked by bonds AB, BC, and CD. The approach is similar to that used for bond angles. Unit vectors perpendicular to the planes ABC and BCD are given by

$$\hat{u}_{N_{ABC}} = \frac{\hat{u}^{CB} \times \hat{u}^{AB}}{|\hat{u}^{CB} \times \hat{u}^{AB}|} \quad (15)$$

$$\hat{u}_{N_{BCD}} = \frac{\hat{u}^{DC} \times \hat{u}^{BC}}{|\hat{u}^{DC} \times \hat{u}^{BC}|}. \quad (16)$$

The dihedral angle force constant is then

$$\frac{1}{k_\phi} = \frac{1}{R_{BA}^2 |\hat{u}_{AB} \times \hat{u}_{BC}|^2 \sum_{i=1}^3 \lambda_i^{AB} |\hat{u}_{N_{ABC}} \cdot \hat{v}_i^{AB}|} + \frac{1}{R_{CD}^2 |\hat{u}_{BC} \times \hat{u}_{CD}|^2 \sum_{i=1}^3 \lambda_i^{DC} |\hat{u}_{N_{BCD}} \cdot \hat{v}_i^{DC}|} \quad (17)$$

IMPROPER DIHEDRAL (OUT-OF-PLANE) ANGLE FORCE CONSTANTS

Let atoms B, C, and D be connected to the central atom A. Then the out-of-plane angle ω_{ABCD} is defined as the angle between planes ABC and BCD. The movement of A perpendicular to the plane BCD feels a restoring force from the bonds AB, AC, and AD. The effective force constant for the movement of A perpendicular to BCD is given by the sum of the three bond contributions:

$$k_{AN} = \sum_{i=1}^3 \lambda_i^{AB} |\hat{u}^N \cdot \hat{v}_i^{AB}| + \sum_{i=1}^3 \lambda_i^{AC} |\hat{u}^N \cdot \hat{v}_i^{AC}| + \sum_{i=1}^3 \lambda_i^{AD} |\hat{u}^N \cdot \hat{v}_i^{AD}|, \quad (18)$$

where \hat{u}^N is a unit vector perpendicular to the plane BCD. Then the out-of-plane force constant for the angle ω_{ABCD} is

$$k_\omega = k_{\omega_{ABCD}} = h_{ABCD}^2 k_{AN}, \quad (19)$$

where h_{ABCD} is the length of projection into the plane BCD of the altitude of triangle ABC (with base BC).

Applications

We have coded the preceding equations in the program FUERZA. It is presently designed to read the Cartesian Hessian tensor from the output of a Gaussian [16] program after a frequency (FREQ) or second derivative of the energy has been requested. The output format of FUERZA is compatible with the input format of the molecular modeling program CHARMM [17]. These features can, of course, be modified to be consistent with other programs.

In the applications that follow, we used a procedure based on density functional theory (DFT) available in the program Gaussian 94 [16] to optimize geometries and compute the second derivatives of the energy. The Becke 88 [18] and the Lee-Yang-Parr [19] functionals were used to represent the exchange and correlation potentials, respectively. However, our method can be implemented with any other DFT, ab initio or semiempirical technique. In the cases to be discussed, FUERZA used the force constants in the output of a frequency DFT calculation to create the intramolecular force field, which was subsequently

used in conjunction with CHARMM for a classical calculation of vibrational frequencies. The extent to which these reproduce the original DFT frequencies is a measure of the quality of the constructed force field. (The DFT procedure being used is known to be effective for vibrational frequencies [20, 21].) In the trivial case of diatomic molecules, exact agreement is obtained, as it must be, since there is only one independent internal coordinate and hence one possible force constant.

In the following, all bond lengths are in Å, angles in degrees, bond force constants in kcal/Å², angular force constants in kcal/rad², frequencies in cm⁻¹, and doubly or higher degenerate vibrational modes are listed only once.

H₂O

The DFT values for the bond length and bond angle are 0.976 and 102.7; the corresponding force constants are 1067 and 80.4, as compared to 900 and 110 in the CHARMM force field. All three eigenvalues of the interaction matrix [K_{HH}] are positive, indicating a stable HH interaction which should be included in the force field. The equilibrium HH distance is 1.249 and the force constant is 31.1. The vibrational frequencies obtained with this force field are 1555, 3674, and 3679; the DFT frequencies are 1636, 3643, and 3754 respectively.

NO₂

The DFT bond lengths and bond angle are 1.224 and 133.1, and the corresponding force constants are 1334 and 242. No stable OO interaction is found. The created force field frequencies are 703, 1201, and 1630, compared to the DFT 713, 1301, and 1586.

CH₃

For this radical in D_{3h} symmetry, the DFT bond length is 1.089 and the bond force constant is 768. The bond angle and out-of-plane force constants are 62 and 12.2. The resulting force field frequencies are 449, 1426, 2997, and 3186, while the DFT are 459, 1386, 3059, and 3236.

CH₃NO₂

It should be noted that parameters for nitro derivatives are not available in any of the standard force fields. The frequencies calculated with the

FUERZA program, with the DFT values given in parentheses, are: 577(572), 606(619), 945(866), 1000(1067), 1081(1091), 1176(1323), 1278(1370), 1294(1436), 1418(1450), 1694(1558), 2912(3014), 3033(3107), and 3064(3136). The first two frequencies are not given, since they correspond to the lowest torsional modes, in which anharmonic effects are particularly significant; accordingly, neither harmonic approximation, empirical nor DFT, is meaningful.

CIS-RH(PH₃)₂(CO)F

The results of an earlier DFT study [22] were used to make a more demanding test of the present approach. The force field frequencies obtained, with the DFT values in parentheses, are: 91(102), 91(107), 91(114), 92(115), 254(271), 260(274), 292(297), 393(403), 408(448), 419(465), 422(470), 434(477), 452(522), 782(530), 801(968), 966(993), 971(1095), 971(1095), 991(1098), 1328(1100), 1925(1935), 2315(2362), 2315(2364), 2339(2386), 2339(2388), 2348(2390), and 2361(2390). The frequencies for the lowest three torsional modes are not given, again because anharmonic effects render them useless.

Conclusion

Overall, the vibrational frequencies obtained with the FUERZA force fields are in very good agreement with those resulting from the DFT original calculations, over a wide range of values. This supports the physical validity of the approach that we have presented for obtaining an intramolecular force field in terms of force constants that are invariant to the choice of internal coordinates. The procedure can be applied to any molecular system for which Cartesian second derivatives of the energy are available.

ACKNOWLEDGMENT

We greatly appreciate the financial support of the Office of Naval Research, through contract No. N00014-95-1-0028.

References

1. B. R. Gelin, *Molecular Modeling of Polymer Structures and Properties* (Hanser Publishers, Munich, 1994).

2. P. L. Hyskens, W. A. P. Luck, and T. Zeegers-Hyskens, Eds., *Intermolecular Forces* (Springer-Verlag, Berlin, 1991).
3. M. Dagher, M. Kobersi, and H. Kobeissi, *J. Comp. Chem.* **16**, 723 (1995).
4. C. J. M. Huige and C. Altona, *J. Comp. Chem.* **16**, 56 (1995).
5. T. Furuki, A. Umeda, M. Sakurai, Y. Inoue, R. Chujo, and K. Harata, *J. Comp. Chem.* **15**, 90 (1994).
6. R. V. Stanton, D. S. Hartsough, and K. M. Merz, Jr., *J. Comp. Chem.* **16**, 113 (1995).
7. D. Cvetko, A. Lausi, A. Morgante, F. Tommasini, P. Cortona, and M. G. Dondi, *J. Comp. Phys.* **100**, 2052 (1994).
8. W. V. Gunsteren, *J. Comp. Phys.* **23**, 327 (1977).
9. J. M. Seminario, M. C. Concha, J. S. Murray, and P. Politzer, *Chem. Phys. Lett.* **225**, 25 (1994).
10. J. M. Seminario, M. C. Concha, and P. Politzer, *J. Chem. Phys.* **102**, 8281 (1995).
11. J. M. Seminario, M. C. Concha, and P. Politzer, *Int. J. Quantum Chem.* **29**, 621 (1995).
12. M. Diem, *Introduction to Modern Vibrational Spectroscopy* (Wiley, New York, 1993).
13. P. Pulay, G. Fogarasi, F. Pang, and J. E. Boggs, *J. Am. Chem. Soc.* **101**, 2550 (1979).
14. A. St-Amant and D. R. Salahub, *Chem. Phys. Lett.* **169**, 387 (1990).
15. A. St-Amant, Ph.D. Thesis (Université de Montréal, 1992).
16. M. J. Frisch, G. W. Trucks, H. B. Schlegel, P. M. W. Gill, B. G. Johnson, M. A. Robb, J. R. Cheeseman, T. Keith, G. A. Petersson, J. A. Montgomery, K. Raghavachari, M. A. Al-Laham, V. G. Zakrzewski, J. V. Ortiz, J. B. Foresman, C. Y. Peng, P. Y. Ayala, W. Chen, M. W. Wong, J. L. Andres, E. S. Replogle, R. Gomperts, R. L. Martin, D. J. Fox, J. S. Binkley, D. J. Defrees, J. Baker, J. P. Stewart, M. Head-Gordon, C. Gonzalez and J. A. Pople, Gaussian 94, Revision B.3, Gaussian, Inc., Pittsburgh PA., 1995.
17. B. R. Brooks, R. E. Brucoleri, B. D. Olafson, D. J. States, S. Swaminathan, and M. Karplus, *J. Comput. Chem.* **4**, 187 (1983).
18. A. D. Becke, *Phys. Rev. A* **33**, 3098 (1988).
19. C. Lee, W. Yang, and R. G. Parr, *Phys. Rev. B* **37**, 785 (1988).
20. B. G. Johnson, P. M. Gill, and J. A. Pople, *J. Chem. Phys.* **98**, 5612 (1993).
21. B. G. Johnson, in *Modern Density Functional Theory: A Tool for Chemistry*, J. Seminario and P. Politzer, Eds. (Elsevier Science, Amsterdam, 1995), Chap. 6.
22. E. A. Salter, A. Wierzbicki, J. M. Seminario, N. W. Hoffman, M. L. Easterling, and J. D. Madura, *J. Phys. Chem.* **98**, 129845 (1994).

Intermolecular Perturbation Theory: Renormalized Interaction Energies

WILLIAM H. ADAMS

*Wright and Rieman Chemistry Laboratories, Rutgers University, New Brunswick, New Jersey 08903;
e-mail: adams@rutchem.rutgers.edu*

Received February 26, 1996; accepted June 5, 1996

ABSTRACT

For intermolecular perturbation theories in which it is assumed that the unperturbed wave function of the composite system is a product of the unperturbed wave functions of its components, and which satisfy one general constraint, we derive two renormalized interaction energy expressions which are more accurate than the perturbation expansions, when all are evaluated to comparable order. This is accomplished by focusing on the parameter λ in terms of which the perturbation expansions are derived rather than on the potential of interaction between components. In the derivation of each renormalized energy formula, we discard zeroth- through infinite-order terms which do not contribute to the interaction energy when the interaction is turned on fully, i.e., when $\lambda = 1$. The first renormalized interaction energy when $\lambda = 1$ is identical in form to the interaction energy in the symmetrized Rayleigh-Schrödinger (SRS) theory, but not in interpretation. The wave function appearing in the renormalized energy cannot generally be that assumed in the SRS theory, and the renormalized energy to zeroth order in λ is not zero. The latter is not surprising because we discarded a zeroth-order term in the derivation. The second renormalized interaction energy formula is derived from the first by using the same set of assumptions and arguments that were used in deriving the first. We expect it to be more accurate than the first, which is expected to be more accurate than the sum of the perturbation energies, all evaluated to comparable order. These expectations are supported by the results of calculations on LiH using two perturbation theories, the polarization approximation and the Amos-Musher theory. The first-order wave functions for both were calculated in the configuration interaction (CI) approximation; then the interaction energies were calculated by summing the perturbation energies through third order and by evaluating the renormalized energy expressions. The perturbation results are compared to interaction energies calculated by full CI with the same basis set. As important as the formulas is the light our analysis throws on the meaning of order in intermolecular perturbation theory. © 1996 John Wiley & Sons, Inc.

Introduction

We show that for a certain class of intermolecular perturbation theories, interaction energies can be calculated more accurately from two renormalized energy formulas than from the energy expansions defined by the perturbation theories, using in each case just the zeroth through n th-order wave functions. In the theories we consider, it is assumed that the unperturbed wave function for two interacting atoms/molecules is the product of the ground-state atomic/molecular wave functions for the noninteracting systems. There are additional conditions that the theories must satisfy. The most important is that they should give, in principle, exact energies and wave functions when carried to infinite order. It is this condition that the simplest intermolecular perturbation theories fail to satisfy, due to the existence, for nearly all systems, of an infinite number of unphysical solutions to the Schrödinger equation, lying lower in energy than the physical ground state.

Unphysical solutions of the Schrödinger equation are those which violate the Pauli exclusion principle. Claverie [1] explained how they become accessible in the simplest intermolecular perturbation theory, the polarization approximation (PA) [2], and that the lowest energy unphysical solutions have lower energies than the physical ground state. Morgan and Simon [3] later observed that there were an infinite number of unphysical solutions of lower energy than the physical ground state in any system containing at least one atom of atomic number greater than 2, and that the physical ground-state energy lies in a continuum of unphysical state energies. Consequently, the PA theory not only gives a divergent energy expansion [4], but cannot be used in principle to calculate the ground-state energy if carried to infinite order [5]. The simplest improvement on the PA theory, the symmetrized Rayleigh-Schrödinger (SRS) theory [6-9], fails similarly [10]. In contrast to these negative results, we have shown that one can circumvent the unphysical states problem by changing the Hamiltonian for the interacting systems in ways that make its lowest energy eigenfunction the physical ground-state function [5, 11, 12]. Perhaps the simplest change is that made in the Amos-Musher (AM) theory [13]. It was relatively inaccurate when applied to H_2^+ [14], but this

defect is corrected significantly by the renormalized energy expressions derived in this study.

An essential element in our derivation of the renormalized interaction energy formulas, and in our understanding of these formulas, is the explicit use of a parameter λ in carrying out the perturbation expansions. It might seem unnecessary to include λ explicitly since it multiplies the perturbing potential \hat{V} in the Hamiltonian for an interacting pair of molecules, but it is the key to deriving and understanding the renormalized energy expressions. In particular, the focus on λ , as we will explain, gives us a mathematical handle for understanding perturbation theory. We feel that an oft-cited defect of intermolecular perturbation theories [2, 15], that orders are not uniquely defined, is more imaginary than real. It is based on the false assumptions that \hat{V} is "weak" and that expansion of the energy and wave function in powers of λ is equivalent to expansion in powers of \hat{V} . If \hat{V} were weak, an infinite number of unphysical states would not be lower in energy than the physical ground state. The renormalized energy formulas show that expansion in λ is not equivalent to expansion in \hat{V} . For example, our first formula gives to zero order in λ the Heitler-London interaction energy. There is no mystery to this because we have identified terms of all orders which cannot contribute to the interaction energy in the limit $\lambda = 1$ and then discarded those terms. The resultant energy expression is identical to that of the SRS perturbation theory, except for its λ dependence and except that the wave function appearing in it cannot be the PA function if the system has more than two electrons. Our second interaction energy formula is derived from the first by applying to it the same reasoning that led to the first.

In the next section we summarize our understanding of the perturbation problem defined by the assumption that the unperturbed wave function for the system is the product of the unperturbed, ground-state wave functions of two atoms/molecules. The renormalized interaction energy formulas are derived in the third section for perturbation theories based on Hamiltonians that satisfy certain general conditions. We infer that the second formula is more accurate than the first, and that both are more accurate than the sum of the perturbation energies when calculated to the same order in the wave function. This section is followed by one in which the Hamiltonians of several published perturbation theories are recast in the form assumed in the derivation of the renor-

malized energy formulas. In the next to last section, we apply the energy formulas to the LiH $^1\Sigma$ ground state using the PA and the AM perturbation theories. The results support our assertion that the renormalized energies are more accurate than the sum of the perturbation theory energies. In addition, the results suggest how one might calculate still more accurate interaction energies than the renormalized energy formulas give. This conjecture is tested, too.

Nature of the Problem

Most of the work on intermolecular perturbation theory published until the 1990s did not take into consideration the unphysical states problem delineated by Claverie [1] and Morgan and Simon [3]. In this section we define our notation as we summarize what the existence of these states implies for perturbation theories based on a zeroth-order wave function which is a product of unperturbed atomic or molecular functions, specific electrons being assigned to each subsystem. The problem is defined by the PA theory.

The PA theory is just the Rayleigh–Schrödinger perturbation theory with a specific choice for the unperturbed Hamiltonian [2]. Let A and B represent two interacting systems, which have, respectively, N_A and N_B electrons. We arbitrarily assign the first N_A electronic position-spin coordinates to A, the coordinates $N_A + 1$ to $N = N_A + N_B$ to B. Let \hat{H} be the nonrelativistic Hamiltonian for the A–B system in the Born–Oppenheimer approximation. The unperturbed Hamiltonian \hat{H}^0 is the Hamiltonian of A when B is absent, plus the Hamiltonian of B when A is absent. The two systems interact via $\hat{V} = \hat{H} - \hat{H}^0$. The lowest energy eigenfunction of \hat{H}^0 is F^0 and its eigenvalue, \mathcal{E}^0 . The function F^0 in our calculations is the spin-coupled product of the A and B ground-state wave functions, and \mathcal{E}^0 is the sum of the A and B ground-state energies. In the PA theory one solves

$$(\hat{H}^0 + \lambda \hat{V})F(\lambda) = \mathcal{E}(\lambda)F(\lambda) \quad (1)$$

by the Rayleigh–Schrödinger method setting

$$F(\lambda) = F^0 + \sum_{n=1}^{\infty} \lambda^n F^{(n)} \quad \text{and} \quad \mathcal{E}(\lambda) = \mathcal{E}^0 + \sum_{n=1}^{\infty} \lambda^n \mathcal{E}^{(n)}. \quad (2)$$

Note that λ has only two physically significant values, zero and one. No attempt is made in the PA theory to exploit the electronic exchange symmetry that is so important for chemical bonding. The result is a theory with major defects: the expansions (2) must diverge for systems containing more than two electrons [1, 4] and, for systems containing one atom of atomic number greater than 2, one cannot give a closed-end prescription for calculating, in principle, the exact ground-state energy [5]. This raises a question as to the significance that should be attached to low-order PA calculations and to refinements of the PA theory.

One can gain a good intuitive understanding of the eigenvalues of (1) at $\lambda = 0$ and 1 by considering the limit of large separations R between A and B. We require $F(\lambda)$ to be antisymmetric in the A electronic coordinates and, separately, in the B electronic coordinates. Thus, the set of $\mathcal{E}(0)$'s equal all possible sums of one unperturbed A and one unperturbed B eigenenergy. For R infinite, some members of the set of $\mathcal{E}(1)$'s equal members of the set of $\mathcal{E}(0)$'s, but there are additional eigenvalues corresponding to states which violate the Pauli exclusion principle. We have explained in some detail the origin of these states for LiH [16]. We have used the configuration interaction (CI) method to solve Eq. (1) nonperturbatively for $^1\Sigma$ LiH for $0 \leq \lambda \leq 1$. Our results show that the $\mathcal{E}(\lambda)$ at finite R have the dependence on λ inferred by Claverie [1], namely, that the lowest eigenvalue $\mathcal{E}_1(\lambda)$ equals \mathcal{E}^0 at $\lambda = 0$, that it shows behavior characteristic of an avoided crossing with $\mathcal{E}_2(\lambda)$ well before $\lambda = 1, \dots$, and that it equals E_1^u , the lowest unphysical state energy, at $\lambda = 1$ [5, 10–12]. We find for LiH, from the equilibrium bond length to infinity, that $\mathcal{E}^0 - E_1^u \cong 1$ hartree, which is much larger than the binding energy of about 0.08 hartree. The magnitude of $\mathcal{E}^0 - E_1^u$ is consistent with the insight of Morgan and Simon [3] in that it suggests that the unphysical continuum at large R begins about 0.5 hartree below \mathcal{E}^0 .

To understand the mathematical properties of the energy expansion in Eq. (2), one lets λ be complex and interprets $\mathcal{E}(\lambda)$ as a multivalued function of λ . The general properties of $\mathcal{E}(\lambda)$ are well understood in the CI approximation [17–19]. In particular, it is known that $\mathcal{E}(\lambda)$ can have only branch point singularities. We denote the sheets of the $\mathcal{E}(\lambda)$ Riemann surface by $\mathcal{E}_k(\lambda)$ and order them so that $\Re \mathcal{E}_k(\lambda) \leq \Re \mathcal{E}_{k+1}(\lambda)$. The eigenfunction corresponding to $\mathcal{E}_k(\lambda)$ is denoted by $F_k(\lambda)$. In an exploratory set of calculations we have found

that the avoided crossing between $\mathcal{E}_1(\lambda)$ and $\mathcal{E}_2(\lambda)$ for LiH arises from a pair of branch points narrowly straddling the real λ axis at $\lambda \approx 0.78$. Thus, the power series expansion [Eq. (2)] of $\mathcal{E}_1(\lambda)$ has a radius of convergence ≈ 0.78 . Only within that radius of convergence does the power series uniquely define $\mathcal{E}(\lambda)$. For $|\lambda|$ greater than the radius of convergence, one can in principle analytically continue the series either along the lowest Riemann sheet or to the second lowest. The physical ground-state energy, however, generally lies on neither of these sheets, but on a sheet that is an indeterminate number of sheets above $\mathcal{E}_1(\lambda)$. In an exact calculation, that indeterminate number is expected to be infinity. One can assume that it is possible by successive analytical continuations of the power series to move from the lowest sheet to the sheet on which the physical ground-state energy lies, but there is zero probability that, after any number of continuations, the desired sheet will have been reached [5].

One naturally conjectures that the simplest way to correct the deficiencies of the PA theory is to project out the unphysical contributions to $F_1(\lambda)$ and calculate the energy from it. This is exactly what is done in the SRS theory [6–9]. Unfortunately, the SRS theory to infinite order is no more accurate for LiH than is the PA theory [10] when one uses $F_1(\lambda)$. One can again imagine analytically continuing the PA expansion from the lowest Riemann sheet to the sheet on which the physical ground-state energy lies, but one still has to carry out an indeterminate, if not infinite, number of successive continuations. This will not be the case for a perturbation theory derived from a Hamiltonian which has no unphysical states below the physical ground state. We show in the next section that if $F_1(\lambda)$ is determined by such a perturbation theory, generally not the PA theory, then the SRS energy expression gives a renormalized interaction energy which sums an infinite number of contributions to the usual perturbation approximation to the interaction energy.

We would use the difficulties that arise in the PA theory from the existence of unphysical states as an argument for abandoning intermolecular perturbation theories based on the choice \hat{H}^0 for the unperturbed Hamiltonian, except that we have shown that there are theories which do not have the defects of the PA theory. These are theories in which $\mathcal{E}(0) = \mathcal{E}^0$ and $\mathcal{E}_1(1) = E_1$, the physical ground-state energy. It is to these theories that the

energy formulas we derive in the next section should be applied. The theories are reviewed in a later section.

Interaction Energy Formulas

We derive two interaction energy formulas which effect partial infinite-order summations of energy expansions for a number of intermolecular perturbation theories. In the derivations we assume that the perturbed wave function $F(\lambda)$ is an eigenfunction of a Hamiltonian $\hat{H}^0 + \lambda\hat{\mathcal{V}}$ and that the perturbed energy $\mathcal{E}(\lambda)$ is the corresponding eigenvalue. It follows that the interaction energy

$$\Delta\mathcal{E}(\lambda) = \mathcal{E}(\lambda) - \mathcal{E}^0 = \lambda \langle F^0 | \hat{\mathcal{V}} | F(\lambda) \rangle \quad (3)$$

when $F(\lambda)$ is normalized so that $\langle F^0 | F(\lambda) \rangle = 1$. Equation (3) gives the interaction energy directly rather than as the difference between two total energies. The potential $\hat{\mathcal{V}}$ is different for each of the perturbation theories considered in the next section, but each satisfies $\hat{\mathcal{A}}\hat{\mathcal{V}} = \hat{\mathcal{A}}\hat{V}$. It follows that

$$\hat{\mathcal{A}}(\hat{H}^0 + \lambda\hat{V})F(\lambda) = \mathcal{E}(\lambda)\hat{\mathcal{A}}F(\lambda). \quad (4)$$

We derive the first interaction energy formula from Eq. (4). It is effectively the SRS energy formula, but its derivation provides a useful understanding of what has been accomplished in deriving that formula. The derivation suggests that one can expect the formula to give more accurate approximations to interaction energies when the $F(\lambda)$ expansion is truncated at n th order than can be obtained from Eq. (3) with the same approximation to $F(\lambda)$. From the understanding gained in deriving the first formula, we are lead to apply to that formula the same series of manipulations. The derivation uses another consequence of $\hat{\mathcal{A}}\hat{\mathcal{V}} = \hat{\mathcal{A}}\hat{V}$, namely, that

$$\hat{\mathcal{A}}(\hat{H}^0 - \mathcal{E}^0)F^{(1)} = \hat{\mathcal{A}}(\mathcal{E}^{(1)} - \hat{V})F^0, \quad (5)$$

where $F^{(1)}$ is the first-order wave function of the theory which defines $F(\lambda)$. The result is a second renormalized interaction energy formula. We expect it to be more accurate than the first.

A key element in the derivations is the commutator identity

$$[\hat{\mathcal{A}}, \hat{H}^0] = [\hat{V}, \hat{\mathcal{A}}]. \quad (6)$$

It is this identity which Hirschfelder called paradoxical [2] because its left side is zeroth order in

\hat{V} , the right, first order. Equation (6) would be paradoxical if the perturbation expansions [Eq. (2)] were developed in powers of \hat{V} rather than λ , but they are not. No λ appears in Eq. (6); both sides of Eq. (6) are zeroth order in λ . At the time Hirschfelder called it paradoxical, it was believed that \hat{V} was a weak perturbation. Given the understanding that we now have of the relationship between the physical and unphysical state eigenvalues of $\hat{H}^0 + \hat{V}$, and the relationship of both to the eigenvalues of \hat{H}^0 , it is unreasonable to assume that \hat{V} is a weak perturbation, suitable for defining orders in an expansion. Furthermore, expansion in \hat{V} is much more complicated than expansion in λ . This is quite clear in the CI approximation in which expansion in \hat{V} means that each element of the \hat{V} matrix should be treated as an independent variable. A power series expansion in terms of λ is simpler, and it gives some mathematical understanding of the properties of $\mathcal{E}(\lambda)$ [17–19].

To derive the first formula, we use Eq. (6) to transform Eq. (4) into

$$\left[\hat{H}^0 \hat{\mathcal{A}} + \hat{V} \hat{\mathcal{A}} + (\lambda - 1) \hat{\mathcal{A}} \hat{V} \right] F(\lambda) = \mathcal{E}(\lambda) \hat{\mathcal{A}} F(\lambda). \quad (7)$$

Next, multiply Eq. (7) from the left by the complex conjugate of F^0 and integrate over all space. Since F^0 is an eigenfunction of \hat{H}^0 and \mathcal{E}^0 is its eigenvalue, it follows that

$$\begin{aligned} \Delta \mathcal{E}(\lambda) &= \mathcal{E}(\lambda) - \mathcal{E}^0 \\ &= \frac{\langle F^0 | \hat{V} \hat{\mathcal{A}} | F(\lambda) \rangle + (\lambda - 1) \langle F^0 | \hat{\mathcal{A}} \hat{V} | F(\lambda) \rangle}{\langle F^0 | \hat{\mathcal{A}} | F(\lambda) \rangle}. \end{aligned} \quad (8)$$

In the discussion which follows, the function $F(\lambda)$ should be regarded generally as the exact, unexpanded eigenfunction of $\hat{H}^0 + \lambda \hat{V}$. Only when discussing order should it be assumed that $F(\lambda)$ is a power series in λ as in Eq. (2).

The term in the numerator of Eq. (8) that is multiplied by $\lambda - 1$ is interesting. It does not contribute to the energy when $\lambda = 1$, but it contributes a term to each order of the λ expansion of $\Delta \mathcal{E}(\lambda)$. What is more interesting is that part of what it contributes in n th order is canceled, when $\lambda = 1$, by part of what it contributes in $n + 1$ th order. For example, it contributes in the

numerator of Eq. (8) to zeroth order $-\langle F^0 | \hat{\mathcal{A}} \hat{V} | F^0 \rangle$ and to first order $\langle F^0 | \hat{\mathcal{A}} \hat{V} | F^0 \rangle - \langle F^0 | \hat{\mathcal{A}} \hat{V} | F^{(1)} \rangle$. The second-order contribution is $\langle F^0 | \hat{\mathcal{A}} \hat{V} | F^{(1)} \rangle - \langle F^0 | \hat{\mathcal{A}} \hat{V} | F^{(2)} \rangle$, and so on. In short, when one truncates the λ expansion of $\Delta \mathcal{E}(\lambda)$ at n th order, one includes terms which do not contribute in infinite order when $\lambda = 1$. For this reason, if one is going to approximate the interaction energy by a truncated expansion in λ , one should derive it from

$$\Delta E_s(\lambda) = \frac{\langle F^0 | \hat{V} \hat{\mathcal{A}} | F(\lambda) \rangle}{\langle F^0 | \hat{\mathcal{A}} | F(\lambda) \rangle}. \quad (9)$$

This is the SRS energy expression except for two differences. First, in the SRS theory it is assumed implicitly that \hat{V} is multiplied by λ ; that is clearly not the case in Eq. (9). Second, the $F(\lambda)$ in Eq. (9) cannot generally be the PA wave function [10].

The problem with using the PA theory $F(\lambda)$ in Eq. (9) arises even when one restricts the theory to the determination of the potential energy surface of the physical ground state. In this case, \mathcal{E}^0 in Eq. (8) should be the lowest eigenvalue of \hat{H}^0 . Thus, we are interested in $\mathcal{E}_1(\lambda)$, the lowest sheet of the $\mathcal{E}(\lambda)$ Riemann surface. For nearly all systems, the PA theory $\mathcal{E}_1(1)$ equals the lowest unphysical state energy and $\mathcal{A}F_1(1) = 0$, i.e., Eq. (8) gives $\Delta \mathcal{E}(\lambda) = 0/0$. In contrast, the Hamiltonians considered in the next section all have $\mathcal{E}_1(1) = E_1$, the physical ground-state energy, and for each, $\mathcal{A}F(1)$ is proportional to the physical ground-state wave function. In the PA theory, $\mathcal{E}_1(1) = E_1$ only for one and two electron systems.

The denominator of Eq. (8) is also interesting. If one substitutes in Eq. (8) the $F(\lambda)$ expansion truncated to n th order, then expands this approximation to $\Delta \mathcal{E}(\lambda)$, the expansion includes contributions of infinite order in λ , i.e., the denominator of Eq. (8) effects an infinite-order summation of selected contributions to the $\Delta \mathcal{E}(\lambda)$ expansion. In fact, we first derived an approximation to the energy formula given below by summing selected terms in the $\Delta \mathcal{E}(\lambda)$ expansion of the AM theory. We conclude that Eq. (9) includes an infinite-order summation of contribution to the $\Delta \mathcal{E}(\lambda)$ expansion. Equation (9) is the first of the renormalized interaction energies.

The importance of the denominator in Eq. (9) increases as the number of electrons increases. To see this, one has only to assume that at large R , the dominant contribution to $F(\lambda)$ is F^0 . Then

$\langle F^0 | \hat{\mathcal{A}} | F(1) \rangle \cong \langle F^0 | \hat{\mathcal{A}} | F^0 \rangle$. For binary systems, as $R \rightarrow \infty$, all permutation contributions to $\langle F^0 | \hat{\mathcal{A}} | F^0 \rangle$ approach zero except that from the identity operation, i.e., $\langle F^0 | \hat{\mathcal{A}} | F^0 \rangle \approx N_A! N_B! / N!$. This equals $\frac{1}{4}$ in our LiH calculations. It will be much smaller for systems containing more electrons.

The expansion of $\Delta E_s(\lambda)$ differs from the expansion of $\Delta \mathcal{E}(\lambda)$ even to the zeroth order in λ . To zeroth order, $\Delta \mathcal{E}(\lambda)$ is zero, but $\Delta E_s(0) = \langle F^0 | \hat{V} \hat{\mathcal{A}} | F^0 \rangle / \langle F^0 | \hat{\mathcal{A}} | F^0 \rangle = \Delta E_{\text{HL}}$, commonly called the Heitler–London energy. It is also the first-order SRS energy. It should not be puzzling that $\Delta E_s(0)$ is nonzero. When we discarded the term in $\Delta \mathcal{E}(\lambda)$ that is multiplied by $\lambda - 1$ to get $\Delta E_s(\lambda)$, we discarded $-\langle F^0 | \hat{\mathcal{A}} \hat{V} | F^0 \rangle$, which is the term which cancels the zeroth-order contribution from $\langle F^0 | \hat{V} \hat{\mathcal{A}} | F(\lambda) \rangle$ to the numerator of $\Delta \mathcal{E}(\lambda)$. That $\Delta E_s(0)$ should equal ΔE_{HL} is not absurd. It is as if one knew an unperturbed Hamiltonian having $\hat{\mathcal{A}} F^0$ for an eigenfunction, with $\mathcal{E}^0 + \Delta E_{\text{HL}}$ as its eigenvalue. A perturbation theory based on that Hamiltonian would give the same zeroth-order contribution to the interaction energy. No such theory has been proposed.

Since in zeroth order $\Delta E_s(\lambda)$ is equal to what is generally regarded as a first-order energy, one should expect that to first order in λ it will include second-order energies $\mathcal{E}^{(2)}$, and so on. To look at these contributions, we have to consider a specific perturbation theory, which we do in the next section. We show there that the numerator of $\Delta E_s(\lambda)$ expanded to first order in λ does include $\mathcal{E}^{(2)}$. There is no reduction in computational effort associated with the shifting of terms from higher to lower order, but one does get higher accuracy.

In the Rayleigh–Schrodinger perturbation theory, one can calculate the energy to third order if one knows the zeroth- and first-order wave functions. This is done by recognizing that the equation which determined $F^{(2)}$ can be used to eliminate $F^{(2)}$ from the third-order energy, i.e., $\mathcal{E}^{(3)} = \langle F^0 | \hat{V} - \mathcal{E}^{(1)} | F^{(2)} \rangle = -\langle F^{(1)} | \hat{H}^0 - \mathcal{E}^0 | F^{(2)} \rangle = \langle F^{(1)} | \hat{V} - \mathcal{E}^{(1)} | F^{(1)} \rangle$. We use Eq. (5) to achieve a similar end. We solve Eq. (5) for $\hat{\mathcal{A}} \hat{V} F^0$, then substitute its Hermitian adjoint into Eq. (8) to obtain $\Delta \mathcal{E}(\lambda) \langle F^0 | \hat{\mathcal{A}} | F(\lambda) \rangle = \langle F^0 | \hat{\mathcal{A}} | F(\lambda) \rangle \mathcal{E}^{(1)} - \langle F^{(1)} | (\hat{H}^0 - \mathcal{E}^0) \hat{\mathcal{A}} | F(\lambda) \rangle + (\lambda - 1) \langle F^0 | \hat{\mathcal{A}} \hat{V} | F(\lambda) \rangle$. Finally, we use Eq. (6) followed by Eq. (4) to arrive at

$$\Delta \mathcal{E}(\lambda) = \frac{\langle F^0 | \hat{\mathcal{A}} | F(\lambda) \rangle \mathcal{E}^{(1)} + \langle F^{(1)} | \hat{V} \hat{\mathcal{A}} | F(\lambda) \rangle + (\lambda - 1) \langle F^0 + F^{(1)} | \hat{\mathcal{A}} \hat{V} | F(\lambda) \rangle}{\langle F^0 + F^{(1)} | \hat{\mathcal{A}} | F(\lambda) \rangle} \quad (10)$$

We assume here that $F^{(1)}$ is calculated with the perturbation theory that is derived from the Hamiltonian which has $F(\lambda)$ as its eigenfunction, although this is not necessary. In addition, we assume again that $\hat{\mathcal{A}} F(1)$ is proportional to the physical ground-state wave function. Equation (10) should be compared to Eq. (8). Note that there is an additional term multiplied by $\lambda - 1$ and that there is an additional term in the denominator. We have achieved a further infinite-order summation of selected contributions to the $\Delta \mathcal{E}(\lambda)$ expansion. Again we discard the terms multiplied by $\lambda - 1$ because they do not contribute to the interaction energy when $\lambda = 1$, the one value of interest. The second renormalized interaction energy formula is

$$\Delta E_l(\lambda) = \frac{\langle F^0 | \hat{\mathcal{A}} | F(\lambda) \rangle \mathcal{E}^{(1)} + \langle F^{(1)} | \hat{V} \hat{\mathcal{A}} | F(\lambda) \rangle}{\langle F^0 + F^{(1)} | \hat{\mathcal{A}} | F(\lambda) \rangle} \quad (11)$$

To zeroth order in λ , Eq. (11) does not vanish. In zeroth order, its numerator includes a contribution that would ordinarily be identified as second order. We show below that $\Delta E_l(1)$ to zeroth order in λ , is identical to $\Delta E_s(1)$ when $F^0 + F^{(1)}$ is substituted for $F(\lambda)$. In Eq. (11) terms have been shifted to lower order not by approximation but by discarding those contributions to the exact $\Delta \mathcal{E}(\lambda)$ of Eq. (10), which vanishes when $\lambda = 1$. We show in the next section that if we substitute $F^0 + \lambda F^{(1)}$ for $F(\lambda)$ in Eq. (11), the resultant approximation to $\Delta E_l(\lambda)$ includes terms that one would customarily classify as third order.

Before we go further it simplifies the later discussion if we introduce a notational convention to indicate approximations made in evaluating Eqs. (9) and (11). We consider only one class of approximations, substituting $F^0 + \lambda F^{(1)} + \dots + \lambda^n F^{(n)}$ for $F(\lambda)$. When this is done, we add a superscript $[n]$ to the E in Eqs. (9) and (11). When we also set $\lambda = 1$ in those formulas, we write simply $\Delta E_s^{[n]}$ and $\Delta E_l^{[n]}$ for the resultant, approximate interaction energies. Translated into the new notation, the observations of the preceding paragraph are that $\Delta E_l^{[0]} = \Delta E_s^{[1]}$ and that $E_l^{[1]}(\lambda)$ includes terms customarily identified as third order. On the basis of

these observations, we conjecture that $\Delta E_I^{[n]}$ is generally more accurate than $\Delta E_S^{[n]}$. Our numerical results for $\Delta E_S^{[1]}$ and $\Delta E_I^{[1]}$ are consistent with this conjecture. Note that in our calculations, we have expanded neither $\Delta E_S^{[n]}(\lambda)$ nor $\Delta E_I^{[n]}(\lambda)$ in a power series in λ .

It is straightforward to show that $\Delta E_I^{[0]} = \Delta E_S^{[1]}$. Note that $\Delta E_I^{[0]} = \Delta \mathcal{E}_I(0)$, the zeroth-order approximation to $\Delta \mathcal{E}(\lambda)$. We have

$$\Delta E_I^{[0]} = \frac{\langle F^0 | \hat{\mathcal{V}} | F^0 \rangle \mathcal{E}^{(1)} + \langle F^{(1)} | \hat{\mathcal{V}} | F^0 \rangle}{\langle F^0 + F^{(1)} | \hat{\mathcal{V}} | F^0 \rangle}$$

and

$$\Delta E_S^{[1]} = \frac{\langle F^0 | \hat{\mathcal{V}} | F^0 + F^{(1)} \rangle}{\langle F^0 | \hat{\mathcal{V}} | F^0 + F^{(1)} \rangle}.$$

If we assume that F^0 and $F^{(1)}$ are real, which is the case in our calculations, then the denominators of $\Delta E_I^{[0]}$ and $\Delta E_S^{[1]}$ are identical. We use Eq. (6), then Eq. (5) in the numerator of $\Delta E_S^{[1]}$ to see that

$$\begin{aligned} \langle F^0 | \hat{\mathcal{V}} | F^0 + F^{(1)} \rangle &= \langle F^0 | \hat{\mathcal{V}} | F^0 \rangle + \langle F^0 | \hat{\mathcal{V}} \hat{V} + \hat{\mathcal{V}} \hat{H}^0 - \hat{H}^0 \hat{\mathcal{V}} | F^{(1)} \rangle \\ &= \langle F^0 | \hat{\mathcal{V}} | F^0 \rangle + \langle F^0 | \hat{\mathcal{V}} \hat{V} | F^{(1)} \rangle \\ &\quad + \langle F^0 | \hat{\mathcal{V}} (\mathcal{E}^{(1)} - \hat{V}) | F^0 \rangle, \end{aligned}$$

which reduces to the numerator of $\Delta E_I^{[0]}$.

It is natural to wonder if a formula more accurate than Eq. (11) might be derived by applying a sequence of operations to it similar to the sequence that led from Eq. (9) to (11). The answer is yes. One can transform $\langle F^{(1)} | \hat{\mathcal{V}} | F(\lambda) \rangle$ in Eq. (10) to bring in $\langle F^{(2)} | \hat{\mathcal{V}} | F(\lambda) \rangle$ and other, lower order terms. Thus, an additional summation of the perturbation expansion can be achieved. We do not present the analysis here because we have not yet done calculations with the resulting formula.

Suitable Perturbation Theories

In the second section, we explained why it is important that intermolecular perturbation theories have $\mathcal{E}_1(\lambda)$'s such that $\mathcal{E}_1(0) = \mathcal{E}^0$ and $\mathcal{E}_1(1) = E_1$, the physical ground-state energy. The energy formulas of the preceding section are strictly applicable only to theories satisfying both conditions. We have recently reviewed which of the existing

perturbation theories can satisfy these conditions [10], but we did not state the eigenvalue equations for each in the form assumed in the preceding section. We do that here. In addition, we show that the second-order AM energy contributes to both $\Delta E_I^{[0]} = \Delta E_S^{[1]}$ when the AM first-order function is substituted in these formulas. Similarly, the third-order AM energy is shown to contribute to $\Delta E_I^{[1]}$.

The $\mathcal{E}_1(\lambda)$'s of the AM theory [13], Hirshfelder's HAV (van der Avoird-Hirschfelder) theory [20] and Polymeropoulos's and the author's theory (AP since PA is taken) [21], satisfy the conditions stated above. The three theories are clearly related. Their wave functions and energies are defined by equations of the form $[\hat{H}^0 + \lambda \hat{\mathcal{V}}(\hat{V} - D(\lambda))]F(\lambda) = \mathcal{E}(\lambda)F(\lambda)$ [10]. The three differ in their definitions of $D(\lambda)$ and in the meaning assigned to the eigenvalue $\mathcal{E}(\lambda)$. In the AM theory $D(\lambda)$ is identically zero, but the Coulomb potential energy between the nuclei must be included in \hat{V} . We write "must" because when it is not, the $\mathcal{E}(\lambda)$ are rapidly varying functions of λ [5]. The AM theory's $\mathcal{E}(\lambda)$ has the properties assumed for $\mathcal{E}(\lambda)$ in the preceding section, namely, $\mathcal{E}_1(0) = \mathcal{E}^0$ and $\mathcal{E}_1(1) = E_1$. Thus, \mathcal{V} in the AM theory is $\mathcal{V}_{\text{AM}} = \hat{\mathcal{V}}\hat{V}$.

In the HAV theory, it is required that $[\hat{H}^0 + \lambda \hat{\mathcal{V}}(\hat{V} - D_{\text{HA}}(\lambda))]F_{\text{HA}}(\lambda) = \mathcal{E}^0 F_{\text{HA}}(\lambda)$, which implicitly defines $D_{\text{HA}}(\lambda)$. We substitute $\mathcal{E}^0 = \mathcal{E}_{\text{HA}}(\lambda) - \lambda D_{\text{HA}}(\lambda)$ in the HAV equation, i.e., we set $\lambda D_{\text{HA}}(\lambda) = \Delta \mathcal{E}_{\text{HA}}(\lambda)$, then rearrange terms so that the $F_{\text{HA}}(\lambda)$ is an eigenfunction of $\hat{H}^0 + \lambda \hat{\mathcal{V}}$ and $\mathcal{E}_{\text{HA}}(\lambda)$ is its eigenvalue. We find $\hat{\mathcal{V}}_{\text{HA}} = \hat{\mathcal{V}}\hat{V} + D_{\text{HA}}(\lambda)(1 - \hat{\mathcal{V}})$. Since $\lambda D_{\text{HA}}(\lambda)$ is identical to $\Delta \mathcal{E}_{\text{HA}}(\lambda)$, one uses $D_{\text{HA}}(\lambda) = \mathcal{E}_{\text{HA}}^{(1)} + \lambda \mathcal{E}_{\text{HA}}^{(2)} + \dots$ to derive the equations which determine the $F_{\text{HA}}^{(n)}$.

In the AP theory $\mathcal{E}(\lambda)$ is defined by requiring that $F_{\text{AP}}(\lambda)$ be least distorted from F^0 in an energy sense [22], under the constraint that $\hat{\mathcal{V}}F_{\text{AP}}(\lambda)$ not vanish. This gives $[\hat{H}^0 + \lambda \hat{\mathcal{V}}(\hat{V} - D_{\text{AP}}(\lambda))]F_{\text{AP}}(\lambda) = \mathcal{E}_{\text{AP}}(\lambda)F_{\text{AP}}(\lambda)$ with $D_{\text{AP}}(\lambda) = \langle F_{\text{AP}}(\lambda) | \hat{\mathcal{V}}\hat{V} | F_{\text{AP}}(\lambda) \rangle / \langle F_{\text{AP}}(\lambda) | \hat{\mathcal{V}} | F_{\text{AP}}(\lambda) \rangle$. We have shown that the AP equation implies that $\hat{\mathcal{V}}F_{\text{AP}}(1)$ is an eigenfunction of $\hat{H}^0 + \hat{V}$ with the eigenvalue $\mathcal{E}_{\text{AP}}(1) + D_{\text{AP}}(1)$. To put the AP equation into the form assumed in the preceding section, we substitute $\mathcal{E}_{\text{AP}}(\lambda) = \mathcal{E}_{\text{AP}}(\lambda) - \lambda D_{\text{AP}}(\lambda)$ and rearrange terms to get $(\hat{H}^0 + \lambda \hat{\mathcal{V}}_{\text{AP}})F_{\text{AP}}(\lambda) = \mathcal{E}_{\text{AP}}(\lambda)F_{\text{AP}}(\lambda)$ where $\hat{\mathcal{V}}_{\text{AP}} = \hat{\mathcal{V}}\hat{V} + D_{\text{AP}}(\lambda)(1 - \hat{\mathcal{V}})$. This is identical in form to $\hat{\mathcal{V}}_{\text{HA}}$, but the two $D(\lambda)$'s are different. In particular, $D_{\text{AP}}(1)$ must be less than $\Delta \mathcal{E}_{\text{AP}}(1)$ because the lowest $\mathcal{E}_{\text{AP}}(1) > \mathcal{E}^0$ [22]. In the HAV theory $D_{\text{HA}}(1) = \Delta \mathcal{E}_{\text{HA}}(1)$. Through first order in the wave

function and second order in the energy, however, the HAV and AP theories are identical [21].

In the last theory we consider, a Hermitian operator $\hat{\mathcal{L}}$ is introduced which satisfies $\hat{\mathcal{L}}F^0 = 0$ and $\hat{\mathcal{L}}\hat{\mathcal{V}} = 0$, and has the property, when added to $\hat{H}^0 + \hat{V}$, of shifting all unphysical energies above

$$\Delta E_{IAM}^{[1]} = \frac{\mathcal{E}_{AM}^{(1)}(\langle F^0 | \hat{\mathcal{V}} | F^0 + 2F_{AM}^{(1)} \rangle + \langle F_{AM}^{(1)} | F_{AM}^{(1)} \rangle) + \mathcal{E}_{AM}^{(2)}\langle F^0 | \hat{\mathcal{V}} | F^0 \rangle + \mathcal{E}_{AM}^{(3)}}{\langle F^0 + F_{AM}^{(1)} | \hat{\mathcal{V}} | F^0 + F_{AM}^{(1)} \rangle}$$

the physical ground-state energy [12]. Two such operators have been constructed explicitly [11, 12], but it should be possible to construct additional ones. With $\hat{\mathcal{V}} = \hat{V} + \hat{\mathcal{L}}$, the lowest eigenvalue in this level shifted (LS) theory can satisfy the conditions $\mathcal{E}_{LS}(0) = \mathcal{E}^0$ and $\mathcal{E}_{LS}(1) = E_1$. The resultant perturbation theory is identical through first order in the wave function and second order in the energy, to the PA theory. We have used the LS theory, without an explicit definition of $\hat{\mathcal{L}}$ to argue that results obtained with the PA and SRS theories are fundamentally valid if only F^0 and $F_{PA}^{(1)}$ were used [5, 11]. In this context, $E_I^{[1]}$ can be regarded as a valid higher order extension of the SRS energy $\Delta E_S^{[1]}$ whereas $\Delta E_S^{[2]}$ cannot.

It is not possible to relate the contributions to $\Delta E_S(\lambda)$ or $\Delta E_I(\lambda)$ to orders in the PA theory because the numerators of both generally depend on matrix elements of $\hat{\mathcal{V}}$, whereas the PA perturbation energies are determined by matrix elements of \hat{V} alone. The AM perturbation theory, on the other hand, is well suited to this task because its perturbation energies are defined by $\mathcal{E}_{AM}^{(n+1)} = \langle F^0 | \hat{\mathcal{V}} | F_{AM}^{(n)} \rangle$ when the normalization $\langle F^0 | F_{AM}(\lambda) \rangle = \langle F^0 | F^0 \rangle = 1$ is imposed. Thus, for the AM theory, the numerator of Eq. (12), assuming real functions, equals $\langle F^0 | \hat{\mathcal{V}} | F^0 \rangle \mathcal{E}_{AM}^{(1)} + \mathcal{E}_{AM}^{(2)}$. This shows that $\Delta E_I^{[0]}$ includes contributions through second order in the perturbation energies although $\Delta E_I^{[0]}$ is the zeroth-order term in the expansion of $\Delta E_I(\lambda)$ in powers of λ . This is not surprising because in the derivation of $\Delta E_I(\lambda)$, we discarded contributions to $\Delta \mathcal{E}(\lambda)$ of all orders in λ .

In the calculations described in the next section, we have calculated the PA and AM wave functions only through first order in λ since it can be argued that it is not practical to go to higher order. This means that we can calculate only $\Delta E_S^{[1]} = \Delta E_I^{[0]}$ and $\Delta E_I^{[1]}$. The numerator of $\Delta E_I^{[1]}$ when the AM functions are used, includes contributions from the first through third order $\mathcal{E}_{AM}^{(n)}$. To show

this, one has first to derive the identity $\mathcal{E}_{AM}^{(3)} = \langle F_{AM}^{(1)} | \hat{\mathcal{V}} | F_{AM}^{(1)} \rangle + \mathcal{E}_{AM}^{(2)}(1 - \langle F^0 | \hat{\mathcal{V}} | F^0 \rangle) - \mathcal{E}_{AM}^{(1)}(\langle F^0 | \hat{\mathcal{V}} | F_{AM}^{(1)} \rangle + \langle F_{AM}^{(1)} | F_{AM}^{(1)} \rangle)$. To do this, we used the equations which determine the first- and second-order AM functions and Eq. (6). It is then straightforward to show that

We include this equation here to show that the numerator is not just a sum of the AM perturbation energies as well as to show that it explicitly includes the third-order energy.

Finally, we must note that the numerator of $\Delta E_S^{[2]}$ can be evaluated using just F^0 and $F^{(1)}$, but that the evaluation of its denominator requires also $F^{(2)}$. We could, of course, truncate the denominator of $\Delta E_S^{[2]}$ to a different order than the numerator, but we have not done so because we feel that it would be inconsistent with the formal analysis in which changes in the denominator are linked to changes in the numerator.

Numerical Test

A numerical test is required to verify the inferences drawn in the preceding sections, namely that $E_I^{[n]}$ is more accurate than $\Delta E_S^{[n]}$ for each perturbation theory, and that both are more accurate than the perturbation energies summed through the highest order calculable with F^0 through $F^{(n)}$. We have calculated only $F^{(1)}$ for the PA and AM theories, which might be thought of as the practical limit for intermolecular perturbation calculations. Using the PA theory, $E_S^{[1]}$ is the interaction energy given by the SRS theory, also known as the symmetrized PA theory [8]. Accordingly, we refer to $\Delta E_S^{[1]}$ calculated with the AM functions as the symmetrized AM (SAM) energy. In the same manner, according to the perturbation functions used in evaluating $\Delta E_I^{[1]}$, we refer to it as the IRS or the IAM energy. The properties of $\Delta E_I^{[1]}$ and $\Delta E_S^{[1]}$ as functions of the nuclear separation R , as exhibited in our calculations, suggest a method by which more accurate approximations to the interaction energy might be obtained than from either $\Delta E_I^{[1]}$ or $\Delta E_S^{[1]}$ alone. We test it as well.

We have chosen to study LiH because it is the simplest system which has an energy spectrum like nearly all other systems, i.e., with an infinite

number of unphysical states below the physical ground-state energy. Our calculations were done with a bideterminantal CI basis in the manner, and with a basis set, we have described previously [5, 10]. The orbital basis set consisted of Li $1s$, $2s$, $2p\sigma$, and $2p\pi$ Hartree-Fock functions and the hydrogen atom $1s$, $2s$, $2p\sigma$, and $2p\pi$ eigenfunctions. Full CI with this basis gave 2840 bideterminants. A finite CI basis set cannot, of course, represent an infinite number of unphysical solutions below the physical ground-state energy, but this one does represent five, including the three lowest. Thus, our calculations allow for effects that a finite number of unphysical states below the physical ground-state energy might introduce. How this may differ from the effect of the infinite number that would be present in an exact calculation is unknown. Our calculations show that the basis set is sufficient to model both short- and long-range interactions between Li and H. It is not large enough to give an accurate LiH potential surface, but that is not our goal. Our goal is to show that $\Delta E_I^{[1]}$ is more accurate than $\Delta E_S^{[1]}$, and that both are more accurate than the corresponding perturbation theories summed through third order in the energy. For that purpose, the basis set is adequate.

The results obtained for the PA, SRS, and IRS energies are summarized in Figure 1. Each line in the figure represents one of the interaction energies divided by the full CI interaction energy. A

value of one for the ratio indicates that the perturbation theory gives the energy exactly. Note that the range of R values extends from short, less than the equilibrium bond length of 3.0 bohrs, to long range where the PA theory if known to give exactly the leading terms in the asymptotic $1/R$ expansion of the energy [23]. That all four curves are approximately equal to one at 20 bohrs, shows that the SRS and IRS energies are also asymptotically correct. It is clear that $\Delta E_{\text{SRS}}^{[1]}$ is much more accurate than the PA energy expansion summed through third order and that $\Delta E_{\text{IRS}}^{[1]}$ is modestly more accurate than $\Delta E_{\text{SRS}}^{[1]}$. These results are consistent with the discussion of the preceding sections. Note that the IRS energy is less than 90% of the exact interaction energy for $R \leq 12$ bohrs, dropping to only 75% at the equilibrium bond length.

The results obtained for the AM, SAM, and IAM energies are presented in Figure 2 in the same manner that results were presented in Figure 1. It is noteworthy that the not one of the curves in Figure 2 approaches 1 as R approaches 20 bohrs. This was expected; the AM theory is known not to give correctly the coefficients of the leading terms in the asymptotic, $1/R$ expansion of the energy for H_2^+ [14]. It is clear from Figure 1 that the SAM energy is more accurate than the AM energy expansion summed through third order and that the IAM energy is more accurate than the SAM en-

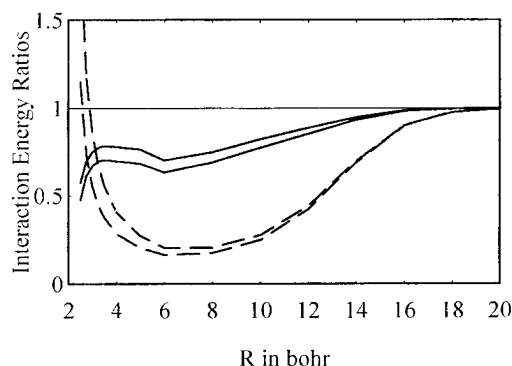


FIGURE 1. For the $^1\Sigma$ LiH ground state, the ratios of the PA, SRS, and IRS interaction energies to the full CI interaction energy are plotted against the nuclear separation R . The lower dashed curve represents the sum of the first- through second-order PA energies; the upper dashed curve, the sum through third order. The lower solid curve represents the SRS interaction energy, the upper solid curve, the IRS. If one of the perturbation theories gave the exact interaction energy, its curve would overlay the light, horizontal line in the graph.

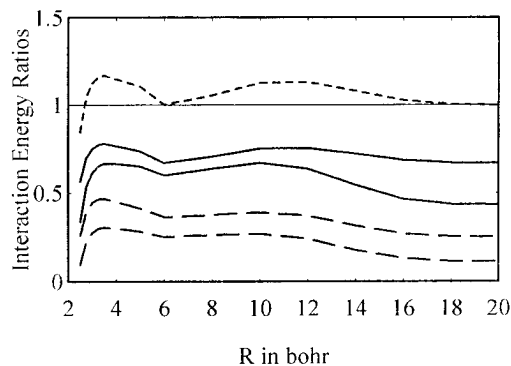


FIGURE 2. For the $^1\Sigma$ LiH ground state, the ratios of the AM, SAM, and IAM interaction energies to the full CI interaction energy are plotted against the nuclear separation R . The lowest dashed curve represents the sum of the first- through second-order AM energies; the dashed curve immediately above it, the sum through third order. The lower solid curve represents the SAM interaction energy; the upper solid curve, the IAM. The short-dash curve represents the corrected IAM interaction energy.

ergy. This is consistent with the inferences drawn from the formal analyses of the preceding sections. The IAM energy is not so accurate as one would wish, equaling, at best, less than 80% of the exact interaction energy at any R . The IRS energy is more accurate than the IAM for $R > 4$ bohrs, but the two are of comparable accuracy at smaller R .

The IAM energy as a function of R exhibits an interesting property: It varies rather slowly with R , giving between 67 and 78% of the exact interaction energy from 3 bohrs, the equilibrium bond length, to 20 bohrs. This is the basis for a speculation. Suppose that in calculations more accurate than the ones presented here, the IAM theory could be expected to give the same fraction f of the exact interaction energy at all R . Since the PA, SRS, and IRS theories are asymptotically correct at large R , one could calculate f at the largest R , then multiply the IAM energies at each R by $1/f$ to get a corrected IAM interaction energy. The short-dash line in Figure 2 shows how this works when we set $f = \Delta E_{\text{IAM}}^{[1]}/E_{\text{IRS}}^{[1]}$, using the $R = 20$ values of those energies. The corrected IAM energy overestimates the interaction energy.

To compare the IRS and corrected IAM energies we have plotted them with the full CI energy in Figure 3. We have not plotted the IAM energy because it is almost indistinguishable from the IRS energy on the scale of the graph. Note that the same range of R values is used in Figure 3 as in

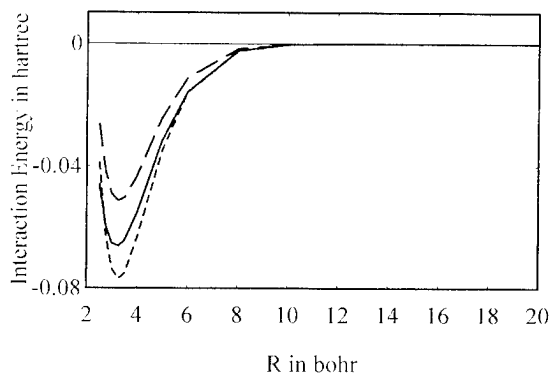


FIGURE 3. For the $^1\Sigma$ LiH ground state, the IRS and the corrected IAM interaction energies, and the full CI interaction energy are shown as functions of R . The solid curve represents the full CI results; the long-dash curve, the IRS results; and the short-dash curve, the corrected IAM results. The IAM results were not plotted because they are indistinguishable from the IRS results on this scale.

the first two figures, even though the energies, on the scale of the graph, are all zero for $R \geq 10$ bohrs. Where the interaction energy is significant, the corrected IAM energy is clearly more accurate than the IRS energy. We are undertaking an extensive series of calculations to see if the method we have used to correct the IAM energies works with larger basis sets for LiH and for other systems.

Conclusions

There is no ambiguity as to order if one focuses on the expansion parameter λ in developing perturbation theory for interacting atoms/molecules from the assumption that the unperturbed wave function for the system is a product of unperturbed atomic/molecular wave functions. The renormalized energy $\Delta E_s(\lambda)$ is more accurate than the sum of the perturbation energies when both are calculated using F^0 through $F^{(n)}$. In turn, $\Delta E_t(\lambda)$ is more accurate than $\Delta E_s(\lambda)$ under the same conditions.

ACKNOWLEDGMENTS

The programs were developed and the calculations were done on computers of Rutgers University Computing Services.

References

1. P. Claverie, *Int. J. Quantum Chem.* **5**, 273 (1971).
2. J. O. Hirschfelder, *Chem. Phys. Lett.* **1**, 325 (1967).
3. J. D. Morgan III and B. Simon, *Int. J. Quantum Chem.* **17**, 1143 (1980).
4. W. Kutzelnigg, *J. Chem. Phys.* **73**, 343 (1980).
5. W. H. Adams, *Chem. Phys. Lett.* **229**, 472 (1994).
6. W. D. Lyons, W. A. Sanders, and J. O. Hirschfelder, *J. Chem. Phys.* **45**, 1075 (1966).
7. P. R. Certain, *J. Chem. Phys.* **49**, 35 (1968).
8. D. N. Chipman, J. D. Bowman, and J. O. Hirschfelder, *J. Chem. Phys.* **59**, 2830 (1973).
9. B. Jeziorski, K. Szalewicz, and G. Chalasinski, *Intern. J. Quantum Chem.* **14**, 271 (1978).
10. W. H. Adams, *Int. J. Quantum Chem.*, to appear.
11. W. H. Adams, *Int. J. Quantum Chem.* **S25**, 165 (1991).
12. W. H. Adams, *J. Math. Chem.* **10**, 1 (1992).
13. A. T. Amos and J. I. Musher, *Chem. Phys. Lett.* **3**, 721 (1969).
14. D. M. Chipman and J. O. Hirschfelder, *J. Chem. Phys.* **59**, 2838 (1973).

15. Cf. I. C. Hayes and A. J. Stone, *Mol. Phys.* **53**, 83 (1984).
16. W. H. Adams, *Int. J. Quantum Chem.* **S24**, 5531 (1990).
17. T. Kato, *Perturbation Theory of Linear Operators*, 2nd ed. (Springer, Berlin, 1980).
18. K. Knopp, *Theory of Functions*, Part II (Dover, New York, 1947) pp. 126-134.
19. J. D. Baker, D. E. Freund, R. N. Hill, and J. D. Morgan III, *Phys. Rev.* **A41**, 247 (1990).
20. J. O. Hirschfelder, *Chem. Phys. Lett.* **1**, 363 (1967).
21. E. E. Polymeropoulos and W. H. Adams, *Phys. Rev.* **A17**, 18 (1978).
22. W. H. Adams, *Phys. Rev. Lett.* **32**, 1093 (1974).
23. B. Jeziorski and W. Kolos, in *Molecular Interactions*, H. Ratajczak and W. J. Orville-Thomas, Ed. (Wiley, New York, 1982), Vol. 3, p. 1.

Many-Electron-Wavepackets Method

H. NAGAO, M. NAKANO,* S. YAMANAKA, S. YAMADA, D. YAMAKI,
I. SHIGEMOTO, S. KIRIBAYASHI, AND K. YAMAGUCHI

Department of Chemistry, Faculty of Science, Osaka University, Toyonaka, Osaka 560, Japan; e-mail for M.N.: mnaka@chem.sci.osaka-u.ac.jp

Y. SHIGETA

Department of Chemistry, Faculty of Science, Kanazawa University, Kakuma Town, Kanazawa 920, Japan

Received February 24, 1996; revised manuscript received April 22, 1996; accepted May 1, 1996

ABSTRACT

We present a computational scheme to study the dynamics of many-electrons in molecular systems by wavepackets method. Several approaches to calculation of nonlinear optical properties for molecules under time-independent or time-dependent external electric fields are presented. Some simple examples of one-dimensional two- or three-electron systems are demonstrated concretely. Implications of these results are discussed in relation to the validity of the many electron wavepackets (MEWP) method. © 1996 John Wiley & Sons, Inc.

Introduction

Heller et al. [1–5] has developed a time-dependent formulation in classical and semiclassical mechanics by using Gaussian wavepackets. The manifold of Gaussian wavepackets is discussed by using the time-dependent variational principle [6]. Numerically exact propagation methods developed by Kosloff et al. [7] indicated that the Laplacian of wave function can be evaluated by using fast Fourier transform (FFT) algorithms. Moreover, time evolution of the wave

function may be obtained in terms of a second-order difference scheme developed by Askar and Cakmak [8]. Feit et al. [9] demonstrated the usefulness of a split-operator time propagation scheme. Tal-Ezer and Kosloff [10] showed that the time evolution may be achieved to machine accuracy by expanding an evolution operator by means of complex Chebyshev polynomials. Kosloff et al. [11] pointed out that eigenfunctions and eigenvalues of Schrödinger equation are determined by solving the Schrödinger equation in imaginary-time evolution and that excited states are obtained by filtering out the lower states. The basic framework of time-dependent quantum mechanical (TDQM)

methods for nuclear dynamics calculations are explained by Kosloff [12]. Leforestier et al. [13] compared time propagation algorithms extensively used so far for the time-dependent Schrödinger equation. Zhang [14] showed that propagation of quantum wavepacket in the interaction picture improves the efficiency of the TDQM method that has emerged as a powerful tool in nuclear dynamics over the last decade.

The TDQM has been applied successfully to study eigenvalue problems, photodissociation, Raman scattering, mode selectivity in chemical reactions, gas-surface scattering, etc. Deumens et al. [15] have presented an overview of methods used for time-dependent treatments of molecules as systems of electrons and nuclei.

The study of molecular systems has traditionally proceeded by solving the electronic problem first to obtain a molecular potential-energy surface (PES) with an associated electronic eigenstate. The dynamics of the molecule is then reduced to the dynamics of the nuclei on that PES, at the classical, semiclassical, or quantum level. It was found that small errors in curvature of the fit can produce significantly different dynamics [16, 17].

Manthe et al. [18] have shown the wavepacket dynamics on three-dimensional PES by the multi-configurational time-dependent Hartree (MCTDH) approach. The ability of the MCTDH approach to an accurate description of a splitting of wavepacket on a saddle-shaped surfaces have been discussed [19,20]. Many applications of the TDQM were performed in various fields.

Zhang et al. [21] presented a computational scheme to propagate wavepackets describing singlet states of two-electron systems, and the low-energy spectrum of helium was computed. Dehnen and Engle [22] calculated the dynamics under the influence of a stronger laser pulse and considered how above-threshold-ionization peaks can be interpreted in terms of momentum-space wave functions. The results were compared with those obtained from calculation using a soft-core potential.

Our interests are in the study of electron wavepackets near the Wannier ridge, strong-field ionization, static and dynamic hyperpolarizabilities of molecular systems, and so on. Our concerns lie in the real spatial dynamics of electrons for such situations in molecular systems. The nonlinear response to the external intense electric field is

described by the hyperpolarizabilities. These have been calculated using several approaches, namely perturbative or nonperturbative theories [23–25] and so on [26, 27]. We have newly proposed some approaches [26, 27] for the nonlinear optical phenomena on the basis of the electron wavepackets dynamics. In order to study the dynamics of electrons in real space, a wavepackets method is presented and is applied to molecular systems. First, we explain our scheme to study the dynamics of many-electron systems with our model Hamiltonian. Then we present three procedures for computing electronic hyperpolarizabilities. Some simple examples for our approach, which is called the many-electron wavepackets (MEWP) method, is then demonstrated. Finally, these results are discussed in connection with the validity of MEWP method.

Theory and Our Scheme

OUR SCHEME

The TDQM method consists of numerically solving the time-dependent Schrödinger equation

$$i \frac{d}{dt} |\varphi(t)\rangle = H |\varphi(t)\rangle, \quad (1)$$

where H is a time-dependent Hamiltonian; $|\varphi(t)\rangle$ is a wave function. The atomic unit $\hbar = m_e = e = 1$ is used throughout this article. Equation (1) is solved by means of some algorithms numerically.

In case of a time-independent Hamiltonian, the solution of Eq. (1) is expressed by the time evolution operator. This exponential function of the time evolution operator is estimated by various schemes, which are the Euler scheme, the simplest Crank–Nicolson scheme, the product formula, the second-order difference scheme, the Chebyshev scheme (CH), and so on.

The CH, which is classified as a global propagator method, is the most accurate and stable method. The CH approximates the exponential function by a Chebyshev polynomial expansion. The error of the CH can be reduced down to the machine limit. These schemes are discussed in detail by Iitaka [28].

In the other case of a time-dependent Hamiltonian, Eq. (1) is solved by some schemes, which are

the Runge-Kutta scheme, the Lanczos scheme, and so on. The accuracy for the long time evolution of these scheme is not so good. But, they are useful to calculate the dynamics for systems with arbitrary Hamiltonian.

Our scheme is as follows:

1. Our model Hamiltonian is derived.
2. The primitive initial wave function is constructed. By propagating the time-independent Schrödinger equation in imaginary time, which is called the relaxation method, the wave function of the ground state is obtained.
3. Using the initial wave function obtained from step 2, the Schrödinger equation is solved and the properties are calculated with the generated wave function at each time step.

MODEL HAMILTONIAN

Now, we derive our model Hamiltonian. We consider the ab initio Hamiltonian for the molecular systems. In the Born-Oppenheimer approximation, the Hamiltonian is written as

$$H = \sum_{\sigma} \int dr \Psi_{\sigma}^{+}(r) \left[-\frac{1}{2} \nabla^2 \right] \Psi_{\sigma}(r) + \sum_{\sigma\rho} \frac{1}{2} \int dr dr' \Psi_{\sigma}^{+}(r) \Psi_{\rho}^{+}(r') \frac{1}{|r-r'|} \times \Psi_{\rho}(r') \Psi_{\sigma}(r) - \sum_{\sigma} \sum_n \int dr \Psi_{\sigma}^{+}(r) \times \frac{Z_n}{|r-R_n|} \Psi_{\sigma}(r), \quad (2)$$

where the first term means the kinetic part, the second is the electronic interaction part, and the third is the nuclear-electron interaction part. $\Psi_{\sigma}^{+}(r)$ [$\Psi_{\sigma}(r)$] means the field operator which is the creation (annihilation) operator for an electron with spin σ at real spatial three-dimensional coordinate r , and satisfies the anticommutation relation.

Here, we introduce an orthogonal basis set $\{\chi_{ijk}(r)\}$ as

$$\chi_{ijk}(r) = \frac{1}{N_{\text{norm}}} \left[\theta \left(x - x_i - \frac{\Delta x}{2} \right) - \theta \left(x - x_i + \frac{\Delta x}{2} \right) \right]$$

$$\times \left[\theta \left(y - y_j - \frac{\Delta y}{2} \right) - \theta \left(y - y_j + \frac{\Delta y}{2} \right) \right] \times \left[\theta \left(z - z_k - \frac{\Delta z}{2} \right) - \theta \left(z - z_k + \frac{\Delta z}{2} \right) \right], \quad (3)$$

where $\theta(x)$ indicates the step function, Δx , Δy , and Δz are the grid intervals when a finite space L is divided into N_g of intervals for each direction. The (ijk) means the (ijk) th interval. $N_{\text{norm}} = \sqrt{\Delta x \Delta y \Delta z}$ is the normalization factor. Then, the field operators are expanded in terms of the basis set $\{\chi_{ijk}(r)\}$ as

$$\Psi_{\sigma}^{+}(r) = \sum_{ijk=1}^n \chi_{ijk}(r) a_{ijk}^{\sigma+}, \quad (4)$$

where $a_{ijk}^{\sigma+}$ (a_{ijk}^{σ}) is the creation (annihilation) operator for the (ijk) th interval. Operators also satisfy the anticommutation relation.

Then, the Hamiltonian in Eq. (2) is rewritten as

$$H = \lim_{\varepsilon \rightarrow 0} \sum_{\sigma} \left\{ -\frac{1}{2\Delta x \varepsilon} \times [a_{i+1,jk}^{\sigma+} a_{ijk}^{\sigma} - 2a_{ijk}^{\sigma+} a_{ijk}^{\sigma} + a_{i-1,jk}^{\sigma+} a_{ijk}^{\sigma}] - \frac{1}{2\Delta y \varepsilon} [a_{ij+1,k}^{\sigma+} a_{ijk}^{\sigma} - 2a_{ijk}^{\sigma+} a_{ijk}^{\sigma} + a_{ij-1,k}^{\sigma+} a_{ijk}^{\sigma}] - \frac{1}{2\Delta z \varepsilon} [a_{ijk+1}^{\sigma+} a_{ijk}^{\sigma} - 2a_{ijk}^{\sigma+} a_{ijk}^{\sigma} + a_{ijk-1}^{\sigma+} a_{ijk}^{\sigma}] \right\} + \frac{1}{2} \sum_{\sigma\rho} \sum_{ijklmn} W_{ijk,lmn}^{\sigma,\rho} a_{ijk}^{\sigma+} a_{lmn}^{\rho+} a_{lmn}^{\rho} a_{ijk}^{\sigma} - \sum_n \sum_{\sigma} \sum_{ijk} w_n^{\sigma} a_{ijk}^{\sigma+} a_{ijk}^{\sigma}, \quad (5)$$

where

$$W_{ijk,lmn}^{\sigma,\rho} = \frac{1}{(\Delta x \Delta y \Delta z)^2} \int_{x_i-\Delta x/2}^{x_i+\Delta x/2} dx \int_{y_j-\Delta y/2}^{y_j+\Delta y/2} dy \times \int_{z_k-\Delta z/2}^{z_k+\Delta z/2} dz \int_{x_l-\Delta x/2}^{x_l+\Delta x/2} dx' \int_{y_m-\Delta y/2}^{y_m+\Delta y/2} dy' \times \int_{z_n-\Delta z/2}^{z_n+\Delta z/2} dz' \frac{1}{|r-r'|}, \quad (6)$$

$$w_{n;ijk,\sigma}^{\sigma} = \frac{1}{\Delta x \Delta y \Delta z} \int_{x_i - \Delta x/2}^{x_i + \Delta x/2} dx \int_{y_j - \Delta y/2}^{y_j + \Delta y/2} dy \int_{z_k - \Delta z/2}^{z_k + \Delta z/2} dz \frac{Z_n}{|r - R_n|}. \quad (7)$$

For the first term in the right-hand side of Eq. (5), we approximate each ε to the grid interval: $2\Delta x\varepsilon \rightarrow 2\Delta x^2$, $2\Delta y\varepsilon \rightarrow 2\Delta y^2$, and $2\Delta z\varepsilon \rightarrow 2\Delta z^2$. Then, it becomes the kinetic Hamiltonian for the finite-difference method. In Eqs. (6) and (7), both integrals for the coulomb interaction, which are called the two-electron integral, are carried out analytically and numerically. Therefore, it is found that the matrix elements for the coulomb interaction are easily obtained. In our model, the Hamiltonian is constructed by the kinetic term for the finite-difference method and the interaction terms are given by expansion in terms of basis set.

Javanainen, Eberly, and Su [29] approximated coulomb potential to the softened coulombic form:

$$\frac{1}{|x|} \approx \frac{1}{\sqrt{1+x^2}}. \quad (8)$$

This approximation implies that the potential retains an asymptotic form of the coulomb potential while eliminating the singularity at the origin. We also use this softened coulombic potential instead of our coulomb matrix element shown as Eqs. (6) and (7).

PRIMITIVE INITIAL WAVE FUNCTION

To obtain the initial wave function used in our last scheme of step 3, we explain how to construct the primitive initial wave function. Our desired initial wave function is generated from this primitive initial wave function by the relaxation method.

The wave function of particles should be antisymmetric:

$$\langle r_1\sigma_1, r_2\sigma_2, \dots, r_N\sigma_N | \psi \rangle = -\langle r_2\sigma_2, r_1\sigma_1, \dots, r_N\sigma_N | \psi \rangle, \quad (9)$$

where r_i indicates the i th coordinate, and σ_i is an up or a down spin state. For an antisymmetric state, the wave function may be written by

$$\langle r_1\sigma_1, r_2\sigma_2, \dots, r_N\sigma_N | \psi \rangle = \frac{1}{\sqrt{N!}} \begin{vmatrix} \langle r_1\sigma_1 | \phi_1 \rangle & \langle r_2\sigma_2 | \phi_1 \rangle & \cdots & \langle r_N\sigma_N | \phi_1 \rangle \\ \langle r_1\sigma_1 | \phi_2 \rangle & \langle r_2\sigma_2 | \phi_2 \rangle & \cdots & \langle r_N\sigma_N | \phi_2 \rangle \\ \vdots & \vdots & \ddots & \vdots \\ \langle r_1\sigma_1 | \phi_N \rangle & \langle r_2\sigma_2 | \phi_N \rangle & \cdots & \langle r_N\sigma_N | \phi_N \rangle \end{vmatrix}. \quad (10)$$

The wave function of the form of Eq. (10) is commonly called a Slater determinant. Though each initial single-particle wave function is arbitrary, we consider a Gaussian wavepacket $|\phi_i\rangle$ of the initial state for i th electron:

$$\langle r_j\rho_j | \phi_i \rangle = \frac{1}{\pi^{1/4} \sqrt{\sigma_i}} \times \exp \left[-\frac{(r_j - r_{0i})^2}{2\sigma_i^2} + ik_{0i}(r_j - r_{0i}) \right], \quad (11)$$

where $|\phi_i\rangle$ is the state vector of i th electron. $\langle r_j|$ means the j th coordinate. ρ_j is the spin for r_j ; r_{0i} and k_{0i} are the grid of the center and the momentum of the i th initial wavepacket, respectively. And σ_i is a dispersion of i th initial wavepacket. We call the wave function shown in Eq. (10) the primitive initial wave function, which is constructed by the single-particle wave function defined in Eq. (11). This wave function is superposed by plural eigenstates. Since our desired initial wave function is the ground state or a particular excited state that is generated from the above primitive initial wave function by the relaxation method, this primitive initial wave function is not so important. But we note that it is significant that the initial wave function is antisymmetric.

BOUNDARY CONDITION

When we carry out the relaxation method or the calculation of the time-dependent wave function and properties, the boundary condition is considered as the following:

$$\begin{aligned} \langle r_1\sigma_1, \dots, r_{ig[k(j)]}=0\sigma_i, \dots, r_N\sigma_N | \psi \rangle \\ = \langle r_1\sigma_1, \dots, r_{ig[k(j)]}=N_g+1\sigma_i, \dots, r_N\sigma_N | \psi \rangle \\ = 0, \end{aligned} \quad (12)$$

where

$$r_{ig[k(j)]} = j \times \Delta x_{ik}$$

$$(i = 1, \dots, N, j = 0, \dots, N_g + 1, k = 1, 2, 3), \quad (13)$$

where x_{ik} ($k = 1, 2, 3$) means $x_{i1} = x_i$ or $x_{i2} = y_i$ or $x_{i3} = z_i$, which is the i th coordinate; $g[k(j)]$ indicates the j th grid number for the x_k direction. On the edge grid of a finite space, the amplitude of the wave function vanishes.

NUMERICAL CALCULATION

We can perform the dynamics of electrons in molecular systems by the following procedure. Using the model Hamiltonian of Eq. (5) and the primitive initial wave function of Eq. (10), we can obtain the ground state and the excited states for each spin state by the relaxation method. We use the CH, since the Hamiltonian is time-independent. Using the generated initial wave function, several properties and the wave functions are calculated.

Approach to the Nonlinear Optical Properties

The MEWP method is considered to be useful particularly for the phenomenon with contributions from electrons in spatially extended regions. Therefore, the nonlinear optical phenomenon may be a good example of the MEWP approach. In this section, after briefly reviewing the conventional approaches to calculation of the nonlinear optical properties, three new approaches based on the MEWP method applicable for some different situations are proposed.

CALCULATION OF HYPERPOLARIZABILITY

In the calculation of static hyperpolarizability, the finite-field method is useful. This procedure consists of the calculation of the total energy or the polarization by a Hamiltonian, including the external electric field, and the differentiation of the total energy (or the polarization) with respect to the external field. It is important to evaluate the error caused by the numerical differentiation. An advantage of such a method is that several standard

quantum chemical calculation methods can be used. In the calculation of static hyperpolarizabilities, we usually use this finite-field (FF) method, i.e., finite-field coupled-Hartree-Fock (FF-CHF) method.

For the time-dependent external field, we can calculate the dynamical hyperpolarizability by the time-dependent Hartree-Fock (TDHF) method [30, 31], the time-dependent perturbation theory (TDPT) [32], the Floquet-Liouville supermatrix (FLSM) method [33], the numerical Liouville approach (NLA) [26], and so on.

MEWP-BASED APPROACHES

Approach via the Finite-Field Method

This approach is a scheme for the time-independent external electric field. By our scheme shown in the previous section, the Schrödinger equation with the external electric field is solved in terms of the relaxation method to obtain the ground state and the total energy. Here, we also use the CH. The static polarizability and hyperpolarizabilities are written as

$$\alpha_{ij}(0) = \left(\frac{\partial \mu_i}{\partial E_j} \right)_{E \rightarrow 0} \quad (14)$$

$$\beta_{ijk}(0) = \left(\frac{\partial \mu_i}{\partial E_j \partial E_k} \right)_{E \rightarrow 0} \quad (15)$$

$$\gamma_{ijkl}(0) = \left(\frac{\partial \mu_i}{\partial E_j \partial E_k \partial E_l} \right)_{E \rightarrow 0}, \quad (16)$$

where

$$P(E) = \mu_0 + \alpha E + \beta E^2 + \gamma E^3 + \dots, \quad (17)$$

$$U_{\text{total}}(E) = U_{\text{total}0} - \mu_0 E - \frac{1}{2} \alpha E^2 - \frac{1}{3} \beta E^3 - \frac{1}{4} \gamma E^4 - \dots, \quad (18)$$

$$\mu_i(E) = - \frac{\partial U_{\text{total}}(E)}{\partial E_i}. \quad (19)$$

$P(E)$ is the polarization, and $U_{\text{total}}(E)$ is the molecular total energy in the presence of electric field. We can obtain hyperpolarizabilities by numerical differentiation as shown in Eqs. (14), (15), and (16).

Approach via the Level Theory (NLA)

We explain another procedure for the dynamical external field. By our scheme mentioned in the

previous section, we have the model Hamiltonian and the initial wave function in the absence of external electric field by the MEWP. Then, the wave function and the total energy of the ground state are obtained. Following Kosloff [11], we can obtain the excited states in order of increasing energy. Therefore, we can get each energy level and each wave function of the system.

In the NLA method [26], which can provide nonperturbative hyperpolarizabilities including the population and coherent relaxation effects, we first perform the static analysis. The transition properties which are the transition energies, the transition moments, and the dipole moments are calculated in terms of the above results obtained by the MEWP. Next, we carry out the dynamic analysis. The polarization $P(t)$ of the system in the external electric field, which has the frequency ω , and the field $\varepsilon(t)$ are generated by numerically solving the Liouville equation including relaxation effects in the Runge-Kutta scheme. The obtained polarization is converted to $P(\omega)$ by the discrete Fourier transformation. Finally, the intensity-dependent nonlinear optical properties $\chi_g^{(n)}(n\omega)$ (NHG) can be obtained by the definition:

$$\chi_g^{(n)}(n\omega) = \frac{P(n\omega)}{n^n \varepsilon^n(\omega)} = \frac{P(n\omega)}{\varepsilon'^n(\omega)}, \quad (20)$$

where $P(n\omega)$ is the n th-order harmonic response. $\varepsilon(\omega)$ indicates an amplitude. $\varepsilon'(\omega) = n\varepsilon(\omega)$ is the amplitude of incident field. Definitions of hyperpolarizabilities for other nonlinear optical phenomena, e.g., EFISH, DFWM, and EFOR, are given in our previous studies [32].

Direct Approach by the MEWP

Following our scheme of steps 1 and 2, we get the initial ground-state wave function in the presence of external field. Using it, the time-dependent Schrödinger equation with the time-dependent external electric field is solved by the MEWP method in the Runge-Kutta or the Lanczos scheme. The polarization $P(t)$ is calculated directly by using the wave function $|\psi(t)\rangle$ for each time step. The polarization $P(t)$ is converted to $P(\omega)$ by the Fourier transformation. And then, we can obtain the n th-order nonlinear properties based on the definition of Eq. (20).

An advantage of this scheme is that we need not calculate the energy level of the system. By using the wavepacket method all schemes have

this advantage. On the other hand, we can calculate the energy levels by our scheme of step 2 or the relaxation method. Therefore, this scheme proves to be a powerful tool in studying problems on the ionization, dynamics under the influence of the strong external field, etc.

A defect of this scheme is that all the contributions from the relaxations cannot be included. Namely, it is not sufficient to simulate phenomenon including resonant processes by only this scheme. However, this approach will be a useful tool to obtain various informations for the systems of our interests.

Examples

In this section, some concrete and simple numerical examples are discussed. For simplicity, we consider the one-dimensional hydrogen molecule, which is two-electron and two-nuclei system. First, we will demonstrate a propagation of the time-independent Schrödinger equation in the imaginary time for this system. Second, we will calculate the nonlinear optical properties of this system by our MEWP approach via the finite-field method (FF-MEWP method) mentioned in the previous section. Later, another example with respect to the chemical reaction of H_3 will be presented.

IMAGINARY TIME EVOLUTION IN THE ABSENCE OF EXTERNAL ELECTRIC FIELD

At the second step in our scheme, we perform the relaxation method in the absence of external electric fields to obtain the initial wave function in the hydrogen molecule system. Table I summarizes parameters constructing the primitive initial wave function. We divide a finite space of 21 a.u. for each electron into 21 grid points. Then, the grid intervals Δx_1 and Δx_2 are 1.0 a.u. The first electron wavepacket is put on the 9th grid point, and the second is set on the 13th grid point. The spin

TABLE I
Parameters used in MEWP method.

L	Δx	Wavepacket 1	Wavepacket 2	Nucleus
21	1.0	$x_{01} = 9$ $k_{01} = 0$ $\sigma_1 = 2.1$ Spin-up	$x_{02} = 13$ $k_{02} = 0$ $\sigma_2 = 2.1$ Spin-down	$X_{01} = 10, X_{02} = 12$

state is the singlet. Each hydrogen nucleus is fixed on the 10th and 12th grid point. Therefore, the distance between atoms is 2.0 a.u.

By the relaxation method in the CH, we can obtain the wave function of the ground state and the excited states. From the primitive initial wave function and the generated final wave function, the total energy E and the square root of the square average with respect to the distance between electrons D_{e-e} , electron and the nucleus D_{e-n} and nuclei D_{n-n} :

$$D_{e-e} = \sqrt{\langle (x_1 - x_2)^2 \rangle}, \quad (21)$$

$$D_{e-n} = \sqrt{\langle (x - X)^2 \rangle}, \quad (22)$$

$$D_{n-n} = \sqrt{\langle (X_1 - X_2)^2 \rangle} \quad (23)$$

are shown in Table II. It is found that the total energy (−1.45992 a.u.) of the singlet ground state is lower than that of the primitive initial state (−1.25275 a.u.). For the distance between electrons, the former is shorter than the latter. The distance between electron and nucleus also becomes short as a result of the imaginary time evolution.

We depict the results using other parameters shown in Table III. Figure 1 displays the square amplitude of the ground states for the singlet and the triplet spin states and the singlet first excited state. All calculations are carried out at the internuclear distance of 1.6 a.u. The square amplitude of a wave function is plotted on a $x_1\sigma_1 + x_2\sigma_2$ plane. The $x_1\sigma_2 - x_2\sigma_2$ plane is composed of four subspaces. There are the $\alpha\text{-}\alpha$ subspace, and $\alpha\text{-}\beta$ subspace, the $\beta\text{-}\alpha$ subspace, and the $\beta\text{-}\beta$ subspace with respect to the spin state for each r -space. Each subspace is expanded by spaces x_1 and x_2 . For the triplet ground state, there is one node on $x_1 = x_2$ line. This means that two electrons are not

TABLE II
Total energy and average distance.

Singlet	Initial wave function	Final wave function
Energy	−1.251748	−1.459917
D_{e-e}	4.262350	2.190121
D_{e-n}	2.577675	1.669181
D_{n-n}	2.0	2.0

TABLE III
Parameters.

L	Δx	Wave- packet 1	Wave- packet 2	Nucleus
13.1	0.1	$x_{01} = 40$ $k_{01} = 0$ $\sigma_1 = 13.1$ Spin-up	$x_{02} = 80$ $k_{02} = 0$ $\sigma_2 = 13.1$ Spin-down	$X_{01} = 58, X_{02} = 74$

in the same place. Thus, spin space is symmetric, and real space becomes antisymmetric. On the other hand, it is found that there is one node, which is different from that for the triplet, for the singlet first excited state. This node is on $x_1 + x_2 = L$ line, where L is the length of the grid, i.e., $L = 33.1$ a.u. And then, the density of the electron is more widely expanded than that of the ground state. The total energy for the singlet ground state is −1.452865 a.u., and that for the triplet ground state becomes −1.198768 a.u. We show the potential curves for the hydrogen molecule by the MEWP method in Figure 2. It is found that in the region where the internuclear distance is short, the difference of the curvature between the MEWP and well-known results by Kolos and Wolniewicz [34] appears, and that in the region where the internuclear distance becomes long, the inequality almost vanishes. However, the qualitative shape of the potential curves obtained by the MEWP is nearly equal to that of Kolos et al.

These results indicate the validity of our scheme and numerical calculations for qualitative studies.

NONLINEAR OPTICAL PROPERTIES VIA THE FINITE-FIELD MEWP METHOD

Next, we calculate the total energy by the imaginary time evolution under static external electric field. The same parameters shown in Table I are used. For each intensity of the electric field, we obtain the properties shown in Table IV. Following our definition, the polarizability and the hyperpolarizability are calculated straightforwardly. However, since we consider the spatial one-dimensional system, they will correspond to α_{xx} , β_{xxx} , and γ_{xxxx} . From these results, the polarizability α_{xx} becomes 12.2395 a.u., and the hyperpolarizability γ_{xxxx} is 306.6565 a.u. Certainly, the value of the β_{xxx} vanishes. In order to confirm the applica-

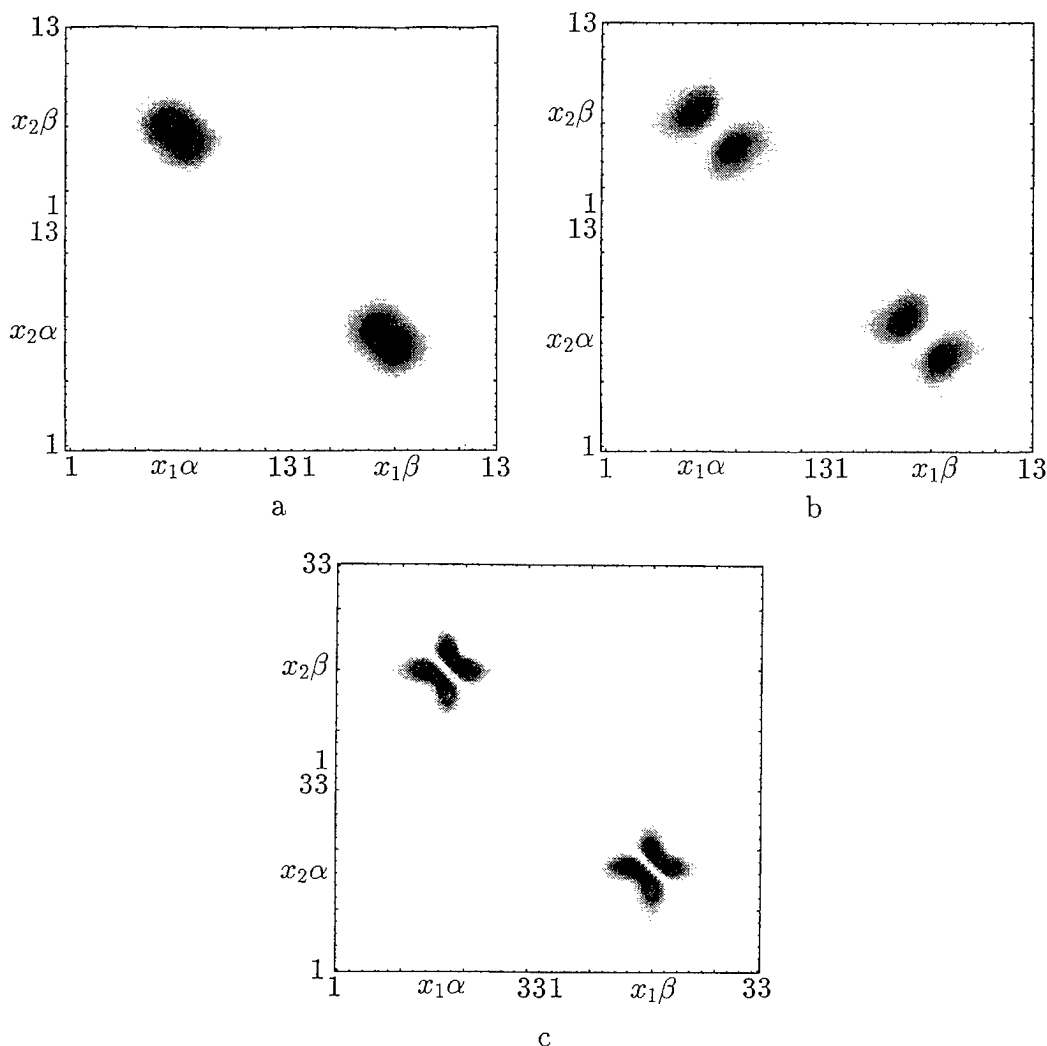


FIGURE 1. Square amplitudes for the singlet and triplet states. The distance between each nucleus is fixed by 1.6 a.u. The amplitude for the singlet ground state is shown in Figure 1(a). Figures 1(b) and 1(c) display those for the triplet ground state and the singlet first excited state.

bility of the FF-MEWP method to the calculation of hyperpolarizabilities, we should further investigate the qualitative behaviors, e.g., variations in hyperpolarizabilities during the bond dissociation, in comparison with *ab initio* results.

OTHER EXAMPLE

Finally, we show the results of the chemical reaction of an H_3 system which is a spatial one-dimensional three-electron system. Parameters are summarized in Table V. Grid size is 20.4 a.u., and the number of the intervals is 51. Therefore, the

grid interval becomes 0.4 a.u. Calculations are carried out under a condition such that both interatomic distances from the central nucleus are equal.

We depict the wave function of the H_3 system in Figure 3. Figure 3 shows that the wave function of three electron system consists of eight subspaces. In a subspace ($x_1\beta - x_2\alpha - x_3\alpha$), the initial wave function and the final wave function obtained by the relaxation method are illustrated in Figures 3(b) and (c), respectively. These figures indicate that the initial wave function is modified into the shape expected from electron-electron coulombic repulsion.

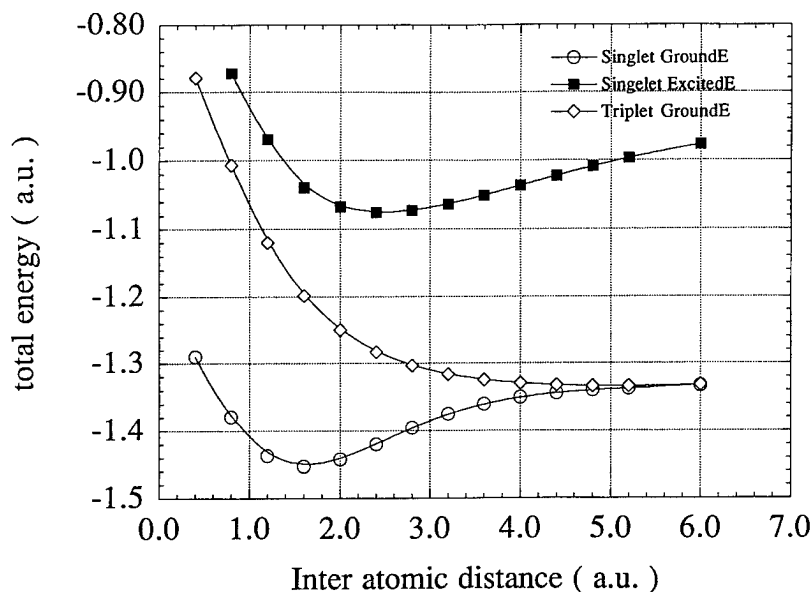


FIGURE 2. Potential curve of a one-dimensional hydrogen molecule. The potential curves for the singlet and triplet spin states are shown.

Figure 4 shows a potential curve of the H_3 system. When the interatomic distance is 2.0 a.u., the total energy takes the lowest value: -2.12039 a.u. On the other hand, total energy of the one-dimensional hydrogen atom is -0.67111 a.u., and that of the one-dimensional hydrogen molecule is -1.45434 a.u. Therefore, because the sum of these total energies is -2.12546 a.u., the energy barrier for the reaction becomes 0.00506489 a.u. The result of Liu [35] by an exact ab initio calculation gives 0.01593600102 a.u. Our result is lower than that of B. Liu, but these results suggest that a qualitative calculation for three electron systems or more electron systems will be able to be performed.

Concluding Remarks

In this study, we have extended the wavepacket method to many-electron systems in a molecule and have proposed some wavepacket approaches to study of the nonlinear optical properties. From some examples presented here, the MEWP method is shown to be applied to the qualitative studies for energies and properties for small molecular systems.

The MEWP method includes the solving process of the spatially three-dimensional or mathematically $3N$ -dimensional Schrödinger equation. Therefore, it is difficult to calculate properties of a such system which is composed of a great number

TABLE IV
Total energy and average distance for each electric field.

Electric field	Energy	D_{e-e}	D_{e-n}	D_{n-n}
0.000	-1.45992	2.19012	1.66918	2.00000
0.005	-1.46007	2.19070	1.68804	2.00000
0.010	-1.46053	2.19248	1.70797	2.00000
0.015	-1.46130	2.19551	1.72905	2.00000

TABLE V
Parameters for H_3 .^a

L	Δx	Wavepacket 1	Wavepacket 2	Wavepacket 3
20.4	0.4	x_{01} $k_{01} = 0$ $\sigma_1 = 5.1$ Spin-up	$x_{02} = 26$ $k_{02} = 0$ $\sigma_2 = 5.1$ spin-down	x_{03} $k_{03} = 0$ $\sigma_3 = 5.1$ Spin-up

^aDistance $x_0 \Delta x = (x_{02} - 26) \Delta x = (26 - x_{01}) \Delta x$.

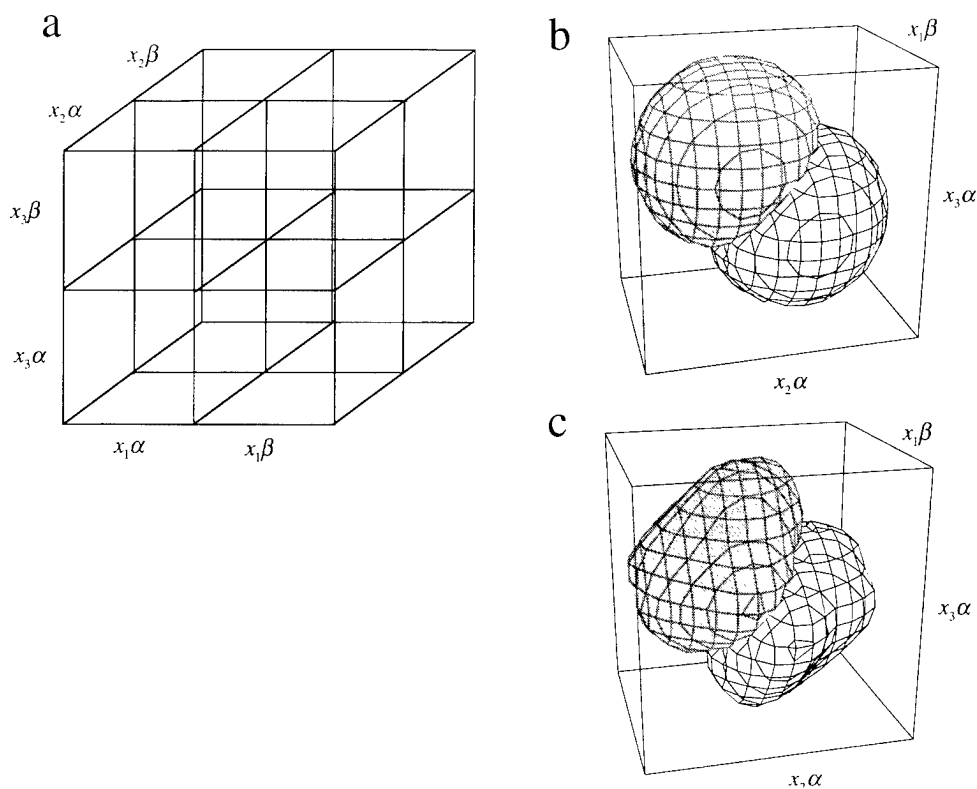


FIGURE 3. Space and spin coordinates for one-dimensional three-electron system is shown in Figure 3(a). Figures 3(b) and 3(c) show the initial wave function and the final wave function is a subspace ($x_1\beta - x_2\alpha - x_3\alpha$).

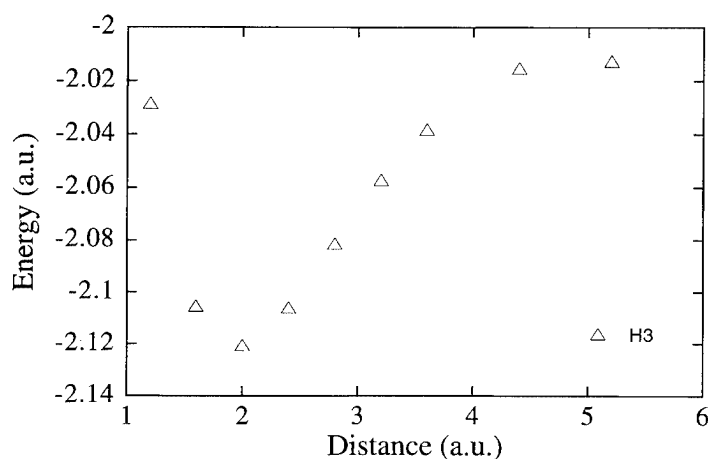


FIGURE 4. Potential curve of a one-dimensional H_3 system with equal H-H bond lengths.

of particles. But we will apply this method to a wide variety of problems which include the double-ionization threshold, the dynamics is highly excited states, electronic nonlinear optical, and magnetic properties by external static and dynamic optical and magnetic fields.

ACKNOWLEDGMENT

We are grateful to the Ministry of Education, Science and Culture of Japan (Specially Promoted Research No. 06101004) for the financial support. All calculations were carried out on the IBM Pow-

erstation models 580 and 3CT. We would like to thank Dr. W. Mori, Dr. S. Takeda, Dr. H. Kawabe, and Dr. K. Nishikawa for their continued encouragement and helpful discussions throughout this work. We also wish to express our grateful acknowledgment to Mr. T. Kawakami, Mr. G. Maruta and Mr. K. Ueda for our instructive discussions.

References

1. E. J. Heller, *J. Chem. Phys.* **62**, 1544 (1975).
2. E. J. Heller, *J. Chem. Phys.* **64**, 63 (1976).
3. S. Y. Lee and E. J. Heller, *J. Chem. Phys.* **76**, 3035 (1982).
4. D. Huber and E. J. Heller, *J. Chem. Phys.* **87**, 5302 (1987).
5. D. Huber and E. J. Heller, *J. Chem. Phys.* **89**, 4752 (1988).
6. F. Arickx, J. Broeckhove, W. Coene, and P. Van Lenven, *Int. J. Quantum Chem.* **20**, 471 (1986).
7. D. Kosloff and R. Kosloff, *J. Comput. Phys.* **52**, 35 (1983).
8. A. Askar and A. S. Cakmak, *J. Chem. Phys.* **68**, 2794 (1978).
9. M. D. Feit, J. A. Fleck, Jr., and A. Steiger, *J. Comput. Phys.* **47**, 412 (1982).
10. H. Tal-Ezer and R. K. Kosloff, *J. Chem. Phys.* **81**, 3967 (1984).
11. R. Kosloff and T. Tal-Ezer, *Chem. Phys. Lett.* **127**, 223 (1986).
12. R. Kosloff, *J. Phys. Chem.* **92**, 2087 (1988).
13. C. Leforestier, R. H. Bisseling, C. Cerjan, M. D. Feit, R. Friesner, A. Guldberg, A. Hammerich, G. Jolicard, W. Karrlein, H.-D. Meyer, N. Lipkin, O. Roucero, and R. Kosloff, *J. Comput. Phys.* **94**, 59 (1991).
14. J. Z. H. Zhang, *Comput. Phys. Com.* **63**, 28 (1991).
15. E. Deumens, A. Diz, R. Longo, and Y. Öhrn, *Rev. Mod. Phys.* **66**, 917 (1994).
16. X. Liu and J. N. Murrell, *J. Chem. Soc. Faraday Trans.* **87**, 435 (1991).
17. A. Agnado, and M. Paniagua, *J. Chem. Phys.* **96**, 1256 (1992).
18. U. Manthe, H. Meyer, and L. S. Cederbaum, *J. Chem. Phys.* **97**, 9062 (1992).
19. R. D. Coalson in *Laser, Molecules and Methods*, J. Hirshfelder, R. Wyatt, and R. Coalson (Eds.) (Wiley, New York, 1989, pp. 605-636).
20. U. Manthe, H. Koppel, and L. S. Cederbaum, *J. Chem. Phys.* **95**, 1708 (1991).
21. L. Zhang, J. M. Feagin, V. Engel, and A. Nakano, *Phys. Rev. A* **49**, 3457 (1994).
22. R. Dehnen and V. Engel, *Phys. Rev. A* **52**, 2288 (1995).
23. T. C. Kavanaugh and R. J. Silbey, *J. Chem. Phys.* **96**, 6443 (1992).
24. K. Wang and S.-I. Chu, *J. Chem. Phys.* **86**, 3225 (1987).
25. B. Dick, R. M. Hochstrasser, *Chem. Phys.* **75**, 133 (1985).
26. M. Nakano and K. Yamaguchi, *Phys. Rev. A* **50**, 2989 (1994).
27. M. Nakano, K. Yamaguchi, Y. Matuzaki, K. Tanaka, and T. Yamabe, *J. Chem. Phys.* **102**, 2986 (1995); *J. Chem. Phys.* **102**, 2996 (1995); *Chem. Phys. Lett.* **234**, 323 (1995); *Chem. Phys. Lett.* **233**, 411 (1995).
28. T. Iitaka, *Phys. Rev. E* **49**, 4684 (1994).
29. J. Javanainen, J. Eberly, and Q. Su, *Phys. Rev. A* **38**, 3430 (1988); Q. Su and J. H. Eberly; *Ibid.*, **44**, 5997 (1991).
30. K. Sasagane, F. Aiga, and R. Itoh, *J. Chem. Phys.* **99**, 3738 (1993).
31. M. Nakano, T. Yoshida, M. Okumura, T. Tsunekawa, and K. Yamaguchi, in *Computer Aided Innovation of New Materials*, Vol. II, M. Doyama, J. Kihara, M. Tanaka, and R. Yamamoto (Eds.) (Elsevier Science, Amsterdam, 1992, p. 221).
32. M. Nakano and K. Yamaguchi, *Chem. Phys. Lett.* **206**, 285 (1993); M. Nakano, I. Shigemoto, S. Yamada, and K. Yamaguchi, *J. Chem. Phys.* **103**, 4175 (1995).
33. T. C. Kavanaugh and R. J. Silbey, *J. Chem. Phys.* **96**, 6443 (1992).
34. W. Kolos and L. Wolniewicz, *J. Chem. Phys.* **41**, 3663 (1964); *J. Chem. Phys.* **41**, 3674 (1964); *J. Chem. Phys.* **43**, 2429 (1965); *J. Chem. Phys.* **49**, 404 (1968).
35. B. Liu, *J. Chem. Phys.* **58**, 1925 (1973).

Stochastic Path-Integral Method for Chemical Reaction Dynamics: Application to the Full 3D H₃ System

MASATAKA NAGAOKA

*Institute for Fundamental Chemistry, 34-4 Takano Nishihiraki-cho, Sakyo-ku, Kyoto 606, Japan;
e-mail: nagaoka@ifc.or.jp*

Received February 25, 1996; revised manuscript received August 6, 1996; accepted August 7, 1996

ABSTRACT

A stochastic path-integral (SPI) technique for chemical reaction dynamics is explored. It is shown that this technique enables the direct computation of the transition amplitude with a finite space-time range, by generating a set of classical paths subject to simultaneous stochastic differential equations. The numerical values of the Boltzmann matrix elements for a harmonic potential are in good agreement with the analytical ones. Within the quantum transition state theory, the flux-flux autocorrelation function is also evaluated at 630 K for the H + H₂ exchange reaction and is found to give a satisfactory agreement with the previous studies. To appraise the influence of the dimensionality, both one-dimensional Eckart potential and a full three-dimensional (3D) Liu-Siegbahn-Truhlar-Horowitz (LSTH) potential calculations have been performed. The calculated values of the Boltzmann matrix elements for the colinear and the full 3D cases are found to deviate slightly from each other in the lower temperature range. The 3D thermal rate constant is in very good agreement with the previous one. © 1996 John Wiley & Sons, Inc.

Introduction

So far, there have been a number of studies in the field of chemical reaction dynamics where the quantum mechanical rate constant is defined through a path-integral formulation. In doing so, the relevant flux-flux autocorrelation functions

consist of complex time propagators with a finite space-time range [1, 2]. Path-integral approaches suggested to date for the estimation of the desired thermodynamic or dynamic quantities generally involve either iterated "short-time" approximation using the Trotter formula or the use of Fourier expansions of the path involved [3]. However, it is still a matter of great concern for theoretical chemists to treat realistic chemical phenomena

where quantum and classical degrees of freedom exist inevitably at the same time or, in other words, to overcome the multidimensionality problem.

The stochastic quantization method (SQM) [3] has succeeded in solving a variety of problems in high-energy physics [4–7]. The prescription of SQM to obtain the usual quantum mechanics depends on the fact that propagators and related quantities can be reduced to n -point functions of the operators [8, 9]. Also, the SQM is based on the equality between the path-integral measure and the Fokker–Planck measure. The latter can be obtained as an equilibrium distribution for dynamical variables by solving a stochastic differential equation (SDE) (e.g., the Langevin equation) [10].

In the field theory for elementary particles, where SQM has been developed, the Feynman boundary condition is implicitly assumed [9]; therefore the two-point functions (i.e., the vacuum expectation values of field operators) are nothing but the transition amplitudes themselves [8, 9]. On the contrary, in quantum statistical mechanics for finite temperature and nonrelativistic quantum mechanics, i.e., the realm of chemical reactions, it is not appropriate to treat a transition amplitude as a vacuum-to-vacuum expectation value in the presence of a source [8]. Instead, the boundary conditions for the motion of classical particles should be such that $x(t_f) = x_f$ and $x(t_i) = x_i$, i.e., boundary conditions with a finite space–time range (the Dirichlet boundary condition [8, 9]).

Therefore, in this article, a new possible procedure of the path-integral method to obtain a transition amplitude with a finite-time range is proposed by combining the quantum transition state theory with SQM, namely, the stochastic path-integral (SPI) method for chemical reaction dynamics. Simple examples are demonstrated by using a harmonic potential, a one-dimensional (1D) Eckart potential and a full three-dimensional (3D) Liu–Siegbahn–Truhlar–Horowitz potential for the thermal exchange reaction of the $\text{H} + \text{H}_2$ system.

Theoretical Treatments

STOCHASTIC QUANTIZATION METHOD AND THE BOLTZMANN MATRIX ELEMENTS

For such problems in *quantum* statistical mechanics at temperature T , SQM assumes the following simultaneous SDE with respect to a new parameter τ which is called “the fictitious time”

(the fifth dimensional parameter with the dimension T^2/M) and is introduced just to describe the quantum mechanical fluctuation around the classical most probable path as a hypothetical stochastic process:

$$\frac{\partial \mathbf{x}(u, \tau)}{\partial \tau} = - \left. \frac{\delta S_E}{\delta \mathbf{x}} \right|_{\mathbf{x}=\mathbf{x}(u, \tau)} + \boldsymbol{\eta}(u, \tau), \quad (1)$$

where \mathbf{x} denotes a set of Cartesian coordinates describing the dynamics and depends not only on the inverse of temperature (or the Euclidean time) u ($0 \leq u \leq \beta\hbar/2$) but also on the fictitious time τ ; S_E is an Euclidean action functional that enables us to calculate the partition function and $\boldsymbol{\eta}$ is a random number vector whose components are Gaussian white noises subject to

$$\langle \eta_i(u, \tau) \rangle = 0, \quad (2)$$

$$\langle \eta_i(u, \tau) \eta_j(u', \tau') \rangle = 2\hbar \delta_{ij} \delta(u - u') \delta(\tau - \tau'). \quad (3)$$

The brackets $\langle \dots \rangle$ stand for the average over $\boldsymbol{\eta}$'s. By solving Eq. (1) under the most suitable boundary conditions for each problem, we obtain a Markov process $\mathbf{x}(u, \tau)$ reflecting not only thermal but also quantum mechanical characteristics of the system. Then, one can retrieve quantum mechanics in the *thermal* equilibrium limit of the hypothetical stochastic process with respect to the parameter τ .

The probability distribution functional $P(\mathbf{x}; \tau)$ with respect to \mathbf{x} satisfies the Fokker–Planck equation [11, 12];

$$\frac{\partial P(\mathbf{x}; \tau)}{\partial \tau} = \hbar \frac{\delta}{\delta \mathbf{x}} \left(\frac{\delta}{\delta \mathbf{x}} + \frac{1}{\hbar} \frac{\delta S_E}{\delta \mathbf{x}} \right) P(\mathbf{x}; \tau), \quad (4)$$

which yields

$$P(\mathbf{x}) = \lim_{\tau \rightarrow \infty} P(\mathbf{x}; \tau) = N \cdot \exp(-S_E/\hbar) \quad (5)$$

at the thermal equilibrium limit with respect to τ , N being the normalization constant [4, 11, 12]. Thus, one can find that the Fokker–Planck measure at the infinite fictitious time limit,

$$d\mu = P_{\text{eq}}(\mathbf{x}) d\mathbf{x} \quad (6)$$

is nothing but the path-integral measure [7].

One typical procedure for extracting quantum mechanical information is to calculate the two-point function $\Delta_{ij}(u - u')$, i.e., two-time Green

function, by using the following relationships [6, 9, 10],

$$\Delta_{ij}(u-u') = N \int D[\mathbf{x}] x_i(u) x_j(u') \exp(-S_E/\hbar) \\ = D_{ij}(u-u'; 0), \quad (7)$$

$$D_{ij}(u-u'; \tau-\tau') \\ = \lim_{\substack{\tau \rightarrow \infty \\ |\tau-\tau'| = \text{fixed}}} \langle x_i(u; \tau) x_j(u'; \tau') \rangle. \quad (8)$$

However, in this article, we will pursue a direct method which can reproduce the path-integral measure under the Dirichlet condition [Eqs. (11) and (12)]. This is a most profitable method for describing time-dependent phenomena in low-energy sciences as chemical reaction dynamics. In that case, the transition amplitude of the Boltzmann operator (the Euclidean time evolution operator) is expressed as follows:

$$\langle \mathbf{x}_f, u_f | \mathbf{x}_i, u_i \rangle \\ = \langle \mathbf{x}_f | \exp(-uH) | \mathbf{x}_i \rangle \\ = N \int D[\mathbf{x}] \exp \left[-\frac{1}{\hbar} \int_{u_i}^{u_f} du L_E \left(\mathbf{x}(u), \frac{d\mathbf{x}(u)}{du} \right) \right], \quad (9)$$

where L_E denotes an Euclidean Lagrangean:

$$L_E \left(\mathbf{x}(u), \frac{d\mathbf{x}(u)}{du} \right) = \frac{1}{2} \frac{d\mathbf{x}(u)}{du} \mathbf{M} \frac{d\mathbf{x}(u)}{du} + V(\mathbf{x}(u)), \quad (10)$$

and \mathbf{M} is a mass matrix. For our purpose, one has to solve the SDE (1), imposing the following

boundary conditions:

$$\begin{cases} \mathbf{x}(u_i, \tau) = \mathbf{x}(u_i, 0) = \mathbf{x}_i & (11) \\ \mathbf{x}(u_f, \tau) = \mathbf{x}(u_f, 0) = \mathbf{x}_f & (12) \end{cases}$$

throughout the fictitious time generation. Only if the equilibrium is reached, can we construct an ensemble of paths $\{\mathbf{x}(u, \tau)\}$ for the boundary condition with two fixed Euclidean space-time boundaries [4, 11, 12]. The pictorial illustration for the scheme is shown in Figure 1.

THERMAL RATE CONSTANT EXPRESSION

In the chemical reaction rate theory, it is well known that the thermal rate constant is expressed as

$$k(T) = Q_R^{-1} \int_0^\infty dt C_f(t), \quad (13)$$

where Q_R is the partition function normalized at the reactant state per unit volume and $C_f(t)$ is the flux-flux autocorrelation function defined as

$$C_f(t) = \text{Tr} [F \exp(u^c H) F \exp(-u^c H)] \\ = \left(\frac{\hbar}{2m} \right)^2 \left(\frac{\partial^2}{\partial \mathbf{x}_f \partial \mathbf{x}_i} \left| \langle \mathbf{x}_f | \exp(-u^c H) | \mathbf{x}_i \rangle \right|^2 \right. \\ \left. - 4 \frac{\partial}{\partial \mathbf{x}_i} \left| \langle \mathbf{x}_f | \exp(-u^c H) | \mathbf{x}_i \rangle \right|^2 \right) \quad (14)$$

with the complex time

$$u^c = \frac{\beta}{2} + i \cdot \frac{t}{\hbar} \quad (15)$$

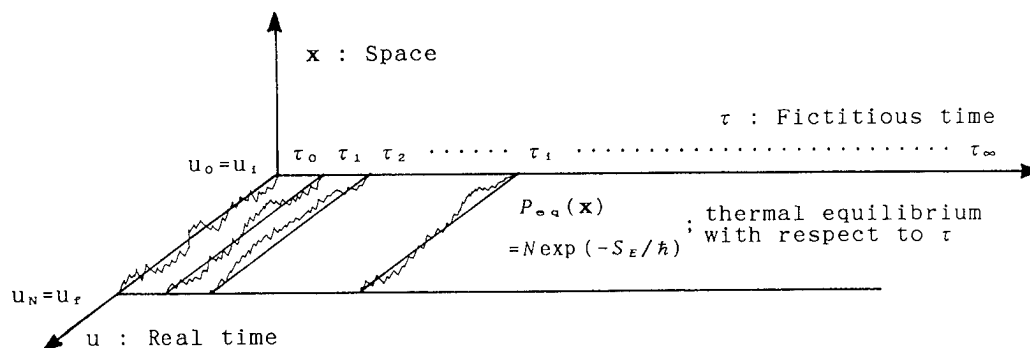


FIGURE 1. Schematic diagram for the stochastic path-integral method. The space axis is represented here by one dimension. The boundary condition is $\mathbf{x}(u_i) = \mathbf{x}(u_f) = \mathbf{x}_i (= \mathbf{x}_f) = 0$.

and the flux operator

$$F = \frac{1}{2} \left[\delta(\mathbf{x}) \frac{\mathbf{p}}{m} + \frac{\mathbf{p}}{m} \delta(\mathbf{x}) \right]. \quad (16)$$

In Eq. (14), the transition amplitude is defined as

$$\begin{aligned} & \langle \mathbf{x}_f | \exp(-u^c H) | \mathbf{x}_i \rangle \\ &= \left(\frac{m}{2\pi\hbar^2 u^c} \right)^{1/2} \exp\left(-\frac{m}{2\hbar^2 u^c} (\mathbf{x}_f - \mathbf{x}_i)^2 \right) \\ & \cdot \Delta(\mathbf{x}_f, \mathbf{x}_i; \beta/2 + it/\hbar). \end{aligned} \quad (17)$$

The left-hand side is the analytic continuation of the transition amplitude of the Boltzmann operator [Eq. (9)],

$$\begin{aligned} \rho(\mathbf{x}_f, \mathbf{x}_i) &= \langle \mathbf{x}_f, \beta\hbar/2 | \mathbf{x}_i, 0 \rangle \\ &= \langle \mathbf{x}_f | \exp(-\beta H/2) | \mathbf{x}_i \rangle, \end{aligned} \quad (18)$$

which is related to the Boltzmann rate constant if the Euclidean time is analytically continued to a complex time $\hbar\beta/2 + it$ [1]. As a result, for estimation of the rate constant, one finally needs the analytic continuation (a.c.) of the SQM value for the potential factor $\Delta(\mathbf{x}_f, \mathbf{x}_i; \beta/2)$ of the transition amplitude as follows:

$$\Delta(\mathbf{x}_f, \mathbf{x}_i; \beta/2 + it/\hbar) = \lim_{u \rightarrow u^c} \text{a.c.} \Delta(\mathbf{x}_f, \mathbf{x}_i; \beta/2). \quad (19)$$

The H + H₂ Exchange Reaction

SIMPLE EXAMPLE: THE HARMONIC BARRIER

In the present study, we employed two 1D and one 3D analytic potentials for the proton exchange reaction in the H + H₂ system. The first one was a harmonic potential:

$$V(x) = \frac{1}{2} m \omega^2 x^2, \quad (20)$$

where the parameters were $\omega = 4.00 \times 10^{14} \text{ (s}^{-1}\text{)}$ and $m = 1.67 \times 10^{-24} \text{ (g)}$. These values were optimally chosen to model a colinear H₃ molecular system.

For each numerical simulation, the Euclidean time axis was discretized into 50 segments between 0 to $\beta\hbar/2$ and that of the fictitious time into 10,000 segments. By setting an arbitrary initial condition for the fictitious time, Eq. (1) was solved and the latter 5000 paths were chosen to make an ensemble $\{x(u_\mu, \tau_\nu)\}$ where μ and ν are integral

suffixes in the ranges between 0 and 50 and between 1 and 5000, respectively. It must be noted that each path, specified by ν , satisfies strictly the Dirichlet boundary condition $x(u_0, \tau_\nu) = x(u_{50}, \tau_\nu) = 0$. To know statistical error estimation, we performed a set of 10 simulations for each temperature by generating 10 sets of random numbers. For each calculation at different temperatures, the same element of the same set of random numbers was assigned to the same lattice points. Each run demanded about 10 s of CPU time in the IBM RISC/6000 355 workstation.

In Table I, the calculated values of the matrix elements of the Boltzmann operator $\langle 0 | \exp(-\beta H/2) | 0 \rangle$ (the Euclidean time transition amplitude) for the harmonic barrier are shown along with the averages, variances, and standard deviations, abbreviated to Avg., Var. and S.d., respectively. The exact values of the matrix elements obtained by analytic expressions are also presented for comparison [13]. The agreement is very good especially for temperatures higher than 500 K in spite of the naive center-difference algorithm. Although we originally used the first-order difference scheme in the numerical algorithm and obtained slightly worse values, a second-order difference scheme was later found to improve those values quite well. However, as is well known in the quantum mechanical simulation, the systematic error became larger as the temperature was lowered [14]. At 300 K, the systematic error in Avg. results in $\sim +40\%$ in comparison to the exact value, although the accidental error is found to be small and with almost the same magnitude, i.e., 2.6–6.4%, throughout the whole temperature range.

In Figure 2, the temperature dependence of the matrix element is plotted for the Avg. and Avg. \pm S.d. values by comparison to the exact ones. Since the transition amplitude itself becomes smaller as the temperature becomes lower, the absolute values of accidental errors at low temperature become small due to the uniformity of percentage of the accidental error.

ONE-DIMENSIONAL ECKART POTENTIAL AND FULL 3-DIMENSIONAL LSTH POTENTIAL

For demonstration of the SPI method, we employed two more realistic potentials for describing the H + H₂ exchange reaction. In the first case, we adopted a 1D Eckart potential, which is often employed as a model potential in a symmetric S_N2

TABLE I

Matrix elements of the Boltzmann operator $\langle s_i | \exp(-H/2kT) | s_i \rangle$ in the case of $s_i = s_j = 0$ for the harmonic oscillator (all values were divided by 10^8).

Data	T (K)							
	300	400	500	600	700	800	900	1000
1	0.5768	0.8106	1.0498	1.2781	1.4948	1.6993	1.8915	2.0718
2	0.6052	0.9184	1.0112	1.1967	1.3739	1.5470	1.7171	1.8836
3	0.5807	0.8322	1.1541	1.3950	1.6152	1.8175	2.0046	2.1783
4	0.6372	0.8082	1.0693	1.2955	1.5114	1.7157	1.9079	2.0881
5	0.5604	0.8900	1.1727	1.4061	1.6218	1.8217	2.0074	2.1803
6	0.5565	0.8073	1.0384	1.2460	1.4360	1.6146	1.7851	1.9494
7	0.5965	0.8875	1.1597	1.4070	1.6306	1.8342	2.0212	2.1943
8	0.5845	0.8644	1.1314	1.3801	1.6094	1.8198	2.0130	2.1911
9	0.6476	0.9375	1.2010	1.4368	1.6490	1.8416	1.9454	2.1826
10	0.5666	0.7725	1.0847	1.3034	1.5032	1.6903	2.0067	2.0371
Avg.	0.5912	0.8529	1.1072	1.3345	1.5445	1.7402	1.9300	2.0957
Var.	0.0010	0.0030	0.0042	0.0066	0.0089	0.0107	0.0112	0.0123
S.d.	0.0310	0.0547	0.0648	0.0810	0.0941	0.1033	0.1060	0.1110
Avg. + S.d.	0.6222	0.9076	1.1721	1.4155	1.6386	1.8434	2.0360	2.2066
Avg. - S.d.	0.5602	0.7982	1.0424	1.2535	1.4504	1.6369	1.8240	1.9847
Analytical ^a	0.3523	0.6659	0.9764	1.2620	1.5190	1.7490	1.9560	2.1450

Data	T (K)							
	1100	1200	1300	1400	1500	1600	1700	1800
1	2.2409	2.3997	2.5494	2.6908	2.8250	2.9525	3.0743	3.1908
2	2.0456	2.2023	2.6353	2.4988	2.6383	2.7723	2.9009	3.0246
3	2.3404	2.4923	2.5651	2.7705	2.8990	3.0213	3.1384	3.2507
4	2.2571	2.4158	2.6370	2.7062	2.8398	2.9669	3.0881	3.2042
5	2.3421	2.4939	2.4084	2.7723	2.9009	3.0234	3.1406	3.2530
6	2.1080	2.2610	2.6488	2.5501	2.6864	2.8174	2.9434	3.0646
7	2.3555	2.5066	2.6540	2.7833	2.9110	3.0327	3.1491	3.2609
8	2.3561	2.5099	2.6175	2.7897	2.9182	3.0404	3.1571	3.2689
9	2.3360	2.4806	2.4992	2.7480	2.8726	2.9922	3.1072	3.2181
10	2.1985	2.3524	2.5369	2.6393	2.8726		3.0239	3.1417
Avg.	2.2580	2.4114	2.5752	2.6949	2.8364	2.9577	3.0723	3.1877
Var.	0.0123	0.0119	0.0063	0.0104	0.0094	0.0095	0.0080	0.0073
S.d.	0.1108	0.1090	0.0794	0.1022	0.0971	0.0976	0.0894	0.0852
Avg. + S.d.	2.3688	2.5204	2.6545	2.7971	2.9335	3.0553	3.1617	3.2729
Avg. - S.d.	2.1472	2.3025	2.4958	2.5927	2.7393	2.8601	2.9829	3.1026
Analytical ^a	2.3170	2.4770	2.6250	2.7650	2.8960	3.0210	3.1390	3.2530

^a Analytical values are calculated by the analytic formula in Feynman and Hibbs (Ref. [13]).

type of chemical reaction [1-3]:

$$V(x) = V_0 \operatorname{sech}^2(x/a), \quad (21)$$

where $V_0 = 7.50$ (kcal/mol) and $a = 3.15$ (Å). In the second case, to understand better the influence of dimensionality for this quantum mechanical process, the full 3D potential prepared by Liu,

Siegbahn, Truhlar, and Horowitz (LSTH), was utilized [15-17]. This has been extensively used for investigating the $H + H_2$ exchange reaction when checking accuracy of different quantum mechanical treatments.

In Figure 3, the temperature dependence of the matrix element is plotted for the 1D Eckart potential and, in Table II, nine sets of the matrix ele-

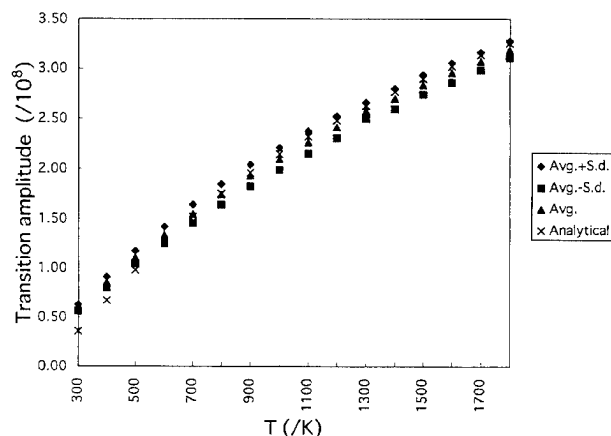


FIGURE 2. Temperature dependence of the transition amplitude for the harmonic potential [Eq. (20)].

ments relating to the potential factor $\Delta(x_f = 0, x_i = 0; u^c)$ and nine corresponding values of the time correlation function $C_f(t)$ are shown from 0 to 20 fs at 630 K in Figure 4. The numerical value estimated by $C_f(t)$ is $3.317 \times 10^{10} \text{ s}^{-1}$ for the thermal rate constant multiplied by Q_R (Table III) and was found to give a reasonable value when the previous values in the temperature range between 200 and 400 K [3] are extrapolated (Fig. 5).

On the other hand, the temperature dependence of the Boltzmann matrix element for the LSTH potential is plotted in Figure 6 for both the colinearly restricted and the full 3D cases at the same time. The corresponding $C_f(t)$'s at 630 K are obtained as shown in Figure 7 and result in 6.272×10^9 and $2.492 \times 10^9 \text{ s}^{-1}$ for kQ_R , respectively. For

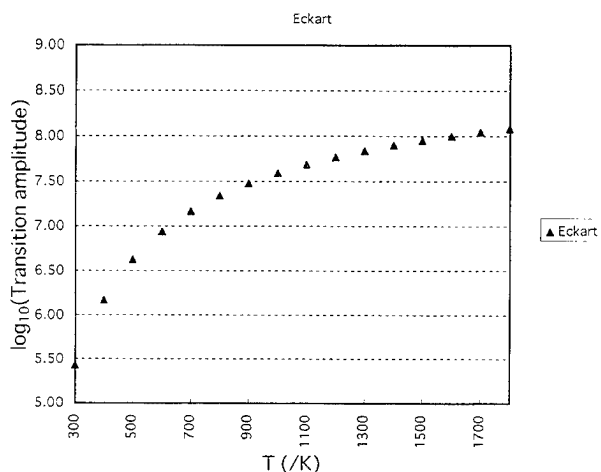


FIGURE 3. Temperature dependence of the transition amplitude for the Eckart potential [Eq. (21)].

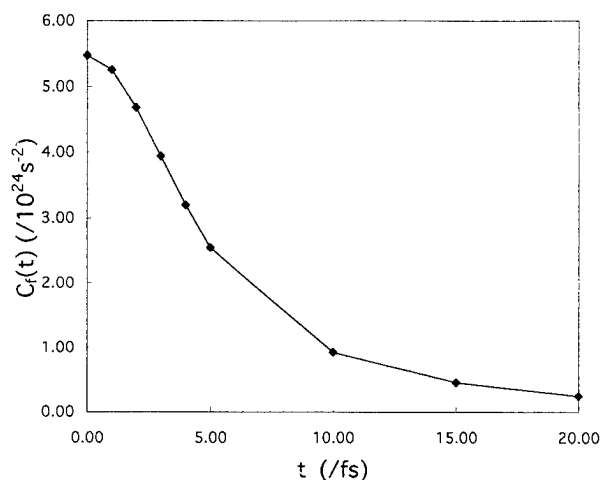


FIGURE 4. Flux-flux autocorrelation function for the Eckart potential, Eq. (21), with $V_0 = 7.50 \text{ kcal/mol}$ and $a = 3.15 \text{ \AA}$, under a temperature of 630 K.

the sake of direct comparison of the rate constant values themselves, the reactant partition function per unit volume Q_R for the 3D case [18–20]:

$$Q_R = \left(\frac{2\pi\mu k_B T}{h^2} \right)^{3/2} \sum_{v,j} (2j+1) \exp\left(\frac{-\epsilon_{v,j}}{k_B T} \right) \quad (22)$$

was calculated for distinguishable-atom H_2 without nuclear spin [18, 19, 21]. μ is the reduced mass, $\epsilon_{v,j}$ is the vibrational-rotational energy of the reactant H_2 diatom [19]. With the numerical value $1.858 \times 10^{22} \text{ molecule cm}^{-3}$ of Q_R for the parameter set A in Ref. 18(a), the present 3D ther-

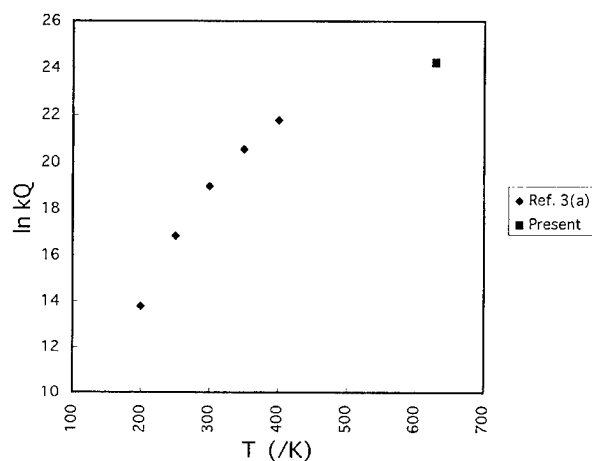


FIGURE 5. Temperature dependence of the thermal rate constant for the Eckart potential. The previous values (♦) are shown also with the present one (■).

TABLE II

Matrix elements relating to the potential factor $\Delta(s_f, s_i; u^c)$ and the time correlation function $C_f(t)$ for $s_f = s_i = 0$ ($T = 630$ K).

t (fs)	$\Delta(0, 0; u^c)$		$ \Delta(0, 0; u^c) ^2$ ($\times 10^{-3}$)	$C_f(t)$ ($\times 10^{24} \text{ s}^{-2}$)
	$\text{Re } \Delta(0, 0; u^c)$ ($\times 10^{-2}$)	$\text{Im } \Delta(0, 0; u^c)$ ($\times 10^{-2}$)		
0.00	5.023	0.000	2.5227	5.463
1.00	4.424	-2.378	2.5228	5.247
2.00	2.771	-4.771	2.5231	4.679
3.00	4.573	-5.004	2.5249	3.936
4.00	-1.967	-4.631	2.5312	3.187
5.00	-3.931	-3.168	2.5484	2.534
10.00	-0.024	5.523	3.0503	0.920
15.00	6.249	0.585	3.9386	0.449
20.00	4.840	-4.661	4.5154	0.239

TABLE III

Thermal rate constant as kQ_R for the Eckart, colinear and 3D models of the $\text{H} + \text{H}_2$ exchange reaction ($T = 630$ K).

T (K)	kQ_R (s^{-1})		
	Eckart	Colinear	3D
630	$3.317\text{E} + 10$	$6.272\text{E} + 09$	$2.492\text{E} + 09^a$

^a The corresponding rate constant k ($T = 630$ K) is $1.341 \times 10^{-13} \text{ cm}^3 \text{ molecule}^{-1} \text{ s}^{-1}$.

mal rate constant k ($T = 630$ K) is converted to $1.341 \times 10^{-13} \text{ cm}^3 \text{ molecule}^{-1} \text{ s}^{-1}$, which is in very good agreement with the previous result in Table IX in Ref. [21]. However, the value is about 10 times larger than that ($\sim 2.000 \times 10^{-15} \text{ cm}^3$

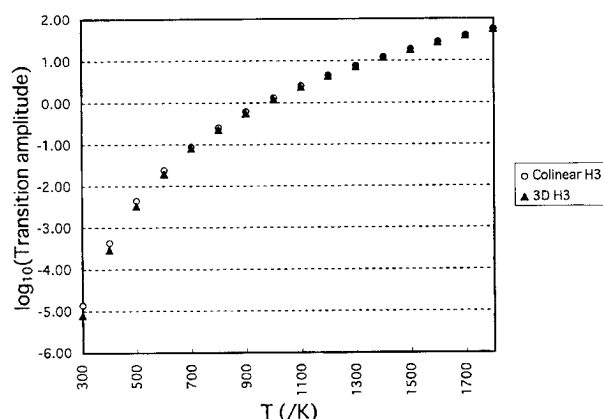


FIGURE 6. Temperature dependence of the transition amplitude for the LSTH potential in the colinearly restricted and the full three-dimensional cases.

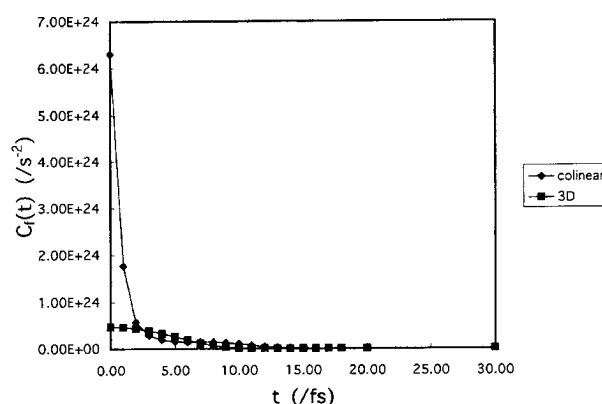


FIGURE 7. Flux-flux autocorrelation function for the LSTH potential in the colinearly restricted and the full three-dimensional cases, under a temperature of 630 K.

molecule $^{-1} \text{ s}^{-1}$) in Ref. [18(a)] since we have utilized the same LSTH potential as Ref. [21] although Ref. [18(a)] adopted the double many-body expansion surface [18(b)].

Furthermore, comparing each matrix element value at the same temperature (Fig. 6), one can understand that the smaller value for the 3D case than for the colinear case (Table III) is originating from its relative smaller values. Because both are based on the same LSTH potential, the relative difference should come from the dimensionality in the two cases. Namely, one should notice that, in the colinear case, there are fewer bath coordinates orthogonal to the reaction coordinate and, therefore, each trajectory, which determines the quantum mechanical transition amplitude as a whole, stays for relatively shorter time than in the 3D

case. Accordingly, the difference in the time of stay results in relatively larger matrix elements and rate constant for the colinear potential.

Concluding Remarks

In the light of the previous examples, we suggest that the stochastic path-integral method can become a promising strategy for many applications in the field of low-energy science, as demonstrated here for a chemical reaction. Furthermore, it should be noted that there exist some merits in this method because it is based on the equation of motion [13]. In addition, we are also convinced that the present method will be regarded as an important milestone in the progress of SQM in the low-energy material sciences.

Although one might regard the present method just as one of the importance sampling methods, in the sense that the ensemble is constructed from the solutions of a stochastic differential equation, which reflects the equation of motion of the system, the method needs not assume any approximation with respect to the potential functional forms, in comparison to usual treatments. Therefore, this approach should, in principle, work for most of the systems with any analytical or numerical force fields for solving the stochastic equation of motion. It is the recent development of quantum chemistry which enabled us to realize analytic potential functions for various realistic chemical reactions that motivate us to do the present study.

ACKNOWLEDGMENTS

The author would like to thank Professor Kenichi Fukui for his enlightening discussions and to acknowledge Professor Tokio Yamabe for his instructive suggestions. He also would like to express his gratitude to the referee for his/her appropriate comments and warm encouragement for completing the present article. The numerical calculations were performed by CONVEX C3210 at the IFC computer room, FACOM VP400E and

VP2600 at the Data Processing Center of Kyoto University, and the SX-3 at the Institute for Molecular Science (IMS). This work was supported by a Grant-in-Aid for Scientific Research from the Ministry of Education, Science and Culture in Japan.

References

1. (a) W. H. Miller, S. D. Schwartz, and J. W. Tromp, *J. Chem. Phys.* **79**, 4889 (1983); (b) K. Yamashita and W. H. Miller, *Ibid.* **82**, 5475 (1985); (c) J. W. Tromp and W. H. Miller, *Ibid.* **90**, 3482 (1986).
2. D. L. Freeman and J. D. Doll, *Adv. Chem. Phys.* **70B**, 139 (1988).
3. (a) R. Lefebvre and N. Moiseyev, *J. Chem. Phys.* **93**, 7173 (1990); (b) R. Lefebvre, V. Ryaboy and N. Moiseyev, *Ibid.* **98**, 8601 (1993); (c) R. Lefebvre, N. Moiseyev, and V. Ryaboy, *Int. J. Quantum Chem.* **51**, 465 (1994).
4. G. Parisi and Y.-S. Wu, *Sci. Sin.* **24**, 483 (1981).
5. M. Namiki, I. Ohba, K. Okano, and Y. Yamanaka, *Prog. Theor. Phys.* **69**, 1580 (1983).
6. (a) M. Namiki, I. Ohba, K. Okano, M. Rikishita, and S. Tanaka, *Prog. Theor. Phys.* **73**, 186 (1985); (b) *Ibid.* **75**, 501 (1986).
7. A. Ukawa and M. Fukugita, *Phys. Rev. Lett.* **55**, 1854 (1985).
8. L. H. Ryder, *Quantum Field Theory* (Cambridge University Press, Cambridge, 1985).
9. B. Sakita and K. Yoshikawa, *Quantum Mechanics of Many Freedom Systems by Path-Integral Method* (Iwanami, Tokyo, 1986).
10. M. Namiki, I. Ohba, and K. Okano, *Prog. Theor. Phys.* **72**, 350 (1984).
11. H. Risken, *The Fokker-Planck Equation*, 2nd ed. (Springer, Berlin, 1989).
12. G. Parisi, *Statistical Field Theory* (Addison-Wesley, New York, 1988).
13. R. P. Feynman and A. R. Hibbs, *Quantum Mechanics and Path Integrals* (McGraw-Hill, New York, 1965).
14. M. Nagaoka, to be submitted.
15. B. Liu, *J. Chem. Phys.* **58**, 1925 (1973).
16. P. Siegbahn and B. Liu, *J. Chem. Phys.* **68**, 2457 (1978).
17. (a) D. G. Truhlar and C. J. Horowitz, *J. Chem. Phys.* **68**, 2466 (1978); (b) *Ibid.* **71**, 1514 (1979).
18. (a) D. C. Chatfield, D. G. Truhlar, and D. W. Schwenke, *J. Chem. Phys.* **94**, 2040 (1991); (b) P. N. Day and D. G. Truhlar, *Ibid.* **94**, 2045 (1991).
19. W. H. Miller, *J. Chem. Phys.* **61**, 1823 (1974).
20. M. Karplus, R. N. Porter, and R. D. Sharma, *J. Chem. Phys.* **43**, 3259 (1965).
21. T. J. Park and J. C. Light, *J. Chem. Phys.* **91**, 974 (1989).

Sinc Collocation in Quantum Chemistry: Solving the Planar Coulomb Schrödinger Equation

VASILIOS G. KOURES AND FRANK E. HARRIS*

*Department of Chemistry, Henry Eyring Bldg., University of Utah, Salt Lake City, Utah 84112;
e-mail for F. E. H.: harris@dirac.chem.utah.edu*

Received March 28, 1996; revised manuscript received July 16, 1996; accepted July 24, 1996

ABSTRACT

Dirac bra-ket notation is introduced for the Whittaker cardinal (Sinc) functions and a previously unreported completeness relation for these quantities is presented and derived. With the use of this completeness relation it becomes simple to transform to a Sinc-basis the eigenvalue equations arising from a light-cone quantization of field theory or the similar equations occurring in nonrelativistic quantum mechanics. The simplicity and power of Sinc-function expansions is illustrated by computation of the eigenvalues and eigenfunctions of the position-space planar Coulomb equation, a problem for which convergence has not been achieved by a variety of other computational methods. © 1996 John Wiley & Sons, Inc.

Introduction

Expansion methods based on Whittaker cardinal functions (usually referred to as Sinc functions) are becoming increasingly recognized as very powerful tools for solving various problems within applied physics and engineering [1]. However, there has been little use of Sinc functions in quantum chemistry, and it has not been clear how to apply Sinc methods within the context of the operator formalism of quantum field theory. In a recent contribution one of us (V.G.K.) has shown how, with the use of Dirac's bra-ket notation and with the derivation of appropriate mathematical

theorems, a Sinc-function approach can be made more transparent and flexible enough to become applicable to problems in a general occupation-number Fock space [2].

The use of Sinc functions constitutes a second step in the direction indicated by our contribution to the 1995 Sanibel Symposium [3]. That work started from the premise that light-cone quantization (LCQ) of quantum field theory was a promising method for solving nonperturbative problems in quantum chemistry, condensed-matter physics, and particle physics, since it led naturally to a rational, closed-form, and relativistically covariant Hamiltonian formulation with a convenient vacuum state. In particular, a discretized LCQ formulation permits gauge theory to be reduced to an eigenvalue problem (for the square of M , the in-

* To whom correspondence should be addressed.

variant mass) involving the light-cone Hamiltonian H_{LC} and a discrete and covariantly regularized Fock space of functions $|n\rangle$:

$$\sum_m \langle n | H_{LC} | m \rangle \langle m | \Psi \rangle = M^2 \langle n | \Psi \rangle. \quad (1)$$

Attempts to solve Eq. (1) with plane waves $|n\rangle$ have produced interesting results, but led to convergence difficulties in problems modeling bound states [4]. Our previous contribution showed how, starting from a plane-wave basis in which nonperturbative renormalization can be properly implemented, one could transform to a localized Gaussian basis. The main drawback of that procedure is the lack of orthogonality of the individual Gaussian functions. The use of a Sinc basis, whose members are orthogonal, provides a route to circumvent that drawback. We have not yet applied Sinc expansions to a fully realistic LCQ problem. However, we can now report results illustrating the power of Sinc-function methods by applying them to a model problem whose solution has not been satisfactorily obtained by other means.

Even though the numerical computation of this model is not of direct interest to quantum chemists, the essential steps which lead to its solution are very relevant. The model is rigorously formulated from a fully relativistic light-cone formulation of quantum electrodynamics (QED) in $2 + 1$ dimensions. We then outline how to derive the planar Coulomb Schrödinger equation by taking the weak-coupling and nonrelativistic limits. A similar need to use a full-fledged quantum field theoretic model as a starting point for solving relativistic many-electron atomic problems is now well established [5]. These atomic models are also initially formulated within a rigorous quantum field theoretic framework and appropriate low-energy limits are then taken to facilitate computation. Novel technical difficulties brought about by such an approach have created a need for new computational paradigms and their tests on simple models.

In this spirit, the remainder of the present study consists of (1) a condensed overview of Sinc methods in Fock space, expressed in Dirac bra-ket notation and including a completeness theorem not previously exhibited in the mathematics literature, followed by (2) a Sinc-method application relevant in quantum field theory and in nonrelativistic quantum mechanics; namely, the position-space radial Coulomb equation in two spatial dimensions.

Sinc kets and Sinc bras

If $a > 0$ and m is an integer, the Sinc function, $S(m, a)(x)$, is defined by [1]

$$S(m, a)(x) = \frac{\sin\left[\frac{\pi}{a}(x - ma)\right]}{\frac{\pi}{a}(x - ma)}. \quad (2)$$

Let's define the Sinc-ket and the Sinc-bra to be, respectively, $|m, a\rangle$ and $\langle m, a|$. We may then express the Sinc function as

$$\langle x | m, a \rangle = S(m, a)(x) = \langle m, a | x \rangle, \quad (3)$$

with the second equality above following from the fact that $S(m, a)(x)$ is real. In order to exploit the full power of the Dirac bra and ket notation [6], we must first establish the completeness relation,

$$\sum_{m=-\infty}^{\infty} |m, a\rangle \langle m, a| = 1, \quad (4)$$

where the 1 on the right-hand side is understood to be the identity operator. To establish this, we first prove the following lemmas:

Lemma 1. The cardinal series for the plane wave, $\sqrt{a/2\pi} e^{ikx}$, with $|k| < \pi/a$ is

$$\sqrt{\frac{a}{2\pi}} e^{ikx} = \sqrt{\frac{a}{2\pi}} \sum_{m=-\infty}^{\infty} S(m, a)(x) e^{ikma}. \quad (5)$$

Proof. Suppose that $\sqrt{a/2\pi} e^{ikx}$ is represented by the power series

$$\sqrt{\frac{a}{2\pi}} e^{ikx} = \sqrt{\frac{a}{2\pi}} \sum_m C_m(x) e^{ikma}. \quad (6)$$

Multiply both sides of Eq. (6) by $\sqrt{a/2\pi} e^{-ikna}$ and integrate over k :

$$\begin{aligned} \frac{a}{2\pi} \int_{-\pi/a}^{\pi/a} dk e^{i(x-na)k} \\ = \sum_{m=-\infty}^{\infty} C_m(x) \frac{a}{2\pi} \int_{-\pi/a}^{\pi/a} dk e^{ik(m-n)a}. \end{aligned} \quad (7)$$

We obtain

$$S(n, a)(x) = \sum_{m=-\infty}^{\infty} C_m(x) \delta_{m,n} = C_n(x), \quad (8)$$

and this completes the proof.

We denote the plane wave, $\sqrt{a/2\pi}e^{-ikx}$, in bra and ket notations as

$$\langle x|k\rangle = \sqrt{\frac{a}{2\pi}} e^{-ikx}. \quad (9)$$

Analogously, we also define

$$\sqrt{\frac{a}{2\pi}} e^{-ikma} = \langle m, a|k\rangle = \langle k|m, a\rangle^*. \quad (10)$$

Equation (5) may now be rewritten as

$$\langle x|k\rangle = \sum_m \langle x|m, a\rangle \langle m, a|k\rangle. \quad (11)$$

We now state the next lemma.

Lemma 2.

$$\sum_m \langle k|m, a\rangle \langle m, a|k'\rangle = \langle k|k'\rangle = \delta(k - k'). \quad (12)$$

Proof. By definition, we reexpress the left side of Eq. (12) as

$$\begin{aligned} \frac{a}{2\pi} \sum_m e^{i(k-k')ma} &= a \sum_n \delta(a(k - k') + 2\pi n) \\ &= \delta(k - k'), \end{aligned} \quad (13)$$

where the last equality follows because $|k - k'| < 2\pi/a$. This completes the proof.

It has already been established that [6]

$$\int_{-\pi/a}^{\pi/a} |k\rangle dk \langle k| = 1 \quad (14)$$

and

$$\int_{-\infty}^{\infty} |x\rangle dx \langle x| = 1. \quad (15)$$

We now use the above closure relations to prove a third lemma.

Lemma 3.

$$\begin{aligned} \sum_{m=-\infty}^{\infty} S(m, a)(x) S(m, a)(y) \\ &= \frac{\sin\left[\frac{\pi}{a}(x - y)\right]}{\frac{\pi}{a}(x - y)} \\ &\approx h\delta(x - y) = \langle x|y\rangle \end{aligned} \quad (16)$$

Proof. The proof of this theorem demonstrates the power of the Dirac bra and ket notation as it makes self-evident the decomposition of the sums and integrals necessary to prove it:

$$\begin{aligned} \sum_{m=-\infty}^{\infty} S(m, a)(x) S(m, a)(y) \\ &= \sum_m \langle x|m, a\rangle \langle m, a|y\rangle \\ &= \sum_m \int_{-\pi/a}^{\pi/a} \int_{-\pi/a}^{\pi/a} \langle x|k\rangle dk \langle k|m, a\rangle \langle m, a|k'\rangle \\ &\quad \times dk' \langle k'|y\rangle \\ &= \left(\frac{a}{2\pi}\right)^2 \int_{-\pi/a}^{\pi/a} \int_{-\pi/a}^{\pi/a} e^{ikx} \left[\sum_m e^{-i(k-k')ma} \right] \\ &\quad \times e^{-ik'y} dk dk' \\ &= \left(\frac{a}{2\pi}\right) \int_{-\pi/a}^{\pi/a} \int_{-\pi/a}^{\pi/a} e^{ikx} e^{-ik'y} \delta(k - k') dk dk' \\ &= \left(\frac{a}{2\pi}\right) \int_{-\pi/a}^{\pi/a} e^{ik(x-y)} dk \\ &= \frac{\sin\left[\frac{\pi}{a}(x - y)\right]}{\frac{\pi}{a}(x - y)}. \end{aligned} \quad (17)$$

It turns out that $\sin[\pi/a(x - y)]/[\pi/a(x - y)]$ is an exact delta function for a large class of square-integrable functions; namely, the Wiener space of functions [1]. For other functional spaces, the error between it and a delta function is exponentially damped [1, 7]. This completes the proof.

The bra and ket notation for a general square-integrable function is

$$\langle x|f\rangle = f(x). \quad (18)$$

In this notation, the sampling of $f(x)$ at the Sinc points ma is given by

$$\langle m, a|f\rangle = f(ma). \quad (19)$$

We may now state the lemma for the cardinal series representation of a function in Wiener space by using the bra and ket notation.

Lemma 4. Let $a > 0$, and let $W(\pi/a)$ denote the Wiener space of functions [1]. Every f in $W(\pi/a)$ has the cardinal series representation

$$\langle x|f\rangle = \sum_{m=-\infty}^{\infty} \langle x|ma\rangle \langle ma|f\rangle. \quad (20)$$

Proof. By the Paley-Wiener theorem [1], $f(x)$ has a Fourier transform:

$$f(x) = \frac{1}{2\pi} \int_{-\pi/a}^{\pi/a} e^{-ikx} F(k) dk. \quad (21)$$

The function F may be represented on the interval $(-\pi/a, \pi/a)$ by its Fourier series expansion,

$$F(x) = \sum_m c_m e^{ik_m a}, \quad (22)$$

with

$$c_m = \frac{a}{2\pi} \int_{-\pi/a}^{\pi/a} e^{-ik_m a} F(k) dk = a f(ma), \quad (23)$$

where the last identity follows from Eq. (21). Upon substituting Eqs. (22) and (23) into Eq. (21) and using the fact that

$$\frac{a}{2\pi} \int_{-\pi/a}^{\pi/a} e^{ik(ma-x)} dk = S(m, a)(x), \quad (24)$$

we get

$$f(x) = \sum_{m=-\infty}^{\infty} S(m, a)(x) f(ma). \quad (25)$$

This completes the proof. Notice that this proof demonstrates that the cardinal series (20) for a function in Wiener space will reproduce the function with zero error. However, even for more general function spaces the error is exponentially damped [1, 7].

These four lemmas are necessary and sufficient to prove the closure relations (4). The upshot of all this is that Eq. (4) may be inserted into any second-quantized Hamiltonian to obtain that Hamiltonian's Sinc-basis representation. In turn, we can now rigorously derive the Sinc-basis representation of the QED light-cone Hamiltonian.

For example, in the bra and ket notation, the momentum space representation of the light-cone Hamiltonian may be written as

$$\begin{aligned} H_{LC} = & \int_{-\pi/a}^{\pi/a} \cdots \int_{-\pi/a}^{\pi/a} \int_{-\pi/a}^{\pi/a} \cdots \int_{-\pi/a}^{\pi/a} |k\rangle dk \langle k| \cdots \\ & \cdots |k'\rangle dk' \langle k'| H_{LC} |k''\rangle dk'' \langle k''| \cdots \\ & \cdots |k'''\rangle dk''' \langle k'''|. \end{aligned} \quad (26)$$

We obtain the Sinc-basis representation by inserting the identity operator (4):

$$\begin{aligned} H_{LC} = & \sum_m \int_k \cdots \sum_{n'} \int_{k'} \int_{k''} \sum_n \cdots \\ & \int_{k'''} \sum_{n''} |m, a\rangle \langle m, a| k\rangle dk \langle k| \cdots \\ & \cdots |m', a\rangle \langle m', a| k'\rangle dk' \langle k'| H_{LC} |k''\rangle \\ & \times dk'' \langle k''| n, a\rangle \langle n, a| \cdots \\ & \cdots |k'''\rangle dk''' \langle k'''| n', a\rangle \langle n', a| \quad (27) \\ = & \sum_m \cdots \sum_{m'} \sum_n \cdots \sum_{n'} |m, a\rangle \langle m, a| \cdots |m', a\rangle \\ & \times \langle m', a| H_{LC} |n, a\rangle \langle n, a| \cdots |n', a\rangle \langle n', a|, \end{aligned} \quad (28)$$

where the appropriate limits of summation and integration are understood. If we now use (28) to operate on a bound state $|\Psi\rangle$, we see by inspection of (1) that we would be dealing with an eigenvalue and matrix diagonalization problem. The bound-state samples are obtained at the Sinc points; we can then use the cardinal series to get the relativistically invariant bound-state amplitudes throughout all space.

Solving the Planar Coulomb Equations

We will now demonstrate the power of the Sinc collocation method by solving the radial Coulomb equation in $d = 2 + 1$. The motives for studying QED in $2 + 1$ dimensions are numerous [7, 8]. The lower dimensions allow a smaller number of degrees of freedom, but the model still possesses independent photon degrees of freedom, unlike the $(1 + 1)$ -dimensional model. The model is super-renormalizable and, when formulated with four-component spinors, it exhibits confinement [8, 9].

The nonrelativistic Coulomb Schrödinger equation is derived from the LCQ formalism as follows [7, 8]. One first derives the discretized light-cone Hamiltonian for $(2 + 1)$ -dimensional QED with four-component spinors. A Tamm-Dancoff integral equation is then obtained for the "positronium" bound states. Taking the weak-coupling limit, one gets a nonrelativistic integral equation which is the momentum-space Coulomb Schrödinger equation; the infrared divergences cancel between the self-mass and one-photon exchange diagrams [8]. The

position-space result is then obtained by a Fourier transform,

$$\left[-\frac{1}{m} \nabla_r^2 + \frac{g^2}{2\pi} (\gamma + \ln mr) \right] \Psi(\mathbf{r}) = E \Psi(\mathbf{r}), \quad (29)$$

where γ is the Euler-Mascheroni constant, m is the mass, and g is the coupling constant. It is convenient to rewrite Eq. (29) in terms of the dimensionless variables $x = \sqrt{mg^2/2\pi} \mathbf{r}$ and $\lambda' = (2\pi/g^2)E + \ln\sqrt{2g^2/m\pi}$. We get

$$(-\nabla_x^2 + \ln x + \gamma + \ln 2) \Psi(x) = \lambda' \Psi(x), \quad (30)$$

or

$$(-\nabla_x^2 + \ln x) \Psi(x) = \lambda \Psi(x), \quad (31)$$

with

$$\lambda = \lambda' - \gamma - \ln 2. \quad (32)$$

The separation of variables, $\Psi(x) = R(x)\Theta(\theta)$, leads to $\Theta(\theta) = \exp(\pm i l \theta)$, where l is the angular momentum quantum number. We are left with a radial differential equation for R which, after using the substitution [9]

$$R(x) = x^{-1/2} f(x), \quad (33)$$

transforms into a differential equation for f :

$$-f''(x) + \left[\frac{4l^2 - 1}{4x^2} + \ln x \right] f(x) = \lambda f(x). \quad (34)$$

This equation for f represents a singular Sturm-Liouville system, and it can be solved by Sinc collocation [1].

The theory of Sinc series (cardinal functions) on the entire real line has been thoroughly developed. As mentioned earlier, for a class of functions known as the Wiener class, the Sinc interpolation and quadrature formulas are exact [1]. However, a more practical application of Sinc approximation of functions which are in a much less restrictive class has also been developed and the absolute errors have been derived via contour integration [1]. In a nutshell, the Wiener functions are entire but a more practical class of functions should have specific growth restrictions on the real line and should be analytic only on an infinite strip centered about the real line,

$$D_S \equiv \{z \in \mathcal{E} : z = x + iy, |y| < d\}. \quad (35)$$

\mathcal{E} denotes the set of complex numbers. It turns out that the absolute error of Sinc interpolation and quadrature on such functions is exponentially damped [1].

For the problem of interest to us we need to use Sinc methods on a function f whose domain is $(0, \infty)$. The more general class just described, however, has a domain which includes the whole real line. This conflict is elegantly circumvented through the use of conformal maps [1]. For example, let ϕ be a one-to-one conformal map from some domain D to domain D_S and let ψ denote the inverse map which is also conformal. If f is analytic in D then $f \circ \psi$ is analytic in D_S . So, if a numerical process has been developed in a domain containing the whole real line, \mathcal{R} , then this process can be carried over to a new domain containing only a proper subset of the real line.

We will shortly see that the domain of interest to us is

$$D \equiv \left\{ w \in \mathcal{E} : |\arg(\sinh(w))| < d \leq \frac{\pi}{2} \right\}. \quad (36)$$

This domain is conformally mapped onto the infinite strip D_S by the function [1]

$$z = \phi(w) = \ln(\sinh(w)). \quad (37)$$

If we let

$$w = \psi(z) = \phi^{-1}(z) = \ln(e^z + \sqrt{1 + e^{2z}}), \quad (38)$$

then

$$\Gamma \equiv \psi(\mathcal{R}) = (0, \infty), \quad (39)$$

as desired. For $a > 0$ and m an integer we define the *Sinc points*

$$x_m \equiv \psi(ma) = \ln(e^{ma} + \sqrt{1 + e^{2ma}}). \quad (40)$$

One may further verify that

$$\begin{aligned} \phi'(x_m) &= \sqrt{1 + e^{-2ma}}, \\ \phi''(x_m) &= -e^{-2ma}, \end{aligned} \quad (41)$$

where the primes denote differentiation with respect to x .

Now, to solve (34) we note that [7]

$$f(x) \approx \sum_{m=-M}^N S(m, a)(\phi(x)) f(x_m), \quad (42)$$

$$f''(x) \approx \sum_{m=-M}^N \left\{ \left[(\phi'(x))^2 \frac{d^2}{d\phi^2} + \phi''(x) \frac{d}{d\phi} \right] \times S(m, a)(\phi(x)) \right\} f(x_m). \quad (43)$$

Since we would like our solution to be normalized, we will also make use of the Sinc quadrature formula [7],

$$\int_0^\infty F(x) dx \approx a \sum_{m=-M}^N \frac{F(x_m)}{\phi'(x_m)}. \quad (44)$$

To evaluate these expansions at a general Sinc point x_n note that

$$\begin{aligned} S(m, a)(\phi(x))|_{x_n} &= \delta_{n,m}^{(0)}, \\ \frac{d}{d\phi} S(m, a)(\phi(x))|_{x_n} &= -\frac{1}{a} \delta_{n,m}^{(1)}, \\ \frac{d^2}{d\phi^2} S(m, a)(\phi(x))|_{x_n} &= \frac{1}{a^2} \delta_{n,m}^{(2)}, \end{aligned} \quad (45)$$

where $\delta_{n,m}^{(0)}$ is the Kronecker delta function and

$$\delta_{n,m}^{(1)} = \begin{cases} 0, & m = n \\ \frac{(-1)^{m-n}}{m-n}, & m \neq n, \end{cases} \quad (46)$$

$$\delta_{n,m}^{(2)} = \begin{cases} -\frac{\pi^2}{3}, & m = n \\ \frac{2(-1)^{m-n+1}}{(m-n)^2}, & m \neq n \end{cases}. \quad (47)$$

Using these results along with (41) we may now approximate (34) via Sinc collocation,

$$\sum_{m=-M}^N [I_{n,m}^{(0)} + I_{n,m}^{(1)} + I_{n,m}^{(2)}] f(x_m) = \lambda f(x_n), \quad (48)$$

where

$$\begin{aligned} I_{n,m}^{(0)} &= \left(\frac{4l^2 - 1}{4x_m^2} + \ln x_m \right) \delta_{n,m}^{(0)} \\ I_{n,m}^{(1)} &= \frac{1}{a} e^{-2ma} \delta_{n,m}^{(1)} \\ I_{n,m}^{(2)} &= -\frac{1}{a^2} (1 + e^{-2ma}) \delta_{n,m}^{(2)}. \end{aligned} \quad (49)$$

In the tradition of LCQ, we have formulated the problem as an eigenvalue and matrix diagonalization problem. The components of the eigenvector $f(x_m)$ can be substituted into (42) to compute the eigenfunction at arbitrary x . Finally, we use (33) to acquire $R(x)$ and we normalize this function by computing the norm, $\sqrt{\int_0^\infty R^2(x) dx}$, using the Sinc quadrature formula (44).

In Table I we list the first five eigenvalues for l ranging from 0 to 4. The diagonalization was performed with MATLAB [10]. The convergence was excellent for all l values but we needed considerably higher M values for $l = 0$ than for $l \neq 0$ [7]. In Ref. [7] the first five $l = 0$ eigenvalues were computed in momentum space:

$$\begin{aligned} \lambda'_0 &= 1.7969, \quad \lambda'_1 = 2.9316, \quad \lambda'_2 = 3.4475, \\ \lambda'_3 &= 3.7858, \quad \lambda'_4 = 4.0380, \end{aligned} \quad (50)$$

where λ' is related to λ in Table I by (32). These momentum space results do not agree with the position-space computations in the literature [9] and additional repeated attempts to get convergence in position space have failed [8]. It was concluded in Ref. [8] that "the previous position space calculation [9] was inaccurate, due to the slow, logarithmic behavior of the potential... The momentum space calculation is much more rapidly convergent."

TABLE I
First five eigenvalues for l ranging from 0 to 4.

	$l = 0$	$l = 1$	$l = 2$	$l = 3$	$l = 4$
λ_0	0.52643626	1.3861862	1.8443720	2.1578468	2.3962798
λ_1	1.6619365	2.0094748	2.2758614	2.4881158	2.6638815
λ_2	2.1870578	2.3943387	2.5800522	2.7390550	2.8772701
λ_3	2.5153639	2.6726676	2.8144703	2.9409664	3.0543788
λ_4	2.7677810	2.8906069	3.0049630	3.1096821	3.3373990

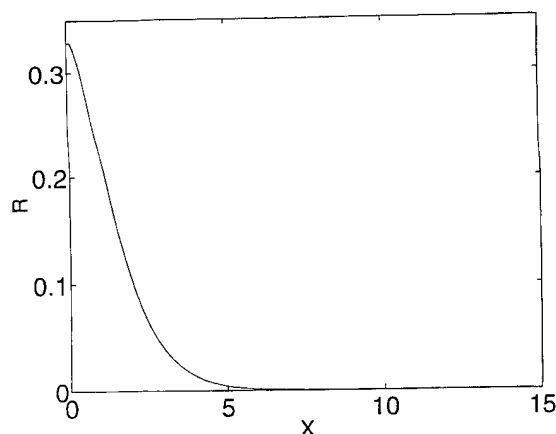


FIGURE 1. Plot of normalized function $R_{0,0}(x)$ for $l = 0$ and $\lambda'_0 = 1.7968$.

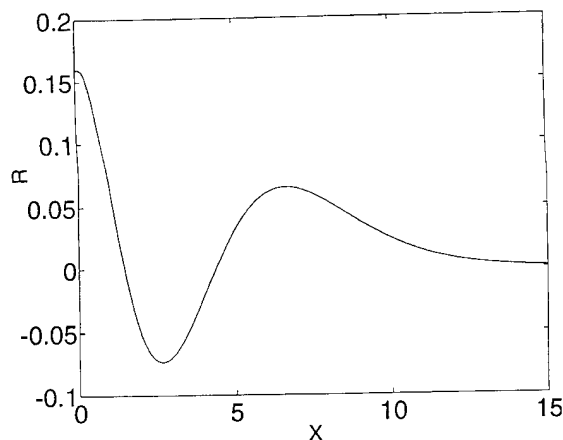


FIGURE 3. Plot of normalized function $R_{2,0}(x)$ for $l = 0$ and $\lambda'_2 = 3.4574$.

On the other hand, if we use (32) to convert the first column of Table I to the parameterization used in Ref. [7] we see that

$$\lambda'_0 = 1.7967991, \quad \lambda'_1 = 2.9322993, \quad \lambda'_2 = 3.4574206, \\ \lambda'_3 = 3.7857268, \quad \lambda'_4 = 4.0381439. \quad (51)$$

These values are in very good agreement with (50), they converge faster, and they are more accurate. Note further that the eigenvalues for $l \neq 0$ are actually in good agreement with the previously reported position space results [9]. (The momentum space calculations in [8] were not carried out for $l \neq 0$.) This leads us to conclude that the slow convergence of the previous position space results

was not due to the slow logarithmic behavior of the potential; rather, it was due to a minor instability caused by the sign-flip of the "centrifugal" part of the potential when $l = 0$.

As promised, it is now very easy to use (42) along with (33) to compute any eigenfunction; these eigenfunctions are easily normalized through the use of the Sinc quadrature result (44). As a representative sample, in Figures 1 to 3 we display the first three normalized eigenfunctions for $l = 0$; note that the number of bumps increases incrementally as we go from $n = 0$ to $n = 2$. Figures 4 to 6 show the first three normalized eigenfunctions for $l = 4$; note that the "centrifugal" barrier causes the bumps to move away from the center, relative to the $l = 0$ plots.

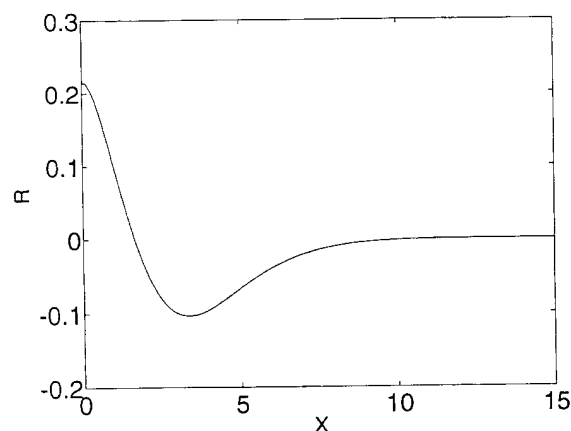


FIGURE 2. Plot of normalized function $R_{1,0}(x)$ for $l = 0$ and $\lambda'_1 = 2.9323$.

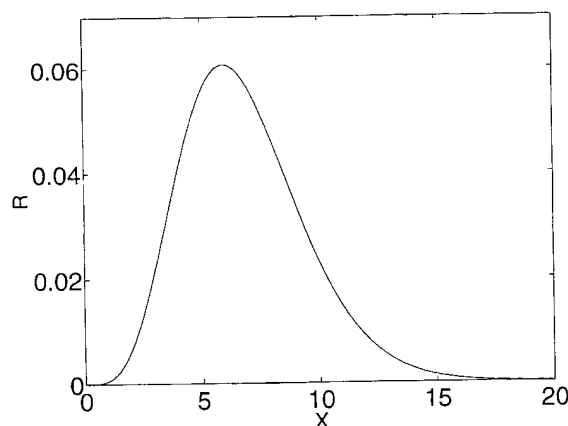


FIGURE 4. Plot of normalized function $R_{0,4}(x)$ for $l = 4$ and $\lambda'_0 = 3.6666$.

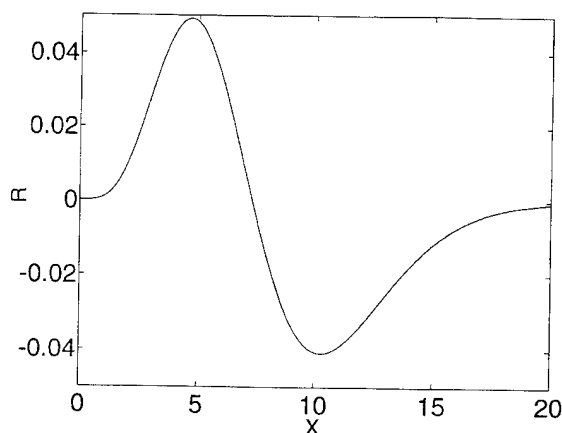


FIGURE 5. Plot of normalized function $R_{1,4}(x)$ for $l = 4$ and $\lambda_1 = 3.9342$.

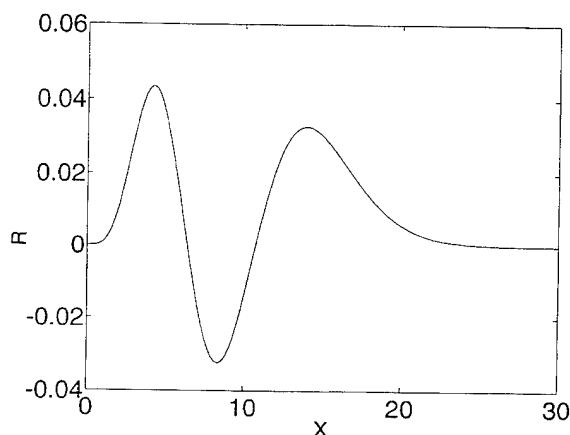


FIGURE 6. Plot of normalized function $R_{2,4}(x)$ for $l = 4$ and $\lambda_2 = 4.1476$.

Conclusion

We have introduced a Dirac bra-ket formulation of the Sinc basis along with an important completeness relation. It is now straightforward to incorporate a Sinc-function representation into any problem which is posed in a second-quantized format such as the light-cone Hamiltonian. Fur-

thermore, we have explicitly demonstrated that Sinc methods provide a very powerful tool for solving the radial Coulomb Schrödinger equation in $d = 2 + 1$. These methods are very accurate and converge very fast. This point is strongly demonstrated by the fact that convergence for the $l = 0$ values could not be attained in position space by other well-known numerical techniques. It is our hope that Sinc methods will be found useful in attacking many other nonperturbative problems in quantum chemistry, condensed matter physics, and related disciplines.

ACKNOWLEDGMENTS

One of us (V.G.K.) gratefully acknowledges professor Frank Stenger for many helpful consultations. This work was supported in part by the Office of Naval Research, contact N0014-93-1-0196.

References

1. F. Stenger, *Numerical Methods Based on Sinc and Analytic Functions*, (Springer-Verlag, New York, 1993).
2. V. G. Koures, *J. of Comp. Physics* **127**, in press.
3. V. G. Koures and F. E. Harris, *Int. J. of Quantum Chem. QCS* **29**, 277 (1995).
4. M. Kaluža and H.-C. Pauli, *Phys. Rev. D* **45**, 2968 (1992); M. Krautgärtner, H.-C. Pauli, and F. Wölz, *Phys. Rev. D* **45**, 3755 (1992).
5. J. Sapirstein in *From Actions to Answers: Proceedings of the 1989 Advanced Study Institute in Elementary Particle Physics*, T. DeGrand and D. Tousaint, Eds. (World-Scientific, Singapore, 1990), p. 655.
6. P. A. M. Dirac, *The Principles of Quantum Mechanics*, 4th ed., sec. 6 (Oxford, New York, 1958); L. I. Schiff, *Quantum Mechanics*, 3rd ed., (McGraw-Hill, New York, 1968), p. 164; J. J. Sakurai, *Modern Quantum Mechanics*, 1st ed., Ch. 1 (Benjamin/Cummings, Menlo Park, CA, 1985).
7. V. G. Koures, quant-ph/9510006, University of Utah preprint UTAH-IDR-CP-05, 1995.
8. A. Tam, C. J. Hamer, and C. M. Yung, *J. Phys. G* **21**, 1463 (1995).
9. C. M. Yung and C. J. Hamer, *Phys. Rev. D* **44**, 2595 (1991).
10. John Little and Cleve Moller, *MATLAB User's Guide* (Mathworks, Inc., Natick, MA, 1993).

On Approximating Electron Repulsion Integrals with Linear Combination of Atomic-Electron Distributions

SEIICHIRO TEN-NO* AND SUEHIRO IWATA

Institute for Molecular Science, Myodaiji, Okazaki, Aichi 444 Japan; e-mail for S.T: tenno@ims.ac.jp

Received February 24, 1996; revised manuscript received April 30, 1996; accepted May 2, 1996

ABSTRACT

We recently investigated some features of atomic-electron distributions which are products of atomic orbitals without linear redundancies. Then, the atomic-electron distributions were employed as expansion functions of molecular charge distributions in the three-center expansion method for electron repulsion integrals. It turned out that the method is very accurate even after substantial reductions of required integrals. We shall illustrate the method and discuss its applicability to many electron theories. © 1996 John Wiley & Sons, Inc.

Introduction

The fundamental scaling properties in many types of ab initio electronic structure calculations are governed by generating and manipulating electron repulsion integrals (ERIs),

$$(ab | cd) = \int d\mathbf{r}_1 d\mathbf{r}_2 \chi_a(d\mathbf{r}_1) \chi_b(d\mathbf{r}_1) r_{12}^{-1} \chi_c(d\mathbf{r}_2) \chi_d(d\mathbf{r}_2). \quad (1)$$

In spite of a great deal of effort toward theoretical and algorithmic developments coupled with increasingly faster electronic computers, the tractable

quality of a wave function is strongly limited with respect to the size of molecules and the quality of basis functions. To overcome this obstacle, there has been a recent resurgence of attempting to approximate ERIs. The pseudospectral approach developed by Friesner and co-workers [1] chooses a spatial grid and transforms basis set and spatial grid representations. This approach scales as $N^2 M_g$ in the context of the Hartree-Fock approximation and $n^2 N_v^2 M_g$ in the localized formulation of Møller-Plesset perturbation theory (LMP2) [2], where N , n , and M_g are numbers of basis functions, occupied orbitals, and grid, respectively, and N_v is fixed virtual space size.

Alternative ways to approximate ERIs employ model distributions to represent products over basis functions, and the resolution identity (RI) over model distributions is substituted into the expres-

*To whom correspondence should be addressed.

sion of ERIs [3]. Some of these approaches are based on the similar ideas used for approximating direct coulombic energy in the linear combination of atomic orbital (LCAO) $X\alpha$ method [4, 5], and charge and transition densities of molecules are expanded into model distributions of auxiliary basis functions. Although these methods gave almost satisfactory results, the optimal ways to generate expansion basis functions were not well-addressed.

Most recently, we focused our attention upon atomic-electron distributions [6, 7], in which all of the linear redundancies of orbital products are removed, and approximated molecular charge distributions with linear combination of atomic-electron distributions (LCAD). The LCAD approximation has following features:

1. Neither independent sets of auxiliary functions nor numerical parameters are needed in approximating ERIs.
2. The number of atomic-electron distributions grows almost linearly not only with respect to the size of molecules but also to the quality of basis functions.
3. The approximation is very accurate since no error occurs in the intra-atomic distributions, and the accuracy is systematically improved according to the quality of basis set used.

The present study will show how this approach can be used to provide particularly convenient procedures for the wave functions of molecules and what new aspects are possible to enhance the electronic structure theory within the method. We shall give a brief review of the method and then explore new possibilities to the many-electron theory, focusing our attention on a multiconfiguration self-consistent field (MCSCF) procedure, where orbital Hessian is not explicitly set up, and direct configuration interaction (CI) methods.

RI-LCAD method

The notion to employ auxiliary functions to reexpand the $\chi_a(\mathbf{r})\chi_b(\mathbf{r})$ distributions is not quite new. In these methods, the auxiliary functions are usually chosen to be proportional to N , N being the number of LCAO basis functions. In the Roothaan-type expansion, the required rank of distributions should be much smaller than $N(N+1)/2$ for large N , since the convergence of distribu-

tions is doubly faster than that of molecular basis functions. Several approximations are conceivable with a given set of auxiliary functions [3]. Vahtas et al. [8] investigated Hartree-Fock energies of different approximations based on RI or the spectral resolution,

$$(ab|cd) \cong \sum_{\kappa} (ab|\kappa)C_{\kappa}^{cd}, \quad (2)$$

or

$$(ab|cd) \cong \sum_{\kappa\lambda} C_{\kappa}^{ab}(\kappa|\lambda)C_{\lambda}^{cd}, \quad (3)$$

where κ, λ, \dots , denote auxiliary functions. The expansion coefficients are determined locally,

$$C_{\kappa}^{ab} = \sum_{\lambda} (\mathbf{S}^{-1})_{\kappa\lambda}(ab\lambda), \quad (4)$$

or nonlocally,

$$C_{\kappa}^{ab} = \sum_{\lambda} (\mathbf{V}^{-1})_{\kappa\lambda}(ab|\lambda), \quad (5)$$

where $(ab\lambda)$ and $S_{\kappa\lambda}$ are three- and two-center overlap integrals, and $(ab|\lambda)$ and $V_{\kappa\lambda} = (\kappa|\lambda)$ are three- and two-center ERIs. The use of nonlocally determined coefficients leads to the same expression of Eq. (2) and (3). For the approximation of ERIs in the LCAO $X\alpha$ and Hartree-Fock calculations [4, 8], the authors concluded that the nonlocally determined coefficients (5) give results superior to a locally determined one (4), since Eq. (5) can be obtained by minimizing the self-repulsion of the residual. In order to realize the computational efficiency and the reduction in disk storage requirement of decomposed quantities in Eqs. (2) or (3), the approximate ERIs are rewritten as,

$$(ab|cd) \cong \sum_{\bar{\kappa}} (ab|\bar{\kappa})[\bar{\kappa}|cd], \quad (6)$$

where

$$(ab|\bar{\kappa}) = \sum_{\kappa} (\mathbf{V}^{-1/2})_{\bar{\kappa}\kappa}(ab|\kappa). \quad (7)$$

This expression is used in the CCSD(T) (singles and doubles coupled-cluster plus a perturbational estimate of the effects of connected triple excitations) models [9] to avoid the input/output (I/O) and storage bottlenecks. In the RI-MP2 [10] and the coupled-cluster methods with approximate integrals, the scaling properties of the calculations are hardly improved, viz. $O(n^2N^2m)$ and $O(n^2N^4)$, m being the number of auxiliary functions, since they explicitly form four-indexed integrals from

three-indexed integrals. Since the usual *ab initio* methods are based on the four-indexed ERIs, additional research is needed to explore optimal ways to use three-indexed integrals. However, the computational effort shifts from I/O to matrix multiplications, which can be handled more efficiently than I/O. We also employ the same expression (6) and (7) in the approximate second-order MCSCF procedure [6, 7], but the three-indexed integrals are used as much as possible in place of the four-indexed integrals. In this case, the most time-consuming part of the molecular orbital (MO) integral transformation step is much more improved and maximum a factor of 8.4 speedup is attained for one MCSCF iteration [7].

The choice of auxiliary functions is apparently dominant over the quality of three-center approximation. Previous researchers tried to construct an independent auxiliary set as compact as possible. Some of them used an even-tempered set and obtained accurate self-consistent field (SCF) energies [8]. However, no systematic contraction scheme has been proposed. Although auxiliary sets have also been used to approximate coulombic potentials in the density functional theory, preliminary experience suggests that the exchange interactions are more complicated than the direct coulombic one. So such expansion sets are not necessarily transferable to the general two-electron interactions. Furthermore, an optimal choice should require one-to-one correspondence of the auxiliary basis sets with a given molecular basis set which varies with the purpose. For these reasons, we have fallen back on the idea of using atomic-electron distributions (ADs) consisting of each atomic basis set,

$$\chi_a(\mathbf{r})\chi_b(\mathbf{r}) \cong \sum_{cc'}^{\text{intra}} c_{cc'}^{ab} \chi_c(\mathbf{r})\chi_{c'}(\mathbf{r}), \quad (8)$$

where the summation runs over intra-atomic distributions. In each set of atomic-electron distributions, they include two different kinds of linear dependencies, viz. the angular and coulombic redundancies (AR and CR) [6, 7]. It should be noted that atomic blocks are dominant in the matrix **V**. Both of the redundancies can be efficiently removed, since we can use full symmetry of each atom, which is independent from the shape of molecules to be calculated. Numerical results indicate that ADs grow proportionally not only with the size of molecules but also with the quality of basis functions, if AR and CR are removed. We

call the RI method plugged into ADs, where the charge distributions are reexpressed by linear combinations of ADs, the RI-LCAD, or simply LCAD approximation. The accuracies of the RI-LCAD are automatically and systematically improved by extending the set of basis functions. Our previous calculations suggest that typical errors of the approximation for molecules consisting of first row atoms are a few $10\mu E_h$ with *d* functions (*g*-ADs) and less than $1\mu E_h$ with *f* functions (*i*-ADs) [7]. To our knowledge, the present LCAD is the most accurate way to approximate ERIs.

MCSCF Method without Setting up Orbital Hessian

We combined the RI-LCAD method with the approximate second-order MCSCF method [6, 7]. Since the MCSCF methods include CI and orbital optimization, the time-consuming steps are strongly dependent on the number of basis functions and the size of CI expansion. We therefore shall not give general inspections on the MCSCF method in this section but focus our attention upon the orbital improvement within the framework of second-order MCSCF theory. Direct CI method combined with the RI-LCAD approximation, which bear some resemblance to the direct MCSCF method, will be given in the next section. For a large majority of MCSCF calculations, the most time-consuming step is the integral transformation required in each MCSCF iteration. It is the most apparent that integral transformation time can be much reduced in the three-center approximation, since the total number of ERIs is much less than that of full integrals. In this case, the integrals transformation is efficiently achieved without difficulty using a code for similarity transformations of symmetric matrices. So if the transformed (three-indexed) integrals can be used in the remaining steps as efficiently as those of four-indexed, the MCSCF method will be more enhanced by the three-center expansion.

In the second-order MCSCF method, solving the Newton-Raphson linear equations in each iteration commonly reduces to an iterative procedure, where the Hessian is multiplied by a trial vector and a sequence of vectors is built [11, 12]. Usually, the number of active orbitals *n* is much smaller than the entire part *N*, and the linear equations are solved quickly in comparison with the integrals transformation step. We therefore set up the or-

bital Hessian matrix explicitly in the approximate second-order MCSCF method with RI-LCAD [6, 7]. There coarse quantities of ERIs are accumulated into Hessian, and four-indexed integrals are not generated explicitly for the gradient and the coulombic-like part of the Hessian,

$$\sum_{\bar{\kappa}=1}^{m(\nu_c)} d_{ij}^{\bar{\kappa}}(ab|\bar{\kappa}) \quad (9)$$

and

$$d_{ij}^{\bar{\kappa}} = \sum_{kl} \Gamma_{ijkl}(kl|\bar{\kappa}), \quad (10)$$

where i, j, k, \dots , and a, b, c, \dots , refer to occupied and virtual orbitals, respectively, Γ denotes two-particle reduced density matrix, and ν_c is a coarse threshold of two-electron contributions to the Hessian. Our previous experience suggests that employing the coarse threshold efficiently simplifies the evaluation of Hessian without any loss of convergence [7]. It is, however, not completely resolved to generate four-indexed integrals for the exchange-like contributions, and this step and the step in Eq. (9) scale as $n^2 N^2 m(\nu_c)$, where $m(\nu_c)$ is a number of distributions within the coarse threshold. One can expend a nontrivial amount of computational effort in these steps, if the active space becomes large both in the LCAD and the usual algorithms.

We can proceed with an alternative method to solve linear equations, where the update vectors are evaluated directly from the elements of the Hessian matrix. Instead of using four-indexed coulombic-like and exchange-like operators, whose one index is transformed to be a restricted one, the basic contributions can be written in the forms:

$$\sum_{\bar{\kappa}=1}^{m(\nu_c)} \sum_j d_{ij}^{\bar{\kappa}} L_{aj}^{\bar{\kappa}} \quad (11)$$

and

$$\sum_{\bar{\kappa}=1}^{m(\nu_c)} \sum_j e_{ij}^{\bar{\kappa}}(aj|\bar{\kappa}), \quad (12)$$

where L denotes three-indexed operator, one index of which is transformed by an arbitrary vector,

$$L_{aj}^{\bar{\kappa}} = \sum_b (ab|\bar{\kappa}) R_{jb} \quad (13)$$

and

$$e_{ij}^{\bar{\kappa}} = \sum_{kl} \Gamma_{ijkl} L_{kl}^{\bar{\kappa}}. \quad (14)$$

The above procedure scales at most $nN^2 m(\nu_c)$, and it is more independent of the size of the active orbitals than setting up Hessian explicitly. So it would be most efficient in the restricted active space (RAS) SCF. It should be noted that the present algorithm is entirely based on the three-indexed integrals, in which four-indexed quantities do not appear. The operations in the entire part consist of simple linear algebra, and we can expect that the method with LCAD approximation can handle many degrees of orbital rotations. The Newton-Raphson procedure requires that the starting orbitals be in a local region close to the global minimum, and it is very stable in such region. However, if one starts from ill-conditioned orbitals, there is no way to attain the global convergence with information of first- and second-order derivatives since the energy function includes infinite-order terms with respect to the antisymmetric exponent \mathbf{R} in the unitary matrix. Werner and Meyer [13, 14] have introduced a method in which the energy is expanded through second order in $\mathbf{T}(\mathbf{R}) = e^{\mathbf{R}} - 1$ and the method is more reliable than the Newton-Raphson procedure. Since the microiteration requires one-index transformation, it is as cheap as the update scheme in the Newton-Raphson procedure. We note that the above mentioned procedure employing three-indexed integrals is applicable to the method with an entirely parallel argument.

Slater Determinant-Based Direct CI Method

The CI method is one of the most popular tools to treat electron correlation effects of ground and excited states. When we use the direct CI algorithm where the Davidson scheme is used, the time-consuming step is the evaluation of σ of the two-electronic part:

$$\sigma_l = \sum_{ijkl} (ij|kl) \sum_J \langle I | \hat{E}_{ij} \hat{E}_{kl} | J \rangle c_J, \quad (15)$$

where \mathbf{c} is a trial vector and \hat{E}_{ij} are generators of unitary group. Siegbahn [15, 16] proposed an algorithm for full CI calculations, which can make good use of pipeline computers, introducing the

resolution of the identity over CSFs,

$$\langle I | \hat{E}_{ij} \hat{E}_{kl} | J \rangle = \sum_K \langle I | \hat{E}_{ij} | K \rangle \langle K | \hat{E}_{kl} | J \rangle. \quad (16)$$

Then the evaluation of σ in Eq. (15) can be written as follows, with, loop over K :

$$\sigma_I = \sum_{ij} \gamma_{ij}^{IK} E_{ij}^K, \quad (17)$$

where γ_{ij}^{IK} are one-electron coupling coefficients,

$$\gamma_{ij}^{IK} = \langle I | \hat{E}_{ij} | K \rangle, \quad (18)$$

whose matrix elements over Gelfand states are ordinarily calculated in the graphical unitary group approach [17, 18], and

$$E_{ij}^K = \sum_{kl} (ij | kl) D_{kl}^K, \quad (19)$$

$$D_{kl}^K = \sum_J \gamma_{ij}^{KJ} c_J. \quad (20)$$

Although this method turns out to be computationally efficient, there remains a demand on I/O facilities for the one-electron formula tape. Abandoning the use of CSFs, Knowles and Handy [19] extended Siegbahn's idea to the use of simple Slater determinants. Although there are two or three times as many determinants as CSFs in a CI expansion and accordingly the matrix multiplication in Eq. (19) increases, the treatment of the coupling coefficients is much more simplified.

We can expect that the RI-LCAD method provides an efficient alternative to the Slater determinant CI illustrated above. In the three-center expansion, the part of Hamiltonian including two-electron generators can be expanded into a combination of square of one-electron operators,

$$\sum_{ijkl} \hat{E}_{ij} \hat{E}_{kl} (ij | kl) \equiv \sum_{\bar{\kappa}} \hat{O}_{\bar{\kappa}}^2, \quad (21)$$

where

$$\hat{O}_{\bar{\kappa}} = \sum_{ij} \hat{E}_{ij} (ij | \bar{\kappa}). \quad (22)$$

Accordingly, the major matrix multiplication step in Eq. (19) can be rewritten

$$E_{ij}^K = \sum_{\bar{\kappa}} (ij | \bar{\kappa}) D_{\bar{\kappa}}^K \quad (23)$$

and

$$D_{\bar{\kappa}}^K = \sum_J \langle K | \hat{O}_{\bar{\kappa}} | J \rangle c_J. \quad (24)$$

Then the scaling property in Eq. (19) changes from n^2 to m , asymptotically. However, since the size of full CI grows rapidly with the numbers of electrons and orbitals, it is usual that a set of basis functions are chosen as active. The original algorithm is also designed with the problem of the complete active space (CAS) SCF method in mind [19], where the square of n often becomes smaller than m . Thinking from a different point of view, we shall explore the possibility of restricted CI algorithms with the Slater determinant-based method.

The problem to be solved here is a CI calculation of a single reference in which the excitation is limited to be X . The most obvious difficulty of introducing intermediate states is that they must span extra spin states which at least interact through the operators \hat{E}_{ai} . We can divide the linear contributions to σ into two parts, viz. intermediate states are within or out of the range of the CI expansion space:

$$\left[\sum_{Y \leq X} \langle I | \hat{O}_{\bar{\kappa}} | Y \rangle \langle Y | \hat{O}_{\bar{\kappa}} | J \rangle \right] + \langle I | \hat{O}_{\bar{\kappa}} | X+1 \rangle \langle X+1 | \hat{O}_{\bar{\kappa}} | J \rangle, \quad (25)$$

where we used abbreviated notation for the summation over intermediates and $\bar{\kappa}$. The size of intermediates out of the CI space makes the calculation wasteful. It is also possible to classify the second contributions into three parts; namely the rank of orbital difference is 2, 1, or 0. For rank = 2, we can rewrite it to σ by introducing $X-1$ electron excited states as; loop over $(X-1)$ and $\bar{\kappa}$;

$$\begin{aligned} & \langle I | \hat{O}_{\bar{\kappa}} | X+1 \rangle \sum_J \langle X+1 | \hat{O}_{\bar{\kappa}} | J \rangle c_J \\ &= A_{I\bar{\kappa}}^{ai, (X-1)} \sum_{bj} A_{j\bar{\kappa}}^{bj, (X-1)} c_J \\ &\quad - A_{I\bar{\kappa}}^{ai, (X-1)} \sum_j A_{j\bar{\kappa}}^{aj, (X-1)} c_J \\ &\quad - A_{I\bar{\kappa}}^{ai, (X-1)} \sum_b A_{j\bar{\kappa}}^{bi, (X-1)} c_J \\ &\quad + c_I (ai | \bar{\kappa})^2, \end{aligned} \quad (26)$$

where a and i indicate created and annihilated orbitals to form a state I from a state belonging to

$X - 1$, and

$$A_{i\bar{k}}^{ai,(X-1)} = \langle I | \hat{E}_{ai} (X - 1) \rangle (ai | \bar{k}]. \quad (27)$$

In the RI-LCAD method, the main contributions therefore can be expressed as a sum of products in each excited state of $X - 1$ and \bar{k} . This expression is no more wasteful and similar convenience can be provided for rank = 0, 1 as well. The present method is restricted within the single reference CI calculation. However, even in the multireference case, we believe that efficient code can be generated based on the RI-LCAD method with a technique similar to the one introduced here.

Conclusion

We have illustrated MCSCF and direct CI methods incorporating the RI-LCAD approximation. In both methods, new ideas are proposed to avoid explicitly setting up four-indexed integrals. These methods therefore enable us to handle smaller size of data and lead to new aspects in the ab initio methods for large molecular systems. Our experience suggests that the LCAD approximation is very accurate not only in the single-determinant wave function but also in the large-scale CI calculations, unless one uses an extremely poor basis set. It should be emphasized that we do not think the entire part of the ab initio method can be improved by adopting three-center expansion. For instance, the SCF or energy part of the MP2 method scales as fourth power of the size of molecules. It is always necessary to transform an index in the three-center expansion and it also scales as N^4 . However, the bottleneck of the computation shifts from the necessity to handle a large number of data to the algebraic manipulations of matrices. So the three-center expansion would be much more suited on parallel computers.

ACKNOWLEDGMENTS

This work is partly supported by the Grant-in-Aids for the Priority Area (No. 04243102) by the Ministry of Education, Science, Sports and Culture, Japan.

References

1. B. H. Greeley, T. V. Russo, D. T. Mainz, R. A. Friesner, J.-M. Langlois, W. A. Goddard III, R. E. Donnelly, Jr. and M. N. Ringnalda, *J. Chem. Phys.* **101**, 4028 (1994), and the references therein.
2. R. B. Murphy, M. D. Beachy, R. A. Friesner, and M. N. Ringnalda, *J. Chem. Phys.* **103**, 1481 (1995).
3. J. Almlöf, in *Modern Electronic Structure Theory Part I*, D. R. Yarkony, Ed. (World Scientific, Singapore, 1995), and references therein.
4. B. I. Dunlap, J. W. D. Connolly, and J. R. Sabin, *J. Chem. Phys.* **71**, 3396 (1979).
5. B. I. Dunlap, J. W. D. Connolly, and J. R. Sabin, *J. Chem. Phys.* **71**, 4993 (1979).
6. S. Ten-no and S. Iwata, *Chem. Phys. Lett.* **240**, 578 (1995).
7. S. Ten-no and S. Iwata, *J. Chem. Phys.*, in press.
8. O. Vahtras, J. Almlöf, and M. W. Feyereisen, *Chem. Phys. Lett.* **213**, 514 (1993).
9. A. P. Rendell and T. J. Lee, *J. Chem. Phys.* **101**, 400 (1994).
10. M. Feyereisen, G. Fitzgerald, and A. Komornicki, *Chem. Phys. Lett.* **208**, 359 (1993).
11. B. H. Lengsfeld III, *J. Chem. Phys.* **77**, 4073 (1982).
12. J. Olsen, D. L. Yeager, and P. Jørgensen, *Adv. Chem. Phys.* **54**, 1 (1983) and the references therein.
13. H.-J. Werner and W. Meyer, *J. Chem. Phys.* **73**, 2342 (1980).
14. H.-J. Werner, *Adv. Chem. Phys.* **69**, 1 (1987).
15. P. E. M. Siegbahn, *Chem. Phys. Lett.* **109**, 417 (1984).
16. P. E. M. Siegbahn, in *Lecture Notes in Quantum Chemistry, European Summer School in Quantum Chemistry*, B. O. Roos Ed. (Springer-Verlag, Berlin, 1992).
17. I. Shavitt, *Int. J. Quantum Chem. Symp.* **12**, 5 (1978).
18. B. Brooks and H. F. Schaefer III, *J. Chem. Phys.* **70**, 5092 (1979); B. Brooks, W. Laidig, P. Saxe, N. Handy, and H. F. Schaefer III, *Phys. Scripta* **21**, 312 (1980).
19. P. J. Knowles and N. C. Handy, *Chem. Phys. Lett.* **111**, 315 (1984).

Multireference Basis-Set Reduction

WOLFGANG WENZEL*

*Department of Physics, Dortmund University, D-44221 Dortmund, Germany
e-mail: wenzel@cip.physik.uni-dortmund.de*

MATTHEW M. STEINER AND KENNETH G. WILSON

Department of Physics, Ohio State University, Columbus, Ohio 43210-1106

Received February 26, 1996; revised manuscript received April 17, 1996; accepted April 25, 1996

ABSTRACT

We review "Hilbert space basis-set reduction" (BSR) as an approach to reduce the computational effort of accurate correlation calculations for large basis sets. We partition the single-particle basis into a small "internal" and a large "external" set. We use the MRCI method for the calculation for that part of configuration space in which only internal orbitals are occupied and perturbatively correct for the remaining configurations using a method similar to Shavitt's B_k method. The present implementation approximates the MRCI result for the unpartitioned basis set, with a significantly reduced computational effort. To demonstrate the viability of the method, we present results for selected states of small molecules (Be_2 , CH_2 , O_3). For the examples investigated, we find that relative energy differences can be reproduced to an accuracy of approximately 1 kcal/mol with a significant computational saving. © 1996 John Wiley & Sons, Inc.

Introduction

In recent years a number of attempts have been made to introduce approximations for the treatment of dynamical correlation effects within the framework of the established methodology of accurate ab initio methods in quantum chemistry. The impetus for such developments stems from the unfavorable scaling of the correlation energy

with the basis-set size, which arises when the many-body wave function is expanded in terms of Slater determinants. Consequently, methods have been proposed to improve either the wave function, e.g. through the introduction of explicit electron-electron cusps [1], or to formulate an effective Hamiltonian [2, 3] to reduce the size of the basis set which must be treated within the established methodology. The latter approach benefits from the realization that perturbative methods cope adequately with the treatment of purely dynamical correlation effects. Additionally there are a number of comprehensive multireference perturbation

*To whom correspondence should be addressed.

theory approaches [4–6] which account for both dynamical and nondynamical correlations effects.

One common objective of such treatments is an adequate description of electronic fluctuations for a zeroth-order wave function which is more complex than the single-determinant closed-shell Hartree–Fock function. It is well known that the systematic approximation of the electronic fluctuations requires the use of a hierarchical sequence of basis sets of increasing size [7]. For nonperturbative methods this increase quickly leads to a prohibitive computational cost even for molecules of moderate size. The underlying assumption for the development of multireference perturbation methods is the existence of an orbital hierarchy, so that only a small subset of the orbitals is occupied in the zeroth-order wave function. This observation suggests a partition of the orbitals basis into two subsets: a small “internal” subset required for the construction of the zeroth-order wave function and a larger “external” one for the treatment of dynamical electronic fluctuations [3].

Introducing projectors P and $Q = 1 - P$ for the internal and external many-body space, respectively, an effective Hamiltonian [2] for the internal many-body space can be written as

$$H_{\text{eff}} = PHP + PHQ(E - QHQ)^{-1}QHP, \quad (1)$$

where the inversion of the many-body operator $(E - QHQ)$ generates a perturbation expansion. Given such an effective Hamiltonian, the internal wave function $\Psi_i = P\Psi$ can be generated by an established method using only the small subset of internal configurations and then expanded to yield the full wave function through the wave operator:

$$\Psi = [1 + (E - QHQ)^{-1}] \Psi_i, \quad (2)$$

which recovers all fluctuation effects implicit in the effective Hamiltonian.

A scaling analysis in the orbital momentum k demonstrates that only terms in lowest-order perturbation theory to Eq. (1) yield corrections of order k^{-2} to the correlation energy, justifying a termination of the perturbation expansion at that level. Unfortunately, in addition to one-particle and two-particle terms, this approach generates a three-particle interaction in the effective Hamiltonian. The corrections arising from the three-particle interaction are of equal importance as those of the two-particle terms. As Wang and Freed observed early on, an omission of this interaction

expansion seriously affects the quality of the approximation [8]. Its treatment, on the other hand, necessitates a computational effort which tends to overwhelm the possible savings gained by this approach.

Description of the Method

Based on these observations, we previously developed a formalism [9] which avoids the explicit introduction of the effective Hamiltonian in favor of a configuration-based approach similar to Shavitt's B_k method [6]. Using an orbital partitioning, we divide the many-body state vector Ψ into an internal and an external part: $\Psi_i = P\Psi$ and $\Psi_x = (1 - P)\Psi$. The internal wave function will be treated with the MRCI method. We do not require the knowledge of the effective Hamiltonian, but only the internal components of the many-body field $\Omega = H\Psi$. These arise from the coupling to both the internal and the external wave function:

$$\Omega_i = P(H\Psi_i + H\Psi_x). \quad (3)$$

The approximate evaluation of the second term in the many-body field corresponds to the implicit evaluation of the second term in the effective Hamiltonian in Eq. (1). In the following we develop a formalism to compute this contribution approximately, a method we refer to as Hilbert space basis-set reduction (BSR).

As noted above, lowest-order perturbation theory captures the most important contributions to the correlation energy. The truncation of the perturbation expansion at this level decouples the external configurations from one another. Therefore we can determine approximate coefficients α_x for the each of the external configurations ϕ_x independently and their contribution to the effective internal field as $\alpha_x H\phi_x$. In determining α_x we go beyond perturbation theory in a fashion which avoids the intruder state problem: for each external configuration we diagonalize the Hamiltonian in the Hilbert space spanned by ϕ_x and the internal wave function Ψ_i , i.e., we solve the eigenvalue problem

$$\begin{pmatrix} \langle \Psi_i | H | \Psi_i \rangle & \langle \Psi_i | H | \phi_x \rangle \\ \langle \phi_x | H | \Psi_i \rangle & \langle \phi_x | H | \phi_x \rangle \end{pmatrix} \begin{pmatrix} 1 \\ \alpha_x \end{pmatrix} = \epsilon_x \begin{pmatrix} 1 \\ \alpha_x \end{pmatrix}. \quad (4)$$

We note that a substitution of the full many-body wave function Ψ for Ψ_i and accounting for

nonorthogonality would yield the exact coefficient for α_x [10]. An expansion in the energy difference $[\langle \Psi_i | H | \Psi_i \rangle - \langle \phi_x | H | \phi_x \rangle]^{-1}$ recovers *all lowest-order terms* in the effective Hamiltonian of Eq. (1), including the crucial three-particle contribution. The sum of the individual energy contributions of all the external configurations is a perturbative estimate of the external energy contribution,

$$\Delta E = \sum_x (\epsilon_x - E_i), \quad (5)$$

where E_i is the energy of the internal wave function. The lowest-order expansion ΔE yields the A_k energy. A similar approach, DCPT2, has recently been introduced as an alternative to MP2 [11].

As the first step in the calculation we omit any external contributions to Ω_i and converge the MRCI wave function in the internal space, yielding a zeroth-order approximation to the internal state $\Psi_i^{(0)}$. For each external configuration, this state is substituted into Eq. (4) and we obtain a first approximation for the external state,

$$\Psi_x^{(1)} = \sum \alpha_x^{(1)} \phi_x, \quad (6)$$

which is used to compute the first correction to the internal many-body field, $\Omega_{ix}^{(1)} = PH\Psi_x^{(1)}$. We then reconverge the internal calculation in the presence of this field, completing conceptually one iteration of the single-state B_k method, arriving at a corrected internal state $\Psi_i^{(1)}$. The energy of this wave function is given as

$$E_{\text{BSR}} = \frac{\langle \Psi_i^{(1)} | H | \Psi_i^{(1)} \rangle + (\langle \Psi_i^{(1)} | \Omega_{ix}^{(1)} \rangle + \text{h.c.}) + E_x}{\langle \Psi_i^{(1)} | \Psi_i^{(1)} \rangle + N_x}, \quad (7)$$

which accounts for the relaxation of the internal wave function in the presence of the field generated by the external configurations. In the expression for the BSR energy we have introduced

$$E_x = \sum_x \alpha_x^2 \langle \phi_x | H | \phi_x \rangle \quad (8)$$

and

$$N_x = \sum_x \alpha_x^2 \quad (9)$$

for the purely external contributions to energy and norm. The most serious error of this approximation arises from the decoupling of the external configurations, which, on the other hand, is re-

sponsible for the significant reduction of the computational effort of this method. We note that the energy in Eq. (7) is not invariant under unitary transformations of the external orbitals. The effort scales as the second power of the number of external orbitals, compared to a fourth-power dependence for the equivalent MRCI.

Results

The underlying hypothesis for the introduction of this method is that it is possible to separate out a sufficiently large part of the basis for an approximate treatment without the introduction of serious differential errors in the potential energy surface. In the following we present a comparison between MRCI/FCI and BSR energies for three small molecules, Be_2 , CH_2 , and O_3 . These molecules were chosen because the treatment of dynamical and nondynamical correlation effects in each example presents a significant challenge to the method.

Be_2 is among the prototypical examples of a molecule which requires an accurate treatment of both dynamical and nondynamical correlation effects in a large basis set and has been widely studied for that reason. A section of the FCI ground-state potential energy surface in a large basis [12] is shown as the long-dashed line in Figure 1. The minimum of the potential energy surface (PES) is found at $r_e = 4.78$ a.u. in good agreement with an experimental value of $r_e = 4.72$ a.u. [13]. If we reduce the basis set for another FCI, calculation to the lowest 22 orbitals, selecting on the basis of the Hartree-Fock energies, the FCI-PES shows no binding in the relevant region (short-dashed line); hence the *entire differential effect* arises from the proper treatment of the contribution of the neglected external orbitals. The state-selected FCI-BSR-PES (full line) captures the important differential contribution of the external orbitals, while introducing an overall absolute error of 1.8 mH. The binding distance $r_e^{(\text{BSR})} = 4.82$ a.u. is in good agreement with that of the FCI calculation.

The computation of the singlet-triplet splitting in methylene is another example where a high-level method and a large single-particle basis are required to obtain the desired accuracy. In Table I we present the results for MRCI and BSR calculations for the singlet and triplet states of methylene at their respective minima, which were deter-

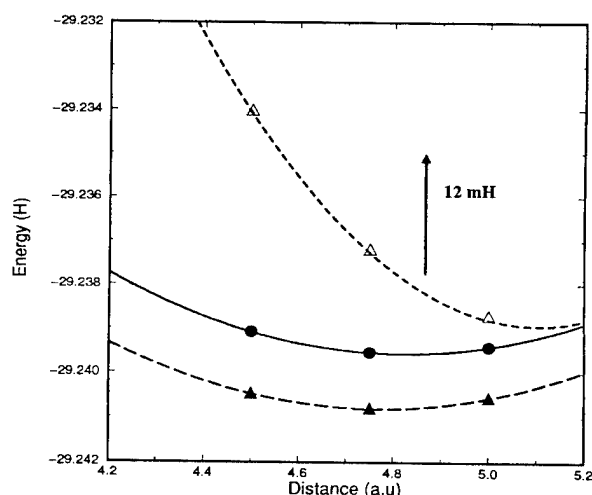


FIGURE 1. FCI and FCI-BSR energies for the beryllium dimer. The FCI energy (long dashed line) in the basis used by Harrison and Handy. The short dashed line shows the FCI potential energy surface for a 22-orbital subset of this basis—it has been shifted down by 12 mH. The full line is the BSR curve including relaxation.

mined by Shavitt [14] in a QZP quality basis. All BSR and MRCI calculations presented here were performed in the frozen-core interacting-space Hilbert space without Davidson correction. The internal orbitals were generated by an all-electron CASSCF calculation, and the remaining orbitals were K-orbitals [15].

Table I demonstrates the absolute energy con-

vergence of the BSR method. The top row shows the results of a six-electron CAS-MRCI calculation at their respective minima. The following three blocks of data correspond to different partitions of the orbitals, with 6, 14, and 48 orbitals in the internal set, respectively. The first entry in each block, labeled E_i , gives the MRCI energy in the internal basis, the second entry the perturbative energy of Eq. (5), and the last entry the BSR energy. The difference between the last two energies is a measure of the importance of the relaxation effects in the last step of the BSR procedure. The last column of each block shows the relative reduction in the number of matrix elements which must be calculated in the BSR vs. the MRCI calculation. The first calculation restricts the internal space to the CAS reference space and gives a predictably large total error; on the other hand the computation effort was reduced by a factor of 1430. The perturbative correction overshoots the MRCI energy by about 12 mH, as is common for an A_k -like method. About half of this error is corrected for in the final relaxation step.

One can now systematically improve upon this calculation. Based on the orbital occupation in the single-particle density matrix or their energy contribution in the first calculation we can select the next important set of orbitals for inclusion into the internal space. A typical threshold for the orbital occupation is about 0.01, but a systematic investigation for an automated selection of the orbitals

TABLE I
Electronic energies for lowest triplet and singlet states of methylene in the frozen-core full-valence complete active-space MRCI and BSR methods at the geometries determined by Shavitt [12].^a

Treatment	N_i/N_x	$^3B_1^b$ (a.u.)	Error (mH)	$^1A_1^c$ (a.u.)	Error (mH)	Comp. speedup ^d
MRCI	82/0	-39.0831	—	-39.0683	—	1
E_i	6/76	-38.9721	111.8	-38.9529	115.4	
$E_i + \Delta E$	6/76	-39.0940	-10.9	-39.0815	-13.2	
E_{BSR}	6/76	-39.0903	-6.7	-39.0771	-8.8	1430
E_i	14/68	-39.0016	83.0	-38.9856	82.7	
$E_i + \Delta E$	14/68	-39.0853	-7.0	-39.0727	-4.4	
E_{BSR}	14/68	-39.0846	-1.5	-39.0713	-3.0	95
E_i	48/34	-39.0463	36.8	-39.0309	37.4	
$E_i + \Delta E$	48/34	-39.0824	0.7	-39.0684	-0.1	
E_{BSR}	48/34	-39.0826	0.5	-39.0684	-0.1	4

^a N_i (N_x) denote the number of internal (external) orbitals in the BSR framework. Six of the internal orbitals are treated in the complete active space. E_i is to the energy of $\Psi_i^{(0)}$. The perturbative energy correction ΔE and the BSR energy E_{BSR} are defined in Eqs. (5) and (7), respectively.

^bGeometry: $R = 1.0779 \text{ \AA}$, $\theta = 132.9^\circ$.

^cGeometry: $R = 1.1086 \text{ \AA}$, $\theta = 102.0^\circ$.

^dThe computational speedup is the fraction of MRCI matrix elements evaluated vs. those used for the BSR calculation.

for the internal space has yet to be undertaken. In this set of 14 orbitals the original six active orbitals will be treated as internal in the MRCI calculation, while the remaining eight will be external in the sense of the MRCI calculation. While the total error of the internal calculation is still quite large, the BSR method now recovers more than 96% of this error, the computational effort is reduced by a factor of 100. The last partition, with 48 internal orbitals, demonstrates convergence of the absolute error, though the computational saving is no longer significant.

An equivalent set of calculations was carried out for the stretched molecule (75 Å) to determine the dissociation energy. In Table II we summarize the results for singlet-triplet splitting and the dissociation energy for the various partitions. For even the smallest internal basis, BSR recovers the full MRCI singlet-triplet splitting and the dissociation energy. Note that none of the energies have been corrected for zero-point vibrations. In the second calculation both energy differences are converged to 1 kcal/mol. The last set of results demonstrates the convergence of the method.

As the final example we present results of an exploratory calculation of the ground state 1A_1 energy surface of ozone. The importance of this molecule to atmospheric chemistry, as well as its interesting properties have spurred a number of theoretical investigations in recent years [16]. While

a number of properties could be adequately described, some features, most notably the dissociation process, remain to be elucidated. Here we focus on the two minima of the ground-state energy surface to test the validity of the BSR approximation. Calculations at the primary minimum were carried out at the experimental geometry; the secondary minimum was determined using an 11 reference MRCI calculation in CASSCF orbitals constrained to D_{3h} symmetry. Dunning's cc-pVTZ basis [17] was used for all calculations. Both the energy of the primary minimum and the location of the secondary minimum compare well with previous studies [16]. The location of the minima and their MRCI energies are given in Table III. We determined the most important orbitals using a BSR calculation in which all nonreference orbitals at both minima were treated in the BSR approximation, yielding a set of 22 internal orbitals. Using only the internal basis, we incur a large differential error in the separation of the two minima. The perturbative step, labeled $E_i + \Delta E$, reduces the relative error to 4.4 mH, while the relaxation step reduces it further to 0.4 mH. The BSR computation cost of the BSR calculation was 7% of that of the corresponding MRCI calculations.

Conclusions

For the examples investigated here the BSR approximation resulted in an adequate energy reso-

TABLE II
Singlet-triplet splitting and dissociation energy of the methylene radical in the frozen-core full-valence complete active-space MRCI and BSR methods.^a

Treatment	N_i/N_x	Splitting (kcal/mol)	Error	D_e (kcal/mol)	error
MRCI	82/0	9.3	—	189.7	—
E_i	6/76	12.0	2.7	169.5	-20.2
$E_i + \Delta E$	6/76	7.8	-1.5	191.9	2.2
E_{BSR}	6/76	8.3	-1.0	191.3	1.6
E_i	14/68	10.4	+1.1	173.1	-16.6
$E_i + \Delta E$	14/68	7.9	-1.4	190.1	0.4
E_{BSR}	14/68	8.3	-1.0	189.3	-0.4
E_i	48/34	9.7	+0.4	184.3	-5.4
$E_i + \Delta E$	48/34	8.7	-0.6	189.7	0.0
E_{BSR}	48/34	8.9	-0.3	189.8	0.1

^aFor symbols and geometries see Table I.

TABLE III

Electronic MRCI and BSR energies for the primary (X^1A_1) and secondary minimum of the ground-state potential energy surface of ozone in a cc-pVTZ basis using CASSCF orbitals in C_{2v} symmetry.^a

Treatment	N_i/N_x	Primary ^b (a.u.)	Error (mH)	Secondary ⁽²⁾ (a.u.)	Error (mH)	Δ_{PS} (mH)	Error (mH)
MRCI	84/0	-225.0482	—	-224.9848	—	63.4	—
E_i	22/62	-224.7880	260.2	-224.7346	250.2	53.4	10.0
$E_i + \Delta E$	22/62	-225.0721	-23.9	-225.0131	-28.3	59.0	4.4
E_{BSR}	22/62	-225.0669	-18.7	-225.0031	-18.1	63.8	0.4

^a N_i (N_x) denote the number of internal (external) orbitals in the BSR framework. There are six (active) valence orbitals. E_i refers to the energy of $\Psi_i^{(0)}$. The perturbative energy correction ΔE and the BSR energy E_{BSR} are defined in Eqs. (5) and (7), respectively.

Δ_{PS} denotes the energy difference between the two minima.

^bGeometry: $R = 2.413 a_0$, $\theta = 116.8^\circ$.

^cGeometry: $R = 2.668 a_0$, $\theta = 60.0^\circ$.

lution of the potential energy surfaces with a significantly reduced computational effort. Building on the effective valence shell Hamiltonian method, we have been able to show that a configuration-based approach can successfully treat the three-particle terms which arise in lowest-order perturbation theory for the effective Hamiltonian. BSR offers a systematic approach to formulate a multireference perturbation theory. Based on an initial run with only a few internal states, the important orbitals can be selected on the basis of either their perturbative energy contribution or according to their occupation. The approximation allows the generation of a single-particle density matrix and thus the computation of properties. The computation of forces and frequencies is a more challenging problem. The present implementation was explicitly designed to approximate an MRCI calculation of the full basis, as such it lacks size consistency. This approach allowed us to test the most significant approximation of the method, namely the neglect of the off-diagonal terms in the external Hamiltonian, against a firmly established method. In the future the requirement to approximate the MRCI will be relaxed to arrive at a size-consistent version of the method.

ACKNOWLEDGMENTS

This work was supported in part by the state government of NRW and the Deutsche Forschungsgemeinschaft. We gratefully acknowledge the use of the computational facilities of the Fraunhofer Society Germany (ISST Dortmund). One of us (W.W.) would like to thank Prof. Morokuma and his group for their hospitality and many stimulating discussions during his stay as a

visiting fellow at the Emerson Center for Computational Science at Emory University. One of us (M.M.S.) was supported by DOE-BES, Division of Material Science (DE-FG02-88ER45347). We acknowledge useful discussions with I. Shavitt, J. W. Wilkins, R. L. Martin, R. J. Bartlett, and H. Keiter.

References

1. W. Kutzelnigg and W. Klopper, *J. Chem. Phys.* **94**, 1985 (1990).
2. P.-O. Löwdin, *J. Chem. Phys.* **19**, 1401 (1951); P.-O. Löwdin, *Int. J. Quantum Chem.* **55**, 77 (1995).
3. K. F. Freed, *Acc. Chem. Res.* **16**, 137 (1983).
4. G. Hose and U. Kaldor, *J. Phys. B* **12**, 3827 (1979); G. Hose, *J. Chem. Phys.* **84**, 4505 (1986).
5. K. Andersson, P.-A. Malmqvist, B. O. Roos, A. J. Sadlej, and K. Wolinski, *J. Phys. Chem.* **94**, 5483 (1990).
6. Z. Gershgorin and I. Shavitt, *Int. J. Quantum Chem.* **2**, 751 (1968); I. Shavitt, *Chem. Phys. Letts.* **192**, 135 (1992).
7. D. Feller, *J. Comp. Phys.* **98**, 7059 (1993).
8. X. C. Wang and K. F. Freed, *J. Chem. Phys.* **91**, 3002 (1989).
9. W. Wenzel and K. G. Wilson, *Phys. Rev. Letts.* **69**, 800 (1992).
10. I. Shavitt, C. F. Bender, A. Pipano, and R. P. Hosteney, *J. Comp. Phys.* **11**, 90 (1973).
11. X. Assfeld, J. E. Almlöf, and D. G. Truhlar, *Chem. Phys. Lett.* **241**, 438 (1995).
12. R. J. Harrison and N. C. Handy, *Chem. Phys. Letts.* **98**, 97 (1983).
13. U. E. Bondybey and J. H. English, *J. Chem. Phys.* **80**, 568 (1984).
14. D. C. Comeau and I. Shavitt, *J. Comp. Phys.* **90**, 6491 (1989).
15. D. Feller and E. R. Davidson, *J. Comp. Phys.* **74**, 3977 (1981).
16. A. Banichvich and S. D. Peyerimhoff, *Chem. Phys.* **174**, 93 (1993).
17. T. H. Dunning, *J. Chem. Phys.* **90**, 1007 (1989).

Basis Set and Correlation Effects on Geometry of Octahedral Second-Row Transition-Metal Complexes

ANDERS BROO

Department of Physical Chemistry, Chalmers University of Technology, 412 96 Göteborg, Sweden

Received February 26, 1996; revised manuscript received April 17, 1996; accepted April 24, 1996

ABSTRACT

An extensive investigation of the basis-set effect on the predicted geometry of the redox pair $[\text{Ru}(\text{NH}_3)_6]^{2+/3+}$ is presented. Basis sets where the core electrons have been replaced with a relativistic core potential as well as all-electron basis sets were tested. Best agreement with observations was obtained with the all-electron basis set MIDI augmented with a set of *f*-type polarization functions on the metal center. Other properties such as the vibration spectrum, the relative energy of the high-spin and low-spin states, and geometry changes upon oxidation/reduction of the central metal are discussed. The importance of electron correlation on the predicted geometry was estimated at the MP2, MP3, MP4(SDQ), CCSD, and CCSD(T) levels of theory. The MIDI(*f*) basis set is then used for other octahedral second-row transition-metal complexes and some other related complexes. The electronic spectrum of $[\text{Ru}(\text{NH}_3)_6]^{2+}$ is also calculated using two different CI computational schemes. Surprisingly good agreement between the predicted electronic spectrum and the observed spectrum are obtained using one of the CI computational schemes. © 1996 John Wiley & Sons, Inc.

Introduction

Ruthenium complexes, especially $[\text{Ru}(\text{bpy})_3]^{2+}$, are among the most experimentally studied metalorganic complexes, due to their unique combination of chemical stability, redox properties, electron and energy-transfer properties, and excited-state reactivity [1], despite that few quantum chemical investigations of ruthenium complexes have been published [2–4]. The

list of computational work on ruthenium complexes is certainly not complete and many works have probably escaped our attention. Until just recently, only semiempirical methods [2, 4a] and density functional theory methods [3] have been used. Part of the problem in applying *ab initio* quantum chemical methods to second-row transition metals is the relative large size, in terms of basis functions, of the metal complexes. Another aspect is the importance of relativistic effects on the electron structure of the metal, which is not properly accounted for in a traditional Hartree–

Fock calculation. Yet another important factor is the so far unclear role of electron correlation on the geometry and binding energy of second-row transition metals [5]. However, attempts have been made to clarify the role of electron correlation on the geometry of second-row metalorganic complexes [6]. The aim of this article was to further study the effect of electron correlation and the effect of the basis set on geometry and geometry changes when the formal oxidation state is changed for the metal ion. This work is concentrated mainly on ruthenium complexes with a nearly octahedral arrangement of the ligands surrounding the central metal ion. Several basis sets and computational methods are used. A compromise between accuracy and computational resource requirements are recommended to be used in future studies.

Computational Details

The ligand field around the central ruthenium ion has octahedral (O_h) symmetry or close to O_h symmetry in most of the ruthenium complexes in this study. The ruthenium ion has either a $4d^6$ electron configuration, Ru(II), or a $4d^5$ electron configuration, Ru(III). Three d orbitals, xz , yz , and xy , are occupied and two, x^2-y^2 and z^2 , are unoccupied. In a perfect O_h ligand field, the occupied d orbitals have t_{2g} symmetry and the unoccupied d orbitals have e_g symmetry. When the perfect O_h symmetry is broken by less symmetric ligands, the occupied d orbitals, as well as the two unoccupied metal orbitals, will be separated in energy. All the Ru(II) complexes are assumed to have a low-spin d^6 metal configuration, since the ligands included in this study are known to produce rather large ligand fields [7]. The Ru(III) complexes are assumed to have a low-spin d^5 metal configuration, which is also observed in most Ru(III) complexes. However, the corresponding high-spin states were calculated in some cases. The highest symmetry a $M(NH_3)_6$ complex can have is D_{3d} . In the D_{3d} symmetry, all the M-N bonds are equal. However, we would like to be able to study Jahn-Teller distortions upon oxidation-state changes. Thus, all geometry optimizations were performed under the C_{2v} symmetry restriction. In the C_{2v} symmetry, three different metal-ligand (M-L) bond distances are possible. When the C_{2v} symmetry restriction is used, the t_{2g} orbitals will be transformed in to an a_2 orbital, an a_1 orbital,

and a b_1 orbital. The e_g orbitals will be transformed into an a_1 orbital and a b_2 orbital. The geometries and a simple molecular orbital (MO) diagram of the studied complexes are found in Figure 1.

All the ab initio geometry optimizations were performed with the GAMESS set of programs or the Gaussian94 program packages [8]. A rather large number of basis sets were tested. The used basis sets are summarized in Table I.

Results and Discussion

$[Ru(NH_3)_6]^{2+}$

The most extensive basis-set study was performed for the $[Ru(NH_3)_6]^{2+}$ complex. The geometry of $[Ru(NH_3)_6]^{2+}$ was optimized using basis set A-I at the Hartree-Fock (HF) level of theory. The results are summarized in Table II. It is evident that the HF method predicts the Ru-N bond length to be much too long compared to what is found in the crystallographic geometry of $[Ru(NH_3)_6]I_2$ [17]. This type of over estimation of the M-L bond length was also found in many $M(H_2O)_6$ complexes studied at the HF level of theory by Åkesson et al. [4h]. In the work by Åkesson et al., both first- and second-row transition metals were considered. They discussed possible sources to the rather large error in the predicted bond lengths and argued that hydrogen bonding to the second solvation shell is one possible source of error. Another possible source of error put forward by Åkesson et al. was that the observed bond lengths are temperature-dependent and crystal effects might also contribute to the differences between theory and observations [4h].

Even though we do not expect that the geometry will be well reproduced at the HF level of theory, we investigated the possible effect of the surrounding media on the predicted geometry of the $[Ru(NH_3)_6]^{2+}$ complex. The geometry of the $[Ru(NH_3)_6]^{2+}$ complex was optimized in the presence of two counterions to form a noncharged complex. Two different counterions were considered: F^- and Cl^- . The effective core potential basis set B was used in this study. The counterions were placed in between the equatorial ligands (see Fig. 1). The $Ru(NH_3)_6F_2$ and the $Ru(NH_3)_6Cl_2$ complexes were optimized under the C_{2v} symmetry constraint. In both complexes, three different Ru-N bond lengths were obtained. For

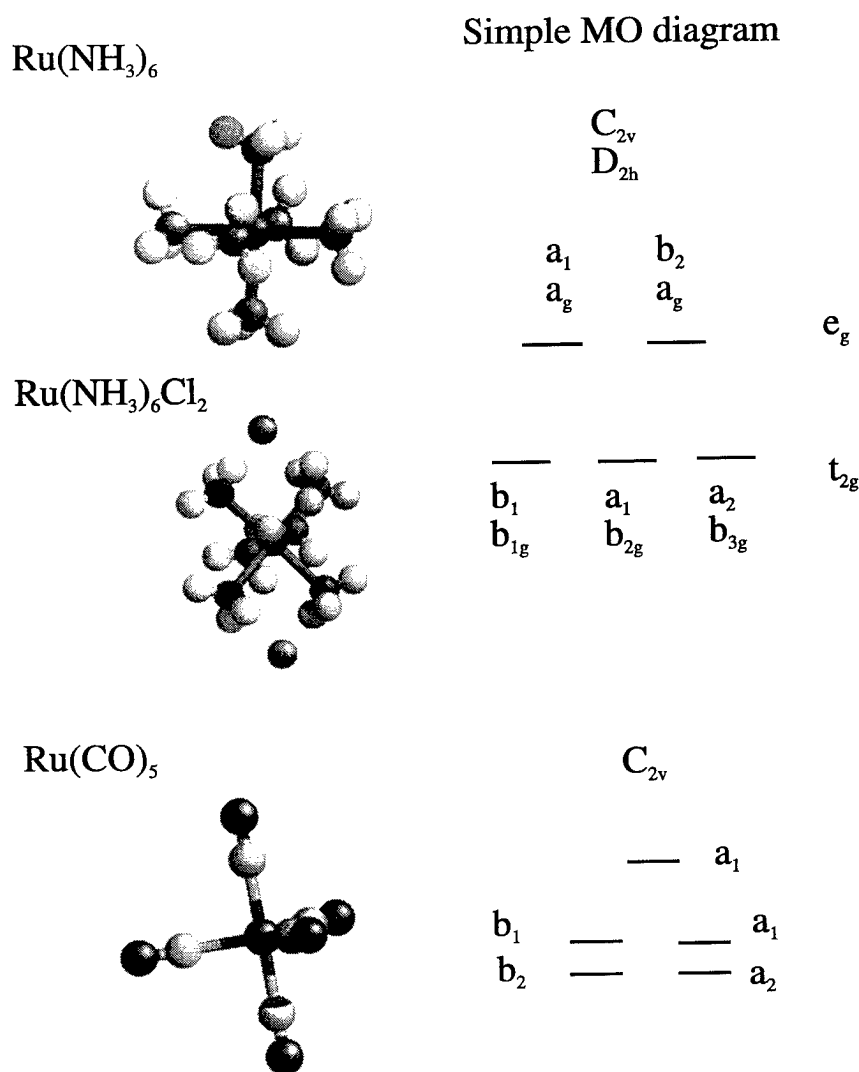


FIGURE 1. A schematic picture of the geometries of some of the metal complexes studied in this work. It is also shown in a simple MO diagram of the 4d orbitals on the metal. The symmetry labels of the MOs in different point groups are also indicated.

$\text{Ru}(\text{NH}_3)_6\text{F}_2$, the Ru—N bond lengths are predicted to be 2.271, 2.247, and 2.246 Å, and for $\text{Ru}(\text{NH}_3)_6\text{Cl}_2$, the Ru—N bond lengths are 2.275, 2.258, and 2.257 Å, compared to the Ru—N bond length 2.286 Å predicted for the “free” complex using basis set B. Thus, a considerable bond-length decrease is induced by the counterions. It is not clear whether the bond-length change is due to steric effects or electronic effects, but it is likely that the steric effects are the most important contribution to the observed bond-length decrease.

The geometry of $[\text{Ru}(\text{NH}_3)_6]^{2+}$ was optimized with different basis sets using the second-order perturbation theory (MP2) to account for some of

the dynamic electron correlation. The predicted geometries are found in Table II together with the HF-predicted geometries. In the MP2 calculations, the core electrons were left uncorrelated. This means that with the ECP basis sets the 12 core electrons on the ligands were left uncorrelated, and for the all-electron calculations, the core electrons of the ligands and the 1s, 2s, 2p, 3s, 3p, 4s, 4p, and 3d electrons on ruthenium were left uncorrelated. With the ECP basis set, the Ru—N bond length is still predicted to be too long compared to what is observed. Electron correlation at the MP2 level of theory decreases the M—L bond length about 0.04 Å for the ECP basis sets. The Ru—N

TABLE I
Summary and description of the basis sets used in this work.

Basis set	Abbreviation	Description
A	SBK + STO-3G	Relativistic effective core potential on Ru where the 28 most inner electrons have been replaced with a core potential [8] and single zeta on N and H [9]
B	SBK + 6-31G	Relativistic effective core potential on Ru where the 28 most inner electrons have been replaced with a core potential [8] and split valence double zeta on N and H [9]
C	HW + 6-31G	Relativistic effective core potential on Ru where the 28 most inner electrons have been replaced with a core potential [10] and split valence double zeta on N and H [9]
D	HW + D95	Relativistic effective core potential on Ru where the 28 most inner electrons have been replaced with a core potential [10] and double zeta on N and H [11]
E	3-21G	Double zeta [12]
F	3-21G(3f)	Double zeta [13] augmented by three <i>f</i> -type polarization functions on Ru ($\alpha = 1.6, 0.4, 0.1$)
G	MIDI	Double zeta [14]
H	MIDI(<i>f</i>)	Double zeta [14] augmented by a set of <i>f</i> -type polarization functions on Ru*
I	MIDI(<i>f</i> , <i>d</i>)	Double zeta [14] augmented by a set of <i>f</i> -type of polarization functions and a set of diffuse <i>p</i> -type functions on Ru* and a set of <i>d</i> -type polarization functions on N

^a The *f*-type polarization function is a three-component contraction which mimic a Slater-type function. The contraction is due to the scheme outlined by Stewart [15] and Walsh et al. [16].

bond length obtained at the MP2 level using the all-electron basis set G is not altered much relative to what is obtained at the HF level. Polarization functions of *f*-type on the metal ion seem to be more important and the geometry is predicted in good agreement with observations at the MP2/MIDI(*f*) level of theory. When the basis set is extended with a set of *d*-type polarization functions on the nitrogen and a set of diffuse *p*-type functions on the metal, the M-L bond length is increased. A similar pattern was also found at the HF level of theory. The effect of a higher level of electron correlation on the geometry will be discussed further in the Property sub-section. The relativistic effect on the geometry was not explicitly investigated since all the ECPs used here include relativistic corrections in the core potential and the all-electron basis sets do not include any relativistic corrections. However, the expected impact on the predicted geometry when the relativistic effects are sufficiently included in the calculations is a shortening of the M-L bond. Thus, the ECP basis-set calculations, which include some of the relativistic effects, should produce shorter bond lengths than do the all-electron basis sets, pro-

vided that the quality of the basis sets is the same in the valence region. Clearly, this is not the case here and we conclude that the ECP basis sets are not sufficiently flexible to be used for this molecule.

An other important issue is whether the correct spin state is obtained or not. The high-spin/low-spin separations is investigated by calculating the energy of the first low-spin state in each irreducible representation and the energy of the corresponding high-spin states of $[\text{Ru}(\text{NH}_3)_6]^{2+}$. Basis set B was used in a set of CASSCF calculations. The rationale for using basis set B is that Åkesson et al. used a similar ECP basis set in an investigation of the high-spin/low-spin separation for some transition-metal hexaaqua complexes with modest success [4h]. We compared the present results with theirs on an equal basis. In the CASSCF calculations, six electrons were distributed in all possible ways among nine active orbitals. The low-spin states were geometry-optimized. The high-spin states were assumed to have all the Ru-N bond lengths equal to 2.26 Å and the geometry of the NH_3 groups was kept as predicted for the 1A_1 state. The corresponding energies and Ru-N bond lengths are summarized in Table III. The 1A_1 low-

TABLE II
HF and MP2-predicted geometries of $[\text{Ru}(\text{NH}_3)_6]^{2+}$ using different basis sets; q_{Ru} , q_{N} , and q_{H} denotes the Mulliken atomic charge on the ruthenium atom, the nitrogen atoms, and the hydrogen atoms, respectively.

	Method basis set														
	HF/A	HF/B	MP2/B	HF/C	HF/D	MP2/D	HF/E	HF/F	HF/G	MP2/G	HF/H	MP2/H	HF/I	MP2/I	Exp. [7]
Ru—N (Å)	2.239	2.286	2.247	2.282	2.273	2.233	2.271	2.265	2.207	2.182	2.209	2.137	2.249	2.161	2.144
N—H (Å)	1.030	1.005	1.030	1.004	1.007	1.030	1.012	1.013	1.018	1.037	1.018	1.037	1.020	1.036	
H—N—H	105.6	107.5	107.0	107.7	107.6	107.1	107.6	107.2	106.4	105.8	106.6	105.8	105.0	104.5	
q_{Ru}	0.12	1.30		1.22	1.18		0.70	1.14	1.17		1.18		0.60		
q_{N}	-0.38	-1.09		-1.03	-1.05		-0.91	-0.96	-0.87		-0.88		-0.86		
q_{H}	0.23	0.40		0.38	0.39		0.37	0.36	0.34		0.34		0.36		

spin state is found as the ground state and is favored by about 170 kJ/mol over the 5A_1 state. Thus, the CASSCF calculations predict the high-spin/low-spin energy ordering in accord with observations [7]. Åkesson et al. [4h] predicted the high-spin state to be the most stable state of the $[\text{Ru}(\text{H}_2\text{O})_6]^{2+}$ complex at both the HF and CASSCF levels of theory in contrast to what is found here for $[\text{Ru}(\text{NH}_3)_6]^{2+}$. However, ammonia is known to produce a larger ligand field splitting than does water [7]. The high-spin/low-spin separation will be further discussed for the $[\text{Ru}(\text{H}_2\text{O})_6]^{2+}$ complex later.

$[\text{Ru}(\text{NH}_3)_6]^{3+}$

The three valent oxidation state of ruthenium has five *d* electrons. The low-spin ground state is a doublet. The " t_{2g} " orbitals have a_1 , a_2 , and b_1 symmetry in the C_{2v} point group. Thus, three different doublets can be constructed with C_{2v} space symmetry. The 2A_1 , 2A_2 , and 2B_1 states were geometry-optimized with the CASSCF method with five active electrons in seven active orbitals. As for the Ru(II) ions, the basis set B was used in the CASSCF calculations. Three almost identical M—L bond lengths are found for all three doublet states (see Table III). The M—L bond lengths are predicted to be much too long compared to the observed one of 2.104 Å in the $[\text{Ru}(\text{NH}_3)_6](\text{BF}_4)_3$ [17]. The 2A_2 state is found to be the most stable state, favored over the 2B_1 state by 28.2 kJ/mol and over the 2A_1 state by 37.8 kJ/mol.

The HF/H and MP2/H model reproduced the observed geometry of the 2+ complex best. Thus, the same basis set was used to predict the geometry of the 3+ complex at the unrestricted Hartree-Fock level (UHF), restricted open-shell Hartree-Fock (ROHF) level, and the second-order perturbation corrected level (UMP2). The optimized geometries of $[\text{Ru}(\text{NH}_3)_6]^{3+}$ are summarized in Table IV. In the ROHF calculations, the state symmetry was allowed to change during the SCF iterations. This resulted in that only two doublet states were geometry-optimized. The 2A_1 state was never accessed in the ROHF calculations, while the UHF and UMP2 geometry optimizations always ended in an 2A state.

$[\text{Ru}(\text{H}_2\text{O})_6]^{2+/3+}$

The geometry of the hexaamine complexes were best reproduced with all-electron basis sets G and

TABLE III

CASSCF-predicted Ru—N bond lengths of the first root in each symmetry with low-spin of $[\text{Ru}(\text{NH}_3)_6]^{2+}$ compared with the high-spin state of each symmetry.

State	Ru—N (Å)	Ru—N (Å)	Ru—N (Å)	Energy (−429. au)
$[\text{Ru}(\text{NH}_3)_6]^{2+}$ Exp. 2.144				
1A_1	2.292	2.292	2.292	.93774
1A_2	2.319	2.322	2.605	.87733
1B_1	2.337	2.337	2.524	.87136
1B_2	2.268	2.478	2.490	.87495
5A_1	2.26	Nonoptimized		.87340
5A_2	2.26	"		.86186
5B_1	2.26	"		.87314
5B_2	2.26	"		.77476
$[\text{Ru}(\text{NH}_3)_6]^{3+}$ Exp. 2.104				
2A_1	2.228	2.208	2.205	.39563
2A_2	2.221	2.214	2.209	.41004
2B_1	2.228	2.221	2.212	.39931

The high-spin states were not geometry-optimized, the geometry of the ammonia was extracted from the MP2/B geometry, and the M—L bond distance was set arbitrary to 2.26 Å. Also shown is the CASSCF-predicted Ru—N bond lengths for the $[\text{Ru}(\text{NH}_3)_6]^{3+}$ complex. The ECP basis set B was used in the CASSCF calculations.

H. Thus, those basis were used for further studies together with ECP basis set B. Even though the ECP basis sets did not reproduce the geometry of the hexamine complexes very well, they are needed for studies of larger systems than what are considered here. Thus, it is of importance to obtain a better knowledge of how well ECP basis sets reproduce the geometry of second-row transition-metal complexes. The geometry of $[\text{Ru}(\text{H}_2\text{O})_6]^{2+}$ was optimized assuming D_{2h} symmetry. The pre-

dicted geometry and the basis set and method dependency are summarized in Table V. The Hartree-Fock model with an ECP basis set predicts the Ru—O bond length to be too long compared to the observed bond length, as was also the case for the Ru—N bond. Åkesson et al. [4h] reported a Ru—O bond length of 2.197 Å for the $[\text{Ru}(\text{H}_2\text{O})_6]^{2+}$ complex at the Hartree-Fock level of theory using the Hey-Wadt ECP basis set [10] on ruthenium and a double zeta basis set on the

TABLE IV

Predicted geometries of $[\text{Ru}(\text{NH}_3)_6]^{3+}$ using the basis sets G and H; q_{Ru} , q_{N} , and q_{H} denotes the Mulliken atomic charge on the ruthenium atom, the nitrogen atoms, and the hydrogen atoms, respectively.

	Method/basis set					Exp. [17]
	ROHF/G 2A_2	UHF/H 2A_1	UMP2/H 2A_2	ROHF/H 2A_2	ROHF/H 2B_2	
Ru—N (Å)	2.151 2.152 2.158	2.159 2.149 2.144	2.123 2.121 2.118	2.149 2.149 2.155	2.148 2.152 2.156	2.104
N—H (Å)	1.024	1.024	1.042	1.024	1.024	
H—N—H	105.3	105.3	105.1	105.6	105.3	
q_{Ru}	1.59	1.50		1.51	1.51	
q_{N}	−0.93	−0.92		−0.92	−0.92	
q_{H}	0.39	0.39		0.39	0.39	

TABLE V

The predicted geometry of $[\text{Ru}(\text{H}_2\text{O})_6]^{2+}$ complex compared with the crystallographic geometry of $[\text{Ru}(\text{H}_2\text{O})_6](\text{C}_7\text{H}_7\text{SO}_3)_2$ [21] and the predicted geometry of $[\text{Ru}(\text{H}_2\text{O})_6]^{3+}$ complex compared with the crystallographic geometry of $[\text{Ru}(\text{H}_2\text{O})_6](\text{C}_7\text{H}_7\text{SO}_3)_3$ [21].

	Method / Basis Set						
	$[\text{Ru}(\text{H}_2\text{O})_6]^{2+}$					$[\text{Ru}(\text{H}_2\text{O})_6]^{3+}$	
	HF/B	HF/G	HF/H	MP2/H	Observed	ROHF/H	Observed
Ru—O (Å)	2.224	2.134	2.162	2.094	2.139	2.105	2.016
	2.224	2.130	2.160	2.088	2.121	2.058	2.030
	2.194	2.108	2.140	2.066	2.107	2.040	2.031
							2.037
							2.019
							2.031
O—H (Å)	0.952	0.973	0.973	0.992		0.982	
H—O—H	110.4			107.8		107.9	
	110.7			107.5		108.2	
	111.9			109.7		110.3	
q_{Ru}		1.38	1.07	1.32		1.39	
q_{O}		-0.77	-0.72	-0.77		-0.73	
q_{H}		0.44	0.44	0.44		0.49	

ligands. Thus, the ECP basis sets predict the Ru—O bond to be too long compared to what is observed. In contrast, Sargent and Hall predicted the geometry of the RuO_4 complex using the same ECP basis set at the Hartree-Fock level of theory in good agreement with observations [4i]. In fact, all basis sets in their work performed remarkably well for the RuO_4 complex, while the M—L bond lengths were not well reproduced at all for the $\text{Ru}(\text{P}(\text{CH}_3)_3)_2(\text{CO})_3$ complex using the same basis set [4i]. The Ru—P bond was predicted to be 0.11 Å too long and the Ru—C bond length was predicted 0.10 Å too long. At first glance, this could appear to be strange. However, the ruthenium atom has a different formal oxidation state in the two complexes. The Ru—O bond lengths of the RuO_4 complex are predicted to be 1.664 Å at the HF/H computational level, which is close to what Sargent and Hall found for all their basis sets [4i].

In the work by Åkesson et al. [4h], only partial geometry optimization was performed of the $[\text{Ru}(\text{H}_2\text{O})_6]^{2+}$ complex. Furthermore, D_{3d} symmetry restrictions were used. Thus, only one Ru—O bond length was obtained. However, the $[\text{Fe}(\text{H}_2\text{O})_6]^{2+}$ was optimized under both D_{3d} and D_{2h} symmetry restrictions and a distorted geometry was obtained for the D_{2h} complex $R_{eq} - R_{ax} = 0.043$ Å [4h]. In the crystallographic-determined geometry, three different Ru—O bond lengths

were found [18]. Bernhard et al. assumed that hydrogen bonding was responsible for the inequality of the Ru—O bond lengths [18]. However, all the geometries of the $[\text{Ru}(\text{H}_2\text{O})_6]^{2+}$ complex reported here have three different Ru—O bond lengths, two almost equal (equatorial) and one a little shorter (axial). By allowing the symmetry to be reduced (Jahn-Teller distortion), we reproduced the observed bond length and the small deviation from perfect D_{3d} symmetry. The bond length difference $R_{eq} - R_{ax}$ was calculated to be 0.02 Å for the $[\text{Ru}(\text{H}_2\text{O})_6]^{2+}$ complex at the HF/H level. Furthermore, Åkesson et al. was not able to reproduce the relative ordering of the high-spin and the low-spin state of the $[\text{Ru}(\text{H}_2\text{O})_6]^{2+}$ complex, not even with an MRCI + Davidson correction calculation [4h]. Using the HF/G model with the HF/G geometry, which is closest to the observed geometry, the high-spin state is predicted to be 45.2 kJ/mol *higher* in energy than the low-spin state in accord with what is observed [18]. Thus, the correct ordering of the high-spin and low-spin states is possible to reproduce if an all-electron basis set is used, but the correct ordering is not obtained with an ECP basis set. The reason for the somewhat disappointing performance of the ECP basis sets might be that the core potential is not flexible enough to account for the core contraction due to the ionic state of the metal. The

ECPs are obtained for neutral molecules and not for the ions that are studied here. It might be necessary to develop different ECPs for different ion charges in order to increase the usefulness of the ECP basis sets.

In Table V is also the ROHF/H-predicted geometry $^2B_{3g}$ state of the $[\text{Ru}(\text{H}_2\text{O})_6]^{3+}$ complex compared with the observed geometry. A rather large Jahn-Teller distortion is found for the Ru(III) hexaaqua complex that was not found for the corresponding hexamine complex. The predicted bond-length change upon reduction of the metal ion $\Delta R = 0.086 \text{ \AA}$ is in good accord with the observed $\Delta R = 0.093 \text{ \AA}$. It has been argued that the different bond-length change for the hexaaqua and hexamine complexes when the ruthenium oxidation state is changed is due to π interaction in the case of H_2O , which is not possible for the NH_3 ligands [18, 19]. The π back-bonding effect should be manifested by an increase of the Mulliken charge of the metal ion. If the Mulliken charge of the ruthenium ion for the hexamine and hexaaqua complexes is compared, a somewhat larger Mulliken charge is found for the hexamine complex. Thus, the bonding π orbital on the water molecules donates a fraction of about 0.1 electron charges to the ruthenium ion (see Tables II, IV and V).

Mo(CO)₆ AND Ru(CO)₅

This far, only ruthenium complexes with small or no back-bonding effects have been considered. We also included a ruthenium carbonyl complex in this study in order to investigate an M-L bond where the back-bonding effects are very important. The molybdenumhexacarbonyl complex was also studied since it has octahedral symmetry and was included in the study by Sargent and Hall [4i]. The formal oxidation state of the central metal is zero. The $\text{Mo}(\text{CO})_6$ complex was geometry-optimized under the O_h symmetry restriction. Thus, all six CO ligands are identical and all the Mo—C bond lengths are equal. At the HF/G level of theory, the Mo—C bond length is predicted to be 2.094 \AA , which is a little longer than the observed 2.063 \AA [20]. The C—O bond length is calculated to be 1.137 \AA compared to the observed 1.145 \AA [20]. Sargent and Hall reported Mo—C bond lengths between 2.122 and 2.092 \AA . The geometry of $\text{Mo}(\text{CO})_6$ is reproduced reasonably well already at the HF level of theory even with a rather compact

all-electron basis set and with the ECP basis sets. The geometry of the $\text{Ru}(\text{CO})_5$ complex was optimized under the C_{2v} symmetry restriction at the HF/G level of theory. Three different Ru—C bond lengths are possible. However, the two different equatorial Ru—C bond lengths were found to be equal. Thus, the Ru—C_{axial} bond length was predicted to be 2.010 \AA and the equatorial Ru—C bond length was predicted to be 1.991 \AA . To the best of my knowledge, no crystallographic geometry is available for the $\text{Ru}(\text{CO})_5$ complex, but the geometry of the related $\text{Ru}(\text{P}(\text{CH}_3)_3)_2(\text{CO})_3$ has been reported [21]. The observed Ru—C is 1.890 \AA , which is 0.11 \AA shorter than what was predicted at the HF/G computational level. That is the largest difference between theory and observations in this work at the HF/G level of theory. However, the crystallographic geometry is perhaps not appropriate for a detailed comparison since the rather large $\text{P}(\text{CH}_3)_3$ might affect the Ru—C bonding situation. Sargent and Hall reported a similar Ru—C bond length for the $\text{Ru}(\text{P}(\text{CH}_3)_3)_2(\text{CO})_3$ complex using both ECP basis sets and all-electron basis sets at the HF level of theory.

PROPERTIES

An interesting question is: Which level of theory is necessary to be used to reproduce properties, such as vibration spectrum or bond-length changes upon oxidation/reduction of the central metal ion? Both these two properties are of importance in electron-transfer theory since the bond-length change and the force constant for the symmetric M-L stretching are proportional to the internal reorganization energy, E_{in} , in the Marcus and Hush model for electron transfer [22]. E_{in} in the case of an ML_6^{2+} — ML_6^{3+} system is given by Eq. (1):

$$E_{in} = \left(\frac{3f_2f_3}{f_2 + f_3} \right) (\Delta R_{M-L})^2, \quad (1)$$

where f_2 and f_3 are the force constants for the breathing mode of the $2+$ and $3+$ complex and ΔR_{M-L} is the metal-ligand bond-length change upon oxidation/reduction.

The observed bond length changes when the $[\text{Ru}(\text{NH}_3)_6]^{2+}$ complex is reduced is 0.04 \AA [17]. At the CASSCF/B level of theory, a bond-length change of 0.075 \AA is predicted. At the HF-UHF/ROHF level of theory with basis set H, a ΔR_{M-L} of 0.058 \AA is predicted. A ΔR_{M-L} of 0.017 \AA is

predicted at the MP2/UMP2/H level of theory. Thus, a rather large spread in the predicted ΔR_{M-L} is obtained and the method dependency is large. The bond-length change upon reduction of the central metal ion is best reproduced at the HF/UHF/ROHF level of theory. However, at the MP2/H level, the geometry is best reproduced. For the $[\text{Ru}(\text{H}_2\text{O})_6]^{2+/3+}$ redox pair, the observed bond-length change was better reproduced (see Table V).

To calculate the full vibration spectrum, the Hess matrix has to be diagonalized. It is a very time-consuming issue if the basis set is large and/or at a high level of electron correlation correction. A full vibrational analysis was performed at the HF-ROHF/G level of theory for the two ruthenium hexamine complexes (see Fig. 2 and Table VI). When the predicted frequencies associated with vibrations within the amino group are scaled by a factor of 0.9, the agreement between the observed frequencies and the predicted frequencies is good. A scaling factor 0.9 for Hartree-Fock vibrational frequencies to obtain a good agreement between theory and observations is generally accepted nowadays. The reasons for scaling the frequencies are the lack of electron

correlation in the calculation and that the vibration analysis neglect the anharmonicity of the vibrations. The skeletal vibrational spectra are reproduced rather well without scaling, which is in accord with that anharmonicity is less important for the low-energy mode since the vibrational amplitude is smaller than for the high-frequency modes. It should be mentioned here that in the vibrational analysis four imaginary frequencies were obtained. The imaginary frequencies are due to rotations of the amino groups in a way to increase the symmetry to the highest possible symmetry (D_{3d}). This small deviation from the highest possible symmetry causes some vibrational mode to be slightly mixed, e.g., the symmetric and asymmetric breathing vibrational mode for the Ru(III) complex are slightly coupled.

At a higher level of theory, the breathing vibration mode was explored by freezing the geometry of the ligands at the MP2/G geometry and varying the Ru—N bond length. The breathing vibration modes are summarized in Table VII. It is interesting to note that the Ru—N bond distance is not changed when higher level of electron correlation is included in the calculation. All the breathing frequencies predicted with the Møller-Plesset-

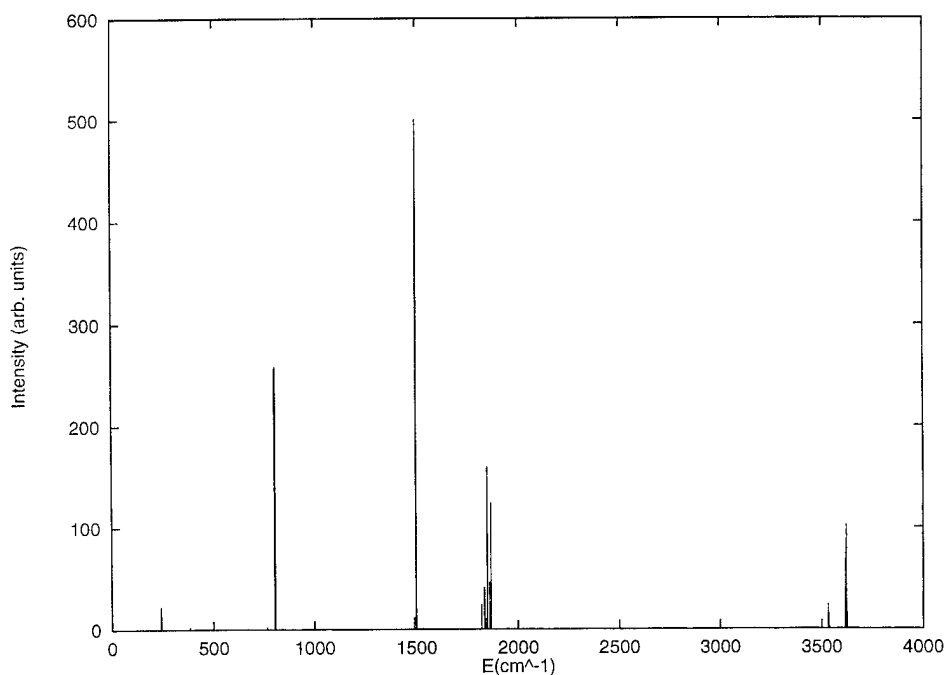


FIGURE 2. The vibrational spectrum of $[\text{Ru}(\text{NH}_3)_6]^{2+}$ calculated at the HF / basis set G level of theory.

TABLE VI

The vibration spectrum of $[\text{Ru}(\text{NH}_3)_6]^{2+/3+}$ as predicted with the HF / G model; the displayed vibration frequencies are unscaled.

	ν_a NH ₃	ν_s NH ₃	δ_a H—N—H	δ_s H—N—H	ρ NH ₃	ν_s M—N	ν M—N	ν_{as} M—N	δ_{as} N—M—N	δ N—M—N
HF / G	~ 3615	3532	1822 – 1867	1499	806	436	397 397	381 382 384	243	240 241
Obsd. ^a	3315	3210	1612	1220	763	409	—	—	—	—
ROHF / G	3540 – 3569	3479 3486	1826 1832 1852	1609 1611 1616	885 890 920	516	462 468	424 435 436	278	248 255
Obsd. ^b	—	—	—	—	—	500	475	463	273	248

^a $[\text{Ru}(\text{NH}_3)_6]\text{Cl}_2$, from [23].

^b $[\text{Ru}(\text{NH}_3)_6]\text{Cl}_3$, from [24].

type treatment of electron correlation are predicted to be too high in energy compared to the observed one, while the coupled cluster calculations predict too low breathing frequencies. A similar pattern was observed in a work on FeCO by Ricca et al. [25]. This pattern can also be taken as an indication on the lack polarization functions on the transition metal, which was shown earlier to have a large effect on the predicted geometry at the MP2 level of theory. However, it was not possible to use a larger basis set in this study due to limitations of the local computer environment.

UV-VIS-SPECTRA

As a final test of the basis sets, the electronic spectrum of the $[\text{Ru}(\text{NH}_3)_6]^{2+}$ was calculated. In this part, only basis set G was used. Meyer reported the electronic spectrum of $[\text{Ru}(\text{NH}_3)_6]^{2+}$ in his thesis work and found a very weak band centered at 3.10 eV, $\epsilon = 30 \text{ M}^{-1} \text{ cm}^{-1}$, and a

somewhat more intense band at 4.51 eV, $\epsilon = 630 \text{ M}^{-1} \text{ cm}^{-1}$ [26]. Both bands are due to Ru $4d \rightarrow 4d^*$ ($t_{2g} \rightarrow e_g$) transitions. It is well known that most ab initio methods do not reproduce transition energies in the UV and visible frequency regions very well. Recent developments of the multireference perturbation theory have, however, shown a promising future in this area [27]. In most ab initio studies of the absorption spectrum, the transition energies must be scaled due to the lack of a good treatment of the dynamic electron correlation in the excited state [28]. Two different types of electronic spectrum calculations are used here. The first method uses HF orbitals as the starting orbitals in a CI calculation where all possible single, double, and triple substitutions within a restricted active space are considered. This is the lowest level of configuration interaction which brings in electron correlation of the excited states [29]. This method will be abbreviated as CI(SDT) hereafter. The second method starts with a small CASSCF calculation where the general density matrices are formed from an average of the ground state and the two lowest excited states. The final CASSCF-optimized orbitals are then used in a CI(SDT) calculation. This method will be abbreviated CAS-CI(SDT) hereafter. In the CI(SDT) calculation, the six t_{2g} electrons were allowed to be excited into the 30 lowest unoccupied molecular orbitals (LUMOs); 20,118 configuration-state functions were generated in this way. The first transition energy was calculated to be 4.79 eV, corresponding to a " $t_{2g} \rightarrow e_g$ " metal-centered transition. Due to symmetry restrictions in the CI calculation, only one transition energy was calculated; however,

TABLE VII

Harmonic breathing mode frequencies of $[\text{Ru}(\text{NH}_3)_6]^{2+}$ as predicted at different levels of theory using the MIDI basis set (basis set G).

	Ru—N (Å)	$\nu(\text{Ru—N})$ (cm ⁻¹)	Experimental (cm ⁻¹) [20]
HF	2.207	436	403–423
MP2	2.182	442	
MP3	2.181	448	
MP4(SDQ)	2.183	446	
CCSD	2.185	383	
CCSD(T)	2.183	382	

two more " $t_{2g} \rightarrow e_g$ " transitions are to be found at about the same energy but with different symmetry. The second transition is predicted at 6.72 eV and has also a " $t_{2g} \rightarrow e_g$ " character. In similarity with *ab initio* CI calculations of the absorption spectrum of the DNA bases [28], the CI(SDT) method predicts the transition energies to be too high in energy. Petke et al. used a scaling factor of about 0.7 to obtain qualitative good agreement with the observed absorption spectra [28]. A similar scaling of the predicted CI(SDT) " $t_{2g} \rightarrow e_g$ " transition energies give the first peak at 3.35 eV and the second peak at 4.70 eV, which still is about 0.2 eV above the observed transition energies. The CAS-CI(SDT) method predicts the first band at 3.02–3.13 eV ($f_{osc} \sim 0.0$) that contains three " $t_{2g} \rightarrow e_g$ " transitions; no symmetry restriction was used in this CI calculation. The second band with three " $t_{2g} \rightarrow e_g$ " transitions are predicted at 4.27–4.35 eV ($f_{osc} \sim 10^{-6}$). The CAS-CI(SDT) transition energies are in excellent agreement with the observed spectrum. However, this very good agreement is likely due to cancellations of errors since a rather compact basis set was used. However, the success of the CAS-CI(SDT) treatment indicates that it is of great importance to optimize the virtual orbital space to obtain qualitative agreement between calculated and observed electronic spectra. This issue is currently under further study in this laboratory. Preliminary results indicate that electronic spectra of organic molecules could be reproduced with high accuracy, without a scaling of the transition energies, using the computational scheme proposed above [CAS-CI(SDT)] [30].

Summary

The basis-set dependency of the predicted geometry of some octahedral ruthenium complexes was reported. *Ab initio* HF calculations with effective core potential basis sets do not reproduce the observed metal M–L bond lengths very well. The geometry is better reproduced if all-electron basis sets are used. Polarization functions of *f*-type on the central metal ion improve the description but the predicted M–L bond lengths are still too long. Electron correlation at the second-order perturbation theory level in combination with an all-electron basis set augmented with a set of *f*-type polarization functions [MP2/MIDI(*f*)] is the minimum level of theory that is needed to reproduce

the geometry of octahedral second-row transition-metal complexes with an acceptable accuracy. A similar level of theory (MP2/6-31G*) has been proven to be sufficient to accurately reproduce the geometry of small and medium-sized molecules [28, 31, 32]. ECP basis sets seem to be too rigid in the core region to reproduce observed geometries of ruthenium complexes when the metal is in an ionic state. When the metal has mostly atomic character, the observed geometries are better reproduced.

Properties such as geometry changes due to reduction/oxidation of the central metal ion are reproduced well already at the HF level of theory. Inclusion of electron correlation does not improve the results. The high-spin/low-spin state separation is predicted in accord with observations at the HF level of theory with the all-electron basis set H in contrast to what, e.g., Åkesson et al. observed for the $[\text{Ru}(\text{H}_2\text{O})_6]^{2+}$ complex and other second-row transition metal complexes using ECP basis sets [4i]. Thus, we conclude that to reproduce the observed high-spin/low-spin separation all-electron basis sets are needed at least for complexes where the metal is in an ionic state.

The full vibration spectrum of $[\text{Ru}(\text{NH}_3)_6]^{2+/3+}$ predicted at the HF/MIDI level of theory agrees reasonably well with the observed spectrum if a linear scaling factor of 0.9 is applied on the calculated frequencies, in similarity with what has been found for small organic molecules. The skeletal vibrational modes are accurately reproduced without any scaling. At a high level of electron correlation, only the breathing vibrational mode has been explored. The MPn methods all predict a breathing mode frequency higher in energy than what is observed and the coupled cluster methods predict the breathing mode too low in energy compared with the observed IR spectrum. Polarization functions are probably needed to reproduce the observed breathing vibrational mode at the electron-correlated level of theory.

The observed electronic spectrum ($t_{2g} \rightarrow e_g$ transitions) of $[\text{Ru}(\text{NH}_3)_6]^{2+}$ is reproduced surprisingly well using basis set G and a novel strategy to do CI calculations on excited states. The strategy can be summarized as follows: First, the important occupied and virtual orbitals are optimized in a small complete active space self-consistent field calculation (CASSCF). For the present complex, this means that the occupied t_{2g} orbitals and the lowest unoccupied e_g orbitals are opti-

mized. The optimized natural orbitals are then used in a CI calculation where all single, double, and triple excitations in a restricted active space are considered [CI(SDT)]. In this case, all MOs that have large metal character are considered in the CI(SDT) calculation. Using this procedure, electron correlation is introduced in a democratic way in both the ground state and the excited states.

ACKNOWLEDGMENTS

This work was financed by grants from the Swedish Natural Science Research Council (NFR). The Center for Parallel Computers (PDC) at Stockholm, Sweden, is acknowledged for a generous supply of computer time.

References

1. A. Juris, V. Balzani, F. Barigelli, S. Campagna, P. Belser, and A. von Zelewsky, *Coord. Chem. Rev.* **84**, 85 (1988).
2. (a) S. Larsson, A. Broo, B. Källebring, and A. Volosov, *Int. J. Quantum Chem., Quant. Biol. Symp.* **15**, 1 (1988); (b) A. Broo and S. Larsson, *Int. J. Quantum Chem., Quant. Biol. Symp.* **16**, 185 (1989); (c) J. R. Reimers and N. S. Hush, *J. Chem. Phys.* **95**, 9773 (1991); (d) J. Zeng, N. S. Hush, and J. R. Reimers, *J. Chem. Phys.* **99**, 10459 (1995); (e) K. K. Stavrev, M. C. Zerner, and T. J. Meyer, *J. Am. Chem. Soc.* **117**, 8684 (1995); (f) S. Woitellier, J. P. Launay, and C. Joachim, *Chem. Phys.* **131**, 481 (1989); (g) C. Joachim, J. P. Launay, and S. Woitellier, *Chem. Phys.* **147**, 131 (1990); (h) C. Joachim and J. P. Launay, *J. Mol. Electr.* **6**, 37 (1990).
3. (a) J. W. Lauher, *Inorg. Chim. Acta* **39**, 119 (1980); (b) M. J. Ondrechen, M. A. Ratner, and D. E. Ellis, *J. Am. Chem. Soc.* **103**, 1656 (1981); (c) M. J. Ondrechen, D. E. Ellis, and M. A. Ratner, *Chem. Phys. Lett.* **109**, 50 (1984); (d) L.-T. Zhang, J. Ko, and M. J. Ondrechen, *J. Am. Chem. Soc.* **109**, 1666 (1987).
4. (a) A. Broo and S. Larsson, *Chem. Phys.* **161**, 363 (1992); (b) M. D. Newton, *J. Phys. Chem.* **92**, 3049 (1988); (c) M. D. Newton, *J. Phys. Chem.* **90**, 3734 (1986); (d) H. Itagaki, N. N. Koga, K. Morokuma, and Y. Saito, *Organometallics* **12**, 1648 (1993); (e) J.-F. Riehl, N. Koga, and K. Morokuma, *J. Am. Chem. Soc.* **116**, 5414 (1994); (f) Y. Wakatsuki, N. Koga, H. Yamazaki, and K. Morokuma, *J. Am. Chem. Soc.* **116**, 8105 (1994); (g) P. E. M. Siegbahn, *J. Phys. Chem.* **99**, 12723 (1995); (h) R. Åkesson, L. G. M. Pettersson, M. Sandström, and U. Wahlgren, *J. Am. Chem. Soc.* **116**, 8691 (1994); (i) A. L. Sargent and M. B. Hall, *J. Comp. Chem.* **12**, 923 (1991).
5. A. Veillard, *Chem. Rev.* **91**, 743 (1991).
6. P. E. M. Siegbahn and M. Svensson, *Chem. Phys. Lett.* **216**, 147 (1993).
7. See, for instance, K. M. Mackay, and R. A. Mackay, *Introduction to Modern Inorganic Chemistry* (International Textbook Co., London, 1981).
8. GAMESS: M. W. Schmidt, K. K. Baldridge, J. A. Boatz, T. S. Elbert, M. S. Gordon, J. H. Jensen, S. Koseki, N. Matsunaga, K. A. Nguyen, S. Su, T. L. Windus, M. Dupuis, and J. A. Montgomery, Jr., *J. Comp. Chem.* **14**, 1347 (1993); M. J. Frisch, G. W. Trucks, H. B. Schlegel, P. M. W. Gill, B. G. Johnson, M. A. Robb, J. R. Cheeseman, T. Keith, G. A. Petersson, J. A. Montgomery, K. Raghavachari, M. A. Al-Laham, V. G. Zakrzewski, J. V. Ortiz, J. B. Foresman, C. Y. Peng, P. Y. Ayala, W. Chen, M. W. Wong, J. L. Andres, E. S. Replogle, R. Gomperts, R. L. Martin, D. J. Fox, J. S. Binkley, D. J. Defrees, J. Baker, J. P. Stewart, M. Head-Gordon, C. Gonzalez, and J. A. Pople, *Gaussian 94, Revision B.3* (Gaussian, Inc., Pittsburgh, PA, 1995).
9. W. J. Stevens, H. Basch, and M. Krauss, *J. Chem. Phys.* **81**, 6026 (1984); W. J. Stevens, H. Basch, M. Krauss, and P. Jasien, *Can. J. Chem.* **70**, 612 (1992); T. R. Cundari and W. J. Stevens, *J. Chem. Phys.* **98**, 5555 (1993).
10. STO-3G: W. J. Hehre, R. F. Stewart, and J. A. Pople, *J. Chem. Phys.* **51**, 2657 (1969); W. J. Hehre, R. Ditchfield, R. F. Stewart, and J. A. Pople, *J. Chem. Phys.* **52**, 2769 (1970); 6-31G: R. Ditchfield, W. J. Hehre, and J. A. Pople, *J. Chem. Phys.* **54**, 724 (1971); W. J. Hehre, R. Ditchfield, and J. A. Pople, *J. Chem. Phys.* **56**, 2257 (1972).
11. P. J. Hay and W. R. Wadt, *J. Chem. Phys.* **82**, 299 (1985).
12. D95: T. H. Dunning, Jr. and P. J. Hay, in *Methods of Electronic Structure Theory*, H. F. Shaefer III, Ed. (Plenum Press, New York, 1977), Chap. 1, pp. 1-27.
13. 3-21G: K. D. Dobbs and W. J. Hehre, *J. Comput. Chem.* **8**, 880 (1987).
14. MIDI: S. Huzinaga, J. Andzelm, M. Klobulowski, E. Radzio-Andzelm, Y. Sakai, and H. Tatewaki, *Gaussian Basis Sets for Molecular Calculations* (Elsevier, Amsterdam, 1984).
15. R. F. Stewart, *J. Chem. Phys.* **52**, 321 (1970).
16. S. P. Walsh, C. W. Bauschlicher, Jr., C. J. Nelin, *J. Chem. Phys.* **79**, 3600 (1983).
17. H. C. Stynes and J. A. Ibers, *Inorg. Chem.* **10**, 2304 (1971).
18. P. Bernhard, H.-B. Bürgi, J. Hauser, H. Lehmann, and A. Ludi, *Inorg. Chem.* **21**, 3936 (1982).
19. W. Böttcher, G. M. Brown, and N. Sutin, *Inorg. Chem.* **18**, 1447 (1979).
20. S. P. Arnese and H. M. Seip, *Acta Chem. Scand.* **20**, 2711 (1966).
21. R. A. Jones, G. Wilkinson, A. M. R. Galas, M. B. Hursthouse, and K. M. A. Malik, *J. Chem. Soc., Dalton Trans.* 1771 (1980).
22. R. A. Marcus, *Discuss. Faraday Soc.* **29**, 21 (1960); *Ibid.*, *Annu. Rev. Phys. Chem.* **15**, 155 (1964); *Ibid.*, *J. Chem. Phys.* **43**, 679 (1965); N. S. Hush, *Trans. Faraday Soc.* **57**, 155 (1961); B. S. Brunschwig, J. Logan, M. D. Newton, and N. Sutin, *J. Am. Chem. Soc.* **102**, 5798 (1980).
23. A. Deak and J. L. Templeton, *Inorg. Chem.* **19**, 1075 (1980).
24. K. H. Schmidt and A. Müller, *Inorg. Chem.* **14**, 2183 (1975).
25. A. Ricca, C. W. Bauschlicher, Jr., and M. Rosi, *J. Phys. Chem.* **98**, 9498 (1994).
26. T. Meyer, PhD. Dissertation (Stanford University, 1966) p. 30, as referenced in P. Ford, D. F. P. Rudd, R. Gaundier, and H. Taube, *J. Am. Chem. Soc.* **90**, 1187 (1968).

27. K. Andersson, P.-Å. Malmqvist, and B. O. Roos, *J. Chem. Phys.* **96**, 1218 (1992).
28. J. D. Petke, G. M. Maggiora, and R. E. Christoffersen, *J. Phys. Chem.* **96**, 6992 (1992); J. D. Petke, G. M. Maggiora, and R. E. Christoffersen, *J. Am. Chem. Soc.* **112**, 5452 (1990).
29. R. J. Bartlett and J. F. Stanton, in *Reviews in Computational Chemistry*, K. B. Lipkowitz and D. B. Boyd, Eds. (VCH, New York, 1994), Vol. 5, Chap. 2, pp. 65-169.
30. A. Broo, manuscript under preparation.
31. A. Broo and A. Holmén, *Chem. Phys.*, in press.
32. W. J. Hehre, L. Radom, P. v. R. Schleyer, and J. A. Pople, in *Ab initio Molecular Orbital Theory* (Wiley, New York, 1986).

Gaussian Fitting Function Basis Sets for Crystalline Silicon: Bond-Centered *s*-Type vs. Site-Centered *f*-Type*

JONATHAN C. BOETTGER

Theoretical Division, Los Alamos National Laboratory, Los Alamos, New Mexico 87545

Received February 25, 1996; revised manuscript received March 28, 1996; accepted April 24, 1996

ABSTRACT

The lattice constant, cohesive energy, bulk modulus, and band gap for Si were calculated with the linear combinations of Gaussian-type orbitals-fitting function (LCGTO-FF) technique using three distinct types of charge density and exchange-correlation fitting function basis sets: (1) site-centered *s*-type GTOs only; (2) site- and bond-centered *s*-type GTOs; and (3) site-centered *s*- and *f*-type GTOs. All three basis sets produce good results for the lattice constant and bulk modulus of Si, but only the two larger basis sets determine the cohesive energy and LDA band gap accurately. The numerical results obtained with the two larger basis sets are in good quantitative agreement with each other and with results from other techniques. © 1996 John Wiley & Sons, Inc.[†]

Introduction

The linear combinations of Gaussian-type orbitals-fitting function (LCGTO-FF) method is an all-electron, full-potential, density functional, electronic structure technique characterized by its use of three independent GTO basis sets to expand the one-electron orbitals, charge density, and exchange correlation (XC) integral kernels. The LCGTO-FF technique is routinely used now to

perform local density approximation (LDA) calculations on molecules [1–3], polymers [4–6], ultra-thin films [7–9], and crystalline solids [10–12]. One of the primary advantages of the LCGTO-FF method over other extant LDA electronic structure techniques is this ability to treat localized (molecular) and periodically extended (crystalline) systems on an equal footing, thereby bridging the long-standing gap between quantum chemistry and solid-state physics. To exploit this advantage of the LCGTO-FF technique fully, a new computer code (GTOFF) [10] was developed recently to perform LCGTO-FF calculations on general systems with 3D, 2D, and 1D (not yet implemented) periodicities.

*The Los Alamos National Laboratory requests that the publisher identify this article as work performed under the auspices of the U.S. Department of Energy.

Although the LCGTO-FF method is, in principle, capable of producing fully consistent results for local and extended systems, in practice, there are at least two potential obstacles to making direct quantitative comparisons between results for such systems. First, there are a number of algorithmic differences between the implementation of the LCGTO-FF method generally employed for the calculations on molecules and polymers [2] and that used for most of the calculations on films and crystalline solids [8-10]. The most significant difference between the two implementations is in the technique used for fitting the XC integral kernels. In the molecular formulation, the unfitted XC integral kernels are formed from the exact electron density, whereas GTOFF forms the unfitted XC kernels from the fitted density. Since formation of the exact electron density is a time-consuming process for crystalline solids [10], the impact of this algorithmic distinction can be most efficiently addressed via molecular calculations and, hence, lies beyond the scope of the present work using GTOFF.

The second potential obstacle to direct comparison of LCGTO-FF calculations for various types of systems is more subtle. LCGTO-FF calculations for molecules occasionally have used bond-centered *s*-type GTO fitting functions to achieve accurate numerical results without including large-*l* GTO fitting functions in the site-centered expansions [13]. In contrast, nearly all calculations for films and crystalline solids have used site-centered fitting functions only, since the higher symmetry of these systems often excludes many components of the larger *l*-type fitting functions and the lengthy Coulomb lattice sums converge more rapidly for the large-*l* charge fitting functions than for the *s*-type charge fitting functions. This systematic difference between the fitting function basis sets used in molecular and crystalline LCGTO-FF calculations raises questions about the relative merits of these two approaches to fitting the charge density and XC kernels and the extent to which results obtained using the two approaches can be compared directly.

In this investigation, these questions are addressed by calculating the properties of crystalline Si, in the cubic diamond structure, with GTOFF, using three types of fitting function basis sets: (1) site-centered *s*-type fitting functions only; (2) site- and bond-centered *s*-type fitting functions; and (3) site-centered *s*- and *f*-type fitting functions. This particular test case has been chosen for several

reasons: Most importantly, cubic Si has well-defined tetrahedral bonds, which ensure that the site-centered *s*-type only basis will be severely taxed. In addition, crystalline Si has been studied recently with at least two other all-electron, full-potential, electronic structure techniques [14, 15], which provide an external reference for the present study. Finally, since Si routinely appears in molecules, polymers, surfaces, and crystals that are of great technological importance, consistent calculations for these various types of systems could prove to be invaluable.

The implementation of the LCGTO-FF method used in GTOFF was discussed in considerable detail elsewhere [8-10]. That discussion will not be repeated here. Instead, the following section discusses only those methodological details that are peculiar to this particular investigation. Results are presented and discussed in the third section. A few concluding remarks are given in the final section.

Computational Details

The orbital basis set used here was derived from Huzinaga's 11*s7p* atomic basis [16]. To reduce the size of the secular matrix, the atomic basis set was contracted into a 6*s4p* basis set using contraction coefficients derived from a series of atomic calculations using the same LDA parameterization as was subsequently used for the crystal (Hedin-Lundqvist [17]). The orbital basis set then was augmented with a single *d*-type GTO, whose exponent was found to minimize approximately the total energy of crystalline Si in a series of test calculations. The final 6*s4p1d* orbital basis set used here is shown in Table I.

The site-centered *s*-type-only charge and XC fitting function basis sets used here each consisted of nine GTOs (see Table II). The exponents for these sets were selected on the basis of previous experience with a wide range of materials and were fine-tuned by requiring that the site-centered *s*-type fitting functions should produce good results for an isolated Si atom. The site-centered *s*-type basis sets were then augmented as desired either with two site-centered *f*-type functions, with only the *xyz* component retained due to symmetry considerations, or by a single *s*-type function in the center of each bond (see Table II). Since there

TABLE I

Gaussian exponents (α) and contraction coefficients (C) of the orbital set used for Si; horizontal lines separate the contractions.

s-Type		p-Type		d-Type	
α	C	α	C	α	C
26737.389	0.0010354	163.73270	0.0118853	0.45	1.00
4076.3786	0.0077158	38.352081	0.0805337		
953.29315	0.0376661	12.021114	0.2705100		
274.58441	0.1368397	4.1845733	0.4640613		
90.681987	0.2433422	1.4827170	1.0000000		
90.681987	0.0924999	0.33498569	1.0000000		
33.529057	0.4327388	0.09699384	1.0000000		
13.457629	0.1933028				
4.0506916	1.0000000				
1.4841839	1.0000000				
0.27044323	1.0000000				
0.09932161	1.0000000				

are two atomic sites and four bond centers in each primitive unit cell of the diamond structure, both augmentation schemes add a total of four GTOs to each of the fitting function basis sets. No effort was made to optimize the exponents of these additional fitting functions.

In all calculations reported here, the Brillouin zone (BZ) integrals were evaluated over the entire BZ on a uniform $6 \times 6 \times 6$ mesh, with 16 irreducible points, using the histogram technique. One-electron eigenvalues were calculated at three additional k -points along the Δ -axis, near the X-point, to allow an accurate determination of the indirect band gap for Si. The SCF portion of each calculation was iterated until the total energy var-

ied by less than $1 \mu\text{Ry/atom}$. All the calculations were nonrelativistic.

Results

For each of the fitting function schemes described above, the total energy of crystalline Si was calculated at six lattice constants: 10.0, 10.1, 10.2, 10.26, 10.3, and 10.4, all in bohr. Binding energies were then obtained by subtracting the energy of an isolated, spin-polarized Si atom, -576.391596 Ry , as determined from an atomic calculation with one additional diffuse p -type GTO added to the orbital basis set to compensate for the effect of the orbital basis functions on neighboring sites during the crystalline calculations. Finally, the equilibrium lattice constants (a_0), cohesive energies (E_c), and bulk moduli (B) were obtained by fitting the calculated binding energies with a slightly modified form [18] of the universal equation of state [19]. Each fit had a standard deviation of less than 0.01 mRy/atom . The equilibrium band gap (E_g) for each series of calculations was then determined via linear interpolation.

In Table III, the equilibrium properties of Si obtained with the three fitting function schemes discussed earlier are compared with results from recent calculations using the scalar-relativistic full-potential linearized muffin-tin orbital (FP-LMTO) method and the full-potential Korringa-Kohn-Rostoker (FKKR) method with fully rela-

TABLE II

Gaussian exponents of the site-centered s-type, site-centered f-type, and bond-centered s-type charge and XC basis sets used for Si.

Charge			XC		
Site s	Site f	Bond s	Site s	Site f	Bond s
1000.00	1.00	1.00	360.00	1.00	1.00
260.00	0.30		90.00	0.30	
72.00			27.00		
24.00			9.00		
8.10			3.00		
2.70			1.00		
0.90			0.36		
0.35			0.17		
0.13			0.08		

TABLE III

The lattice constant (a_0 , in bohr), static lattice cohesive energy (E_c , in eV / atom), bulk modulus (B , in GPa), and band gap (E_g , in eV) obtained here for silicon with the LCGTO-FF method, using three different fitting function basis sets, compared with previous results from FP-LMTO [14] and FKRR [15] calculations and experimental data [20]; except B , which is taken from [21].

	a_0	E_c	B	E_g
FP-LMTO	10.22	5.18	95	
FKRR	10.24		96	0.49
Site s	10.25	5.26	101	0.76
Site s + bond s	10.25	5.14	97	0.52
Site s + site f	10.25	5.14	99	0.51
Experiment	10.26	4.63	98	1.17

tivistic cores and nonrelativistic valence electrons. Table III also lists experimental values for the various parameters [20, 21]. Several interesting features are readily apparent in Table III: First, the lattice constants and bulk moduli obtained here with the three fitting function schemes are nearly identical, with the lattice constants varying by less than 0.1% and the bulk moduli varying by about 4%, a negligible variation for a fitted second derivative. This insensitivity of a_0 and B to changes in the fitting function basis sets reflects the overall robustness of the fitting algorithms used in GTOFF, especially the variational charge fit [1]. The various LCGTO-FF results for a_0 and B are all in slightly better agreement with the experimental data than are the corresponding FP-LMTO and FKRR results.

Although the cohesive energies obtained with the different fitting function schemes vary only by 0.12 eV/atom ($\approx 2\%$), that energy difference is significant. The cohesive energy from the s -type only calculation is *larger* than are the cohesive energies obtained with the richer basis sets because the variational charge fit procedure ensures that the fitted Coulomb energy is a *lower* bound to the exact Coulomb energy [1]. The virtually perfect agreement between the cohesive energies obtained with the two augmented fitting function basis sets once again demonstrates the robustness of the fitting function algorithms being used here, i.e., any reasonable extension of the basis set beyond the s -type-only approximation is sufficient to achieve a well-converged result for the cohesive energy. The cohesive energies obtained with the augmented

fitting function basis sets differ from the FP-LMTO value by only 0.04 eV ($< 1\%$), an excellent agreement for two completely different electronic structure techniques. All the theoretical results exhibit the usual LDA overbinding.

The parameter in Table III that best illustrates the overall inadequacy of the s -type-only approximation is the band gap. The s -type-only basis set produces a band gap (0.76 eV) that is roughly 0.25 eV larger than the band gaps obtained with the two richer fitting function basis sets (0.51 and 0.52 eV) or with other electronic structure methods, 0.49 eV [15] \rightarrow 0.52 eV [22]. This sensitivity of the band gap to the richness of the fitting function basis is not surprising given the variational nature of the charge fit procedure. The one-electron eigenvalues for the unoccupied states and the band gap have no variational significance during an electronic structure calculation and, thus, will be "sacrificed" to ensure that the occupied one-electron eigenvalues are well represented. As was true for the cohesive energy, either augmentation scheme provides enough additional flexibility in the fitting function basis set to allow a precise estimate of the LDA band gap, which is, as usual [22], much smaller than the experimental gap of 1.17 eV [20].

Conclusions

It has been demonstrated here that the LCGTO-FF technique is an exceptionally robust electronic structure method for determining the ground-state properties of crystals within the context of the LDA. Even the crudest fitting function basis set used here, the site-centered s -type-only basis set, produces excellent results for the lattice constant and bulk modulus of Si and only misses the converged cohesive energy by 0.12 eV/atom. This is a remarkable result given the fact that crystalline Si should be one of the more difficult systems to describe with GTO fitting functions, due to its highly directional tetrahedral bonding.

The LCGTO-FF method has a substantially more difficult time describing the band gap of crystalline Si, since the gap is not a ground-state property. For this reason, the site-centered s -type-only basis set proved inadequate for determining the band gap and should not be used for any application in which the conduction states of a tetrahedral semiconductor must be described accu-

rately. The band gap can be determined accurately if the site-centered *s*-type basis set is augmented with either site-centered *f*-type GTOs or bond-centered *s*-type GTOs.

The results obtained for crystalline Si with the two types of augmented fitting function basis sets are nearly indistinguishable. This result suggests that LCGTO-FF cluster calculations using bond-centered *s*-type fitting functions should be fully consistent with LCGTO-FF crystalline calculations using site-centered *f*-type fitting functions, so long as there are no significant algorithmic differences between the codes used for the two calculations.

ACKNOWLEDGMENT

This work was supported by the U.S. Department of Energy.

References

1. B. I. Dunlap, J. W. D. Connolly, and J. R. Sabin, *J. Chem. Phys.* **7**, 3396 (1979); *Ibid.*, *J. Chem. Phys.* **71**, 4993 (1979).
2. B. I. Dunlap and N. Rösch, *Adv. Quantum Chem.* **21**, 317 (1990).
3. J. L. Ballester and B. I. Dunlap, *Phys. Rev. A* **45**, 7985 (1992).
4. J. W. Mintmire and C. T. White, *Phys. Rev. Lett.* **50**, 101 (1983); *Ibid.*, *Phys. Rev. B* **27**, 1447 (1983).
5. J. W. Mintmire and C. T. White, *Phys. Rev. B* **28**, 3283 (1983).
6. J. W. Mintmire, *Phys. Rev. B* **39**, 13350 (1989).
7. J. W. Mintmire, J. R. Sabin, and S. B. Trickey, *Phys. Rev. B* **26**, 1743 (1982).
8. J. C. Boettger, *Inter. J. Quantum Chem. Symp.* **27**, 147 (1993); also see, J. C. Boettger and S. B. Trickey, *Phys. Rev. B* **32**, 1356 (1985).
9. U. Birkenheuer, J. C. Boettger, and N. Rösch, *J. Chem. Phys.* **100**, 6826 (1994).
10. J. C. Boettger, *Int. J. Quantum Chem. Symp.* **29**, 197 (1995).
11. J. C. Boettger and S. B. Trickey, *Phys. Rev. B* **51**, 15623 (1995).
12. J. C. Boettger and J. M. Wills, unpublished.
13. B. I. Dunlap, personal communication.
14. A. K. McMahan, J. E. Klepeis, M. van Schilfgaarde, and M. Methfessel, *Phys. Rev. B* **50**, 10742 (1994).
15. S. Bei der Kellen, Y. Oh, E. Badraxe, and A. J. Freeman, *Phys. Rev. B* **51**, 9560 (1995), and references therein.
16. S. Huzinaga, *Approximate Atomic Functions II*, Report (Dept. of Chemistry, University of Alberta, 1971).
17. L. Hedin and B. I. Lundqvist, *J. Phys. C* **4**, 2064 (1971).
18. J. C. Boettger and S. B. Trickey, *Phys. Rev. B* **53**, 3007 (1996).
19. A. Banerjee and J. R. Smith, *Phys. Rev. B* **37**, 6632 (1988).
20. C. Kittel, *Introduction To Solid State Physics*, 5th ed. (Wiley, New York, 1976).
21. P. Becker and G. Mana, *Metrologia* **31**, 203 (1994).
22. M. Schlüter and L. J. Sham, *Adv. in Quantum Chem.* **21**, 97 (1990).

Reaction Energetics of Tetrahedrane and Other Hydrocarbons: Ab Initio and Density Functional Treatments

JORGE M. SEMINARIO AND PETER POLITZER

Department of Chemistry, University of New Orleans, New Orleans, Louisiana 70148

HUMBERTO J. SOSGUN M.*

Department of Chemistry, UMIST P.O. Box 88, Manchester, M60 1QD, United Kingdom

ANGÉLICA G. ZACARÍAS AND MIGUEL CASTRO

Departamento de Física y Química Teórica, y Departamento de Química Inorgánica, Universidad Nacional Autónoma de México, C.P. 04510, México D.F., México

Received March 1, 1996; accepted April 18, 1996

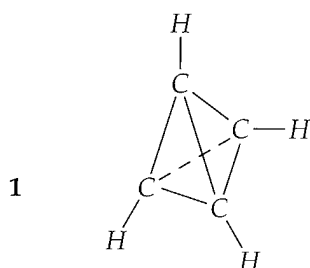
ABSTRACT

Reaction energetics of the highly strained tetrahedrane molecule, as well as some smaller hydrocarbons, were computed at the ab initio MP4, QCISD (T), G1, and G2 levels and also by several density functional (DF) approaches: VWN(LDA), PW86, BLYP, and B3LYP. A variety of basis sets were used in the DF calculations. For atomization processes, nonlocal DF procedures are superior to MP4 and QCI. For the other reactions, B3LYP is the most reliable DF approach and is overall competitive with MP4 and QCISD (T), although the MP4/6-311G(2df, p) results are generally the closest to the experimental and/or the G2 values. There is no consistent correlation between the accuracy of the DF results and the size of the basis set. © 1996 John Wiley & Sons, Inc.

* On leave from Departamento de Química, Facultad Experimental de Ciencias, La Universidad de Zulia, Maracaibo, Venezuela.

Introduction

While a considerable amount of evidence already attests to the effectiveness of nonlocal density functional methods for computing molecular properties and reaction energetics [1–26], there remains a continuing need to evaluate various combinations of exchange and correlation functionals and basis sets. In the present work, we extended such comparative investigations to the highly strained molecule tetrahedrane, 1:



This compound has not yet been isolated [27], although it has been claimed to be an intermediate in several reactions [28]. Estimates of strain energy [27] and a quantitative measure of bond bending [29] both confirm its extremely strained nature. Our present objective was to compare the results of various ab initio and density functional treatments of this molecule and its reaction energetics, as well as those of some smaller hydrocarbons.

Methods

We computed the geometries and energies of tetrahedrane and some other hydrocarbons with several ab initio and density functional (DF) methods. The former included Hartree–Fock (HF), Møller–Plesset perturbation theory (MP), and quadratic configuration interaction (QCI). The density functional procedures involved the Becke (B) [30] and Becke three-parameter-hybrid (B3) [31] exchange functionals and the Perdew-86 (P86) [32]

TABLE I
Ab initio energies and geometries for tetrahedrane.

Method	Energy (Hartrees)	Bond lengths (Å)	
		C—C	C—H
HF / 6-31G(d)	–153.59789	1.463	1.062
HF / 6-31G(d, p)	–153.60704	1.463	1.062
HF / 6-311G(d, p)	–153.63451	1.465	1.062
MP2 / 6-31G(d, p)	–154.14019	1.478	1.067
MP2 = Full / 6-31G(d, p)	–154.16113	1.476	1.066
MP2 / 6-311G(d, p)	–154.19211	1.484	1.072
MP2 = Full / 6-311G(d, p)	–154.26843	1.482	1.071
MP2 / 6-311G(2df, p)	–154.27430	1.476	1.070
HF / 6-311G(d, p) // MP2 / 6-311G(d, p)	–153.63339	1.484	1.072
HF / 6-311 + G(d, p) // MP2 / 6-311G(d, p)	–153.63499	1.484	1.072
HF / 6-311G(2df, p) // MP2 / 6-311G(d, p)	–153.64308	1.484	1.072
HF / 6-311 + G(3df, 2p) // MP2 / 6-311G(d, p)	–153.64958	1.484	1.072
MP2 / 6-311 + G(d, p) // MP2 / 6-311G(d, p)	–154.19584	1.484	1.072
MP3 / 6-311G(d, p) // MP2 / 6-311G(d, p)	–154.21238	1.484	1.072
MP3 / 6-311 + G(d, p) // MP2 / 6-311G(d, p)	–154.21543	1.484	1.072
QCISD(T) / 6-311G(d, p) // MP2 / 6-311G(d, p)	–154.24319	1.484	1.072
MP4 / 6-311G(d, p) // MP2 / 6-311G(d, p)	–154.24359	1.484	1.072
MP4 / 6-311 + G(d, p) // MP2 / 6-311G(d, p)	–154.24719	1.484	1.072
MP2 / 6-311G(2df, p) // MP2 / 6-311G(d, p)	–154.27418	1.484	1.072
MP3 / 6-311G(2df, p) // MP2 / 6-311G(d, p)	–154.29230	1.484	1.072
MP2 / 6-311 + G(3df, 2p) // MP2 / 6-311G(d, p)	–154.29308	1.484	1.072
MP4 / 6-311G(2df, p) // MP2 / 6-311G(d, p)	–154.32804	1.484	1.072
G1 // MP2 / 6-311G(d, p)	–154.33482	1.484	1.072
G2 // MP2 / 6-311G(d, p)	–154.33858	1.484	1.072

and Lee, Yang, and Parr (LYP) [33] correlation functionals. All this work was carried out with the Gaussian 92/DFT and Gaussian 94 programs [34, 35]. A variety of basis sets, some including a considerable number of polarization terms, were used; these are enumerated in Tables I and II.

We also used the code *deMon* [36, 37] for a DF calculation with the Perdew-Wang (PW 86) exchange-correlation functional [32, 38, 39] and, for completeness, a local density approximation (LDA) treatment with the Vosko-Wilk-Nusair (VWN) correlation functional [40]. The basis set for these *deMon* studies was the DZVP2 [41], which is similar to the Gaussian 6-31G(*d, p*). In addition, auxiliary basis sets containing *s*-, *p*-, and *d*-type functions were used to fit the density and the exchange/correlation potential and energies [41].

Since no experimental data are available for tetrahedrane, we compared our results to values obtained by the *ab initio* Gaussian-1 (G1) and Gaussian-2 (G2) procedures, which were designed to achieve a very high level of accuracy [42-44]. For the latter, we used MP2/6-311G(*d, p*)-opti-

mized geometries instead of the prescribed MP2/6-31G(*d*) and improved the energies through subsequent MP4/6-311+G(3*df, 2p*) and QCISD(T)/6-311+G(3*df, 2p*) calculations plus empirical corrections. These results are generally expected to be accurate to within < 2 kcal/mol [42-44], although larger errors have been reported in certain instances [45, 46].

Results and Discussion

TETRAHEDRANE ENERGIES AND GEOMETRIES

The total energies and optimized bond lengths obtained for tetrahedrane by the various approaches are given in Tables I and II. The *ab initio* results include a series of single-point calculations at various levels using a fixed geometry, the MP2/6-311G(*d, p*).

A striking feature of the computed bond lengths is their uniformity. If the HF (uncorrelated) values

TABLE II
Density functional energies and geometries for tetrahedrane.

Method	Energy (Hartrees)	Bond lengths (Å)	
		C—C	C—H
VWN / DZVP2(LDA)	-153.24990	1.485	1.082
BLYP / 6-31G(<i>d</i>)	-154.55969	1.493	1.080
BLYP / 6-31G(<i>d, p</i>)	-154.56745	1.493	1.078
BLYP / 6-311G(<i>d, p</i>)	-154.60545	1.492	1.076
BLYP / 6-311+G(<i>d, p</i>)	-154.60825	1.492	1.076
BLYP / 6-311G(2 <i>df, p</i>)	-154.61283	1.486	1.075
BLYP / 6-311+G(2 <i>df, p</i>)	-154.61575	1.487	1.076
BLYP / 6-311+G(2 <i>df, 2pd</i>)	-154.61881	1.487	1.074
BLYP / 6-311+G(3 <i>df, 2p</i>)	-154.61989	1.487	1.074
BLYP / 6-311+G(3 <i>df, 2pd</i>)	-154.62061	1.487	1.074
BLYP / 6-311++G(3 <i>df, 3pd</i>)	-154.62107	1.487	1.074
B3LYP / 6-31G(<i>d</i>)	-154.63669	1.479	1.073
B3LYP / 6-31G(<i>d, p</i>)	-154.64466	1.479	1.072
B3LYP / 6-311G(<i>d, p</i>)	-154.67888	1.479	1.070
B3LYP / 6-311+G(<i>d, p</i>)	-154.68109	1.475	1.068
B3LYP / 6-311G(2 <i>df, p</i>)	-154.68697	1.474	1.069
B3LYP / 6-311+G(2 <i>df, p</i>)	-154.68929	1.474	1.069
B3LYP / 6-311+G(2 <i>df, 2pd</i>)	-154.69224	1.474	1.068
B3LYP / 6-311+G(3 <i>df, 2p</i>)	-154.69350	1.474	1.068
B3LYP / 6-311+G(3 <i>df, 2pd</i>)	-154.69411	1.474	1.068
B3LYP / 6-311++G(3 <i>df, 3pd</i>)	-154.69447	1.475	1.068
BP86 / 6-311++G(3 <i>df, 3pd</i>)	-154.69672	1.484	1.077
PW86 / DZVP2	-154.87135	1.494	1.079
B3P86 / 6-31++G(3 <i>df, 3pd</i>)	-155.20317	1.470	1.068

TABLE III
Calculated total energies (Hartrees) and zero-point energies (kcal/mol) of reactants and products in Eqs. (1)–(5).

Method	H	C	H ₂	CH	CH ₄	C ₂ H ₂	C ₂ H ₄	C ₂ H ₆	C ₄ H ₄
Total energies									
MP4/6-311G(d,p) ^a	-0.49981	-37.76430	-1.16772	-38.38606	-40.40503	-77.13994	-78.38239	-79.61452	-154.24359
MP4/6-311+G(d,p) ^a	-0.49981	-37.76520	-1.16772	-38.38775	-40.40533	-77.14186	-78.38425	-79.61518	-154.24719
MP4/6-311G(2df,p) ^a	-0.49981	-37.77483	-1.16772	-38.40073	-40.42466	-77.17987	-78.42246	-79.65286	-154.32804
QCISD(T)/6-311G(d,p) ^a	-0.49981	-37.76669	-1.16832	-38.38959	-40.40589	-77.13976	-78.38414	-79.61579	-154.24319
G1 ^a	-0.50000	-37.78464	-1.16501	-38.41220	-40.40772	-77.18602	-78.41401	-79.62656	-154.33482
G2 ^b	-0.50000	-37.78432	-1.16636	-38.41258	-40.41088	-77.18574	-78.41593	-79.63090	-154.33858
VWN/DZVP2(LDA) ^c	-0.47637	-37.46400	-1.13696	-38.08767	-40.11150	-76.60440	-77.84131	-79.05973	-153.24990
PW86/DZVP2 ^c	-0.50000	-37.89129	-1.18334	-38.53250	-40.57768	-77.43840	-78.70338	-79.94750	-154.87135
BLYP/6-31G(d)	-0.49545	-37.83202	-1.16526	-38.46084	-40.47913	-77.29129	-78.53712	-79.76322	-154.55969
BLYP/6-311G(d,p)	-0.49545	-37.83202	-1.16791	-38.46238	-40.48467	-77.29521	-78.54340	-79.77149	-154.56745
BLYP/6-311+G(d,p)	-0.49755	-37.84267	-1.16917	-38.47434	-40.49623	-77.32273	-78.56603	-79.79199	-154.60545
BLYP/6-311G(2df,p)	-0.49755	-37.84447	-1.16917	-38.47691	-40.49651	-77.32513	-78.56787	-79.79241	-154.60825
BLYP/6-311+G(2df,p)	-0.49755	-37.84285	-1.16917	-38.47565	-40.49743	-77.32642	-78.56958	-79.79457	-154.61283
BLYP/6-311+G(2df,2pd)	-0.49755	-37.84465	-1.16917	-38.47809	-40.49780	-77.32858	-78.57144	-79.79512	-154.61575
BLYP/6-311+G(3df,2p)	-0.49755	-37.84465	-1.16960	-38.47874	-40.50018	-77.33024	-78.57402	-79.79861	-154.61881
BLYP/6-311+G(3df,2pd)	-0.49755	-37.84468	-1.16960	-38.47871	-40.49930	-77.33030	-78.57339	-79.79725	-154.61989
BLYP/6-311+G(3df,3pd)	-0.49755	-37.84468	-1.16960	-38.47897	-40.50015	-77.33065	-78.57436	-79.79865	-154.62061
B3LYP/6-31G(d)	-0.50027	-37.84468	-1.16961	-38.47910	-40.50006	-77.33071	-78.57447	-79.79872	-154.62107
B3LYP/6-31G(d,p)	-0.50027	-37.84628	-1.17548	-38.47916	-40.51839	-77.32565	-78.58746	-79.83042	-154.63669
B3LYP/6-311G(d,p)	-0.50216	-37.84628	-1.17854	-38.48080	-40.52402	-77.32957	-78.59381	-79.83874	-154.64466
B3LYP/6-311+G(d,p)	-0.50216	-37.85599	-1.17957	-38.49198	-40.53375	-77.35470	-78.61398	-79.85626	-154.67888
B3LYP/6-311+G(2df,p)	-0.50216	-37.85727	-1.17957	-38.49401	-40.53393	-77.35665	-78.61551	-79.85654	-154.68109
B3LYP/6-311+G(2df,p)	-0.50216	-37.85745	-1.17957	-38.49331	-40.53500	-77.35873	-78.61773	-79.85895	-154.68697
B3LYP/6-311+G(2df,2pd)	-0.50216	-37.85745	-1.18001	-38.49521	-40.53525	-77.36047	-78.61930	-79.85935	-154.68929
B3LYP/6-311+G(3df,2p)	-0.50216	-37.85747	-1.18001	-38.49584	-40.53756	-77.36203	-78.62178	-79.86272	-154.69224
B3LYP/6-311+G(3df,2pd)	-0.50216	-37.85747	-1.18001	-38.49586	-40.53679	-77.36200	-78.62120	-79.86155	-154.69350
B3LYP/6-311+G(3df,3pd)	-0.50226	-37.85747	-1.18003	-38.49607	-40.53756	-77.36230	-78.62206	-79.86281	-154.69411
Zero-point energies									
ZPE(G) ^d	0	0	5.9	3.9	26.8	16.5	30.7	44.7	36.3
ZPE(DFT) ^e	0	0	6.3	4.1	28.0	16.9	31.9	46.7	37.3

^a From [42], except C₄H₄, which is from Table I.

^b From [44], except C₄H₄, which is from Table I.

^c From [11], except C₄H₄, which is from Table II.

^d From [42], except C₄H₄, which is computed in this work.

^e Computed in this work at the B3LYP/6-311+G(3df,3pd) level.

are excluded, the range in the C—C distances is only 1.470–1.494 Å, and for the C—H, 1.068–1.079 Å. The nature of the theoretical approach is more significant than is the particular basis set being used; e.g., the C—C bond lengths obtained at the BLYP level are all within a range of only 0.007 Å, whereas replacing the B exchange functional by the B3 typically decreases the C—C distance by about 0.013 Å.

The B3 exchange functional also has a very consistent effect upon the energies when coupled with LYP correlation. For any particular basis set, the B3LYP total energy is about 0.074 Hartree

more negative than is the BLYP. However, with the P86 correlation functional, replacing the B exchange by B3 lowers the energy by fully 0.5 Hartree.

The effect of the basis set is brought out particularly clearly by the various ab initio single-point calculations with the same MP2/6-311G(*d, p*) geometry (Table I). For example, in two instances, MP2 energies are lower than those of MP4, because the former basis sets have more polarization functions. The significance of these in describing this highly strained molecule with its markedly bent bonds [29] is demonstrated by the improve-

TABLE IV
Calculated atomization energies (kcal/mol).

Method	H ₂	CH	CH ₄	C ₂ H ₂	C ₂ H ₄	C ₂ H ₆	Average error
Ab initio							
MP4/6-311G(<i>d, p</i>) ^a	99.6	72.6	375.8	367.4	505.5	637.5	17.4
MP4/6-311+G(<i>d, p</i>) ^a	99.6	73.1	375.4	367.4	505.6	636.7	17.5
MP4/6-311G(2 <i>df, p</i>) ^a	99.6	75.2	381.5	379.2	517.5	648.3	10.3
QCISD(T)/6-311G(<i>d, p</i>) ^a	99.9	73.3	374.8	364.2	503.6	635.3	18.6
G1 ^b	103.5	80.0	391.0	387.0	530.1	663.5	1.4
G2 ^c	104.4	80.5	393.2	387.2	531.7	666.6	0.8
Density functional							
VWN/DZVP2(LDA) ^d	109.3	88.4	437.7	437.2	600.5	752.5	43.8
PW86/DZVP2 ^d	108.7	84.6	402.8	394.6	545.9	684.3	9.7
BLYP/6-31G(<i>d</i>)	103.1	79.6	389.5	382.4	527.3	660.2	3.4
BLYP/6-31G(<i>d, p</i>)	104.8	80.6	393.0	384.9	531.3	665.4	1.4
BLYP/6-311G(<i>d, p</i>)	102.9	80.1	388.3	386.1	526.9	657.0	3.6
BLYP/6-311+G(<i>d, p</i>)	102.9	80.6	387.4	385.4	525.7	655.0	4.5
BLYP/6-311G(2 <i>df, p</i>)	102.9	80.8	388.9	388.2	528.9	658.4	2.7
BLYP/6-311+G(2 <i>df, p</i>)	102.9	81.2	388.0	387.3	527.8	656.5	3.6
BLYP/6-311+G(2 <i>df, 2pd</i>)	103.2	81.6	389.5	388.4	529.4	658.7	2.6
BLYP/6-311+G(3 <i>df, 2p</i>)	103.2	81.6	389.0	388.4	528.9	657.8	2.9
BLYP/6-311+G(3 <i>df, 2pd</i>)	103.2	81.7	389.5	388.6	529.6	658.7	2.5
BLYP/6-311++G(3 <i>df, 3pd</i>)	103.0	81.7	389.0	388.4	529.2	658.1	2.8
B3LYP/6-31G(<i>d</i>)	103.5	79.2	393.1	380.0	528.9	666.3	2.3
B3LYP/6-31G(<i>d, p</i>)	105.4	80.2	396.7	382.5	532.9	671.6	3.2
B3LYP/6-311G(<i>d, p</i>)	103.7	79.9	391.9	383.7	528.7	663.3	2.1
B3LYP/6-311+G(<i>d, p</i>)	103.7	80.4	391.2	383.3	528.0	661.8	2.7
B3LYP/6-311G(2 <i>df, p</i>)	103.7	80.6	392.6	386.0	530.8	664.7	1.1
B3LYP/6-311+G(2 <i>df, p</i>)	103.7	81.0	391.9	385.5	530.2	663.4	1.7
B3LYP/6-311+G(2 <i>df, 2pd</i>)	103.9	81.4	393.4	386.5	531.7	665.5	1.1
B3LYP/6-311+G(3 <i>df, 2p</i>)	103.9	81.4	392.9	386.4	531.3	664.7	1.2
B3LYP/6-311+G(3 <i>df, 2pd</i>)	103.9	81.6	393.4	385.6	531.9	665.5	1.0
B3LYP/6-311++G(3 <i>df, 3pd</i>)	103.8	81.5	393.0	386.5	531.6	665.1	1.1
Experiment ^e	103.3	80.0	392.5	388.9	531.9	666.2	0.0

^a Calculated using energies from [42].

^b [42].

^c [44].

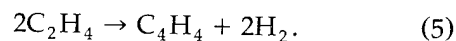
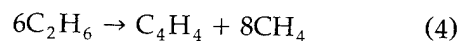
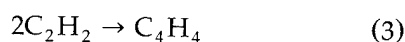
^d [11].

^e Calculated from data in Table VIII.

ment observed in going from MP2/6-311G(*d, p*) to MP2/6-311G(2*df, p*)/MP2/6-311G(*d, p*). The additional *d* and *f* functions on the carbons lower the energy by 0.08207 Hartree (51.5 kcal/mol), a quantity of chemical significance.

REACTION ENERGISTICS

Some hypothetical reactions involving tetrahedrane are shown as Eqs. (1)–(5):



In Table III are listed computed energies for the reactants and products in Eqs. (1)–(5). The *ab initio* values are taken from elsewhere [42, 44], except for tetrahedrane, and are based on MP2 = FULL/6-31G(*d*) geometries; the tetrahedrane energies are from Table I. The density functional values are from the present work, except as indicated. The zero-point energies [ZPE(G)] were obtained in the course of the G1 and G2 procedures [42, 44] and

TABLE V
Calculated ΔE values (kcal/mol) for reactions shown in Eqs. (6)–(10).

Method	Eq. (6)	Eq. (7)	Eq. (8)	Eq. (9)	Eq. (10)	Average Error
Ab initio						
MP4/6-311G(<i>d, p</i>) ^a	222.1	−41.9	−6.3	−38.6	−32.4	2.7
MP4/6-311+G(<i>d, p</i>) ^a	221.2	−41.2	−7.0	−38.6	−31.6	2.5
MP4/6-311G(2 <i>df, p</i>) ^a	228.8	−39.8	−7.4	−38.7	−31.3	0.6
QCISD(T)/6-311G(<i>d, p</i>) ^a	217.6	−42.3	−7.8	−39.5	−31.7	3.1
G1 ^a	226.9	−39.4	−9.7	−39.5	−29.8	1.0
G2 ^b	226.3	−39.8	−9.6	−40.1	−30.5	0.9
Density functional						
VWN/DZVP2(LDA) ^c	260.5	−69.6	−11.3	−54.0	−42.7	17.9
PW86/DZVP2 ^c	225.5	−47.4	−12.8	−42.5	−29.7	3.8
BLYP/6-31G(<i>d</i>)	223.2	−40.1	−12.1	−41.8	−29.8	2.5
BLYP/6-31G(<i>d, p</i>)	223.7	−39.3	−12.3	−41.6	−29.3	2.6
BLYP/6-311G(<i>d, p</i>)	225.9	−31.6	−10.6	−37.8	−27.2	3.8
BLYP/6-311+G(<i>d, p</i>)	224.2	−30.2	−11.1	−37.4	−26.3	4.8
BLYP/6-311G(2 <i>df, p</i>)	226.6	−31.2	−11.1	−37.7	−26.6	3.9
BLYP/6-311+G(2 <i>df, p</i>)	224.9	−29.9	−11.7	−37.5	−25.8	4.9
BLYP/6-311+G(2 <i>df, 2pd</i>)	225.1	−29.5	−11.7	−37.8	−26.1	4.8
BLYP/6-311+G(3 <i>df, 2p</i>)	225.2	−29.1	−11.7	−37.4	−25.6	5.1
BLYP/6-311+G(3 <i>df, 2pd</i>)	225.1	−29.4	−11.9	−37.8	−25.9	4.9
BLYP/6-311++G(3 <i>df, 3pd</i>)	225.0	−29.7	−11.9	−37.8	−25.9	4.9
B3LYP/6-31G(<i>d</i>)	221.7	−46.5	−11.5	−45.4	−33.9	5.0
B3LYP/6-31G(<i>d, p</i>)	222.1	−45.6	−11.8	−45.0	−33.2	4.6
B3LYP/6-311G(<i>d, p</i>)	223.9	−38.4	−10.3	−41.3	−30.9	2.1
B3LYP/6-311+G(<i>d, p</i>)	222.5	−37.2	−10.9	−41.0	−30.1	2.7
B3LYP/6-311G(2 <i>df, p</i>)	224.7	−37.8	−10.8	−41.1	−30.3	2.1
B3LYP/6-311+G(2 <i>df, p</i>)	223.4	−36.8	−11.5	−41.0	−29.5	2.8
B3LYP/6-311+G(2 <i>df, 2pd</i>)	223.6	−36.4	−11.5	−41.3	−29.8	2.9
B3LYP/6-311+G(3 <i>df, 2p</i>)	223.6	−36.1	−11.5	−41.0	−29.4	2.9
B3LYP/6-311+G(3 <i>df, 2pd</i>)	223.5	−36.4	−11.6	−41.3	−29.7	2.9
B3LYP/6-311++G(3 <i>df, 3pd</i>)	223.4	−36.7	−11.6	−41.3	−29.6	2.9
Experiment ^d	228.9	−40.0	−8.7	−39.8	−31.0	0.0

^a Calculated using energies from [42].

^b Calculated using energies from [44].

^c Calculated using energies from [11].

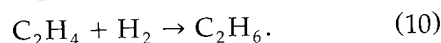
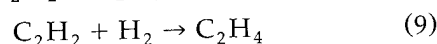
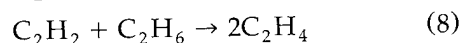
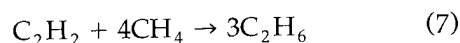
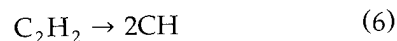
^d Calculated from data in Table VIII.

were used in computing the MP4 and QCI reaction energetics; the ZPE(DF) were calculated at the B3LYP/6-311++G(3df,3pd) level and were used for all DF reaction energetics.

As a test of the data in Table III, Table IV presents the computed atomization energies of the molecules in Eqs. (1)–(5). Experimentally determined values are also included. As anticipated, the largest average error is for the VWN/DZVP2 results; the local density approximation is known to be very poor for calculating bond-breaking energies [47–49]. However, Table IV shows a clear superiority of the nonlocal DF procedures, especially the BLYP and B3LYP, over the MP4 and QCI, which are consistently too low. Indeed, the B3LYP approach is able to achieve the same level of accuracy as do the G1 and G2, provided that *f* polarization functions are included in the basis set. It is interesting to note that diffuse functions have

a detrimental effect upon the BLYP and B3LYP results, possibly reflecting a basis-set superposition error.

As further tests, we used the data in Table III to compute ΔE for each of the reactions shown as Eqs. (6)–(10). The results are in Table V:



The disparity between the accuracies of the ab initio and DF procedures that was observed for the atomization energies (Table IV) is not in evidence in reactions (6)–(10). Instead, the poorest overall

TABLE VI
Calculated ΔE values (kcal/mol) of reactions involving tetrahydrene, Eqs. (1)–(5).

Method	Eq. (1)	Eq. (2)	Eq. (3)	Eq. (4)	Eq. (5)
Ab initio					
MP4/6-311G(d,p)	708.7	–418.2	26.1	109.9	103.3
MP4/6-311+G(d,p)	708.7	–416.2	26.2	108.6	103.4
MP4/6-311G(2df,p)	735.2	–434.3	23.2	102.7	100.6
QCISD(T)/6-311G(d,p)	702.4	–409.1	26.1	110.6	105.0
G1	750.7	–430.5	23.4	102.1	102.4
G2	753.8	–431.9	20.6	100.3	100.8
Density functional					
VWN/DZVP2(SDA)	896.7	–543.2	–22.3	116.9	85.7
PW86/DZVP2	782.3	–444.1	6.9	101.7	91.9
BLYP/6-31G(d)	746.9	–428.4	17.9	98.1	101.5
BLYP/6-31G(d,p)	751.8	–429.4	17.9	96.6	101.2
BLYP/6-311G(d,p)	743.7	–423.3	28.6	91.9	104.2
BLYP/6-311+G(d,p)	740.9	–418.6	29.9	90.3	104.7
BLYP/6-311G(2df,p)	747.8	–424.6	28.6	90.9	104.0
BLYP/6-311+G(2df,p)	745.2	–420.3	29.5	89.3	104.5
BLYP/6-311+G(2df,2pd)	747.1	–420.6	29.7	88.6	105.3
BLYP/6-311+G(3df,2p)	747.7	–421.3	29.1	87.2	103.8
BLYP/6-311+G(3df,2pd)	748.1	–421.1	29.1	87.8	104.6
BLYP/6-311++G(3df,3pd)	748.0	–421.1	28.8	88.2	104.4
B3LYP/6-31G(d)	747.4	–430.8	12.7	105.7	103.6
B3LYP/6-31G(d,p)	752.4	–431.6	12.6	103.8	102.7
B3LYP/6-311G(d,p)	744.7	–425.1	22.7	99.4	105.2
B3LYP/6-311+G(d,p)	742.9	–421.3	23.7	98.2	105.8
B3LYP/6-311G(2df,p)	749.4	–426.8	22.7	98.2	104.9
B3LYP/6-311+G(2df,p)	747.6	–423.5	23.4	97.0	105.4
B3LYP/6-311+G(2df,2pd)	749.5	–423.7	23.5	96.3	106.1
B3LYP/6-311+G(3df,2p)	750.2	–424.5	22.7	94.9	104.6
B3LYP/6-311+G(3df,2pd)	750.6	–424.3	22.7	95.4	105.3
B3LYP/6-311++G(3df,3pd)	750.5	–424.4	22.5	95.9	105.0

results are now shown by the BLYP method for reaction (7) and, to a lesser extent, reaction (10). It is interesting that the BLYP values actually become worse as the basis set is expanded. The B3LYP calculations, on the other hand, are comparable in accuracy to the MP4 and QCISD(T), except for the smallest basis sets. Again, as for the atomization energies, the inclusion of diffuse functions gives poorer energies by both the BLYP and B3LYP approaches.

Proceeding now to the reactions actually involving tetrahedrane [Eqs. (1)–(5)], Table VI lists the ΔE values obtained using the data in Table III. For the reaction in Eq. (1), the atomization of tetrahedrane, the MP4 and QCI results appear to be too low, as would be expected on the basis of Table IV. The BLYP and B3LYP values approach much more closely the G1 and G2. For the other reactions, the B3LYP results tend to be superior to the

BLYP and are overall comparable in accuracy to the ab initio (if we take the G2 as our standard); however, the MP4/6-311G(2df, p) are clearly the best, as they were also for the reactions in Eqs. (6)–(10). Except for the VWN/DZVP2(LDA), the largest errors were obtained with the QCISD(T) and the PW86/DZVP2 procedures.

A point of interest concerning Eq. (4) is that it depicts an "isodesmic" reaction, i.e., one in which the number of bonds of each formal type remains the same. ΔE for such a reaction is sometimes interpreted as reflecting any deviations from additivity of bond energies and, hence, is used as a measure of anomalous energetic effects, such as strain [50]. By this reasoning, the ΔE values listed in Table VI for Eq. (4) indicate that tetrahedrane has a strain energy of approximately 100 kcal/mol. On the other hand, other approaches to estimating strain energy, also involving G2 calculations, have

TABLE VII
Tetrahedrane enthalpies of formation at 0 K (kcal / mol) computed from Eqs. (1)–(5).

Method	Eq. (1)	Eq. (2)	Eq. (3)	Eq. (4)	Eq. (5)
Ab initio					
MP4 / 6-311G(d, p)	177.7	148.2	134.7	138.5	132.3
MP4 / 6-311 + G(d, p)	177.7	150.2	134.8	137.2	132.4
MP4 / 6-311G(2df, p)	151.2	132.1	131.8	131.3	129.6
QCISD(T) / 6-311G(d, p)	184.0	157.3	134.7	139.2	134.0
G1	135.7	135.9	132.0	130.7	131.4
G2	132.6	134.5	129.2	128.9	129.7
Density functional					
VWN / DZVP2(SDA)	– 10.3	23.2	86.3	145.5	114.7
PW86 / DZVP2	104.1	122.3	115.5	130.3	120.9
BLYP / 6-31G(d)	139.5	138.0	126.5	126.7	130.5
BLYP / 6-31G(d, p)	134.6	137.0	126.5	125.2	130.2
BLYP / 6-311G(d, p)	142.7	143.1	137.2	120.5	133.2
BLYP / 6-311 + G(d, p)	145.5	147.8	138.5	118.9	133.7
BLYP / 6-311G(2df, p)	138.6	141.8	137.2	119.5	133.0
BLYP / 6-311 + G(2df, p)	141.2	146.1	138.1	117.9	133.5
BLYP / 6-311 + G(2df, 2pd)	139.3	145.8	138.3	117.2	134.3
BLYP / 6-311 + G(3df, 2p)	138.7	145.1	137.7	115.8	132.8
BLYP / 6-311 + G(3df, 2pd)	138.3	145.3	137.7	116.4	133.6
BLYP / 6-311 + + G(3df, 3pd)	138.4	145.3	137.4	116.8	133.4
B3LYP / 6-31G(d)	139.0	135.6	121.3	134.3	132.5
B3LYP / 6-31G(d, p)	134.0	134.8	121.2	132.4	131.7
B3LYP / 6-311G(d, p)	141.7	141.3	131.3	128.0	134.2
B3LYP / 6-311 + G(d, p)	143.5	145.1	132.3	126.8	134.7
B3LYP / 6-311G(2df, p)	137.0	139.6	131.3	126.8	133.8
B3LYP / 6-311 + G(2df, p)	138.8	142.9	132.0	125.6	134.4
B3LYP / 6-311 + G(2df, 2pd)	136.9	142.7	132.1	124.9	135.1
B3LYP / 6-311 + G(3df, 2p)	136.2	141.9	131.3	123.5	133.5
B3LYP / 6-311 + G(3df, 2pd)	135.8	142.1	131.3	124.0	134.2
B3LYP / 6-311 + + G(3df, 3pd)	135.9	142.0	131.1	124.5	134.0

TABLE VIII
Experimental enthalpies of formation at
0 K (kcal/mol).^a

System	$\Delta H_{f,0K}^0$
H (g)	51.626
H ₂ (g)	0
C (g)	169.98
CH (g)	141.6
CH ₄ (g)	-15.970
C ₂ H ₂ (g)	54.3
C ₂ H ₄ (g)	14.515
C ₂ H ₆ (g)	-16.523

^a Except for C₂H₂, these data are from [52]. The value for C₂H₂ was calculated using its experimental atomization energy as given in [42].

recently yielded values greater than 130 kcal/mol [51]. Indeed, Maier noted that strain energies from 97 to 150 kcal/mol have been attributed to tetrahedrane [27]. This simply illustrates the difficulty in trying to describe quantitatively a property for which there is no rigorous definition.

ENTHALPY OF FORMATION

In principle, the enthalpy of formation at 0 K of tetrahedrane can be determined from the ΔE for any of the reactions in Eqs. (1)–(5) if $\Delta H_{f,0K}^0$ is known for each of the other reactants and products. The results obtained in this manner, using the experimental data in Table VIII, are given in Table VII. The G1 and G2 procedures yield average values of 133.1 and 131.0 kcal/mol, respectively, over ranges of less than 6 kcal/mol. (These are in reasonable agreement with other calculated values [51, 53, 54].) For all our other computational approaches, the heats of formation predicted from Eqs. (1)–(5) cover much larger ranges, although the MP4/6-311G(2df, p) values are very consistent if that for Eq. (1) is excluded. (The latter is based upon the atomization process, and we have already pointed out that the MP4 and QCI methods give relatively poor atomization energies.) Thus, even though the B3LYP/6-311 + G(3df, 3pd) average is 133.5 kcal/mol, quite close to the G2, the range is 17.5 kcal/mol.

Conclusions

In the comparisons that have been made in this

work, the B3LYP procedure has been found to be the most reliable of the density functional methods that were investigated and generally competitive with ab initio MP4 and QCISD(T) techniques.

A notable feature of both the BLYP and B3LYP results is the absence of any consistent correlation between their accuracy and the size of the basis set. Evidence of this can be found throughout Tables IV–VII. Thus, the BLYP/6-31G(d) ΔE values for Eqs. (2)–(5) are distinctly better than are the BLYP/6-311 + G(3df, 2pd); as another example, the average of the B3LYP/6-31G(d, p) enthalpies of formation is 130.8 kcal/mol, nearly matching the G2 131.0, and the range is only 13.6 kcal/mol, while the corresponding B3LYP/6-311 + G(3df, 2pd) figures are 133.5 and 18.1 kcal/mol, respectively. It is clear that a larger basis set, which, of course, increases the demands upon computational resources, is not a reliable means of achieving greater accuracy. A similar conclusion was reached by Hertwig and Koch in a DFT study of homonuclear diatomic molecules [22].

ACKNOWLEDGMENTS

We greatly appreciate the financial support provided by the Office of Naval Research through Contract No. N00014-95-1-0028 and Program Officer Dr. Richard S. Miller and by the CONICIT-Venezuela, Cray Research Inc. (Project SC-002295), and DGAPAUNAM-Mexico (Project IN101295). We also thank DGSCA/UNAM-Mexico for access to the Cray-YMP4/464.

References

1. E. Clementi and S. J. Chakravorty, *J. Chem. Phys.* **93**, 2591 (1990).
2. G. Fitzgerald and J. Andzelm, *J. Phys. Chem.* **95**, 10531 (1991).
3. G. L. Gutsev and T. Ziegler, *J. Phys. Chem.* **95**, 7220 (1991).
4. L. Fan and T. Ziegler, *J. Am. Chem. Soc.* **114**, 10890 (1992).
5. J. M. Pérez-Jordá, E. San-Fabián, and F. Moscardó, *Phys. Rev. A* **45**, 4407 (1992).
6. C. W. Murray, G. J. Laming, N. C. Handy, and R. D. Amos, *Chem. Phys. Lett.* **199**, 551 (1992).
7. G. E. Scuseria, *J. Chem. Phys.* **97**, 7528 (1992).
8. P. M. W. Gill, B. G. Johnson, and J. A. Pople, *Int. J. Quantum. Chem., Quantum. Chem. Symp.* **26**, 319 (1992).
9. A. D. Becke, *J. Chem. Phys.* **97**, 9173 (1992); *Ibid.* **98**, 5648 (1993).
10. J. M. Seminario, M. C. Concha, and P. Politzer, *Int. J. Quantum. Chem., Quantum. Chem. Symp.* **27**, 263 (1993).

11. J. M. Seminario, *Chem. Phys. Lett.* **206**, 547 (1993).
12. B. G. Johnson, P. M. W. Gill, and J. A. Pople, *J. Chem. Phys.* **98**, 5612 (1993).
13. J. Cioslowski and A. Nanayakkara, *J. Chem. Phys.* **99**, 5163 (1993).
14. J. Andzelm, C. Sosa, and R. A. Eades, *J. Phys. Chem.* **97**, 4664 (1993).
15. L. Deng, V. Branchadell, and T. Ziegler, *J. Am. Chem. Soc.* **116**, 10645 (1994).
16. L. A. Eriksson, J. Wang, R. J. Boyd, and S. Lunell, *J. Phys. Chem.* **98**, 792 (1994).
17. Z. Latajka and Y. Bouteiller, *J. Chem. Phys.* **101**, 9793 (1994).
18. N. Oliphant and R. J. Bartlett, *J. Chem. Phys.* **100**, 6550 (1994).
19. J. M. Seminario, *Int. J. Quantum. Chem., Quantum. Chem. Symp.* **28**, 655 (1994).
20. Y. Zheng, J. J. Neville, C. E. Brion, Y. Wang, and E. R. Davidson, *Chem. Phys.* **188**, 109 (1994).
21. B. G. Johnson, in *Modern Density Functional Theory: A Tool for Chemistry*, J. M. Seminario and P. Politzer, Eds. (Elsevier, Amsterdam, 1995), Chap. 6.
22. R. H. Hertwig and W. Koch, *J. Comp. Chem.* **16**, 576 (1995).
23. S. Suhai, *Phys. Rev. B* **51**, 16553 (1995); *Ibid.* **52**, 1674 (1995).
24. P. J. Hay, *J. Phys. Chem.* **100**, 5 (1996).
25. J. Hrusák, H. Friedrichs, H. Schwarz, H. Razafinjanahary, and H. Chermette, *J. Phys. Chem.* **100**, 100 (1996).
26. P. Politzer and P. Lane, *J. Mol. Struct. (Theochem)* (in press).
27. G. Maier, *Angew. Chem., Int. Ed. Engl.* **27**, 309 (1988).
28. A. Greenberg and J. F. Liebman, *Strained Organic Molecules* (Academic Press, New York, 1978).
29. P. Politzer, L. Abrahamsén, P. Sjöberg, and P. R. Laurence, *Chem. Phys. Lett.* **102**, 74 (1983).
30. A. D. Becke, *Phys. Rev. A* **38**, 3098 (1988).
31. A. D. Becke, *J. Chem. Phys.* **98**, 5648 (1993).
32. J. P. Perdew, *Phys. Rev. B* **33**, 8822 (1986).
33. C. Lee, W. Yang, and R. G. Parr, *Phys. Rev. B* **37**, 785 (1988).
34. M. J. Frisch, G. W. Trucks, H. B. Schlegel, P. M. W. Gill, B. G. Johnson, M. W. Wong, J. B. Foresman, M. A. Robb, M. Head-Gordon, E. S. Replogle, R. Gomperts, J. L. Andres, K. Raghavachari, J. S. Binkley, C. Gonzalez, R. L. Martin, D. J. Fox, D. J. DeFrees, J. Baker, J. J. P. Stewart, and J. A. Pople, *Gaussian 92/DFT. Revision G.2* (Gaussian, Inc., Pittsburgh, PA, 1993).
35. M. J. Frisch, G. W. Trucks, H. B. Schlegel, P. M. W. Gill, B. G. Johnson, M. A. Robb, J. R. Cheeseman, T. A. Keith, G. A. Petersson, J. A. Montgomery, K. Raghavachari, M. A. Al-Laham, V. G. Zakrzewski, J. V. Ortiz, J. B. Foresman, J. Cioslowski, B. B. Stefanov, A. Nanayakkara, M. Challacombe, C. Y. Peng, P. Y. Ayala, W. Chen, M. W. Wong, J. L. Andres, E. S. Replogle, R. Gomperts, R. L. Martin, D. J. Fox, J. S. Binkley, D. J. DeFrees, J. Baker, J. P. Stewart, M. Head-Gordon, C. Gonzalez, and J. A. Pople, *Gaussian 94 (Revision B.3)* (Gaussian, Inc., Pittsburgh, PA, 1995).
36. A. St. Amant and D. R. Salahub, *Chem. Phys. Lett.* **169**, 387 (1990).
37. D. R. Salahub, R. Fournier, P. Mlynarski, I. Papai, A. St. Amant, and J. Ushio, in *Density Functional Methods in Chemistry*, J. K. Labanowski and J. W. Andzelm, Eds. (Springer-Verlag, New York, 1991), Chap. 6.
38. J. P. Perdew and Y. Wang, *Phys. Rev. B* **33**, 8800 (1986).
39. J. P. Perdew, *Phys. Rev. B* **34**, 7406 (1986).
40. S. H. Vosko, L. Wilk, and M. Nusair, *Can. J. Phys.* **58**, 1200 (1980).
41. N. Godbout and D. R. Salahub, *Can. J. Chem.* **70**, 560 (1992).
42. J. A. Pople, M. Head-Gordon, D. J. Fox, K. Raghavachari, and L. A. Curtiss, *J. Chem. Phys.* **90**, 5622 (1989).
43. L. A. Curtiss, C. Jones, G. W. Trucks, K. Raghavachari, and J. A. Pople, *J. Chem. Phys.* **93**, 2537 (1990).
44. L. A. Curtiss, K. Raghavachari, G. W. Trucks, and J. A. Pople, *J. Chem. Phys.* **94**, 7221 (1991).
45. G. A. Peterson and J. Mantzaris, *J. Am. Chem. Soc.* **113**, 2486 (1991).
46. A. Nicolaides and L. Radom, *J. Phys. Chem.* **98**, 3092 (1994).
47. A. D. Becke, *J. Chem. Phys.* **84**, 4524 (1986).
48. M. Grodzicki, J. M. Seminario, and P. Politzer, *J. Chem. Phys.* **94**, 1668 (1991).
49. T. Ziegler, *Chem. Rev.* **91**, 651 (1991).
50. W. J. Hehre, L. Radom, P. v. R. Schleyer, and J. A. Pople, *Ab Initio Molecular Orbital Theory* (Wiley-Interscience, New York, 1986).
51. M. N. Glukhovtsev, S. Laiter, and A. Pross, *J. Phys. Chem.* **99**, 6828 (1995).
52. D. R. Lide, Ed., *Handbook of Chemistry and Physics*, 71st ed. (CRC Press, Boca Raton, FL, 1990).
53. H. Kollmar, *J. Am. Chem. Soc.* **102**, 2617 (1980).
54. R. L. Disch, J. M. Schulman, and M. L. Sabio, *J. Am. Chem. Soc.* **107**, 1904 (1985).

Attempts Toward a Pair Density Functional Theory

PAUL ZIESCHE

Max Planck Institute for Physics of Complex Systems, Bayreuther Str. 40, D-01187 Dresden, Germany; e-mail: pz@idefix.mpiPKS-dresden.mpg.de

Received March 25, 1996; accepted June 25, 1996

ABSTRACT

A generalized density functional theory (DFT) is proposed based on a generalized Hohenberg–Kohn theorem with the pair density as the key quantity and the kinetic energy as a universal functional of the pair density. It is assumed that there exists an effective interaction potential which, via the corresponding two-particle (2P) Schrödinger equation, generates 2P orbitals (geminals) from which follows the pair density, just as in the conventional DFT the density follows from 1P orbitals (as the solutions of an effective 1P Schrödinger equation). According to three different representations (natural spectral resolutions) of the pair density or the cumulant pair densities in terms of geminals, three versions of a pair DFT (PDFT) are formally sketched. Also considered are the relation between electron correlation and particle-number fluctuations in fragments of the system and the use of the pair density for an estimation of such fluctuations. © 1996 John Wiley & Sons, Inc.

1. Introduction

Density functional theory (DFT) provides us with the ground state (GS) energy E of an interacting many-electron system (finite or extended) and the GS density $\rho(1)$, the diagonal of the one-particle (1P) reduced density matrix (RDM) $\gamma(1,1')$, referred to below as the 1-matrix. [The shorthands $1 = (\mathbf{r}_1, \sigma_1)$ and $\int d1 = \sum_{\sigma_1} \int d^3r_1$ are used.] The electrons are bound by an external potential $v_{\text{ext}}(1)$ and interact via $v_{\text{int}}(1,2)$, the electron–electron repulsion e^2/r_{12} . The inputs of

the effective 1P scheme after Kohn and Sham (KS) are the external potential $v_{\text{ext}}(1)$ and an approximation for the exchange (X) and correlation (C) energy E_{XC} as a functional of the density $\rho(1)$. Several review papers and monographs show the “triumphal march” of DFT in solid-state theory and quantum chemistry [1–21], recent papers deal with improvements, refinements, extensions, generalizations, benchmark checking, connections with related theories [22–25, 70]. Although “the density has its charm and power” [26], it gives “only” the probability of finding an electron at “1” and besides this the average number of electrons in an arbitrarily chosen fragment Ω of the whole space

(e.g., the region around an atom or of a bond in a molecule) via

$$N_{\Omega} = \int_{\Omega} d1 \rho(1), \quad (1.1)$$

which, of course, approaches the total number of electrons N for Ω approaching the total space.

Obviously, further information about the quantum kinematics of the GS of a correlated electron system is contained in the 1-matrix $\gamma(1, 1')$ and in the two-particle (2P) or pair density $n(1; 2)$, which is the diagonal of the 2-matrix and which is normalized according to

$$\int \frac{d1d2}{2!} n(1; 2) = \left(\frac{N}{2} \right),$$

the total number of electron pairs, as well as in higher-order RDMs [27]. The 1-matrix and pair density yield the density via $\rho(1) = \gamma(1, 1)$ and

$$\rho(1) = \int \frac{d2}{N-1} n(1; 2), \quad (1.2)$$

respectively. In addition to this from $\gamma(1, 1')$ follows the momentum distribution, which contains—in the case of crystalline metals—the Fermi surface, and generally follow the q -order nonidempotency (per particle)

$$c(q) = 1 - \frac{1}{N} \text{Tr}(\gamma)^q, \quad c(1) = 0,$$

and from $c'(1)$ the correlation “entropy” (per particle)

$$s = -\frac{1}{N} \text{Tr}(\gamma) \ln(\gamma)$$

as recently discussed quantitative measures (on the 1P level) of the qualitative term correlation strength [28–31, 36]. Originally Löwdin [32] suggested studying the meaning of $\text{Tr}(\gamma - \gamma^2)$ which is just $Nc(2)$ with the second-order nonidempotency $c(2)$, in the following denoted by c . [A side remark: from $c(q)$ follows the Tsallis entropy $s(q) = c(q)/(q-1)$ with $s(1) = s$ [33].] For other measures of the correlation strength based on particle-number fluctuations cf. [34] or on configurational interaction (CI) cf. [35, 36].

The pair density gives the probability of finding an electron pair with one electron at “1” and one electron at “2,” and it again yields the average

number of electron pairs in a fragment Ω via

$$\int_{\Omega} \frac{d1d2}{2!} n(1; 2) = \left(\frac{N}{2} \right)_{\Omega}, \quad (1.3)$$

which of course approaches $\left(\frac{N}{2} \right)$, the total numbers of electron pairs, for $\Omega \rightarrow \infty$.

This allows the calculation of the particle-number fluctuations in a fragment Ω , because of

$$\left(\frac{N}{2} \right)_{\Omega} = \frac{1}{2!} [(N^2)_{\Omega} - N_{\Omega}],$$

and the definition of the variance as

$$\begin{aligned} (\Delta N_{\Omega})^2 &= (N^2)_{\Omega} - (N_{\Omega})^2 \\ &= \int_{\Omega} d1d2 n(1; 2) - N_{\Omega}(N_{\Omega} - 1). \end{aligned} \quad (1.4)$$

Then $P_{\Omega}(M)$, the probability of finding M ($= 0, 1, \dots, N$) electrons in Ω , can be obtained approximately from N_{Ω} and ΔN_{Ω} maximizing its information entropy

$$S_{\Omega} = - \sum_M P_{\Omega}(M) \ln P_{\Omega}(M).$$

The result is $P_{\Omega}(M) = C \exp(-\alpha(M - \beta)^2)$ with α, β, C to be determined from N_{Ω} , ΔN_{Ω} , and the normalization. For the exact particle number probability in Ω higher-order distribution functions would be needed [37–39]:

$$P_{\Omega}(M) = \frac{(\Theta_{\Omega})^M}{M!} \sum_{M'=0}^{N-M} \frac{(-\Theta_{\Omega})^{M'}}{M'!} n_{M+M'}. \quad (1.5)$$

Here the notation

$$(\Theta_{\Omega})^M n_M = \int_{\Omega} d1 \cdots \int_{\Omega} dM n(1, \dots, M)$$

is used, $n_0 = 1$. In terms of the cumulant expansion

$$\begin{aligned} n(1) &= \rho(1), \\ n(1; 2) &= \rho(1)\rho(2) - w(1; 2), \\ n(1; 2; 3) &= \rho(1)\rho(2)\rho(3) - \rho(1)w(2; 3) \\ &\quad - \rho(2)w(3; 1) \\ &\quad - \rho(3)w(1; 2) + w(1; 2; 3), \end{aligned}$$

etc., the variance is

$$(\Delta N_{\Omega})^2 = N_{\Omega} - W_{\Omega}^{(2)}, \quad W_{\Omega}^{(2)} = \int_{\Omega} d1d2 w(1; 2), \quad (1.6)$$

and

$$P_{\Omega}(M) = \left\{ \exp \left[-\frac{1}{2} W_{\Omega}^{(2)} \left(\frac{\partial}{\partial N_{\Omega}} \right)^2 + \dots \right] \right\} \times \frac{(N_{\Omega})^M}{M!} \exp_{N-M}(-N_{\Omega}) \quad (1.7)$$

describes the deviation from the (classical) Poisson distribution due to X and C hidden in the hierarchical series $W_{\Omega}^{(2)}, W_{\Omega}^{(3)}, \dots$. The index $N - M$ at "exp" means that the power series stops with $(-N_{\Omega})^{N-M}/N - M!$.

The relations between correlation and fluctuations are discussed by Fulde [34]. Therein the molecule C_2H_2 is considered as an example, and the probability of finding in the ground state 0, 1, ... or 8 valence electrons at a C-atom is considered. The average value is 4, but the variance depends on whether or not correlations are taken into account. A correlation-induced narrowing is found accompanied by a suppression of fluctuations: The probability for configurations with large deviations from the average value, i.e., 0 or 1, respectively, 7 or 8 valence electrons essentially goes down (to almost zero). Similarly in [71] a detailed fluctuation analysis for H_2 and N_2 is performed. So the pair density gives a deeper insight into the internal dynamical structure of an interacting electron system, especially into the mutual relation between correlation and fluctuations. A striking example in favor of the pair density is the uniform electron gas, where the density $\rho(1) = \text{const}$ has no structure whereas the spin parallel and antiparallel pair densities with the Fermi and Coulomb holes, respectively, have rich structures with curvature and cusp properties for small electron-electron separations and Friedel oscillations for large separations. For a recent discussion of pair densities in the H_2 molecule cf. Gritsenko et al. [23]. For strongly correlated electron systems with dominating on-site electron-electron repulsion, the pair density approach is possibly an appropriate access or starting point. Of course, the price for more information is the need to deal with a more complicated function. With all this in mind one may perhaps say: if available, $n(1;2)$ would have even more charm and power than $\rho(1)$.

For finite systems quantum chemical methods (e.g., CI = configurational interaction, CC = coupled cluster, MP = Møller-Plesset) allow in

principle the calculation of the pair density. But for extended systems (crystals) the Hartree-Fock (HF) approximation (which falsely yields for metals a vanishing density of states at the Fermi energy) does not take into account correlation, and DFT gives "only" $\rho(1)$ and E (for the GS). The methods developed by Fulde et al. (use of cumulants for size consistency, to avoid for extended systems ghosts/spurious terms $\approx N^2, N^3, \dots$; use of projection and partitioning techniques as promoted long ago by Löwdin; use of local operators to describe the correlation hole; use of incremental methods to calculate GS and binding energies) have until now been successfully applied "only" to nonmetallic systems [34]. So the additional availability of calculational/computational schemes which provide the pair density especially for extended systems (both nonmetallic and metallic) seems to be highly desirable. For bosons a pair density functional theory (PDFT) has been proposed [40]. For fermions the ideas of a PDFT [41] as well as a (generalized) HF method for electron pairs [42] have been presented recently. Here we try to push the PDFT idea a step further.

The advantage of DFT is its applicability to finite as well as extended (metallic as well as insulating/semiconducting) systems: The effective 1P or KS equation survives the thermodynamic limit (TDL). In case it is really possible to develop a practicable PDFT, its advantage should be again its applicability not only to finite but also to extended systems: Also the effective 2P equation should survive the TDL.

The present work—a formal sketch of ideas toward a PDFT of the GS—has the following structure: Section 2 clarifies some basic notation. Section 3 considers the different possible spectral resolutions of the 2-matrix and its cumulant components. The derivation of DFT (Sec. 4) is formally transferred to obtain similarly (and bearing in mind the spectral resolutions of Sec. 3) three versions of PDFT (Sec. 5). Section 6 presents some discussion, open questions, and an outlook.

2. The System and Its Quantities

For simplicity relativistic effects are neglected (spin-independent Hamiltonian) and the nuclei are resting at given positions (adiabatic approximation). The Hamiltonian of this Schrödinger-

Born–Oppenheimer world

$$\hat{H} = \hat{T} + \hat{V}_{\text{ext}} + \hat{V}_{\text{int}} \quad (2.1)$$

describes the electronic structure of atoms, Hooke law models, molecules, clusters, solids as well as finite and extended jellium models. The 1P part of \hat{H} is $\hat{H}_0 = \sum_i \hat{h}_0(i)$ with $\hat{h}_0(i) = \hat{t}(i) + v_{\text{ext}}(i)$ and $\hat{t}(i) = -(\hbar^2/2m)\Delta_i$. The interaction term $\hat{V}_{\text{int}} = \sum_{i < j} v_{\text{int}}(i, j)$ includes a coupling constant λ varying between 0 and 1.

The correlated antisymmetric wave function (of the GS) is normalized as

$$\int \frac{d1 \cdots dN}{N!} |\Psi(1, \dots, N)|^2 = 1, \quad i = (\underline{r}_i, \sigma_i),$$

$$\int di = \sum_{\sigma_i} \int d^3 r_i,$$

and yields the (nonidempotent) 1-matrix:

$$\gamma(1, 1') = \int \frac{d2 \cdots dN}{(N-1)!} \Psi(1, 2, \dots, N) \times \Psi^*(1', 2, \dots, N), \quad (2.2)$$

and the 2-matrix (with $2' = 2$):

$$\begin{aligned} n(1, 1'; 2) &= \int \frac{d3 \cdots dN}{(N-2)!} \Psi(1, 2, 3, \dots, N) \\ &\times \Psi^*(1', 2, 3, \dots, N). \end{aligned} \quad (2.3)$$

Density and pair density are then $\rho(1) = \gamma(1, 1)$ and $n(1; 2) = n(1, 1; 2)$, respectively. The “components” of the GS energy $E = T + V_{\text{ext}} + V_{\text{int}}$ in terms of RDMs are

$$T[\gamma] = \int d1 \hat{t}(1) \gamma(1, 1')|_{1'=1}, \quad (2.4)$$

$$V_{\text{ext}}[\rho] = \int d1 \rho(1) v_{\text{ext}}(1), \quad (2.5)$$

$$V_{\text{int}}[n] = \int \frac{d1 d2}{2!} n(1; 2) v_{\text{int}}(1, 2), \quad (2.6)$$

or with $n(1; 2) = \rho(1)\rho(2) - w(1; 2)$ and $V_{\text{int}} = V_H + V_{\text{XC}}$:

$$V_H[\rho] = \frac{1}{2} \int d1 \rho(1) \int d2 \rho(2) v_{\text{int}}(1, 2), \quad (2.7)$$

$$V_{\text{XC}}[w] = - \int \frac{d1 d2}{2!} w(1; 2) v_{\text{int}}(1, 2), \quad (2.8)$$

or with $w(1; 2) = |\gamma(1, 2)|^2 + c \cdot u(1; 2)$ and $V_{\text{XC}} = V_X + V_C$:

$$V_X[\gamma] = - \int \frac{d1 d2}{2!} \gamma(1, 2) \gamma(2, 1) v_{\text{int}}(1, 2), \quad (2.9)$$

$$V_C[u] = - \int \frac{d1 d2}{2!} u(1, 2) c \cdot v_{\text{int}}(1, 2). \quad (2.10)$$

H means “Hartree” and V_X and V_C are referred to as cumulant X energy and cumulant C energy, respectively. Note that γ in V_X is not the idempotent HF 1-matrix. In [43] the difference between $|\gamma|^2$ and $|\gamma|_{\text{HF}}^2$ is referred to as “correlation induced X-hole narrowing”; therein this narrowing and also V_X and V_C as functions of r_s are illustrated for the uniform electron gas using data for the momentum distribution (which agrees for this simple model case with the natural occupation numbers).

The cumulant pair densities $w(1; 2)$ and $u(1; 2)$ are the diagonals of the cumulant matrices (CMs) $w(1, 1'; 2)$ and $u(1, 1'; 2)$, respectively. The 1P and 2P eigenfunctions of the RDMs and CMs are decorated with tilde to distinguish them from the 1P orbitals and geminals of DTF and PDTF, respectively.

3. Reduced Density Matrices and Their Spectral Resolutions

The 1-matrix $\gamma(1, 1')$ can be written in terms of its orthonormal eigenfunctions (NSOs = natural spin orbitals) $\tilde{\psi}_\kappa(1)$ and eigenvalues (NONs = natural occupation numbers) \tilde{n}_κ according to

$$\gamma(1, 1') = \sum_\kappa \tilde{\psi}_\kappa(1) \tilde{n}_\kappa \tilde{\psi}_\kappa^*(1') \quad (3.1)$$

with $\sum_\kappa \tilde{n}_\kappa = N$ and $0 \leq \tilde{n}_\kappa \leq 1$.

The q -order nonidempotency $c(q) = 1 - (1/N) \sum_\kappa (\tilde{n}_\kappa)^q$ and the correlation entropy $s = -(1/N) \sum_\kappa \tilde{n}_\kappa \ln \tilde{n}_\kappa$ measure the correlation strength (on the 1P level). In the following the notation c will be used for the second-order nonidempotency $c(2) = 1 - \text{Tr}(\gamma^2)/N$.

For the spectral resolution of the pair density $n(1; 2)$ in terms of geminals, there are three possibilities.

a. Version I: Here the pair density is given directly in terms of orthonormal natural geminals $\tilde{\psi}_\kappa(1, 2)$ and the corresponding geminal occupation

numbers (GON) \tilde{n}_K via

$$n(1;2) = \sum_K \tilde{n}_K |\tilde{\psi}_K(1,2)|^2 \quad (3.2)$$

with $\sum_K \tilde{n}_K = \binom{N}{2}$ and $0 \leq \tilde{n}_K (\leq [N/2])$. Whereas κ is a 1P quantum number, here K is a 2P quantum number. The geminals $\tilde{\psi}_K(1,2)$ are antisymmetric and normalized according to $\int d1d2 |\tilde{\psi}_K(1,2)|^2/2! = 1$. Each geminal has a 1-matrix:

$$\gamma_K(1,1') = \int d2 \tilde{\psi}_K(1,2) \tilde{\psi}_K^*(1',2),$$

$$\int d1 \gamma_K(1,1) = 2,$$

again with the spectral resolution

$$\gamma_K(1,1') = \sum_{\kappa} \tilde{\psi}_{\kappa}^K(1) \tilde{n}_{\kappa}^K [\tilde{\psi}_{\kappa}^K(1')]^*, \quad \sum_{\kappa} \tilde{n}_{\kappa}^K = 2,$$

and with the correlation entropy

$$s_K = -\frac{1}{2} \sum_{\kappa} \tilde{n}_{\kappa}^K \ln \tilde{n}_{\kappa}^K \geq 0.$$

From the "partial" 1-matrix $\gamma_K(1,1')$ follows the "total" 1-matrix:

$$\gamma(1,1') = \int \frac{d2}{N-1} n(1,1';2) \quad (3.3)$$

via

$$\gamma(1,1') = \frac{1}{N-1} \sum_K \tilde{n}_K \gamma_K(1,1').$$

[From the contraction (3.3) follows for $1' = 1$ the more simple contraction (1.2).]

The GS energy takes the form $E = E_0 + V_{\text{int}}$ with

$$E_0 = \sum_{\kappa} \tilde{n}_{\kappa} h_{\kappa}^0, \quad V_{\text{int}} = \sum_K \tilde{n}_K v_K^{\text{int}} \quad (3.4)$$

and with the (diagonal) matrix elements

$$h_{\kappa}^0 = \int d1 \tilde{\psi}_{\kappa}^*(1) \hat{h}_0(1) \tilde{\psi}_{\kappa}(1) = \langle \kappa | h_0 | \kappa \rangle,$$

$$v_K^{\text{int}} = \int \frac{d1d2}{2!} \tilde{\psi}_K^*(1,2) v_{\text{int}}(1,2) \tilde{\psi}_K(1,2)$$

$$= \langle K | v_{\text{int}} | K \rangle.$$

b. Version II: Here the pair density is decomposed into a Hartree term and a remainder (which

describes XC beyond "Hartree"):

$$n(1;2) = \rho(1)\rho(2) - w(1;2). \quad (3.5)$$

The cumulant pair density $w(1;2)$ including X has the contraction

$$\rho(1) = \int d2 w(1;2). \quad (3.6)$$

Note the difference compared to Eq. (1.2). And $w(1;2)$ is the diagonal of a corresponding 2-matrix $w(1,1';2)$ with the contraction

$$\gamma(1,1') = \int d2 w(1,1';2). \quad (3.7)$$

If one would like to express this (unsymmetric) matrix $w(1,1';2)$ in terms of symmetric and antisymmetric geminals, then one needs to decompose this matrix into a symmetric and an antisymmetric part. The result for $w(1;2)$ is

$$w(1;2) = \frac{1}{2} \sum_{K_+} \tilde{n}_{K_+} |\tilde{\psi}_{K_+}^+(1,2)|^2$$

$$- \frac{1}{2} \sum_{K_-} \tilde{n}_{K_-} |\tilde{\psi}_{K_-}^-(1,2)|^2. \quad (3.8)$$

The first term contains the symmetric geminals

$$\tilde{\psi}_{K_+}^+(1,2)$$

$$= \begin{cases} \tilde{\psi}_{\kappa_1}(1) \tilde{\psi}_{\kappa_2}(2) + \tilde{\psi}_{\kappa_1}(2) \tilde{\psi}_{\kappa_2}(1) & \text{for } \kappa_1 \neq \kappa_2 \\ \sqrt{2} \tilde{\psi}_{\kappa_1}(1) \tilde{\psi}_{\kappa_2}(2) & \text{for } \kappa_1 = \kappa_2 \end{cases}$$

$$(3.9)$$

and occupation numbers

$$\tilde{n}_{K_+} = \tilde{n}_{\kappa_1} \tilde{n}_{\kappa_2} \leq 1 \quad \text{with} \quad \sum_{K_+} = \sum_{\kappa_1 < \kappa_2}$$

and

$$\sum_{K_+} \tilde{n}_{K_+} = \frac{1}{2} N(N+1) - Nc, \quad (3.10)$$

[c denotes the second-order nonidempotency $c(2) = 1 - \text{Tr}(\gamma^2)/N$.] These symmetric geminals are uncorrelated because they are single permanents [built up of the NSOs $\tilde{\psi}_{\kappa}(1)$ like determinants with all plus signs]. Their 1-matrices are explicitly given by

$$\gamma_{K_+}(1,1') = \tilde{\psi}_{\kappa_1}(1) \tilde{\psi}_{\kappa_1}^*(1') + \tilde{\psi}_{\kappa_2}(1) \tilde{\psi}_{\kappa_2}^*(1'),$$

containing (spin dependent!) occupation numbers 1 (for $\kappa_1 \neq \kappa_2$) and 2 (for $\kappa_1 = \kappa_2$). The second term of Eq. (3.8) contains antisymmetric geminals $\tilde{\psi}_{K-}^-(1, 2)$ and occupation numbers \tilde{n}_{K-} with

$$\sum_{K-} \tilde{n}_{K-} = \frac{1}{2} N(N-1) - Nc. \quad (3.11)$$

These antisymmetric geminals are correlated, i.e., they are sums of 2P Slater determinants. Their 1-matrices

$$\gamma_{K-}(1, 1') = \int d2 \tilde{\psi}_{K-}^-(1, 2) [\tilde{\psi}_{K-}^-(1', 2)]^*$$

have spectral resolutions

$$\gamma_{K-}(1, 1') = \sum_{\kappa} \tilde{\psi}_{\kappa}^{K-}(1) \tilde{n}_{\kappa}^{K-} [\tilde{\psi}_{\kappa}^{K-}(1')]^*, \quad \sum_{\kappa} \tilde{n}_{\kappa}^{K-} = 2$$

and correlation entropies

$$s_{K-} = -\frac{1}{2} \sum_{\kappa} \tilde{n}_{\kappa}^{K-} \ln \tilde{n}_{\kappa}^{K-} \geq 0.$$

The GS energy $E = E_0 + V_H + V_{XC}$ contains now

$$V_H = \frac{1}{2} \sum_{\kappa_1, \kappa_2} \tilde{n}_{\kappa_1} \tilde{n}_{\kappa_2} v_{\kappa_1, \kappa_1; \kappa_2, \kappa_2}^{\text{int}}, \quad (3.12)$$

$$V_{XC} = -\frac{1}{2} \sum_{K+} \tilde{n}_{K+} v_{K+}^{\text{int}} + \frac{1}{2} \sum_{K-} \tilde{n}_{K-} v_{K-}^{\text{int}},$$

where

$$v_{\kappa_1, \kappa_1'; \kappa_2, \kappa_2'}^{\text{int}} = \int d1 \tilde{\psi}_{\kappa_1}^*(1) \tilde{\psi}_{\kappa_1'}(1) \int d2 \tilde{\psi}_{\kappa_2}^*(2) \tilde{\psi}_{\kappa_2'}(2) v_{\text{int}}(1, 2).$$

The $v_{K\pm}^{\text{int}}$ are similarly defined as in Eq. (3.4).

c. *Version III*: Here the "correlation only" (X not including) cumulant pair density $u(1; 2)$ is considered. It is defined via

$$n(1; 2) = \rho(1)\rho(2) - |\gamma(1, 2)|^2 - c \cdot u(1; 2); \quad (3.13)$$

because of $\int d2 n(1; 2) = (N-1)\rho(1)$ it has the contraction property

$$c \int d2 u(1; 2) = \rho(1) - \int d2 |\gamma(1, 2)|^2, \quad (3.14)$$

which follows from the more general contraction

of the matrix $u(1, 1'; 2)$:

$$c \int d2 u(1, 1'; 2) = \gamma(1, 1') - \int d2 \gamma(1, 2) \gamma(2, 1'). \quad (3.15)$$

Furthermore $u(1; 2)$ has the normalization $c \int d1 d2 u(1; 2) = N - \int d1 d2 |\gamma(1, 2)|^2$ or

$$\int d1 d2 u(1; 2) = N \quad (3.16)$$

and the spectral resolution

$$u(1; 2) = \sum_K \tilde{n}_K |\tilde{\psi}_K(1, 2)|^2. \quad (3.17)$$

The antisymmetric geminals and the occupation numbers are, of course, different from those of Eq. (3.2); for simplicity an additional index to distinguish them will not be introduced. Here the occupation numbers \tilde{n}_K are normalized to

$$\sum_K \tilde{n}_K = \frac{N}{2}. \quad (3.18)$$

Again similar as in version I each of these correlated geminals $\tilde{\psi}_K(1, 2)$ has a 1-matrix $\gamma_K(1, 1')$ with a corresponding spectral resolution and a correlation entropy s_K . Here the relation between the "total" 1-matrix $\gamma(1, 1')$ and the "partial" 1-matrix $\gamma_K(1, 1')$ is more complicated:

$$\gamma(1, 1') - \int d2 \gamma(1, 2) \gamma(2, 1') = c \sum_K \tilde{n}_K \gamma_K(1, 1').$$

The GS energy $E = E_0 + V_H + V_X + V_C$ contains now

$$V_X = -\frac{1}{2} \sum_{\kappa_1, \kappa_2} \tilde{n}_{\kappa_1} \tilde{n}_{\kappa_2} v_{\kappa_1, \kappa_2; \kappa_2, \kappa_1}^{\text{int}}, \quad (3.19)$$

$$V_C = -\sum_K \tilde{n}_K c \cdot v_K^{\text{int}}.$$

Note the role of the second-order nonidempotency renormalizing the coupling constant λ of the bare electron-electron repulsion $v_{\text{int}}(1, 2)$ and note the cancellation of the self-interaction terms (arising from $\kappa_1 = \kappa_2$) in the V_H and V_X terms, similarly as this is known from the HF approximation.

4. Density Functional Theory

The DFT starts with the 1:1 correspondence between the external potential and the density

(Hohenberg-Kohn theorem). So the energy and its "components" T and V are for fixed $v_{\text{ext}}(1)$ functionals of $\rho(1)$. The external potential expectation value is an explicitly given linear functional:

$$V_{\text{ext}}[\rho] = \int d1 \rho(1) v_{\text{ext}}(1). \quad (4.1)$$

The kinetic energy functionally depends on $\rho(1)$ because the 1-matrix $\gamma(1, 1')$ is a functional of $\rho(1)$. The interaction energy depends functionally on $\rho(1)$ because the pair density $n(1; 2)$ is a functional of $\rho(1)$.

Now in view of the RDM analysis of Section 3 these unknown functionals are made partially explicit under the assumption that there exists an effective (local) 1P potential $v_{\text{eff}}(1)$ which is a functional of $\rho(1)$ and which causes orthonormal 1P orbitals $\psi_\kappa(1)$ and 1P energies ϵ_κ in such a way that the GS density of the interacting system is given by

$$\rho(1) = \sum_{\kappa}^{\text{occ}} |\psi_\kappa(1)|^2 \quad (4.2)$$

as a variational ansatz (v representability) and the GS energy follows as $E[\rho]$.

To derive this effective 1P Schrödinger equation for the orbitals $\psi_\kappa(1)$ the 1-matrix $\gamma(1, 1')$ is decomposed according to

$$\gamma(1, 1') = \sum_{\kappa}^{\text{occ}} \psi_\kappa(1) \psi_\kappa^*(1') + \Delta\gamma(1, 1') \quad (4.3)$$

into an idempotent part (first term) and an unknown remainder (second term) with the property $\Delta\gamma(1, 1) = 0$. This yields the ansatz (4.2) and makes the "total" 1-matrix $\gamma(1, 1')$ nonidempotent. Thus the kinetic energy

$$T[\gamma[\rho]] = \sum_{\kappa}^{\text{occ}} \langle \kappa | \hat{t} | \kappa \rangle + \Delta T[\rho] \quad (4.4)$$

consists of an explicitly given orbital part $T_s[\psi_\kappa[\rho]]$ [note that the 1P orbitals $\psi_\kappa(1)$ are functionals of $\rho(1)$] and an unknown remainder. The pair density $n(1; 2)$ is decomposed as

$$n(1; 2) = \rho(1)\rho(2) + \Delta n(1; 2) \quad (4.5)$$

[comparison with Eq. (3.5) shows $\Delta n(1; 2) = -w(1; 2)$], so the interaction energy

$$V_{\text{int}}[n[\rho]] = V_H[\rho] + \Delta V[\rho] \quad (4.6)$$

consists of the explicitly given Hartree term and an unknown remainder. The sum of the unknown remainders is denoted with $E_{\text{XC}}[\rho]$; in it nonidempotency and fluctuations caused by XC are hidden. So the energy density functional is given by

$$E[\rho] = T_s[\psi_\kappa[\rho]] + V_{\text{ext}}[\rho] + V_H[\rho] + E_{\text{XC}}[\rho]. \quad (4.7)$$

Minimizing this functional under the constraint $\int d1 \rho(1) = N$ yields the KS equation

$$\left[\hat{h}_0(1) + v_H(1) + \frac{\delta E_{\text{XC}}[\rho]}{\delta \rho(1)} \right] \psi_\kappa(1) = \epsilon_\kappa \psi_\kappa(1), \quad (4.8)$$

where $v_H(1) = \int d2 \rho(2) v_{\text{int}}(1, 2)$ is the Hartree potential. Note the difference between the KS orbitals $\psi_\kappa(1)$ and the NSOs $\tilde{\psi}_\kappa(1)$. Their dissimilarity together with the difference between the NONs \tilde{n}_κ and their KS parties n_κ ($= 0$ and 1) are contained in $\Delta\gamma(1, 1')$ and thus in $\Delta T[\rho]$ which is part of $E_{\text{XC}}[\rho]$.

In the same way that KS-DFT is obtained, three types of PDFTs are derived, thereby bearing in mind the spectral resolutions of the pair density and its cumulant pair densities.

5. Pair Density Functional Theory

The PDFT starts with the correspondence between the external and interaction potentials on the one hand and the pair density on the other hand (generalized Hohenberg-Kohn theorem, cf. Appendix). So the energy and its "components" T and V , also $\gamma(1, 1')$ and $\rho(1)$ are for fixed $v_{\text{ext}}(1)$ and $v_{\text{int}}(1, 2)$ functionals of $n(1; 2)$. Their detailed representation depends on which PDFT version (I, II, III) is considered. In each of these versions it is assumed that there exists an effective 2P Schrödinger equation generating orthonormal geminals in such a way that the true pair density and the true cumulant pair densities are given by geminals just as in the conventional DFT the density is given by 1P orbitals (v representability). Because "scientists have not yet learned to think in terms of $\binom{N}{2}$ geminals, rather than in N orbitals" (Davidson [27], p. 97) there is on the one hand a "mental barrier," on the other hand it seems worthwhile to overcome it.

PDFT I: GEMINAL REPRESENTATION OF THE PAIR DENSITY $n(1; 2)$

Here the interaction energy $V_{\text{int}}[n]$ is given by Eq. (2.6). With the contraction (1.2) the external potential expectation is

$$V_{\text{ext}}[\rho[n]] = \int \frac{d1d2}{2!} n(1; 2) \frac{1}{N-1} \times [v_{\text{ext}}(1) + v_{\text{ext}}(2)]. \quad (5.1)$$

The 2-matrix (with $2' = 2$)

$$n(1, 1'; 2) = \sum_K^{\text{occ}} \psi_K(1, 2) \psi_K^*(1', 2) + \Delta n(1, 1'; 2) \quad (5.2)$$

is decomposed into a geminal part and an unknown remainder, which describes XC beyond the first term and has the property $\Delta n(1, 1; 2) = 0$ so that $1' = 1$ leaves

$$n(1; 2) = \sum_K^{\text{occ}} |\psi_K(1, 2)|^2 \quad (5.3)$$

as a variational ansatz for the pair density in terms of $\binom{N}{2}$ orthonormal antisymmetric geminals. With the contraction (3.3) the kinetic energy

$$T[\gamma[n]] = \sum_K^{\text{occ}} \frac{1}{N-1} \langle K | \hat{t}(1) + \hat{t}(2) | K \rangle + T_{\text{XC}}[n] \quad (5.4)$$

consists then of a part, explicitly given in terms of geminals [which are functionals of $n(1; 2)$] and an unknown remainder.

Minimizing the sum of $T, V_{\text{ext}}, V_{\text{int}}$ under the constraint $\int d1d2 n(1; 2) = N(N-1)$ yields the effective 2P Schrödinger equation

$$\left\{ \frac{1}{N-1} [\hat{h}_0(1) + \hat{h}_0(2)] + v_{\text{int}}(1, 2) + \frac{\delta T_{\text{XC}}[n]}{\delta n(1; 2)} \right\} \psi_K(1, 2) = \epsilon_K \psi_K(1, 2), \quad (5.5)$$

where XC makes the bare interaction "effective." Its self-consistent (sc) solution gives via Eq. (5.3) the GS pair density, from which follows the GS density by the contraction (1.2), as well as the GS

energy

$$E = \sum_K^{\text{occ}} \epsilon_K + T_{\text{XC}}[n] - \int \frac{d1d2}{2!} n(1; 2) \frac{\delta T_{\text{XC}}[n]}{\delta n(1; 2)}. \quad (5.6)$$

The 2P Hamiltonian of Eq. (5.5) corresponds (without the correlation correction—last term) to the reduced 2P Hamiltonian of Coleman [44].

PDFT II: GEMINAL REPRESENTATION OF THE EXCHANGE INCLUDING CUMULANT PAIR DENSITY $w(1; 2)$

Here the starting points are Eq. (3.5) and the decomposition of the cumulant 2-matrix (with $2' = 2$):

$$w(1, 1'; 2) = \frac{1}{2} \sum_{K_+}^{\text{occ}} \psi_{K_+}^+(1, 2) [\psi_{K_+}^+(1', 2)]^* - \frac{1}{2} \sum_{K_-}^{\text{occ}} \psi_{K_-}^-(1, 2) [\psi_{K_-}^-(1', 2)]^* + \Delta w(1, 1'; 2) \quad (5.7)$$

into two geminal parts and an unknown remainder which describes XC beyond the first terms and which has the property $\Delta w(1, 1; 2) = 0$ so that

$$w(1; 2) = \frac{1}{2} \sum_{K_+}^{\text{occ}} |\psi_{K_+}^+(1, 2)|^2 - \frac{1}{2} \sum_{K_-}^{\text{occ}} |\psi_{K_-}^-(1, 2)|^2 \quad (5.8)$$

is a variational ansatz for the cumulant pair density $w(1; 2)$ in terms of $N(N+1)/2$ symmetric geminals and $N(N-1)/2$ antisymmetric geminals. With the contraction (3.7) the kinetic energy

$$T[\gamma[w]] = \frac{1}{2} \sum_{K_+}^{\text{occ}} \langle K_+ | \hat{t}(1) + \hat{t}(2) | K_+ \rangle - \frac{1}{2} \sum_{K_-}^{\text{occ}} \langle K_- | \hat{t}(1) + \hat{t}(2) | K_- \rangle + T_{\text{XC}}[w] \quad (5.9)$$

consists then of a part, explicitly given in terms of geminals [which are functionals of $w(1; 2)$] and an unknown remainder. With the contraction (3.6) the external potential expectation is

$$V_{\text{ext}}[\rho[w]] = \int \frac{d1d2}{2!} w(1; 2) [v_{\text{ext}}(1) + v_{\text{ext}}(2)], \quad (5.10)$$

and the interaction energy $V_{\text{int}} = V_H + V_{\text{XC}}$ is given by Eqs. (2.7) and (2.8).

Minimizing the sum of T , V_{ext} , and V_{int} under the constraint $\int d1d2 w(1;2) = N$ yields the effective 2P Schrödinger equation:

$$\left\{ \hat{h}_H(1) + \hat{h}_H(2) - v_{\text{int}}(1,2) + \frac{\delta T_{\text{XC}}[w]}{\delta w(1;2)} \right\} \psi_K(1,2) = \epsilon_K \psi_K(1,2), \quad (5.11)$$

where $\hat{h}_H(1) = \hat{h}_0(1) + v_H(1)$. Again the bare interaction potential v_{int} [here with a minus sign arising from the minus sign in Eq. (3.5)] is made effective by an additional XC term.

The sc solution of Eq. (5.11) gives via Eqs. (5.8) and (3.6) the GS density and via Eq. (3.5) the GS pair density as well as the GS energy:

$$E = \frac{1}{2} \sum_{K_+}^{\text{occ}} \epsilon_{K_+} - \frac{1}{2} \sum_{K_-}^{\text{occ}} \epsilon_{K_-} - V_H[\rho[w]] + T_{\text{XC}}[w] - \int \frac{d1d2}{2!} w(1;2) \frac{\partial T_{\text{XC}}[w]}{\partial w(1;2)}. \quad (5.12)$$

Solving Eq. (5.11) the use of Hartree orbitals should be appropriate.

PDFT III: GEMINAL REPRESENTATION OF THE CORRELATION ONLY (EXCHANGE NOT INCLUDING) CUMULANT PAIR DENSITY $u(1,2)$

PDFT III goes a step further by using Eq. (3.12) and representing part of the cumulant pair density $u(1;2)$ in terms of antisymmetric geminals. Note that this scheme needs also the nonidempotent 1-matrix (at least approximately), which enters here not only the kinetic energy $T[\gamma]$ but also the cumulant X energy $V_X[\gamma]$, cf. Eqs. (2.4) and (2.8), and which yields the second-order nonidempotency $c = 1 - \text{Tr}(\gamma^2)/N$. Here the decomposition

$$u(1,1';2) = u_0(1,1';2) + \Delta u(1,1';2),$$

$$u_0(1,1';2) = \sum_K^{\text{occ}} \psi_K(1,2) \psi_K^*(1',2) \quad (5.13)$$

into a geminal part and an unknown remainder with the property $\Delta u(1,1';2) = 0$ provides

$$u(1;2) = \sum_K^{\text{occ}} |\psi_K(1,2)|^2 \quad (5.14)$$

as a variational ansatz for the cumulant pair den-

sity $u(1;2)$ in terms of $N/2$ antisymmetric geminals.

Now the 1-matrix γ is related to the ansatz (5.13) via the contraction (3.15). Consequently the (explicitly from geminals constructable) part γ_0 follows from $u_0(1,1';2)$ via

$$\gamma_0(1,1') = \int d2 \gamma_0(1,2) \gamma_0(2,1') = c_0 \int d2 u_0(1,1';2), \quad (5.15)$$

while the unknown remainder Δu causes the unknown remainder $\Delta \gamma$ via

$$\Delta \gamma(1,1') = \int d2 [\Delta \gamma(1,2) \gamma_0(2,1') + \gamma_0(1,2) \Delta \gamma(2,1') + \Delta \gamma(1,2) \Delta \gamma(2,1')] = c_0 \int d2 \Delta u(1,1';2) + \Delta c \int d2 u_0(1,1';2). \quad (5.16)$$

The use of $\gamma = \gamma_0 + \Delta \gamma$ in $T[\gamma]$ and $V_X[\gamma]$ leads to the complicated task of performing the variation of T with $\psi_K^*(1,2)$ via Eq. (5.15). In addition a consequence of $\gamma = \gamma_0 + \Delta \gamma$ is $\rho = \rho_0 + \Delta \rho$ which causes also unknown remainders not only of T and V_X , but also of V_{ext} and V_H .

With the simplifying assumption $(n_K)^2 \approx n_K \sum_K (n_K)^2 / N$ the nonlinear contraction (3.15) emerges the more simple linear form

$$\gamma(1,1') \approx \int d2 u(1,1';2), \quad (5.17)$$

which leads together with the ansatz (5.13) to the kinetic energy

$$T[\gamma[u]] = \sum_K^{\text{occ}} \langle K | \hat{t}(1) + \hat{t}(2) | K \rangle + \Delta T[u]. \quad (5.18)$$

The external potential expectation is

$$V_{\text{ext}}[\rho[u]] = \int \frac{d1d2}{2!} u(1;2) [v_{\text{ext}}(1) + v_{\text{ext}}(2)]. \quad (5.19)$$

The interaction energy $V_{\text{int}} = V_H + V_X + V_C$ is taken from Eqs. (2.7), (2.9), and (2.10) with $V_X[\gamma] = V_X[\gamma_0] + \Delta V_X[u]$. The sum of $\Delta T[u]$ and $\Delta V_X[u]$ is denoted $E_{\text{XC}}[u]$.

Minimizing the sum of T , V_{ext} , and V_{int} under the constraint $\int d1d2 u(1;2) = N$ yields now the effective 2P Schrödinger equation

$$\left\{ \hat{h}_{\text{HF}}(1) + \hat{h}_{\text{HF}}(2) - c_0 v_{\text{int}}(1,2) + \frac{\delta E_{\text{XC}}[u]}{\delta u(1;2)} \right\} \psi_K(1,2) = \epsilon_K \psi_K(1,2), \quad (5.20)$$

where $\hat{h}_{\text{HF}}(1) = \hat{h}_H(1) + \hat{v}_X(1)$ with $\hat{v}_X(1)f(1) = -\int d2 \gamma_0(1,2)v_{\text{int}}(2)f(2)$. As in version II the interaction has a minus sign, following from the minus sign of the last term in Eq. (3.13). Besides this, the second-order nonidempotency $c_0 = 1 - \text{Tr}(\gamma_0)^2/N$ appears as a factor renormalizing the bare interaction potential self-consistently. Again as in versions I and II an additional XC term makes the interaction effective. Deriving Eq. (5.20) terms arising from $\Delta c = c - c_0$ and from the functional derivative of the second-order nonidempotency have been deleted.

The sc solution of Eq. (5.20) gives via Eqs. (5.14) and (5.17) the approximate 1-matrix $\gamma_0(1,1')$ from which follows c_0 and $\rho(1)$, via Eq. (3.13) the GS pair density $n(1;2)$, and the GS energy

$$E = \sum_K^{\text{occ}} \epsilon_K - V_H[\rho[u]] - V_X[\gamma_0[u]] + E_{\text{XC}}[u] - \int \frac{d1d2}{2!} u(1;2) \frac{\delta E_{\text{XC}}[u]}{\delta u(1;2)}. \quad (5.21)$$

Solving Eq. (5.20) the geminals are suitably expanded in HF orbitals.

Summarizing and comparing the presented PDFT versions one may say:

Version I: Here the effective 2P Hamiltonian contains N , the total number of electrons explicitly. So it seems not appropriate for the TDL.

Version II: Here not only antisymmetric but also symmetric geminals appear and the density [via contracting Eq. (5.8) by integration over 2] proves to be the difference between two (large?) terms.

Version III: Here pair density and (nonidempotent) 1-matrix have to be calculated simultaneously and the XC term is not purely "kinetic" (as this is the case for versions I and II); it has also a "component" resulting from part of the potential (interaction) energy.

Versions II and III: The geminals of the cumulant pair densities $w(1;2)$ and $u(1;2)$ result from effective 2P Hamiltonians which contain the electron-

electron interaction with a minus sign, as if electrons would attract each other.

From a size consistency point of view version III seems perhaps to be the most appropriate one. But there are still flaws which one should try to overcome [e.g., replace the condition $\Delta u(1,1;2) = 0$ (or add to it) the requirement $\int d2 \Delta u(1,1';2) = 0$?].

6. Some Discussions, Open Questions, and Outlook

1. Even if the proposed schemes for the calculation of the pair density survive a critical analysis (possibly after corrections or modifications, e.g., with GONs $\neq 1$?), then the task remains at first to find reasonable approximations for the effective interaction.

a. One way could be to find scaling properties and to exploit them. To find the minimum of $E[n]$ one can first define the kinetic energy as a functional of the pair density with the constrained-search idea of Levy [45]:

$$T[n] = \lim_{\Psi \rightarrow n(1;2)} \frac{\langle \Psi | \hat{T} | \Psi \rangle}{\langle \Psi | \Psi \rangle}, \quad (6.1)$$

and then minimize $T[n] + V[n]$ under the constraint $\int d1d2 n(1;2) = N(N-1)$. Perhaps the scaling properties of $T[n]$ and consequently of $T_{\text{XC}}[n]$ and $T_{\text{XC}}[w]$ can be used to find explicit expressions (functionals). Based on the local scaling method an energy functional of the pair density has been derived [46].

b. Another way is to say that with each effective interaction a (static) dielectric function (DF) is defined which contains (beyond random-phase approximation) local-field corrections being related to the pair density via the static structure factor, cf. e.g. [47]. Possibly the "correct" DF includes higher-order response (beyond the linear one) via corresponding functional dependences. For different kinds of DFs (describing screening between two test charges or between a test charge and an electron or between two electrons), cf. [48]. For DFs of inhomogeneous systems, cf. [49]. For a relation between DF and pair correlation via the fluctuation-dissipation theorem within DFT, cf. [68].

2. Another task is to make the spin dependence more explicit by distinguishing between parallel and antiparallel pair densities.

a. A question in this connection is: Must the geminals be (restricted) eigenfunctions of the total spin $\hat{s}_1 + \hat{s}_2$ of the electron pair?

b. Another question: How to treat the total spin \hat{S} of the N -electron system on the way to an effective 2P equation?

3. The task to solve a 2P Schrödinger equation becomes easy for two model cases: the uniform electron gas and the Hooke's law model. Separation of the (free, respectively, harmonic) center-of-mass motion leaves behind the 1P problem for the relative motion.

4. How one can make use of the equation of motion:

$$\begin{aligned} & [\hat{h}_0(1) - \hat{h}_0^*(1')] \gamma(1, 1') \\ &= - \int d2 [v_{\text{int}}(1, 2) - v_{\text{int}}^*(1', 2)] n(1, 1'; 2) \quad (6.2) \end{aligned}$$

and, following from it, of the continuity equation and the local stress theorem (or momentum balance) [50]?

5. What is known from detailed quantum chemical studies of atoms and molecules about the structure (the eigenvalues) of the 2-matrix and its cumulant matrices and—possibly following thereof—would it be more appropriate to modify the decompositions (5.2), (5.7), and (5.13)? This may be especially important for cases where "super-geminals" appear with large GONs [51].

a. Do cases where ODLRO (= off-diagonal long-range order) appears need a special treatment?

b. A (at that time) controversial paper on superconductivity from a pair density is [52].

c. Do the Lagrange parameters ϵ_K in Eqs. (5.5), (5.11), and (5.20) have any physical meaning?

d. How does strong electron correlation show its peculiarities in the 1- and 2-matrices?

6. What are the relations between DFT and PDFT? In this connection one may ask: If a good DFT calculation is done, is it then reasonable/possible to think about an additional succeeding PDFT-like treatment of the 1-matrix remainder $\Delta\gamma(1, 1')$ and the pair density remainder $\Delta n(1; 2)$ hidden in the XC functional $E_{\text{XC}}[\rho]$ of DFT. Such a version IV should be derived under the constraint of an already known (from DFT) density.

7. Recently the N representability of the pair density was studied [53]. To what extent the results obtained therein have an impact on the considerations of Section 5 remains to be checked. For

the purpose of deriving effective 2P Schrödinger equations it seems to be sufficient that only the variational ansätze (5.3), (5.8), and (5.14) result from N particle wave functions.

In addition to further questions and references mentioned in [41] (cf. references [18–22] therein) in the following other hints to papers are listed, which might have relationship with the proposed PDFT:

a. There exists a rich literature on antisymmetrized geminal power (AGP) wave functions, cf. [8] and [54]; in [55] the 2-matrix of the AGP wave function has been studied.

b. Functionals of the 1-matrix and of the pair density are discussed, e.g., in [56–58] and [46], respectively.

c. What, if any, is the relationship of Section 5 to the density matrix hierarchy decoupling schemes of [59] and [60]? Therein the 2-matrix is approximated in terms of the 1-matrix, respectively, a "density equation" is derived, which yields the 2-matrix without any use of the many-electron wave function!

d. Another way of exploiting density matrices is to obtain the XC potential (of the Kohn–Sham scheme) from low-order density matrices [61].

d. What, if any, is the relationship to the Euler–Lagrange equation of [62] resulting from a trial wave function with a local correlation factor?

e. What, if any, is the relationship to quantum chemical methods (especially CC) [34, 72]?

f. In [69] an effective interaction (instead of the bare Coulomb interaction) is introduced so that already a single determinant of 1P orbitals (Coulomb-hole HF) or the linear combination of a few determinants give reasonable results for the density and the energy. Is there a relationship between this effective interaction and that of PDFT?

Finally the hope is expressed that the different approaches of quantum chemistry and solid-state theory to tackle the problems of weak and strong electron correlation in small and extended systems, crystalline (metallic and nonmetallic, perfect and with imperfections) as well as disordered (alloyed and amorphous) materials without and with pairing phenomena, with hard and soft reactivity, etc. can be brought to a fruitful/prolific interaction with the result of a unified theory of electron correlation, knowing that electron correlation is, of course, not only matter of the GS but of all the states of a system and their more or less hard or soft response when perturbing the system with external fields or when changing the number of electrons ("particle bath" as a sort of an external

"field"). For a historical review of the development of the electron correlation problem cf. [63]. In the future theory of electron correlation the GS pair density surely will have its firm place; although it is a more complicated quantum kinematic quantity (compared with the density), it may give finally a more clear/lucid picture of the internal dynamical structure of a many-electron system in its GS.

Appendix: Generalized Hohenberg-Kohn Theorem

0. In [64] a Hohenberg-Kohn theorem for the nondegenerate GS of an interacting system with a nonlocal external potential has been proven. Similar work is in [65, 66]. Here the variation of the pair density (and following from it also of the density) with local external and interaction potentials are considered.

1. For given $v_{\text{ext}}(1)$ and $v_{\text{int}}(1,2)$ the Hamiltonian \hat{H} may have a (nondegenerate) GS characterized by E, Ψ and, following from Ψ , by $n(1;2)$ and $\rho(1) = \int d2 n(1;2)/(N-1)$. Other potentials $v'_{\text{ext}}(1)$ and $v'_{\text{int}}(1,2)$ yield E', Ψ' , and $n'(1;2), \rho'(1)$. The assumption $n'(1;2) = n(1;2)$ leads to

$$E < E' + \int d1 \rho(1) [v_{\text{ext}}(1) - v'_{\text{ext}}(1)] + \int \frac{d1 d2}{2!} n(1;2) [v_{\text{int}}(1,2) - v'_{\text{int}}(1,2)]$$

and a similar inequality with primed and unprimed quantities exchanged. So $E + E' < E' + E$ would result showing the above assumption to be wrong. Conclusion from this contradiction: $n'(1;2) \neq n(1;2)$ when $v'_{\text{ext}}(1) \neq v_{\text{ext}}(1)$ and/or $v'_{\text{int}}(1,2) \neq v_{\text{int}}(1,2)$.

2. For given $v_{\text{ext}}(1)$ and $v_{\text{int}}(1,2)$ the GS energy is a functional of the pair density: $E[n] = T[n] + V_{\text{ext}}[n] + V_{\text{int}}[n]$. The pair density n_0 of the GS Ψ_0 minimizes $E[n]$ and this minimum $E[n_0]$ is the GS energy E_0 . Proof: Assume a state $\Psi_1 (\neq \Psi_0)$ which yields a pair density $n_1(1;2)$ and minimizes the kinetic energy according to Eq. (6.1), then

$$E_0 = \langle \Psi_0 | \hat{H} | \Psi_0 \rangle \leq \langle \Psi_1 | \hat{H} | \Psi_1 \rangle = E[n_1].$$

3. In [67] (the author thanks N. Ashcroft for giving a hint to this reference), it is similarly shown that under given conditions of (temperature and) density, the pair potential $v_{\text{int}}(1,2)$, which gives

rise to a given radial distribution function $n(1;2)$, is unique up to a constant.

Note added in proof: The DFT literature [1-21] is continued by H. Eschrig, *The Fundamentals of Density Functional Theory* (Teubner, Stuttgart, 1996).

ACKNOWLEDGMENTS

Discussions with H. Beck, A. J. Coleman, G. Diener, E. K. U. Gross, A. Holas, W. John, K. V. Kladko, M. Levy, P.-O. Löwdin, N. H. March, Y. Öhrn, J. P. Perdew, S. B. Trickey, R. Schumann are gratefully acknowledged. The author thanks P. Fulde for supporting this work and for several hints, J. P. Perdew and W. Stephan for critically reading the manuscript, and H. Scherrer and H. Wonn for technical help.

References

1. A. K. Rajagopal, *Adv. Chem. Phys.* **41**, 59 (1980); A. S. Bamzai and B. M. Deb, *Rev. Mod. Phys.* **53**, 95 (1981).
2. J. Keller and J. L. Gázquez, Eds., *Density Functional Theory* (Springer, Berlin, 1983).
3. R. G. Parr, *Ann. Rev. Phys. Chem.* **34**, 631 (1983).
4. P. Ziesche and G. Lehmann, Eds., *Ergebnisse in der Elektrophysik der Metalle* (Akademie Verlag und Springer Verlag, Berlin, 1983); G. Lehmann and P. Ziesche, *Electronic Properties of Metals* (Elsevier, Amsterdam, 1990); see also [73].
5. J. Callaway and N. H. March, *Solid State Phys.* **38**, 135 (1984).
6. J. P. Dahl and J. Avery, Eds., *Local Density Approximation in Quantum Chemistry and Solid State Physics* (Plenum, New York, 1984).
7. R. M. Dreizler and J. da Providência, Eds., *Density Functional Methods in Physics* (Plenum, New York, 1985).
8. R. Erdahl and V. H. Smith, Jr., Eds., *Density Matrices and Density Functionals* (Reidel, Dordrecht, 1987).
9. N. H. March and B. M. Deb, *The Single-Particle Density in Physics and Chemistry* (Academic, New York, 1987).
10. R. G. Parr and W. Yang, *Density Functional Theory of Atoms and Molecules* (Oxford University, New York, 1989); A. Goursot and H. Chermette, Eds., *J. Chim. Phys. Physicochim. Biol.* **86**(4), 647, 1989, special issue on application of density functional theory to properties of inorganic systems; E. Clementi and S. J. Chakravorty, *A Comparative Study of Density Functional Models to Estimate Molecular Atomization Energies*, IBM Research Report, KGN-215, 1990.
11. E. S. Kryachko and E. V. Ludena, *Energy Density Functional Theory of Many-Electron Systems* (Kluwer, Dordrecht, 1990).

12. S. B. Trickey, Ed., *Density Functional Theory of Many-Fermion Systems*, Adv. in Quantum Chem. **21** (Academic, San Diego, 1990).
13. R. M. Dreizler and E. K. U. Gross, *Density Functional Theory* (Springer, Berlin, 1990).
14. J. K. Labanowski and J. W. Andzelm, Eds., *Density Functional Methods in Chemistry* (Springer, Berlin, 1991).
15. N. H. March, *Electron Density Theory of Atoms and Molecules* (Academic, London, 1992).
16. N. Russo, Ed., Int. J. Quantum Chem. **52**(4), (1994) [special issue].
17. E. K. U. Gross and R. M. Dreizler, Eds., *Density Functional Theory* (Plenum, New York, 1995).
18. D. E. Ellis, Ed., *Density Functional Theory of Molecules, Clusters, and Solids* (Kluwer, Dordrecht, 1995).
19. D. P. Chong, Ed., *Recent Advances in Density Functional Methods*, Part I, Rec. Adv. in Comput. Chem. **1** (World Scientific, Singapore, 1995); J. M. Seminario and P. Politzer, Eds., *Modern Density Functional Theory: A Tool for Chemistry*, Theor. Comput. Chem. **2** (Elsevier, Amsterdam, 1995).
20. R. F. Nalewajski, Ed., *Topics in Current Chemistry* (Springer, Berlin, 1995); R. F. Nalewajski, Ed., Int. J. Quantum Chem. **56**(4, 5, 6) (1995) [special issues].
21. B. B. Laird, R. Ross, and T. Ziegler, Eds., *Chemical Applications of Density Functional*, American Chemical Society Symposium Series (American Chemical Society, Washington, DC, 1996).
22. C. A. Ullrich and E. K. U. Gross, Austral. J. Phys. **49**, 103 (1996); M. Petersilka, U. J. Gossmann, and E. K. U. Gross, Phys. Rev. Lett. **76**, 1212 (1996); M. Büchner, J. F. Dobson, and E. K. U. Gross, submitted.
23. M. A. Buijse, Ph.D. Thesis, Vrije Universiteit Amsterdam, 1991; R. van Leeuwen, Ph.D. Thesis, Vrije Universiteit Amsterdam, 1994; P. Süle, O. V. Gritsenko, Á. Nagy, and E. J. Baerends, J. Chem. Phys. **103**, 10085 (1995); O. V. Gritsenko, R. van Leeuwen, and E. J. Baerends, to appear.
24. M. Levy, Phys. Rev. A **52**, R4313 (1995); M. Levy and A. Görling, Phys. Rev. B **53**, 969 (1996); A. Seidl, A. Görling, P. Vogl, J. A. Majewski, and M. Levy, Phys. Rev. B **53**, 3764 (1996).
25. J. P. Perdew and K. Burke, Int. J. Quantum Chem. **57**, 309 (1996); K. Burke, J. P. Perdew, and M. Ernzerhof, to appear; J. P. Perdew, M. Ernzerhof, K. Burke, and A. Savin, to appear; J. P. Perdew, K. Burke, and Y. Wang, submitted; M. Ernzerhof, K. Burke, and J. P. Perdew, J. Chem. Phys., in press; A. Zupan, J. P. Perdew, K. Burke, and M. Causá, submitted.
26. M. Levy and J. P. Perdew, in *Density Functional Methods in Physics*, R. M. Dreizler and J. da Providência, Eds. (Plenum, New York, 1985), p. 11.
27. E. R. Davidson, *Reduced Density Matrices in Quantum Chemistry* (Academic, New York, 1976). In a series of papers the "geometry of density matrices" has been studied: J. E. Harriman, Phys. Rev. A **17**, 1249, 1257 (1978); Int. J. Quantum Chem. **15**, 611 (1979); Phys. Rev. A **27**, 632 (1983); for the asymptotics of RDMs, cf., e.g., K. A. Dawson and N. H. March, J. Chem. Phys. **82**, 1967 (1985) and M. Ernzerhof et al. in Ref. [25]; for the "structure of Fermion density matrices" cf. A. J. Coleman, Rev. Mod. Phys. **35**, 668 (1963); J. Math. Phys. **13**, 214 (1972); and J. Low Temperature Phys. **74**, 1 (1989) and references therein.
28. D. Collins, Z. Naturforsch. A **48**(1/2), 68 (1993).
29. P. Ziesche, Int. J. Quantum Chem. **56**, 363 (1995); P. Ziesche, in *Information. New Questions to a Multidisciplinary Concept*, K. Kornwachs and K. Jacoby, Eds. (Akademie Verlag, Berlin, 1996), p. 119.
30. P. Gersdorf, W. John, J. P. Perdew, and P. Ziesche, preprint mpi-mks 95/09/001, Dresden, 1995, and Int. J. Quantum Chem., in press.
31. R. O. Esquivel, A. L. Rodríguez, R. P. Sagar, M. Hô, and V. H. Smith, Jr., Phys. Rev. A **54**, 259 (1996); J. C. Ramirez, C. Soriano, R. O. Esquivel, R. P. Sagar, M. Hô, and V. H. Smith, Jr., to appear; M. Hô, R. P. Sagar, V. H. Smith, Jr., and R. O. Esquivel, J. Phys. B **27**, 5149 (1994) study atomic information entropies built up from position or momentum space densities.
32. P.-O. Löwdin, in *Density Matrices and Density Functionals*, R. Erdahl and V. H. Smith, Jr., Eds. (Reidel, Dordrecht, 1987), p. 21.
33. C. Tsallis, J. Stat. Phys. **52**, 479 (1988).
34. P. Fulde, *Electron Correlation in Molecules and Solids* (Springer, Berlin, 1991, 3rd enlarged edition, 1995).
35. R. Grobe, K. Rzążewski, and J. H. Eberly, J. Phys. B **27**, L503 (1994).
36. P. Gersdorf, Ph.D. Thesis, TU Dresden, 1996.
37. P. Ziesche, Habilitation Thesis, TU Dresden 1967; P. Ziesche and V. A. Sagrebnov, JINR P4-8220, Dubna, 1974.
38. R. Lenk, Ann. Physik (Leipzig) **19**, 88 (1967).
39. R. F. Bader, *Atoms in Molecules* (Clarendon, Oxford, 1990), p. 332.
40. E. Krotscheck, Phys. Lett. A **190**, 201 (1994).
41. P. Ziesche, Phys. Lett. A **195**, 213 (1994).
42. A. Gonis, T. C. Schulthess, J. van Ek, and P. E. A. Turchi, Phys. Rev. Lett. **77**, 2981 (1996); A. Gonis and T. C. Schulthess, to appear.
43. P. Ziesche, Solid State Commun. **82**, 597 (1992).
44. A. J. Coleman, in *Density Matrices and Density Functionals*, R. Erdahl and V. H. Smith, Jr., Eds. (Reidel, Dordrecht, 1987), p. 5; a recent paper dealing with pion distributions and the spectra of reduced Hamiltonians is A. J. Coleman, E. P. Yukalova, and V. I. Yukalov, Int. J. Quantum Chem. **54**, 211 (1995).
45. M. Levy, Proc. Natl. Acad. Sci. USA **76**, 6062 (1979); see also S. M. Valone, J. Chem. Phys. **73**, 1344 (1980).
46. T. Koga, J. Quantum Chem. **93**, 5856 (1990).
47. P. Vashishta and K. S. Singwi, Phys. Rev. B **6**, 875 (1972); G. Senatore and N. H. March, Rev. Mod. Phys. **66**, 445 (1994).
48. L. Kleinman, Phys. Rev. **172**, 383 (1968).
49. M. Taut, J. Phys.: Condens. Matter **4**, 9595 (1992).
50. P. Ziesche, in *Density Functional Theory*, E. K. U. Gross and R. M. Dreizler, Eds. (Plenum, New York, 1995), p. 559 and references therein.
51. In V. H. Smith's group the Be GS was naturally analyzed and the largest GON was appreciably greater than 1 (they use the term "supergeminals" for such cases); very large GONs equalling $[N/2]$ appear for very special wave functions ("extrem AGP"), cf. Ref. [8], p. 35, C. N. Yang, Rev.

- Mod. Phys. **34**, 694 (1962), and F. Sasaki, Phys. Rev. **138**, B1338 (1965).
52. A. J. Coleman, in *Quantum Statistics and the Many-Body Problem*, S. B. Trickey, W. Kirk, and J. Dufty, Eds. (Plenum, New York, 1975), p. 239.
53. E. R. Davidson, Chem. Phys. Lett. **246**, 209 (1995); earlier papers dealing with the N representability of the pair density are, e.g., M. B. Ruskai, Phys. Rev. **183**, 129 (1969) and **A5**, 1336 (1972), cf. also Ref. [8] and references therein; A. Soirat, M. Flocco, and L. Massa, Int. J. Quantum Chem. **49**, 291 (1994) deal with N -representable density functional density matrices.
54. J. V. Ortiz, B. Weiner, and Y. Öhrn, Int. J. Quantum Chem. **S15**, 113 (1981).
55. M. Rosina, in *Reduced Density Operators with Application to Physical and Chemical Systems* (Queen's Papers in Pure and Applied Mathematics, No. 40), R. M. Erdahl, Ed. (Queen's University, Kingston, Ontario, 1974).
56. S. M. Valone and J. F. Capitani, Phys. Rev. A **23**, 2127 (1981).
57. A. Savin, Phys. Rev. A **52**, R1805 (1995).
58. M. Levy and A. Görling, Phys. Rev. A **52**, R1808 (1995).
59. C. Valdemoro, Phys. Rev. A **45**, 4462 (1992); F. Colmenero, C. Pérez del Valle, and C. Valdemoro, Phys. Rev. A **47**, 971 and 979 (1993).
60. H. Nakatsuji, Phys. Rev. A **14**, 41 (1976); H. Nakatsuji and K. Yasuda, Phys. Rev. Lett. **76**, 1039 (1996).
61. A. Holas and N. H. March, Int. J. Quantum Chem., in press.
62. J.-P. Blaizot and G. Ripka, *Quantum Theory of Finite Systems* (MIT Press, Cambridge/Massachusetts, 1986), p. 626.
63. P.-O. Löwdin, Int. J. Quantum Chem. **55**, 77 (1995) and Int. J. Quantum Chem. **55** (2, 3) (1995).
64. T. L. Gilbert, Phys. Rev. **B12**, 2111 (1975).
65. R. A. Donnelly and R. G. Parr, J. Chem. Phys. **69**, 4431 (1978).
66. E. Meron and J. Katriel, Phys. Lett. **61A**, 19 (1977).
67. R. L. Henderson, Phys. Lett. **49A**, 197 (1974).
68. E. Chacón and P. Tarazona, Phys. Rev. **B37**, 4013 (1988).
69. E. Clementi and G. Corongiu, in *Methods and Techniques in Computational Chemistry* (METECC-95), E. Clementi and G. Corongiu, Eds. (STEF, Cagliari, 1995), p. 1.
70. A. Eguiluz, 36th Sanibel Symposium (St. Augustine, Febr. 24–March 2, 1996).
71. M. Mödl, M. Dolg, P. Fulde, and H. Stoll, J. Chem. Phys., in press.
72. I. Lindgren and J. Morrison, *Atomic Many-Body Theory* (Springer, Berlin, 1982).
73. P. Ziesche and H. Eschrig, Eds., *Electronic Structure of Solids '91* (Akademie Verlag, Berlin, 1991).

On the Optimal Mixing of the Exchange Energy and the Electron–Electron Interaction Part of the Exchange–Correlation Energy

OLEG V. GRITSENKO, ROBERT VAN LEEUWEN, AND EVERT JAN BAERENDS

Afdeling Theoretische Chemie, Vrije Universiteit, De Boelelaan 1083, 1081 HV, Amsterdam, The Netherlands

Received February 25, 1996; accepted May 20, 1996

ABSTRACT

The optimal mixing coefficient C of the exchange energy E_x and the electron–electron interaction part of the exchange–correlation energy W_{xc}^1 in the formula for the total exchange–correlation energy E_{xc} was expressed through the ratio of the kinetic T_c and potential W_c contributions to the correlation energy E_c . This expression can be derived from a Heavyside step function model of the dependence of W_{xc}^λ on the coupling parameter of the electron interaction λ . Values of T_c and W_c obtained from ab initio wave functions were used to estimate C for a number of atoms and molecules. A strong dependence of T_c , W_c , and C on the bond distance was demonstrated for the case of the H_2 molecule. T_c and C approach zero in the bond-dissociation limit; so for an electron–pair bond, the admixing of exact exchange to obtain an accurate E_{xc} is strongly dependent on the bond length and has to disappear for weak interaction/large bond distances. The potential of the exchange–correlation hole constructed for H_2 from an ab initio second-order density matrix was compared with its generalized gradient approximation (GGA). © 1996 John Wiley & Sons, Inc.

Introduction

Exchange and correlation energies as defined in density functional theory (DFT) [1, 2] are

different quantities than the conventional ones used in ab initio quantum chemistry. They are defined with respect to the determinantal wave function of Kohn–Sham orbitals rather than with respect to the Hartree–Fock determinantal wave function. We briefly recall the relevant definitions.

The exact total energy of an interacting electron system is written as

$$E = T + \int \rho(\mathbf{r})v(\mathbf{r})d\mathbf{r} + \frac{1}{2} \int \frac{\rho(\mathbf{r}_1)\rho(\mathbf{r}_2)}{|\mathbf{r}_1 - \mathbf{r}_2|} + W_{xc}, \quad (1)$$

where W_{xc} is the exchange-correlation part of the electron-electron interaction energy, which can be written employing either the two-electron density matrix $\Gamma(\mathbf{r}_1s_1, \mathbf{r}_2s_2)$ or the pair-correlation factor $g(\mathbf{r}_1, \mathbf{r}_2)$:

$$\begin{aligned} W_{xc}[\rho] &= \frac{1}{2} \sum_{s_1, s_2} \int \frac{\Gamma(\mathbf{r}_1s_1, \mathbf{r}_2s_2)}{|\mathbf{r}_1 - \mathbf{r}_2|} d\mathbf{r}_1 d\mathbf{r}_2 \\ &\quad - \frac{1}{2} \int \frac{\rho(\mathbf{r}_1)\rho(\mathbf{r}_2)}{|\mathbf{r}_1 - \mathbf{r}_2|} d\mathbf{r}_1 d\mathbf{r}_2 \\ &= \int \frac{\rho(\mathbf{r}_1)[g(\mathbf{r}_1, \mathbf{r}_2) - 1]\rho(\mathbf{r}_2)}{|\mathbf{r}_1 - \mathbf{r}_2|} d\mathbf{r}_1 d\mathbf{r}_2. \end{aligned} \quad (2)$$

The energy of the Kohn-Sham determinantal wave function Ψ_s is

$$\begin{aligned} E^{KS} &= \langle \Psi_s | H | \Psi_s \rangle \\ &= T_s + \int \rho(\mathbf{r})v(\mathbf{r})d\mathbf{r} \\ &\quad + \frac{1}{2} \int \frac{\rho(\mathbf{r}_1)\rho(\mathbf{r}_2)}{|\mathbf{r}_1 - \mathbf{r}_2|} d\mathbf{r}_1 d\mathbf{r}_2 + E_x, \end{aligned} \quad (4)$$

which defines the exchange energy in terms of the Kohn-Sham orbitals [see Eq. (17) below]. The exchange-correlation energy E_{xc} of DFT is now defined by writing the exact total energy in the following form:

$$\begin{aligned} E &= T_s + \int \rho(\mathbf{r})v(\mathbf{r})d\mathbf{r} \\ &\quad + \frac{1}{2} \int \frac{\rho(\mathbf{r}_1)\rho(\mathbf{r}_2)}{|\mathbf{r}_1 - \mathbf{r}_2|} d\mathbf{r}_1 d\mathbf{r}_2 + E_{xc}. \end{aligned} \quad (5)$$

Note that E_{xc} incorporates, apart from the electron-electron interaction term W_{xc} , also the difference between the exact and Kohn-Sham kinetic energies, $T - T_s$. The Kohn-Sham kinetic energy T_s is just the kinetic energy of independent parti-

cles occupying the Kohn-Sham orbitals:

$$T_s = -\frac{1}{2} \sum_{i=1}^N \int \phi_i^*(\mathbf{r}) \nabla^2 \phi_i(\mathbf{r}) d\mathbf{r}. \quad (6)$$

The following definitions are now self-explanatory:

$$\begin{aligned} E_c &= E - E^{KS} = E_{xc} - E_x \\ T_c &= T - T_s \\ E_{xc} &= E_x + E_c \\ W_{xc} &= E_x + W_c \\ E_{xc} &= W_{xc} + T_c = E_x + W_c + T_c \\ E_c &= W_c + T_c. \end{aligned} \quad (7)$$

The contributions W_{xc} and W_c will be referred to as the electron-electron potential energy parts (or just potential parts) of the exchange-correlation and correlation energies, respectively. It is interesting to observe that the DFT definition of the correlation energy E_c does not involve, as does the conventional definition, correlation corrections to electron-nuclear and Hartree electron-electron interaction energies, since the exact and Kohn-Sham one-electron densities do not differ, while the exact and Hartree-Fock one-electron densities do. The DFT definitions will not differ much from the conventional ones in systems where there is little near-degeneracy correlation and the Hartree-Fock approximation is a good zero-order starting point. In systems with strong near-degeneracy correlation, however, the Hartree-Fock density may differ strongly from the exact one and the DFT quantities are very different from the conventional ones [3, 4].

A key formula of DFT to obtain the exchange-correlation energy $E_{xc}[\rho]$ of a many-electron system is an integral [5-7] over the coupling parameter λ of the electron interaction λ/r_{12} :

$$\begin{aligned} E_{xc}[\rho] &= \int \int_0^1 \frac{\rho(\mathbf{r}_1)[g^\lambda(\mathbf{r}_1, \mathbf{r}_2) - 1]\rho(\mathbf{r}_2)}{|\mathbf{r}_1 - \mathbf{r}_2|} d\lambda d\mathbf{r}_1 d\mathbf{r}_2, \end{aligned} \quad (9)$$

where $\rho(\mathbf{r})$ is the electron density and $g^\lambda(\mathbf{r}_1, \mathbf{r}_2)$ is the pair-correlation function of a system in which the electron-electron interaction is λ/r_{12} and in which an "external" potential $v^\lambda(\mathbf{r})$ is present of such a form that the one-electron density $\rho^\lambda(\mathbf{r})$ corresponding to the exact wavefunction Ψ^λ is equal to the exact density $\rho(\mathbf{r})$ of the fully interacting system at each λ . Usually, the integration over

λ is effectively carried out first and $E_{xc}[\rho]$ is expressed as the spatial integral

$$E_{xc}[\rho] = \int \frac{\rho(\mathbf{r}_1)[\bar{g}(\mathbf{r}_1, \mathbf{r}_2) - 1]\rho(\mathbf{r}_2)}{|\mathbf{r}_1 - \mathbf{r}_2|} d\mathbf{r}_1 d\mathbf{r}_2 \quad (10)$$

of the coupling constant integrated pair-correlation function $\bar{g}(\mathbf{r}_1, \mathbf{r}_2)$:

$$\bar{g}(\mathbf{r}_1, \mathbf{r}_2) = \int_0^1 g^\lambda(\mathbf{r}_1, \mathbf{r}_2) d\lambda. \quad (11)$$

Numerous approximations of $\bar{g}(\mathbf{r}_1, \mathbf{r}_2)$ were used in DFT to calculate $E_{xc}[\rho]$ via Eq. (10).

One can, alternatively, carry out first the spatial integrations in Eq. (10) and represent $E_{xc}[\rho]$ as an integral of the electron-electron interaction energy part $W_{xc}^\lambda[\rho]$ of the exchange-correlation energy of electrons in the model system with the pair-correlation function $g^\lambda(\mathbf{r}_1, \mathbf{r}_2)$:

$$E_{xc}[\rho] = \int_0^1 W_{xc}^\lambda[\rho] d\lambda. \quad (12)$$

In its turn, $W_{xc}^\lambda[\rho]$ may be expressed as an integral of the potential of the exchange-correlation hole $v_{xc}^{hole, \lambda}(\mathbf{r})$:

$$W_{xc}^\lambda[\rho] = \frac{1}{2} \int \rho(\mathbf{r}) v_{xc}^{hole, \lambda}(\mathbf{r}) d\mathbf{r}, \quad (13)$$

$$v_{xc}^{hole, \lambda}(\mathbf{r}_1) = \int \frac{\rho(\mathbf{r}_2)[g^\lambda(\mathbf{r}_1, \mathbf{r}_2) - 1]}{|\mathbf{r}_1 - \mathbf{r}_2|} d\mathbf{r}_2. \quad (14)$$

Expression (12) can also be used as a basis for the DFT approximations. In particular, Becke proposed in [8] to approximate the dependence of W_{xc}^λ on λ with a linear function, so that integral (12) is calculated in this approximation via the simple trapezoidal rule ("half-and-half" formula):

$$E_{xc}[\rho]^{mod} = \frac{1}{2} W_{xc}^1[\rho] + \frac{1}{2} E_x[\rho], \quad (15)$$

where $E_x[\rho] \equiv W_{xc}^0[\rho]$ is the exchange energy of the Kohn-Sham ($\lambda = 0$) system, the pair-correlation function of which, $[g^0(\mathbf{r}_1, \mathbf{r}_2) - 1]$, of course, only describes the exchange hole. With W_{xc}^1 approximated with the functional W_{xc}^{LSDA} of the local spin-density approximation (LSDA) [9] and with the rigorous exchange functional E_x of the Kohn-Sham (KS) orbitals (the latter were obtained from the self-consistent LSDA calculations) for-

mula (15) provides reasonable accuracy for the calculated atomization energies E_a of a representative set of molecules. A linear combination of W_{xc}^{LSDA} and E_x with the coefficients fitted to experimental data yields substantially better E_a values [8] and an empirical combination of E_x with four approximate exchange and correlation functionals [10] reproduces also total atomic energies, atomic and molecular ionization potentials, and molecular proton affinities.

The question arises, What is the optimal mixing of W_{xc}^1 and E_x to provide an accurate E_{xc} value for a given system? In this article, an exact mixing coefficient C is expressed through the ratio of the kinetic T_c and potential W_c contributions to the correlation energy E_c . This mixing can be derived from a Heaviside step function model of the dependence of W_{xc}^λ on λ , which is an alternative to the linear interpolation model of Becke. Values of T_c and W_c obtained using accurate quantities (ρ, E, T, E_x) from ab initio wave functions are used to estimate C for a number of atoms and molecules. The dependence of T_c , W_c , and C on the bond distance is analyzed in the case of the H_2 molecule and an accurate asymptotic formula for T_c is obtained for the bond dissociation limit. The shape of the potential $v_{xc}^{hole, 1}$ as function of the electron coordinate \mathbf{r} is obtained from an accurate ab initio second-order density matrix for H_2 [11, 12] and is compared to its generalized gradient approximation (GGA) [13-15].

A Mixing Formula and a Model of the λ Dependence

In this article, a mixing formula of the type

$$E_{xc}[\rho]^{mod} = (1 - C)W_{xc}^1 + CE_x \quad (16)$$

is considered, which mixes the upper and the lower limits of the integral (12). In the case of $\lambda = 0$, the general formula (13) for W_{xc}^λ can be rewritten in terms of the occupied KS orbitals $\phi_i(\mathbf{r})$:

$$W_{xc}^0[\rho] \equiv E_x[\rho] = -\frac{1}{2} \sum_{i=1}^N \sum_{j=1}^N \times \int \frac{\phi_i(\mathbf{r}_1)\phi_i^*(\mathbf{r}_2)\phi_j^*(\mathbf{r}_1)\phi_j(\mathbf{r}_2)}{|\mathbf{r}_1 - \mathbf{r}_2|} d\mathbf{r}_1 d\mathbf{r}_2. \quad (17)$$

The difference between $W_{xc}^1[\rho]$ and $E_x[\rho]$ is the potential energy part $W_c[\rho]$ of the correlation energy [cf. Eqs. (8)]:

$$W_{xc}^1[\rho] - E_x[\rho] = W_c[\rho] = \frac{1}{2} \int \rho(r) v_c^{hole,1}(r) dr, \quad (18)$$

where $v_c^{hole,1}$ is the potential of the Coulomb hole, the difference between the complete hole described by $[g^{\lambda=1}(r_1, r_2) - 1]$ and the exchange hole described by $[g^0(r_1, r_2) - 1]$. The integrand of Eq. (12) is the exchange-correlation part of the electron-electron potential energy, but the integration over λ produces the total $E_{xc}[\rho]$ including its kinetic contribution T_c :

$$E_{xc}[\rho] = \int_0^1 W_{xc}^\lambda[\rho] d\lambda = E_x[\rho] + W_c[\rho] + T_c[\rho]. \quad (19)$$

For a particular many-electron system, the exact value of the mixing coefficient C in formula (16) can be defined from the requirement that (16) should reproduce the accurate value of $E_{xc}[\rho]$:

$$E_{xc}[\rho] = E_x[\rho] + W_c[\rho] + T_c[\rho], \quad (20)$$

$$\begin{aligned} E_{xc}^{mod,\lambda}[\rho] &= (1 - C)W_{xc}^{\lambda=1} + CE_x \\ &= E_x[\rho] + W_c[\rho] + T_c[\rho]. \end{aligned} \quad (21)$$

From Eqs. (8) [cf. also (18)], the expression for C follows:

$$C = -\frac{T_c}{W_c}. \quad (22)$$

The ratio (22) provides a theoretical estimate for the optimal mixing coefficient of the exchange-correlation and exchange functionals in the formula for E_{xc} .

The mixing formula (16) can be derived from a model, in which the λ dependence of W_{xc}^λ is approximated with the Heavyside step function $\theta(x)$:

$$W_{xc}^{mod,\lambda} = \theta(\lambda - C)(W_{xc}^1 - E_x) + E_x, \quad (23)$$

$$\theta(x) = \begin{cases} 1 & \text{if } x > 0 \\ 0 & \text{if } x \leq 0. \end{cases}$$

The integration of (23) over λ yields the mixing formula (16). The step-function model (23) can be considered as an alternative to Becke's linear inter-

polation model:

$$W_{xc}^{mod,\lambda} = \lambda W_{xc}^1 + (1 - \lambda)E_x, \quad (24)$$

the latter yielding after the λ integration the trapezoidal rule formula (15). Contrary to model (24) with its relatively smooth dependence on λ , Eq. (23) models a sharp dependence with a region $\lambda \leq C$ of weak Coulomb correlation, where $W_{xc}^{mod,\lambda}$ is assumed to be equal to its exchange-only limit E_x and a region $\lambda > C$ of strong Coulomb correlation, where $W_{xc}^{mod,\lambda}$ is assumed to be equal to its full strength limit W_{xc}^1 . In the weakly correlated mode, the system is assumed to have the exchange-only pair-correlation function $g^0(r_1, r_2)$, while the full-strength pair-correlation function $g^1(r_1, r_2)$ is attributed to the strongly correlated mode. The mixing coefficient C in this model has the meaning of a critical coupling strength, at which the transition occurs from the weakly correlated system to the strongly correlated system. In the next sections, the optimal mixing coefficient C will be estimated from the available data on T_c and the Coulomb correlation energy E_c and the dependence of C on the bond distance will be studied in the case of the H_2 molecule.

The Ratio $-T_c/W_c$ for Atoms and Molecules

Table I represents values of T_c obtained for a number of atoms [16] and molecules [17, 18] and the corresponding values of W_c and $C = -T_c/W_c$. The values for T_c were obtained as the difference

$$T_c^{CI} = T^{CI} - T_s \quad (25)$$

of the kinetic energy T^{CI} calculated for the system with the configuration interaction (CI) method and T_s , the latter being obtained by available methods [19, 20] to construct the KS orbitals and potential from the CI electron density. W_c is evaluated as

$$W_c = E_{c, HF}^{CI} - T_c^{CI}, \quad (26)$$

where the (CI approximation to the) conventional correlation energy $E_{c, HF}^{CI}$ is the difference between the total energies of the CI and Hartree-Fock methods:

$$E_{c, HF}^{CI} = E^{CI} - E^{HF}, \quad (27)$$

as it is traditionally defined in quantum chemistry. Note that we are approximating here the DFT correlation energy or, rather, the best CI approxi-

TABLE I
Correlation energy components (au) and their ratios.

System	T_c	W_c	C
He	0.037	-0.079	0.47
Li	0.038	-0.083	0.46
Be	0.074	-0.168	0.44
B	0.095	-0.216	0.44
C	0.12	-0.272	0.44
N	0.15	-0.330	0.45
O	0.19	-0.435	0.44
F	0.24	-0.546	0.44
Ne	0.30	-0.676	0.44
Na	0.31	-0.696	0.44
Mg	0.34	-0.752	0.45
Al	0.35	-0.765	0.46
Si	0.36	-0.781	0.46
P	0.41	-0.862	0.47
H ₂	0.032	-0.071	0.45
LiH	0.057	-0.134	0.43
BH	0.099	-0.236	0.42
HF	0.237	-0.541	0.44

mation to it,

$$E_c^{CI} = E^{CI} - E^{KS}[\rho], \quad (28)$$

by the conventional correlation energy $E_{c, HF}^{CI}$. This replacement is acceptable, for the present purpose of interpretation, for atoms and for the chosen molecules at their equilibrium geometry, because in this case, the Hartree-Fock electron density ρ^{HF} is close to the correlated density ρ , so that $E^{KS}[\rho]$ and E^{HF} values should also be close to each other. The accuracy of the CI wave function varies from system to system, so that a comparison of absolute values of T_c and W_c is not always meaningful. On the other hand, their ratio C is expected to be less influenced by the errors of the limited CI.

For eight of 18 systems considered, C has the same value $C = 0.44$, while for the other systems, deviations from this value are not large and C varies within the range 0.43–0.47. It follows from these results that for the considered atoms and for molecules at the equilibrium geometry (at least if there are not strong correlation effects at the equilibrium geometry) the optimal mixing is not very sensitive to the type of the system and E_{xc} can be reproduced with the following combination of ac-

curate functionals:

$$E_{xc}[\rho] \approx 0.56W_{xc}^1 + 0.44E_x, \quad (29)$$

which is not far from the "half-and-half" formula (15) of Becke. In terms of the Heavyside step function model (23), it means that the region of strong Coulomb correlation spans a slightly larger portion of the interval $0 \leq \lambda \leq 1$ and at the coupling strength value $\lambda = 0.44$ the system undergoes a transition from the weakly correlated mode to the strongly correlated mode.

Note that if, instead of the functional T_c of DFT and W_c of Eq. (26), their conventional quantum chemical analogs $T_{c, HF}$ and $W_{c, HF}$,

$$T_{c, HF} = T - T^{HF}, \quad (30)$$

$$W_{c, HF} = E_{c, HF} - T_{c, HF}, \quad (31)$$

$$E_{c, HF} = E - E^{HF}, \quad (32)$$

are inserted in (22), C would be always equal to 0.5 because of the virial theorem, which holds true for the exact solution, as well as for the Hartree-Fock solution with the total and kinetic energies E^{HF} , T^{HF} , and electron density ρ^{HF} . Levy et al. [21] recently made the analogous observation that eq. (15) would be exact in case the virial relation $E_{c, HF} = -T_{c, HF}$ would also hold for E_c and T_c . This is in agreement with our exact relation $C = -T_c/(E_c - T_c)$. The reason for the lower values of C obtained (see Table I) is the difference between T_s and T_{HF} . By its definition, the KS kinetic functional $T_s[\rho]$ minimizes the kinetic energy (6) for the correlated density ρ . This density is usually somewhat more contracted around the nuclei (the exact kinetic energy is higher than the HF kinetic energy) and the minimal kinetic energy for ρ^{exact} is still higher than is T_{HF} . As a result, C of Eq. (22) is consistently lower than $C = -T_{c, HF}/W_{c, HF} = 0.5$.

From the results presented, one can conclude that for atoms and for molecules at the equilibrium geometry the model with the step-function λ dependence provides only a slight alteration in comparison with the linear interpolation model. However, the step-function model has a definite advantage over the linear model for the process of molecular dissociation, because of the well-known deficiency of the exchange-only functionals in the bond dissociation limit. In the next section, the dependence of T_c and C on the bond distance will be considered for the simplest case of the H₂ molecule.

H₂: The Dependence of T_c and C on the Bond Distance

T_c and C exhibit a strong dependence on the bond distance and in the bond dissociation limit of the H₂ molecule both T_c and C approach zero. To establish this trend, we shall derive first the asymptotic expression for T_c . In the bond dissociation limit, the H₂ molecule is described properly with the Heitler–London wave function $\Psi^{HL}(x_1, x_2)$:

$$\Psi^{HL}(x_1, x_2) = \frac{a^*(r_1)b(r_2) + a^*(r_2)b(r_1)}{2(1 + S_{ab}^2)^{\frac{1}{2}}} \times [\alpha(s_1)\beta(s_2) - \alpha(s_2)\beta(s_1)], \quad (33)$$

where $a(r)$ and $b(r)$ are the 1s-type atomic orbitals located on the H atoms A and B , $\alpha(i)$ and $\beta(i)$ are the one-electron spin functions, and S_{ab} is the overlap integral:

$$S_{ab} = \int a^*(r)b(r) dr. \quad (34)$$

A convenient feature of the KS theory is that in the dissociation limit the KS system of H₂ is properly described with the one-determinantal wave function $\Psi_s(x_1, x_2)$ formed from the σ_g combinations of the 1s orbitals $a(r)$ and $b(r)$ (except possibly at the bond midpoint):

$$\Psi_s(x_1, x_2) = \frac{(a^*(r_1) + b^*(r_1))(a(r_2) + b(r_2))}{2\sqrt{2}(1 + S_{ab})} \times [\alpha(s_1)\beta(s_2) - \alpha(s_2)\beta(s_1)], \quad (35)$$

since just $\Psi_s(x_1, x_2)$ generates the ground-state density $\rho(r)$ in this limit. Subtracting the kinetic energy obtained with $\Psi_s(x_1, x_2)$ from that obtained with $\Psi^{HL}(x_1, x_2)$, one can derive an asymptotic expression for T_c :

$$T_c = \langle \Psi^{HL} | \hat{T} | \Psi^{HL} \rangle - \langle \Psi_s | \hat{T} | \Psi_s \rangle = \frac{2(T_a S_{ab} - T_{ab})(1 - S_{ab})}{(1 + S_{ab})(1 + S_{ab}^2)}, \quad (36)$$

where T_a and T_{ab} are the kinetic integrals:

$$T_a = -\frac{1}{2} \int a^*(r) \nabla^2 a(r) dr, \quad (37)$$

$$T_{ab} = -\frac{1}{2} \int a^*(r) \nabla^2 b(r) dr. \quad (38)$$

The difference between the total energies obtained with $\Psi^{HL}(x_1, x_2)$ and $\Psi_s(x_1, x_2)$, the correlation energy, E_c , approaches with increasing H—H distance its exact finite limiting value -0.3125 au [22]. On the other hand, T_c , the difference (36) between the corresponding kinetic energies decreases with decreasing S_{ab} and T_{ab} at longer bond distances and it becomes zero in the infinite separation limit:

$$T_c \rightarrow 0, R(H-H) \rightarrow \infty. \quad (39)$$

Note a striking difference between T_c and the conventional kinetic contribution $T_{c, HF}$: The latter function approaches in this limit the finite value 0.2565 au [4].

As a consequence of the asymptotics (36), the optimal mixing coefficient C of Eq. (22) decreases with decreasing T_c and becomes zero in the infinite separation limit:

$$C = -\frac{T_c}{W_c} \rightarrow 0, R(H-H) \rightarrow \infty, \quad (40)$$

so that the mixing formula (16) correctly reduces to W_{xc}^1 :

$$E_{xc}^{mod} = (1 - C)W_{xc}^1 + CE_x \rightarrow W_{xc}^1, R(H-H) \rightarrow \infty. \quad (41)$$

In terms of the Heavyside step-function model (23), Eq. (40) means that in the infinite separation limit for all λ but $\lambda = 0$ the system is in the strongly correlated mode. This is physically reasonable in view of the negligible interaction between the H atoms at infinite distance, so that the model offers a physically correct picture [23, 24]. For all $\lambda > 0$, the interaction term λ/r_{12} will favor the Heitler–London wave function $\Psi^{HL}(x_1, x_2)$ [Eq. (33)] in which two electrons are residing on different atoms. Only for $\lambda = 0$, the exact wave function for the noninteracting electrons is just the KS determinant $\Psi_s(x_1, x_2)$ of Eq. (35). The $\lambda = 0$ point, however, becomes unimportant in the cou-

pling constant integration for the pair-correlation function and we have

$$\begin{aligned} \lim_{R \rightarrow \infty} \bar{g}(r_1, r_2) \\ = \lim_{R \rightarrow \infty} \int_0^1 g^\lambda(r_1, r_2) d\lambda = \int_0^1 g^1(r_1, r_2) d\lambda \\ = g^1(r_1, r_2). \end{aligned} \quad (42)$$

In this case, the step-function model has a definite advantage over the linear interpolation model of Eq. (24), which for each λ appears to mix $\Psi^{HL}(x_1, x_2)$ and $\Psi_s(x_1, x_2)$, leading to an unwarranted E_x contribution to E_{xc} . As a result, the mixing formula (16) provides in this case a considerable improvement over Becke's "half-and-half" formula.

To study the dependence of T_c , W_c , and C for a wide range of bond distances $R(\text{H-H})$, we use T_c and E_c values calculated in [25] at several distances from a full-CI wave function. In this case, the rigorous quantity E_c^{CI} of Eq. (28) was used to estimate $W_c = E_c - T_c$, since the difference between E_c^{CI} and $E_{c, HF}^{CI}$ becomes appreciable at longer distances. The Hartree-Fock one-electron density deviates quite strongly from the exact density at longer bond distances, to the extent that the conventional correlation corrections to the one-electron energies, the Hartree-Fock electron-nuclear potential energy and the Hartree-Fock kinetic energy, become larger in magnitude than the correlation correction to the two-electron part of the energy [4]. The assumptions made in compiling Table I would not be justified for dissociating H_2 . In Figure 1, the plots of $T_c(R)$, $W_c(R)$, and $C(R)$ as functions of $R(\text{H-H})$ are presented. One can see from Figure 1 that in the interval of $R = 1-4$ au T_c shows a slight dependence on R , reaching its maximum $T_c = 0.042$ Hartrees at $R = 3$ au. For longer distances, T_c gradually decreases, approaching zero asymptotically (39). On the other hand, the absolute value of W_c increases monotonically with increasing R . As a result, their ratio C gradually decreases with increasing R ; the only exception is a local plateau of $C(R)$ in the interval $R = 2.0-2.5$ au. From these results, one can conclude that, at least in the considered case of the H_2 molecule, the optimal mixing coefficient C depends strongly on the bond distance.

The conclusions reached here on the asymptotics of T_c can be generalized for the case of a many-electron homonuclear molecule. In this case, the value of T_c in the dissociation limit becomes

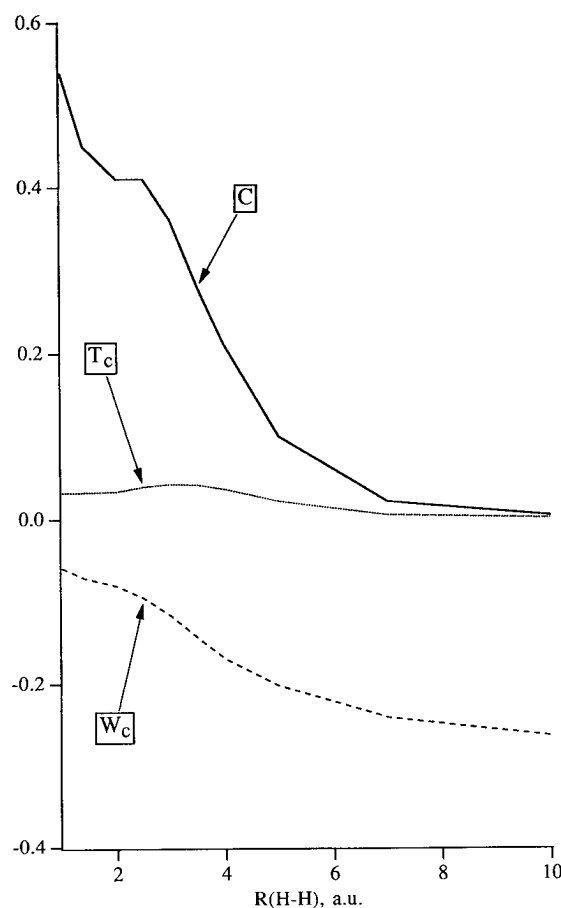


FIGURE 1. T_c , W_c (au), and C as functions of the bond distance for the H_2 molecule.

equal to the sum of the T_c contributions of the atomic fragments. The λ -integrated exchange-correlation hole for a reference electron on one of the atomic fragments will then be equal to the λ -integrated hole of the atom itself. In the particular case of the H_2 molecule, this leads to the established asymptotics (39), because for the one-electron H atom, $T_c = 0$.

Conclusions

In this article, the exact coefficient C of mixing of the exchange E_x and the exchange-correlation potential energy W_{xc}^1 in the formula for the total exchange-correlation energy E_{xc} was expressed through the ratio of the kinetic T_c and potential W_c contributions to the correlation energy E_c . This mixing corresponds to a Heaviside step-function model of the dependence of W_{xc}^λ on

λ , where C has the meaning of a critical coupling strength, at which the transition occurs from the weakly correlated system to the strongly correlated system. Values of T_c and W_c obtained from CI wave functions were used to estimate C for a number of atoms and molecules. For the H_2 molecule, the strong dependence of T_c , W_c , and C on the bond distance was demonstrated and an accurate asymptotic formula for T_c was obtained, according to which T_c and C approach zero in the bond-dissociation limit. This dependence of the admixing of "exact exchange" on the bond distance should be taken into account in the actual applications of mixing formulas.

To apply various mixing formulas, one has to approximate W_{xc}^1 with one of the currently available approximate functionals. Thus, the problem of the quality of the approximate functionals W_{xc}^{mod} arises. The potential of the exchange–correlation hole $v_{xc}^{hole,1}(r)$ which, according to Eq. (13), yields the potential energy $W_{xc}^1[\rho]$, may be used to ob-

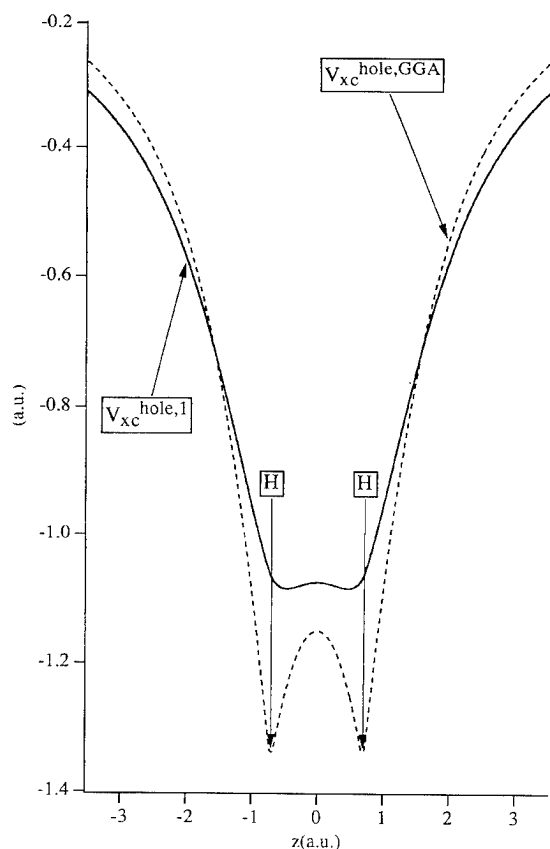


FIGURE 2. Comparison of the potential of the exchange–correlation hole and its GGA approximation (au) for the H_2 molecule at $R(H-H) = 1.401$ au.

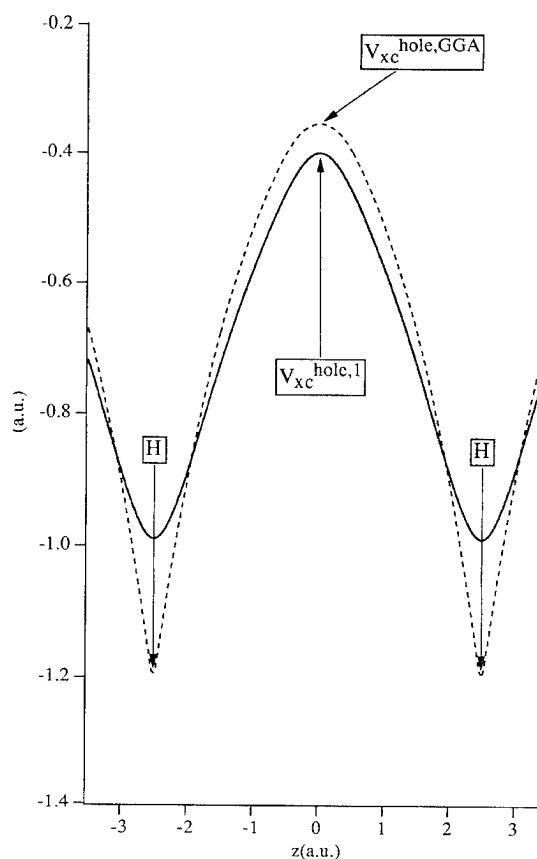


FIGURE 3. Comparison of the potential of the exchange–correlation hole and its GGA approximation (au) for the H_2 molecule at $R(H-H) = 5.0$ au.

tain some insight in the quality of the r -dependence of approximations to the exchange–correlation energy density. In Figures 2 and 3, the essentially accurate potential $v_{xc}^{hole,1}$ obtained for the H_2 molecule from the full-CI second-order density matrix [11, 12] at the equilibrium bond distance and at the long distance $R(H-H) = 5$ au is represented as a function of the distance Z from the bond midpoint. It is compared with its GGA model $v_{xc}^{hole,GGA}$, which is calculated via the following formula:

$$v_{xc}^{hole,GGA}(\mathbf{r}) = 2\epsilon_x^{LDA}(\mathbf{r}) + 2\epsilon_x^B(\mathbf{r}) + 2\epsilon_c^{PW}(\mathbf{r}) - 2t_c^{PW}(\mathbf{r}). \quad (43)$$

Here, ϵ_x^{LDA} is the exchange energy density (per particle) of the local density approximation (LDA), $2\epsilon_x^B$ is the gradient-dependent correction to ϵ_x^{LDA} of Becke [13], ϵ_c^{PW} is the Coulomb correlation energy density of Perdew and Wang [9, 14, 15], and $t_c^{PW}(\mathbf{r})$ is the kinetic correlation energy den-

TABLE II
Exchange-correlation energy (au) and its components for the H₂ molecule.

$R(\text{H-H})$ (au)	E_x	E_x^{GGA}	E_x^{LDA}	E_x^{B}	W_c	W_c^{PW}	W_{xc}^{GGA}	W_{xc}^1
1.401	-0.661	-0.658	-0.569	-0.089	-0.071	-0.081	-0.739	-0.732
5.0	-0.410	-0.512	-0.423	-0.089	-0.207	-0.057	-0.569	-0.617

sity, which is obtained by the partial differentiation of $\epsilon_c^{\text{PW}}(\mathbf{r})$ [26-28]:

$$t_c^{\text{PW}}(\mathbf{r}) = -\epsilon_x(r_s) r_s \frac{\partial}{\partial r_s} \left[\frac{\epsilon_c^{\text{PW}}(r_s, x; \mathbf{r})}{\epsilon_x(r_s)} \right], \quad (44)$$

$$\epsilon_x(r_s) = -\frac{0.458}{r_s}, \quad (45)$$

$$r_s = \left[\frac{4}{3} \pi \rho(\mathbf{r}) \right]^{-\frac{1}{3}}, \quad (46)$$

$$x = \frac{|\nabla \rho(\mathbf{r})|}{\rho^{\frac{4}{3}}}. \quad (47)$$

Insertion of $v_{xc}^{\text{hole,GGA}}(\mathbf{r})$ of Eq. (43) into the integral (13) yields the exchange-correlation potential energy of GGA: W_{xc}^{GGA} .

In Table II, W_{xc}^{GGA} values calculated for $R(\text{H-H}) = 1.401$ and 5.0 au are presented together with the contributions to W_{xc}^{GGA} from the LDA exchange functional E_x^{LDA} , the Becke correction E_x^{B} , and the correlation contribution W_c^{PW} . They are compared with the corresponding values of the exact W_{xc}^1 , obtained by integration of $v_{xc}^{\text{hole,1}}$, and its contributions, the exchange energies E_x and correlation energies W_c . One can see from Table II that at the equilibrium distance GGA reproduces W_{xc}^1 very nicely; the corresponding difference is only 7 mHartrees. The LDA value E_x^{LDA} is lower than the accurate E_x , but the Becke correction compensates the difference, so that both exchange and correlation contributions are reproduced well within the GGA.

For the long distance $R = 5.0$ au, the E_x value becomes 251 mHartrees smaller (in an absolute sense) than that for the equilibrium distance, since in the former case, the exchange hole is delocalized over two well-separated H atoms. An increase of the left-right Coulomb correlation W_c from -0.071 to -0.207 due to the strong near-degeneracy effect, leading to a more pronounced Coulomb hole [4], compensates more than half of the above-mentioned difference, and the total W_{xc}^1 value at $R = 5.0$ au is only 115 mHartrees smaller than that for

$R = 1.401$ au. This reflects the fact that delocalization of the exchange hole at long bond distances is effectively compensated by delocalization of the Coulomb hole, so that the total exchange-correlation hole remains essentially localized around the reference electron [4].

The GGA correlation functional W_c^{PW} fails to reproduce the near-degeneracy effect at large bond length; it is only 27.5% of the exact W_c (see Table II) at $R = 5.0$ au. Its value is 150 mHartrees too small, being even smaller than that at $R = 1.401$ au. However, the GGA exchange functional ($E_x^{\text{GGA}} = E_x^{\text{LDA}} + E_x^{\text{B}}$) simulates a major part of the correlation: Its value at $R = 5.0$ au is ca. 100 mHartrees larger (more negative) than that of the accurate KS functional E_x . This comes about by the E_x^{LDA} being now slightly larger than E_x (13 mHartrees larger, not ca. 90 mHartrees smaller as is the case at $R = 1.401$ au) and the Becke correction, being equally large as at $R = 1.401$ au, adding an overcorrection of 89 mHartrees. This yields about a 100 mHartrees too negative E_x^{GGA} , which partly compensates the 150 mHartrees too small GGA correlation contribution W_c^{PW} , resulting in a total W_{xc}^{GGA} that is "only" ca. 50 mHartrees smaller than W_{xc}^1 .

A comparison of the hole potentials $v_{xc}^{\text{hole,1}}$ and $v_{xc}^{\text{hole,GGA}}$ shows appreciable local deviations (See Figs. 2 and 3). For both bond distances considered, $v_{xc}^{\text{hole,GGA}}$ is more attractive than is $v_{xc}^{\text{hole,1}}$ in the neighborhood of the H nuclei and it is less attractive in the outer region of the H₂ molecule. In the bonding region, $v_{xc}^{\text{hole,GGA}}$ is more attractive than is $v_{xc}^{\text{hole,1}}$ for $R = 1.401$ au (see Fig. 2), while it is less attractive in this region for $R = 5.0$ au (see Fig. 3). The errors of opposite sign from the different regions cancel each other when $v_{xc}^{\text{hole,GGA}}$ is integrated via Eq. (13), thus providing the above-mentioned reasonable W_{xc}^{GGA} values.

One can conclude from the present results that further work is needed to develop an approximate functional $v_{xc}^{\text{hole,mod}}$, which will yield better W_{xc} values at longer distances and will provide a better approximation locally. In this respect, a promis-

ing way is not to split the functional into exchange and correlation parts, but try to develop from the very beginning a combined exchange–correlation approximation, which allows to retain a localized model of the exchange–correlation hole. The corresponding work is in progress.

ACKNOWLEDGMENTS

We gratefully acknowledge funding by the Netherlands Foundation for Scientific Research (NWO) and the Stichting Fundamenteel Onderzoek der Materie (FOM).

References

1. R. M. Dreizler and E. K. U. Gross, *Density Functional Theory: An Approach to the Quantum Many-Body Problem* (Springer-Verlag, Berlin, 1990).
2. R. G. Parr and W. Yang, *Density Functional Theory of Atoms and Molecules* (Oxford University Press, New York, 1989).
3. E. J. Baerends, O. V. Gritsenko, and R. van Leeuwen, in *Density Functional Methods in Chemistry*, B. Ross, R. C. Laird, and T. Ziegler, Eds., ACS Symposium Series, 629 (American Chemical Society, Washington, DC, 1995).
4. M. A. Buijse and E. J. Baerends, in *Electronic Density Functional Theory of Molecules, Clusters and Solids*, D. E. Ellis, Ed. (Kluwer, Dordrecht, 1995).
5. J. Harris and R. O. Jones, *J. Phys. F* **4**, 1170 (1974).
6. D. C. Langreth and J. P. Perdew, *Solid State Commun.* **17**, 425 (1975).
7. O. Gunnarsson and B. I. Lundqvist, *Phys. Rev. B* **13**, 4274 (1976).
8. A. D. Becke, *J. Chem. Phys.* **98**, 1372 (1993).
9. J. P. Perdew and Y. Wang, *Phys. Rev. B* **45**, 13244 (1992).
10. A. D. Becke, *J. Chem. Phys.* **98**, 5648 (1993).
11. M. A. Buijse, E. J. Baerends, and J. G. Snijders, *Phys. Rev. A* **40**, 4190 (1989).
12. P. Süle, O. V. Gritsenko, Á. Nagy, and E. J. Baerends, *J. Chem. Phys.* **103**, 10085 (1995).
13. A. D. Becke, *Phys. Rev. A* **38**, 3098 (1988).
14. Y. Wang and J. P. Perdew, *Phys. Rev. B* **44**, 13298 (1991).
15. J. P. Perdew, J. A. Chevary, S. H. Vosko, K. A. Jackson, M. R. Pederson, D. J. Singh, and C. Fiolhais, *Phys. Rev. B* **46**, 6671 (1992).
16. R. C. Morrison and Q. Zhao, *Phys. Rev. A* **51**, 1980 (1995).
17. O. V. Gritsenko, R. van Leeuwen, and E. J. Baerends, *Phys. Rev. A* **52**, 1870 (1995).
18. O. V. Gritsenko, R. van Leeuwen, and E. J. Baerends, *Top. Curr. Chem.* (in press).
19. Q. Zhao, R. C. Morrison, and R. G. Parr, *Phys. Rev. A* **50**, 2138 (1994).
20. R. van Leeuwen and E. J. Baerends, *Phys. Rev. A* **49**, 2421 (1994).
21. M. Levy, N. H. March, and N. C. Handy, *J. Chem. Phys.* **104**, 1989 (1996).
22. J. C. Slater, *Quantum Theory of Molecules and Solids* (McGraw-Hill, New York, 1974), Vol. 4.
23. J. P. Perdew, A. Savin, and K. Burke, *Phys. Rev. A* **51**, 4531 (1995).
24. R. van Leeuwen, O. V. Gritsenko, and E. J. Baerends, unpublished.
25. R. van Leeuwen, PhD Thesis (Vrije Universiteit, Amsterdam, The Netherlands, 1994).
26. M. Levy and J. P. Perdew, *Phys. Rev. A* **32**, 2010 (1985).
27. J. P. Perdew, *Phys. Lett. A* **165**, 79 (1992).
28. A. Görling, M. Levy, and J. P. Perdew, *Phys. Rev. B* **47**, 1167 (1993).

Resemblance Analysis of Molecular Systems on the Grounds of DFT-Evaluated Parameters. Platinum Complexes and Their Anticancer Activity

L. SCHULZ* and H. CHOJNACKI

Wyb. Wyspińskiego 27, 50-370 Wrocław, Institute of Physical and Theoretical Chemistry, Wrocław Technical University, Poland

Received February 26, 1996; revised manuscript received April 17, 1996; accepted August 5, 1996

ABSTRACT

The molecular properties characterizing diammine platinum complexes have by way of example been analyzed and selected because of their role in anticancer activity. The research was done with the use of the nonstandard quantitative method to compare molecular properties resulting from density functional theory (DFT). Among different molecular parameters considered, the multipole moment components were found mainly to have clear correspondence to the trans (anticancer neutral) and cis classes of platinum complexes. The results led to the selection and conjecture of the specific significance of some molecular characteristics contrasted with other assemblies of parameters. © 1996 John Wiley & Sons, Inc.

Formulation of the Problem

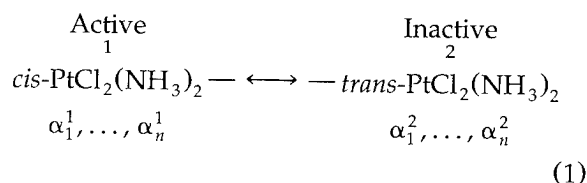
The invention of Rosenberg [1] of the filamentous growth of *Escherichia coli* during electrolysis with platinum electrodes can serve as the example of an unplanned result and as an investi-

gation to find factors which could have influence on the cell growth.

It is well known [2–5] that the cis form of diammine platinum complexes is the necessary condition to observe anticancer activity. Hence, if some physico-chemical properties of the two Pt complexes (active and inactive) are similar, then it can be supposed these properties have doubtful relevance to the activity considered. Otherwise, the same properties (under similar conditions)

*To whom correspondence should be addressed.

would be assumed to underlie mutually excluding phenomena, e.g.:



matched by a resemblance under $\alpha_1^1, \dots, \alpha_n^1$ and $\alpha_1^2, \dots, \alpha_n^2$ do not show these quantities involved in the anticancer mechanisms. Oppositely, if the compounds of system (1) are differentiated (unmatched) under the families of properties $\beta_1^1, \dots, \beta_k^1$ and $\beta_1^2, \dots, \beta_k^2$, then these properties can have an anticancer relevance.

The first task to resolve this problem is how to split the matched system (1) and to differentiate as far as possible the considered compounds according to their inhibiting cancer abilities. Some molecular parameters are commonly considered for their relevance to the anticancer activity [2–5]. The properties to be investigated in this study are sequences $\alpha_1^i, \dots, \alpha_n^i$ of parameters evaluated for particular platinum complexes (indexed by i). Quantitative properties $\alpha_1^i, \dots, \alpha_n^i$ have been determined for cis and trans conformations with the same or different nonammine ligands.

The second step pursued was looking for subsequences $\alpha_{\nu_1}^i, \dots, \alpha_{\nu_k}^i$ such that if $\alpha_{\nu_1}^i, \dots, \alpha_{\nu_k}^i$ was matched by the resemblance with $\alpha_{\nu_1}^j, \dots, \alpha_{\nu_k}^j$, then i and j should simultaneously denote cis or simultaneously trans conformers. Thus, if for each Pt complex i from the set considered the sequence $\alpha_{\nu_1}^i, \dots, \alpha_{\nu_k}^i$ fulfills the condition just mentioned, then ν_1, \dots, ν_k are indexing quantities distinguished from $\alpha_1^i, \dots, \alpha_n^i$ to parallel the cis–trans dichotomy.

What are parameter discriminating procedures and how to prove the existence of the subsequences postulated is shown below.

Computational

The electronic structure of the systems under consideration has been calculated within the density functional theory (DFT). All the calculations were performed with the BLYP functional [6] for the fully optimized geometries at the all-valence MOPAC level [7]. The final, first time computed results for platinum-coordinated complexes are listed in Tables I–IV.

TABLE I
Calculated dipole moments (Debye) for cis and trans conformations of platinum compounds.

Molecule	Cis	Trans
PtCl ₂ (NH ₃) ₂	13.49	0.00
PtF ₂ (NH ₃) ₂	12.18	0.00
Pt(OH) ₂ (NH ₃) ₂	8.99	0.00
PTClF(NH ₃) ₂	12.98	1.29
Pt(OH)F(NH ₃) ₂	13.30	1.67
Pt(OH)Cl(NH ₃) ₂	11.41	2.83
Pt(SH) ₂ (NH ₃) ₂	1.68	0.00
PtBr ₂ (NH ₃) ₂	11.94	0.00
PtBrCl(NH ₃) ₂	12.75	1.06

If x denotes a compound having characteristics $\alpha_1, \dots, \alpha_n$, then the relevant set spectrum [8] is defined as follows:

$$fx = \oplus \{\alpha_i\} \quad \text{for } i = 1, \dots, l,$$

i.e., fx is the coproduct of one-element sets including particular quantities. This allows one to find the general factors of similarity $FS(fx, fy)$ and dissimilarity $FD(fx, fy)$ for two molecules x and y considered. The factors with the relation of tolerance t have been determined in [8]:

$$\begin{aligned} FS(a, b) &\stackrel{\text{df}}{=} |(a \times b) \cup (b \times a) \cap t|, \\ FD(a, b) &\stackrel{\text{df}}{=} |a \setminus \text{dom}((a \times b) \cap t)| \\ &\quad + |b \setminus \text{im}((a \times b) \cap t)|, \end{aligned} \quad (2)$$

where a, b are finite sets and domain (dom) and image (im) of the relations indicated have been involved.

Two quantities α_k^i and α_k^j are recognized to fulfill t if their difference $|\alpha_k^i - \alpha_k^j|$ is less than the average difference in the set of quantities of the k kind. The distance between two compounds x and y is estimated by the following formula

$$d(x, y) = \frac{FD(fx, fy)}{FD(fx, fy) + FS(fx, fy)}. \quad (3)$$

Such determined distance has the following properties: (i) for each molecule x from the set established:

$$d(x, x) = 0;$$

TABLE II
Calculated main quadrupole moment components (Debye-Ang) for cis and trans conformations of platinum compounds.

Molecule	Cis form			Trans form		
	Q_{xx}	Q_{yy}	Q_{zz}	Q_{xx}	Q_{yy}	Q_{zz}
PtCl ₂ (NH ₃) ₂	-67.1	-62.4	-67.4	-67.1	-40.9	-94.3
PtF ₂ (NH ₃) ₂	-48.9	-47.1	-49.3	-48.9	-24.9	-69.4
Pt(OH) ₂ (NH ₃) ₂	-53.5	-43.6	-42.9	-53.4	-30.4	-54.0
PtClF(NH ₃) ₂	-56.8	-56.3	-58.0	-58.0	-32.9	-81.7
Pt(OH)F(NH ₃) ₂	-40.3	-51.6	-48.6	-51.2	-27.8	-61.6
Pt(OH)Cl(NH ₃) ₂	-59.8	-48.1	-60.3	-60.3	-35.7	-73.4
Pt(SH) ₂ (NH ₃) ₂	-64.7	-51.9	-51.0	-65.0	-54.3	-49.8
PtBr ₂ (NH ₃) ₂	-78.1	-65.7	-79.0	-78.0	-53.9	-103.1
PtBrCl(NH ₃) ₂	-65.7	-71.0	-72.7	-72.6	-47.4	-99.4

(ii) for each molecules x and y from the set considered:

$$d(x, y) = d(y, x) \quad (\text{symmetry}).$$

The distance mentioned is particularly a pseudometric when the tolerance t is an identity (cf. [8]). Using distance d , one can determine relations between the objects compared simply by imposing useful conditions on the function d involved:

$$(x, y) \text{ fulfills } r \text{ if and only if } (x, y) \in X \times X \text{ and } \Phi(x, y, d),$$

where the required properties are established by

the condition Φ . If the condition(s) $\Phi(x, y, d)$ are fulfilled, then the points x, y are matched:

$$x \rightarrow -y,$$

otherwise, they remain unmatched. Hence, a graph equivalent to relation r can be constructed. For example, in [9], the recurrent procedure to choose the nearest neighbor(s) after rejecting all previously chosen objects has been applied, i.e., x_{i+1} is such that for each

$$y' \in X \setminus \{x_1, \dots, x_i\}: d(x_i, x_{i+1}) \leq d(x_i, y').$$

In this work, the rejected set $\{x_1, \dots, x_i\}$ of elements has been restricted to one-element set $\{x_i\}$, i.e., it generally holds that (x, y) fulfills r if and

TABLE III
Calculated octupole main-moment components (Debye-Ang**3) for cis and trans conformations of platinum compounds.

Molecule	Cis form			Trans form		
	O_{xxx}	O_{yyy}	O_{zzz}	O_{xxx}	O_{yyy}	O_{zzz}
PtCl ₂ (NH ₃) ₂	1.9	83.8	0.0	0.0	0.0	0.0
PtF ₂ (NH ₃) ₂	0.0	0.0	-26.8	0.0	0.0	0.0
Pt(OH) ₂ (NH ₃) ₂	0.0	0.0	-10.9	0.0	0.0	0.0
PtClF(NH ₃) ₂	-87.7	40.5	1.8	0.0	0.0	37.9
Pt(OH)F(NH ₃) ₂	-21.5	51.5	0.0	0.0	0.0	-26.7
Pt(OH)Cl(NH ₃) ₂	80.8	13.4	0.1	0.0	0.0	67.3
Pt(SH) ₂ (NH ₃) ₂	0.0	0.0	36.4	0.0	0.0	1.4
PtBr ₂ (NH ₃) ₂	-2.0	60.3	0.0	0.0	0.0	0.0
PtBrCl(NH ₃) ₂	-56.8	-85.1	1.9	0.0	0.0	-55.4

TABLE IV

Calculated hexadecapole main-moment components (Debye-Ang^{*3}) for cis and trans conformations of platinum compounds.

Molecule	Cis form			Trans form		
	H_{xxxx}	H_{yyyy}	H_{zzzz}	H_{xxxx}	H_{yyyy}	H_{zzzz}
PtCl ₂ (NH ₃) ₂	-87.3	-619.6	-696.8	-87.4	-300.2	-1127.4
PtF ₂ (NH ₃) ₂	-56.0	-336.8	-347.4	-56.7	-292.4	-398.8
Pt(OH) ₂ (NH ₃) ₂	-65.0	-360.3	-342.8	-65.1	-317.7	-254.5
PtClF(NH ₃) ₂	-649.5	-361.8	-71.6	-71.9	-295.9	-728.0
Pt(OH)F(NH ₃) ₂	-272.0	-365.0	-47.7	-60.9	-306.8	-326.8
Pt(OH)Cl(NH ₃) ₂	-667.6	-281.2	-76.2	-76.2	-309.4	-637.9
Pt(SH) ₂ (NH ₃) ₂	-82.1	-793.6	-705.7	-83.3	-396.4	-958.7
PtBr ₂ (NH ₃) ₂	-101.3	-660.2	-899.0	-101.4	-335.1	-1469.9
PtBrCl(NH ₃) ₂	-731.0	-668.1	-94.5	-94.5	-316.9	-1316.4

only if $x, y \in X$ and for each $y' \in X \setminus \{x\}$: $d(x, y) \leq d(x, y')$. This all enables one to distinguish classes with growing relevance, generally regarding the fixed condition Φ . If $(x, y) \in r$, then (y, x) does not necessarily fulfill relation r , i.e., it takes place (x, y) -asymmetric matching. The symmetric matching shows a closer proximity between x and y .

The classes of resemblance of the first kind have, in general, elements (vertices) keeping only a rough kinship between each other. They are equivalence classes of the quotient set X/r^- where r^- is the equivalence closure of r . The equivalence classes of this kind can include the asymmetric matching.

The classes of resemblance of the second kind, i.e., the elements of the quotient set $X/(r \cap r^{-1})^-$ are more closely related regarding their similarity. Only symmetric matching is possible between the vertices of a fixed equivalence class. Even more closely related are vertices in the classes of resemblance of the third kind, which are determined as maximal elements with the following property: $a \times a \subseteq r$. Any two vertices of such a class are related by the symmetric matching. If the class a_3 is of the third kind, then there exist class of resemblance a_2 of the second kind and class of resemblance a_1 of the first kind such that $a_3 \subseteq a_2 \subseteq a_1$. The classes of resemblance of all kinds have been considered to reveal the possible properties responsible for the anticancer activity.

The experimental thesis to regard trans isomers considered as inactive leads to the utmost differentiation $F_0 = \{B, B'\}$ (utmost mixing $F_1 = \{X\}$) such

that

$$X = B \cup B' \quad \text{and} \quad B \cap B' = \emptyset,$$

where X is the set of compounds and B and B' are sets of cis and trans forms, respectively. If F is a family of finite sets [e.g., X/r^- or $X/(r \cap r^{-1})^-$], then its set spectrum is the union of sets of the form

$$a^2 \setminus ([\text{dom}((a \cap B) \times (a \cap B'))]^2 \cup [\text{im}((a \cap B) \times (a \cap B'))]^2), \quad \text{for } a \in F,$$

where $a^2 = a \times a$ for short. For example, $fF_0 = B^2 \cup B'^2$ and $fF_1 = (B \times B') \cup (B' \times B)$ which implies including only (cis, cis) and (trans, trans) pairs into fF_0 , and (cis, trans) and (trans, cis) pairs of compounds into fF_1 . Thus, distance [Eq. (3)] (with the identity taken as tolerance t) between F and F_0 (or F_1) can easily be determined. This distance turned out very useful in selecting procedures.

To summarize:

1. Any chosen sequence of parameters $\alpha_1, \dots, \alpha_n$ determined for each compound of X does allow one to establish the relation r and using it to distinguish the family F of resemblance classes (of the fixed kind) covering X .
2. Pattern F_0 consists of two classes cis and trans forms, respectively.
3. Another family is defined as $F_1 = \{X\}$, where no discrimination between cis and trans conformations occurs.

4. $d(F, F_0) = 1$ if and only if each class of F includes the cis-trans pair of compounds.
5. $d(F, F_1) = 1$ if and only if no class of F includes a cis-trans pair of compounds, i.e., the full separation of cis and trans forms takes place. If $d(F, F_0) = 0$, then $F = F_0$.

Hence, if parameters $\alpha_1^i, \dots, \alpha_n^i$ (for i indexing all complexes from the fixed set) induce full separation or close to 1 distance $d(F, F_1)$, then they can be considered as accompanying the cis-trans dichotomy and therefore having potential relevance to the activity or inactivity. Otherwise, such a relevance cannot be recognized.

Additionally, distance $d(F, F_0)$ has been taken into account as an auxiliary. It estimates the "crumbling" of X if $d(F, F_1)$ is constant.

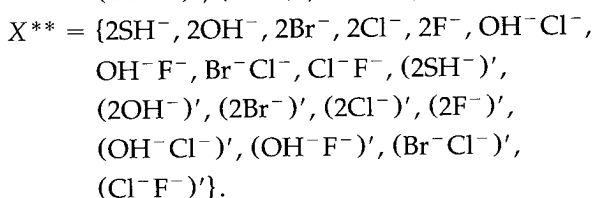
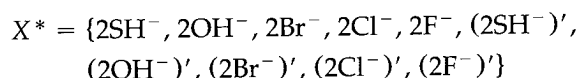
Selecting Anticancer Properties for Platinum Complexes

The series of quantities computed by DFT were leading to distinguishing classes of resemblance of the second kind. They were determined for the family X of platinum (II) complexes with the SH^- , OH^- , Br^- , Cl^- , F^- ligands.

It is of great interest to know the behavior of system (1) under quantities of various kinds and to know the distances under the pattern partition F_0 . Table V includes comparison results computed for electron affinity (A), electronegativity (ELN), nuclear repulsion energy (NUC), total energy (HF), and other properties as stated for set X of Pt complexes where $X = \{2\text{OH}^-, 2\text{Cl}^-, 2\text{F}^-, (2\text{OH}^-)', (2\text{Cl}^-)', (2\text{F}^-)'\}$ [only the nonammine ligands are indicated and the trans forms are primed; e.g., $(2\text{Cl}^-)'$ stands for *trans*- $\text{PtCl}_2(\text{NH}_3)_2$].

In the case of Table V, the unmatched status of (1) appears only when the dipole moment is involved. For one case of constants of rotation the full separation [$d(F, F_1) = 1$] has been reached.

In spite of alterations of system of compounds using Mg(II) , Be(II) , and Ca(II) complexes with the same ligands, the results were not better than those presented in Table V. Hence, the results of Table V indicate the dipole moment alone as inducing cis-trans separation. After turning to multipoles, the marked proximity under uttermost differentiation F_0 has been fixed for some multipole moments in X analyzed under their activity-inactivity relevance. For this reason, a more detailed analysis has been made for dipole, quadrupole, octupole, and hexadecapole moments. The various structural modifications of the Pt complexes can throw light on the cancer-pertinent mechanisms (cf., e.g., [10]). Hence, mixed functions in the nonammine ligands have been introduced. Also, the number of compounds in the systems analyzed was gradually increased. The extended systems of Pt complexes (denoted according to the convention mentioned) are the following:



Establishing matching (1) and computing distances under utmost differentiation F_0 (mixing F_1) was the task potentially revealing invariant kinship in the systems gradually extended. The searched family of parameters have to show minimal dis-

TABLE V
Differentiation of Pt complexes under physicochemical properties (X)

No.	Properties cumulated	System (1) matched (+) unmatched (-)	Distance of the pattern: $d(F, F_0)$	Cumulation with dipole moment	
				System (1)	Distance of the pattern $d(F, F_0)$
1	A, NUC, HF	+	1	+	0.60000
2	ELN, NUC, HF	+	1	+	1
3	Const. of rotation	+	1	-	0.44444
4	Polarizability	+	1	-	0.90909

TABLE VI
Matching and distances ($\times 10^2$) for multipole moments and their components.^a

Parameters	Cumulation with dipole moment												
	X		X*		X**		X		X*		X**		
	<i>m</i>	Dist.	<i>m</i>	Dist.	<i>m</i>	Dist.	<i>m</i>	Dist.	<i>m</i>	Dist.	<i>m</i>	Dist.	
Dipole mom.	—	0 100	—	83.333 83.333	—	54.762 97.479	—	0 100	—	83.333 83.333	—	54.762 97.479	$d(F, F_0)$ $d(F, F_1)$
Quadrup. mom.	+	100 0	+	100 56.000	+	97.283 86.826	+	83.333 72.727	+	100 32.000	+	97.727 65.269	$d(F, F_1)$ $d(F, F_1)$
Octupole mom.	—	33.333 100	—	36.000 100	—	78.824 95.960	—	22.222 100	—	36.000 100	—	80.357 96.823	$d(F, F_0)$ $d(F, F_1)$
Hexadecap mom.	—	86.364 80.952	—	85.185 93.103	—	48.765 100	—	55.556 100	—	89.655 85.714	—	81.482 100	$d(F, F_0)$ $d(F, F_1)$
HEXC	—	44.444 100	—	56.000 100	—	61.728 100	—	44.444 100	—	68.000 100	—	81.482 100	$d(F, F_0)$ $d(F, F_1)$

^aWhere *m* shows matching status of system (1) as in Table V.

tance $d(F, F_0)$ and maximal value of $d(F, F_1)$. Moreover, these distances should exhibit a stability under extensions. Testing the systems introduced, the following results have been obtained (Table VI). HEXC is a choice of hexadecapole moment components consisting of all of them after rejecting five components (i.e., XXXX, ZZZZ, XYYY, XXZZ, YYZZ). The distances for this assembly are the best results attained here in looking for invariants. Cumulating HEXC with dipole moment yields the similar status but with the greater standard deviation (0.09 and 0.19, respectively).

In an alternative computational way, other than (2) factors of similarity and dissimilarity can be used. For example,

$$FD(a_i, a_j) = \mu(a_i \triangle a_j),$$

$$FS(a_i, a_j) = \mu(a_i \cap a_j),$$

where a_i, a_j are some neighborhoods of α^i and α^j , respectively, and μ is a measure (e.g., the measure of Lebesgue). Using these factors the hexadecapole distances have been determined for X^{**} (for the resemblance classes of the first kind):

$$d(F, F_0) = 0.97521, \quad d(F, F_1) = 0.49438.$$

For HEXC assembly the results are as follows:

$$d(F', F_0) = 0.78652, \quad d(F', F_1) = 0.92.$$

Thus, distance $d(F', F_1)$ is close to 1, showing the small fraction of mixed classes in F' (under HEXC). The existence of invariants and alternative, resulting in principle in the same algorithms, does prompt a good reason for further testing assemblies of parameters pertinent to the activity considered.

Discussion and Conclusions

From the results of our calculations, we conclude that only some molecular properties enable one to discriminate an active and nonactive system. These conditions are fulfilled solely by higher than dipole, multipole moments. It seems that the best are components of the hexadecapole moments. However, it seems strange that typical molecular parameters like ionization energy, electron affinity, total energy, and correlation corrections are unable to distinguish between those two groups of molecular systems.

It should be stressed that parameters are discriminated on the grounds of the distances between the induced collections of compounds (resemblance classes) and F_0, F_1 families. These estimations depend of the fixed pattern. In this work, the trans and cis conformations have been taken as such a pattern in view of their well-known

experimentally established activity-inactivity relationship.

Since dipole moment induces the ideal partition $F = F_0$ (cf., Table VI) for system X , a pitfall arises when making conclusions on the pertinence of this moment to the cis-trans discrimination. To improve and test the conclusion, $\text{Pt}(\text{SH})_2(\text{NH}_3)_2$ complex has been included (X^*), and thereafter the partition F induced contained mixed classes [i.e., $d(F, F_1) < 1$]. Thus, the negative result of the test has been obtained. It is so since the complex just considered has relatively much smaller value of the dipole moment than cis conformers (of X^*), and therefore this dipole moment shows a better kinship to the trans forms. Generally, the parameters, being out of the pertinence desired, disturb the cis-trans dichotomy affecting induced partitions when the database is enriched. On the contrary, the properties looked for should not induce cis-trans mixing in the resemblance classes after substitutions of new ligands.

This is a hard postulate since even the existence of such properties within a finite family of the considered parameters is difficult to be a priori assumed. Therefore, the discriminated family of multipole components HEXC, inducing the partition desired in the gradually enriched systems, shows the method of the resemblance analysis, enabling one to find quite new criterion for the separation of cis and trans forms.

In view of the example considered, it can be noted that the cancer diseases are one of the most serious challenges for modern science, particularly, the "reading" of cancer cells by drugs (cf., e.g., the concepts of lectins [11] or long-range carcinogenic effects [12]) illustrate the complexity of this problem. The analysis performed here allows one to frame the hypothesis on the specific significance of some molecular parameters in the anticancer action. It is easily seen that the electric molecular

parameters and their symmetry in platinum complexes should play an essential role in the mechanisms of their activity. However, their character, which is necessary for the desired effect, remains unknown or is difficult to determine. On the other hand, the general idea to pursue some multipoles does not seem groundless and can probably be helpful in predicting ways to stimulate anticancer inhibition.

The extensions or modifications of the method illustrated can be of great interest in looking for efficient ways in drug design and selecting useful properties.

Note added in proof: Annotation performed within C.E.C. COST D3 Action.

References

1. B. Rosenberg, *Nucleic Acid Metal Ion Reactions*, in T. G. Spiro, Ed. (Wiley, New York, 1980), p. 1.
2. T. A. Connors and J. J. Roberts, *Platinum Coordination Complexes in Cancer Chemotherapy* (Springer, Berlin, 1974).
3. S. E. Sherman and S. J. Lippard, *Chem. Rev.* **87**, 1153 (1987).
4. J. L. van der Veer and J. Reedijk, *Chem. Br.* **24**, 775 (1988).
5. J. Reedijk, A. M. J. Fichtinger-Schepman, A. T. van Oosterom, and P. van de Putte, *Structure and Bonding* **67** (Springer, Berlin, 1987), p. 53.
6. M. J. Frisch, G. W. Trucks, H. B. Schlegel, P. M. W. Gill, B. G. Johnson, M. W. Wong, J. B. Foresman, M. A. Robb, M. Head-Gordon, E. S. Replogle, R. Gomperts, J. L. Andres, K. Raghavachari, J. S. Binkley, C. Gonzalez, R. L. Martin, D. J. Fox, D. J. Defrees, J. Baker, J. J. P. Stewart, and J. A. Pople, *Gaussian 92/DFT, Revision G.4*, (Gaussian, Inc., Pittsburgh, 1993).
7. J. J. P. Stewart, *J. Comp. Chem.* **10**, 209 (1989).
8. L. Schulz, *Appl. Math. Comp.* **41**, 1 (1991).
9. L. Schulz, *J. Mol. Struct. (Theochem)* **231**, 367 (1991).
10. M. Alink, H. Nakahara, T. Hirano, K. Inagaki, M. Nakanishi, J. Kidani, and J. Reedijk, *Inorg. Chem.* **30**, 1236 (1991).
11. F. Cramer, *Chaos and Order* (VCH, Weinheim 1993).
12. J. Ladik, *Anticancer Res.* **14**, 209 (1994).

Spin-Multiplet Energies from Time-Dependent Density Functional Theory

M. PETERSILKA AND E. K. U. GROSS*

*Institut für Theoretische Physik, Universität Würzburg, Am Hubland, D-97074 Würzburg, Germany;
e-mail for E. K. U. G.: gross@physik.uni-wuerzburg.de*

Received March 28, 1996; accepted May 2, 1996

ABSTRACT

Starting from a formally exact density-functional representation of the frequency-dependent linear density response and exploiting the fact that the latter has poles at the true excitation energies, we develop a density-functional method for the calculation of excitation energies. Simple additive corrections to the Kohn-Sham single-particle transition energies are derived whose actual computation only requires the ordinary static Kohn-Sham orbitals and the corresponding eigenvalues. Numerical results are presented for spin-singlet and triplet energies. © 1996 John Wiley & Sons, Inc.

Introduction

In recent years, density-functional theory (DFT) [1–5] has enjoyed increasing popularity in the field of quantum chemistry. The computational simplicity of the Kohn-Sham scheme and the availability of reliable exchange-correlation (xc) functionals allow accurate calculations even for very large systems [6,7]. The traditional density-functional formalism of Hohenberg, Kohn, and Sham [1,2] is mainly a ground-state theory. In view of the advantages of DFT, a generalization allowing the calculation of excitation spectra is highly desirable, especially since most experimen-

tal data are obtained by spectroscopical techniques. One might be tempted to interpret the Kohn-Sham single-particle energy differences as excitation energies. This interpretation, however, has no rigorous basis and in practice the Kohn-Sham orbital energy differences deviate by 10–50% from the true excitation energies. Another deficiency of the Kohn-Sham orbital energy spectrum is the fact that it shows no multiplet splittings.

To deal with excited states, several extensions of ground-state DFT have been proposed which rely either on the Rayleigh-Ritz principle for the lowest eigenstate of each symmetry class [8–10] or on a variational principle for ensembles [11–16]. A practical difficulty of these approaches is that the respective xc energy functionals depend on the

*To whom correspondence should be addressed.

symmetry labels of the state considered or on the particular ensemble. Until today, little is known about the explicit form of these excited-state xc functionals although significant progress has recently been made in the ensemble formalism [17–22].

In this article we are going to elaborate on a different approach [23–25] to the calculation of excitation energies which is based on time-dependent density-functional theory (TDDFT) [26]. In the linear response regime TDDFT has been applied rather successfully to the photo-response of atoms and molecules [27–31]. Dynamical hyperpolarizabilities have also been calculated [32] and first applications beyond the perturbative regime have emerged [33–35]. For a recent review of TDDFT and its applications, see [36].

To calculate excitation energies from TDDFT we use the fact that the frequency-dependent linear density response of a finite system exhibits discrete poles at the true (correlated) excitation energies of the unperturbed system. It can be shown [23] that the exact linear density response of an interacting system can be written as the linear density response of a noninteracting (Kohn–Sham) system to an effective perturbation. The basic idea is to use this formally exact representation of the frequency-dependent linear density response to calculate the shifts of the Kohn–Sham orbital energy differences (which are the poles of the Kohn–Sham response function) toward the true excitation energies in a systematic way. This program has recently been carried out [23] rather successfully to the calculation of singlet excitation energies. The purpose of the present article is to extend the scheme to incorporate spin degrees of freedom. This will allow us to calculate the excitation energies of spin multiplets.

Method

The frequency-dependent linear density response $n_{1\sigma}(\mathbf{r}, \omega)$ of interacting electrons with spin σ to a frequency-dependent perturbation $v_{1\nu}(\mathbf{y}, \omega)$ is usually written in terms of the full response function $\chi_{\sigma\nu}$ as

$$n_{1\sigma}(\mathbf{r}, \omega) = \sum_{\nu} \int d^3y \chi_{\sigma\nu}(\mathbf{r}, \mathbf{y}; \omega) v_{1\nu}(\mathbf{y}, \omega). \quad (1)$$

Alternatively, the exact frequency-dependent spin-density response can be calculated (self-con-

sistently) from

$$n_{1\sigma}(\mathbf{r}, \omega) = \sum_{\nu} \int d^3y \chi_{s\sigma\nu}(\mathbf{r}, \mathbf{y}; \omega) v_{s1\nu}(\mathbf{y}, \omega) \quad (2)$$

as the response of noninteracting (Kohn–Sham) particles subject to the effective potential

$$\begin{aligned} v_{s1\nu}(\mathbf{y}, \omega) &= v_{1\nu}(\mathbf{y}, \omega) \\ &+ \sum_{\nu'} \int d^3y' \left(\frac{1}{|\mathbf{y} - \mathbf{y}'|} + f_{xc\nu\nu'}(\mathbf{y}, \mathbf{y}'; \omega) \right) \\ &\times n_{1\nu'}(\mathbf{y}', \omega). \end{aligned} \quad (3)$$

Here the spin-dependent exchange-correlation kernel f_{xc} is given by the Fourier transform of

$$f_{xc\sigma\sigma'}(\mathbf{r}, t, \mathbf{r}', t') := \left. \frac{\delta v_{xc\sigma} [n_{\uparrow}, n_{\downarrow}](\mathbf{r}, t)}{\delta n_{\sigma'}(\mathbf{r}', t')} \right|_{n_{0\uparrow}, n_{0\downarrow}} \quad (4)$$

with respect to $(t - t')$. The proof that Eqs. (2)–(4) represent the exact linear spin-density response of the interacting system is based on the spin-dependent generalization [37] of TDDFT. The argument follows step by step the proof for the spin-independent case given in Ref. [23] and will therefore not be repeated here. The response function χ_s of the Kohn–Sham system can be expressed in terms of the unperturbed static Kohn–Sham spin orbitals $\phi_{j\sigma}$ as

$$\begin{aligned} \chi_{s\sigma\sigma'}(\mathbf{r}, \mathbf{r}'; \omega) &= \delta_{\sigma\sigma'} \sum_{j,k} (f_{k\sigma} - f_{j\sigma}) \\ &\times \frac{\phi_{j\sigma}(\mathbf{r}) \phi_{k\sigma}^*(\mathbf{r}) \phi_{j\sigma}^*(\mathbf{r}') \phi_{k\sigma}(\mathbf{r}')}{\omega - (\epsilon_{j\sigma} - \epsilon_{k\sigma}) + i\eta}, \end{aligned} \quad (5)$$

where $f_{k\sigma}, f_{j\sigma}$ are the Fermi occupation factors (1 or 0). The summations in (5) run over all unperturbed Kohn–Sham orbitals, including the continuum states. Note that the Kohn–Sham response function (5) is diagonal in the spin variable and exhibits poles at frequencies $\omega_{jk\sigma} \equiv \epsilon_{j\sigma} - \epsilon_{k\sigma}$ corresponding to Kohn–Sham single-particle excitations within the same spin space. In order to calculate the shifts toward the true excitation energies

Ω of the interacting system, we rewrite Eq. (2) as

$$\begin{aligned} \sum_{\nu'} \int d^3 y' \left\{ \delta_{\sigma\nu'} \delta(\mathbf{r} - \mathbf{y}') - \sum_{\nu} \int d^3 y \chi_{s\sigma\nu}(\mathbf{r}, \mathbf{y}; \omega) \right. \\ \left. \times \left[\frac{1}{|\mathbf{y} - \mathbf{y}'|} + f_{xc\nu\nu'}(\mathbf{y}, \mathbf{y}'; \omega) \right] \right\} n_{1\nu'}(\mathbf{y}', \omega) \\ = \sum_{\nu} \int d^3 y \chi_{s\sigma\nu}(\mathbf{r}, \mathbf{y}; \omega) v_{1\nu}(\mathbf{y}, \omega). \end{aligned} \quad (6)$$

In general, the true excitation energies Ω are not identical with the Kohn–Sham excitation energies $\omega_{jk\sigma}$. Therefore, the right-hand side of Eq. (6) remains finite for $\omega \rightarrow \Omega$. Since, on the other hand, the exact spin-density response $n_{1\sigma}$, has poles at the true excitation energies Ω , the integral operator acting on $n_{1\sigma}$ on the left-hand side of Eq. (6) cannot be invertible for $\omega \rightarrow \Omega$. This is easily seen by reductio ad absurdum: Assuming the inverse operator existed, its action on both sides of Eq. (6) would result in a finite right-hand side for $\omega \rightarrow \Omega$ in contradiction to the fact that $n_{1\sigma}$, remaining on the left-hand side, has a pole at $\omega = \Omega$.

Consequently, the true excitation energies Ω are characterized as those frequencies where the integral operator acting on the spin-density vector in Eq. (6) is not invertible or, equivalently, where the eigenvalues of this operator vanish. If the delta function in Eq. (6) is integrated out, the true excitation energies Ω are those frequencies where the eigenvalues $\lambda(\omega)$ of

$$\begin{aligned} \sum_{\nu'} \int d^3 y' \sum_{\nu} \int d^3 y \chi_{s\sigma\nu}(\mathbf{r}, \mathbf{y}; \omega) \\ \times \left[\frac{1}{|\mathbf{y} - \mathbf{y}'|} + f_{xc\nu\nu'}(\mathbf{y}, \mathbf{y}'; \omega) \right] \gamma_{\nu'}(\mathbf{y}', \omega) \\ = \lambda(\omega) \gamma_{\sigma}(\mathbf{r}, \omega) \end{aligned} \quad (7)$$

satisfy

$$\lambda(\Omega) = 1. \quad (8)$$

This condition rigorously determines the true excitation spectrum of the interacting system considered.

For notational convenience, we introduce double indices $q \equiv (j, k)$ so that $\omega_{q\sigma} \equiv \epsilon_{j\sigma} - \epsilon_{k\sigma}$ denotes the excitation energy of the single-particle transition ($j\sigma \rightarrow k\sigma$). Moreover, we define

$$\Phi_{q\sigma}(\mathbf{r}) := \phi_{k\sigma}(\mathbf{r})^* \phi_{j\sigma}(\mathbf{r}), \quad (9)$$

$$\alpha_{q\sigma} := f_{k\sigma} - f_{j\sigma} \quad (10)$$

and set

$$\begin{aligned} \xi_{q\sigma}(\omega) := \sum_{\nu'} \int d^3 y' \int d^3 y \Phi_{q\sigma}(\mathbf{y})^* \\ \times \left[\frac{1}{|\mathbf{y} - \mathbf{y}'|} + f_{xc\sigma\nu'}(\mathbf{y}, \mathbf{y}'; \omega) \right] \gamma_{\nu'}(\mathbf{y}', \omega). \end{aligned} \quad (11)$$

With these definitions, Eq. (7) takes the form

$$\sum_q \frac{\alpha_{q\sigma} \Phi_{q\sigma}(\mathbf{r})}{\omega - \omega_{q\sigma} + i\eta} \xi_{q\sigma}(\omega) = \lambda(\omega) \gamma_{\sigma}(\mathbf{r}, \omega). \quad (12)$$

Solving this equation for $\gamma_{\sigma}(\mathbf{r}, \omega)$ and reinserting the result on the right-hand side of Eq. (11) leads to

$$\sum_{\sigma'} \sum_{q'} \frac{M_{q\sigma q'\sigma'}(\omega)}{\omega - \omega_{q'\sigma'} + i\eta} \xi_{q'\sigma'}(\omega) = \lambda(\omega) \xi_{q\sigma}(\omega). \quad (13)$$

Here we have introduced the matrix elements

$$\begin{aligned} M_{q\sigma q'\sigma'}(\omega) \\ = \alpha_{q'\sigma'} \int d^3 r \int d^3 r' \Phi_{q'\sigma'}^*(\mathbf{r}) \\ \times \left[\frac{1}{|\mathbf{r} - \mathbf{r}'|} + f_{xc\sigma\sigma'}(\mathbf{r}, \mathbf{r}'; \omega) \right] \Phi_{q\sigma}(\mathbf{r}'). \end{aligned} \quad (14)$$

Note that the summation in Eq. (13) extends over all single-particle transitions $q'\sigma'$ between occupied and unoccupied Kohn–Sham (KS) orbitals, including the continuum states. Up to this point, no approximations have been made. In order to actually calculate $\lambda(\omega)$, the eigenvalue problem (13) has to be truncated in one way or another. One possibility is to expand all quantities in Eq. (13) about one particular KS orbital energy difference $\omega_{p\tau}$:

$$\xi_{q\sigma}(\omega) = \xi_{q\sigma}(\omega_{p\tau}) + \left. \frac{d\xi_{q\sigma}(\omega)}{d\omega} \right|_{\omega_{p\tau}} (\omega - \omega_{p\tau}) + \dots \quad (15)$$

$$\lambda(\omega) = \frac{A(\omega_{p\tau})}{\omega - \omega_{p\tau}} + B(\omega_{p\tau}) + \dots \quad (16)$$

The matrix elements with $\omega_{p\tau} \neq \omega_{q'\sigma'}$ can be expanded into a Taylor series:

$$\begin{aligned} \frac{M_{q\sigma q'\sigma'}(\omega)}{\omega - \omega_{q'\sigma'} + i\eta} &= \frac{M_{q\sigma q'\sigma'}(\omega_{p\tau})}{\omega_{p\tau} - \omega_{q'\sigma'} + i\eta} \\ &+ \frac{d}{d\omega} \left[\frac{M_{q\sigma q'\sigma'}(\omega)}{\omega - \omega_{q'\sigma'} + i\eta} \right]_{\omega_{p\tau}} (\omega - \omega_{p\tau}) + \dots \end{aligned} \quad (17)$$

whereas, for $\omega_{p\tau} = \omega_{q'\sigma'}$, the matrix elements have to be represented by a Laurent series:

$$\begin{aligned} \frac{M_{q\sigma q'\sigma'}(\omega)}{\omega - \omega_{q'\sigma'} + i\eta} &= \frac{M_{q\sigma q'\sigma'}(\omega_{p\tau})}{\omega - \omega_{p\tau} + i\eta} \\ &+ \frac{dM_{q\sigma q'\sigma'}(\omega)}{d\omega} \Big|_{\omega_{p\tau}} + \dots \end{aligned} \quad (18)$$

Inserting Eqs. (15)–(18) into Eq. (13) the coefficients A and B are readily identified. If the pole $\omega_{p\tau}$ is nondegenerate, one finds

$$A(\omega_{p\tau}) = M_{p\tau p\tau}(\omega_{p\tau}) \quad (19)$$

and

$$\begin{aligned} B(\omega_{p\tau}) &= \frac{dM_{p\tau p\tau}}{d\omega} \Big|_{\omega_{p\tau}} + \frac{1}{M_{p\tau p\tau}(\omega_{p\tau})} \\ &\times \sum_{q'\sigma' \neq p\tau} \frac{M_{p\tau q'\sigma'}(\omega_{p\tau}) M_{q'\sigma' p\tau}(\omega_{p\tau})}{\omega_{p\tau} - \omega_{q'\sigma'} + i\eta}. \end{aligned} \quad (20)$$

The corresponding eigenvector (in lowest order) is given by

$$\xi_{q\sigma} = \frac{1}{A(\omega_{p\tau})} M_{q\sigma p\tau}(\omega_{p\tau}) \xi_{p\tau} \quad (21)$$

with $(p\tau)$ fixed. The number $\xi_{p\tau}$ is free and can be chosen to properly normalize the vector ξ .

If the pole $\omega_{p\tau}$ is K -fold degenerate,

$$\omega_{p_1\tau_1} = \omega_{p_2\tau_2} = \dots = \omega_{p_K\tau_K} \equiv \omega_0, \quad (22)$$

the lowest-order coefficient A in Eq. (16) is determined by the following matrix equation:

$$\begin{aligned} \sum_{k=1}^K M_{p_i\tau_i p_k\tau_k}(\omega_0) \xi_{p_k\tau_k}^{(n)} &= A_n(\omega_0) \xi_{p_i\tau_i}^{(n)}, \\ i &= 1, \dots, K. \end{aligned} \quad (23)$$

In general, one obtains K different eigenvalues A_1, \dots, A_K . Then the remaining components of the corresponding eigenvectors $\xi^{(n)}$ can be calculated from

$$\xi_{q\sigma}^{(n)} = \frac{1}{A_n(\omega_0)} \sum_{k=1}^K M_{q\sigma p_k\tau_k}(\omega_0) \xi_{p_k\tau_k}^{(n)}, \quad (24)$$

once the eigenvalue problem (23) has been solved. Assuming that the true excitation energy Ω is not too far away from ω_0 , it will be sufficient to consider only the lowest-order terms of the above Laurent expansions. In particular, we set

$$\lambda_n(\omega) \approx \frac{A_n(\omega_0)}{\omega - \omega_0}. \quad (25)$$

The condition (8) and its complex conjugate, $\lambda^*(\Omega) = 1$, then lead, in this order, to a compact expression for the excitation energies:

$$\Omega_n = \omega_0 + \mathcal{R} A_n(\omega_0). \quad (26)$$

This is the central result of our analysis. Equation (26) shows that a single KS pole can lead to several many-body excitation energies. The corresponding oscillator strengths can be obtained [25] from the eigenvectors $\xi^{(n)}$ and the KS oscillator strengths.

Application to Closed-Shell Systems

In this section, we will apply the above formalism to systems with spin-unpolarized ground states. For these systems, the Kohn–Sham orbital eigenvalues are degenerate with respect to the spin variable, which implies a lack of spin-multiplet structure in the Kohn–Sham spectrum. In the following, we demonstrate how this is restored by the lowest-order corrections (26). Assuming that there are no further degeneracies besides the spin degeneracy, Eq. (23) reduces to the following (2×2) eigenvalue problem:

$$\sum_{\sigma'=\uparrow, \downarrow} M_{p\sigma p\sigma'}(\omega_0) \xi_{p\sigma'}(\omega_0) = A \xi_{p\sigma}(\omega_0). \quad (27)$$

For spin-saturated systems, one finds $M_{p\uparrow p\uparrow} = M_{p\downarrow p\downarrow}$ and $M_{p\uparrow p\downarrow} = M_{p\downarrow p\uparrow}$, so that the eigen-

values of Eq. (27) are given by

$$A_{1,2} = M_{p\uparrow p\uparrow} \pm M_{p\uparrow p\downarrow}. \quad (28)$$

By Eq. (26), the resulting excitation energies are

$$\Omega_1 = \omega_0 + \mathcal{R}\{M_{p\uparrow p\uparrow} + M_{p\uparrow p\downarrow}\} \quad (29)$$

$$\Omega_2 = \omega_0 + \mathcal{R}\{M_{p\uparrow p\uparrow} - M_{p\uparrow p\downarrow}\}. \quad (30)$$

Inserting the explicit form of the matrix elements (14), one finds

$$\Omega_1 = \omega_0 + 2\mathcal{R} \int d^3r \int d^3r' \Phi_p^*(\mathbf{r}) \times \left[\frac{1}{|\mathbf{r} - \mathbf{r}'|} + f_{xc}(\mathbf{r}, \mathbf{r}'; \omega_0) \right] \Phi_p(\mathbf{r}') \quad (31)$$

$$\Omega_2 = \omega_0 + 2\mathcal{R} \int d^3r \int d^3r' \Phi_p^*(\mathbf{r}) \times \mu_0^2 G_{xc}(\mathbf{r}, \mathbf{r}'; \omega_0) \Phi_p(\mathbf{r}') \quad (32)$$

where

$$f_{xc}(\mathbf{r}, \mathbf{r}'; \omega) = \frac{1}{4} \sum_{\sigma, \sigma' = \uparrow, \downarrow} f_{xc\sigma\sigma'}(\mathbf{r}, \mathbf{r}'; \omega) \quad (33)$$

and

$$G_{xc}(\mathbf{r}, \mathbf{r}'; \omega) = \frac{1}{4\mu_0^2} \sum_{\sigma, \sigma' = \uparrow, \downarrow} (\beta_{\sigma\sigma'}) f_{xc\sigma\sigma'}(\mathbf{r}, \mathbf{r}'; \omega); \quad (34)$$

μ_0 denotes the Bohr magneton and $\beta_{\sigma\sigma'} = 1$ for $\sigma = \sigma'$ and $\beta_{\sigma\sigma'} = -1$ for $\sigma \neq \sigma'$. For simplicity, we have dropped the spin index of $\Phi_{p\sigma}$ in Eqs. (31) and (32). [This is possible only if the unperturbed KS ground-state determinant is spin-saturated since, in this case, $\phi_{j\uparrow}(\mathbf{r}) = \phi_{j\downarrow}(\mathbf{r})$ for all j .]

The quantity G_{xc} gives rise to exchange and correlation effects in the Kohn-Sham equation for the linear response of the frequency-dependent magnetization density $m(\mathbf{r}, \omega) = \mu_0[n_{\uparrow}(\mathbf{r}, \omega) - n_{\downarrow}(\mathbf{r}, \omega)]$ [37].

The fact that the magnetization density response naturally involves spin-flip processes suggests that Ω_2 represents the spin-triplet excitation energies of many-electron systems with spin-saturated ground states. The corresponding spin-singlet excitation energies, on the other hand, are given by Ω_1 . This assignment will be given further support by the numerical results presented in the next section.

Results and Discussion

Apart from the truncation of the expansions (15)–(18), two further approximations are necessary in the described TDDFT calculation of excitation energies:

1. The frequency-dependent xc kernels f_{xc} and G_{xc} have to be approximated.
2. The static Kohn-Sham orbitals entering Eqs. (31) and (32) through Eq. (9) have to be calculated with an approximate (static) potential v_{xc}^{stat} .

As an application of the method, we consider the lowest excitation energies of the alkaline earths and the elements of the zinc series. Here, in addition to the degeneracy with respect to the spin index, the $s \rightarrow p$ transitions under consideration are threefold degenerate in the magnetic quantum number m of the "final" state. Hence, we have a six-fold degenerate pole and Eq. (23) is a (6×6) eigenvalue problem. In our case, however, the matrix $M_{p_i\tau_i p_k\tau_k}$ in Eq. (23) consists of three identical (2×2) blocks, leading only to two distinct corrections, independent of m , as it should be. The resulting triplet states are still degenerate with respect to the total angular momentum quantum number because the spin-orbit coupling is not accounted for in the nonrelativistic Kohn-Sham equations.

In Tables I–IV we show excitation energies calculated from Eqs. (31) and (32). The calculation of Table I employs the ordinary local density approximation (LDA) for v_{xc}^{stat} (using the parametrization of Vosko, Wilk, and Nusair [38]) and the so-called adiabatic LDA (ALDA) for the xc kernels:

$$f_{xc}^{\text{ALDA}}[n_0](\mathbf{r}, \mathbf{r}'; \omega) = \delta(\mathbf{r} - \mathbf{r}') \frac{\partial^2}{\partial \rho^2} \left[\rho \epsilon_{xc}^{\text{hom}}(\rho, \zeta) \right] \Big|_{(\rho=n_0(\mathbf{r}), \zeta=0)} \quad (35)$$

and [39]

$$G_{xc}^{\text{ALDA}}[n_0](\mathbf{r}, \mathbf{r}'; \omega) = \delta(\mathbf{r} - \mathbf{r}') \frac{1}{\mu_0^2 n(\mathbf{r})} \frac{\partial^2}{\partial \zeta^2} \times \left[\epsilon_{xc}^{\text{hom}}(\rho, \zeta) \right] \Big|_{(\rho=n_0(\mathbf{r}), \zeta=0)}. \quad (36)$$

TABLE I
Lowest $S \rightarrow P$ excitation energies of
various atoms.^a

Atom	State	Ω_{exp}	Ω^{LDA}	$\Omega(\Delta_{\text{SCF}})$	ω_0^{LDA}
Be	1P_1	0.388	0.399	0.331	0.257
	3P_0	0.200			
	3P_1	0.200	0.192	0.181	0.257
	3P_2	0.200			
Mg	1P_1	0.319	0.351	0.299	0.249
	3P_0	0.199			
	3P_1	0.199	0.209	0.206	0.249
	3P_2	0.200			
Ca	1P_1	0.216	0.263	0.211	0.176
	3P_0	0.138			
	3P_1	0.139	0.145	0.144	0.176
	3P_2	0.140			
Zn	1P_1	0.426	0.477	0.403	0.352
	3P_0	0.294			
	3P_1	0.296	0.314	0.316	0.352
	3P_2	0.300			
Sr	1P_1	0.198	0.241	0.193	0.163
	3P_0	0.130			
	3P_1	0.132	0.136	0.135	0.163
	3P_2	0.136			
Cd	1P_1	0.398	0.427	0.346	0.303
	3P_0	0.274			
	3P_1	0.279	0.269	0.272	0.303
	3P_2	0.290			

^aThe experimental values (first column) [44] are compared with results calculated from Eq. (31) for the singlet and from Eq. (32) for the triplet (second column) and with ordinary LDA- Δ_{SCF} values (third column). The LDA was employed for $v_{\text{xc}}^{\text{stat}}$ and the ALDA for the xc kernels. The corresponding Kohn-Sham orbital energy differences ω_0 are shown in the last column (all values in rydbergs).

For the xc energy per particle, $\epsilon_{\text{xc}}^{\text{hom}}$, of the homogeneous electron gas and its second derivative with respect to the relative spin polarization $\zeta := (n_{\uparrow} - n_{\downarrow})/n$, also called the xc contribution to the "spin-stiffness coefficient," we use the parametrization of Ref. [38].

The calculation of Table II uses the x-only optimized effective potential (OEP) for $v_{\text{xc}}^{\text{stat}}$ in the approximation of Krieger, Li, and Iafrate [40] and for f_{xc} the kernel

$$f_{\text{xc}}^{\text{TDOEP}}[n_0](\mathbf{r}, \mathbf{r}'; \omega) = - \frac{2|\sum_k f_k \phi_k(\mathbf{r}) \phi_k^*(\mathbf{r}')|^2}{|\mathbf{r} - \mathbf{r}'| n_0(\mathbf{r}) n_0(\mathbf{r}')} , \quad (37)$$

which is based on the time-dependent OEP method in the x-only approximation [23,41].

TABLE II
Lowest $S \rightarrow P$ excitation energies of
various atoms.^a

Atom	State	Ω_{exp}	Ω^{OEP}	$\Omega(\Delta_{\text{SCF}})$	ω_0^{OEP}
Be	1P_1	0.388	0.392	0.331	0.259
	3P_0	0.200			
	3P_1	0.200	0.138	0.181	0.259
	3P_2	0.200			
Mg	1P_1	0.319	0.327	0.299	0.234
	3P_0	0.199			
	3P_1	0.199	0.151	0.206	0.234
	3P_2	0.200			
Ca	1P_1	0.216	0.234	0.211	0.157
	3P_0	0.138			
	3P_1	0.139	0.090	0.144	0.157
	3P_2	0.140			
Zn	1P_1	0.426	0.422	0.403	0.314
	3P_0	0.294			
	3P_1	0.296	0.250	0.316	0.314
	3P_2	0.300			
Sr	1P_1	0.198	0.210	0.193	0.141
	3P_0	0.130			
	3P_1	0.132	0.081	0.135	0.141
	3P_2	0.136			
Cd	1P_1	0.398	0.376	0.346	0.269
	3P_0	0.274			
	3P_1	0.279	0.211	0.272	0.269
	3P_2	0.290			

^aThe experimental values (first column) [44] are compared with results calculated from Eq. (31) for the singlet and from Eq. (32) for the triplet (second column) and with ordinary LDA- Δ_{SCF} values (third column). The x-only optimized effective potential was used for $v_{\text{xc}}^{\text{stat}}$ and the approximate TDOEP kernels (37) and (38). The corresponding Kohn-Sham orbital energy differences ω_0 are shown in the last column (all values in rydbergs).

The mean absolute deviation from the experimental singlet spectrum for the excitation energies calculated from Eq. (31) is 36 mryd for the pure LDA calculation of Table I and 11 mryd for the x-only OEP calculation of Table II.

In Table III we show the results of a "hybrid" calculation (OEP + ALDA) which employs the x-only OEP for $v_{\text{xc}}^{\text{stat}}$ and the ALDA (including local exchange and correlation terms) for the xc kernels. The results of this calculation are of similar quality as the x-only OEP calculation of Table II. The mean absolute deviation from experiment is 15 mryd. Thus, for the singlet spectrum, the OEP values are clearly superior to the LDA results and are also better than the usual LDA- Δ_{SCF} values, which deviate on the average by 27 mryd from the experi-

TABLE III
Lowest $S \rightarrow P$ excitation energies of various atoms.^a

Atom	State	Ω_{exp}	$\Omega^{\text{OEP+ALDA}}$	$\Omega(\Delta_{\text{SCF}})$	ω_0^{OEP}
Be	1P_1	0.388	0.398	0.331	0.259
	3P_0	0.200			
	3P_1	0.200	0.196	0.181	0.259
	3P_2	0.200			
Mg	1P_1	0.319	0.329	0.299	0.234
	3P_0	0.199			
	3P_1	0.199	0.196	0.206	0.234
	3P_2	0.200			
Ca	1P_1	0.216	0.236	0.211	0.157
	3P_0	0.138			
	3P_1	0.139	0.129	0.144	0.157
	3P_2	0.140			
Zn	1P_1	0.426	0.417	0.403	0.314
	3P_0	0.294			
	3P_1	0.296	0.280	0.316	0.314
	3P_2	0.300			
Sr	1P_1	0.198	0.211	0.193	0.141
	3P_0	0.130			
	3P_1	0.132	0.117	0.135	0.141
	3P_2	0.136			
Cd	1P_1	0.398	0.370	0.346	0.269
	3P_0	0.274			
	3P_1	0.279	0.239	0.272	0.269
	3P_2	0.290			

^aThe experimental values (first column) [44] are compared with results calculated from Eq. (31) for the singlet and from Eq. (32) for the triplet (second column) and with ordinary LDA- Δ_{SCF} values (third column). The x-only optimized effective potential was used for $v_{\text{xc}}^{\text{stat}}$ and the ALDA (including exchange and correlation terms) for the xc kernels. The corresponding Kohn-Sham orbital energy differences ω_0 are shown in the last column (all values in rydbergs).

mental data. This can be traced back to the sensitivity of the unoccupied orbitals and their energy eigenvalues to the asymptotic behavior of the Kohn-Sham potential. One major reason for the superiority of the optimized effective potential is the fact that it is self-interaction free and therefore has the correct $-1/r$ tail (while the LDA potential falls off exponentially). We note in passing that since the optimized effective potential decreases correctly for all orbitals, it is also superior to the Hartree-Fock (HF) potential, which is self-interaction free only for the occupied orbitals but not for the unoccupied ones. Consequently, HF orbital energy differences are typically too large.

The triplet spectrum obtained from Eq. (32) within the LDA deviates on the average from

TABLE IV
Singlet-triplet separations for the lowest $S \rightarrow P$ transitions of various atoms calculated with different approximations of the xc-functionals (see text) in comparison with experimental values [44] (EXP).^a

Atom	J	EXP	LDA	OEP	OEP + ALDA	Δ_{SCF}
Be	0	0.188				
	1	0.188	0.207	0.253	0.202	0.150
	2	0.188				
Mg	0	0.120				
	1	0.120	0.142	0.175	0.133	0.094
	2	0.120				
Ca	0	0.077				
	1	0.077	0.118	0.144	0.107	0.067
	2	0.076				
Zn	0	0.132				
	1	0.130	0.164	0.172	0.136	0.087
	2	0.126				
Sr	0	0.067				
	1	0.066	0.105	0.129	0.094	0.058
	2	0.062				
Cd	0	0.124				
	1	0.119	0.158	0.165	0.131	0.074
	2	0.108				
δ			0.033	0.057	0.018	0.028

^aJ is the total angular momentum quantum number of the triplet state; δ denotes the mean absolute deviation of the calculated values from the experimental ones (all values in rydbergs).

experiment by 9 mryd, which is slightly better than the mean absolute deviation of 10 mryd of the LDA- Δ_{SCF} spectrum. However, in spite of the fact that the OEP provides self-interaction free orbitals, it reproduces the triplet spectrum less accurately: the average deviation from experiment is 55 mryd, as can be seen from Table II. This is a consequence of the fact that we have employed the time-dependent x-only approximation for the kernel $f_{\text{xc}\sigma\sigma'}$. This approximation neglects the correlation between electrons of antiparallel spin and leads to an xc kernel which is diagonal in spin space. Accordingly, from Eqs. (33) and (34), we have within the x-only TDOEP

$$G_{\text{xc}}^{\text{TDOEP}}[n](\mathbf{r}, \mathbf{r}'; \omega) = \frac{1}{\mu_0^2} f_{\text{xc}}^{\text{TDOEP}}[n](\mathbf{r}, \mathbf{r}'; \omega). \quad (38)$$

We expect that the OEP triplet energies can be improved considerably by adding appropriate correlation terms [42, 43] to the TDOEP xc kernels.

This expectation is backed by the observation that when the x-only OEP approximation of v_{xc}^{stat} is combined with a local density prescription (ALDA) for exchange and correlation in the xc kernels f_{xc} and G_{xc} , the triplet spectrum is reproduced fairly well by Eq. (32). This can be seen from Table III, where the calculated triplet spectrum deviates on the average by 15 mryd from the experimentally measured one.

To complete the discussion of the various approximate xc functionals employed, we list the singlet-triplet separations for the lowest $S \rightarrow P$ transitions of the alkaline earth elements and the zinc series in Table IV. Obviously, by calculating $\Omega_1 - \Omega_2$ from Eqs. (31) and (32), the Kohn-Sham excitation energies ω_0 and hence all the errors contained in the approximate Kohn-Sham eigenvalues cancel out. Again, the mean absolute deviation δ from experiment clearly shows that singlet-triplet splittings are well reproduced only if correlation is included in the xc kernels. The best results are obtained when the ground-state potential is self-interaction free (OEP + ALDA).

Summary and Conclusion

We have developed a formally exact scheme of calculating excitation energies from TDDFT. Within that scheme, we arrived at compact approximate expressions for the excitation energies which performed quite well in practical calculations of singlet and triplet excitations. The calculation involves only known ground-state quantities, i.e., the ordinary static Kohn-Sham orbitals and the corresponding Kohn-Sham eigenvalues. Thus the scheme described here requires only one self-consistent Kohn-Sham calculation, whereas the so-called Δ_{SCF} procedure involves linear combinations of two or more self-consistent total energies [9].

In spite of the fact that we focused our attention to the lowest transition energies of closed-shell systems, and spin-multiplets, the method is also capable of dealing with spatial multiplets, higher excitations, and open-shell systems. Work along these lines is in progress.

ACKNOWLEDGMENTS

We thank T. Grabo for useful discussions. This work was supported in part by the Deutsche Forschungsgemeinschaft.

References

1. P. Hohenberg and W. Kohn, Phys. Rev. **136**, B864 (1964).
2. W. Kohn and L. J. Sham, Phys. Rev. **140**, A1133 (1965).
3. R. G. Parr and W. Yang, Density-Functional Theory of Atoms and Molecules (Oxford University Press, New York, 1989).
4. R. M. Dreizler and E. K. U. Gross, Density Functional Theory, An Approach to the Quantum Many-Body Problem (Springer, Berlin, 1990).
5. E. K. U. Gross and R. M. Dreizler, Eds., Density Functional Theory, Vol. 337 of NATO ASI Series B, (Plenum Press, New York, 1995).
6. J. P. Lu and W. Yang, Phys. Rev. B **49**, 11421 (1994).
7. Q. Zhao and W. Yang, J. Chem. Phys. **102**, 9598 (1995).
8. O. Gunnarsson and B. I. Lundqvist, Phys. Rev. B **13**, 4274 (1976).
9. T. Ziegler, A. Rauk, and E. J. Baerends, Theoret. Chim. Acta **43**, 261 (1977).
10. U. von Barth, Phys. Rev. A **20**, 1693 (1979).
11. A. Theophilou, J. Phys. C **12**, 5419 (1979).
12. N. Hadjisavvas and A. Theophilou, Phys. Rev. A **32**, 720 (1985).
13. W. Kohn, Phys. Rev. A **34**, 5419 (1986).
14. E. K. U. Gross, L. N. Oliveira, and W. Kohn, Phys. Rev. A **37**, 2805 (1988).
15. E. K. U. Gross, L. N. Oliveira, and W. Kohn, Phys. Rev. A **37**, 2809 (1988).
16. L. N. Oliveira, E. K. U. Gross, and W. Kohn, Phys. Rev. A **37**, 2821 (1988).
17. A. Nagy, Phys. Rev. A **42**, 4388 (1990).
18. A. Nagy, J. Phys. B **24**, 4691 (1991).
19. A. Nagy, Phys. Rev. A **49**, 3074 (1994).
20. A. Nagy, Int. J. Quantum Chem. Symp. **29**, 297 (1995).
21. M. Levy, Phys. Rev. A **52**, R4313 (1995).
22. P. K. Chattaraj, S. K. Ghosh, S. Liu, and R. G. Parr, Int. J. Quant. Chem., to appear.
23. M. Petersilka, U. J. Gossmann, and E. K. U. Gross, Phys. Rev. Lett. **76**, 1212 (1996).
24. M. Petersilka, Diplomarbeit, Universität Würzburg, 1993.
25. M. Petersilka, U. J. Gossmann, and E. K. U. Gross, to appear.
26. E. Runge and E. K. U. Gross, Phys. Rev. Lett. **52**, 997 (1984).
27. A. Zangwill and P. Soven, Phys. Rev. A **21**, 1561 (1980).
28. Z. H. Levine and P. Soven, Phys. Rev. A **29**, 625 (1984).
29. S. J. A. van Gisbergen, J. G. Snijders, and E. J. Baerends, J. Chem. Phys. **103**, 9347 (1995).
30. M. Stener, P. Decleva, and A. Lisini, J. Phys. B **28**, 4973 (1995).
31. G. D. Mahan and K. R. Subbaswamy, Local Density Theory of Polarizability (Plenum Press, New York, 1990).
32. G. Senatore and K. R. Subbaswamy, Phys. Rev. A **35**, 2440 (1987).
33. B. Galdrikian, M. Sherwin, and B. Birnir, Phys. Rev. B **49**, 13744 (1994).

34. C. A. Ullrich, U. J. Gossmann, and E. K. U. Gross, *Ber. Bunsenges. Phys. Chem.* **99**, 488 (1995).
35. C. A. Ullrich, S. Erhard, and E. K. U. Gross, in *Super Intense Laser Atom Physics IV*, H. G. Muller, Ed. (Kluwer, Dordrecht, 1996).
36. E. K. U. Gross, J. F. Dobson, and M. Petersilka, in *Density Functional Theory*, R. F. Nalewajski, Ed., Springer Series Topics in Current Chemistry, Vol. 181 (Springer, Berlin, Heidelberg, 1996).
37. K. L. Liu and S. H. Vosko, *Can. J. Phys.* **67**, 1015 (1989).
38. S. H. Vosko, L. Wilk, and M. Nusair, *Can. J. Phys.* **58**, 1200 (1980).
39. K. L. Liu, *Can. J. Phys.* **69**, 573 (1991).
40. J. B. Krieger, Y. Li, and G. J. Iafrate, *Phys. Rev. A* **45**, 101 (1992).
41. C. A. Ullrich, U. J. Gossmann, and E. K. U. Gross, *Rev. Lett.* **74**, 872 (1995).
42. T. Grabo and E. K. U. Gross, *Chem. Phys. Lett.* **240**, 141 (1995).
43. E. K. U. Gross, M. Petersilka, and T. Grabo, in *Density Functional Methods in Chemistry*, T. Ziegler, Ed. (American Chemical Society, Washington, D.C., 1996).
44. C. E. Moore, *Nat. Stand. Ref. Data Ser. (U.S. Nat. Bur. Stand.)* **35**, Vol. I, II, and III (1971).

Simple Modification of the Lee–Yang–Parr Correlation Functional to Satisfy Exact Nonuniform Scaling Requirements

STANISLAV IVANOV

Department of Chemistry and Quantum Theory Group, Tulane University, New Orleans, Louisiana 70118; e-mail: stan@mailhost.tcs.tulane.edu

Received February 29, 1996; accepted July 17, 1996

ABSTRACT

In density functional theory (DFT) the exchange–correlation energy has to be approximated. One of the most widely used approximations to the correlation component, the Lee–Yang–Parr (LYP) functional does not obey nonuniform scaling requirements. We propose a modifying function that makes this functional satisfy nonuniform scaling constraints. As a result, two modified LYP functionals are suggested. One of them, optimized in a preliminary way, exhibits some properties better than the original LYP functional. This implies that nonuniform scaling requirements convey very important information and all approximate functionals in DFT should be made to satisfy these requirements. Our modifying factor could be used to improve the nonuniform scaling properties not only of $E_c^{\text{LYP}}[n]$ but also of most functionals which do not obey these conditions. © 1996 John Wiley & Sons, Inc.

Introduction

Density functional theory (DFT) has provided a machinery for effective quantum calculations replacing the traditional wave function approach by the electron density description of the system under investigation. This methodology

is attractive for large systems because the density depends only upon three spatial coordinates, regardless of the size of the system [1–4]. For computational purposes the exact exchange–correlation (xc) functional, $E_{xc}[n]$, must be approximated, and conveniently $E_{xc}[n]$ is separated in the following way, $E_{xc}[n] = E_x[n] + E_c[n]$ (Ref. [5]). In order to arrive at the very best approximations to $E_{xc}[n]$, one needs knowledge of conditions

reflecting the properties of the exact exchange–correlation energy.

We will concentrate our attention on the exact correlation component, $E_c[n]$, only and more specifically on the nonuniform scaling properties of the well-known Lee–Yang–Parr (LYP) approximation to $E_c[n]$. We propose a modifying factor that makes this approximation obey nonuniform scaling constraints. Our factor is not sensitive to uniform scaling but furnishes the correct nonuniform scaling behavior and could be used to improve most functionals that do not obey the nonuniform scaling requirements. Uniform and nonuniform scaling, when used with other constraints, turns out to be very powerful for constructing new approximations or improving upon the properties of already existing ones.

Define three types of scaled densities:

$$n_\lambda(x, y, z) \equiv \lambda^3 n(\lambda x, \lambda y, \lambda z), \quad (1)$$

$$n_\lambda^x(x, y, z) \equiv \lambda n(\lambda x, y, z), \quad (2)$$

$$n_{\lambda\lambda}^{xy}(x, y, z) \equiv \lambda^2 n(\lambda x, \lambda y, z). \quad (3)$$

Equation (1) represents a uniformly scaled density, and (2) and (3) nonuniformly scaled densities. With these definitions, the following equalities and inequalities have been established for the exact correlation energy [6, 7].

$$\lim_{\lambda \rightarrow \infty} E_c[n_\lambda] > -\infty, \quad (4)$$

$$\lim_{\lambda \rightarrow \infty} E_c[n_\lambda] < 0, \quad (5)$$

$$E_c[n_\lambda] \sim -\lambda, \quad \lambda \rightarrow 0, \quad (6)$$

$$\lim_{\lambda \rightarrow \infty} E_c[n_\lambda^x] = 0, \quad (7)$$

$$\lim_{\lambda \rightarrow 0} \lambda^{-1} E_c[n_{\lambda\lambda}^{xy}] = 0. \quad (8)$$

Modifications for LYP Functional

Next, we will focus our attention on one of the most commonly used approximations to the exact correlation energy, the functional of LYP [8]. This functional stems from the Colle–Salvetti formula for the correlation energy [9]. The LYP functional for spin-nonpolarized system has the following

form:

$$\begin{aligned} E_c^{\text{LYP}}[n] &= \int \frac{(-a)n}{1 + dn^{-1/3}} \\ &\times \left\{ 1 + b \left[c_F - \frac{17|\nabla n|^2}{72n^{8/3}} + \frac{21\nabla^2 n}{72n^{5/3}} \right] e^{-cn^{-1/3}} \right\} d\mathbf{r}. \end{aligned} \quad (9)$$

By integrating by parts, one eliminates the term containing the Laplacian of density [9], and expression (9) simplifies to

$$\begin{aligned} E_c^{\text{LYP}}[n] &= \int \frac{(-a)n}{1 + dn^{-1/3}} \\ &\times \left\{ 1 + b \left[c_F - \frac{17|\nabla n|^2}{72n^{8/3}} Q(n) \right] e^{-cn^{-1/3}} \right\} d\mathbf{r}, \end{aligned} \quad (10)$$

with

$$Q(n) = 1 - \frac{7}{17} \left[2 - cn^{-1/3} - \frac{dn^{-1/3}}{1 + dn^{-1/3}} \right]. \quad (11)$$

The values of the constants for both versions are $a = 0.049$, $b = 0.132$, $d = 0.349$, $c = 0.2533$, and $c_F = (\frac{3}{10})(3\pi^2)^{2/3}$. The spin-dependent forms of (9) and (10) are given in Refs. [8] and [10], respectively.

The LYP approximation satisfies conditions (4) through (6) but does *not* obey equalities (7) and (8). Instead,

$$\lim_{\lambda \rightarrow \infty} E_c^{\text{LYP}}[n_\lambda^x] \rightarrow \infty, \quad (12)$$

$$\lim_{\lambda \rightarrow 0} \lambda^{-1} E_c^{\text{LYP}}[n_{\lambda\lambda}^{xy}] \rightarrow -\infty. \quad (13)$$

In order to improve the scaling properties of the LYP functional, we suggest the following modifying function that simply multiplies the integrands in Eqs. (9) and (10). Our factor reads

$$f(n) = \exp \left(-K \frac{|\nabla n|^2}{n(\mathbf{r})^{8/3}} \right) \quad (14)$$

and makes the LYP formula obey constraints (7) and (8). Note that the proposed function $f(n)$ is not sensitive to uniform scaling, but it is submissive to nonuniform scaling as required by (7) and (8). In expression (14), K is left as a positive adjustable parameter; K should be a positive constant in order to prevent any divergence of the integrand. In the limiting case, $K = 0$, $f(n)$ becomes 1, and the original LYP functional is recovered. Corresponding to expressions (9) and (10), the following modifications of LYP result:

$$E_c^{\text{LYPM1}}[n] = \int (-a)n \frac{e^{-K[|\nabla n|^2/n(r)8/3]}}{1 + dn^{-1/3}} \times \left\{ 1 + b \left[c_F - \frac{17|\nabla n|^2}{72n^{8/3}} + \frac{21\nabla^2 n}{72n^{5/3}} \right] e^{-cn^{-1/3}} \right\} d\mathbf{r} \quad (15)$$

$$E_c^{\text{LYPM2}}[n] = \int (-a)n \frac{e^{-K[|\nabla n|^2/n(r)8/3]}}{1 + dn^{-1/3}} \times \left\{ 1 + b \left[c_F - \frac{17|\nabla n|^2}{72n^{8/3}} Q(n) \right] e^{-cn^{-1/3}} \right\} d\mathbf{r}. \quad (16)$$

To obtain Eq. (16) from Eq. (10), we multiplied the integrand by $f(n)$ after Eq. (9) had been integrated by parts.

To demonstrate how $f(n)$ improves the scaling properties of $E_c^{\text{LYP}}[n]$, we will apply condition (7) to formula (16) to arrive at

$$\lim_{\lambda \rightarrow \infty} E_c^{\text{LYPM2}}[n_\lambda^x] = \lim_{\lambda \rightarrow \infty} \int \frac{(-a)n(x, y, z)}{1 + \lambda^{-1/3} dn^{-1/3}} \times \exp \left[-K \frac{\left| \lambda^2 \frac{\partial n(x, y, z)}{\partial x} + \lambda \frac{\partial n(x, y, z)}{\partial y} + \lambda \frac{\partial n(x, y, z)}{\partial z} \right|^2}{\lambda^{8/3} n^{8/3}(x, y, z)} \right] \times \left\{ 1 + b \left[c_F - \frac{1}{24} \frac{\left| \lambda^2 \frac{\partial n(x, y, z)}{\partial x} + \lambda \frac{\partial n(x, y, z)}{\partial y} + \lambda \frac{\partial n(x, y, z)}{\partial z} \right|^2}{\lambda^{8/3} n^{8/3}(x, y, z)} \right] \right\} dx dy dz = 0, \quad (17)$$

where

$$\lim_{\lambda \rightarrow \infty} Q(n_\lambda^x) = \frac{3}{17}$$

$$\lim_{\lambda \rightarrow \infty} e^{-c\lambda^{-1/3}n(x, y, z)^{-1/3}} = 1$$

have been used. [A corresponding result applies with expression (15).]

Observe that the exponential function in (17) approaches zero much faster than the function in the curly brackets and the limit becomes zero. Following the same pattern, it can be easily shown that both modifications satisfy condition (8) as well.

Spin-dependent forms of our suggested functionals could be obtained by multiplying spin-polarized forms in Refs. [8] and [10]. Since $f(n)$ involves only the total density of the system.

In order to find the values of the adjustable parameters, we have varied, thus far, only one of the parameters in the original LYP functional, denoted by a . We have looked for a combination between a and K , for each modification, that gives as good results for atomic systems as $E_c^{\text{LYP}}[n]$. For the first modification, Eq. (15), we have obtained a viable set of $a = 0.052$ and $K = 0.002$. However, we have not yet been able to find a good combination of a and K for $E_c^{\text{LYPM2}}[n]$ because it is extremely sensitive to the value of K . Consequently, one should try to optimize the second modification more thoroughly by varying all constants in it.

TABLE I
Correlation energies / negative values^a

Atom / ion	Exp. ^b	$K = 0.0 /$ $a = 0.049$	$K = 0.002 /$ $a = 0.052$
He	0.042	0.0436221	0.0417904
Li ⁺	0.0435	0.047370	0.045582
Be ²⁺	0.0443	0.0488703	0.0473012
Be	0.094	0.0942098	0.0903355
B ⁺	0.111	0.106204	0.102123
Ne	0.387	0.382075	0.386307
Ar	0.79	0.748027	0.763763
Kr	—	1.74216	1.80303

^aDensities are obtained from Clementi–Roetti orbitals.^bThe experimental values are taken from the original paper by Lee, Yang, and Parr [8].

Numerical Results

We present some numerical results showing some improvement of the properties of the $E_c^{\text{LYPM1}}[n]$ versus $E_c^{\text{LYP}}[n]$. First we calculated the correlation energies of some atomic systems. The third column in Table I, where $K = 0.0$ and $a = 0.049$, gives the correlation energies calculated with the original LYP approximation using our integration program. The fourth column gives the correlation energies computed by means of formula (15) with $K = 0.002/a = 0.052$.

Next, we will utilize some recently derived relationships from DFT perturbation theory in order to compare the properties of $E_c^{\text{LYP}}[n]$ and $E_c^{\text{LYPM1}}[n]$. It has been shown by Görling and Levy [11] that

$$E_c^{(2)}[n] = - \sum_{l=1}^{\infty} |\langle \Phi_l | \Delta V | \Phi_0 \rangle|^2 / (E_l - E_0), \quad (18)$$

with

$$\Delta V = \hat{V}_{ee} - \sum_{i=1}^N \left[\int \frac{n(\mathbf{r}_i) d\mathbf{r}}{|\mathbf{r}_i - \mathbf{r}|} + v_x([n]; \mathbf{r}_i) \right], \quad (19)$$

where Φ_0 is that noninteracting Kohn–Sham ground-state determinant which yields n , and E_0 is the sum of the orbital energies of Φ_0 . The determinants Φ_l are the excited states of $H_{\text{KS}}[n]$ with the respective energies E_l 's, where $H_{\text{KS}}[n]$ is the Kohn–Sham noninteracting Hamiltonian. $E_c^{(2)}$ is the leading term in the following expansion for the correlation energy of the scaled density:

$$E_c[n_\lambda] = E_c^{(2)}[n] + \lambda^{-1} E_c^{(3)}[n] + \lambda^{-2} E_c^{(4)}[n] + \dots \quad (20)$$

This fact implies that $\lim_{\lambda \rightarrow \infty} E_c[n_\lambda] \simeq E_c[n]$, or that $E_c[n]$ is relatively insensitive to scaling, except when n is nearly uniform and integrates to a large number of electrons.

Table II demonstrates that for most of the considered systems our modified functional exhibits smaller sensitivity upon uniform scaling than the original LYP functional.

Finally, we turn our attention to two exact bounds on the high-density limit of the correlation energy and its functional derivative obtained by Ivanov, Lopez-Boada, Görling, and Levy [12]. The conditions are held for a two-electron hydrogen-like density of the form

$$n(\mathbf{r}) = \frac{2Z^3}{\pi} e^{-2Zr} \quad (21)$$

or, $n(\mathbf{r}) = 2|1s|^2$, where $1s = (Z^{3/2}/\sqrt{\pi})e^{-Zr}$ in atomic units. From the recent work of Chakravorty

TABLE II
Correlation energies / negative values^a

Atom / ion	$E_c^{\text{LYP}}[n]$	$E_c^{(2)\text{LYP}}[n]$	$E_c^{\text{LYPM1}}[n]$	$E_c^{(2)\text{LYPM1}}[n]$
He	0.0436221	0.0578889	0.0417904	0.0519484
Li ⁺	0.0473702	0.0577638	0.045582	0.0513296
Be ²⁺	0.0488703	0.0570887	0.0473012	0.0510797
Be	0.0942098	0.157741	0.0903355	0.142842
B ⁺	0.106204	0.157977	0.102123	0.143258
Ne	0.382075	0.537544	0.386307	0.525429
Ar	0.748027	1.03754	0.763763	1.03109
Kr	1.74216	2.2082	1.80303	2.25591

^aDensities are obtained from Clementi–Roetti orbitals: $E_c^{(2)\text{LYP}}[n]$ is the result of taking the limit of $E_c^{\text{LYP}}[n_\lambda]$ as λ goes to infinity; $E_c^{(2)\text{LYPM1}}[n]$ is the result of taking the limit of $E_c^{\text{LYPM1}}[n_\lambda]$ as λ goes to infinity.

and Davidson [13] and from our independent work, we ascertain that

$$E_c^{(2)}[n] = -0.046663 \quad (\text{in a.u.}). \quad (22)$$

Moreover, we [12] have obtained

$$\int v_c^{(2)}([n], \mathbf{r}) n(\mathbf{r}) d\mathbf{r} = 0.12868 \quad (\text{in a.u.}), \quad (23)$$

where $v_c^{(2)}([n], \mathbf{r})$ is the functional derivative of $E_c^{(2)}[n]$ with respect to $n(\mathbf{r})$.

	Condition (22)	Condition (23)
Exact value	-0.046663	0.128680
$E_c^{\text{LYP}}[n]$	-0.056481	-0.108922
$E_c^{\text{LYPM}^2}[n]$	-0.050375	-0.098721

It is seen that the modified functional gives results closer to theoretical values than the original LYP approximation. Both approximations have wrong signs when condition (23) is applied. This is not surprising since the form of the original $E_c^{\text{LYP}}[n]$ was not designed with the functional derivative in mind. (It can be demonstrated that the inclusion of $f(n)$ cannot change the sign of

$$\int v_c^{(2)\text{LYPM}^1}([n], \mathbf{r}) n(\mathbf{r}) d\mathbf{r}$$

for any $K > 0$.) Finally, since completion of this work, the refined GGA correlation energy functional of Perdew, Burke, and Ernzerhof [14] has been tested with respect to condition (22) and found to give $E_c^{(2)}[n] = -0.0482$ a.u.

Concluding Comments

Following nonuniform scaling requirements, we have proposed a modifying factor that makes $E_c^{\text{LYP}}[n]$ obey constraints (8) and (9). Even though we optimized one of our suggested functionals, $E_c^{\text{LYPM}^2}[n]$, in a preliminary way, the modified version has certain better properties than the original LYP formula. It is anticipated, in the future, that both modified functionals, Eqs. (15) and (16), will be optimized with respect to all parameters, to

closely reproduce the improved "exact" correlation energies by Chakravorty et al. [15]. This implies that nonuniform scaling conveys important information for approximating $E_c[n]$. Moreover, our modifying function could be used to improve nonuniform scaling properties of any functional which does not obey constraints (7) and (8), provided upon nonuniform scaling $f(n)$ dominates the violating term as far as the asymptotic behavior is concerned and approaches the correct limits faster.

ACKNOWLEDGMENT

It am extremely thankful to Mel Levy for his valuable comments and suggestions. This research has been supported by the National Institute of Standards and Technology.

References

1. P. Hohenberg and W. Kohn, Phys. Rev. B **136**, 864 (1964); W. Kohn and L. J. Sham, Phys. Rev. A **140**, 1133 (1965).
2. R. Parr and W. Yang, *Density Functional Theory of Atoms and Molecules* (Oxford University Press, Oxford, 1989), and all references therein.
3. M. Levy, Proc. Natl. Acad. Sci. (USA) **76**, 6062 (1979); M. Levy, Bull. Am. Phys. Soc. **24**, 626 (1979).
4. E. Lieb, Rev. Modern Phys. **53**, 603 (1981) and references therein.
5. M. Levy and J. P. Perdew, Phys. Rev. A **32**, 2010 (1985).
6. M. Levy, Phys. Rev. A **43**, 4637 (1991).
7. A. Görling and M. Levy, Phys. Rev. B **45**, 1509 (1992). See also M. Levy and A. Görling, Phil. Mag. **69**, 763 (1994).
8. C. Lee, W. Yang, and R. G. Parr, Phys. Rev. B **37**, 785 (1988).
9. R. Colle and D. Salvetti, Theor. Chim. Acta **70**, 407 (1975).
10. B. Miehlich, A. Savin, H. Stoll, and H. Preuss, Chem. Phys. Lett. **157**, 200 (1989).
11. A. Görling and M. Levy, Phys. Rev. B **47**, 13105 (1993).
12. S. Ivanov, R. Lopez-Boada, A. Görling, and M. Levy, unpublished.
13. S. J. Chakravorty and E. R. Davidson, J. Phys. Chem. **100**, 6167 (1996).
14. J. P. Perdew, K. Burke, and M. Ernzerhof, Phys. Rev. Lett., 1996, in press.
15. S. J. Chakravorty, S. R. Gwaltney, E. R. Davidson, F. A. Parpia, and C. Froese Fisher, Phys. Rev. A **47**, 3649 (1993).

DFT Calculations of Alternative Structures in the Allyl-Nickel Catalyzed Polymerization of Butadiene

H. BOEGEL* AND S. TOBISCH

Institute of Physical Chemistry (Merseburg), Martin Luther University of Halle, D-06099 Halle, Germany

Received March 29, 1996; revised manuscript received July 22, 1996; accepted August 2, 1996

ABSTRACT

The π -allyl insertion mechanism of the 1,4-*cis* polymerization of butadiene by means of allyl-nickel catalysts has been studied theoretically by density functional theory (DFT) for the ligand free cationic butenyl nickel(II) complexes $[\text{Ni}(\text{C}_3\text{H}_5)(\text{C}_4\text{H}_6)]^+$, **I**, $[\text{Ni}(\text{C}_3\text{H}_5)(\text{C}_4\text{H}_6)(\text{C}_2\text{H}_4)]^+$, **II**, and $[\text{Ni}(\text{C}_7\text{H}_{11})(\text{C}_4\text{H}_6)]^+$, **III**. DFT energy profiles have been determined for the insertion of *s-cis*-butadiene into the anti- η^3 -butenyl nickel(II) bond in the supine and prone orientation of the reacting ligands. One of the objectives of the study was to support the proposed π -allyl insertion mechanism. With increasing size of the model compound there is better agreement between the calculated reaction and activation energies in relation to the known experimental behavior. Among the different arrangements (anti- or syn-butenyl) of the allylic end of the growing polymer chain and the relative orientation (supine or prone) of cisoid butadiene at the catalytic site, the anti-butenyl/prone reacts in compound **III** with a small activation barrier (8.2 kcal/mol) to the product (–5.7 kcal/mol). The stabilizing effect of the coordination of an additional double bond of the growing polymer chain for the correct description of the geometrical and energetical aspects of the insertion reaction was demonstrated by **II**. The results support the *s-cis*-butadiene insertion into the anti- η^3 -butenyl nickel(II) bond according to the proposed π -allyl mechanism. © 1996 John Wiley & Sons, Inc.

Introduction

The stereospecific polymerization of butadiene can be directed to the desired 1,4-*cis*-polybutadiene. This is an important process in the chemical industry for producing so-called synthetic rubber. Allyl-nickel compounds and allyl

compounds of other transition metal ions catalyze the C—C bond formation with high *cis* selectivity. The reaction mechanism is much more complicated than it is for mono-olefins (Ziegler-Natta polymerization). From the experimental observations at the moment there are two mechanisms in the very complex reaction scheme proposed. The allylic end of the growing polymer chain interacts with a butadiene monomer, both coordinated in the sphere of a catalytic center. The σ -allyl mecha-

*To whom correspondence should be addressed.

nism first suggested by Cossee and Arlman [1] describes the C—C bond formation by a nucleophilic attack of the η^1 -coordinated butenyl end to the coordinated butadiene. The second mechanism is the π -allyl insertion introduced by Taube et al. [2].

The aim of this research is to investigate the mechanism of the π -allyl insertion by reliable ab initio calculations of those allyl-/butadiene-nickel species (models of key structures) in their equilibrium structures of educts and products. The second task is to locate and characterize the transition states for those reactions.

In a previous study [3] we reported the reliability of density functional theory (DFT) and Hartree-Fock (HF) calculations in describing the structure of such experimentally very well known compounds like *bis*(η^3 -allyl)nickel and syn-crotyl-cyclooctadiene-nickel, and intermediates of (η^3 -allyl)(butadiene)nickel [4]. In the HF calculations different basis sets of double-zeta (DZ) and triple-zeta (TZ) quality and pseudopotentials were used, but the results at the HF-level are not as good as the corresponding DFT calculations. As an important conclusion for the calculation of organo-nickel compounds, the reliability of the DFT approach with nonlocal gradient corrections is of the same good quality as post-HF results, but not so time consuming.

The structural models for the calculations had been taken from the mechanistic investigations and x-ray studies of Taube et al. [5] of the cationic C_{12} -allyl nickel(II) complex [$Ni(C_{12}H_{19})](B(C_6H_3)(CF_3)_2)_4$]. They have proved conclusively that the cationic polybutadienyl butadiene nickel(II) complex [$RC_3H_4Ni(C_4H_6)^+$] is the real catalyst for the 1,4-cis polymerization of butadiene. A generally accepted mechanistic scheme for the catalysis of the cis- and trans-1,4 polymerization of butadiene by allyl nickel(II) complexes was proposed. The different reactivity of the anti- and the syn-butenyl nickel(II) complex with respect to the mode of butadiene coordination should show whether the insertion process is a cis or trans insertion step of the catalytic reaction.

Computational Details

The approximate density functional calculations reported here were performed with the DGauss program and the UniChem interface [6] on a CRAY supercomputer.

All calculations were carried out using the local spin density approximation (LDA) with Slater's exchange functional [7(a),(b)] and the Vosko-Wilk-Nusair parameterization on the homogeneous electron gas for correlation [7(c)], augmented by gradient corrections to the exchange-correlation (xc) potential. Gradient corrections for exchange were based on the functional of Becke [7(d)] and for correlation were based on Perdew [7(e)], Lee-Yang-Parr [7(f)], and Stoll-Pavlidou-Preuss [7(g)]. The Becke-Perdew functionals were either added variationally within the self-consistent field (SCF) procedure (LDA/BP-NLSCF) or added perturbatively to the LDA energies (LDA/BP). The other correlation functionals were added together with the Becke functional either variationally (LDA/BLYP-NLSCF) or as perturbation (LDA/BSPP).

All electron Gaussian orbital basis sets were used for all atoms. The calculations were performed with two different basis sets from the DGauss basis-set library, denoted DZVP and TZVP. Our standard DZVP basis is a 15s/9p/5d set contracted to (63321/531/41) for nickel [8(a)], a 9s/5p/1d set contracted to (621/41/1) for carbon [8(b)], and a 4s/1p set contracted to (31/1) for hydrogen [8(b)]. A corresponding auxiliary basis set was used for the fitting of the charge density [8(b)]. The TZVP basis set consisted of orbital function with the contraction patterns (63321/5211/41), (7111/411/1), and (311/1) for Ni [8(a)], C [8(b)], and H [8(b)], respectively.

The numerical integration was done using a standard fine-meshed grid of adequate quality. The energetic effect of tighter meshed grids was estimated to be less than 0.2 kcal/mol, as indicated by single-point calculations with more than twice as many integration points as in our standard fine grid.

The geometry optimization and the saddle point search were performed at the LDA and the LDA/BP-NLSCF level of approximation by utilizing analytical gradients/hessians according to standard algorithms. No symmetry constraints were imposed in any optimization. The stationary points were exactly identified by the curvature of the potential surface at these points corresponding to the eigenvalues of the analytically calculated hessians.

Single-point calculations at the optimized stationary points at the LSDA/BP-NLSCF level with our standard basis set were performed using the LDA/BLYP-NLSCF functional as well as the larger

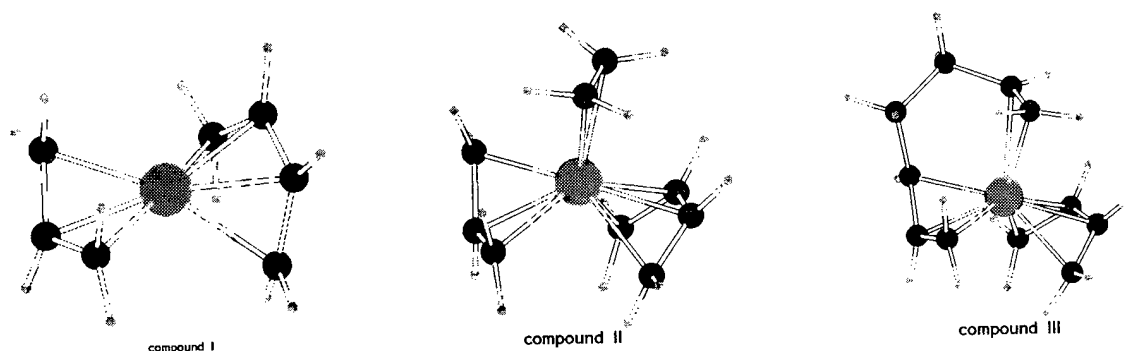


FIGURE 1. Model compounds taken into account (here only the prone orientation of allyl part with respect to the butadiene ligand, in the supine orientation the *cis*-butadiene ligand is with its open side oriented above, similar to the allyl part). The two carbon atoms in front of the structures are forming the new C—C bond of the insertion reaction of butadiene and providing the "new" allylic part to the attached monomer unit, to the end of the growing polymer chain.

TZVP basis in connection with the LDA/BP-NLSCF functional. Also the LDA/BP and LDA/BSPP functionals were utilized in single-point calculations at the optimized stationary points at the LDA level with our standard basis set.

Results and Discussion

We shall here present the results from our DFT calculations on the cationic $[(C_3H_5)Ni(C_4H_6)]^+$, **I**, $[(C_3H_5)(C_2H_4)Ni(C_4H_6)]^+$, **II**, and $[(C_7H_{11})Ni(C_4H_6)]^+$, **III**, complexes (see Fig. 1).

These were chosen as models of the real active catalyst, the cationic polybutadienyl butadiene nickel(II) complex $[R-C_3H_4Ni(C_4H_6)]^+$. The structures of the educts were derived from preliminary investigations [9] of the η^3 -butenyl coordination in anti- and syn-conformation of the corresponding cationic C_{12} -allyl nickel(II) complexes. In each of the above model systems two arrangements were investigated: the "supine" (the reacting η^2/η^4 -butadiene and η^3 -butenyl group oriented back to back) and the "prone" (reacting η^2/η^4 -butadiene and η^3 -butenyl group oriented back to front).

In the smallest $[(C_3H_5)Ni(C_4H_6)]^+$ complex, **I**, no distinction between anti and syn coordination

TABLE I
Calculated energy profile for the π -allyl insertion in the cationic $[(C_3H_5)Ni(C_4H_6)]^+$ system (kcal/mol).^a
The structures are η^4 -butadiene (a), η^2 -butadiene (b) educt, transition state (c), and product (d) in supine (1) and prone (2) orientation.

System	LDA/BP-NLSCF ^b	LDA ^b	LDA/BLYP-NLSCF ^c	LDA/BP ^d	LDA/BSPP ^d
1a	0.0	0.0	0.0	0.0	0.0
1b	17.7	32.2	12.8	23.3	10.1
1c	24.0	24.7	26.3	27.0	30.0
1d	7.0	11.4	7.8	12.1	12.5
2a	-6.9	-2.2	-6.6	-2.1	-1.6
2b	18.6	32.8	13.6	23.5	9.7
2c	18.6	14.3	21.6	18.3	23.9
2d	-0.3	4.0	0.7	4.6	5.0

^aThe supine η^4 -butadiene educt (**1a**) was chosen as arbitrary reference point.

^bComplete optimized structures.

^cSingle-point calculations using LDA/BP-NLSCF optimized structures.

^dSingle-point calculations using LDA optimized structures.

of the η^3 -butenyl group is possible. Also, we do not expect large differences between the educts, products, and transition states in supine and prone arrangement, respectively, considering the lack of coordinative saturation of nickel in this simple model.

The more realistic $[(C_3H_5)(C_2H_4)Ni(C_4H_6)]^+$ complex, **II**, contains an additional ethylene ligand in an orientation above the nickel that takes into account the specific orientation of an η^3 -butenyl group in the anti conformation. Here it is important to see how the ethylene ligand stabilizes the transition states for the supine and prone configuration in a different way.

In the biggest model $[(C_7H_{11})Ni(C_4H_6)]^+$, **III**, under investigation here, the stabilizing ethylene itself is part of the growing polymer chain.

An indication for the reliability of the standard DZVP basis is given by single-point calculations at the LDA/BP-NLSCF optimized structures using the larger TZVP basis. The relative energetic changes are sufficiently small, about 1 kcal/mol for the supine and up to 4 kcal/mol for the prone arrangement.

CATIONIC $[(C_3H_5)(C_2H_4)Ni(C_4H_6)]^+$ COMPLEX

Single-point LDA/BLYP-NLSCF calculations give quite similar energetics as for the LDA/BP-NLSCF level. The insertion reaction is about 8 kcal/mol endothermic, and the activation energies

were calculated to be of the same order for supine and prone orientations (26 and 28 kcal/mol, respectively). Only the η^2 -butadiene educts (**1b**, **2b**) are about 5 kcal/mol more stabilized relative to the η^4 -butadiene educts (**1a**, **2a**), distinctly below the transition states (see Table I). Although structural relaxation was not included, we would not expect any dramatic changes, if a complete LDA/BLYP-NLSCF optimization was performed.

At the LDA level there is a clear kinetic and thermodynamic preference for the prone versus the supine orientation. The supine reaction is about twice as endothermic as the prone reaction, 11 kcal/mol and 6 kcal/mol, respectively. The activation energies were calculated to be 25 kcal/mol (supine) and 16 kcal/mol (prone), and the η^2 -butadiene educts (**1b**, **2b**) are clearly above the transition states. These considerable differences with respect to the gradient-corrected functionals can hardly be accepted from a chemical point of view for the similar reaction models lacking any steric hindrance. We guess the inadequate xc-treatment at the LDA level is responsible for this failure. Perturbatively adding the BP corrections at the LDA-optimized stationary points (LDA/BP) cannot overcome this behavior. The insertion turns out to be 12 or 7 kcal/mol endothermic and activation energies of 27 or 20 kcal/mol for the supine or prone orientation. Also the LDA/BSPP level was unable to give a suitable energetic description. So we cannot agree with the commonly used mixed

TABLE II

Calculated energy profile for the π -allyl insertion in the cationic $[(C_3H_5)(C_2H_4)Ni(C_4H_6)]^+$ system (kcal/mol).^a The structures are η^4 -butadiene (a), η^2 -butadiene (b) educt, transition state (c), and product (d) in supine (3) and prone (4) orientation.

System	LDA/BP-NLSCF ^b	LDA ^b	LDA/BLYP-NLSCF ^c	LDA/BP ^d	LDA/BSPP ^d
3a	0.0	0.0	0.0	0.0	0.0
3b	3.6	12.6	-1.3	5.4	-6.6
3c	26.4	26.9	26.8	27.8	28.6
3d	-8.5	-8.4	-7.7	-6.7	-4.7
4a	2.8	3.9	2.9	4.0	3.7
4b	5.3	11.8	0.6	4.6	-7.3
4c	6.7	6.9	9.0	9.9	14.2
4d	-14.4	-7.4	-13.4	-8.2	-10.1

^aThe supine η^4 -butadiene educt (**3a**) was chosen as arbitrary reference point.

^bComplete optimized structures.

^cSingle-point calculations using LDA/BP-NLSCF optimized structures.

^dSingle-point calculations using LDA optimized structures.

computational treatment, to perform optimizations at the LDA level followed by a perturbative addition of gradient corrections.

CATIONIC $[(C_3H_5)(C_2H_4)Ni(C_4H_6)]^+$ COMPLEX

The optimized structures of the η^4 -butadiene educt (**3a**, **4a**), the η^2 -butadiene educt (**3b**, **4b**), the transition state (**3c**, **4c**), and the product (**3d**, **4d**) for the supine/prone arrangement are compared in Table II, respectively. All optimized structures have no symmetry.

The most remarkable differences between the supine and prone coordination mode, influenced by the ethylene ligand, occurred for the transition states (**3c**, **4c**). They differ in the two possible geometrical arrangements, observed for the d^8 transition metal configuration. The supine transition state **3c** can be described as tetragonal pyramidal and the prone system **4c** as trigonal bipyramidal. The transition states were located at a carbon to carbon distance of 2.155 and 2.079 Å, for **3c**, **4c**, respectively, for the performed σ -bond. These are noticeably larger than for **1c**, **2c**, indicating an earlier occurrence at the potential surfaces than for **1c**, **2c**. By comparing the transition states for supine (**3c**) and prone (**4c**) orientation, it can be concluded that the former appears product-like whereas **4c** appears educt-like.

The simpler $[(C_3H_5)Ni(C_4H_6)]^+$ model (discussed in the previous section) is able to give essential insights into the mechanism, derived from the located transition state structures. But only by the inclusion of an additional ethylene ligand could we overcome the lack of coordinative unsaturation at the nickel center. A different picture between the supine and prone arrangement results. The coordinative interaction of the ethylene with Ni(II) is very similar at each stage of the reaction, as indicated by the nearly identical ligand geometry distortion, regardless of whether the allylic and butadiene moieties are supine or prone oriented.

As found for the $[C_7H_{11}Ni]^+$ system the Ni-C distances are found to be noticeably shorter at the LDA than at the LDA/BP-NLSCF level. The above-discussed geometrical aspects for the educts, products, and transition states are found also without including gradient corrections. Greater deviations from the LDA/BP-NLSCF geometries occur for the transition states **3c**, **4c**. Two different geo-

metrical arrangements are revealed, tetragonal pyramidal with 2.084 Å for **3c** and trigonal bipyramidal with 2.079 Å for the CC σ -bond for **4c**.

In free optimizations starting downhill from marginally distorted transition state geometries, that is with an elongated and shortened CC distance (which is mainly involved in the reaction coordinate), proved that the two transition states correspond to the η^4 -butadiene educts (**3a**, **4a**) and the products (**3d**, **4d**), respectively.

The calculated energy profile at several levels of theory using the standard DZVP basis is reported in Table II. From the above-discussed geometrical aspects of the insertion reaction we would expect a noticeable energetic difference especially for the transition states, resulting in quite different activation energies for supine and prone arrangements. Due to the inclusion of the ethylene ligand, Tolman's 18-16 electron rule should be fulfilled; we also expect more realistic reaction energies, compared with the experiment.

First we discuss the energetics for the complete optimized structures at the LDA/BP-NLSCF level. In contrast to the simpler $[(C_3H_5)Ni(C_4H_6)]^+$ model the insertion reaction was calculated to be exothermic in both arrangements, 8.5 kcal/mol for supine and about twice as much, i.e., 17 kcal/mol (Table II), for prone. Also the η^4 - (**3a**, **4a**) and η^2 - (**3b**, **4b**) educts are energetically similar, with the η^4 -educts favored by about 3 kcal/mol. So from the energetic point of view both educts are eligible as reactants for the true insertion reaction, but the η^2 -educts should be ruled out according to deductions from the principle of least structure variation. The most important difference was found for the transition states. Whereas for the supine mode a

TABLE III
Calculated energy profile at the LDA/BP-NLSCF level for the π -allyl insertion in the $[(anti-C_7H_{11})Ni(C_4H_6)]^+$ system (kcal/mol).^a The structures are η^4 -butadiene (a), η^2 -butadiene (b) educt, transition state (c), and product (d).

Structure	Supine (5)	Prone (6)
a	0.0	3.9
b	11.5	12.8
c	25.2	12.2
d	-4.7	-1.8

^aThe supine η^4 -butadiene educt (**5a**) was chosen as reference point.

similar activation energy of about 26 kcal/mol as for the $[(C_3H_5)Ni(C_4H_6)]^+$ model arises, only about 4 kcal/mol was calculated for the prone mode. So besides the thermodynamic preference, the prone orientation should also be kinetically quite feasible.

The calculated reaction energies are not influenced by using the larger TZVP basis at the LDA/BP-NLSCF level. Also the activation energy for supine remains the same, whereas for prone about 6 kcal/mol was calculated.

Quite similar energetics result from single-point LDA/BLYP-NLSCF calculations using the optimized LDA/BP-NLSCF structures. The prone insertion was twice as exothermic as supine, i.e., about 16 and 8 kcal/mol, and the activation energies were calculated to be about 27 or 6 kcal/mol for supine or prone. The largest deviation of approximately 5 kcal/mol appears in the case of the η^2 -educts. At the LDA/BP-NLSCF level the η^4 -educts are slightly more stable than the η^2 -educts, but at the LDA/BLYP-NLSCF level that relation is

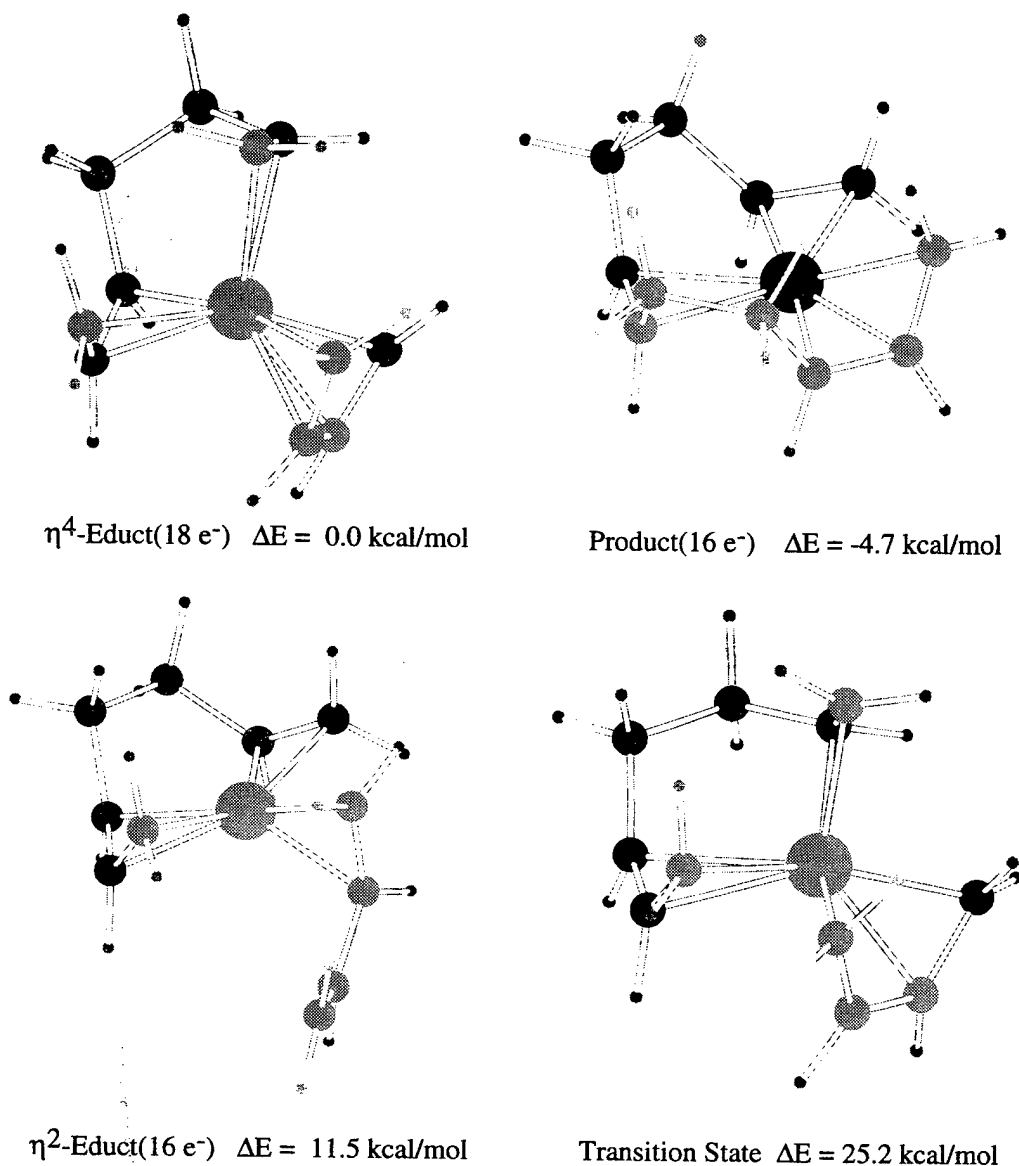


FIGURE 2. Modeling of the π -allyl insertion mechanism (antibutenyl configuration) (SUPINE)[Ni(η^3, η^2 -C₇H₁₁)(η^2/η^4 -*cis*-C₄H₆)]⁺ (DZVP/A1-Basis VWN BP NLSCF XC grid-fine, relative energies, ANTI-Butenyl SUPINE η^4 -educt is the reference point).

turned around. The energetic effects caused by a complete optimization at the LDA/BLYP-NLSCF level were estimated to be negligible.

The relative energetics of the insertion reaction are surprisingly well described at the LDA level compared to the more reliable gradient-corrected functionals. The prone insertion is thermodynamically preferred over supine, although by only about 3 kcal/mol. The calculated activation barriers of about 27 or 3 kcal/mol for supine or prone agree quite well with the LDA/BP-NLSCF values. On the other hand unlike the gradient-corrected functionals, a rather large energy difference between the η^4 - and η^2 -educts appears. Taking the strik-

ingly good energetically description at the LDA level into account, than the fairly good agreement between the perturbatively added BP corrections (LDA/BP) and the full self-consistent BP treatment (LDA/BP-NLSCF) is not so unexpected. Although we do not have any real measure for the reliability of the calculated energetics for the investigated systems, for example, by means of highly correlated ab initio methods, at the moment we are worried about the reliability of the LDA/BSPP calculated energetics. More elaborate calculations on small organyl-nickel compounds at the coupled-cluster singles and doubles (CCSD(T)) level have been started.

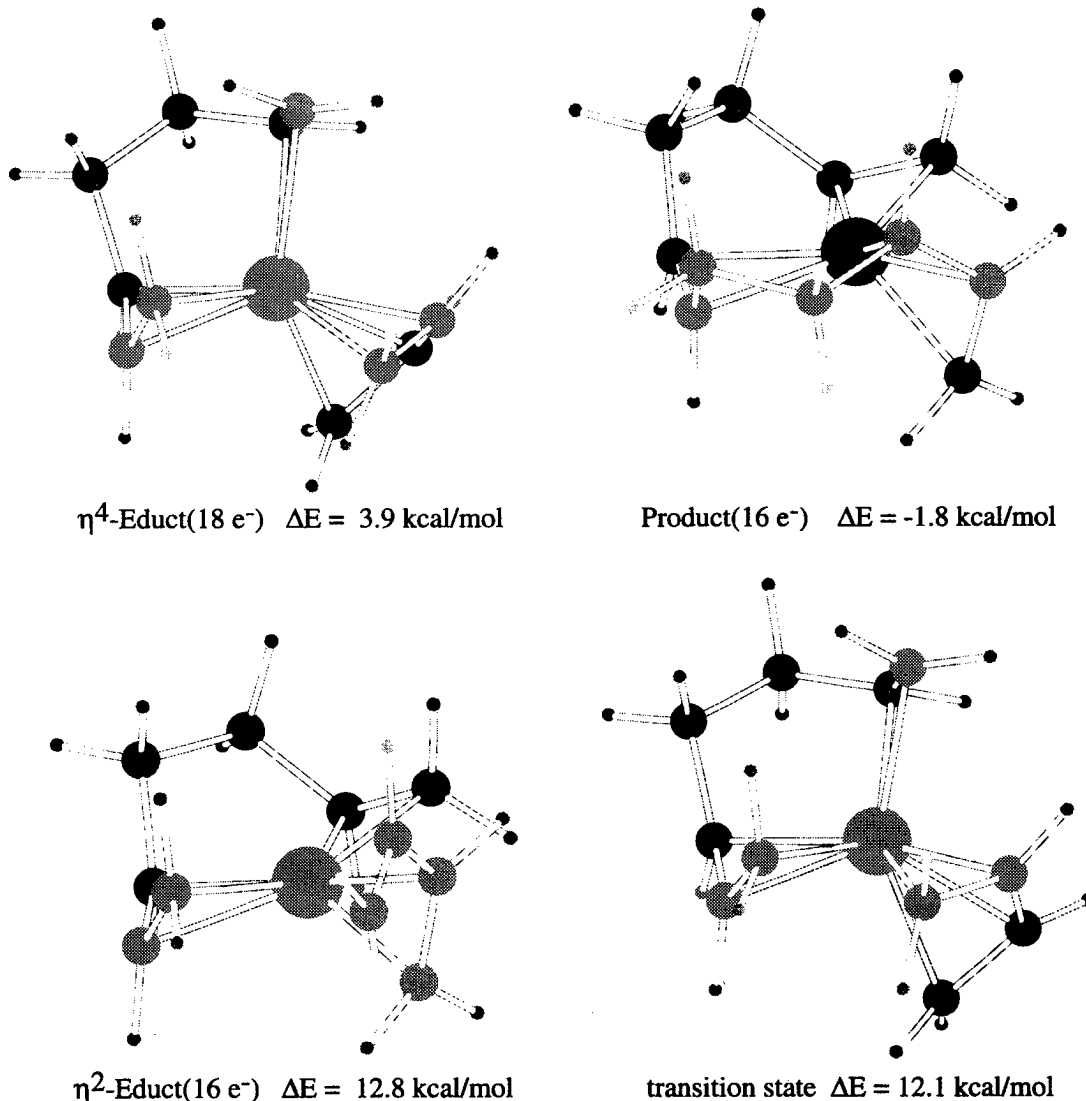


FIGURE 3. Modeling of the π -allyl insertion mechanism (antibutenyl configuration) (PRONE) $[\text{Ni}(\eta^3, \eta^2\text{-C}_7\text{H}_{11})(\eta^2/\eta^4\text{-cis-C}_4\text{H}_6)]^+$ (DZVP / Al-Basis VWN BP NLSCF XC grid-fine, relative energies, ANTI-Butenyl SUPINE η^4 -Educt is the reference point).

At the LDA/BSPP level, which should be suitable to overcome the error introduced by self-interaction, the η^2 -educt results considerably more stable than the η^4 -educt.

A detailed mechanistic interpretation and comparison of these models (1, 2, 3, 4) and their role in describing the catalytic chemical insertion reaction of butadiene will be given in a separate more chemical-oriented work [4].

CATIONIC $[(C_7H_{11})Ni(C_4H_6)]^+$ COMPLEX

In conclusion of the models described above, the additional ethylene ligand gave a reliable picture of the insertion process. Here we want to investigate its effect, to be part of the growing polymer chain. The calculations were performed at the LDA/BP-NLSCF level for an antibutenyl conformation of the growing end of the polymer, which transforms during the insertion to a cis unit of the polymer. This model (5, 6) takes into account all the essential coordination as it is proposed for the reaction mechanism [5] for the real catalyst.

It was found that the orientation of the η^2 -olefinic part of the polymer is quite similar to the ethylene ligand in the models discussed (3, 4) above. Furthermore the allyl part in the educts is very similar to those in the products, which is important for the overall process.

The supine orientation gives slightly more stable educts (5a) and products (5d) (see Table III), but the activation energy for the prone orientation is essentially smaller (only 12 kcal/mol) than for the supine (25 kcal/mol). Therefore the reaction starts from the prone orientation, which is not the most stable one. This agrees with nuclear magnetic resonance (NMR) investigations of labeled compounds in the 1,4-cis-polybutadiene [10], which had been interpreted to arise from prone orientations.

The optimized structures of educts, transition states, and products for supine (Fig. 2) and prone orientation (Fig. 3) are summarized.

Conclusions

The aim of this research was to study the insertion of s-cis-butadiene into the anti- η^3 -butenyl-nickel(II) bond attempting to support the proposed π -allyl insertion mechanism for the 1,4-cis polymerization of butadiene. The investigations were

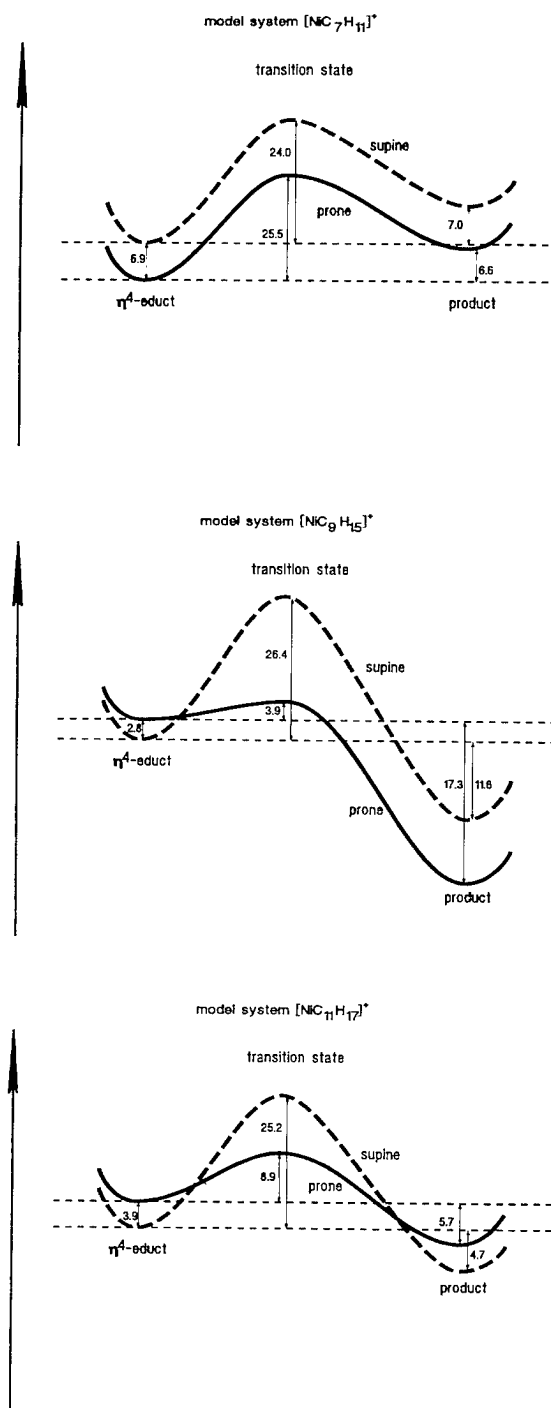


FIGURE 4. Calculated energy profiles (kcal/mol) for the insertion of butadiene into the allyl-nickel bond for supine and prone orientation in the three model compounds (I, II, III).

done on model compounds of increasing complexity, the $[(C_3H_5)Ni(C_4H_6)]^+$, $[(C_3H_5)(C_2H_4)Ni(C_4H_6)]^+$, and $[(C_7H_{11})Ni(C_4H_6)]^+$ system, modeling the ligand-free cationic butenyl nickel(II) complex.

For the $[(C_3H_5)Ni(C_4H_6)]^+$ complex no clear difference for both the main geometrical parameters and the reaction profile between the supine and prone coordination mode was appeared. The necessity of the incorporation of the next double bond of the growing polymer chain for a correct picture of the geometrical and energetical aspects was clear demonstrated by the $[(C_3H_5)(C_2H_4)Ni(C_4H_6)]^+$ and $[(C_7H_{11})Ni(C_4H_6)]^+$ systems. A clear difference between the supine and prone orientation has occurred for these systems, especially realized at the transition states. The product-like supine transition state **3c**, **5c** can be described as tetragonal pyramidal and the rather educt-like prone transition state **4c**, **6c** as trigonal bipyramidal structure.

As a result of the lack of coordinative saturation of Ni(II) in the $[(C_3H_5)Ni(C_4H_6)]^+$ system, the insertion was calculated to be endothermic with an activation barrier of about 25 kcal/mol. For the $[(C_3H_5)(C_2H_4)Ni(C_4H_6)]^+$ model a noticeable thermodynamic and kinetic preference of the prone over the supine orientation has occurred. The insertion was determined to be exothermic by about 8.5 or 17 kcal/mol with a barrier of about 26 or 4 kcal/mol for supine or prone, respectively. For the biggest model $[(C_7H_{11})Ni(C_4H_6)]^+$ the insertion is 5 or 6 kcal/mol and the barrier is 25 or 8 kcal/mol for supine or prone. The insertion reaction proceeds from the prone orientation. Figure 4 compares the energy profiles for supine and prone orientations of all three models at the LDA/BP-NLSCF level.

The transition states can be characterized by a nearly complete change in hybridization of the reaction centers at the carbon atoms of the newly to form C—C σ -bond from sp^2 to sp^3 . As a consequence this C—C σ -bond is coordinated lower and moved away from the nickel coordination sphere, while the other ligands remain π -coordinated to Ni(II).

From a theoretical point of view the usage of gradient-corrected functionals is recommended for a reliable description of the investigated reactions. Very similar energy profiles were derived with both the LDA/BP-NLSCF and the LDA/BLYP-NLSCF treatment. Also for the geometries of the

optimized structures we would expect no significant difference between these functionals. Although the nickel–ligand interaction was not properly described at the LDA level, the relative geometrical changes are comparable to the former one. For the estimation of the energetics the LDA, even by perturbatively adding of gradient corrections, is not able to give a well-balanced energetic description.

In further studies we will extend our investigations on one hand to the use of more elaborated methods to study the reliability of the DFT calculations and on the other hand we want to continue in study the catalytic reaction scheme of butadiene in monoligand nickel(II) complexes.

ACKNOWLEDGMENTS

This work was supported by the German Bundesministerium für Forschung und Technologie (BMFT). We acknowledge excellent service by the computer centers ZIB Berlin, URZ Magdeburg, and HLRZ Jülich.

References

- (a) P. Cossee, in *Stereochemistry of Macromolecules*, Vol. 1, A. D. Ketley, Ed. (Marcel Dekker, New York, 1967), p. 145. (b) E. J. Arlman, *J. Catal.* **5**, 178 (1966).
- R. Taube and J. Langlotz, *Makromol. Chem.* **194**, 705 (1993).
- S. Tobisch and H. Bögel, *Int. J. Quant. Chem.* **56**, 575 (1995).
- S. Tobisch, H. Bögel, and R. Taube, *Organometallics* **15**, 3563 (1996).
- (a) R. Taube and S. Wache, *J. Organomet. Chem.* **428**, 431 (1992). (b) S. Wache and R. Taube, *J. Organomet. Chem.* **456**, 137 (1993).
- (a) J. Andzelm and E. Wimmer, *Physica B* **172**, 307 (1991). (b) J. Andzelm, in *Density Functional Methods in Chemistry*, J. Labanowski and J. Andzelm, Eds. (Springer, Berlin, 1991); DGAUSS and UniChem are software packages available from Cray Research.
- (a) P. A. M. Dirac, *Proc. Cambridge Philos. Soc.* **26**, 376 (1930). (b) J. C. Slater, *Phys. Rev.* **81**, 385 (1951). (c) S. H. Vosko, L. Wilk, and M. Nusair, *Can. J. Phys.* **58**, 1200 (1980). (d) A. D. Becke, *Phys. Rev. A* **38**, 3098 (1988). (e) J. P. Perdew, *Phys. Rev. B* **33**, 8822 (1986). (f) C. Lee, W. Yang, and R. G. Parr, *Phys. Rev. B* **37**, 785 (1988). (g) H. Stoll, C. M. E. Pavlidou, and H. Preuss, *Theor. Chim. Acta* **49**, 143 (1978).
- (a) DGAUSS basis-set library. (b) N. Godbout, D. R. Salahub, J. Andzelm, and E. Wimmer, *Can. J. Chem.* **70**, 560 (1992).
- S. Tobisch, unpublished data.
- L. Porri, G. Natta, and M. C. Gallazzi, *J. Polym. Sci. C* **16**, 2525 (1967).

Density Functional Study of $\text{Fe}_2\text{-N}_2$

ANGELICA ZACARIAS AND MIGUEL CASTRO*

Departamento de Fisica y Quimica Teorica, Facultad de Quimica, Universidad Nacional Autonoma de Mexico, Ciudad Universitaria, C.P. 04510 Mexico D.F., Mexico; e-mail for M. C.: castro@papalotl.pquim.unam.mx

Received March 30, 1996; revised manuscript received July 22, 1996; accepted July 30, 1996

ABSTRACT

The interaction of two iron atoms with molecular nitrogen was studied by means of density functional techniques. Calculations were of the *all-electron* type, and both conventional local and gradient-dependent approximate (GDA) models were used. A ground state (GS) of linear structure was found for $\text{Fe}_2\text{-N}_2$ with $2S + 1 = 7$; whereas a distorted tetrahedral structure, being also a septuplet, was located at 4.0 and 14.3 kcal/mol above the GS, at the local and GDA levels of theory, respectively. The N–N bond is moderately perturbed in the GS, but it is strongly activated in the tetrahedral mode: It has bond orders of 2.6 and 1.5, vibrational frequencies of 2148 and 1496 cm^{-1} , and equilibrium bond lengths of 1.14 and 1.24 Å, for the linear and tetrahedral geometries, respectively. These values are 3.0, 2359 cm^{-1} , and 1.095 Å, for free N_2 . At GDA level of theory, the $\text{Fe}_2\text{-N}_2$ binding energy is 15 kcal/mol, which is bigger than that of Fe-N_2 (9 kcal/mol). The π -back donation, in the linear GS, is of 0.31 electrons, but the total charge transfer, from Fe_2 to N_2 , is only 0.05 units. This is relevant in comparison with the tetrahedral mode, where the Fe_2 to N_2 total charge transfer is of 0.45 electrons, yielding a stronger activated N_2 moiety. © 1996 John Wiley & Sons, Inc.

Introduction

The experimental and theoretical study of the interaction of molecular species with transition metals (TM) is nowadays an active field of research. Large efforts are devoted to determine the mechanism of activation that some molecules (such as N_2 , N_2O , O_2 , etc.) experience in the presences of TMs [1–6]. Surfaces, organometallic com-

plexes, and enzymes represent some catalytic systems responsible for many important chemical reactions that occur in biological and industrial processes. They usually contain one or two types of TMs surrounded by some ligands [1] (e.g., nitro-genase contains Fe, Mo, S, and H atoms). So far, it is not totally clear which metallic site is preferred for the activation; also the role played by the ligands attached to, or surrounding the metallic centers is not known. Nonetheless it is expected that both the metal–metal and metal–ligand interactions within the enzyme or complex will pro-

* To whom correspondence should be addressed.

mote a electronic state of optimal catalytic capability. The study of the catalytic properties has been focused on a fragment of the whole system. This small piece commonly contains a TM atom joined to some ligands, in the case of enzymes, or joined to a small number of TM atoms, in the case of metallic surfaces; this TM atom will be labeled as TM*. This kind of approach reduces the problem to the study of a TM*-L system, which is more amenable for the search of lowest energy structures, transition states, activation energies, etc., that occurs during the catalytic processes. A limitation of this approach is in the choice of a structure for the active site, which is more difficult to select for an enzyme.

On the other hand, a theoretical study of the whole enzyme-molecule system is beyond the state of the art both of the computational methodologies and of the available computational facilities. One reason for such limitation originates from the complicated nature of the exchange-correlation (XC) that arises when TM atoms are involved. For instance, it is well known that the Hartree-Fock (HF) level of theory is a very bad starting point for TMs, and that their treatment at least requires a second order Møller-Plesset perturbation theory (MP2) approach (at this level, the nonlocal XC operator scales as N^5), or even higher, but with a consequent higher order scaling, for a reasonable accounting of XC. On the other hand, density functional theory (DFT) accounts for XC of many electron systems through local, and presumably, more accurate gradient-corrected functionals and at the same time scale as N^3 (or even lower when cutoffs are employed). Then, DFT base methods may be used for the study of molecules interacting with TM systems [3, 4].

In an attempt to understand the activation of molecular nitrogen by systems containing Fe atoms—organometallic complexes [1] and enzymes (i.e., nitrogenase)—we have recently started a theoretical study of the interaction of N_2 with Fe, Fe_2 , Fe_2S_2 , $FeMoS_2$, and up in order to reach a cluster's size where the activation mechanism has been switched on. The goal is to obtain a characterization of the site that is responsible of the N_2 fixation and to get insight about the role that the metal-metal and metal-ligand interactions, wherein the cluster, play in that kind of process.

In a previous work [6], we reported the results of Fe- N_2 . Two lowest energy states were found (linear and triangular triplets), at which the bonding of N_2 is strongly perturbed by the Fe atom [6].

Now, we are going to discuss the lowest energy structures that result from the interaction of Fe_2 with N_2 .

Computational Procedure

The study was done through first-principles *all-electron* calculations with the program deMonKS [7]: a *Linear Combination of Gaussian-type Orbitals* (LCGTO) DFT-based method. Here, the local spin density approximation (LSDA) was included as in Vosko et al. [8] while the gradient-dependent approximations (GDA) were those of Perdew and Wang for exchange [9], and Perdew for correlation [10]. The GDA potential was included in the Kohn-Sham potential during the self-consistent-field (SCF) procedure [7]. Orbital basis sets of DZVP2 quality [(63321/5211*/41 +) for Fe and (721/51/1*) for N], optimized explicitly for DFT calculations [11], were used. They contain *p*-polarization and *d*-diffuse functions. Additional auxiliary bases of Gaussian-type orbitals were employed to describe the charge density (CD) and the XC potential. During the iterative step, the CD is fitted analytically, while the XC potential is fitted numerically on a fine grid. At the end of the SCF procedure, the XC contributions to the energy and energy gradients are calculated by numerical integration on an augmented set of grid points [12]. By means of the Broyden-Fletcher-Goldfarb-Shanno algorithm [13], the geometries were optimized by minimizing the norm of the gradient (with a 10^{-5} a.u. threshold). A tolerance convergence criteria of 10^{-6} a.u. was used for the total energy and of 10^{-5} a.u. for the electronic density. These criteria are needed for a correct determination of the lowest energy structure for a given TM-L geometry, since it was observed that, in some cases, there are several coordination modes within a small energy range [3, 4]. Finally, a vibrational analysis, under the harmonic approximation, was done for the optimized geometries. This gives information about the stability or nature, a minimum or a transition state, of the optimized geometry.

Results and Discussions

We have started the study of Fe_2 - N_2 by choosing some input geometries (see Fig. 1). The geometry optimization of these starting structures was

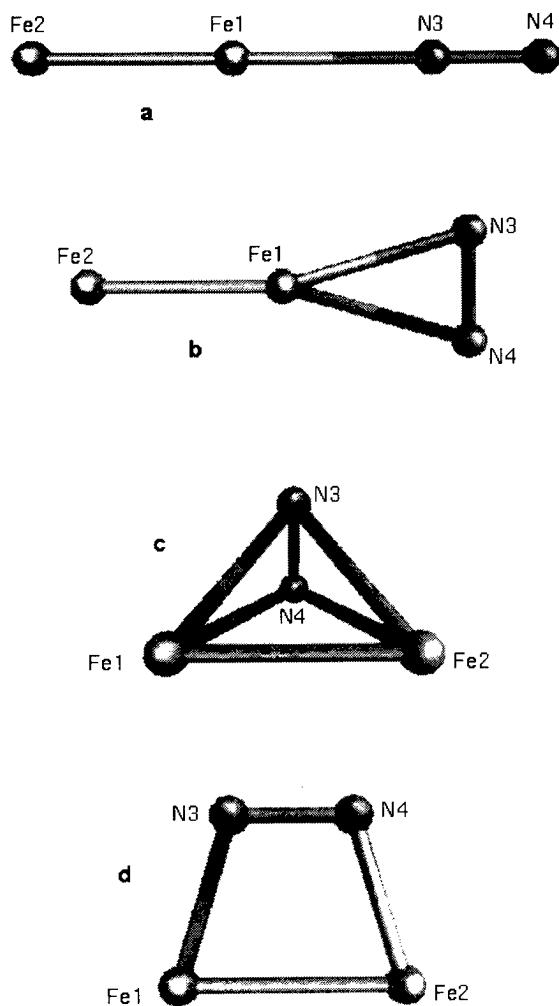


FIGURE 1. Some input geometries for the $\text{Fe}_2\text{-N}_2$ coordination modes.

done for several electronic states of different total spin S or multiplicity $M = 2S + 1$. In all cases, the initial N-N, Fe-N, and Fe-Fe internuclear distances were 1.095, 2.0, and 2.0 Å, respectively. This initial guess yields a plethora of possibilities for the $\text{Fe}_2\text{-N}_2$ coordination modes. Figure 2 shows some optimized geometries. Visualization techniques, as implemented in UniChem [14], were used to follow the evolution of the $\text{Fe}_2\text{-N}_2$ structures during the geometry optimization procedure. Initial and final structures, as obtained with UniChem, are shown in Figures 1 and 2. Also the density contour plots were obtained with the use of UniChem, coupled, in this case, with the program Dgauss [15], which was used for the generation of the electronic density of the optimized structure. The density contour plots for the GSs of Fe_2 and N_2 are

reported in Figure 3, and those for some located $\text{Fe}_2\text{-N}_2$ structures are reported in Figure 4.

In general, high-spin states are energetically more favored for $\text{Fe}_2\text{-N}_2$ (which shows preferences for $M = 7$ and $M = 5$ states, with the former lying deeper in energy) as compared with $\text{Fe}_2\text{-N}_2$, which has preferences for $M = 3$ and $M = 5$ states [6]. Some of these lowest energy structures are contained within an small energy range (of about 5 kcal/mol), and they have different dimensionality and/or multiplicity; see Figure 2. The values in parenthesis show the relative stability at GDA level, which, in principle, is a better approach than LSDA. These two levels of theory yield a different energy position for some states, which reveals both the complicated nature of XC in systems involving TM atoms and the complicated nature of the potential energy surface of $\text{Fe}_2\text{-N}_2$. For example, the two-dimensional septuplet is a transition state, since its vibrational analysis yields an imaginary frequency, but while LSDA locates it at +7.6 kcal/mol, with respect to the GS, GDA locates this state at only +2.7 kcal/mol above the GS. Moreover, there is agreement between GDA and LSDA in that the GS is the linear septuplet; but these two approaches give a different ordering for the remaining states. Now, we are going to discuss the main features of the $\text{Fe}_2\text{-N}_2$ structures. Table I shows the calculated equilibrium bond lengths, R_e , and Table II shows the vibrational frequencies, ω_e , as well as the ΔR and $\Delta\omega$ changes experienced by N_2 . Table III presents a Mulliken population analysis for the valence electrons of the GS; while Table IV contains the gross populations that the N and Fe atoms have in the $\text{Fe}_2\text{-N}_2$ structures. Finally, the binding energies, D_e computed at LSDA and GDA levels of theory, are reported in Table V.

$\text{Fe}_2\text{-N}_2$, THE *END-ON* GROUND STATE

A linear structure, with $M = 7$, was found as the GS for $\text{Fe}_2\text{-N}_2$. The linear quintet was found ≈ 16 kcal/mol higher in energy. In the $\text{Fe}_2\text{-N}_2$ *end on* mode, the R_e and ω_e of N_2 are, with respect to free N_2 , enlarged and reduced by 0.019 Å (0.017 Å) and by 195 cm^{-1} (179 cm^{-1}), respectively, at LSDA (GDA) level of theory. These results imply a reduction of the multiple bond of N_2 . Indeed, a Mayer bond order (BO) analysis [16] yields a BO of 2.6 for N_2 in $\text{Fe}_2\text{-N}_2$. (free N_2 has BO = 3.0). That is, the bonding of the N_2 moiety

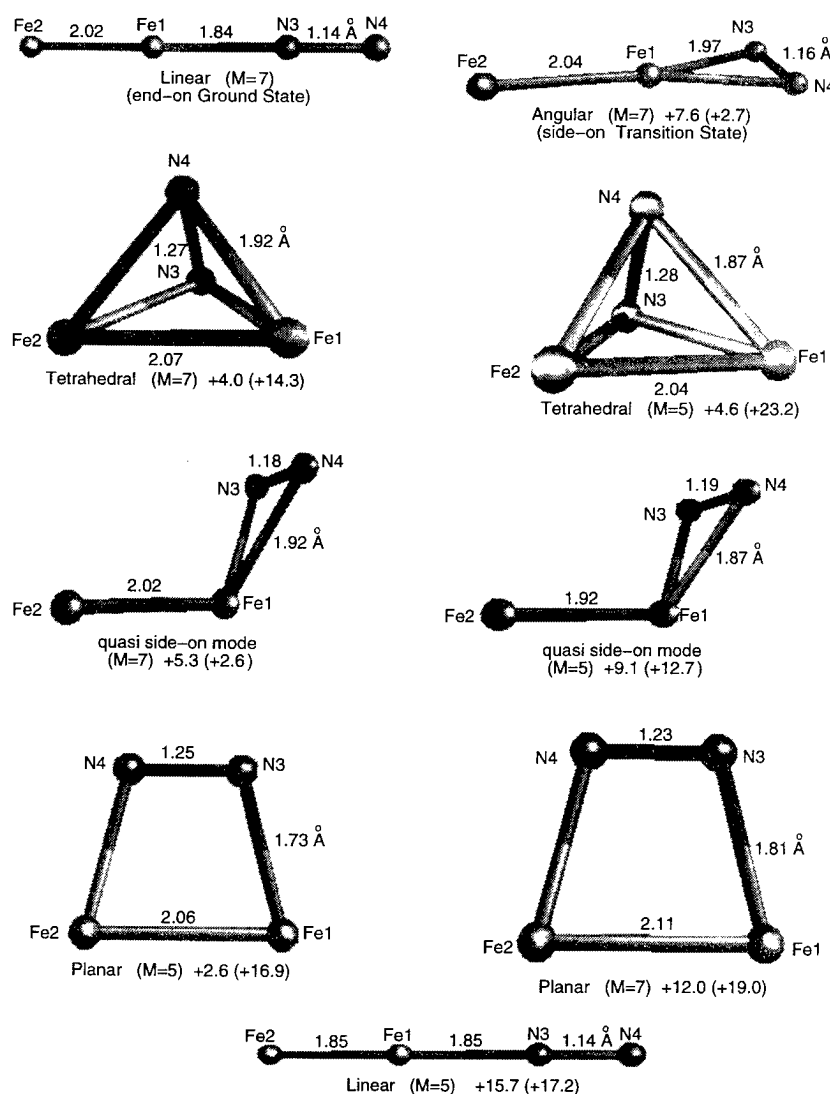


FIGURE 2. Optimized geometries for the lowest energy structures of $\text{Fe}_2\text{-N}_2$. LSDA and GDA (values in parenthesis) relative energies are indicated as well as the LSDA equilibrium bond lengths.

has been reduced by less than a half bond. In linear TM-L systems a synergistic ligand to metal (a σ -donation) and metal-to-ligand (a π -back donation) charge transfer mechanism is operative. This last is a measure of the TM-L bond strength. In the GS of $\text{Fe}_2\text{-N}_2$ there is a σ -donation of 0.325 electrons and a π -back donation of 0.314 electrons; see Table II. (These values are smaller than those of the triplet linear GS of $\text{Fe}_2\text{-N}_2$, where there are σ - and π -back donations of 0.37 and 0.73 electrons, respectively [6]. The smaller π -back donation in $\text{Fe}_2\text{-N}_2$ is due to the fact that the Fe atom, which is bonding directly to N_2 , is also bonding, through some π -electrons, with the other Fe atom.) This π metal-to-ligand charge transfer, although a modest

value, accounts for the high stability exhibited by the linear septuplet. The total density contour plot for the GS [see Fig. 4(a)] reveals some accumulation of charge density in the metal (Fe_1)-ligand (N_3) region, which accounts for a high bond strength. In fact, in this one-dimensional geometry is where the Fe-N distance reaches its shortest value (see Fig. 2) and its highest binding energy. $\text{Fe}_2\text{-N}_2$ have a metal-ligand D_e of 30.3 and 14.6 kcal/mol at the LSDA and GDA schemes, respectively. (These D_e 's were computed with respect to the GSs of Fe_2 and N_2 free molecules. Note that the quintet linear state of $\text{Fe}_2\text{-N}_2$ is unbound, at GDA level of theory.) On the other hand, there is a very small total charge transfer from Fe_2 to N_2 ,

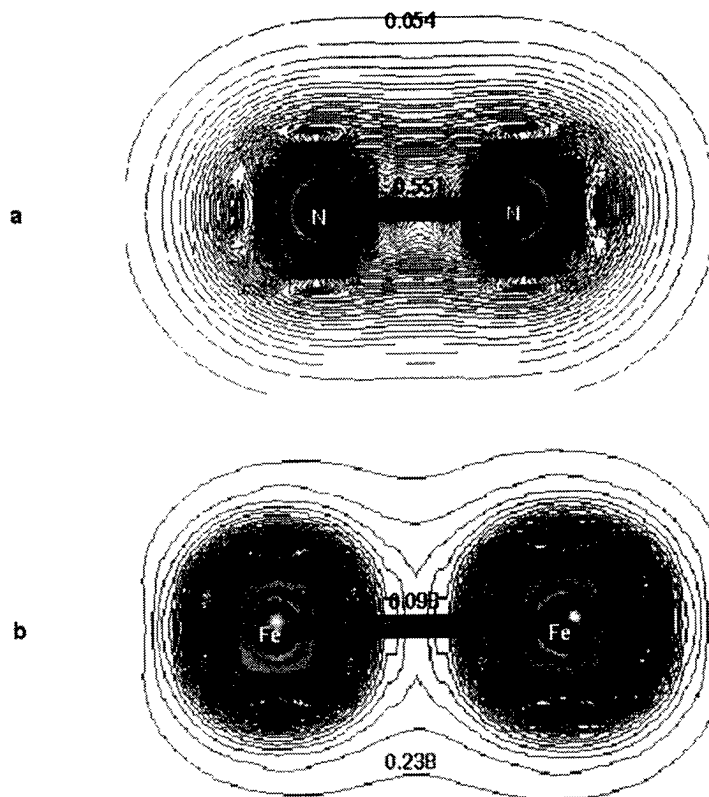


FIGURE 3. Total density contour plots for (a) free N_2 and (b) free Fe_2 .

which is of about 0.05 units; see Table III. This last fact accounts for the relatively small perturbation of the N-N bonding by Fe_2 (the transferred electrons goes into antibonding π -type molecular orbitals of N_2). Summarizing, the main findings for the computed GS are: the metal-ligand D_e for the linear septuplet is the biggest one, (see Table V), but the perturbation experienced by N_2 is relatively small.

$\text{Fe}_2\text{-N}_2$, A *SIDE-ON* TRANSITION STATE

The two-dimensional (2D) septuplet of $\text{Fe}_2\text{-N}_2$ was located as a transition state (TS), since its vibrational analysis yields an imaginary frequency. The N-N bonding experiences a bigger perturbation in the TS than in the GS. For example, in the TS the N-N distance (1.16 Å) and the (from Fe_2 to N_2) total charge transfer (0.1 units) are bigger than the corresponding values for the GS. The 2D septuplet may be the starting point that gives rise to $\text{Fe}_2\text{-N}_2$ coordination modes in which the N_2 moiety is more strongly perturbed by Fe_2 . Below, we will show these kind of states.

$\text{Fe}_2\text{-N}_2$, A *QUASI SIDE-ON*, $M = 7$, COORDINATION MODE

As shown above, the side-on mode is unstable. We have found that this type of coordination (in which the N centers are mostly bonding to a single Fe atom) is stabilized by bending the N_2 molecule out of the plane by about 54° . This yields the structure labeled as "*quasi side-on*" in Figure 2. This structure is stable in both septuplet and quintet (which is bent by 63° out of the plane) states (with the septuplet lower in energy), since their vibrational analysis does not produce imaginary values. In the septuplet quasi side-on mode, the R_e and ω_e of N_2 are 1.18 Å and 1902 cm^{-1} , respectively. These values produce ΔR and $\Delta\omega$ shifts of $+0.058\text{ Å}$ and -441 cm^{-1} , respectively. These changes are bigger than those of the linear GS, and they reflect a moderate but important reduction of the N-N bond strength. In fact, in the $M = 7$ quasi side-on structure there is a total charge transfer, from Fe_2 to N_2 , of 0.14 electrons. As expected, most of this charge, 0.13 units, is transferred from the Fe atom that is directly bonded to the N_2

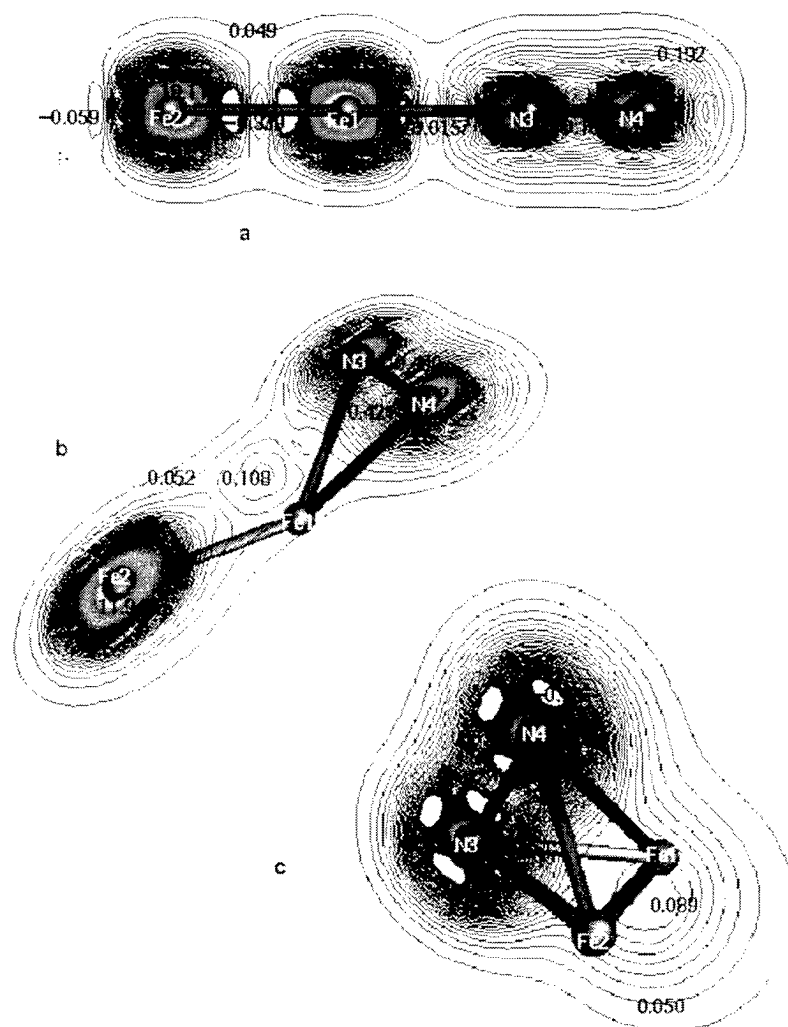


FIGURE 4. Total density contour plots for (a) linear GS, (b) quasi-side on, and (c) tetrahedral coordination modes of $\text{Fe}_2\text{-N}_2$.

moiety. However, we have observed that there is some interaction, presumably of bonding type, among the iron atom (labeled as Fe2) that is far away from N_2 , and the nitrogen centers. This is reflected by the total electronic density contour plot, displayed in Figure 4(b). This kind of interaction could originate the appearance of directional forces that would move the N centers into a position at which they are able to interact more equally, and more effectively, with the two Fe centers. Below, we will address this type of mode.

$\text{Fe}_2\text{-N}_2$. THE TETRAHEDRAL, $M = 7$ AND 5, COORDINATION MODES

A tetrahedral-like approach of N_2 to Fe_2 [see Fig. 1(c)] yields a distorted tetrahedron, as an

stable structure for $\text{Fe}_2\text{-N}_2$ (see Fig. 2). High spin states, $M = 7$ and 5, occur in this geometry. They are quasi-degenerate at LSDA level of theory. But the introduction of GDA corrections puts the quintet at 8.9 kcal/mol above the septuplet. In these states, the two N atoms are equally bonded to both of the two Fe atoms. The Fe-N R_e 's are equal to 1.92 Å (1.87 Å), and the N-N distance is of 1.26 Å (1.28 Å) for the $M = 7$ ($M = 5$) state. This gives, with respect to free N_2 , $\Delta R = 0.14$ Å for $M = 7$, and $\Delta R = 0.17$ Å for $M = 5$. In these tetrahedral modes occurs the biggest enlargements of the N-N bond lengths, which means a substantial weakening of the N-N bond. This is also implied by the huge reductions of the N_2 frequencies (in $\text{Fe}_2\text{-N}_2$). These $\Delta\omega$ changes are, with respect to the free N_2 value (2343 cm^{-1}), -847 and -951 cm^{-1} , for the

TABLE I

Equilibrium bond lengths for the calculated structures of $\text{Fe}_2\text{-N}_2$. ΔR changes of N_2 are also indicated. GDA values are shown in parenthesis.

Structures	M	R_e (Å)			ΔR (N-N)
		N-N	Fe-N	Fe-Fe	
Linear	7	1.137 (1.146)	1.837 (1.929)	2.018 (2.016)	0.019 (0.017)
	5	1.139 (1.147)	1.846 (1.951)	1.853 (1.856)	0.021 (0.018)
Tetrahedral	7	1.256 (1.221)	1.924 (1.87)	2.068 (2.017)	0.138 (0.092)
	5	1.283 (1.301)	1.867 (1.90)	2.041 (2.030)	0.165 (0.172)
Angular	7	1.164 (1.165)	1.966 (2.109)	2.036 (2.023)	0.046 (0.036)
Quasi side-on	7	1.176 (1.167)	1.923 (2.104)	2.024 (2.024)	0.058 (0.038)
	5	1.187 (1.194)	1.868 (1.930)	1.916 (1.928)	0.069 (0.065)
Planar	7	1.227 (1.239)	1.810 (1.852)	2.108 (2.102)	0.109 (0.110)
	5	1.251 (1.267)	1.727 (1.756)	2.108 (2.059)	0.133 (138)
Calculated at LSDA ^a		1.118 (1.129)			0.020 (0.031)
Experimental ^b		1.098			

^a For free N_2 .

^b For free N_2 ; from Refs. 5 and 17.

$M = 7$ and 5 states, respectively. In fact, the N-N bond strength (in $\text{Fe}_2\text{-N}_2$) is 1.5, which is a much weaker bond than the triple bond of free N_2 . Also, there are large total charge transfers from Fe_2 to N_2 : They are equal to 0.44 and 0.52 electrons for the $M = 7$ and 5 states, respectively. These transferred electrons go into high-energy antibonding molecular orbitals of N_2 . The density contour plots, for the $M = 7$ tetrahedral state [see Fig. 4(c)], reveal that the electronic charge is highly polarized toward the N atoms. In fact, this picture implies

that, in this septuplet coordination mode, the N_2 moiety is strongly perturbed or truly activated by the Fe atoms. This activation is slightly bigger in the quintet state, which is higher in energy than the septuplet one. It is to be remarked that the biggest structural changes (experienced by N_2) are coupled with huge total charge transfers (from Fe_2 to N_2). In fact, this occurs in the quintet tetrahedral state, and to a lesser extent in the septuplet one. However, at GDA level of theory, the D_e for the septuplet is very small, about 0.3 kcal/mol,

TABLE II

Vibrational frequencies, ω_e , for the calculated $\text{Fe}_2\text{-N}_2$ structures.

Structures	M	ω_e (cm^{-1})			$\Delta \omega$
		N-N	Fe-N	Fe-Fe	
Linear	7	2148 (2071)	450 (387)	332 (332)	-195 (-179)
	5	2136	368	491	-207
Tetrahedral	7	1496	515, 431	438	-847
	5	1392	601, 626	373	-951
Angular	7	(1934)	(208, 322)	(415)	(-316)
Quasi side-on	7	1902	369, 434	379	-441
	5	1837	492, 502	423	-506
Planar	7	1589	499, 579	328	-754
	5	1455	336, 635	373	-888
Calculated at LSDA ^a		2343 (2250)			-16 (-109)
Experimental ^b		2359			

^a For free N_2 .

^b For free N_2 ; from Refs. 5 and 17.

TABLE III

Eigenvalues and occupation numbers, per atom and per angular momentum component, for the valence electrons of the ground state of $\text{Fe}_2\text{-N}_2$.

Orb.	n_i	ϵ_i	Fe1			Fe2			N3		N4	
			s	p	d	s	p	d	s	p	s	p
α												
1 σ	1	-28.009	—	—	—	0.01	-0.02	—	0.37	0.06	0.46	0.13
2 σ	1	-15.212	—	—	—	0.03	0.02	0.03	0.42	0.25	0.24	0.02
1 π	2	-11.763	—	—	—	—	—	0.01	—	0.54	—	0.43
3 σ	1	-11.232	—	—	0.01	0.04	0.03	0.03	0.02	0.21	0.22	0.44
2 π	2	-7.213	—	—	0.57	—	—	0.41	—	—	—	0.02
4 σ	1	-7.175	—	—	0.64	—	0.04	0.30	0.01	0.01	—	0.01
1 δ	2	-6.742	—	—	0.77	—	—	0.23	—	—	—	—
2 δ	2	-6.146	—	—	0.23	—	—	0.77	—	—	—	—
5 σ	1	-5.802	0.64	—	-0.02	0.32	0.03	0.04	—	—	—	—
3 π	2	-5.392	—	0.01	0.40	—	0.02	0.47	—	0.03	—	0.07
6 σ	1	-5.049	0.14	—	0.31	0.07	0.02	0.47	—	-0.01	—	—
4 π	0	-2.995	—	0.06	0.02	—	0.10	0.08	—	0.35	—	0.39
β												
1 σ	1	-27.966	—	—	—	0.01	-0.02	—	0.38	0.06	0.46	0.13
2 σ	1	-15.157	—	—	—	0.03	0.02	0.02	0.42	0.27	0.24	0.02
1 π	2	-11.667	—	—	—	—	—	0.01	—	0.55	—	0.42
3 σ	1	-11.120	—	—	0.01	0.04	0.03	0.03	0.02	0.21	0.22	0.44
4 σ	1	-5.573	0.33	—	0.26	0.10	0.13	0.14	0.01	0.02	—	0.01
2 π	2	-5.370	—	0.01	0.39	—	0.01	0.54	—	0.01	—	0.04
5 σ	1	-5.017	0.25	0.01	0.23	0.22	-0.01	0.31	—	-0.01	—	—
1 δ	1	-4.233	—	—	0.47	—	—	0.53	—	—	—	—
2 δ	0	-3.703	—	—	0.38	—	0.06	0.12	—	0.18	—	0.18
σ -donation		0.325										
π -back-donation		0.314										

while there is no positive D_e for the quintet state (it is about -8.6 kcal/mol). The enlargement of the cluster or improvement of the model (i.e., the use of Fe_2S_2 or FeMoS_2) in order to obtain a better description of the active site may enhance the stabilization of these types of coordination modes. We are searching currently these possibilities; results will be reported elsewhere.

$\text{Fe}_2\text{-N}_2$, THE PLANAR, $M=5$ AND 7, COORDINATION MODES

A parallel approach of N_2 to Fe_2 produces two planar coordination modes of $\text{Fe}_2\text{-N}_2$ with $M=5$ and 7. These two states differ by only ≈ 2 kcal/mol; see Figure 2. The two N atoms in these planar modes are equally bonded to the two Fe

TABLE IV

Mulliken populations for the lowest energy states of $\text{Fe}_2\text{-N}_2$. The dipole moment, μ , is also indicated.

Atom	Linear	Tetrahedral		Quasi side-on	
	$M=7$	$M=7$	$M=5$	$M=7$	$M=5$
Fe1	26.00 (26.03)	25.77 (25.79)	25.74 (25.72)	25.87 (25.90)	25.89 (25.86)
Fe2	25.95 (25.93)	25.78 (25.87)	25.74 (25.73)	25.99 (26.01)	25.95 (25.97)
N3	7.03 (7.02)	7.22 (7.16)	7.26 (7.28)	7.07 (7.05)	7.08 (7.09)
N4	7.02 (7.01)	7.22 (7.19)	7.26 (7.28)	7.07 (7.05)	7.08 (7.09)
μ	1.058 (0.605)	1.105 (1.104)	3.379	1.561 (0.992)	2.005 (1.823)

TABLE V
Binding energies, D_e for the computed states
of $\text{Fe}_2\text{-N}_2$.

$\text{Fe}_2\text{-N}_2$	M	D_e (kcal/mol)	
		LSDA	GDA
Linear	7	30.258	14.627
	5	14.577	-2.541
Tetrahedral	7	26.274	0.311
	5	25.673	8.566
Angular	7	22.659	11.918
Quasi side-on	7	24.962	12.088
	5	21.146	1.972
Planar	7	18.104	-4.486
	5	27.661	-2.234

centers. The N-N distance is of 1.25 Å (1.23 Å) for the $M = 5$ ($M = 7$) state. This gives (with respect to free N_2) enlargements of 0.13 Å for $M = 5$ and of 0.11 Å for $M = 7$, for the N-N R_e . There are also big reductions (888 cm^{-1} for $M = 5$ and 754 cm^{-1} for $M = 7$) for the ω value of N_2 . Consistently, there are large total charge transfers, from Fe_2 to N_2 ; they are 0.40 and 0.38 electrons for the $M = 5$ and 7 states, respectively. These changes of N_2 are relatively big (particularly those for $M = 5$), but smaller than those observed in the tetrahedral modes, and implies a substantial reduction of the N-N bond.

Conclusions

A systematic study of the $\text{Fe}_2\text{-N}_2$ coordination modes was done by means of the program deMon-KS, a DFT-based method. The calculated ground state corresponds to a linear geometry, with $M = 7$, in which the metal-ligand binding energy reaches its highest value, and where N_2 shows a relatively small perturbation by the Fe atoms. A highest activation of N_2 occurs in the tetrahedral $\text{Fe}_2\text{-N}_2$ geometry, which is stable in both quintet and septuplet high spin states. Indeed, the bond length and vibrational frequency of N_2 are considerably enlarged and reduced, respectively, in these tetrahedra modes. These changes indicates that N_2 is truly activated in this type of geometries, where the two N atoms interact equally with the two Fe centers. These results suggest a strong correlation between the electronic charge transfer (from the metal to the moiety) and the activation experienced by N_2 (measured by the extent of its struc-

tural changes). Big structural changes of N_2 were also observed in the planar coordination modes, although to a lesser extent than those in the tetrahedrals.

Going to a bigger cluster, in order to achieve an improvement in the description of the active site, our preliminary results of $\text{Fe}_2\text{S}_2\text{-N}_2$ indicates that the sulfur atoms further enhance the activation experienced by N_2 . Studies to determine the role played by both sulfur and molybdenum atoms in the catalytic process are in progress in our laboratory; results will be published elsewhere [18].

ACKNOWLEDGMENTS

We are indebted with Prof. Dennis R. Salahub for allowing us the use of the program deMon-KS. Financial support both from Cray Inc., under project SC-002295, and from DGAPA-UNAM, under project IN-101295, are greatly appreciated as is the access to the supercomputer Cray YMP4/464 at DGSCA-UNAM.

References

- (a) J. Kim and D. C. Rees, *Biochemistry* **33**, 389 (1994). (b) R. R. Eady and G. J. Leigh, *J. Chem. Soc., Dalton Trans.* 2739 (1994). (c) J. Chatt, G. J. Leigh, and R. L. Richards, *J. Chem. Soc. (A)* 2243 (1970). (d) P. Sobota and B. Jezowska-Trzebiatowska, *J. Organomet. Chem.* **131**, 341, (1977). (e) S. Sakaki, K. Morokuma, and K. Ohkubo, *J. Am. Chem. Soc.* **107**, 2686 (1985). (f) R. A. Henderson, J. R. Dilworth, A. Hills, D. L. Hughes, C. Macdonald, A. N. Stephens, and D. R. M. Walton, *J. Chem. Soc., Dalton Trans.* 1077 (1990). (g) P. S. Wagenknecht and J. R. Norton, *J. Am. Chem. Soc.* **117**, 1841 (1995). (h) D. Cruz-Garritz, G. Domenzain, and H. Torrens, *Rev. Soc. Quim. Mex.* **30** 11 (1986), and reference therein.
- D. R. Salahub and N. Russo, Ed., *Metal-Ligand Interactions: From Atoms, to Clusters, to Surfaces*, NATO-ASI (Kluwer Academic, Dordrecht, 1992).
- M. Castro, D. R. Salahub, and R. Fournier, *J. Chem. Phys.* **100**, 8233 (1994), and references therein.
- S. Sirois, M. Castro, and D. R. Salahub, *Int. J. Quantum Chem.: Q. Chem. Symp.* **28**, 645 (1994).
- C. W. Bauschlicher, Jr., and L. M. Pettersson, *J. Chem. Phys.* **87**, 2129 (1987), and references therein.
- A. Zacarias, H. Torrens, and M. Castro, *Int. J. Quantum Chem.*, to appear.
- (a) A. St-Amant and D. R. Salahub, *Chem. Phys. Lett.* **169**, 387 (1990). (b) D. R. Salahub, R. Fournier, P. Mlynarsky, I. Papai, A. St-Amant, and J. Ushio, in *Density Functional Methods in Chemistry*, J. Labanowski and J. Andzelm, Eds. (Springer, New York, 1991).
- S. H. Vosko, L. Wilks, and M. Nusair, *Can. J. Phys.* **58**, 1200 (1980).
- J. P. Perdew and Y. Wang, *Phys. Rev. B* **33**, 8800 (1986).

10. J. P. Perdew, Phys. Rev. B **33**, 8822 (1986); Phys. Rev. B **34**, 7406E (1986).
11. N. Godbout, D. R. Salahub, J. Andzelm, and E. Wimmer, Can. J. Chem. **70**, 60 (1992).
12. deMon User's Guide, version 1.0 beta (Biosym Technologies, San Diego, 1992).
13. See, H. B. Schlegel, in *Ab Initio Methods in Quantum Chemistry I*, K. P. Lawley, Ed. (Wiley, New York, 1987).
14. Unichem is a commercial computational package available from Cray Research. For details see: D. A. Dixon, G. Fitzgerald, and T. Raeuchle, in *Data Visualization in Molecular Science*, J. E. Bowie, Ed. (Addison-Wesley, New York, 1995).
15. J. Andzelm, in *Density Functional Methods in Chemistry*, J. Labanowski and J. W. Andzelm, Eds. (Springer Verlag, New York, 1991).
16. I. Mayer, J. Mol. Struct. (Theochem) **149**, 81 (1987).
17. K. P. Huber and G. Herzberg, *Molecular Spectra and Molecular Structure* (Van Nostrand Reinhold, New York, 1979).
18. A. Zacarias, F. Bohr, and M. Castro, in preparation.

Electronic Structure and Properties of MCO and M₅CO Carbonyls (M = Fe, Ni, Cu) by Density Functional Methods

RAMON M. SOSA*

Institute of Physics, Faculty of Engineering, Avda. J. Herrera y Reissig 565, Montevideo 11300, Uruguay; e-mail: crsosa@fing.edu.uy

PATRICIA GARDIOL

Institute of Physics, Faculty of Sciences, Tristan Narvaja 1674, Montevideo 10773, Uruguay

Received February 25, 1996; revised manuscript received July 17, 1996; accepted July 18, 1996

ABSTRACT

Density functional theory (DFT) calculations of the electronic structure and properties of Fe, Ni, and Cu carbonyls with one and five transition-element atoms are reported, due to their importance in heterogeneous catalysis (especially in Fischer-Tropsch synthesis). The local density approximation (LDA) with the Vosko-Wilk-Nussain (VWN) correlation functional as well as the generalized gradient approximation (GGA) using Becke's 1988 exchange functional and Perdew's 1986 correlation functional (BP method) were applied to the study of the clusters using a triple-zeta plus polarization (TZP) basis set. Triplet and quintuplet states for FeCO, singlet and triplet for NiCO, and doublet for CuCO were considered, and optimization of energy at the LDA/BP level for these cases was done. Dissociation energies in M and CO fragments, frequencies, and population analysis were performed. Geometry optimization of the distance between the C atom and the clusters M₅ (with geometries taken from the crystals) were carried out and the dissociation energy in fragments M₅ and CO as well as population analysis at the optimized geometries were also done. Comparison between our results and some others published using ab initio and density functional methods were performed. © 1996 John Wiley & Sons, Inc.

*To whom correspondence should be addressed.

Introduction

Carbonyls of transition elements are a very important class of compounds for several reasons. One of these is that they are considered to be the first step in the reaction of CO with H₂ catalyzed by transition elements (Fischer–Tropsch synthesis) which, from the industrial point of view, is of paramount importance due to the large number of chemicals that can be obtained from it. The initial step of the chain of reactions is the chemisorption of CO on materials which contain such elements. The simplest model for these materials is one atom. That is where the importance of the MCO compounds comes from. There are many experimental and theoretical studies of these carbonyls, and our theoretical study uses one of the important methodologies: the density functional theory (DFT) in one of the successful versions developed at present.

As a further step it is natural to consider, as suitable models for real materials, clusters or crystals of the elements involved and to use the appropriate computational techniques.

In order to compare the results of the MCO and M_{*n*}CO calculations (*n* = 2, 3, ...), we must use the same computational level in both cases, and, therefore the cluster size must not be too large. These calculations must provide accurate predictions at least for the equilibrium molecular geometries, dissociation energies, and vibrational frequencies. For this reason we have studied, besides the MCO, the M₅CO compounds with symmetry C_{4v} that involve transition-atom clusters with geometries taken from the crystal. Models with fewer or larger number of atoms are scarce in the current literature [1–3].

The transition elements considered in this report Cu, Ni, and Fe, are important in the Fischer–Tropsch synthesis and present quite different difficulties. The Cu case is the simplest because of its electronic structure as compared to Ni and Fe.

Important points in our study are the prediction of the place where the CO will be preferentially adsorbed, the geometry of the adsorbate–substrate and the energy involved in such adsorption.

We will focus our interest in the geometrical and energetical aspects of the systems under consideration rather than in the bonding of the car-

bonyls that are extensively considered in the literature.

Method

The calculations reported in this work are based on the Kohn–Sham approach to the DFT with the methodology of Baerends and co-workers [4, 5].

The density functional, also called the exchange-and-correlation (XC) functional, consists of a local part [local density approximation (LDA)] and a so-called gradient correction [generalized gradient approximation (GGA)]. Initially, the LDA used by the calculation of the exchange energy Ex(LDA) was that proposed by Slater [6] (X α approximation); version that includes also a correlation part, which is used in this report, is that proposed by Vosko, Wilk, and Nusair (VWN) [7].

The GGA introduces terms depending on the gradient of the electron density that account for inhomogeneity in order to describe the nonuniform electron gas in the case of atomic systems. GGA is the sum of two terms: the exchange and the correlation ones. The introduction of these terms, correcting LDA, usually gives better results for comparison with experimental data for molecular geometries, bond energies, etc.

We have several possibilities using the ADF program for the GGA calculations. The one used in this report is the Becke's calculation [8] for the exchange term and the Perdew's [9] for the correlation. The method is called LDA/BP.

Slater orbitals (STO) basis set for the molecular orbital (MO) expansion linear combination of atomic orbitals (LCAO) method were used. For the transition elements an uncontracted triple zeta (three 3*d* and three 4*s*) and one 4*p* were used as the valence basis set and 2*s* and 1*p* for the frozen core shell (FC). In order to establish the orthogonality of the valence MO, with the FC, it is necessary to add *s* and *p* orbitals to the valence set. We add 4*s* and 3*p* and we have in this way 14 STO for the valence set.

For the main elements (C and O) we set up also a triple zeta basis set with 3*s* and 3*p* and one polarization *d* STO; we add also 1*s* to have the valence orbitals orthogonal to the FC 1*s*. We have, therefore, 8 STO for the valence basis set.

We can consider the molecular symmetry in order to have the overlap and Fock matrices block-diagonal by using symmetry-adapted linear combinations of the above mentioned STO.

A set of auxiliary *s*, *p*, *d*, *f*, and *g* STO centered on each nucleus were used to fit the electronic density. For each transition metal atom 34 STO were used and for C and O 20 STO were used. In this way integrals involving electronic density (such as Coulomb potentials) were evaluated using these auxiliary functions and then taking linear combination of these integrals. The coefficients of these linear combinations were evaluated in each SCF cycle.

The matrix elements of the overlap and Fock matrices were calculated by numerical integration. The success of the DFT methods such as the ADF is due, among other reasons, to the existence of accurate and very efficient numerical methods for the calculation of integrals using STO functions [10].

Instead of calculating total energies, as most methods do, ADF calculates bond energies according to Ziegler's procedure [11]. These bond energies are the difference between the total energy of a molecule (or atom) and those of the atoms (or fragments) in established reference states.

Optimization of the geometry at the LDA/BP level was done for all the geometrical parameters in the case of the MCO compounds: triplet and quintuplet for FeCO, singlet and triplet for NiCO, and doublet for CuCO.

Mulliken population analysis was carried out and the intermolecular charge distribution and related dipole moment as well as the vibrational frequencies were calculated for each molecule.

We have several possibilities for the M₅ clusters in the case of M₅CO compounds. Ni and Cu crystals have fcc (face-centered cubic) elementary cells and the Fe has a bcc (body-centered cubic) one.

In the first two cases we have selected two cluster models, one that we call "planar" and symbolized by (5, 0) that has the five atoms on the top face. The other that is called "hollow" and symbolized by (4, 1) has the four center atoms of the lateral cubic faces and one atom located at the center of the bottom face (see Figs. 1 and 2). We have used the nomenclature given in [2].

In the case of Fe₅ we have selected the hollow (4, 1) model, taking the four Fe atoms of the square top face and the central cubic Fe atom.

The CO group was oriented normal to the M₄ plane and passing through its center. In one calculation (CuCO) we have tilted the CO group, to take into account the nonlinearity of the CuCO molecule, and the CuCO plane was taken parallel

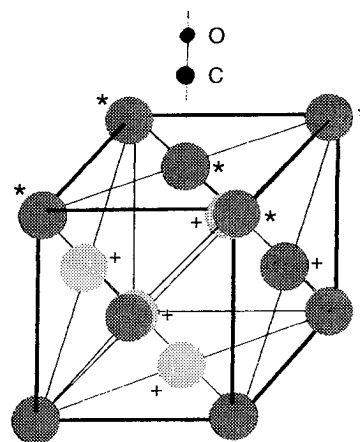


FIGURE 1.

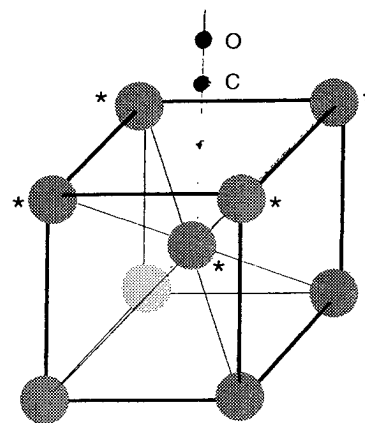


FIGURE 2.

to one side of the M₄ square, but the results obtained do not change significant.

Optimization of the distance *d* between the C atom and the M₄ plane, with the CO distance unchanged at the value optimized in the MCO calculation, was the first step of the calculation. This was done at the selected electronic configuration with the lowest energy.

All calculations were done at the unrestricted level, giving initially the total number of alpha and beta spin electrons. We checked the electronic configuration after the self-consistent field (SCF) convergence to see if the lowest unoccupied molecular orbital (LUMO) is lower in energy than the highest occupied molecular orbital (HOMO) both for alpha and beta spin.

If this was not satisfied, we changed the configuration accordingly (making sure that the energy decreased) until we got the lowest value.

We have the very cumbersome problem of the oscillation in energy when working with transition elements, where occupied and empty orbital levels are very close in energy. This is particularly difficult in the case of the M_5 clusters for Ni and Fe cases. The level shift technique of Saunders and Hillier in many cases solves the problem.

Two procedures were used to obtain the sum-of-fragments energy (E_{sof}): one was to increase the M-C distance until a constant value of the energy was reached (asymptotic energy) and the other was to calculate directly the energies of the fragments M (or M_5) and CO.

Results and Discussion

MCO (M = Fe, Ni, Cu) CASE

Molecular Geometries

Optimized geometries, as well as bond and dissociation energies and electronic configurations are summarized in Table I.

All calculations reported were done at the LDA/BP level. It is well known [12] that the predictions for molecular geometries are improved when the BP corrections are included in the LDA methodology, resulting in values very close to the experimental ones. In general, DFT methods are in many cases far superior to Hartree-Fock (HF) ones, in particular for metal-ligand bond lengths.

For CuCO a linear geometry was supposed [13], but the bond energy between Cu and CO was almost null. Optimization of the energy without this restriction gives a nonlinear geometry, as was pointed out by Fournier [14], with a significantly higher bond energy. His calculation method is

very similar to the ADF that we are using in this report.

Our results (Table I) were similar to the ones from [14] (1.858/1.160/142.8), where the symbol ($d/d'/a$) means $d = d(\text{MC})$, $d' = d(\text{CO})$, and $a = \text{angle}(\text{M-C-O})$.

Summarizing the results we have:

(1.906/1.160/136.7)	Table I
(1.858/1.160/142.8)	[14]
(1.963/1.132/153.1)	[15]

The result from [15] is the most exact of the several reported there.

The ground state was $2A'$ with the electronic configuration (11 4/10 4) in the symmetry group C_s where the symbol means 11 electrons in a' and 4 in a'' orbitals for alpha spin and 10 electrons in a' and 4 in a'' orbitals for beta spin.

For NiCO we have considered the two lowest energy states: the ground state whose geometry is linear and is a singlet (1Σ) with the configuration (6 6 2/6 6 2) (6 electrons in σ orbitals, 6 in π orbitals, and 2 in δ orbitals both for alpha and beta spin), and the first electronic excited state is a triplet with a bent geometry with the configuration (11 4/9 4).

Many calculations for NiCO have been reported in the literature. Among others, we consider those of references [14] and [16] (DFT) ([14] at the LDA level and [16] at the LDA/BP level), [13] (ab initio CASSCF), [17] (ab initio MRSDCI-CIPSI) in order to compare with those of Table I.

A general review about ab initio calculations of structure and molecular properties of transition-metal organometallics is given in [18].

TABLE I
Molecular geometries, bond and dissociation energies, and electronic configurations of the MCO compounds.

Molecule / state	Molecular geometry			Bond energy	Dissociation energy ^a	Electronic configuration
	$d(\text{MC})(\text{\AA})$	$d(\text{CO})(\text{\AA})$	$\angle \text{MCO} (\text{deg})$	$E (\text{a.u.})$	$D_e (\text{kcal/mol})$	
CuCO($2A'$)	1.9057	1.1600	136.7	-0.575237	16.05 (16.03)	(11 4/10 4)
NiCO(1Σ)	1.6614	1.1692	180.0	-0.660224	63.93 (62.84)	(6 6 2/6 6 2)
NiCO($3A'$)	1.8575	1.1633	143.2	-0.605832	31.10 (28.25)	(11 4/9 4)
FeCO(3Σ)	1.6972	1.1731	180.0	-0.753607	58.74 (55.34)	(6 6 2/6 6 0)
FeCO($5A''$)	1.8626	1.1656	164.6	-0.741648	35.70 (40.34)	(11 4/8 3)

^a Parentheses values calculated from E_{sof} .

For the linear NiCO(1Σ) we have:

(1.661/1.169)	Table I
(1.663/1.715)	[16]
(1.637/1.167)	[14]
(1.693/1.164)	[13]

For the bent NiCO(3A'):

(1.876/1.163/143.2)	Table I
(1.788/1.162/147.5)	[14]

As we can see from these results, the general agreement is rather good. It must be pointed out that our calculations are all at the LDA/BP level and that without the BP corrections the metal-ligand bond lengths are underestimated by an average of 0.05 Å, and the BP corrections reduce the error to an average of 0.01 Å [12]. Bond angles, in general, are not influenced significantly by these corrections.

We observe from our results an increase of 0.22 Å for the Ni-C and a reduction of 0.006 Å for the d(C-O) distances as well as a change in the bond angle Ni-C-O from 180° to 143° when we go from the ground to the first excited state.

In the case of FeCO we have a linear triplet 3Σ ground state and a bent quintuplet 5A'' first excited state. A comparison between reported geometries and ours is given below.

FeCO(3Σ):

(1.697/1.173)	Table I
(1.660/1.175)	[14]
(1.809/1.190)	[17]
(2.039/1.256)	[19]

FeCO(5A''):

(1.863/1.166/164.6)	Table I
(1.808/1.160/158.1)	[14]
(1.900/1.201/180)	[17]

The agreement between [14] and ours is rather good (taking into account the above-mentioned calculated levels). The bond distances of [17] are a little bit higher and, furthermore, the geometry of the excited state was, apparently, taken to be linear.

Dissociation Energies

Bond energies for the MCO compounds are given in Table I for the above-mentioned states at the equilibrium geometry.

The asymptotic energy was obtained at approximately 4.0 Å where we can consider the molecule dissociated into the M and CO fragments. The identification of the state of these fragments is interesting. This is done by calculating the energies of selected states of these fragments that reproduce these constant energies (that we call asymptotic energies).

Starting with CuCO we have an asymptotic (bond) energy of -0.54968 a.u. For the fragments we have $E\{\text{Cu}(s1d9)\} = -0.00941$ a.u. (it is not zero because this is not the reference state chosen for the Cu atom) and $E\{\text{CO}(1.1600)\} = -0.539719$ a.u., and their sum is -0.54966 a.u., in very good agreement with the asymptotic energy. The difference between the minimum reported in Table I and the asymptotic energy is 16.05 kcal/mol (1 a.u. = 627.5 kcal/mol). The analog if using E_{sof} is 16.03 kcal/mol.

In this way we identify the state of the products as Cu(s1d9) and CO(1Σ) (the ground state for CO). The experimental value reported in [17] is 16.6 kcal/mol, in very close agreement with ours. Reported values are 20.3 (19.6) kcal/mol in [16], 19.4 kcal/mol in [17] (but the linear geometry was considered here). A value of 22.72 kcal/mol was quoted in [12] where the ADF method was used (but in [1] in which an earlier version of the ADF method was used a value of 12 kcal/mol was given). However, only in [16] and ours, a bent geometry was assumed.

In the case of NiCO, we consider the singlet ground state 1Σ with a configuration (6 6 2/6 6 2) and the corresponding asymptotic energy is -0.55853 a.u. In this case, the SCF convergence is difficult to reach, and it was necessary to introduce a level shift of 0.1 a.u. So we have perhaps, an error in this value. The E_{sof} of the fragments Ni and CO that fits better this value is the one corresponding to Ni(s1d9) with a bond energy (with respect to the reference state) of -0.021245 a.u. that added to -0.538842 a.u. corresponding to CO(1.1692 Å) gives -0.560087 a.u., in relative good agreement with the asymptotic energy. With the equilibrium value of Table I and the sum of fragments we have 62.84 kcal/mol.

This is quite a high value compared with those reported in the literature. However, a higher value

of 79.0 kcal/mol by a DFT method was reported in [20]. In [16] a value of 54.5 kcal/mol is given, but as a result of the most accurate calculations and experiments a value of about 40 kcal/mol seems to be quite acceptable. For example, a Coupled Cluster Singles, Doubles (Triples) (CCSD(T)) calculation with a large basis gives a value of 38.0 kcal/mol [21].

The lowest excited triplet state is 33.8 kcal/mol above the ground state (36 kcal/mol according to [16]). As we said, the equilibrium geometry is bent (symmetry Cs). The electronic configuration is (11 4/9 4) and the asymptotic energy is -0.556276 a.u. The values of E_{sof} are -0.560799 a.u. if we adopt for CO (C–O distance equal to 1.1633 Å) the value -0.539554 a.u. and for Ni(*s1d9*) the value -0.009941 a.u. and -0.572375 a.u. if consider instead the Ni(*s2d8*) state, whose energy is -0.032821 a.u. The asymptotic energy is closest to the first value, so we can identify the dissociated state of the Ni atom as the *s1d9* one.

With the asymptotic value the dissociation energy is 31.10 kcal/mol, but if we consider the E_{sof} ones, this result moves to 28.25 kcal/mol for Ni(*s1d9*) and 21.00 kcal/mol for Ni(*s2d8*). These values are compared with 18 kcal/mol found in [14]. In [13] the geometry considered for this excited state is a linear one.

Let us consider now the states of FeCO. The ground state is a linear triplet (3Σ) with an asymptotic energy of -0.6600 a.u. and its configuration is (6 6 2/6 6 0).

The states of the fragments Fe and CO that give the best fit for this value are CO($1\Sigma +$; 1.1731) with a bond energy of -0.538511 a.u. and Fe(*s1d7*) quintuplet with a bond energy of -0.104308 a.u. The E_{sof} value is, therefore, -0.665422 a.u. giving a dissociation energy of 55.34 kcal/mol. If we use

instead the asymptotic energy, it changes to 58.74 kcal/mol.

Reported values for this energy are 49(33) kcal/mol [14], 30.9 kcal/mol [17] (experimental values between 25.1 and 36.9 are reported here), and 28.6 kcal/mol [13].

Our calculated value is about 18 kcal/mol higher relative to the average value of 40 kcal/mol. This is surprising because DFT methods are considered to yield results at a very good level of accuracy when the BP corrections are made (at the LDA level, however, errors of about 100% are common) [12].

Something similar happens in the case of NiCO ground state, whose corresponding difference is about 23 kcal/mol.

The first electronic excited state for FeCO is the bent quintuplet FeCO($5A''$) with the configuration (11 4/8 3), 7.50 kcal/mol above the ground state. The asymptotic energy is -0.684752 a.u. when we specify 15 and 11 as the total number of alpha and beta electrons, respectively, and consider the geometry at $d(\text{Fe-C}) = 5.0$ Å as linear. The CO ground-state energy is -0.539340 a.u. If we adopt the *s1d7* quintet state for Fe, the sum of the fragments energy is -0.666251 a.u. On the other hand, if we choose the *s2d6* quintet state for Fe, we get a value of -0.677357 a.u. The asymptotic energy is closer to the last value, whence we can correlate the dissociated state of Fe with the quintet *s2d6*. We have, consequently, the value 40.34 kcal/mol for the dissociation energy using the E_{sof} value and 35.70 kcal/mol using the asymptotic energy.

Reported values are: 31 kcal/mol in [14], 13.4 kcal/mol in [17], and 22.6 and 18.5 kcal/mol in [13]; the last value was obtained at higher computational level than the previous 22.6 kcal/mol. In

TABLE II
Atomic charges and dipole moments for the MCO compounds.

Molecule / state	Atomic charges						Dipole moment (D)
	M(s)	M(p)	M(d)	M	C	O	
CuCO(2)	0.1011	-0.2214	0.2235	0.1032	0.2064	-0.3096	0.7014
NiCO(1)	0.3042	-0.0566	-0.1100	0.1376	0.2404	-0.3780	3.5023
NiCO(3)	0.0461	-0.2581	0.3251	0.1132	0.2136	-0.3268	0.9997
FeCO(3)	0.0304	-0.0655	0.2290	0.1939	0.1866	-0.3805	3.2350
FeCO(5)	0.1407	-0.3826	0.4315	0.1896	0.1488	-0.3384	0.7694

the two last references the FeCO molecule was supposed to be linear.

Atomic Charges and Dipole Moments

We consider in this report the Mulliken's population analysis as the method of choice for obtaining the charge distribution in the molecule. In order to understand the data that are displayed in Tables II, III, and IV we consider the case of the CuCO molecule at the equilibrium geometry.

The Elementary Atomic Basis Functions (BAS) population is given for the orbitals *s*, *p* and *d*, in this order, for Cu, C, and O and for alpha and beta spin:

Alpha spin			Beta spin		
Cu	<i>s</i>	1.7301	Cu	<i>s</i>	1.1688
	<i>p</i>	3.1669		<i>p</i>	3.0545
	<i>d</i>	4.8968		<i>d</i>	4.8797
C	<i>s</i>	0.7750	C	<i>s</i>	0.7279
	<i>p</i>	1.2042		<i>p</i>	0.9994
	<i>d</i>	0.0445		<i>d</i>	0.0427
O	<i>s</i>	0.9364	O	<i>s</i>	0.9362
	<i>p</i>	2.2171		<i>p</i>	2.1613
	<i>d</i>	0.0291		<i>d</i>	0.0295

The differences between the corresponding numbers are the spin polarization that are shown in Table IV for the metal (Cu in our case). The

TABLE III
Spin densities on the metal atom for MCO compounds.

Molecule / state	d(s)	d(p)	d(d)
CuCO(2)	0.5613	0.1124	-0.0171
NiCO(3)	0.5581	0.1440	1.0537
FeCO(3)	-0.2202	-0.0133	2.4964
FeCO(5)	0.7241	0.2590	3.1361

TABLE IV
Overlap populations C-M for the MCO compounds.

Molecule / state	Alfa	Beta	Total
CuCO(2)	0.1293	0.1447	0.2740
NiCO(1)	0.2076	0.2076	0.4152
NiCO(3)	0.1439	0.1789	0.3228
FeCO(3)	0.1877	0.2124	0.4001
FeCO(5)	0.1674	0.2032	0.3706

corresponding sums for Cu are 2.8989 for *s* orbitals, 6.2214 for *p*, and 9.7765 for *d*, and they give the total (alpha + beta spin) population as the valence contribution. If we adopt the valence configuration: (3*s*)²(3*p*)⁶(4*s*)¹(3*d*)¹⁰, then we have 3*s*,6*p*,10*d* electrons that give us the net electronic charge 0.1011 for *s* orbitals, -0.2214 for *p*, and 0.2235 for *d*. These are the values in Table II labeled as M(*s*)M(*p*)M(*d*). The sum of these three numbers gives the value 0.1032 labeled M in Table II.

This number can also be obtained from the total alpha + beta population for Cu that amounts, in our case, to 18.8968. For Cu (atomic number 29) we have 10 core electrons and, therefore, 19 valence electrons. The net charge for Cu is, therefore, 0.1032. Similarly, we can obtain 0.2064 and -0.3096 as the net charges for C and O, respectively.

In Table II we also report the dipole moment (in Debye), and it is interesting to compare some dipole moments reported in the literature with ours.

This comparison give the results:

CuCO(2):

0.7014 D	Table II
0.64 D	[16] (0.68 D at LDA level)
3.49 D	[17] (linear geometry)
3.74 D (2.74 D)	[13] (linear geometry)

NiCO(1):

3.5023 D	Table II
3.42 D	[16]
3.18 D (4.55 D)	[13]

NiCO(3):

0.9997 D	Table II
2.69 D (1.63 D)	[13]

FeCO(3):

3.2350 D	Table II
1.38 D	[17]
2.18 D	[19]

FeCO(5):

0.7694 D	Table II
1.55 D	[17]
0.762 D (1.85 D)	[13]

As we can see from these results, the agreement with DFT calculations of [16] is quite good, but the other calculation gives results coincident with ours only in a few cases.

Overlap Populations

We consider only the overlap populations between the C and the M atoms, which are a measure of the C–O bond strength. We expect to find, therefore, a relationship between this population and the dissociation energy of the CO group. From the data of Tables I, III, IV we have, taken in increasing order the overlap populations:

CuCO	(0.2740, 16.03)	(overlap population and dissociation energy, in parentheses, respectively)
NiCO(3)	(0.3228, 28.25)	
FeCO(5)	(0.3706, 40.34)	
FeCO(3)	(0.4001, 55.34)	
NiCO(1)	(0.4152, 62.84)	

This relationship can be graphed and the corresponding curve is quite smooth. CuCO gives the lowest overlap population and NiCO(1) the highest.

Vibrational Frequencies

Vibrational frequencies (in cm^{-1}) for the MCO molecules are displayed in Table V as well as intensities (in parentheses) in km/mol . We compare these values with those reported in the literature. The three values considered are: f_1 for the bending M–C–O mode, f_2 for the stretching of the M–C bond, and the highest f_3 corresponding to the stretching of the C–O bond.

Comparison with vibrational frequencies reported in the literature give the results:

CuCO(2):

231(13)	386(7)	1951(848)	Table V
237(23)	439(6)	1978(906)	[16]
—	363	2075	[15]
—	320	2010	(experimental value quoted in [17])

243(18) 517(7) 2026(861) [14] (here an experimental value of 2042 for f_3 is quoted).

NiCO(1) (we have a great deal of calculations to compare with from which we have made the following selection):

342(10)	617(0.2)	2005(530)	Table V
311(12)	614(2)	2019(565)	[16] (an experimental value of 2028 for f_3 is quoted)
324(11)	646(2)	2076(524)	[14]
—	—	2010–2074	[19]

NiCO(3):

243(20)	460(9)	1939(861)	Table IV
265(25)	551(10)	2017(871)	[14]

FeCO(3):

357(5)	574(26)	1948(986)	Table V
341(13)	638(5)	2020(680)	[14] (an experimental value of 1930 is quoted for f_3).
	546	1986	[17]
	320	1546	[19]

FeCO(5):

153(51)	462(6)	1960(551)	Table V
241(45)	542(10)	2003(659)	[14]
	552	1876	[17]

We conclude that the agreement of our values with the experimental ones are very satisfactory as well as with those from [14]. Our calculations are at the LDA/BP level (those of [14] are at the LDA level), and it is considered that LDA corrections (such as the GGA ones) usually improve the results of the frequencies obtained by DFT methods [22].

M₅CO (M = Fe, Ni, Cu) CASES

In Tables VI and VII the relevant parameters that we have calculated in this report are displayed.

In Table VI we report the optimized distance from the C atom to the center of the M₄ square keeping the CO distance fixed at the value of the corresponding MCO compound. Only in the case of CuCO have we optimized this distance.

In the cases of Cu₅CO and Ni₅CO we have the two choices for the cluster M₅ those of (5, 0) and (4, 1); for the Fe₅CO we have only the (4, 1) cluster

geometry among the M₅ clusters of C_{4v} symmetry.

We report bond energies at equilibrium and E_{sof} energies. The difference between these two values is the vertical dissociation energy that is also reported as well as the corresponding configuration using the symmetry C_{4v} (symmetries are a_1, a_2, b_1, b_2, e_1 , in that order). We have also calculated asymptotic energies and checked that they agree with the corresponding E_{sof} energies. The energy of CO was obtained at the bond distance used in the M₅CO calculations. We subtracted

TABLE V
Vibrational frequencies f (cm⁻¹) and (in parentheses) intensity in (km / mol) for MCO compounds.

Molecule / state	f_1 stretch. (MC)	f_2 bend.	f_3 stretch. CO
CuCO(2)	231 (13)	386 (7)	1951 (848)
NiCO(1)	342 (10)	617 (0.2)	2005 (530)
NiCO(3)	243 (20)	460 (9)	1939 (861)
FeCO(3)	357 (5)	574 (26)	1948 (986)
FeCO(5)	153 (51)	462 (6)	1960 (551)

TABLE VI
Distance d from C to the M₄ plane (Å), bond energy E (a.u.), E_{sof} (a.u.), dissociation energy D_e (kcal / mol), and electronic configuration for the M₅CO compounds.

Molecule / state	d	E	E_{sof}	D_e	Configuration
Cu ₅ CO(2A ₁)(5,0)	1.80	-0.791656	-0.752472	24.59	(13 3 7 4 26 / 12 3 7 4 26)
Cu ₅ CO(2E ₁)(5,0)	1.90	-0.793778	-0.783390	6.52	(13 3 7 4 26 / 13 3 7 4 25)
Cu ₅ CO(2A ₁)(4,1)	0.85	-0.707294	-0.673491	21.21	(13 3 7 4 26 / 12 3 7 4 26)
Cu ₅ CO(2E ₁)(4,1)	1.73	-0.719386	-0.713274	3.86	(13 3 7 4 26 / 13 3 7 4 25)
Ni ₅ CO(1)(5,0)	1.70	-0.956774	-0.893778	33.37	(12 3 7 4 24 / 12 2 7 4 25)
Ni ₅ CO(1)(4,1)	0.00	-0.863319	-0.820598	19.07	(12 3 7 4 24 / 12 2 7 4 25)
Ni ₅ CO(3)(5,0)	1.80	-0.957368	-0.896044	38.48	(12 3 6 4 26 / 12 3 6 3 25)
Ni ₅ CO(3)(4,1)	0.10	-0.850991	-0.820598	19.07	(12 3 6 4 26 / 12 3 6 3 25)
Fe ₅ CO(3)(4,1)	1.05	-1.543196	-1.498714	27.86	(12 2 4 6 22 / 12 2 3 5 22)
Fe ₅ CO(5)(4,1)	1.15	-1.585505	-1.498714	54.56	(11 3 3 6 24 / 12 1 3 6 21)

TABLE VII
Net atomic charges and dipole moments (D) of the M₅CO compounds.

Molecule / state	$q(M_1)$	$q(M)$	$q(C)$	$q(O)$	$q(CO)$	Dipole moment
Cu ₅ CO(2)(5,0)	-0.2842	0.0729	0.3324	-0.3400	-0.0076	0.4747
Cu ₅ CO(2)(4,1)	0.1049	0.0183	0.1478	-0.3258	-0.1780	0.4241
Fe ₅ CO(3)(4,1)	-0.0026	0.0460	0.2124	-0.3940	-0.1816	0.1990
Fe ₅ CO(5)(4,1)	0.0422	0.0321	0.2281	-0.3989	-0.1708	0.5176
Ni ₅ CO(1)(5,0)	-0.1815	0.0660	0.2963	-0.3786	-0.0823	0.0920
Ni ₅ CO(1)(4,1)	0.1669	0.0458	0.0171	-0.3671	-0.3500	0.3019
Ni ₅ CO(3)(5,0)	-0.1995	0.0655	0.2937	-0.3562	-0.0625	0.0976
Ni ₅ CO(3)(4,1)	0.1419	0.0552	-0.0248	-0.3380	-0.3682	0.8143

from the occupation numbers for the alpha and beta spin the corresponding ones to CO in the symmetry C4V, that are (3 0 0 0 2/3 0 0 0 2), and we obtained the occupational numbers for the M_5 fragment.

Consider as an example the case of the Fe_5CO quintuplet. The bond energy at 3.0 Å is -1.490355 a.u. and the configuration is (11 3 3 6 24/12 1 3 6 21). The configuration for the Fe_5 fragment is, therefore (9 3 3 3 22/9 1 3 6 19), and its bond energy is -0.953107 a.u. The CO bond energy at the CO distance of 1.17 Å is -0.538758 a.u., whence the E_{sof} is -1.491865 Å, agreeing with the calculated energy at 3.0 Å.

The reason for this checking is that in some cases we had to shift the virtual orbitals because of convergence problems, and this might introduce some uncertainty in the energy. These problems appeared very often at large bond distances when we wanted to calculate the asymptotic energies.

It is interesting to assess the influence on the energy of the position of the ring M_4 when it is moved along the axis of the MCO molecule considered in the linear geometry.

At long distances between the center of the M_4 square and the M of the MCO, the energy of the system is the sum of the energies of MCO and M_4 . This is natural because the interaction between the two fragments is negligible. When the two fragments become closer, the energy drops when, as in this case, there is an attractive interaction between the two molecules. This continues until an equilibrium situation is set up, and then the energy begins to increase.

In the case of NiCO at long distances between the square Ni_4 and the NiCO the energy is -0.818 a.u., that is, the sum of the energies of the NiCO (1) -0.660 (from Table I) and of the square Ni_4 that was calculated at the experimental geometry of the Ni crystal and was -0.158 a.u.

When the Ni_4 square moves toward the Ni atom of NiCO, the energy drops until a minimum is reached at which the energy is -0.956774 a.u. This happens when the Ni of the NiCO is in the center of the Ni_4 square ($d = 1.70$ Å) and we are in the case of the cluster (5, 1) (see Table VI).

When the Ni_4 square continues to move toward the C atom and the Ni atom of the NiCO is on the other side of this square, the energy begins to increase, and this continues until the distance of this fifth Ni atom from the Ni_4 square is the corresponding to the Ni(4,1) cluster. In this case the energy increases up to the value -0.863619

a.u. according to Table VI and the distance d of the C atom from the center of the Ni_4 square is 0.0 Å. This particular distance in the case of Cu_5CO is 0.85 Å and in the case of $Ni_5CO(3)$ is 0.65 Å.

Bond Distances and Dissociation Energy

Let us consider, in the first place the case of Cu_5CO . There are two studies from Baerends et al. [1, 2] in which this compound with the geometries (5,0) and (4,1) and symmetries C4V were studied. This was done at the LDA level instead of at the LDA/BP as was done in this report.

According to Tables I and VI the distance C- Cu_1 changes from 1.91 to 1.80 Å when we move from $CuCO$ to Cu_5CO (5,0) due to additional effect of the Cu_4 group and, at the same time, the dissociation energy is increased from 16.0 to 24.6 kcal/mol, meaning a more stable C- Cu_1 bond. On the other hand, when we consider the cluster (4,1) whose equilibrium distance from the C to the Cu_4 plane is 0.85 Å and taking into account that the distance from the Cu_1 to that plane is 1.795 Å, the distance C- Cu_1 is 2.60 Å, larger than the corresponding one to the (5,0) case, and the dissociation energy is therefore lower (21.2 kcal/mol in Table VI).

Contrary to the conclusion reached in [1], the most stable place for CO to interact with the Cu crystal is the top position, and the hollow position would be a little bit less preferred. In [1] the distances from C to the Cu_4 plane are 1.93 Å (ours is 1.80 Å) for the (5,0) case and 1.39 Å (1.217 Å in [2]) for the (4,1) one (ours is 0.85 Å). The experimental distance reported is 1.90 Å, agreeing with the top site adsorption. The dissociation energies reported in [1] are very different from ours (14.6 kcal/mol) (22.72 kcal/mol in [12]) (ours is 24.6 kcal/mol) for the (5,0) case and 30.9 kcal/mol (38.0 kcal/mol in [12]) (ours 21.2 kcal/mol) for the (4,1) one. The experimental one is 15 kcal/mol, as reported in [1].

We consider now the $Ni_5CO(1)$ case. Going from NiCO to Ni_5CO (5,0) the distance C- Ni_1 changes from 1.66 to 1.70 Å and the dissociation energy from 63.9 to 39.52 kcal/mol, meaning that the bond C- Ni_1 is weaker when the Ni_4 group interacts with NiCO, and therefore the distance C- Ni_1 must increase somewhat, in agreement with our results.

When Ni_4 moves toward the C atom the cluster (4,1) is set up with a distance of 1.76 Å from Ni_1 to the Ni_4 plane, then this C atom is on the Ni_4 plane ($d = 0$ according to the Table VI). The distance

C-Ni₁ is 1.76 Å, a little longer than in the (5,0) case, and the dissociation energy is lowered from 39.52 k in the (5,0) case to 22.1 kcal/mol.

The only reported data we found were in [23], where a value of 2.04 Å of the C-Ni₁ is given for the (5,0) case (ours is 1.70 Å), but we have used the BP correction.

Moving to the Ni₅CO(3) case, we find the interesting fact that for the cluster (5,0) this triplet state is a little more stable than the singlet one by 1.42 kcal/mol, contrary to the NiCO(3) where the singlet is more stable than the triplet by 34.13 kcal/mol. This situation is opposite to the case of the (4,1) cluster, where the singlet is more stable than the triplet by 7.79 kcal/mol.

The C-N₁ distance is changed from 1.88 Å in NiCO to 1.80 Å in Ni₅CO (5,0) and to 2.41 Å in the (4,1) case. The corresponding dissociation energies are 31.10 kcal/mol from Table I and 38.48 kcal/mol for the (5,0) case and 15.0 kcal for the (4,1) one. This shows us that the behavior for the triplet state of Ni₅CO is different from the singlet case. The maximum interaction of the Ni₄ group with NiCO, that occurs in the (5,0) cluster, shortens the C-Ni₁ bond and therefore increases the bond energy. For the (4,1) case the distance from C to the Ni₄ plane is 0.65 Å and as a consequence the distance to Ni₁ is 2.41 Å, which is longer than the corresponding to Ni-C in NiCO (1.88 Å). The bond energy reduces to 15.0 kcal/mol, less than the 31.10 kcal/mol value corresponding to the NiCO case.

Similarly to the CuCO case, for both, the NiCO(1) and NiCO(3), the top position from the energetical point of view is preferred to the hollow one.

For Fe₅CO we have only the case (4,1). We observe from Table VI that the Fe₅CO quintuplet is more stable than the triplet by 28.2 kcal/mol.

The fifth Fe atom is 1.435 Å from the Fe₄ plane, therefore, according to Table VI, the distance C-Fe₁ is 2.485 Å for the triplet Fe₅CO and 2.535 for the quintuplet.

For the triplet the distance C-Fe changes from 1.70 to 2.49 Å and the dissociation energy drops from 58.74 kcal/mol for the triplet FeCO to 27.86 kcal/mol for the triplet Fe₅CO. This means that the C-Fe bond is now weaker. In the case of the quintuplet, the distance C-Fe₁ is also increased from 1.86 to 2.54 Å, but the corresponding dissociation energy does not drop, as in the previous case, but increases from 35.70 to 56.12 kcal/mol. This could be rationalized if the effect of the Fe₄ group were greater than the change of the C-Fe₁ distance, so the direction in which the change of dissociation energy occurs would be more influenced by the presence of this Fe₄ group than for the change in the Fe-C distance. It is also interesting to note that, for the FeCO case, the triplet is more stable than the quintuplet, contrary to the Fe₅CO case where the quintuplet is more stable than the triplet.

Atomic Charges and Dipole Moments

In Table VII the net gross atomic charges of the metal atom M₁ and the rest the M₄ atoms, as well as C, O, and CO, and the dipole moments are displayed.

Observing those values we conclude:

1. Going from the MCO to the M₅CO(5,0) cases, there is a significant lowering of the negative CO charge, meaning that electronic charge is flowing from CO to the M₅ group. Dipole moments are also reduced, meaning that the electric charge is more smoothly distributed.

TABLE VIII
Overlap populations C-M of M₅CO compounds.

Molecule / state	Alpha		Beta		Total		
	CM ₁	CM ₂	CM ₁	CM ₂	CM ₁	CM ₂	CM
Cu ₅ CO(2)(5,0)	0.1495	0.0042	0.1560	0.0226	0.3055	0.0268	0.4127
Cu ₅ CO(2)(4,1)	-0.0161	0.0374	0.0430	0.0690	0.0269	0.1067	0.4537
Ni ₅ CO(1)(5,0)	0.1640	0.0199	0.1742	0.0226	0.3382	0.0425	0.5082
Ni ₅ CO(1)(4,1)	0.1452	0.0403	0.1442	0.0476	0.2894	0.0879	0.6410
Ni ₅ CO(3)(5,0)	0.1753	0.0177	0.1787	0.0202	0.3540	0.0379	0.5056
Ni ₅ CO(3)(4,1)	0.1436	0.0545	0.1167	0.0603	0.2603	0.1148	0.7195
Fe ₅ CO(3)(4,1)	0.0355	0.0496	-0.0118	0.0575	0.0237	0.1071	0.4521
Fe ₅ CO(5)(4,1)	0.0125	0.0633	-0.0224	0.064	-0.0099	0.1273	0.4993

2. Unlike the MCO, in the $M_5CO(4,1)$ cases what takes place is an increase in the electronic charge of the CO group, except in the Fe_5CO triplet and quintuplet cases, where there is only a small reduction in this charge and the dipole moments are reduced too.
3. In the singlet and triplet Ni_5CO cases, comparing the (5,0) with the similar (4,1) cases, we observe that the electronic charge of the CO group is increased as well as the dipole moments. On the other hand, in the Cu_5CO cases, both the CO electric charge and the dipole moments, remain almost unchanged.

Overlap populations

In Table VIII the overlap populations of the C- M_1 and the four C- M_2 bonds for alpha and beta spin are shown, as well as the total alpha plus beta spin. The total overlap population between C and M_5 is $CM = CM_1 + 4CM_2$. This is displayed in the last column and is the corresponding to the C-M bond of the MCO compounds.

As in the case of the MCO compounds we can observe a close relationship between the total overlap population of the C and the M_5 cluster and the dissociation energy. In the case of the (5,0) clusters we have that increased values of the overlap populations are in the order $Cu_5CO(2E_1)(0.3420)$, $Cu_5C(2A_1)(0.4127)$, ..., and the highest values are those of the Ni_5CO singlet (0.5082) and triplet (0.5086), and they have also a very similar dissociation energy. In the case of the (4,1) clusters the situation is not so clear.

Conclusions

The DFT method at the LDA/BP level is very satisfactory for the predictions of equilibrium geometries, dissociation energies, and vibrational frequencies, as well as dipole moments for MCO compounds when compared to experimental values.

For M_5CO compounds the theoretical values, given in this report, are comparable with the few experimental values available.

In particular our calculations have established that:

1. $CuCO$ is bent in the doublet ground state, and this is also true for triplet $NiCO$ and

quintuplet $FeCO$. The ground states for $NiCO$ (singlet) and $FeCO$ (triplet) are linear.

2. Dissociation energies calculated using bond asymptotic energies are, in general, quite close to those obtained using the sum-of-fragments energies.
3. There is a close relationship between the dissociation energy and the overlap population of the M-C bond for the MCO and M_5CO (5,0) compounds.
4. Bond energies are lower in the (5,0) cases compared to the (4,1) ones. The dissociation energies are lower for the (4,1) cases compared to the (5,0) ones.
5. Cu_5CO has two states with almost the same bond energy but with very different dissociation energies in the case (5,0). On the contrary, in the (4,1) case, the state $2E_1$ is much more stable and has much lower dissociation energy than the $2A_1$ state.
6. The (4,1) case of Ni_5CO , similarly to $NiCO$, has the singlet more stable than the triplet, but this behavior is reversed in the (5,0) case.
7. For Fe_5CO , the quintuplet is more stable than the triplet, opposite to $FeCO$ where the triplet is more stable than the quintuplet.

ACKNOWLEDGMENTS

The support of the CONICYT (Consejo Nacional de Investigaciones Cientificas y Tecnologicas) of Uruguay is gratefully acknowledged.

References

1. D. Post and E. J. Baerends, *J. Chem. Phys.* **78**, 5663 (1983).
2. G. te Velde and E. J. Baerends, *Chem. Phys.* **177**, 399 (1993).
3. A. C. Pavao, M. Braga, C. A. Taft, B. L. Hammond, and W. A. Lester, Jr. *Phys. Rev. B* **44**, 1910 (1991).
4. ADF 2.0.1, SCM, *Theoretical Chemistry* (Wrije Universiteit, Amsterdam) E. J. Baerends, D. E. Ellis, and P. Ross, *Chem. Phys.* **2**, 41 (1973); G. te Velde and E. J. Baerends, *J. Comp. Phys.* **99**, 84 (1992).
5. W. Kohn and L. J. Sham, *Phys. Rev. A* **140**, 1133 (1965).
6. J. C. Slater, *Phys. Rev.* **81**, 381 (1952).
7. S. J. Vosko, L. Wilk, and M. Nusair, *Can. J. Phys.* **58**, 1200 (1980).
8. A. D. Becke, *Phys. Rev. A* **38**, 3098 (1988).
9. J. P. Perdew, *Phys. Rev. B* **33**, 8822 (1986); errata: *B* **34**, 7406 (1986).
10. P. M. Boerrigter, G. te Velde, and E. J. Baerends, *Int. J. Quantum Chem.* **33**, 87 (1988).

11. T. Ziegler and A. Rauk, *Theor. Chim. Acta* **46**, 1 (1977).
12. L. Fang and T. Ziegler, *J. Chem. Phys.* **95**, 7401 (1991).
13. C. W. Bauschlicher Jr., P. S. Bagus, C. J. Nelin, and B. O. Ross, *J. Chem. Phys.* **85**, 354 (1986).
14. R. Fournier, *J. Chem. Phys.* **99**, 1801 (1993).
15. C. W. Bauschlicher, *J. Chem. Phys.* **100**, 1215 (1993).
16. R. Fournier, *J. Chem. Phys.* **98**, 8041 (1993).
17. G. Berthier, A. Daoudi and M. Suard, *J. Mol. Struct (Theor. chem)* **179**, 407 (1988).
18. A. Veillard, *Chem. Rev.* **91**, 743 (1991).
19. C. W. Bauschlicher, Jr. and L. G. M. Pettersson, *J. Chem. Phys.* **87**, 2129 (1987).
20. B. I. Dunlap, H. L. Yu, and P. R. Antoniewicz, *Phys. Rev. A* **25**, 25 (1982).
21. M. R. A. Blomberg, P. E. M. Siegbahn, T. J. Lee, A. P. Rendell, and J. E. Rice, *J. Chem. Phys.* **95**, 5898 (1991).
22. T. Ziegler, *Chem. Rev.* **91**, 651 (1991).
23. N. Rosch, in *Cluster Models for Surface Phenomena*, G. Pacchioni, P. S. Bagus, F. Parmigianni, Eds. (NATO ASI Series, Series B, Phys. Vol. 283, Plenum, New York, 1992) p. 251.

Ensemble Density Functional Theory for Inhomogeneous Fractional Quantum Hall Systems

O. HEINONEN,* M. I. LUBIN, AND M. D. JOHNSON

Department of Physics, University of Central Florida, Orlando, Florida 32816-2385; e-mail for O.H.: ogh@physics.ucf.edu

Received February 26, 1996; revised manuscript received March 19, 1996; accepted March 19, 1996

ABSTRACT

The fractional quantum Hall effect (FQHE) occurs at a certain magnetic field strengths $B^*(n)$ in a two-dimensional electron gas of density n at strong magnetic fields perpendicular to the plane of the electron gas. At these magnetic fields strengths, the system is incompressible, i.e., there is a finite cost in energy for creating charge density fluctuations in the bulk, while the boundary of the electron gas has gapless modes of density waves. The bulk energy gap arises because of the strong electron-electron interactions. While there are very good models for infinite homogeneous systems and for the gapless excitations of the boundary of the electron gas, computational methods to accurately model finite, inhomogeneous systems with more than about 10 electrons have not been available until very recently. We will here review an ensemble density functional approach to studying the ground state of large inhomogeneous spin-polarized FQHE systems. © 1996 John Wiley & Sons, Inc.

Introduction

The fractional quantum Hall effect (FQHE) is manifested in a two-dimensional electron gas (2DEG) in a strong magnetic field oriented perpendicular to the plane of the electrons [1]. The effect was discovered as a transport anomaly. This is still the "Hallmark" of the effect, even though there

are now a host of other phenomena associated with the effect, which have been studied experimentally. In a transport measurement it is noted that at certain strengths $B^*(n)$, which depend on the density n of the 2DEG, current can flow without any dissipation. That is, there is no voltage drop along the flow of the current. At the same time, the Hall voltage perpendicular to both the direction of the current and of the magnetic field is observed to attain a quantized value for a small, but finite, range of magnetic field or density, de-

* To whom correspondence should be addressed.

pending on which quantity is varied in the experiment. The effect is understood to be the result of an excitation gap in the spectrum of an infinite 2DEG at these magnetic fields, so that there is a finite cost in energy to be paid for making density fluctuations in the system. This means that the 2DEG is incompressible. In general, the magnetic field strengths $B^*(n)$ at which the quantum Hall transport anomalies are observed are related to the density through the filling factor $\nu = 2\pi l_B^2 n$, with $l_B = \sqrt{\hbar c/(eB)}$ the magnetic length. The quantum Hall effect was first discovered [2] at integer filling factors. In this integer quantum Hall effect, the energy gap is nothing but the kinetic energy gap $\hbar\omega_c = \hbar eB/(m^*c)$. Later, the fractional quantum Hall effect was discovered [3] at certain rational filling factors of the form $\nu = p/q$, with p and q relative primes, and q odd. In the FQHE, the excitation gap is a consequence of the strong electron-electron interactions.

Our understanding of the origin of the FQHE started with Laughlin's seminal study of 1983 [4], which dealt with the simplest fractions $\nu = 1/m$, with m an odd integer. At these values of ν , there are on the average m magnetic flux quanta $\Phi_0 = hc/e$ per electron. In that work, Laughlin constructed a variational wave function for spin-polarized systems in strong magnetic fields, strong enough that the splitting $\hbar\omega_c$ between the magnetic subbands, or Landau levels, can be taken to be infinite. The wave function can then be constructed from single-particle states entirely within the lowest Landau level. Laughlin wrote the variational wave function as

$$\Psi_m \propto \prod_{i,j} (z_i - z_j)^m \exp\left[-\frac{1}{4} \sum_k |z_k|^2\right], \quad (1)$$

where m is an odd integer, and $z_j = x_j + iy_j$ is the coordinate of the j th electron in complex notation. This wave function is an eigenstate of angular momentum. Laughlin went on to demonstrate that the system having the wave function of Eq. (1) is an incompressible liquid with $\nu = 1/m$, m odd, and with an energy gap to excitations, and that the elementary excitations are fractionally charged quasi-holes or quasi-particles of charge $e^* = \pm e/m$. The origin of the energy gap can be understood in the so-called pseudo-potential representation of the electron-electron interactions [5]. Here, the electron-electron interaction $V(\mathbf{r}_i - \mathbf{r}_j)$ between electrons i and j is decomposed into strengths V_l in relative angular momentum chan-

nels $l = 0, 1, 2, \dots$, of the two electrons. For any realistic interaction $V(\mathbf{r}_i - \mathbf{r}_j)$, it turns out that $V_0 > V_1 > V_2 \dots$. Consider the case $\nu = \frac{1}{3}$. In this case, the lowest angular momentum pseudo-potential that enters into the $m = 3$ Laughlin description is V_1 , the interaction energy of two electrons of unit relative angular momentum (in units of \hbar). (Even relative angular momenta are not permissible for spin-polarized electron wave functions, since they have to be antisymmetric under interchange of electron coordinates). The Laughlin wave function is a very cleverly constructed highly correlated state which completely excludes unit relative angular momentum between any two electrons, and is furthermore the only state which satisfies this property at $\nu = \frac{1}{3}$. Therefore, any excited state must contain some electrons with unit relative angular momentum. The energy gap is due to the cost of this, and hence is of order V_1 . Note that because of the nature of the correlations between the electrons, which are contained in the factors $(z_i - z_j)^m$, the Laughlin wave function cannot be expressed as a single Slater determinant of single-particle states in the lowest Landau level. Figure 1 depicts the exchange-correlation energy per particle for infinite, homogeneous FQHE systems vs. filling factor. The cusps at filling factors $\nu = \frac{1}{3}, \frac{2}{5}, \frac{3}{5}$, and $\nu = \frac{2}{3}$ have been included to scale, and these filling factors marked by vertical lines for clarity. Note that these cusps are barely visible on this scale, yet they are responsible for all the physics of the FQHE!

More modern theories of the FQHE are based on the so-called composite fermions. This idea was originated by Jain [6] who noted that the $m = 3$ Laughlin wave function can be written as $\Pi(z_i - z_j)^2 \Psi_1$, where $\Psi_1 = \Pi(z_i - z_j) \exp[-\frac{1}{4} \sum_k |z_k|^2]$ is the Slater determinant wave function of a filled lowest Landau level. Because of constraints on the Hilbert space, Ψ_1 is an exact eigenstate of an interacting electron system at $\nu = 1$. Although Ψ_1 need not in general be the ground state of the interacting system, it is if the Landau level splitting $\hbar\omega_c$ is much greater than the scale of the Coulomb interaction, $e^2/(\epsilon_0 l_B)$, and if the external potential is sufficiently well behaved [7], e.g., it is caused by a uniform positive background charge density, and we will assume that these conditions are satisfied. Multiplication by the Jastrow factor $\Pi(z_i - z_j)^2$ makes the total wave function Ψ_3 vanish as the cube of the separation of two electrons when they approach each other, rather than linearly. In the two-dimensional world of the FQHE,

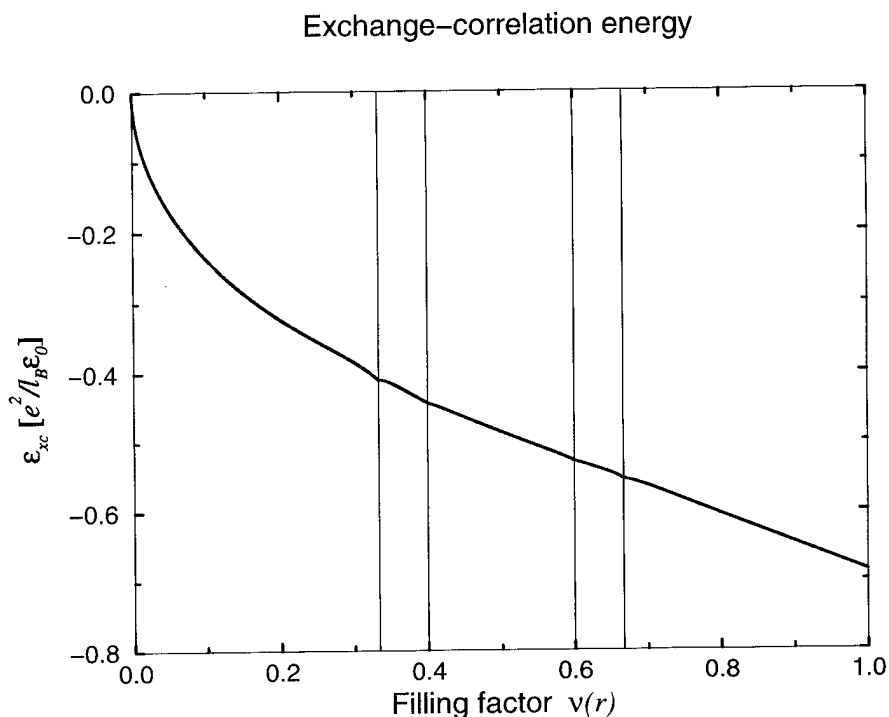


FIGURE 1. The ground-state energy ϵ_{xc} per particle of an infinite, homogeneous, spin-polarized FQHE system is depicted as a function of filling factor. The cusps at $\nu = \frac{1}{3}$, $\frac{2}{5}$, $\frac{3}{5}$, and $\nu = \frac{2}{3}$ are included (these filling factors are indicated by vertical lines for clarity).

a zero of the wave function at a fixed point z_0 produces a phase factor of 2π when an electron adiabatically encircles z_0 . This is equivalent to adding a flux-tube containing a single-flux quantum Φ_0 at z_0 . This is purely an Aharonov-Bohm phase—no magnetic field is added anywhere except at z_0 , where the wave function vanishes. Therefore, the FQHE at $m = 3$ can be interpreted as a system of electrons at $\nu = 1$, but with two flux quanta added to the position of each electron. These composite objects, electrons plus an integer number of flux quanta, are called composite fermions. So one can say that the fractional quantum Hall effect at $\nu = \frac{1}{3}$ is an integer quantum Hall effect ($\nu = 1$) of composite fermions. This generation of FQHE states from composite fermions was subsequently generalized to all FQHE fractions. One way of studying FQHE systems of electrons theoretically is to perform a singular gauge transformation [8], which is a gauge transformation in which an odd number of flux quanta is added to the position of each electron. The transformed wave function is thus a wave function for composite fermions. In a Lagrangian formulation, a term has to be added to the La-

grangian to ensure that the flux tubes indeed are located at the electrons. The resulting term in the Lagrangian is called the Chern-Simons term, and is well known from earlier topological field theories.

Finite Systems

We have outlined above how the electron-electron interactions in an infinite, homogeneous system produce the excitation gap. It is important to note that these gaps are only for excitations in the *bulk* of the system. When a system is bounded there *must* be gapless excitations located at the boundaries of the system. The following simple argument, due to MacDonald [7], demonstrates this point. Consider a finite system in which the chemical potential μ lies in the bulk "charge gap," i.e., we have to pay the price of the energy gap to introduce particles to the bulk of the system. Now imagine that the chemical potential is increased an infinitesimal amount $\delta\mu$, and consider the resulting change in the current density. In the bulk, the current density cannot change since $\delta\mu$ is infinites-

imal and cannot overcome the energy gap in the bulk. It follows that if there is a change in the current density as a response to $\delta\mu$, this must be located at the edges of the system. Current conservation also requires that if there is a resulting change in the current along the edge, this change must be constant along the edge. We can relate the change in current δI to the change in orbital magnetization through

$$\delta I = \frac{c}{A} \delta M, \quad (2)$$

where A is the total area of the system. This relation is nothing but the equation for the magnetic moment of a current loop. But we can write δM in terms of $\delta\mu$ using a Maxwell relation:

$$\delta M = \left. \frac{\partial M}{\partial \mu} \right|_B \delta\mu = \left. \frac{\partial N}{\partial B} \right|_\mu \delta\mu, \quad (3)$$

where N is the total number of electrons. By combining Eqs. (2) and (3) we arrive at

$$\frac{\delta I}{\delta \mu} = c \left. \frac{\partial n}{\partial B} \right|_\mu. \quad (4)$$

Since $\partial n / \partial B$ is nonzero, it follows that $\delta I / \delta \mu$ is nonzero, and we conclude that there must be gapless excitations of the system, and that these excitations must be localized to the edges. Since all experimental systems are finite and inhomogeneous, the low-energy properties probed by experiments must be determined by the gapless edge excitations. Advances in semiconductor nanofabrication technologies have lead to the possibility of manufacturing systems which are extremely inhomogeneous and, in practice, dominated by edges. As an example, recent experiments have even been performed on tiny quantum dots, with about 30 electrons on them [9, 10]. In order to accurately understand the experiments and inhomogeneous FQHE systems in general, we must have a way of accurately calculating their properties. Certain aspects of inhomogeneous FQHE systems have been studied by different techniques. For example, field theories can be constructed to study the low-energy limit of the gapless edge excitations [11]. Composite fermion methods have been used in a Hartree approximation to study finite FQHE systems [12, 13]. In this approach, the Chern-Simons term, arising from the singular gauge transformation, and the electron-electron interaction are treated in a self-consistent Hartree approximation.

The hope is then that the most important aspects of the electron-electron correlations are included in this approximation. Near $\nu = 1$, at which the Slater determinant Ψ_1 is the exact ground state, it makes sense to use the Hartree-Fock approximation, and the stability of a quantum dot at $\nu = 1$ as a function of confining potential has been studied in this approximation [14, 15]. The edge structure has also been studied using semiclassical methods [16, 17] in which the electron-electron interaction is included at the Hartree level, and it is furthermore assumed that all potentials vary on a length scale much larger than l_B . Beenakker [16], and Chklovskii, and Glazman [17] demonstrated that the edge of an integer quantum Hall system, in which the correlation energies between the electrons can be ignored, consists of a sequence of compressible and incompressible strips. Imagine going from the bulk of an integer quantum Hall effect, with ν -filled Landau levels in the bulk (so that the chemical potential lies above the energy of these ν Landau levels) toward an edge. There is an external potential confining the system, and this potential rises toward the edge, causing the Landau levels to bend upward near the edge. The compressible strips occur where the chemical potential crosses a Landau level. There are then both empty and occupied single-particle states available, and the electron gas can screen the external potential perfectly. Eventually this Landau level bends upward, rising above the chemical potential. There are then no more empty single particle states, and changing the electron density would involve a cost of energy of the order of $\hbar \omega_c$, the spacing between the Landau levels. Thus, an incompressible strip forms. Here, the electrons cannot screen the external potential. Further out on the edge, the chemical potential crosses the next lower Landau level, and a new compressible strip forms. Thus, whenever the chemical potential lies between two Landau levels, the electron gas is incompressible, and the electron density is constant, while the total potential varies. On the other hand, whenever the chemical potential crosses a Landau level, the electron gas can screen perfectly the external potential, and the electron density varies while the total potential remains constant. The width of the incompressible strips is then determined by the length over which the confining potential varies an amount equal to the energy gap $\hbar \omega_c$. The origin of the compressible and incompressible strips are the energy gaps, which are the kinetic energy gaps $\hbar \omega_c$ in the case of the integer quantum Hall effect.

But it is easy to heuristically generalize the argument to include the energy gaps causing the FQHE [17]. The conclusion is then that there should be compressible and incompressible strips, with the density of the incompressible strips fixed at the density of an FQHE fraction. The width of each incompressible strip is then fixed by the length over which the confining potential varies an amount equal to the energy gap of the FQHE fraction corresponding to the density of that strip.

Finite, inhomogeneous systems have also been studied by direct numerical diagonalizations [18]. At the present, numerical diagonalizations are limited to systems with about 10 electrons.

It is highly desirable to have a computational approach which accurately includes electron-electron correlations and can handle inhomogeneous systems with on the order of 10^2 – 10^3 electrons. One such approach is in principle valid for any interacting electron system is the density functional theory (DFT) [19–21]. There have been some attempts to apply density functional theory to the FQHE.

Ferconi and Vignale [22] applied current density functional theory [23] to small, parabolically confined quantum Hall systems and showed that the current density functional theory gave good results for the ground-state energy and spin polarization near $\nu = 1$. However, the energy gaps due to correlation effects were not included in that calculation. Ferconi, Geller, and Vignale [24] also recently studied FQHE systems within the spirit of the DFT using an extended Thomas–Fermi approximation at low, but nonzero, temperatures. In this, the kinetic energy was treated as a local functional, as in the standard Thomas–Fermi approximation, while the exchange-correlation energy was included in a local density approximation (LDA). This extended Thomas–Fermi approximation is valid in the limit of very slowly varying confining potential. Ferconi, Geller, and Vignale focused on the incompressible and compressible strips at an edge of an FQHE system and obtained results in agreement with the predictions by Chklovskii, Shklovskii, and Glazman [17].

We have developed for the fractional quantum Hall effect an ensemble DFT scheme within the local density approximation and have applied it to spin-polarized circularly symmetric quantum dots [25]. In our approach, the kinetic energy is treated exactly, and the density represented by Kohn–Sham orbitals. The results are in good agreement with results obtained by semiclassical

[16, 17, 24], Hartree–Fock [14, 15] (for cases where the correlations do not play a major role), and exact diagonalization methods [26]. Our calculations show that the exchange and correlation effects of the FQHE are very well represented by the LDA and that our approach provides a computational scheme to model large inhomogeneous FQHE systems. We note that there exist previous formal DFTs for strongly correlated systems, in particular for high-temperature superconductors [27], and DFT calculations of high- T_c materials [28] and transition-metal oxides [29]. However, ours are, to the best of our knowledge, the first practical LDA–DFT calculations of a strongly correlated system in strong magnetic fields, and demonstrate the usefulness of the LDA–DFT in studying large inhomogeneous FQHE systems.

Ensemble Density Functional Theory Approach

In typical DFT calculations of systems of N_{el} electrons, the standard Kohn–Sham (KS) scheme [30] is implemented in which the particle density $n(\mathbf{r})$ is expressed in terms of a Slater determinant of $N \geq N_{el}$ KS orbitals, $\psi_\alpha(\mathbf{r})$. These obey an effective single-particle Schrödinger equation $H_{eff} \psi_\alpha = \epsilon_\alpha \psi_\alpha$, which is solved self-consistently by occupying the N_{el} KS orbitals with the lowest eigenvalues, ϵ_α , and iterating. This scheme works well in practice for systems for which the true electron density can be represented by a single Slater determinant of single-particle wave functions. However, when the KS orbitals are degenerate at the Fermi energy (which we identify with the largest ϵ_α of the occupied orbitals) there is an ambiguity of how to occupy these degenerate orbitals. There exists an extension of DFT which is formally able to deal with this situation. This extension is called ensemble DFT [20, 21], and in it, the density of the system is represented by an ensemble of Slater determinants of KS orbitals. However, while it can be shown using ensemble DFT that such a representation of the density is rigorous, it cannot be shown *how* the degenerate KS orbitals at the Fermi energy should be occupied, i.e., there has not been available a practical computational scheme for ensemble density functional theory.

We argued above that the Laughlin wave function cannot be represented as a Slater determinant of single-particle wave functions. Therefore, one may suspect that the density of a general FQHE

system cannot be represented by a single Slater determinant. We will now argue that this is indeed the case. Consider a FQHE system in the xy plane with the magnetic field along the \hat{z} axis. A circularly symmetric external potential $V_{\text{ext}}(\mathbf{r}) = V_{\text{ext}}(r)$ (due, e.g., to a uniform positive background charge density) confines the systems such that the density is fixed with a local filling of $\nu = \frac{1}{3}$ up to an edge at r_0 ($r_0 \gg l_B$) where the density falls to zero within a distance of order l_B . That such systems exist is well demonstrated by the excellent agreement between the Laughlin wave function and experiments, and by many numerical calculations [31, 26]. Due to the circular symmetry we can label single-particle orbitals by angular momentum m , and by a Landau level index $n \geq 0$. The orbitals $\psi_{m,n}(\mathbf{r})$ are centered on circles of radii $r_m \approx \sqrt{2ml} l_B$ with Gaussian fall-offs for $r \ll r_m$ and $r \gg r_m$. The single-particle orbitals with $n = 0$ are then in the bulk all degenerate, and the degeneracy is not lifted by electron-electron interactions since the system is homogeneous in the bulk. Only the orbital $\psi_{0,0}$ is nonzero at the origin—all others vanish at $r = 0$. In order to obtain a constant density at $\nu = \frac{1}{3}$ even at the center of the system, all single-particle orbitals in the bulk with $n = 0$ must have occupancies $\frac{1}{3}$. If the Fermi energy lay above the energies of the bulk orbitals, they would all be filled and one would have $\nu = 1$. Therefore, to get occupancies $\frac{1}{3}$ the Fermi energy must lie at the degenerate energy $\epsilon_{m,0}$ of these orbitals. Thus, in applying DFT to the FQHE we can expect a huge degeneracy of KS orbitals at the Fermi energy, and they must all have fractional occupancies. Consequently, the particle density cannot be expressed in terms of a single Slater determinant. Instead, the density has to be constructed from an ensemble of Slater determinants, i.e., the orbitals at the Fermi energy are assigned fractional occupation numbers, just as the Laughlin wave function for $\nu = \frac{1}{3}$ is not a single Slater determinant, but a highly correlated state with average occupancies of $\frac{1}{3}$ of single-particle states. Therefore, one might expect from the outset that one has to use ensemble density functional theory—the standard Kohn-Sham scheme may not converge.

Although ensemble DFT has been developed formally, there are in practice few examples of applications and calculations using ensemble DFT for ground-state calculations. A significant aspect of our work is that we have developed an ensemble scheme which is practical and useful for the

study of the FQHE. In ensemble DFT, any physical density $n(\mathbf{r})$ can be represented by $n(\mathbf{r}) = \sum_{m,n} f_{m,n} |\psi_{m,n}(\mathbf{r})|^2$, where $f_{m,n}$ are occupation numbers satisfying $0 \leq f_{m,n} \leq 1$, and the orbitals $\psi_{m,n}$ satisfy the equation

$$\left\{ \frac{1}{2m^*} \left[\mathbf{p} + \frac{e}{c} \mathbf{A}(\mathbf{r}) \right]^2 + V_{\text{ext}}(\mathbf{r}) + V_H(\mathbf{r}) + V_{\text{xc}}(\mathbf{r}, \mathbf{B}) \right\} \psi_{m,n}(\mathbf{r}) = \epsilon_{m,n} \psi_{m,n}(\mathbf{r}), \quad (5)$$

where $\nabla \times \mathbf{A}(\mathbf{r}) = \mathbf{B}(\mathbf{r})$. In Eq. (5), $V_H(\mathbf{r})$ is the Hartree interaction of the two-dimensional electrons, and, as usual, $V_{\text{xc}}(\mathbf{r}, \mathbf{B})$ is the exchange-correlation potential, defined as a functional derivative of the exchange-correlation energy $E_{\text{xc}}[n(\mathbf{r}), \mathbf{B}]$ of the system with respect to density:

$$V_{\text{xc}}(\mathbf{r}, \mathbf{B}) = \frac{\delta E_{\text{xc}}[n(\mathbf{r}), \mathbf{B}]}{\delta n(\mathbf{r})} \Big|_{\mathbf{B}}.$$

(We will hereafter not explicitly indicate the parametric dependence of V_{xc} and E_{xc} on \mathbf{B} .) For the case of the FQHE, we know that the exchange-correlation potential will be crucial, as it contains all the effects of the electron correlations which cause the FQHE in the first place, and a major part of the DFT application is to come up with an accurate model of E_{xc} and so of V_{xc} . Leaving this question aside for a moment, and assuming that we have succeeded in doing so, the practical question is then how to determine the KS orbitals and their occupancies in the presence in degeneracies. We devised an empirical scheme, which means that after a lot of trial and error we made some educated guesses that work. Our scheme produces a set of occupancies for the KS orbitals which satisfy some minimum requirements, namely (a) the scheme converges to physical densities (to the best of our knowledge) for FQHE systems, (b) it reproduces finite temperature DFT distributions at finite temperatures, and (c) it reproduces the standard Kohn-Sham scheme for systems whose densities can be represented by a single Slater determinant.

In our scheme, we start with input occupancies and single-particle orbitals and iterate the system N_{eq} times using the KS scheme. The number N_{eq} is chosen large enough (about 20–30 in practical calculations) that the density is close to the final density after N_{eq} iterations. If the density of the system could be represented by a single Slater determinant of the KS orbitals, we would now essentially be done. However, in this system there

are now in general many degenerate or near-degenerate orbitals at the Fermi energy. After each iteration, the Kohn–Sham scheme chooses to occupy the N_{el} orbitals with the lowest eigenvalues, corresponding to making a distinct Slater determinant of these orbitals. But there will be small fluctuations in the density between each iteration, which cause a different subset of these (near) degenerate orbitals to be occupied after each iteration. This corresponds to constructing different Slater determinants after each iteration, and the occupation numbers f_{mn} of these orbitals are zero or unity more or less at random after each iteration. This means that the computations will never converge. However, the *average* occupancies, i.e., the occupancies averaged over many iterations, become well defined and approach a definite value, e.g., $\frac{1}{3}$ for orbitals localized in a region where the local filling factor is close to $\nu = \frac{1}{3}$. Therefore, we use these average occupancies to construct an ensemble by accumulating running average occupancies $\langle f_{mn} \rangle$ after the initial N_{eq} iterations:

$$\langle f_{mn} \rangle = \frac{1}{N_{\text{it}} - N_{\text{eq}}} \sum_{i=N_{\text{eq}}+1}^{N_{\text{it}}} f_{mn,i} \quad (6)$$

where $f_{mn,i}$ is the occupation number (0 or 1) of orbital ψ_{mn} after the i th iteration, and use these to calculate densities. Thus, our algorithm essentially picks a different (near) degenerate Slater determinant after each iteration, and these determinants are all weighted equally in the ensemble. It is clear that this scheme reduces to the KS scheme for which the density can be represented by a single Slater determinant of KS orbitals (for which the KS scheme picks only the one Slater determinant which gives the ground state density) for N_{eq} large enough. We have numerically verified that a finite-temperature version of our scheme converges to a thermal ensemble at finite temperatures down to temperatures of the order of $10^{-3} \hbar \omega_c / k_B$. We have also performed some Monte Carlo simulations about the ensemble obtained by our scheme. In these simulations, we used a Metropolis algorithm to randomly change the occupation numbers about our converged solution, keeping the chemical potential fixed. The free energy of the new set of occupation numbers was calculated self-consistently. If the free energy decreased, this set was kept, and if the free energy increased, the set was kept if a random number was smaller than $\exp[-\Delta F / k_B T^*]$, where ΔF is the change in free

energy, and T^* a fictitious temperature. The results were that to within numerical accuracy our ensemble DFT scheme gives the lowest free energy. As a condition for convergence, we typically demanded that the difference between the input and output ensemble densities, $n_{\text{in}}(r)$ and $n_{\text{out}}(r)$, of one iteration should satisfy

$$\frac{2\pi}{N_{\text{el}}} \int_0^\infty |n_{\text{in}}(r) - n_{\text{out}}(r)| r dr < 10^{-3}. \quad (7)$$

Practical density functional theory calculations hinge on the availability of good approximations for the exchange-correlation potential V_{xc} , which enters in the effective Schrödinger equation for the KS orbitals. The simplest, and probably the most commonly used, approximation is the local density approximation (LDA). In this approximation, the exchange-correlation energy is assumed to be a *local function* of density, so that the total exchange-correlation energy consists of contributions from the local density of the system. Thus, in this approximation one writes $E_{\text{xc}}/N = \int d\mathbf{r} \epsilon_{\text{xc}}(\nu) n(\mathbf{r})$, where $\epsilon_{\text{xc}}(\nu)$ is the exchange-correlation energy per particle in a *homogeneous* system of constant density $n = \nu / (2\pi l_B^2)$ and filling factor ν . In other words, in the LDA one assumes that the system is locally homogeneous, i.e., the system can locally be approximated to have the energy per particle of an infinite, homogeneous system of the local density. This approximation obviously makes sense if the density of the system varies on a very long length scale, while it could be questionable for systems in which the density varies on some microscopic length scale. However, experience has shown that the LDA often works surprisingly well, even for systems in which the electron density is strongly inhomogeneous [19]. In fact, the first application of LDA–DFT was to calculate the work function of simple metals [32], so these were systems which were terminated with densities varying on the scale of a Bohr radius! Nevertheless, the LDA–DFT gave quite good results, vastly superior to those of the Hartree or Hartree–Fock approximation. In the FQHE, the length scale of exchange-correlation interactions and density fluctuations is given by the magnetic length l_B due to the Gaussian fall-off of any single-particle basis in which the interacting Hamiltonian is expanded. The densities are relatively smooth on this length scale, which gives us additional hope that the LDA will work well for the FQHE, too. In addition, the cusps in the exchange-correlation energy will sup-

press density fluctuations, so in this sense one can actually expect the basic physics of the FQHE to make the LDA a good approximation.

In conventional LDA-DFT calculation, the exchange-correlation energy ϵ_{xc} is obtained by interpolating between the exchange-correlation energies per particle of systems with vanishing and infinite densities, respectively, for which exact results are known. Analogously, following Rasolt and Perrot [33], we obtain our exchange-correlation energy by interpolating between two limits for which the result is known very accurately. In our case, the two limits are $B \rightarrow \infty$, and $B \rightarrow 0$, respectively, and we stitch them together using a Padé approximant [33]. Thus, we write for the exchange-correlation energy per particle of a uniform electron gas in a constant magnetic field:

$$\epsilon_{xc}(\nu) = \frac{\epsilon_{xc}^{\text{FQHE}}(\nu) + \nu^4 \epsilon_{xc}^{\text{TC}}[n(\nu)]}{1 + \nu^4}. \quad (8)$$

Here, $\epsilon_{xc}^{\text{TC}}$ is the zero-magnetic field result for a 2DEG obtained by Tanatar and Ceperley [34]. The term $\epsilon_{xc}^{\text{FQHE}}(\nu)$ is the $B \rightarrow \infty$ limit, which is the exchange-correlation energy of the FQHE in a system for which only single-particle states in the lowest Landau level are occupied. This contribution consists of two terms. The first one is a smooth interpolation formula $\epsilon_{xc}^{\text{LWM}}(\nu)$ due to Levesque, Weiss, and MacDonald [35] between ground-state energies at some rational fillings. The second one, $\epsilon_{xc}^{\text{C}}(\nu)$, is all-important for the study of the FQHE. This term contains the cusps in the ground-state energy which cause the FQHE. Here we have used a simple model which captures the essential physics. We model $\epsilon_{xc}^{\text{C}}(\nu)$ by constructing it to be zero at values of $\nu = p/q$ which display the FQHE. Near $\nu = p/q$, $\epsilon_{xc}^{\text{C}}(\nu)$ is linear and has at $\nu = p/q$ a discontinuity in the slope related to the chemical potential gap $\Delta\mu = q(|\Delta_p| + |\Delta_h|)$. Here $\Delta_{p,h}$ are the quasiparticle (hole) creation energies which can be obtained from the literature [36, 37] at fractions $\nu = p/q$. Farther away from $\nu = p/q$, $\epsilon_{xc}^{\text{C}}(\nu)$ decays to zero. Finally, in the LDA $V_{xc}(r)$ is obtained from $\epsilon_{xc}(\nu)$ as

$$V_{xc}(r) = \left. \frac{\partial[\nu \epsilon_{xc}(\nu)]}{\partial \nu} \right|_{\nu=\nu(r)}$$

at constant B . In our calculations, we restrict ourselves to include only the cusps at $\nu = \frac{1}{3}, \frac{2}{5}, \frac{3}{5}$ and $\nu = \frac{2}{3}$, which are the strongest fractions. These are some the fractions of the form $\nu = p/(2p \pm 1)$

generated by the so-called V_1 model, in which only the pseudo-potential V_1 is included.

A technical difficulty arises in the LDA: The discontinuities in $V_{xc}(r)$ in the LDA give rise to a numerical instability. The reason is that an arbitrarily small fluctuation in charge density close to an FQHE fraction give rise to a finite change in energy. Imagine that the local filling factor $\nu(r)$ in some neighborhood of a point r is very close to, but less than, say, $\frac{1}{3}$ after one iteration. In this neighborhood, the local exchange-correlation potential will then form a potential well with sharp barriers at the points around r where $\nu(r) = \frac{1}{3}$. During the next iteration, charge will then be poured into this well. As a result, the local filling factor will after this iteration exceed $\frac{1}{3}$, and in this neighborhood V_{xc} now forms a potential barrier of finite height. So in the next iteration, charge is removed from this neighborhood, and so on. We can see that this leads to serious convergence problems. To overcome this, we made the compressibility of the system finite, but very small, corresponding to a finite, but very large, curvature instead of a pointlike cusp in ϵ_{xc} at the FQHE fractions. In other words, instead of having a steplike discontinuity $\Delta\mu$ in the chemical potential, it rises smoothly an amount $\Delta\mu$ over an interval γ in the filling factor. What worked very well in practice was to have the discontinuity in chemical potential occur over an interval of filling factor γ of magnitude 10^{-3} . This corresponds to a sound velocity of about 10^6 m/s in the electron gas, which is 3 orders of magnitude larger than the Fermi velocity of a 2DEG at densities typical for the FQHE. In general, the finite compressibility does not lead to any spurious physical effects so long as the energy of density fluctuations on a size of the order of the systems size is larger than any other relevant energy in the problem. The only noticeable effect is that incompressible plateaus, at which the density would be perfectly constant were the compressibility zero, will have density fluctuations on a scale of γ . Figure 2 depicts V_{xc} used in our calculations as a function of filling factor.

Applications to Quantum Dots

We have self-consistently solved the KS equations [Eqs. (5)] for a spin-polarized quantum dot in a parabolic external potential, $V_{\text{ext}}(r) = \frac{1}{2}m^*\Omega^2 r^2$,

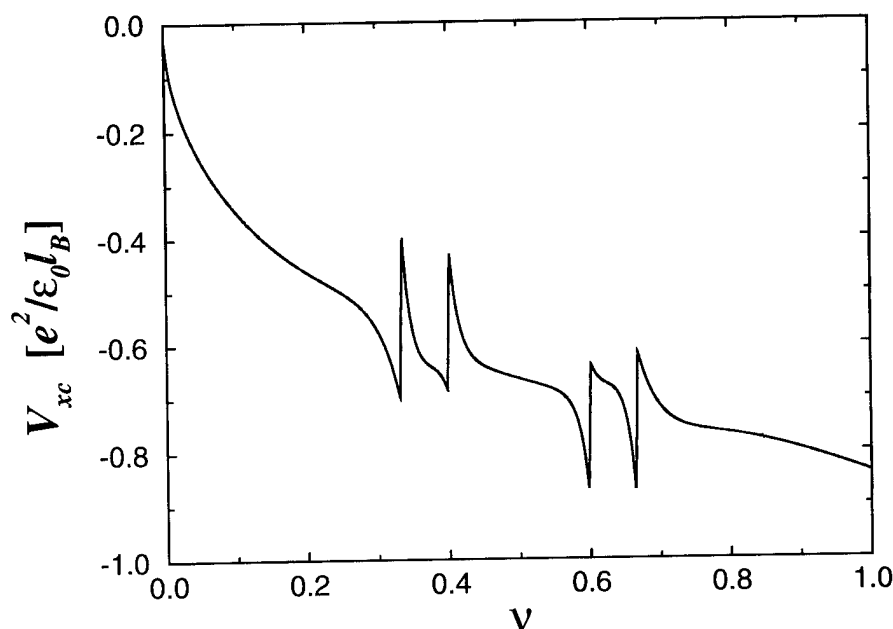


FIGURE 2. Exchange-correlation potential V_{xc} as function of filling factor in units of $e^2/(\epsilon_0 l_B)$ for $0 \leq \nu \leq 1$. The increase in V_{xc} at an FQHE filling occurs over a range of filling factor of 0.004.

by expanding the KS orbitals $\psi_{mm}(\mathbf{r}) = e^{im\phi}\phi_{mn}(r)$ in the eigenstates of

$$H_0 = \frac{1}{2m^*} \left[\mathbf{p} + \frac{e}{c} \mathbf{A}(\mathbf{r}) \right]^2.$$

We use the cylindrical gauge, $\mathbf{A}(\mathbf{r}) = \frac{1}{2}Br\hat{\phi}$, and include the four lowest Landau levels ($n = 0, \dots, 3$). We chose the static dielectric constant $\epsilon_0 = 13.6$, appropriate for GaAs, and a confining potential of strength [9] $\hbar\Omega = 1.6$ meV.

The use of our LDA-DFT scheme is illustrated by a study of the edge reconstruction of the quantum dot as a function of magnetic field strength. As is known from Hartree-Fock and exact diagonalizations [12–15, 16], for strong confinement the quantum dot forms a maximum density droplet in which the density is uniform at $\nu = 1$ in the interior, and falls off rapidly to zero at $r \approx \sqrt{2N}l_B = r_0$. As the magnetic field strength increases, a “lump” of density breaks off, leaving a “hole” or deficit at about $r = r_0$. This effect is due to the short-ranged attractive exchange interaction: It is energetically favorable to have a lump of density break off so that the system can take advantage of the exchange energy in the lump. As B is further increased, the correlations will cause incompressible

strips with densities $\nu = p/q$ to appear [16, 17, 24, 38] on the edges, and incompressible droplets to form in the bulk at densities $\nu = p/q$. Figure 3 depicts various states of edge reconstruction obtained by us as the magnetic field strength is increased. The value of B for which the exchange lump appears compares very well with the value found by De Chamon and Wen [15] in Hartree-Fock and numerical diagonalizations. At higher fields still, incompressible strips appear at the edges, and incompressible droplets are formed in the bulk. In Figure 4 we show occupancies for the KS orbitals for a finite-temperature calculation with $N_{el} = 40$, $B = 4.45$ T, and $T = 0.0003e^2/(\epsilon_0 l_B k_B)$. The diamonds depict the converged ensemble occupancies for the KS single-particle states using our ensemble scheme. At this finite temperature, we calculated the thermal occupancies of the KS orbitals after each iteration, and these “instantaneous” thermal occupancies were then averaged using our ensemble scheme. The temperature was sufficiently low that the instantaneous thermal occupancies were essentially 0 or 1 before convergence. The continuous curve shows the instantaneous thermal occupancies obtained after a particular iteration after convergence has been achieved. This figure then clearly shows that

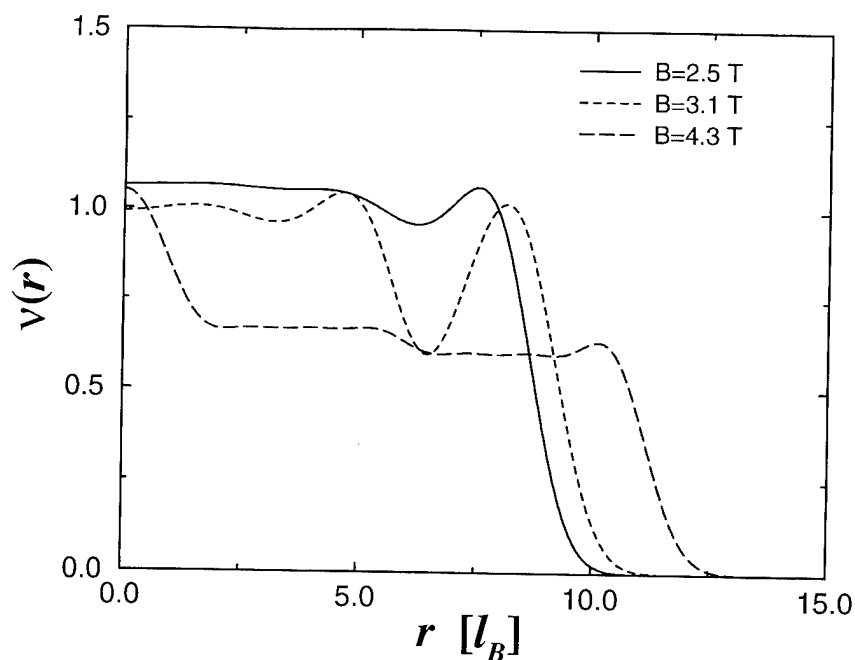


FIGURE 3. Edge reconstruction of a quantum dot as the magnetic field strength is increased. Plotted here is the local filling factor $\nu(r)$ for a parabolic quantum dot with $\hbar U = 1.6$ meV and 40 electrons. For magnetic field strengths $B < 2.5$ T the dot forms a maximum density droplet, and for $B \approx 3.0$ T, an exchange hole is formed. For stronger magnetic fields, incompressible regions form, separated by compressible strips.

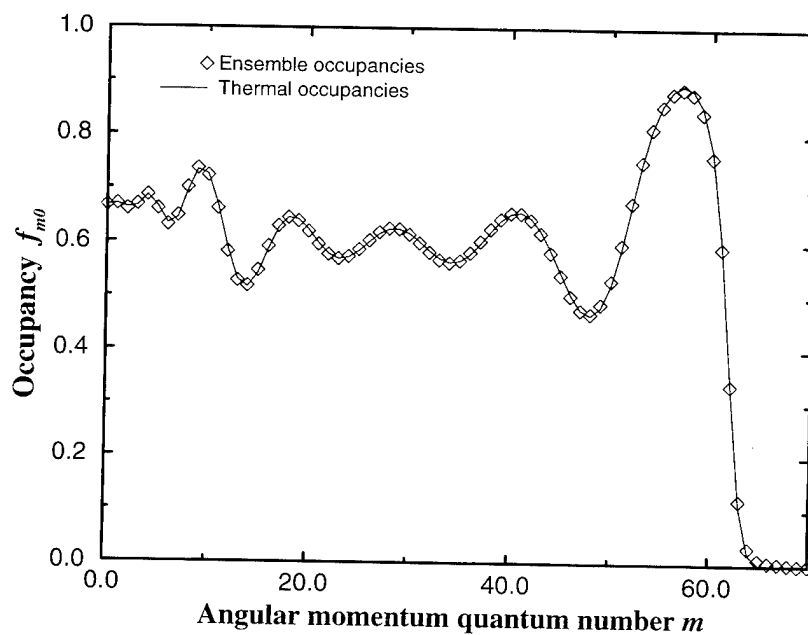


FIGURE 4. Ensemble (diamonds) and instantaneous (solid line) thermal occupancies for $N_{el} = 40$, $B = 4.45$ T, and $T = 0.0003 \text{ e}^2 / (\epsilon_0 l_B k_B)$ after convergence.

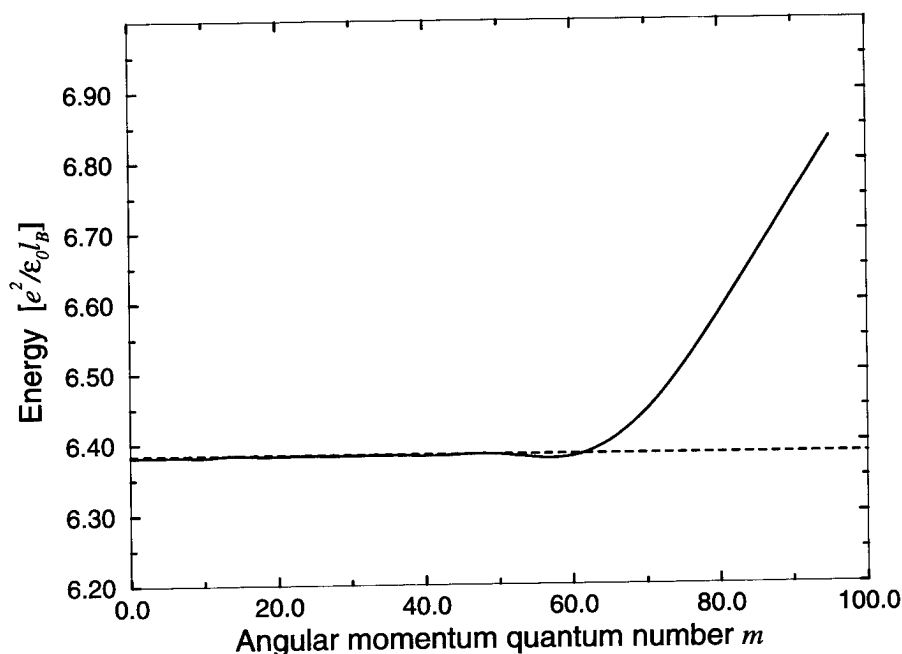


FIGURE 5. Eigenvalues of the lowest Landau-level Kohn-Sham orbitals for $N_{el} = 40$ and $B = 4.45$ T as a function of angular momentum quantum number. The chemical potential is indicated by the dashed line.

our ensemble occupancies (in this case at a low, but nonzero, temperature) converged to the thermal occupancies. Note that this particular temperature is so low that no standard finite-temperature scheme could be used to achieve convergence.

Figure 5 depicts the eigenvalues of the KS orbitals for $N_{el} = 40$, and $B = 4.45$ T. The dashed line indicates the chemical potential of the system. This figure then shows that all KS orbitals in the bulk are in fact degenerate. It may at first seem paradoxical that the eigenvalues are degenerate on an incompressible strip, since, according to the picture by Chklovskii, Shklovskii, and Glazman [17], on such a strip the density is constant, while the total potential varies (since the electrons cannot screen the external potential). If the total potential varies, then ought not the eigenvalues of the KS orbitals localized on that strip vary, too, since these then in general are subjected to different potential energies? The problem with this argument as applied to DFT is that it ignores the effect of the exchange-correlation potential. As the external and Hartree potentials vary across the strip, the exchange-correlation potential varies across its discontinuity so as to completely screen out the external and Hartree potentials. The discontinuity in V_{xc} does *not* mean that this potential is fixed at the lower limit of its discontinuity while

the density is fixed at an incompressible strip. What it does mean is that V_{xc} is free to achieve any value across its discontinuity so as to completely screen out the external and Hartree potentials. In this way, it is perhaps better to think of incompressibility as the limit of a finite compressibility approaching zero. A strip can then remain incompressible with constant density so long as V_{xc} can screen the external and Hartree potentials, so the width of the incompressible strip is given by the distance over which the external plus Hartree potentials varies an amount given by the energy gap associated with the density at that strip. Also, all bulk KS states are degenerate at the chemical potential. When a single particle is added, the chemical potential simply increases a small amount, and all KS orbitals are again degenerate at the chemical potential. We also would like to emphasize that incompressible regions that appear in these calculations are not due to the presence of a uniform positive background density which tends to fix the bulk density at the value of the background density.

There is also another edge effect caused by correlations. For particular, stiff confining potentials, so-called composite edges [26, 39] can appear. These can be thought of as particle-hole conjugates of uniform incompressible droplets.

Consider a droplet with a bulk density corresponding to $\nu = \frac{1}{3}$, falling off to zero at the edge. An incompressible droplet with a bulk density of $\nu = \frac{2}{3}$ is obtained by particle-hole conjugation. However, at the edge, the density will first *rise* to $\nu = 1$ (since the density of the $\nu = \frac{1}{3}$ droplet drops to zero), and then eventually drop to zero. Note that this argument is based on particle-hole conjugation, which is an exact symmetry of the lowest Landau level [40], and it is unclear if composite edges exist in real systems, which do not strictly obey particle-hole symmetry.

Figure 6 depicts the particle density (inset) for a system where the confining potential is supplied by a uniform positive background charge density $n_+ = 2/(6\pi l_B^2)$ (so that the corresponding filling factor is $\nu_+ = \frac{2}{3}$) for $r < r_0$, and falling linearly to zero over a distance a for $a > r_0$, where r_0 is fixed by charge neutrality. Thus, the parameter a is a convenient parameter with which one can control the stiffness of the confining potential [15]. From this figure, we see that for $a = 0$, the system forms a composite edge, even though our system does not obey particle-hole symmetry. We therefore conclude that such edges can exist in real systems. As a is increased, the edge undergoes an instabil-

ity and reconstruction, and eventually forms incompressible strips.

Conclusion and Summary

In conclusion, we have showed that ensemble density functional theory can be applied to the FQHE. This opens the door to doing realistic calculations for large systems. We believe that our results are also significant in that they are the first LDA-DFT calculations of a strongly correlated system in a strong magnetic field, and they are (to the best of our knowledge) the first practical ensemble DFT calculations. There are, however, still many issues that need to be resolved, and new directions to go. For example, our calculations were of a spin-polarized system. As is well known [7], the spin degree of freedom is very important, even for magnetic fields of the order of 10 T. The reason is that the effective g factor in GaAs is very small, so small that the ratio between the Zeeman splitting and the cyclotron energy is about 2%. This leads to the possibility of FQHE ground states which are not spin-polarized. It also gives rise to so-called charge-spin-texture excitations near $\nu =$

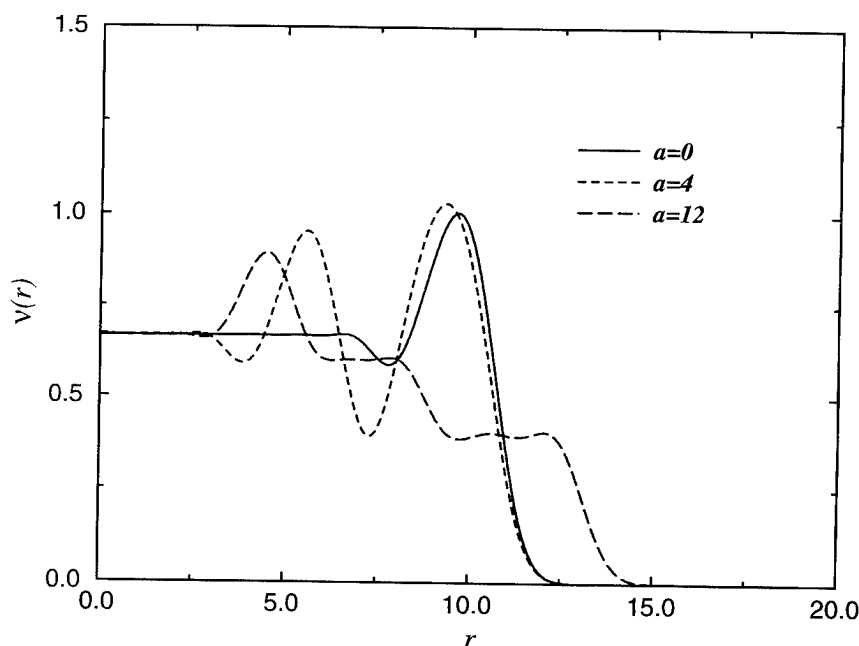


FIGURE 6. Local filling factor $\nu(r)$ as a function of r (in units of l_B) for a system of 45 electrons in a magnetic field of $B = 5.0$ T. The confining potential is due to a positive background charge density at $\nu_+ = \frac{2}{3}$ in the bulk, and falling linearly to zero within a distance a near the edge. For a stiff edge ($a = 0$), the system forms a composite edge with $\nu(r)$ rising toward unity near the edge. As a increases, the edge becomes softer and undergoes a reconstruction to a sequence of incompressible strips.

$1/m$, $m = 1, 3, \dots$. These excitations are lower in energy than a simple singlet particle-hole pair, and believed to be responsible for the observed [41] rapid destruction of the spin polarization near $\nu = 1$. Correctly including the spin degree of freedom to account for this involves a DFT for Heisenberg spins. We are presently, together with J. Kinaret (Chalmers University of Technology), developing such a theory.

ACKNOWLEDGMENT

The authors would like to thank M. Ferconi, M. Geller, and G. Vignale for helpful discussions and for sharing their results prior to publications, and K. Burke and E. K. U. Gross for useful comments about the DFT. One of us (O.H.) would like to thank Chalmers Institute of Technology, where part of the numerical work was done. This work was supported by the NSF through grant DMR93-01433.

References

1. R. E. Prange and S. M. Girvin, Eds., *The Quantum Hall Effect* (Springer, New York, 1987).
2. K. von Klitzing, G. Dorda, and M. Pepper, Phys. Rev. Lett. **45**, 494 (1980).
3. D. C. Tsui, H. L. Störmer, and A. C. Gossard, Phys. Rev. Lett. **48**, 1559 (1982).
4. R. B. Laughlin, Phys. Rev. Lett. **50**, 1395 (1983).
5. F. D. M. Haldane, Phys. Rev. Lett. **51**, 605 (1983).
6. J. Jain, Phys. Rev. B **40**, 8079 (1989).
7. See, for example, A. H. MacDonald, in *Quantum Transport in Semiconductor Microstructures*, B. Kramer, Ed. (Kluwer Academic, Hingham, MA, 1996).
8. For a review, see, for example, E. Fradkin, *Field Theories of Condensed Matter Systems* (Addison-Wesley, Redwood City, 1991).
9. P. L. McEuen, E. B. Foxman, J. Kinaret, U. Meirav, M. A. Kastner, N. S. Wingreen, and S. J. Wind, Phys. Rev. B **45**, 11419 (1992).
10. O. Klein, C. De C. Chamon, D. Tang, D. M. Abusch-Magder, U. Meirav, X.-G. Wen, M. A. Kastner, and S. J. Wind, Phys. Rev. Lett. **74**, 785 (1995).
11. X.-G. Wen, Phys. Rev. B **44**, 5708 (1991).
12. L. Brey, Phys. Rev. B **50**, 11861 (1994).
13. D. B. Chklovskii, Phys. Rev. B **51**, 9895 (1995).
14. A. H. MacDonald, S. R. E. Yang, and M. D. Johnson, Aust. J. Phys. **46**, 345 (1993).
15. C. De C. Chamon and X. G. Wen, Phys. Rev. B **49**, 8227 (1994).
16. C. W. J. Beenakker, Phys. Rev. Lett. **64**, 216 (1990).
17. D. B. Chklovskii, B. I. Shklovskii, and L. I. Glazman, Phys. Rev. B **46**, 4026 (1992).
18. See, for example, S.-R. Eric Yang, A. H. MacDonald, and M. D. Johnson, Phys. Rev. Lett. **71**, 3194 (1993).
19. W. Kohn and P. Vashista, in *Theory of the Inhomogeneous Electron Gas*, S. Lundqvist and N. March, Eds. (Plenum, New York, 1983).
20. R. M. Dreizler and E. K. U. Gross, *Density Functional Theory: An Approach to the Quantum Many-Body Problem*, (Springer, Berlin, 1990).
21. R. G. Parr and W. Yang, *Density-Functional Theory of Atoms and Molecules*. (Oxford University Press, New York, 1989).
22. M. Ferconi and G. Vignale, Phys. Rev. B **50**, 14722 (1994).
23. G. Vignale and M. Rasolt, Phys. Rev. Lett. **59**, 2360 (1987); Phys. Rev. B **37**, 10685 (1988).
24. M. Ferconi, M. Geller, and G. Vignale, Phys. Rev. B **52**, 16357 (1995).
25. O. Heinonen, M. I. Lubin and M. D. Johnson, Phys. Rev. Lett. **75**, 4110 (1985).
26. M. D. Johnson and A. H. MacDonald, Phys. Rev. Lett. **67**, 2060 (1991).
27. E. K. U. Gross, L. N. de Oliveira and W. Kohn, Phys. Rev. A **37**, 2805 (1988); Phys. Rev. A **37**, 2809 (1988).
28. W. Pickett, Rev. Mod. Phys. **61**, 433 (1989).
29. A. Svane and O. Gunnarsson, Phys. Rev. Lett. **65**, 1148 (1990); Z. Szotek, W. Temmerman, and H. Winter, Phys. Rev. B **47**, 4029 (1993).
30. W. Kohn and L. J. Sham, Phys. Rev. **140**, A1133 (1965).
31. F. D. M. Haldane in Ref. [1].
32. N. D. Lang and W. Kohn, Phys. Rev. B **1**, 4555 (1970).
33. M. Rasolt and F. Perrot, Phys. Rev. Lett. **17**, 2563 (1992).
34. B. Tanatar and D. M. Ceperley, Phys. Rev. B **39**, 5005 (1989); Y. Kwon, D. M. Ceperley, and R. M. Martin, Phys. Rev. B **48**, 12037 (1993).
35. D. Levesque, J. J. Weiss, and A. H. MacDonald, Phys. Rev. B **30**, 1056 (1984).
36. R. Morf and B. I. Halperin, Phys. Rev. B **33**, 221 (1986).
37. N. d'Ambrumenil and R. Morf, Phys. Rev. B **40**, 6108 (1989).
38. B. Y. Gelfand and B. I. Halperin, Phys. Rev. B **49**, 1994.
39. A. H. MacDonald, Phys. Rev. Lett. **64**, 222 (1990).
40. Note, however, that for a finite system the Hilbert space for the holes has to be restricted. See Ref. [26].
41. S. E. Barrett, R. Tycko, L. N. Pfeiffer, and K. W. West, Phys. Rev. Lett. **74**, 5112 (1995).

Linear Response and Quasiparticle Calculations as Probes of the Kohn–Sham Eigenvalues in Metals

ADOLFO G. EGUILUZ

Department of Physics and Astronomy, University of Tennessee, Knoxville, TN 37996-1200; Solid State Division, Oak Ridge National Laboratory, Oak Ridge, TN 37831-6030; e-mail: eguiluz@utk.edu*

Received April 19, 1996; revised manuscript received June 4, 1996; accepted June 5, 1996

ABSTRACT

The Kohn–Sham eigenvalues were formally introduced into density functional theory as Lagrange multipliers in the implementation of the minimum principle for the total energy of a many-electron system. No general results are available concerning the physical significance of these one-electron eigenvalues (with the exception of the highest occupied level, which equals the Fermi energy). Recent *ab initio* calculations of dynamical response in metals make explicit use of the Kohn–Sham band structure, and associated wave functions, through the use of spectral representations. This opens up the possibility of examining the significance of the eigenvalues at an “empirical” level, i.e., through direct comparison with the results of spectroscopic measurements. A particularly interesting example is afforded by new inelastic x-ray scattering experiments on Al. For a special wave vector transfer, $q_0 \approx 1.5k_F$, the measured spectrum provides a direct mapping of the Kohn–Sham noninteracting spectrum. For a range of wave vectors about q_0 , the bare Kohn–Sham spectrum still reproduces all the main features of the measurements; this suggests that, in this metal, the Kohn–Sham eigenvalues are good approximations to the quasiparticle energies. We also discuss the interplay between Kohn–Sham bands and the energy of the “anomalous” plasmon in Cs, whose dispersion bears a signature of the excited-state band structure. Finally, and in a more formal framework, we outline the results of a first-principles comparison between quasiparticle amplitudes and Kohn–Sham wave functions at a jellium surface; the latter turn out to be excellent approximations to the former. © 1996 John Wiley & Sons, Inc.

* Managed by Lockheed Martin Energy Research Corp. for the U.S. Department of Energy under contract DE-AC05-96OR22464.

Introduction

Density functional theory is a powerful approach to the many-body problem of interacting electrons [1]. In particular, Kohn and Sham [2] established a rigorous mapping between the intractable problem of interacting electrons (e.g., the $\sim 10^{23}$ valence electrons in a metal) and the much simpler problem of fictitious noninteracting electrons moving in an effective, local, energy-independent potential which contains all the many-body effects (these effects strongly influence most properties of metals). The great practical interest of this scheme resides in the fact that the self-consistent solution of the Kohn-Sham equation yields the density for which the energy of the ground state of the interacting system takes on its minimum value. The scheme would be exact, i.e., the density would equal the exact many-body density, if the exact form of the exchange-correlation energy functional $E_{xc}[n]$ were known—which, of course, it is not.

The local density approximation (LDA) is the simplest nontrivial ansatz for $E_{xc}[n]$. This approximation, already discussed in the two original papers on density functional theory [1, 2], has turned out to work surprisingly well in practice. When LDA-based density functional calculations are performed strictly within the confines of the method—the ground state of the interacting system—the success stories have been many [3–5]. Typically, lattice parameters, bulk moduli, phonon frequencies, and other observables which are functionals of the ground-state electron density, are nowadays obtained from first principles—that is, using as input only the atomic number for the species under study, and an available approximate result for the correlation energy of the uniform electron gas—and they agree with experiment very well. For strongly correlated systems such as the heavy Fermions, the high- T_c cuprates, and even for a conventional itinerant ferromagnet such as Fe, the limitations of the LDA, and its spin-polarized counterpart, LSDA, must be dealt with [6–8]. In some cases, gradient corrections to the LSDA functional may improve the results (e.g., the ground state of Fe) [9]. For the magnetic systems, the quality of the results may even depend on the details of the parametrization of the correlation energy for the uniform electron gas [10].

Now, there is another class of physical problems for which the information contained in the Kohn-Sham equation has been used rather routinely—and, basically, out of necessity. Specifically, the Lagrange multipliers of the theory, the Kohn-Sham eigenvalues (typically, evaluated within the LDA) are commonly used for the interpretation of spectra obtained via photoemission [11] (which probes the occupied states) and inverse photoemission [12] (which probes the empty states). This procedure has proved successful in many cases, at least in a practical sense [11, 12]. However, in others it has not—the band-gap problem in semiconductors [13, 14] being a classic example. [We recall that the origin of this problem is not the approximate nature of the LDA; the optical excitation across the gap is strongly influenced by the dynamical electron-hole (exciton) attraction [15], which is a many-body process outside the one-electron Kohn-Sham scheme.]

The question of how good the Kohn-Sham eigenvalues are as an approximation to the excitation energies is receiving a great deal of attention these days [16, 17]—particularly for finite systems, such as atoms and molecules [16]. (In the case of atoms, there is the additional issue that the LDA yields poor eigenvalues, since in this approximation the one-electron potential decays exponentially, rather than as the inverse power of the distance from the nucleus [3].) Of course, anybody doing spectroscopy would probably agree that what is needed are quasiparticle band structures (and their lifetimes), as these are the “energy levels” which photoelectrons probe. However, quasiparticle band structure calculations in the presence of the periodic ionic potential are still rather rare [18], and, for the most part, confined to semiconductors (Ref. [19] is an exception) and to relatively simple treatments of the correlation problem, such as the dynamically screened Hartree-Fock [20]—or GW [21]—approximation. More elaborate treatments of dynamical correlations are at the present stage the province of discrete models of highly correlated materials, such as the two-dimensional Hubbard model [22].

In this article we examine the question of the interconnection between the Kohn-Sham band structure and real electronic excitations in metals at both an “empirical” level and at a more “fundamental” level. For the most part, we confine the presentation to the empirical category, by which we mean detailed comparison with measured spectra. *Such comparisons are now becoming possible*

because of recent advances on the theoretical front, by virtue of which loss spectra can be calculated *ab initio*, that is, with use of a realistic representation for the Kohn-Sham states in crystals (as opposed to, e.g., jellium model-based calculations); see Ref. [23], and references therein.

A very recent inelastic x-ray scattering investigation of Al provides an excellent test case, as in that study a wave vector transfer is identified ($q = q_0 \approx 1.5k_F$) for which the x-ray photons couple directly with *noninteracting* electron-hole pairs [24]. We find that the "Kohn-Sham spectrum" agrees very well with the x-ray data obtained for this unique experimental condition. Away from this condition, the x-rays, of course, excite dressed electron-hole pairs. Yet, in general, for wave vectors which are large enough that the coherent aspects of the electronic response are suppressed, the *bare* Kohn-Sham (LDA-) spectrum still displays all the main features of the measured spectra. This finding suggests that the unoccupied Kohn-Sham bands are not too different from quasiparticle bands, even at energies as high as 60 eV above the Fermi level. (Quasiparticle lifetimes are outside this argument.)

The heaviest alkali metal, Cs, is another interesting system for which to address the same issue. This possibility arises because it turns out that interband transitions into empty states just above ω_p [25] influence the measured "anomalous" dispersion [26] of the Cs plasmon appreciably. While other physical effects—such as correlation—also play a role, even for small wave vectors [25], our presentation highlights the interplay between selected Kohn-Sham bands and the measured plasmon energy. This interplay is such that it leads to a negative plasmon dispersion [27] for small wave vectors.

A message that comes out of these studies of electronic excitations in prototype metals is that we expect that a "many-body loop," which would start with a Kohn-Sham band structure, and would proceed by renormalizing the bands via dynamical self-energy insertions, should converge rather quickly. Of course, a wider variety of metallic systems needs to be investigated along similar lines.

Finally, we present a sketch of a first-principles comparison [28] between quasiparticle theory and density functional theory at a jellium surface—this study belongs in the "fundamental" category. The emphasis is placed on states which are self-bound to the surface by long-range Coulomb correlations,

the image states [29]. The Kohn-Sham eigenfunctions for these states—which must be calculated without invoking the LDA, as this approximation ignores long-range correlations—turn out to be excellent approximations to the corresponding quasiparticle amplitudes. Furthermore, the quasiparticle energy shifts are found to be quite small. Thus, at least as far as the manifestations of the *real part* of the electron self-energy are concerned, the Kohn-Sham states represent the quasiparticle states near the vacuum level (~ 4 eV above the Fermi level) very well.

Linear Response

For the purposes of our inquiry into the possible experimental manifestation of the Kohn-Sham states, it is convenient to begin with the following spectral representation for the spatial Fourier transform of the noninteracting electron-hole polarizability $\chi^{(0;KS)}(\mathbf{x}, \mathbf{x}'; \omega)$,

$$\begin{aligned} \chi_{\mathbf{G}, \mathbf{G}'}^{(0;KS)}(\mathbf{q}; \omega) &= \frac{1}{\Omega_N} \sum_{\mathbf{k}} \sum_{n, n'}^{BZ} \frac{f_{\mathbf{k}, n} - f_{\mathbf{k}+\mathbf{q}, n'}}{E_{\mathbf{k}, n} - E_{\mathbf{k}+\mathbf{q}, n'} + \hbar(\omega + i\eta)} \\ &\quad \times \langle \mathbf{k}, n | e^{-i(\mathbf{q}+\mathbf{G}) \cdot \hat{\mathbf{x}}} | \mathbf{k} + \mathbf{q}, n' \rangle \\ &\quad \times \langle \mathbf{k} + \mathbf{q}, n' | e^{i(\mathbf{q}+\mathbf{G}') \cdot \hat{\mathbf{x}}} | \mathbf{k}, n \rangle, \end{aligned} \quad (1)$$

where Ω_N is the normalization volume and \mathbf{G} is a vector of the reciprocal lattice. The label KS added to the polarizability serves as a reminder that the "noninteracting" electrons we have in mind are those described by Kohn-Sham eigenfunctions and eigenvalues ("independent" may be a better denomination than noninteracting, since the Kohn-Sham electrons experience a mean field which includes exchange-correlation effects). The matrix elements in Eq. (1) are evaluated by expanding the one-electron Bloch (Kohn-Sham) states in an appropriate basis; the expansion coefficients are obtained from the self-consistent solution of the Kohn-Sham ground state. In principle, Eq. (1), and the discussion which follows, refer to an exact implementation of density functional theory; in practice, most calculations—in particular, the physical results discussed in the next two sections—start from a band structure obtained within the LDA. [Some details of the numerical evaluation of Eq. (1), and of the ensuing loss spec-

trum (number of bands included, sampling of the Brillouin zone, size of the response matrices, etc.), can be found in Refs. [25, 30–32].

In the time-dependent version of density functional theory (this method is a relatively recent development) [33, 34], the true density response function $\chi(\mathbf{x}, \mathbf{x}'; \omega)$ obeys an integral equation of the form

$$\chi = \tilde{\chi} + \tilde{\chi} \nu \chi, \quad (2)$$

where ν denotes the bare Coulomb interaction and $\tilde{\chi}$ is the “irreducible polarizability,” related to $\chi^{(0;KS)}$ via the equation

$$\tilde{\chi}^{-1} = (\chi^{(0;KS)})^{-1} - f_{xc}^{KS}, \quad (3)$$

where the “vertex correction” f_{xc}^{KS} is rigorously given by the functional derivative of the *time-dependent* exchange-correlation potential [34] with respect to the fluctuating density, i.e.,

$$f_{xc}^{KS} \equiv \frac{\delta V_{xc}(\mathbf{x}, t)}{\delta n(\mathbf{x}', t')}. \quad (4)$$

We note that we have chosen to write Eqs. (2) and (3) in a form which facilitates the comparison with the diagrammatic approach [35]. To this end, we furthermore write the solution of Eq. (2) à la Hubbard [36], i.e.,

$$\chi = \chi^{(0;KS)} \{1 - \nu(1 - G^{KS}) \chi^{(0;KS)}\}^{-1}, \quad (5)$$

a result which follows immediately from Eqs. (2) and (3) upon introducing the “many-body local-field factor” $G^{KS}(\mathbf{q}, \omega)$ [35, 36], defined such that $f_{xc}^{KS} = -\nu G^{KS}$. [Note that, while for the jellium model the density response function χ is a scalar, for the general case of band electrons in a periodic crystal potential, all elements of Eq. (5) must be understood as matrices in reciprocal space.]

In the time-dependent density functional framework [33, 34], Eq. (5) is formally *exact*. However, not much is known explicitly about the functional form of $V_{xc}(\mathbf{x}, t)$. (For recent work on the treatment of dynamical correlations in jellium, see Ref. [37]; exchange-only calculations for atoms within the so-called optimized effective potential are discussed in Ref. [34].) Most calculations of response within density functional theory—particularly in the presence of the crystal structure—have so far resorted to making an adiabatic ansatz, such as the “time-dependent” LDA (or TDLDA) [38], in which

$f_{xc}^{KS} = \int d^3x e^{-i\mathbf{q}\cdot\mathbf{x}} dV_{xc}(\mathbf{x})/dn(\mathbf{x})$, where $V_{xc}(n)$ is the exchange-correlation potential obtained in an LDA ground-state calculation.

In diagrammatic approaches to the electronic-response problem, it is rather customary to introduce the random-phase approximation (RPA) for the irreducible polarizability, $\chi^{(0)}$, as the reference density response for noninteracting electrons [39]. In that case, the counterpart of Eq. (5) can be written as

$$\chi = \chi^{(0)} \{1 - \nu(1 - G) \chi^{(0)}\}^{-1}, \quad (6)$$

where we have introduced a general many-body local-field factor $G(\mathbf{q}, \omega)$. We stress that Eq. (6) may also be viewed as giving the exact density response function—if we agree that *all* the effects of correlation are to be included in $G(\mathbf{q}, \omega)$. Of course, this is just a definition; in actual calculations, the local-field factor is obtained only approximately [35]. Note also that the propagators which define $\chi^{(0)}$ are *bare* [40] (i.e., they contain no self-energy or exchange-correlation, effects), and this translates into the result that, although the spectral representation for $\chi^{(0)}$ has the same form as Eq. (1), the energy eigenvalues and matrix elements are to be obtained for the *Hartree* one-electron Hamiltonian.

As just indicated, the two “pictures”—i.e., the response methods based on either Eq. (5) or Eq. (6)—formally yield the same exact density response. However, the respectively noninteracting polarizabilities, $\chi^{(0;KS)}$ and $\chi^{(0)}$ are, in general, different (an exception is encountered in the case of Al investigated below); thus, the corresponding many-body local field factors must be different as well. In fact, from Eqs. (5) and (6) it is a simple exercise to obtain the following relation between them [41]:

$$G^{KS} - G = \nu^{-1} \{ (\chi^{(0)})^{-1} - (\chi^{(0;KS)})^{-1} \}. \quad (7)$$

Traditionally, the many-body aspects of the electronic response have been discussed via the diagrammatic approach [Eq. (6)], whose implementation has been mostly restricted to the jellium model [35]. However, the physics discussed in the next two sections is outside this time-honored model; one must then tackle the spectrum of excitations of real crystals. As is well known, calculations for crystals are the established domain of the Kohn–Sham method—as far as ground-state observables are concerned. Equation (7) provides a

convenient link between both approaches to the treatment of the effects of correlation in the density response function χ .

Probing the Kohn-Sham States in Aluminum with X-rays

Larson et al. [24] have very recently performed extensive measurements of the dynamical structure factor of Al at the Oak Ridge National Laboratory x-ray beam line at Brookhaven's National Synchrotron Light Source. The emphasis was placed on wave vectors $q \sim 2k_F$, as calculations by Fleszar et al. [31] had raised the possibility that such measurements could be used to prove the details of the short-range electron-electron correlations. This wave vector regime is, of course, central to Hartree-Fock theory, which predicts a spin density wave instability in the electron gas [42]. Furthermore, the large wave vector response has a long history of interest in connection with the famous double-peak loss structure of the inelastic x-ray spectrum of simple systems; see Refs. [31, 43, 44], and references therein.

We recall that the cross section for inelastic x-ray scattering is proportional to the dynamical structure factor $S(\mathbf{q}, \omega)$, given by the equation

$$S(\mathbf{q}; \omega) = -2\hbar\Omega_N \text{Im } \chi_{G=0, G'=0}(\mathbf{q}; \omega). \quad (8)$$

Thus, the cross section is directly obtained from the solution of Eq. (5). Inspection of the experimental data [24] readily shows that the x-ray spectrum of Al contains a distinct "crossover" from a regime ($q < k_F$) for which mean-field response (the RPA) works well, to a regime ($q > k_F$) where it does not. An equivalent way to phrase this is to state that for $q > k_F$ the response becomes predominantly incoherent—which is precisely the regime that we must have access to, if we are to isolate the response of the one-electron states. Note that this regime is not easily accessible with other probes, such as inelastic electron scattering.

In fact, the large impact of correlation for $q > k_F$ and energies up to $\hbar\omega \sim 40$ eV made possible the first *experimental* determination of the many-body local-field factor for Al for large wave vectors [24]. In brief, such determination proceeds by "inverting" Eq. (5) (whose left-hand side corresponds to the measured data) to extract the local-field factor [45] on the basis of the knowledge of the noninteracting spectrum $S^{(0;KS)}(\mathbf{q}, \omega)$ —which obtains from

Eq. (8) upon replacing the true response χ by its noninteracting counterpart given by Eq. (1); such replacement is equivalent to setting $\nu(q) \equiv 0$ in Eq. (5). Remarkably, the measured local-field factor, $G_{\text{exp}}^{\text{KS}}(\mathbf{q}, \omega)$, turns out to be much stronger than predicted by theory for $q \rightarrow 2k_F$ [46–50]—with one exception [49]; this result is indicative of strong many-body correlations.

From the perspective of the present article, the key feature of the experiments of Larson et al. [24] which we want to focus on is that $G_{\text{exp}}^{\text{KS}}(\mathbf{q}, \omega)$ equals unity for $q \equiv q_0 \sim 1.5k_F$. Most importantly, this result holds (approximately) over a large frequency interval—the data of Ref. [24] are consistent with a weak ω dependence of the local-field factor for energies less than ~ 35 eV; furthermore, $G_{\text{exp}}^{\text{KS}}(\mathbf{q}, \omega)$ turns out to be predominantly real in this spectral region. Thus, for $q = q_0$ conditions are realized such that from Eq. (5) it follows that $S(\mathbf{q}_0, \omega) \approx S^{(0;KS)}(\mathbf{q}_0, \omega)$ (i.e., $\text{Im } \chi \approx \text{Im } \chi^{(0;KS)}$ for $q = q_0$) over a rather wide frequency interval—which includes the double-peak loss structure. This situation is striking, since it means that, for $q = q_0$, the x-rays photons probe the response of noninteracting (independent) electron-hole pairs. *This provides us with the opportunity of "taking a look" at the Kohn-Sham eigenvalues (band structure).*

The above statement is borne out by the results of Figure 1, in which we compare explicitly the x-ray data for $q = q_0$ with the Kohn-Sham spectrum $S^{(0;KS)}(\mathbf{q}_0, \omega)$, obtained in the LDA. The agreement between both spectra is extremely good; note that we are comparing absolute intensities, and that the calculation contains no adjustable parameters. Clearly, then, for $q = q_0$ the measured spectrum provides a direct physical realization of the Kohn-Sham excited-state one-electron band structure. We are not aware of a similar example in any other experimental context.

[The exaggerated feature in $S^{(0;KS)}(\mathbf{q}_0, \omega)$ at $\hbar\omega \sim 40$ eV is probably due to residual effects of the Coulomb interaction, i.e., to the approximate nature of the equality $G_{\text{exp}}^{\text{KS}}(\mathbf{q}_0, \omega) = 1$ over the frequency range covered by the data shown in Figure 1. In addition, for $\hbar\omega \sim 40$ eV, and for higher frequencies as well, the data are rather insensitive to the effects of correlation—this increases the intrinsic error of the measured value of local-field factor for such frequencies [24].]

Now, the definition of the "special" wave vector q_0 was made on the basis of Eq. (5), i.e., in the context of the density functional approach to dynamical response. We noted above that the many-

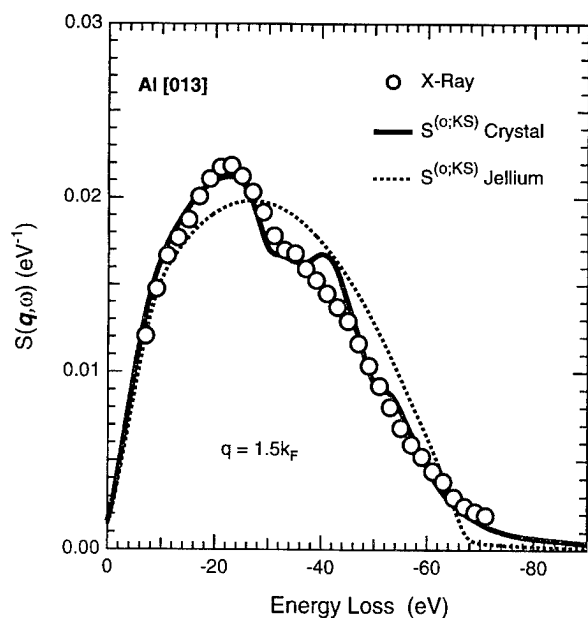


FIGURE 1. Inelastic x-ray spectrum of Al for $q = q_0 = 1.5k_F$ —the wave vector for which $G_{\text{exp}}^{\text{KS}}(\mathbf{q}, \omega) \cong 1$, as determined in Ref. [24] (see text). The empty circles are the measurements of Larson et al. [24]. The solid curve corresponds to $S^{(0;\text{KS})}(\mathbf{q}_0, \omega)$, which is the loss spectrum for “bare” Kohn–Sham electrons, obtained by replacing Eq. (1) into Eq. (8). For comparison, the corresponding noninteracting spectrum for jellium (Lindhard function) is also shown.

body local-field factor introduced in the diagrammatic approach differs, in general, from its density functional counterpart; see Eq. (7). Thus, on first sight it may seem that the preceding analysis may contain an element of ambiguity in the assignment of the balance between the band structure and many-body effects. However, there is no ambiguity; explicit calculation shows that, for Al, the “truly noninteracting” response $\chi^{(0)}$ evaluated in Hartree (RPA) theory is identical, on the scale of Figure 1, with the Kohn–Sham noninteracting response $\chi^{(0;\text{KS})}$. From this result it follows that $G^{\text{KS}} = G$, at least for the domain of wave vectors and frequencies relevant to the experiments of Ref. [24]. Thus, the significance of the wave vector q_0 for the x-ray spectrum of Al is identical in both “pictures.”

Thus far we have argued that, for a special experimental condition, which materializes for $q = q_0$, the x-rays excite “bare” Kohn–Sham electrons. What about other wave vectors?—how different is the measured response from $\chi^{(0;\text{KS})}$ in

the general case? We stress that this argument refers to a comparison of the data with $\chi^{(0;\text{KS})}$, not with the full (“dressed”) response χ .

The answer to the question just posed is contained in Figure 2. For pedagogical reasons, we show results for both the smaller q regime (left panel), in which the response is dominated by the collective mode (plasmon), and for a range of wave vectors about q_0 , for which the response is manifestly incoherent (right panel). It is apparent that, in the incoherent regime, the response of independent Kohn–Sham electrons, $S^{(0;\text{KS})}(\mathbf{q}, \omega)$, provides a rather good approximation to the x-ray data—it reproduces the fine structure of the measured spectra quite well, and the absolute intensities are not that far off. (A more exhaustive series of measurements, including data for even larger wave vectors, is presented in Ref. [24].) We interpret this result as a strong indication that, for Al, the Kohn–Sham eigenvalues and wave functions are good first approximations to their quasiparticle counterparts—even for excited states which are as far away from the Fermi surface as are probed by the data of Figure 2.

We finish this discussion with an overview of the method of analysis presented above. One may still ask what response scheme—based on Kohn–Sham or RPA noninteracting polarizabilities—is more suitable, in general, for the purposes of analyzing the x-ray data. Both approaches are entirely equivalent within the jellium model, since in that case the Kohn–Sham wave functions are plane waves, and the many-body effect contained in $V_{\text{xc}}(n)$ amounts to a trivial shift of all the eigenvalues. However, a metal would not even bind in the absence of electron correlations (which is why the calculation of the noninteracting RPA response $\chi^{(0)}$ alluded to above was performed by clamping the crystal at the lattice constant for which the total energy minimizes in LDA), and this favors the procedure adopted above—i.e., the extraction of the local-field factor based on Eq. (5), not on Eq. (6). The opposite viewpoint was adopted in Ref. [24], but, as noted above, for Al there is no difference. [Incidentally, on first sight, the fact that, for Al, $\chi^{(0;\text{KS})} = \chi^{(0)}$ may appear to imply that the inelastic x-ray spectrum of this metal is well reproduced by the jellium model; we emphasize that this is *not* the case, as Figure 1 clearly illustrates.]

For a metal with localized electrons at the Fermi level, such as Pd, $\chi^{(0;\text{KS})}$ and $\chi^{(0)}$ are quite different [51] (the correlation effect contained in $V_{\text{xc}}(n)$ leads to a narrowing of the occupied d -band com-

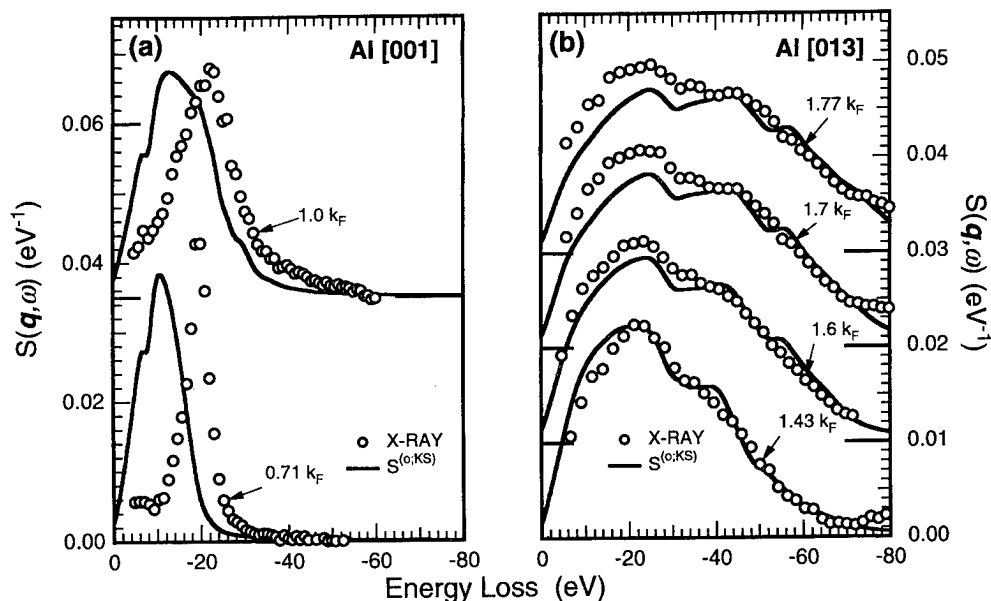


FIGURE 2. Comparison of measured inelastic x-ray spectra of Al [24] for a variety of wave vectors with the corresponding loss spectra for independent Kohn-Sham electrons, $S^{(0;KS)}(\mathbf{q}, \omega)$. See text for details.

plex), and thus the respective many-body local-field factors are intrinsically different. Since the LDA provides a valuable starting point for the treatment of correlation in crystals, we anticipate that forthcoming experiments on the transition metals (which will make use of new sources of hard x-rays, such as the Advanced Photon Source at Argonne) will be analyzed on the basis of Eq. (5)—if desired, the transformation to the RPA-based picture can be performed via Eq. (7).

Interplay between Kohn-Sham Bands and the Dielectric Response of Cesium

The dielectric response of Cs provides us with another example of the “empirical” manifestation of the Kohn-Sham band structure in the excitation spectrum of metals. High-resolution electron energy loss measurements by vom Felde et al. [26] have shown that the plasmon dispersion relation of the heavy alkalis differs drastically from the picture of the collective response of the simple metals held for many years—ever since the development of the RPA for the interacting electron gas [39]. In the case of Cs, instead of a “conventional” (upward) parabolic dispersion curve, controlled by the compressibility, the energy of the plasmon

disperses downward for $q \rightarrow 0$; furthermore, the dispersion curve remains quite flat for large wave vectors.

In Figure 3 (which centers on the small wave vector domain) we show the measured plasmon dispersion relation [26], together with our calculated dispersion curve for Cs [25] and for electrons in jellium with the bulk density of Cs ($r_s = 5.6$). (A negative plasmon dispersion for a realistic model of Cs was first reported in Ref. [27].) The theoretical dispersion curve was obtained from the position of the main peak in the loss spectrum $S(\mathbf{q}, \omega)$ given by Eq. (8). Clearly, there is excellent agreement with experiment. The key physical ingredients behind this agreement are [25]: the effects of the band structure, the matrix nature of the response, which reflects the contribution to the polarizability from the spatially localized $5p$ semi-core states, and the related enhancement of the importance of the many-body Coulomb correlations for *small* wave vectors.

In keeping with the theme of this presentation, we proceed to highlight the role of the Kohn-Sham band structure. We do this with reference to Figure 4, in which the central issue is the effect of the *unoccupied* bands on the position of the root of the equation $\text{Re } \epsilon_{\mathbf{G}=0, \mathbf{G}'=0}(\mathbf{q}; \omega) = 0$ —an alternative definition of the energy of the plasmon for a given

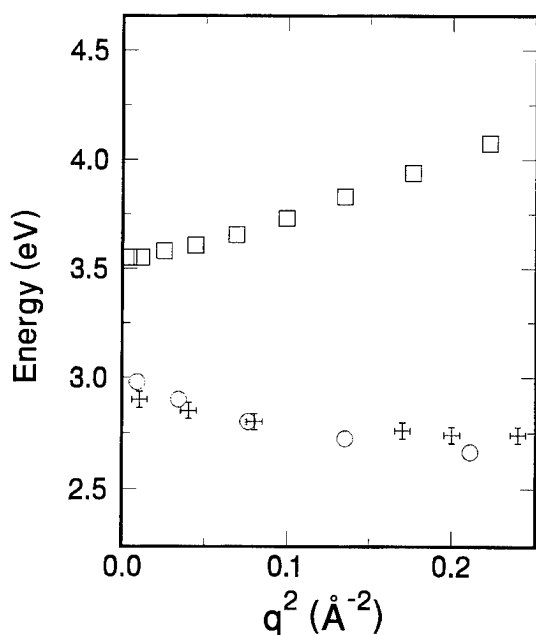


FIGURE 3. Plasmon dispersion relation in Cs for small wave vectors along the (110) direction. The figure shows the experimental data of Ref. [26] (crosses) and the crystal calculation of Ref. [25] (full circles), together with the RPA dispersion curve for jellium (empty squares). (In the crystal calculation the 5p semicore states were treated as valence states; furthermore, that calculation includes the effects of the crystal local fields and of a many-body local-field, or vertex correction [25].)

q . Now the exact dielectric function is given by $\epsilon = 1 - \nu\tilde{\chi}$ [see Eq. (3)], where, in general, all quantities are matrices in reciprocal space. For independent Kohn-Sham electrons we have $\epsilon^{\text{KS}} = 1 - \nu\chi^{(0;\text{KS})}$; since we are focusing on the empty states, in Figure 4 we have not included the contribution from the semicore states [25], in which case the response becomes predominantly diagonal, and this is why only the $\mathbf{G} = 0, \mathbf{G}' = 0$ element of the dielectric function enters the present argument.

Figure 4 shows, in the frequency region in the vicinity of the plasmon energy (~ 3 eV), $\text{Re } \epsilon_{\mathbf{G}=0, \mathbf{G}'=0}^{\text{KS}}(\mathbf{q}; \omega)$ calculated for "real" Cs (solid curve) and its counterpart for jellium (long dashes). First, it is apparent that the zero of the (real part of the) dielectric function of the crystal is shifted downward relative to its position for the jellium model—the location of the respective zero of $\text{Re } \epsilon_{\mathbf{G}=0, \mathbf{G}'=0}^{\text{KS}}(\mathbf{q}; \omega)$ is indicated by a pair of arrows. The negative plasmon dispersion for $q \rightarrow 0$ is traced to

this shift [32], whose magnitude is wave vector dependent.

Next, we draw attention to the curve in short dashes, which corresponds to the dielectric function of the crystal obtained upon eliminating from Eq. (1) the contribution from final states corresponding to a narrow complex of Kohn-Sham bands lying just above the plasmon energy. The inset of Figure 4 shows the calculated density of (Kohn-Sham) states (DOS); the lower local maximum in the DOS (note that it occurs at ~ 3 eV!) due to the bands in question is highlighted by an arrow. These bands, which are predominantly of d -like symmetry [52], roughly span the 3–4 eV range. As seen in the figure, in the absence of those interband transitions, the root of $\text{Re } \epsilon_{\mathbf{G}=0, \mathbf{G}'=0}^{\text{KS}}(\mathbf{q}; \omega) = 0$ for the crystal coincides with its frequency position for jellium. In that case the anomaly goes away—the plasmon dispersion is then solely determined by the compressibility, which is of course positive, since the system is stable, and the plasmon disperses upward [53].

[Although for small wave vectors the spectral weight of the one-electron transitions just identified is small [32], they involve final states which are nearly degenerate with the plasmon; furthermore, the real part of the dielectric function of the crystal reaches its zero quite gradually, as seen in Figure 4. Both features of the excitation spectrum of Cs contribute to the sensitivity of the energy of the plasmon to small "perturbations," such as introduced by the unoccupied Kohn-Sham bands whose effect is highlighted in the figure.]

To reiterate: If we remove the spiky complex in the Kohn-Sham DOS which lies just above ω_p , the dispersion relation of the plasmon of Cs changes qualitatively—it becomes the same as that for electrons in jellium (cf. Fig. 3). Thus the plasmon of Cs embodies a remarkable signature of the Kohn-Sham excited-state band structure. The impact of these one-electron (Kohn-Sham) transitions on the dielectric function of Cs is such that, in conjunction with other physical effects which prove important in the present problem—crystal local fields, electron-electron correlations—excellent agreement with the measured plasmon dispersion relation is obtained for small wave vectors [25].

In summary: Although there is no general Koopmans-like theorem relating the Kohn-Sham one-electron states to electronic excitations, the above results for the plasmon of Cs, together with the direct observation of $S^{(0;\text{KS})}(\mathbf{q}, \omega)$ on which we based our discussion of the x-ray spectrum of Al

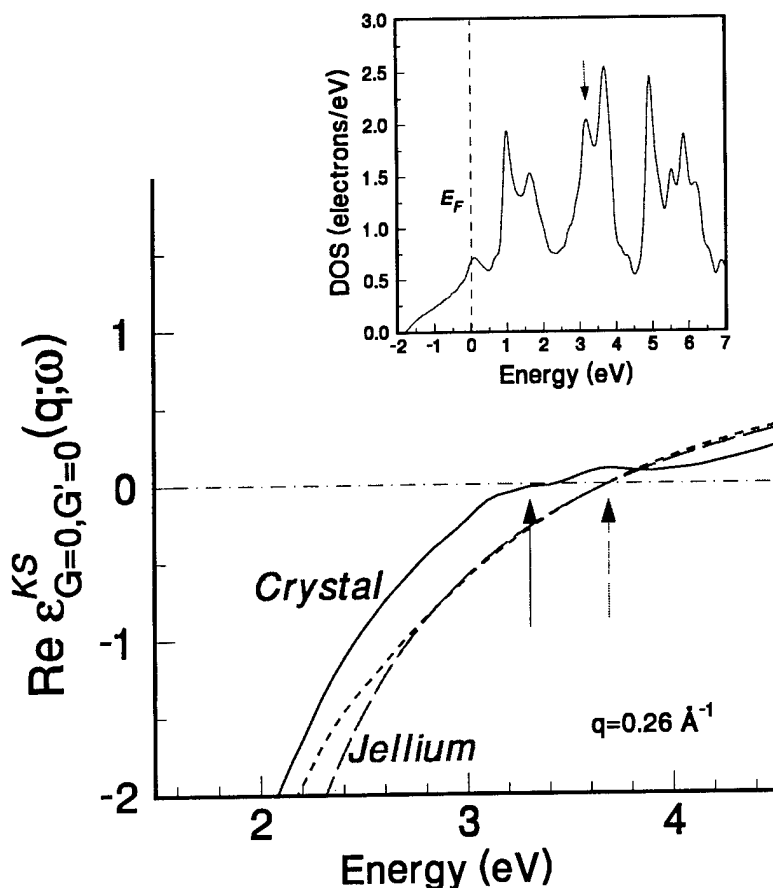


FIGURE 4. $\text{Re } \epsilon_{G=0, G'=0}^{KS}(\mathbf{q}; \omega)$ for Cs (solid curve) and for its jellium counterpart (long dashes), in the vicinity of ω_p (~ 3 eV). The position of the respective zero of the (real part of the) dielectric function is indicated by an arrow. The wave vector \mathbf{q} is along the (110) direction. The short dashes represent the result of excluding from Eq. (1) the contribution from the spiky complex in the DOS (see inset) lying just above ω_p . [In the present case (cf. Fig. 3) the crystal calculation does not include the effect of the semicore states.]

for large wave vectors, provide concrete examples in which *dynamical* polarizabilities obtained from Kohn-Sham electrons compare with experiment quite well. Ongoing calculations for a metal with *d*-like orbitals at the Fermi surface, namely Pd, tend to agree with this finding [51].

Of course, by its very nature, an "empirical" study such as the one we have outlined for Al and Cs can only be deemed as being "suggestive." Nonetheless, on the basis of the above presentation we propose that, for these metals, the Kohn-Sham independent electrons provide a good first approximation to the true quasiparticle states (with the caveat that the quasiparticle lifetimes are beyond the realm of the Kohn-Sham scheme). Clearly, more fundamental investigations, based on the

evaluation of quasiparticle band structures (including lifetimes), must be undertaken. Such calculations may be feasible; *the above discussion gives us the hope that the Kohn-Sham band structure may be such a good initial "guess" that (the computationally expensive) many-body self-consistency may be achieved in a few iteration steps.*

Quasiparticles and Kohn-Sham Electrons at a Jellium Surface

The spectrum of electronic excitations can be obtained from the solution of the Dyson equation for the one-electron Green's function, or, equivalently, by the self-consistent solution of the quasi-

particle equation [54]:

$$\begin{aligned} & \left(-\frac{\hbar^2}{2m} \nabla^2 + V_H(\mathbf{x}) \right) \Psi_{QP}(\mathbf{x}, E_{QP}) \\ & + \int d^3x' \Sigma_{xc}(\mathbf{x}, \mathbf{x}'; E_{QP}) \Psi_{QP}(\mathbf{x}', E_{QP}) \\ & = E_{QP} \Psi_{QP}(\mathbf{x}, E_{QP}), \end{aligned} \quad (9)$$

where $\Psi_{QP}(\mathbf{x}, E_{QP})$ is a quasiparticle amplitude and E_{QP} is the corresponding eigenvalue—which, we recall, corresponds to a physical excitation energy of the many-electron system in a metal, as probed, for example, by an electron added in the inverse photoemission process. In Eq. (9) we have introduced the electron self-energy, $\Sigma_{xc}(\mathbf{x}, \mathbf{x}'; E)$, which plays the role of a complex, nonlocal, energy-dependent “potential” in which the quasiparticle propagates—and which the quasiparticle actually sets up self-consistently. In the calculations on which the following outline is based, the self-energy was evaluated in the so-called GW approximation [20, 21], in which

$$\begin{aligned} \Sigma_{xc}(\mathbf{x}, \mathbf{x}'; E) = & \frac{i}{2\pi} \int dE' e^{iE'\eta} G(\mathbf{x}, \mathbf{x}'; E + E') \\ & \times W(\mathbf{x}, \mathbf{x}'; E'), \end{aligned} \quad (10)$$

where $G(\mathbf{x}, \mathbf{x}'; E)$ is the one-electron Green's function, and $W(\mathbf{x}, \mathbf{x}'; E)$ is the dynamically screened electron-electron interaction, given by the equation $W = v + v\chi v$, where χ is the time-ordered counterpart of the density response function introduced in Eq. (2). We note that a description of the screening consistent with the neglect of vertex corrections in Eq. (10) requires that the density response χ used in the evaluation of W be the solution to Eq. (2) for $\tilde{\chi} = \chi^{(0)}$ —which is the RPA, obtained also from Eq. (6) with $G(\mathbf{q}, \omega) \equiv 0$. [The exact self-energy is formally given by $\Sigma_{xc} = GW\Gamma$, where Γ is the vertex function; $\Gamma = 1$ in Eq. (10).]

The solutions of Eqs. (9) and (10) have been compared in detail [28] with the self-consistent solutions of the much simpler Kohn-Sham equation,

$$\left(-\frac{\hbar^2}{2m} \nabla^2 + V_H(\mathbf{x}) + V_{xc}(\mathbf{x}) \right) \phi_v(\mathbf{x}) = E_v \phi_v(\mathbf{x}), \quad (11)$$

for the case of a metal surface modeled by jellium—this model affords a tractable realization of a strongly inhomogeneous interacting electron sys-

tem. The emphasis was placed on states which are bound by the image tail of the surface barrier, namely the image states [29] (which are resonances, in the absence of a band gap). The physics of these states is governed by the dual features of long-range Coulomb correlations and strong charge localization at the surface.

Now, in the LDA, $V_{xc}(\mathbf{x})$ is a *function* of the *local* value of the density $n(\mathbf{x})$, and this leads to a surface barrier which decays exponentially into the vacuum outside the surface. By contrast, the correct surface barrier has a long-range z^{-1} tail. Thus, the image states are entirely beyond the realm of the LDA, which is the approximation for correlation for which Eq. (11) is typically solved.

A scheme was developed for going beyond the LDA in Eq. (11) in a nonperturbative fashion [55, 56]. By nonperturbative we mean that the rapid rate of decay of the electron density at the surface is treated exactly, i.e., without appeal to gradient expansions—which is a must, in the present case. In essence, this scheme starts out from the observation that long-range correlations in the presence of the self-consistent electron density profile at the surface are naturally included into the self-energy given by Eq. (10), and thus into the quasiparticle states given by Eq. (9), already at the level of the RPA, via the response function χ . The idea is then to feed the long-range correlations into $V_{xc}(\mathbf{x})$ through their insertion into $\Sigma_{xc}(\mathbf{x}, \mathbf{x}'; E)$ by solving an exact integral equation [57] which relates both “potentials.” From the solution of that equation for $V_{xc}(\mathbf{x})$, a nonlocal relation between V_{xc} and n was subsequently established [56, 58]; this relation allows us to perform electronic surface structure calculations which have built in the effects of the long-range Coulomb correlations, and thus the image states, absent in the LDA.

In Figure 5 we compare the quasiparticle amplitude $\Psi(\mathbf{q}_{\parallel}, E_{QP}; z)$ with the corresponding Kohn-Sham wave function $\phi_v(\mathbf{q}_{\parallel}, z)$ —obtained from Eq. (11) in the presence of the “nonlocal” V_{xc} obtained as just described. The figure refers to the $n = 1$ image state (resonance) of Al, modeled with jellium with $r_s = 2.07$, for a representative value of the wave vector parallel to the surface, \mathbf{q}_{\parallel} , and energy eigenvalue E_{QP} , for the quasiparticle state. Clearly, the two wave functions are nearly identical.

The above result is remarkable in view of the fact that the physics of the image problem is controlled by correlation, while in the bulk (of a semiconductor), for which a similar result was previ-

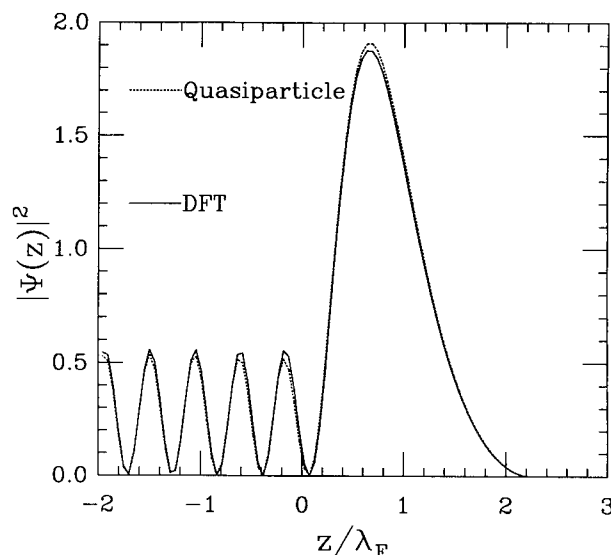


FIGURE 5. Comparison of the modulus square of the quasiparticle amplitude $\Psi_{QP}(\mathbf{q}_{\parallel}, E_{QP}; z)$ and the density functional wave function $\phi_n(\mathbf{q}_{\parallel}, z)$ for the $n = 1$ image state (resonance) of Al, modeled by a jellium surface with $r_s = 2.07$. The calculation was performed for $E_{QP} = 0.3E_F$, and $q_{\parallel} = 0.2k_F$ [28].

ously obtained [59], correlation plays a lesser role in establishing the nature of the one-electron potential. Since in Figure 5 the Kohn-Sham and quasiparticle calculations were performed at the same level in the treatment of the electron-electron interaction (the RPA), we feel that this a posteriori success of the Kohn-Sham wave functions may be general—i.e., it will hold for calculations which derive from more sophisticated treatments of correlation than contained in Eq. (10).

Additionally, the quasiparticle energy shift, that is, the difference $E_{QP} - E_{KS}$ was found to be small. Specifically, this difference was found to be ≈ 0.02 eV for $q_{\parallel} = 0$, which should be compared with the binding energy of the state, ~ 0.5 eV, measured from the vacuum level. This result is deemed to be typical of the present problem, as for Al the quasiparticle effective mass is very close to unity; the fact that the center of mass of the image state is far into the vacuum (see Fig. 5) should lead to an even smaller many-body mass enhancement.

A physical interpretation for the almost perfect overlap between the quasiparticle amplitudes and Kohn-Sham wave functions for the image states was given by Deisz et al. [28] on the basis of an effective, local quasiparticle potential, $U_{eff}^{QP}(z)$, constructed as a spatial integral over the electron self-energy, weighted by the quasiparticle ampli-

tude [28]. It was found that the relatively weak nonlocality of $\text{Re } \Sigma_{xc}^{QP}$ outside the surface has the consequence that $U_{eff}^{QP}(z)$ is well approximated by $V_{xc}(z)$ over the energy range corresponding to the image states. This energy domain is of the order of 4 eV above the Fermi surface.

Of course, the quasiparticle spectrum is richer than its Kohn-Sham counterpart, since the former contains the physical effect of the damping of the excited electronic states. Novel features of the energy dependence of the quasiparticle states outside the surface have been found [60]; in particular, the conventional $(E - E_F)^2$ scaling of Fermi liquid theory has been shown to hold for an increasingly small range above the Fermi level as the quasiparticle moves out into the vacuum. In other words, when the quasiparticle is outside the surface, large corrections to quadratic scaling are obtained for most energies for which such scaling holds in the bulk. These corrections are traced to the suppression of decay channels involving one electron final states above the Fermi energy [60].

ACKNOWLEDGMENTS

The author would like to acknowledge fruitful collaboration on the work discussed in this article with (in alphabetical order) John Deisz, Andrzej Fleszar, and Ben Larson. I thank Hardy Gross for useful discussions during the symposium. I acknowledge support from National Science Foundation Grant No. DMR-9207747/9596022 and the National Energy Research Supercomputer Center.

References

1. P. Hohenberg and W. Kohn, *Phys. Rev.* **136**, B864 (1964).
2. W. Kohn and L. J. Sham, *Phys. Rev.* **140**, A1133 (1965).
3. S. Lundqvist and N. H. March, Eds., *Theory of the Inhomogeneous Electron Gas* (Plenum, New York, 1983).
4. S. B. Trickey, Ed., *Density Functional Theory of Many-Fermion Systems* (Academic, New York, 1990).
5. E. K. U. Gross and R. M. Dreizler, Eds., *Density Functional Theory* (Plenum, New York, 1994); R. M. Dreizler and E. K. U. Gross, *Density Functional Theory: An Approach to the Quantum Many-Body Problem* (Springer-Verlag, Berlin, 1990).
6. D. M. Bylander and L. Kleinman, *Phys. Rev. B* **49**, 1608 (1994).
7. D. J. Singh and W. E. Pickett, *Phys. Rev. B* **44**, 7715 (1991).
8. M. M. Steiner, R. C. Albers, D. J. Scalapino, and L. J. Sham, *Phys. Rev. B* **43**, 1637 (1991); M. M. Steiner, R. C. Albers, and L. J. Sham, *Phys. Rev. B* **45**, 13272 (1992).

9. D. J. Singh, W. E. Pickett, and H. Krakauer, *Phys. Rev. B* **43**, 11628 (1991); D. J. Singh and J. Ashkenazi, *Phys. Rev. B* **46**, 11570 (1992).
10. D. J. Singh, D. P. Clougherty, J. M. MacLaren, R. C. Albers, and C. S. Wang, *Phys. Rev. B* **44**, 7701 (1991); J. P. Perdew and Y. Wang, *Phys. Rev. B* **45**, 13244 (1992); J. P. Perdew, J. A. Chevary, S. H. Vosko, K. A. Jackson, M. R. Pederson, D. J. Singh, and C. Fiolhais, *Phys. Rev. B* **46**, 6671 (1992).
11. J. W. Inglesfield and E. W. Plummer, in *Angle Resolved Photoemission, Theory and Current Applications*, S. D. Kevan, Ed. (Elsevier, Amsterdam, 1992), p. 15.
12. N. V. Smith, *Rep. Prog. Phys.* **51**, 1227 (1988); F. J. Himpsel, *Surf. Sci. Rep.* **12**, 1 (1990).
13. M. S. Hybertsen and S. G. Louie, *Phys. Rev. Lett.* **55**, 1418 (1985).
14. R. W. Godby, M. Schlüter, and L. J. Sham, *Phys. Rev. Lett.* **56**, 2415 (1986).
15. G. Strinati, H. J. Mattausch, and W. Hanke, *Phys. Rev. B* **25**, 2867 (1982).
16. See, in particular, A. Savin and C. J. Umrigar, *Bull. Am. Phys. Soc.* **41**, 64 (1996); M. Levy, *Bull. Am. Phys. Soc.* **41**, 64 (1996); J. P. Modiset and P. Nordlander, **41**, 64 (1996).
17. M. Petersilka and E. K. U. Gross, *Int. J. Quantum Chem. S.*, submitted; G. E. Engel and W. E. Pickett, *Bull. Am. Phys. Soc.* **41**, 64 (1996).
18. For a recent review, see S. G. Louie, *Surf. Sci.* **299/300**, 346 (1994).
19. F. Aryasetiawan, *Phys. Rev. B* **46**, 13051 (1992).
20. J. J. Quinn and R. A. Ferrell, *Phys. Rev.* **112**, 812 (1958).
21. L. Hedin, *Phys. Rev.* **139**, A796 (1965).
22. W. von der Linden, *Phys. Rep.* **220**, 53 (1992).
23. A. G. Eguiluz and A. A. Quong, in *Dynamical Properties of Solids*, G. K. Horton and A. A. Maradudin, Eds. (North-Holland, Amsterdam, 1995), Vol. 7, p. 425.
24. B. C. Larson, J. Z. Tischler, E. D. Isaacs, P. Zschack, A. Fleszar, and A. G. Eguiluz, *Phys. Rev. Lett.*, in press.
25. A. Fleszar, R. Stumpf, and A. G. Eguiluz, *Phys. Rev. Lett.*, submitted.
26. A. vom Felde, J. Sprösser-Prou, and J. Fink, *Phys. Rev. B* **40**, 10181 (1989).
27. F. Aryasetiawan and K. Karlsson, *Phys. Rev. Lett.* **73**, 1679 (1994).
28. J. J. Deisz, A. G. Eguiluz, and W. Hanke, *Phys. Rev. Lett.* **71**, 2793 (1993).
29. P. M. Echenique and J. B. Pendry, *Prog. Surf. Sci.* **32**, 11 (1990), and references therein; R. Fischer, S. Schuppler, N. Fischer, Th. Fauster, and W. Steinmann, *Phys. Rev. Lett.* **70**, 654 (1993).
30. A. A. Quong and A. G. Eguiluz, *Phys. Rev. Lett.* **70**, 3955 (1993).
31. A. Fleszar, A. A. Quong, and A. G. Eguiluz, *Phys. Rev. Lett.* **74**, 590 (1995).
32. A. G. Eguiluz, A. Fleszar, and J. Gaspar, *Nucl. Instrum. Methods B* **96**, 550 (1995).
33. E. Runge and E. K. U. Gross, *Phys. Rev. Lett.* **52**, 997 (1984); E. K. U. Gross and W. Kohn, *Adv. Quant. Chem.* **21**, 255 (1990).
34. M. Petersilka, U. J. Gossmann, and E. K. U. Gross, *Phys. Rev. Lett.* **76**, 1212 (1996), and references therein.
35. A. Holas, P. K. Aravind, and K. S. Singwi, *Phys. Rev. B* **20**, 4912 (1979); K. Awa, H. Yasuhara, and T. Asahi, *Phys. Rev. B* **25**, 3687 (1982); G. Vignale and K. S. Singwi, *Phys. Rev. B* **32**, 2156 (1985); F. Green, D. Neilson, and J. Szymanski, *Phys. Rev. B* **35**, 124 (1987).
36. J. Hubbard, *Proc. R. Soc. London A* **243**, 336 (1957).
37. S. Conti, H. M. Böhm, and M. P. Tosi, preprint.
38. A. Zangwill and P. Soven, *Phys. Rev. A* **21**, 1561 (1980).
39. D. Pines and P. Nozières, *The Theory of Quantum Liquids* (Benjamin, New York, 1966), Vol. 1.
40. G. D. Mahan, *Many-Particle Physics*, 2nd ed. (Plenum, New York, 1990), p. 435.
41. A result equivalent to Eq. (7) was obtained independently by E. K. U. Gross (private communication).
42. A. W. Overhauser, in *Highlights of Condensed-Matter Theory*, F. Bassani, F. Fumi, and M. P. Tosi, Eds. (North-Holland, Amsterdam, 1985), p. 194.
43. P. M. Platzman and P. Eisenberger *Phys. Rev. Lett.* **33**, 152 (1974); P. M. Platzman, E. D. Isaacs, H. Williams, P. Zschack, and G. E. Ice, *Phys. Rev. B* **46**, 12943 (1992), and references therein.
44. N. E. Maddocks, R. W. Godby, and R. J. Needs, *Europhys. Lett.* **27**, 681 (1994); *Phys. Rev. B* **49**, 8502 (1994).
45. We note that, since $G^{KS}(\mathbf{q}, \omega)$ is complex, the "inversion" of the data is not trivial; the interested reader is referred to Ref. [24] for details.
46. P. Vashishta and K. S. Singwi, *Phys. Rev. B* **6**, 875 (1972).
47. K. Utsumi and S. Ichimaru, *Phys. Rev. B* **22**, 5203 (1980); *Phys. Rev. B* **23**, 3291 (1981).
48. C. F. Richardson and N. W. Ashcroft, *Phys. Rev. B* **50**, 8170 (1994).
49. F. Brosens, J. T. Devreese, and Lemmens, *Phys. Rev. B* **21**, 1363 (1980); F. Brosens and J. T. Devreese, *Phys. Stat. Sol. (B)* **147**, 173 (1988).
50. S. Moroni, D. M. Ceperley, and G. Senatore, *Phys. Rev. Lett.* **75**, 689 (1995).
51. J. A. Gaspar, A. Fleszar, and A. G. Eguiluz, to appear.
52. D. A. Papaconstantopoulos, *Handbook of the Band Structure of Elemental Solids* (Plenum, New York, 1986), p. 50.
53. A. many-body mechanism for the anomalous Cs plasmon has been proposed, within the jellium model, by H. M. Böhm, S. Conti, and M. Tosi, *J. Phys. Condens. Matter* **8**, 781 (1996). See also Ref. [37].
54. L. Hedin and S. Lundqvist, in *Solid State Physics*, H. Ehrenreich, F. Seitz, and D. Turnbull, Eds. (Academic, New York, 1969), Vol. 23, p. 1.
55. A. G. Eguiluz, M. Heinrichsmeier, A. Fleszar, and W. Hanke, *Phys. Rev. Lett.* **68**, 1359 (1992).
56. A. G. Eguiluz, J. J. Deisz, M. Heinrichsmeier, A. Fleszar, and W. Hanke, *Int. J. Quantum Chem.: Quantum Chem. Symposium* **26**, 837 (1992).
57. L. J. Sham and M. Schlüter, *Phys. Rev. Lett.* **51**, 1888 (1983).
58. M. Heinrichsmeier, A. Fleszar, W. Hanke, and A. G. Eguiluz, preprint.
59. M. S. Hybertsen and S. G. Louie, *Phys. Rev. B* **34**, 5390 (1986).
60. J. J. Deisz and A.G. Eguiluz, preprint.

Intensity and Polarization of Light Emitted in Slow Ion–Atom Collisions

HERBERT F. M. DACOSTA,* DAVID A. MICHA,
AND KEITH RUNGE

Quantum Theory Project, University of Florida, Gainesville, Florida 32611-8435; e-mail for H.F.M.D: dacosta@qtp.ufl.edu

Received March 29, 1996; revised manuscript received June 4, 1996; accepted August 6, 1996

ABSTRACT

We study the intensity and polarization of light emitted during slow ion–atom collisions. We describe the nuclei as moving along classical trajectories while the electronic rearrangement is treated using time-dependent molecular orbitals. The intensity of emitted light is calculated from the diatomic time-dependent dipole. We evaluate the diatomic dipole matrix elements involving $1s$, $2s$, and $2p$ traveling atomic orbitals suitable for time-dependent collision studies. We calculate the intensity and the polarization of light emitted in $p + H(1s)$ collisions at kinetic energies from 10 to 1000 eV, for several impact parameters, changing over time. The emitted intensity goes through a maximum as the collision energy increases and lasts between 10 and 1 fs; the polarized light components parallel and perpendicular to the incoming beam direction show pronounced dependences on impact parameters and time. © 1996 John Wiley & Sons, Inc.

Introduction

Several contributions have shown how electrons jump between two nuclei during slow ion–atom collisions [1–7]. In our previous work, we developed a time-dependent theory of ion–atom collisions which provides details of the time evolution of the diatomic's properties [8–13]. Our previously calculated Figure 1 [13] presents the target H $1s$ -orbital population in collisions

with H^+ at a laboratory projectile kinetic energy $E = 10$ eV and impact parameter $b = 1.0$ a.u. One can see the temporal charge rearrangement that leads to an oscillating electric dipole for the collision complex, which does therefore emit light.

We have recently presented [14] a quantitative study of the light emission, where we have calculated its time evolution and spectral distribution in $H^+ + H(1s)$ collisions, at projectile (H^+) energies of 10 and 100 eV at a single typical impact parameter, and we have analyzed the wavelength $\lambda = c/\nu$ components of the emitted light packet. In the present work we calculate the intensity and polarization of emitted light integrated over the light

*To whom correspondence should be addressed.

detector angles for varying impact parameters and collision energies, and as functions of the time lapsed during collisions. The calculations involve the evaluation of the dipole matrix elements for $1s$, $2s$, and $2p$ orbitals over time, insofar as $2s$ and $2p$ orbitals are important for collisions occurring at Lab energies of the order of 100 eV and higher. We consider only the free-to-free transition, since the radiative recombination leading to formation of H_2^+ has been found to have small cross sections (below about 10^{-5} a.u., compared to electron transfer cross sections around 10^2 a.u.) due to the small values of their Franck-Condon factors [15, 16].

We adopt a semiclassical treatment with the nuclei moving along classical trajectories, and we calculate the intensity of light emitted from the classical electromagnetic flux. The expectation value of the time-dependent electric dipole is obtained from the electronic density matrix, calculated in a basis of traveling atomic orbitals previously introduced in the calculation of collision cross sections [12, 13].

In the conventional language of molecular electronic spectra, light emission leads to a transition between stationary electronic states of $H + H^+$, which are coupled to the nuclear motions and change nuclear trajectories. In our treatment, electronic and nuclear motions are coupled over time, and we can describe changes of trajectories as the electron state changes. The electronic rearrangement is accurately treated by a quantal (time-dependent molecular orbital) calculation which has

been shown to give correct answers for cross sections and orbital polarization parameters [12, 13, 17]. Our classical description of the electromagnetic field means that we are describing photon emission in a probabilistic way, with the absolute value squared of the field giving the relative probability of emission at a given time.

The procedure we follow here may be compared with the conventional procedure using stationary molecular states. For free-to-free transitions, these states are first generated in the absence of light for the continuum energies and the electronic states of interest. Then the transition dipole is calculated between stationary states, and from this one obtains emission rates. The wavelengths and intensities of emitted light vary in accordance with the distance dependence of states and transition dipoles, which enter the rates through Franck-Condon factors. For the $H + H^+$ system, the initial state has the electron localized at one of the protons, and must therefore be written as a combination of the σ_g and σ_u stationary states of H_2^+ . In our procedure, we instead generate nonstationary (time-dependent) states chosen initially to localize the electron at one of the protons. The system is evolved in time, again in the absence of light, to generate a time-dependent dipole which oscillates due to the electron jumps between protons. This takes the place of transitions between the σ_g and σ_u orbitals of H_2^+ . From the time-dependent dipole, it is possible to calculate transient light emission, as we show in what follows. The Fourier transform of the emission intensity gives

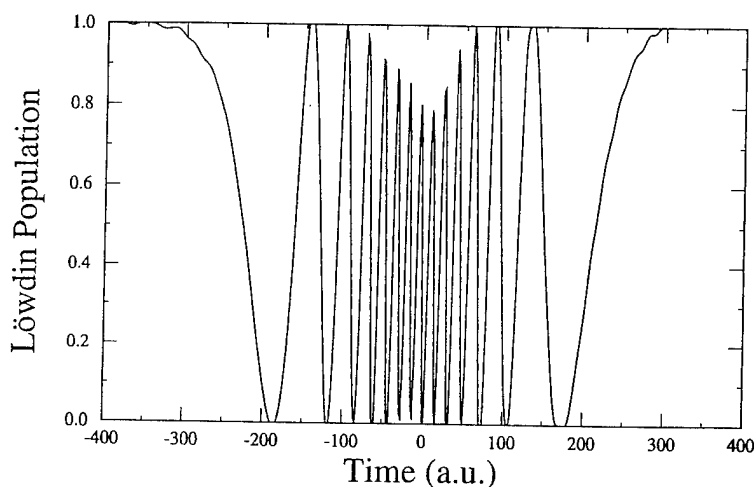


FIGURE 1. Löwdin population of the target $1s$ state vs. time in a.u. in a 10-eV proton-hydrogen-atom collision at $b = 1.0$ a.u.

the distribution of emitted frequencies and could be rewritten in terms of stationary electronic states. The present time-dependent calculation provides instead a straightforward procedure for transient emission. The energy carried away by an emitted photon must be small compared with the total energy of the diatomic system. This is indeed the case for $\text{H} + \text{H}^+$, insofar as the emitted photon energies are below about 5 eV, as found from the diatomic potential energy differences and also from Ref. [14], while the molecular energies we consider go from 1000 down to 10 eV. At the lower value, a more accurate treatment would include the electromagnetic energy in the calculation of the molecular dynamics from the outset, but this would not change the qualitative description at our low energies, and would be negligible at our high energies.

INTENSITY AND POLARIZATION OF THE EMITTED LIGHT

Our starting point is the eikonal/time-dependent Hartree-Fock (Eik/TDHF) method reported earlier [12], which describes the time evolution of coupled electronic and nuclear motions during collisions. We are interested in one-electron collisions for which the Fock operator reduces to the one-electron Hamiltonian \hat{H} and we work with the eikonal/time-dependent molecular orbital (Eik/TDMO) approach [13]. This formulation is developed in terms of the density operator and its density-matrix derived in a basis of traveling atomic orbitals. In the next step the electric and magnetic fields of the oscillating dipole and the Poynting flux vector are derived. Integrating the expression for the intensity of light emitted into a given solid angle over a sphere of radius r_{LD} (the distance from the Lab frame region to the light detector) produces the intensity I_k of light emitted in a given polarization k . Integration of I_k over time gives the polarization energy E_k .

Eikonal / Time-Dependent Molecular Orbital Method

We express the electron density operator as

$$\hat{\rho} = |\psi\rangle\langle\psi|, \quad (1)$$

where the time-dependent molecular orbital $\psi(t)$ is written as a linear combination of traveling

atomic orbitals ξ_μ ,

$$\begin{aligned} \psi(\mathbf{r}, t) &= \sum_{\mu} \xi_{\mu}(\mathbf{r}, t) c_{\mu}(t), \\ \xi_{\mu}(\mathbf{r}, t) &= \chi_{\mu}(\mathbf{r}) T_m(\mathbf{r}, t), \end{aligned} \quad (2)$$

with $\chi_{\mu}(\mathbf{r})$ an atomic orbital centered at proton position $\mathbf{R}_m(t)$, $m = a, b$, for the electron at position \mathbf{r} , and with the electron translation factor $T_m(\mathbf{r}, t)$ given by

$$T_m(\mathbf{r}, t) = \exp \left\{ i m_e \left[\mathbf{v}_m(t) \cdot \mathbf{r} - \int_{t_a}^t dt' v_m^2(t')/2 \right] \right\}, \quad (3)$$

where \mathbf{v}_m is the velocity vector of proton m , t_i is the initial time, and m_e is the electron mass.

Following the notation used for molecular orbital calculations [18] we write the atomic orbitals (AOs) as linear combinations of Gaussian functions $g_{l\kappa}$

$$\chi_{nl\kappa}(\mathbf{r}_{ml}; 1) = \sum_{j=1}^J d_{nl,j} g_{l\kappa}(\mathbf{r}_{ml}; \alpha_{nl,j}), \quad (4)$$

with $J = 6$, where \mathbf{r}_{ml} is the distance from electron 1 to nucleus m , $\kappa = x, y, z$ for $l = 1$. The Gaussian functions we have used are (for $\mathbf{R}_m = 0$),

$$\begin{aligned} g_s(\mathbf{r}, \alpha) &= \left(\frac{2\alpha}{\pi} \right)^{3/4} \exp(-\alpha r^2), \\ g_{p_\xi}(\mathbf{r}, \alpha) &= \left(\frac{2^7 \alpha^5}{\pi^3} \right)^{1/4} \xi \exp(-\alpha r^2), \end{aligned} \quad (5)$$

with $\xi = x, y, z$, and the exponential coefficients $\alpha_{nl,j}$ and expansion coefficients $d_{nl,j}$ taken from previous work [10, 13].

The density operator in the basis of traveling atomic orbitals is

$$\hat{\rho}(t) = \sum_{\mu\nu} |\xi_{\mu}\rangle P_{\mu\nu} \langle \xi_{\nu}|, \quad (6)$$

where $P_{\mu\nu}$ is the $(\mu\nu)$ element of the density matrix \mathbf{P} , which is given by

$$P_{\mu\nu}(t) = \sum_{\text{occ } i} c_{\mu i}(t) [c_{\nu i}(t)]^*. \quad (7)$$

For one-electron systems the TDHF equation for the electronic density operator becomes

$$\hat{H}\hat{\rho} - \hat{\rho}\hat{H} = i\hbar \frac{\partial \hat{\rho}}{\partial t}. \quad (8)$$

This equation is coupled to the equation for the proton trajectories, which are determined by the classical Hamilton's equations for the system, in terms of an effective Hamiltonian average over electronic states I with weight w_I [12],

$$H = \langle\langle \hat{H} \rangle\rangle = \sum_I w_I \text{tr}(\hat{\rho}_I \hat{H})$$

$$\frac{d\mathbf{R}}{dt} = \frac{\partial H}{\partial \mathbf{P}},$$

$$\frac{d\mathbf{P}}{dt} = -\frac{\partial H}{\partial \mathbf{R}}. \quad (9)$$

Equations (8) and (9) are solved self-consistently to generate a dynamically screened Coulomb potential. Since we take the collision to occur in the (x, z) -plane, the internuclear distance is given by

$$R(t) = \sqrt{[X_P(t) - X_T(t)]^2 + [Z_P(t) - Z_T(t)]^2}, \quad (10)$$

with the subscripts P and T referring to the projectile and target nuclei, respectively.

Evaluation of the Electric Dipole

For a single electron, the electronic component of the electric dipole in terms of the electronic density matrix $P_{\mu\nu}$ is

$$\mathbf{D}_{\text{el}}(t) = \langle \psi(t) | \mathbf{D}_{\text{el}} | \psi(t) \rangle = - \sum_{\mu, \nu} P_{\mu\nu}(t) \langle \xi_\nu | \mathbf{r} | \xi_\mu \rangle, \quad (11)$$

in atomic units.

The total electric dipole \mathbf{D} is given by

$$\mathbf{D} = \mathbf{D}_{\text{nuc}} + \mathbf{D}_{\text{el}} = \mathbf{D}(t; b, v_p), \quad (12)$$

where the nuclear component of the electric dipole is

$$\mathbf{D}_{\text{nuc}} = Z_T \mathbf{R}_T(t) + Z_P \mathbf{R}_P(t), \quad (13)$$

with Z_T and Z_P , being the nuclear charges and $\mathbf{R}_T(t)$ and $\mathbf{R}_P(t)$ being the trajectories.

The distance from an electron 1 to the origin \mathbf{r}_1 , is given by

$$\mathbf{r}_1 = \mathbf{R}_m + \mathbf{r}_{m1}, \quad (14)$$

where \mathbf{R}_m is the distance from the nucleus m to the origin. Then, the Cartesian components of \mathbf{r}_1 are $x_1 = X_m + x_{m1}$, $y_1 = Y_m + y_{m1}$, and $z_1 = Z_m + z_{m1}$, and the dipole matrix elements are as in the example below:

$$\langle \xi_{m1s} | x | \xi_{n1s} \rangle = \sum_j \sum_l d_{m1s,j}^* d_{n1s,l}$$

$$\times \langle g_{ms}(\alpha_j) | T_m^* T_n | g_{ns}(\alpha_l) \rangle X_n$$

$$+ \sum_j \sum_l d_{m1s,j}^* d_{n1s,j}$$

$$\times \langle g_{ms}(\alpha_j) | T_m^* T_n | g_{np_x}(\alpha_l) \rangle \frac{1}{2\sqrt{\alpha_l}}, \quad (15)$$

where use was made of the property of the Gaussian functions

$$x g_s(\alpha_l) = g_{p_x}(\alpha_l) / (2\sqrt{\alpha_l}). \quad (16)$$

The other matrix elements are derived in a similar way.

Electric and Magnetic Fields and the Poynting Vector

We assume that the collision occurs in the (x, z) -plane, with the initial projectile velocity parallel to the $+z$ -axis. The light detector (LD) is located at vector position \mathbf{r}_{LD} . We introduce two sets of coordinates to describe it: $(r_{\text{LD}}, \Theta'_{\text{LD}}, \Phi'_{\text{LD}})$ in a coordinate system where the z' axis is kept in the direction of $\mathbf{D}(t)$, and rotates with time (Θ'_{LD} is the angle between the dipole and the light detector) and $(r_{\text{LD}}, \Theta_{\text{LD}}, \Phi_{\text{LD}})$ in the Lab frame [Fig. 2(a)]. In Figure 2(b) we illustrate the dynamics of the oscillating dipole with the dipole orientation angle θ being defined as the angle between the z' and z -axes in the Lab frame.

In SI units, the electric \mathbf{E} and magnetic \mathbf{B} fields for the light emitted by the dipole are given by [19]

$$\mathbf{E}(\mathbf{r}_{\text{LD}}, t) = \frac{\mu_0}{4\pi r} [\mathbf{r}_{\text{LD}} (\mathbf{n}_r \cdot \ddot{\mathbf{D}}(t_r)) \mathbf{n}_r - \ddot{\mathbf{D}}(t_r)] \quad (17)$$

and

$$\mathbf{B}(\mathbf{r}_{\text{LD}}, t) = -\frac{\mu_0}{4\pi r_{\text{LD}} c} [\mathbf{n}_r \times \ddot{\mathbf{D}}(t_r)], \quad (18)$$

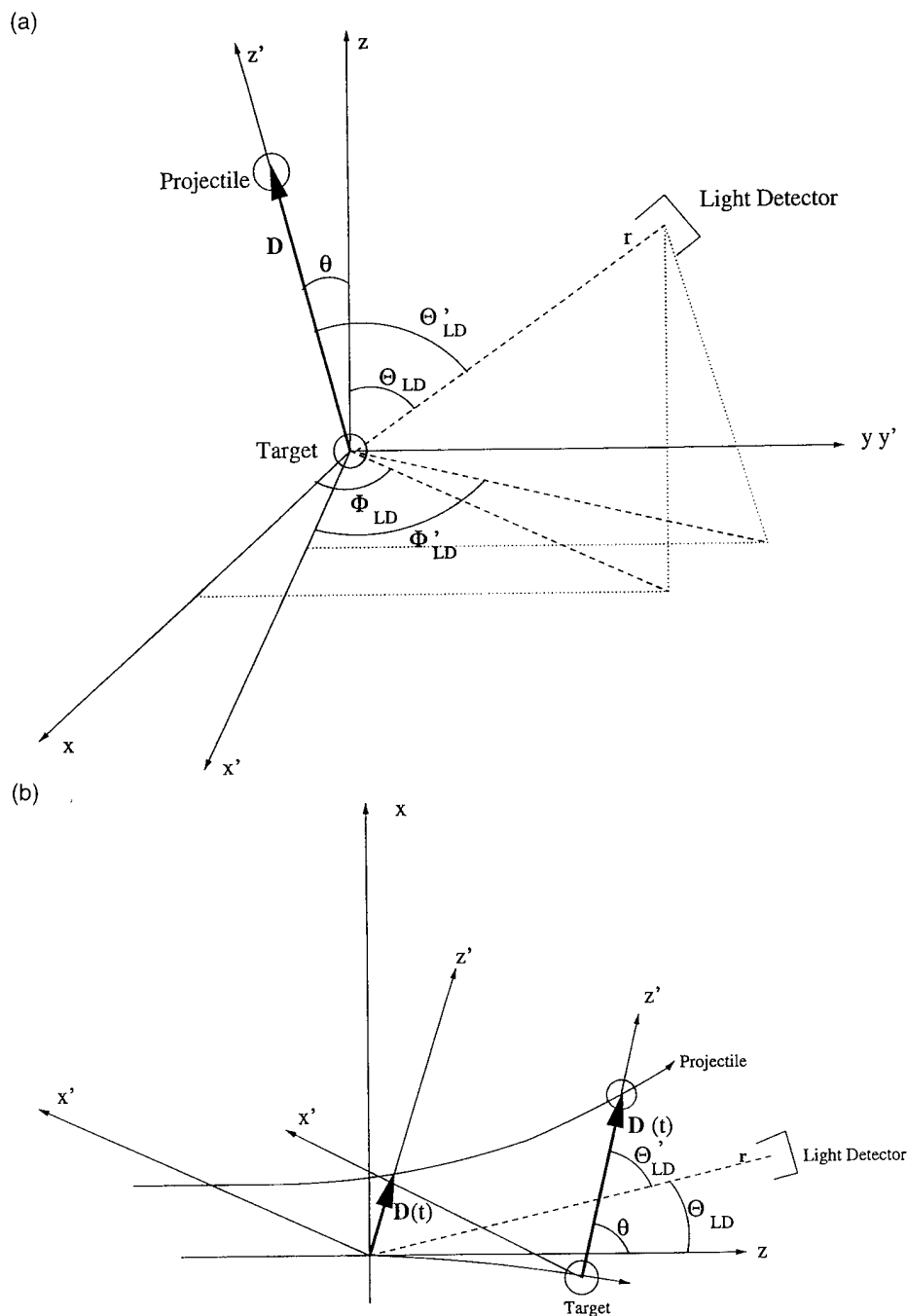


FIGURE 2. (a) Coordinate systems and light detector positions for proton-hydrogen-atom collisions; (b) similar to (a) including the nuclear trajectories.

where μ_0 is the permeability of free space, r_{LD} is the location of the light detector, $t_r = t - r_{LD}/c$ and $\mathbf{n}_r = \mathbf{r}_{LD}/r_{LD}$.

We express the total electric dipole as

$$\mathbf{D} = D_z \mathbf{n}_{z'}, \quad (19)$$

where

$$\mathbf{n}_{z'} = \cos(\Theta'_{LD}) \mathbf{n}_r - \sin(\Theta'_{LD}) \mathbf{n}_{\Theta'}, \quad (20)$$

with $\mathbf{n}_{\Theta'}$ the unit vector in the direction of increasing Θ'_{LD} .

Using Eqs. (19) and (20) we can rewrite \mathbf{E} and \mathbf{B} as

$$\mathbf{E}(\mathbf{r}_{\text{LD}}, t) = \frac{\mu_0}{4\pi} \ddot{D}(t_r) \left(\frac{\sin(\Theta'_{\text{LD}})}{r_{\text{LD}}} \right) \mathbf{n}_{\Theta'}, \quad (21)$$

$$\mathbf{B}(\mathbf{r}_{\text{LD}}, t) = \frac{\mu_0}{4\pi c} \ddot{D}(t_r) \left(\frac{\sin(\Theta'_{\text{LD}})}{r_{\text{LD}}} \right) \mathbf{n}_{\Phi'}, \quad (22)$$

with $\mathbf{n}_{\Phi'}$ the unit vector in the direction of increasing Φ'_{LD} .

Then the Poynting flux vector is given by

$$\begin{aligned} \mathbf{S}(\mathbf{r}_{\text{LD}}, t) &= \frac{1}{\mu_0} (\mathbf{E} \times \mathbf{B}) \\ &= \frac{\mu_0}{16\pi^2 c} [\ddot{D}(t_r)]^2 \frac{\sin^2(\Theta'_{\text{LD}})}{r_{\text{LD}}^2} \mathbf{n}_{\text{LD}}. \end{aligned} \quad (23)$$

We need \mathbf{S} in the Lab frame, where we use the coordinate system (x, y, z) . We find the detector angle Θ'_{LD} in the Lab frame in terms of the dipole orientation angle $\theta(t; b, v_p) = \arccos(D_z/D)$ (with $D^2 = D_x^2 + D_z^2$), and the detector angles Θ_{LD} and Φ_{LD} , by recognizing [from Fig. 2(a)] that

$$\begin{aligned} r_z &= r_{\text{LD}} \cos(\Theta_{\text{LD}}), \\ r_x &= r_{\text{LD}} \sin(\Theta_{\text{LD}}) \cos(\Phi_{\text{LD}}), \\ r_{z'} &= r_{\text{LD}} \cos(\Theta'_{\text{LD}}) = r_z \cos(\theta) + r_x \sin(\theta), \end{aligned} \quad (24)$$

yields

$$\begin{aligned} \cos(\Theta'_{\text{LD}}) &= \cos(\Theta_{\text{LD}}) \cos(\theta) \\ &+ \sin(\Theta_{\text{LD}}) \cos(\Phi_{\text{LD}}) \sin(\theta). \end{aligned} \quad (25)$$

Intensity and Polarization of Emitted Light

In this work we are interested in looking at the intensities and polarizations of light emitted by an oscillating dipole. The intensity of light emitted into solid angle $d\Omega_{\text{LD}}$ by a dipole component along $k = x, z$, for fixed impact parameter b and a nearby detector (with $r_{\text{LD}}/c \ll t$) is

$$\left(\frac{dI_k}{d\Omega_{\text{LD}}} \right)_b = \mathbf{S} \cdot \mathbf{n}_L r_L^2 = \frac{\mu_0}{16\pi^2 c} \ddot{D}_k(t)^2 \sin^2(\Theta'_{\text{LD}}). \quad (26)$$

Integration over $d\Omega_{\text{LD}}$, with

$$d\Omega_{\text{LD}} = \sin(\Theta_{\text{LD}}) d\Theta_{\text{LD}} d\Phi_{\text{LD}}, \quad (27)$$

yields

$$I_k(t; b, v_p) = \frac{1}{4\pi\epsilon_0} \frac{2[\ddot{D}_k(t; b, v_p)]^2}{3c^2}. \quad (28)$$

We obtain the energy E_k emitted per collision, for each polarization, by integrating over time the k polarization of the intensity of light emitted I_k :

$$E_k = \int I_k dt. \quad (29)$$

Results and Conclusion

We consider the case where the light has been collected over all angles and calculate the integrated intensity given by Eq. (29).

Figures 3 and 4 present results for I_x and I_z vs. time vs. impact parameter for protons of energy 10.0 eV. Figures 5 and 6 present similar results for 100.0 eV. The lowest b value shown is $b = 0.1$ a.u., and the others are multiples of 0.5 a.u.

From Figures 3 and 4, we observe that the x polarization (perpendicular to the velocity of the incoming proton) of the intensity of emitted light integrated over time goes through a maximum for impact parameters b around 1.0 a.u. and has a very small value for head-on collisions near $b = 0.0$ a.u. The integrated intensity with z polarization (parallel to the incoming proton velocity) is on the other hand largest at $b = 0$, and then falls with increasing b values. The light emitted over time is found to appear only during the collision and lasts about 400 a.u. or about 10 fs. Figures 5 and 6 show similar dependences with impact parameter and time, but the duration of light emission is shorter, as we would expect for a faster collision, and show transient emission lasting about 2.5 fs.

To obtain the magnitudes of the transient emission, we calculated the average total light energy emitted per collision for the impact parameters of 1.0 and 1.5 a.u. by integrating over time. Results are presented in Table I, for the x and z polarizations and also for their sum. Our calculations, done in atomic units, have been converted to Joules per mole to give an estimate of the amount of energy emitted at each impact parameter. This corresponds to a given deflection angle into the detector, and would have to be integrated over

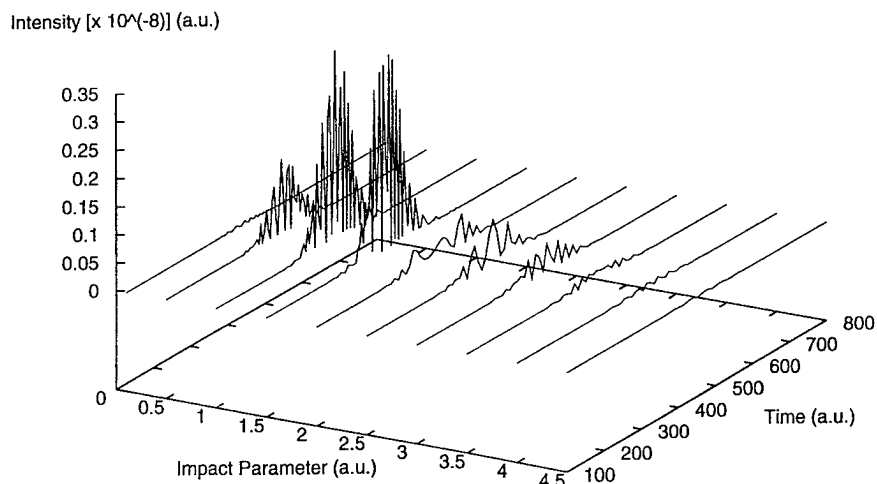


FIGURE 3. The x component of the intensity vs. time vs. impact parameter for $H^+ + H(1s)$ collisions for a collision energy of 10 eV.

angles to obtain the total light energy emitted over all angles for all times. For a single trajectory, we find that the magnitude of light emission appears to go through a maximum as collision energy increases from 10 to 1000 eV; this is observed for the two impact parameters we include in Table I and appears to be a general feature of the transient emission. The values in Table I can be used to estimate the number of emitted photons at each energy. For typical light emission energy of 1 J/mol and photon energy of 4 eV = 6.40×10^{-19} J, the number of photons emitted by 1 mol of $H + H^+$ would be 1.56×10^{18} . A beam-gas experiment at

one of the given energies and impact parameters would give a somewhat lower number of photons, while in a crossed-beam experiment the number would be much lower; but in any case it appears to us that there would be enough emitted photons to experimentally detect the transient emission.

In conclusion, we have characterized the nature of transient light emission with a computational approach which proved before to be reliable for collisional properties. Light emission following ion-atom collisions has been observed and measured before, but to our knowledge it has not been studied at our low collisions energies, for which

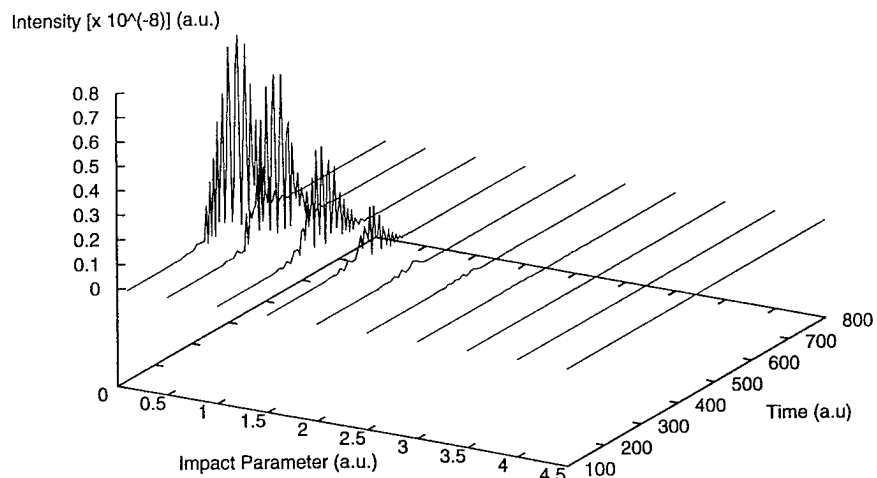


FIGURE 4. Similar to Fig. 3 for the z component.

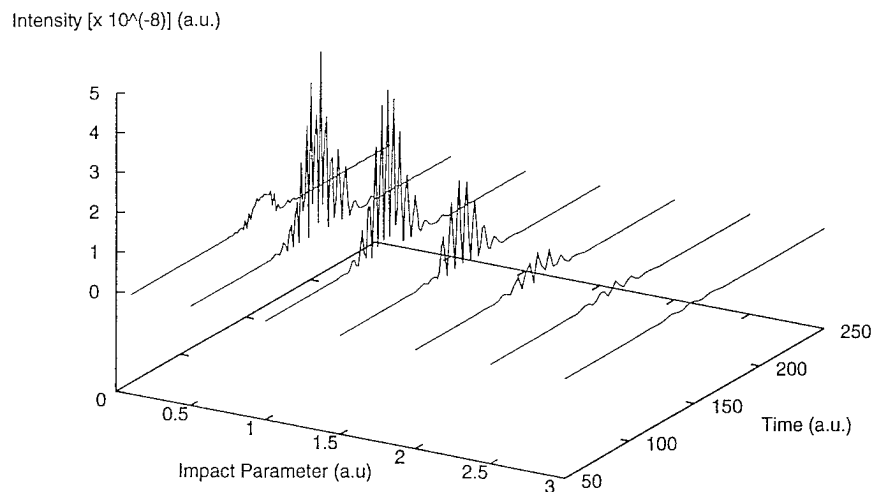


FIGURE 5. The x component of the intensity vs. time vs. impact parameter $H^+ + H(1s)$ collisions for a collision energy of 100 eV.

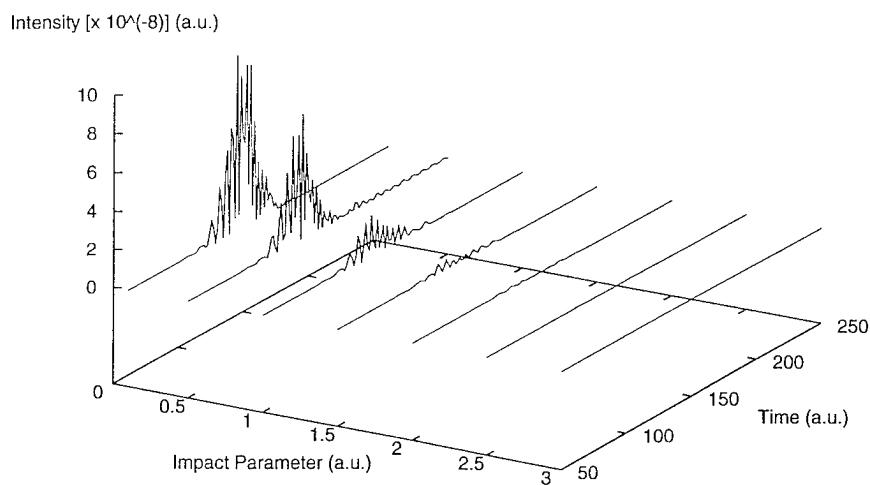


FIGURE 6. Similar to Fig. 5 for the z component.

TABLE I

Light energy emitted per collision for $H^+ + H(1s)$ collisions for impact parameters $b = 1.0$ a.u. and $b = 1.5$ a.u., integrated over time.

Impact parameter (a.u.)	Emission energy (J/mol)	Collision energies				
		(10 eV)	100 eV	500 eV	700 eV	1000 eV
1.0	E_x	0.460	1.578	0.402	0.335	0.393
	E_z	0.578	0.890	0.834	0.758	0.692
	$E_x + E_z$	1.038	2.468	1.236	1.093	1.085
1.5	E_x	0.514	0.889	0.361	0.298	0.271
	E_z	0.227	0.288	0.309	0.310	0.306
	$E_x + E_z$	0.741	1.177	0.670	0.608	0.577

repeated electron transfer is present. Light emission due to polarization of target or projectile atoms in slow collisions has been theoretically studied before and has been labeled atomic bremsstrahlung [20]. Light emission in our case comes instead not from transient atomic states but from transient molecular states resulting from the temporary sharing of electrons, and therefore has a different distribution of intensities over time and wavelengths. The present study indicates that transient light emission should appear in many collision phenomena involving electronic rearrangement, and provides an estimate of the properties of the emitted light.

ACKNOWLEDGMENTS

This work has been supported by grants from the U.S. National Science Foundation and the Office of Naval Research.

References

1. R. McCarroll, in *Atomic and Molecular Collision Theory*, F. A. Gianturco, Ed. (Plenum, New York, 1980), Ch. 2.
2. T. G. Winter, C. M. Dutta, and N. F. Lane, *Phys. Rev. A* **31**, 2702 (1985).
3. J. D. Garcia, *Nuclear Instr. Meth. Phys. Res. A* **240**, 552 (1985).
4. C. Harel and A. Salin, in *Electronic and Atomic Collisions*, H. B. Gilbody et al., Eds. (Elsevier, Amsterdam, 1988), p. 631.
5. M. Kimura and N. F. Lane, *Adv. At. Mol. Opt. Phys.* **26**, 79 (1990).
6. W. Fritsch and C. D. Lin, *Phys. Rep.* **202**, 1 (1991).
7. B. H. Bransden and M. R. C. McDowell, *Charge Exchange and the Theory of Ion-Atom Collisions* (Oxford University Press, New York, 1992).
8. B. Gazdy and D. A. Micha, *Phys. Rev. A* **36**, 546 (1987).
9. K. Runge, D. A. Micha, and E. Q. Feng, *Int. J. Quantum Chem. Symp.* **24**, 781 (1990).
10. K. Runge, Ph. D. Dissertation, University of Florida, (1993).
11. D. A. Micha, *Intern. J. Quantum Chem.* **51**, 499 (1994).
12. D. A. Micha and K. Runge, *Phys. Rev. A* **50**, 322 (1994).
13. K. Runge and D. A. Micha, *Phys. Rev. A* **53**, 1388 (1996).
14. D. A. Micha, K. Runge, and H. F. M. DaCosta, *Chem. Phys. Lett.*, **256**, 321 (1996).
15. B. Zygelman, A. Dalgarno, M. Kimura, and N. F. Lane, *Phys. Rev. A* **40**, 2340 (1989).
16. P. C. Stancil, J. F. Babb, and A. Dalgarno, *Astrophys. J.* **414**, 672 (1993).
17. D. A. Micha and K. Runge, *Chem. Phys. Lett.* **238**, 132 (1995).
18. W. J. Hehre, R. Ditchfield, R. F. Stewart, and J. A. Pople, *J. Chem. Phys.* **52**, 2769 (1970).
19. D. J. Griffiths, *Introduction to Electrodynamics*, 2nd ed. (Prentice-Hall, Englewood Cliffs, NJ, 1989) Ch. 9.
20. M. Ya. Amusia, *Phys. Rep.* **162**, 249 (1988).

Hybrid Quantum/Classical Studies of Photodissociation and Recombination of $I_2(A)$ in Rare Gas Matrices: A Linear Chain Model

HUA GUO* AND LI LIU

Department of Chemistry, University of Toledo, Toledo, OH 43606: e-mail for H. G.:
hguo@uoft02.utoledo.edu

Received February 24, 1996; revised manuscript received April 1, 1996; accepted April 3, 1996

ABSTRACT

A hybrid quantum/classical model is developed for the photodissociation and recombination dynamics of an I_2 molecule in low-temperature rare-gas (Rg) matrices. The simplified model consists of an I_2 molecule embedded in a linear chain of Rg atoms. The aggregate is partitioned into a quantum system and a classical bath, which are self-consistently coupled. Two partitioning schemes are used. The first treats the I-I coordinate quantum mechanically and the Rg coordinates classically. The second and more reliable scheme includes in the quantum system both the I-I mode and the symmetric motion of the two nearest Rg atoms. Both models show substantial energy transfer from the dissociating I_2 to the solvent, followed by coherent vibrational motion of the recombined I_2 . It is found that the one-dimensional quantum/classical scheme is consistent with its higher dimensional counterpart, although the latter shows much faster dephasing. © 1996 John Wiley & Sons, Inc.

1. Introduction

In many extended systems, a complete quantum-mechanical characterization of dynamics is formidable and often unnecessary. However, there is ample evidence indicating that a pure

classical treatment is not always sufficient. To address this dilemma, it is common to partition the aggregate into a system and the surrounding bath [1]. The system is usually defined as a collection of several modes where the primary dynamics takes place, while the bath consists of the less involved modes coupled to the system. Such a separation represents a good approximation when the system and bath are weakly coupled and when their frequencies are significantly different.

* To whom correspondence should be addressed.

A commonly used formulation of the system-bath separation is the so-called hybrid classical/quantum scheme [2]. In this method, the dynamics of the system is described by a quantum wave packet while that of the bath is by classical trajectories. The system and the bath are coupled self-consistently via the Ehrenfest theorem [3]. Namely, the system is subjected to an instantaneous mean-field determined by the bath and vice versa. Energy exchange between the system and bath is allowed, albeit indirectly. This approach focuses on the primary dynamics in the system without neglecting the influence of the bath. It is numerically efficient and amenable to large and weakly coupled systems.

It should be realized that the aforementioned scheme can be considered as the quantum/classical version of the so-called time-dependent Hartree (TDH) or self-consistent field (TDSCF) approximation [2, 4–6], in which the total wave function is assumed to be separable. Thus, the hybrid method inherits the deficiencies of the TDH approximation, in addition to the classical approximation. A major concern [7] of the hybrid approach is the separability of the quantum-classical subsystems. In this work, we attempt to address this issue in a well-defined simple system, i.e., the photodissociation and recombination of I_2 in a linear rare-gas (Rg) matrix.

II. Linear Chain Model

In this work, we are primarily concerned with the photodissociation and recombination of I_2 embedded in a cryogenic rare-gas (Kr) matrix. This system (I_2 -solvent) has been extensively investigated and served as a prototype for condensed phase bond breaking processes [8]. With a femtosecond pump/probe scheme, coherent vibrational motion of the recombined I_2 has been observed for a few picoseconds after the initial excitation to the A state [9, 10]. Experimental evidence also indicated that the caging of I_2 in its A state is complete. Our simplified model [11–13] used here is loosely based on the I_2 -Rg system. In this so-called linear chain (LC) model, an I_2 molecule is embedded in a one-dimensional aggregate of 100 rare-gas atoms, as shown in Figure 1. The LC model is expected to be a reasonable approximation for the short-time dynamics because the rota-

tion of the I_2 moiety is very slow [14]. On the other hand, the neglect of solvent atoms in three dimensions renders the LC model a qualitative one. Thus, no direct comparison with experiments is attempted. The I - I interaction potentials for the X and A states are given in the Morse form while the I -Rg and Rg-Rg interactions are represented by Lennard-Jones 6–12 potentials. Only the nearest interactions are included in the model. The parameters of the potentials are given elsewhere [13]. The potentials of the I_2 system are displayed in Figure 1.

III. Hybrid Quantum/Classical Methods

In order to facilitate a direct comparison between the two quantum/classical models used here, we restrict ourselves to a matrix temperature of 0 K. Under such idealized conditions, the I_2 center-of-mass motion can be ignored and the rare-gas atoms oscillate symmetrically relative to the center of the chain. It has been shown previously that the dynamics at a finite but low temperature does not change qualitatively [12].

The hybrid quantum/classical approach considers the total Hamiltonian as the sum of terms representing the system, the bath, and the interaction between them:

$$H = H_s + H_b + H_{sb} \quad (1)$$

The quantum wave packet of the system is the solution of the time-dependent Schrödinger equation, which can be written for a two-state problem as follows ($\hbar = 1$):

$$i \frac{\partial}{\partial t} \begin{bmatrix} \varphi_1 \\ \varphi_2 \end{bmatrix} = \begin{bmatrix} H_{s1}^{\text{eff}} & H_{12} \\ H_{21} & H_{s2}^{\text{eff}} \end{bmatrix} \begin{bmatrix} \varphi_1 \\ \varphi_2 \end{bmatrix}, \quad (2)$$

where φ_i ($i = 1, 2$) represent the nuclear wave functions on the two adiabatic electronic surfaces corresponding to the X and A states, respectively. The off-diagonal terms in the Hamiltonian matrix denote radiative couplings responsible for the excitation, which are modeled in this work by a short temporal function with a central frequency:

$$H_{12} = H_{21}^* = A e^{-\gamma t^2} e^{i\omega t}. \quad (3)$$

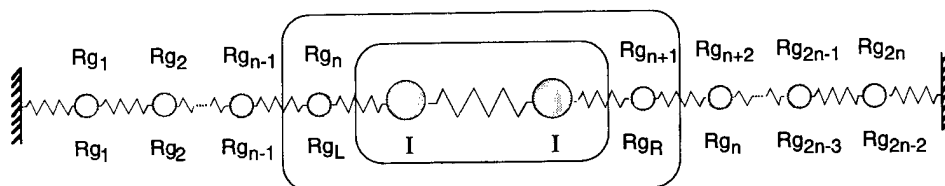
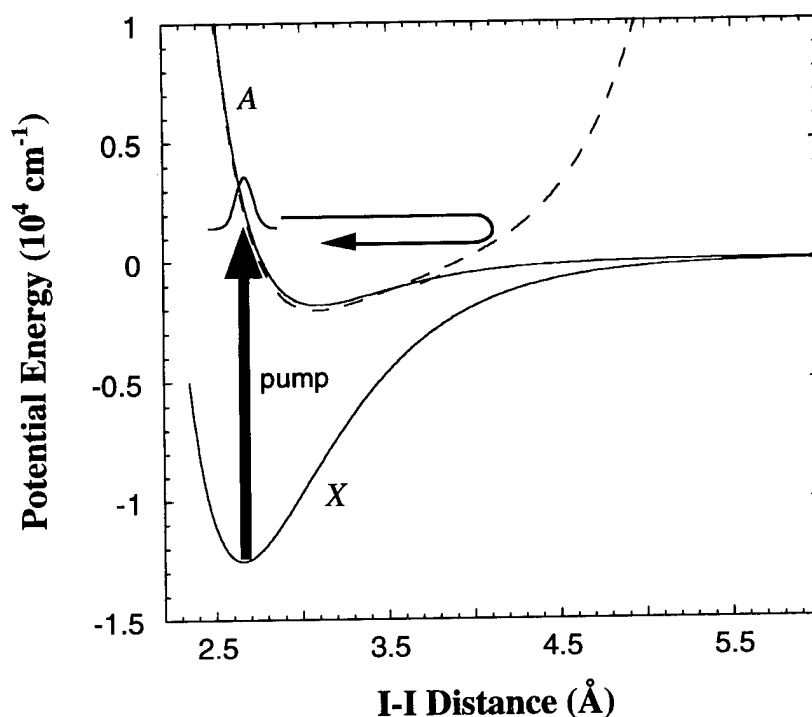


FIGURE 1. Upper panel: one-dimensional potential energy curves for the I-I coordinate. The pump scheme is indicated by a vertical bold arrow. The presence of the solvent wall (dashed line) prevents complete dissociation. Lower panel: geometry of the linear chain model for I_2 embedded in rare-gas (Rg) atoms. The two boxes indicate the quantum system in the two hybrid quantum/classical schemes used in this work. The upper labels are for the 1DQ/C model and lower ones are for the 2DQ/C model.

The equations of motion for the classical bath are given below in Hamilton's form:

$$\frac{dq_i}{dt} = \frac{\partial H_b^{\text{eff}}}{\partial p_i}, \quad \frac{dp_i}{dt} = -\frac{\partial H_b^{\text{eff}}}{\partial q_i}. \quad (4)$$

The system is initially on the ground state and the excitation occurs in the time span of the excitation pulse. The quantum wave packet of the system is propagated using a short iterative Lanczos method [15]. The fast Fourier transform method [15] is used to evaluate the action of the Hamiltonian. The classical equations are solved using the

velocity Verlet method [16]. The quantum and classical equations of motion are integrated simultaneously. The self-consistent propagation allows energy flow between the quantum and classical modes.

A. ONE-DIMENSIONAL QUANTUM/CLASSICAL (1DQ/C) MODEL

In this model, only the dynamics along the I-I internuclear distance is treated quantum mechanically and the rare-gas atoms are described classically. The quantum system is illustrated in the lower panel of Figure 1 by the inner box. The

Hamiltonians for the system, the bath, and the system/bath interaction are given below:

$$\mathbf{H}_s = \frac{P_X^2}{2\mu_{I-I}} + V_{I-I}(X), \quad (5a)$$

$$\mathbf{H}_b = \sum_{i=1}^{100} \frac{p_i^2}{2m} + V_b(q), \quad (5b)$$

$$\mathbf{H}_{sb} = 2V_{I-Rg}(X, q), \quad (5c)$$

where m and μ_{I-I} are the mass of Rg and the reduced mass of I_2 , respectively. The quantum degree of freedom X is the I-I internuclear distance while the collective bath coordinate q denotes the classical displacements of the 100 Rg atoms in the matrix. The effective Hamiltonians for the system and the bath are given below:

$$\mathbf{H}_s^{\text{eff}} = \frac{P_X^2}{2\mu_{I-I}} + V_{I-I}(X) + 2\langle V_{I-Rg}(X, q) \rangle_q, \quad (6a)$$

$$\mathbf{H}_b^{\text{eff}} = \sum_{i=1}^{100} \frac{p_i^2}{2m} + V_b(q) + 2\langle V_{I-Rg}(X, q) \rangle_X. \quad (6b)$$

For the quantum system, the mean-field potential is determined by the instantaneous positions of the classical particles in the bath (q). For the bath particles, however, the effective potential is averaged over the quantum mode according to the Ehrenfest theorem [3]:

$$\langle V_{I-Rg}(X, q) \rangle_X = \int_0^\infty dX \varphi^*(X, t) V_{I-Rg}(X, q) \varphi(X, t). \quad (7)$$

The mean-field potential is only calculated for the excited state.

B. TWO-DIMENSIONAL QUANTUM/CLASSICAL (2DQ/C) MODEL

In this more elaborate model, the symmetric motion of the two rare-gas atoms nearest to the I_2 moiety is included in the quantum system, as shown by the outer box in the lower panel of Figure 1. The classical bath includes all the remaining rare-gas atoms. The corresponding Hamiltonians are

$$\mathbf{H}_s = \frac{P_X^2}{2\mu_{I-I}} + \frac{P_Y^2}{2\mu_{Rg-Rg}} + V_{I-I}(X) + 2V_{I-Rg}(X, Y), \quad (8a)$$

$$\mathbf{H}_b = \sum_{i=1}^{98} \frac{p_i^2}{2m} + V_b(q'), \quad (8b)$$

$$\mathbf{H}_{sb} = 2V_{Rg-Rg'}(Y, q'), \quad (8c)$$

where $Y = q_R - q_L$ (q_R and q_L are the displacements of the two rare-gas atoms nearest to the I_2 moiety) and $\mu_{Rg-Rg'}$ is the corresponding reduced mass. Note that in this model the bath has 98 atoms and the system-bath interaction is between two solvent atoms (Rg-Rg'). Similarly, the effective Hamiltonians for the system ($I_2 \cdot Rg_2$) and the bath (98 Rg') are

$$\mathbf{H}_s^{\text{eff}} = \frac{P_X^2}{2\mu_{I-I}} + \frac{P_Y^2}{2\mu_{Rg-Rg}} + V_{I-I}(X) + 2V_{I-Rg}(X, Y) + 2\langle V_{Rg-Rg'}(Y, q') \rangle_{q'} \quad (9a)$$

$$\mathbf{H}_b^{\text{eff}} = \sum_{i=1}^{98} \frac{p_i^2}{2m} + V_b(q') + 2\langle V_{Rg-Rg'}(Y, q') \rangle_{X, Y}. \quad (9b)$$

Note that the I-Rg interaction is explicitly taken into account in the system Hamiltonian. The effective potentials are treated in a similar manner to the 1DQ/C system. For example, the mean-field potential for the classical bath is as follows:

$$\begin{aligned} \langle V_{Rg-Rg'}(Y, q') \rangle_{X, Y} &= \int_0^\infty dX \int_0^\infty dY \varphi^*(X, Y, t) \\ &\quad \times V_{Rg-Rg'}(Y, q') \varphi(X, Y, t), \end{aligned} \quad (10)$$

where Rg denotes a rare gas atom in the system and Rg' its nearest neighbor in the bath.

The idea of explicitly including in the system some strongly coupled bath modes is not entirely new [17, 18]. The 2DQ/C model proposed here removes some crucial deficiencies in the 1DQ/C model. It treats the dynamics between the I_2 and its adjacent rare-gas atoms exactly and quantum mechanically. The 2DQ/C method is thus expected to yield much more reliable results and serves here as a benchmark to assess the validity of the 1DQ/C model.

IV. Results

We concentrate here on the comparison between the 1DQ/C and 2DQ/C models for the I_2 -Kr₁₀₀

system. A 734-nm laser pulse with a width of 100 fs is used to excite the system from its ground state to the excited A state. Figure 2 displays the averaged I-I distance (a) and the energy (b) of the system calculated from the two models. Starting at the ground-state equilibrium geometry (~ 2.8 Å), the I-I distance increases rapidly during the initial phase of dissociation, owing to the strong repulsive potential of the A state. It quickly reaches its maximum at ~ 4.2 Å in a few hundred femtoseconds. Because of the "cage effect," however, the dissociation of I_2 is blocked by the solvent. Subsequently, the I_2 moiety oscillates near a new equilibrium geometry. The agreement between the 1DQ/C and 2DQ/C models, as shown by Figure 2(a), is generally satisfactory. Quantitatively, the 2DQ/C model (dotted line) shows stronger and more regular oscillations in the first 1 ps and more pronounced dephasing at long times (> 2 ps). The dephasing can be attributed to the diffusive wave packet in the two-dimensional phase space [13].

The caging of the highly energetic fragments is accompanied by drastic energy transfer from the

fragments to the solvent atoms. It can be seen from Figure 2b that the energy loss in the 1DQ/C model occurs in the first ~ 300 fs. It takes a little longer to achieve similar energy loss in the 2DQ/C model because the system now includes two neighboring Kr atoms. Quantitatively, the amount of energy transferred to the bath is somewhat larger in the 2DQ/C model (dotted line). This difference may be attributed to the inclusion of the I-Rg interaction in the quantum system, which provides a better description of the energy transfer from I_2 to its adjacent Rg atoms. Concurrent with the I_2 energy loss, the energy of the rare-gas matrix increases (not shown here) and the total energy (system plus bath) is conserved. The kinetic energy of the rare-gas atoms is propagated outward in the solvent chain as a shock wave [11–13]. After the initial energy loss due to the fragment-solvent collision, further vibrational relaxation becomes less efficient due to the oversimplification of the LC model.

Similar observations have been obtained in three-dimensional classical molecular dynamics studies of the same system by Martens and co-workers [9, 10]. However, it should be pointed out that the quantum coherence, which stems from the interference between coherently populated vibrational states, is fundamentally different from the classical vibrational oscillation. The retention of the vibrational coherence after significant energy transfer is due to the impulsive nature of the collision and to the low temperature of the matrix.

The wave packet motion in the I-I degree of freedom is presented for the two models in Figure 3. In the 2DQ/C model, the one-dimensional reduced density is defined as follows:

$$\varphi^2(X, t) = \int dY \varphi^*(X, Y, t) \varphi(X, Y, t). \quad (11)$$

Overall, the two methods give qualitatively similar results, even at very long times (~ 2 ps). In order to quantitatively compare the two models, we calculate the overlap between the moduli of the two wave packets:

$$S = \frac{\langle |\varphi^{1DQ/C}| |\varphi^{2DQ/C}| \rangle}{\sqrt{\langle \varphi^{1DQ/C} | \varphi^{1DQ/C} \rangle \langle \varphi^{2DQ/C} | \varphi^{2DQ/C} \rangle}}, \quad (12)$$

where the modulus is defined as

$$|\varphi^{2DQ/C}| = \sqrt{\varphi^2}. \quad (13)$$

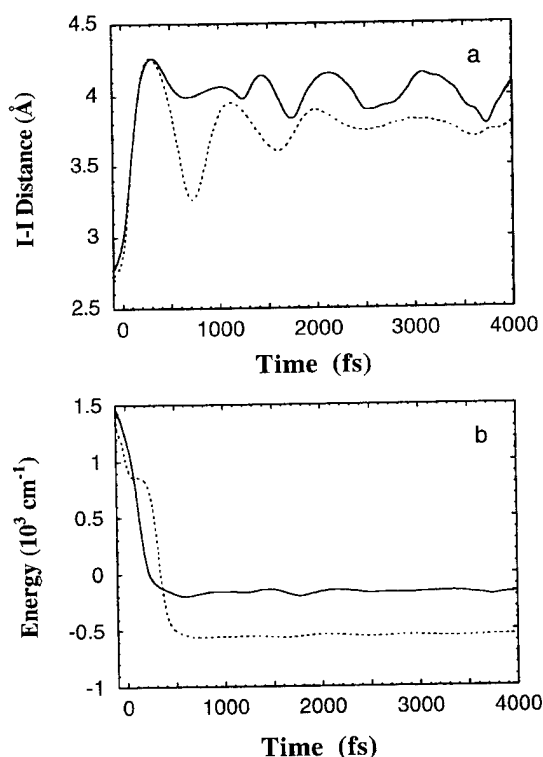


FIGURE 2. Averaged I-I distance (a) and averaged energy of the system (b) as a function of time. The solid and dotted lines are the 1DQ/C and 2DQ/C models, respectively.

The denominator in Eq. (12) is used to normalize the wave functions in both models. This is necessary because the population on the *A* state is not normalized and is a function of time during pumping. Since we are primarily interested in the dynamics in coordinate space, rather than in energy space, the phase factors of the wave packets are

ignored. The overlap is displayed in Figure 4. At the center of the pump pulse ($t = 0$), the overlap between the two models is very close to unity. Subsequently, the overlap deteriorates as the collision between the iodine fragments and the nearby rare-gas atoms takes place. It recovers near 1300 fs where the wave packet again reaches the outer

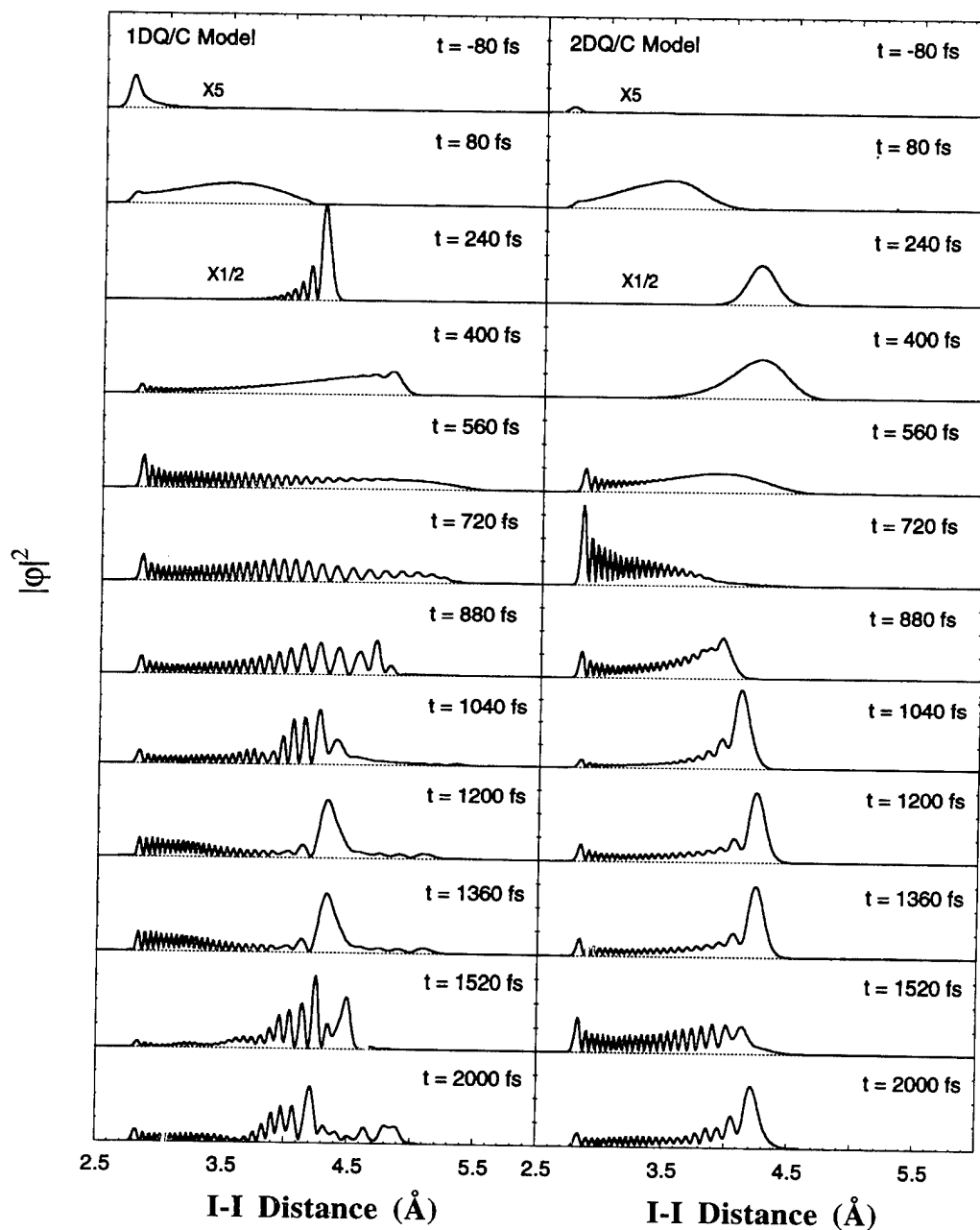


FIGURE 3. Snapshots of the I-I wave packet motion of the I_2-Kr_{100} system for the 1DQ/C and 2DQ/C models.

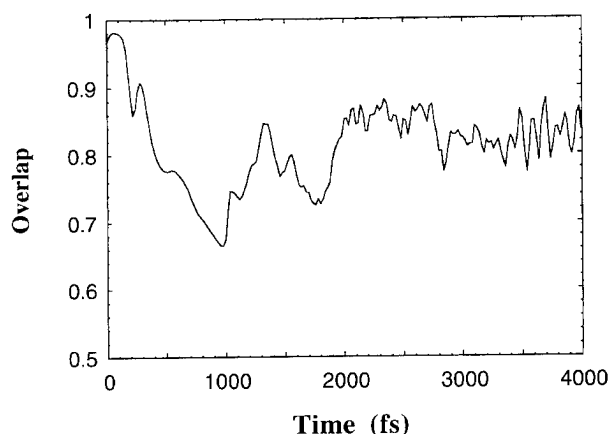


FIGURE 4. Overlap between the moduli of the wave packets for the two models (see text).

turning point. Beyond 2000 fs, the overlap between the 1DQ/C and 2DQ/C models becomes stabilized near $\sim 80\%$.

The above comparison of the two models clearly illustrates that the validity of the 1DQ/C model depends very much on the type of quantities to be extracted from the dynamics. The 1DQ/C model is certainly capable of capturing some major dynamical features of the dissociation-recombination process, such as the impulsive energy transfer between the dissociating fragments and the solvent atoms and the retention of the vibrational coherence after the collision. However, it fails to describe the destruction of the coherence on a relatively long time scale. This failure of the 1DQ/C model in this aspect can be directly related to the mean-field approximation that restricts the I-I wave packet to one dimension.

V. Conclusions

In this work, we have examined the validity of the hybrid quantum/classical methodology in studying the photodissociation and recombination dynamics of I_2 in rare-gas matrices. The validity of the system-bath separation is explored by two models within the linear chain approximation. The simpler model (1DQ/C) treats the I-I coordinate quantum mechanically and the remaining bath modes classically. This method is often used in condensed phase systems. The more sophisticated model (2DQ/C) includes in the system both the I-I mode and the symmetric mode of the two

adjacent rare-gas atoms. It provides a better representation of the dynamics because of the exact treatment of the I-Rg interaction.

The 1DQ/C model is shown to reproduce the significant energy transfer between the dissociating fragments and the solvent atoms. It also shows coherent wave packet motion after the energy transfer. However, this model gives a relatively poor representation of the dephasing process. Overall, the 1DQ/C model appears to provide a reasonably accurate representation of the short-time dynamics.

The hybrid quantum/classical method based on the time-dependent Hartree approximation combines a quantum treatment of the system with an approximated classical characterization of the bath. When applied prudently, it represents an efficient and useful tool in studying chemical processes with large dimensionalities. It should, however, be borne in mind that this method involves a number of potentially fatal approximations. It works best when the system-bath coupling is weak and the mass of the bath atoms is heavy. Its validity deteriorates with time so that the long-time dynamics is unreliable. Highly averaged attributes are usually more trustworthy than state-resolved quantities.

ACKNOWLEDGMENTS

This work was supported by the donors of Petroleum Research Fund, administered by American Chemical Society, and by the National Science Foundation (CHE-9411934).

References

1. R. P. Feynman and A. P. Hibbs, *Quantum Mechanics and Path Integrals* (McGraw-Hill, New York, 1965).
2. R. B. Gerber, V. Buch, and M. A. Ratner, *J. Chem. Phys.* **77**, 3022 (1982).
3. G. D. Billing, *Comp. Phys. Rep.* **1**, 237 (1984).
4. P. A. M. Dirac, *Proc. Cambridge Philos. Soc.* **26**, 376 (1930).
5. J. Frenkel, *Wave Mechanics* (Oxford University Press, Oxford, 1934).
6. A. D. McLachlan, *Mole. Phys.* **8**, 39 (1964).
7. K. Haug and H. Metiu, *J. Chem. Phys.* **97**, 4781 (1992).
8. A. L. Harris, J. K. Brown, and C. B. Harris, *Ann. Rev. Phys. Chem.* **39**, 341 (1988).
9. R. Zadoyan, Z. Li, P. Ashjian, C. C. Martens, and V. A. Apkarian, *Chem. Phys. Lett.* **218**, 504 (1994).

10. R. Zadoyan, Z. Li, C. C. Martens, and V. A. Apkarian, *J. Chem. Phys.* **101**, 6648 (1994).
11. L. Liu and H. Guo, *Chem. Phys. Lett.* **237**, 299 (1995).
12. L. Liu and H. Guo, *J. Chem. Phys.* **103**, 7851 (1995).
13. L. Liu and H. Guo, *J. Chem. Phys.* **104**, 528 (1996).
14. M. Messina and R. D. Coalson, *J. Chem. Phys.* **90**, 4015 (1989).
15. R. Kosloff, *J. Phys. Chem.* **92**, 2087 (1988).
16. M. P. Allen and D. J. Tildesley, *Computer Simulation of Liquids* (Oxford University, Oxford, 1986).
17. N. Makri, *Chem. Phys. Lett.* **169**, 541 (1990).
18. B. Vekhter, M. A. Ratner, and R. B. Gerber, *J. Chem. Phys.* **99**, 7916 (1993).

Fourier Space for Accurate Ab Initio RHF Band Structure Calculations on Chainlike Systems

I. FLAMANT, J. G. FRIPIAT, AND J. DELHALLE*

Laboratoire de Chimie Théorique Appliquée, Facultés Universitaires Notre-Dame de la Paix, 61, rue de Bruxelles, B-5000 Namur, Belgium; e-mail for J. D.: joseph.delhalle@fundp.ac.be

Received February 24, 1996; accepted February 24, 1996

ABSTRACT

Minimal basis-set (STO-3G) direct and Fourier space restricted Hartree–Fock (RHF) calculations on the infinite regular (metallic) and alternating chains of lithium molecules, $(-\text{Li}_2^-)_x$, are reported to illustrate two advantages of the Fourier representation method: accurate calculation of all lattice summations and faithful reproduction of the genuine features of the RHF approach for metallic cases. © 1996 John Wiley & Sons, Inc.

Introduction

Restricted Hartree–Fock (RHF) linear combination of atomic orbitals (LCAO) calculations on extended chains with one-dimensional periodicity [1] have become routine. Most of the numerical and algorithmic difficulties associated with the study of these systems are understood now (basis-set extension and possible linear dependencies, lattice summations, self-consistent field (SCF) convergence, computational effort, etc.) and, if not yet fully controllable, the possible negative effects on the quality of the results have been

pointed out. It is interesting to note that essentially all practical calculations in this area are carried out in the configuration or direct space (DS) approach.

In the DS approach, the Coulomb and exchange contributions are treated on a different footing [2]. The Coulomb (Madelung) sums are computed generally using a multipole expansion of the two-electron integrals in the asymptotic regime of small overlap of the interacting charge distributions. The convergence of the summations of the exchange contributions is fixed by the decay of the LCAO-density matrix elements making the implementation of a multipole expansion-based algorithm more difficult. At present, the exchange lattice summations are still evaluated on a trial-and-error basis by repeated calculations with varying numbers of interacting cells to assess the convergence.

*To whom correspondence should be addressed.

If acceptable in the case of insulators and semiconductors, the procedure cannot be applied realistically to systems characterized by partial band occupancy. Indeed, to reproduce the genuine features of the HF description of the metallic situation [3] (notwithstanding its physically undesirable character) the number of interacting cells to be taken into account would be prohibitively expensive. This surely explains that the vast majority of the reported applications are on insulators and semiconductors.

The Fourier space (FS) representation [4] is a promising direction to investigate for the evaluation of both the Coulomb and exchange lattice sums on a consistent basis. Very recently, it has been shown that combining the Poisson summation formula and the Ewald method in the context of gaussian basis sets [5] can be used to compute accurately these summations. Practical implementation, however, requires the development of efficient algorithms for the two-electron integrals. The purpose of this work is to compare the results obtained for the linear chain of lithium molecules treated in a basis of *s*-type gaussian functions by the FS and DS approaches.

The article is planned as follows: In the theoretical section the model system is described briefly. Also introduced in this section are the basic RHF equations that will be needed and some numerical aspects to help in appraising the difference between the DS and FS methods. In the result section we compare numerical results on the lithium chains obtained with both approaches. The work ends with a few remarks on future developments.

Theoretical Considerations

MODEL SYSTEM

The model system used for the present comparison is the linear chain of lithium molecules with n_e ($n_e = 6$) electrons per unit cell distributed along the *z* axis, which is chosen as the direction of periodicity (Fig. 1). The interatomic distance in the unit cell is kept fixed and is equal to 5.5 a.u., which is close to the *ab initio* HF value (5.52 a.u.) obtained for the Li_2 molecule with the STO-3G basis set using the Gaussian 92 program [6]. In this work three values of the unit cell length a_0 have been considered, 11.0, 12.0 and 13.0 a.u., to cover situations ranging from an even distribution of atoms to cases of increasing alternancy. In a RHF description it must be pointed out that to a $(-\text{Li}_2-)_x$ chain with equidistant atoms does not correspond the metallic situation, but the symmetry broken solution. Accordingly, the band structures for the three values of a_0 will all exhibit a gap at the edge of the Brillouin zone.

The DS calculations have been performed with the PLH program [2] and the calculations in FS using a new prototype program, FTCHAIN. In all cases, the criterion for convergence of the iterative SCF procedure on the density matrix elements is set equal to 10^{-6} . Calculations have been carried out using two atomic *s* functions on each atom, each function described by three gaussians to mimic Slater functions of exponents $\zeta_{1s} = 2.69$ and $\zeta_{2s} = 0.65$ [7]. It must be pointed out that this fairly localized minimal basis set has been selected on purpose to guarantee everywhere reliability

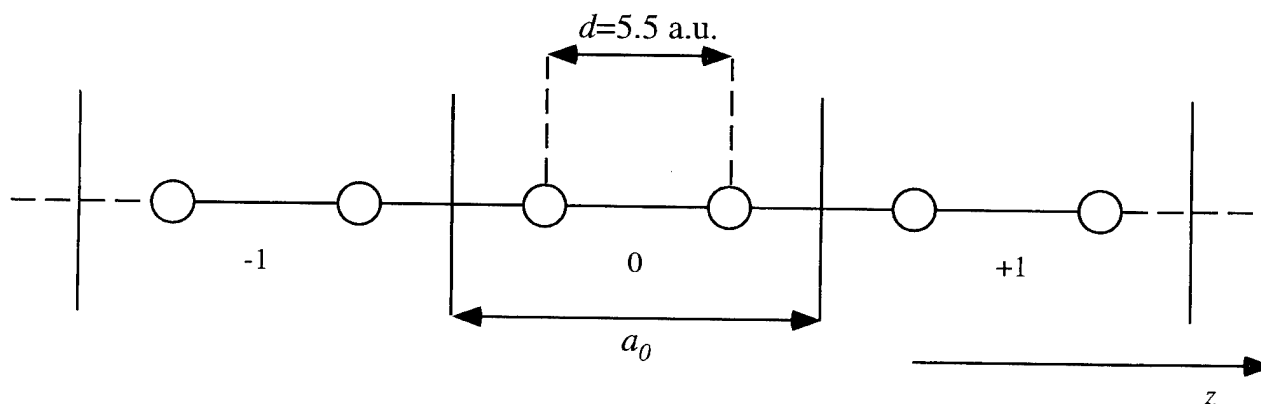


FIGURE 1. Schematic picture of the infinite chains of lithium molecules, $(-\text{Li}_2-)_x$, considered in this work. The values of a_0 , the unit cell length, are 11.0, 12.0, and 13.0 a.u. The interatomic distance in the unit cell, d , is equal to 5.5 a.u. The *z* axis is the direction of periodicity.

and accuracy of the multipole expansion used in the PLH program to evaluate the Madelung terms.

RELEVANT RHF EXPRESSIONS

The RHF Bloch states $\phi_n(k, \mathbf{r})$ are doubly occupied up to the Fermi energy E_F and orthonormalized as shown in the following equation:

$$\int d\mathbf{r} \phi_n^*(k', \mathbf{r}) \phi_n(k, \mathbf{r}) = N \delta_{k'k} \delta_{n'n} \quad (1)$$

$N(N \rightarrow \infty)$ is the total number of cells in the system, the lattice sites are identified by the integers m, m' , and $m'' (= 0, \pm 1, \pm 2, \dots)$, and n and n' are the band indices. In our notation, the wavenumber k is expressed in units of $2\pi/a_0$ and is defined in the Brillouin zone (BZ), i.e., $k \in [-\frac{1}{2}, \frac{1}{2}]$. The Bloch states

$$\phi_n(k, \mathbf{r}) = \sum_p C_{pn}(k) b_p(k, \mathbf{r}) \quad (2)$$

are expressed in terms of Bloch sums $b_p(k, \mathbf{r})$

$$\begin{aligned} b_p(k, \mathbf{r}) &= \sum_{m=-\infty}^{\infty} e^{ik2\pi m} \chi_p(\mathbf{r} - \mathbf{A}_p - ma_0 \mathbf{e}_z) \\ &= \sum_{m=-\infty}^{\infty} e^{ik2\pi m} \chi_p^m(\mathbf{r}), \end{aligned} \quad (3)$$

where p and vector \mathbf{A}_p represent the index and the center in the unit cell of the atomic function, χ_p , respectively.

The charge neutrality condition of the chain is given by

$$\int_{\text{BZ}} dk \sum_n \theta_n(k) = n_e \quad (4)$$

with the occupation function $\theta_n(k)$ defined as

$$\theta_n(k) = \begin{cases} 2 & \text{if } \varepsilon_n(k) \leq E_F \\ 0 & \text{if } \varepsilon_n(k) > E_F. \end{cases} \quad (5)$$

The RHF equations of the Bloch states and the energy bands $\varepsilon_n(k)$ are

$$\begin{aligned} F(\mathbf{r}_1) \phi_n(k, \mathbf{r}_1) \\ = \left[-\frac{\nabla^2(\mathbf{r}_1)}{2} - \sum_{m=-\infty}^{\infty} \sum_{a=1}^M \frac{Z_a}{|\mathbf{r}_1 - \mathbf{A}_a - ma_0 \mathbf{e}_z|} \right] \end{aligned}$$

$$\begin{aligned} &+ \int_{\text{BZ}} dk' \sum_{n'} \theta_{n'}(k') \\ &\times \int d\mathbf{r}_2 \frac{\phi_n^*(k', \mathbf{r}_2) \phi_{n'}(k', \mathbf{r}_2)}{|\mathbf{r}_1 - \mathbf{r}_2|} \Big] \phi_n(k, \mathbf{r}_1) \\ &- \frac{1}{2} \int_{\text{BZ}} dk' \sum_{n'} \theta_{n'}(k') \\ &\times \int d\mathbf{r}_2 \frac{\phi_n^*(k', \mathbf{r}_2) \phi_n(k, \mathbf{r}_2)}{|\mathbf{r}_1 - \mathbf{r}_2|} \phi_{n'}(k', \mathbf{r}_1) \\ &= \varepsilon_n(k) \phi_n(k, \mathbf{r}_1), \end{aligned} \quad (6)$$

where $F(\mathbf{r}_1)$ is the Fock operator in the restricted form for double occupancy of the Bloch states; Z_a and vector \mathbf{A}_a define the charge and the position of atom a , respectively, and M is the number of atoms ($M = 2$ in this work). Equation (6) can be expressed in terms of the atomic functions as

$$\sum_q F_{pq}(k) C_{qn}(k) = \varepsilon_n(k) \sum_q S_{pq}(k) C_{qn}(k), \quad (7)$$

where $F_{pq}(k)$ and $S_{pq}(k)$ are the elements of the LCAO Fock $\mathbf{F}(k)$ and overlap $\mathbf{S}(k)$ matrices, defined as

$$F_{pq}(k) = N^{-1} \int d\mathbf{r} b_p^*(k, \mathbf{r}) F(\mathbf{r}) b_q(k, \mathbf{r}) \quad (8)$$

and

$$S_{pq}(k) = N^{-1} \int d\mathbf{r} b_p^*(k, \mathbf{r}) b_q(k, \mathbf{r}). \quad (9)$$

The Fock matrix elements are composed of three terms:

$$F_{pq}(k) = T_{pq}(k) + V_{pq}(k) + X_{pq}(k), \quad (10)$$

where $T_{pq}(k)$ is the kinetic energy, $V_{pq}(k)$ the classical electrostatic energy, which includes the electron-nuclear attraction and the electron-electron repulsion contributions, and $X_{pq}(k)$ the exchange energy. Analysis of the problem in these terms with respect to the convergence of the lattice sums which enter in their definition, and the analytic properties of the LCAO density matrix elements $P_{pq}(k)$

$$P_{pq}(k) = \sum_n C_{pn}(k) C_{qn}^*(k) \theta_n(k) \quad (11)$$

in the BZ, as well as the consequences on the RHF results are well documented [8].

COMPUTATIONAL ASPECTS

In this section, we briefly contrast the way the matrix elements are computed in the DS and FS approaches.

$$\begin{aligned}
 V_{pq}(k) &= \sum_{m=-N_x}^{N_x} e^{2\pi i k m} \left\{ \sum_{m''=-\infty}^{\infty} \left[\sum_{m'=-N_x}^{N_x} \left\{ \sum_{rs} P_{rs}^{m'} \begin{pmatrix} 0 & m \\ p & q \end{pmatrix} \begin{vmatrix} m'' & m' + m'' \\ r & s \end{vmatrix} \right\} - V_{pq}^m(m'') \right] \right\} \\
 &= \sum_{m=-N_x}^{N_x} e^{2\pi i k m} \left\{ \sum_{m''=-N_c}^{N_c} \left[\sum_{m'=-N_x}^{N_x} \sum_{rs} P_{rs}^{m'} \left\{ \begin{pmatrix} 0 & m \\ p & q \end{pmatrix} \begin{vmatrix} m'' & m' + m'' \\ r & s \end{vmatrix} - \frac{1}{n_e} S_{rs}^{m'} V_{pq}^m(m'') \right\} \right] \right\} \\
 &\quad + \text{long range correction,}
 \end{aligned} \tag{14}$$

$$X_{pq}(k) = -\frac{1}{2} \sum_{m=-N_x}^{N_x} e^{2\pi i k m} \sum_{rs} \left\{ \sum_{m', m''=-N_x}^{N_x} P_{rs}^{m'-m-m''} \begin{pmatrix} 0 & m' \\ p & s \end{pmatrix} \begin{vmatrix} m + m'' & m \\ r & q \end{vmatrix} \right\}, \tag{15}$$

where N_x is the limit used in the lattice summations appearing in the exchange and in the Coulomb terms. In the Coulomb terms, however, the summation over m'' decays like $|m''|^{-1}$. Hence, the summation over m'' is partitioned in a short-range region ($-N_c \leq m'' \leq +N_c$) where all integrals are calculated in a standard way. Outside of this region a multipole expansion is applied and the infinite summations are carried out explicitly using the properties of Riemann zeta functions. S_{pq}^m , T_{pq}^m , $V_{pq}^m(m'')$, and

$$\begin{pmatrix} 0 & m \\ p & q \end{pmatrix} \begin{vmatrix} m' & m'' \\ r & s \end{vmatrix},$$

respectively, are the overlap, kinetic, nuclear attraction and two-electron integrals between the atomic functions used to represent the Bloch state $\phi_n(k, \mathbf{r})$:

$$S_{pq}^m = \int d\mathbf{r} \chi_p^0(\mathbf{r}) \chi_q^m(\mathbf{r}), \tag{16}$$

$$T_{pq}^m = \int d\mathbf{r} \chi_p^0(\mathbf{r}) \left[\frac{-\nabla^2}{2} \right] \chi_q^m(\mathbf{r}), \tag{17}$$

Direct Space

In the configuration-space approach, the different components are expressed as

$$S_{pq}(k) = \sum_{m=-N_x}^{N_x} e^{2\pi i k m} S_{pq}^m, \tag{12}$$

$$T_{pq}(k) = \sum_{m=-N_x}^{N_x} e^{2\pi i k m} T_{pq}^m, \tag{13}$$

$$\begin{aligned}
 V_{pq}^m(m'') &= \sum_{a=1}^M \int d\mathbf{r} \chi_p^0(\mathbf{r} - \mathbf{A}_p) \\
 &\quad \times \left[\frac{Z_a}{|\mathbf{r} - \mathbf{A}_a - m'' a \mathbf{e}_z|} \right] \chi_q^m(\mathbf{r}) \tag{18}
 \end{aligned}$$

$$\begin{aligned}
 &\begin{pmatrix} 0 & m \\ p & q \end{pmatrix} \begin{vmatrix} m' & m'' \\ r & s \end{vmatrix} \\
 &= \int d\mathbf{r}_1 \int d\mathbf{r}_2 \frac{\chi_p^0(\mathbf{r}_1) \chi_q^m(\mathbf{r}_1) \chi_r^{m'}(\mathbf{r}_2) \chi_s^{m''}(\mathbf{r}_2)}{|\mathbf{r}_1 - \mathbf{r}_2|}, \tag{19}
 \end{aligned}$$

where P_{rs}^m is the m th Fourier coefficient of the complex Fourier series representing $P_{rs}(k)$,

$$P_{rs}^m = \int_{-1/2}^{1/2} dk e^{-2\pi i k m} P_{rs}(k). \tag{20}$$

In this work, only s type atomic orbitals located on the z axis are used:

$$\chi_p^m(\mathbf{r}) = \left(\frac{2\alpha_p}{\pi} \right)^{3/4} \exp \left[-\alpha_p (\mathbf{r} - \mathbf{A}_p - m a_0 \mathbf{e}_z)^2 \right], \tag{21}$$

and the above integrals take the particular forms:

$$S_{pq}^m = \left(\frac{4\alpha_p\alpha_q}{\pi} \right)^{3/4} \left(\frac{\pi}{\alpha_p + \alpha_q} \right)^{3/2} \times \exp \left(- \frac{\alpha_p\alpha_q}{\alpha_p + \alpha_q} |\mathbf{A}_q - \mathbf{A}_p + m a_0 \mathbf{e}_z|^2 \right), \quad (22)$$

$$T_{pq}^m = \left(\frac{1}{\alpha_p + \alpha_q} \right) \times \left\{ 3\alpha_p\alpha_q - 2 \frac{(\alpha_p\alpha_q)^2}{(\alpha_p + \alpha_q)} |\mathbf{A}_q - \mathbf{A}_p + m a_0 \mathbf{e}_z|^2 \right\} S_{pq}^m, \quad (23)$$

$$V_{pq}^m(m'') = \frac{2(\alpha_p + \alpha_q)^{1/2}}{\pi^{1/2}} S_{pq}^m \sum_a^M Z_a \times F_0 \left((\alpha_p + \alpha_q)(\mathbf{G}_{pq}^m - \mathbf{A}_a + m'' a_0 \mathbf{e}_z)^2 \right), \quad (24)$$

$$\begin{pmatrix} 0 & m \\ p & q \end{pmatrix} \begin{pmatrix} M'' & m'' + m' \\ r & s \end{pmatrix} = 2 \sqrt{\frac{(\alpha_p + \alpha_q)(\alpha_r + \alpha_s)}{\pi(\alpha_p + \alpha_q + \alpha_r + \alpha_s)}} S_{pq}^m S_{rs}^{m'} \times F_0 \left(\frac{(\alpha_p + \alpha_q)(\alpha_r + \alpha_s)}{\alpha_p + \alpha_q + \alpha_r + \alpha_s} (m'' a_0 \mathbf{e}_z + \mathbf{G}_{rs}^{m'} - \mathbf{G}_{pq}^m)^2 \right), \quad (25)$$

where \mathbf{G}_{pq}^m and $\mathbf{G}_{rs}^{m'}$ are the centers of the gaussians that result of the product of two gaussians $\chi_p^0(r)$ and $\chi_q^m(r)$, and $\chi_r^0(r)$ and $\chi_s^{m'}(r)$,

$$\mathbf{G}_{pq}^m = \frac{\alpha_p \mathbf{A}_p + \alpha_q (\mathbf{A}_q + m a_0 \mathbf{e}_z)}{\alpha_p + \alpha_q}. \quad (26)$$

$F_0(t)$ is related to the error function,

$$F_0(t) = \int_0^1 \exp(-tu^2) du = \frac{1}{2} \sqrt{\frac{\pi}{t}} \operatorname{erf}(\sqrt{t}) \quad (t > 0).$$

Fourier Space

In the Fourier transform approach, the expressions for the Coulomb and the exchange terms are:

$$V_{pq}(k) = (\pi a_0)^{-1} \sum_{rs} \int_{\text{BZ}} dk' P_{rs}(k') \sum_{\mu} \int \frac{d\mathbf{q}_0}{\mathbf{q}_0^2 + \mu^2} S_{pq}(k, \mathbf{q}_{\mu}) \times \left[S_{rs}(k', -\mathbf{q}_{\mu}) - \frac{1}{n_e} S_{rs}(k', 0) \left(\sum_{a=1}^M Z_a e^{2\pi i \mathbf{q}_{\mu} \cdot \mathbf{A}_a} \right) \right], \quad (27)$$

$$X_{pq}(k) = -(2\pi a_0)^{-1} \sum_{rs} \int_{\text{BZ}} dk' P_{rs}(k') \times \sum_{\mu} \int \frac{d\mathbf{q}_0}{\mathbf{q}_0^2 + (\mu + k - k')^2} \times S_{ps}(k', \mathbf{q}_{\mu+k-k'}) S_{rq}(k, -\mathbf{q}_{\mu+k-k'}), \quad (28)$$

where $\mathbf{q} \Leftrightarrow (q_x, q_y, q_z)$ and $\mathbf{q}_{\mu} \Leftrightarrow (q_x, q_y, \mu)$.

In these equations, the generalized overlap $S_{pq}(k, \mathbf{q})$ integral is defined by:

$$S_{pq}(k, \mathbf{q}) = \sum_m e^{i2\pi m k} \langle \chi_p^0 | e^{i2\pi a_0^{-1} \mathbf{q} \cdot \mathbf{r}} | \chi_q^m \rangle. \quad (29)$$

In the case of *s*-atomic orbitals, the generalized overlap integral has, after factorization in the $\mathbf{q}_x, \mathbf{q}_y$, and \mathbf{q}_z components, the following analytical expression:

$$S_{pq}(k, \mathbf{q}) = S_{pq}^{(x,y)} S_{pq}^{(z)}(k, q_z) e^{i2\pi \mathbf{q} \cdot \mathbf{G}_{pq}^0} \times \exp \left[- \frac{\pi^2}{a_0^2} \frac{1}{(\alpha_p + \alpha_q)} \mathbf{q}^2 \right] \quad (30)$$

with $S_{pq}^{(x,y)}$ defined as:

$$S_{pq}^{(x,y)} = \left(\frac{4\alpha_p\alpha_q}{\pi} \right)^{1/2} \left(\frac{\pi}{\alpha_p + \alpha_q} \right) \times \exp \left\{ - \frac{\alpha_p\alpha_q}{\alpha_p + \alpha_q} \left[(A_{x,p} - A_{x,q})^2 + (A_{y,p} - A_{y,q})^2 \right] \right\}. \quad (31)$$

The *z*-component $S_{pq}^{(z)}$ involves a lattice summation that can always be made to converge rapidly by choosing one of the two equivalent forms (32a) or (32b) linked by the Poisson formula according

to the particular values of the gaussian exponents,

$$S_{pq}^{(z)}(k, q_z) = \left(\frac{4\alpha_p\alpha_q}{\pi} \right)^{1/4} \left(\frac{\pi}{\alpha_p + \alpha_q} \right)^{1/2} \\ \times \sum_m \exp \left[2\pi i m \left(k + \frac{\alpha_q}{\alpha_p + \alpha_q} q_z \right) - \frac{\alpha_p\alpha_q}{\alpha_p + \alpha_q} (ma_0 + A_{z,q} - A_{z,p})^2 \right] \quad (32a)$$

or

$$S_{pq}^{(z)}(k, q_z) = \frac{\pi}{a_0} \left(\frac{4\alpha_p\alpha_q}{\pi} \right)^{1/4} \left(\frac{1}{\alpha_p\alpha_q} \right)^{1/2} \\ \times \exp \left[-\frac{2\pi}{a_0} i (A_{z,q} - A_{z,p}) \left(k + \frac{\alpha_q}{\alpha_p + \alpha_q} q_z \right) \right] \\ \times \sum_m \exp \left[-\frac{2\pi}{a_0} i m (A_{z,q} - A_{z,p}) - \frac{\pi^2}{a_0^2} \right. \\ \left. \times \frac{\alpha_p + \alpha_q}{\alpha_p\alpha_q} \left(k + m + \frac{\alpha_q}{\alpha_p + \alpha_q} q_z \right)^2 \right] \quad (32b)$$

Using these relations, the Coulomb and exchange terms then become:

$$V_{pq}(k) = a_0^{-1} \sum_{rs} \int_{-1/2}^{1/2} dk' P_{rs}(k') \\ \times \sum_{\mu} S_{pq}^{(xy)} S_{rs}^{(xy)} S_{pq}^{(z)}(k, \mu) \\ \times \left[S_{rs}^{(z)}(k', -\mu) e^{(2\pi i \mu / a_0)(G_{z,pq}^0 - G_{z,rs}^0)} E_1(\gamma \mu^2) - \frac{1}{n_e} S_{rs}^{(z)}(k', 0) \sum_a Z_a e^{(2\pi i \mu / a_0)(G_{z,pq}^0 - A_z)} E_1(\delta \mu^2) \right] \quad (33)$$

and

$$X_{pq}(k) = -\frac{1}{2a_0} \sum_{rs} \int_{-1/2}^{1/2} dk' P_{rs}(k') S_{ps}^{(xy)} S_{rq}^{(xy)}$$

$$\times \sum_{\mu} S_{ps}^{(z)}(k', (\mu + k - k')) \\ \times S_{rq}^{(z)}(k, -(\mu + k - k')) \\ \times e^{(2\pi / a_0) i (\mu + k - k') (G_{z,ps}^0 - G_{z,rq}^0)} \\ \times E_1(\eta (\mu + k - k')^2). \quad (34)$$

In these expressions, γ , δ , and η are respectively defined as:

$$\gamma = \left(\frac{\pi}{a_0} \right)^2 \left(\frac{1}{\alpha_p + \alpha_q} + \frac{1}{\alpha_r + \alpha_s} \right), \\ \delta = \left(\frac{\pi}{a_0} \right)^2 \left(\frac{1}{\alpha_p + \alpha_q} \right), \\ \eta = \left(\frac{\pi}{a_0} \right)^2 \left(\frac{1}{\alpha_p + \alpha_s} + \frac{1}{\alpha_r + \alpha_q} \right).$$

The rate of convergence of these lattice summations can be slow if the γ , δ , or η values are small, or alternatively when $(\alpha_p + \alpha_q)$ or $(\alpha_r + \alpha_s)$ are large. Rapidly convergent series are obtained using a combination of the Ewald technique [9] and the Poisson formula [10], the latter being applicable thanks to the gaussian expansion of the atomic functions.

The numerical integration over k' is carried out with the same quadrature scheme and integration points for both the Coulomb and exchange contributions. The method is based on a grid of equidistant points (in our case 33 k' points in the first Brillouin zone) and Newton-Cotes formulas [11]. The numerical integration procedure has specifically been designed to handle analytically the singularity in the exchange part. The integration weights needed to treat the singular integrand occurring in the exchange term in a suitable way have been constructed from the Lagrange interpolation formulas [11]. Reference 5 contains more details about this newly proposed computational technique.

Results

First, we analyze comparatively the results obtained with the DS and FS approaches for the three values of the unit cell length ($a_0 = 11.0, 12.0$, and 13.0 a.u.). Then, to further illustrate the power of the FS approach, we report results on the symmetry constrained metallic situation.

TABLE I

Energy values $\varepsilon(k)$ of the occupied and unoccupied valence bands at selected k points and the band gaps, W , for the infinite chain of lithium molecules, $(-\text{Li}_2-)_x$, with (a) $a_0 = 11.0$, (b) 12.0, and (c) 13.0 a.u. computed with the DS and FS approaches. (Energies are in atomic units.)

$\varepsilon(k)$	(a)		(b)		(c)	
	DS	FS	DS	FS	DS	FS
occ.						
$\varepsilon(0.0)$	-0.228535	-0.228533	-0.217075	-0.217076	-0.207408	-0.207410
$\varepsilon(0.125)$	-0.223255	-0.223254	-0.212417	-0.212417	-0.203517	-0.203519
$\varepsilon(0.25)$	-0.206738	-0.206730	-0.198218	-0.198217	-0.192080	-0.192079
$\varepsilon(0.375)$	-0.177521	-0.177518	-0.175256	-0.175256	-0.175418	-0.175416
$\varepsilon(0.5)$	-0.149940	-0.149992	-0.158195	-0.158195	-0.165188	-0.165188
unocc.						
$\varepsilon(0.0)$	0.152080	0.152152	0.119592	0.119599	0.093216	0.093201
$\varepsilon(0.125)$	0.111178	0.111210	0.089544	0.089549	0.071268	0.071260
$\varepsilon(0.25)$	0.040393	0.040367	0.032494	0.032492	0.026775	0.026771
$\varepsilon(0.375)$	-0.021191	-0.021217	-0.018549	-0.018553	-0.013423	-0.013424
$\varepsilon(0.5)$	-0.058807	-0.058761	-0.044671	-0.044673	-0.031566	-0.0311561
W	0.091133	0.091231	0.113524	0.113522	0.133622	0.133627
n_{it}	57	38	10	22	8	18

LITHIUM CHAINS WITH $a_0 = 11.0$, 12.0, AND 13.0 a.u.

The valence band structures obtained by the DS and FS approaches for $(-\text{Li}_2-)_x$ with $a_0 = 11.0$, 12.0, and 13.0 a.u. are shown in Figure 2 where

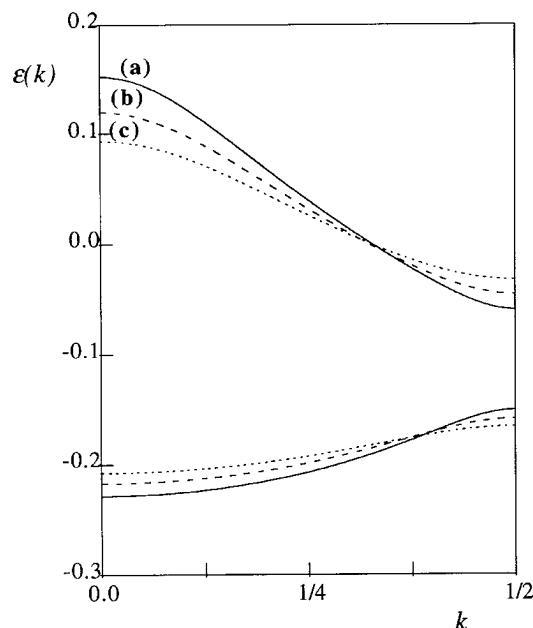


FIGURE 2. Valence bands obtained by the DS and FS approaches for the infinite chain of lithium molecules, $(-\text{Li}_2-)_x$, with (a) $a_0 = 11.0$, (b) 12.0, and (c) 13.0 a.u. Energies are in atomic units.

they are denoted by (a), (b), and (c), respectively. The DS results have been obtained with $N_x = 10$, the maximum number of interacting cells that can presently be taken into account in the PLH program to compute the exchange contributions to the Fock matrix elements, Eq. (15). Selected energy values $\varepsilon(k)$ of the occupied and unoccupied valence bands, and the band gaps W obtained by the two approaches are listed in Table I. The number of iterations n_{it} needed to achieve convergence of the density matrices within the preassigned threshold is also indicated. Overall, the DS and FS results compare fairly well and their graphs in Figure 2 are indeed indistinguishable. Nevertheless from data in Table I, one can notice that the more alternant the situation is, the better the agreement between the two approaches. To trace the origin of this discrepancy, it is useful to analyze the changes during the iterations of the energy band values obtained by the DS approach for the chain of equidistant atoms (a).

The first iteration starts with a guess density matrix based on the diagonal elements of the overlap matrix $S(k)$:

$$P_{pp}^{(0)}(k) = S_{pp}^{-1}(k)\theta_{pp}(k), \quad (35)$$

where $\theta_{pp}(k) = 2$ for $k \in [-\frac{1}{4}, \frac{1}{4}]$ and 1 for $k \in ([-\frac{1}{2}, -\frac{1}{4}] \cup [\frac{1}{4}, \frac{1}{2}])$, $p = 1s$ and $2s$. The valence band structures corresponding to the first (dashed line) and last (continuous line) iterations of the

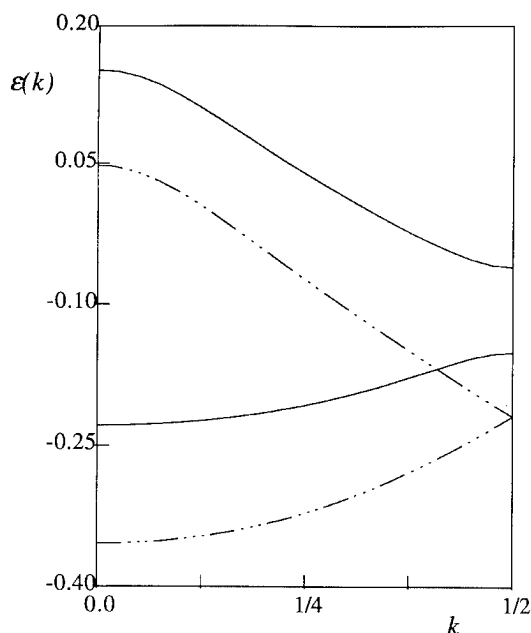


FIGURE 3. Energy valence band obtained by the DS approach for the infinite chain of lithium molecules, $(-\text{Li}_2-)_x$, at the first (dashed line) and last (continuous line) iterations of the SCF procedure. Energies are in atomic units.

SCF procedure are shown in Figure 3. At the first iteration the band structure is degenerate (to within accuracy of the calculations) at the edge of the Brillouin zone ($k = 0.5$). As the iterations proceed, the degeneracy is progressively lifted and the solution converges toward the energetically more stable symmetry broken solution. Figures 4a1 and 4a2 compare the graph of the density matrix element P_{2s-2s}^m with respect to m at the first and last iterations. The corresponding values are given in Table II. It is observed that the decay of these elements is rather slow ($\sim |m|^{-1}$) [8] at the first iteration since it corresponds to a "numerically transient" metallic situation. At the end of the SCF process a gap has opened up (Fig. 3) and the decay is now of the exponential type as theoretically predicted for the nondegenerate cases [8]. The actual rate of the exponential decay is governed by the analytical features of the one-electron states and energies with respect to k (see appendix in Ref. 8c). To a first approximation, the convergence rate can be related to the energy band gap [8b]. This can be verified with case (b) ($a_0 = 12.0$ a.u.) for which the gap is slightly larger than for (a) (Fig. 2); the corresponding density matrix elements, also given in Table II and plotted in Figure

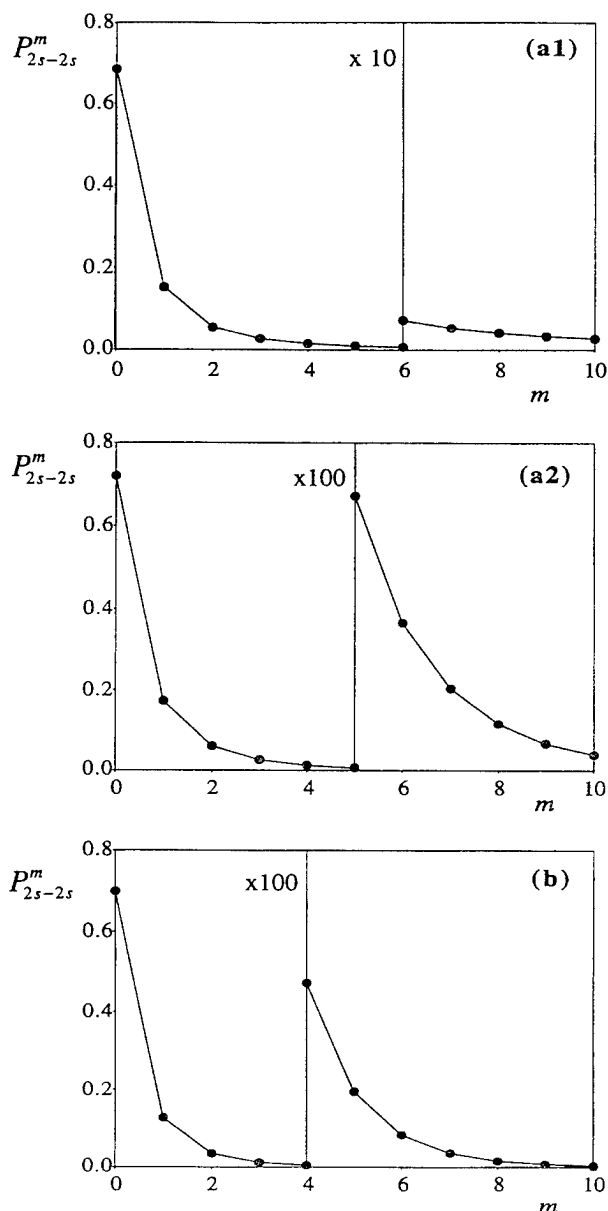


FIGURE 4. Graphs of the evolution with respect to m of the density matrix element P_{2s-2s}^m for the infinite chain of lithium molecules with $a_0 = 11.0$ a.u. at the (a1) first and (a2) last iterations of the SCF procedure and with (b) $a_0 = 12.0$ a.u. at the last iteration.

4b, indeed decay faster than for (a). Thus, the larger discrepancy between the direct space and Fourier space results (Table I) noted for the chain of evenly distributed lithium atoms (a) indicate that the number of interacting cells, $|N_x| = 10$, used to evaluate the exchange contributions is not enough to reach 5 decimal digits accuracy.

TABLE II

Values with respect to m of the density matrix element P_{2s-2s}^m for the infinite chain of lithium molecules with $a_0 = 11.0$ a.u. at the (a1) first and (a2) last iterations of the SCF procedure and with (b) $a_0 = 12.0$ a.u. at the last iteration.

m	(a1)	(a2)	(b)
0	0.685031	0.720026	0.699199
1	-0.151910	-0.172434	-0.127620
2	0.546705×10^{-1}	0.601288×10^{-1}	0.352045×10^{-1}
3	-0.266155×10^{-1}	-0.261654×10^{-1}	-0.121790×10^{-1}
4	0.155983×10^{-1}	0.128804×10^{-1}	0.472761×10^{-1}
5	-0.102099×10^{-1}	-0.672170×10^{-2}	-0.194125×10^{-2}
6	0.721343×10^{-2}	0.365573×10^{-2}	0.829047×10^{-3}
7	-0.537895×10^{-2}	-0.203782×10^{-2}	-0.362483×10^{-3}
8	0.417780×10^{-2}	0.115738×10^{-2}	0.161329×10^{-3}
9	-0.334927×10^{-2}	-0.666340×10^{-3}	-0.727299×10^{-4}
10	0.275415×10^{-2}	0.390831×10^{-3}	0.332536×10^{-4}

To further assess the importance of the number of interacting cells taken into account to evaluate the exchange terms in DS calculations, we have computed the band structure (the occupied and the unoccupied valence band) for the chain of evenly distributed lithium atoms (a) with $N_x = 2, 3, 5$, and 10. Energies at selected k points and band gaps are listed in Table III, and the valence band structures are plotted in Figure 5. For the sake of clarity, $N_x = 5$ is omitted in Figure 5. It appears that even if the graphs are essentially stabilized for $N_x = 3$, the values in Table III show that significant variations in the energies still persist.

SYMMETRY-CONSTRAINED METALLIC CHAIN

As we have just seen, even in nondegenerate situations with gaps as large as 0.094 a.u. or 2.5 eV, DS-RHF band structures can still be sensitive to the number of interacting cells through their exchange contributions. Here we wish to show that the FS approach applied to compute the band structure of the symmetry-constrained metallic solution of $(-Li)_x$ (one Li atom per unit cell) leads to the genuine features of the RHF approach, namely the vanishing of the density of states at the Fermi level. The results given in Table IV and Figures 6 and 7, reveal that, except in the vicinity

TABLE III

Energy values $\varepsilon(k)$ of the occupied and unoccupied valence bands at selected k points and the band gaps, W , for the infinite chain of evenly distributed Li atoms and for the DS and FS approaches. In the DS calculations, different numbers of interacting cells (N_x) have been considered. (Energies are in atomic units.)

$\varepsilon(k)$	DS				FS
	$N_x = 2$	$N_x = 3$	$N_x = 5$	$N_x = 10$	
occ.					
$\varepsilon(0.0)$	-0.229288	-0.228249	-0.228475	-0.228535	-0.228533
$\varepsilon(0.125)$	-0.223232	-0.223475	-0.223290	-0.223255	-0.223254
$\varepsilon(0.25)$	-0.205896	-0.206686	-0.206758	-0.206738	-0.206730
$\varepsilon(0.375)$	-0.177509	-0.177305	-0.177470	-0.177521	-0.177518
$\varepsilon(0.5)$	-0.151701	-0.150501	-0.150016	-0.149940	-0.149992
unocc.					
$\varepsilon(0.0)$	0.164063	0.147813	0.151261	0.152080	0.152152
$\varepsilon(0.125)$	0.104394	0.114752	0.111203	0.111178	0.111210
$\varepsilon(0.25)$	0.039743	0.037917	0.040868	0.040393	0.040367
$\varepsilon(0.375)$	-0.017581	-0.019508	-0.021235	-0.021191	-0.021217
$\varepsilon(0.5)$	-0.061858	-0.059989	-0.059054	-0.058807	-0.058761
W	0.089843	0.090512	0.090962	0.091133	0.091231

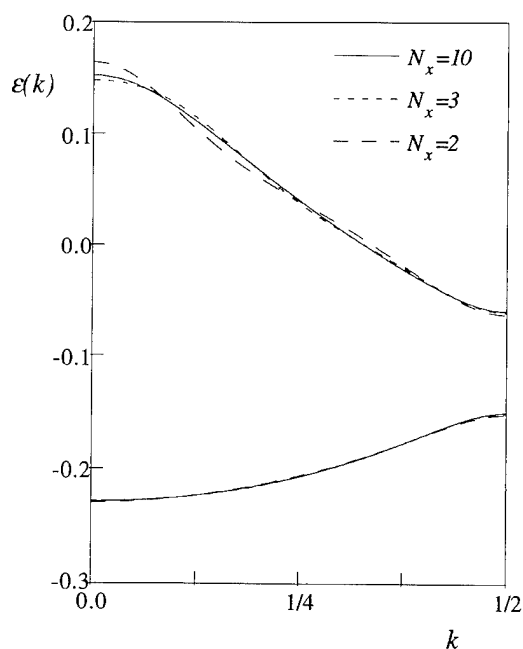


FIGURE 5. Valence bands obtained by the DS approach for the infinite chain of evenly distributed Li atoms using different numbers of interacting cells (N_x). Energy values are in atomic units.

of $k = k_F$, the band structures for the metallic and symmetry-broken solutions are almost identical. Thus, it seems from this application that the general features of the electronic structures, in particular the band widths, are not better nor less well

TABLE IV
Energy values $\varepsilon(k)$ of the occupied and unoccupied valence bands at selected k points and the band gaps, W , obtained for the symmetry-constrained metallic (dotted line) and the symmetry-broken (continuous line) solutions. (Energies are in atomic units.)

$\varepsilon(k)$	DS	FS
occ.		
$\varepsilon(0.0)$	-0.228535	-0.229977
$\varepsilon(0.125)$	-0.223255	-0.224647
$\varepsilon(0.25)$	-0.206738	-0.207620
$\varepsilon(0.375)$	-0.177521	-0.174672
$\varepsilon(0.5)$	-0.149940	-0.104701
unocc.		
$\varepsilon(0.0)$	0.152080	0.152798
$\varepsilon(0.125)$	0.111178	0.111863
$\varepsilon(0.25)$	0.040393	0.040592
$\varepsilon(0.375)$	-0.021191	-0.024702
$\varepsilon(0.5)$	-0.058807	-0.104701
W	0.091133	0.0

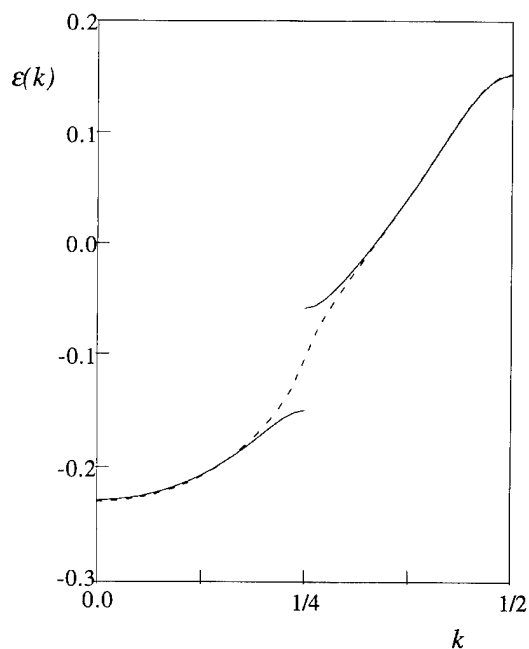


FIGURE 6. Valence bands obtained for the symmetry-constrained metallic (dotted line) and symmetry-broken (continuous line) solutions. To facilitate comparison, the DS valence band has been unfolded. Energy values are in atomic units.

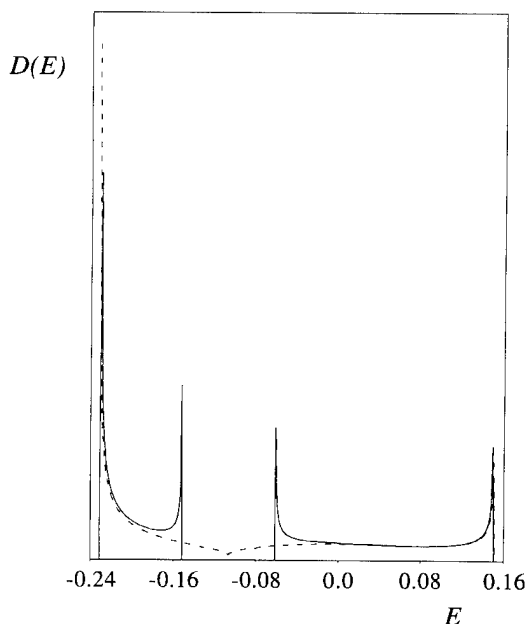


FIGURE 7. Valence density of states $D(E)$ obtained for the symmetry-constrained metallic (dotted line) and symmetry-broken (continuous line) solutions. Energy values are in atomic units and the density of states values are in arbitrary units.

described in metals than in insulators at the RHF level.

The graphs of the valence density of states obtained for the metallic (dotted line) and symmetry-broken (continuous line) solutions are shown in Figure 7. In the case of the metallic solution and within the resolution of the density of states calculations reported here, the special behavior of RHF metallic cases is apparent. A more detailed analysis of the valence and core bands of the symmetry-constrained metallic case can be found in Ref. 12.

Concluding Remarks

From this work, the following concluding remarks can be made:

1. Even for systems with gaps of the order of 2.5 eV, typically case (a), the importance of the number of interacting cells contributing to the exchange terms is still felt beyond 10 neighbors. It must be further stressed that these observations are made for a localized minimal basis which is a rather favorable situation from a numerical point of view. Even if it could be argued that the net effect does not modify qualitatively the final picture in the case studied here, a similar analysis on complex systems where more diffuse bases are generally used is thus necessary.

2. The FS approach constitutes a suitable framework for accurate evaluations of all lattice sums for localized as well as delocalized bases. As such, it appears as a way to avoid the difficult problem of selecting the number of interacting cells needed in a particular application.

3. To our knowledge, the FS approach is presently the only approach capable of a proper description of RHF symmetry-constrained metallic solutions of realistic systems.

4. On a more pragmatic ground, these comparisons constitute checks on the reliability of our FS and DS codes.

Our Fourier transform code (FTCHAIN) is still in a prototype phase, but it has already contributed to illustrate the merits of the Fourier representation in the context of calculations of the electronic structure of extended chains. Ongoing work to bring it to a more applicable stage includes the rather demanding task of obtaining working forms for new types of integrals and the corresponding computer routines.

ACKNOWLEDGMENTS

All calculations have been performed on the IBM RS6000 Models 730 and 560 of the Namur Scientific Computing Facility (Namur-SCF). The authors gratefully acknowledge the financial support of the FNRS-FRFC, the "Loterie Nationale" for the convention No. 9.4593.92, and the FNRS within the framework of the "Action d'impulsion à la recherche fondamentale" of the Belgian Ministry of Science under the convention D.4511.93.

References

1. (a) T. E. Peacock and R. McWeeny, *Proc. Phys. Soc. London* **74**, 385 (1959). (b) S. Yomosa, *J. Phys. Soc. Jpn.* **19**, 1718 (1964). (c) G. Del Re, J. Iadik, and G. Biczio, *Phys. Rev.* **155**, 977 (1967). (d) J. M. André, L. Gouverneur, and G. Leroy, *Int. J. Quantum Chem.* **1**, 427 (1967).
2. J. M. André, D. H. Mosley, B. Champagne, J. Delhalle, J. G. Fripiat, J. L. Brédas, D. J. Vanderveken, and D. P. Vercouteren, *Methods and Techniques in Computational Chemistry (METECC-94)*, E. Clementi, Ed. (Stef. Cagliari, 1993), Vol. B. J. G. Fripiat, D. H. Mosley, B. Champagne, and J. M. André, PLH-93 from METECC-94.
3. (a) F. Seitz, *The Modern Theory of Solids* (McGraw-Hill, New York, 1940). (b) P. Fulde, *Electron Correlation in Molecules and Solids* (Springer-Verlag, Berlin, 1991).
4. (a) F. E. Harris and J. H. Monkhorst, *Phys. Rev.* **B2**, 4400 (1970). (b) F. E. Harris, *J. Chem. Phys.* **56**, 4422 (1972). (c) J. Delhalle and F. E. Harris, *Phys. Rev.* **B31**, 6755 (1985).
5. J. Delhalle, J. Cizek, I. Flamant, J. L. Calais, and J. G. Fripiat, *J. Chem. Phys.* **101**, 10717 (1994).
6. Gaussian-92/DFT, Revision F.2, M. J. Frisch, G. W. Trucks, H. B. Schlegel, P. M. W. Gill, B. G. Johnson, M. W. Wong, J. B. Foresman, M. A. Robb, M. Head-Gordon, E. S. Replogle, R. Gomperts, J. L. Andres, K. Raghavachari, J. S. Binkley, C. Gonzalez, R. L. Martin, D. J. Fox, D. J. Defrees, J. Baker, J. J. P. Stewart, and J. A. Pople, Gaussian, Inc., Pittsburgh PA, 1993.
7. R. Poirier, R. Kari, and I. G. Csizmadia, *Handbook of Gaussian Basis Sets* (Elsevier, New York, 1985).
8. (a) H. J. Monkhorst, *Phys. Rev. B* **20**, 1504 (1979). (b) H. J. Monkhorst and M. Kertesz, *Phys. Rev. B* **24**, 3025 (1981). (c) J. Delhalle and J. L. Calais, *J. Chem. Phys.* **85**, 5286 (1986).
9. P. P. Ewald, *Ann. Phys.* **64**, 253 (1921).
10. P. Henrici, *Applied and Computational Complex Analysis* (Wiley, New York, 1977), Vol. 2.
11. M. Abramowitz and I. A. Stegun, *Handbook of Mathematical Functions* (Dover, New York, 1968).
12. I. Flamant, J. Delhalle, and J. G. Fripiat, submitted for publication.

Iodine-Doped Transpolyacetylene

G. P. DAS*

Systan Corporation, 4126 Linden Ave, Dayton, Ohio 45432; e-mail: dasgp@picard.ml.wpafb.af.mil

A. T. YEATES AND D. S. DUDIS

WL / MLBP, WPAFB, Ohio 45433

Received February 28, 1996; accepted April 2, 1996

ABSTRACT

With a view to elucidate and develop a model for the mechanism of conduction in doped transpolyacetylene (t-PA), we have carried out an ab initio study of the ground and excited state of transoctatetraene in the presence of an iodine atom. While the ground state is calculated as characterized by a slightly distorted alternating bond geometry, with iodine remaining largely neutral on top of the plane of the polyene near roughly the midpoint of the chain axis, the excited state has the geometry characterized by a solitonic distortion with the octatetraene carrying a net positive charge close to 0.7e. The bandgap [highest occupied to lowest unoccupied molecular orbital (HOMO-LUMO) gap] is computed to be nearly 0.8 eV. Moreover, the excited-state energy appears very insensitive to the position of iodine along the axis of the octatetraene chain. As an extension of an earlier calculation on the transport of charge by a charged soliton, a similar calculation is performed on a $C_8H_{10}^+$ "kink" traveling along the backbone of $C_{12}H_{14}^+$, yielding very similar results. A computer code has been developed to compute the transport velocity of charge based on the above model and can be used in conjunction with the GAMESS program package. © 1996 John Wiley & Sons, Inc.

Introduction

When doped even at a very low level, transpolyacetylene (t-PA) exhibits very high conductivity [1, 2]. In understanding the way charge is transported in organic systems under the influence of an electric field, one has to take into account many details of the system beyond those

required in understanding conduction in metals and inorganic semiconductors. While the latter is amenable to interpretation in terms of largely free electrons or holes, the conductivity in organic systems appears to be a truly many-body phenomenon where not only is such reduction to free electrons inappropriate, but also the electron-nuclear coupling seems to be too strong to be treated as perturbation. First proposed by Su, Schrieffer, and Heeger (SSH) [3], the traveling soliton waves are now generally accepted as repre-

* To whom correspondence should be addressed.

sending the predominant mode of electrical conduction in doped transacetylene and perhaps other similar organic polymeric systems. In this soliton model of electrical conduction the electrical energy is carried by positively or negatively charged solitons which are, in fact, "kinks" in an otherwise periodic Peierls bond-alternated geometry.

The solitonic transport theory developed so far as relied almost exclusively on the SSH model Hamiltonian or its variants [3]. Because of the very approximate nature of these models, however, even though the reality of charged solitons as carriers of electrical energy is now accepted universally, the predictions of their mobility [4-6] based on these models remain unconvincing. This is notwithstanding the fact that several all-electron semiempirical [7] and ab initio [8] studies on the structure of charged solitons reveal roughly the same features as obtained from the SSH models. We have recently carried out an ab initio evaluation of the transport velocity of a positively charged soliton and made an estimate of the conductivity based on these calculations [2]. In this analysis several assumptions have been made. First, the positively charged solitons are assumed to be the dominant carriers. Moreover, the excitonic energy (i.e., the energy of these carriers relative to the ground state) is taken to be of the order of 1 eV. Also the solitonic charge is assumed to be not pinned by the dopant counterions and moving almost freely along the direction of the chain axis. In the present work we shall try to justify these assumptions again in the ab initio framework. For this, we restrict ourselves to the case of a single iodine atom interacting with a *trans*-octatetraene molecule. This represents perhaps the simplest prototype (computationally speaking) of the real doped t-PA system. Upon satisfying ourselves that the underlying assumptions of the model are borne out, we reevaluate the transport velocity of a positively charged octatetraene kink as it moves along the chain axis of the oligomer $C_{12}H_{14}^+$ under the influence of an external voltage.

Characterization of the Iodine-doped Polyene System

In carrying out the investigation as outlined above we must describe adequately both the ground and excited states of the total system as the charge moves along its length. We can achieve

this by using the complete active space self-consistent field (CASSCF) wavefunctions built out of the total π -orbital space treated as the active space. However, the CASSCF process runs into difficulties here because of the weak mixing of the σ - and π -orbitals due to the breakdown of the "planar" symmetry of the polyene in the presence of the iodine atom. An unrestrained CASSCF will scramble the σ - and π -orbitals among each other beyond recognition, leading to undesirable inclusion of the σ -correlation. Moreover, this will also cause the MCSCF convergence, particularly for the excited states, to be poor since the partially occupied π -orbitals have orbital energies that are very similar to the higher lying σ -orbitals. In this work we solve this problem as follows: We first obtain the occupied σ -orbital and the occupied and virtual π -orbital from a restricted Hartree-Fock (RHF) calculation on the polyene (without the iodine). We also get the occupied σ - and π -orbitals for iodine. These orbitals are then combined, ordered in accordance with the basis set of the combined system, IC_8H_{10} , and then orthonormalized. Let us denote this set as $\{\sigma_i^0\}$ and $\{\pi_i^0\}$. We now carry out an open-shell RHF on the combined system. Let the corresponding occupied and unoccupied orbitals be denoted as $\{\phi_j\}$. We now transform these orbitals into the σ - and π -like orbitals $\{\sigma_i\}$ and $\{\pi_i\}$, respectively, as follows:

$$\begin{aligned}\sigma_i^{(oc)} &= \sum_{j \in oc} \langle \sigma_i^0 | \phi_j \rangle \phi_j, \\ \pi_i^{(oc)} &= \sum_{j \in oc} \langle \pi_i^{0(oc)} | \phi_j \rangle \phi_j, \\ \pi_i^{(un)} &= \sum_{j \in un} \langle \pi_i^{0(un)} | \phi_j \rangle \phi_j,\end{aligned}\quad (1)$$

where the symbols oc and un denote respectively the occupied and virtual orbitals. These orbitals $\{\sigma_i\}$ and $\{\pi_i\}$ are then used as the starting orbital sets for the CASSCF runs where we impose the additional constraint that the σ -like orbitals mix only within the space that is orthogonal to the π -like orbitals, while the π 's mix only among themselves.

Since an analytic approach of geometry optimization is ruled out because of the constraints on CASSCF, in order to simplify the geometry search process, we make the following further approximations: First, we truncate the π -space to consist only of the lowest N (the number of "heavy" atoms) π -orbitals, thus obviating the need of the

rotation of the π -orbitals during the CASSCF optimization. The error due to this constraint, we believe, is minimal as far as the geometry optimization is concerned since the changes of geometry in our case bring about mostly bond breaking and forming without much of a participation of the nonvalence π -space (which, in the case of a minimal basis, as we choose for the first stage of our calculation, is absent anyway). This approximation clearly reduces the orbital optimization problem to simply the optimization of the closed-shell σ -orbitals. Also, in the search for the minimum in the potential energy surface, we avoid a complete geometry optimization by keeping frozen all the lengths of the truly σ -bonds such as CH throughout at their values obtained for the polyene in its ground state. Moreover, we assume that the polyene molecule remains strictly planar. This is presumably a good approximation since in both the ground and excited states iodine is quite far away from the plane of the polyene molecule, making it highly unlikely for the latter to be significantly nonplanar.

Calculations and Results on the Polyene Plus Iodine System

For studying the influence of a counterion, in this case I^- , we adopt the following basis: We treat iodine in the effective core potential (ECP) framework using the Hay-Wadt ECP basis. For octatetraene we use the STO-3G basis, which is known to lead to a reasonably good geometry for such systems.

In Figure 1 we plot the bond lengths of the system $I + C_8H_{10}$ in its ground and first excited states. It is evident that the ground-state geometry is very close to that of the undoped Peierls alter-

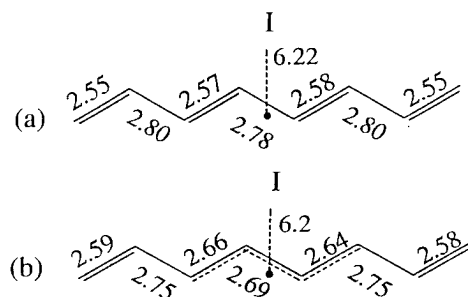


FIGURE 1. Bond distances (in bohrs) for the ground (a) and excited (b) states of $C_8H_{10}I$.

nating-bond polyene, while the excited state corresponds to a solitonic kink (a soliton-antisoliton pair). The Mulliken charges carried by iodine in these states are respectively -0.033 and -0.694 and the excitonic energy is 0.76 eV. Table I shows the excited-state energy and the Mulliken charge on iodine as functions of the distance of iodine from one end of the octatetraene (all other geometry parameters being optimized within the restrictions described above). It is evident that the excited-state energy is quite insensitive to where the iodine is located. It is, however, interesting to note that the charges on iodine vary significantly as the solitonic kink moves away from iodine.

We conclude from the above calculations that the assumptions underlying the modeling of charge transport in terms of a traveling charged soliton are justified, at least at the level of calculations described above. Once the geometry is optimized for both the ground and excited states, we recompute the excitation energy at the level of the 3-21G basis for all the atoms. The difference of 0.07 eV in the excitation energies going from STO-3G to 3-21G (shown in parentheses in Table I) is sufficiently small such that the general conclusions drawn here based on STO-3G are very likely sound.

Evaluation of Charge Transport Velocity

Calculations on the charge transport are now carried out by assuming a positively charged larger polyene, in our case, $C_{12}H_{14}^+$. The model of charge transport that we pursue here is similar to the one used in [2]. This is diagrammatically sketched in

TABLE I
CASSCF excitonic energy of the first excited state and Mulliken charge on iodine as functions of iodine distance measured from the "left"-most carbon.^a

$x(A)$	Excitonic energy (hartrees)	Mulliken charge on I
0.44	0.03321	-0.616
0.94	0.03311	-0.611
1.44	0.03069	-0.651
1.94	0.02954	-0.706
2.44	0.02854 (0.03111)	-0.694
2.94	0.03302	-0.612

^a The ground state CASSCF energy = -316.21123 hartrees at the ground-state optimized geometry.

Figure 2. We review below the steps involved in calculating the velocity of transport of charge. (i) First we obtain the ground-state wavefunction of the total neutral system, in this case, $C_{12}H_{14}$. This is done at the RHF level. (ii) The π -orbitals $\{\pi_i\}$ are localized in the following manner: We consider two sets of elementary localized π -orbitals, one consisting of all the bonding orbitals and the other of antibonding ones belonging to each double bond. These are symmetrically orthonormalized. We denote the resulting orbitals as $\{\pi_i^b\}$ and $\{\pi_i^a\}$ respectively. The π -orbitals obtained from step (i) are now projected on to these orbitals:

$$\begin{aligned}\pi_i^{(oc)} &= \sum_j \langle \pi_i^b | \pi_j^{(oc)} \rangle \pi_j^{(oc)}, \\ \pi_i^{(un)} &= \sum_j \langle \pi_i^a | \pi_j^{(un)} \rangle \pi_j^{(un)}.\end{aligned}\quad (2)$$

(iii) A part of the oligomer is now selected (to be called the "charged unit") as carrying the charge and a restricted open-shell Hartree-Fock (ROHF) calculation is carried out where only the π -orbitals belonging to the charged unit are optimized with the constraint that they be orthogonal to the rest of the π -orbitals. The σ -orbitals are, however, optimized for all geometries. This is followed by a relocation of the π -orbitals on the charged unit (along the lines indicated above). A geometry optimization of the total system is now carried out using a singles-and-doubles configuration interaction (CI) where only the π -electrons of the charged unit are promoted. This will give us both the equilibrium geometry and the normal modes with the charge located within the charge unit selected. (iv) The total wavefunction is now constructed as a linear combination of the global Born-Oppen-

heimer (GBO) products Φ, G_i , each defining a "charge unit" [9]. The matrix elements and overlaps are given by:

$$\begin{aligned}H'_{ij} &\equiv \langle \Phi_i | H_{el} - \mathcal{E}_{el} | \Phi_j \rangle \langle G_i | G_j \rangle, \\ S'_{ij} &\equiv \langle \Phi_i | \Phi_j \rangle \langle G_i | G_j \rangle,\end{aligned}\quad (3)$$

where H_{el} and \mathcal{E}_{el} are respectively the electronic Hamiltonian and electronic energy of each charge unit and the electron integrals are computed at the equilibrium geometry of either the i th or the j th charge unit. In our singles-and-doubles representation of the electronic wavefunctions (see above), assuming that Φ_i and Φ_j are the same except for a translation that transforms Φ_i into Φ_j or vice versa, it is easy to show that, to a good approximation (neglecting virtual space contribution),

$$\begin{aligned}\langle \Phi_i | \Phi_j \rangle &\cong \sum_a B_{ia} B_{ja}, \\ \langle \Phi_i | H_{el} - \mathcal{E}_{el} | \Phi_j \rangle &\cong \sum_a B_{ia} B_{ja} (\mathcal{E}_a - \mathcal{E}_{el}) \\ &\quad + \sum_{a \neq b} B_{ia} B_{jb} \mathcal{E}_{ab},\end{aligned}\quad (4)$$

where

$$\begin{aligned}\Phi_i &\cong \sum_a B_{ia} \Pi_a \\ \Pi_a &\equiv \pi_1^2 \pi_2^2 \cdots \pi_{a-1}^2 \pi_a \pi_{a+1}^2 \cdots \\ \mathcal{E}_a &= \langle \pi_a | H_{el} | \pi_a \rangle\end{aligned}\quad (5)$$

(v) The general solution of the time-dependent problem is

$$\Psi(\mathbf{r}, \mathbf{R}, t) = \sum_{\lambda} C_{\lambda} \Psi^{(\lambda)} e^{i\mathcal{E}_{\lambda} t / \hbar}.\quad (6)$$

If we assume that at $t = 0$ the system is in the nonsteady localized state Φ_1 , that is, the charge is localized in the first charge unit, we have

$$\begin{aligned}\sum_{\lambda} C_{\lambda} A_1^{(\lambda)} &= 1, \\ \sum_{\lambda} C_{\lambda} A_i^{(\lambda)} &= 0, \quad i \neq 1\end{aligned}\quad (7)$$

The probability that at a later time the charge resides on the charge unit number 2 is given by

$$\begin{aligned}P_2 &= \left| \sum_{\lambda} C_{\lambda} A_2^{(\lambda)} e^{i\mathcal{E}_{\lambda} t / \hbar} \right|^2 \\ &= 4 \sum_{\lambda, \lambda'} C_{\lambda} C_{\lambda'} A_2^{(\lambda)} A_2^{(\lambda')} \sin^2 \frac{\mathcal{E}_{\lambda'} - \mathcal{E}_{\lambda}}{2\hbar} t\end{aligned}\quad (8)$$

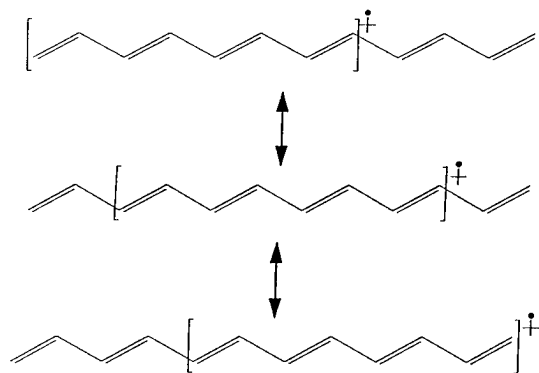


FIGURE 2. Scheme for modeling transport of charge along the backbone of a $C_{12}H_{14}$ radical cation.

assuming both C_λ and $A_i^{(\lambda)}$ to be real. This attains its maximum at a time t given by

$$\sum C_\lambda C_{\lambda'} A_2^{(\lambda)} A_2^{(\lambda')} \left(\frac{\mathcal{E}_{\lambda'} - \mathcal{E}_\lambda}{\hbar} \right) \sin \frac{\mathcal{E}_{\lambda'} - \mathcal{E}_\lambda}{\hbar} \tau = 0. \quad (9)$$

In the present case Eq. (3) involves three charge units, leading to three eigenvalues of which the higher two are nearly degenerate. Thus Eq. (9) leads to

$$\sin \frac{\mathcal{E}_2 - \mathcal{E}_1}{\hbar} \tau = 0 \quad \text{or} \quad \tau = \frac{\pi \hbar}{\mathcal{E}_2 - \mathcal{E}_1}, \quad (10)$$

whence the transport velocity is given by

$$v = 0.256 \times (a \text{ in bohrs}) \times (\Delta E \text{ in eV}) \times 10^7 \text{ cm/s}, \quad (11)$$

where a is the approximate repetition length in polyacetylene and ΔE is the width of the excitonic energy band.

We shall now describe our calculations on the transport of charge in $C_{12}H_{14}^+$. We have found [9] the choice of the STO-3G basis for these calculations to be adequate for preliminary estimates. As shown in Figure 3, the general features of the geometry of $C_{12}H_{14}^+$ optimized at the semiempirical and ab initio SCF levels with STO-3G and 3-21G basis sets are very similar. For the case at hand the values of the various overlaps and matrix elements [Eq. (3)] are shown in Table II. The solution of the corresponding secular equation yields the following energies: $E_1 = -0.030$, $E_2 = -0.002$, and $E_3 = 0.001$ hartrees. Hence the transport velocity is calculated to be approximately 0.9×10^7 cm/s. This is very similar to the value obtained in

TABLE II
Values of S_{ij} and H'_{ij} [Eq. 3].^a

Parameters	Values
S'_{12}	-0.78676
S'_{13}	0.39086
H'_{12}	-1.7222 ($\times 10^{-3}$ hartrees)
H'_{13}	1.0981 ($\times 10^{-3}$ hartrees)

^a S'_{23} and H'_{23} are assumed equal to S'_{12} and H'_{12} , respectively.

[9] with a shorter chain with a pure charged soliton. Thus we arrive at the important conclusion that the size of the "charged unit" does not seriously affect the calculated transport velocity. Such high velocities have been shown [9] to be crucial for the occurrence of high conductivity in t-PA.

As we have noted in [9], however, the charge transport velocity is substantially reduced (by nearly 40%) when 3-21G basis is used instead of STO-3G in the transport calculation. The resulting value is then in approximate agreement with the value $v^{(s)} = 0.12 \times 10^7$ cm/s reported by Su [6] based on the SSH Hamiltonian.

Code for Computing Charge Transport

We have automated the above steps by developing a code and installing it in the GAMESS environment. A flow diagram is given in Figure 4. The code requires as input the occupied and virtual orbitals resulting from an RHF calculation on the neutral backbone system (restricted here to be

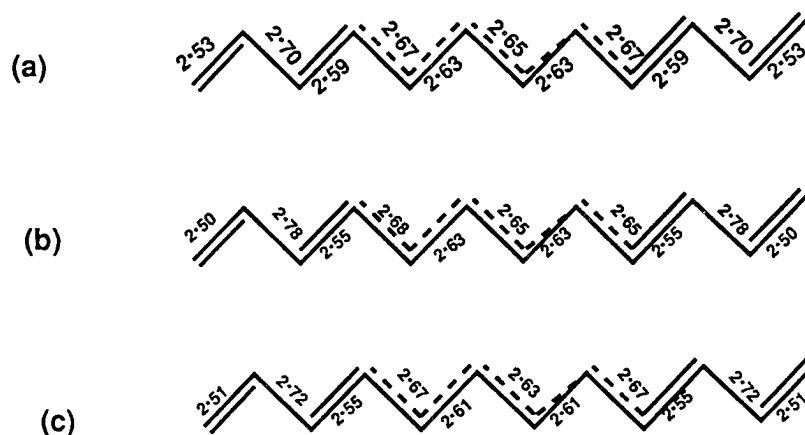


FIGURE 3. Geometry of $C_{12}H_{14}^+$ with bond distances shown in bohrs optimized at (a) the semiempirical (AM1) level and the ab initio SCF level with (b) STO-3G and (c) 3-21G bases.

planar). The code then localizes the π -orbitals, performs new ROHF at each of a set of grid points as defined by the input, yielding new σ -orbitals, and then performs singles-and-doubles CI over the localized π -orbitals. The single and double excitations are chosen so as to represent the bond breaking and bond forming that lead to the input-specified location of the charged kink. These CI energies are then used to perform the vibrational analysis. If any of the frequencies is imaginary, the system is displaced in the direction of the normal

mode of imaginary frequency with the largest absolute value until the energy attains a rough minimum, whereupon the above steps are repeated again. On the other hand, if the vibrational frequencies are all real, the new equilibrium geometry is obtained by solving for the displacements that lead to zero gradients (in the quadratic approximation) on the potential surface. If the deviation between the new and old geometries is larger than a given threshold, the above steps are repeated. Otherwise the geometry is assumed converged. The corresponding normal modes and frequencies are then used to obtain the overlaps of vibrational functions according to Eq. (4). Also the overlaps between the electronic wavefunctions and the corresponding Hamiltonian matrix elements are calculated according to Eq. (4). The global secular equation is then solved, leading to the parameter ΔE of Eq. (11).

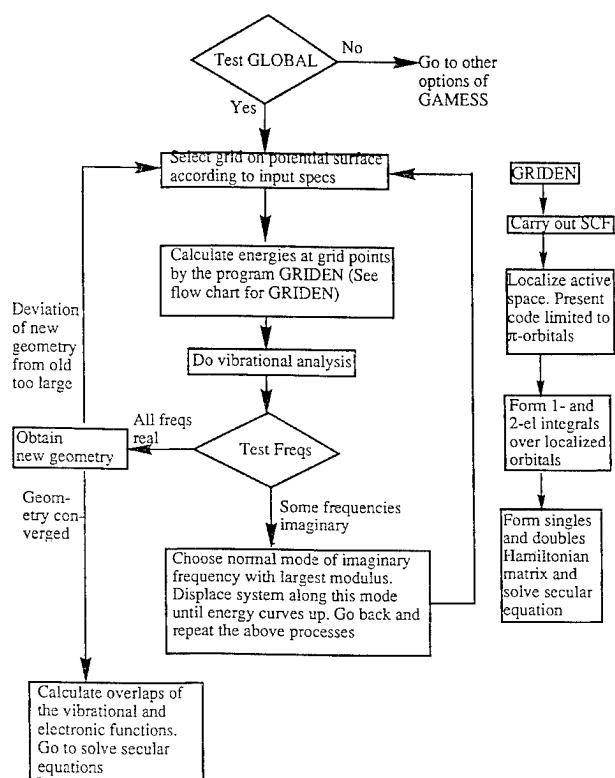


FIGURE 4. Flow chart for global solution of molecular Schrödinger equation.

References

1. H. Shirakawa, E. J. Louis, A. G. McDiarmid, C. K. Chiang, and A. J. Heeger, *J. Chem Soc. Comm.* **1977**, 578 (1977).
2. *Proceedings of the International Conference on Low-Dimensional Conductors*, Boulder, CO, Aug. 9-14, 1981, A. J. Epstein and E. M. Conwell, eds., *Mol. Cryst. Liq. Cryst.* **77** (1981); **83** (1982).
3. W. P. Su, J. R. Schrieffer, and A. J. Heeger, *Phys. Rev. Lett.* **42**, 1698 (1979); *Phys. Rev. B* **22**, 2099 (1980).
4. S. Kivelson, *Phys. Rev. Lett.* **46**, 1344 (1981).
5. S. Kivelson, *Phys. Rev. B* **25**, 3798 (1982).
6. W. P. Su, *Handbook of Conducting Polymers* vol. 11, T. A. Skotheim, Ed. (Marcel Dekker, New York, 1989), pp. 757-794.
7. D. S. Boudreaux, R. R. Chance, J. L. Brédas, and R. Silbey, *Phys. Rev. B* **28**, 6927 (1983).
8. H. O. Villar, M. Dupuis, and E. Clementi, *Phys. Rev. B* **37**, 2520 (1988).
9. G. P. Das and A. T. Yeates, *Int. J. Quant. Chem.*, **59**, 251 (1996).

Theoretical Study of the X-ray Photoionization Spectra of Polycycloalkanes

M. DELEUZE* AND J. DELHALLE

Laboratoire de Chimie Théorique Appliquée, Facultés Universitaires Notre-Dame de la Paix, Rue de Bruxelles 61, B-5000 Namur, Belgium; e-mail for M. D.: deleuze@scf.fundp.ac.be

Received February 24, 1996; accepted February 29, 1996

ABSTRACT

The dependence of X-ray photoionization spectra on structural characteristics is assessed by one-particle Green's function calculations on the nearly isomeric adamantane, 1,4-dimethyl bicyclo [2,2,2] octane and 1,1,4,4-tetramethyl cyclohexane compounds. These calculations are carried out using the quasi-particle approximation and the diagonal 2ph-TDA renormalization scheme for the self-energy. The simulated spectra fingerprint remarkably the atomic connectivity from their inner valence part, through the interplay of energy degeneracies and the influence of torsional strains on electron binding energies. The boundary region between the inner and outer valence bands provides also specific signatures for molecular characteristics pertaining to conformational questions, namely the enforced conversion from the chair to the boat form of the cyclohexane units generating these compounds. © 1996 John Wiley & Sons, Inc.

Introduction

Photoelectron spectroscopy has been successfully used for more than two decades to investigate the electronic structure and the chemical bonding characteristics of molecules in the gas, liquid, and solid phases. As is well known, this spectroscopy gives a direct access from core level shifts to the chemical composition and inhomogeneity in the top layers of organic and inorganic

solids. It is as such one of the most currently used analytical devices. On the other hand, the valence bands have received so far much less attention. By comparison with the results of reliable quantum mechanical calculations, however, valence photoionization spectra can also provide [1] invaluable information on the molecular architecture of the investigated compounds. This comprises not only the overall atomic connectivity (primary structure or configuration) but also the possibility [2–7] of tracing more subtle changes of the molecular conformation (or secondary structure). Owing to its high sensitivity to the mixing of orbitals through

*To whom correspondence should be addressed.

the interplay of cross-section effects, X-ray photoionization spectroscopy (XPS) is particularly well-suited to fingerprint molecular conformations.

Recent theoretical investigations on the electronic structure of large saturated hydrocarbons have disclosed evidence for a mixing of the C_{2s} and $C_{2p} + H_{1s}$ states at the border of the inner and outer valence bands, due to the development of long-range methylenic hyperconjugation effects over zig-zag planar chains [6] or related cyclic structures [7]. These interactions yield highly specific XPS conformational signatures in a binding energy interval comprised between 14 and 22 eV, which could be for instance exploited [8] in a definite identification [9] of the leading fold stacking sequence in the [110]'s growth sector of polyethylene. These studies have generated further investigations on polypropylene [10] or self-assembled layers of alkane-thiol compounds [11]. Long-range methylenic hyperconjugation have also provided a consistent explanation [12] for the origin of valence XP spectra differences of *n*-tridecane in solid and gas phases, considering the thermal agitation prevailing in the gas phase.

Previous works [13] have shown the value of studying gas-phase model molecules to provide a detailed analysis of the core level structure of polymers. Their virtue resides not only in the higher resolution achieved in gas phase but also in the separation of intramolecular characteristics (chemical bonding, vibrational influences on the line profiles, origin of the nonstoichiometric ratios of peak areas) from intermolecular interactions (polarization of neighboring molecules, phonon broadening, structural disorder, etc.) and related solid-state effects limiting the resolution (surface charging). One limitation with *n*-alkanes samples is that the chains adopt different conformations in the gas phase, the proportion of which is hard to define. As a result of the ring closure constraints, the cycloalkane compounds, at least the smallest ones, exhibit in comparison a much better defined molecular architecture. The rigid chair form prevailing for cyclohexane is in particular very well-suited to investigate the effects of long-range methylenic hyperconjugation. As shown in [7, 9, 14], a cyclic conversion from the chair to the boat or twisted-boat forms of cyclohexane could be easily followed from XPS measurements, if the latter conformer, lying 4.2 kcal above the global energy minimum, could be stabilized and isolated,

which is, to our knowledge, impossible in practice nowadays. Nevertheless, this conversion can be followed indirectly, by enforcing the chair and the boat forms of cyclohexane in polycycloalkane structures.

Thus, in the present study, we have chosen to consider the adamantane, the 1,4-dimethyl bicyclo [2,2,2] octane and the 1,1,4,4-tetramethyl cyclohexane compounds, which are of very close chemical nature and nearly isomeric pairwise, but strongly differ in their overall connectivity. A few ultraviolet photoelectron spectra are available [15] for adamantane and hetero derivatives, in studies which essentially focus on the outer valence region. Except for a recent work [16] based on outer valence Green's function (OVGF [17]) calculations, their interpretation has been advanced by comparison with semi-empirical theoretical data. No measurement of the inner valence structure of adamantane from X-ray photoionization spectroscopy has been reported to date. There is also, to our knowledge, no experimental record available for the 1,4-dimethyl bicyclo [2,2,2] octane and the 1,1,4,4-tetramethyl cyclohexane compounds.

In order to evaluate on correlated grounds XPS fingerprints for the molecular structure of polycycloalkanes, the valence ionization spectra of these compounds have been, in this preliminary study, evaluated using simple one-particle Green's function schemes in the quasi-particle approximation [6, 7].

Model Systems and Computational Aspects

Among the many saturated hydrocarbon compounds available today, adamantane has the unique cage structure of a tetrahedron of CH groups embedded in an octahedron of CH_2 groups. The basic pattern found in this molecule is the chair form of cyclohexane, which is consistently reproduced along each of the 3-fold axis of its T_d symmetry group. The 1,4-dimethyl bicyclo [2,2,2] octane compound has been selected in this study, in order to build with the same number of carbons as adamantane a rigid cage structure of D_{3h} symmetry based on the boat form of cyclohexane. The chair form of cyclohexane is most conveniently recovered from the latter structure by considering the closely related 1,1,4,4-tetramethyl cyclohexane compound of C_{2h} symmetry.

The photoelectron spectra of these compounds have been computed on the basis of RHF/STO-3G optimized geometries. The molecular structures studied are shown in Figure 1. Previous comparisons carried out on linear alkanes [6, 7, 9] or cycloalkanes [9] have pointed the adequacy of simple Green's function calculations carried out on the assumption of a quasi-particle picture of ionization, when has been recently assessed [14] by a detailed series of Green's function calculations accounting for multistate interactions in an algebraic diagrammatic construction (ADC) scheme [18] being exact through third order in correlation. As shown in this study, the idea of a one-particle process for the ionization of saturated hydrocarbons can be retained nearly over the whole valence region, up to a general threshold of about 23 eV. Beyond that threshold, the innermost ionization lines in the C_{2s} region tend to break into many shake-up lines of comparable strength, as a result of severe hole-mixing effects [19] in the molecular cation. Particularly relevant for the present purpose is that the main spectral features fingerprinting the development of long-range methylenic hyperconjugation remain free [18] of satellites. At this point, it is useful to recall that configurational and conformational signatures in the XPS spectra of saturated hydrocarbons find essentially their

origin in the nodal characteristics of the molecular orbitals. These signatures can therefore be consistently analyzed [6a, 7] in terms of the relative distribution of main lines, which appears to be mostly unaffected [18] by basis-set effects.

As the Green's function is in this case dominantly diagonal, one can legitimately consider related forms of the second-order self-energy derived from a renormalization [20] of excitation energies through first-order in correlation in the so-called diagonal 2ph-TDA (two-particle-hole Tamm-Dankoff Approximation) scheme [21]. In spite of inherent drawbacks such as a loss of size consistency [22], this scheme has enabled [6a, 7, 9] overall a satisfactory reproduction of the photoionization spectra of saturated hydrocarbons, in regards with the relative positions of peaks and their intensity or the width and shape of bands. Accurate absolute values are beyond reach with this approximation, as a result of the neglect of electron correlation in the reference ground state, yielding typically an underestimation of the electron binding energies by about 1 eV. This approach has been preferred to other schemes of decoupling of the many-body problem, like the second-order (MBGF2) or shifted Born collision (SBC) approximations [21] for the self-energy. The reason of this choice is that for linear alkanes, it

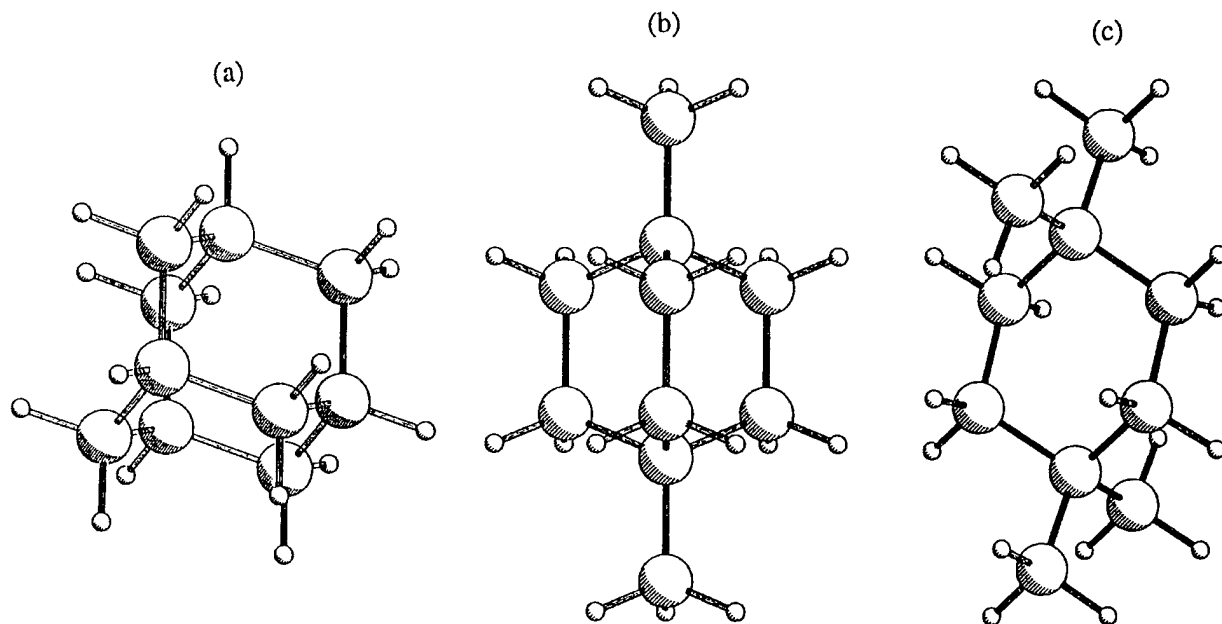


FIGURE 1. Selected structures: (a) adamantane, (b) 1,4-dimethyl bicyclo [2,2,2] octane, and (c) 1,1,4,4-tetramethyl cyclohexane.

has enabled [6b, 9] a calculation of the relative positions of inner valence ionization lines within less than 4% of error with respect to experiment.

Photoionization intensities have been evaluated using the parametric Gelius model [23] for molecular orbital cross sections; the relative atomic photoionization cross sections used for C_{2s} , C_{2p} , and H_{1s} being 100.0, 7.69, and 0.00, respectively (core atomic functions do not significantly participate in the molecular orbitals of the valence region). Although this simple model implies the use of a minimal basis set, it reflects nicely [9, 14] the influence of the C_{2s} - C_{2p} mixing of states at the border of the inner and outer valence regions arising with the development of methylenic hyperconjugation effects [6a] on the calculated photoionization intensities. For a better account of many-body effects, the Gelius cross sections, obtained from an uncorrelated model, are multiplied by the corresponding pole strength factors Γ_c as obtained from a one-electron Green's function calculation. More details on the technical aspects of these calculations can be found in [6b].

The simulated XPS spectra shown in this work are constructed from a superposition of peaks centered at the Koopmans and 2ph-TDA/QP values for electron binding energies, respectively. In these spectra, the ionization lines have been convoluted using a spread function based on a linear combination of one gaussian and one lorentzian curve with equal weight and a full width at half the maximum of 1.1 eV, in order to account roughly for vibrational broadening, as well as the experimental resolution characteristics allowed with the most recent gas-phase X-ray spectrometers [24].

Results and Discussion

GENERAL OBSERVATIONS

The convoluted spectra of the selected compounds are displayed in Figure 2 at the Koopmans and diagonal 2ph-TDA/QP levels of approximation. In the latter case, the computed main lines are also given as a spike spectrum. The detailed molecular orbital cross sections and Green's function data used to construct these convolutions are given in Table I, together with results obtained using other decoupling schemes of the many-body problem. Except for a shift and a contraction of bands toward lower binding energies, the Koop-

mans and diagonal 2ph-TDA/QP spectra are overall essentially similar, a result of a balance in the convolution procedure between the relaxation effects on binding energies and the dispersion of photoionization intensity into secondary processes [1, 6a].

Two bands of rather different intensity can be distinguished on the selected energy scale, justifying a somewhat arbitrary [6a] classification of the valence molecular orbitals of saturated hydrocarbon compounds in terms of inner valence levels dominated by C_{2s} atomic contributions and of outer valence levels of leading ($C_{2p} + H_{1s}$) character. Owing to their large number and to their diffuse character, the latter molecular orbitals yield poorly structured bands of low photoionization intensity, from which it is usually difficult to extract specific information on the molecular structure. Therefore, in this contribution, attention is mainly focused on the inner valence levels.

As shown (Table I) by the values obtained for pole strengths, the molecular orbital picture is well preserved nearly over the whole range of binding energies, justifying the use of diagonal approximations for the self-energy and its kernel. Great care has, however, to be exercised for a definite conclusion, as a minimal STO-3G basis set yields shake-up states of artificially too high energy and tends therefore to limit the fragmentation of ionization lines into satellites. In direct relationships with the results given in [6b, 9] and [14], the pole strengths obtained for the innermost levels of the investigated compounds drop significantly at the 2ph-TDA level of approximation, an observation which suggests a complete breakdown of the molecular orbital picture of ionization of an electron out of those levels in Green's function calculations of the ADC type, based on larger basis sets. Since these levels fall far apart from each other, their fragmentation tail should simply yield a smoothing and broadening of the convoluted band profile at the bottom of the inner valence region. As in [9] and [14], the idea of a one-particle process of ionization can be on the other hand reasonably retained below an approximate threshold of 23 eV on electron binding energies.

In Figure 3, we compare our theoretical results to the inner valence binding energy data obtained by R. Boschi et al. [15e] from He(II) photoelectron spectroscopy measurements on adamantane. As clearly shown by the slope of linear correlations

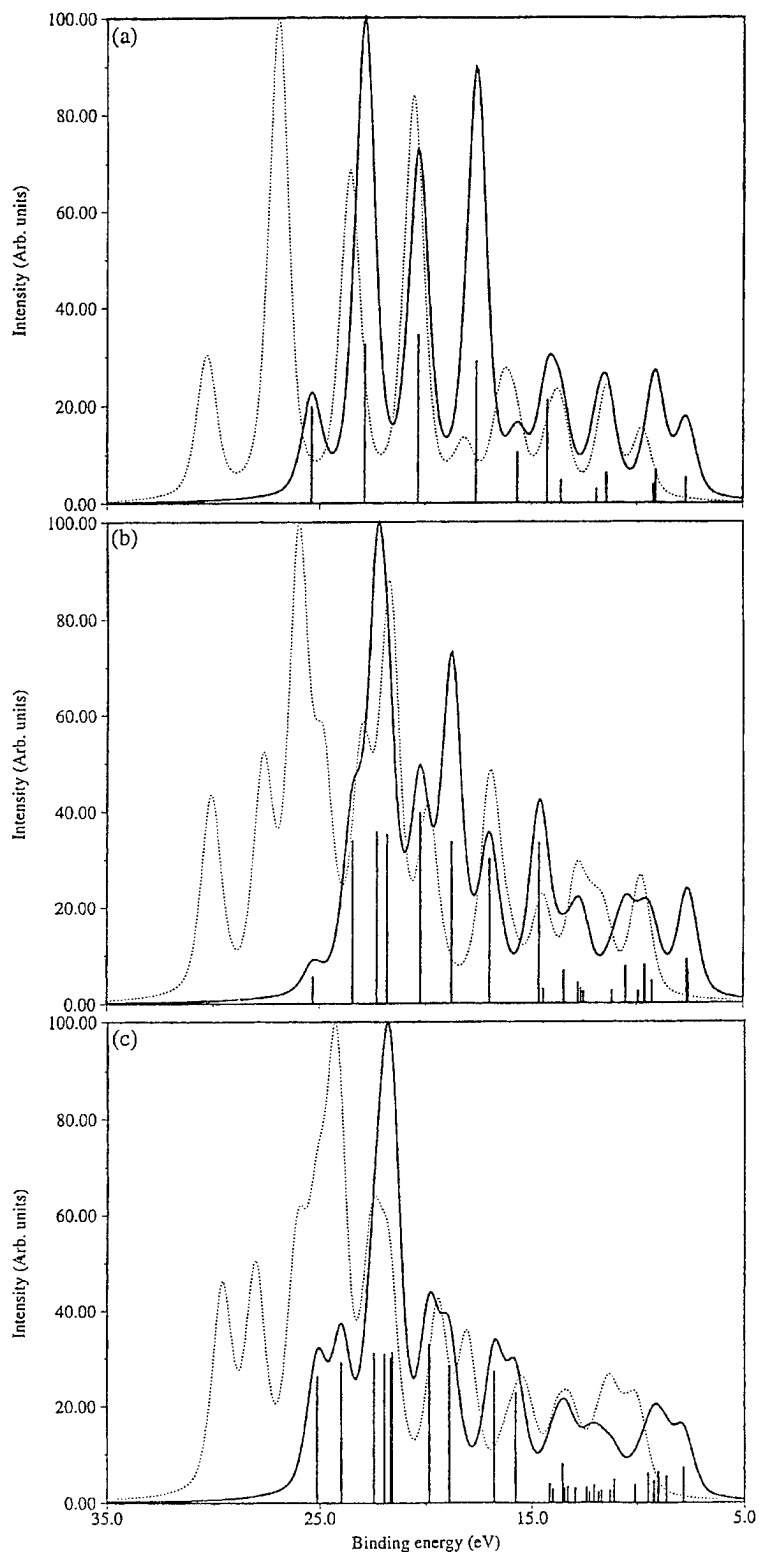


FIGURE 2. X-ray theoretical photoionization spectra of (a) adamantane, (b) 1,4-dimethyl bicyclo [2,2,2] octane, and (c) 1,1,4,4-tetramethyl cyclohexane, at the HF / Koopmans (dotted line) and diagonal 2ph-TDA (full line) levels of description.

TABLE I
Theoretical electron binding energies (in eV) and Gelius XPS molecular orbital cross sections (pole strengths in brackets).

Molecule	level	Koopmans	QP2	SBC	Diagonal 2ph-TDA	σ
Adamantane (T_d)						
	$1a_1$	30.32	27.10 (0.880)	26.16 (0.804)	25.40 (0.551)	77.39
	$1t_2$	26.98	24.21 (0.897)	23.45 (0.840)	22.90 (0.789)	88.52
	$1e$	23.58	21.40 (0.915)	20.78 (0.869)	20.34 (0.830)	88.89
	$2t_2$	20.57	18.56 (0.921)	18.00 (0.880)	17.62 (0.847)	73.69
	$2a_1$	18.18	16.46 (0.929)	15.99 (0.894)	15.67 (0.867)	25.72
	$3a_1$	16.40	14.92 (0.938)	14.53 (0.907)	14.26 (0.885)	51.26
	$3t_2$	15.79	14.27 (0.936)	13.87 (0.906)	13.60 (0.884)	11.45
	$1t_1$	14.21	12.59 (0.933)	12.18 (0.904)	11.91 (0.883)	7.01
	$4t_2$	13.69	12.09 (0.935)	11.69 (0.907)	11.43 (0.887)	15.13
	$2t_1$	11.44	9.82 (0.934)	9.44 (0.908)	9.10 (0.889)	9.34
	$2e$	11.42	9.73 (0.932)	9.34 (0.905)	9.10 (0.887)	16.44
	$5t_2$	9.76	8.22 (0.937)	7.89 (0.913)	7.68 (0.896)	12.45
1,4-Dimethyl bicyclo [2,2,2] octane (D_{3h})						
	$1a'_1$	30.09	26.87 (0.880)	25.93 (0.800)	25.31 (0.135)	79.21
	$1a'_2$	27.64	24.81 (0.894)	24.02 (0.833)	23.44 (0.761)	87.05
	$1e'$	26.00	23.52 (0.904)	22.81 (0.850)	22.29 (0.796)	87.67
	$2a'_1$	24.84	22.79 (0.918)	22.23 (0.873)	21.81 (0.832)	82.59
	$2a'_2$	22.99	21.12 (0.925)	20.62 (0.887)	20.25 (0.852)	90.83
	$1e''$	21.70	19.72 (0.921)	19.16 (0.879)	18.77 (0.844)	77.59
	$3a'_1$	19.87	17.89 (0.922)	17.36 (0.883)	16.99 (0.851)	69.10
	$3a'_2$	16.97	15.35 (0.935)	14.94 (0.904)	14.65 (0.880)	74.14
	$2e'$	16.75	15.16 (0.932)	14.72 (0.900)	14.44 (0.876)	6.59
	$4a'_1$	16.02	14.23 (0.926)	13.78 (0.894)	13.48 (0.870)	15.18
	$2e''$	14.54	13.32 (0.945)	13.00 (0.922)	12.80 (0.905)	9.34
	$1a'_2$	14.47	13.12 (0.942)	12.76 (0.915)	12.53 (0.897)	5.15
	$3e'$	14.47	13.19 (0.944)	12.86 (0.920)	12.66 (0.903)	6.32
	$2e''$	12.93	11.70 (0.946)	11.38 (0.923)	11.18 (0.907)	5.61
	$4e'$	12.85	11.12 (0.933)	10.79 (0.905)	10.54 (0.885)	16.61
	$4a'_2$	12.13	10.29 (0.926)	9.88 (0.899)	9.62 (0.879)	17.51
	$1a'_1$	11.61	10.41 (0.948)	10.11 (0.926)	9.93 (0.911)	5.39
	$5e'$	11.57	9.90 (0.932)	9.52 (0.906)	9.28 (0.887)	10.10
	$5a'_1$	9.90	8.22 (0.931)	7.86 (0.907)	7.64 (0.889)	19.60
	$3e''$	9.76	8.17 (0.935)	7.80 (0.910)	7.59 (0.893)	14.71
1,1,4,4-Tetramethyl cyclohexane (C_{2h})						
	$1a_g$	29.61	26.58 (0.887)	25.77 (0.822)	25.14 (0.742)	80.97
	$1b_u$	28.05	25.27 (0.895)	24.55 (0.839)	24.01 (0.778)	85.42
	$1a_u$	26.09	23.61 (0.906)	22.96 (0.856)	22.48 (0.812)	87.35
	$2a_g$	25.15	22.97 (0.915)	22.39 (0.870)	21.98 (0.830)	84.93
	$2b_u$	24.31	22.50 (0.926)	22.02 (0.888)	21.68 (0.856)	80.09
	$3a_g$	24.18	22.39 (0.927)	21.92 (0.891)	21.60 (0.860)	83.15
	$3b_u$	22.59	20.69 (0.925)	20.20 (0.888)	19.86 (0.857)	87.51
	$1b_g$	21.77	19.79 (0.921)	19.27 (0.882)	18.90 (0.850)	76.24
	$4a_g$	19.45	17.56 (0.925)	17.10 (0.892)	16.78 (0.865)	71.85
	$4b_u$	18.06	16.44 (0.918)	16.04 (0.905)	15.77 (0.881)	59.09
	$5a_g$	16.35	14.80 (0.934)	14.42 (0.907)	14.17 (0.885)	10.13

TABLE I
(Continued).

Molecule	level	Koopmans	QP2	SBC	Diagonal 2ph-TDA	σ
	$2b_g$	16.07	14.62 (0.939)	14.25 (0.912)	14.01 (0.892)	7.04
	$5b_u$	15.55	14.14 (0.941)	13.79 (0.914)	13.57 (0.895)	20.24
	$2a_u$	15.51	14.05 (0.938)	13.70 (0.912)	13.47 (0.893)	7.74

displayed in this figure, the $1t_2$, $1e$, $2t_2$, $2a_1$ HF one-electron levels of adamantane fall in an energy range that is too large by about 36% as compared with experiment, a defect which reduces to an error of 20, 16, and 12% with the diagonal second-order, SBC, and 2ph-TDA results, respectively. These slopes are significantly larger than the ones obtained in the same conditions [6b] for gas-phase samples of *n*-alkane chains (respectively, HF: 1.27; QP2: 1.13; SBC: 1.07; 2ph-TDA: 1.00), reflecting the enhanced role played by electronic relaxation effects in a polycyclic structure. This relates to a

lowering of the fundamental gap as a result of torsional strains.

INFLUENCE OF THE ATOMIC CONNECTIVITY

Striking differences can be observed in these bands from one compound to the other, confirming the proposition that the valence region of XP spectra can be successfully used to extract information on the molecular structure. In this case, the XPS fingerprints relate to combined variations on

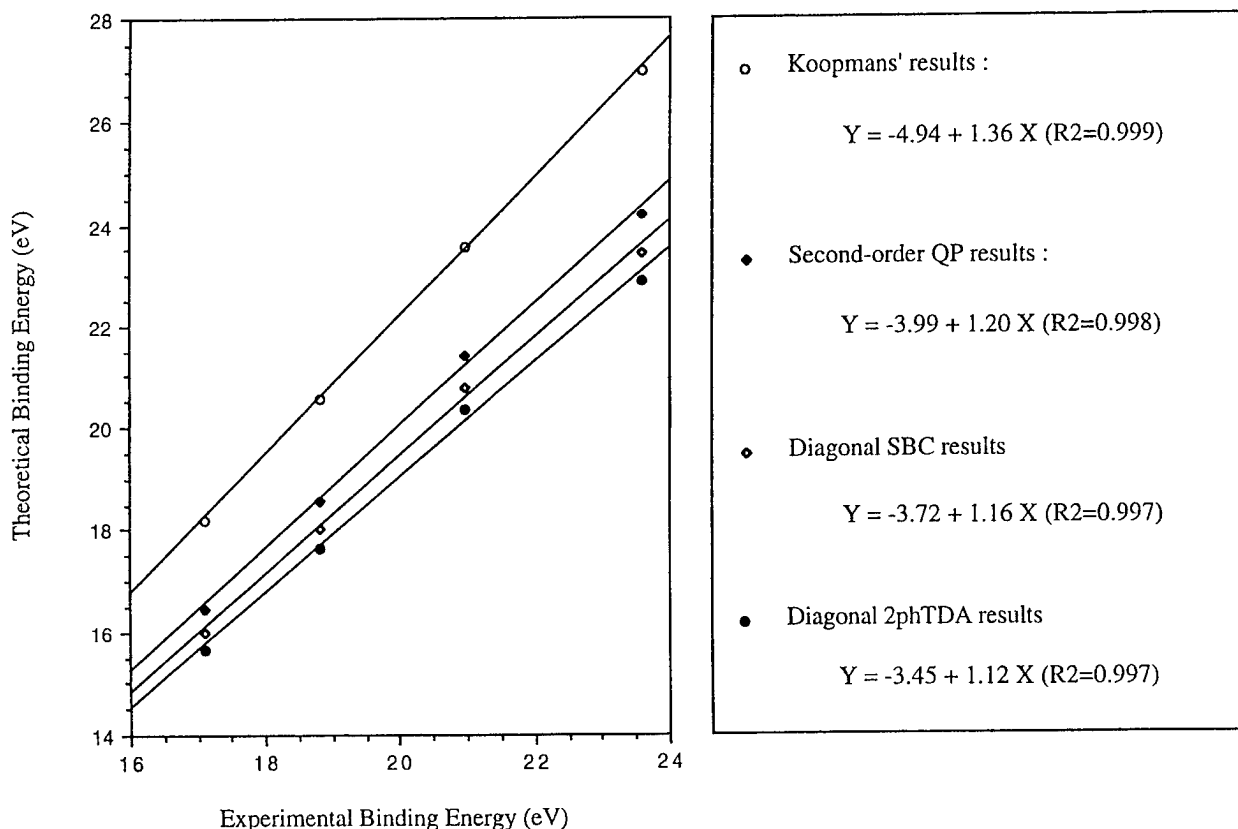


FIGURE 3. Correlation between theoretical and experimental [15e] inner valence binding energies of adamantane.

the connectivity, torsional strains in polycyclic structures, and transannular or long-range interactions, an observation which is worth further analysis.

The inner and outer valence bands fall by 1.6 eV apart in the ionization spectrum of 1,1,4,4-tetramethyl cyclohexane, whereas the topmost C_{2s} level of 1,4-dimethyl bicyclo [2,2,2] octane compound lies only 0.2 eV above the first outer valence level. From the intensity of the individual ionization lines, the C_{2s} and $C_{2p} + H_{1s}$ bands clearly interpenetrate in the XP spectrum of adamantane. This overall behavior relates to an enhancement of torsional strains with the closure and fusion of one, three, and four six-membered rings, respectively, yielding [9] a stronger energy dispersion of the C_{2s} and $C_{2p} + H_{1s}$ one-electron levels.

From their overall aspect, the outer valence bands of the selected compounds present some similarity, with the emergence of four rather poorly resolved substructures. On the other hand, the atomic connectivity affects heavily the overall aspect of the convoluted inner valence bands, through the interplay of energy degeneracies and line positions. Four peaks can be clearly distinguished in the C_{2s} band of adamantane, the intensity of which directly reflects the degree of degeneracy of the corresponding levels, $1a_1$, $1t_2$, $1e$, $2t_2$, successively. As shown in Figure 2(a), $2a_1$ level falling in the border energy range with the outer valence band should most likely remain hidden in the convoluted XPS background. The 1,4-dimethyl bicyclo [2,2,2] octane compound yields six peaks in the convoluted C_{2s} band, which can be assigned to the following sets of orbitals, successively: ($1a'_1$); ($1a'_2$, $1e'$, and $2a'_1$); ($2a''_2$); ($1e''$); ($3a'_1$); ($3a''_2$). Only four well-resolved structures emerge from the inner valence band of the 1,1,4,4-tetramethyl cyclohexane compound, which from their energy location and relative intensity remind the C_{2s} energy structure of the 1,4-dimethyl bicyclo [2,2,2] octane compound.

INFLUENCE OF TRANSANNULAR INTERACTIONS

The boundary energy region between the inner and outer valence bands exhibit also specific differences from one compound to the other, which cannot be easily rationalized considering atomic connectivity only. These changes relate to a modulation of long-range interactions with variations on

the molecular architecture, and can be as such regarded as probes of conformational characteristics.

From the computed photoionization cross sections (Table I), the $2a_1$ orbital of adamantane can be shown to be dominantly of ($C_{2p} + H_{1s}$) character, whereas the $3a_1$ orbital is clearly dominated by C_{2s} atomic contributions. In the convoluted XP spectrum [Fig. 2(a)], this feature is fingerprinted by the disappearance of the $2a_1$ level in the computed background and by the emergence of a relatively intense peak at 14.3 eV, in an energy region normally assigned to the outer valence band. As for the chair form of cyclohexane [6b, 9] or zig-zag planar chains of polyethylene [6a, 9], this particularly strong mixing of the $C_{2s}/(C_{2p} + H_{1s})$ orbitals at the border of the inner and outer valence bands typically relates to the development of through-space interactions between the methylenic C-H bond (also referred as σ -conjugation effects [25]). It is in this case very strongly favored by the overlap of the inner and outer valence energy ranges due to the ring constraints in a cage structure on the one hand, and on the other hand by the topology of the involved orbitals, $2a_1$ and $3a_1$, enabling a hyperconjugation pattern fully consistent with the tetrahedral symmetry group. In comparison, when considering the chair form of cyclohexane, this mixing is limited by an energy interval of about 2.0 eV between the inner and outer valence regions, and by the presence of a nodal surface in orbitals belonging to the a_{2u} irreducible representation of the D_{3d} symmetry group. Similar considerations prevail with zig-zag planar forms of large n -alkane chains, in which the boundary orbitals of the inner and outer valence regions exhibit also a nodal surface following roughly the carbon backbone.

Long-range methylenic hyperconjugation, on the other hand, is forbidden with the 1,4-dimethyl bicyclo [2,2,2] octane compound, since it can be regarded as a fusion of boat forms [6b] of cyclohexane. The computed photoionization cross sections differ markedly from the inner and outer valence bands (Table I), confirming the absence of a mixing of the $C_{2s}/(C_{2p} + H_{1s})$ character of the boundary orbitals, in spite of their very weak energy separation. Accordingly, the $3a''_2$ orbital emerges intensively and distinctively at the top of the inner valence region, 2.35 eV above the nearest inner valence energy level, corresponding to the $3a'_1$ orbital.

Methylenic hyperconjugation interactions are recovered with the 1,1,4,4-tetramethyl cyclohexane compound, through the interplay of a mixing of the $C_{2s}/(C_{2p} + H_{1s})$ character of the $4b_u$ and $5b_u$ orbitals, as reflected by their XPS photoionization cross sections. Besides the emergence of a rather intense peak at 13.6 eV, relating directly to the $5b_u$ orbital, this mixing contributes to a net stabilization of the topmost C_{2s} level by 1.1 eV in comparison with the 1,4-dimethyl bicyclo [2,2,2] octane compound. In this case, the highest C_{2s} level cannot be resolved from the energy level below.

Conclusions

The goal of this work was an assessment of specific fingerprints of the molecular architecture in the X-ray photoionization spectra (XPS) of polycyclic hydrocarbons, the adamantane and the 1,4-dimethyl bicyclo [2,2,2] octane compounds and of the 1,1,4,4-tetramethyl derivative of cyclohexane. The inner valence XP spectra of these molecules exhibit striking signatures for their molecular primary structure (atomic connectivity), through the interplay of electronic degeneracies and the influence of cyclic strains on binding energies. Owing to the sensitivity of X-ray photoionization cross sections to the development of transannular methylenic hyperconjugation, these spectra can also be successfully used to follow the conversion from the chair to the boat form of the cyclohexane unit on which these compounds are based. As confirmed in this study, the boundary region between the inner and outer valence bands generate specific signatures for molecular characteristics pertaining to conformational questions.

The results presented in this study have been obtained using the quasi-particle approximation for a one-electron Green's function scheme based on the diagonal 2ph-TDA renormalization of the self-energy. Although electronic configuration mixing effects in the cation are not explicitly considered in this approximation, one can reasonably retain, by comparison with previous works on related compounds, the idea of one-particle picture of ionization nearly over the whole range of valence binding energies, except above an approximate threshold of 23 eV where ionization lines should most likely split into dense structures of shake-up lines. To cope with multistate interactions, as well as with electronic correlation in the

reference ground state, one should consider specific high-order approximations of the one-electron Green's function such as the third-order algebraic diagrammatic construction [ADC (3)] scheme.

Another limitation in our simulations result from the use of a parametric model based on a noncorrelated approach for the evaluation of photoionization cross sections. In the long-run, photoionization intensities should be computed using nonparametric techniques implemented [26] in the framework of the Green's function approach. Vibronic coupling effects [27] in systems with numerous electronic degeneracies should also be considered.

ACKNOWLEDGMENTS

One of us (M. D.) is grateful to the FNRS (the Belgian National Fund for Scientific Research) for his Senior Research position.

References

1. J. Delhalle, M. Deleuze, *J. Mol. Struct. (Theochem)* **261**, 187 (1992).
2. (a) P. Boulanger, R. Lazzaroni, J. Verbist, and J. Delhalle, *Chem. Phys. Lett.* **129**, 275 (1986); (b) P. Boulanger, J. Riga, J. Verbist, and J. Delhalle, *Macromolecules* **21**, 173 (1989); (c) P. Boulanger, C. Magermans, J. Verbist, J. Delhalle, and D. S. Urch, *Macromolecules* **24**, 2757 (1989); (d) M. Deleuze, J. Delhalle, D. H. Mosley, and J.-M. André, *Phys. Scrip.* **51**, 111 (1995).
3. J. Delhalle, S. Delhalle, and J. Riga, *J. Chem. Soc., Faraday Trans. 2* **83**, 503 (1988).
4. G. Hennico, J. Delhalle, G. Boiziau, and G. Lecayon, *J. Chem. Soc. Faraday Trans.* **86**, 1025 (1990).
5. (a) J. V. Ortiz, *J. Am. Chem. Soc.* **110**, 4522 (1988); (b) J. V. Ortiz, *Macromolecules* **21**, 1189 (1988); (c) J. V. Ortiz, *J. Chem. Phys.* **94**, 6064 (1991); (d) J. V. Ortiz, *Macromolecules* **26**, 7282 (1993).
6. (a) M. Deleuze, J. P. Denis, J. Delhalle, and B. T. Pickup, *J. Phys. Chem.* **97**, 5115 (1993); (b) M. Deleuze, J. Delhalle, and B. T. Pickup, *Chem. Phys.* **175**, 427 (1993).
7. M. Deleuze, J. Delhalle, B. T. Pickup, *J. Phys. Chem.* **98**, 2382 (1994).
8. J. Delhalle, J. P. Denis, M. Deleuze, J. Riga, and M. Dosière, *Chem. Phys. Lett.* **210**, 21 (1993).
9. M. Deleuze, J. Delhalle, B. T. Pickup, and S. Svensson, *J. Am. Chem. Soc.* **116**, 10517 (1994).
10. I. Flamant, D. H. Mosley, M. Deleuze, J. M. André, and J. Delhalle, *Int. J. Quantum Chem.* **S28**, 469 (1994).
11. (a) A.-S. Duwez, J. Riga, J. Ghijssen, J. J. Pireaux, J. Verbist, and J. Delhalle, *J. Electron Spectr. Rel. Phenom.*, to appear; (b) A.-S. Duwez, J. Riga, B. Y. Han, and J. Delhalle, *Probing*

- the Surface Molecular Structure in the UPS Spectra of Octadecanethiol and 1-Cyclohexyl-12-Dodecanethiol Self-Assembled on Gold*, to appear; (c) A.-S. Duwez, J. Ghijsen, J. Riga, M. Deleuze, J. Delhalle, and R. L. Johnson, *Surface Molecular Structure of Self-assembled Alkanethiols Evidenced by Photoemission with Synchrotron Radiation*, to appear.
12. J. Riga, J. Delhalle, M. Deleuze, J. J. Pireaux, and J. J. Verbist, *Surf. Int. Anal.* **22**, 507 (1994).
 13. (a) A. N. d. Brito, M. P. Keane, N. Correia, S. Svensson, and U. Gelius, *Surf. Interf. Sci. Anal.* **17**, 94 (1991); (b) A. N. d. Brito, N. Correia, S. Svensson, and H. Ågren, *J. Chem. Phys.* **95**, 2965 (1991); (c) G. Beamson and D. Briggs, *Mol. Phys.* **76**, 919 (1992); (d) A. N. d. Brito, S. Svensson, H. Ågren, and J. Delhalle, *J. Electron Spectrosc. Rel. Phenom.* **63**, 239 (1993).
 14. M. Deleuze and L. S. Cederbaum, *J. Chem. Phys.*, submitted.
 15. (a) N. Bodor, M. J. S. Dewar, and S. D. Worley, *J. Am. Chem. Soc.* **92**, 19 (1970); (b) G. D. Mateescu, *Tetrahedron Lett.* 5285 (1972); (c) S. D. Worley, G. D. Mateescu, C. W. McFarland, R. C. Fort, Jr., and C. F. Dheley, *J. Am. Chem. Soc.* **95**, 7580 (1973); (d) W. Schmidt, *Tetrahedron* **29**, 2129 (1973); (e) R. Boschi, W. Schmidt, R. J. Suffolk, B. T. Wilkins, H. J. Lempka, and J. N. A. Ridyard, *J. Electron Spectr. Rel. Phenom.* **2**, 377 (1973); (f) C. Worell, J. W. Verhoeven, and W. N. Speckamp, *Tetrahedron* **30**, 3525 (1974); (g) B. Kovac and L. Klasine, *Croat. Chem. Acta* **51**, 55 (1978); (h) R. Gleiter, M. Kobayashi, and J. Kuthan, *Tetrahedron* **32**, 2775 (1976); (i) S. F. Nelsen and J. M. Buschek, *J. Am. Chem. Soc.* **69**, 7930 (1994).
 16. V. Galasso, *J. Mol. Struct. (Theochem)* **336**, 47 (1995).
 17. L. S. Cederbaum, *J. Phys. B* **8**, 290 (1975).
 18. J. Schirmer, L. S. Cederbaum, and O. Walter, *Phys. Rev. A* **28**, 1237 (1983).
 19. L. S. Cederbaum, W. Domcke, J. Schirmer, and W. von Niessen, *Adv. Chem. Phys.* **65**, 115 (1986).
 20. O. Walter and J. Schirmer, *J. Phys. B* **14**, 3805 (1981).
 21. Y. Öhm and G. Born, *Adv. Quantum Chem.* **13**, 1 (1981).
 22. M. Deleuze, J. Delhalle, B. T. Pickup, and J.-L. Calais, *Adv. Quantum Chem.* **26**, 35 (1995).
 23. U. Gelius, *J. Electron. Spectr. Rel. Phenom.* **5**, 985 (1974).
 24. U. Gelius, L. Asplund, E. Basilier, S. Hedman, K. Helene-lund, and K. Siegbahn, *Nucl. Instrum. Methods* **B1**, 85 (1985).
 25. C. Castiglioni, M. Gussoni, and G. Zerbi, *J. Chem. Phys.* **95**, 7144 (1991).
 26. M. Deleuze, B. T. Pickup, and J. Delhalle, *Mol. Phys.* **83**, 655 (1994).
 27. H. Köppel, W. Domcke, and L. S. Cederbaum, *Adv. Chem. Phys.* **57**, 59 (1984).

Molecular Shape Transitions in Grafted Polymers Under Geometrical Confinement

GUSTAVO A. ARTECA

Département de Chimie et Biochimie, Laurentian University—Université Laurentienne, Ramsey Lake Road, Sudbury, Ontario, Canada P3E 2C6; e-mail: gustavo@nickel.laurentian.ca

Received February 25, 1996; accepted February 29, 1996

ABSTRACT

Many applications involve the use of macromolecules at interfaces, including adhesion, lubrication, and the manufacture of surfaces resistant to wear. Modeling these systems requires an understanding of how the dominant conformational features of a macromolecule are modified by the presence of a boundary. In this work, we are interested in monitoring the shape changes that accompany the configurational rearrangements of a single polymer chain near a hard plane. We provide a detailed characterization of essential molecular shape features of compressed grafted chains. These chains are modeled by three-dimensional (off-lattice) walks with excluded-volume interaction, anchored to a flat surface by a terminal point. Compression is induced by confining the chains between two parallel walls. For these systems, we have studied how shape descriptors depend on polymer size and the separation between walls. We show that compression causes a number of nontrivial changes in shape (shape transitions). In particular, we show that the most compact chains found during compression are neither spheroidal nor maximally self-entangled. Maximal entanglements are found in chains that are already mostly "flattened" toward the surface. The present results provide new insights that can be useful in the design of interfaces with targeted properties. © 1996 John Wiley & Sons, Inc.

Introduction

There is a considerable interest in modeling the behavior of macromolecules at solid-liquid interfaces [1–3]. These systems find many applications, including surface wetting, crystal growth, adhesion, film spreading, lubrication, and

oil recovery. The design of size-exclusion chromatographic phases, filters, and surfaces resistant to wear is also based on the properties of confined polymers. The properties of macromolecules at thin interphases are also central for understanding the functions of biological membranes.

Several models have been proposed for studying the effect of boundary conditions on chain molecules. Two typical approaches are usually fol-

lowed, where: (a) macromolecules are anchored at the solid-liquid interface and (b) macromolecules form a liquid interphase, confined between two solid phases. Some specific examples have considered: (i) grafting of a chain to a surface (i.e., terminal-point chemisorption) to form a "brush" [4-10], (ii) adsorption of the entire chain [5, 11-13], (iii) macromolecules geometrically confined within planar impenetrable surfaces, e.g., slabs [14, 15] and prisms [15], (iv) confinement in realistic channels [16], nanotubes [17, 18], liquid layers [19], and (v) adsorption in the presence of an irregular boundary (e.g., a pore) [20]. All these models include usually chain-chain and chain-surface interactions in various forms, from the simple excluded-volume interaction [5] to detailed hydrogen-bonding and solvation [21].

Recent results confirm that polymer size is greatly affected by the presence of a surface [22], its texture [23], and interphase thickness [24]. Computer simulations complement these observations. They provide us with a microscopic picture of how the shape and size of the dominant chain configurations are modified by a boundary.

Computer simulations of confined chains usually monitor some ad hoc molecular size features, from the components of the radius of gyration in preferential directions [10, 14, 19] to the distribution of end-to-end distances [25] and persistence length [26]. Topological properties of cyclic polymers (e.g., knot probabilities) have also been studied in terms of geometrical confinement [13, 15, 27]. Yet, a systematic study of how distinct shape features are affected by boundary conditions is lacking. Here, we present a detailed approach where independent aspects of geometrical shape are monitored simultaneously.

We have studied how distinct molecular shape features of grafted chains are affected by compression. Only linear chains are considered here. Chains are considered in "swollen" (excluded-volume) configurations and they are modeled by off-lattice (self-avoiding) walks, grafted to a plane. Compression is introduced by placing the chains between two "hard" (impenetrable) walls with variable separation. (For general scaling properties of random walks in the presence of a surface, see Ref. [28] and others therein. Some effects of confinement on branched polymers are discussed in Ref. [29].)

We use grafting as a device to control the deformability of the chains and produce reasonable cut-offs on the "pressure" that can be applied on

them. The effect of grafting on the configurational properties of long chains is minor. In the limit of short chains, however, grafting and excluded volume allow us to reproduce the usual experimental observation that small polymers are fairly rigid and difficult to deform by compression. Our present goal is to study the behavior of all shape features of a single chain, confined to an interphase with variable thickness. Entanglements with other chains and the possibility of full chain adsorption are not considered here. Similarly, we will neglect attractive interactions and thus eliminate the possibility of forming compact globules. Compactness will only be controlled by varying the confinement between walls.

For these model chains, we have computed configurationally averaged descriptors associated with three distinct shape features: size, anisometry, and entanglement complexity. We have also characterized the occurrence of shape transitions due to compression. The relation between self-entanglements, anisometry, and polymer size has recently been studied for various homopolymers [30, 31] and protein backbones [31-33]. In this work, we show that the interrelation between the above shape features is greatly modified when a boundary is taken into account. In contrast with "free" polymers, compression can lead to structures that are compact according to size, but whose configurations are neither spheroidal nor very entangled.

The next sections deal with the construction of the model chains, their shape characterization, and the onset of shape transitions by compression inside a slab with impenetrable walls. We show that the use of several independent shape features, rather than a single descriptor, can provide a detailed characterization of structural changes.

Grafted Polymer Model with Confinement

We study conformational transitions in polymers with small to intermediate size. These polymers (with typically less than 100 monomers) comprise a large number of cases with practical interest. These chains are well represented by off-lattice models [34]. Here, we use a "necklace" model (a Pearson random walk), consisting of a string of n identical "beads," with a constant bonded-bead distance ℓ (Kuhn's length). We simulate the effect of a "good solvent" [5, 35] by including an ex-

cluded-volume interaction. This is a purely repulsive interaction characterized by the condition that all nonbonded monomers must be at a distance larger than or equal to r_{ex} , the radius of excluded volume. [This imposes a restriction on the polymer shape: in the limit of $r_{\text{ex}} \rightarrow 2\ell$ the chain can only be a rigid rod.]

Our goal is to explore only the effect of confinement on grafted chains with variable length. The parameters ℓ and r_{ex} are kept constant. Our present choice ($\ell = 3.8 \text{ \AA}$ and $r_{\text{ex}} = 6 \text{ \AA}$) generates chains that mimic unfolded (solvated) proteins, in absence of confinement. A smaller r_{ex} value is not convenient since it produces compact chains that instead resemble polymers in poor solvents. Our main results depend, however, little on ℓ .

Grafting and confinement are simulated as follows: A terminal point of the chain is attached to a planar wall. Then, the chain is allowed to "grow" by random walks of length ℓ within two parallel (hard-plane) walls separated by a distance L . All configurations that violate the condition of excluded volume or grow outside the region for confinement are rejected. The procedure is equivalent to a Monte Carlo sampling of configurational space, where all accepted conformers have zero energy and all rejected conformers have infinite energy. An example of an "accepted" ($n = 100$) configuration is given in Figure 1. Successful configurations will be indicated by $\{K_i\}$. This approach is sufficient to explain simple size and shape features in free chains [31, 34]. In this work, we expand the procedure to chains subject to boundary conditions. Our goal is study confined polymers by using the same shape descriptors that are useful for free chains.

Often, descriptors of size and anisometry are adapted to the particular geometrical features of the chosen confinement [5, 10, 15, 35–41]. For example, in the case of placing a chain between two parallel planes, one can analyze the components of the radius of gyration and the asphericity in the directions parallel and perpendicular to the walls. This approach may not be useful for other confinement geometries. Elsewhere [33] we have shown that the simultaneous use of distinct shape descriptors can uncover subtle changes in molecular shape induced by temperature. For the present study of confined polymers, we use three descriptors that are independent from each other.

The chosen descriptors characterize the shape of freely rotating polymers [33]. In our present case, the chains are not created in isolation, but rather

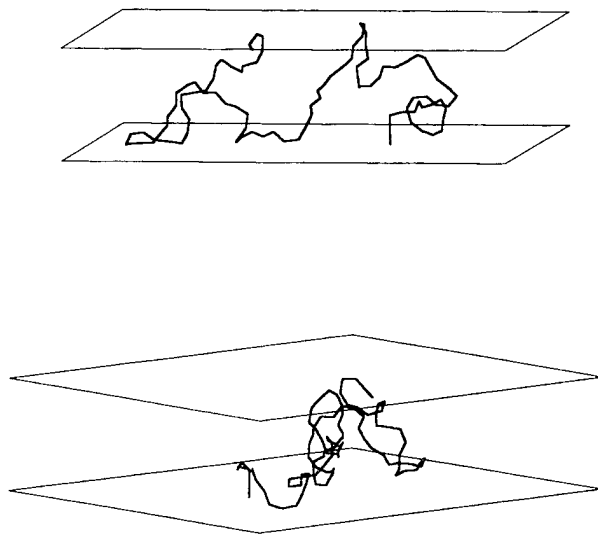


FIGURE 1. Two views of a typical random polymer configuration confined between two parallel planes. (The example corresponds to $n = 100$ beads, a step length of $\ell = 3.8 \text{ \AA}$, and a radius of excluded volume of $r_{\text{ex}} = 6.0 \text{ \AA}$. The separation between planes is 30 \AA .)

grown between two parallel planes and grafted to one of them. The subsequent analysis of these chains as if in isolation may introduce a problem in sampling. Note that all K_i configurations, derived from each other by translation and rotation, will have the same shape description. Yet, not all of them would necessarily be "successful configurations" if grafted and grown under confinement. To circumvent this issue, we deal with a slightly modified subset of configurations that can unequivocally be associated with grafting. Their construction is as follows: (a) the first three monomer beads are chosen collinear and perpendicular to the wall; (b) the confined Pearson walk with excluded volume is built starting from the fourth bead, located at a distance ℓ from the third collinear bead (see Fig. 1).

The condition that the chains start with three collinear beads grafted perpendicularly provides an unambiguous specification on how to "insert" an isolated polymer within the slab and anchor it to the surface by one end. Moreover, note that the probability that the last three beads ($n - 2$, $n - 1$, n) will place themselves randomly collinear is virtually zero. Thus, in practice, it will only be possible to "graft back" a selected configuration K_i at one end of the chain, the one with the three collinear beads. Its shape characterization will unequivocally be associated with a "successful" con-

figuration. Nonetheless, this special condition for grafting has little influence on the shape of long chains.

There exists a minimum value of L (L_{\min}) below which no polymer configurations are found. With the first three beads collinear, this critical wall separation increases, but the difference is only significant for chains with $n \leq 10$. For the parameters ℓ and r_{ex} used here, conformers were always found for wall separations larger than 8.5 Å, regardless of the n value. This value is comparable to a very small molecular cavity [10, 14, 18].

Detailed Molecular Shape Description

We have evaluated shape descriptors on the configurations selected according to the above criteria. The descriptors characterize three distinct shape features: (a) size and compactness, described by the span R and the instantaneous radius of gyration R_G [35]; (b) anisotropy, described by the asphericity Ω [37, 38]; and (c) the entanglement complexity, described by the mean number of overcrossings, \bar{N} [42]. These three properties have already been used to monitor dynamical shape transitions in biopolymers [33].

The evaluation of the descriptors has been discussed elsewhere in detail [33]. We summarize here the main elements. Let $\{\mathbf{r}_i, i = 1, 2, \dots, n\}$ be the coordinates associated with a chain configuration K_i . The origin of the coordinate system is at the geometric centre of the chain. The instantaneous radius of gyration R_G and the span R are simply given as:

$$R_G^2 = \frac{1}{n} \sum_{i=1}^n r_i^2, \quad r_i = \|\mathbf{r}_i\|, \quad (1a)$$

$$R = \max_{\{i\}} r_i. \quad (1b)$$

A number of so-called shape factors have been proposed in the literature to account for the configurational anisotropy [36–40]. In our case, we resort to R_G and R to characterize size, whereas we use the asphericity for measuring anisotropy [40]:

$$\Omega = \frac{1}{2} \left\{ \sum_{i=1}^2 \sum_{j=i+1}^3 (\lambda_i - \lambda_j)^2 \right\} \left\{ \sum_{i=1}^3 \lambda_i \right\}^{-2}, \quad (2)$$

defined in terms of the three principal moments of inertia $\{\lambda_i\}$. Spheroidal chains exhibit $\Omega \sim 0$, whereas prolate chains satisfy $\Omega \sim \frac{1}{4}$.

Finally, we use the probability distribution of overcrossings as a measure of the complexity of self-entanglements in a chain [42]. In the present context, the term "self-entanglement" is meant to convey how the linear chains "coil and twist over themselves." (Note that we deal with a single chain that in general will not be grafted to both surfaces, and thus they will not form knots or braids.) The distribution of overcrossings provides a geometrical characterization of the complexity of these "coils" that is independent, in general, from size and anisotropy features. The distribution, indicated as $\{A_N(n)\}$, gives the probability of observing N overcrossings when projecting the bonding pattern of a rigid n -atom macromolecular conformation onto two dimensions. (The overcrossings are the points where two bonds appear to "cross" when projected to a plane.) In practice, $\{A_N(n)\}$ is evaluated by averaging over a large series of randomized projections (typically 5×10^4 points) [42]. Here, we use a single parameter to describe the type of entanglements obtained, namely the mean number of overcrossings \bar{N} defined as:

$$\bar{N} = \sum_{N=0}^{\max N} N A_N(n),$$

$$\max N = (n-3)(n-2)/2. \quad (3)$$

This descriptor captures some essential folding features: In swollen or disentangled chains we expect $\bar{N} \rightarrow 0$, whereas \bar{N} will take large values in convoluted or entangled polymers.

For each polymer of length n , we have computed configurational averages of the above descriptors over many chains. If D_i is the value of a generic descriptor D at a successful configuration K_i , reliable (and conservative) estimates for the configurational mean $\langle D \rangle$ can be obtained by averaging over sequences of the computed descriptor (D_1, D_2, \dots), as follows:

$$\langle D \rangle = \frac{1}{N-1} \sum_{k=2}^{N \geq 2} \sum_{i=1}^{k \geq 2} D_i/k. \quad (4)$$

We have added enough configurations to reach 3-significant-figure accuracy in $\langle R_G^2 \rangle^{1/2}$. The simultaneous use of $\langle R_G^2 \rangle^{1/2}$, $\langle R \rangle$, $\langle \Omega \rangle$, and $\langle \bar{N} \rangle$ should provide a detailed picture of all relevant molecular shape features for compressed chains. In free chains, some degree of correlation is found between descriptors [33, 34]. For example, a decrease in size is accompanied by an increase in

entanglements and a decrease in asphericity. This behavior is contrasted below with the results for various wall separations L .

Shape Transitions Induced by Compressing a Grafted Polymer

Intuitively, the behavior of the grafted chains in the limit of large L values (i.e., weak confinement) and small L values (i.e., strong confinement) could be predicted: (a) Long grafted chains with no confinement should resemble free chains. For the chosen ℓ and r_{ex} parameters, this means slightly prolate configurations ($\langle\Omega\rangle \sim 0.1$). There are no attractive interactions between beads that can turn the chain into a spherical globule. (b) When compression is applied, the chains should become smaller, more spheroidal, and entangled. Therefore, we expect that $\langle R_G^2 \rangle^{1/2}$, $\langle R \rangle$, and $\langle\Omega\rangle$ should initially decrease when L decreases, whereas $\langle\bar{N}\rangle$ should increase under the same conditions. (c) Under strong confinement (i.e., with wall separations approaching L_{min}), the chains will be squashed along directions parallel to the surface. The resulting configurations will be oblate, large in size (not compact), and unentangled. Therefore, we expect the behavior of the shape descriptors near L_{min} to be the opposite to that for large L values, i.e., $\langle R_G^2 \rangle^{1/2}$, $\langle R \rangle$, and $\langle\Omega\rangle$ will increase (and $\langle\bar{N}\rangle$ decrease) with compression. Figure 2 illustrates this behavior for representative configurations of an $n = 100$ chain at large, intermediate, and small wall separations ($L = 50 \text{ \AA}$, 30 \AA , and 10 \AA , respectively).

The above analysis suggests that, at least for large n values, size and anisometry descriptors will exhibit a minimum as a function of L , and the averaged mean number of overcrossings will have a maximum for some L value. Let $L^*(D)$ be the wall separation at which the descriptor D has a critical point (i.e., $[\partial\langle D \rangle / \partial L]_{L^*} = 0$). As we show below, the positions of the critical points for size, anisometry, and entanglement complexity [$L^*(R_G)$, $L^*(\Omega)$, and $L^*(\bar{N})$, respectively] are not coincident.

The occurrence of a minimum radius of gyration in chains enclosed in various geometries has already been reported [10, 15]. Our results confirm the same behavior for confined chains grafted onto a surface. Figure 3 shows the configurationally averaged radius of gyration as a function of L for $n = 75$ chains. The molecular size has a minimum

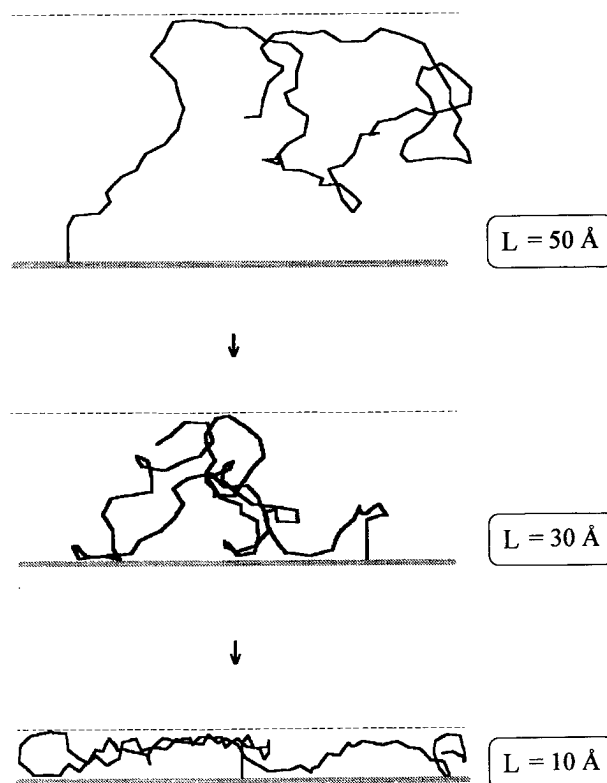


FIGURE 2. Typical changes in polymer configuration due to compression. (The parameters for the chain are the same as in Fig. 1. The separation between walls is indicated to the right.)

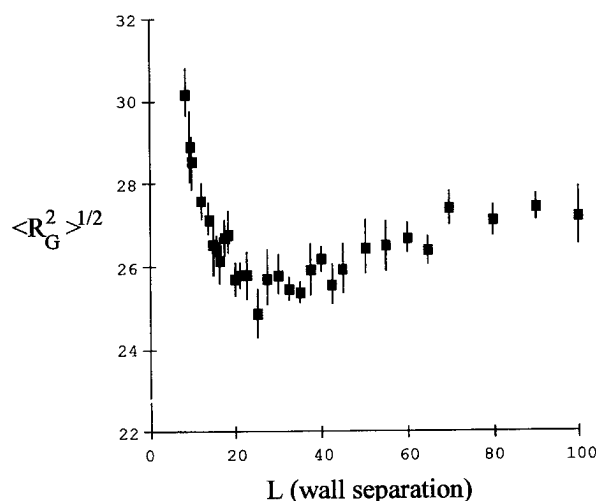


FIGURE 3. Change in mean radius of gyration of a $n = 75$ chain ($\ell = 3.8 \text{ \AA}$, $r_{\text{ex}} = 6.0 \text{ \AA}$) with compression. (Wall separation and radius of gyration in angstroms. The error bars represent the uncertainty in the mean values after configurational sampling.)

at approximately 30 Å [i.e., $L^*(R_G) \approx L^*(R) \sim 30$ Å]. This minimum is rather flat, as the averaged molecular size changes little between $L \sim 20$ and 40 Å.

The mean number of overcrossings and the average asphericity (Figs. 4 and 5, respectively) complement the picture of how the shape of the $n = 75$ chains is affected by compression. The most entangled configurations are found in the regime of strong confinement [$L^*(\bar{N}) \sim 20$ Å], whereas spheroidal ones appear at weaker confinement [$L^*(\Omega) \sim 45$ Å]. By comparing the results in Figures 3–5, it is clear that the maximum in entanglement complexity is found for oblate chains that are not very compact. Note, however, that $\langle \bar{N} \rangle$ changes fast as L is further reduced. As expected, the large and flat chains found at very strong compression ($L \sim 10$ Å) are not entangled.

The above results indicate that different shape features are affected differently by confinement. Size, compactness, anisometry, and entanglement complexity are not trivially related when the boundary conditions are changed. This trend is also found at other chain lengths. Figures 6–8 show the three averaged shape descriptors for chains with $n = 20$. Again, the positions of the critical points for the various descriptors do not coincide. The most compact conformations (i.e., those with smallest $\langle R_G^2 \rangle$) are found to be oblate rather than spheroidal. Note that a maximum in

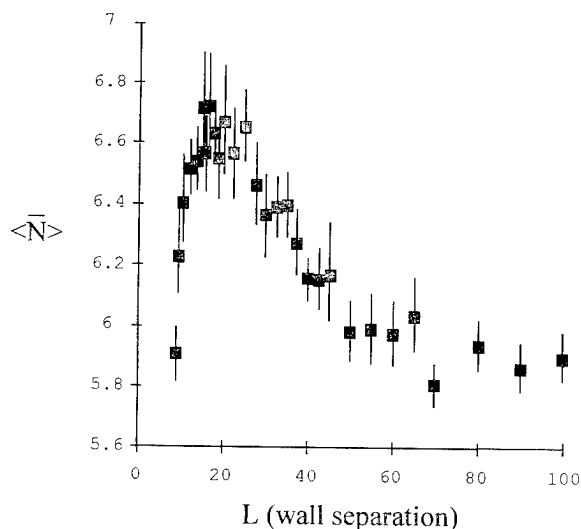


FIGURE 4. Change in the configurationally averaged mean number of overcrossings of a $n = 75$ chain with compression. (Wall separation is in angstroms. Simulation conditions are the same as in Fig. 3.)

entanglement complexity appears at very strong confinement [$L^*(\bar{N}) \sim 10$ Å], just above the threshold below which no conformers are found [$L_{\min} \sim 8.5$ Å]. This critical point is not detected for chains shorter than $n = 20$. In these cases, $\langle \bar{N} \rangle$ increases monotonically during compression.

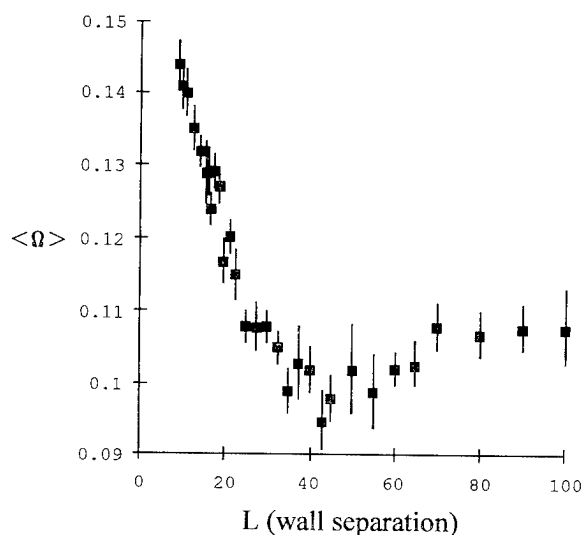


FIGURE 5. Change in the configurationally averaged asphericity of a $n = 75$ chain with compression. (Wall separation is in angstroms. Simulation conditions are the same as in Fig. 3.)

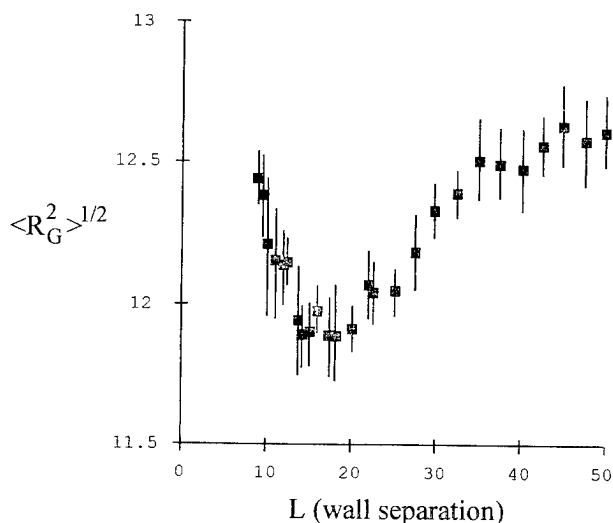


FIGURE 6. Change in mean radius of gyration of a $n = 20$ chain ($\ell = 3.8$ angstroms, $r_{\text{ex}} = 6.0$ Å) with compression. (Wall separation and radius of gyration in Å. The error bars represent the uncertainty in the mean values after configurational sampling.)

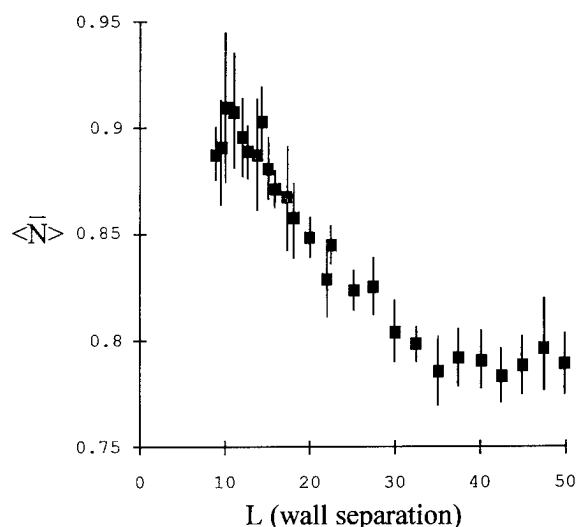


FIGURE 7. Change in the configurationally averaged mean number of overcrossings of a $n = 20$ chain with compression. [Wall separation is in angstroms. Simulation conditions are the same as in Fig. 6.]

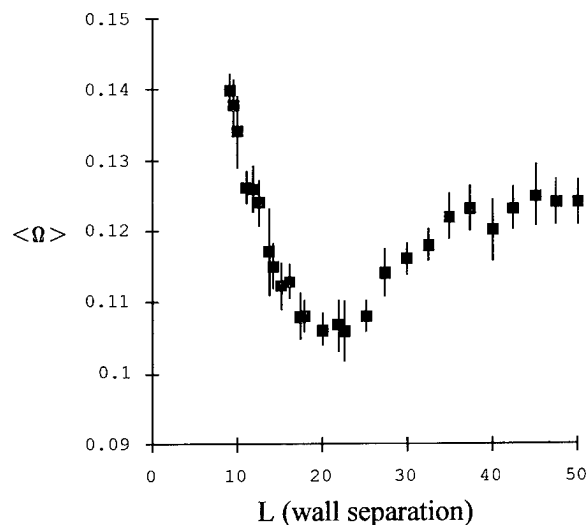


FIGURE 8. Change in the configurationally averaged asphericity of a $n = 20$ chain with compression. (Wall separation is in angstroms. Simulation conditions are the same as in Fig. 6.)

The critical behavior of shape descriptors is summarized in Table I for polymers with $n \leq 100$. A number of observations can be made from these approximate estimates:

1. Over the small range of polymers considered, the wall separation leading to the most compact conformations increases approximately linearly with n . As well, the value of $\min \langle R_G^2 \rangle^{1/2}$ (a minimum over L , for n constant) appears to be linear with n .

2. The minimum value of asphericity is virtually the same for all chains, that is, all polymers reach a similar "spheroidal regime" at some point during the compression. The actual position of this minimum [$L^*(\Omega)$] varies with the polymer length. Nevertheless, its change is easily predicted. Let R_∞

be the value of the average span in the limit of large wall separations ($R_\infty = \lim_{L \rightarrow \infty} \langle R \rangle$). For the examples in Table I, we find that the span of the nonconfined chains and the wall separation that leads to the most spheroidal chains are virtually indistinguishable (at 95% confidence level and values in angstroms):

$$L^*(\Omega) \approx (0.97 \pm 0.15) R_\infty + (0.3 \pm 4.9). \quad (5)$$

These results suggest that the asphericity is not a very discriminating shape descriptor. Asphericity alone provides little insight into the structural changes taking place during compression, beyond giving a first indication on the chain's reorientation toward the boundary surface. In order to

TABLE I
Estimated critical values of configurationally averaged shape descriptors for grafted chains of various lengths.^a

n	$\min \langle R_G^2 \rangle^{1/2}$	$L^*(R_G)$	$\max \langle \bar{N} \rangle$	$L^*(\bar{N})$	$\min \langle \Omega \rangle$	$L^*(\Omega)$
10	—	—	—	—	0.104 ± 0.003	12 ± 1
20	11.9 ± 0.1	17 ± 3	0.92 ± 0.03	10 ± 1	0.106 ± 0.004	21 ± 1
50	20.7 ± 0.3	25 ± 5	3.76 ± 0.05	13 ± 1	0.101 ± 0.004	35 ± 3
75	25.5 ± 0.5	30 ± 3	6.8 ± 0.1	16 ± 2	0.100 ± 0.003	45 ± 5
100	30.0 ± 0.5	40 ± 5	9.9 ± 0.1	20 ± 3	0.099 ± 0.003	50 ± 5

^a[Radius of gyration and wall separations L^* in angstroms. Due to the configurational restrictions imposed on the model chains, the shortest chains (e.g., $n = 10$) exhibit no extrema for the descriptors of size and entanglement. The estimated values of $\max \bar{N}$ are less accurate due to the intrinsic errors in computing mean overcrossing numbers, in addition to the fluctuations associated with the configurational sampling.]

obtain more detailed information, one should analyze the individual principal moments of inertia (cf. eq. (2)).

3. In the range of polymers considered, the wall separation leading to the most entangled conformations is rather small [$L^*(\bar{N}) \sim L^*(R_G)/2$], and it also increases with n . The results suggest that the entanglement complexity is maximized just before a rapid "configurational transition" leading to flattened chains almost adhered to the surface.

Figure 9 conveys the differences in shape descriptors from another viewpoint. The figure gives the dependence of the span $\langle R \rangle$ on the separation between walls. We observe the occurrence of rather flat minima, for all n (except $n = 10$). The dashed lines to the left and right of the minima represent the approximate wall separations for the maxima in entanglements and minima in asphericity, respectively. This figure suggests an interesting interrelation between the three shape descriptors: (a) The minimum in asphericity marks the onset of boundary effects on the chains' size; (b) the minimum in molecular size defines a regime where the confinement forces the chains into compact, increasingly entangled, and oblate configurations; and (c) the maximum in entanglement complexity marks the limits to compactness. Further squeezing brings about a rapid variation in molecular size. Since the configurational "space" accessible

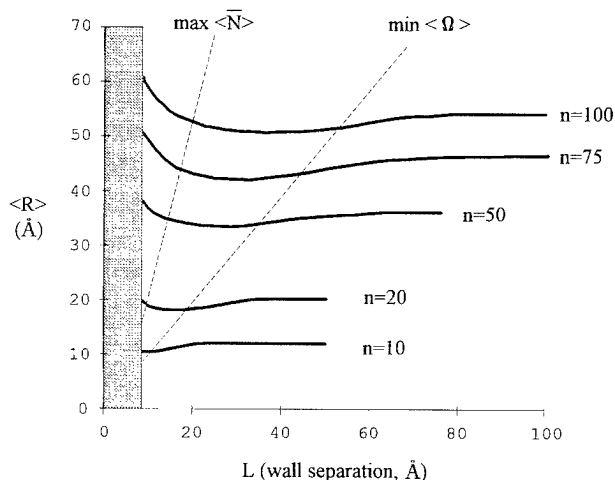


FIGURE 9. Change in chain span as a function of the wall separation for polymers of various lengths. (The dashed lines to the left and right represent qualitatively the values of $\langle R \rangle$ and L associated with the maximum degree of entanglement and the minimum asphericity, respectively. The gray area gives the L values where no chains are possible.)

to long chains is very reduced for $L < L^*(\bar{N})$, the chains are quickly forced to adopt laterally spread, open, and unentangled structures. Note that excluded volume will pose a smaller constraint for shorter chains. Therefore, a decrease in entanglement complexity brought with further compression may not be visible before reaching the critical L_{\min} value.

Further Comments and Conclusions

The improved design of interphases with desired structural properties requires appropriate tools to analyze how molecular shape is modified by various control factors (e.g., interphase thickness, density of grafting, temperature, and solvation). In the present work, we have shown that three descriptors (associated with independent shape features) can provide a detailed characterization of configurational transitions in compressed polymers. The results show that it is not necessary to use ad hoc descriptors "adapted" to the nature of the particular geometrical confinement considered.

The present study indicates that the terms "compactness," "sphericity," and "entanglement" are not interchangeable for the compressed chains. Summarizing, we have found that: (i) compressed chains reach their smallest size for configurations which are not the ones closest to sphericity and (ii) the maximum entanglement complexity occurs for rather flat conformers that are not maximally compact. Therefore, it is clear that the interplay between these shape features cannot be captured by a single descriptor.

The same procedure presented here should be valuable to study configurational transitions in more realistic polymer models. A number of effects, omitted in this work, should introduce important shape changes. For instance, we have restricted our study to confinement on "hard" polymer chains with variable length. We have excluded attractive interactions between monomers or between the polymer and the surface, as well as avoided the explicit presence of molecules in the liquid phase. Moreover, whereas the presence of grafting poses a reasonable limit to the accessible compression, it plays little role in modifying the shape of long chains. This is due to the fact that we have only considered single-chain effects (i.e., a grafted surface with low surface coverage of poly-

mers). A less diluted surface grafting between attractive chains will of course affect enormously the nature of their entanglements. The role of these factors on polymer shape transitions will be discussed elsewhere.

ACKNOWLEDGMENT

I thank N. D. Grant (Sudbury) for her comments on the manuscript. This work was supported by the Fonds de Recherche de l'Université Laurentienne (FRUL) and a grant from the Natural Sciences and Engineering Research Council (NSERC) of Canada.

References

1. J. Israelachvili, *Intermolecular and Surface Forces* (Academic Press, London, 1991).
2. I. Sanchez, (Ed.), *Physics of Polymer Surfaces and Interfaces* (Butterworth-Heinemann, Boston, 1992).
3. G. J. Fleer, M. A. Cohen-Stuart, J. M. H. M. Scheutjens, T. Cosgrove, and B. Vincent, *Polymers at Interfaces* (Chapman and Hall, London, 1993).
4. P.-G. de Gennes, *Rep. Prog. Phys.* **32**, 187 (1969).
5. P.-G. de Gennes, *Scaling Concepts in Polymer Physics* (Cornell University Press, Ithaca, 1985).
6. M. N. Barber, A. J. Guttmann, K. M. Middlemiss, G. M. Torrie, and S. G. Whittington, *J. Phys. A* **11**, 1833 (1978).
7. K. F. Freed, *J. Chem. Phys.* **79**, 3121 (1983).
8. A. Baumgärtner, in *Applications of the Monte Carlo Method in Statistical Physics*, K. Binder, Ed. (Springer-Verlag, Berlin, 1987) [and references therein].
9. K. Binder, P.-Y. Lai, and J. Wittmer, *Faraday Discuss.* **98**, 97 (1994).
10. G. H. Peters and D. J. Tildesley, *Phys. Rev. E* **52**, 1882 (1995).
11. R. Hentschke and R. G. Winkler, *J. Chem. Phys.* **99**, 5528 (1993).
12. R. Hegger and P. Grassberger, *J. Phys. A* **27**, 4069 (1994).
13. C. Vanderzande, *J. Phys. A* **28**, 3681 (1995).
14. R. G. Winkler, A. Gerstmaier, P. Reineker, T. Matsuda, and D. Y. Yoon, *Int. J. Quantum Chem.* **52**, 437 (1994).
15. M. C. Tesi, E. J. Janse van Rensburg, E. Orlandini, and S. G. Whittington, *J. Phys. A* **27**, 347 (1994).
16. B. Smit and T. L. M. Maesen, *Nature* **374**, 42 (1995).
17. R. S. Ruoff, *Nature* **372**, 731 (1995).
18. H. Dai, E. W. Wong, Y. Z. Lu, S. Fan, and C. M. Lieber, *Nature* **375**, 769 (1995).
19. Y. Kong, C. W. Manke, W. G. Madden, and A. G. Schlijper, *Int. J. Thermophys.* **15**, 1093 (1994).
20. P.-G. de Gennes, *C. R. Acad. Sci. Paris, Sér. IIb*, **320**, 85 (1995).
21. A. Raudino and F. Zuccarello, *J. Mol. Struct. (Theochem)* **314**, 125 (1994).
22. S. Kumar, H. Tang, and I. Szleifer, *Mol. Phys.* **81**, 867 (1994).
23. K. Tupper, R. J. Colton, and D. W. Brenner, *Langmuir* **10**, 2041 (1994).
24. P. Ray and K. Binder, *Europhys. Lett.* **27**, 53 (1994).
25. G. K. Stratouras and M. K. Kosmas, *J. Chem. Phys.* **102**, 2239 (1995).
26. J. Hendricks, T. Kawakatsu, K. Kawasaki, and W. Zimmermann, *Phys. Rev. E* **51**, 2658 (1995).
27. E. Orlandini, E. J. Janse van Rensburg, M. C. Tesi, and S. G. Whittington, *J. Phys. A* **27**, 335 (1994).
28. K. De'Bell and T. Lookman, *Rev. Mod. Phys.* **65**, 87 (1993).
29. A. Grosberg, A. Gutin, and E. Shakhnovich, *Macromolecules* **28**, 3718 (1995).
30. G. A. Arteca, *Int. J. Quantum Chem., QCS* **28**, 433 (1994).
31. G. A. Arteca, *Phys. Rev. E* **49**, 2417 (1994).
32. G. A. Arteca, *Phys. Rev. E* **51**, 2600 (1995).
33. G. A. Arteca, *Biopolymers* **35**, 393 (1995).
34. G. A. Arteca, *J. Phys. Chem.* **97**, 13831 (1993).
35. P. J. Flory, *Statistical Mechanics of Chain Molecules* (Interscience, New York, 1969).
36. K. Šolc, *Macromolecules* **6**, 378 (1973).
37. J. Rudnick and G. Gaspari, *J. Phys. A* **19**, L 191 (1986).
38. J. Rudnick and G. Gaspari, *Science* **237**, 384 (1987).
39. H. W. Diehl and E. Eisenriegler, *J. Phys. A* **22**, L 87 (1989).
40. A. Baumgärtner, *J. Chem. Phys.* **98**, 7496 (1993).
41. G. Zifferer, *J. Chem. Phys.* **102**, 3720 (1995).
42. G. A. Arteca, *Biopolymers* **33**, 1829 (1993).

Modification of the Local Self-Consistent Field Method for Modeling Surface Reactivity of Covalent Solids

L. G. GORB*,†

Institute of Colloid and Water Chemistry, Academy of Sciences of Ukraine, 42 Vernadsky Ave., 252142 Ukraine

J.-L. RIVAIL,* V. THERY, AND D. RINALDI

Laboratoire de Chimie Théorique, Unité de Recherche Associée au CNRS n° 510, Université Henri Poincaré, Nancy 1, BP 239, 54506 Vandoeuvre-les Nancy Cedex, France

Received March 28, 1996; revised manuscript received May 31, 1996; accepted June 5, 1996

ABSTRACT

The local self-consistent field (LSCF) method which allows full SCF computations on a fragment of very long molecular systems represented by a classical force field has been adapted to the description of nonmetallic crystals. The periodicity of the network is achieved by modifying self-consistently the basic parameters of the classical subsystem (charges, geometric parameters) along the SCF iterative scheme. The method is tested on α -cristobalite. The parametrization of the quantum classical junction, achieved by localized bond orbitals has been performed with the help of a fragment located in the bulk. The stability of the method with respect to the size of the fragment and the size of the crystalline sample appears to be very good. The properties of fully hydroxylated (010) surface are corrected described. Modeling of water adsorption on the ideal surface as well as on two kinds of surface defects gives rise to very reasonable results with an absorption energies of ca 10 kcal/mol which are close to the upper limit of the experimental data. This preliminary study appears to be quite encouraging regarding the possibilities of using this method, which can be considered as an extension of the embedded cluster approach to covalent solids. Many applications to surface chemical reactivity studies can be imagined. © 1996 John Wiley & Sons, Inc.

* To whom correspondence should be addressed.

† Current address: Department of Chemistry, Jackson State University, Jackson, MS, 39217-0510.

Introduction

Theoretical studies of chemical reactivity require the use of quantum mechanics (QM) in order to be able to describe the modification of the electronic structure of the reactants. This is now quite a common method for the study of reactions in the gas phase. When the reaction involves the chemical participation of the surface of a solid, the quantum chemical study of the exceedingly large system becomes a very difficult problem. In the case of nonmetallic surfaces one often replaces the whole solid by a small part of it in which the valence rules are fulfilled, for the dangling bonds, by extra atoms (usually hydrogen) and performs the computations with the usual molecular codes at the *ab initio*, density functional or semiempirical levels of approximation [1–6]. In such approaches the size of the clusters is limited and the level of accuracy is rather low. For instance, the cluster $\text{H}_{54}\text{Si}_{25}\text{O}_{25}$, model of a silica surface, has been computed at the 3-21 G level [7] and larger clusters with about 100 Si and O atoms were investigated at the MNDO level [8]. In addition long-range electrostatic interactions which are present in crystals are either omitted or roughly reintroduced [9, 10] in such models.

Another approach consists of using periodic Hartree–Fock computations [11] on a periodic two-dimensional slab of the crystal structure [12], but this method suffers some serious limitations too: The slab cannot be very thick and the influence of the bulk crystal is not very well represented. Moreover the periodicity makes difficult the introduction of some irregularities or defects. New computational approaches, based on the Car–Parrinello formalism [13] seem very promising [14, 15], in particular for modeling metal surfaces. However, they usually require large computer facilities and suffer some limitations which make alternative approaches still desirable.

In the case in which the interactions can be considered at the physical level, modeling of large systems can be conveniently achieved by means of molecular mechanics (MM). For instance, the energetics of zeolite frameworks [16, 17], the localization of adsorbed molecules in silicalite channels [18, 19], and amorphous substances [20] have been approached successfully with such models.

In the case of chemical interactions one usually assumes that the electronic perturbation created by a local interaction in a large system becomes negligible at some distance of the interaction center so that one immediately thinks of limiting the quantum chemical computation to this part of the system, provided that one is able to include the interaction with the rest of the system in the computation scheme and treat properly the boundary between the quantum and the classical parts of the system. This last point is straightforward in the case of molecular solutions in which it is easy to chemically define the solute and the solvent molecules which here play the role of the classical surroundings [21–25], giving rise to hybrid QM-MM methods. This is also true for molecular crystals in which one may introduce a Madelung potential due to the surrounding molecules [26]. The task becomes far more difficult when there is no chemical discontinuity between the quantum and the classical parts of the system such as in macromolecules or in nonmetallic solids. The idea of using localized orbitals is not so recent [27] and offers various levels of approximation for the reactive part and for the surroundings [28–30]. Valence bond treatments are an alternative to overcome the difficulty [31]. Recently, a simple modification of the usual Roothaan equations [32] used in molecular Hartree–Fock computations have been proposed under the denomination of local self-consistent field (LSCF) method [33] which enables us to treat quantum mechanically part of a large system while the boundary between the quantum and classical subsystem is properly treated. The method consists in representing the electron pairs involved in the chemical bonds connecting the quantum and classical subsystems by localized orbitals and by constraining the molecular orbitals in the quantum subsystem to remain orthogonal to these localized orbitals. The rest of the system is represented by a classical force field, and the two subsystems interact through electrostatic and van der Waals interactions. The analytic derivatives of energy with respect to the atomic coordinates have been established for the quantum subsystem giving rise to a classical quantum force field (CQFF) [34] which allows geometry optimization and even molecular dynamics computations. This methodology has been tested successfully on protein and enzymatic systems. The present work mainly deals with the implementation of the method for the study of the surface reactivity of covalent solids.

After having solved the technical details inherent to solid state, we chose to test the method by modeling a silica surface. It is well known that silicon oxide is one of the most abundant components of Earth's crust, but silica is also a widely studied solid by computational approaches, using either quantum [6, 35–37] or classical [18, 38, 39] mechanics. Solid silica exists in many different crystalline forms [40] in which the basic units, most often a tetrahedral SiO_4 motif, share its apices with the neighboring tetrahedrons, the various geometric arrangements of these connectivities leading to the different well-defined crystalline forms. In this study we limit ourselves to the hydroxylated (010) surface of α -cristobalite.

This study will be organized as follows. In the next section we briefly recall the principles of the LSCF method and the modifications made necessary by its extension to the study of solid surfaces. The applications to α -cristobalite are described in the third section. The parametrization of the quantum classical junction is detailed and tested on a quantum subsystem located in the bulk of the crystal. The results regarding the geometry and electronic structure of a regular (010) surface are given and simple examples of surface irregularities are presented. The results are briefly discussed in the fourth section and the last section is devoted to the conclusion.

Extension of the LSCF Method

The principles of the LSCF method have been described previously [33]. The whole system is divided into the quantum subsystem (S) and its classical environment (E). The chemical bonds linking the atoms of S (frontier atoms) to E are assumed to be represented by predefined localized orbitals built with hybrid orbitals. The hybrid orbital of the frontier atom belonging to S is called the frozen hybrid orbital. At the NDDO level of approximation [41] which will be used here, the only parameters we need to introduce are the (i) the s content of the normalized frozen hybrid orbital of each frontier atom of S . This quantity will be denominated a . (ii) The diagonal element P_{ll} of the density matrix corresponding to each hybrid orbital in the localized bond orbital linking S to E .

This pair of parameters is assumed to be transferable and is usually predetermined on a model system computed quantum chemically with the

same method as used in the forthcoming computations. At the NDDO level of approximation the energy of the systems is expressed by:

$$\begin{aligned}
 E = & \sum_{\mu} \sum_{\nu} P_{\mu\nu} \left\{ H_{\mu\nu} + \frac{1}{2} \sum_{\lambda} \sum_{\eta} P_{\lambda\eta} \left[(\mu\nu|\lambda\eta) - \frac{1}{2} (\mu\eta|\lambda\nu) \right] \right\} \\
 & + \sum_l P_{ll} \left\{ \sum_{\mu} \sum_{\nu} P_{\mu\nu} \left[(\mu\nu|ll) - \frac{1}{2} (\mu l|\nu l) \right] \right\} \\
 & + \sum_{l'} \frac{1}{2} P_{l'l'} (ll|l'l') \\
 & + \sum_{A \in E} Q_A (ll|s_A s_A) + \sum_{K \in S} Z_K (ll|s_K s_K) \Bigg\} \\
 & + \frac{1}{2} \sum_{K \in S} \sum_{\substack{L \in S \\ L \neq K}} Z_K Z_L f_{KL} \\
 & + \sum_{A \in E} \left\{ Q_A \sum_{\mu} \sum_{\nu} P_{\mu\nu} (\mu\nu|s_A s_A) \right. \\
 & \left. + \sum_{K \in S} Z_K [Z_A f_{KA} - P_A (s_K s_K|s_A s_A)] \right\} \\
 & + V(E) + V'(E, S). \quad (1)
 \end{aligned}$$

In this equation $P_{\mu\nu}$ denotes the density matrix element corresponding to atomic orbitals $|\mu\rangle$ and $|\nu\rangle$ of subsystem S (orthogonalized to the frozen hybrid orbitals). The semi-empirical core-core atomic repulsion function is symbolized by f_{KA} and, according to the NDDO formalism, the Coulomb interaction between two atomic charges A and K is assumed to be proportional to the Coulomb integral between s functions s_A and s_K , respectively. The equivalent valence electronic population of a classical atom A is simply defined by $P_A = Z_A - Q_A$ where Z_A is the number of valence electrons. Therefore, the first line of Eq. (1) represents the Hartree-Fock energy of electrons in S ; the second sum corresponds to the potential energy of the electronic population of the frozen hybrid orbitals. The third sum is the core-core atomic repulsion in S and the fourth one stands for the electrostatic interaction between subsystems S and E . The two extra terms $V(E)$ and $V'(E, S)$ represent, respectively, the potential energy of the classical subsystem and all interactions between the two subsystems E and S , except the electrostatic ones.

The derivation of the Hartree-Fock equations from this expression of E is straightforward and the computation of one- and two-electron integrals of Eq. (1) involving hybrid atomic orbitals requires simple linear transformation of standard integrals as explained in Ref. [33].

The extension of this formalism to crystalline solids can be performed at least in two different manners. We can choose a finite piece of crystal, especially if the atoms are assumed to be fixed, and compute the interaction of the quantum subsystems with all the atoms of E as it is the case in proteins. The macroscopic size of the crystal may be simulated by using an Ewald sum [42] to extend the classical environment to infinity. In the present preliminary study we chose the first method in order to analyze the convergence of the results when the size of the sample is increased. In order to take into account the volume and the surface periodic arrangement of the atoms, the code has been modified in such a way that the net charges located on the atoms of the classical subsystem, and which are used to define the electrostatic interaction of the two subsystems, are set equal to the net charges computed on the equivalent atoms of the quantum subsystem. This adjustment is performed by iterations until the self-consistency is reached. Similarly, the code allows an optimization of the geometric parameters of the surface atoms in the quantum part, and these parameters are repeated in the classical part of the surface in order to achieve the two-dimensional periodicity of a regular surface.

The input data of the program are the basic parameters a and P_{II} of the frozen orbitals and the atomic coordinates of the unit cell of the crystal. The code generates finite size samples by repeating this cell N times along the three directions of space, to create an assembly of N^3 unit cells.

The surfaces are generated by a cleavage plane defined by the equation

$$hx + ky + lz = D_i \quad (2)$$

in which h , k , and l are the Miller indices of the plane and D_i is an integer. By varying D_i , one defines planes with the same atomic structure. In the case of finite samples as defined above, different values of D_i generate surfaces limiting a crystal sample with a variable number of atoms for a given value of N . Consequently, by changing N and D_i one can study the influence of the size of the bulk and of the extension of the surface on the computed properties.

Computation and Results

DEFINITION OF THE PARAMETERS

The test system investigated is α -cristobalite. This crystal has a tetragonal $P4_12_1$ space group symmetry [40]. The pseudocubic prismatic cell contains 12 atoms and its parameters are $a_0 = b_0 = 4.9733 \text{ \AA}$ and $c_0 = 6.9262 \text{ \AA}$.

In the computations reported here the frontier atoms of the quantum subsystem are oxygen atoms. The basic parameters a and P_{II} are adjusted on the O-Si bonds surrounding a SiO_4 tetrahedron located in the bulk of the crystal. We used a pentamer Si_5O_{16} [Fig. 1(b)] located at the center of

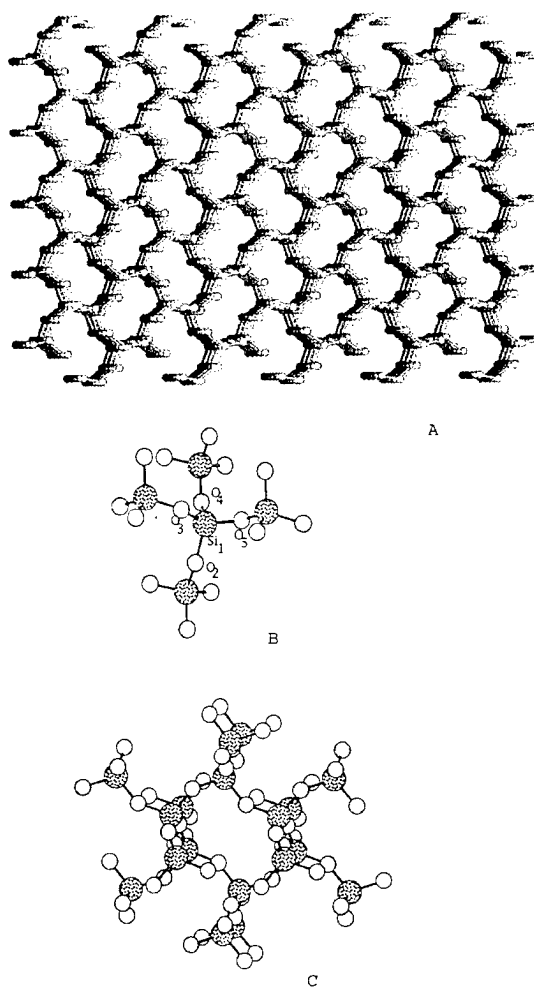


FIGURE 1. General view (A) and the quantum systems (B, C) for the modeling of a bulk.

TABLE I
Self-consistent Si and O charges and precalculated parameters of the MNDO-AM1 and the MNDO-PM3 levels.

Units ^a	Atoms ^b	MNDO-AM1				MNDO-PM3			
		q_{Si}	q_{O}	P_{ss}	a	q_{Si}	q_{O}	P_{ss}	a
125	1500	2.090	-1.045	1.526	0.79	1.590	-0.795	1.370	0.79
343	4116	2.130	-1.064	1.534	0.79	1.760	-0.880	1.420	0.79
729	8748	2.170	-1.085	1.540	0.79	1.890	-0.945	1.450	0.79
1331	15972	2.190	-1.095	1.544	0.79	1.980	-0.990	1.480	0.79

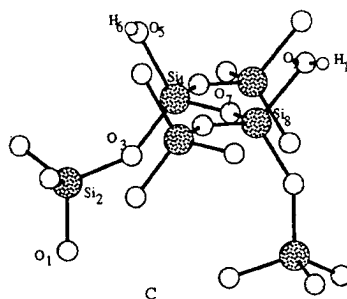
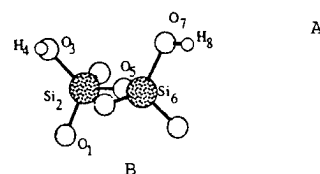
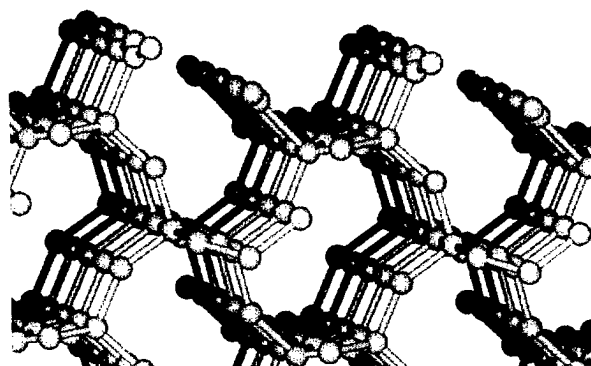
^a Total number of elementary units.^b Total number of atoms in quantum and classical subsystems.

pseudocubic samples of variable size. We used four different samples, containing 125, 343, 729, and 1331 crystallographic unit cells (1500, 4116, 8748, and 15972 atoms) [Fig. 1(a)]. The parameters are adjusted self-consistently.

The computations have been carried on by both AM1 [43] and PM3 [44] methods. AM1 is used with its native parametrization. In the case of PM3 we had to modify the ρ_0 parameter of silicon. We simply transferred the value used in AM1 ($\rho_0^{\text{Si}} = 1.38544$). The values obtained are collected in Table I, together with the self-consistent values of the charges.

In order to check the reliability of the method, a second computation has been performed with a larger cluster embedded in the same crystal samples. We chose a 12-member silicon oxygen ring with the stoichiometric formula $\text{Si}_{18}\text{O}_{54}$ [Fig. 1(c)]. The charges computed in the quantum subsystem, by using the parameters determined with the smaller cluster, are compared with the charges

computed on the latter. Due to the boundary conditions, the charges are not rigorously the same on the various atoms of the same element. We give in Table II the averaged value of these charges. The

**FIGURE 2.** General view (A) and the quantum systems (B, C) for the modeling of the surface with a regular structure.**TABLE II**
Average values of Si and O charges, calculated for clusters B and C (Fig. 1).

Cluster	Units ^a	Atoms ^a	MNDO-AM1		MNDO-PM3	
			Q_{Si}	Q_{O}	Q_{Si}	Q_{O}
B ^b	—	33	2.015	-0.972	1.324	-0.571
B	125	1500	2.091	-1.048	1.592	-0.790
C	125	1500	2.071	-1.040	1.650	-0.789
B	343	4116	2.134	-1.071	1.760	-0.848
C	343	4116	2.130	-1.067	1.826	-0.877
B	729	8748	2.168	-1.086	1.885	-0.909
C	729	8748	2.164	-1.084	1.952	-0.935
B	1331	15972	2.191	-1.097	1.975	-0.958
C	1331	15972	2.189	-1.096	2.044	-0.988

^a The definition was given in Table I.^b Data for the molecular cluster.

TABLE III
Values of optimized parameters for cluster B (Fig. 2).

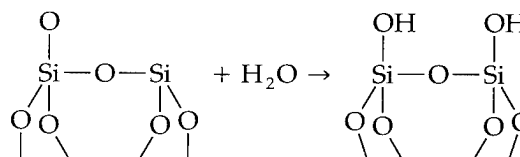
Atoms ^a	D_i^b	Approx.	$R_{H_4O_3}$	$\langle H_4O_3Si_2 \rangle$	$\langle H_4O_3Si_2O_1 \rangle$	$R_{O_3Si_2}$	$\langle O_3Si_2O_5Si^e \rangle$	$R_{H_8O_7}$	$\langle H_8O_7Si_6 \rangle$	$\langle H_8O_7Si_6O_5 \rangle$	$R_{O_7Si_6}$	$\langle O_7Si_6O_5 \rangle$
750	2	AM1	0.946	116.1	81.1	1.765	3.2	0.948	114.6	156.4	1.756	106.4
750	2	PM3	0.946	113.5	70.9	1.723	3.1	0.945	113.6	171.6	1.715	106.2
1050	3	AM1	0.946	116.4	81.1	1.764	3.2	0.947	114.9	159.1	1.755	106.3
1350	4	AM1	0.946	116.6	81.2	1.763	3.2	0.947	115.1	161.8	1.754	106.2
1470	2	AM1	0.946	116.1	77.0	1.765	3.9	0.947	114.5	153.5	1.756	107.1
3822	6	AM1	0.946	116.9	76.9	1.761	4.1	0.947	115.1	157.7	1.754	107.1
2430	2	AM1	0.946	116.1	71.7	1.765	4.2	0.947	114.5	155.0	1.757	107.3
8262	8	AM1	0.946	117.1	73.4	1.761	4.5	0.946	115.2	157.4	1.755	107.5
3630	2	AM1	0.946	116.2	69.4	1.765	4.5	0.947	114.5	156.1	1.757	107.3
15 ^c	—	AM1	0.947	116.8	121.7	1.740	2.8	0.945	116.6	106.6	1.758	111.7
15 ^c	—	PM3	0.945	116.1	123.7	1.699	2.3	0.944	117.0	94.4	1.712	109.0
15 ^d	—	AM1	0.949	117.6	147.2	1.730	20.4	0.948	117.8	89.0	1.730	109.3
15 ^d	—	PM3	0.945	116.4	131.8	1.690	28.3	0.944	116.4	93.9	1.689	110.2

^a The definition was given in Table I.^b For the definition of D_i see Eq. (2).^c Corresponds to the molecular cluster with the same number of the optimized parameters.^d Corresponds to the fully optimized molecular cluster.

convergence is quite good, and the charges compare quite well with the classical charges optimized of the rest of the crystal. The same quantities computed on the isolated molecular cluster ($Si_5O_{16}H_{12}$) depart noticeably from the data obtained on the embedded cluster. The absolute values of charges are higher at the MNDO-AM1 level because the charges of molecular cluster for these systems are higher for the MNDO-AM1 method (see Table II). We also briefly mention that the results obtained by AM1 seem in better agreement with ab initio computations which suggest a charge close to -1 on oxygen [45]. In other respects both methods have the same tendencies.

MODELING OF THE HYDROXYLATED (010) SURFACE

The dangling bonds of (010) α -cristobalite surface belong to Si and O unsaturated atoms. These surface atoms are considered as chemisorption sites for polar molecules, especially for water, which generates an hydroxylic layer on the surface. The reaction may be depicted by the general scheme:

**TABLE IV**
Values of optimized parameters for cluster C (Fig. 2) at the MNDO-AM1 level.

Atoms ^a	D_i^b	$R_{H_6O_5}$	$\langle H_6O_5Si_4 \rangle$	$\langle H_6O_5Si_4O_3 \rangle$	$R_{O_5Si_4}$	$\langle O_5Si_4O_3 \rangle$	$R_{H_{10}O_9}$	$\langle H_{10}O_9Si_8 \rangle$	$\langle H_{10}O_9Si_8O_7 \rangle$	$R_{O_9Si_8}$	$\langle Si_8O_9O_7 \rangle$
750	2	0.948	115.8	78.0	1.762	112.1	0.947	114.6	185.3	1.757	106.4
1050	3	0.948	116.1	77.1	1.760	112.4	0.947	114.7	189.5	1.757	106.3
1350	4	0.948	116.2	78.3	1.760	112.3	0.947	114.8	190.2	1.757	107.2
1470	2	0.948	115.9	74.1	1.761	112.2	0.947	114.6	182.8	1.757	107.2
39 ^c	—	0.947	115.9	137.2	1.746	111.1	0.947	115.3	115.3	1.744	110.4
39 ^d	—	0.947	116.0	146.4	1.725	112.4	0.949	115.7	115.7	1.729	112.0

^a The definition was given in Table I.^b For the definition of D_i see Eq. (2).^c Corresponds to the molecular cluster with the same number of the optimized parameters.^d Corresponds to the fully optimized molecular cluster.

TABLE V
Average values of atomic charges for cluster B (Fig. 2).

Atoms ^a	D_i^b	Approx.	Q_{O_1}	Q_{Si_2}	Q_{O_3}	Q_{H_4}	Q_{O_5}
750	2	AM1	-0.978	1.948	-0.744	0.220	-1.000
750	2	PM3	-0.683	1.336	-0.574	0.179	-0.665
1050	3	AM1	-0.982	1.959	-0.747	0.222	-1.003
1350	4	AM1	-0.984	1.964	-0.748	0.223	-1.005
1470	2	AM1	-0.999	1.955	-0.745	0.218	-1.004
3822	6	AM1	-0.999	1.984	-0.754	0.223	-1.015
2430	2	AM1	-0.998	1.959	-0.747	0.218	-1.008
8262	8	AM1	-1.009	2.001	-0.760	0.224	-1.023
3630	2	AM1	-1.004	1.962	-0.748	0.218	-1.010
15 ^c	—	AM1	-0.820	1.990	-0.735	0.223	-0.847
15 ^c	—	PM3	-0.616	1.317	-0.536	0.185	-0.552
15 ^d	—	AM1	-0.673	1.775	-0.673	0.245	-0.776
15 ^d	—	PM3	-0.510	1.223	-0.507	0.202	-0.541

^a The definition was given in Table I.^b For the definition of D_i see Eq. (2).^c Corresponds to the molecular cluster with the same number of the optimized parameters.^d Corresponds to the fully optimized molecular cluster.

The ideal hydroxylated (010) α -cristobalite is shown of Figure 2(a). The hydroxyl groups all occupy vicinal positions according to the usual classification [46].

Structure of the Ideal Surface

In order to analyze the electronic properties of the surface, we performed some LSCF computations on two clusters of variable size with the formulas $Si_2O_7H_2$ and $Si_6O_{19}H_2$ that contain two vicinal hydroxyl groups [Fig. 2(b) and 2(c)]. Table III collects the results obtained with cluster B for a variable number of atoms in the classical system,

including the free cluster. The corresponding results for cluster C can be found in Table IV. Again one notices that the conclusions do not depend significantly neither on the size of the cluster nor on the size of the classical subsystem. Nevertheless, the results corresponding to the free cluster depart strongly from all the other ones for the orientation of the OH groups (see the values $\langle H_4O_3Si_2O_1 \rangle$ and $\langle H_8O_7Si_6O_5 \rangle$ in the Table III and $\langle H_6O_5Si_4O_3 \rangle$ in the Table IV).

The main difference between the atoms on the surface compared with the bulk is the electronic charge (Tables V and VI). The absolute value of the charge of the hydroxylic oxygen atoms is less

TABLE VI
Average value of atomic charges for cluster C (Fig. 2) at the MNDO-AM1 level.

Atoms ^a	D_i^b	Q_{O_1}	Q_{Si_2}	Q_{O_3}	Q_{Si_4}	Q_{O_5}	Q_{H_6}	Q_{O_7}
750	2	-1.014	2.014	-0.995	1.940	-0.840	0.223	-1.000
1050	3	-1.017	2.028	-1.000	1.948	-0.852	0.225	-1.005
1350	4	-1.019	2.034	-0.996	1.947	-0.853	0.226	-1.010
1470	2	-1.024	2.022	-1.003	1.946	-0.847	0.223	-1.003
39 ^c	—	-0.804	2.013	-0.888	1.921	-0.750	0.225	-0.906
39 ^d	—	-0.687	1.781	-0.842	1.935	-0.668	0.239	-0.865

^a The definition was given in Table I.^b For the definition of D_i see Eq. (2).^c Corresponds to the molecular cluster with the same number of the optimized parameters.^d Corresponds to the fully optimized molecular cluster.

TABLE VII
Geometry (A and degree) for clusters B and D
(Fig. 3) at the MNDO-PM3 level.^{a, b}

Cluster	Parameter	Value
B	R _{O2H3}	0.957(0946)
	R _{H3O5}	2.654
	R _{H6O7}	1.783
	R _{O7H8}	0.945(0946)
	R _{H4O5}	0.970(0.951)
	R _{H6O5}	0.957(0.951)
	∠H4O5H6	106.8(107.7)
	∠H3O2Si8	116.6(112.8)
D	∠H8O7Si9	116.8(112.9)
	R _{O1H2}	0.946(0.945)
	R _{H4O1}	1.759
	R _{O3H6}	1.904
	R _{H4O3}	0.967(0.951)
	R _{H5O3}	0.954(0.951)
	R _{H6O7}	0.948(0946)
	∠H4O3H5	106.9(107.7)
	∠H2O1Si9	114.6(112.8)
	∠H6O7Si8	114.1(113.5)

^a Values in parentheses correspond to isolated clusters or to isolated water molecule.

^b Surface has been defined with Atoms = 750, $D_i = 2$.

TABLE VIII
Geometry (A and degree) for clusters B and D (Fig. 4)
at the MNDO-PM3 level.

Parameter	Cluster B	Cluster D
R _{Si2O3}	1.699	1.701
R _{O3Si4}	1.708	1.702
R _{Si4O5}	1.696	1.697
R _{O5Si6}	1.707	1.708
R _{Si4O7}	1.704	1.703
R _{Si4O9}	1.715	1.719
R _{H8O7}	0.948	0.948
R _{H10O9}	0.945	0.945
∠O1Si2O3	87.4	87.5
∠Si2O3Si4	110.7	111.0
∠O3Si4O5	125.2	125.1
∠Si4O6Si6	117.7	117.6
∠O5Si6O1	90.4	90.4
∠H8O7Si4	113.9	114.4
∠H10O9Si4	112.8	114.5
∠O7Si4O9	102.7	101.7
R _{H11O12}	—	0.968
R _{H13O12}	—	0.954
R _{O9H11}	—	1.768
∠H11O12H13	—	106.6

than the corresponding quantity for oxygens coordinated with two surface silicon atoms, and the oxygen atoms of the bulk bear the greatest charge. The same variation is observed for the positive charge of the silicon atoms. These observations indicate that the Si–O bonds are less polarized near the surface than in the bulk, as expected, since a condensed phase is a polarizable medium which favors charge separation.

The barrier to internal rotation of one OH group on the surface can be easily estimated. The results range from 2.9 to 5.9 kcal/mol depending on the size of the bulk. They meet the known experimental data [47].

Finally one notices that the results obtained by the PM3 method are in agreement with those obtained by AM1.

Interaction of a Water Molecule with the Ideal Surface

This study has been performed at the PM3 level. The full geometry optimization of a water molecule interacting with the hydroxylated surface shows two stable conformations in which the adsorbed molecule interact with the hydrogen atom of a OH group and with the oxygen atom of a OH group. These two situations correspond to the cases in which one hydrogen atom (H_6) of the adsorbed molecule is hydrogen bonded to the O_7H_8 group [Fig. 3(a) and (b)] or both hydrogen atom (H_4) and oxygen (O_3) are involved in a bifurcated interaction [Fig. 3(c) and (d)]. In both cases (Table VII) the hydrogen bonds with the oxygen atom of the hydroxylic group are rather short (1.78 Å or less) although the hydrogen bonds involving the oxygen atom of the adsorbed water molecule are closer to the usual bonds in water dimers (1.90 Å). The interaction energies are of the same order of magnitude [11.5 and 10.4 kcal/mol for structures (b) and (d)]. These values are in the observed experimental range [5, 48, 49], although they appear as slightly overestimated.

Modeling Surface Defects

Silica surfaces can hardly be considered as ideally regular surfaces [50–52]. Most of the theoretical approaches deal with point defects [5]. We shall here consider two special cases: an extra SiO_2

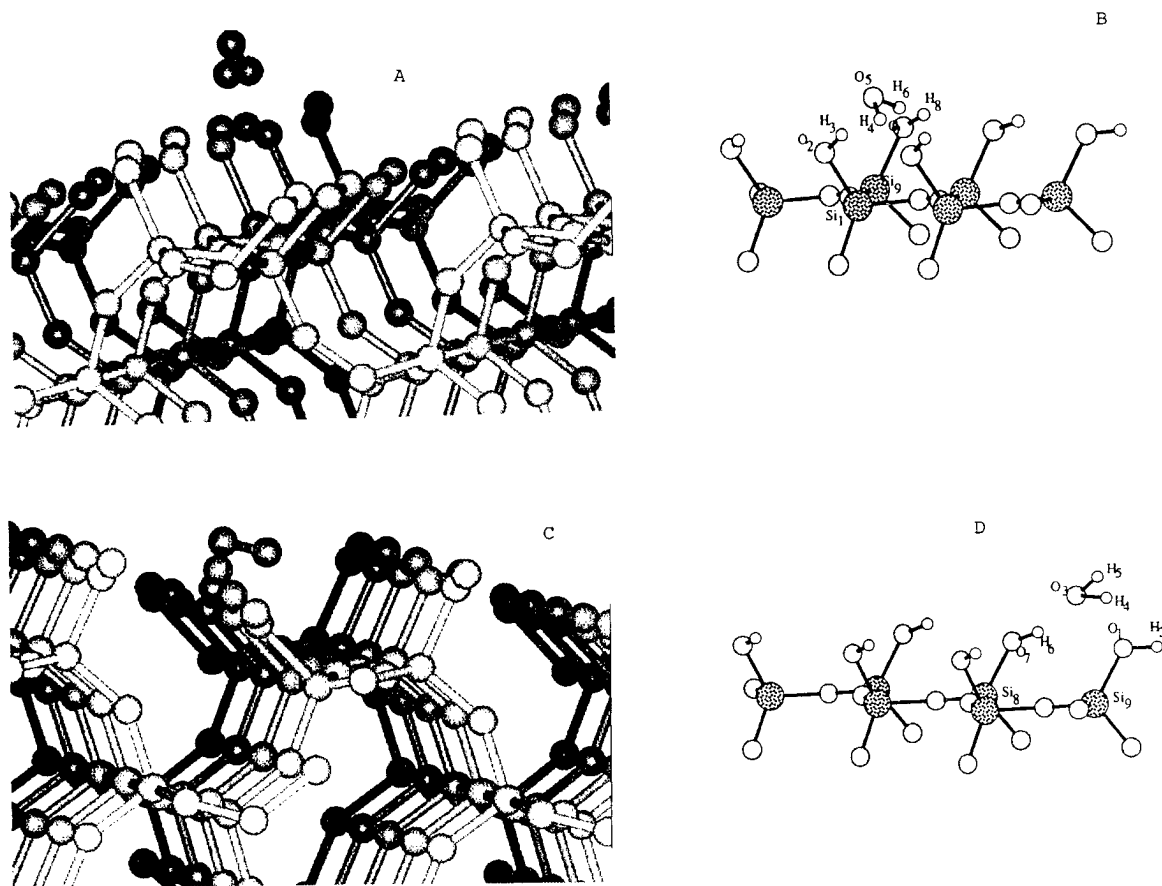


FIGURE 3. General view (A, C) and the quantum systems (B, D) for the modeling of water adsorption on a surface with a regular structure.

group added to the ideal (010) surface and a crystal edge.

The extra SiO_2 group, represented on Figure 4(a) is modeled by a quantum cluster schematized in Figure 4(b) (formula $\text{Si}_7\text{O}_{21}\text{H}_6$). The presence of this chemically bonded extra group introduces a local perturbation in the bond angles and bond lengths (Table VIII). One possible structure of a water molecule adsorbed on this defect is represented in Figures 4(c) and 4(d) (the interacting atoms are O_9 and H_{11}). The energy of interaction found in this case is 10.2 kcal/mol, very close to the values obtained on the ideal surface.

We finally considered the edge of a (010) plane represented in Figure 5. The uneven geometry of the silanol groups is clearly visible on this figure. The energy of interaction of a water molecule with these groups was again found equal to 10.2 kcal/mol.

Discussion

Although the main aim of this work is to test the extension of the LSCF method to crystal surfaces, especially to its capability for modeling their chemical properties, the preliminary results obtained on the (010) surface of α -cristobalite already give some interesting indications on the chemical properties of the surface.

The most striking result is the great stability of the computed properties with the size of the quantum subsystem either in the bulk or on the surface. This should give confidence in the method. The other very clear result arises from the comparison of the geometric features of an isolate surface cluster with an imbedded one which exhibits larger differences, indicating that the conclusions drawn

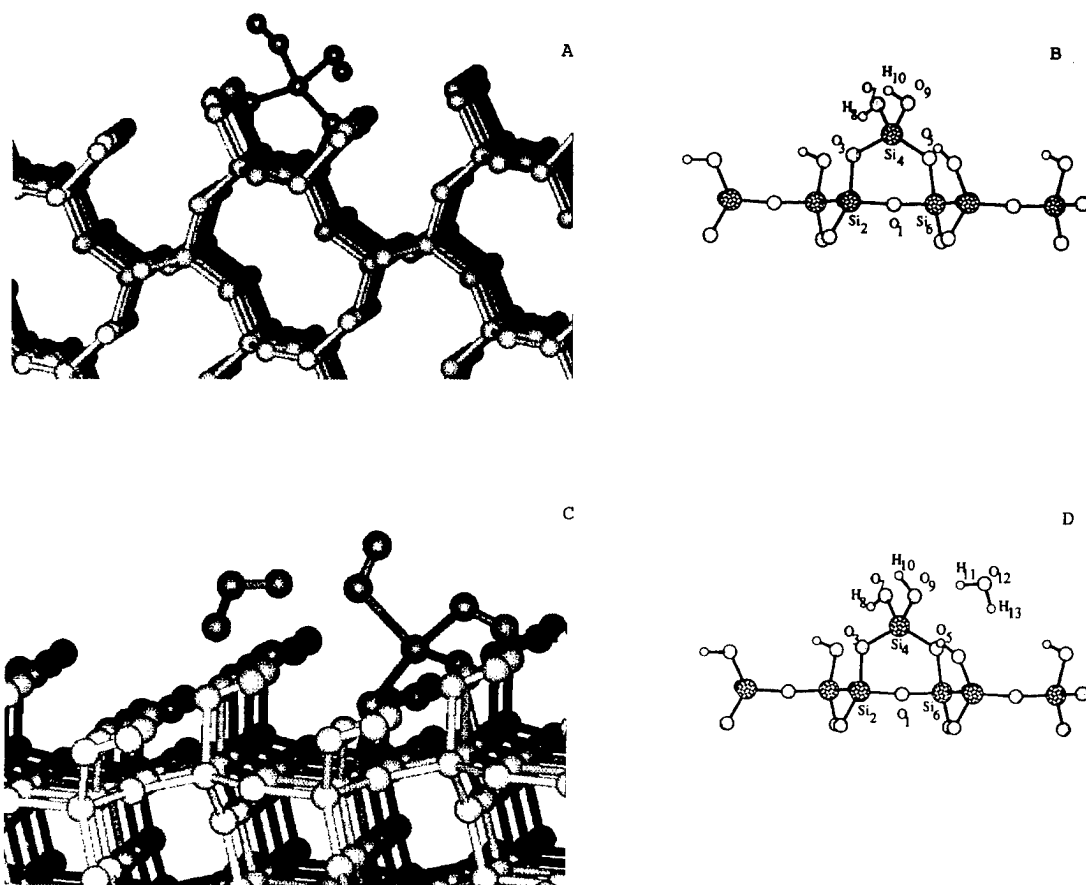


FIGURE 4. General view (A, C) and the quantum systems (B, D) for the modeling of a surface with irregular structure.

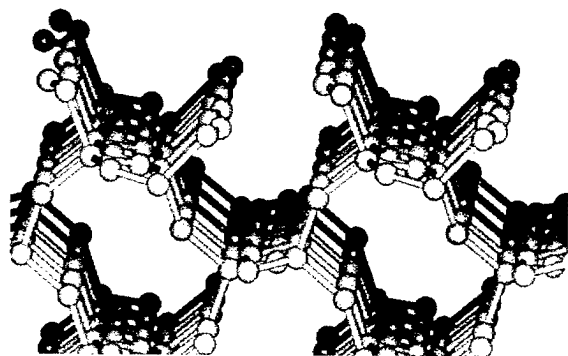


FIGURE 5. General view of a corner of (010) α -cristobalite surface.

from the study of small molecular clusters intended for representing the surface of a solid may be somewhat erroneous.

The only chemical property studied here is the energy of interaction of a water molecule with the hydroxylated (010) surfaces. The unexpected result is the small range of variation of these energies.

This could mean that this interaction involves the properties of individual OH groups and that these properties do not vary much from one place to another, as expected for covalent bonds.

This method is well adapted to the study of other physical properties, such as vibrational frequencies [36], as well as chemical reactivity such as acidity or basicity of surface groups or the influence of chemical defects (substitution of one atom by another element). It should be tested in this way in the near future.

Conclusion

The extension of the LSCF method to periodic systems appears to be quite an appropriate tool to perform quantum chemical computations on a cluster of any size (provided that the computational requirements do not exceed the possibilities of the computer in use) interacting with the rest of

the solid and linked to it by localized bond orbitals which minimize the electronic discontinuity between the two systems. When such a cluster is located at the surface of the solid, it allows the study of chemical properties of the surface and of chemical reactions in which this surface is involved.

This computational scheme, which was originally devised for modeling biopolymers, can also be used for amorphous solids provided that one is able to generate the structure of these solids and to define a chemical similarity between the atoms of the quantum part and those of the rest of the system, in order to achieve the self-consistency in the charge distribution.

In its present form, the method works very efficiently at the NDDO semi-empirical level, due to the assumed orthogonality of the atomic orbitals. The basic principles of the method are also valid at the *ab initio* level, but they require a full orthogonalization of the quantum subsystem to the localized bond orbitals which separate the classical and the quantum subsystem. This additional subroutine is under development in the Nancy group. Therefore, the local self-consistent field method [33] together with the classical-quantum force field [34] appear as a natural extension of the embedded cluster methods to covalent solids and thus offer some very appealing prospects.

ACKNOWLEDGMENTS

This work has been performed with the financial support of the Centre National de la Recherche Scientifique (France), while one of us (L.G.G.) was staying at Nancy thanks to a CNRS-Academy of Sciences of Ukraine exchange program. The authors would like to express their gratitude to this organization.

References

1. I. D. Mikheikin, I. A. Abronin, and G. M. Zhidomirov, *J. Mol. Catal.* **1**, 435 (1978).
2. G. B. Gibbs, *Am. Mineral.* **67**, 421 (1982).
3. J. Sauer, *J. Chem. Rev.* **89**, 199 (1989).
4. S. Beran and J. Dubsky, *J. Phys. Chem.* **83**, 2538 (1979).
5. P. Uglierio, V. R. Sanders, and E. Garone, *J. Phys. Chem.* **93**, 5210 (1989).
6. Z. M. Zhidomirov and V. B. Kazansky, *Adv. Catal.* **34**, 131 (1986).
7. H. V. Brand, L. A. Curtiss, and L. E. Iton, *J. Phys. Chem.* **96**, 7725 (1992).
8. A. Redondo and P. J. Hay, *J. Phys. Chem.* **97**, 11754 (1993).
9. S. Beran, *Chem. Phys. Lett.* **91**, 86 (1982).
10. N. U. Zhanpeisov, G. M. Zhidomirov, and M. Baerns, *Zhurn. Struct. Khim.* **35**, 12 (1994) (in Russian).
11. C. Pisani, R. Dovesi, and C. Roetti, *Lecture Notes in Chemistry*, Vol. 48, p. 1 (Springer Verlag, Heidelberg, 1988).
12. R. Orlando, C. Pisani, E. Ruiz, and P. Sautet, *Surface Sci.* **275**, 482 (1992).
13. R. Car and M. Parrinello, *Phys. Rev. Lett.* **55**, 2471 (1985).
14. M. C. Payne, E. Tarnow, P. D. Bristowe, and J. D. Joannopoulos, *Mol. Simul.* **4**, 79 (1989).
15. J. Furthmueller, J. Hafner, and G. Kresse, *Europhys. Lett.* **28**, 659 (1994); *Phys. Rev. B*, **53**, 7334 (1996).
16. G. Ooms, R. A. van Santen, C. J. J. Ouden, R. A. Jacson, and C. R. Catlow, *J. Phys. Chem.* **92**, 4462 (1988).
17. S. M. Tomlinson, R. A. Jackson, and R. A. Catlow, *J. Chem. Soc. Chem. Commun.* **1990**, 813 (1990).
18. F. Vigne-Maeder, in *Modelling of Molecular Structures and Properties, Proceedings of International Meeting, Nancy, France, 11-15 September 1989*, J.-L. Rivail, Ed., p. 135 (Elsevier, Amsterdam, 1990).
19. A. K. Nowak, A. K. Chetham, and J. M. Thomas, *Mol. Simul.* **2**, 353 (1989).
20. A. Nakano, L. Bi, R. K. Kalia, and P. Vashista, *Phys. Rev.* **49B**, 9441 (1994).
21. U. C. Singh and P. A. Kolman, *J. Comp. Chem.* **7**, 718 (1986).
22. P. A. Bash, M. J. Field, and M. Karplus, *J. Am. Chem. Soc.* **109**, 8092 (1987).
23. J. Gao and X. Xia, *Science* **258**, 63 (1992).
24. I. Tuñon, M. T. C. Martins-Costa, C. Millot, and M. F. Ruiz-Lopez, *J. Mol. Mod.* **1995**, 196 (1995).
25. I. Tuñon, M. T. C. Martins-Costa, C. Millot, M. F. Ruiz-Lopez, and J.-L. Rivail, *J. Comp. Chem.* **17**, 19 (1996).
26. J. G. Angyan and B. Silvi, *J. Phys. Chem.* **86**, 6957 (1987).
27. A. Warshel and E. M. Levitt, *J. Mol. Biol.* **103**, 227 (1976).
28. G. Naray-Szabo and P. R. Surjan, *Chem. Phys. Lett.* **96**, 499 (1983).
29. G. Naray-Szabo, *Croat. Chim. Acta* **57**, 901 (1987).
30. G. G. Ferenczy, J.-L. Rivail, P. R. Surjan, and G. Naray-Szabo, *J. Comp. Chem.* **13**, 830 (1992).
31. F. Bernardi, M. Olivucci, and M. A. Robb, *J. Am. Chem. Soc.* **114**, 1606 (1992).
32. C. C. J. Roothaan, *Rev. Mod. Phys.* **23**, 69 (1951).
33. V. Thery, D. Rinaldi, J.-L. Rivail, B. Maigret, and G. G. Ferenczy, *J. Comp. Chem.* **15**, 269 (1995).
34. G. Monard, M. Loos, V. Thery, K. Baka, and J. L. Rivail, *Int. J. Quantum Chem.*, **58**, 153 (1996).
35. B. Silvi, *J. Mol. Struct. (Theochem)* **226**, 29 (1991).
36. M. Gordon, R. Damrauer, and M. Krempf, *J. Phys. Chem.* **97**, 7820 (1993).
37. A. G. Pelmeshnikov, G. Morosi, and A. Gamba, *J. Phys. Chem.* **96**, 7422 (1992).
38. C. J. J. Den Ouden, B. Smit, A. F. H. Wiers, R. A. Jacson, and A. K. Nowak, *Mol. Simul.* **4**, 121 (1989).
39. S. D. Pickett, A. K. Nowak, A. K. Cheetham, and J. M. Thomas, *Mol. Simul.* **2**, 353 (1989).

40. R. W. G. Wyckoff, *Crystall. Structures*, Vol. 1 (Wiley, Interscience, New York, 1965), p. 316.
41. J. A. Pople, D. P. Santry, and G. A. Segal, *J. Chem. Phys.* **43**, 5129 (1965).
42. P. P. Ewald, *Ann. Physik* **64**, 253 (1921).
43. M. J. S. Dewar, E. G. Zoebisch, E. F. Healy, and J. J. P. Stewart, *J. Am. Chem. Soc.* **107**, 3902 (1985).
44. J. J. P. Stewart, *J. Comp. Chem.* **10**, 209, 221 (1989).
45. K. A. van Genechten, W. J. Mortie, and P. Geerlings, *J. Chem. Phys.* **86**, 5063 (1987).
46. A. V. Kiselev and I. V. Ligin, *Infrared Spectra of Surface Compounds*, (Wiley, New York, 1975).
47. I.-S. Chuang, D. R. Kinney, and G. E. Maciel, *J. Am. Chem. Soc.* **115**, 8695 (1993).
48. K. Klier and A. C. Zettlemoyer, *J. Colloid Interface Sci.* **58**, 216 (1977).
49. K. R. Lange, *J. Colloid Interface Sci.* **20**, 231 (1965).
50. J. Datka, M. Boczar, and P. Pymarowich, *J. Catal.* **114**, 368 (1988).
51. J. J. Boland, *Phys. Rev. Lett.* **65**, 3325 (1990).
52. R. A. Evarestov, E. A. Katomin, and A. N. Ermoshkin, *Molecular Models of Points Defects in Solids* (Zinante, Riga, 1983).

Self-Expansion and Compression of Charged Clusters of Stabilized Jellium

ARMANDO VIEIRA, CARLOS FIOLEAIS, AND
MARTA BRAJCZEWSKA*

Departamento de Fisica, Universidade de Coimbra, P-3000 Coimbra, Portugal; e-mail for M. B.: marta@feor4.fis.uc.pt

JOHN P. PERDEW

Department of Physics and Quantum Theory Group, Tulane University, New Orleans, Louisiana 70118

Received February 25, 1996; accepted February 28, 1996

ABSTRACT

In a positively charged metallic cluster, surface tension tends to enhance the ionic density with respect to its bulk value, while surface-charge repulsion tends to reduce it. Using the stabilized jellium model, we examine the self-expansion and compression of positively charged clusters of simply metals. Quantal results from the Kohn–Sham equations using the local density approximation are compared with continuous results from the liquid drop model. The positive background is constrained to a spherical shape. Numerical results for the equilibrium radius and the elastic stiffness are presented for singly and doubly positively charged aluminum, sodium, and cesium clusters of 1–20 atoms. Self-expansion occurs for small charged clusters of sodium and cesium, but not of aluminum. The effect of the expansion or compression on the ionization energies is analyzed. For Al_6 , we also consider net charges greater than 2^+ . The results of the stabilized jellium model for self-compression are compared with those of other models, including the SAPS (spherical averaged pseudopotential model). © 1996 John Wiley & Sons, Inc.

1. Introduction

The stabilized jellium model (SJM) or structureless pseudopotential model [1] is a simple modification of the jellium model. In the jell-

ium model, the ions are replaced by a continuous charge background of density $\bar{n} = 3/(4\pi r_s^3)$, truncated sharply at a cluster radius $R = r_s N_0^{1/3}$, where N_0 is the number of valence electrons in the neutral cluster. This model is widely used in the physics of metal clusters, since the precise position of the ions is not important for many physical properties. Stabilized jellium as well as jellium

*To whom correspondence should be addressed.

may be deformed, but we limit our consideration here to spherical shapes.

Bulk jellium ($N_0 \rightarrow \infty$) is unstable at density parameters which are very different from that of sodium ($r_s^B = 3.93$ bohr). (We adopt atomic units in which $e = m = \hbar = 1$.) The SJM cures the main deficiencies of the jellium model, namely unrealistic binding energies at all densities, unrealistic bulk moduli for metals with low valence electron density such as cesium ($r_s = 5.62$ bohr), and unrealistic surface energies for high valence electron density metals such as aluminum ($r_s = 2.07$ bohr). The SJM retains the simplicity and universality of jellium, as the only inputs to these models are the bulk density parameter r_s and the valence z . In the SJM, we subtract the spurious self-repulsion of the jellium charge inside each Wigner-Seitz sphere and then add a constant potential acting on the electrons inside the cluster. This constant potential, different for each metal, is designed so that the bulk metal is stable at the observed valence-electron density r_s (i.e., the pressure P vanishes at the experimental r_s).

In previous works, the surface properties [2], the energetics of small clusters and cohesive properties of bulk metals [3], and a number of fragmentation processes of charged clusters [4] were explored in the framework of the SJM. In all those works the density parameter of the clusters was taken to be r_s^B , the bulk density parameter. However, stabilized jellium permits adjustment of the background density so that the energy per particle of a cluster is minimal [5, 6]. A neutral cluster with $r_s = r_s^* < r_s^B$ has a lower energy than a cluster with r_s^B . This effect, which cannot be described in the jellium model, is simply explained, within the liquid drop model (LDM), by the surface tension. It is called "self-compression" and has analogs in nuclear physics [7] and in the physics of helium droplets.

In the present work, the SJM is employed to study not only the self-compression but also the self-expansion of charged clusters of simple metals. The magnitude of self-compression should be reduced for charged systems. Self-expansion is expected if the Coulomb repulsion of the excess charge overwhelms the surface tension. We use the Kohn-Sham equations of density functional theory in the local density approximation (LDA), and the LDM, considering clusters of three different metals (Al, Na, and Cs), which cover the range of physical

densities, with single and double positive charges.

Let us see how the main reasoning used to introduce the self-compression of neutral clusters can be extended to the case of charged ones. The constant potential is an average of the difference between an electron-ion pseudopotential and the jellium electron-background potential in a unit cell. It can therefore be expressed in terms of a pseudopotential "core radius" r_c . Then the bulk stability condition is

$$\lim_{N_0 \rightarrow \infty} \frac{\partial}{\partial r_s} \left(\frac{E_0}{N_0} \right) \bigg|_{r_s = r_s^B} = 0, \quad (1.1)$$

where $E_0 = E(N_0, r_s, z, r_c)$ is the total energy of the neutral cluster in the SJM. Equation (1.1) fixes $r_c = r_c(r_s^B, z)$ for each metal.

The equilibrium positive-background density parameter r_s^* for a neutral cluster with a finite number N_0 of valence electrons is the solution of the following equation:

$$\frac{\partial}{\partial r_s} \left(\frac{E_0}{N_0} \right) \bigg|_{r_s = r_s^*} = 0, \quad (1.2)$$

where the derivative is evaluated using the same r_c as in Eq. (1.1) (assuming transferability of the pseudopotential from the bulk to the cluster environment).

The elastic stiffness or inverse compressibility of the neutral cluster measures the curvature of the energy with respect to r_s , around the point r_s^* . It is defined by:

$$B_0 = \frac{1}{12\pi r_s^*} \frac{\partial^2}{\partial r_s^2} \left(\frac{E_0}{N_0} \right) \bigg|_{r_s = r_s^*}. \quad (1.3)$$

It is a function of N_0 , r_s^* , z , and r_c . This second derivative goes over to the bulk modulus B^B when $N_0 \rightarrow \infty$.

If we ionize the cluster, the number of valence electrons becomes $N = N_0 + \nu$, with N_0 the number of valence electrons of the neutral system and ν the number of excess electrons (e.g., for a cluster with a single positive charge, $\nu = -1$). The energy of the charged cluster may be evaluated by solving the self-consistent Kohn-Sham [8] equations and filling up in sequence the available single-particle levels. It can also be evaluated using the LDM for charged systems [9, 10], in which we disregard

shell fluctuations. In either case, the equilibrium radius of the positive background is $R = r_s^* N_0^{1/3}$, with the equilibrium density parameter defined by

$$\left. \frac{\partial}{\partial r_s} \left(\frac{E}{N} \right) \right|_{r_s=r_s^*} = 0, \quad (1.4)$$

where $E = E(N_0, r_s, z, r_c, \nu)$ is the total energy of the charged cluster. We have expansion if $r_s^* > r_s^B$ or compression if $r_s^* < r_s^B$.

The elastic stiffness of the charged cluster,

$$B = \frac{1}{12\pi r_s^*} \frac{\partial^2}{\partial r_s^2} \left(\frac{E}{N} \right) \bigg|_{r_s=r_s^*}, \quad (1.5)$$

is different from the stiffness of a neutral cluster. Besides N_0 , r_s^* , z , and r_c , it depends on the charge ν .

We shall determine r_s^* and related physical properties as functions of N_0 and ν for different metals (different sets of r_s^B and z).

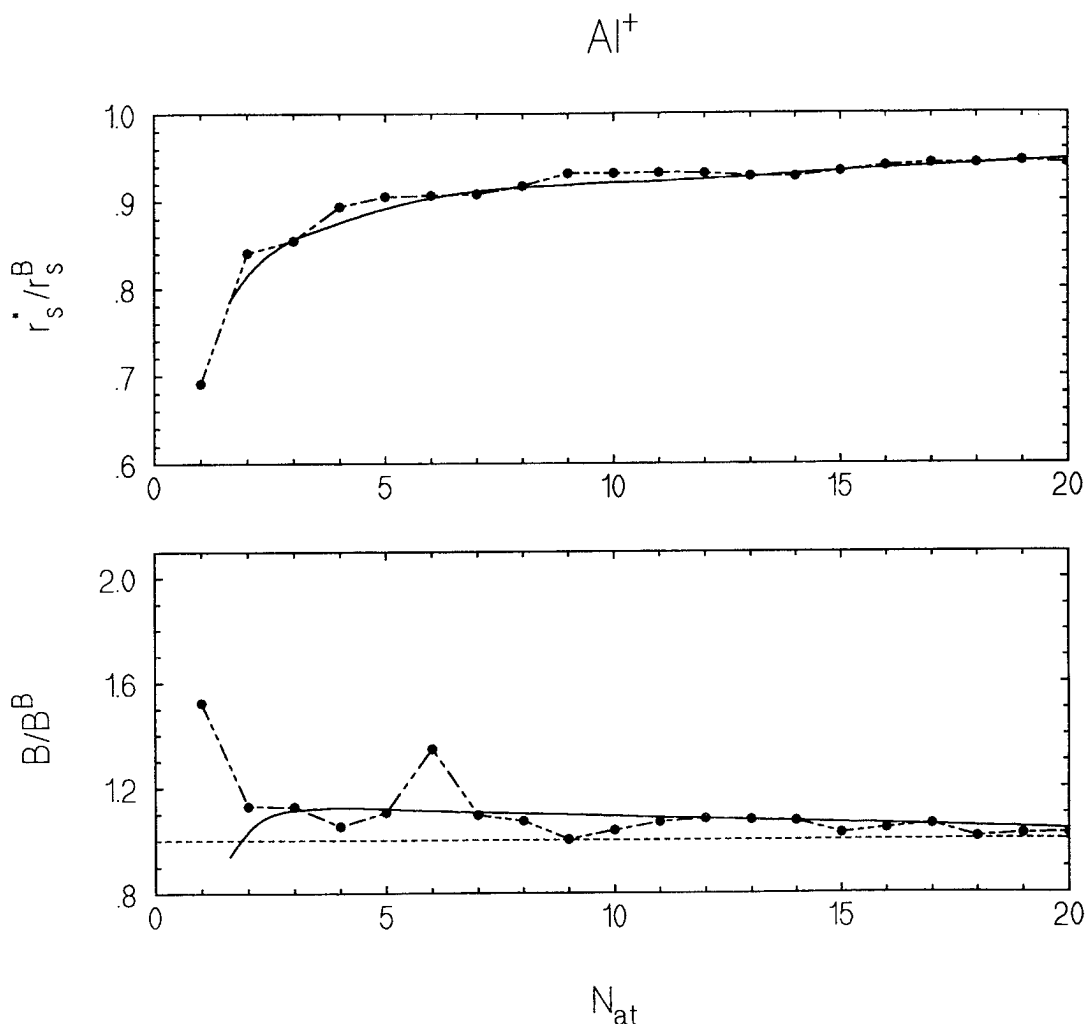


FIGURE 1. (a) Ratio of the equilibrium density parameter r_s^* to its bulk value r_s^B as a function of number of atoms $N_{at} = N_0/z$, for a singly charged cluster of stabilized jellium representing Al^+ . Heavy dots: LDA Kohn–Sham results. Solid curve: Exact numerical solution within the LDM. These results should be compared with those for neutral clusters [5, 6]. Note, however, that in Ref. [5] the local spin density (LSD) was used instead of the LDA and, in Refs. [5, 6], the densities of Na and Cs were $r_s^B = 3.99$ and $r_s^B = 5.63$, in contrast with the present $T = 0$ values $r_s^B = 3.93$ and $r_s^B = 5.62$. (b) Ratio of the elastic stiffness to its bulk value as a function of number of atoms for Al^+ .

In the next section we elaborate on the LDM for charged clusters. In Section 3, we present and discuss the quantal and liquid drop results, and in Section 4 the main conclusions are drawn.

2. Energy of the Charged System

To evaluate the energy of a charged system, we use the Kohn–Sham equations in the LDA, with the Perdew–Wang parametrization [11] for the correlation energy. The quantal equations which were solved are explicitly written in Refs. [3, 4].

The LDM for a charged system deserves more attention, since it is not so well known. In this model, the energy of a neutral cluster is written as

a power series of the valence electron number $N_0^{1/3}$:

$$E_0 = a_v(r_s, z, r_c)N_0 + a_s(r_s, z, r_c)N_0^{2/3} + a_c(r_s, z, r_c)N_0^{1/3} + \dots, \quad (2.1)$$

where a_v is the average energy per electron for a bulk system of uniform density, a_s is the surface energy coefficient, and a_c is the curvature energy coefficient. This expression can be derived using density functional techniques by developing the density of the cluster around the density profile of the planar surface (Lang–Kohn calculation) [2]. This procedure, which goes under the name of “leptodermous expansion” since it applies to systems with thin skin, allows us to evaluate the surface and curvature energies [7]. Although Eq.

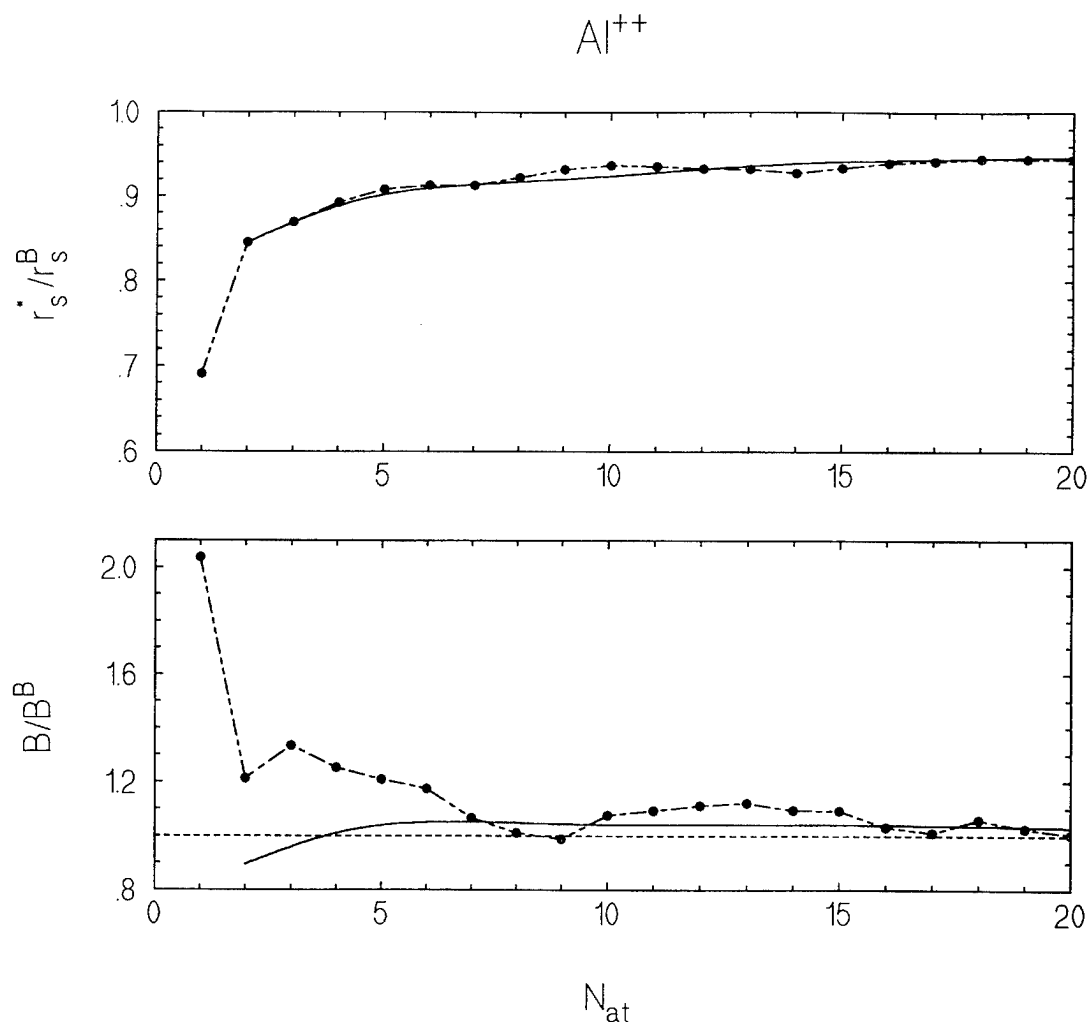


FIGURE 2. Same as Fig. 1, For Al^{2+} .

(2.1) is strictly valid for $N_0 \rightarrow \infty$, it provides a useful average of the shell-structure oscillations of the quantal result and may be accurate even in the atomic limit $N_0 = 1$ [3, 12].

The energy of a charged cluster may also be described by a continuous approximation. In Refs. [9, 10] the following liquid drop formula of a charged cluster with ν excessive electrons has been obtained in the jellium model:

$$E = E_0 - \nu \left(W + \frac{c}{R} \right) + \frac{\nu^2}{2(R + \delta)}, \quad (2.2)$$

where W is the work function, c is a size correction to the work function, and δ is the distance from the image plane to the jellium edge of the planar surface. In Eq. (2.2), $-(W + c/R)$ is the chemical potential of the neutral cluster; its contribution of order R^{-2} is currently unknown. If we

replace the jellium LDM coefficients by those of the SJM, the expression (2.2) is still valid for stabilized jellium, given the similarity of the two energy functionals. It has been used in Ref. [4, 13] without any self-expansion or compression effects. We stress that the LDM formula (2.2) is only justified when the charge ν is small in comparison with the total number of electrons $N = N_0 + \nu$.

The ionization energy and the electron affinity may be derived from Eq. (2.2):

$$I = E(\nu = -1) - E(\nu = 0) \\ = W + \left(\frac{1}{2} + c \right) \frac{1}{R + \delta}, \quad (2.3)$$

$$A = E(\nu = 0) - E(\nu = 1) \\ = W + \left(-\frac{1}{2} + c \right) \frac{1}{R + \delta}. \quad (2.4)$$

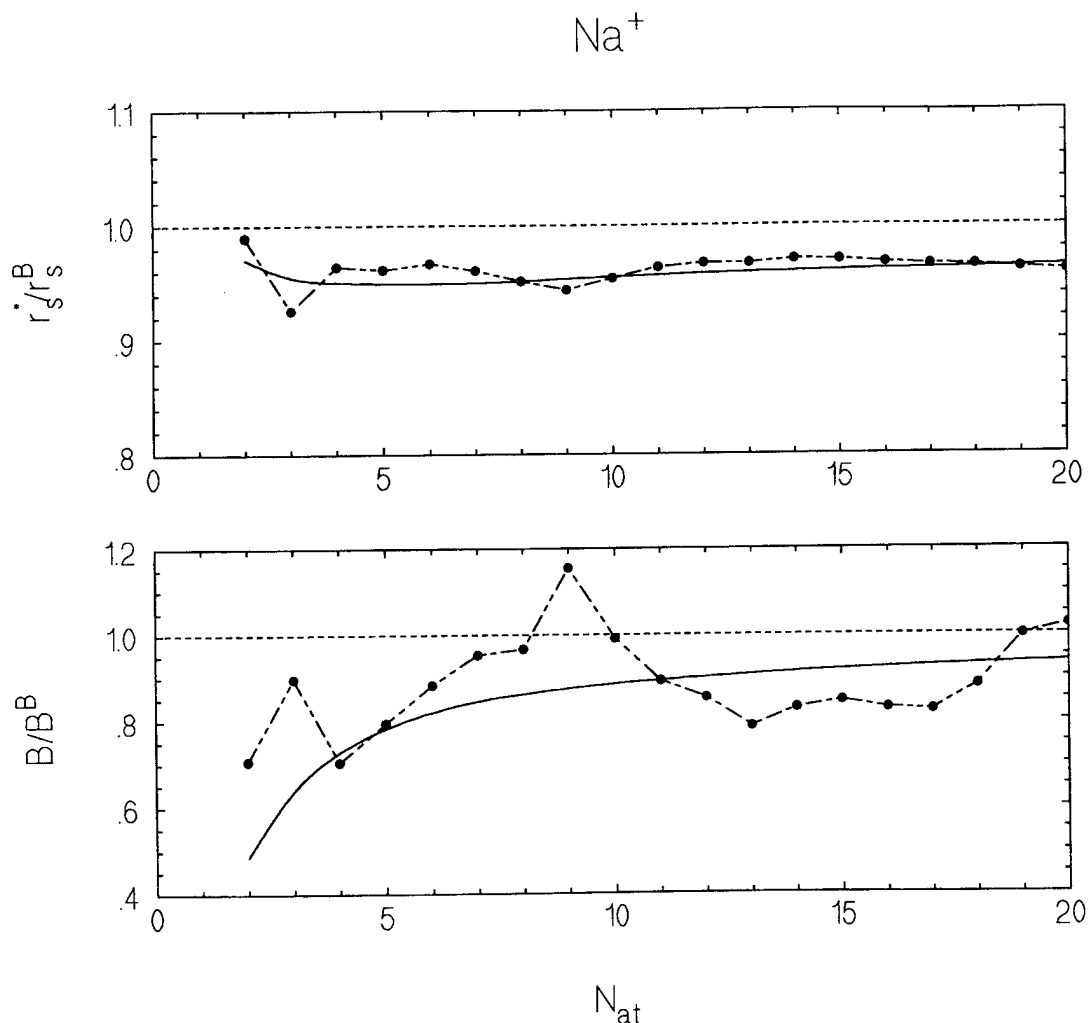


FIGURE 3. Same as Fig. 1, for Na^+ .

Therefore, once values of W and c are available, the SJM can predict ionizations and affinities for finite systems. The work function is given by the same surface calculation which yields a_s and a_c [2]. Lacking any first principles calculation of c , we have evaluated it by taking finite singly charged and neutral clusters and considering an extended Thomas-Fermi approximation (TFDW-4) for the kinetic energy functional of the self-consistent density. Then, fitting the ionization energy by the formula (2.3) yields $c = -0.1$ in the case of Al [4], close to the value known for jellium ($c = -0.07$) [14]. Since in the jellium model c is approximately independent of r_s , we assume that the same is true for the SJM. Finally, δ was taken from Ref. [15].

The ionization energy is always positive, but within the jellium-LDA approach the electron

affinity is negative for small clusters. That is also the case for stabilized jellium-LDA. It is interesting to investigate the number of particles for which the affinity turns out to be positive. From Eq. (2.4), the condition $A \geq 0$ is equivalent to:

$$N_0 \geq \left(\frac{\frac{1}{2} - c}{r_s W} - \frac{\delta}{r_2} \right)^3. \quad (2.5)$$

More generally, the affinity of order ν is defined by

$$A(\nu) = E(\nu - 1) - E(\nu). \quad (2.6)$$

This quantity is positive if

$$N_0 \geq \left(\frac{\nu - \frac{1}{2} - c}{r_s W} - \frac{\delta}{r_s} \right)^3. \quad (2.7)$$

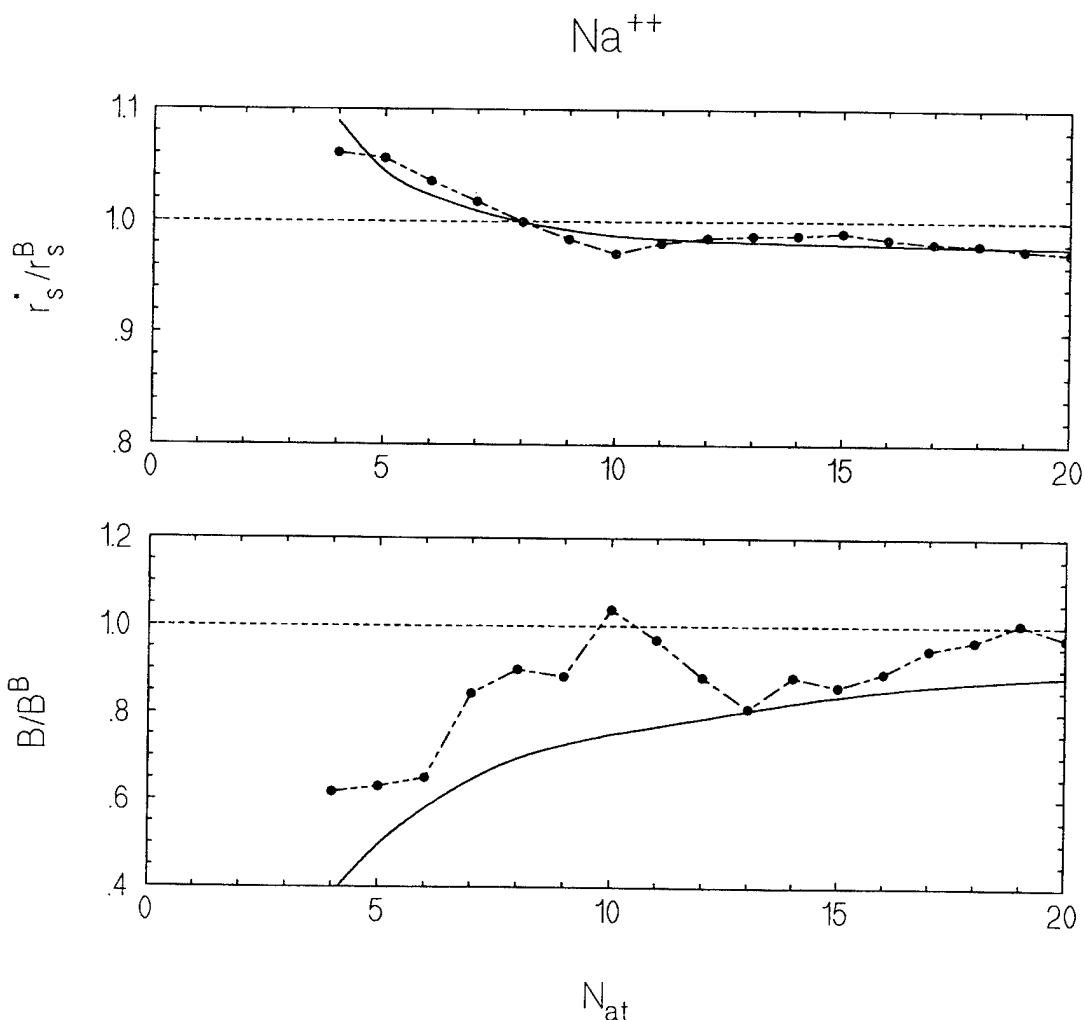


FIGURE 4. Same as Fig. 1, for Na^{2+} .

The results on the limits of stability for negative ions are displayed in Table I.

The solution of (1.4) with the energy given by (2.2) is found numerically, since the r_s dependence of the LDM coefficients a_s , a_c , and W is known from numerical planar surface calculations. The coefficients c and δ are assumed to remain constant when compression changes the density of each metal.

The LDM can be used to make simple estimates of the transition from expansion to contraction. We use the Taylor expansion of Ref. [5] around the bulk density parameter:

$$E = E(r_s^B) + (r_s - r_s^B)E' + \frac{1}{2}(r_s - r_s^B)^2 E'' + \dots \quad (2.8)$$

with $E' = \partial E / \partial r_s|_{r_s=r_s^B} = a'_s N_0^{2/3} + a'_c N_0^{1/3}$, and $E'' = \partial^2 E / \partial r_s^2|_{r_s=r_s^B}$. The equilibrium condition leads to

$$r_s^* - R_s^B \simeq -E'/E''. \quad (2.9)$$

The condition $r_s^* = r_s^B$ is then equivalent to $E' = 0$ or, considering only the surface and the Coulomb term (with $\delta = 0$):

$$a'_s N_0^{2/3} - \frac{\nu^2}{2(r_s^B)^2 N_0^{1/3}} = 0. \quad (2.10)$$

For $\nu = -2$, this happens at $N_0 = 3$ for aluminum, $N_0 = 9$ for sodium, and $N_0 = 11$ for cesium. (The values of the derivatives a'_s appear in Ref. [5].) Clearly, these guesses for the transition from expansion to contraction are only reasonable if the

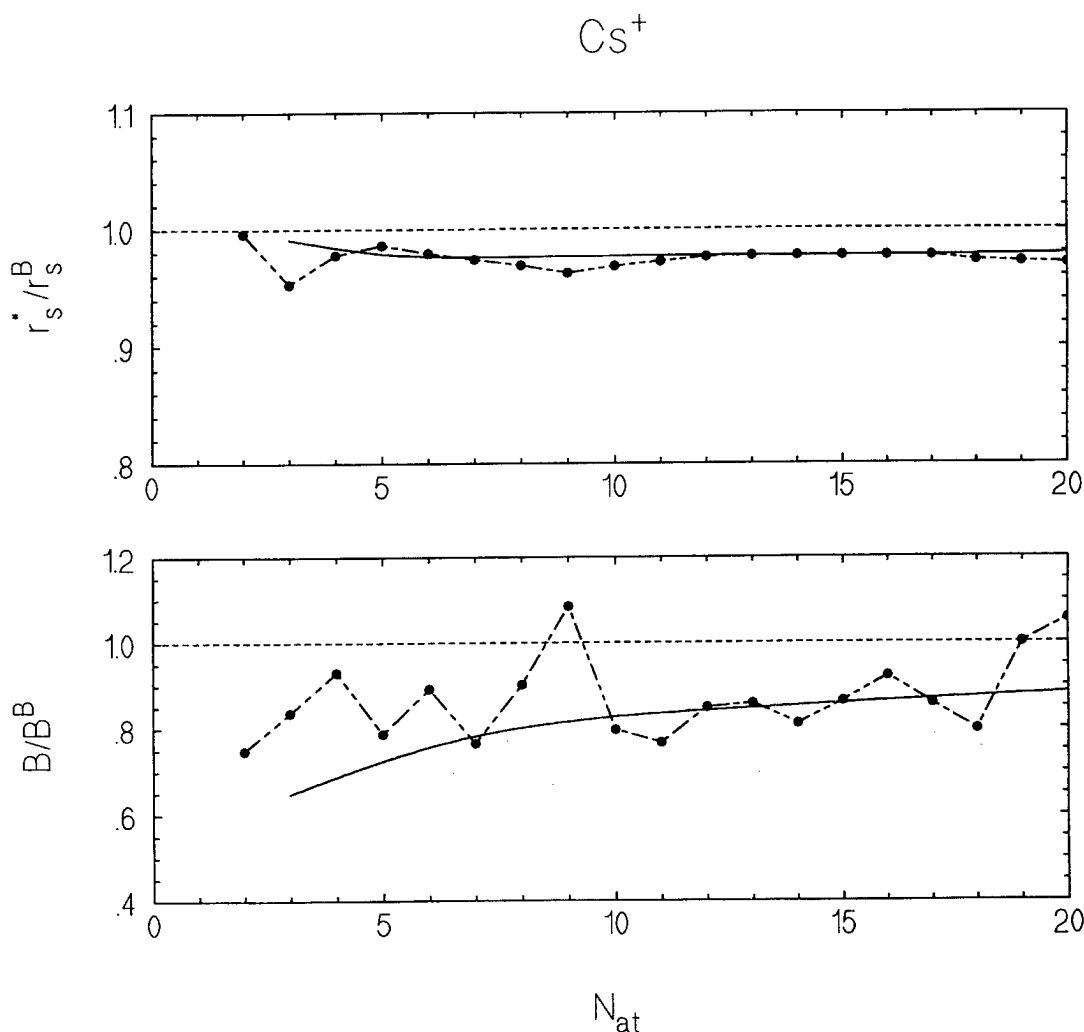


FIGURE 5. Same as Fig. 1, for Cs^+ .

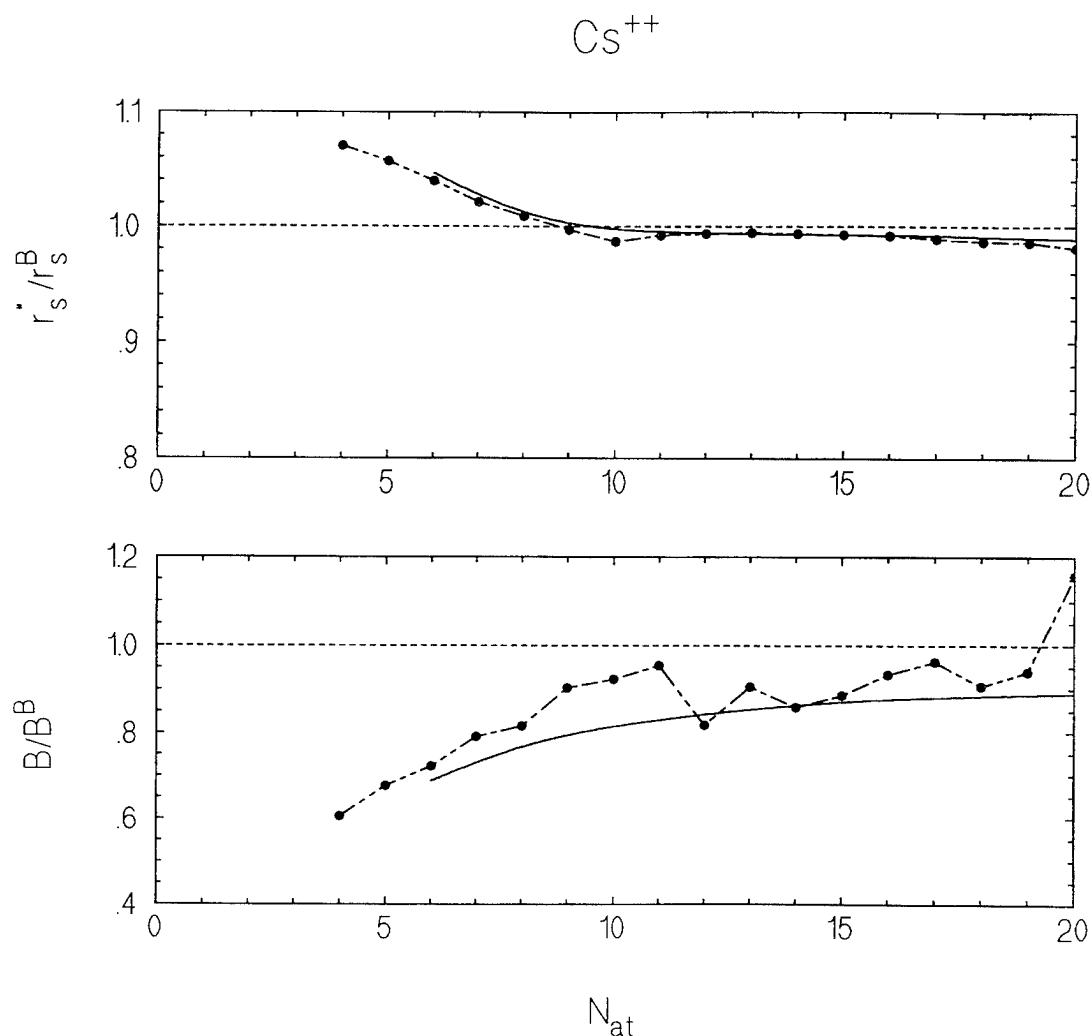
FIGURE 6. Same as Fig. 1, for Cs^{2+} .

TABLE I

The smallest integer value of N_0 for which the electron affinity of the $(N_0 + \nu - 1)$ valence electron cluster is positive, according to Eq. (2.7).^a

ν	Al ($r_s^B = 2.07$, $z = 3$)	Na ($r_s^B = 3.93$, $z = 1$)	Cs ($r_s^B = 5.62$, $z = 1$)
1	3	2	2
2	90	42	33
3	435	210	153
4	1216	554	423

^aThe smallest neutral cluster of stabilized jellium that can bind ν excess electrons has N_0 valence electrons. The results are similar to those of the jellium model [26].

truncation of the Taylor expansion (2.8) is a good approximation to the exact LDM result, and if the excluded terms in (2.10) may be neglected.

3. Results

In Refs. [5, 6] we have found for neutral systems with up to 20 atoms that:

1. Small clusters display self-compression $r_s^* \leq r_s^B$, i.e., the ionic density is higher in the cluster than in bulk.

2. Quantal shell effects produce local minima in r_s^* and local maxima in B for closed-shell clusters $N_0 = 2, 8$, etc.

Figures 1(a)–6(a) show the ratio of the equilibrium density parameter r_s^* to its bulk value r_s^B as a function of the number of atoms $N_{\text{at}} = N_0/z$, for Al^+ , Al^{2+} , Na^+ , Na^{2+} , Cs^+ , and Cs^{2+} , respectively. From these figures we see that Al^+ and Al^{2+} show self-compression for all sizes, although this compression is not so pronounced as in the neutral case. This is due to the high surface tension of Al. On the contrary, Na^{2+} and Cs^{2+} exhibit self-expansion for small clusters and self-compression for large clusters. The transition takes place at $N_{\text{at}} = 8$ and $N_{\text{at}} = 9$, respectively, using the LDM (and the Kohn–Sham approach gives practically the same transition). Na^+ and Cs^+ always show self-compression. The simple rule given by Eq. (2.11) makes a good estimate of the transition from dilatation to contraction, except for Al where the truncated Taylor expansion is not accurate [6]. In the asymptotic limit ($N_0 \rightarrow \infty$), a fixed net charge is negligible so that the asymptotic expression (Ref. [5]) for r_s in the neutral case still holds in the charged case. As in the neutral case, the LDM provides a good average of the quantal results, and quantal shell effects are evident in the curves r_s^*/r_s^B versus N_{at} .

The elastic stiffness was calculated numerically by making a least-squares fit of a fourth-order polynomial to the curve $E(N_0, r_s, z, r_c, \nu)$, around the minimum r_s^* , in the quantal as well as in the liquid drop cases. Figures 1(b)–6(b) show the ratio of the elastic stiffness to its bulk value as a function of the number of atoms, for Al^+ , Al^{2+} , Na^+ , Na^{2+} , Cs^+ , and Cs^{2+} , respectively. We conclude that in the LDM picture for Al^{2+} , bigger clusters are harder than the bulk and smaller clusters are softer. (The same was found for neutral clusters in Ref. [5], where the asymptotic $N \rightarrow \infty$ correction to the bulk modulus was positive for Al but negative for Na and Cs). The crossover occurs at $N_0 = 4$. On the contrary, the quantal calculations for Al always show a cluster stiffness higher than that of the bulk. These observations may have technological implications. Na and Cs clusters charged or neutral, are always softer than the bulk in the LDM picture. The quantal results show fluctuations, with some clusters harder than the bulk material.

The role of the charge is to decrease the elastic stiffness. Disagreement between the LDM and the quantal stiffnesses for very small charged clusters indicates that the LDM may be failing in those cases. For some very small clusters, we do not find solutions for the equilibrium radius. The disap-

pearance of such solutions is prefigured by a sudden drop in the elastic stiffness.

Ionization energies are affected by the expansion or compression. We can define two ionization energies: one "vertical," where the density parameter is frozen at the value of the neutral system, and another "relaxed," where both the neutral and the charged system are allowed to minimize their energies with respect to r_s . The first is more realistic, since in a real ionization process the ions do not have time enough to readjust their positions. Figure 7 shows the vertical ionization energy for Cs, in comparison with that calculated for the bulk density (without any compression or expansion). The stronger self-contraction that occurs for closed-shell clusters leads to a stronger binding of the least-bound electron and thus enhances the shell-structure fluctuations of the ionization energy.

4. Conclusions

We have examined the self-expansion and self-compression of singly and doubly positively charged clusters of stabilized jellium. We have found that, for a range of densities which cover Na and Cs, self-expansion occurs for smaller doubly charged clusters and self-compression for larger ones. However, for high densities, such as that of Al, self-compression prevails for the net charges considered here. If the charge increases further, self-expansion appears even for Al, and for very large charges the phenomenon of "blow up" (Coulomb explosion) arises via disappearance of a solution for the background equilibrium radius (see Figure 8).

Note that the recently proposed "ultimate jellium model" [16], unlike the stabilized or standard jellium models, does not admit solutions for any positively charged clusters.

Typically the charged liquid drop model yields a useful average of the quantal results. But it fails to give results for some very small charged clusters, where the quantal method still applies.

Finally, let us discuss the experimental and theoretical information available on the compression and expansion of charged clusters. Lattice compression or dilatation has been observed in many cases (see Ref. [17]), but the experimental data are contradictory. The observed clusters are bound to

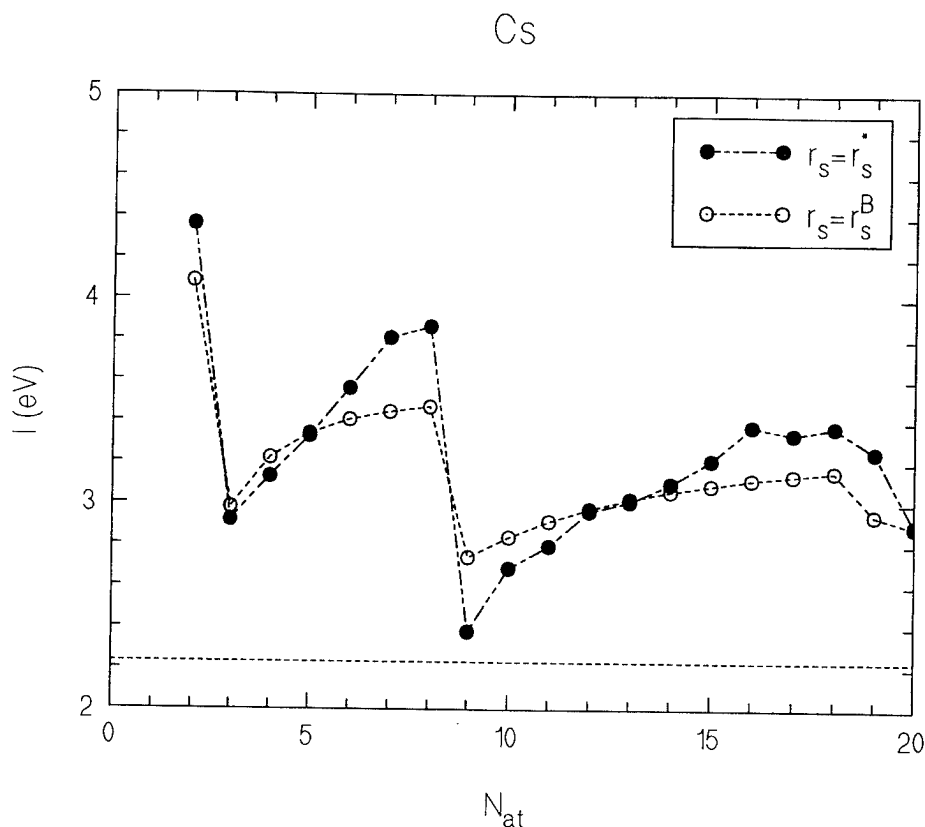


FIGURE 7. First ionization energy of Cs, in the SJM, where the neutral clusters have relaxed background density r_s^* and the charged clusters have the same density, in comparison with calculations where both neutral and charged clusters have the bulk background density r_s^B . The dashed horizontal line indicates the work function.

a surface, and the effect of the substrate is not well understood.

It is interesting to compare the self-compression of a neutral system predicted by the SJM with a similar compression given by atomistic calculations. The spherical averaged pseudopotential model (SAPS) [18] is a model which has an intermediate degree of sophistication between the SJM and full atomistic calculations. In Refs. [19, 20], the SAPS was used to predict an inhomogeneous contraction of a Cs cluster, in which the ions in the inner layers are more closely packed than those near the surface. The SAPS has been used recently to calculate the frequency of the "breathing" mode, where the ions oscillate while maintaining spherical symmetry [21]. In the SJM framework, we can infer the frequency of this mode from the bulk modulus via Eq. (21) of Ref. [21]. The result for Na ($\hbar\omega_0 = 23N^{-1/3}$ meV) does not differ very much from that obtained in the SAPS. (A good fit [21] is given by $\hbar\omega_0 = a + bN^{-1/3}$, with $a = 0.6$ meV and $b = 30$ meV). This suggests that the SAPS is similar to the SJM. The SAPS may also be used to

evaluate contraction or dilatation of charged systems and is probably somewhat more realistic than any continuous background model.

In Ref. [22], some of the present authors have evaluated the contraction of six-atom clusters of different metals (Li, Na, Mg, and Al), using a linear combination of atomic orbitals local density molecular code but considering only the octahedral shape. The results were only qualitatively comparable with those of the SJM.

Some theoretical calculations on small neutral and charged aluminum clusters with unrestricted geometry are available. In Ref. [23], density functional calculations (with a local spin density approximation for the exchange-correlation energy) and finite-temperature molecular dynamics are applied to neutral and singly charged aluminum clusters, with the number of atoms ranging up to 10. In Ref. [24], an all-electron study on neutral, singly, and doubly charged aluminum clusters (for 2–6 atoms) is carried out within the Kohn–Sham formalism, including gradient corrections to the exchange and correlation energy. In Ref. [25], the

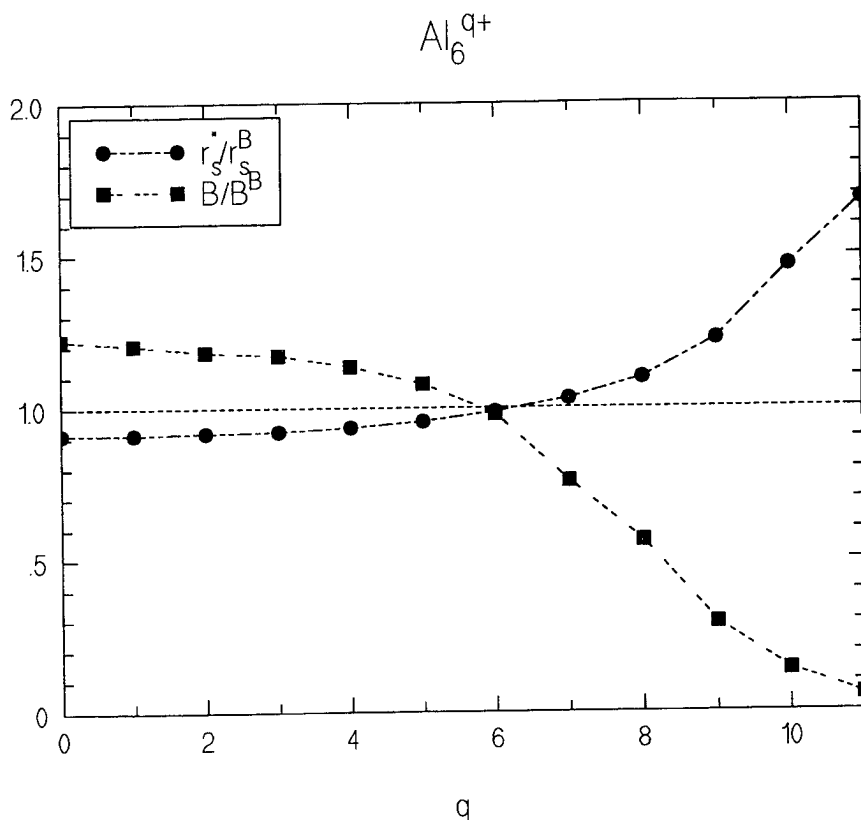


FIGURE 8. Elastic stiffness B and equilibrium density parameter r_s^* calculated by the Kohn-Sham method for the spherical SJM of Al_6^{q+} . There is no self-consistent solution for $q \geq 12$.

structure and properties of singly positively and negatively charged (1–5 atoms) aluminum clusters are investigated by using the linear combination of Gaussian type orbitals method, employing local and nonlocal spin density approximations and a model core potential that allows the explicit treatment of $3s^2 3p^1$ valence electrons. In all these studies the average bond length tends to be smaller in smaller clusters, in agreement with our own results. But, again, the agreement is more qualitative than quantitative. Charged clusters show a smaller bond-length reduction than neutral ones.

We plan to study the SAPS for several charged metallic clusters and to carry out more exact calculations for the charged six-atom clusters with restricted and unrestricted geometries.

ACKNOWLEDGMENTS

We acknowledge useful discussions with A. Mañanes and L. C. Balbás. The work of two of the authors (J. P. P. and C. F.) was supported by

NATO Collaborative Research Grant No. 910623. This work has been partially supported by the Praxis XXI Program (Project 2/2.1/FIS/26/94), the Commission of the European Communities (Contract ERB-SC1-CT92-0770), the Junta Nacional de Investigação Científica e Tecnológica (Project PBIC/C/FIS/2216/95), and the U.S. National Science Foundation (Grant No. DMR95-21353).

References

1. J. P. Perdew, H. Q. Tran, and E. D. Smith, *Phys. Rev. B* **42**, 11627 (1990).
2. C. Fiolhais and J. P. Perdew, *Phys. Rev. B* **45**, 6207 (1992).
3. M. Bralczevska, C. Fiolhais, and J. P. Perdew, *Int. J. Quantum Chem. S* **27**, 249 (1993).
4. A. Vieira, M. Bralczevska, and C. Fiolhais, *Int. J. Quantum Chem.* **56**, 239 (1995).
5. J. P. Perdew, M. Bralczevska, and C. Fiolhais, *Solid State Commun.* **88**, 795 (1993).
6. M. Bralczevska, C. Fiolhais, A. Vieira, and J. P. Perdew, in *Many-Body Physics*, C. Fiolhais et al., Eds. (World Scientific, Singapore, 1994), p. 455.

7. M. Brack, C. Guet, and H.-B. Håkansson, *Phys. Rep.* **123**, 275 (1985).
8. W. Kohn and L. J. Sham, *Phys. Rev.* **140**, A1133 (1965).
9. J. P. Perdew, in *Condensed Matter Theories*, J. Keller, Ed. (Plenum, New York, 1989), vol. 4.
10. M. Seidl and M. Brack, *Annals of Physics (N.Y.)* **245**, 275 (1996); M. Seidl and J. P. Perdew, *Phys. Rev. B* **50**, 5744 (1994).
11. J. P. Perdew and Y. Wang, *Phys. Rev. B* **45**, 13244 (1992).
12. J. P. Perdew, P. Ziesche, and C. Fiolhais, *Phys. Rev. B* **47**, 16460 (1993); P. Ziesche, J. P. Perdew, and C. Fiolhais, *Phys. Rev. B* **49**, 7916 (1994). These articles describe voids and monovacancies within the stabilized jellium and liquid drop models.
13. A. Vieira and C. Fiolhais, *Z. Phys. D*, to appear.
14. E. Engel and J. P. Perdew, *Phys. Rev. B* **43**, 1331 (1991).
15. A. Kiejna, *Phys. Rev. B* **47**, 7361 (1993).
16. M. Koskinen, P. O. Lipas, and M. Manninen, *Z. Phys. D* **35**, 285 (1995).
17. E. L. Nagaev, *Sov. Phys. Usp.* **35**, 747 (1992).
18. M. P. Iñiguez, M. J. López, J. A. Alonso, and J. M. Soler, *Z. Phys. D* **13**, 171 (1989).
19. A. Mañanes, J. A. Alonso, U. Lammers, and G. Borstel, *Phys. Rev. B* **44**, 7273 (1991).
20. A. Mañanes, private communication.
21. J. G. Aguilar, A. Mañanes, F. Duque, M. J. López, M. P. Iñiguez, and J. A. Alonso, *Int. J. Quantum Chem.*, to appear.
22. F. Nogueira, C. Fiolhais, J. He, J. P. Perdew, and A. Rubio, *J. Phys.: Condens. Matter* **8**, 287 (1996).
23. R. O. Jones, *Phys. Rev. Lett.* **67**, 224 (1991).
24. A. Martínez and A. Vela, *Phys. Rev. B* **49**, 17464 (1994).
25. P. Calaminici, N. Russo, and M. Toscano, *Z. Phys. D* **33**, 281 (1995).
26. J. P. Perdew, *Phys. Rev. B* **37**, 6175 (1988).

Free Energy in Relation to Order Parameter in Magnets and Pyroelectrics

N. H. MARCH

University of Oxford, Oxford OX1 3QR, United Kingdom

A. M. L. NIP AND J. A. TUSZYŃSKI*

Department of Physics, University of Alberta, Edmonton, Alberta, Canada T6G 2J1

Received February 26, 1996; revised manuscript received July 18, 1996; accepted July 18, 1996

ABSTRACT

Theoretical models will be presented in which the internal energy of (a) a ferromagnet and (b) a pyroelectric material is expressed in terms of magnetization and electric polarization, respectively. For the ferromagnet, simple models of elementary excitations (e.g., spin wave theory in an insulator, to which Stoner excitations must be added in a metal) lead to formulas for the internal energy at low temperature as power laws in the change of magnetization from its saturation value. An unconventional use of two order parameters, the sublattice magnetization plus the metallic discontinuity in momentum distribution at the Fermi surface, allows the phase transition between metallic and insulating states of antiferromagnets to be treated at $T = 0$, the three-dimensional transition-metal dichalcogenides being an example here. The treatment of the internal energy of the ferromagnet is then extended to include the entropy also, using specifically the Ising model in nonzero external magnetic field. Its relevance to the Landau theory of phase transitions will be emphasized. Some comments will finally be made about the analogue for pyroelectrics. © 1996 John Wiley & Sons, Inc.

Introduction

The concept of the order parameter is, of course, central to the theory of phase transitions. In the present work, we shall be concerned

with magnets—both ferro and antiferro—where the magnetization is the crucial quantity, and with pyroelectrics, where the polarization, or dipole moment per unit volume, plays a central role. A little more specifically, the order parameter of the transition from a paramagnetic to a ferromagnetic state with long-range magnetic order is the magnetization M . This transition is second-order; e.g., the susceptibility and specific heat, second-order

*To whom correspondence should be addressed.

derivatives of the free energy, diverge at the transition.

Though we shall deal at some length with ferromagnets, we shall also make reference to the antiferromagnetic case. Thus we should note that an antiferromagnet exhibits phase transitions at nonzero field. In this case a series of ordered phases are characterized by different order parameters related to components of the sublattice magnetization [1].

The final case treated in the present study is that of pyroelectric materials. The phenomenon of pyroelectricity, which is observable through the temperature dependence of the electric dipole moment, is important technologically for infrared detection. It will be treated here along with magnets, though the models employed below are more primitive than in the case of magnetic systems.

The outline of the study is then as follows. Immediately below the exact Onsager solution of the two-dimensional Ising model [2,3] will be shown to yield a unique plot of the internal energy of such a ferromagnetic description in terms of the order parameter, the magnetization. Then by discussing low-lying elementary excitations in (a) insulating ferromagnets using spin wave theory [4] and (b) metallic ferromagnets in terms of Stoner excitations [5], the form of the internal energy in terms of the change from the saturation magnetization as the temperature is raised from $T = 0$ will be set out. Following this, a brief discussion will be given in the main text of the treatment of the metal-insulator transition, now at $T = 0$, between two antiferromagnetic phases, the detailed phenomenology in terms of sublattice magnetization, the conventional order parameter, plus a second, unconventional choice at $T = 0$, being given in the Appendix.

To discuss the free energy, the focus on the internal energy must be expanded to embrace the entropy. In doing this, attention will be restricted to the ferromagnetic case. A generalization of the study of Tuszyński and Wierzbicki [6] is effected in this section by employing now the one-dimensional Ising model in a nonzero external magnetic field. It is shown, when entropy is related again to the order parameter, that the results thereby obtained reduce to those of Ref. [6] when the interaction between spins is finally "switched off."

A brief treatment of the internal energy in pyroelectric materials is then given by analogy with the magnetic case, and some predictions as to low-temperature behavior follow.

Internal Energy of Ferromagnet in Terms of Magnetization

We turn first to discuss the internal energy of a ferromagnet in relation to the order parameter, the magnetization M . We start from the model of the two-dimensional Ising Hamiltonian, solved in exact form by Onsager [2]. The magnetization is given in convenient form by Callaway [3]. As Grout and March [7] emphasized, one can thereby express the internal energy, known also in closed form as a function of T in this simple model, by solving two equations simultaneously, in terms of the magnetization $M(T)$. The result is shown in Figure 1.

What is of interest when we turn to realistic magnetic materials below, both insulating and metallic ferromagnets, is the deviation from the saturation magnetization $M(T = 0) \equiv M_0$: say

$$\Delta M = M_0 - M(T). \quad (1)$$

Then, it can be seen from Figure 1 that, in the two-dimensional Ising model:

$$E_0 - E(T) = \text{constant } \Delta M \text{ (at small } \Delta M \text{ or low } T). \quad (2)$$

It can be shown, in fact [7] that for all Ising models, Eq. (2) is true at sufficiently low temperature.

LOW-LYING EXCITATIONS IN THREE-DIMENSIONAL MAGNETS

In an insulating ferromagnet in three dimensions, one can express the predictions of spin wave

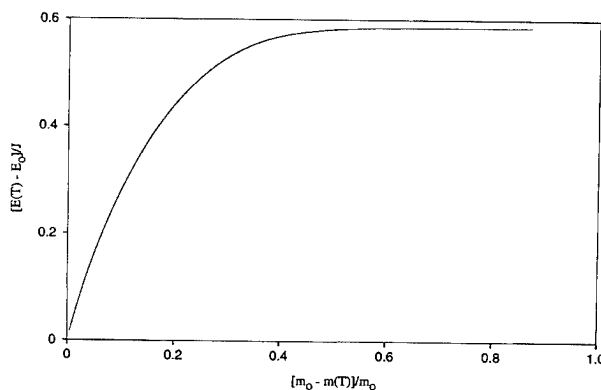


FIGURE 1. $[E(T) - E_0]/J$ vs. $[m(0) - m(T)]/m(0)$ in two-dimensional Ising model (after Grout and March [7]).

theory very simply for the low-lying excitations: (i) the magnon dispersion relation $\omega_q \propto q^2$, translates readily into the form of internal energy

$$E(T) - E_0 \propto T^{5/2} \text{ (at low } T), \quad (3)$$

whereas (ii) the deviation of magnetization from the saturation value is given by

$$\Delta M \propto T^{3/2}, \quad (4)$$

a law first derived long ago by Bloch. Inverting Eq. (4) to obtain $T \propto (\Delta M)^{2/3}$, and substitution in Eq. (3) yields the desired result for an insulating ferromagnet at low temperature:

$$E(T) - E_0 \propto (\Delta M)^{5/3} \text{ (for an insulator at low } T). \quad (5)$$

Turning to metallic ferromagnets, such as Ni, one has single-particle or Stoner excitations, and these, it turns out, dominate aspects of the low-temperature thermodynamics in the metallic materials. In particular, one has instead of Eq. (3)

$$E(T) - E_0 \propto T^2 \text{ (for a metallic ferromagnet at low } T). \quad (6)$$

However, the magnetization is still dominated by the spin waves. Substituting therefore, according to Eq. (4), $T \propto (\Delta M)^{2/3}$ but now into eq. (6), one obtains immediately for the metallic magnet:

$$E(T) - E_0 \propto (\Delta M)^{4/3}. \quad (7)$$

These results are evidently rather different from the Ising model prediction (2) and are the correct results for the low-temperature behavior of three-dimensional magnets; insulating according to Eq. (5) and metallic having behavior (7). In other words, the low-temperature expansion of $E_0 - E(T)$ in powers of ΔM is now nonanalytic around $T = 0$ at leading order.

Metal-Insulator Transition at $T = 0$ Between Two Antiferromagnetic Phases

March et al. [8] proposed to build a phenomenological theory of metal-insulator transitions at $T = 0$ using the discontinuity, q say, in the electronic momentum distribution at the Fermi surface of the metallic phase as the order parameter. In

this way they were able usefully to treat (a) the transition between electron liquid and Wigner electron crystal in the jellium model and (b) the transition induced in a metal described by the Hubbard Hamiltonian to an insulating phase as the energy it costs to put two electrons on the same site with antiparallel spins is increased from, say U , to some critical value U_c .

Below, we add this order parameter to the conventional one—the sublattice magnetization—to treat the metal-insulator transition between two antiferromagnetic phases at $T = 0$: see also Ferraz et al. [9]. This treatment, summarized below, was designed with the three-dimensional transition-metal chalcogenides in mind. A schematic phase diagram for the specific case of $\text{NiS}_{2-x}\text{Se}_x$ is drawn, for example, by Czjzek et al. [10].

To model such a phase diagram, it is quite clear that one must introduce strong electron-electron correlations in narrow energy bands, which is just the situation for which the Hubbard Hamiltonian was invented. Writing this for a half-filled doubly degenerate band one has, in a customary notation:

$$\begin{aligned} H = & \sum_{f,g,\alpha,\sigma} t_{fg} (a_{f\alpha\sigma}^\dagger a_{g\alpha\sigma} + a_{g\alpha\sigma}^\dagger a_{f\alpha\sigma}) \\ & + U \sum_g \left(\sum_\alpha n_{g\alpha\uparrow} \right) \left(\sum_\alpha n_{g\alpha\downarrow} \right) \\ & + (U - J) \sum_{g,\sigma} n_{g1\sigma} n_{g2\sigma}. \end{aligned} \quad (8)$$

In Eq. (8), J is the interatomic exchange integral, and the index $\alpha = 1$ and 2 denotes the two orbitals. One then associates the metal-insulator transition within this framework with a decrease in the ratio of the band width, proportional to t_{fg} , to the correlation energy U , and J , through some critical value, as discussed by Mott [11]. In the three-dimensional transition-metal chalcogenides cited above, namely $\text{NiS}_{2-x}\text{Se}_x$, the band width will clearly depend on x , since the transfer of an electron between Ni sites will occur via an anion.

The phenomenological model employed here generalizes the work of March et al. [8] to antiferromagnetic phases as follows. While the fermiology of an antiferromagnetic metal is a somewhat complex problem, it is assumed in the phenomenology that some, average, discontinuity in the momentum distribution, again defined as q , can be used as one order parameter in the antiferromagnetic metal-insulator transition. The details are set out in the Appendix, and in particular in

Eq. (A1) the internal energy $E(q, M)$ is expanded, following Landau, in the two order parameters, q already defined above, and the conventional one, the sublattice magnetization M .

As set out in the Appendix, minimization of the internal energy $E(q, M)$ leads to the simple prediction that the difference between the sublattice magnetization in the metallic (m) and the insulating (i) phases is proportional to the discontinuity q :

$$M_m - M_i \propto q. \quad (9)$$

This Eq. (9) would seem to be of interest in connection with magnetic properties of two antiferromagnetic phases around the metal-insulator transition and seems worthy of attempts to test it experimentally. This would mean low-temperature measurements of sublattice magnetization in two antiferromagnetic phases and also positron annihilation, or Compton profile experiments on the metallic phase near the transition.

So far, the discussion has focused entirely on internal energy E . To complete the thermodynamic description, one must also know the entropy. The results of our very recent investigation, via again the Ising model, are the focus of the ensuing discussion. Then, the combined considerations, leading to the free energy will be related to the Landau theory.

Expressions for Entropy

In earlier work [6], the entropy S of an assembly of noninteracting spins of arbitrary magnitude J as a function $S(m)$ of the magnetization m induced by an applied external magnetic field H has been derived. This entropy is given implicitly by the two coupled equations below:

$$\frac{S}{Nk_B} = \ln \left\{ \frac{\sinh[(2J+1)g\mu_B\nu/2]}{\sinh(g\mu_B\nu/2)} \right\} + m\nu \quad (10)$$

and

$$-2m = g\mu_B \left\{ (2J+1) \coth \left[\frac{(2J+1)}{2} g\mu_B\nu \right] - \coth \left(\frac{g\mu_B\nu}{2} \right) \right\}, \quad (11)$$

where m denotes mean magnetization per particle: $m = M/N$ and ν is a Lagrange multiplier. For $J = \frac{1}{2}$, this reduces to the well-known expression [12]:

$$\frac{S_{1/2}}{Nk_B} = \ln(2) - \frac{1}{2} \ln(1 - \sigma^2) - \sigma \tanh^{-1}(\sigma), \quad (12)$$

where σ is the reduced magnetization defined by $\sigma = M/(g\mu_B N)$. Equation (12) is plotted in Figure 2. Here, our main aim is to generalize this result to apply to interacting spins, and thereby to make contact with the approximate theory of Landau [13].

To proceed, we start out from well-established results [3, 14] for (i) equilibrium magnetization as a function of temperature at $H = 0$ and (ii) the Helmholtz free energy $F = E - TS$ for the two-dimensional Ising model in zero field. The magnetization m can be written in the explicit form: [14] for $T < T_c$

$$m = \frac{(1 + e^{-4\beta\epsilon})^{1/4} (1 - 6e^{-4\beta\epsilon} + e^{-8\beta\epsilon})^{1/8}}{\sqrt{1 - e^{-4\beta\epsilon}}}. \quad (13)$$

Here, $\beta = 1/(k_B T)$ while ϵ measures the interaction strength and is related to the critical temperature T_c by $k_B T_c = 2.269\epsilon$. The entropy S per site can be obtained as a function of $\beta\epsilon$ also through $TS = E - F$, where the Helmholtz free energy F per site is given by [14]:

$$\beta F = \ln[2 \cosh(2\beta\epsilon)] - \frac{1}{2\pi} \int_0^\pi d\phi \ln \left[\frac{1}{2} \left(1 + \sqrt{1 - \delta^2 \sin^2 \phi} \right) \right], \quad (14)$$

where $\delta = 2 \sinh(2\beta\epsilon) / \cosh^2(2\beta\epsilon)$. The internal energy per site [7] takes the form

$$\beta E = -\beta\epsilon \coth(2\beta\epsilon) \left\{ 1 + \frac{2}{\pi} [2 \tanh^2(\beta\epsilon) - 1] \times \int_0^{\pi/2} \frac{d\phi}{\sqrt{1 - \delta^2 \sin^2 \phi}} \right\}. \quad (15)$$

Using these results [Eqs. (13)–(15)], the entropy S is plotted for this model as a unique function of the equilibrium magnetization m in Figure 3. This complements the plot of $E(m)$ given in Ref. [7].

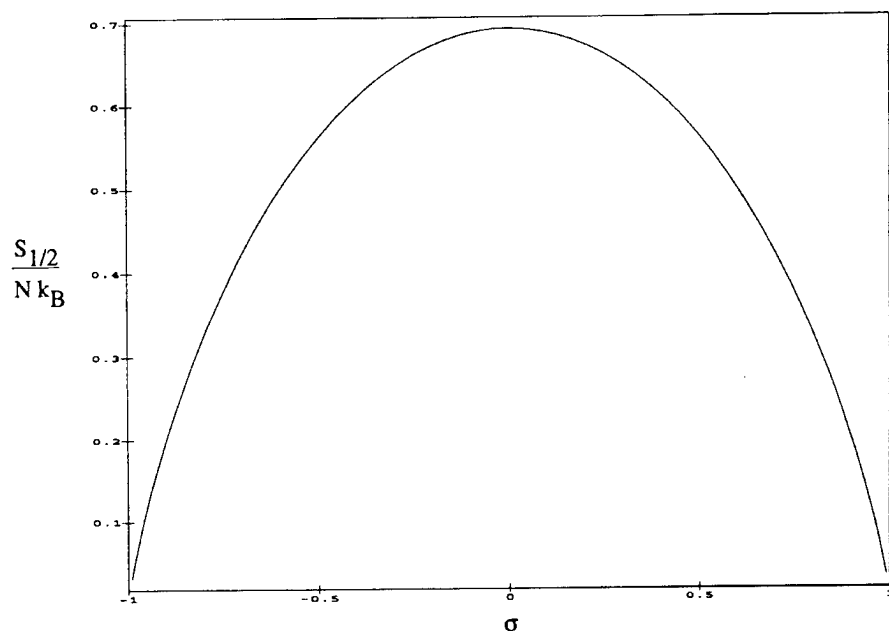


FIGURE 2. Entropy $S_{1/2} N k_B$ (for $J = \frac{1}{2}$) of Eq. (12) as a function of the reduced magnetization σ [6, 12] for an ensemble of noninteracting spins.

Naturally since $m = 0$ for $T > T_c$, such plots apply only for $T \leq T_c$. When we consider $S(m)$ in Figure 3 in relation to the noninteracting results of Ref. [6] and Figure 2, the maximum entropy per site $S_{\text{nonint}}/k_B = \ln(2)$, is, as expected, substantially re-

duced by the presence of interactions, measured by the energy ϵ in Eqs. (13)–(15).

To make closer contact with the work of Ref. [6], we turn next to consider the one-dimensional Ising model in the nonzero external field H . The magne-

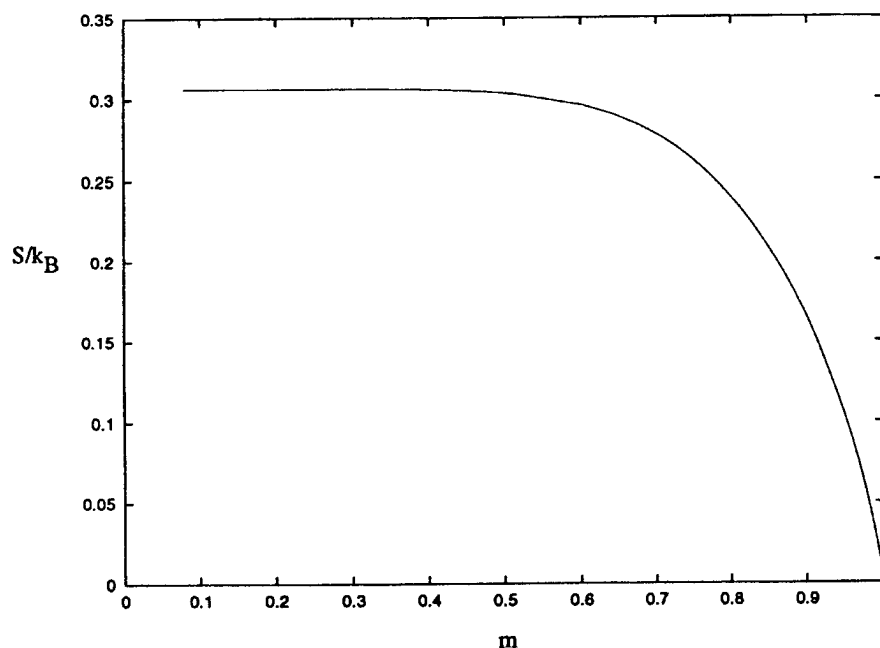


FIGURE 3. Entropy per Boltzmann constant as a function of the equilibrium magnetization m for the two-dimensional Ising model.

tization m can now be written in terms of $\beta\epsilon$ and $\beta H \equiv h$ as [14]

$$m = \frac{\sinh(h)}{\sqrt{\cosh^2(h) - 2e^{-2\beta\epsilon} \sinh(2\beta\epsilon)}}. \quad (16)$$

For this one-dimensional model, the Gibbs energy G per site is given in the simplest form by:

$$\beta G(\beta\epsilon, h) = -\beta\epsilon - \ln \left[\cosh(h) + \frac{\sinh(h)}{m} \right]. \quad (17)$$

Using the thermodynamic relation $S = -(\partial G / \partial T)_H$, one can find S in terms of the equilibrium magnetization m and $\beta\epsilon$. A plot of S versus these two variables (h and $\beta\epsilon$) is shown in Figure 4.

To summarize this section, we have established

the way the entropy of an interacting spin system can be expressed in terms of the equilibrium magnetization. This has been done for (i) the two-dimensional Ising model in zero field and (ii) the one-dimensional Ising model in an applied field. Particularly through example (ii), contact can be made with the result of Ref. [6] for noninteracting spins. Note that the related computer simulation results of Stump [15] for the two-dimensional Ising model in an external field, in contrast to our approach, were concerned with the entropy $S \equiv S(E, m)$, as a function of internal energy and magnetization.

Relation to Landau Theory

Landau theory [13] can be taken to start out from an approximate form of free energy as a

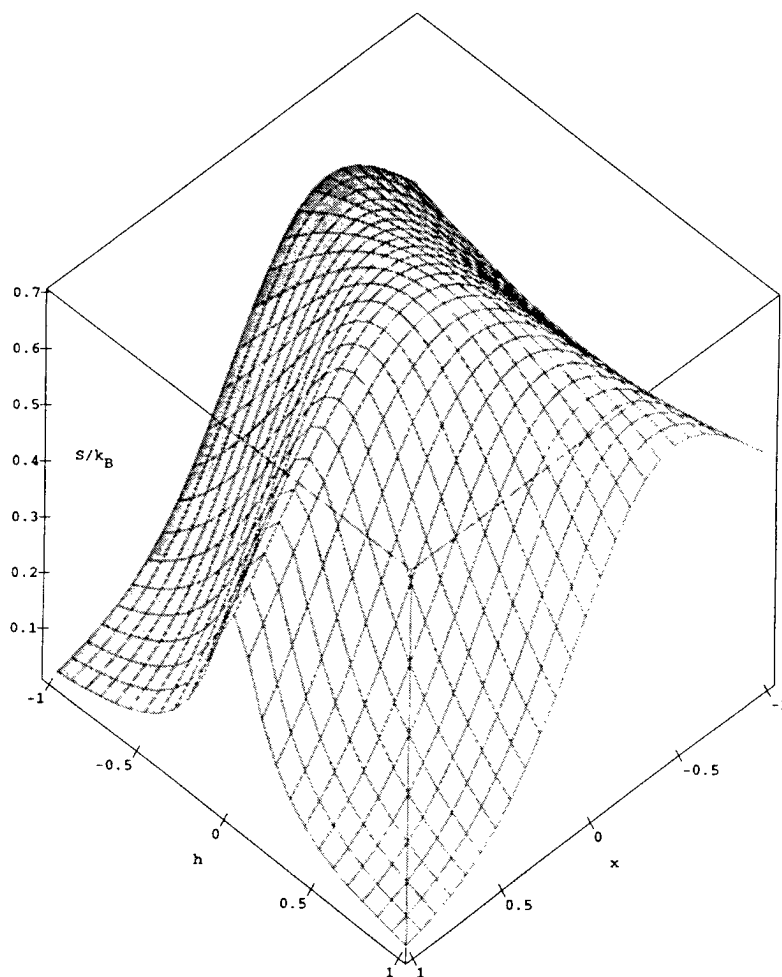


FIGURE 4. A three-dimensional surface plot of the entropy per Boltzmann constant as a function of $x \equiv \beta\epsilon$ and $h \equiv \beta H$ for the one-dimensional Ising model in the presence of a magnetic field.

function of the magnetization m and the temperature T , namely

$$F(m, T) = E(m, T) - TS(m, T). \quad (18)$$

Assuming that Eq. (18) is sufficiently general to apply away from equilibrium, one now performs the minimization of F with respect to m at constant T to find

$$\left. \frac{\partial F}{\partial m} \right|_T = 0 = \left. \frac{\partial E}{\partial m} \right|_T - T \left. \frac{\partial S}{\partial m} \right|_T. \quad (19)$$

To establish contact between this Eq. (19), valid on the minimum of the free energy, and the results presented earlier, we have taken the (equilibrium) relations between S and m and E and m in the two-dimensional Ising model in zero magnetic field and have plotted the two derivatives $(\partial E/\partial m)_T$ and $(\partial TS/\partial m)_T$ in Figure 5 against magnetization m . What is remarkable to us is that, over an extensive range of magnetization, coming away from the critical point, Eq. (19) is well satisfied. However, as one nears the region where the magnetization is approaching saturation, some inadequacies in using our results for large values of magnetization are being exposed.

In this context, we note the results for (three-dimensional) insulating and metallic ferromagnets near the saturation value of the magnetization. Power laws ($n/3$, with n integer) emerge for the internal energy ΔE in the two cases in terms of the deviation from the saturation magnetization $\Delta m = m(0) - m(T)$, by consideration of the low-lying excitations in the two types of ferromagnet. Evidently, near $T = 0$, Δm is a satisfactory order parameter though the internal energy is non-analytic in Δm .

In contrast, the Landau theory concerns itself with an expansion around the critical temperature T_c , where the magnetization m (the order parameter in the examples treated in the present work) is itself small. Clearly, to extend the Landau theory, one must, at the very least, interpolate successfully between the Landau limit and the nonanalytic behavior in Eqs. (5) and (7).

Analogous Treatment of Pyroelectric Materials

Especially as the theory and experiment are much less extensively studied, especially at low temperatures, it is appropriate to follow the above

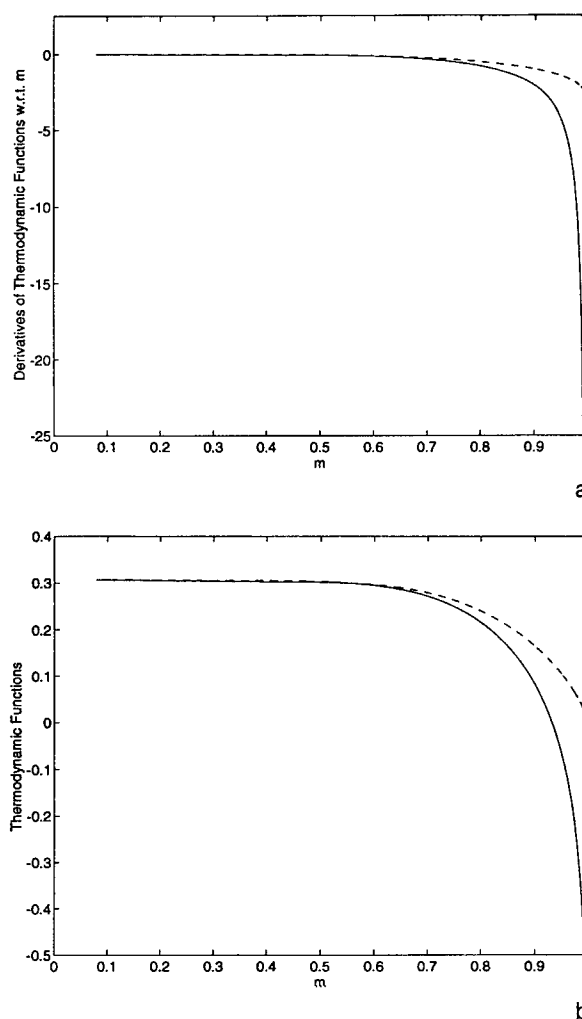


FIGURE 5. (a) Derivatives of βE (solid line) and S/k_B (dashed line) with respect to m at constant temperature T as functions of m . (b) A comparison of the profiles between the βE (solid) and the S/k_B (dashed) curves as functions of m is made by adding a positive constant (0.93) to the βE curve.

discussion of magnets with some comments on the analogue for pyroelectrics [16, 17].

Very briefly, changes in the electric polarization of solids can be brought about by various means. These embrace the application of a strain (piezoelectricity). It is pyroelectrics we focus on in this section. It is relevant to note here that ferroelectrics constitute a technologically important class of materials, in which the polarization can be switched by application of an electric field—see, for example, the book by Lines and Glass [16] and the review by Resta [17]. The work of King-Smith and Vanderbilt [18] should also be mentioned in the above context.

Below, the low-temperature behavior of the pyroelectric coefficient is the focus. We stress that in noncentrosymmetric crystals, the measurable quantity is the temperature dependence of the electric dipole moment: not the polarization $p(T)$ itself. Early important theoretical work was that of Born [19].

Let us proceed first by analogy with ferromagnets and write the deviations of internal energy E and polarization p from their zero temperature values as

$$\Delta E = c_t(\Delta p)^t \quad \text{where } \Delta p \propto T^s. \quad (20)$$

To recover from these low-temperature forms, with exponents t and s to be determined, the Debye T^3 law for the specific heat associated with acoustic phonon excitations we require that $\Delta E \propto T^4$ and hence

$$ts = 4. \quad (21)$$

Elsewhere, models have been considered to determine the low-temperature exponents t and s , respectively. We mention here the work of Ohmura et al. [20], where the starting point is the well-known Dick-Overhauser shell model. These workers argue that due to the deformation of the electronic charge clouds as the ions vibrate, the Dick-Overhauser exchange charge has a quadratic temperature dependence in the low-temperature limit. This leads to an (observable) pyroelectric coefficient (essentially $d\Delta p/dt$) proportional to T , and hence $s = 2$ in Eq. (20). Then from Eq. (21), $t = 2$, which would be what one would assert in a molecular field treatment. This result, compatible as noted above with a shell model, would be changed in a (less realistic) rigid ion model, which leads to $\Delta p \propto T^4$ and hence $t = 1$ in Eqs. (20) and (21). This is hence to be compared with the Ising model result discussed above for magnets where $\Delta E \propto \Delta m$ at low temperatures: a result differing from the realistic low-temperature behavior in Eqs. (5) and (7) for insulating and itinerant electron magnets, respectively.

However, we must stress that experiment has not yet confirmed the shell-model prediction of a linear temperature dependence of the pyroelectric coefficient at low temperature, though the simple model of Ohmura et al. predicts a value of $2 \times 10^{-7} \mu\text{cm}^{-2} \text{K}^{-1}$ at 5 K, which agrees reasonably with that measured by Lines [21] for LiTaO_3 . It is relevant in the context above to note that Grout et al. [22] give upper bounds to the pyroelectric coefficient.

But at low temperatures, both the shell-model and the rigid-ion predictions are compatible with the bounds, so a full microscopic theory transcending these models is still required.

Discussion and Summary

The internal energy of a ferromagnet has first been treated from the point of view of the two-dimensional Ising model. One consequence of working out the change in internal energy from its ground-state limit in terms of the deviation ΔM of the magnetization from its saturation value is the linear relation at low temperatures. This is modified in both insulating and metallic three-dimensional ferromagnets to exhibit an exponent correction c : $\Delta E \propto (\Delta M)^{1+c}$, where the fractional exponent c is $\frac{2}{3}$ for insulating magnets and $\frac{1}{3}$ for metallic systems. At $T = 0$, another order parameter is valuable in discussing the metal-insulator transition between two antiferromagnetic phases. This is the discontinuity in the momentum distribution of the metal at the Fermi surface, the further order parameter being the customary sublattice magnetization. The internal energy has also been treated at low temperatures in pyroelectrics where, in contrast to the magnets, the low-lying excitations are acoustic phononlike.

The ferromagnet in the Ising framework has finally been reconsidered in relation to the entropy, needed of course to construct the free energy appearing in the Landau theory of phase transitions. The results of our analysis are of significance to a number of particular applications, two of which, ferromagnets and pyroelectrics, have been discussed in the article.

Appendix: Unconventional Order Parameter for Metal-Insulator Transition Between Antiferromagnetic Phases

In this Appendix we shall summarize an unconventional phenomenological approach to the treatment of the metal-insulator transition at $T = 0$ between phases which both exhibit cooperative antiferromagnetic ordering. Following the ideas set out in the main text, we must first note that to model the phase diagram (the case of three-dimensional transition-metal dichalcogenides is a specific

example; see, e.g., the schematic phase diagram in Ref [10]) of such systems requires the incorporation of strong correlation interactions in narrow energy bands. In the text, this situation is modeled by the Hubbard Hamiltonian, written there for a half-filled doubly degenerate band.

PHENOMENOLOGICAL MODEL IN TERMS OF METALLIC DISCONTINUITY AT FERMİ SURFACE

In accord with the approach of March et al. [8], the discontinuity at the Fermi surface is to be used as an order parameter to describe the metal-insulator phase transition at absolute zero of temperature. Then (see also Chapman and March [23] at elevated temperatures), in the region of the transition in the metallic side one expands E in both the discontinuity, q say, and the difference ΔM between the sublattice magnetizations, as a further order parameter as discussed in the body of the text. Then near the transition, and following the spirit of Landau theory of phase transitions,

$$E(q, \Delta M) = E_0 + E_1 q + \frac{1}{2} E_2 q^2 + a \Delta M + \frac{1}{2} b (\Delta M)^2 + \lambda q \Delta M + \dots, \quad (\text{A1})$$

where $\Delta M = M_{\text{met}} - M_{\text{ins}} < 0$, since it will be supposed that there is magnetic saturation in the insulating phase. Also

$$a = \beta(U_c - U) \geq 0, \quad E_1 = -\alpha(U_c - U) \leq 0 \quad (\text{A2})$$

with α , β , b , E_2 , and λ all being taken as positive quantities. The physical significance of λ is that this parameter reflects the dependence on magnetization of the formation of electron-hole pairs.

Carrying out the minimization of $E(q, \Delta M)$ in Eq. (A1) with respect to q and ΔM then gives

$$\Delta M = \frac{[(\alpha\lambda/E_2) + b][U_c - U]}{(\lambda^2/E_2) - b} \quad (\text{A3})$$

and

$$q = \frac{[\beta + (\alpha\beta/\lambda)][U_c - U]}{(E_2 b/\lambda) - \lambda}. \quad (\text{A4})$$

Since $\Delta M \leq 0$ as argued above, we must have $\lambda^2/E_2 b < 1$. It is evident from Eqs. (A3) and (A4) that both ΔM and q , in this model, go continuously to zero at $U \rightarrow U_c$. It immediately follows

from Eqs. (A3) and (A4) that $\Delta M \propto q$, as discussed in the body of the text. Experimental tests of this relation as the metal-insulator transition is approached from the metallic phase would be of considerable interest but these would be required at the lowest feasible temperatures.

ACKNOWLEDGMENTS

We wish to thank Professor J. Stephenson for stimulating discussions. One of us (J.T.) acknowledges support from NSERC (Canada). Another of us (N.H.M.) had partial financial support from the University of Alberta (Edmonton) during a visit in early 1995. He wishes to thank Professors A. Z. Capri and G. R. Freeman, and their colleagues, for generous hospitality. Partial financial support from the Office of Naval Research (USA) and especially the encouragement of Dr. P. Schmidt, are gratefully acknowledged by N.H.M.

References

1. R. B. Stinchcombe, in *Polymers, Liquid Crystals and Low-Dimensional Solids*, N. H. March and M. P. Tosi, Eds. (Plenum, New York, 1984), p. 335.
2. L. Onsager, *Phys. Rev.* **65**, 117 (1944).
3. See, for example, J. Callaway, *Quantum Theory of the Solid State*, Part A (Academic, New York, 1974), p. 136.
4. C. Kittel, *Quantum Theory of Solids* (Wiley, New York, 1963).
5. See, for instance, W. Jones and N. H. March, *Theoretical Solid-State Physics* (Dover, New York, 1985).
6. J. A. Tuszynski and W. Wierzbicki, *Am. J. Phys.* **59**, 555 (1991).
7. P. J. Grout and N. H. March, *Phys. Rev. B* **14**, 4027 (1976).
8. N. H. March, M. Suzuki, and M. Parrinello, *Phys. Rev. B* **19**, 2027 (1979).
9. A. Ferraz, R. G. Chapman, N. H. March, B. Alascio, and C. M. Sayers, *Solid State Commun.* **57**, 937 (1986).
10. G. Czjzek, J. Fink, H. Schmidt, G. Krill, M. F. Lapierre, P. Panissod, F. Gautier, and C. Robert, *J. Magn. Matter* **3**, 58 (1976).
11. See, e.g., N. F. Mott, *Metal-Insulator Transitions* (Taylor and Francis, London, 1974).
12. J. S. Smart, *Phys. Rev.*, **90**, 55 (1953).
13. L. D. Landau and E. M. Lifshitz, *Statistical Physics* (Pergamon Press, London, 1959).
14. L. E. Reichl, *A Modern Course in Statistical Physics* (University of Texas Press, Austin, 1980).
15. D. R. Stump, *Phys. Rev. A* **36**, 4439 (1987).
16. M. E. Lines and A. M. Glass, *Principles and Applications of Ferroelectrics and Related Materials* (Clarendon, Oxford, 1977).
17. R. Resta, *Ferroelectrics* **136**, 51 (1992).

18. R. D. King-Smith and D. Vanderbilt, *Phys. Rev. B* **47**, 165 (1993).
19. M. Born, *Rev. Mod. Phys.* **17**, 245 (1945).
20. Y. Ohmura, P. J. Grout, and N. H. March, *J. Phys. Chem. Solids* **42**, 323 (1981).
21. M. E. Lines, *Phys. Rev. B* **15**, 388 (1977).
22. P. J. Grout, N. H. March, and T. L. Thorp, *J. Phys. C* **8**, 2167 (1975).
23. R. G. Chapman and N. H. March, *Phys. Rev. B* **38**, 792 (1988).

Behavior of Carriers in δ -Doped Quantum Wells Under In-Plane Magnetic Fields

A. T. LINO AND E. K. TAKAHASHI

Departamento de Ciências Físicas, Universidade Federal de Uberlândia, C.P. 593, CEP 38400-902, Uberlândia - MG, Brazil

L. M. R. SCOLFARO AND J. R. LEITE

Instituto de Física, Universidade de São Paulo, C.P. 66318, CEP 05389-970, São Paulo - SP, Brazil

Received February 24, 1996; revised manuscript received April 17, 1996; accepted April 25, 1996

ABSTRACT

Self-consistent electronic structure calculations of δ -doped quantum wells (QW) in the presence of in-plane magnetic fields B up to 20 Tesla are carried out within the frameworks of the effective mass and the local density approximations. QWs composed of two layers of $\text{Ga}_{1-x}\text{Al}_x\text{As}$, separated by a layer of GaAs with a donor δ -doped sheet in the center, are considered. The width of the GaAs layer was varied from 100 to 400 Å. It is shown that the diamagnetic shift increases with the increasing of the GaAs QW width. The magnetic field induces remarkable changes in the energy dispersions of electrons and holes, along an in-plane direction perpendicular to B . The most striking effect occurs in the nature of the band gap of these systems. We found that the valence band displays a double-maximum character instead of a single maximum at the center of the Brillouin zone. © 1996 John Wiley & Sons, Inc.

Introduction

Recently, an increasing interest has been revealed in the use of the δ -doping concept to produce very high carrier concentration two-dimensional (2D) semiconductor structures of several applications, including devices and the gener-

ation of high-mobility 2D electron gas systems [1]. Such structures are obtained by atomic layer doping of epitaxially grown, e.g., GaAs or GaAlAs crystals. An ideal δ -doping profile is achieved by confining the dopant atoms to a crystal monolayer, generating a V-shaped potential well in the host material. The presence of a 2D electron gas with a characteristic subband structure in the V-shaped potential well has been confirmed by several ex-

perimental and theoretical works [2–5]. The lack, however, of confinement of the minority carriers, i.e., holes in the case of n - δ -doping, has brought difficulties, for instance, on the use of optical experiments to investigate this kind of system [6–8].

Additional information on the physics of these δ -doped structures can be obtained when the δ -layer lies, e.g., within a quantum well (QW), since the QW barriers may provide an extra degree of control to the number and population of typically various confined subbands [9–11]. This has been also achieved by building up a superlattice of such δ -layers, which allows for the needed minority carriers confinement [2, 3].

The effects of a magnetic field on the 2D electron gas in semiconductor heterostructures have been the subject of intensive investigations. Particularly, in the well-known modulation-doped quantum well (MDQW) structures, the behavior of 2D carriers under the influence of an in-plane magnetic field B has been widely studied both theoretically [12–14] and experimentally [15, 16]. A double-minimum character of the electron energy dispersion with a magnetic field-induced indirect band gap has been predicted [14] and confirmed by photoluminescence measurements [16]. In these MDQWs, the doping in the barriers provides the required confinement of holes in the valence band, therefore making possible optical transitions within the well to be observed. The electronic subbands of an isolated n - δ -doped layer in bulk GaAs under a magnetic field parallel to the plane of the donor atoms have also been studied through magnetoconductivity experiments [17]. An increase of the bottom of each electron subband energy level due to the diamagnetic shift was seen. No attempts, however, have been done to investigate the effect of the in-plane magnetic field on the holes in the valence band of such δ -doped layers.

In this work, we present detailed calculation results for the electronic structure of an n -type δ -doped layer placed at the center of GaAs/ $\text{Al}_x\text{Ga}_{1-x}\text{As}$ QWs ($x = 0.3$), under in-plane magnetic fields B up to 20 Tesla. Calculations, based on the self-consistent (SCF) one-electron state solution of the Schrödinger equation and the Poisson equation, were performed for a sheet donor concentration $N_s = 7.0 \times 10^{12} \text{ cm}^{-2}$ and different values of the QW widths L_w . Many-body effects such as exchange and correlation were taken into account within the local density approximation (LDA). The effects of the field on the electron and hole subband structures were analyzed. It is shown that

the hole energy dispersion has a double maximum, which is more pronounced as the QW becomes larger, whereas the electron dispersions keep the single minima at $k = 0$. Thus, the band gap is predicted to become indirect. For such δ -doped type-I QWs, the valence band discontinuity provides the required confinement of the holes for optical investigations. Besides, the presence of an in-plane magnetic field may give further support for probing the nature of the conduction–valence band gap.

Theory

The system considered is a GaAs/ $\text{Ga}_{1-x}\text{Al}_x\text{As}$ QW with a silicon- δ -doped layer at its center. We use the effective-mass approximation [18] to describe the electrons in the host semiconductor heterostructure and replace the localized donor charges by a z -dependent charge density which has been averaged over the x - y plane. A schematic representation of the layers in the system investigated here is depicted in Figure 1. All Si donors are assumed to be ionized and uniformly distributed within a range of 2 Å. Since low temperature is usually employed to reduce diffusion of silicon out of the doped plane, no significant spread of the donors is expected [1]. The electrons released by the donors form a quasi-2D electron gas which screens the potential of the positive charges.

The electron–electron interactions in the conduction band can then be separated into a Hartree (Coulomb) contribution due to the electrostatic potential of the total electron density and an exchange–correlation term. Hohenberg et al. [19] showed that the exchange–correlation potential can be obtained by taking the functional derivative of the exchange and correlation part of the ground-state energy with respect to the electron density; in general, the exchange–correlation potential energy is an unknown functional of the electron density $n(z)$. In the simplest approximation, i.e., the LDA, the exchange–correlation potential is approxi-

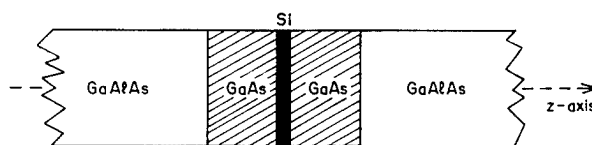


FIGURE 1. Schematic representation of the GaAs / GaAlAs QW with a silicon δ -doped layer in the center.

mated by the exchange–correlation contribution to the chemical potential of a homogeneous electron gas having a uniform electron density which equals the local electron density $n(z)$ of the inhomogeneous system. It is interesting to point out that this simple approximation works surprisingly well and has been currently used with great success to obtain ground-state properties of several systems [20].

The magnetic field was assumed to be along the y axis $\mathbf{B} = (0, B, 0)$, for which the gauge $\mathbf{A} = (Bz, 0, 0)$ has been chosen, with z being the direction perpendicular to the layers or to the QW. The problem is in the LDA reduced to a one-particle Schrödinger equation, with electrons moving in an effective potential which is a sum of the Coulombic and the exchange–correlation potentials, plus the magnetic potential. The calculations are performed at temperature $T = 0$ K.

The electronic states will be denoted by the wave function $\Phi(x, y, z)$ which due to the translational symmetry in the x - y plane can be written as

$$\Phi = e^{ik_x x} e^{ik_y y} \Psi(z), \quad (1)$$

where k_x and k_y are components of the wave vector $\mathbf{k} \equiv (k_x, k_y, 0)$ and $\Psi(z)$ is the solution of the one-dimensional Schrödinger equation, which is solved for each state i :

$$\left[-\frac{\hbar^2}{2m^*} \frac{d^2}{dz^2} + V_C(z) + V_{XC}(z) + V_B(z) \right] \Psi_i(z) = E_i \Psi_i(z), \quad (2)$$

with m^* being the electron effective mass. Here, $V_C + V_{XC} + V_B$ is the effective potential, given by the sum of the Coulombic potential $V_C(z)$, the local exchange potential $V_{XC}(z)$, and the magnetic potential $V_B(z)$. The potential $V_B(z)$ generated by the magnetic field is given by [14]

$$V_B(z) = \frac{1}{2} m^* \omega_c^2 (z + k_x l^2)^2, \quad (3)$$

where $\omega_c = eB/m^*$ is cyclotron frequency, e is the electronic charge, and $l = \sqrt{\hbar/(eB)}$ is the magnetic length. The magnetic potential $V_B(z)$ depends on the in-plane wave vector k_x perpendicular to B . Thus, the energies related to the transverse axis x have the form $E_i(k_x)$, so that the total energy of the carrier is

$$E_T = \frac{\hbar^2}{2m^*} k_y^2 + E_i(k_x). \quad (4)$$

We consider a finite layer of thickness $2d$ with a 3D density of donors n_D . Thus, $N_S = 2 \times d \times n_D$ is the Si donor concentration per unit area. As mentioned before, it is assumed that all the Si atoms are ionized, supplying the electrons to form the 2D electron gas. Therefore, the 2D electron density equals the sheet donor density N_S . The Coulombic potential $V_C(z)$ due to the electrostatic electron–electron and electron–ionized donor interactions, is obtained from the Poisson equation

$$\frac{d^2 V_C}{dz^2} = -\frac{e^2}{\epsilon} [n(z) - n_D], \quad (5)$$

where ϵ is the dielectric constant, and $n(z)$, the electron gas density given by

$$n(z) = \sum_i N_S^i(k_x) |\Psi_i(z)|^2, \quad (6)$$

with $N_S^i(k_x)$ being the number of electrons per unit area in the i th subband, which is given by

$$N_S^i(k_x) = \frac{1}{\pi^2} \left[\frac{2m^*}{\hbar^2} (E_F - E_i(k_x)) \right]^{1/2}, \quad (7)$$

where E_F is the Fermi energy obtained from the condition

$$N_S = \int_{-\infty}^{+\infty} \sum_{i=1}^{\infty} N_S^i(k_x) \Theta[E_F - E_i(k_x)] dk_x. \quad (8)$$

In the above expression, Θ is the Heaviside step function.

For the exchange–correlation potential $V_{XC}(z)$, we used the simple analytic expression suggested by Hedin and Lundqvist [21]:

$$V_{XC}(z) = -\frac{e^2}{2\epsilon a_0^*} \frac{2}{\pi \alpha r_s} \left[1 + 0.0368 r_s \ln \left(1 + \frac{21}{r_s} \right) \right], \quad (9)$$

with $a_0^* = \epsilon a_0 (\frac{m}{m^*})$ being the effective Bohr radius, $r_s = \{[4\pi a_0^{*3} n(z)]/3\}^{-1/3}$, and $\alpha = [4/(9\pi)]^{1/3}$ is a numerical constant.

The value $x = 0.3$ was assumed for the Al concentration in the alloy and the currently used 60–40% rule for the conduction-to-valence band discontinuity was adopted [22]. This leads to a barrier height of 226 meV for the QW where the electrons are confined. The values used for m^* and ϵ are $0.068m$ and $12.53\epsilon_0$, respectively, where m is the free electron mass, and ϵ_0 , the vacuum permittivity [23].

We are dealing here with an n -type δ -doping system where the majority carriers are electrons. To obtain the one-particle energy states for the minority carriers, we assumed that they are submitted to the SCF potential calculated for the electrons. This assumption is valid as long as one keeps the hole density very low. For a hole gas of a finite density, a proper treatment is required to obtain the valence band dispersion curves [24]. According to the low-density limit assumed here, the holes are submitted to the repulsive potential calculated for the electrons and confined by the valence band potential of the QW, which, for $x = 0.3$, has a height of 148 meV. The confined energy states for the holes are then calculated by considering these one-particle external potentials and a value of $0.36m$ for the heavy-hole effective mass in the Schrödinger equation [23]. We neglected the effects of the magnetic field on the light-hole valence band, since any occupation of this band may be ruled out in the description of electron-hole recombination transitions of the n -type δ -doped QWs investigated here [7]. Changes in the effective masses within the GaAlAs barriers were also neglected. In spite of the fact that nonparabolicity effects of the valence bands have not been taken into account in the present work, the inclusion of such effects is not expected to alter qualitatively the conclusions made here and is in progress.

Results and Discussion

In Figure 2, we show the conduction band potential profile and energy levels for a δ -doped QW with typical values of sheet donor concentration $N_S = 7.0 \times 10^{12} \text{ cm}^{-2}$ and well width $L_W = 100 \text{ \AA}$. Two subbands E_0 and E_1 are found occupied, below the Fermi energy E_F . Within the QW, there is still an empty level E_2 which appears well above E_F . This latter energy level may be important in absorption and absorption-related optical experiments [11, 25]. The δ -doped layer is responsible for the spikelike potential profile seen in Figure 2, in which lies the lowest energy level E_0 comprising most of the 2D electrons.

Some general effects of the magnetic field B on the carriers are best illustrated assuming $N_S = 0$, i.e., an undoped QW. In this case, $V(z) = V_C(z) + V_{XC}(z)$ is just a square-well potential. Figure 3 shows the energy dispersions along the in-axis k_x of the first electron and hole subbands for $N_S = 0$

and $L_W = 150 \text{ \AA}$ and two values of B : $B = 0$ and $B = 20T$. The results displayed in this figure show that the magnetic field increases the electron-hole recombination energy, which is seen by the large diamagnetic shifts at $k_x = 0$. Figure 3 also shows a flattening of the dispersion curves for both electrons and holes for $B \neq 0$ [14].

The effect of the magnetic field on the electronic structure of the δ -doped QW is first considered in Figure 4. There, energy dispersion curves for a sheet donor concentration of $N_S = 3.5 \times 10^{12} \text{ cm}^{-2}$ and a QW width of $L_W = 150 \text{ \AA}$ are shown. Solid lines correspond to values in the absence of magnetic field ($B = 0$) and dashed lines are related to $B = 20T$. First, we analyze the results depicted in Figure 4 for $B = 0$. The presence of the δ -doped layer is responsible for a strong attractive potential which is partially screened by the Hartree potential generated by the electrons. This makes the carriers to feel higher barriers, therefore being more localized around the doped plane. The energy levels appear several meV above the bottom of the potential well, which was taken as the energy zero. This is a characteristic picture of the subbands inside δ -doped QWs [5, 7]. The presence of the magnetic field flattens the energy dispersions and gives rise to relatively small diamagnetic shifts if compared to the undoped QW, as expected (see Fig. 3).

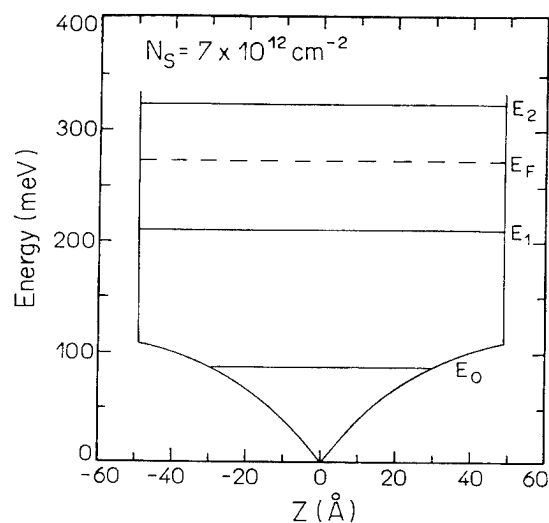


FIGURE 2. Conduction band potential profile and energy levels for a typical n - δ -doped QW with a sheet donor concentration $N_S = 7.0 \times 10^{12} \text{ cm}^{-2}$ and a well width $L_W = 100 \text{ \AA}$. The subbands E_0 and E_1 are occupied. The Fermi energy E_F is indicated by a dashed line.

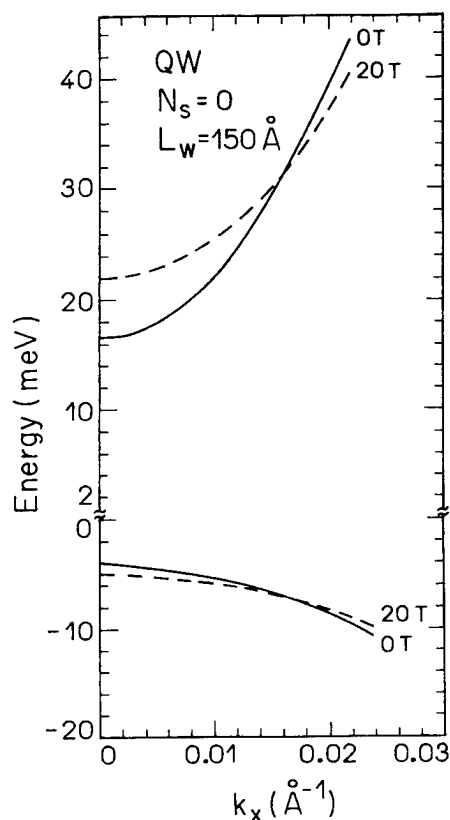


FIGURE 3. Energy dispersion curves for an undoped QW ($N_s = 0$) with $L_w = 150$ Å for $B = 0$ (solid line) and $B = 20$ T (dashed line). The zero in the energy scale is taken at the bottom of the conduction band at $k_x = 0$ for electrons and at the top of the valence band at the same k -point for holes.

In Figure 5 we present the energy dispersions for electron and hole subbands, for different values of magnetic fields for three well widths $L_w = 100, 200$, and 400 Å and a fixed sheet donor concentration $N_s = 7.0 \times 10^{12} \text{ cm}^{-2}$. As expected, with the increasing of L_w , the energy of the electron subbands is lowered, with higher levels starting to be populated. For $L_w = 400$ Å, already four subbands are occupied at $k_x = 0$. For such a large well width, the system behaves essentially as an isolated δ -doped layer [5, 17]; the compositional band offset does not affect the δ potential. This can also be concluded by analyzing the charge distribution within the QWs. For the larger QW width, the total charge density is found essentially localized around the doped plane, with no penetration in the GaAlAs barriers. It is worth mentioning that, contrarily, for the 100 Å width QW, the barriers play a relevant effect on the electronic

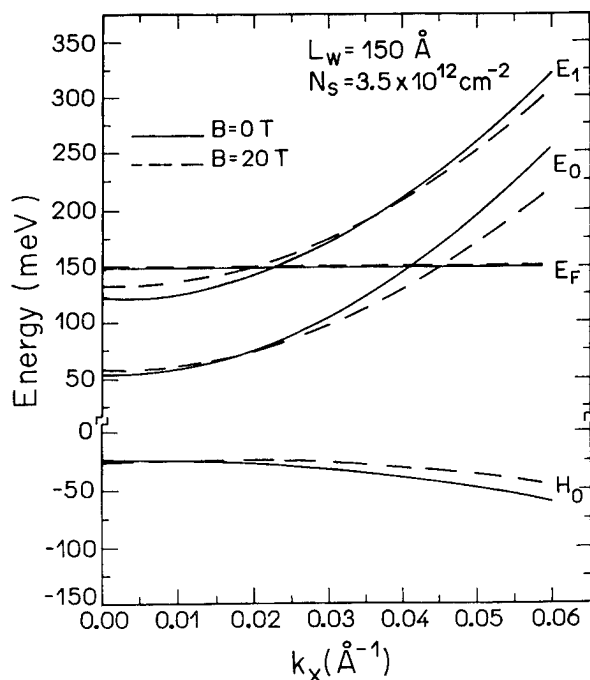


FIGURE 4. Energy dispersions of electrons and holes for an n - δ -doped QW with $L_w = 150$ Å and $N_s = 3.5 \times 10^{12} \text{ cm}^{-2}$ for $B = 0$ (solid line) and $B = 20$ T (dashed line). The Fermi energy E_F is also shown. The zero in the energy scale is taken as in Figure 3.

states confinement, which is reflected by the extension of the wave functions within the barrier regions [26]. The main effects of the magnetic field, as seen in Figure 4, are the increase of the subband levels at $k_x = 0$ (diamagnetic shift) and a flattening of the dispersion curves as one moves away from $k_x = 0$. In contrast to what has been observed in MDQWs [14], the effect of B is more pronounced for the higher electronic subbands. This feature was also seen in previous investigations reported on [17] for the case of an isolated δ -layer in GaAs.

The most striking characteristic observed in the electronic structure of the δ -doped QWs investigated here under the effect of a parallel magnetic field is that the maximum of the hole energy dispersion curves moves out from the center of the Brillouin zone (BZ) already for moderate values of the field, whereas the electron dispersions keep the single minima at $k_x = 0$. To emphasize the behavior of the hole bands, Figure 6 depicts the hole energy dispersions only, in a larger scale, for the δ -doped QW of $L_w = 400$ Å and $N_s = 7.0 \times 10^{12} \text{ cm}^{-2}$ for the several values taken for B . The dou-

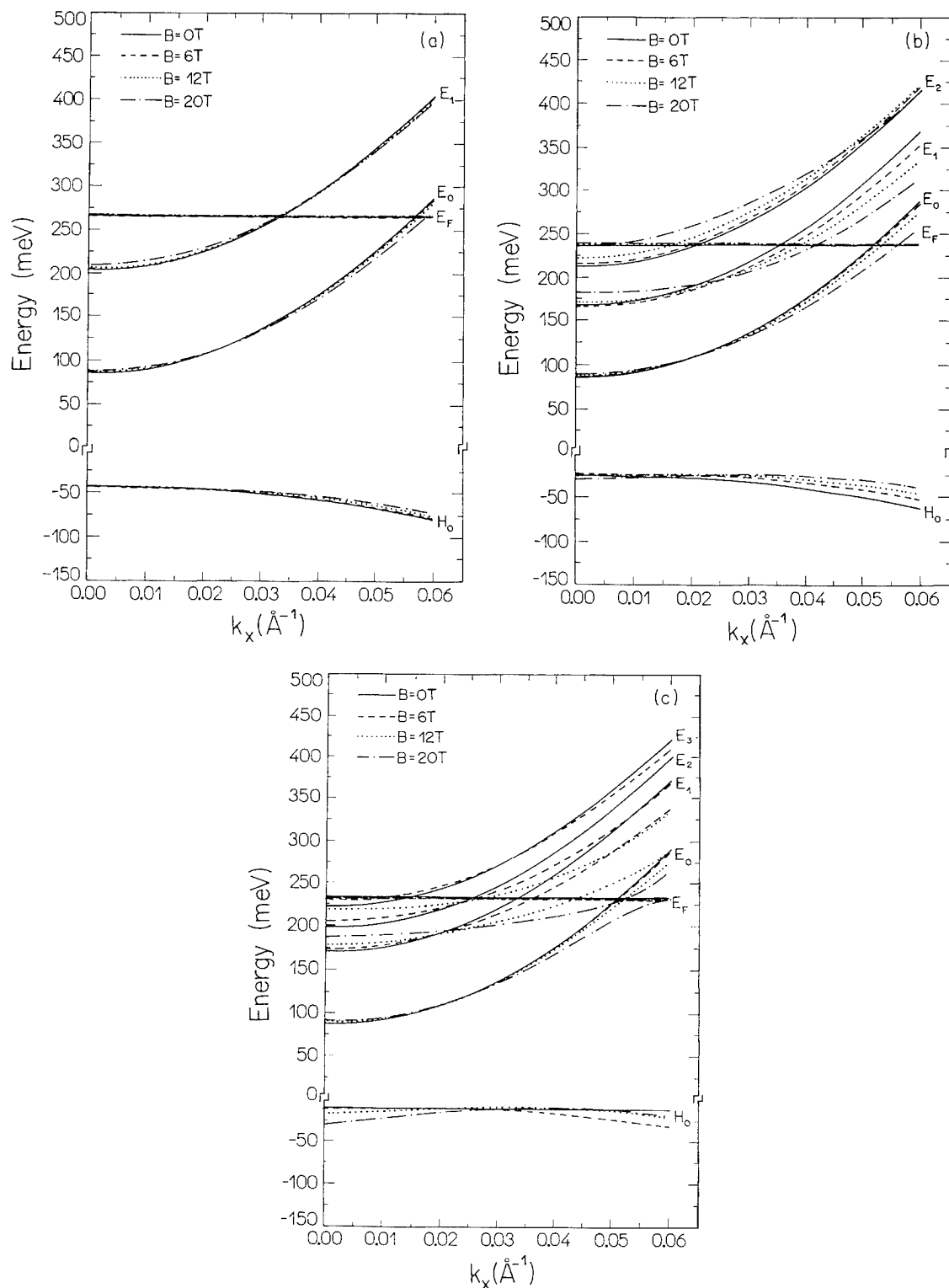


FIGURE 5. Energy dispersions of electrons and holes, at different magnetic fields, for a sheet donor concentration $N_S = 7.0 \times 10^{12} \text{ cm}^{-2}$ and well width (a) 100 Å, (b) 200 Å, and (c) 400 Å. The zeros in the energy scales correspond to the conduction band edge (electrons) and valence band edge (holes) for $k_x = 0$. The Fermi energy E_F is also shown.

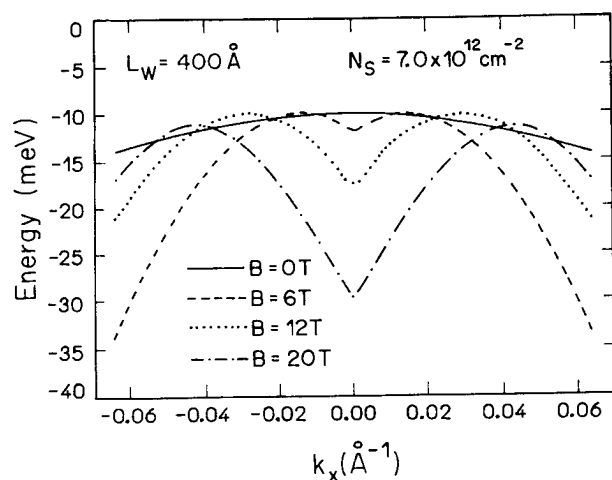


FIGURE 6. Heavy hole subbands, as extracted from Figure 5(c), for different values of the magnetic field, for an n - δ -doped QW of $L_W = 400$ Å and sheet donor concentration $N_S = 7.0 \times 10^{12} \text{ cm}^{-2}$. The zero of energy was placed at the top of the valence band QW for $k_x = 0$.

ble-maximum character is clearly seen. This characteristic behavior is also observed for the narrower QWs, although it is more pronounced as the QW width increases. Therefore, under the influence of the magnetic field, these systems become indirect-gap materials. This is a novel effect, which has been predicted for MDQWs. Nevertheless, the induced indirect-gap in the later systems is due to the displacement of the minimum in the first electron subband and has been attributed to the effect of the magnetic field on the electronic charge redistribution [14]. The effect is more remarkable as the QW becomes larger and the electrons lying in the lowest subband are more sensitive to the self-consistent repulsive Coulombic potential, which in the case of MDQWs is generated by the doping in the barriers. For the δ -doped QWs studied here, such a situation takes place for the carriers in the lowest hole subband. Similarly, the holes in this subband are directly affected by the repulsive potential created by the positive charges in the δ -sheet.

Conclusions

We have shown that the in-plane magnetic field leads to significant effects on the electronic ground-state properties of δ -doped GaAs/GaAlAs QWs. The magnetic field brakes the symmetry of the V-shaped δ -doped QW by bending one side of

the square potential, thus changing the electronic charge distribution and the electron energy dispersion curves. However, we verified that even for intense magnetic fields the Fermi level position remains quite stable and the minimum of the occupied conduction bands stays at the center of the BZ. This finding differs from that observed for the MDQW structures where the magnetic field induces a double-minimum character in the occupied conduction bands.

The magnetic field-dependent SCF potential obtained from the calculations is then used to solve the effective-mass Schrödinger equation for a single hole at the valence band of the δ -doped GaAs/GaAlAs QWs. We show that the one-hole energy dispersion curves display a remarkable feature due to the magnetic field, which is the displacement of the maxima of the valence bands out from the center of the BZ. In conclusion, the magnetic field leads to a double maximum character for the valence band, therefore indicating that an indirect band gap behavior is expected for these systems. It is worth mentioning that this interesting behavior is predicted to occur even for moderate values of the magnetic field.

The results reported here are expected to be useful for the analysis of optical measurements performed on δ -doped layers: first, because of the extra degree of control provided by the QW barriers, which allows for the necessary hole confinement for electron-to-hole recombinations be observed, and, second, as previously done for MDQWs, the indirect-band gap behavior predicted here for δ -doped QWs could be further studied, e.g., through photoluminescence experiments under parallel magnetic fields.

ACKNOWLEDGMENTS

The authors wish to thank CNPq (Brazilian Agency), and A. T. L. particularly also FAPEMIG (Brazilian Agency) and the Universidade Federal de Uberlândia for partial financial support.

References

1. E. F. Schubert, *Semicond. and Semimet.* **40**, 1 (1994).
2. S. M. Shibli, L. M. R. Scolfaro, J. R. Leite, C. A. C. Mendonça, F. Plentz, and E. A. Meneses, *Appl. Phys. Lett.* **60**, 2895 (1992).

3. C. A. C. Mendonça, F. Plentz, J. B. B. Oliveira, E. A. Meneses, L. M. R. Scolfaro, D. Beliaev, S. M. Shibli, and J. R. Leite, *Phys. Rev. B* **48**, 12316 (1993).
4. R. Enderlein, G. M. Sipahi, L. M. R. Scolfaro, J. R. Leite, and I. F. L. Dias, *Mater. Sci. Eng.* **B35**, 396 (1995).
5. L. M. R. Scolfaro, D. Beliaev, J. R. Leite, A. T. Lino, and E. K. Takahashi, *Int. J. Quantum Chem.* **S28**, 667 (1994).
6. J. Wagner, A. Fisher, and K. Ploog, *Phys. Rev. B* **42**, 7280 (1990).
7. C. A. C. Mendonça, L. M. R. Scolfaro, J. B. B. Oliveira, F. Plentz, M. Micovic, J. R. Leite, and E. A. Meneses, *Superlat. Microstruct.* **12**, 257 (1992).
8. A. Tabata, A. M. Ceschin, A. A. Quivy, A. Levine, J. R. Leite, R. Enderlein, J. B. B. Oliveira, E. Laureto, and J. L. Gonçalves, *Mater. Sci. Eng. B* **35**, 401 (1995).
9. M.-L. Ke and B. Hamilton, *Phys. Rev. B* **47**, 4790 (1993).
10. L. M. R. Scolfaro, J. R. Leite, C. A. C. Mendonça, D. Beliaev, S. M. Shibli, E. C. F. da Silva, and E. A. Meneses, *Mater. Sci. Forum* **143-147**, 669 (1994).
11. A. M. Cechin, A. A. Quivy, J. A. N. T. Soares, R. Enderlein, A. Tabata, L. M. R. Scolfaro, E. C. F. da Silva, J. R. Leite, J. B. B. Oliveira, and E. A. Meneses, *Superlat. Microstruct.* **15**, 333 (1994).
12. T. Ando, *J. Phys. Soc. Jpn.* **39**, 411 (1975); *Ibid.* **44**, 475 (1978).
13. W. Zawadzki, S. Klahn, and U. Merkt, *Phys. Rev. B* **33**, 6916 (1986).
14. G. M. G. Oliveira, V. M. S. Gomes, A. S. Chaves, J. R. Leite, and J. M. Worlock, *Phys. Rev. B* **35**, 2896 (1987).
15. S. Oelting, U. Merkt, and J. P. Kotthaus, *Surf. Sci.* **170**, 402 (1986).
16. D. M. Whittaker, T. A. Fisher, P. E. Simmonds, M. S. Skolnick, and R. S. Smith, *Phys. Rev. Lett.* **67**, 887 (1991).
17. A. Zrenner, H. Reisinger, F. Koch, K. Ploog, and J. C. Maan, *Phys. Rev. B* **33**, 5607 (1986).
18. J. M. Luttinger and W. Kohn, *Phys. Rev.* **97**, 869 (1955).
19. P. Hohenberg and W. Kohn, *Phys. Rev. B* **136**, 864 (1964); W. Kohn and L. J. Sham, *Ibid.* **140**, A1133 (1965); L. J. Sham and W. Kohn, *Ibid.* **145**, 561 (1966).
20. See, e.g., R. O. Jones and O. Gunnarsson, *Rev. Mod. Phys.* **61**, 689 (1989).
21. L. Hedin and B. I. Lundqvist, *J. Phys. C* **4**, 2064 (1971).
22. T. Hayakawa, T. Suyama, K. Takahashi, M. Kondo, S. Yamamoto, S. Yano, and T. Hijikata, *Surf. Sci.* **174**, 76 (1986).
23. O. Madelung, Ed., *Physics of Group-IV and III-V Compounds*, Landolt-Bornstein, New Series, Group III, Vol. 17 (Springer-Verlag, Berlin, 1982).
24. G. M. Sipahi, R. Enderlein, L. M. R. Scolfaro, and J. R. Leite, *Phys. Rev.* **B53**, 9930 (1996).
25. J. A. N. T. Soares, D. Beliaev, R. Enderlein, L. M. R. Scolfaro, M. Saito, and J. R. Leite, *Mater. Sci. Eng. B* **35**, 267 (1995).
26. E. K. Takahashi, A. T. Lino, and L. M. R. Scolfaro, *Int. J. Mod. Phys. B*, in press.

Computational Studies of Less Common Fullerene-Related Species

SHYI-LONG LEE,* MEI-LING SUN, AND ZDENĚK SLANINA†

*Department of Chemistry, National Chung-Cheng University, Ming-Hsiung, Chia-Yi 62117, Taiwan;
e-mail for S.-L. L.: sllee@nas01.ccu.edu.tw*

Received February 24, 1996; accepted March 1, 1996

ABSTRACT

The contribution reports results of ongoing computations of various cage structures differing from the well-known buckminsterfullerene in the number of carbon atoms (C_{80}) in their coordination or in the types of rings involved (C_{59}). The computations have supplied a complete description of the seven isolated-pentagon-rule (IPR) isomers of C_{80} (i.e., a system not yet observed) at the semiempirical AM1 and SAM1 levels; their energetics was also evaluated at ab initio Hartree-Fock level in small basis sets. The ground-state structure of the system possesses a D_{5d} symmetry, but at supposed synthetic conditions a structure of D_2 symmetry is the most populated, i.e. temperature represents an important factor in the stability relationships. One of the IPR isomers exhibits an I_h topological symmetry, but it undergoes a Jahn-Teller distortion and its symmetry is actually reduced to D_2 . The C_{59} serves as an example of odd-numbered carbon clusters, and new rules are reported for the pentagon/hexagon pattern in the odd clusters, yielding a variable number of the pentagons. Moreover, other rings are considered and the computed ground state of the system in fact contains an eight-membered ring (while the next lowest species exhibits a nine-membered ring). Their relative stabilities are not very sensitive to temperature. Altogether 19 isomers of C_{59} are treated at the AM1 level. In contrast to even-numbered fullerenes, with odd fullerenes the cages cannot be built from three-coordinated carbon atoms only. Hence, we have to allow for two- or even four-coordinated atoms. For example, if we consider one two-coordinated carbon atom (and the rest three-coordinated) the number of pentagons drops to 10. If we allow for just one four-coordinated atom, the number of pentagons changes to 14. Let the number of two-coordinated carbon atoms be p , and the number of four-coordinated q . If we still allow only for pentagons and hexagons, it holds for the number of pentagons $n_5 = -2p + 2q + 12$. © 1996 John Wiley & Sons, Inc.

* To whom correspondence should be addressed.

† On a leave of absence from the Academy of Sciences of the Czech Republic, Prague.

Introduction

Fullerenes became known to chemist recently enough, i.e., at times when computational chemistry, and especially molecular mechanics and semiempirical quantum chemistry, could provide useful information during the surge of interest in these molecules. Owing to the tremendous development of computational hardware in the 1970s and 1980s, computational chemistry could well follow the C_{60} discovery, and even supply useful support to further advances. Computational chemistry is now playing the role of a real partner in fullerene research where theory and experiment are mutually complementary tools. In this article we shall illustrate fullerene computations with two less conventional systems, with C_{80} and C_{59} .

The Isolated-Pentagon-Rule (IPR) Isomers of C_{80}

Three mixtures of fullerene isomers were studied in detail by now, namely C_{78} [1-5], C_{82} [6-13], and C_{84} [14-31]. The missing system, C_{80} , has received limited attention [32, 33], apparently because the particular fullerene set has not been isolated yet. For the three isolated and characterized systems it has been demonstrated [5, 13, 30, 31] that they cannot be understood without considering temperature effects. Although interisomeric separation energies are important, they themselves alone cannot determine the relative stabilities at elevated temperatures. The temperatures in fullerene syntheses are high, and thus entropy contributions can even overcompensate the enthalpy terms. This was shown not only on fullerene systems but also for small carbon clusters [34] and with silicon clusters [35].

There are seven topologically different C_{80} structures [36] which obey the isolated pentagon rule (the structures are coded A-G, which correspond to the letters used in Ref. 33, see Fig. 1). In this section, the AM1 computations on C_{80} are reported together with their relative stability evaluations.

The geometry optimizations were performed with the implementation of the AM1 semiempirical quantum chemical method [37] in the Spartan program package [38] installed at an Iris/Silicon

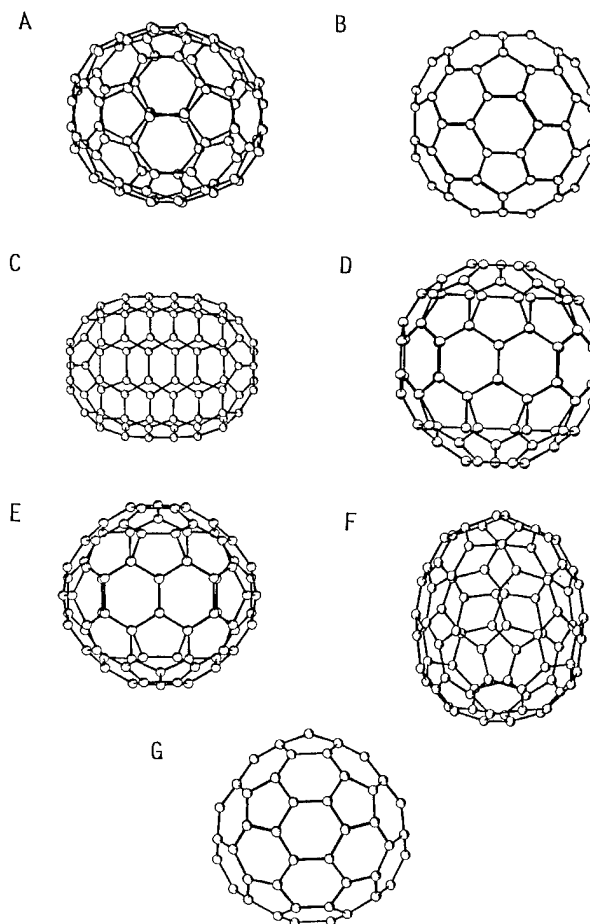


FIGURE 1. AM1 optimized IPR structures of C_{80} .

Graphics XZ4000 workstation. The optimizations were performed without any symmetry constraints in Cartesian coordinates and with analytically constructed energy gradient. In the AM1 optimized geometries, the harmonic vibrational analysis was carried out by a numerical differentiation of the analytical energy gradient. The vibrational calculations were mainly performed with the Gaussian 92 [39] though some cases of poor self-consistent field (SCF) convergence were retreated with the SCF convergers built in the MOPAC 5.0 [40] program package. The vibrational analysis helped in clarification of the stationary point nature, in the vibrational spectra prediction, and in partition function construction.

Relative concentrations of the seven isomers were computed as the mole fractions w_i , using the isomeric partition functions q_i within the rigid-rotor and harmonic-oscillator approximation. In the terms of q_i and the ground-state energy $\Delta H_{0,i}^{\circ}$ the

mole fractions are given [41]:

$$w_i = \frac{q_i \exp[-\Delta H_{0,i}^0/(RT)]}{\sum_{j=1}^7 q_j \exp[-\Delta H_{0,j}^0/(RT)]}, \quad (1)$$

where R is the gas constant and T the absolute temperature. The conventional heats of formation at room temperature were converted to heats of formation at the absolute zero temperature, and finally the vibrational zero-point energy was extracted. Hence, the relative potential energies ΔE_{rel} resulted from the treatment.

Chirality contribution is to be considered with Eq. (1). There is no asymmetric carbon atom in the conventional sense in the fullerene cages (with three coordinated carbon atoms), nevertheless, some of the structures are still chiral, i.e., they are not superimposable upon their mirror image. This structural dissymmetry can readily be recognized from the point group of symmetry as the presence of no reflection symmetry, i.e., absence of rotation-reflection axes S_n : only the C_n , D_n , T , O , and I groups obey the requirement. For an enantiomeric pair its partition function q_i in Eq. (1) has to be doubled (if we assume the presence of both optical isomers, which seems natural under fullerene synthesis conditions).

Symmetry of the optimized structures has been determined by a procedure that allows for a precision of the computed coordinates as a variable parameter, ϵ . The origin of the coordinate system is placed in the center of charge (defined similarly to the center of mass)—the point is the only candidate for possible center of symmetry. Candidates for C_2 axes are either lines connecting any two nuclei or perpendicular bisectors of the distance between any two nuclei of the same kind. Then C_n axes with $n > 2$, S_n and S_{2n} axes, and planes of symmetry are investigated. The symmetry operations found have to create one of the known symmetry groups. For each symmetry operation considered, coordinates of the interrelated atoms before and after symmetry operation are checked with respect to ϵ . If the coordinates are identical within the accuracy ϵ (i.e., the largest difference is smaller than ϵ) a symmetry element has been found at the accuracy level ϵ .

Of the seven IPR C_{80} structures, the species **B** is especially interesting. It has a topological symmetry I_h . However, according to the concept of the Goldberg polyhedra [42], it has to be an open shell

and it has to undergo a Jahn-Teller distortion toward lower energy and lower symmetry. This indeed happens in our AM1 calculations, though the geometry distortions are quite small. This is in agreement with the findings for charged C_{60} species [43–45] where the Jahn-Teller geometry distortions are of the order of 10^{-3} Å only. The symmetry of the **B** structure is relaxed to D_2 , however, the determination of the symmetry deserves a comment. The computations were performed in the Cartesian coordinates, hence, the coordinates of the symmetry-related atoms can be subject to a numerical inaccuracy. If we want to extract the related symmetry group, we have to allow for some threshold variation or accuracy ϵ in the coordinates when we judge symmetry relationships. For very low value (e.g., 10^{-5} Å) of such a threshold ϵ we can find simply C_1 symmetry and only after its increase (say to 10^{-4} or 10^{-3} Å) a correct symmetry appears (and a further increase, e.g., to 10^{-2} Å, may produce an artificially high symmetry). Apparently the threshold choice should be related to the precision with which the coordinates themselves are computed. It should also be realized that a usage of internal coordinates with the strict symmetry requirements may not necessarily help as a possible imaginary frequency may be quite small (HF/STO-3G calculations [46] lead to D_{5d} symmetry, however, without vibrational analysis). Using such threshold variation we determined the symmetries presented in Table I. The results were consistent with exception of the **E** and **G** cases where reoptimization of already optimized structure sometimes resulted in a symmetry change that, however, was not permanent. Apparently, the numerical precision available was not sufficient to resolve the problem, and therefore we list two alternatives of symmetry for the two particular cases. However, we preferred the lower symmetry for them in the relative stability calculations, though we checked the effects of the higher symmetries, too—vide infra. Clearly enough, each of the **E** and **G** species is just one structure with well-established energy, etc., only the symmetry is not easy to decide owing to numerical imprecisions in Cartesian coordinates (the details on the computerized symmetry-finding procedure will be published elsewhere [47]).

The computations (both at room and at absolute zero temperature) point out the **C** isomer (D_{5d} symmetry) as the system ground state, being followed by the **A** species of a D_2 symmetry. This is in agreement with density functional computa-

TABLE I
The AM1 structures^a and energetics^b of the IPR structures of C₈₀.

Species	A (cm ⁻¹)	B (cm ⁻¹)	C (cm ⁻¹)	$\Delta H_{f,298,rel}^o$ (kJ/mol)	ΔE_{rel} (kJ/mol)	SAM1 ^c (kJ/mol)	HF/3-21G ^d (kJ/mol)
A <i>D</i> ₂	0.00179	0.00150	0.00142	21	22	17	10
B <i>D</i> ₂	0.00157	0.00156	0.00155	273	301	314	423
C <i>D</i> _{5d}	0.00188	0.00142	0.00142	0	0	0	0
D <i>C</i> _{2v}	0.00157	0.00156	0.00155	132	144	154	216
E <i>C</i> ₂ / <i>C</i> _{2v}	0.00167	0.00156	0.00146	73	77	75	98
F <i>C</i> ₂	0.00166	0.00165	0.00140	132	137	138	154
G <i>C</i> ₁ / <i>C</i> _s	0.00163	0.00156	0.00151	104	110	115	158

^a The rotational constants A, B, and C, and symmetries.

^b Relative heats of formation at room temperature ($\Delta H_{f,298,rel}^o$) or relative potential energies (ΔE_{rel}).

^c The SAM1 computed ΔE_{rel} terms.

^d The HF/3-21G ΔE_{rel} terms computed in the SAM1 optimized geometries.

tions [33]. We also computed the HOMO-LUMO gaps of the species and found the values 4.0, 4.02, 4.14, 4.15, 4.31, 4.72, and 4.95 eV for the **D**, **F**, **B**, **G**, **E**, **C**, and **A** isomers. Hence, the stability order deduced from the HOMO-LUMO gaps is not identical with the potential-energy order. We also checked the computed separation energies by the newly introduced SAM1 semiempirical method [48] (i.e., the geometries were fully reoptimized at the SAM1 level). Figure 2 shows that the results are basically parallel. However, the total values of the heats of formation differ as the SAM1 terms are considerably lower (but for the relative stabilities only relative heats of formation matter). Moreover, we also checked the relative potential energies ΔE_{rel} at an ab initio Hartree-Fock level, namely in the standard 3-21G basis set (HF/3-21G), though the ab initio computations were performed in the optimized SAM1 geometries (Table I). The semiempirical and ab initio results essentially agree. There is only a stability interchange between structures **F** and **G**. Experiments cannot supply separation energies for fullerene isomers at present. With the experimental information it is virtually impossible to decide which set of the computed separation energies is the best (though the question is not critical owing to the proximity of the results).

The vibrational calculations confirmed that all the seven localized stationary points are local energy minima as there was no imaginary frequency. Table II presents only 12 wavenumbers, selected out of 234 terms, for each isomer, namely the lowest, highest, and 10 infrared (IR) most intense wavenumbers. Even for those few representative

lines, we can see that the isomers are vibrationally different. In particular, the most intense line is located in different spectral regions for various structures. Of the seven isomers only the **C** species exhibits symmetry-adapted degeneracies (which is also seen in Table II). It has been well known that quantum chemical vibrational frequencies are somewhat overestimated comparing to experiment, and thus, scaling down (by a factor of about 0.9) is important for spectral predictions. But in

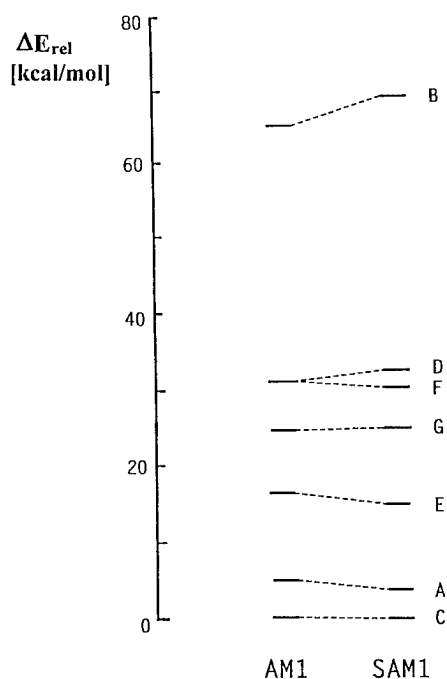


FIGURE 2. AM1 and SAM1 computed relative heats of formation of the IPR structures of C₈₀.

TABLE II
The AM1 lowest (ω_{\min}), 10 most intense^a (ω_{int}), and highest (ω_{\max}) harmonic vibrational wavenumbers (in cm^{-1}) for the IPR structures of C_{80} .

Species	$\omega_{\min} / \omega_{\text{int}}$	ω_{int}	ω_{int}	ω_{int}	ω_{int}	$\omega_{\text{int}} / \omega_{\max}$
A	211	918 (61)	1383 (65)	1540 (57)	1557 (51)	1604 (52)
	1616 (79)	1630 (53)	1747 (82)	1777 (67)	1832 (100)	1843
B	150	1102 (57)	1221 (64)	1235 (51)	1350 (100)	1363 (94)
	1369 (89)	1457 (72)	1532 (89)	1615 (67)	1641 (88)	1775
C	201	1436 (17)	1465 (26)	1582 (24)	1582 (24)	1610 (62)
	1610 (69)	1778 (100)	1802 (29)	1804 (19)	1804 (21)	1818
D	214	897 (43)	1247 (42)	1253 (36)	1326 (100)	1327 (40)
	1404 (45)	1487 (58)	1524 (36)	1670 (38)	1761 (34)	1902
E	224	904 (77)	1342 (58)	1347 (69)	1370 (92)	1380 (67)
	1505 (100)	1530 (43)	1622 (90)	1630 (78)	1830 (57)	1881
F	214	896 (100)	1295 (27)	1307 (64)	1334 (72)	1381 (85)
	1528 (27)	1677 (38)	1797 (52)	1807 (43)	1807 (42)	1863
G	227	900 (19)	1328 (100)	1356 (27)	1378 (16)	1489 (20)
	1505 (32)	1507 (14)	1611 (16)	1656 (19)	1779 (17)	1902

^a The relative IR intensities of ω_{int} are given in parentheses; the most intense frequency has the relative intensity of 100 (arbitrary units).

fact, such a uniform scaling has a negligible effect [41] for Eq. (1). Therefore, no scaling of the computed vibrational frequencies was applied in this study. Needless to add, IR intensity has spectral but no thermodynamic significance—in Eq. (1) all vibrational modes must be considered with equal significance. Although lower frequencies are generally more important for thermodynamic functions, it is the overall interplay of all the 234

modes that after all matters for the relative isomeric concentrations.

Table III reports the temperature evolution of the relative concentrations, w_i , for the seven-membered mixture under the thermodynamic equilibrium conditions. At very low temperatures the ground-state structures, **C**, has to prevail, and the relative concentrations of other structure have to obey the $\Delta H_{f,0,\text{rel}}^\circ$ order. But at higher tempera-

TABLE III
The AM1 equilibrium relative populations (%) of the IPR structures of C_{80} .

T (K)	A	B	C	D	E	F	G
500	3.20	4×10^{-24}	96.8	5×10^{-11}	3×10^{-5}	2×10^{-11}	4×10^{-8}
1000	30.0	1×10^{-9}	69.8	5×10^{-4}	0.17	1×10^{-4}	0.01
1485 ^a	48.6	9×10^{-5}	48.6	0.08	2.19	0.02	0.46
1500	49.0	1×10^{-4}	48.1	0.08	2.31	0.02	0.50
2000 ^b	53.9	0.03	34.3	1.00	7.48	0.23	3.06
	56.9	0.03	36.2	1.06	3.95	0.24	1.62
2500	49.3	0.67	24.2	3.87	13.1	0.83	7.93
3000	39.8	4.82	16.4	8.19	16.4	1.66	12.8
3345 ^a	31.9	12.0	12.0	10.8	16.4	2.14	14.7
3711 ^a	23.7	23.7	8.28	12.3	14.8	2.38	14.9
4000	18.1	34.4	6.00	12.5	12.8	2.37	13.9
5000	6.55	65.5	1.91	9.39	6.45	1.71	8.51

^a Two-structure equimolarity point.

^b The lower line for 2000 K (in *italics*) results from the C_{2v} and C_s symmetries of the **E** and **G** isomers, respectively (see Table I).

tures preexponential factors in Eq. (1) become important (while the importance of the exponential part is gradually decreased). At a temperature of 1485 K the A species reaches equimolarity with the C species and beyond that point is always more populated. Nevertheless, at considerably high temperatures (above 3700 K) actually the B species becomes the most populated one (though the temperatures are probably already too high from a practical point of view). This surprising high-temperature importance of the B isomer originates in the fact that it has the lowest low-frequency terms, though the chirality enhancement is relevant, too. Other four structures (D–G) are less important though not entirely negligible. It is of interest to note that the two structures with somewhat unclear symmetries, E and G, in fact do not change the overall picture even if their alternative (higher) symmetries are considered instead (as demonstrated for a temperature of 2000 K). Unfortunately, we cannot confront the computations with an observation yet.

A complex isomeric interplay can also be visualized in terms of heat capacity, namely as the difference between the standard molar heat capacity at constant pressure of the equilibrium isomeric mixture (the overall value C_p°) and a partial value $C_{p,i}^\circ$ belonging to one selected reference isomer, for example, C. This difference, the isomerism contribution $\delta C_{p,C}$, can frequently exhibit [41] a sharp temperature maximum (which could even be seen in the overall C_p° term). Such maximum is present in the C_{80} system, too, and it is quite pronounced. It is reached at about 3782 K and amounts to substantial 98.8 J/K mol⁻¹ (though it is only about 5% of the C_p° term at the temperature).

The reported considerable thermal effects on the relative isomeric stabilities result from an interplay between rotational, vibrational, potential-energy terms, and chirality factors. The whole scheme, however, refers to a thermodynamic equilibrium, though only to the interisomeric equilibrium. We can hardly say anything on the degree to which this presumption is satisfied in a future experiment. After all, fullerene synthesis is probably controlled by kinetics rather than by thermodynamics and it may explain why the C_{80} has not yet been isolated. Other explanation could be based on different charge distributions in the molecules (possibly connected with different solubility or adsorption properties). However, the most positive and most negative Mulliken charge in the A and C structures is about comparable with the AM1 val-

ues for C_{70} (though the spatial distribution of charges matters, too). Overall, computations predict that under the supposed fullerene-synthesis conditions the species A and C should primarily be produced (and the former one in a larger amount), and possibly other isomers in less significant concentrations. The proportions are, however, quite temperature sensitive and thus the particular temperature regime must be known.

Computations of C_{59}

Fullerenes are usually considered as even-atom cages built from pentagons and hexagons (while other related species are sometimes called pseudo-fullerenes). However, odd-numbered carbon aggregates have also been observed [49–51] around both $n = 60$ and $n = 120$. The observations are based on mass spectrometry and structural relationships are not well known. Hence, computations are useful and the computed structure of C_{61} was reported [42]. The computations [42] pointed out that rings other than pentagons and hexagons could also be significant, e.g., three- and seven-membered cycles. In fact, even with even-numbered fullerenes some other rings have occasionally been considered [43–57]. This section deals with computations of C_{59} , its structures, energetics, vibrations, and thermodynamics.

In contrast to even-numbered fullerenes, with odd fullerenes we cannot build the cage from three-coordinated carbon atoms only; this immediately follows from the relationship valid in conventional fullerenes between the number of atoms V and the number of bonds E : $3V = 2E$. Hence, we have to allow for two- or even four-coordinated atoms. Using Euler's theorem we can show that the number of pentagons (if we allow only for five- and six-membered rings) is generally different from 12. For example, if we consider one two-coordinated carbon atom (and the rest three-coordinated) the number of pentagons drops to 10. If we allow for just one four-coordinated atom, the number of pentagons changes to 14. With six two-coordinated atoms we can completely avoid pentagons. Rules are of course different if we include, for example, heptagons. With one heptagon and one two-coordinated carbon atom, the number of pentagons drops to 11, etc.

We can go even further and consider simultaneously two-, three-, and four-coordinated atoms in a

cage. Let the number of two-coordinated carbon atoms be p , and the number of four-coordinated q . If we still allow only pentagons and hexagons, we can evaluate the number of pentagons, n_5 , from Euler's formula:

$$n_5 = -2p + 2q + 12, \quad (2)$$

which of course reduces to the 12 pentagons if $p = q = 0$. There is a possibility that $n_5 = 0$, and also some parity requirements and value limitations.

One possible way to generate C_{59} topologies is to take a C_{58} structure and add two-coordinate carbon atom to a selected C-C bond. It is a useful approach though not all C_{59} structures can be generated this way. Moreover, we should consider all possible C_{58} isomers. This is of course impossible as it is estimated [58] that there should be, for example, 1037 isomers of C_{58} of C_1 symmetry (thus producing $1037 \times 87 = 90,219$ structures of C_{59}). Therefore we decided to limit ourselves only to the lowest known [59] structure of C_{58} . It has a topological symmetry C_{3v} , but it undergoes a Jahn-Teller distortion (Fig. 3).

We first selected the shortest and the longest bonds in the ground-state structure of C_{58} and added one carbon atom to them. It has turned out that the long C-C bonds led to considerably lower energies of the final C_{59} species. Therefore we concentrated on particularly long 6/6 and 5/6 bonds of the original C_{58} cage. Table IV surveys

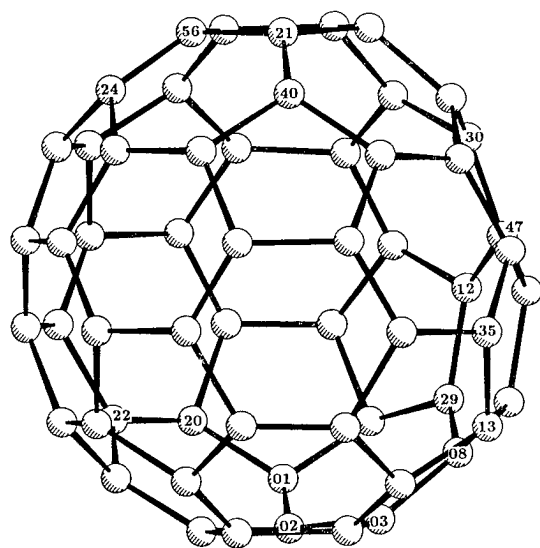


FIGURE 3. AM1 structure of C_{58} used in generation of some C_{59} isomers.

TABLE IV
AM1 energetics of the selected C_{59} structures.

Label ^a	Bridge ^b	Bridged Bond (Å)	$\Delta H_{f,298}^o$ (kJ/mol)	$\Delta H_{f,298,r}^o$ (kJ/mol)
6/8 ^c	5/7	2.319	4617	0
5/9 ^c	4/8	2.264	4670	52
12290 ^d	5/6	2.305	4695	77
0308 ^d	6/6	2.322	4701	83
7/7 ^c	6/6	2.331	4736	119
1335	5/5	1.592	4757	139
6/7 ^c	5/6	2.357	4780	163
1335o	5/5	2.177	4789	172
0203o	5/6	2.338	4810	193
0203	5/6	1.631	4819	201
1229	5/6	1.691	4822	205
0102	6/6	2.220	4822	205
2022	6/6	1.559	4828	211
2140	6/6	1.550	4829	212
2456	6/6	1.574	4840	222
3047	6/6	1.582	4878	260
3i ^e			5269	651
6/8i	5/7	1.524	5319	702
2456i	6/6	1.461	5356	739

^a The four-digit labels (see Fig. 3) for the numbering of atoms involved in the bridging. Suffix o denotes an open structure (in order to distinguish from the related closed structure); suffix i denotes an internal (in cage) location of the 59th carbon atom. The two-digit labels refer to structures not derived by a simple bridging and denote the rings in which the two-coordinated carbon atom is involved.

^b The type of the bond bridged over.

^c See Figure 4.

^d See Figure 5.

^e The 59th atom is bonded inside the cage to one atom only.

the computed results and uses numbering from Figure 3. Owing to addition of the C atom, C-C bond (6/6, 5/6, or 5/5) can either remain or can be broken as clearly indicated by the bond lengths of the critical bonds after the full geometry optimization. Figure 4 presents two lowest C_{59} structures derived from C_{58} . The bridged bonds in Figure 4 are of 5/6 and 6/6 types, and both structures are open (the critical bond broken); this creates one and two heptagons, respectively, in the C_{59} cage.

Another, less systematic way of C_{59} generation can start from C_{60} : remove one carbon atom, and reconstruct the cage. By this approach we could generate four additional structures (Fig. 5). They contain one eight- (6/8), one nine- (5/9), three seven- (7/7), and two seven-membered rings (6/7). In both generation approaches we tried to create a

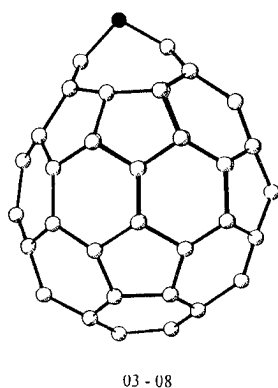
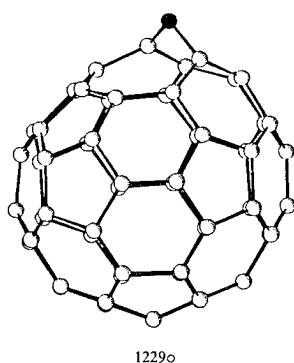


FIGURE 4. Two low-energy C_{59} structures derived from C_{58} in Figure 3.

structure with a four-coordinated carbon atom but the geometry optimizations never converged to such a structure. Finally, we also optimized three structures with the 59th atom inside (and not outside) the cage; they are all high in energy (Table IV).

We can select a limited set of four isomers, the ground state and three species separated from it by less than 100 kJ/mol. The ground state contains eight-membered ring (6/8, C_1 symmetry), being followed by the species with nine-membered ring

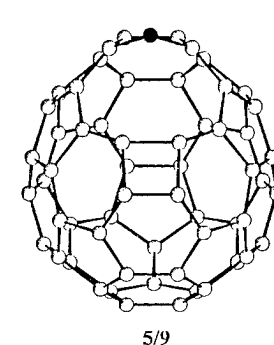
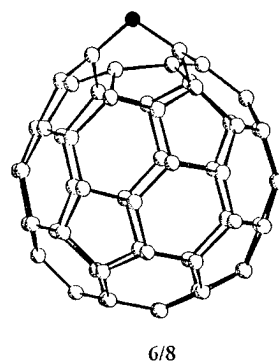
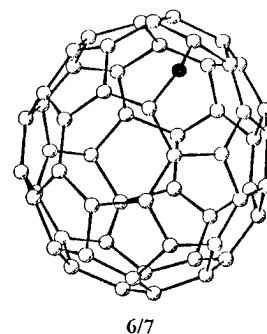
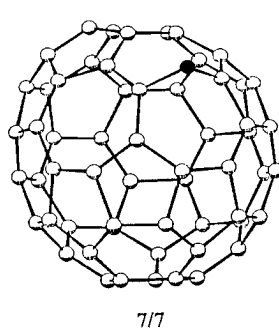


FIGURE 5. Four low-energy C_{59} structures not derived from C_{58} in Figure 3.

(5/9, C_s symmetry). Then, two structures derived from Figure 3 follow, 1229o (C_1 symmetry) and 0308 (C_s symmetry). The computed HOMO-LUMO gaps of the 6/8, 5/9, 1229o, and 0308 structures are 5.7, 6.4, 3.9, and 4.9 eV, respectively. Hence, they do not exactly follow the stability order given by the heats of formation at room temperature (Table IV).

Table V presents rotational constants and three intense IR lines for the four low-energy structures of C_{59} . Variation in the rotational constants is not very significant. However, there are differences in

TABLE V
AM1 computed structural and vibrational characteristics of the four lowest C_{59} isomers.^a

Isomer	A (cm ⁻¹)	B (cm ⁻¹)	C (cm ⁻¹)	ω_i^b (cm ⁻¹)
6/8	0.00299	0.00279	0.00277	1692 / 100
5/9	0.00297	0.00279	0.00275	1286 / 100
1229o	0.00300	0.00281	0.00278	1061 / 100
0308	0.00296	0.00286	0.00278	1444 / 79

^a See Table IV and Figures 4 and 5.

^b Only the three IR most intense vibrational wavenumbers are presented followed by their relative IR intensities (after the slash).

TABLE VI
Temperature dependency of the equilibrium mole fractions w_i of the four lowest C_{59} isomers.^a

Isomer	w_i (%)						
	500 ^b	1000 ^b	1500 ^b	2000 ^b	2500 ^b	3000 ^b	4000 ^b
6/8	100.0	99.83	98.40	94.89	89.73	83.87	72.70
5/9	3×10^{-4}	0.16	1.31	3.67	6.59	9.46	14.00
1229o	7×10^{-7}	8×10^{-3}	0.20	0.99	2.47	4.42	8.69
0308	1×10^{-7}	3×10^{-3}	0.09	0.46	1.21	2.25	4.62

^a See Table IV for the structure labeling.

^b Temperature in K.

the positions of the IR intense lines, and they could play some role in experimental identification of the structures.

Although the energy separation of the four low-energy isomers is rather small, entropy does not compensate it in this particular case. As can be seen in Table VI, the ground-state structure **6/8** remains the far most populated, prevailing species even at very high temperatures. However, this result is valid only for the thermodynamic equilibrium, and we cannot decide if this should really happen in an experiment. There may be differences in kinetic barriers between the structures originated in simple additions of one carbon atom to C_{58} and the structures produced by reorganization after a carbon release from C_{60} (the first channel may be more common). Finally, it is interesting to note the position of C_{59} with respect to C_{60} in the AM1 computed heats of formation per particle—it is higher by about 10.4 kJ/mol atom. The supposed AM1 ground state of C_{58} is placed about 8.17 kJ/mol atom above C_{60} . From this point of view, the C_{59} species are actually not particularly high in energy.

As a two-coordinated carbon atom is involved, we can ask about triplet electronic states. There is a difficulty in computing their separation energies. The unrestricted HF (UHF) treatment has better convergency properties over the open-shell restricted Hartree-Fock procedure (ROHF). However, the energies from the UHF treatment are not directly comparable with the values for closed-shell structures (owing to the higher flexibility of the UHF wave function the stabilities of triplet species are overestimated [52]). On the other hand, the ROHF computations frequently diverge.

This study points out some interesting, new geometrical relationships in fullerenes, once we relax the carbon coordination number. Moreover, it indicates that arrangements with larger rings

tend to be energetically more convenient in the odd fullerenes. A deeper insight, however, requires some knowledge on kinetics of the formation processes. The suggested approach could also be applied to other odd-numbered species, like C_{57} or C_{55} , known from mass spectra [50], too.

Note Added in Proof. Michel et al. [60] reported separation of a C_{80} species for which they concluded D_2 symmetry, this being in agreement with our prediction for higher temperatures (Table III, species **A**).

ACKNOWLEDGMENTS

Acknowledgments are made to the National Science Council, Taiwan, and the National Chung-Cheng University for financial support. The authors also thank the National Center for High-Performance Computing in Hsinchu for computer time on the Convex C3840 and SPP 1000.

References

1. P. W. Fowler, R. C. Batten, and D. E. Manolopoulos, *J. Chem. Soc., Faraday Trans.* **87**, 3103 (1991).
2. F. Diederich, R. L. Whetten, C. Thilgen, R. Ettl, I. Chao, and M. M. Alvarez, *Science* **254**, 1768 (1991).
3. K. Kikuchi, N. Nakahara, T. Wakabayashi, S. Suzuki, H. Shiromaru, Y. Miyake, K. Saito, I. Ikemoto, M. Kainosho, and Y. Achiba, *Nature* **357**, 142 (1992).
4. D. Bakowies, A. Geleßus, and W. Thiel, *Chem. Phys. Lett.* **197**, 324 (1992).
5. Z. Slanina, J.-P. François, D. Bakowies, and W. Thiel, *J. Mol. Struct. (THEOCHEM)* **279**, 213 (1993).
6. K. Kikuchi, N. Nakahara, T. Wakabayashi, M., Honda, H. Matsumiya, T. Moriwaki, S. Suzuki, H. Shiromaru, K. Saito, K. Yamauchi, I. Ikemoto, and Y. Achiba, *Chem. Phys. Lett.* **188**, 177 (1992).

7. M. Hoinkis, C. S. Yannoni, D. S. Bethune, J. R. Salem, R. D. Johnson, M. S. Crowder, and M. S. de Vries, *Chem. Phys. Lett.* **198**, 461 (1992).
8. S. Nagase, K. Kobayashi, T. Kato, and Y. Achiba, *Chem. Phys. Lett.* **201**, 475 (1993).
9. G. Orlandi, F. Zerbetto, and P. W. Fowler, *J. Phys. Chem.* **97**, 13575 (1993).
10. M. Okada, K. Okahara, K. Tanaka, and T. Yamabe, *Chem. Phys. Lett.* **209**, 91 (1993).
11. S. Nagase and K. Kobayashi, *Chem. Phys. Lett.* **214**, 57 (1993).
12. X. Q. Wang, C. Z. Wang, B. L. Zhang, and K. M. Ho, *Chem. Phys. Lett.* **217**, 199 (1994).
13. Z. Slanina, S.-L. Lee, K. Kobayashi, and S. Nagase, *J. Mol. Struct. (THEOCHEM)* **339**, 89 (1995).
14. F. Diederich, R. Ettl, Y. Rubin, R. L. Whetten, R. Beck, M. Alvarez, S. Anz, D. Sensharma, F. Wudl, K. C. Khemani, and A. Koch, *Science* **252**, 548 (1991).
15. R. D. Beck, P. S. John, M. M. Alvarez, F. Deiderich, and R. L. Whetten, *J. Phys. Chem.* **95**, 8402 (1991).
16. K. Kikuchi, N. Nakahara, M. Honda, S. Suzuki, K. Saito, H. Shiromaru, K. Yamauchi, I. Ikemoto, T. Kuramochi, S. Hino, and Y. Achiba, *Chem. Lett.* 1607 (1991).
17. K. A. Caldwell, D. E. Giblin, and M. L. Gross, *J. Am. Chem. Soc.* **114**, 3743 (1991).
18. S. Hino, K. Matsumoto, S. Hasegawa, K. Kamiya, H. Inokuchi, T. Morikawa, T. Takahashi, K. Seki, K. Kikuchi, S. Suzuki, I. Ikemoto, and Y. Achiba, *Chem. Phys. Lett.* **190**, 169 (1992).
19. J. F. Anacleto, H. Perreault, R. K. Boyd, S. Pleasance, M. A. Quilliam, P. G. Sim, J. B. Howard, Y. Makarovsky, and A. L. Lafleur, *Commun. Mass Spectr.* **6**, 214 (1992).
20. K. Raghavachari and C. M. Rohlfing, *J. Phys. Chem.* **95**, 5768 (1991).
21. P. W. Fowler, *J. Chem. Soc., Faraday Trans.* **87**, 1945 (1991).
22. D. Bakowies and W. Thiel, *J. Am. Chem. Soc.* **113**, 3704 (1991).
23. F. Negri, G. Orlandi, and F. Zerbetto, *Chem. Phys. Lett.* **189**, 495 (1992).
24. P. W. Fowler, D. E. Manolopoulos, and R. P. Ryan, *J. Chem. Soc., Chem. Commun.* 408 (1992).
25. K. Raghavachari, *Chem. Phys. Lett.* **190**, 397 (1992).
26. X.-Q. Wang, C. Z. Wang, B. L. Zhang, and K. M. Ho, *Phys. Rev. Lett.* **69**, 69 (1992).
27. D. Bakowies, M. Kolb, W. Thiel, S. Richard, R. Ahlrichs, and M. M. Kappes, *Chem. Phys. Lett.* **200**, 411 (1992).
28. D. E. Manolopoulos, P. W. Fowler, R. Taylor, H. W. Kroto, and D. R. M. Walton, *J. Chem. Soc., Faraday Trans.* **88**, 3117 (1992).
29. P. W. Fowler, D. E. Manolopoulos, and R. P. Ryan, *Carbon* **30**, 1235 (1992).
30. Z. Slanina, J.-P. François, M. Kolb, D. Bakowies, and W. Thiel, *Fullerene Sci. Technol.* **1**, 221 (1993).
31. Z. Slanina and S.-L. Lee, *NanoStruct. Mater.* **4**, 39 (1994).
32. S. J. Woo, E. Kim, and Y. H. Lee, *Phys. Rev. B* **47**, 6721 (1993).
33. K. Nakao, N. Kurita, and M. Fujita, *Phys. Rev. B* **49**, 11415 (1994).
34. Z. Slanina, *Chem. Phys. Lett.* **173**, 164 (1990).
35. Z. Slanina, S.-L. Lee, K. Kobayashi, and S. Nagase, *J. Mol. Struct. (THEOCHEM)* **312**, 175 (1994).
36. D. E. Manolopoulos and P. W. Fowler, *J. Chem. Phys.* **96**, 7603 (1992).
37. M. J. S. Dewar, E. G. Zoebisch, E. F. Healy, and J. J. P. Stewart, *J. Am. Chem. Soc.* **107**, 3902 (1985).
38. W. J. Hehre, L. D. Burke, and A. J. Schusterman, SPARTAN (Wavefunction, Inc., Irvine, 1993).
39. M. J. Frisch, G. W. Trucks, M. Head-Gordon, P. M. W. Gill, M. W. Wong, J. B. Foresman, B. G. Johnson, H. B. Schlegel, M. A. Robb, E. S. Replogle, R. Gomperts, J. L. Andres, K. Raghavachari, J. S. Binkley, C. Gonzalez, R. L. Martin, D. J. Fox, D. J. Defrees, J. Baker, J. J. P. Stewart, and J. A. Pople, "GAUSSIAN 92, Revision C" (Gaussian Inc., Pittsburgh, 1992).
40. J. J. P. Stewart, MOPAC 5.0 (QCPE 455, Indiana University, 1990).
41. Z. Slanina, *Int. Rev. Phys. Chem.* **6**, 251 (1987).
42. P. W. Fowler, *Chem. Phys. Lett.* **131**, 444 (1986).
43. R. D. Bendale, J. F. Stanton, and M. C. Zerner, *Chem. Phys. Lett.* **194**, 467 (1992).
44. N. Koga and K. Morokuma, *Chem. Phys. Lett.* **196**, 191 (1992).
45. R. Saito, G. Dresselhaus, and M. S. Dresselhaus, *Chem. Phys. Lett.* **210**, 159 (1993).
46. G. E. Scuseria, In *Buckminsterfullerenes*, W. E. Billups and M. A. Ciufolini, Eds. (VCH, New York, 1993).
47. F. Uhlík, Z. Slanina, and S.-L. Lee, to appear.
48. M. J. S. Dewar, C. Jie, and J. Yu, *Tetrahedron Lett.* **49**, 5003 (1993).
49. J. F. Christian, Z. Wan, and S. L. Anderson, *J. Phys. Chem.* **96**, 3574 (1992).
50. J.-P. Deng, D.-D. Ju, G.-R. Her, C.-Y. Mou, C.-J. Chen, Y.-Y. Lin, and C.-C. Han, *J. Phys. Chem.* **97**, 11575 (1993).
51. S. W. McElvany, J. H. Callahan, M. M. Ross, L. D. Lamb, and D. R. Huffman, *Science* **260**, 1632 (1993).
52. Z. Slanina and S.-L. Lee, *J. Mol. Struct. (THEOCHEM)* **304**, 173 (1994).
53. A. D. J. Haymet, *Chem. Phys. Lett.* **122**, 421 (1985).
54. T. I. Shibuya and M. Yoshitani, *Chem. Phys. Lett.* **137**, 13 (1987).
55. R. L. Murry and G. E. Scuseria, *Science* **263**, 791 (1994).
56. B. I. Dunlap and R. Taylor, *J. Phys. Chem.* **98**, 11018 (1994).
57. Z. Slanina and S.-L. Lee, *Fullerene Sci. Technol.*, to appear.
58. D. Babić, D. J. Klein, and C. H. Sah, *Chem. Phys. Lett.* **211**, 235 (1993).
59. R. E. Stanton, *J. Phys. Chem.* **96**, 111 (1992).
60. R. Michel, D. Fuchs, E. Werner, H. Eisler, S. Richard, F. Hennrich, C. Lehner, M. Fanti, F. Zerbetto, and M. M. Kappes, *International Winterschool on Electronic Properties of Novel Materials*, Kirchberg, 1996, p. 70.

Investigation on the Interaction on and the Rotation of C_{60} in Alkali-Doped Complexes $A_X A'_{3-X} C_{60}$ ($X = 1, 2, 3$; $A, A' = \text{Alkali}$)

JI-MIN YAN* and CHUAN-BAO ZHU

Institute of Chemistry, Academia Sinica, Beijing 100080, People's Republic of China; email for J.-M. Y.: huangsi@rose.cnc.ac.cn

ZHI-JIN XU

Institute of Chemistry, Academia Sinica, Beijing 100080, People's Republic of China; and Institute of Applied Physics and Computational Mathematics, Beijing 100088, People's Republic of China

Received February 25, 1996; revised manuscript received April 18, 1996; accepted April 24, 1996

ABSTRACT

The interaction on and the rotation of C_{60} in alkali-doped C_{60} solids, $A_X A'_{3-X} C_{60}$ ($X = 1, 2, 3$; $A, A' = \text{alkali}$), have been calculated with Buckingham potential model. The results show that the total interaction on C_{60} changes dramatically when the pure C_{60} solid is alkali-doped into K_3C_{60} . The interaction on C_{60} in K_3C_{60} is about 20 times greater than that in pure C_{60} . And the main component in the former, occupying $> 90\%$ is electrostatic, while in the latter, the main components, occupying $> 90\%$, are dispersive and repulsive. The results also show that in contrast to the whole-region free rapid rotation of C_{60} molecule in its pure solid, the rotation of C_{60} in K_3C_{60} is mostly forbidden due to a 10 times increase (reaching about 300 kJ/mol) in potential barrier, except for the region from 0° to 50° where a broad, smooth, and shallow potential well exists. Calculations for alkali-doped complexes other than K_3C_{60} , i.e., $A_X A'_{3-X} C_{60}$ ($X = 1, 2, 3$; $A, A' = K, Rb, Cs$), come to the same conclusion. Finally, an interesting and meaningful result is that the superconducting transition temperatures of $A_X A'_{3-X} C_{60}$ ($X = 1, 2, 3$; $A, A' = K, Rb, Cs$) change inversely with the total interactions on C_{60} .

© 1995 John Wiley & Sons, Inc.

*To whom correspondence should be addressed.

Introduction

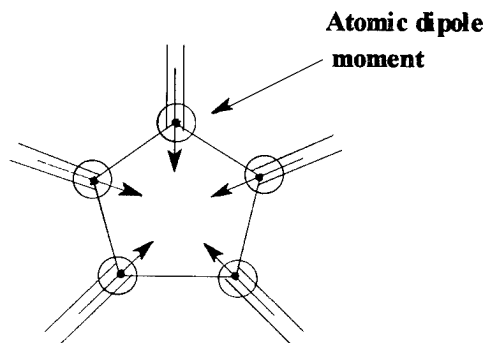
Pure C_{60} solid is an insulator, whose C_{60} molecules rotate very rapidly on the lattice points [1-4]. However, alkali-doped C_{60} solids, $A_x A'_{3-x} C_{60}$ ($x = 1, 2, 3$; $A, A' = K, Rb, Cs$), are not only conductors but also superconductors at low temperatures [5-16], and the rotation of C_{60} molecules are assumed to be forbidden by the lattice geometry [5, 11]. Clearly, the properties of alkali-doped C_{60} solids are very different from those of pure C_{60} solid. Scientists have been interested in this issue and contributed a great deal to the literature [15, 17-37]. Generally, they have paid more attention to the lattice geometry. It is held that the lattice of C_{60} solid expands after being doped with alkali atoms, and then the frontier energy bands become narrow and the density of states on the Fermi surface increases, so that the superconducting transition temperature T_C increases [15, 16, 29, 37]. As for the dynamics properties, some authors also hold that the free rapid rotations of C_{60} molecules are forbidden after the solid is doped with alkali atoms, since there is no room for C_{60} molecules to rotate [5, 11]. However, the expansions of the lattice constant are small, about 0.004 nm from C_{60} solid to K_3C_{60} solid and about 0.032 nm from K_3C_{60} solid to $RbCs_2C_{60}$ solid. It is not convincing that simply such small expansions change an insulator into superconductors and even raise the transition temperatures from 2.5 to 33 K [6, 7, 12, 13]. Furthermore, the distance between an A (or A') and a C on C_{60} is much longer than the sum of their van der Waals radii, therefore one may wonder how the free rapid rotation of C_{60} could be forbidden simply by the lattice geometry. In short, the insignificant variations of lattice constant cannot satisfactorily explain the sudden property changes for the solid from being insulator to being superconductor and for C_{60} molecules from being able to rotate freely and rapidly to being forbidden from that. In this study we consider the sudden change of physical interaction on C_{60} , instead of the lattice geometrical change, as the essential reason for the sudden property changes mentioned above. The interactions on C_{60} in both pure C_{60} solid and alkali-doped C_{60} solids, $A_x A'_{3-x} C_{60}$ ($x = 1, 2, 3$; A, A'

= K, Rb, Cs), have been calculated, and the results show that there is a sudden change in interaction from the former to the latter, which corresponds to the sudden change of C_{60} 's rotation and the conversion from insulator to superconductor.

Computational Model

Alkali-doped C_{60} solids, $A_x A'_{3-x} C_{60}$ ($x = 1, 2, 3$; $A, A' = K, Rb, Cs$), all have the same crystallography features as the pure C_{60} solid. They all belong to the face-centered-cubic (fcc) structure form, in which A and/or A' atoms occupy both the tetrahedral and the octahedral interstitial sites [7, 8, 10-12, 19]. For each C_{60} in $A_x A'_{3-x} C_{60}$, there are 12 nearest neighbors of C_{60} and 14 nearest neighbors of A and/or A'. Of these alkali atoms 8 are filled in the rooms of 8 tetrahedrons and 6 in the rooms of 6 octahedrons. Since the room volume of the tetrahedron is smaller than that of the octahedron, the alkali atom with smaller radius will first reside in the room of tetrahedron. In order to express the computational model for the interactions on C_{60} clearly and accurately, the form of Table I is used, where the center C_{60} is put at the origin point in a Cartesian coordinate system and it rotates around the axis [1 1 1].

In C_{60} solid, although each C atom in C_{60} is electroneutral, because each C links with one short (or double) bond and two long (or single) bond, the atomic point dipole moment on each C atom is not equal to zero, shown as follows:

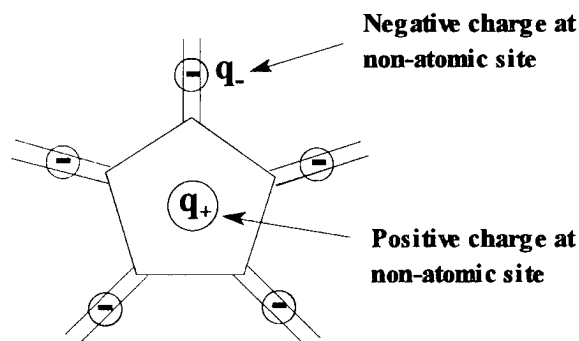


It is inconvenient to operate atomic point dipole moments. Therefore, to make the operation convenience, the distribution of atomic site dipole moments is transformed to the distribution of

TABLE I
The coordinates of the neighbors around the center C₆₀.

Sort and number of neighbors	Coordinate	State
Four C ₆₀	$(\frac{1}{2}, \frac{1}{2}, 0), (\frac{1}{2}, -\frac{1}{2}, 0)$ $(-\frac{1}{2}, -\frac{1}{2}, 0), (\frac{1}{2}, -\frac{1}{2}, 0)$	On xy plane and rotating synchronously with center C ₆₀ around the $[1 \bar{1} \bar{1}]$ axis
Four C ₆₀	$(0, \frac{1}{2}, \frac{1}{2}), (0, -\frac{1}{2}, \frac{1}{2}),$ $(0, -\frac{1}{2}, -\frac{1}{2}), (0, \frac{1}{2}, -\frac{1}{2})$	On yz plane and rotating synchronously with center C ₆₀ around the $[\bar{1} 1 \bar{1}]$ axis
Four C ₆₀	$(\frac{1}{2}, 0, \frac{1}{2}), (\frac{1}{2}, 0, -\frac{1}{2}),$ $(-\frac{1}{2}, 0, -\frac{1}{2}), (-\frac{1}{2}, 0, \frac{1}{2})$	On zx plane and rotating synchronously with center C ₆₀ around the $[\bar{1} \bar{1} 1]$ axis
Eight A and / or A'	$(\frac{1}{4}, \frac{1}{4}, \frac{1}{4}), (-\frac{1}{4}, \frac{1}{4}, \frac{1}{4}),$ $(-\frac{1}{4}, -\frac{1}{4}, \frac{1}{4}), (\frac{1}{4}, -\frac{1}{4}, \frac{1}{4}),$ $(\frac{1}{4}, \frac{1}{4}, -\frac{1}{4}), (-\frac{1}{4}, \frac{1}{4}, -\frac{1}{4}),$ $(-\frac{1}{4}, -\frac{1}{4}, -\frac{1}{4}), (\frac{1}{4}, -\frac{1}{4}, -\frac{1}{4})$	At the center of tetrahedron composed of four C ₆₀ 's
Six A and / or A'	$(\frac{1}{2}, 0, 0), (-\frac{1}{2}, 0, 0),$ $(0, \frac{1}{2}, 0), (0, -\frac{1}{2}, 0),$ $(0, 0, \frac{1}{2}), (0, 0, -\frac{1}{2})$	At the center of octahedron composed of six C ₆₀ 's

nonatomic site charges as follows:



This is to say that there is a nonatomic site positive charge with $Q^+ = 5q$ on each of the 12 centers of five-membered ring, and a nonatomic site negative charge with $Q^- = 2q$ on each of the 30 centers of short bond, q being the effective charge. It has been already known from simulation that $q = 0.13|e|$ [38]. It follows that the interactions on nonatomic site charges should also be considered in calculation.

Interaction Potential

In solids of pure C₆₀ and A_XA'_{3-X}C₆₀ (X = 1, 2, 3; A, A' = K, Rb, Cs), the distance between two

atoms on different molecules or components is larger than the sum of their van der Waals radii; therefore it is convenient and accurate using Buckingham [40, 41] potential to calculate the interaction of atom pairs mentioned above.

For the sake of conciseness, the calculating formulas of interaction on the center C₆₀ are only given in some detail in the case of when A = A' (= K). It is easy to transform these formulas into those when A ≠ A'. The calculation includes two steps, in which the first step is to calculate the interaction on C₆₀ in pure C₆₀ solid, namely $E(C_{60})$:

$$E_{\text{rep}}(C_{60})(\omega) = \sum_{i=1}^{60} \sum_{k=1}^{12} \sum_{j=1}^{60} B_{C-C} \times \exp[-C_{C-C} \cdot r_{ij(k)}(\omega)], \quad (1)$$

$$E_{\text{dis}}(C_{60})(\omega) = \sum_{i=1}^{60} \sum_{k=1}^{12} \sum_{j=1}^{60} A_{C-C} r_{ij(k)}^{-6}(\omega), \quad (2)$$

$$E_{\text{es}}(C_{60})(\omega) = \sum_{i=1}^{12} \sum_{k=1}^{12} \sum_{j=1}^{12} Q_{pi} Q_{pj} r_{ij(k)}^{-1}(\omega) + \sum_{i=1}^{12} \sum_{k=1}^{12} \sum_{j=1}^{30} Q_{pi} Q_{nj} r_{ij(k)}^{-1}(\omega)$$

$$\begin{aligned}
& + \sum_{i=1}^{30} \sum_{k=1}^{12} \sum_{j=1}^{12} Q_{ni} Q_{pj} r_{ij(k)}^{-1}(\omega) \\
& + \sum_{i=1}^{30} \sum_{k=1}^{12} \sum_{j=1}^{30} Q_{ni} Q_{nj} r_{ij(k)}^{-1}(\omega). \quad (3)
\end{aligned}$$

The second step is to calculate the interactions on C_{60} in alkali-doped C_{60} solid, namely $E(K_3C_{60})$:

$$\begin{aligned}
E_{\text{rep}}(K_3C_{60})(\omega) &= E'_{\text{rep}}(C_{60})(\omega) \\
&+ \sum_{i=1}^{60} \sum_{j=1}^8 B_{C-K} \exp[-C_{C-K} r_{ij}(\omega)] \\
&+ \sum_{i=1}^{60} \sum_{j=1}^6 B_{C-K} \exp[-C_{C-K} r'_{ij}(\omega)], \quad (4)
\end{aligned}$$

$$\begin{aligned}
E_{\text{dis}}(K_3C_{60})(\omega) &= E'_{\text{dis}}(C_{60})(\omega) \\
&+ \sum_{i=1}^{60} \sum_{j=1}^8 A_{C-K} r_{ij}^{-6}(\omega) \\
&+ \sum_{i=1}^{60} \sum_{j=1}^6 A_{C-K} r'_{ij}^{-6}(\omega), \quad (5)
\end{aligned}$$

$$\begin{aligned}
E_{\text{es}}(K_3C_{60})(\omega) &= E'_{\text{es}}(C_{60})(\omega) \\
&+ \sum_{i=1}^{60} \sum_{j=1}^8 Q_{Ci} Q_{Kj} r_{ij}^{-1}(\omega) \\
&+ \sum_{i=1}^{60} \sum_{j=1}^6 Q_{Ci} Q_{Kj} r'_{ij}^{-1}(\omega) \\
&+ \sum_{i=1}^{12} \sum_{j=1}^8 Q_{pi} Q_{Kj} r_{ij}^{-1}(\omega) \\
&+ \sum_{i=1}^{12} \sum_{j=1}^6 Q_{pi} Q_{Kj} r'_{ij}^{-1}(\omega) \\
&+ \sum_{i=1}^{30} \sum_{j=1}^8 Q_{ni} Q_{Kj} r_{ij}^{-1}(\omega)
\end{aligned}$$

$$\begin{aligned}
& + \sum_{i=1}^{30} \sum_{j=1}^6 Q_{ni} Q_{Kj} r'_{ij}^{-1}(\omega) \\
& + \sum_{i=1}^{60} \sum_{k=1}^{12} \sum_{j=1}^{60} Q_{Ck} Q_{Cj(k)} r_{ij(k)}^{-1}(\omega) \\
& + \sum_{i=1}^{60} \sum_{k=1}^{12} \sum_{j=1}^{12} Q_{Ci} Q_{pj(k)} r_{ij(k)}^{-1}(\omega) \\
& + \sum_{i=1}^{60} \sum_{k=1}^{12} \sum_{j=1}^{30} Q_{Ci} Q_{nj(k)} r_{ij(k)}^{-1}(\omega) \\
& + \sum_{i=1}^{12} \sum_{k=1}^{12} \sum_{j=1}^{60} Q_{pi} Q_{Cj(k)} r_{ij(k)}^{-1}(\omega) \\
& + \sum_{i=1}^{30} \sum_{k=1}^{12} \sum_{j=1}^{60} Q_{ni} Q_{Cj(k)} r_{ij(k)}^{-1}(\omega), \quad (6)
\end{aligned}$$

where ω is the rotation angle of the C_{60} molecules, and the $E'(C_{60})$ denotes the corresponding interaction on C_{60} as in the pure C_{60} solid, but the lattice constant is already changed into the one as that in the K-doped C_{60} solid, K_3C_{60} solid.

The coupling potential parameters needed in the calculation are listed in Table II.

Interaction on C_{60} and Transition Temperatures of the Superconductors

Pure C_{60} solid is an insulator, but $A_X A'_{3-X} C_{60}$ ($X = 1, 2, 3$; $A, A' = K, Rb, Cs$) are superconductors, and it has been noted that the transition temperatures T_C have a parallel relationship with their lattice constants a . In the literature, it has been held because of the increasing of the lattice constant, the energy bands will be changed to narrow, and then the density of states on the Fermi surface increases, so that the transition temperatures T_C increase. After A and/or A' are filled into the C_{60} solid, the lattice of the doped solid is

TABLE II
Coupling potential parameters for some atom pairs.

Atom pair	B (kJ/mol)	C (nm ⁻¹)	A (10 ⁻⁸ kJ · nm ⁶ /mol)	Refs.
C-C	369743.0	0.36000	-24.39800	[39, 40]
K-C	11791.062	0.30450	-6.89781	[41, 42]
Rb-C	11058.562	0.28675	-8.67123	[41, 42]
Cs-C	10215.256	0.28184	-9.34565	[41, 42]

expanded, but it is a gradual, not a sudden change. Therefore, this geometrical factor of cell change may not be a good reason for the sudden change of the electricity and the superconductivity.

In this work, the interactions on C₆₀ in C₆₀ solid and in A_XA'_{3-X}C₆₀ (X = 1, 2, 3; A, A' = K, Rb, Cs) solids have been calculated. From the computational results, it is seen that there is a sudden change for the interactions on C₆₀ from in pure C₆₀ solid (-435.5 kJ/mol) to in alkali-doped C₆₀ solids, A_XA'_{3-X}C₆₀ (X = 1, 2, 3; A, A' = K, Rb, Cs), for example, -9517.1 kJ/mol for K₃C₆₀. Therefore, it will be important and interesting to associate the physical factor of interaction on C₆₀ with the superconducting transition temperature T_C, and the relationship between them is shown in Table III.

From the data listed in Table III, it can be easily seen that there is an antiparallel change relationship between the superconducting temperatures T_C and the interactions on C₆₀ in A_XA'_{3-X}C₆₀ (X = 1, 2, 3; A, A' = K, Rb, Cs) solids. One can see this relationship more clearly from Figure 1.

The Interaction on and the Rotation Dynamics of C₆₀

A series of interaction on C₆₀ in the range of $\omega = 0-120^\circ$ have been calculated, which are shown in Figure 2. For ease of comparison, the relative interaction $RE(\omega) = E(\omega) - E(0)$ is used in this figure.

Figure 2 shows that the absolute values of the total interaction E_{tot} on C₆₀ in K₃C₆₀ solid is about 20 times greater than that in pure C₆₀ solid, and the corresponding relative variation in K₃C₆₀ solid is about 10 times greater than that in C₆₀ solid; the absolute value of the electrostatic interaction E_{es} on C₆₀ in K₃C₆₀ solid is about 60 times greater than that in solid C₆₀, and the corresponding relative variation in K₃C₆₀ solid is about 15 times

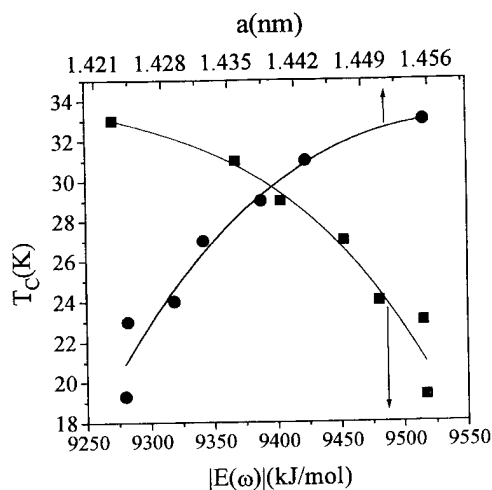


FIGURE 1. Transition temperatures T_C vs. interactions |E(ω)| on C₆₀ or lattice constants a.

greater than that in C₆₀ solid; the repulsive and the dispersive interactions in two systems do not change too much. It is also seen that the electrostatic interaction is the essential component in K₃C₆₀ solid, being > 90%, but the repulsive and the dispersive interactions are the essential components in the C₆₀ solid, being > 90%.

Making a comparison of the potential barriers between two systems of the pure C₆₀ solid and the alkali-doped C₆₀ solid, K₃C₆₀ solid, it can be seen that in pure C₆₀ solid, the rotation potential barrier is low, ~ 31 kJ/mol, which can be overcome by the thermomotion. Then the C₆₀ molecule can rotate rapidly and freely; while in alkali-doped C₆₀ solid, K₃C₆₀ solid, the potential barrier is high, up to ~ 280 kJ/mol, which cannot be overcome by thermomotion. Therefore, the rotation of the C₆₀ molecule will be forbidden in K₃C₆₀ solid. But it is also seen that there is a broad and smooth potential well in the region from 0° to 50°. Then the C₆₀ molecule can rotate in this region at room temperature. In other words, the rotation of C₆₀ molecule

TABLE III
Comparison of the interactions on C₆₀ and the superconducting transition temperatures (nm; kJ/mol; K).

Solid	C ₆₀	K ₃ C ₆₀	K ₂ RbC ₆₀	K ₂ CsC ₆₀	KRb ₂ C ₆₀	Rb ₃ C ₆₀	Rb ₂ CsC ₆₀	RbCs ₂ C ₆₀
a	1.420	1.4240	1.4243	1.4292	1.4323	1.4384	1.4431	1.4555
E _{tot} (0)	-435.5	-9517.1	-9515.1	-9480.7	-9452.9	-9403.4	-9368.1	-9271.7
T _C		19.3	23	24	27	29	31	33

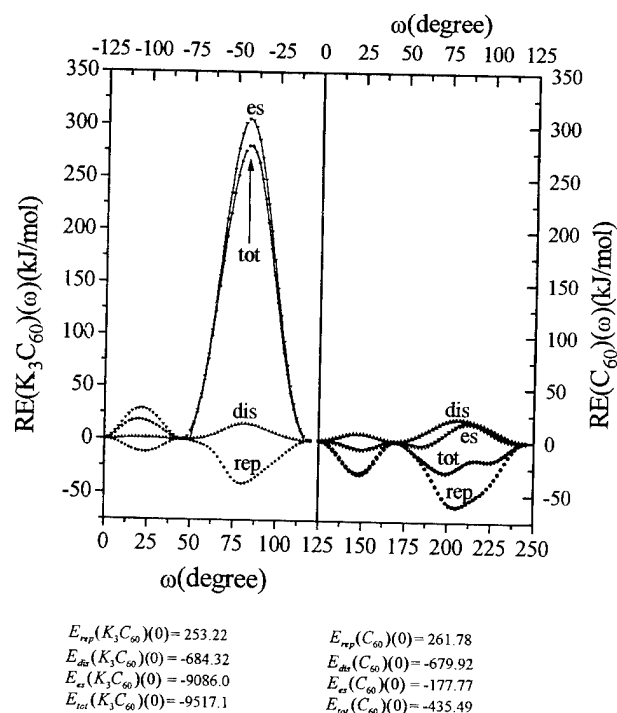


FIGURE 2. Relative interaction energy $RE(\omega)$ vs. rotation angle ω .

is only forbidden to a small region about $0-50^\circ$. That is to say that the rotation of C_{60} molecule in alkali-doped C_{60} solid is neither wholly free nor wholly forbidden, where C_{60} can rotate in a small region. This conclusion is not in agreement with those from other authors [5, 11, 24]. About the rotation of C_{60} in K_3C_{60} solid, there are two points of view in the literature, namely one is that the rotation of C_{60} molecule is wholly forbidden because of the geometrical factor [5, 11]. From our computational results it is seen that it is the higher potential barrier coming from the interaction on C_{60} in its alkali-doped complex that confines the free rotation of C_{60} molecule. Another viewpoint is that the rotation of C_{60} molecule is expected to be free wholly according to the line width of ^{13}C -NMR spectra of K_3C_{60} solid [24]. Although the spectrum peak is not broad, it is not narrow enough to be seen as a line. Therefore, it is not exact evidence to demonstrate that the rotation of C_{60} molecule is wholly free as that in pure C_{60} solid. In addition, it is not very reasonable to make a conclusion just from the test of the ^{13}C -NMR spectra. Now, these two distinctly contrary viewpoints are united into one viewpoint as shown above.

ACKNOWLEDGMENTS

This work was supported by the National Natural Science Foundation of China and a grant from Institute of Chemistry, Academia Sinica, to which we are grateful.

References

1. R. Taylor, R. C. Hare, A. K. Abdul-Sadaa, and H. Kroto, *J. Chem. Soc. Chem. Commun.* **20**, 1423 (1990).
2. R. Tycko, R. C. Haddon, G. Dabbagh, S. H. Glarum, D. C. Douglass, and A. M. Mujsce, *J. Phys. Chem.* **95**, 518 (1991).
3. C. Yannoni, R. D. Johnson, G. Meijer, D. S. Bethune, and J. R. Salem, *J. Phys. Chem.* **95**, 9 (1991).
4. J. M. Yan and Z. J. Xu, *J. Mol. Struct. (THEOCHEM)* **312**, 179 (1994).
5. R. C. Haddon, A. F. Hebard, M. J. Rosseinsky, D. W. Murphy, S. J. Duclos, K. B. Lyons, B. Miller, J. M. Rosamilla, R. M. Fleming, A. R. Kortan, S. H. Glarum, A. V. Makhija, A. J. Muller, R. H. Eick, S. M. Zahurak, R. Tycko, G. Dabbagh, and F. A. Thiel, *Nature* **350**, 320 (1991).
6. A. F. Hebard, M. J. Rosseinsky, R. C. Haddon, D. W. Murphy, S. H. Glarum, T. T. M. Paalstra, A. P. Ramirez, and A. R. Kortan, *Nature* **350**, 600 (1991).
7. M. J. Rosseinsky, A. P. Ramirez, S. H. Glarum, D. W. Murphy, R. C. Haddon, A. F. Hebard, T. T. M. Paalstra, A. R. Kortan, S. M. Zhurak, and A. V. Makhija, *Phys. Rev. Lett.* **66**, 2830 (1991).
8. K. Holczer, O. Klein, S.-M. Huang, R. B. Kaner, K.-J. Fu, R. L. Whetten, and F. Diederich, *Science* **252**, 1154 (1991).
9. P. J. Benning, J. L. Martins, J. H. Weaver, L. P. F. Chibante, and R. E. Smalley, *Science* **252**, 1417 (1991).
10. K. Tanigaki, I. Hirose, T. W. Ebbesen, J. Mizuki, Y. Shimakawa, Y. Kubo, J. S. Tsai, and S. Kuroshima, *Nature* **356**, 419 (1992).
11. P. W. Stephens, L. Mihaly, P. L. Lee, R. L. Whetten, S.-M. Huang, R. Kaner, F. Diederich, and K. Holczer, *Nature* **351**, 632 (1991).
12. K. Tanigaki, T. W. Ebbesen, S. Saito, J. Mizuki, T. S. Tsai, Y. Kubo, and S. Kuroshima, *Nature* **352**, 222 (1991).
13. A. P. Kelty, C.-C. Chen, and C. M. Lieber, *Nature* **352**, 223 (1991).
14. R. M. Fleming, M. J. Rosseinsky, A. P. Ramirez, D. W. Murphy, J. C. Tully, R. C. Haddon, T. Siegrist, R. Tycko, S. H. Glarum, P. Marsh, G. Dabbagh, S. M. Zahurak, A. V. Makhija, and C. Hampton, *Nature* **352**, 701 (1991).
15. R. M. Fleming, A. P. Ramirez, M. J. Rosseinsky, D. W. Murphy, R. C. Haddon, S. M. Zahurak, and A. V. Makhija, *Nature* **352**, 787 (1991).
16. C.-C. Chen, S. P. Kelty, and C. M. Lieber, *Science* **253**, 886 (1991).
17. O. Zhou, J. E. Fischer, N. Coustel, S. Kycia, Q. Zhu, A. M. McGhie, W. J. Romanow, J. P. McCauley, Jr, and A. B. Smith III, *Nature* **351**, 462 (1991).
18. G. K. Wertheim, J. E. Rowe, D. N. Buchanan, E. E. Chaban, A. F. Hebard, A. R. Kortan, A. V. Makhija, and R. C. Haddon, *Science* **252**, 1419 (1991).

19. G. Sparr, J. D. Thompson, S.-M. Huang, R. B. Kaner, F. Diederich, R. L. Whetten, G. Gruner, and K. Holczer, *Science* **252**, 1829 (1991).
20. Y. Z. Li, M. Chander, J. C. Patrin, J. H. Weaver, L. P. F. Chibante, and R. E. Smalley, *Science* **253**, 429 (1991).
21. E. Sohmen, J. Fink, and W. Kratschmer, *Eurphys. Lett.* **17**, 51 (1992).
22. C. T. Chen, L. H. Tjeng, P. Rudolf, G. Meigs, J. E. Rowe, J. Chen, J. P. McCauley, A. B. Smith, A. R. McGhie, W. J. Romanow, and E. Plummer, *Nature* **352**, 603 (1991).
23. Y. J. Uemura, A. Keren, L. P. Lee, G. M. Luke, B. J. Sternlieb, W. D. Wu, J. H. Brewer, R. L. Whetten, S.-M. Huang, S. Lin, R. B. Kaner, F. Diederich, S. Donovan, G. Gruner, and K. Holczer, *Nature* **352**, 605 (1991).
24. R. Tycko, G. Dabbagh, M. J. Rosseinsky, D. W. Murphy, R. M. Fleming, A. P. Ramirez, and J. C. Tully, *Science* **253**, 884 (1991).
25. K. Holczer, O. Klein, G. Gruner, J. D. Thompson, F. Diederich, and R. L. Whetten, *Phys. Rev. Lett.* **67**, 271 (1991).
26. C. Steven, and W. E. Pickett, *Science* **254**, 842 (1991).
27. Z. Zhang, C.-C. Chen, S. P. Kelty, H. Dai, and C. M. Lieber, *Nature* **353**, 333 (1991).
28. O. Zhou, J. E. Fischer, P. A. Heiney, N. Coustel, J. P. McCauley, and A. B. Smith, *Science* **255**, 833 (1992).
29. G. Sparr, J. D. Thompson, R. L. Whetten, S.-M. Huang, R. B. Kaner, F. Diederich, G. Gruner, and K. Holczer, *Phys. Rev. Lett.* **68**, 1228 (1992).
30. C. Gu, F. Stepniak, D. M. Poirier, M. B. Jost, P. J. Benning, Y. Chen, T. R. Ohno, J. L. Martins, J. H. Weaver, J. Fure, and R. E. Smalley, *Phys. Rev. B* **45**, 6348 (1992).
31. C. M. Varma, J. Zaanen, and K. Raghavachari, *Science* **254**, 989 (1991).
32. F. C. Zhang, M. Ogata, and T. M. Rice, *Phys. Rev. Lett.* **67**, 3452 (1991).
33. M. Schluter, M. Lanoo, M. Needles, G. A. Baraff, and D. Tomanek, *Phys. Rev. Lett.* **68**, 526 (1991).
34. A. P. Ramirez, M. J. Rosseinsky, D. W. Murphy, and R. C. Haddon, *Phys. Rev. Lett.* **69**, 1687 (1992).
35. S. Chakravarty, S. A. Kivelson, M. I. Salkola, and S. Tewari, *Science* **256**, 1306 (1992).
36. R. A. Jishi, and M. S. Dresselhaus, *Phys. Rev. B* **45**, 2597 (1992).
37. J.-M. Yan, *Chinese Chem. Lett.* **4**, 159 (1993).
38. Z.-J. Xu, and J.-M. Yan, *Acta Physico-Chimica Sinica*, **11**, 991 (1995).
39. D. E. Williams, and D. J. Houpt, *Acta Crystallogr. Sect. B: Struct. Sci.* **B42**, 286 (1986).
40. D. E. Williams and J.-M. Yan, *Adv. Atomic Mol. Phys.* **23**, 87 (1987).
41. C.-B. Zhu, and J.-M. Yan, *Chinese Sci. Bull.* **40**, 1789 (1995).
42. J.-M. Yan, and C.-B. Zhu, *J. Mol. Struct. (THEOCHEM)* **358**, 167 (1995).

Comparison of Theoretical Models of Solvation

KRASSIMIR K. STAVREV, TOOMAS TAMM, AND
MICHAEL C. ZERNER

Quantum Theory Project, University of Florida, Gainesville, Florida 32611-8435

Received April 17, 1996; accepted May 20, 1996

ABSTRACT

In this work, we examine several continuum models for estimating the free energy of solvation. We find statistically that the best overall one-parameter fit depends only on whether there is a hydrogen bond or not. Within the non-hydrogen-bonded set of molecules, a three-parameter fit including molecular volume, molecular surface area, and the electrostatic component from *any* reaction field model is quite successful. We do not find a strong bias for any of the dielectric models, although the PCM model of Tomasi and co-workers seems to slightly surpass the others. Within the hydrogen-bonded set of compounds, a good fit can be obtained simply by considering the surface accessible area of each atom, together with a dispersion and electrostatic interaction descriptor (a six-parameter fit). Such a model, containing primarily nonquantum chemical descriptors, extrapolates very well to the solvation energies of the non-hydrogen-bonded set with an overall $R^2 = 0.9334$. © 1996 John Wiley & Sons, Inc.

Introduction

The use of continuum models for simulating solvent effects in quantum chemistry has a history of more than two decades. The publication of several recent reviews on the subject [1, 2] indicates that the area has reached a certain level of maturity and acceptance. Many articles are now in the literature using one model or another ad-

ressing the differences that one obtains between quantum chemical calculations in the gas phase and modeled in solution.

In spite of some debate, most of these models are very successful in describing the chemistry that they examine if the solvent is not water or potentially hydrogen bonding to the solute. It is possible in these cases that models based upon the dielectric properties of the solvent alone have reached their limits, at least in predicting such properties as heats of solution. Current research is

shifting toward the dynamic aspects of solvent-solute interactions, using various combined classical/quantum models [3-9]. Another approach that we are examining is super-molecule quantum mechanics in which the quantum motif contains the solute and several solvent molecules from the first solvation shell, all embedded in a dielectric continuum.

Despite the existence of several continuum models of solvation, most of them appear to be implemented in different quantum chemical environments and, in many cases, exist only as local modifications to available codes. Access to these codes is in some cases limited to the research groups themselves and their closest collaborators. Only a limited number of methods (SCRf in MOPAC [10] and GAUSSIAN [11], COSMO [12] in MOPAC [13], SM* methods [14-18] in AMSOL [19]) have been made publicly available in quantum chemical packages.

As a consequence of the above, there appear to be very few (if any) comparisons of the several different approaches to the problem of solvation, in which all factors not relevant to the particular model would be eliminated. Here, we examine and compare several theoretical approaches to the different components of the free energies of solvation, using the same Hamiltonian, basis set, and set of test compounds.

Methods Studied

The free energy of solvation is usually described as consisting of the following components [2, 20-22]:

$$\Delta G_{\text{sol}} = W(M/S) - RT \ln \left(\frac{q_{\text{rot},g} q_{\text{vib},g}}{q_{\text{rot},s} q_{\text{vib},s}} \right) - RT \ln \left(\frac{n_{M,g} \Lambda_{M,g}^3}{n_{M,s} \Lambda_{M,s}^3} \right) \quad (1)$$

$$W(M/S) = \Delta G_{\text{el}} + \Delta G_{\text{cav}} + \Delta G_{\text{dis}} + \Delta G_{\text{rep}}. \quad (2)$$

Here, $W(M/S)$ is the coupling work of solvent (S) and solute (M); $q_{\text{rot},g}$, $q_{\text{vib},g}$, $q_{\text{rot},s}$, and $q_{\text{vib},s}$ are the microscopic partition functions for rotation and vibration of M, in the gas phase and in solution; $n_{M,g}$ and $n_{M,s}$ are the numerical densities of M molecules; and $\Lambda_{M,g}$ and $\Lambda_{M,s}$ are the momentum partition functions. The free-energy components of

the coupling work come from the electrostatic interaction (ΔG_{el}), cavitation (ΔG_{cav}), dispersion (ΔG_{dis}), and repulsion (ΔG_{rep}).

The current work concentrates on the ΔG_{el} , ΔG_{cav} and ΔG_{dis} , as these are the major components of ΔG_{sol} . The other components are generally considered to be negligibly small.

ELECTROSTATIC INTERACTION ENERGY

The term most studied, and that with the greatest number of methods available for its calculation, is the electrostatic interaction term, ΔG_{el} . Within the continuum approach, it is typically modeled as the energy of building up a charge on a cavity surface, in the presence of the electric field created by the solute. The solvent is modeled as a (usually isotropic) dielectric medium, characterized by its dielectric constant, ϵ . For cavities of spherical or ellipsoidal shape, analytical solutions exist for the Poisson equation:

$$\nabla^2 \phi(\mathbf{r}) = - \frac{4\pi \rho(\mathbf{r})}{\epsilon}, \quad (3)$$

where ϕ is the electrostatic potential and ρ is the charge density at the point \mathbf{r} . For other shapes of cavities, and ϵ different from infinity, one has to resort to numerical methods of solving the electrostatic problem.

The Poisson equation for a point dipole in a spherical cavity was applied to the phenomenon of solvation by Onsager in the 1936 [23]. Inclusion of the respective interaction terms into a quantum-chemical Hamiltonian was first proposed by Hylton, Christoffersen, and Hall [24], with implementations following shortly thereafter from several groups [25,26]. In the current study, we compared the models employing spherical and ellipsoidal cavities. Due to limitations of the implementation available to us, the electric field created by the solute was expanded up to hexadecapole moments when spherical cavities were considered. For ellipsoidal cavities, only the dipole-level expansion was available and studied. Traditionally, this class of methods has been called the self-consistent reaction field (SCRf) [25,26].

There are two approaches for inclusion of the solvent-solute interactions into the Hamiltonian, depending on the assumptions of the derivations [27]. The terms "model A" and "model B" have been used for these in the past. Model A freely

varies the total energy of the system

$$E_{\text{univ}} = E_{\text{quantum}}(\Psi) + E_{\text{interaction}}(\Psi), \quad (4)$$

subject to the normalization of the wave function Ψ , ($\langle \Psi | \Psi \rangle = 1$) and a Hamiltonian is derived of the form

$$H^A = H_0 + 2H_{\text{interaction}} \quad (5)$$

and

$$W^A \equiv \langle \Psi | H | \Psi \rangle = \langle \Psi | H_0 | \Psi \rangle + 2E_{\text{interaction}}. \quad (6)$$

The factor of two arises because of the quadratic dependence of the interaction energy, $E_{\text{interaction}}$, on the wave function Ψ , and for this reason, W must be corrected for the loss of free energy that the solvent experiences when disturbed by the solute:

$$E_{\text{univ}} = W^A - E_{\text{interaction}}. \quad (7)$$

Model B introduces a second Lagrange constraint such that the quantum chemical energy yields E_{univ} directly, with

$$\begin{aligned} H^B &= H_0 + H_{\text{interaction}} \\ E_{\text{univ}} &= W^B. \end{aligned} \quad (8)$$

SCRF models are generally of type A, whereas direct reaction field models are generally of type B. For more details, the reader is referred to [27]. Both approaches were included, when available, in the current study.

The most successful and widely known algorithm for solving the Poisson equation for a cavity of a general shape in quantum chemical calculations is likely the polarizable continuum model (PCM), introduced by Miertuș, Scrocco, and Tomasi in 1981 [28]. In our implementation of the PCM model [29], the electric field of the solute was derived from its molecular charge distribution expanded as a set of point charges and point dipoles centered at the nuclei. While less rigorous than the direct calculation of the electrostatic potential at the cavity surface, it is remarkably faster and has been shown to produce results of comparable accuracy to the full treatment [30]. Different approaches can be used for estimating the atomic point charges, of which the Mulliken and ZDO charges are readily available. These approximations bring the model close to the Generalized Born model [31–36]. In the case where atomic point dipoles were also included, these were calcu-

lated within the ZDO approximation, and the corresponding ZDO point charges were used as the remaining part of the expansion. For an ab initio implementation, inclusion of the two-center dipole terms would be required.

A method which can be viewed as positioned between the above two is the multicavity (MCa) SCRF approach, proposed by Karelson, Tamm, and Zerner in 1993 [37]. Here, the molecule is partitioned into rotationally invariant groups (fragments), each embedded in a spherical cavity with its own Onsager-type reaction field. The original formulation included additional terms for interfragment reaction field interactions. The approach was revised prior to the current study, and in the latest implementation, the interfragment interaction terms have been omitted. The justification behind this change will be published elsewhere.

CAVITATION ENERGY

The energy associated with the formation of a cavity inside the solvent is usually termed the cavitation energy, ΔG_{cav} . The most widespread approach toward its estimation is likely the scaled particle theory, originally introduced by Pierotti [38].

Another widely used approach is based on the assumption that the cavitation energy is roughly proportional to the surface area of the solute. Various solvent-accessible surface area (SASA)-based approaches are known from the literature [39–41]. For the current study, a straightforward linear relationship

$$\Delta G_{\text{cav}} = \sigma A, \quad (9)$$

where A is the surface area and σ is a proportionality factor, was adopted.

A more sophisticated elaboration of the same approach has been used in the successful SM1-SM5 solvent models introduced by Cramer and co-workers [14–18]. In this case, proportionality factors (named "surface tensions" by the authors) are established for each type of atom in the molecule, where "type" denotes either a chemical element or an element in a certain molecular environment. In the later models, hydrogen atoms are not assigned separate surface tensions, but those of the bonded atoms are adjusted according to the number of attached hydrogens. For this study, the most straightforward approach was chosen, where the exposed surface area for each different element

was multiplied by a proportionality factor:

$$\Delta G_{\text{cav}} = \sum_{k=1}^N \sigma_k A_k, \quad (10)$$

where N is the number of atoms in the molecule; A_k , the exposed surface area of the atom; and σ_k , a proportionality factor (surface tension). In this case, there are different values for σ_k for each different element, independent of its bonding environment.

DISPERSION ENERGY

For the current study, only two methods of evaluating the dispersion energy were at our disposal. The first one is the configuration interaction (CI)-based approach developed by Rösch and Zerner [42], which has given very good results for describing solvent shifts in electronic spectra. The second approach is based on the experimentally known fact that larger molecules have higher dispersion energies, and the dispersion is roughly proportional to the volume of the molecule:

$$\Delta G_{\text{dis}} = \varrho V, \quad (11)$$

where V is molecular volume, and ϱ , a proportionality factor.

ENERGY OF HYDROGEN BONDS

Hydrogen bonding is a phenomenon which is traditionally studied outside of continuum solvation models, due to its high specificity and directionality, caused by association energies considerably greater than kT , the thermal energy. For the pure energetic effect, however, it was found important (and sufficient for the current study) to include a single parameter, "hydrogen-bonding energy," which would be set at a fixed value for the molecules which are known to form hydrogen bonds and to zero otherwise. This parameter will be called the "hydrogen-bonding descriptor" in the subsequent text.

Calculations

For the current study, a set of 30 small organic molecules was assembled. The main selection criteria were a diversity of functional groups and structures, availability of experimental geometries, densities, and free energies of solvation in water.

The compounds and the related experimental data are assembled in Table I. Crystallographic structures were used, and no geometry optimization was attempted in the solution-phase quantum chemical calculations. This might have allowed for a more complete comparison of the different models of solvation. However, we felt that we did not want to compare, at least not yet, errors in geometric predictions using a model only of modest accuracy is estimating gas-phase geometries (INDO/1). This will be a source of error, however, in our comparisons [43,44].

All calculations were performed using the INDO/1 Hamiltonian [45–47] as implemented in the ZINDO [48] program. The CI calculations necessary for calculation of the dispersion energies were performed using a spherical cavity.

Cavity sizes for spherical cavities were calculated from the mass density (d), molecular weight (M), and Avogadro's number (N_A):

$$R = \left(\frac{10^{24} \cdot M}{d \cdot N_A} \right)^{1/3} = 0.732 \left(\frac{M}{d} \right) (\text{\AA}), \quad (12)$$

assuming no empty space between the molecules. For the elliptical cavities, the same volume was preserved, but the ratio of the axes of the ellipsoid was adjusted according to the moments of inertia of the molecule. For purposes of calculating these moments, the atomic volumes, not masses, were used.

The cavity shapes for the PCM models were obtained from the GEPOL93 [49] algorithm, as van der Waals surfaces, using radii compiled by Bondi [50]. There have been suggestions in the literature to multiply Bondi's radii by 1.2 (see, e.g., [2] for a discussion and further references). We found that such multiplication decreases the electrostatic solvation energies on the average by $1.73 = 1.2^3$ times, with a very high correlation between the energies obtained by using the modified and unmodified radii ($R^2 = 0.998$). Therefore, we dropped the multiplier and assumed that any necessary adjustments will be done at the data analysis stage. The GEPOL93 algorithm also supplied us with the total and partial surface areas for cavitation energy calculations, as well as another set of molecular volumes. The latter correlated very well with the mass density volumes [eq. (12)], and due to their general availability, the GEPOL volumes were used

TABLE I
The solute molecules in this study.

Name of molecule	ΔG_{sol}	Classification	H bond
Methane	1.93	Hydrocarbon	N
Ethane	1.77	Hydrocarbon	N
Propane	1.98	Hydrocarbon	N
2-Methylpropane	2.28	Hydrocarbon	N
Cyclohexane	1.24	Hydrocarbon	N
Octane	2.89	Hydrocarbon	N
Benzene	-0.88	Aromatic	N
Toluene	-0.77	Aromatic	N
Ethylbenzene	-0.60	Aromatic	N
Acetic acid	-6.70	Acid	Y
Pyridine	-4.70	Heterocycle	Y
Chloromethane	-0.56	Chlorinated hydrocarbon	N
Chloroform	-1.07	Chlorinated hydrocarbon	N
Dichloromethane	-1.41	Chlorinated hydrocarbon	N
Acetone	-3.85	Ketone	Y
Methylamine	-4.56	Amine	Y
Nitroethane	-3.71	Nitro compound	Y
Acetonitrile	-3.90	Nitrile	Y
Trimethylamine	-3.24	Amine	Y
Aniline	-4.90	Aromatic amine	Y
Nitrobenzene	-4.12	Aromatic nitro	Y
Methanol	-5.10	Alcohol	Y
Ethanol	-5.05	Alcohol	Y
1-Propanol	-4.83	Alcohol	Y
1-Butanol	-4.72	Alcohol	Y
tert-Butanol	-4.51	Alcohol	Y
1-Hexanol	-4.36	Alcohol	Y
Cyclohexanol	-5.48	Alcohol	Y
Phenol	-6.62	Aromatic alcohol	Y

for the present study. The experimental ΔG_{sol} of solvation in water were taken from the compilation by Cabani et al. [51].

The results were analyzed using the CODESSA [52] statistical-analysis package, utilizing the correlation and heuristics methods available therein. In keeping with the terminology used in the field of Linear Structure-Activity Relationships, the various calculated values from the various models will be called *descriptors*. The quality of the fits was judged by the square of the correlation coefficient (R^2), by the sign and value of the regression coefficients (multipliers in front of the corresponding descriptor values in the regression formula), and by the cross-validated R^2 . The latter is a figure which measures the predictive power of a fit by leaving out the data points one by one, repeating the correlation for the rest, predicting the left-out experimental value from the regression, and then

correlating predicted values with the actual one. We consider R^2 and $R^2(\text{CV})$ values above 0.9 satisfactory for predictions in complex areas like studies of solvation energetics.

Results and Discussion

DEPENDENCE OF THE COMPONENTS OF SOLVATION ENERGY ON CAVITY SIZE

The only solute-specific parameter that enters the equations of the solvation energy, which is not directly obtainable from quantum chemistry, is the size (and shape, for PCM-type models) of the cavity. To investigate this dependence, the various components for the simplest spherical cavity model, along with cavitation energy by Pierotti, and dispersion energy by Rösch and Zerner, were

calculated and plotted as a function of cavity size. For the case of acetone, the plot is reproduced in Figure 1.

It is immediately clear that all components of the solvation energy become more positive as the size of the cavity increases. The dependence is especially sharp for the sum of the three components, which can be used as the estimate for the total free energy of solvation. For example, when the cavity size is decreased by 10% from the mass-density value, the total calculated solvation energy decreases from -3 to -8 kcal/mol—far beyond any experimental error and probably beyond the expected error of the calculation.

Since there is no generally approved and tested method to calculate the cavity size, it is often approached as a parameter of the model. There is also no proof that the optimum values for the radii for calculating the different components of the solvation energies are similar. However, in the range close to the optimal radius, the components of the solvation energy depend monotonically upon the radius. Therefore, it was found justified to use multilinear regression in fitting the calculated components of the solvation energy to experimental data. The regression coefficients can be converted back into coefficients usable for scaling the sizes of the cavity from the values used in this study into a single optimal scaling factor for each model, but we have not done so here.

SINGLE-PARAMETER CORRELATIONS

In some early studies, the electrostatic interaction energies have been used as a measure of the whole solute-solvent interaction, without additional corrections for the cavitation and dispersion. According to the results of the current study, none of the available electrostatic interaction energy models yields results which correlate well with the experimental data. The best correlation [$R^2 = 0.4882$, $R^2(\text{CV}) = 0.4165$, Fig. 2] was achieved for the multicavity SCRF model:

$$\Delta G_{\text{solv}} = 0.52\Delta G_{\text{electrostatic}} - 0.60. \quad (13)$$

Surprisingly, the hydrogen-bonding descriptor correlated remarkably well with the experimental solvation energies [$R^2 = 0.8285$, $R^2(\text{CV}) = 0.7997$, Fig. 3], dividing the data into two classes of non-hydrogen-bonding and hydrogen-bonding molecules, with the average energy of the hydrogen bond estimated at -5.3 kcal/mol. The latter value is in good agreement with the generally accepted values of 3–9 kcal/mol for a hydrogen bond [see, e.g., [53], p. 454]. Trying to anticipate how many hydrogen bonds a compound possessed did not improve the statistical fit.

Since the solvation energies appear to be largely dominated by the hydrogen bonding, the compounds were subdivided into two groups: hydro-

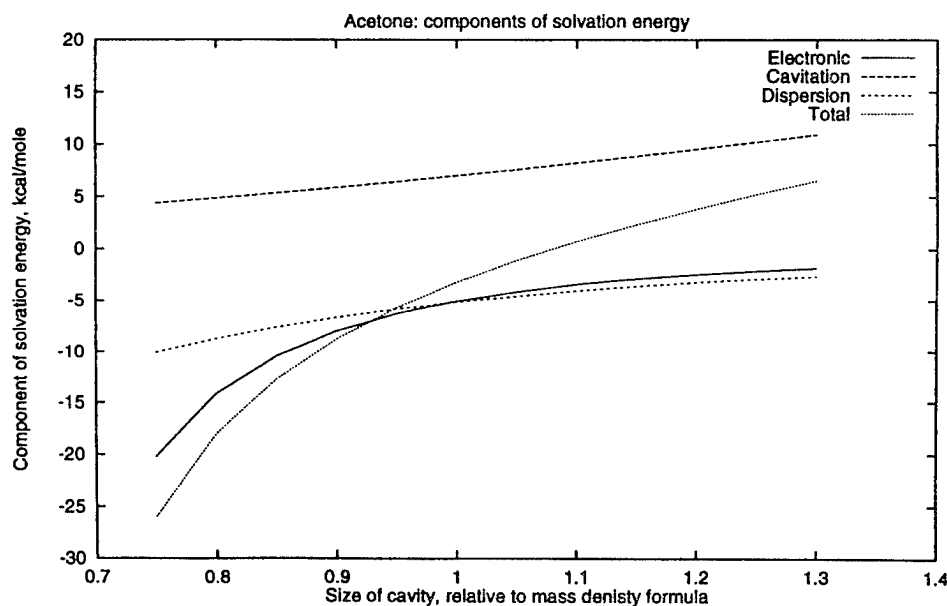


FIGURE 1. Components of the calculated solvation energy of acetone in water.

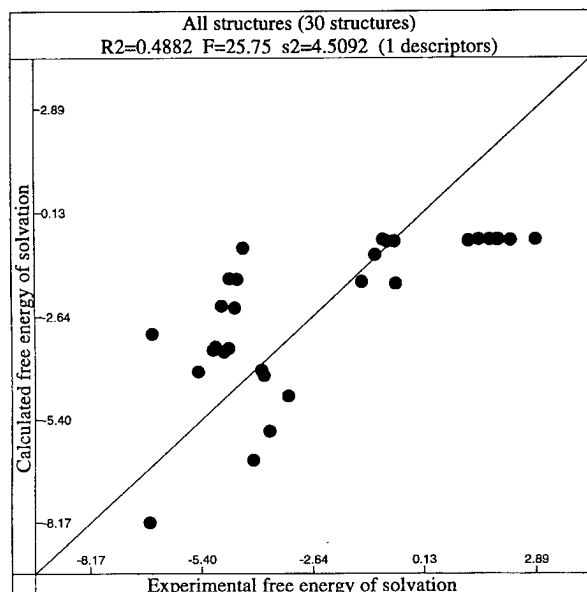


FIGURE 2. Correlation between the calculated multicavity SCRF and the experimental solvation energies of all 30 compounds.

gen-bonding and non-hydrogen-bonding. There were 17 hydrogen-bonding and 13 non-hydrogen-bonding structures in the set. Most of the remaining correlations were performed on the two groups separately.

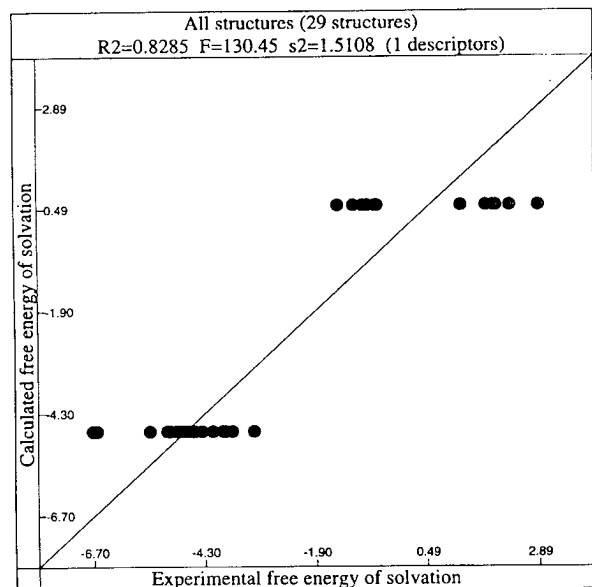


FIGURE 3. Correlation between the hydrogen-bonding descriptor and the experimental solvation energies of all 30 compounds.

NON-HYDROGEN-BONDING COMPOUNDS

For this group, three parameters appeared to be the minimum amount necessary to achieve a correlation of the experimental solvation energies with the R^2 higher than 0.9. The best fit was obtained with the PCM model (electrostatic potential from Mulliken charges), surface area, and volume, as parameters [$R^2 = 0.9513$, $R^2(\text{CV}) = 0.9144$, Fig. 4]:

$$\Delta G_{\text{solv}} = 0.63\Delta G_{\text{electrostatic}} + 0.27S - 0.34V - 1.7. \quad (14)$$

The coefficient 0.63 in front of the calculated electrostatic contribution would be brought to 1.0 by using a scaling factor for the van der Waals radii equal to 1.17, close to 1.2 as discussed above. Replacing the PCM/Mulliken electrostatic interaction descriptor with any other one of the electrostatic descriptors did not lead to a much worse correlation; R^2 in all cases was above 0.87.

Leaving out any of the three descriptors, however, did lead to a significant degradation of the fit, with typical correlation coefficients as low as $R^2 = 0.5$. We conclude here that at least one descriptor for each of cavitation, dispersion, and electrostatic components of the solvation energy is required to describe the energetics of solvation of the non-hydrogen-bonding compounds.

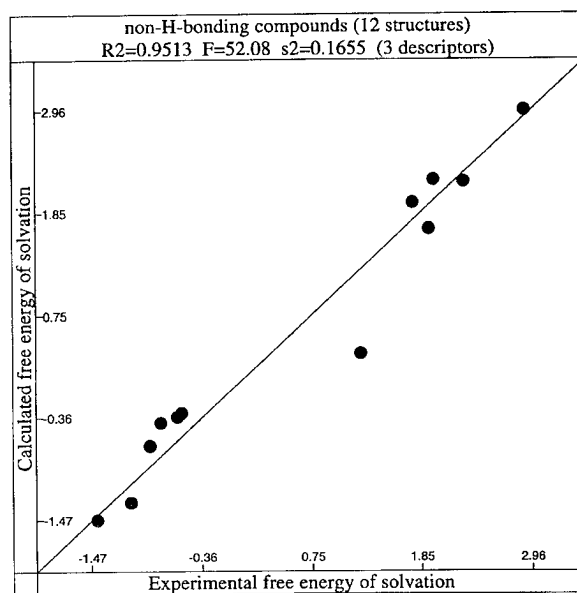


FIGURE 4. The best three-parameter correlation for the non-hydrogen bonding compounds.

At the same time, there is a little dependence of the final results on the choice of the particular models chosen for either of the components. Also, the more complex (CI) method for the calculation of dispersion energy [42] does not appear to have advantages over the far more trivial molecular volume model, at least for ΔG_{sol} ($R^2 = 0.7777$ for PCM electrostatics, surface area, and CI dispersion; $R^2 = 0.5993$ if Pierotti's cavitation energy is substituted for the surface area).

HYDROGEN-BONDING COMPOUNDS

Aside from the overall energy of a hydrogen bond, as described earlier, there appears to be no single good descriptor to characterize the solvation energy for this group of compounds. Reasonably good correlations could only be achieved when the partial atomic surface area descriptors were involved. This apparently accounts for the different ability of the atoms to form hydrogen bonds and is at the heart of such methods as described by Cramer and Truhlar [14–18]. These are features of geometric structure rather than directly dependent on electronic structure.

The best correlation results from inclusion of the partial surface areas, along with spherical cavity dipole-level SCRF electronic energies. The correlation coefficient is still not very good, $R^2 = 0.6296$. Addition of dispersion term raises the correlation coefficient to $R^2 = 0.7812$ (here the elliptical cavity model performed better than the spherical), but the $R^2(\text{CV})$, i.e., the predictive power of the model, remains extremely low, 0.3952 (Fig. 5). The plot indicates a relatively uniform distribution of errors, unlikely to be improved by adding another descriptor. The coefficient in front of the electrostatic term, -0.54 , is indicative of the low influence of the electrostatic energy contribution into the total ΔG_{sol} .

A similar set of parameters, with the addition of the surface area of chlorine and the hydrogen-bonding descriptor, and using the spherical cavity electrostatic contribution, is well capable of predicting the solvation energies in the whole data set. The errors are all below 1 kcal/mole, with a $R^2 = 0.9443$ and $R^2(\text{CV}) = 0.8226$ (Fig. 6). We conclude that the approach adopted by the developers of the SM* models will be the most successful one, applicable to both non-hydrogen-bonding and hydrogen-bonding compounds.

The downside of this multiparameter approach, however, is the fact that removal of the electro-

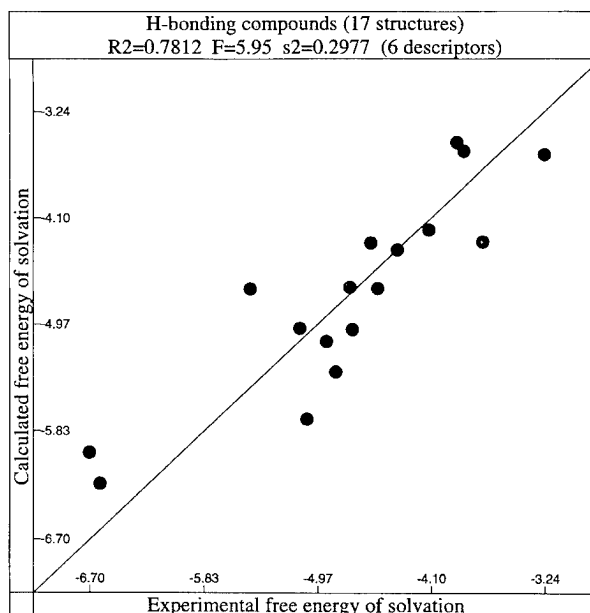


FIGURE 5. The best six-parameter correlation for the hydrogen-bonding compounds.

static component does not lower of the quality of the fit significantly ($R^2 = 0.6296$). It appears that solvation energy can be described by descriptors devoid of quantum theory. The influence of the solvent on the electronic structure, as well as electronic properties of the solute other than energy, is not expected, however, to be described accurately

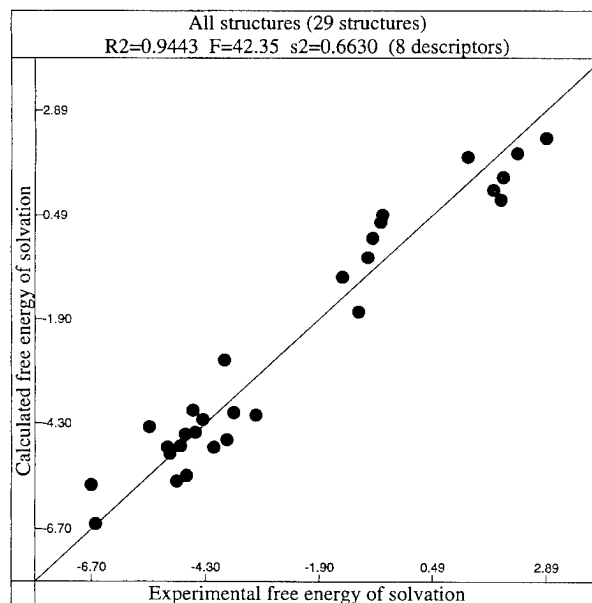


FIGURE 6. The best correlation (8 parameters) for the entire set of compounds.

without quantum chemistry. It is also a reasonable conclusion to expect, that for hydrogen-bonded systems, supermolecule calculations are required if greater accuracy is the objective.

Conclusions

The current study indicates that the best descriptors for free energy of solvation, ΔG_{solv} , presently come from models that do not require quantum chemical calculations. While the importance of various continuum models in the description of the influence of solvents on the electronic structure of the solute cannot be overestimated, the property most often sought after and quoted, namely, free energy of solvation, can still be best described by simple multilinear correlation models.

For hydrogen bonding, there appears to be no general quantum mechanical approach aside from supermolecule calculations or mixed quantum classical models that include strong interactions specifically. While the non-quantum-mechanical simple descriptors are quite capable of estimating the free energies of solvation, these models have no influence whatsoever on the electronic structure resulting from single-molecule quantum chemistry calculations. The various continuum methods studied all give results of similar quality, and none of them can be singled out by this study to be the "best" in calculating ΔG_{solv} .

Acknowledgments

This work was supported in part from a grant from the Office of Naval Research and from NSF CHE-9312651 and has benefited greatly from discussions with Mati Karelson (Tartu). We are grateful to Victor Lobanov and Alan Katritzky (Florida) for a copy of CODESSA.

References

1. C. J. Cramer and D. G. Truhlar, *Rev. Comput. Chem.* **6**, 1 (1993).
2. J. Tomasi and M. Persico, *Chem. Rev.* **94**, 2027 (1994).
3. A. Warshel and M. Levitt, *J. Mol. Biol.* **103**, 227 (1976).
4. U. C. Singh and P. A. Kollman, *J. Comput. Chem.* **7**, 718 (1987).
5. M. J. Field, P. A. Bash, and M. Karplus, *J. Comput. Chem.* **11**, 700 (1990).
6. J. Gao, *J. Phys. Chem.* **96**, 6432 (1992).
7. J. Gao and X. Xia, *Science* **258**, 631 (1992).
8. J. Gao, *J. Am. Chem. Soc.* **117**, 8600 (1995).
9. M. A. Thompson and G. K. Schenter, *J. Phys. Chem.* **99**, 6374 (1995).
10. M. M. Karelson, T. Tamm, A. R. Katritzky, S. J. Cato, and M. C. Zerner, *Tetrahedron Comput. Method.* **2**, 295 (1989).
11. M. J. Frisch, G. W. Trucks, H. B. Schlegel, P. M. Gill, B. G. Johnson, M. A. Robb, J. R. Cheeseman, T. A. Keith, G. A. Peterson, J. A. Montgomery, K. Raghavachari, M. A. Al-Laham, V. G. Zakrzewski, J. V. Ortiz, J. B. Foresman, J. Cioslowski, B. B. Stefanov, A. Nanayakkara, M. Challacombe, C. Y. Peng, P. Y. Ayala, W. Chen, M. W. Wong, J. L. Andres, E. S. Replogle, R. Gomperts, R. L. Martin, D. J. Fox, J. S. Binkley, D. J. Detrees, J. Baker, J. P. Stewart, M. Head-Gordon, C. Gonzalez, and J. Pople, *Gaussian* (Gaussian, Inc., Pittsburgh, PA).
12. A. Klamt and G. Schuurmann, *J. Chem. Soc., Perkin Trans.* **2**, 799 (1993).
13. MOPAC Version 7.0 © (Fujitsu Ltd., 1993).
14. C. J. Cramer and D. G. Truhlar, *J. Am. Chem. Soc.* **113**, 8305 (1991).
15. C. J. Cramer and D. G. Truhlar, *Science* **256**, 213 (1992).
16. C. J. Cramer and D. G. Truhlar, *J. Comput. Chem.* **13**, 1089 (1992).
17. D. J. Giesen, C. J. Cramer, and D. G. Truhlar, *J. Phys. Chem.* **99**, 7137 (1995).
18. D. G. Truhlar, presented at the ACS meeting (New Orleans, March 1996).
19. C. J. Cramer and D. G. Truhlar, AMSOL (Program 606 Quantum Chemistry Program Exchange, Indiana University, Bloomington, IN).
20. A. Ben-Naim, *Water and Aqueous Solutions* (Plenum Press, New York, 1974).
21. A. Ben-Naim, *J. Phys. Chem.* **82**, 792 (1978).
22. A. Ben-Naim, *Solvation Thermodynamics* (Plenum Press, New York, 1987).
23. L. Onsager, *J. Am. Chem. Soc.* **58**, 1486 (1936).
24. J. Hylton, R. E. Christoffersen, and G. G. Hall, *Chem. Phys. Lett.* **26**, 501 (1974).
25. O. Tapia and O. Goscinski, *Mol. Phys.* **29**, 1653 (1975).
26. J.-L. Rivail and D. Rinaldi, *Chem. Phys.* **18**, 233 (1976).
27. M. M. Karelson and M. C. Zerner, *J. Phys. Chem.* **96**, 6949 (1992).
28. S. Miertuș, E. Scrocco, and J. Tomasi, *Chem. Phys.* **55**, 117 (1981).
29. K. K. Stavrev, T. Tamm, and M. C. Zerner, *4th Conference on Current Trends in Computational Chemistry* (Vicksburg, MS, Nov. 3-4, 1995), p. 111.
30. T. Fox and N. Rösch, *J. Mol. Struct. (Theochem)* **276**, 2791 (1992).
31. M. Born, *Z. Phys.* **1**, 45 (1920).
32. I. Fischer-Hjalmars and A. Henriksson-Enflo, *Chem. Phys.* **24**, 167 (1977).
33. G. Klopman and P. Andreozzi, *Theor. Chim. Acta (Berl.)* **55**, 77 (1980).

34. R. Constanciel and R. Contreras, *Theor. Chim. Acta (Berl.)* **65**, 1 (1984).
35. R. Contreras and A. Aizman, *Int. J. Quantum Chem.* **27**, 293 (1985).
36. T. Kozaki, K. Morihashi, and O. Kikuchi, *J. Am. Chem. Soc.* **111**, 1547 (1989).
37. M. Karelson, T. Tamm, and M. C. Zerner, *J. Phys. Chem.* **97**, 11901 (1993).
38. R. A. Pierotti, *Chem. Rev.* **76**, 717 (1976).
39. R. B. Hermann, *J. Phys. Chem.* **76**, 2754 (1972).
40. R. B. Hermann, *J. Phys. Chem.* **79**, 163 (1975).
41. G. D. Rose, A. R. Geselowitz, G. J. Lesser, R. H. Lee, and M. H. Zehfus, *Science* **229**, 834 (1985).
42. N. Rösch and M. C. Zerner, *J. Phys. Chem.* **98**, 5817 (1994).
43. M. Karelson, A. R. Katritzky, M. Szafran, and M. C. Zerner, *J. Chem. Soc., Perkin Trans.*, 195 (1990).
44. M. Karelson, A. R. Katritzky, M. Szafran, and M. C. Zerner, *J. Org. Chem.* **54**, 6030 (1989).
45. M. C. Zerner, G. H. Loew, R. F. Kirchner, and U. T. Müller-Westerhoff, *J. Am. Chem. Soc.* **102**, 589 (1980).
46. J. E. Ridley and M. C. Zerner, *Theor. Chim. Acta (Berl.)* **32**, 111 (1973).
47. A. Bacon and M. Zerner, *Theor. Chim. Acta (Berl.)* **53**, 21 (1979).
48. M. C. Zerner, ZINDO program package (Quantum Theory Project, University of Florida, Gainesville, FL).
49. J. L. Pascual-Ahuir, E. Silla, J. Tomasi, and R. Bonaccorsi, *J. Comput. Chem.* **8**, 778 (1987).
50. A. Bondi, *J. Phys. Chem.* **68**, 441 (1964).
51. S. Cabani, P. Gianni, V. Mollica, and L. Lepori, *J. Sol. Chem.* **10**, 563 (1981).
52. CODESSA © 1995 (University of Florida; distributed by SemiChem, Inc. 7128 Summit, Shawnee, KS 66216).
53. R. H. Petrucci and W. S. Harwood, *General Chemistry: Principles and Modern Applications* (Prentice Hall, Englewood Cliffs, NH, 1993).

Using Theoretical Descriptors to Model Solvent Effects in the Isomerization of *cis*-Stilbene

R. ANDREW MCGILL, JANE K. RICE, A. P. BARONAVSKI, AND
J. C. OWRUTSKY

Chemistry Division, Naval Research Laboratory, Washington, DC 20375

ALFRED H. LOWREY*

Laboratory for the Structure of Matter, Naval Research Laboratory, Washington, DC 20375

KRASSIMIR K. STAVREV, TOOMAS TAMM, AND
MICHAEL C. ZERNER

Quantum Theory Project, University of Florida, Gainesville, Florida 32611-8435

Received March 28, 1996; revised manuscript received May 21, 1996; accepted May 28, 1996

ABSTRACT

Experimental observations of the photoinduced excited-state lifetime of *cis*-stilbene have shown a distinct dependence on solvation processes. The rate of decay, dominated by a *cis-trans* isomerization, is more rapid in polar solvents than in nonpolar solvents. Linear solvation energy relationship (LSER) techniques show that this can be explained in terms of polarity and polarizability parameters for the solvent. Theoretical linear solvation energy relationship (TLSER) analysis shows that this can be explained in terms of solvent polarizability and electrostatic basicity. New TLSER descriptors based on calculated solvent bond dipole parameters are also successful in describing this solvent dependence. Solvent-dependent dipole moments are calculated for an approximate stilbene transition-state geometry using the polarizable continuum model (PCM), which suggests the usefulness of a more detailed study of this photoisomerization process using current solvation theory and computational techniques. © 1996 John Wiley & Sons, Inc.

*To whom correspondence should be addressed.

Introduction

Reaction dynamics in solution is a complex phenomenon not easily explained by theoretical or experimental models [1]. The photoinduced isomerization of stilbene between *cis* and *trans* forms is a well-studied unimolecular phenomenon [2, 3] and has been previously treated with solvent viscosity models to describe solvent influence on the internal rotation about the ethylenic central bond. These models, however, do not seem to account for some experimental observations, particularly when studied in dipolar solvents [1, 3]. Considerable research has focused on the mechanisms that contribute to this phenomenon using concepts such as internal/external energy reorganizations and time-dependent solvent "friction" [1].

This manuscript describes the results of regression studies of the solvent dependence of photoinduced excited-state *cis*-stilbene relaxation rates which are dominated by *cis*-*trans* isomerization. Regression techniques have a long history of successful elucidation of basic phenomena affected by solute/solvent interactions [4, 5]. Using well-established descriptors associated with various models for solute/solvent interactions, regression techniques employ statistical analysis to identify important solvent and solute solubility factors associated with variations in experimental observations. These calculations are fast and are extremely useful for identifying models worthy of more elaborate development [6].

Previously, Rice and Baronavski [9] and McGill and co-workers [7] modeled the effects of solvent on the excited-state *cis*-stilbene lifetime. The ultrafast dynamics of *cis*-stilbene in solution were monitored using ~ 100 ns laser systems: Experimental lifetime data in a wide range of dipolar and nonpolar solvents were gathered from several independent laboratories [8–14].

LSER ANALYSIS

The solvent dependence of these lifetimes were studied using the techniques of linear solvation energy relationships (LSER). Multiple regression analysis of log isomerization rates, $\ln k$, were performed based on variations of empirical multipa-

rameter solvation equations developed by Koppel, Palm, Makitra, and Pirig [KPMP] [15–18] and Kamlet, Abraham, and Taft [KAT] [19]. These equations have been shown to be capable of correlating, predicting, and elucidating hundreds of physiochemical properties and reactivity parameters of diverse types [4, 19, 20]. Both the KPMP and KAT equations contain solvent descriptors for solvent polarity such as π_1 or $f(\epsilon)$; hydrogen-bonding acidity α_1 or electrophilicity E ; hydrogen-bonding basicity β_1 or nucleophilicity B ; and cavity formation δ_H^2 . However, in contrast to the KPMP solvation equation, the KAT equation does not contain a separate parameter that describes the solvent molecular polarizability. To include such a parameter, the refractive index function $f(n)$ was used to replace the solvent parameter which models the polarizability of the solvent lone pair and π electrons R_1 , as opposed to the whole molecule. In addition to using the usual solvent dipolar descriptors, $f(\epsilon)$ and π_1 for the KPMP and KAT solvation equations, the molecular dipole moment, μ , was also examined as an alternative to these parameters. The three primary equations utilized were

$$\ln(k) = \ln(k_0) + p \times f(n)_1 + s \times \pi_1 + a \times \alpha_1 + b \times \beta_1 + h \times \delta_H^2 \quad (1)$$

$$\ln(k) = \ln(k_0) + p \times f(n)_1 + m \times \mu + a \times \alpha_1 + b \times \beta_1 + h \times \delta_H^2 \quad (2)$$

$$\ln(k) = \ln(k_0) + A_1 \times f(n)_1 + A_2 f(\epsilon)_1 + A_5 \times E + A_4 \times B + A_3 \times \delta_H^2 \quad (3)$$

TLSER ANALYSIS

The work reported here focuses on using the theoretical linear solvation energy relationships technique developed by Famini and co-workers [6, 20, 21]. They developed the theoretical linear solvation energy relationship (TLSER) method based on a systematic study of this problem. The TLSER formulation of the regression equations is given by [6]

$$\log(P) = a \times V_{mc} + b \times \pi_i + c \times \epsilon_B + d \times q_- + e \times \epsilon_A + f \times q_{h+} + g \quad (4)$$

The definitions of these terms are given in Table I.

TABLE I
Definitions of TLSER descriptors.

Symbol	Name	Definition	Units	Meaning
V_{mc}	Molecular volume	Molecular volume	100 Å	Cavity / steric
π_1	Polarizability index	Polarizability (V_{mc})	none	Polarizability
ε_B	"Covalent" HB basicity	$0.30 - (E(h) - E(lw) / 100)$	heV	HBAB
$q -$	"Electrostatic" HB basicity	Maximum $ (-) $ charge on an atom	acu	HBAB
ε_A	"Covalent" HB acidity	$0.30 - (E(1) - E(hw) / 100)$	heV	HBDA
q_{h+}	"Electrostatic" HB acidity	Maximum $ (+) $ charge on an H atom	acu	HBDA

Å = angstrom; heV = hectoelectron volt; acu = atomic charge unit, HB = hydrogen bond; $E(1)$ = LUMO energy; $E(h)$ = HOMO energy; $E(lw)$ and $E(hw)$ refer to the E (LUMO) and E (HOMO) for water, respectively; $| |$ indicates absolute magnitudes; HBAB = hydrogen bond acceptor basicity; HBDA = hydrogen-bond donor acidity.

The molecules of interest for these studies are relatively large. Therefore, the TLSER method relies on the semiempirical formulations for molecular orbital calculations [22, 23], most notably the well-documented and extensive functionalities available in the MOPAC package [24]. These descriptors have been successfully used to characterize a range of properties ranging from charcoal absorption, HPLC retention index, electronic absorption of a pyridinium ylide, octanol-water partition coefficients, pK_a and the reaction rate constant for hydrolysis of organophosphonothioates in different solvents [20, 25].

One of the principal reasons for this study was the recent development of an empirical model by McGill and co-workers [7] which characterizes the excited-state *cis*-stilbene decay rate as a process dependent on two main opposing effects controlled by the solvent molecular polarity and polarizability. In the spirit of the TLSER philosophy, Fager and Famini [26] developed proposed descriptors derived from bond dipoles as calculated by MOPAC [24]. Use of these dipole descriptors is still in the preliminary development stage. The proposed descriptors are the total molecular dipole μ^T , the maximum bond dipole μ^M , and the average bond dipole μ^A . The bond dipole is defined as the positive difference between the calculated atomic charges multiplied by the bond length for the two atoms participating in a bond.

Results

The TLSER descriptors for the various solvents along with the associated experimental lifetimes and rates are given in Table II. Calculations were made for some hydrocarbons which were not part of the experimental data set for the purpose of seeing if the regressions predict useful values for future experiments. Since molecular dipoles are of interest in this study, TLSER descriptors were calculated for stilbene geometries optimized with MNDO using a two-state configuration interaction. Both the *cis* and *trans* forms were optimized and an approximate geometry for a transition state was obtained by searching the ethylenic torsion coordinate at 5° intervals. The CI-optimized geometry holding the torsion at 105.0° exhibited the highest heat of formation. The customary TLSER descriptors were calculated holding these three geometries fixed [26]. These geometries are shown in Figure 1. The descriptors for the *cis*, *trans*, and the approximate transition state are given in Table III. Since the TLSER descriptors are often not greatly sensitive to molecular conformation [6], the approximate transition-state geometry is a good representation for the purposes of this study. This may be observed in Table III where most of the TLSER descriptors vary between the *cis* and *trans* conformations by 1% or less. The calculated de-

TABLE II
TLSER descriptors for solvents.

Solvent ^a	Volume	Polarizability	Eb ^b	Q ⁻	Ea ^b	Q ⁺	μ^T	μ^M	μ^A	Experimental lifetime (ps)	Experimental ln k Rate ^b
Acetonitrile	41.06	0.1034	0.1177	0.1146	0.1622	0.0209	0.7675	0.3577	0.1535	0.38	0.968
Cycloheptane	116.71	0.1119	0.1276	0.0054	0.1460	0.0037	0.1237	0.0100	0.0059	1.52	-0.419
Cyclohexane	99.97	0.1116	0.1286	0.0092	0.1461	0.0050	0.1840	0.0158	0.0102	1.37	-0.315
Cyclononane	150.94	0.1117	0.1287	0.0040	0.1462	0.0065	0.1078	0.0115	0.0040	c	c
Cyclooctane	137.53	0.1094	0.1292	0.0029	0.1457	0.0032	0.0765	0.0068	0.0032	1.62	-0.482
Cyclopentane	86.09	0.1062	0.1250	0.0165	0.1462	0.0082	0.2744	0.0274	0.0183	1.25	-0.223
n-Decane	184.44	0.1056	0.1275	0.0218	0.1466	0.0045	0.7295	0.0787	0.0235	1.27	-0.239
1-Decanol	184.76	0.1092	0.1328	0.3236	0.1466	0.1805	2.3157	0.6742	0.0724	1.13	-0.122
Diethyl ether	87.02	0.1034	0.1365	0.3423	0.1456	0.0071	2.8536	0.7162	0.2038	0.66	0.416
DMSO ^a	68.54	0.1101	0.1475	0.7204	0.1734	0.0500	8.0154	2.4601	0.8906	0.59	0.528
1,4-Dioxane	83.48	0.1075	0.1391	0.3230	0.1478	0.0327	3.6174	0.6384	0.2584	0.73	0.315
n-Dodecane	224.52	0.1037	0.1281	0.0218	0.1470	0.0045	0.7887	0.0787	0.0213	1.35	-0.300
Ethanol	50.92	0.0983	0.1324	0.3235	0.1442	0.1783	1.7092	0.6501	0.2136	0.62	0.478
Ethyl acetate	84.38	0.1073	0.1314	0.3570	0.1687	0.0260	3.7324	0.9377	0.2871	0.54	0.616
n-Heptane	133.64	0.1032	0.1258	0.0217	0.1455	0.0045	0.6390	0.0786	0.0290	c	c
n-Hexadecane	289.49	0.1067	0.1289	0.0218	0.1474	0.0045	0.9074	0.0787	0.0185	1.59	-0.464
n-Hexane	115.2	0.1033	0.1252	0.0218	0.1450	0.0045	0.6062	0.0787	0.0319	1.05	-0.049
hmpa ^a	177.11	0.1153	0.1451	0.6559	0.1874	0.0111	24.0137	3.1901	0.8576	0.83	0.186
Methanol	33.67	0.0932	0.1314	0.3291	0.1402	0.1803	1.9036	0.7258	0.3807	0.50	0.693
mth-2-butn ^a	95.89	0.1040	0.1255	0.0666	0.1453	0.0126	1.0273	0.1670	0.0642	1.00	0.000
mthcyclhxn ^a	118.85	0.1096	0.1293	0.0560	0.1465	0.0110	0.7224	0.1523	0.0344	1.37	-0.315
n-Nonane	169.3	0.1039	0.1270	0.0218	0.1463	0.0045	0.6997	0.0787	0.0250	1.21	-0.191
n-Octane	151.42	0.1036	0.1265	0.0218	0.1460	0.0045	0.6699	0.0787	0.0268	1.16	-0.148
n-Pentadecane	271.8	0.1066	0.1288	0.0218	0.1473	0.0045	0.8780	0.0787	0.0191	c	c
n-Pentane	97.4	0.1028	0.1240	0.0217	0.1446	0.0045	0.5809	0.0786	0.0363	0.97	0.030
1-Pentanol	101.93	0.1045	0.1336	0.3234	0.1462	0.1790	2.2997	0.6679	0.1353	0.94	0.062
2-Propanol	68.04	0.1010	0.1335	0.3200	0.1450	0.1781	1.5821	0.5893	0.1438	0.80	0.223
Propionitrile	61.23	0.1005	0.1197	0.1055	0.1620	0.0291	0.5967	0.2802	0.0746	0.46	0.777
n-Tetradecane	247.04	0.1096	0.1286	0.0218	0.1472	0.0045	0.8475	0.0787	0.0197	1.44	-0.365
n-Tridecane	238.85	0.1054	0.1284	0.0218	0.1471	0.0045	0.8186	0.0787	0.0205	1.37	-0.315
tm224pntne ^a	145.9	0.1065	0.1293	0.1045	0.1461	0.0057	2.4571	0.2421	0.0983	1.10	-0.095
n-Undecane	202.35	0.1057	0.1278	0.0218	0.1468	0.0045	0.7592	0.0787	0.0223	c	c

^aDMSO = dimethyl sulfoxide, hmpa = hexamethylphosphoramide, mth-2-butn = 2-methylbutane, mthcyclhxn = methylcyclohexane, tm224pntne = 2,2,4-trimethylpentane.

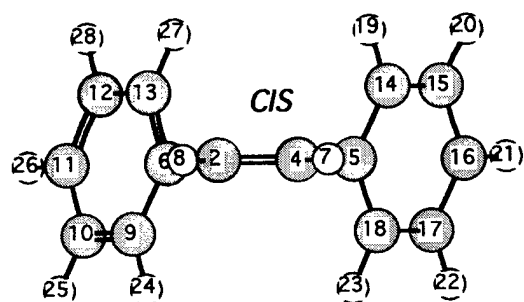
^bEb = electrostatic basicity; Ea = electrostatic acidity.

^cNot part of experimental data set; calculations included for illustrative purposes.

scriptors for the approximate transition state show variations that range from < 1% to as large as 11%. The changes observed in the calculated dipole descriptors in Table III support the molecular dipole model for the solvent dependence of this isomerization. These calculations are viewed as probes of significant trends in complex processes and are meant to be suggestive rather than quantitative.

The TLSER regressions were performed using the isomerization rate data shown in Table II. Because of the limited amount of experimental data, and because of large cross correlations between descriptors for this data set, it was essential

to search for the minimum set of descriptors that appeared significant. Using the established TLSER descriptors, the regression analysis demonstrated that the stilbene isomerization rate data were best represented by the molecular polarizability π_i and the electrostatic basicity q_- . The regression results are given in Table IV. During the search for minimum descriptors, it became apparent that the data for acetonitrile, propionitrile, and ethyl acetate were not well represented by the TLSER descriptors and they were removed from the regression as outliers whose residuals rates were well over three standard deviations removed from the rest of the data (Fig. 2). Nitrogen compounds, in particular



Approximate Transition State

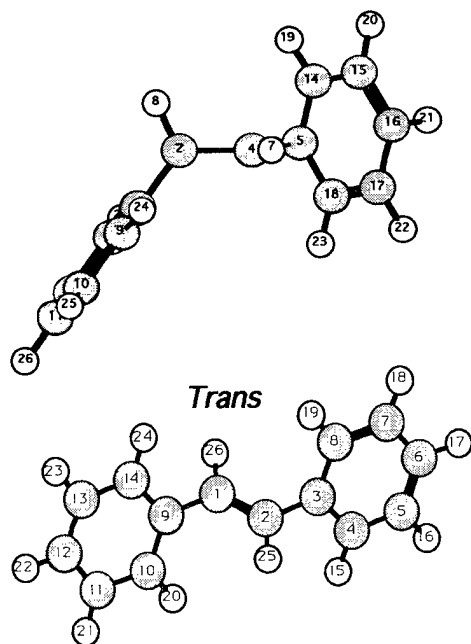


FIGURE 1. MNDO geometries of *cis*-stilbene, an approximate transition state with torsion around the ethylenic bond of 105.0° and *trans*-stilbene using a two-state configuration interaction.

acetonitrile, have often proven difficult to represent with this methodology, perhaps because of well-known difficulties in semiempirical calculations for these molecules [27]. At this time, it is not understood why ethyl acetate is not well represented by TLSE for this data set.

The VIF is the variable inflation factor used to measure cross-correlation among descriptors in the regression analysis. It is defined as

$$\text{VIF} = 1/(1 - R^2), \quad (5)$$

where R is the correlation coefficient of one variable against the others in the regression set. In the TLSE methodology, values of $1 < \text{VIF} < 5$ are considered acceptable. Because the proposed dipole descriptors are not yet well characterized, and because of the limited amount of experimental data, much stricter criteria were employed here in suggesting the significance of various descriptors for the rate of isomerization. For example, including the molecular volume descriptor in the above regression improves the R^2 value, increasing it to 0.941 and reducing the RMS residual to 0.086. However, the two-tail P value for the volume term is 0.0005 and the VIF factor for the volume is 1.41. While these are acceptable values, and the coefficient for the volume contribution is negative in accord with the proposed model for isomerization, the changes in statistical measures suggest that more data are necessary for a definitive analysis. Similarly, a regression using the TLSE polarizability and covalent basicity yielded goodness-of-fit values $R = 0.921$ and $R^2 = 0.848$, however, the VIF for the polarizability vs. the electrostatic basicity (E_b) was 1.1.

Regression analysis of this isomerization data using the proposed dipole descriptors was greatly aided by the VIF analysis of cross-correlation. There is not a strictly defined direct relationship between the TLSE descriptors and these proposed dipole quantities, even though they are all strictly defined in terms of results from the MOPAC calculations

TABLE III
TLSE descriptors for stilbene MNDO geometries optimized using two-state configuration interaction.

Stilbene configuration	V mol	Pi-I	Eb	Q -	Ea	Qh +	Total	Max	Average
<i>cis</i> -Stilbene	178.15	0.1358	0.1535	0.0644	0.1758	0.0599	1.7417	0.1353	0.0645
<i>trans</i> -Stilbene	177.00	0.1415	0.1535	0.0645	0.1764	0.0602	1.7786	0.1357	0.0659
TS ~ 105°	179.24	0.1519	0.1670	0.0655	0.1844	0.0680	1.7983	0.1442	0.0666

TABLE IV

TLSE regression on stilbene isomerization rates: $\ln(k) = b \times \pi_1 + d \times q - + \text{intercept}$
 ($n = 24$, $r = 0.945$, $sd = 0.114$); $R = 0.945$, $R^2 = 0.892$, $\text{Adj } R^2 = 0.882$, and $\text{RMS residual} = 0.114$.

	<i>b</i>	<i>d</i>	Intercept
Coefficient	-38.800	1.289	3.850
±	5.022	0.810	0.531
<i>t</i> value	-7.726	11.540	7.248
<i>P</i> (two-tail)	< 0.001	< 0.001	< 0.001
VIF	1.00	1.00	
Std. coefficient	-0.542	0.810	3.850

Solvent	Experimental $\ln(k)$	Calculated $\ln(k)$	Residual
Acetonitrile (avg, [11, 13])	.968	-.014	.981
Cycloheptane [8]	-.419	-.484	.066
Cyclohexane [9]	-.315	-.468	.153
Cyclononane	—	-.478	—
Cyclooctane [8]	-.482	-.391	-.092
Cyclopentane [8]	-.223	-.249	.026
<i>n</i> -Decane [11]	-.239	-.219	-.020
1-Decanol [8]	-.122	.030	-.153
Diethyl ether [8]	.416	.280	.136
DMSO (avg, [8, 11])	.528	.507	.021
Dioxane	.315	.096	.219
<i>n</i> -Dodecane [11]	-.300	-.145	-.155
Ethanol [8]	.478	.453	.025
Ethyl acetate [8]	.616	.147	.469
Heptane	—	-.126	—
<i>n</i> -Hexadecane [14]	-.464	-.262	-.202
<i>n</i> -Hexane (avg, [8, 10, 12–14])	-.049	-.130	.081
hmpa [8]	.186	.222	-.036
Methanol (avg, [9, 11, 12])	.693	.658	.035
mth-2-butn [14]	.000	-.099	.099
mthcylhxn [8]	-.315	-.330	.015
<i>n</i> -Nonane [13]	-.191	-.153	-.038
<i>n</i> -Octane [13]	-.148	-.141	-.007
Pentadecane	—	-.258	—
<i>n</i> -Pentane [8]	.030	-.110	.141
Pentanol [11]	.062	.213	-.151
Propan-2-ol [11]	.223	.344	-.121
Propionitrile [8]	.777	.087	.690
Tetradecane [10]	-.365	-.374	.009
Tridecane	—	-.211	—
tm224patne [14]	-.095	-.147	.052
Undecane	—	-.223	—

See footnote a to Table II for abbreviations.

[24, 26]. Based on the regression results above, and the model proposed by McGill and co-workers [7], the polarizability term was chosen as the most significant TLSE descriptor. In the process of minimizing additional descriptors, the best regression analysis was achieved by combining the po-

larizability and the average dipole descriptors μ^A . These regression statistics are given in Table V.

Regression using the polarizability and the total dipole descriptor, μ^T , yielded goodness of fit values $R = 0.787$ and $R^2 = 0.64$. Using the maximum dipole descriptor, μ^M , and the polarizability

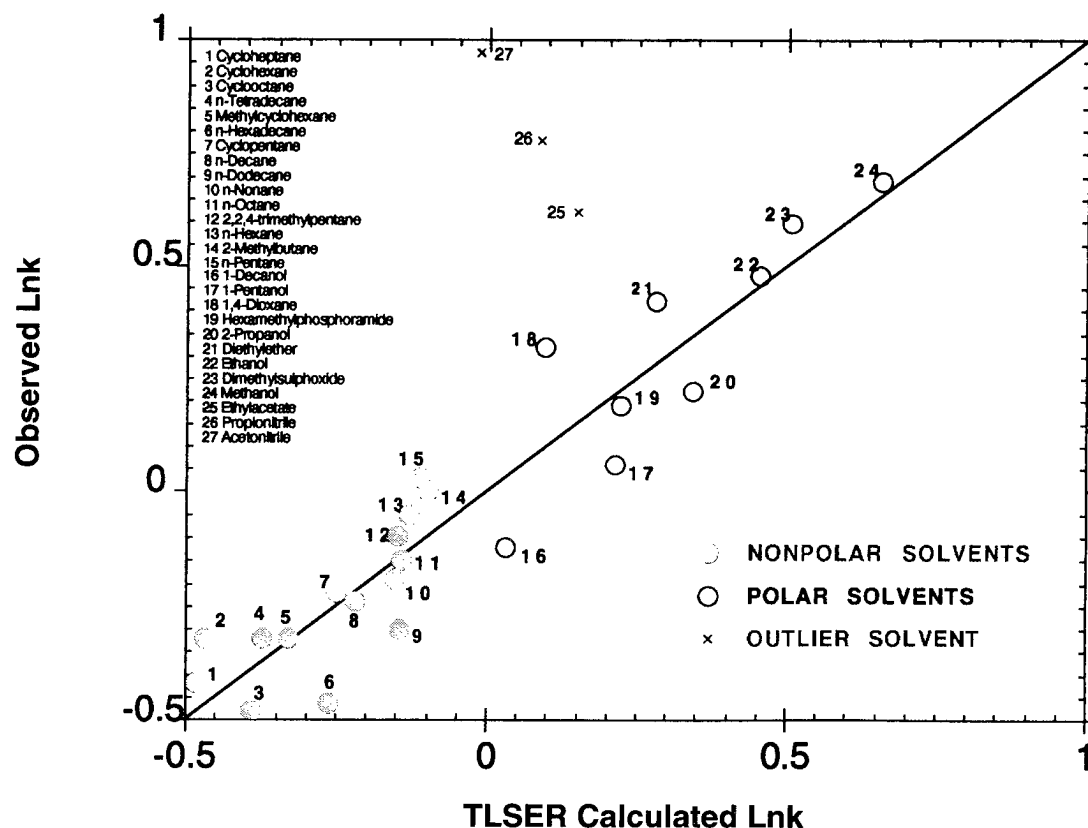


FIGURE 2. Observed vs. TLSEr calculated transition rates for solvent-dependent photoisomerization of stilbene. The regression line is shown for the final regression with the outliers removed.

yielded goodness of fit values $R = 0.900$ and $R^2 = 0.810$. The VIF factor for the polarizability and the μ^M descriptor is 1.09, suggesting a stronger cross-correlation between these two descriptors as perhaps the explanation for the less satisfactory good-

TABLE V
Regression equation and statistics using polarizability and average dipole descriptors:
 $\ln(k) = b \times \pi_1 + m_3 \times \mu^A + \text{intercept}$
($n = 24$, $r = 0.913$, $sd = 0.141$); $R = 0.913$,
 $R^2 = 0.833$, $\text{Adj } R^2 = 0.818$, and $\text{RMS residual} = 0.141$.

	b	m_3	Intercept
Coefficient	-44.827	1.086	4.544
\pm	6.326	0.783	0.667
t value	-7.086	8.858	6.808
P (two-tail)	< 0.001	< 0.001	< 0.001
VIF	1.03	1.03	
Std. coefficient	-0.626	0.783	4.544

ness of fit. The volume descriptor is found to contribute to the regression analysis in a manner similar to the contribution with the polarizability and electrostatic basicity. Using the volume descriptor along with the μ^A dipole descriptor increases the goodness of fit to yield $R = 0.953$ and $R^2 = 0.907$, but the VIF for the volume is 1.35 and the VIF for the AVG descriptor increases to 1.20.

Because models for the isomerization process for *cis-trans*-stilbene need not necessarily involve significant hydrogen-bonding or cavity term effects, it is possible to simplify Eqs. (1)–(3) by removal of the last three terms. The resulting regressions for all the data shown in Table II are

$$\ln(k) = 2.21 - 10.07 \times f(n)_1 + 1.06 \times \pi_1$$

$$(n = 30, r = 0.980, sd = 0.09) \quad (6)$$

$$\ln(k) = 2.14 - 9.61 \times f(n)_1 + 0.24 \times \mu$$

$$(n = 30, r = 0.975, sd = 0.11) \quad (7)$$

$$\ln(k) = 1.33 - 8.32 \times f(n)_1 + 2.45 \times f(\epsilon)$$

$$(n = 30, r = 0.906, sd = 0.19). \quad (8)$$

From these equations, it is clear that the photoisomerization of *cis*-stilbene to *trans*-stilbene may be explained in terms of a polar transition state. These equations show positive contributions from terms representing the polarity of the solvent such that more polar solvents increase the isomerization rate. Opposing this is a term representing induced molecular polarizability which retards the isomerization and dominates the different equations. This suggests that polarizable term interactions, between the transition state and polarizable solvents, result in attractions between molecules. Coupled with polarizability interactions between solvent molecules, this indicates an increased "sip-stick"-type friction for the phenyl group as it rotates about the central carbon-carbon bond toward *trans*-stilbene. More polarizable solvents thus retard the isomerization rate.

Discussion

The results of the MNDO-CI(2) calculations are consistent with other theoretical models for the isomerization of *cis*-stilbene [3]. The *trans* form exhibits a slightly lower heat of formation (60.7 kcal) than does the *cis* form (61.1 kcal) and both forms exhibit similar structures around the ethylenic bond with only minor variations in optimized geometric parameters. The approximate model for the transition-state geometry, calculated for ethylenic torsion fixed at 105.0° away from the *cis* orientation, shows sharp differences in optimized geometric parameters, with the central bond at 1.467 Å compared to 1.345 Å for the initial *cis* and *trans* forms. The C—C bond length to the phenyl groups is approximately the same as the central bond in the twisted form, averaging 1.466 Å, which is slightly smaller than the average 1.480 Å found in the planar forms. The lengthening of the central bond is consistent with results from vibrational analysis [3].

EMPIRICAL LSER VS. THEORETICAL TLSER MODEL

The different *cis*-*trans*-stilbene equations developed by multiple linear regression of empirical and theoretically derived solubility parameters show very similar trends and similar statistical quality. However, the LSER empirical model does provide a slightly better fit to the data and can model all the different solvent data, whereas for

the TLSER model, the nitrogen-containing solvents and ethyl acetate had to be removed from the data set as outliers from the model. In both models, increasing solvent "polarity" advances isomerization rates and increasing solvent polarizability retards isomerization rates, and the latter dominates the process even for the most dipolar solvents studied. Dipolar solvents interact with a polar stilbene transition state, providing a more favorable reaction pathway via a lower-energy transition state. Polarizable solvents interact with stilbene and surrounding layers of solvent molecules to form a friction barrier to rotation of the phenyl group from the transition state through to the *trans* isomer. Increasing solvent polarizability leads to larger microscopic friction.

From the stilbene equations developed, we can now use them to predict new isomerization rates and evaluate term contributions to examine which solvation factors dominate the process. For the empirically developed LSER Eq. (9) and the theoretically developed TLSER Eq. (10), the term contributions are listed for some representative solvents.

A comparison of "polar" terms in Table VI(a) shows that there is very good agreement in the LSER and TLSER term contributions. It is not surprising therefore to find that μ and q_- are very well correlated [Eq. (11)] for the stilbene solvent set after elimination of the two nitrile containing solvents.

Similarly, a comparison of "polarizability" terms [Table VI(b)] also shows some very similar trends for homologs and between different families. The relatively constant difference between the magnitude of the terms for solvents can be traced to the difference of the regression constants from the two LSER and TLSER equations. The direct comparisons are shown in Table VI(c). A plot of $f(n)$ vs. π_1 for all the solvents in Eq. (12) is also quite reasonable, although the scatter of the plot reduces the correlation coefficient:

$$\ln(k) = 2.14 - 9.61 \cdot f(n)_1 + 0.24 \cdot \mu \quad (9)$$

$$\ln(k) = 3.85 - 38.8 \cdot \pi_1 + 1.29 \cdot q \quad (10)$$

$$\mu = -0.13 + 5.39 q_- \quad r = 0.99 \quad (11)$$

$$f(n)_1 = -0.15 + 3.72 \cdot \pi_1 \quad r = 0.85. \quad (12)$$

Also in this work, stilbene was studied using the polarizable continuum model (PCM) [28] as

TABLE VI
Comparison of LSER and TLSER polarity terms, polarizability terms, and regressions.

(a) Comparison of LSER and TLSER polarity terms		
Solvent	LSER dipolar term 0.24 μ	TLSER dipolar term 1.29 $q -$
<i>n</i> -Hexane	0.00	0.03
<i>n</i> -Decane	0.00	0.03
<i>n</i> -Tetradecane	0.00	0.03
Cyclohexane	0.00	0.01
Cyclooctane	0.00	0.00
Methanol	0.41	0.42
Pentanol	0.40	0.42
Decanol	0.39	0.42
Dimethyl sulfoxide	0.95	0.93
Ethyl acetate	0.43	0.46
Diethyl ether	0.28	0.44

(b) Comparison of LSER and TLSER polarizability terms		
Solvent	LSER polarizability term $-9.61 f(n)$	TLSER polarizability term $-38.8 \pi_1$
<i>n</i> -Hexane	-2.21	-4.01
<i>n</i> -Decane	-2.40	-4.10
<i>n</i> -Tetradecane	-2.50	-4.25
Cyclohexane	-2.50	-4.33
Cyclooctane	-2.59	-4.24
Methanol	-1.92	-3.62
Pentanol	-2.40	-4.05
Decanol	-2.50	-4.24
Dimethyl sulfoxide	-2.69	-4.27
Ethyl acetate	-2.21	-4.16
Diethyl ether	-2.11	-4.01

(c) Comparison of LSER and TLSER regressions							
Solvent	Ln obs (1 / t)	ln k_0	0.24 μ	$-9.61 (n)$	ln k_0	1.29 $q -$	$-38.8 \pi_1$
<i>n</i> -Pentane	0.000	2.14	0.00	-2.11	3.85	0.03	-3.99
<i>n</i> -Hexane	-0.100	2.14	0.00	-2.21	3.85	0.03	-4.01
<i>n</i> -Octane	-0.148	2.14	0.00	-2.31	3.85	0.03	-4.02
<i>n</i> -Nonane	-0.191	2.14	0.00	-2.40	3.85	0.03	-4.03
<i>n</i> -Decane	-0.239	2.14	0.00	-2.40	3.85	0.03	-4.10
<i>n</i> -Dodecane	-0.300	2.14	0.00	-2.40	3.85	0.03	-4.02
<i>n</i> -Tetradecane	-0.322	2.14	0.00	-2.50	3.85	0.03	-4.25
Cyclopentane	-0.223	2.14	0.00	-2.40	3.85	0.02	-4.12
Cyclohexane	-0.315	2.14	0.00	-2.50	3.85	0.01	-4.33
Cycloheptane	-0.419	2.14	0.00	-2.59	3.85	0.00	-4.34
Cyclooctane	-0.482	2.14	0.00	-2.59	3.85	0.00	-4.24
Methylcyclohexane	-0.315	2.14	0.00	-2.40	3.85	0.07	-4.25
Methanol	0.693	2.14	0.41	-1.92	3.85	0.42	-3.62
Ethanol	0.478	2.14	0.41	-2.11	3.85	0.42	-3.81
Propan-2-ol	0.223	2.14	0.40	-2.21	.85	0.41	-3.92
Pentanol	0.062	2.14	0.40	-2.40	.85	0.42	-4.05

(Continued)

(Continued)

TABLE VI
(Continued)

(c) Comparison of LSER and TLSER regressions							
Solvent	Ln obs (1/t)	ln k_0	0.24 μ	-9.61 (n)	ln k_0	1.29 q -	-38.8 π_1
Decanol	-0.122	2.14	0.39	-2.50	.85	0.42	-4.24
Acetonitrile	0.968	2.14	0.94	-2.02	3.85	0.15	-4.00
Propionitrile	0.777	2.14	0.97	-2.11	3.85	0.14	-3.90
Dimethyl sulfoxide	0.598	2.14	0.95	-2.69	3.85	0.93	-4.27
HMPA	0.186	2.14		-2.59	3.85	0.85	-4.47
Ethyl acetate	0.616	2.14	0.43	-2.21	3.85	0.46	-4.16
Diethyl ether	0.416	2.14	0.28	-2.11	3.85	0.44	-4.01

implemented in the ZINDO program [29–33]. The model develops a realistic shape of the cavity around the solute by surrounding each atom by intersecting spheres with radii equal to the van der Waals radii. The surface is divided into patches (tesserae) by a triangulation technique [34–36]. Each tessera is represented by a point which carries the entire charge of that patch.

The PCM model used in this work was presented in detail elsewhere [37, 38]. The new features of the PCM model developed include several different approaches for estimating the electrostatic potential of the solute. Charges derived from the Mulliken population analysis, from the zero differential overlap (ZDO) density matrix, and from the ZDO density matrix plus point atomic dipoles were implemented to estimate the electrostatic potential on the tessera. In addition, we made algorithmic improvements, including calculating the charges on the tessera internal to the self-consistent field (SCF) procedure, that speed up the calculations significantly and lead to a good agreement between the calculated and experimental solvation energies.

The results obtained from preliminary calculations [37, 38] show that the "ZDO charge dipole" approximation to estimate the solution electrostatic potential appears to be most suitable for the description of the solvent-solute interactions. Therefore, we chose this latter method for our studies on *cis*-stilbene.

According to the general expression (PCM),

$$\sigma(r) = \frac{1 - \epsilon}{4\pi\epsilon} \cdot \frac{\partial}{\partial n} [\phi_p(r) + \phi_\sigma(r)], \quad (13)$$

the charge density on the cavity surface $\sigma(r)$ is a function of the dielectric constant of the medium, ϵ . The electrostatic part of the total energy, E_{polar} , is thus screened through ϵ which is the only solvent characteristic within the time-independent PCM model.

The dipole moments of *cis*-stilbene and those for the geometry calculated as an approximation for a transition-state structure in gas phase (twist angle = 105.0°) were calculated via PCM in a variety of solvents. The results are given in Table VII. These dipole moments alone can reproduce the experimental decay rates with a statistical data fit of $R = 0.774$ with an rms error of 0.26. A regression with these dipoles and the molecular volume yields a statistical data fit of $R = 0.84$ and an rms error of 0.23.

A significant question in this study is the link between different computational approaches for obtaining the solvation descriptors. A regression analysis on the PCM calculated TS dipoles shows that the TLSER q^+ is correlated with a goodness of fit of 0.95 over the solvent molecules data set without the outliers. This goodness of fit does not change appreciably when the solvent molecules in Table II, for which there is no experimental data, are also included in the regression. However, the goodness of fit deteriorates dramatically to 0.77 when the outlier molecules, acetonitrile, propionitrile, and ethyl acetate, are included in the regression. This suggests that current advances in solvation theory such as the PCM can provide significant insight into solvation descriptors such as those used in the TLSER and in the LSER empirical descriptor set.

TABLE VII
PCM dipole moments calculated for approximate transition-state (TS-105) and *cis*-stilbene geometries.

Solvent	Dielectric Constant	TS-105 (D)	<i>cis</i> -Stilbene (D)	Experimental lifetime (ps)
Gas phase	1.000	0.590	0.319	0.32
Acetonitrile	37.500	0.846	0.548	0.38
Cycloheptane	1.965	0.680	0.402	1.52
Cyclohexane	2.023	0.683	0.405	1.37
Cyclononane ^a	2.000	0.682	0.404	—
Cyclooctane ^a	2.000	0.682	0.404	1.37
Cyclopentane	1.965	0.680	0.402	1.25
Decane	1.991	0.682	0.403	1.27
Decanol	8.100	0.803	0.511	1.26
Diethyl ether	4.335	0.763	0.475	0.66
Dimethyl sulfoxide	4.700	0.767	0.480	0.59
Dioxane	2.209	0.695	0.414	0.73
Dodecane	2.015	0.683	0.405	1.35
Ethanol	24.300	0.839	0.542	0.62
Ethyl acetate	6.020	0.787	0.496	0.54
Heptane	1.920	0.678	0.399	—
Hexadecane ^a	2.000	0.682	0.404	1.59
Hexane	1.890	0.675	0.397	1.05
hmpa ^a	2.000	0.682	0.404	0.83
Methanol	32.630	0.844	0.546	0.50
2-Methylbutane	1.843	0.672	0.394	1.00
Methylcyclohexane	2.020	0.683	0.405	1.37
Nonane	1.972	0.681	0.402	1.21
Octane	1.948	0.679	0.401	1.16
Pentadecane ^a	2.000	0.682	0.404	—
Pentane	1.844	0.672	0.394	0.97
Pentanol	13.900	0.825	0.530	0.94
Propan-2-ol	18.300	0.835	0.537	0.46
Propionitrile ^b	37.50	0.846	0.548	0.46
Tetradecane ^a	2.000	0.682	0.404	1.37
Tridecane ^a	2.000	0.682	0.404	1.44
2,2,4-Trimethylpentane	1.940	0.679	0.401	1.10
Undecane	2.005	0.682	0.404	—

^ahmpa = hexamethylphosphoramide. Dielectric constant assumed to be = 2.0.^bDielectric constant assumed equal to that of acetonitrile.

ACKNOWLEDGMENT

This work was supported in part through a grant from the Office of Naval Research (M. C. Z.).

References

1. D. Raftery, R. J. Sension, and R. M. Hochstrasser, in *Activated Barrier Crossing*, G. R. Fleming and P. Hangii, Eds. (World Scientific, Rucer Edge, NJ, 1993), pp. 163–205.
2. R. M. Hochstrasser, *Pure Appl. Chem.* **52**, 2683 (1980).
3. D. H. Waldeck, *Chem. Rev.* **91**, 415 (1991).
4. C. Hansch, *Acc. Chem. Res.* **26**, 147 (1993).
5. P. Politzer and J. S. Murray, Eds., *Quantitative Treatment of Solute/Solvent Interactions* (Elsevier, Amsterdam, 1994), Vol. 1.
6. G. R. Famini and L. Y. Wilson, in *Quantitative Treatment of Solute/Solvent Interactions*, P. Politzer and J. S. Murray, Eds. (Elsevier, Amsterdam, 1994), Vol. 1, pp. 213–241.
7. R. A. McGill, J. K. Rice, A. P. Baronavski, and J. C. Owrrutsky, in *ERDEC Meeting on Solute/Solvent Interactions*, G. R. Famini, Ed. (U.S. Army CBDCOM: APG, MD, 1994).
8. J. K. Rice, A. P. Baronavski, and J. C. Owrrutsky, unpublished data.
9. J. K. Rice and A. P. Baronavski, *J. Chem. Phys.* **93**, 3359 (1992).
10. D. C. Todd, J. M. Jean, S. J. Rosenthal, J. Ruggerio, D. Yang, and G. R. Fleming, *J. Chem. Phys.* **93**, 8568 (1990).

11. D. C. Todd and G. R. Fleming, *J. Chem. Phys.* **98**, 269 (1993).
12. R. J. Sension, S. T. Repinec, A. Z. Szarka, and R. M. Hochstrasser, *J. Chem. Phys.* **98**, 6291 (1993).
13. L. Nikowa, D. Schwarzer, J. Troe, and J. Schroder, *J. Chem. Phys.* **93**, 4827 (1992).
14. S. Abrash, S. Repinec, and R. M. Hochstrasser, *J. Chem. Phys.* **93**, 1041 (1990).
15. I. A. Koppel and V. A. Palm, *Org. React. USSR* **8**, 291 (1971).
16. I. A. Koppel and V. A. Palm, in *Advances in Linear Free Energy Relationships*, N. B. Chapman and J. Shorter, Eds. (Plenum, London, 1972).
17. R. G. Makitra, Y. N. Pirig, A. M. Zeliznyi, V. L. Daniel de Aguar, V. L. Mikolajev, and V. A. Ramanov, *Org. React. USSR* **14**, 421 (1977).
18. R. G. Makitra and Y. N. Pirig, *Org. React. USSR* **16**, 535 (1979).
19. M. J. Kamlet and R. W. Taft, *Acta Chem. Scand.* **39**, 611 (1985).
20. C. J. Cramer, G. R. Famini, and A. H. Lowrey, *Acc. Chem. Res.* **26**, 599 (1993).
21. A. H. Lowrey, C. J. Cramer, J. J. Urban, and G. R. Famini, *Comput. Chem.* **19**, 209 (1995).
22. J. J. P. Stewart, in *Reviews of Computational Chemistry*, K. B. Lipkowitz and D. B. Boyd, Eds. (VCH, New York, 1990), Vol. 1, pp. 45-118.
23. M. C. Zerner, in *Reviews of Computational Chemistry*, K. B. Lipkowitz and D. B. Boyd, Eds. (VCH, New York, 1991), Vol. 2, pp. 313-365.
24. J. J. P. Stewart, *QCPE Bull.* **10**, 86 (1990).
25. G. R. Famini, C. A. Penski, and L. Y. Wilson, in *Meeting on Solute/Solvent Interactions*, G. R. Famini, Ed. (U.S. Army Chemical Research Development and Engineering Center, Aberdeen Proving Grounds, Maryland, 1992), Vol. CRDEC-SP-009, pp. 71-75.
26. J. A. Fager and G. R. Famini, MADCAP program package (Axis Technologies).
27. L. Wilson, private communication.
28. J. Tomasi and M. Persico, *Chem. Rev.* **94**, 2027 (1994).
29. M. C. Zerner, ZINDO program package (Quantum Theory Project, University of Florida).
30. M. C. Zerner, G. H. Loew, R. F. Kirchner, and U. T. Mueller-Westerhoff, *J. Amer. Chem. Soc.* **102**, 589 (1980).
31. J. Ridley and M. C. Zerner, *Theor. Chim. Acta* **32**, 111 (1973).
32. W. D. Edwards and M. C. Zerner, *Theor. Chim. Acta* **72**, 347 (1987).
33. A. D. Bacon and M. C. Zerner, *Theor. Chim. Acta* **53**, 21 (1979).
34. J. L. Pascual-Ahuir, E. Silla, J. Tomasi, and R. J. Bonacorsi, *Comput. Chem.* **8**, 778 (1987).
35. J. L. Pascual-Ahuir and E. Silla, *J. Comput. Chem.* **11**, 1047 (1990).
36. E. Silla, I. Tunon, and J. L. Pascual-Ahuir, *J. Comput. Chem.* **12**, 1077 (1991).
37. K. K. Stavrev, T. Tamm, and M. C. Zerner, in *4th Conference on Current Trends in Computational Chemistry* (U.S. Army Waterways Experimental Station, Vicksburg, MS, 1995), p. 111.
38. K. K. Stavrev, T. Tamm, and M. C. Zerner, *Int. J. Quant. Chem.* **60** (7), 373 (1996).

Does the Proton-Transfer Reaction Take Place in the Ground State of Phenol-(H₂O)₄ Clusters?

HIDEKAZU WATANABE AND SUEHIRO IWATA

Graduate University for Advanced Studies, and Institute for Molecular Science, Okazaki 444, Japan

Received February 24, 1996; revised manuscript received April 17, 1996; accepted April 24, 1996

ABSTRACT

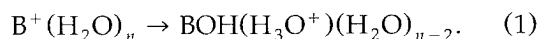
In recent experimental studies of infrared (IR) spectra of hydrated phenol clusters, the Mikami and Ebata group at Tohoku University attributed apparently two very different spectra to PhOH(H₂O)₄. The first spectrum has a wide transparent region between 3500 and 3700 cm⁻¹, which they named a window region. The second spectrum has several absorption bands in this window region. Our previous study revealed that the first spectrum was assigned to the isomers which have a single-ring structure of a hydrogen-bonding network of OH's of phenol and waters. The experimentalists suggested that the second spectrum might be identified to a proton-transferred phenol-water cluster. In the present article, the geometrical structures of proton-transferred hydrated phenol clusters were determined with the *ab initio* molecular orbital method and their IR spectra were calculated. The proton-transferred phenol-water cluster is at a stable local minimum, but the energy is much higher than that of the most stable nontransferred cluster. The calculated IR spectrum has a still wider window region and is far different from the experimental spectrum of the second type. © 1996 John Wiley & Sons, Inc.

Introduction

The proton-transfer reaction is one of the typical chemical reactions. As described even in high school textbooks, a part of the water molecules in pure bulk water are dissociated to the oxonium ion H₃O⁺ and the hydroxyl ion OH⁻. The dissociation constant of pure water K_w is 1.0×10^{-14} at room temperature. Here is an intriguing question in cluster chemistry: Does the proton-transfer reac-

tion take place in small water clusters? Very recently, Lee et al. theoretically predicted that proton-transferred clusters could exist in such small water clusters as H₃O⁺OH⁻(H₂O)₃ and H₃O⁺OH⁻(H₂O)₆ [1]. They are much less stable than are the well-investigated normal water clusters (H₂O)₅ and (H₂O)₈ [2-12], but the proton-transferred water clusters are at a stable local minima. When the cluster has an acidic nature, the proton-transfer reaction more easily takes place. Recently, we reported that in the hydrated singly

charged boron cation–water clusters $B^+(H_2O)_n$ the proton-transfer reaction proceeds without any barrier for $n \geq 2$ [13]:



Phenol is one of the fundamental organic acids. One can expect that the possibility of the proton-transfer reaction in hydrated phenol clusters is higher than in pure water clusters. This possibility was first noticed by the Mikami group at Tohoku University, when they studied the infra-red (IR) spectra of phenol–water clusters $PhOH(H_2O)_n$ (for $n \leq 4$), [14, 15]. Up to $n = 3$, the observed spectra have a transparent region between antisymmetric and symmetric stretching modes of water molecules around $3500\text{--}3700\text{ cm}^{-1}$. The region is named the "window region" by Mikami's group [14–16]. Our previous theoretical studies revealed that the spectra having a window region are assigned to the isomers of a single-ring structure consisting of an OH of phenol and an OH of each of n water [17]. In their "mass-selected" experiments, two different IR spectra were attributed to $PhOH(H_2O)_4$. One of the spectra is similar to those for $n = 2$ and 3 and is identified to the isomers of a ring structure. On the other hand, the other has

no window region and shows several absorption bands in this region. To explain this second spectrum, the proton-transferred phenol–water clusters were suggested [14, 15].

In the present article, the geometric structures of proton-transferred phenol–water clusters, which are regarded as derivatives of proton-transferred water clusters reported in [1], are determined with the ab initio molecular orbital method. The IR spectra of the proton-transferred phenol–water clusters as well as pure water clusters are calculated, and the possibility of identification of the second type of spectrum in [14, 15] is examined.

Method

The closed-shell self-consistent field (SCF) molecular orbital method is used for optimization of the geometries and for evaluation of the IR spectra. The basis sets used are 6-31 + G* for oxygen atoms and the 6-31G* set for the rest of atoms (carbon and hydrogen). It is important to place diffuse functions on the oxygen for describing the hydroxyl anion OH^- . In [1], the basis set used is 6-31 + G** for all atoms. For $(H_2O)_5$ and

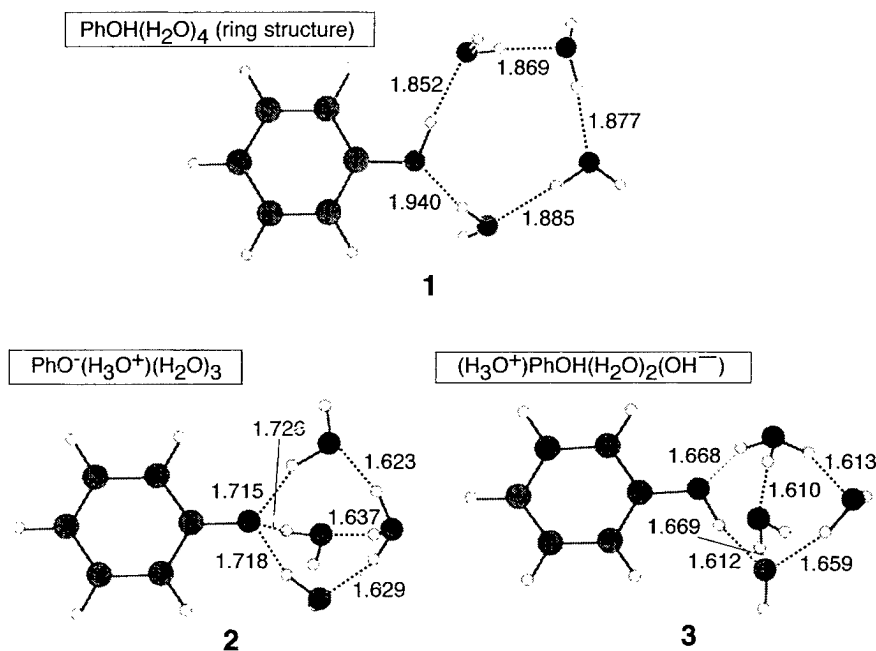


FIGURE 1. Structures of ring type (1) of $PhOH(H_2O)_4$ cluster and proton-transferred clusters of (2) $PhO^-(H_3O^+)(H_2O)_3$ and (3) $(H_3O^+)PhOH(H_2O)_2(OH^-)$. The geometric parameters were determined with the SCF/6-31 + G* method. Units are given in Å.

H₃O⁺(H₂O)₃OH⁻, the total energies are recalculated with the frozen-core second-order Møller-Plesset perturbation (MP2) method. The present basis set is smaller than that in [1], but large enough to describe the dissociation to ion-pair clusters. The scaling factor for harmonic frequencies is 0.8976, which is fixed by adjusting the symmetric and antisymmetric stretching modes of a free water molecule. Programs used are GAUSSIAN 92 and GAUSSIAN 94 packages [18, 19].

Results and Discussion

In our previous work [17], the most stable isomer of PhOH(H₂O)₄ has a single-ring structure consisting of the hydrogen-bonding network of OH groups of phenol and water molecules. Structure 1 in Figure 1 depicts the ring structure of the PhOH(H₂O)₄ cluster. Structures 2 and 3 are two proton-transferred phenol-water clusters PhOH(H₂O)₄, which are regarded as derivatives of the proton-transferred pure water cluster (H₃O⁺)(H₂O)₃(OH⁻) reported in [1]. Isomer 2 has the structure PhO⁻(H₂O)₃H₃O⁺, in which a proton of phenol is transferred to an oxonium ion. On the other hand, isomer 3 has the structure H₃O⁺PhOH(H₂O)₂OH⁻, in which a proton of water is transferred. The proton-transferred cluster (H₃O⁺)(H₂O)₃(OH⁻) has a C₃ symmetry and the C₃ axis is through the oxygen atom of the oxonium ion H₃O⁺ via the hydroxyl ion OH⁻. In structures 2 and 3, the local C₃ symmetry is almost preserved, although an OH⁻ ion in the water clusters is replaced with a PhO⁻ ion in the phenol-water clusters.

The relative energies of proton-transferred phenol-water and pure water clusters are summarized in Table I. Although a stable local minimum is found for PhO⁻(H₂O)₃H₃O⁺ (structure 2), the total energy is 138.43(144.49) kJ/mol higher than that of the ring PhOH(H₂O)₄ (structure 1) without (with) zero-point vibration correction. Isomer 2 is more stable than is isomer 3, as is expected from chemical common sense that the acidity of PhOH is stronger than that of H₂O. The energy difference between isomers 2 and 3 is 23.62 kJ/mol without a zero-point vibration collection and 23.56 kJ/mol with a zero-point vibration collection. The energy difference between isomers 1 and 3 is almost the same as the energy difference between (H₂O)₅ and H₃O⁺(H₂O)₃OH⁻, because the generated ion pair is the same. The energy difference between (H₂O)₅ and H₃O⁺(H₂O)₃OH⁻ with the SCF approximation is overestimated compared with that in [1]. But the single-point MP2 (frozen core) energy is in good agreement with that in [1], in spite of the smaller basis set. Thus, if we assume that the electron correlation effect on the proton-transfer reaction is similar to each other for the clusters (H₂O)₅ and PhOH(H₂O)₄, we may be able to discuss qualitatively the stability of the PhOH(H₂O)₄ and its ion-pair clusters.

The calculated infrared stick spectra of the clusters in the —OH frequency region are shown in Figure 2. Their numerals are summarized in Table II. Only dominant components are given for assignments of each absorption band in Figure 2 and Table II. Spectrum A in Figure 2 shows the stick spectra of a free water molecule, an oxonium ion H₃O⁺, and a hydroxyl ion OH⁻ for comparison. The calculated stick spectra of proton-trans-

TABLE I
Relative energy difference without zero-point vibration ($-\Delta E$) and with zero-point vibration ($-\Delta E_{\text{zpv}}$) correlation of the proton-transferred PhOH(H₂O)₄ and (H₂O)₅ clusters.

		$-\Delta E$	$-\Delta E_{\text{zpv}}$	
			SCF	MP2//SCF
PhOH(H ₂ O) ₄ (ring)	(1)	+0.00	+0.00	
PhO ⁻ (H ₂ O) ₃ H ₃ O ⁺	(2)	+138.43	+144.49	
H ₃ O ⁺ PhOH(H ₂ O) ₂ (OH ⁻)	(3)	+162.05	+168.05	
(H ₂ O) ₅ (ring)		+0.00	+0.00	+0.00 (+0.00)
H ₃ O ⁺ (H ₂ O) ₃ OH ⁻		+159.84	+168.69	+100.74 (+92.05)

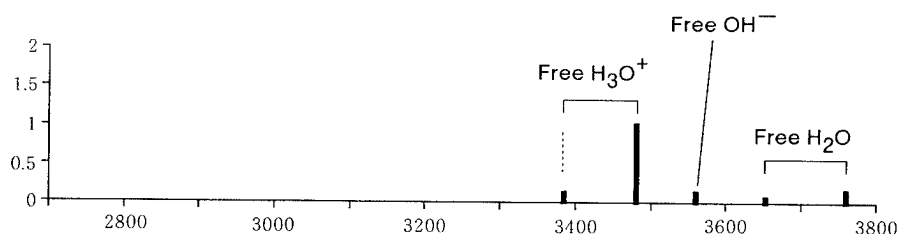
For $-\Delta E_{\text{zpv}}$ with MP2 (frozen core) evaluation, the zero-point vibration energies with the SCF level of approximation are added into the total energies calculated with the single-point MP2 (frozen core) level of approximation. Energy standards are set at the most stable ring isomers of PhOH(H₂O)₄ and (H₂O)₅. The values in parentheses are in [1] with the MP2/6-31 + G** level of approximation. Units are given in kJ/mol.

ferred clusters $(\text{H}_3\text{O}^+)(\text{H}_2\text{O})_3(\text{OH}^-)$, $\text{PhO}^- (\text{H}_2\text{O})_3(\text{H}_3\text{O}^+)$ (structure 2), and $(\text{H}_3\text{O}^+)\text{PhOH} (\text{H}_2\text{O})_2(\text{OH}^-)$ (structure 3) are spectra B, C, and D, respectively.

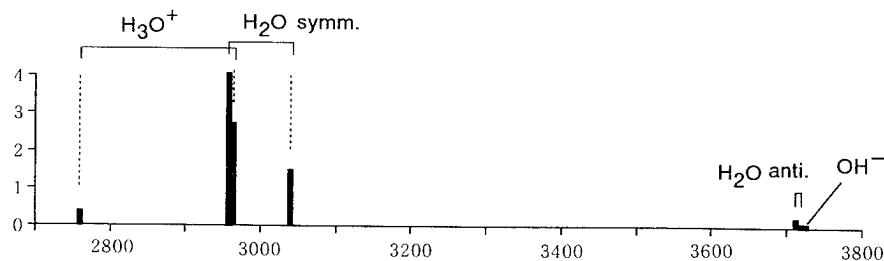
In previous theoretical studies, the IR spectra of the pure water cluster $(\text{H}_2\text{O})_n$ [2, 3] and hydrated phenol clusters $\text{PhOH}(\text{H}_2\text{O})_n$ [17], both of which have a single-ring structure, had similar character-

istics in the spectra. The antisymmetric stretching modes of water molecules do not move much. In contrast, the symmetric stretching modes of water molecules show large shifts toward the lower energy from a free water. The former mode is more or less localized in nonhydrogen bonding OH's, and the latter is on a hydrogen-bonding OH, forming a ring. In phenol-water clusters, the OH

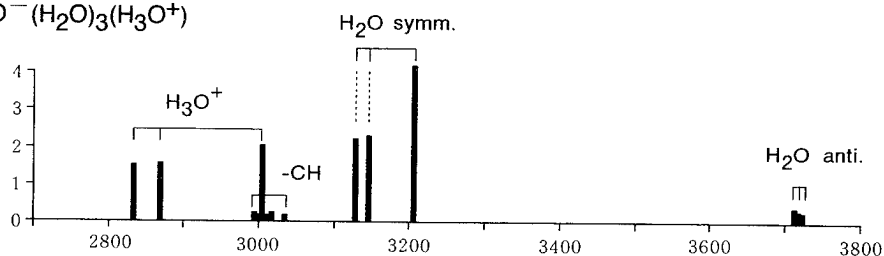
A. Free H_2O , OH^- , and (H_3O^+)



B. $(\text{H}_3\text{O}^+)(\text{H}_2\text{O})_3(\text{OH}^-)$



C. $\text{PhO}^- (\text{H}_2\text{O})_3(\text{H}_3\text{O}^+)$



D. $(\text{H}_3\text{O}^+)\text{PhOH}(\text{H}_2\text{O})_2(\text{OH}^-)$

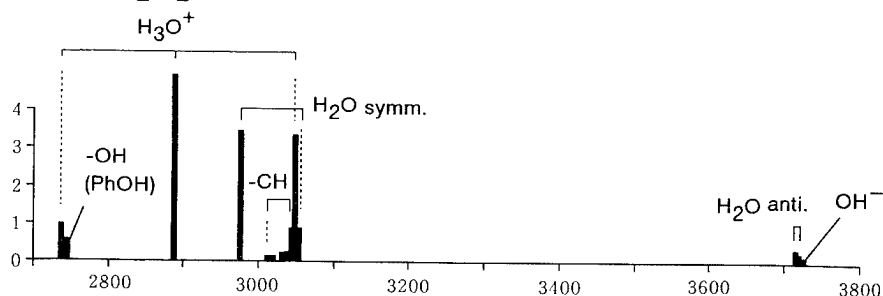


FIGURE 2. Calculated IR spectra of proton-transferred clusters and relative species: (A) water, oxonium ion, and hydroxyl ion; (B) $\text{H}_3\text{O}^+(\text{H}_2\text{O})_3\text{OH}^-$; (C) $\text{PhO}^-(\text{H}_3\text{O}^+)(\text{H}_2\text{O})_3$; (D) $(\text{H}_3\text{O}^+)\text{PhOH}(\text{H}_2\text{O})_3(\text{OH}^-)$. Only dominant components are given for assignments.

stretching mode of the phenol molecule also shifts toward the low frequency. The low-frequency shifts of symmetric stretching modes of water and the OH mode of phenol become larger for a large cluster size. In other words, the window region [14–16] is wider for a larger cluster size n in (H₂O) _{n} and PhOH(H₂O) _{n} of a ring structure. For the ring structure of PhOH(H₂O)₄, the experimental absorption bands of the OH stretching of PhOH and symmetric stretching of water appear in the region about 3150–3450 cm⁻¹, and the window region is around 3450–3700 cm⁻¹.

But as shown in Figure 2, the window region of proton-transferred clusters is much wider than that of the nontransferred ring structure of PhOH(H₂O)₄. In the calculated spectrum **B** for (H₃O⁺)(H₂O)₃(OH⁻) in Figure 2, the window region is range 3050–3700 cm⁻¹. The window region of spectrum **D** (for structure **3**) is almost as large as spectrum **B**. The window region of spectrum **C** (for structure **2**) is 3200–3700 cm⁻¹, a little narrower than that of spectrum **B**. It is, however, still wider than of the window region of PhOH(H₂O)₄. By hydrogen-bonding formation, the stretching modes of water and the OH stretching of phenol as well as the degenerate OH modes of oxonium ion H₃O⁺ shift substantially toward the low frequency.

According to the analysis by Schiöberg and Luck [20], the band shifts of water molecules are related to the strength of the basicity of the proton-accepting molecule. When the strong base molecule is bonded to a water as a proton acceptor, the base molecule attracts strongly a hydrogen atom of a water molecule. Thus, the OH bond of the water becomes weak and the frequency of OH stretching becomes lower. The very wide window regions of proton-transferred clusters are due to the much strong basicity of the hydroxyl ion OH⁻. Because the basicity of PhO⁻ is weaker than that of OH⁻, the window region in spectrum **C** for PhO⁻(H₃O⁺)(H₂O)₃ is somewhat narrower than in spectrum **B**. The width of the window region of spectrum **D** is almost same as that of spectrum **B** because the anion in (H₃O⁺)PhOH(H₂O)₂(OH⁻) is a hydroxyl ion, the same as in (H₃O⁺)(H₂O)₃(OH⁻).

In contrast, the high-frequency modes of water molecules in the cluster do not move much; the parentage of these modes is the antisymmetric mode of a water molecules. When two OH bonds are not equivalent by hydrogen bonding, this mode

becomes localized on a free (nonhydrogen bonding) OH. At the limit of complete decoupling of two OH modes, the frequency of the free OH mode is given as [20]

$$\nu_{\text{lim}} = \frac{\nu_1 + \nu_3}{2}, \quad (2)$$

where ν_1 and ν_3 are the frequencies of symmetric and antisymmetric modes of a *free* water. In the present case, $\nu_1 = 3653$ and $\nu_3 = 3750$, and, thus, $\nu_{\text{lim}} = (\nu_1 + \nu_3)/2 = 3702$ [cm⁻¹]. In these proton-transferred clusters, the frequencies of "unshifted" modes are about 3715 cm⁻¹, very close to 3702 cm⁻¹. In other words, two OH modes of a water in clusters are decoupled, which is evidence that water molecules in proton-transferred clusters are bonding to a strong base.

TABLE II
Calculated harmonic frequencies (cm⁻¹) and IR intensities (km/mol) of proton-transferred clusters and several associated moieties in the OH frequency region; only dominant components are written for assignments.

Frequency	Intensity	Assignment
<u>H₂O</u>		
3653	23.4	sym.
3750	87.5	anti.
<u>H₃O⁺</u>		
3385	62.6	
3481	598.6	
3481	598.6	
<u>OH⁻</u>		
3561	80.4	
<u>PhO⁻(H₂O)₃(H₃O⁺)</u>		
2832	836.4	H ₃ O ⁺
2867	876.4	H ₃ O ⁺
2993	68.9	—CH str.
2996	5.2	—CH str.
3004	1140.2	H ₃ O ⁺
3010	10.5	—CH str.
3015	88.4	—CH str.
3033	31.4	—CH str.
3127	1259.5	H ₂ O
3145	1324.3	H ₂ O
3205	2436.5	H ₂ O
3714	156.6	H ₂ O
3716	115.9	H ₂ O
3718	90.0	H ₂ O

(Continued)

TABLE II
(continued)

Frequency	Intensity	Assignment
$(\text{H}_3\text{O}^+)(\text{H}_2\text{O})_3\text{OH}^+$		
2761	212.7	H_3O^+
2761	212.7	H_3O^+
2958	2398.4	H_2O
2958	2398.4	H_2O
2961	1619.0	H_3O^+
3041	888.6	H_2O
3716	142.1	H_2O
3716	142.1	H_2O
3718	4.4	H_2O
3723	12.7	OH^- str.
$(\text{H}_3\text{O}^+)\text{PhOH}(\text{H}_2\text{O})_2(\text{OH}^-)$		
2738	516.0	H_3O^+
2746	271.0	OH of PhOH
2888	2908.4	H_3O^+
2974	2003.1	H_2O
3012	9.7	—CH str.
3020	9.4	—CH str.
3032	59.2	—CH str.
3039	56.0	—CH str.
3044	470.6	—CH str.
3048	1942.5	H_3O^+
3052	465.2	H_2O
3716	145.3	H_2O
3717	63.9	H_2O
3721	17.0	OH^- str.

Conclusion

The IR spectra of proton-transferred clusters have a very wide window region because of the strong basicity of OH^- and PhO^- . The possibility of the identification of the second spectrum of $\text{PhOH}(\text{H}_2\text{O})_4$ to such proton-transferred clusters is ruled out. An alternative species for the second spectrum is a larger size of clusters than $\text{PhOH}(\text{H}_2\text{O})_4$. In [17], we demonstrated that several IR bands are found in region $3500\text{--}3700\text{ cm}^{-1}$, if the cluster has a water molecule with both of the hydrogen atoms of the molecule bonded to other water molecules. The water molecule in which two hydrogens are bonded to base molecules was named the "double proton donor" by Jordan and Zwier's group [21, 22]. Some isomers of $\text{PhOH}(\text{H}_2\text{O})_5$ contain two such double proton donor waters. The second spectrum could be assigned to one of those isomers. It might be difficult

to experimentally find the proton-transferred clusters in such small clusters as $\text{PhOH}(\text{H}_2\text{O})_4$ and $(\text{H}_2\text{O})_5$ because of their instability. But one could obtain the proton-transferred clusters in larger sizes by matrix isolation techniques. By measuring the IR spectra, the wide window region could be a key of detecting the proton-transferred clusters.

ACKNOWLEDGMENTS

We acknowledge Professors Ebata and Mikami for bringing us the present research project and for stimulating discussion. H. W. thanks the Research Fellowships of the Japan Society for the Promotion of Science for Young Scientists for financial support. This work was partially supported by the Grant-in-Aids for Scientific Research (No. 04640458) and for the Priority Area (No. 04243102) by the Ministry of Education, Science, Sports and Culture, Japan.

References

1. C. Lee, C. Sosa, and J. J. Novoa, *J. Chem. Phys.* **103**, 4360 (1995).
2. S. S. Xantheas and T. H. Dunning, Jr., *J. Chem. Phys.* **99**, 8774 (1993).
3. E. Honegger and S. Leutwyler, *J. Chem. Phys.* **88**, 2582 (1988).
4. K.-P. Schröder, *Chem. Phys.* **123**, 91 (1988).
5. J. O. Jensen, P. N. Krishnan, and L. A. Bruke, *Chem. Phys. Lett.* **246**, 13 (1995).
6. S. S. Xantheas, *J. Chem. Phys.* **100**, 7523 (1994).
7. S. S. Xantheas, *J. Chem. Phys.* **102**, 4505 (1995).
8. G. Brink and L. Glasser, *J. Phys. Chem.* **88**, 3412 (1984).
9. C. J. Tsai and K. D. Jordan, *J. Phys. Chem.* **97**, 5208 (1993).
10. C. J. Tsai and K. D. Jordan, *J. Chem. Phys.* **95**, 3850 (1991).
11. D. J. Wales and I. Omine, *J. Chem. Phys.* **98**, 7245 (1993).
12. K. S. Kim, M. Dupuis, G. C. Lie, and E. Clementi, *Chem. Phys. Lett.* **131**, 451 (1986).
13. H. Watanabe and S. Iwata, *J. Phys. Chem.* **100**, 3377 (1996).
14. N. Mikami, *Bull. Chem. Soc. Jpn.* **68**, 683 (1995).
15. T. Watanabe, T. Ebata, S. Tanabe, and N. Mikami, *J. Chem. Phys.* (in press).
16. S. Tanabe, T. Ebata, M. Fujii, and N. Mikami, *Chem. Phys. Lett.* **215**, 347 (1993).
17. H. Watanabe and Iwata, *J. Chem. Phys.* (in press).
18. M. J. Frisch, G. W. Trucks, M. Head-Gordon, P. M. W. Gill, M. W. Wong, J. B. Foresman, B. G. Johnson, H. B. Schlegel, M. A. Robb, E. S. Replogle, R. Gomperts, J. L. Andres, K. Raghavachari, J. S. Binkley, C. Gonzalez, R. L. Martin, D. J. Fox, D. J. Defrees, J. Baker, J. J. P. Stewart, and J. A. Pople, *Gaussian 92, Revision E.2* (Gaussian, Inc., Pittsburgh, PA, 1992).

19. M. J. Frisch, G. W. Trucks, H. B. Schlegel, P. M. W. Gill, B. G. Johnson, M. A. Robb, J. R. Cheeseman, T. Keith, G. A. Petersson, J. A. Montgomery, K. Raghavachari, M. A. Al-Laham, V. G. Zakrzewski, J. V. Ortiz, J. B. Foresman, J. Cioslowski, B. B. Stefanov, A. Nanayakkara, M. Challacombe, C. Y. Peng, P. Y. Ayala, W. Chen, M. W. Wong, J. L. Andres, E. S. Replogle, R. Gomperts, R. L. Martin, D. J. Fox, J. S. Binkley, D. J. Defrees, J. Baker, J. P. Stewart, M. Head-Gordon, C. Gonzalez, and J. A. Pople, *Gaussian 94, Revision B.2* (Gaussian, Inc., Pittsburgh, PA, 1995).
20. D. Schiöberg and W. A. P. Luck, *J. Chem. Soc. Faraday Trans. 75*, 762 (1979).
21. K. Kim, K. Jordan, and T. S. Zwier, *J. Am. Chem. Soc.* **116**, 11568 (1994).
22. R. N. Pribble and T. S. Zwier, *Science* **265**, 75 (1994).

Generalized Conductor-like Screening Model (GCOSMO) for Solvation: An Assessment of Its Accuracy and Applicability

THANH N. TRUONG,* UYEN N. NGUYEN, AND EUGENE V. STEFANOVICH†

Department of Chemistry, University of Utah, Salt Lake City, Utah 84112

Received March 28, 1996; revised manuscript received May 27, 1996; accepted May 29, 1996

ABSTRACT

We present an assessment on the accuracy of a dielectric continuum solvation model, the generalized conductor-like screening model (GCOSMO), for predicting hydration free energies, tautomeric equilibria, and reaction profiles in solution. © 1996 John Wiley & Sons, Inc.

Introduction

For the past half century, quantum chemistry has made significant progress in the development of theory as well as its applications to predict physical properties of gas-phase processes. Recently, theoretical efforts have been shifting focus toward solution chemistry. In particular, many theoretical approaches have been proposed for modeling solvation. The dielectric continuum ap-

proach [1–3], however, offers the simplest methodology for incorporating solvent effects into a wide range of *ab initio* molecular orbital (MO) and density functional theory (DFT) levels of theory. In the dielectric continuum approach, the solvated system is modeled as the solute inside a cavity surrounded by a dielectric continuum medium characterized by the dielectric constant ϵ . Models based on molecular-shape cavities have been shown to provide a more accurate description of solvent-solute interactions than those based on simple spherical or ellipsoidal cavity [1, 3]. For molecular-shape cavities, several promising approaches have been introduced. In particular, the SMx models [1], which are based on the generalized Born formal-

* To whom correspondence should be addressed.

† On leave from the Institute of Chemical Physics, University of Latvia, 19 Rainis, Blvd., Riga, LV 1586, Latvia.

ism within the semiempirical molecular orbital theory, are quite successful in calculating free energy of solvation. However, the deficiency of the semiempirical molecular orbital wave function makes them less useful for modeling reactions in solution. Thus, to model reactions in solution, more accurate representation of the solute is required such as using DFT or *ab initio* molecular orbital theories. In this case, one can use the DFT/PB model [4–7], which combines DFT for solute density distribution and the Poisson–Boltzmann (PB) method for interaction with the dielectric continuum medium. Alternatively, the polarizable continuum model (PCM) [3, 8] can be employed. This model based on the Poisson boundary condition has been implemented at the DFT and *ab initio* MO levels of theory. Although both the DFT/PB and PCM models can provide accurate description of the solute in the dielectric cavity, their use is computationally rather expensive. Several approximations have also been developed. In the reaction field factors approach [9], the PCM equations are simplified by using multipole expansion for the solute density. We recently suggested the generalized conductor-like screening model (GCOSMO), which is based on the COSMO model originally proposed by Klamt and Schrümann within the semiempirical MO formalism [10]. In GCOSMO, accurate *ab initio* electronic wave function can be used for solute electrons and nonelectrostatic contributions are added to the free energy of solvation [11–14]. GCOSMO approximate boundary condition allows significant reduction in computational demand as compared to the DFT/PB and PCM-based models while maintaining comparable accuracy. Since DFT/PB, PCM, and GCOSMO models were implemented within the DFT and/or *ab initio* MO theory, they can be employed for quantitative modeling of reactions in solution. However, before

extensive use of these models to real systems, thorough analyses of their accuracy should be performed.

Accuracy of continuum solvation models depends on (1) boundary conditions on the surface of the cavity, (2) the atomic radii used in determining the cavity size, and (3) the validity of the continuum approximation itself. In this study, we focus our attention on how these three factors affect the accuracy of the GCOSMO model.

The GCOSMO model uses the boundary condition from a cavity in a conductor and then scales

the surface charges for a dielectric medium. This is fundamentally different from the exact boundary condition used in the PCM model. In our previous study [11], we have shown a good agreement between GCOSMO and PCM hydration energies for a large set of molecules and ions when the same atomic radii were used. This shows that the GCOSMO approximation is quite accurate for solvents with high dielectric constants such as water. However, in principle, the GCOSMO scaling procedure may yield errors for solvents with low dielectric constants, though no systematic analysis has been done. To estimate the magnitude of these errors, here we compare results from GCOSMO and PCM calculations with experimental data for the tautomeric equilibria between 2-hydroxypyridine and 2-pyridone in several solvents having a wide range of dielectric constants.

In our previous work [11], we optimized a set of atomic radii for construction of molecular cavities for both GCOSMO and PCM calculations. With these atomic radii, GCOSMO model reproduces experimental hydration energies with an average unsigned difference of about 1 kcal/mol for neutral solutes and of order 2–4 kcal/mol for ions that were used in the fit. It is desirable to test applicability of these radii for a larger set of molecules and ions that were not included in the fit. In this study, we calculated hydration free energies for 39 molecules and 5 ions playing an important role in protein structure and function.

Finally, in this study, we perform a GCOSMO study on hydration effects on the potential surface for the proton transfer reaction in the $[H_3N-H-NH_3]^+$ system. Comparison of these results with previous QM/MM Monte Carlo simulations [15] provides a test of the applicability of the GCOSMO model for modeling of reaction profiles in solutions and also illustrates the use of GCOSMO gradient in determining geometries of stationary points on the free energy surface.

This study is organized as follows. In the theory section we present a brief overview of the GCOSMO model. The application section is divided into three parts: the first examines solvent effects on the tautomeric equilibria of 2-hydroxypyridine/2-pyridone in different solvents. The second provides a test of fitted atomic radii by calculating free energies of solvation for a large number of molecules and ions which were not studied by the GCOSMO earlier. The third discusses hydration effects on the potential surface the proton

transfer reaction in the $[\text{H}_3\text{N}-\text{H}-\text{NH}_3]^+$ system. Finally, conclusions and future directions are given.

Theory

GENERALIZED CONDUCTOR-LIKE SCREENING MODEL (GCOSMO)

The GCOSMO model is a generalization of the semiempirical COSMO method [10] to have an accurate ab initio description for the solute charge density and also to include dispersion, repulsion, and cavity formation contributions to the free energy. The GCOSMO model was incorporated into classical ab initio MO and DFT frameworks. The central approximation of this model is to scale the screening conductor surface charge by a factor of $f(\epsilon) = (\epsilon - 1)/\epsilon$ to satisfy the Gauss theorem for the total surface charge for a solute in a dielectric medium specified by the dielectric constant ϵ . The screening conductor surface charge can be obtained directly from the boundary condition that the total potential on the surface of the cavity in a conductor is zero:

$$\sum_i \frac{z_i}{|\mathbf{R} - \mathbf{R}_i|} - \int_V \frac{\rho(\mathbf{r}')}{|\mathbf{r} - \mathbf{r}'|} d^3r' + \int_S \frac{\sigma(\mathbf{r}')}{|\mathbf{r} - \mathbf{r}'|} d^2r' = 0, \quad (1)$$

where z_i and \mathbf{R}_i are values and positions of N nuclear charges, $\rho(\mathbf{r})$ is the solute electronic density and the solvent reaction field is represented by the surface charge density $\sigma(\mathbf{r})$.

Within the boundary element approach, a cavity boundary is defined by M surface elements with areas $\{S_u\}$. The surface charge density at each surface element is approximated as a point charge, $\{q_u\}$, located at the center of that element, $\{t_u\}$. The surface charge distribution is then given by

$$\mathbf{q} = -f(\epsilon)\mathbf{A}^{-1}(\mathbf{B}\mathbf{z} + \mathbf{c}), \quad (2)$$

where \mathbf{A} , \mathbf{B} , and \mathbf{c} are $M \times M$, $M \times N$, and $M \times 1$ matrices, respectively, with matrix elements defined by [10]

$$A_{uv} = \frac{1}{|\mathbf{t}_u - \mathbf{t}_v|} \quad \text{for } u \neq v \quad \text{and} \quad A_{uu} = 1.07 \sqrt{\frac{4\pi}{S_u}}, \quad (3)$$

$$B_{ui} = \frac{1}{|\mathbf{t}_u - \mathbf{R}_i|}, \quad (4)$$

$$c_u = - \int \frac{\rho(\mathbf{r})}{|\mathbf{r} - \mathbf{t}_u|} d^3r, \quad (5)$$

and \mathbf{z} is the vector of N nuclear charges. The total free energy of the whole system (solute + surface charges) is then given by

$$E_{\text{tot}} = \sum_{\mu\nu} P_{\mu\nu} \left(H_{\mu\nu} + \frac{1}{2} G_{\mu\nu} \right) - \frac{1}{2} f(\epsilon) \mathbf{z}^+ \mathbf{B}^+ \mathbf{A}^{-1} \mathbf{B} \mathbf{z} + E_{\text{nn}} + \Delta G_{\text{nonels}}, \quad (9)$$

where E_{nn} is the solute nuclear-nuclear repulsion. The solvent contributions to the one- and two-electron terms of the Fock matrix elements ($H_{\mu\nu}$ and $G_{\mu\nu}$, respectively) are expressed as

$$H_{\mu\nu}^s = -f(\epsilon) \mathbf{z}^+ \mathbf{B}^+ \mathbf{A}^{-1} \mathbf{L}_{\mu\nu}, \quad (10)$$

$$G_{\mu\nu}^s = -f(\epsilon) \mathbf{c}^+ \mathbf{A}^{-1} \mathbf{L}_{\mu\nu}, \quad (11)$$

where

$$L_{\mu\nu}^u = - \left\langle \mu \left| \frac{1}{|\mathbf{r} - \mathbf{t}_u|} \right| \nu \right\rangle, \quad (8)$$

and $P_{\mu\nu}$ is the density matrix element; ΔG_{nonels} is the non-electrostatic part of the free energy of solvation that includes the dispersion, repulsion, and cavity formation contributions. For the dispersion and short-range repulsion contributions, we adopted Floris et al. method [16]. For the cavity formation term, we employed the scaled particle fluid theory of Pierotti [17], which was transformed by Huron and Claverie [18] into an atom-molecule-type formalism. Other non-electrostatic contributions—such as an entropy change due to the solvent reorganization, an enthalpy change due to changes in the solute vibrational and rotational degrees of freedom, a charge transfer to the solvent, non-electrostatic components of the solute-solvent hydrogen bonding, etc.—are effectively included in the atomic radii defining the cavity boundary. The cavity boundary was defined by the solvent-excluding surface (also known as molecular surface) proposed by Richard [19]. Note

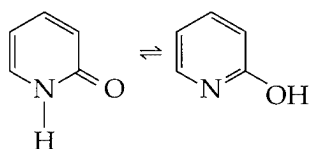
that in some cases when the solute can make strong hydrogen bonds with solvent molecules, the GCOSMO approach can be improved by including several explicit solvent molecules. This will be discussed more details in a separate report.

We have implemented the above formalism into the HF, MP2, CIS, and local and non-local DFT theories. Our results indicate that GCOSMO solvation energy gradient and Hessian calculations on the average require only about 10–20% more computational time as compared to corresponding gas-phase calculations. This is noticeably faster than other existing *ab initio* MO or DFT dielectric continuum models based on a general cavity.

Applications

TAUTOMERIC EQUILIBRIA OF 2-HYDROXYPYRIDINE / 2-PYRIDONE IN SOLUTIONS

Tautomeric equilibria of heterocyclic compounds in solution are very sensitive to the solvent–solute interaction, thus providing excellent tests for accuracy of different solvation models. These properties have also been the subjects of recent reviews [1, 2, 20] due to their importance in biological systems. In this study, we consider the tautomeric equilibria of 2-hydroxypyridine/2-pyridone in different solvents as shown below:



Previous studies showed that almost all dielectric continuum models correctly predict the differential free energies of solvation for this system. We use this well-behaved system here mainly to test the accuracy of GCOSMO boundary condition and optimized atomic radii for solvents other than water by comparing our results with experimental data and with PCM calculations which employs an exact Poisson dielectric continuum boundary condition. We refer readers to an excellent review by Cramer and Truhlar for more discussion on the accuracy of other continuum solvation models for this system [2].

Gas-phase geometries for both 2-hydroxypyridine and 2-pyridone were optimized at the sec-

ond-order Møller–Plesset perturbation theory level using the 6-31G** basis set. These structures were used in solvation calculations for solvents with dielectric constants ϵ equal to 2, 5, 36, and 78, which correspond to cyclohexane, dimethyl ether, acetonitrile, and water, respectively. Free energies of solvation were calculated by using both PCM and GCOSMO models with our atomic radii. The van der Waals surface was used for the PCM model as implemented in the Gaussian 94 program. We found that the non-electrostatic terms contribute only about 0.1 kcal/mol in the calculated differential free energies of hydration, thus they were not included here.

Calculated differential free energies of solvation are listed in Table I along with experimental data [21]. For $\epsilon = 5$, the PCM surface charges do not converge for 2-hydroxypyridine. This convergent problem is due to the iterative procedure for calculating surface charges. Recent closure relation and matrix inversion formulations of the PCM model [22] may elevate this problem. For aqueous solvent, GCOSMO yields the error of 0.8 kcal/mol compared to the experiment. As expected, the GCOSMO surface charge scaling approximation produces larger errors for less polar solvents. It should be noted that both 2-hydroxypyridine and 2-pyridone have hydrogen bonding groups which would have strong interactions with first-solvation-shell waters. A good agreement with experimental data may result from cancelation of errors from specific hydrogen bond effects in both tautomers that were not included in the present and previous continuum calculations. A detailed analysis of modeling hydrogen bonding effects in conjunction with the dielectric continuum approach will be presented in a forthcoming study. The agreement between GCOSMO and PCM results for

TABLE I
Difference between free energies of solvation (kcal / mol) for 2-hydroxypyridine and 2-pyridone in solutes with different dielectric constant ϵ .

Model / Hamiltonian / Basis	$\epsilon = 2$	$\epsilon = 5$	$\epsilon = 36$	$\epsilon = 78$
GCOSMO / MP2 / 6-31G**	2.0	3.8	4.9	5.1
PCM / MP2 / 6-31G**	1.6	NC ^b	4.5	4.7
Experiment ^a	1.1	1.8	3.8	4.3

^a Ref. [21].

^b Not converged.

a wide range of solvents not only validates the boundary approximation used in GCOSMO but also opens the possibility for more quantitative quantum continuum solvation studies.

HYDRATION FREE ENERGIES

Using our recently optimized atomic radii (H: 1.172; C_σ: 2.096; C_{σπ}: 1.635; N_{hb}: 1.738; N_{nhb}: 2.126; O: 1.576; F: 1.28; P: 2.279; S: 2.023; Cl: 1.75) [11], we have calculated hydration free energies for a set of 39 neutral molecules and 5 ions which are of interest in biochemistry. GCOSMO calculations were done at the HF/6-31G* level using the gas-phase optimized geometries at the same level of theory. For dispersion and repulsion interactions between the solute with solvent water hydrogen and oxygen atoms, coefficients are taken from the OPLS force field [23]. Recall that in our previous study [11] we found rather small differences between hydration free energies calculated at the HF, DFT, and MP2 levels. Thus, we expect that DFT and MP2 theories would show the same trend as the present HF results. The calculated HF/6-31G* hydration free energies are listed in Table II along with available experimental data. We found that GCOSMO yields hydration free energies for neutral nonaromatic molecules with a RMS (root-mean square) difference with experiments of about 1.3 kcal/mol. This is consistent with our previous finding. An interesting new result is that for aromatic molecules, GCOSMO tends to overestimate the hydration free energies with a RMS error of about 2.6 kcal/mol. A careful examination of the fitting procedure [11] for atomic radii shows that the *sp*² carbon radius (1.635 Å) attempts to account for both hydrogen bonding effects in acids, acetones, and amides as well as resonance effects in aromatic compounds. However, the *sp*² carbon radius is biased toward the former since it has more experimental values used in the fit. Consequently, the *sp*² carbon radius is too small and effectively overestimates the resonance effects for aromatic compounds. For ions, the RMS error is about 5 kcal/mol, which is about the same range as in our previous study. Note that the wave functions for anions are quite diffuse. As a result, there is a non-negligible portion of the solute electron density outside of the cavity; this yields consistently smaller hydration free energies for anions as seen in Table II. Therefore, more accurate fitting of atomic radii is required with the use of carefully selected set of target species.

TABLE II
Calculated and experimental hydration free energies (in kilocalories per mole).

Solutes	$\Delta G_{\text{hyd}}^{\text{HF}}$	$\Delta G_{\text{hyd}}^{\text{exp}}$
<i>Neutral (nonaromatic)</i>		
Ethanol	-4.90	-4.9
1-Propanol	-4.39	-4.8
Isopropanol	-4.46	-4.8
Dimethylamine	-1.77	-4.3
Ethylthiol	-1.32	-1.3
Methyl-ethylsulfide	-1.88	-1.5
Dimethylsulfide	-0.94	-1.4
Diethylsulfide	0.25	-1.3
Butanone	-3.89	-3.6
2-Pentanone	-3.70	-3.5
3-Pentanone	-2.82	-3.4
Acetaldehyde	-4.58	-3.5
Propionic acid	-7.78	-6.5
acetamide	-11.36	-9.7
Propionamide	-10.35	-9.4
N-methylacetamide	-8.97	-10.0
N-p-Guanidine	-11.61	-11.0
Trimethylamine	0.19	-3.2
1-Propylamine	-2.89	-4.4
2-Methoxyethanol	-6.70	-6.8
2-Methoxypropane	-0.19	-2.0
3-pentanone	-3.64	-3.4
Ethylacetate	-4.27	-3.1
Methyl-butanoate	-3.39	-2.8
Methyl-propanoate	-4.02	-2.9
Methylformate	-5.40	-2.8
N-methylacetamide	-9.04	-10.0
Piperazine	-5.77	-7.4
Pro-2-en-1-ol	-4.64	-5.0
RMS error	1.27	
<i>Neutral (aromatic)</i>		
Benzene	-2.95	-0.9
Toluene	-2.01	-0.9
4-Methylpyridine	-2.76	-4.9
P-cresole	-7.91	-6.1
2-Methylphenol	-7.72	-5.9
Methylindole	-7.47	-5.9
Methylimidazole	-11.42	-10.0
Aniline	-7.28	-4.9
Acetophenone	-8.47	-4.6
Benzaldehyde	-9.29	-4.0
RMS error	2.64	
<i>Ions</i>		
N-Butylammonium	-63.6	-69
Methyl-thiol ion	-72.4	-74
Propionate ion	-73.4	-79
P-cresole ion	-66.5	-75
Methylimidazolium	-66.9	-64
RMS error	5.4	

SOLVENT EFFECTS ON POTENTIAL ENERGY SURFACE FOR THE PROTON TRANSFER IN $\text{H}_3\text{N} \cdots \text{HNH}_3^+$

Proton transfer reactions are fundamentally important in many chemical and biological processes and are the subjects of numerous theoretical and experimental studies. Since proton transfer in biological systems occurs under the influence of the protein and aqueous environments, environmental effects are of profound importance for modeling its reaction mechanisms. In this study, we provide an analysis of the potential energy surface of the proton transfer in the $\text{H}_3\text{N} \cdots \text{HNH}_3^+$ system in aqueous solution, which is often being used as a model for proton transfer in biological systems. In particular, McCammon and co-workers [24] have constructed an analytical potential function for the gas-phase reaction based on the MP2/6-31G* energies and pointed out that the N-N vibration of the donor and acceptor fragments has a noticeable effect on the barrier to proton transfer. Gao [15] has performed hybrid QM/MM simulations based on the AM1 semiempirical Hamiltonian for the quantum region to obtain a two-dimensional potential energy surface for this reaction and noted that hydration effects further raise the barrier at large N-N distances.

Geometries of the ion-dipole complex and saddle point were fully optimized at the MP2/6-31G** level of theory in both the gas phase and in aqueous solution. Optimized geometrical parameters and barrier heights are listed in Table III. We found that the aqueous environment has a significant effect on the geometry of the ion-dipole complex due to the large total dipole but has a little effect on the structure of the zero-dipole transition state, even though the difference in hydration energies of the complex and transition state is only 1.5 kcal/mol. In particular, the NH_4 bond distance (R_1) of the ammonium shortens from 1.134 to 1.058 Å while the hydrogen bond (R_2) elongates from 1.533 to 1.801 Å when transferring from the gas phase to aqueous solution. This is consistent with previous finding on the similar $[\text{H}_2\text{O} \cdots \text{H} \cdots \text{OH}_2]^+$ system using the PCM solvation model [25]. As pointed out in previous studies [15, 25], the charge distribution is more delocalized at the transition state; consequently the transition state is less solvated compared to that of the ion-dipole complex. This leads to an increase in the proton transfer barrier by 1.5 kcal/mol from its values in the gas phase of 0.45 kcal/mol. Similar

TABLE III
Geometrical parameters (bond lengths in angstroms and angles in degrees) of stationary points and barrier heights (kilocalories per mole) to proton transfer in both the gas phase and aqueous solution.

	Gas phase		Solution	
	Complex	TS	Complex	TS
R_1	1.134	1.298	1.058	1.296
R_2	1.533		1.801	
α	110.7	111.8	109.9	111.7
β	112.7		112.8	
ΔE or $\Delta\Delta G$	0.0	0.45	0.0	1.94
ΔG_{solv}			70.4	68.9

increase of 1.24 kcal/mol was found for the barrier of the proton transfer in the $[\text{H}_2\text{O} \cdots \text{H} \cdots \text{OH}_2]^+$ system using the PCM solvation model [25]. However, our result is a factor of 2 smaller than Gao's prediction of 3 kcal/mol using QM/MM-AM1/OPLS approach [15]. This difference could result from several factors. One is the solvent-solute hydrogen bond effects which is treated in an average manner in our continuum calculations. But including specific first-solvation-shell hydrogen bond effects in a discrete continuum model was found to lower the proton transfer barrier for the $[\text{H}_2\text{O} \cdots \text{H} \cdots \text{OH}_2]^+$ system [25]. The other factor is the difference in the solute electronic wave functions, MP2 in our calculations as compared to AM1 in Gao's simulations [15]. However, as mentioned earlier, our previous study [12] showed that solvation energy is not very sensitive to the quality of the solute wave function (though only HF, MP2, and DFT levels were considered). More study is certainly needed to sort out the origins of this discrepancy.

To provide a quantitative understanding of the hydration effects on the potential energy surface of this reaction particularly along the N-N stretching mode, we have calculated the potential curves for proton transfer between two nitrogen atoms separated by distances $R_{\text{NN}} = 2.5, 2.75, \text{ and } 3 \text{ Å}$, respectively, both in the gas phase and in aqueous

solution. Since the spectator R_{NH} bond distances and HNN angles remain nearly constant about 1.02 Å and 111.6°, respectively, at the reactant and transition state, they are assumed to be fixed. These potential curves plotted versus the reaction coordinate are shown in Figure 1. The reaction coordinate used here is defined as the difference in the distances from the transferring proton to the acceptor and the donor nitrogens. In general, our results agree well with those obtained from QM/MM Monte Carlo simulations by Gao. In particular, at $R_{NN} = 2.5$ Å, the free energy surface is barrierless to proton transfer. However, as the N–N distance increases the barrier to proton transfer also increases but at a faster rate in the presence of aqueous solvent. Furthermore, the ion–dipole complex is more stabilized by the aqueous solvent as the N–N distance increases making the complex minimum flatten out relative to that of the gas-phase minimum. These features have been discussed in details by Gao. The general agreement between our results and those from Gao's QM/MM simulations [15] leads to an important conclusion that the simple and efficient GCOSMO model can be used effectively for reaction profile calculations instead of expensive simulations. This allows one to use more sophisticated quantum mechanical methods that is essential for quantita-

tive description of bond-breaking and -forming processes in solution and to consider realistic reacting systems with reasonable computational cost. In addition, the availability of GCOSMO first and second energy derivatives allows one to study solvent effects on the reaction coordinates which have not been addressed in the past. Such effects will be discussed in a forthcoming study.

Conclusion

The GCOSMO continuum solvation model has shown considerable promise in modeling equilibria, structure, and reactivity of reactions in solutions. In many cases, like tautomeric equilibrium in 2-hydroxypyridine/2-pyridone and proton transfer reaction in the $H_3N-H-HN_3^+$ system studied here, the use of the dielectric continuum GCOSMO model is justified, as shown by comparison with more rigorous PCM and QM/MM results. In such cases, the main advantage of the GCOSMO model is the computational efficiency in calculating solvation free energy and its derivatives. The accuracy of about 1 kcal/mol for hydration free energies of neutral nonaromatic solutes and slightly larger for aromatic solutes and ions is comparable to the more rigorous PCM model. More work is needed to improve the atomic radii for defining the cavity and to include specific hydrogen bonding effects. Extending this model to study solvent effects on electronic absorption and vibrational spectra is currently under way in our laboratory.

ACKNOWLEDGMENT

This work is supported in part by the University of Utah and by the National Science Foundation through a Young Investigator Award to T.N.T.

References

1. C. J. Cramer and D. G. Truhlar, in *Reviews in Computational Chemistry*, K. B. Lipkowitz and D. B. Boyd, Eds. (VCH Publishers, New York, 1994) p. 1.
2. C. J. Cramer and D. G. Truhlar, in *Solvent Effects and Chemical Reactivity*, O. Tapia and J. Bertrán, Eds. (Kluwer, Dordrecht, 1996) p. 1.
3. J. Tomasi and M. Persico, *Chem. Rev.* **94**, 2027 (1994).
4. J. L. Chen, L. Noodleman, D. A. Case, and D. Bashford, *J. Phys. Chem.* **98**, 11059 (1994).

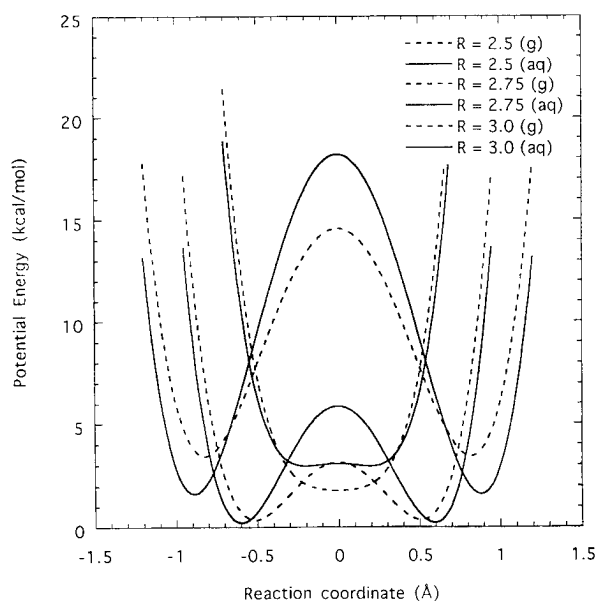


FIGURE 1.

5. A. A. Rashin, M. A. Bukatin, J. Andzelm, and A. T. Hagler, *Biophys. Chem.* **51**, 375 (1994).
6. D. J. Tannor, B. Marten, R. Murphy, R. A. Friesner, D. Sitkoff, A. Nicholls, M. Ringnalda, W. A. Goddard, and B. Honig, *J. Am. Chem. Soc.* **116**, 11875 (1994).
7. K. Baldridge, R. Fine, and A. Hagler, *J. Comp. Chem.* **15**, 1217 (1994).
8. S. Miertus, E. Scrocco, and J. Tomasi, *Chem. Phys.* **55**, 117 (1981).
9. V. Dillet, D. Rinaldi, and J. L. Rivail, *J. Phys. Chem.* **98**, 5034 (1994).
10. A. Klamt and G. Schüürmann, *J. Chem. Soc., Perkin Trans. II*, 799 (1993).
11. E. V. Stefanovich and T. N. Truong, *Chem. Phys. Lett.* **244**, 65 (1995).
12. T. N. Truong and E. V. Stefanovich, *Chem. Phys. Lett.* **240**, 253 (1995).
13. T. N. Truong and E. V. Stefanovich, *J. Phys. Chem.* **99**, 14700 (1995).
14. T. N. Truong and E. V. Stefanovich, *J. Chem. Phys.* **103**, 3709 (1995).
15. J. Gao, In *Reviews in Computational Chemistry*, K. B. Lipkowitz and D. B. Boyd, Eds. (VCH Publishers, New York, 1996) p. 119.
16. F. M. Floris, J. Tomasi, and J. L. P. Ahuir, *J. Comp. Chem.* **12**, 784 (1991).
17. R. A. Pierotti, *Chem. Rev.* **76**, 717 (1976).
18. M. J. Huron and P. Claverie, *J. Phys. Chem.* **76**, 2123 (1972).
19. F. M. Richards, *An. Rev. Biophys. Bioeng.* **6**, 151 (1977).
20. J. S. Kwiatkowski, T. J. Zielinski, and R. Rein, *Adv. Quantum Chem.* **18**, 85 (1986).
21. P. Beak, *Acc. Chem. Res.* **10**, 186 (1977).
22. E. L. Coitiño, J. Tomasi, and R. Cammi, *J. Comp. Chem.* **16**, 20 (1995).
23. W. L. Jorgensen and J. Tirado-Rives, *J. Am. Chem. Soc.* **110**, 1657 (1988).
24. L. Jaroszewski, B. Lesyng, J. J. Tanner, and J. A. McCammon, *Chem. Phys. Lett.* **175**, 282 (1990).
25. F. R. Tortonda, J. L. Pascual-Ahuir, E. Silla, and I. Tuñón, *J. Phys. Chem.* **97**, 11087 (1993).

Analysis of Chemical Bonding in C₂ Using Dyson Orbitals

WEI TONG AND ROBERT C. MORRISON

Department of Chemistry, East Carolina University, Greenville, North Carolina 27858

ORVILLE W. DAY, JR.

Department of Physics, East Carolina University, Greenville, North Carolina, 27858

Received February 24, 1996; revised manuscript received May 20, 1996; accepted May 24, 1996

ABSTRACT

Multireference configuration interaction wave functions with single and double excitations were calculated for the $^1\Sigma_g^+$ ground state of the C₂ molecule and the excited states of C₂⁺ with symmetries $^2\Sigma_g^+$, $^2\Sigma_u^-$, $^2\Pi_u$, and $^2\Pi_g$. The corresponding σ_g , σ_u , π_u , and π_g valence Dyson orbitals were calculated. Most of the density due to the valence electrons is accounted for by three σ_g , one σ_u , and one degenerate pair of π_u Dyson orbitals. Electron correlation plays an important role in the bond strength of C₂ by increasing the occupation of the σ_g valence orbitals and decreasing the occupation of the σ_u and π_u valence orbitals. © 1996 John Wiley & Sons, Inc.

Introduction

A number of experimental [1] and theoretical [2–11] studies of C₂ were conducted to determine potential energy curves, spectroscopic constants, electron affinity, and ionization potentials and to identify the energy positions of several of its excited states. The $^1\Sigma_g^+$ ground state, $\text{KK}(2\sigma_g)^2(2\sigma_u)^2(1\pi_u)^4$, is only slightly below, 0.09 eV, the $^3\Pi_u$ excited state, $\text{KK}(2\sigma_g)^2(2\sigma_u)^2(1\pi_u)^3(3\sigma_g)^1$ [12].

The experimental bond energy, D_e , for C₂ is 0.234 au [12], but the Hartree–Fock value is only 0.029 au [10]. The near degeneracy of the $2\sigma_u$, $3\sigma_g$, $1\pi_u$, and $1\pi_g$ orbitals and the large spatial overlap of the $2\sigma_u$ and $3\sigma_g$ orbitals are thought to contribute to the stability of C₂ [2]. The conventional bond-order analysis of the self-consistent-field (SCF) single-configuration $^1\Sigma_g^+$ wave function leads to the prediction that C₂ has a double π bond. Configuration interaction (CI) wave functions for C₂ typically have a coefficient of about 0.88 for the primary configuration and a coefficient of about 0.32 for the configuration

$KK(2\sigma_g)^2(1\pi_u)^4(3\sigma_g)^2$. One effect of the correlated wave function is to increase the amount of σ bonding in C_2 .

Dyson orbitals (DOs), also called generalized overlap amplitudes and Feynman–Dyson amplitudes, were used for a qualitative analysis of chemical bonding in oligosilanes [13] and carbon clusters [14]. In this article, we examine the chemical bonding in C_2 using DOs.

Dyson spin orbitals (DSOs) can be defined as [15, 16]

$$g_i(\mathbf{x}) = m_i^{-1/2} \int \Psi_i^{N-1}(\mathbf{x}_1, \mathbf{x}_2, \dots, \mathbf{x}_{N-1}) \\ \times \Psi^N(\mathbf{x}_1, \mathbf{x}_2, \dots, \mathbf{x}_{N-1}, \mathbf{x}) \\ \times d\mathbf{x}_1 d\mathbf{x}_2 \dots d\mathbf{x}_{N-1}, \quad (1)$$

where \mathbf{x}_i represents the spatial and spin coordinates of the i th electron. The $m_i^{-1/2}$ serve as normalization constants in Eq. (1) and can be interpreted as occupation numbers when expanding the density in terms of g_i :

$$\rho(\mathbf{x}) = \sum_i m_i |g_i(\mathbf{x})|^2. \quad (2)$$

The DSO occupation numbers, m_i , sum to N , the number of electrons. In general, they are not equal to the natural spin orbital (NSO) occupation numbers.

The DSOs can be written as the product of a spatial part times a spin part $g_i(\mathbf{x}) = g_i(\mathbf{r})\sigma_i$. For the singlet state considered here, $g_i(\mathbf{r})$ is the same for both α and β spin parts. We refer to the $g_i(\mathbf{r})$ as the DOs and will refer to DSOs, the $g_i(\mathbf{x})$, mainly with reference to discussing their occupation numbers.

The N -electron wave function can be expanded in terms of the DOs and the wave functions for the $(N-1)$ -electron states:

$$\Psi^N = \sum_i \left(\frac{m_i}{N} \right)^{1/2} g_i(\mathbf{r}_N) \sigma_i \Psi_i^{N-1}(\mathbf{x}_1, \dots, \mathbf{x}_{N-1}). \quad (3)$$

The $g_i(\mathbf{r})$ are the orbitals occupied by one electron if the others occupy an eigenfunction of the ionic system of $(N-1)$ electrons. The DOs are physically meaningful, since the square of the Fourier transform into momentum space of individual orbitals can be measured by electron momentum spectroscopy [17].

Although certain DOs with the same spin are predicted to have the same long-range decay [18, 19] related to the lowest ionization potential (IP), calculations on the Li atom suggest that they may have intermediate-range decays which depend on their associated IPs [20]. DOs with higher IPs tend to decay more rapidly at intermediate distances. The most diffuse DOs appear to be associated with the lower states of the ion. DOs associated with higher excited states of the ion, higher IPs of the N -electron system, appear to be more compact, to have fewer nodes and to decay more rapidly. DOs associated with higher IPs for H_2 contribute to building up the electron density at the nucleus and in the bonding region [21].

Calculations and Results

Multireference configuration interaction with single and double excitations (MRSDCI) wave functions were calculated for C_2 and for the excited states of C_2^+ having symmetries $^2\Sigma_g^+$, $^2\Sigma_u^-$, $^2\Pi_u$, and $^2\Pi_g$. Calculations were performed at the C_2 equilibrium internuclear distance $r_e = 2.348$ bohr using the MELD [22, 23] programs which include a program for calculating DOs. The basis set consisted of 14s, 12p, 3d, 2f, and 1g Cartesian Gaussian functions. All Cartesian components were kept. The 14s, 12p, and 3d orbitals are taken from Wang's 228-CGTO-2 basis set [24] and the 2f and 1g functions are the correlated orbitals for carbon from Dunning [25]. The SCF energy in this basis set is -75.4065 au.

Configurations in the MRSDCI wave functions were dropped if their second-order perturbation theory contributions were less than 1×10^{-5} . This resulted in 51,105 configurations for the C_2 ground state, 33,595 configurations for the $^2\Sigma_g^+$ states of C_2^+ , 42,934 configurations for the $^2\Sigma_u^-$ states of C_2^+ , 35,044 configurations for the $^2\Pi_u$ states of C_2^+ , and 57,222 configurations for the $^2\Pi_g$ states of C_2^+ using D_{2h} symmetry. The total computed CI energy of C_2 is -75.83235 au, which accounts for 82% of the correlation energy. (The exact total energy is estimated to be -75.9255 au using -37.8450 au for the total nonrelativistic energy of the carbon atom [26] and the experimental dissociation energy $D_e = 147.8$ kcal/mol [27].)

The highest NSO [28] occupation numbers for the ground state of C_2 are listed in Table I. The

TABLE I
NSO occupation numbers.

	σ_g	π_u	σ_u	π_g
1	0.9993	0.9680	0.9993	0.0251
2	0.9875	0.0031	0.8527	0.0009
3	0.1296	0.0012	0.0053	
4	0.0031		0.0014	
5	0.0031		0.0008	
6	0.0019			
2*sum ^a	4.2688	3.8892 ^b	3.7186	0.1040 ^b

^aThe factor of 2 accounts for both α and β spin types.^bThe extra factor of 2 accounts for the spatial degeneracy of the π orbitals.

large amount of correlation between the $\text{KK}(2\sigma_g)^2(2\sigma_u)^2(1\pi_u)^4$ and $\text{KK}(2\sigma_g)^2(1\pi_u)^4(3\sigma_g)^2$ configurations is illustrated by the high occupation number of 0.1396 for the $3\sigma_g$ NSO and the low occupation number of 0.8527 for the $2\sigma_u$ NSO. These occupation numbers would be expected to be near 0 and 1.0, respectively, for a wave function that had little correlation. The sum of the spin-traced occupation numbers is about 4.3 for the σ_g natural orbitals (NOs) and about 3.7 for the σ_u NOs. The occupation of the π_u NSO, while down slightly, is not reduced nearly as much as the $2\sigma_u$ NSO. Electron correlation has the effect of contributing to the stability of the molecule by reducing the density contribution of the antibonding orbitals.

The number of Dyson orbitals that could be determined for each symmetry of the C_2^+ ion is the same as the number of configurations in the wave function, many more than the number of SCF orbitals in a finite basis set. We label DOs by the symbol nXm , where X is the symmetry label, n is the principal SCF quantum number within a given symmetry type, and m is an index which orders DOs according to their IP within a given n and X . The first σ_g DO is $3\sigma_g1$, the second is $3\sigma_g2$, the third is $2\sigma_g1$, and so on.

The first 13 IPs and DSO occupation numbers are listed in Table II for the σ_g , σ_u , π_g , and π_u orbital symmetries. All the π_u DOs listed in Table II are $1\pi_u m$, all listed σ_u are $2\sigma_u m$, and all listed π_g are $1\pi_g m$. DOs corresponding to the core orbitals $1\sigma_g$ and $1\sigma_u$ were not calculated because they correspond to excited states of the ion that were higher than we were able to compute. The six DOs that make significant contributions to the valence density are the $3\sigma_g2$, $2\sigma_g1$, $2\sigma_g3$, and $2\sigma_u1$ and the two $1\pi_u1$ DOs.

If the wave functions had coefficients near 1 for the dominant configurations and coefficients near 0 for the others, the occupation numbers for both the NSOs and the DSOs would be near 0 and 1. The largest occupation number for the $1\pi_u$ DSO is 0.9237, near 1, while the largest occupation number for the $2\sigma_u$ DSOs is 0.8076. Three of the σ_g valence DSOs which have significant occupancy are the $3\sigma_g2$ DSO with an occupation number

TABLE II
IPs and DSO generalized overlap amplitudes (GOA) occupation numbers for C₂ for $R = 2.348$ au.

DO	IP(σ_g)	$m(\sigma_g)$	IP(σ_u)	$m(\sigma_u)$	IP(π_u)	$m(\pi_u)$	IP(π_g)	$m(\pi_g)$
1	0.5911	0.0009	0.5867	0.8076	0.4932	0.9237	0.5677	0.0038
2	0.8519	0.1335	0.8371	0.0041	0.7459	0.0001	0.7372	0.0013
3	1.0593	0.2179	1.1032	$< 10^{-4}$	0.8487	0.0002	0.9107	0.0013
4	1.1756	0.0199	1.1922	0.0008	0.9919	0.0003	0.9574	0.0003
5	1.2287	0.4261	1.2127	0.0034	1.0370	0.0019	1.1457	0.0051
6	1.2599	0.0084	1.2937	0.0005	1.0606	$< 10^{-4}$	1.1907	0.0002
7	1.2972	0.0285	1.3091	0.0010	1.1346	0.0001	1.2560	$< 10^{-4}$
8	1.3372	0.0110	1.3647	0.0011	1.1910	0.0002	1.2665	0.0004
9	1.3516	0.0657	1.3725	$< 10^{-4}$	1.2024	$< 10^{-4}$	1.2685	$< 10^{-4}$
10	1.3687	0.0043	1.3774	$< 10^{-4}$	1.2310	$< 10^{-4}$	1.2863	$< 10^{-4}$
11	1.3812	0.0022	1.3864	0.0002	1.2538	0.0009	1.2957	0.0001
12	1.4030	0.0004	1.4198	$< 10^{-4}$	1.2837	0.0011	1.3012	$< 10^{-4}$
13	1.4340	0.0002	1.4253	0.0009	1.3086	0.0023	1.3167	0.0003
Σm_i		0.9190		0.8196		0.9308		0.0128

0.1335, the $2\sigma_g1$ DSO with an occupation number of 0.2179, and the $2\sigma_g3$ DSO with an occupation number of 0.4261. The other valence-shell DSOs have occupation numbers less than 0.1.

The perspective plots of the $3\sigma_g2$, $2\sigma_g1$, and $2\sigma_g3$ DOs are shown in Figures 1–3, respectively. The $3\sigma_g2$ DO is similar to the $3\sigma_g$ SCF virtual orbital. The $2\sigma_g1$ DO and $2\sigma_g3$ DO are similar to the $2\sigma_g$ SCF orbital. The $3\sigma_g2$, $2\sigma_g1$, and $2\sigma_g3$ DOs have amplitudes of 0.4187, 0.3945, and 0.3647, respectively, at the bond midpoint compared to values of 0.3705 and 0.2816 for the $2\sigma_g$ and $3\sigma_g$ SCF orbitals. The $3\sigma_g2$ DO bond-midpoint amplitude is significantly higher than is the bond-midpoint amplitude for the $3\sigma_g$ SCF orbital, an indication that occupation of the $3\sigma_g2$ DO would contribute to the bond strength more than would that of the $3\sigma_g$ SCF orbital.

The overlaps of the valence DOs with the selected SCF orbitals are given in Table III. The $3\sigma_g1$ DO is a mixture of -0.2598 $2\sigma_g$ and 0.8846 $3\sigma_g$ SCF orbitals and contains significant contributions, > 0.1 , from higher SCF virtual orbitals. The $3\sigma_g2$ DO is a mixture of 0.4645 $2\sigma_g$ and 0.8707 $3\sigma_g$ SCF orbitals. The $2\sigma_g1$ and $2\sigma_g3$ DOs are primarily the $2\sigma_g$ SCF orbital. The $2\sigma_u1$ DO is essentially the $2\sigma_u$ SCF orbital and the $1\pi_u1$ DO is essentially the $1\pi_u$ SCF orbital. The σ_g DOs gain increasing amounts of $2\sigma_g$ SCF character going across Table III from $3\sigma_g1$ to $2\sigma_g3$.

The sums of the first 13 DO occupation numbers for each symmetry are 0.9308 for the π_u DOs, 0.9190 for the σ_g DOs, 0.8196 for the σ_u DOs, and 0.0128 for the π_g DOs. These sums are for only a very small fraction of the DOs, but they are consistent with the increased σ_g NO occupancy and

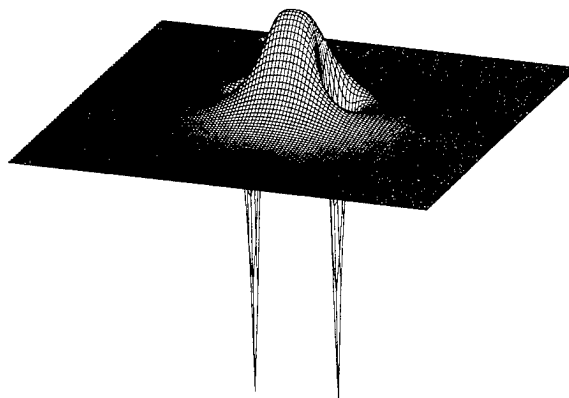


FIGURE 2. Perspective plot of the $2\sigma_g1$ DO.

decreased σ_u NO occupancy compared to the SCF orbitals.

One indication of an orbital's contribution to bonding is the fraction of its density that lies in the bond. We calculated partially integrated orbital densities by integrating the orbital density over the x and y coordinates, taking the internuclear axis to be along the z axis. This gives the total density in the xy plane at each point along the internuclear axis.

The partially integrated densities of the $3\sigma_g2$, $2\sigma_g1$, and $2\sigma_g3$ DOs are shown in Figure 4 and the partially integrated densities of the $2\sigma_u1$ and $1\pi_u1$ DOs are shown in Figure 5. There are small peaks at the nuclear positions for the $2\sigma_g1$ DO, the $2\sigma_g3$ DO, and the $2\sigma_u1$ DOs. The highest peaks of the partially integrated densities are in the bonding region for the σ_g and π_u orbitals and are outside the bonding region for the antibonding $2\sigma_u1$ DO.

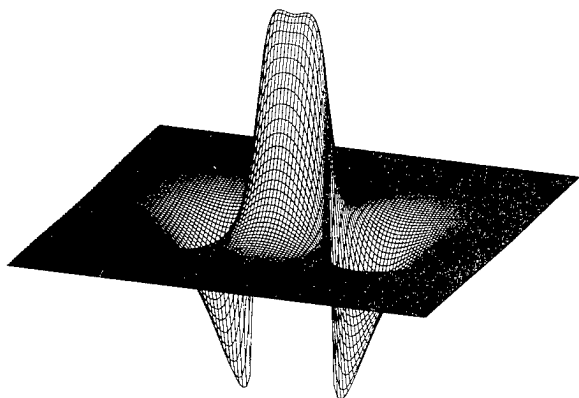


FIGURE 1. Perspective plot of the $3\sigma_g2$ DO.

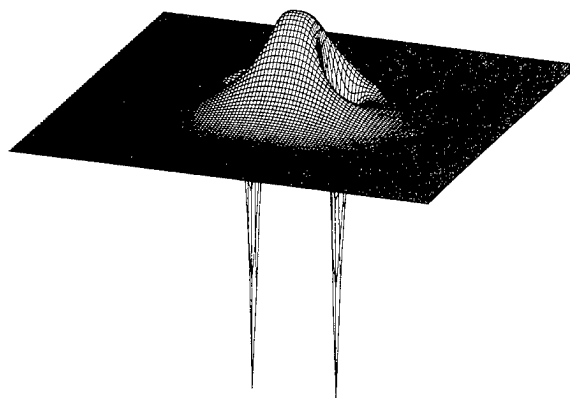


FIGURE 3. Perspective plot of the $2\sigma_g3$ DO.

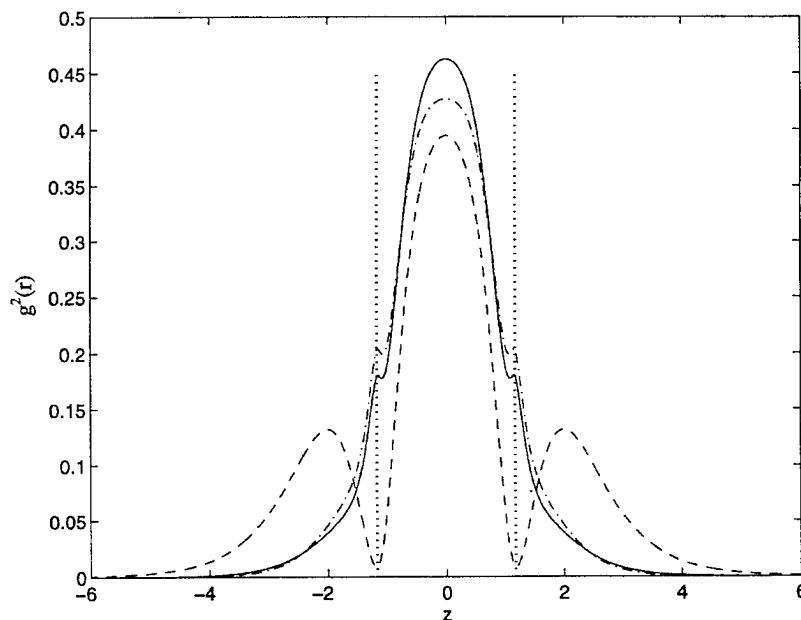
TABLE III
Overlap of the DOs with the SCF orbitals.

ϕ	$3\sigma_g$ 1 DO	$3\sigma_g$ 2 DO	$2\sigma_g$ 1 DO	$2\sigma_g$ 2 DO	$2\sigma_g$ 3 DO
m	0.0009	0.1335	0.2179	0.0199	0.4261
$\langle 1\sigma_g \text{SCF} \phi \rangle$	0.0029	-0.0034	-0.0016	0.9×10^{-4}	0.0020
$\langle 2\sigma_g \text{SCF} \phi \rangle$	-0.2598	0.4645	0.9983	0.9996	0.9998
$\langle 3\sigma_g \text{SCF} \phi \rangle$	0.8846	0.8707	0.0323	-0.0169	0.0123
ϕ	$1\pi_u$ 1 DO				
m	0.9237				
$\langle 1\pi_u \text{SCF} \phi \rangle$	0.9999				
ϕ	$2\sigma_u$ 1 DO				
m	0.8076				
$\langle 2\sigma_u \text{SCF} \phi \rangle$	0.9993				

In Eq. (2), the total density is obtained by multiplying the DO densities by their respective occupation numbers and summing. The partially integrated DO densities times their occupation numbers are plotted in Figure 6 for the $3\sigma_g$ 2, $2\sigma_g$ 1, and $2\sigma_g$ 3 and in Figure 7 for the $2\sigma_u$ 1 and $1\pi_u$ 1 DOs. All these orbitals make significant contributions to the electron density and the σ_g and $1\pi_u$ DOs contribute to building up the density in between the two atoms. The $3\sigma_g$ 2 DO is not expected

to contribute to the bond strength as much as do the two $2\sigma_g$ Dyson orbitals because it contains a large component of the $3\sigma_g$ SCF orbital, but it has a smaller occupation number and makes a smaller contribution to the total density than that of the other two σ_g Dyson orbitals.

Bader et al. [29] analyzed the SCF density of C₂ and other diatomic molecules in terms of Berlin's [30] binding and antibinding regions. Electron density in the binding region produces attractive

**FIGURE 4.** Partially integrated densities of (dashed line) the $3\sigma_g$ 2 DO, (solid line) the $2\sigma_g$ 1 DO, and (dashed-dotted line) the $2\sigma_g$ 3 DO. Vertical dotted lines indicate atomic positions.

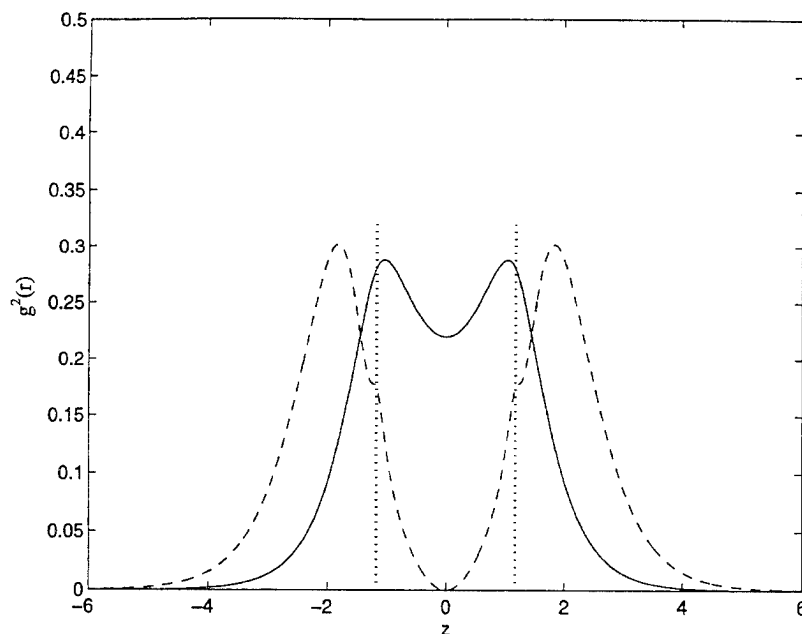


FIGURE 5. Partially integrated densities of (dashed line) the $2\sigma_u1$ DO, and (solid line) the $1\pi_u1$ DO. Vertical dotted lines indicate atomic positions.

forces on the nuclei, pulling them together, whereas electron density in the antibinding region pushes the nuclei apart. The calculated fraction of the density in the binding region for the SCF density of C_2 is 0.60 [29]. The SCF binding density fraction

computed with the current basis is 0.602 and the binding density fraction computed from the CI density is 0.598 for C_2 . They are essentially the same, indicating that the additional bond strength determined by the CI calculation does not come

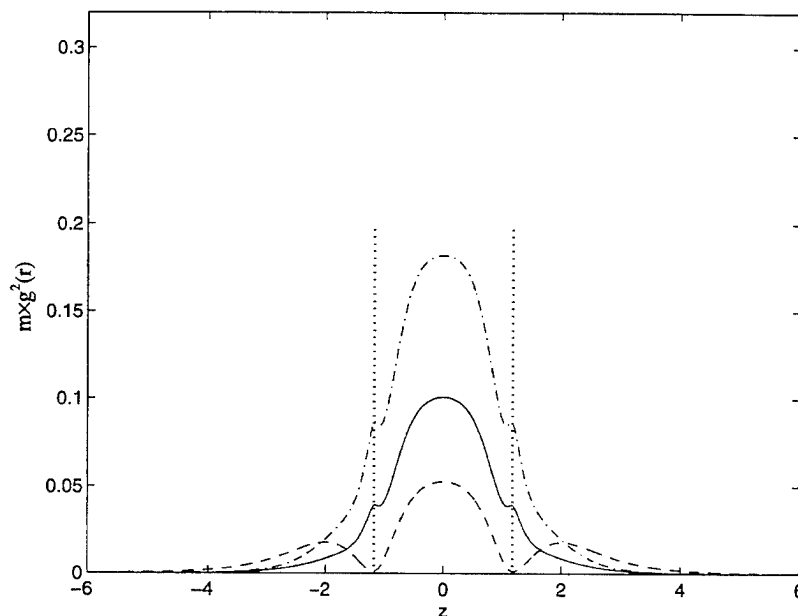


FIGURE 6. Partially integrated densities times their occupation numbers for (dashed line) the $3\sigma_g2$ DO, (solid line) the $2\sigma_g1$ DO, and (dashed-dotted line) the $2\sigma_g3$ DO. Vertical dotted lines indicate atomic positions.

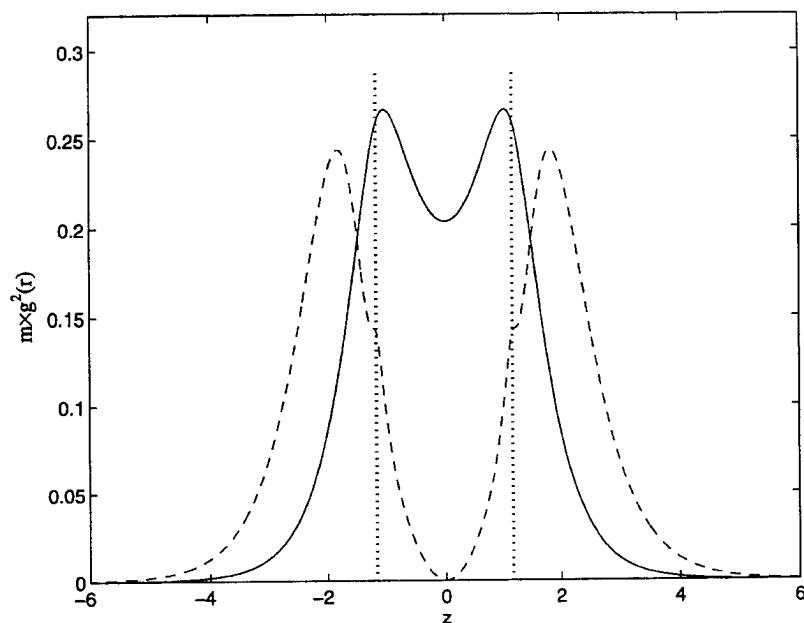


FIGURE 7. Partially integrated densities times their occupation numbers for (dashed line) the $1\sigma_g1$ DO and (solid line) the $1\pi_u1$ DO. Vertical dotted lines indicate atomic positions.

from transfer of electron density from the antibonding region to the binding region. The difference between the CI density and the SCF density is shown in Figure 8. The CI density is more contracted than is the SCF density all along the bond

axis except at the nuclei, where it is reduced. The additional bond strength associated with the CI density appears to come from a higher density along the bond axis rather than from a higher density in the Berlin binding region.

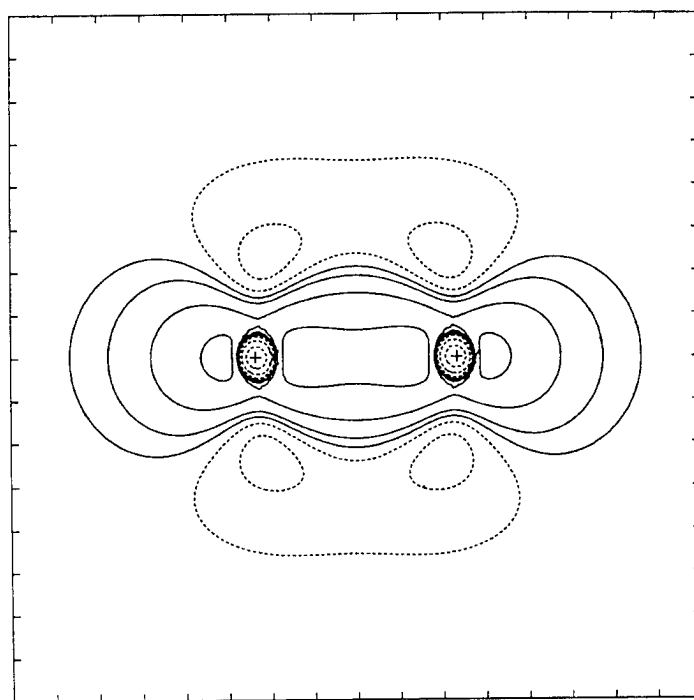


FIGURE 8. Density difference map for $\rho(\text{CI}) - \rho(\text{SCF})$ for C_2 .

TABLE IV
Binding density fractions for Dyson and SCF orbitals.

Orbital	Fraction
$3\sigma_g$ 2 DO	0.5988
$2\sigma_g$ 1 DO	0.8712
$2\sigma_g$ 3 DO	0.8571
$2\sigma_u$ 1 DO	0.2267
$1\pi_u$ 1 DO	0.7388
$1\sigma_g$ SCF	0.5078
$1\sigma_u$ SCF	0.5074
$2\sigma_g$ SCF	0.8498
$2\sigma_u$ SCF	0.2488
$3\sigma_g$ SCF	0.2710
$1\pi_u$ SCF	0.7499

The binding density fractions for the SCF orbitals and selected DOs are listed in Table IV. The $1\sigma_g$ and $1\sigma_u$ SCF orbitals have binding density fractions of about 0.5, consistent with their non-bonding character. The $2\sigma_g$ SCF orbital has a binding density fraction of 0.8498, the antibonding $2\sigma_u$ SCF orbital has a binding density fraction of 0.2488, and the $3\sigma_g$ SCF orbital has a binding density fraction of only 0.2710. The equilibrium bond distance of the $^2\Sigma_g^+$, $KK(2\sigma_g)^2(2\sigma_u)^2(1\pi_u)^4(3\sigma_g)^1$ state of C_2^- is 2.396 bohr, about 0.048 bohr greater than the equilibrium bond distance of the ground state of C_2 . This is consistent with the low binding density fraction of the $3\sigma_g$ SCF orbital and is an indication that occupation of this orbital weakens the bond. The $3\sigma_g$ 2, the $2\sigma_g$ 1, and $2\sigma_g$ 3 DOs have binding density fractions of 0.5988, 0.8712, and 0.8571, respectively, and occupation of these orbitals is expected to contribute to the bond strength.

Conclusions

Electron correlation plays a significant role in chemical bonding in the C_2 molecule. An examination of the NSO occupation numbers shows an increase in the occupation of the σ_g NSOs and a decrease in the occupation of the σ_u and π_u NSOs. The net effect is to increase the density along the bond axis.

The occupation of the σ_g valence DOs is spread over three main DOs, all of which contribute to building up the electron density in the binding

region. Occupation of the $3\sigma_g$ 1 DO places increased density at the bond midpoint. Occupation of DOs which build up electron density in the binding region and at the bond midpoint goes hand in hand with increased bond strength due to electron correlation.

ACKNOWLEDGMENTS

The authors wish to acknowledge discussions concerning basis sets with Dr. Yan Alexander Wang. The authors also acknowledge the support of the National Science Foundation for a grant to East Carolina University.

References

1. W. Weltner, Jr. and R. J. Van Zee, *Chem. Rev.* **89**, 1713 (1989) for a review and references.
2. M. Zeitz, S. D. Peyerimhoff, and R. J. Buenker, *Chem. Phys. Lett.* **58**, 487 (1978).
3. M. Dupuis and B. Liu, *J. Chem. Phys.* **73**, 337 (1980).
4. J. A. Nichols and J. Simons, *J. Chem. Phys.* **86**, 6972 (1987).
5. W. P. Kraemer and B. O. Roos, *Chem. Phys.* **118**, 345 (1987).
6. C. W. Bauschlicher, Jr. and S. R. Langhoff, *J. Chem. Phys.* **87**, 2919 (1987).
7. R. S. Grev and H. F. Schaefer III, *J. Chem. Phys.* **96**, 1850 (1992).
8. J. D. Watts and R. J. Bartlett, *J. Chem. Phys.* **96**, 6073 (1992).
9. R. S. Grev and H. F. Schaefer III, *J. Chem. Phys.* **96**, 6850 (1992).
10. K. A. Peterson, R. A. Kendell, and T. H. Dunning, Jr., *J. Chem. Phys.* **99**, (1993).
11. K. A. Peterson, *J. Chem. Phys.* **102**, 262 (1995).
12. K. P. Huber and G. Herzberg, *Molecular Spectra and Molecular Structure IV. Constants of Diatomic Molecules* (Van Nostrand, Princeton, NJ, 1979).
13. J. V. Ortiz, *J. Chem. Phys.* **94**, 6064 (1991).
14. J. V. Ortiz, *J. Chem. Phys.* **102**, 294 (1995).
15. O. Goscinski and P. Lindner, *J. Math. Phys.* **11**, 1313 (1970).
16. O. W. Day, Jr., *Int. J. Quantum Chem.* **57**, 547 (1996).
17. P. Duffy, S. A. C. Clark, C. E. Brion, M. E. Casida, D. P. Chong, E. R. Davidson, and C. Maxwell, *Chem. Phys.* **165**, 183 (1992), and references therein.
18. J. Katriel and E. R. Davidson, *Proc. Natl. Acad. Sci. U.S.A.* **77**, 4403 (1980).
19. C. O. Ambladh and U. von Barth, *Phys. Rev.* **B31**, 3231 (1985).
20. R. C. Morrison, J. R. Mizell, Jr., and O. W. Day, Jr., *Int. J. Quantum Chem.* **57**, 355 (1996).

21. R. C. Morrison, W. Tong, and O. W. Day, Jr., *Int. J. Quantum Chem.* **59**, 0000 (1996).
22. E. R. Davidson, Quantum Chemistry Program Exchange No. 580.
23. E. R. Davidson, in *Modern Techniques in Computational Chemistry: MOTECC-90*, E. Clementi, Ed. (ESCOM, Leiden, 1990), p. 417.
24. Y. A. Wang, PhD Thesis (Indiana University, 1995).
25. T. H. Dunning, Jr., *J. Chem. Phys.* **90**, 1007 (1989).
26. S. J. Chakravorty, S. R. Gwaltney, E. R. Davidson, F. A. Parpia, and C. F. Fischer, *Phys. Rev. A* **47**, 3649 (1993).
27. R. S. Urdahl, Y. Bao, and W. M. Jackson, *Chem. Phys. Lett.* **178**, 425 (1991).
28. P.-O. Löwdin, *Phys. Rev.* **97**, 1474 (1955).
29. R. F. W. Bader, W. H. Henneker, and P. E. Cade, *J. Chem. Phys.* **46**, 3341 (1967).
30. T. Berlin, *J. Chem. Phys.* **19**, 208 (1951).

Polarizabilities of Heteroaromatic Molecules: Azines Revisited

ROBERT J. DOERKSEN AND AJIT J. THAKKAR*

Department of Chemistry, University of New Brunswick, Fredericton, NB E3B 6E2, Canada

Received February 25, 1996; accepted March 7, 1996

ABSTRACT

Ab initio electron-correlated calculations of the equilibrium geometries, dipole moments, and static dipole polarizabilities are reported for benzene and 12 heteroaromatic six-membered rings obtained from it by aza-substitution. Our geometries and dipole moments agree well with available experimental microwave determinations. The polarizabilities are in reasonable agreement with the fragmentary experimental data available. Uncoupled Hartree-Fock calculations indicate that as much as half the polarizability comes from the σ -electrons. Simple empirical formulas based on atom- and bond-additive models correlate the calculated polarizabilities of 33 five- and six-membered heteroaromatic rings (10 azoles, 10 oxazoles, 13 azines) quite well. The correlation improves significantly if systematic data of uniform quality are used. © 1996 John Wiley & Sons, Inc.

Introduction

Polarizabilities determine long-range intermolecular induction and dispersion forces, low-energy electron-molecule scattering cross sections, Langevin capture cross sections in ion-neutral collisions, and various phenomena such as collision-induced spectral line shifts [1, 2]. We have begun a systematic study of the polarizabilities of heteroaromatic molecules [3–6] to build a sizable body of accurate polarizability data for such molecules, to examine the utility and limits of simple models for these polarizabilities, and to

study the connection between polarizability and aromaticity. We have previously studied four families of heteroaromatic molecules: azines [3], azoles [4], oxopurines [5], and oxazoles [6]. However, our study of the azines (aza-benzenes) [3] differs from our subsequent ones [4–6] in that (i) a mix of experimental and calculated geometries was used rather than a consistent set of calculated geometries, (ii) a poorer basis set was used for some of the polarizability calculations, (iii) 5 of the 12 possible aza-substitutions were not considered, (iv) additive models were not reported, and (v) no attempt was made to separate the σ - and π -electron contributions to the polarizability.

The purpose of this study is to revisit the azines and remove these shortcomings. We report systematic, electron-correlated, ab initio calculations

* To whom correspondence should be addressed.

of the equilibrium geometries, dipole moments, and static dipole polarizabilities of benzene and all 12 aza-benzenes. Uncoupled Hartree-Fock calculations are used to determine the fraction of the mean polarizability that arises from the π -electrons. Additive and other simple models for the polarizabilities of the 13 azines, 10 azoles, and 10 oxazoles are discussed and empirical formulas are given that fit the polarizabilities of these 33 molecules quite well.

Methods and Definitions

Only a concise summary of our methods is given here because full details were given in previous work [4] which used the same computational methods. Equilibrium geometries for all 13 azines were computed using all-electron, second-order Møller-Plesset (MP2) perturbation theory [7, 8] and the 6-31G* basis set [9]. The dipole moments and polarizabilities were calculated by the finite-field method [10, 11] using self-consistent-field (SCF) and valence MP2 field-dependent energies computed with GAUSSIAN-90 [12]. The finite-field SCF polarizabilities are equivalent to coupled Hartree-Fock (CHF) ones [11, 13]. We used a [5s3p2d/3s2p] basis set, denoted C in Ref. [4], of contracted Gaussian-type functions (GTF) for the finite-field calculations. It consists of a [4s2p/2s] double-zeta substrate [14] augmented by [1s1p/1s] diffuse GTF, and [2d/2p] polarization GTF—one optimized for electron correlation [15] and the other for polarizabilities [4]. We compute uncoupled Hartree-Fock (UCHF) polarizabilities [16] to estimate the relative contribution of the π -electrons.

The molecules were placed on the yz plane to block diagonalize the polarizability tensor whose eigenvalues $\alpha_1 = \alpha_{xx} \leq \alpha_2 \leq \alpha_3$ determine the mean:

$$\bar{\alpha} = \frac{1}{3}(\alpha_{xx} + \alpha_{yy} + \alpha_{zz}) = \frac{1}{3}(\alpha_1 + \alpha_2 + \alpha_3) \quad (1)$$

and the difference between the mean in-plane and out-of-plane components:

$$\begin{aligned} \Delta_1 \alpha &= \alpha_{\parallel} - \alpha_{\perp} = \frac{1}{2}(\alpha_{yy} + \alpha_{zz}) - \alpha_{xx} \\ &= \frac{1}{2}(\alpha_2 + \alpha_3) - \alpha_1. \end{aligned} \quad (2)$$

The Kerr anisotropy and the in-plane anisotropy, respectively, are

$$\Delta_2 \alpha = \left[\frac{(\alpha_1 - \alpha_2)^2 + (\alpha_2 - \alpha_3)^2 + (\alpha_3 - \alpha_1)^2}{2} \right]^{1/2} \quad (3)$$

$$\Delta_3 \alpha = [(\Delta_2 \alpha)^2 - (\Delta_1 \alpha)^2]^{1/2} = \frac{\sqrt{3}}{2}(\alpha_3 - \alpha_2). \quad (4)$$

Atomic units are used in this work for polarizabilities.

Equilibrium Geometries

Figure 1 is a scale drawing of our MP2/6-31G* equilibrium geometries for the 13 azines. The MP2/6-31G* bond lengths were remarkably similar in all the azines; CC bonds were between 138.5 and 139.6 pm, CN and NN bonds between 133.5 and 134.7 pm, and CH bonds between 108.5 and 108.8 pm. A comparison of our structures with experimental [17–25] and other ab initio calculations [26–35] follows.

Seven of our geometries are not tabulated because they are very similar to previously reported calculations. MP2/6-31G* geometries for benzene, pentazine, and hexazine were reported previously [26, 27, 29]. Raman [17] and infrared (IR) [25] spectroscopy leads to a similar geometry for benzene. There are no published experimental geometries for pentazine and hexazine because they have not yet been isolated [27, 29]. Our 1,3,5-triazine geometry coincides exactly with an MP2/6-31G** calculation of Creuzet and Langlet [31]. They discussed the good agreement with an experimental Raman structure [18]. There is even better agreement with the combined electron diffraction (ED), Raman, and calculated r_g geometry of 1,3,5-triazine [22] which differs from ours by less than 0.1 pm and 0.1° except that their CH bond is 1.8 pm longer. Our unlisted MP2/6-31G* geometries for 1,2,3-triazine and 1,4-diazine are within 0.2 pm and 0.1° of their frozen core counterparts [32, 33]. Fischer et al. [32] found fair agreement between their MP2 calculation and an X-ray structure [21] for 1,2,3-triazine. Our geometry for 1,4-diazine dif-

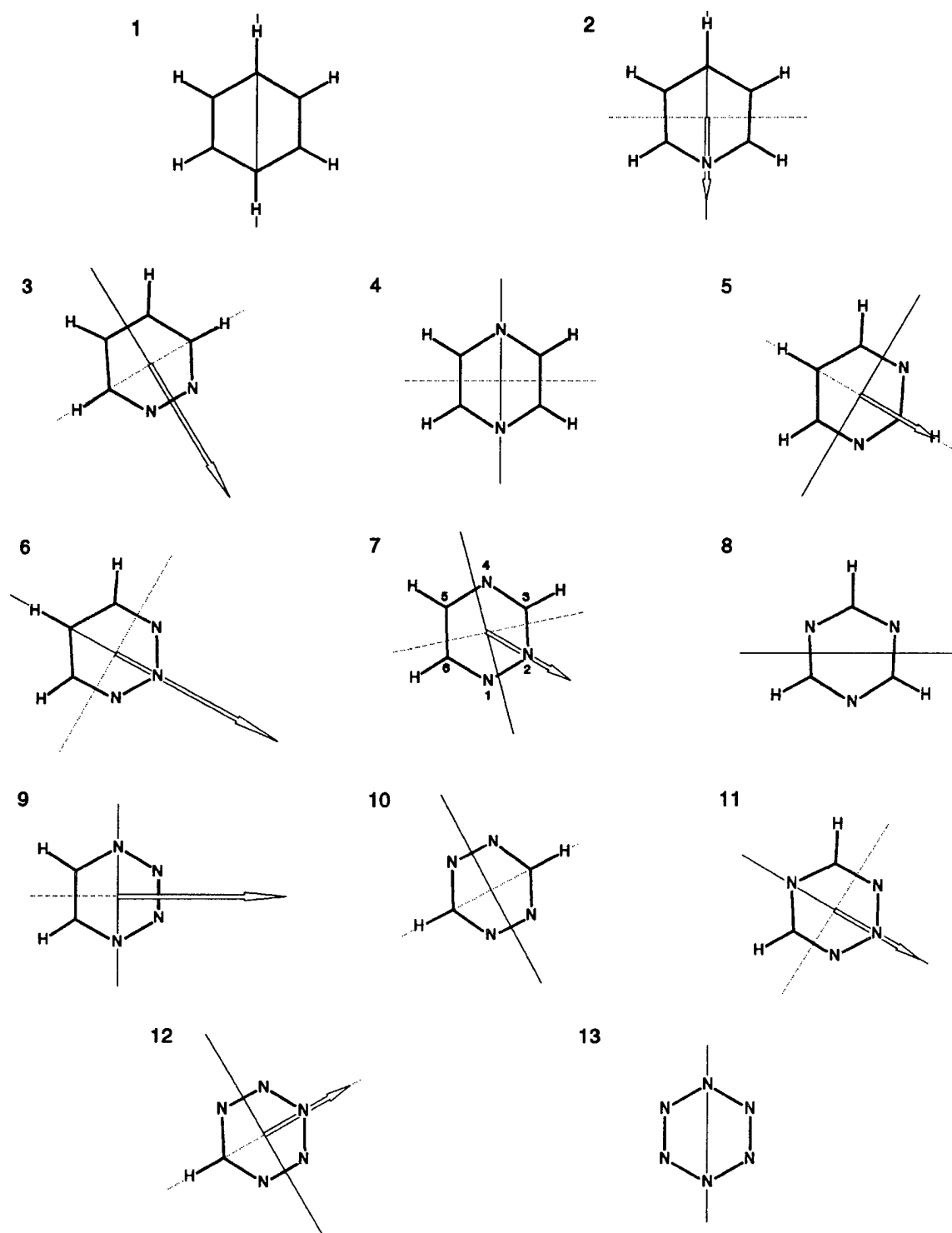


FIGURE 1. The azines at their MP2/6-31G* optimized geometry: benzene (1), pyridine (2), 1,2-diazine or pyridazine (3), 1,4-diazine or pyrazine (4), 1,3-diazine or pyrimidine (5), 1,2,3-triazine (6), 1,2,4-triazine (7), 1,3,5-triazine or s-triazine (8), 1,2,3,4-tetrazine (9), 1,2,4,5-tetrazine or s-tetrazine (10), 1,2,3,5-tetrazine (11), pentazine (12), and hexazine (13). MP2/C dipole moments are shown to scale, with the arrow head pointing to the negative end. The solid line is the a axis of inertia and the dotted line is the α_3 axis of polarizability (not specified for symmetric tops).

fers by about 0.5 pm and $< 1.1^\circ$ from the r_α structure obtained by Cradock et al. [23] using electron diffraction and liquid-crystal (LC) nuclear magnetic resonance (NMR) data. Our unreported geometry for 1,2,4,5-tetrazine is very similar to an MP2/6-311G** calculation [35] except that our NN bond is 0.4 pm longer. The same work [35] included a CASPT2/ANO geometry in closer agreement to the microwave (MW) r_s structure [20]. However, the experimental parameters have rather large uncertainties; for example, the NN bond length of 132.56 ± 1.6 pm [20] does not rule out our MP2/6-31G* value of 133.9 pm.

Table I lists our calculated geometries for the other six azines. We are unaware of previous electron-correlated geometries for pyridine and 1,3-diazine, although SCF geometries have been published in 6-31G* and 6-31G** basis sets [36, 37] among others. Our MP2/6-31G* geometry for 1,2-diazine has bond lengths that differ from their

MP2/6-311G** counterparts [30] by up to 1.7 pm. Table I shows that our pyridine geometry agrees with the microwave r_s substitution structure [19] within 0.6 pm and 0.3° . Our geometries for 1,2- and 1,3-diazine are in reasonable agreement with the r_α structures obtained by Cradock et al. [23, 24] by combining ED, MW, and LC-NMR data. Table I shows that the average absolute discrepancies are 0.7 pm and 0.5° , but the largest bond length differences are 1.3 pm for CN in 1,3-diazine and 1.5 pm for C4H in 1,2-diazine.

Table I compares our geometries for the other three azines with previous calculations because we are unaware of any experimental geometries. The recent MP2/TZVP geometry [34] for 1,2,4-triazine has virtually identical bond angles but longer ring bonds and shorter CH bonds with an average difference of 0.5 pm. Table I shows that our bond lengths differ from CISD/DZP ones [28] by an average and maximum of 1.6 and 3.8 pm for

TABLE I
Comparison of MP2/6-31G* geometries with others. Bond lengths in picometers and bond angles in degrees.

	Pyridine		1,2-diazine		1,3-diazine		1,2,4-triazine		1,2,3,4-tetrazine		1,2,3,5-tetrazine	
	MP2	Exp. ^a	MP2	Exp. ^b	MP2	Exp. ^b	MP2	MP2 ^c	MP2	CISD ^d	MP2	CISD ^d
1-2	134.4	133.8	134.7	133.7	134.1	132.8	134.7	134.1	134.6	133.0	133.8	131.1
2-3	139.4	139.4	134.3	133.8			134.0	133.6	133.5	129.7		
3-4	139.3	139.2	139.6	140.0	134.3	135.0	134.6	134.2			134.3	133.3
4-5			138.5	138.5	139.1	139.3	133.5	133.2	133.7	131.4	133.6	132.3
5-6							139.6	139.4	139.0	139.6		
6-1							134.0	133.6				
2-H	108.8	108.7			108.7	108.2						
3-H	108.6	108.3	108.7	107.9			108.6	107.9				
4-H	108.7	108.2	108.6	107.1	108.8	107.9					108.7	108.1
5-H					108.5	108.7	108.8	108.1	108.6	108.0		
6-H							108.6	108.0				
612	116.8	116.9	119.0	119.4	115.6	116.0	117.6	117.5	117.8	118.3	118.2	118.2
123	123.8	123.8			127.4	128.0	118.0	118.1	121.7	121.9	119.8	120.5
234	118.7	118.5	124.1	123.8			127.4	127.5				
345	118.4	118.4	116.9		122.3	121.2	114.1	113.9			125.6	125.3
456					116.9	117.8	120.7	120.7	120.6	119.8	112.6	112.5
561							122.3	122.3				
H23	120.5	120.2										
H34	121.2	121.4	121.4	121.3			117.1	117.2				
H45			122.2	122.5	121.5	120.9					118.1	118.5
H56							121.9	121.7	123.1	123.0		
H61							115.6	115.7				

^aMW r_s structure, Ref. [19].

^bED, MW, LC-NMR structure, Refs. [23, 24].

^cTZVP basis, Ref. [34].

^dDZP basis, Ref. [28].

1,2,3,4-tetrazine and 1.1 and 2.7 pm for 1,2,3,5-tetrazine. All but the CC bond are shorter. Angles differ by as much as 0.8°.

Dipole Moments

Five of the molecules have a zero dipole moment; Figure 1 shows, to scale, the magnitudes, orientations, and polarities of the dipole moments of the other eight azines. Figure 1 also shows the inertial a axis corresponding to the smallest principal moment of inertia. The orientation of the dipole moment is determined by symmetry except in 1,2,4-triazine whose MP2/C dipole moment makes an angle of 45.19° with the a axis. In each azine, the negative end of the dipole moment points to the region with the most nitrogens.

Our MP2/C dipole moments are listed in Table II. Half are higher and half lower than the unlisted SCF/C dipole moments by an average of 1.5% and a maximum of 3%. The dipole moments obtained by microwave Stark spectroscopy, 2.215D for pyridine [38], 4.22D for 1,2-diazine [39], and 2.334D for 1,3-diazine [40], are 0.13–0.16D (or 4–6%) lower than our MP2/C values. Somewhat better agreement with experiment was obtained by Palmer et al. who reported MRCI/TZVP dipole moments of 2.275D, 4.343D, and 2.383D for pyridine [41], 1,2-diazine [42], and 1,3-diazine [43], respectively. For the other azines, there are no experimental dipole

moments available, and our calculations are more accurate than previous ones. Palmer et al. [44] reported minimal basis SCF dipole moments (at ad hoc geometries) for all eight azines which are on average 16% lower than our SCF/C values. Mó et al. reported [45] SCF/6-31G*//SCF/6-31G dipole moments for seven azines; they differ from our SCF/C values by an average of 1.6% and a maximum of 4.4%.

Polarizabilities

Figure 1 shows the MP2/C principal axis of highest polarizability—the α_3 axis. It lies on a symmetry axis except in 1,2,4-triazine where it makes a 86.31° angle with the inertial a axis. The α_3 axis is generally more distant from the less polarizable nitrogen atoms than the α_2 axis. The three symmetric tops have an isotropic in-plane polarizability, and a nonunique α_3 axis, which is therefore not shown in Figure 1.

Our MP2/C polarizabilities are listed in Table II. Figures 2 and 3 show that MP2/C polarizabilities are higher than the CHF/C values by an average of 4.2% and 7% for $\bar{\alpha}$ and $\Delta_1\alpha$, respectively, with maximum differences of 7.2 and 12% for s -triazine. The UCHF/C $\bar{\alpha}$ and $\Delta_1\alpha$, respectively, are 3 and 10% different from the CHF/C results on average, but are 12 and 26% higher for the worst-case hexazine.

TABLE II
MP2/C dipole moments in Debyes and polarizabilities in atomic units at the MP2/6-31G* geometries. The π -fractions f of the UCHF polarizabilities are given as percentages.

	μ	α_1	α_2	α_3	$\bar{\alpha}$	$\Delta_1\alpha$	$\Delta_2\alpha$	$\Delta_3\alpha$	$f(\perp, \pi)$	$f(\parallel, \pi)$
Benzene		45.17	81.33	81.33	69.28	36.16	36.16	0.00	62.0	56.1
Pyridine	2.36	41.08	73.23	77.55	63.95	34.31	34.51	3.74	59.2	54.8
1,2-Diazine	4.38	37.81	69.70	71.38	59.63	32.73	32.76	1.46	56.8	54.3
1,4-Diazine		37.34	65.50	74.36	59.06	32.59	33.48	7.67	56.7	54.8
1,3-Diazine	2.46	37.44	67.78	70.75	58.65	31.82	31.93	2.57	55.9	52.7
1,2,3-Triazine	5.20	34.98	64.02	64.56	54.52	29.31	29.31	0.47	54.2	53.5
1,2,4-Triazine	2.72	34.60	60.90	67.16	54.22	29.43	29.93	5.42	53.7	53.4
1,3,5-Triazine		34.20	62.89	62.89	53.33	28.69	28.69	0.00	51.9	49.9
1,2,3,4-Tetrazine	4.71	32.34	57.33	60.64	50.11	26.65	26.80	2.86	51.6	53.2
1,2,4,5-Tetrazine		32.50	55.88	61.52	49.97	26.20	26.65	4.88	51.3	54.0
1,2,3,5-Tetrazine	2.73	32.23	56.41	60.85	49.83	26.40	26.68	3.85	50.5	51.8
Pentazine	2.78	30.49	52.52	55.39	46.13	23.47	23.60	2.49	48.8	52.9
Hexazine		28.98	49.16	49.16	42.44	20.18	20.18	0.00	46.8	53.2

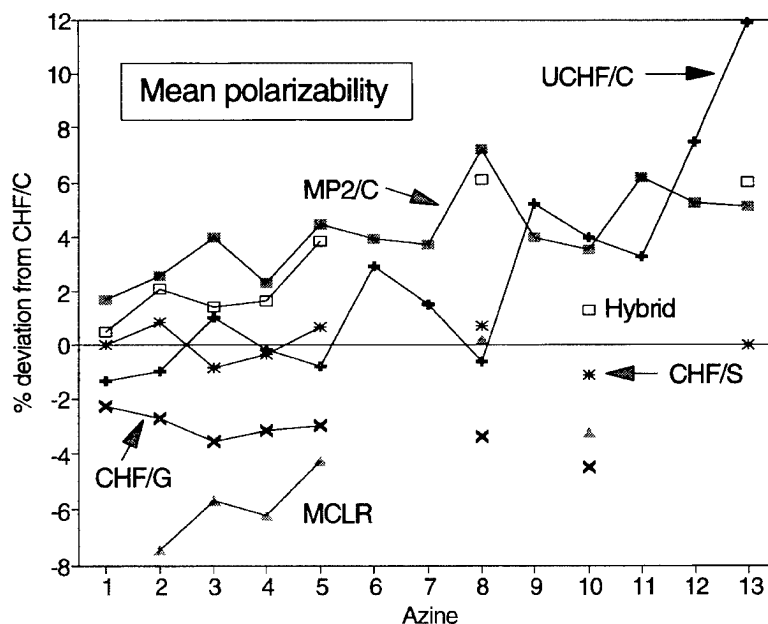


FIGURE 2. Percent differences between the mean polarizability computed by a given method and its counterpart calculated at the CHF/C level. The numbering system for the azines is defined in Figure 1.

A comparison with previous CHF calculations is also made in Figures 2 and 3. Hinchliffe et al.'s [37, 46] CHF calculations using a 6-311G + 3d,3p basis set, denoted CHF/G, are consistently 3 and 5% below our CHF/C results for $\bar{\alpha}$ and $\Delta_1\alpha$, respectively, because their basis set is less appro-

priate for polarizabilities. By contrast, CHF results [3, 47] obtained using Sadlej's basis [48] designed specifically for polarizabilities, denoted CHF/S, are very close to our CHF/C values; the differences average only 0.6% for $\bar{\alpha}$ and 1.4% for $\Delta_1\alpha$. Even these small differences are chiefly due to

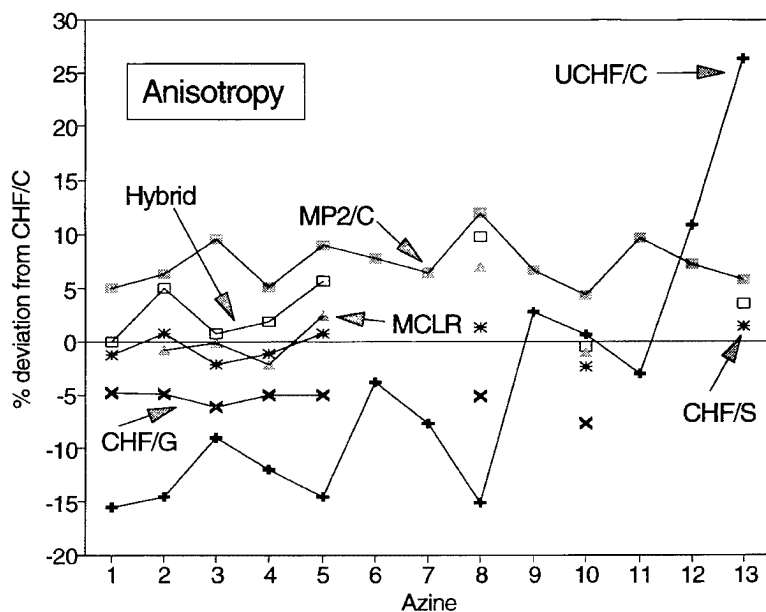


FIGURE 3. Percent differences between the polarizability anisotropy $\Delta_1\alpha$ computed by a given method and its counterpart calculated at the CHF/C level. The numbering system for the azines is defined in Figure 1.

small differences in geometry. To confirm this, we calculated UCHF/C polarizabilities at the geometries (denoted //exp) used in Refs. [3, 47]. The (UCHF/C//MP2/6-31G*-UCHF/C//exp) differences always agreed in sign and rough magnitude with the (CHF/C//MP2/6-31G*-CHF/S//exp) differences.

A comparison with previous correlated calculations is also made in Figures 2 and 3. Some older calculations discussed previously [3] are not mentioned here. The MCLR $\bar{\alpha}$ of Knuts et al. [49] are significantly lower (4.5% on average) than even our CHF/C values. Moreover, their MCLR results are lower than their own RPA values whereas all other calculations predict that correlation raises $\bar{\alpha}$ for the azines. Their MCLR values, obtained at the geometry of benzene for all the azines, are probably unreliable. By contrast, the MP2/S(adlej) polarizabilities [3] for three azines differ from the MP2/C values by only 1 and 2% for $\bar{\alpha}$ and $\Delta_1\alpha$, respectively. Again the small differences are due to small geometrical differences. We found the MP2/C values for *s*-tetrazine using the same geometry [20] as in Ref. [3] to be 49.44, 25.66, and 26.07 for $\bar{\alpha}$, $\Delta_1\alpha$, and $\Delta_2\alpha$, respectively, which is within 0.1 of the MP2/S result [3]. Schütz et al. [35] reported very similar CASPT2/S//CASPT2/ANO values of 49.2, 25, and 25.3 a.u. for $\bar{\alpha}$, $\Delta_1\alpha$, and $\Delta_2\alpha$, respectively. Archibong and Thakkar [3] reported hybrid polarizabilities calculated by combining CHF/S or MP2/S values with higher order correlation corrections computed with Spackman's smaller basis set [50]. Figures 2 and 3 show that there is no uniformity to the differences, averaging 1.2 and 3.6% for $\bar{\alpha}$ and $\Delta_1\alpha$, respectively, between their hybrid results and our MP2/C values. Our uniform MP2/C results are likely to be more reliable.

There have been many experimental measurements of the polarizability of benzene but only two in the gas phase. Alms et al. [51] extrapolated refractivity data and Rayleigh scattering depolarization ratios to zero frequency to find $\bar{\alpha} = 67.48$ and $\Delta_1\alpha = 35.0$. Gentle and Ritchie [52] used the temperature dependence of electro-optical Kerr effect measurements, and Rayleigh scattering depolarization ratios at optical frequencies, to find a zero frequency value of $\Delta_1\alpha = 38.5 \pm 1.2$ after correcting for vibronic effects. These measured values are in good agreement with our MP2/C values of $\bar{\alpha} = 69.3$ and $\Delta_1\alpha = 36.2$ given that we have omitted the effects of zero-point vibrational motion.

There has been much less experimental work on the polarizabilities of the other azines. The only gas-phase result we are aware of is a value of $\Delta_1\alpha = 5.4$ for *s*-tetrazine obtained by laser Stark spectroscopy [53]; however, this value is almost five times as small as theoretical calculations [3, 35, 53] which are all close to our MP2/C value of 26.2. This huge discrepancy has not yet been resolved. Battaglia and Ritchie [54] extracted polarizabilities from dipole moments, molar refractions, and molar Kerr and Cotton-Mouton constants measured at 633 nm for benzene and five azines dissolved in dioxane. They had to assume $\Delta_3\alpha = 0$ to carry out the analysis; Table II shows that this assumption is most nearly valid in 1,2-diazine and least valid in 1,4-diazine. They determined $\bar{\alpha}$ to be 70.4, 64.3, 56.7, and 50.4 for benzene, pyridine, the diazines, and *s*-triazine, respectively. These values differ from our MP2/C results by an average of 3.4% and a maximum of 6.2%. Battaglia and Ritchie [54] found $\Delta_1\alpha \approx \Delta_2\alpha \approx 25.4, 25.5, 26.4, 27.3, 29.2$, and 29.1 for benzene, pyridine, 1,2-diazine, 1,4-diazine, 1,3-diazine, and *s*-triazine, respectively. These anisotropies are lower than our MP2/C values by amounts ranging from 30 to 9% except for *s*-triazine where their value is only 1.5% higher than ours. Given that Battaglia and Ritchie's polarizabilities are for a wavelength of 633 nm in dioxane solution and based on a questionable assumption, the agreement with our infinite wavelength calculations for nonvibrating isolated molecules is as good as can be hoped for.

Finally, note from Table II that the UCHF π -fraction of the transverse polarizability decreases with aza-substitution from 62% in benzene to 47% in hexazine. The UCHF π -fraction of the mean in-plane polarizability varies more erratically between 50 and 56%. These fractions are very similar to those obtained from a nonempirical Unsöld approximation by Mulder et al. [55].

Polarizability Models

Molecular polarizabilities have long been modeled as a sum of contributions from the constituent atoms [56, 57]. Such models work rather well for ab initio polarizabilities of many organic [58] and heteroaromatic molecules [4, 6]. Here we examine models that can describe simultaneously the polarizabilities of 10 azoles [4], 10 oxazoles [6], and the

13 azines. The simplest is the additive atom model:

$$\alpha \approx B_1 n_H + B_2 n_C + B_3 n_N + B_4 n_O \quad (5)$$

in which n_i is the number of atoms of type i . The parameters, obtained by linear regression of our MP2/C polarizabilities for 33 molecules, are listed in Table III with the model's average absolute error δ_a and maximum error δ_m . Model 5 predicts the average polarizability of 33 heteroaromatic molecules with $\delta_a = 1.1\%$ and $\delta_m = 3\%$. The coefficient of the n_i term can be interpreted as the polarizability of an atom of type i in a planar heteroaromatic molecule; Table III shows that these coefficients are smaller than free atom polarizabilities [2]. When model 5 is applied to the anisotropy $\Delta_1 \alpha$, the errors are tripled. Addition of a molecular "volume" term, taken to be $A^{3/2}$ as in Ref. [6], where A is the area enclosed by the ring, yields the model

$$\alpha \approx B_1 n_H + B_2 n_C + B_3 n_N + B_4 n_O + B_5 A^{3/2}. \quad (6)$$

Table III shows that this model improves δ_a to 0.66 and 3% for $\bar{\alpha}$ and $\Delta_1 \alpha$, respectively. Unfortunately, the coefficients of the n_i terms no longer have a simple interpretation.

A more elaborate model uses additive contributions from connections [4]

$$\alpha \approx a n_{NH} + b n_{CH} + c n_{CC} + d n_{CN} + e n_{NN} + f n_{CO} + g n_{NO} \quad (7)$$

where n_{ij} is the number of connections (or bonds, making no distinction between single and multiple bonds) between atoms of types i and j . For our 33 molecules, there are two constraints upon the n_{ij} : $2n_{CH} = 2n_{CC} + n_{CN} + n_{CO}$ and the number of intraring connections = $6 - (n_{NH} + n_{NO} + n_{CO})$. Thus Eq. (7) reduces to

$$\alpha \approx C_1 + C_2 n_{NN} + C_3 n_{CN} + C_4 n_{CC} + C_5 n_{NO} + C_6 n_{CO}. \quad (8)$$

Table III shows that model 8 is a slight improvement over model 6. Adding a $A^{3/2}$ term to model 8 does not improve it. Numerical experiments, and previous correlations between polarizability and electronegativity [59], led us to a term involving the energies of the frontier orbitals:

$$\alpha \approx C_1 + C_2 n_{NN} + C_3 n_{CN} + C_4 n_{CC} + C_5 n_{NO} + C_6 n_{CO} + C_7 / \chi \quad (9)$$

in which $\chi = (\epsilon_{LUMO} - \epsilon_{HOMO})/2$ can be thought of as an approximation to the hardness. Table III shows that model 9 gives an excellent prediction of $\bar{\alpha}$ ($\delta_a = 0.36\%$, $\delta_m = 1.2\%$), and a reasonable one of $\Delta_1 \alpha$ ($\delta_a = 2\%$, $\delta_m = 6\%$).

The accuracy of our simple models is somewhat higher than might have been expected. We think this is so partly because the 33 heteroaromatic molecules are closely related and partly because our polarizability database is of uniform quality.

TABLE III
Parameters (in atomic units) and errors of various polarizability models. Model numbers refer to equations in the main text and an asterisk indicates that a nonuniform data base was used.

	$\bar{\alpha}$ Model						$\Delta_1 \alpha$ Model			
	5	6	8*	8	9*	9	5	6	8	9
B_1	1.1	11.5	0	0	0	0	-2.87	1.93	0	0
B_2	10.3	-6.56	0	0	0	0	8.82	1.1	0	0
B_3	6.86	1.14	0	0	0	0	3.74	1.113	0	0
B_4	2.8	7.5	0	0	0	0	-1.7	0.5	0	0
B_5	0	0.52	0	0	0	0	0	0.24	0	0
C_1	0	0	8.6	7.1	-3.33	-2.45	0	0	-16.89	0.1
C_2	0	0	5.5	5.78	6.5	6.56	0	0	6.5	5.1
C_3	0	0	7.43	7.75	8.22	8.38	0	0	7.684	6.6
C_4	0	0	10.05	10.4	10.58	10.8	0	0	8.8	8
C_5	0	0	3.1	3.4	4.6	4.6	0	0	5.8	3.6
C_6	0	0	4.8	5	5.7	5.8	0	0	5.81	4.45
C_7	0	0	0	0	1.604	1.29	0	0	0	-2.3
$\delta_a(\%)$	1.1	0.66	0.75	0.59	0.45	0.36	3.4	3.0	2.7	2.0
$\delta_m(\%)$	3.4	2.6	2.8	2.0	1.9	1.2	11.	13.	10.	6.

To demonstrate this latter point, we include in Table III models 8* and 9* obtained by fitting Eqs. (8) and (9) to our polarizability database with eight azine polarizabilities of this work replaced by the hybrid results of Ref. [3]. Table III shows clearly that the error measures for models 8* and 9* are noticeably larger than those for models 8 and 9.

These models utilize only isotropic information and therefore work better for the mean polarizability $\bar{\alpha}$ than for the anisotropy $\Delta_1\alpha$. The Kerr anisotropy $\Delta_2\alpha$ can be described by these models with an accuracy slightly worse than that obtained for $\Delta_1\alpha$. However, an accurate model for the in-plane anisotropy $\Delta_3\alpha$ requires anisotropic information. We are trying to develop such models.

ACKNOWLEDGMENT

This work was supported by the Natural Sciences and Engineering Research Council (NSERC) of Canada. One of us (R.J.D.) thanks NSERC for a postgraduate scholarship.

References

1. A. D. Buckingham, *Adv. Chem. Phys.* **12**, 107 (1967).
2. T. M. Miller and B. Bederson, *Adv. At. Mol. Phys.* **13**, 1 (1977); **25**, 37 (1988).
3. E. F. Archibong and A. J. Thakkar, *Mol. Phys.* **81**, 557 (1994).
4. N. El-Bakali Kassimi, R. J. Doerksen, and A. J. Thakkar, *J. Phys. Chem.* **99**, 12790 (1995).
5. N. El-Bakali Kassimi and A. J. Thakkar, *J. Mol. Struct. (Theochem)*, to appear.
6. N. El-Bakali Kassimi, R. J. Doerksen, and A. J. Thakkar, *J. Phys. Chem.*, to appear.
7. C. Møller and M. S. Plesset, *Phys. Rev.* **46**, 618 (1934).
8. R. J. Bartlett, *Ann. Rev. Phys. Chem.* **32**, 359 (1981).
9. P. C. Hariharan and J. A. Pople, *Chem. Phys. Lett.* **66**, 217 (1972).
10. H. D. Cohen and C. C. J. Roothaan, *J. Chem. Phys.* **43**, S34 (1965).
11. C. E. Dykstra, *Ab Initio Calculation of the Structures and Properties of Molecules* (Elsevier, Amsterdam, 1988).
12. M. J. Frisch, M. Head-Gordon, G. W. Trucks, J. B. Foresman, H. B. Schlegel, K. Raghavachari, M. A. Robb, J. S. Binkley, C. Gonzalez, D. J. Defrees, D. J. Fox, R. A. Whiteside, R. Seeger, C. F. Melius, J. Baker, R. L. Martin, L. R. Kahn, J. J. P. Stewart, S. Topiol, and J. A. Pople, *Gaussian 90*, Revision J, Gaussian, Inc., Pittsburgh, PA, 1990.
13. T. C. Caves and M. Karplus, *J. Chem. Phys.* **50**, 3649 (1969).
14. A. J. Thakkar, T. Koga, M. Saito, and R. E. Hoffmeyer, *Int. J. Quantum Chem. Symp.* **27**, 343 (1993).
15. T. H. Dunning, Jr., *J. Chem. Phys.* **90**, 1007 (1989).
16. A. Dalgarno, *Adv. Phys.* **11**, 281 (1962).
17. B. P. Stoicheff, *Can. J. Phys.* **32**, 339 (1954).
18. J. E. Lancaster and B. P. Stoicheff, *Can. J. Phys.* **34**, 1016 (1956).
19. F. Mata, M. J. Quintana, and G. O. Sørensen, *J. Mol. Struct.* **42**, 1 (1977).
20. V. A. Job and K. K. Innes, *J. Mol. Spectr.* **71**, 299 (1978).
21. H. Neunhoeffer, M. Clausen, H. Vötter, H. Ohl, C. Krüger, and K. Angermund, *Liebigs. Ann. Chem.* 1732 (1985).
22. W. Pyckhout, I. Callaerts, C. Van Alsenoy, H. J. Geise, A. Almenningen, and R. Seip, *J. Mol. Struct.* **147**, 321 (1986).
23. S. Cradock, P. B. Liescheski, D. W. H. Rankin, and H. E. Robertson, *J. Am. Chem. Soc.* **110**, 2758 (1988).
24. S. Cradock, C. Purves, and D. W. H. Rankin, *J. Mol. Struct.* **220**, 193 (1990).
25. J. Plíva, J. W. C. Johns, and L. Goodman, *J. Mol. Spectrosc.* **148**, 427 (1991).
26. K. B. Wiberg, private communication in A. G. Ozkabak and L. Goodman, *J. Chem. Phys.* **87**, 2564 (1987).
27. M. T. Nguyen, *J. Phys. Chem.* **94**, 6923 (1990).
28. J. R. Thomas, G. E. Quench, and H. F. Schaefer III, *J. Org. Chem.* **56**, 539 (1991).
29. P. Politzer, J. S. Murray, J. M. Seminario, and R. S. Miller, *J. Mol. Struct. (Theochem)* **262**, 155 (1992).
30. J. Cioslowski, J. Sauer, J. Hetzenegger, T. Karcher, and T. Hierstetter, *J. Am. Chem. Soc.* **115**, 1353 (1993).
31. S. Creuzet and J. Langlet, *Chem. Phys. Lett.* **208**, 511 (1993). They omitted the CH bond length; ours is 108.8 pm.
32. G. Fischer, A. U. Nwankwoala, M. P. Olliff, and A. P. Scott, *J. Mol. Spectrosc.* **161**, 388 (1993). They omitted the CNN bond angle; ours is 122.2°.
33. L. Zhu and P. Johnson, *J. Chem. Phys.* **99**, 2322 (1993).
34. M. H. Palmer, I. C. Walker, M. F. Guest, and M. R. F. Siggel, *Chem. Phys.* **201**, 381 (1995).
35. M. Schütz, J. Hutter, and H. P. Lüthi, *J. Chem. Phys.* **103**, 7048 (1995).
36. K. B. Wiberg, D. Nakaji, and C. M. Breneman, *J. Am. Chem. Soc.* **111**, 4178 (1989).
37. A. Hinchcliffe and H. J. Soscún M., *J. Mol. Struct. (Theochem)* **304**, 109 (1994).
38. G. O. Sørensen, L. Mahler, and N. Rastrup-Andersen, *J. Mol. Struct.* **20**, 119 (1974).
39. W. Werner, H. Dreizler, and H. D. Rudolph, *Z. Naturforsch.* **22a**, 531 (1967).
40. G. L. Blackman, R. D. Brown, and F. R. Burden, *J. Mol. Spectrosc.* **35**, 444 (1970).
41. I. C. Walker, M. H. Palmer, and A. Hopkirk, *Chem. Phys.* **141**, 365 (1989).
42. M. H. Palmer and I. C. Walker, *Chem. Phys.* **157**, 187 (1991).
43. M. H. Palmer, I. C. Walker, M. F. Guest, and A. Hopkirk, *Chem. Phys.* **147**, 19 (1990).
44. M. H. Palmer, R. H. Findlay, and A. J. Gaskell, *J. Chem. Soc. Perkin II*, 420 (1974).
45. O. Mó, J. L. G. de Paz, and M. Yáñez, *J. Molec. Struct. (Theochem)* **150**, 135 (1987).

46. A. Hinchliffe and H. J. Soscún M., *J. Mol. Struct.* **300**, 1 (1993).
47. P. Lazzeretti, M. Malagoli, and R. Zanasi, *Chem. Phys. Lett.* **167**, 101 (1990).
48. A. J. Sadlej, *Coll. Czech. Chem. Commun.* **53**, 1995 (1988).
49. S. Knuts, O. Vahtras, and H. Ågren, *J. Molec. Struct. (Theorchem)* **279**, 249 (1993).
50. M. A. Spackman, *J. Phys. Chem.* **93**, 7594 (1989).
51. G. R. Alms, A. K. Burnham, and W. H. Flygare, *J. Chem. Phys.* **63**, 3321 (1975).
52. I. R. Gentle and G. L. D. Ritchie, *J. Phys. Chem.* **93**, 7740 (1989).
53. S. Heitz, D. Weidauer, and A. Hese, *J. Chem. Phys.* **95**, 7952 (1991).
54. M. R. Battaglia and G. L. D. Ritchie, *J. Chem. Soc. Perkin II* 897 (1977).
55. F. Mulder, G. van Dijk, and C. Huiszoon, *Mol. Phys.* **38**, 577 (1979).
56. J. R. Tessman, A. H. Kahn, and W. Shockley, *Phys. Rev.* **92**, 890 (1953).
57. K. J. Miller, *J. Am. Chem. Soc.* **112**, 8533 (1990).
58. J. M. Stout and C. E. Dykstra, *J. Am. Chem. Soc.* **117**, 5127 (1995).
59. J. K. Nagle, *J. Am. Chem. Soc.* **112**, 4741 (1990).

Negative Hydrogen and Helium in a Variety of Debye Plasmas

LI ZHANG and PETER WINKLER*

Department of Physics, University of Nevada, Reno, Nevada 89557; e-mail for P.W.: winkler@rigel.physics.unr.edu

Received February 29, 1996; revised manuscript received April 1, 1996; accepted April 4, 1996

ABSTRACT

Aspects of the influence of a strong Debye plasma environment on the negative hydrogen ion and the neutral helium atom have been studied. Contrary to earlier work, in the present calculation all interactions have been screened. This increases the stability of the systems to the extent that neither the H^- ion nor the ground state of helium will lose an electron by pressure ionization. It has been found that the charge distribution of H^- remains remarkably constant over a vast range of values of the Debye parameter D .

© 1996 John Wiley & Sons, Inc.

Introduction

In the investigation of plasmas consisting of atomic ions and electrons a good understanding of the interaction potential among those species is essential. Compared to the free-space case the force between the charges is modified due to short-range order and static and dynamical screening effects introduced by neighboring ions and fast electrons, respectively. These modifications effect one-electron properties (e.g., spectral lines which serve as key quantities in plasma diagnostics) as well as properties involving more than one elec-

tron (e.g., dielectronic recombination rates which account for plasma losses). Extending the usual Debye-Hückel treatment of screening to encompass also dynamic screening effects due to ion motions is an important research area in its own right. Such research is expected to be noticeably facilitated by the incorporation of the static screening effects into the calculation of atomic properties and processes right from scratch. Doing so, one can then formulate a procedure which allows the simultaneous evaluation of level broadening and of the lowering of the continuum threshold—both on the same footing.

In a recent study [1] the numerical pair function method of our earlier studies of the Debye potential [2] has been replaced by a variational calculation employing correlated wave functions. This change was needed in order to achieve high accu-

*To whom correspondence should be addressed.

racy in calculations of not only the ground-state energies of the negative hydrogen ion and the helium atom but also of some excited states of the latter system, as well as the radial one-electron density function of such systems under various plasma conditions. In this investigation the attractive Coulomb potential between the electron and the nucleus has been replaced by a screened potential of the Debye type $Z \exp(-r/D)/r$. Varying the Debye length D from infinity—which corresponds to no screening—to small values, different plasma conditions can be simulated. Since the Debye parameter is a function of both the electron density n_e and the electron temperature T_e , a particular value of D corresponds to a range of plasma conditions. It is, however, meaningful to associate smaller values of D with stronger screening. The earlier studies, not including screening of the electron-electron interaction, indicated that the assumedly very fragile H^- ion may in reality be more stable in weak-to-moderate plasma conditions than initially assumed. The inclusion of Debye screening into the electron interaction in the present work corroborates these findings strongly. As expected, this modification leads to a further increase of stability for a H^- ion embedded in a Debye plasma. Since screening in one form or the other is a fact on plasmas, the gross features of the present calculation, which is strictly based on the validity of the Debye model, may well serve as a general outline of trends under more general conditions. The detailed interpretation of the numerical results, however, requires caution: The Debye potential may not always be appropriate to model a real plasma. In particular, in the range of small values of the Debye parameter D , close to (or even smaller than) the average interparticle distance, the interpretation of the present results in terms of a plasma is not reasonable. However, even in those regions the results represent properties of the Debye potential which have not been studied before. In particular, by extending a similar study by Rogers and co-workers [3] of the hydrogen atom to two-electron systems, it was possible to extract accurate ionization energies for the helium atom and, above all, detachment energies for H^- . Over most of the range of D values covered in the present work, the results are indeed representative for typical effects of screening on the binding energy and the electron distribution of small atoms.

The Calculations

The nonrelativistic Hamiltonian

$$H = -\frac{1}{2}\nabla_1^2 - \frac{1}{2}\nabla_2^2 - \frac{Z \exp(-r_1/D)}{r_1} - \frac{Z \exp(-r_2/D)}{r_2} + \frac{\exp(-r_{12}/D)}{r_{12}}, \quad (1)$$

describing two-electron systems in a Debye plasma characterized by the parameter D , has been diagonalized in a basis of correlated functions of the following type:

$$\varphi_{klm}(r_1, r_2, r_{12}) = N_{klm} (e^{-\alpha_k r_1} e^{-\beta_l r_2} \pm e^{-\beta_l r_1} e^{-\alpha_k r_2}) \times e^{-\gamma_m r_{12}}. \quad (2)$$

The variables r_1 and r_2 are the radial coordinates of the two electrons and the variable r_{12} stands for the distance between them, while the quantity N_{klm} is a normalization factor. Expansions of this type have previously been shown to be very efficient in obtaining highly accurate variational wave functions for S states of two-electron atoms [4]. The two signs correspond to singlet and triplet states, respectively. The nonlinear parameters α_k , β_l , and γ_m have been preselected so as to approximate a definite integral optimally as described in the earlier reference which introduced these functions as a particular type of integral transform wave functions. The linear parameters are determined in the usual variational procedure by solving the generalized eigenvalue equation

$$(H - SE)\Phi = 0. \quad (3)$$

Here H and S stand for the Hamiltonian and overlap matrices, respectively. Since the main goal of this study has been to evaluate all of the binding energy of the H^- ion embedded in a pure Debye plasma without overestimating the effect, a comparatively large basis set of 220 functions of the type given in Eq. (2) has been used. The use of correlated wave functions containing the interelectronic distance r_{12} as a dynamical variable in connection with the Debye potential is very convenient because all integrals can be expressed in closed form modifying the closed-form expressions given in [4].

The radial one-electron density function is obtained by integrating the two-electron density ex-

pression over the coordinate of one of the particles as well as over the angular variables of the other, which in the present case of spherically symmetric states reduces to applying a factor of 4π :

$$P(r_1) = 4\pi \int d^2r_2 \Phi^*(\mathbf{r}_1\mathbf{r}_2)\Phi(\mathbf{r}_1\mathbf{r}_2). \quad (4)$$

In the present study we focus on the lowest bound state to obtain information about the spatial extension of the systems in various plasma environments. Hence, in Eq. (4) the quantity Φ stands for the ground-state wave function but could be replaced by the eigenfunction of any excited state to evaluate the density of that state.

Although an extension of the correlated wave function approach to atoms with more than two electrons may not be practical, the treatment of systems of particles interacting via Yukawa forces by an appropriate modification of more standard methods of quantum chemistry or atomic theory is possible. In fact, systems of particles interacting via Yukawa forces have been studied early on in nuclear physics, e.g., by Swiatecki [5]. This reference contains also the formulas for the interaction integrals of particles described by wave functions

of Gaussian type, i.e., $\exp(-\alpha r^2)$, or interacting via Yukawa forces. The adaptation to systems with both attractive and repulsive screened interactions and the interpretation of the results as meaningful for ions embedded in a plasma, however, is new and promises interesting results, in particular, for the further study of atomic processes in plasmas.

All calculations have been performed in extended precision on the Hewlett-Packard 9000 735/125 computer system of the Physics Department of the University of Nevada at Reno.

Results

RESULTS FOR THE ENERGIES

The results for the ground-state energies of both the negative hydrogen ion and the neutral hydrogen atom, which have been reported before [1], are summarized in Figure 1. Although the results for large values of the Debye parameter D are not displayed here for the sake of readability in the low D region, the results for large but finite values of D are represented directly as detachment energies in Figure 2. For $D \rightarrow \infty$, the energy curves for

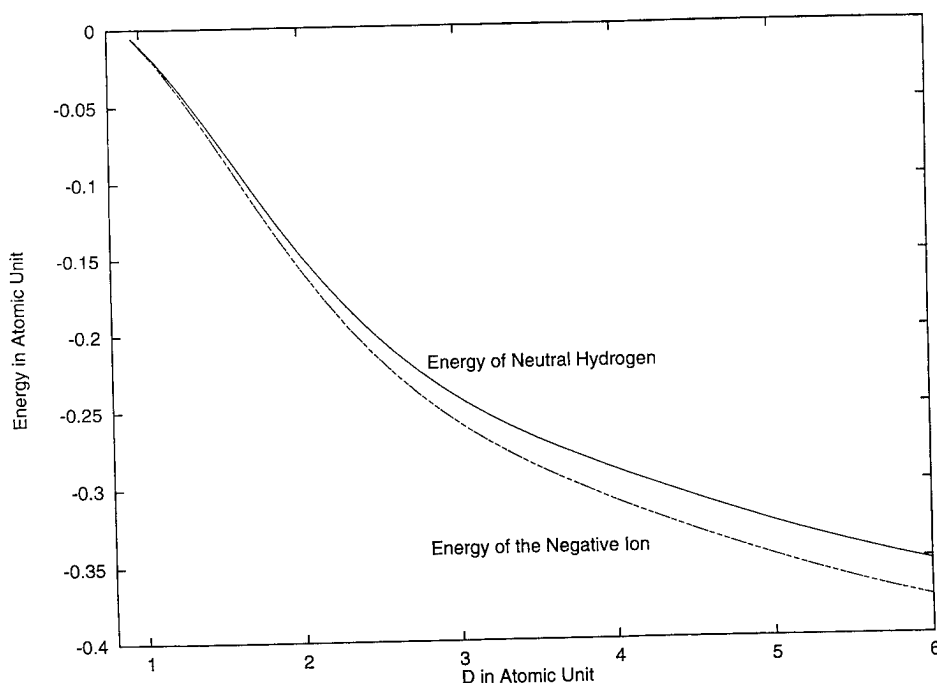


FIGURE 1. The energy of the negative hydrogen ion vs. the screening parameter D compared to the ground-state energy of the hydrogen atom under the same plasma conditions. The ionic system is bound over the whole range of D values in which the neutral system is also capable of supporting at least one bound state.

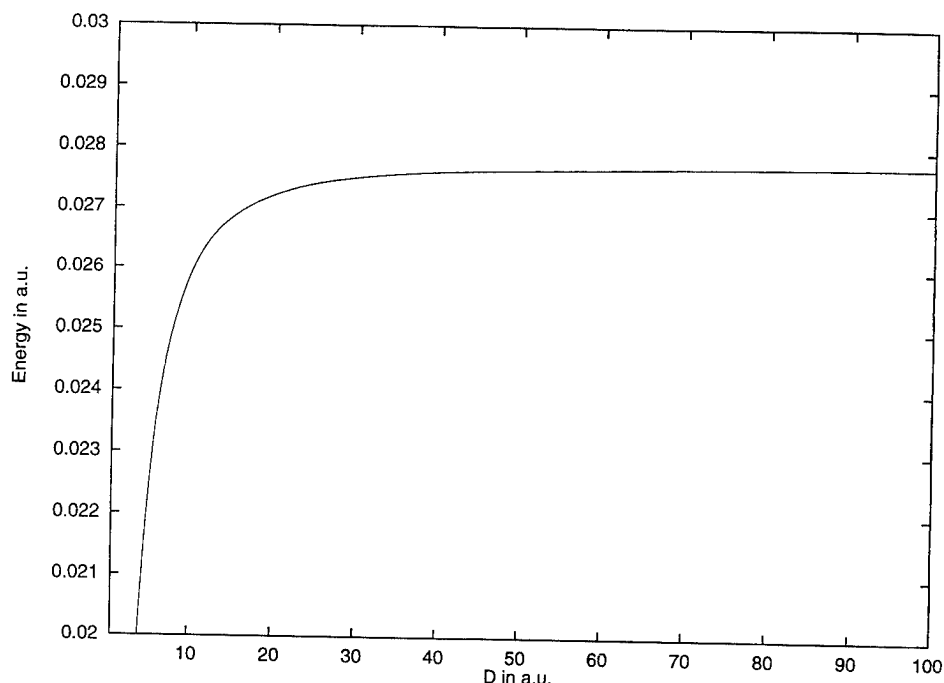


FIGURE 2. Detachment energy for the negative hydrogen ion vs. the Debye length D .

H^- and H approach smoothly the corresponding vacuum values of -0.52775 and -0.5 a.u., respectively.

In fact, our findings indicate that the negative hydrogen ions survives increasing plasma conditions as well as neutral hydrogen does and that both species lose their binding property simultaneously as a function of decreasing values of D . The smallest value of D for which binding of the two-electron system has still been obtained (although with a tiny value of the detachment energy of 0.68×10^{-4} a.u.) is $D = 0.860$ a.u. This value is so close to the value obtained by Rogers and co-workers [3] for the limit beyond which not even neutral hydrogen is able to support a bound state that it is safe to state as our main finding the fact that, in a pure Debye potential, there is no way for the negative ion to lose its second electron due to pressure ionization. Any detachment that occurs is due to the action of one-particle operators such as collisions with other particles or photons. As a function of decreasing values of D the detachment energy of H^- decreases initially very slowly from its vacuum value of 0.0277 a.u. and holds still a sizable 0.0234 a.u. at $D = 6$. From then on it drops rapidly.

The corresponding results for the helium atom in comparison to the ground-state energy of the

helium ion are presented in Figure 3. Again it has been found that both systems lose their capability to support bound states at the same value of D . More precisely, we calculated this to happen at $D = 0.4311$ a.u. for the helium ion. The critical point of no binding for the first two excited singlet S states of helium is noticeably different from this value: $D = 0.460$ a.u. for the $(1s2s)$ state and $D = 0.4957$ a.u. for the $(1s3s)$ state. Since the excited states of helium are pushed into the continuum in a region of D values where the positive helium ion still carries a bound ground-state—though barely so—the corresponding curves in Figure 3 do intersect. For higher excited states this crossing will occur at values of D which still represent plasma situations. In these regions, pressure ionization of one Rydberg electron is possible even in a real Debye plasma. In Figure 4 the ionization energies of the neutral helium atom are plotted versus the Debye length D .

RESULTS FOR THE ONE-ELECTRON RADIAL DENSITY

The one-electron radial density has been calculated for the negative hydrogen ion under various plasma conditions mainly in order to study the spatial extension of this system as it becomes less

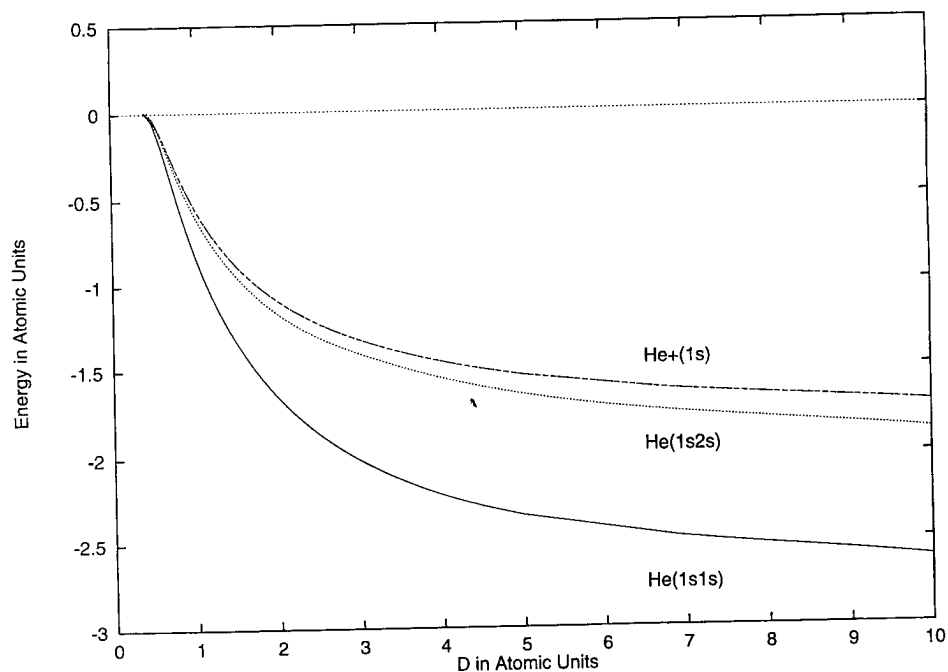


FIGURE 3. The energy of the two lowest $1S$ states of the helium atom vs. the screening parameter D compared to the ground-state energy of the positive helium ion under the same plasma conditions. While the ground state of He is bound over the whole range of D values for which there is a bound state of the ion, the curve of the excited He state crosses the ionic curve, although this is not noticeable in the graph.

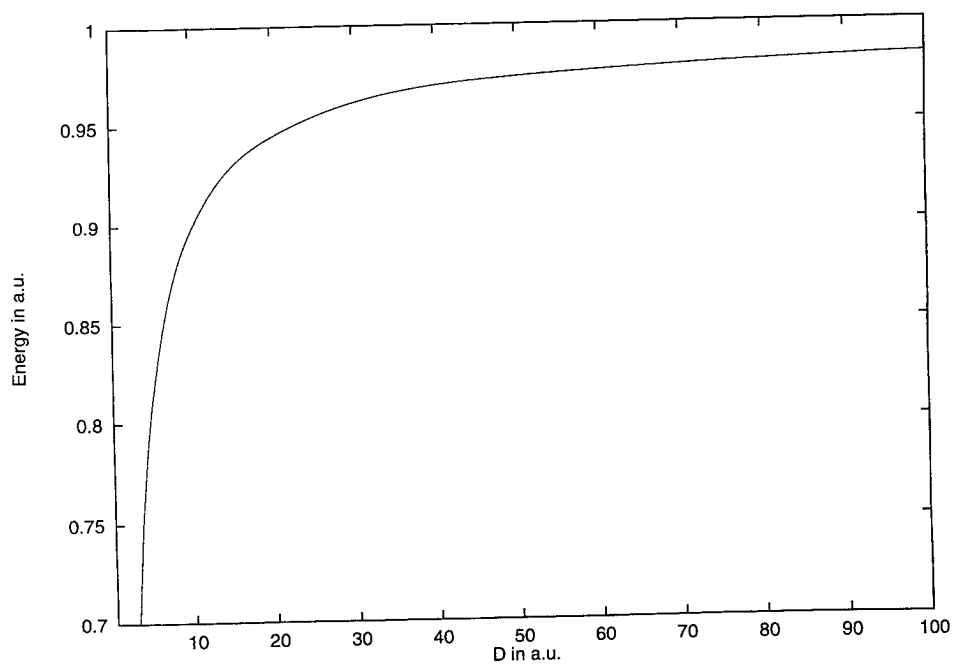


FIGURE 4. Ionization energy for the neutral helium atom vs. the Debye length D .

and less bound with decreasing value of D . This effect is frequently addressed as "lowering of the continuum threshold." The expectation is that H^- increases in spatial extension with the reduction of the binding energy. This is indeed the case as shown in Figure 5. However, this increase in size occurs in a region of small D values which is not representative of a plasma. The most prominent feature of these results is rather the high degree of stability the ion exhibits in various plasma conditions. There is very little change in the density from $D = 20,000$ a.u. to $D = 4$ a.u. A small shift of electron density from the inner regions toward the tail of the distribution is noticeable. The most striking feature, however, is the fact that we do not see more of it. Even at $D = 2$ a.u. the curve retains its maximum at roughly the same position. From then on, however, the charge distribution changes noticeably. The lowest curve, corresponding to $D = 0.860$ a.u., is so extended that within a region of $r \leq 80$ a.u. not more than 25% of the total charge is collected. The relative constancy of both the detachment energy and the electron distribution of H^- accounts well for its property to

enhance the opacity of plasmas. The unexpectedly high degree of stability of the ion points toward its presence even in high-density laboratory plasmas as opposed to just in astrophysical plasmas.

SOME SPECULATIVE RESULTS

While the Debye theory postulates a uniform screening potential between two charges, it seems plausible to assume that local fluctuations of the screening are not only possible but rather the rule. If that is so, it may be argued that the electrons, being light particles, can be more efficient in taking advantage of such local fluctuations than an electron-ion pair which has one less mobile partner. In particular, it may be argued that electron pairs will preferably move into regions with higher screening potential (i.e., lower values of D) because this will lower the energy of the system and that electron pairs are more efficient to do so than electron-ion pairs. In order to explore the rudiments of an emerging theory of such ideas, we have studied cases in which the values of the Debye parameter for the electron-electron interac-

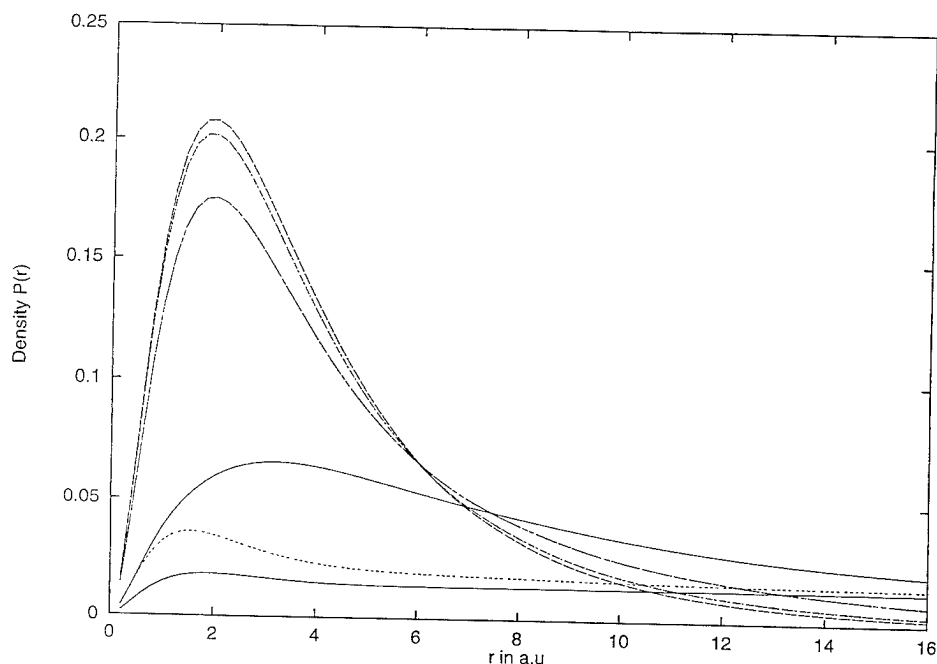


FIGURE 5. The radial one-electron density of the negative hydrogen ion in various plasma environments. The top curve (taken at the maximum) represents the density at a value of $D = 2000$ a.u., while the lower curves correspond to a series of values of $D = 4, 2, 1, 0.875$, and 0.860 a.u., respectively.

tion was chosen different from those of the electron-nucleus potential. In practice, we have augmented the last term of the Hamiltonian Eq. (1) by a scaling factor y to read $\exp(-yr_{12}/D)/r_{12}$ while the other terms remain unchanged. By changing y one can modify the screening of the electron interaction relative to the other interactions. Results of these calculations are presented in Table I. The most interesting feature of this scenario is the possibility of excited states of H^- . Although here only states of S symmetry have been included, it is likely that bound states of higher angular momentum do exist. Then one would expect low-energy electromagnetic transitions, which, if identifiable, might serve diagnostic purposes. Astrophysical spectra usually have lots of broadened

low-energy transition lines so that the identification of such transitions may be difficult. Laboratory plasma have a much better chance for the detection.

Summary

While in previous work the screening effects were applied only to the electron-ion interaction, the present study extends Debye screening also to the electron-electron interaction. A variational calculation of the ground-state energy of the negative hydrogen ion has been performed for various plasma conditions characterized by different val-

TABLE I
Binding energies of the negative hydrogen ion are listed for various values of the screening parameter D and various values of the scaling factor y by which the screening of the electron-electron interaction can be modified without affecting the screening of the electron nuclear potential. For comparison, the values for neutral hydrogen (1s) are given in column 2. Multiple entries in columns 2-5 indicate the existence of excited states of $1S$ symmetry

	H Atom	Negative Hydrogen Ion			
		$y = 1.0$	$y = 1.1$	$y = 1.5$	$y = 2.0$
$D = 200.0$	0.49502	0.52276	0.52325 0.49517	0.52520 0.49642 0.49578	0.52760 0.49801 0.49684
$D = 100.0$	0.49007	0.51780	0.51876 0.49033	0.52254 0.49237 0.49109	0.52717 0.49501 0.49275
$D = 50.0$	0.48030	0.50795	0.50978 0.48060	0.51693 0.48361 0.48131	0.52554 0.48761 0.48319
$D = 30.0$	0.46748	0.49499	0.49785 0.46772	0.50894 0.47127 0.46804	0.52203 0.47618 0.46968
$D = 20.0$	0.45182	0.47904	0.48303 0.45192	0.49829 0.45545 0.45188	0.51590 0.46066 0.45284
$D = 15.0$	0.43653	0.46338	0.46834	0.48706 0.43960	0.50827 0.44461 0.43673
$D = 10.0$	0.40706	0.43295	0.43942	0.46340 0.40867	0.48975 0.41252
$D = 8.0$	0.38588	0.41092	0.41821	0.44499 0.38656	0.47387 0.38929
$D = 6.0$	0.35226	0.37568	0.38390	0.41372	0.44507 0.35312
$D = 4.0$	0.29092	0.31074	0.31960	0.35135	0.38351

ues of the Debye parameter D . This results in a considerable increase in stability of the ion as compared to the case of an unscreened interaction (i.e., with only the electron-ion potential screened).

As an example of related research, we refer to a study by Scheibner, Weisheit, and Lane [6] of plasma screening effects on proton-impact excitation of positive ions. In this work two screened ions interact via a Debye force.

ACKNOWLEDGMENT

This work was supported by the Division of Chemical Sciences, Office of Basic Energy Sciences,

Office of Energy Research, U.S. Department of Energy.

References

1. P. Winkler, Brief Report, Phys. Rev. E, to appear.
2. Z. Wang and P. Winkler, Phys. Rev. A **52**, 216 (1995).
3. F. J. Rogers, H. C. Graboske, Jr., and D. J. Harwood; Phys. Rev. A **1**, 1577 (1970).
4. P. Winkler and R. N. Porter, J. Chem. Phys. **61**, 2038 (1974).
5. W. J. Swiatecki, Proc. Roy. Soc. A **205**, 238 (1951).
6. K. Scheibner, J. C. Weisheit, and N. F. Lane, Phys. Rev. A **35**, 1252 (1987).

Condensed-Phase Effects on the Conformational Equilibrium of Ethylene Glycol

B. J. COSTA CABRAL

*Departamento de Química e Bioquímica, Faculdade de Ciências da Universidade de Lisboa, 1700 Lisboa, Portugal, and *Centro de Física da Matéria Condensada da Universidade de Lisboa, Av. Professor Gama Pinto, 2, 1699 Lisboa, Portugal; e-mail: ben@alf1.cii.fc.ul.pt*

Received February 25, 1996; accepted May 7, 1996

ABSTRACT

Density functional calculations for ethylene glycol ($\text{CH}_2\text{OHCH}_2\text{OH}$) in the gas and in a dielectric medium are reported. The condensed-phase calculations are based on the self-consistent reaction field approach and the environment has the dielectric constant of liquid methanol. NPT Monte Carlo simulations of ethylene glycol (ETG) in liquid methanol are also reported. The simulations were carried out for three conformers of ETG (tGg', gGg', and tTt). Comparison between SCRF results for the conformational equilibrium in the gas and in the dielectric suggests that the tGg' conformer is slightly stabilized relative to the gGg' conformer in the solvent. However, the energy difference between them is less than 1.0 kJ/mol, which indicates that frequent interconversions between the tGg' and gGg' conformers are expected in the condensed phase. The all-trans conformer (tTt) is higher than the most stable conformer in the gas by 14 kJ/mol. Monte Carlo simulations predict that the tGg' and gGg' conformers have very similar energies in the solvent. However, the simulations also show, in agreement with experimental data, that the tTt conformer is stabilized in liquid methanol, relative to the gas phase. The microscopic mechanism leading to the stabilization of the tTt conformer in the liquid is related to the differential hydrogen-bonding formation between the ETG conformers and the methanol molecules. © 1996 John Wiley & Sons, Inc.

*Address for correspondence.

Introduction

Interest in the study of polyols has been recently emphasized by the research of potent HIV-1 protease inhibitors [1, 2]. One of the simplest polyols (a diol) is ethylene glycol ($\text{CH}_2\text{OHCH}_2\text{OH}$ = ETG). This molecule is a model system to discuss the formation of intramolecular hydrogen bonding. Ab initio studies of ETG are also a good test for the quantum chemical prediction of the relative stability due to the presence of several conformational local minima.

Another interesting aspect of ETG is that the interactions of this molecule with an environment can induce important changes on the conformational equilibrium. This effect is particularly important in hydrogen-bonding solvents. In these cases, competition between internal and external hydrogen-bonding formation changes the conformational equilibrium of the solvated molecule relative to the gas-phase monomer. In addition, the solvation of polyols in water or hydrogen-bonding solvents reduces the formation of hydrogen-bonded networks and modifies the dynamics leading to the phase transitions of the pure solvents.

Several experimental studies on the conformational equilibrium of ETG have been reported [3–14]. Theoretical studies on the conformational equilibrium of ETG were the research theme of several works [15–30]. However, some relevant aspects in the theoretical modeling of this molecule, as, e.g., electronic correlation effects on the conformational equilibrium, were analyzed only recently [21].

Ab initio studies of ETG [15–28] predict, in agreement with experimental results, that two conformers with an internal hydrogen bond (gGg' and tGg') are the predominant structures in the gas. The energy difference between them is very dependent on the theoretical level of the calculations [28]. This is related to the fact, verified by the most recent theoretical studies of ETG [21–28], that the energy difference between tGg' and gGg' conformers is less than 1.5 kJ/mol.

Theoretical studies on the conformational equilibrium of ETG in condensed phases are few and very recent [26–31]. Some of these studies were based on Monte Carlo [26–27] and molecular dynamics [30, 31] methods and analyzed the solvation of ETG in water [26–31] and carbon tetrachlo-

ride [30]. Very recent molecular dynamics simulations of ETG in water and in xenon have been also reported [31]. Other theoretical studies of ETG in the condensed phase were based on self-consistent reaction field (SCRF) calculations, using the continuum model approach [28, 29]. The simplifications introduced by this approach and the limitations of the method are well known. However, by including in the Hamiltonian of the solvated molecule the interaction with the environment, SCRF methods [32–37] provide the capability to model quantum chemical solvent effects in a self-consistent way.

A theoretical study on the modifications of the ETG conformational equilibrium when it is solvated in liquid methanol is presented reported. Two different approaches were used: density functional SCRF calculations and Monte Carlo simulations. The interest to perform statistical mechanics computer simulations of ETG in liquid methanol is related to hydrogen-bonding formation and also to the fact that a small reorganization of the solvent is expected considering the similarity between ETG and two methanol molecules. The results are compared to experimental data and with other theoretical studies.

Computational Details

DENSITY FUNCTIONAL CALCULATIONS

The density functional calculations were performed using for the exchange the Becke functional [38a] and for correlation the Lee, Yang, and Parr functional [39] (BLYP). Additional calculations using a hybrid functional including a mixture of Hartree-Fock exchange with DFT exchange-correlation (Becke's parameter function) [38b] which is being represented by B3LYP are also reported. To assess the importance of electronic correlation effects, some calculations with the Becke exchange correlation only (HFB) were carried out. The calculations were performed with the G92/DFT program [40] and the 6-31G** and 6-311G** basis sets were used.

Three ETG conformers, defined by the relative orientations of the O—H group around the C—C—O plane (Fig. 1) and the angle between C—C—O planes, are considered. The conformers are tGg', gGg', and tTt. There are 10 different conformers of ETG. These three conformers were selected because it is known that tGg' and gGg'

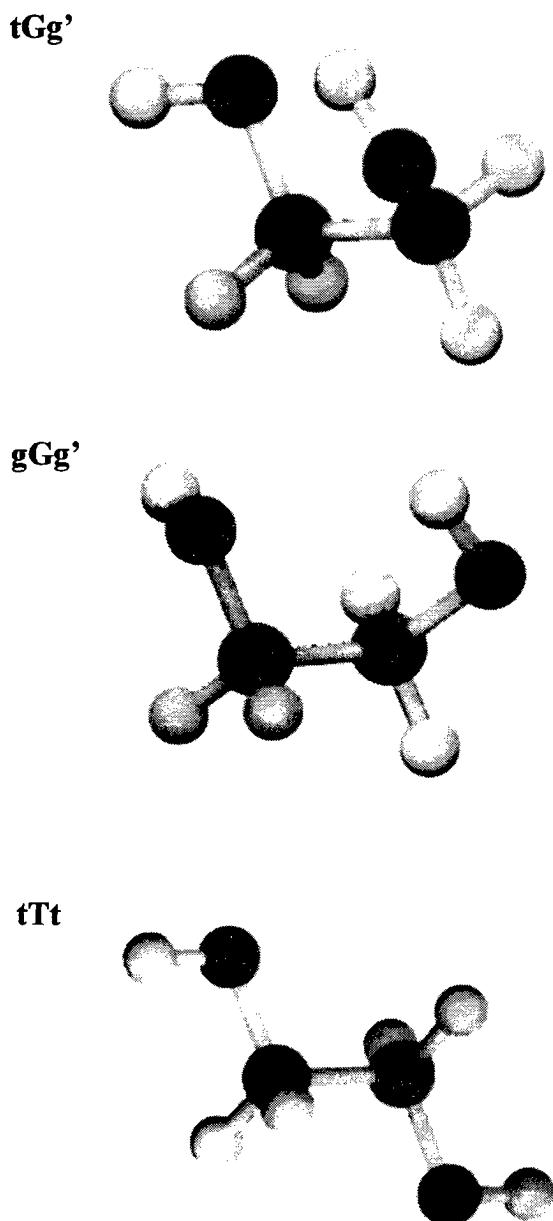


FIGURE 1. tGg', gGg', and tTt conformers of ETG.

are the most stable in the gas phase and also because experimental information predicts a significant stabilization of the tTt conformer in ETG pure liquid [9].

Quantum chemical calculations in the condensed phase have been based on the self-consistent reaction field (SCRF) approach [32–37]. In this approach, the solute molecule is placed in a cavity, which is presently assumed to be spherical of radius a_0 (Onsager cavity radius). The environ-

ment is represented by a dielectric medium of constant ϵ . The Onsager cavity radius for the different conformers was in the 3.48–3.51 Å range. The value of the dielectric constant was that of liquid methanol ($\epsilon = 33.6$). Recent developments in the SCRF are reported in [36, 37].

The G92/DFT implementation [34, 35] of the SCRF approach includes only the Born and Onsager contributions to the reaction field. They are related, respectively, to the total charge and dipole moment of the solute. It is known that for some systems the contributions to the reaction field due to higher-order multipolar moments can be important [37]. In addition, the all-trans conformer (tTt) has no permanent dipolar moment and the present implementation of the SCRF it is not adequate to model the solvation of this conformer.

MONTE CARLO SIMULATIONS

The Monte Carlo simulations for ETG solvated in liquid methanol were carried out with one solute molecule and 127 solvent molecules in a cube with periodic boundary conditions. The ETG molecule was represented by six interaction sites, which are the ethyl group and the hydrogen and oxygen atoms. The methanol molecule was represented by three interaction sites which are the methyl group and the hydrogen and oxygen atoms. The OPLS intermolecular potential function was used to model the site-site interactions and the parameters were those proposed by Jorgensen [41].

A preferential sampling algorithm [42], adequate to simulate dilute solutions, was used. The Markov chain was generated by the usual Metropolis algorithm in the NPT ensemble [43] that is particularly convenient to model mixtures and dilute solutions.

The Monte Carlo simulations of ETG in liquid methanol were carried out for the three ETG conformers (tGg', gGg', and tTt). The geometry of each conformer was the theoretical gas-phase geometry and has been kept constant during the simulations. The main advantage of this procedure is that the relaxation of the solvent around a particular conformer is assured and that the statistics related to the solute-solvent properties is accurate. A similar approach was recently used in the simulations of ETG solvated in water and in Xe carried out by Hayashi et al. [31]. Although ETG is a very flexible molecule, it should be observed that the main purpose of the present simulations is to pro-

vide detailed information on the differential solvation of the three conformers (gGg', tGg', and tTt).

The simulations were carried out at 25°C and 1 atm of pressure. For each conformer, $4-6 \times 10^6$ Monte Carlo steps (one step corresponding to the trial move of one solvent particle), were performed for equilibration. The coordinates of the solute molecule were perturbed each 50–200 steps. The volume of the system was perturbed each 2500 steps. The stochastic parameters related to the translations and rotations of the solute, translations, and rotations of the solvent molecules and volume perturbations were adjusted in order that ~50% of the generated configurations are accepted. Additional $8-12 \times 10^6$ steps were generated to estimate the reported final averages.

Results and Discussion

DENSITY FUNCTIONAL CALCULATIONS

Density functional calculations for the ETG conformers in the gas phase and in a dielectric representing liquid methanol are reported in Table I. The present analysis is oriented to the discussion of energy differences and dipole moments. A further analysis of the geometries and vibrational frequencies of ETG and ETG-(H₂O)_n complexes is in progress and will be reported elsewhere.

The energy differences relative to the tGg' conformer range from -1.97 to 0.18 kJ/mol. There is almost no difference between the HFB/6-31G** and BLYP/6-31G** calculations. A significant reduction (0.87 kJ/mol) of the energy difference be-

tween the tGg' and gGg' conformers can be observed when we move from the 6-31G** to the 6-311G** basis set. B3LYP results are significantly different from the BLYP results, reducing considerably the energy difference between the conformers. Excepting the B3LYP/6-311G** calculation (0.18 kJ/mol), all other calculations predict that the gGg' conformer is slightly favored in the gas. The B3LYP/6-311G** result is in good agreement with the MP2/6-311G** value (0.25 kJ/mol) predicted by Teppen et al. [25] and is slightly lower than an MP2/6-31G* (0.7 kJ/mol) calculation [21]. ZPVE correction to this energy is 0.12 kJ/mol at the HF/6-31G* level [26, 27].

The experimental studies clearly indicate that these two conformers are the most stable in the gas phase. The relative stability of the tGg' and gGg' conformers, however, is much more difficult to assess. Takeuchi and Tasumi [11] suggested the possible coexistence of the two conformers in low-temperature argon matrices. Walder et al. [10] interpreted the microwave spectrum of ETG in terms of the gGg' conformer only. Kristiansen et al. [12] predicted that gGg' is 1.4 (4) kJ/mol less stable than is tGg' at 300 K. Comparison among the present calculations, other theoretical results, and experimental works suggests that both tGg' and gGg' conformers coexist in the gas phase. The all-trans conformer is 14 kJ/mol higher than the gGg' conformer (BLYP/6-31G**), which is in good agreement with the value (13.6 kJ/mol) predicted by Oie et al. [23].

The present DFT/SCRF calculations predict that the solvation free-energy difference between tGg'

TABLE I

Total energies^a (in au), O—C—C—O dihedral angle φ (in deg.), dipole moment μ (in Debye), and energy difference relative to the tGg' conformer ΔE (in kJ/mol).

Gas	gGg'			tGg'			
	Energy	φ	μ	Energy	φ	μ	ΔE
HFB/6-31G**	-229.02260	56.9	2.2	-229.02187	63.3	2.3	-1.93
BLYP/6-31G**	-230.17616	53.9	2.3	-230.17541	60.2	2.4	-1.97
BLYP/6-311G**	-230.24689	55.1	2.3	-230.24648	61.1	2.4	-1.1
B3LYP/6-31G**	-230.25757	54.5	2.4	-230.25735	59.8	2.5	-0.57
B3LYP/6-311G**	-230.32318	55.6	2.4	-230.32325	60.6	2.5	0.18
Dielectric ^b							
B3LYP/6-311G**	-230.32499	53.8	2.9	-230.32525	57.9	3.1	0.68

^aTotal energies (in au) for the all-trans conformer are -230.16952 (BLYP/6-31G**) and -230.25221 (B3LYP/6-31G**).

^bThe Onsager cavity radius for the tGg' and gGg' are, respectively, 3.5 and 3.49 Å.

The dielectric constant was 33.6 (liquid methanol).

and gGg' conformers is -0.7 kJ/mol. Solvation free-energy differences between gGg' and tGg' conformers in water and other solvents were discussed by several theoretical studies [26–31]. In general, they predict that gGg' is better solvated. However, a recent molecular dynamics simulation by Hayashi et al. [31] suggests that there is a preference for the tGg' in aqueous solution. A previous Hartree–Fock/SCRF calculation of Alagona and Ghio [29] predicted that the difference in the solvation free energy between tGg' and gGg' was 2.7 kJ/mol. Another continuum model study by Cramer and Truhlar [28] based on AM1 calculations predicted that this difference was 0.8 kJ/mol. The present DFT/SCRF calculations also predict a reduction of the O—C—C—O dihedral angle (φ) for the tGg' conformer. The angle φ changes from 60.6° in the gas to 57.9° in the dielectric. A similar reduction in the dihedral angle φ can be observed for the gGg' conformer.

The present calculations at the B3LYP/6-311G** level predict that the dipole moments (see Table I) for the two most stable conformers in the gas phase are 2.4 D (gGg') and 2.5 D (tGg'). These values are in excellent agreement with experiment (2.3 ± 0.1 D) [7a]. SCRF calculations predict that the values of the dipole moment in the dielectric medium representing liquid methanol are significantly higher. They are 2.9 D (gGg') and 3.1 D (tGg'). This result is in very good agreement with experimental data for the neat liquid (3.5 – 4.0 D) [5]. The observed increase of the dipolar moment of ETG in the liquid and the difference between the values for the two conformers is in the present model coherent with a better solvation of the tGg' conformer.

MONTE CARLO SIMULATIONS

Thermal properties for ETG solvated in methanol are reported in Table II. The solute–solvent interaction energies (E_{sx}) for the three conformers show that the tGg' and gGg' have similar interaction energies with methanol (-110.9 kJ/mol).

The partition of E_{sx} in E_{sx-12} , E_{sx-6} , and E_{sx-1} also suggests that for tGg' a higher solute–solvent repulsive energy is compensated by the E_{sx-6} attractive contribution. The solute–solvent interaction energy for the tTt conformer is -106.7 kJ/mol. Comparison between E_{ss} and V from the simulations of ETG in liquid methanol and those from the simulations of the neat liquid (E_{ss}^* and V^*)

TABLE II
Thermal data for NPT Monte Carlo simulations of ETG in liquid methanol.

	tGg'	gGg'	tTt
E_{sx}	-110.9 ± 4 (-131.4) ^a	-110.9 ± 4 (-136.0) ^a	-106.7 ± 4 (-133.1) ^a
E_{sx-12}	68.2	64.8	65.7
E_{sx-6}	-86.2	-82.0	-81.2
E_{sx-1}	-92.9	-93.7	-91.2
E_{ss}	-35.0 ± 2	-35.4 ± 2	-35.5 ± 2
V	9161 ± 50	9089 ± 45	9193 ± 50
E_{ss}^*	-34.7		
V^{*b}	9070 ± 40		

The pressure is 1 atm and the temperature 298 K. Energies are in kJ/mol. Volumes are in \AA^3 . E_{sx} is the total solute–solvent energy. E_{sx-12} , E_{sx-6} , and E_{sx-1} are, respectively, the r^{-12} , r^{-6} , and Coulombic interaction energies between the solute and the solvent. E_{ss} is the solvent total energy. E_{ss}^* and V^* are, respectively, the energy and volume of pure methanol.

^aFor ETG solvated in liquid water from [26].

^bFrom the simulations of liquid methanol [41].

suggests that solvation of ETG in liquid methanol does not induce a significant reorganization of the solvent. This is expected, since ETG can be seen as being formed by two molecular fragments similar to methanol. Thus, the energy difference between the tTt conformer and the tGg' and gGg' conformers in liquid methanol can be estimated as ~ 4.2 kJ/mol. If we compare this value with the gas-phase energy difference (14.0 kJ/mol at B3LYP/6-311G**), it is suggested that solvation of ETG in liquid methanol stabilizes the tTt conformer relative to the gas phase. This result is in agreement with experimental data for the neat liquid by Pruettiangkura et al. [9]. These authors predicted that the effect of solvation on the conformational energy difference was to induce a relatively large stabilization of the all-*trans* rotamer in pure ETG by 6.3 kJ/mol. The present study for ETG solvated in methanol indicates that the tTt conformer is stabilized by ~ 9.8 kJ/mol relative to the gas phase.

The site–site distribution functions for the correlations between the ETG oxygen atom and the methanol methyl site [O—CH₃(M)], the ethyl ETG site, and the methanol oxygen atom [CH₂—O(M)] are reported in Figures 2 and 3. O—CH₃(M) (Fig. 2) shows for all the three conformers a maximum about 3.5 \AA , which is less pronounced for the gGg' conformer. The CH₂—O(M) site–site correlation

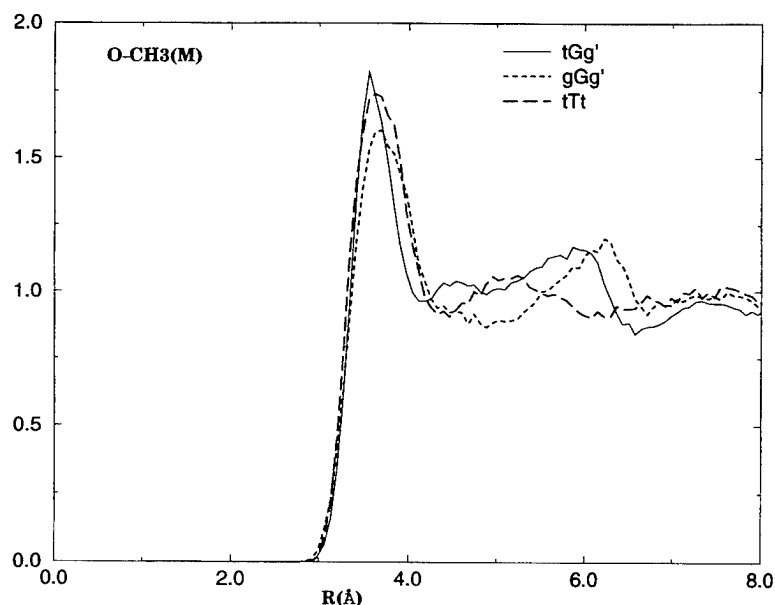


FIGURE 2. O—CH₃(M) site-site distribution functions for the three conformers of ETG in liquid methanol.

functions present a first maximum 3.6 Å. For the tGg' conformer, there is second maximum at 3.9 Å, which reflects, in this case, the different roles played by the CH₂ sites. Also indicated is the formation of a second coordination shell, after a second maximum, which is for all the three conformers at ~5.0 Å.

The correlations between oxygen and hydrogen atoms are reported in Figures 4 and 5. The correlations between the ETG oxygen atom and the methanol hydrogen (Fig. 4) and the ETG hydrogen atom and the methanol oxygen (Fig. 5) are very different for the three conformers. As illustrated in Figure 4, for the all-*trans* conformer, the height of

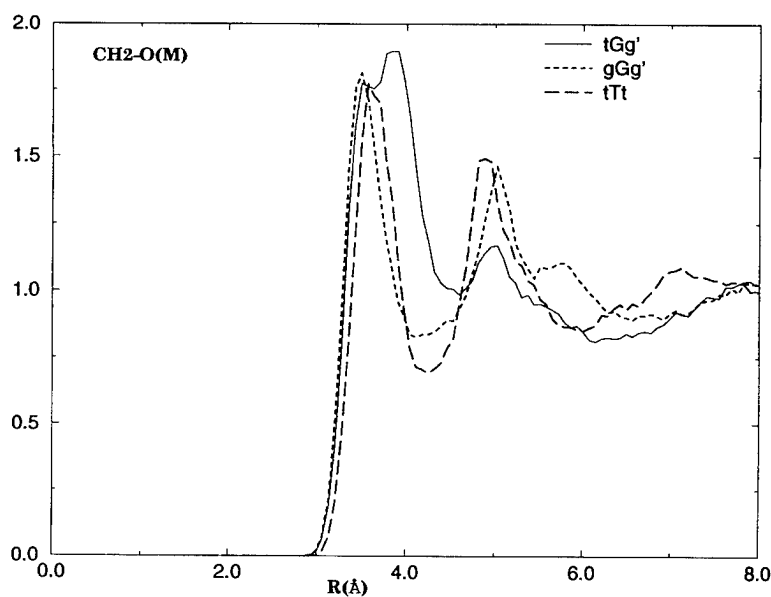


FIGURE 3. O—CH₂(M) site-site distribution functions for the three conformers of ETG in liquid methanol.

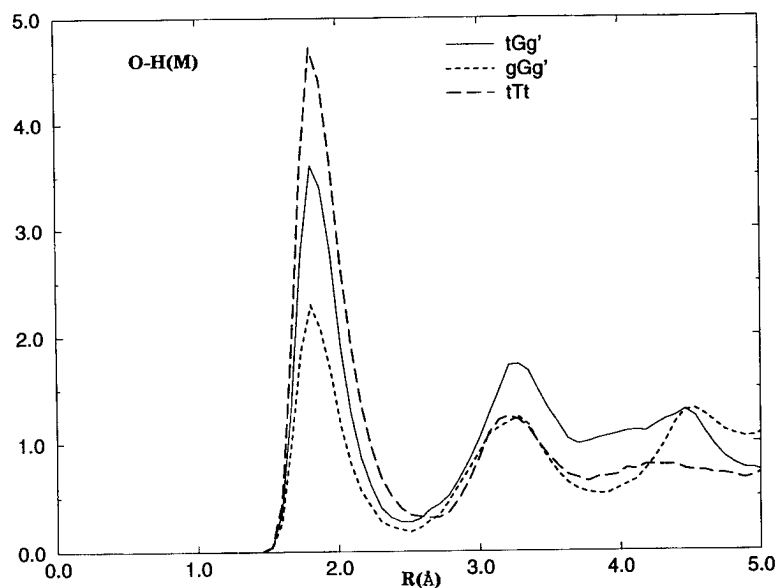


FIGURE 4. O—H(M) site-site distribution functions for the three conformers of ETG in liquid methanol.

the first maximum is significantly higher than those corresponding to the tGg' and gGg' . The O—H(M) distribution functions show that the tTt conformer, when comparison is made with the two other conformers (tGg' and gGg'), is the preferential proton acceptor conformer. It is also illustrated in

Figure 4 that for tGg' correlations between O—H(M) are favored after the first coordination shell.

Figure 5 suggests that the H—O(M) site-site correlation functions for the three conformers are not very different, although the approaching of

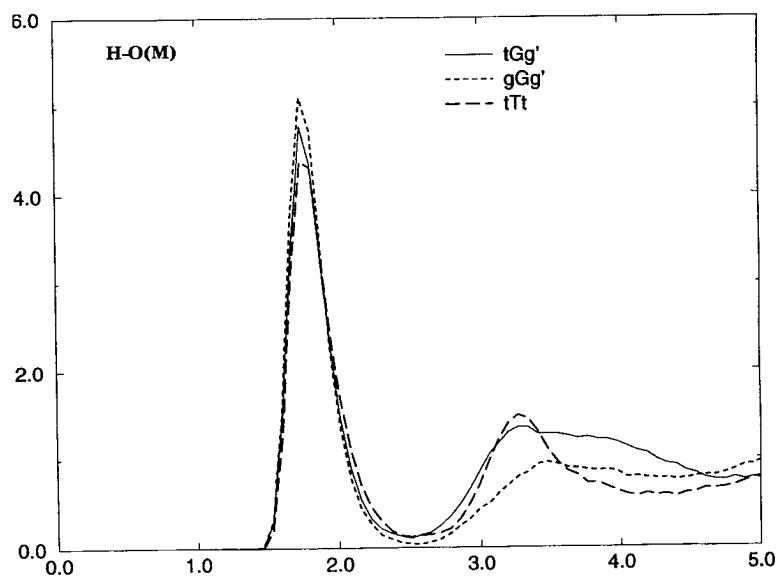


FIGURE 5. H—O(M) site-site distribution functions for the three conformers of ETG in liquid methanol.

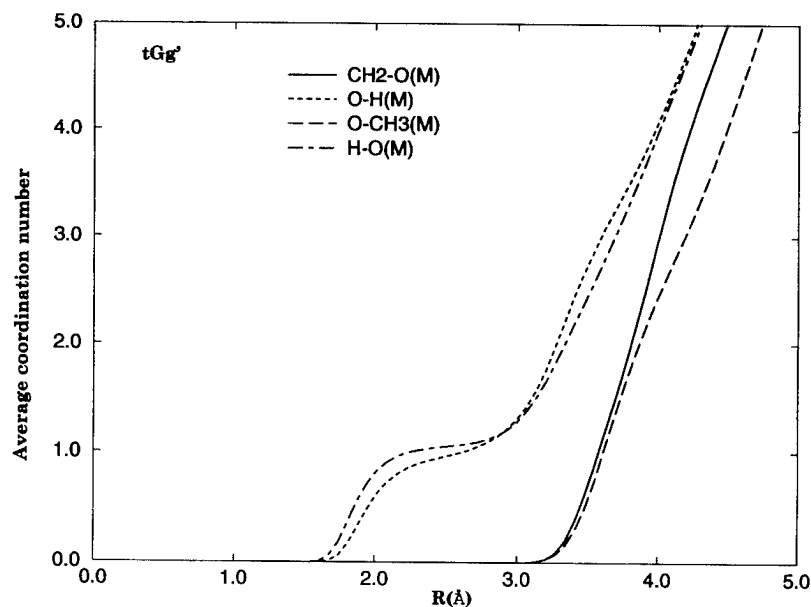


FIGURE 6. Average coordination numbers as a function of the site-site distances for the tGg' conformer in liquid methanol.

oxygen methanol atoms to ETG hydrogens seems slightly more important for the gGg' conformer. However, this figure also suggests that after the first coordination shell the approaching of O(M) atoms is more favored to tTt and tGg' conformers.

This is related to the second maximum of the correlation functions at ~ 3.4 Å.

Figures 6–8 report the average coordination numbers as a function of the distance between the sites, respectively, for the tGg', gGg', and tTt con-

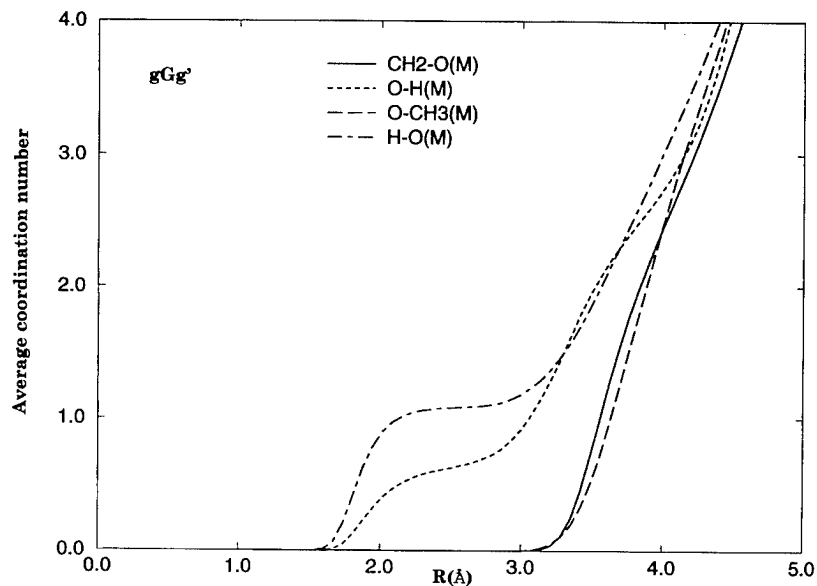


FIGURE 7. Average coordination numbers as a function of the site-site distances for the gGg' conformer in liquid methanol.

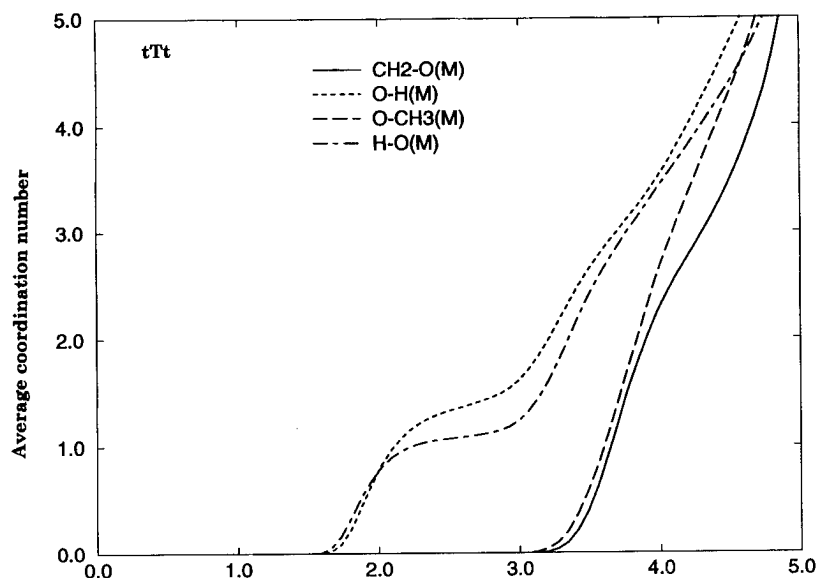


FIGURE 8. Average coordination numbers as a function of the site-site distances for the tTt conformer in liquid methanol.

formers. For the tGg' conformer, Figure 6 shows that given one oxygen ETG atom there is one methanol hydrogen atom at ~ 2.9 Å and that for one hydrogen ETG atom there is one methanol oxygen at ~ 2.0 Å. In Figure 7, a competition between $\text{CH}_2\text{—O(M)}$ and $\text{O—CH}_3\text{(M)}$ correlations for the gGg' conformer is illustrated by the crossing of the coordination numbers at ~ 3.3 and ~ 3.9 Å.

The formation of plateaux in the average coordination curves, as a function of the distances between the sites, illustrates the definition of the first coordination shell. This effect is particularly important in the O—H correlations and it is related to the value of the minima in the site-site distribution functions. Figure 8 shows the coordination numbers for the tTt conformer. The correlations between O—H(M) (dashed curve) for this conformer are clearly more important than for the two other conformers (Figs. 6 and 7). This suggests, in agreement with the data for thermal properties, that hydrogen bonding plays a very important role to stabilize the ETG all-*trans* conformer in liquid methanol.

Conclusions

The modifications relative to the gas phase of several molecular properties of ETG when it is solvated in liquid methanol were analyzed. DFT

calculations for different conformers of ETG in the gas and in a dielectric medium modeling liquid methanol were reported. The calculations were performed with different representations for the exchange-correlation functionals. The condensed-phase calculations based on the DFT/SCRF approach predict that for ETG solvated in a dielectric there is a small stabilization of tGg' relative to gGg'.

Monte Carlo simulations of ETG in liquid methanol showed that tGg' and gGg' have similar interactions with liquid methanol and that a very small reorganization of the solvent is observed. However, the simulations also predict, in agreement with experiment data, an important stabilization, relative to the gas-phase equilibrium, of the all-*trans* conformer. The microscopic mechanisms leading to this stabilization were analyzed through the calculation of site-site correlation functions and were related to the specific role played by the all-*trans* ETG conformer as a proton acceptor in liquid methanol.

References

1. D. J. Kempf, D. W. Norbeck, L. Codavici, X. C. Wang, W. E. Kohlbrenner, N. Wideburg, D. A. Paul, M. Knigge, S. Vasavanonda, A. Craig-Kennard, A. Saldivar, W. Rosenbrook, J. J. Clement, and J. Erickson, *J. Med. Chem.* **33**, 2687 (1990).
2. D. J. Kempf, L. Codavici, X. C. Wang, W. E. Kohlbrenner, N. Wideburg, A. Saldivar, S. Vasavanonda, K. C. Marsh,

- P. Bryant, H. L. Sham, B. E. Green, D. A. Betebenner, J. Erickson, and D. Norbeck, *J. Med. Chem.* **36**, 320 (1993).
3. O. Bastiensen, *Acta Chem. Scand.* **3**, 415 (1949).
4. P. Buckley and P. A. Guiguère, *Can. J. Chem.* **45**, 397 (1967).
5. K. G. Pachler and P. L. Wessels, *J. Mol. Struct.* **6**, 471 (1970).
6. T.-K. Ha, H. Frei, R. Meyer, and H. S. H. Günthard, *Theor. Chim. Acta* **34**, 277 (1974).
7. (a) F. Podo, G. Nemethy, R. L. Indovina, and L. Radics, *Mol. Phys.* **27**, 521 (1974); (b) V. Viti, P. L. Indovina, F. Podo, L. Radics, and G. Nemethy, *Mol. Phys.* **27**, 541 (1974).
8. H. Frei, T.-K. Ha, R. Meyer, and H. S. H. Günthard, *Chem. Phys.* **25**, 271 (1977).
9. P. Pruetiangkura, S. Ho, and M. Schwartz, *Spectrosc. Lett.* **12**, 679 (1979).
10. E. Walder, A. Bauder, and H. S. H. Günthard, *Chem. Phys. Lett.* **51**, 223 (1980).
11. H. Takeuchi and M. Tasumi, *Chem. Phys.* **77**, 21 (1983).
12. P.-E. Kristiansen, K.-M. Marstokk, and H. Møllendal, *Acta Chem. Scand., Ser. A* **41**, 403 (1987).
13. C. G. Park and M. Tasumi, *J. Phys. Chem.* **95**, 2757 (1991).
14. V. Crupi, M. P. Jannelli, S. Magazu, G. Maisano, D. Majolini, P. Migliardo, and D. Sirna, *Mol. Phys.* **84**, 645 (1995).
15. L. Radom, W. A. Lathan, W. J. Hehre, and J. A. Pople, *J. Am. Chem. Soc.* **95**, 693 (1973).
16. F. Podo, G. Nemethy, P. L. Indovina, L. Radics, and V. Viti, *Mol. Phys.* **27**, 521 (1974).
17. J. Almlöf and H. Stymne, *Chem. Phys. Lett.* **33**, 118 (1975).
18. S. Melber and K. Rasmussen, *J. Mol. Struct.* **57**, 215 (1979).
19. C. van Alsenoy, L. van den Enden, and L. Schäfer, *J. Mol. Struct. (Theochem)* **108**, 121 (1984).
20. K. Morokuma and H. Sugeta, *Chem. Phys. Lett.* **134**, 23 (1987).
21. B. J. Costa Cabral, L. M. P. C. Albuquerque, and F. M. S. Silva Fernandes, *Theor. Chim. Acta* **78**, 271 (1991).
22. M. A. Murcko and R. A. DiPaola, *J. Am. Chem. Soc.* **114**, 10010 (1992).
23. T. Oie, I. A. Topol, and S. K. Burt, *J. Phys. Chem.* **98**, 1121 (1994).
24. T.-S. Yeh, Y.-P. Chang, and T.-M. Su, *J. Phys. Chem.* **98**, 8921 (1994).
25. B. J. Teppen, M. Cao, R. F. Frey, and C. van Alsenoy, *J. Mol. Struct. (Theochem)* **120**, 169 (1994).
26. P. I. Nagy, W. J. Dunn III, G. Alagona, and C. Ghio, *J. Am. Chem. Soc.* **113**, 6719 (1991).
27. P. I. Nagy, W. J. Dunn III, G. Alagona, and C. Ghio, *J. Am. Chem. Soc.* **114**, 4752 (1992).
28. C. J. Cramer and D. G. Truhlar, *J. Am. Chem. Soc.* **116**, 3892 (1994).
29. G. Alagona and C. Ghio, *J. Mol. Struct. (Theochem)* **254**, 287 (1992).
30. R. W. W. Hooft, B. P. van Eijck, and J. Kroon, *J. Chem. Phys.* **97**, 3639 (1992).
31. H. Hayashi, H. Tanaka, and K. Nakanishi, *J. Chem. Soc., Faraday. Trans.* **91**, 31 (1995).
32. O. Tapia and O. Goscinski, *Mol. Phys.* **29**, 1653 (1975).
33. J. L. Rivail and D. Rinaldi, *Chem. Phys.* **18**, 233 (1976).
34. M. W. Wong, K. B. Wiberg, and M. Frisch, *J. Chem. Phys.* **95**, 8991 (1991).
35. M. W. Wong, M. J. Frisch, and K. Wiberg, *J. Am. Chem. Soc.* **113**, 4776 (1991).
36. V. Dillet, D. Rinaldi, J. G. Angyán, and J. L. Rivail, *Chem. Phys. Lett.* **202**, 18 (1993).
37. M. F. Ruiz López, F. Bohr, M. T. C. Martins-Costa, and D. Rinaldi, *Chem. Phys. Lett.* **221**, 109 (1994).
38. (a) A. D. Becke, *Phys. Rev. A* **38**, 3098 (1988); (b) A. D. Becke, *J. Chem. Phys.* **98**, 1372 (1993).
39. C. Lee, W. Yang, and R. G. Parr, *Phys. Rev. B* **37**, 785 (1988).
40. G92/DFT: M. J. Frisch, G. W. Trucks, M. Head-Gordon, P. M. Gill, M. W. Wong, J. B. Foresman, B. J. Johnson, H. B. Schlegel, M. Robb, E. S. Replogle, R. Gomperts, J. L. Andres, K. Raghavachari, J. S. Binkley, C. Gonzalez, R. L. Martin, D. J. Fox, D. J. DeFrees, J. Baker, J. J. P. Stewart and J. A. Pople, *Gaussian 92* (Gaussian Inc., Pittsburgh, PA, 1992).
41. W. L. Jorgensen, *J. Phys. Chem.* **90**, 1276 (1986).
42. J. C. Owicki, ACS Symposium Series 86, American Chemical Society, Washington, DC, 1978, p. 159.
43. M. P. Allen and D. J. Tildesley, *Computer Simulation of Liquids* (Oxford University Press, Oxford, 1988).

The π, π^* State in Formaldehyde and Thioformaldehyde

F. GREIN AND M. R. J. HACHEY

Department of Chemistry, University of New Brunswick, Bag Service #45222, Fredericton, New Brunswick, Canada E3B 6E2; e-mail (F.G.): fritz@unb.ca

Received March 26, 1996; revised manuscript received June 11, 1996; accepted June 13, 1996

ABSTRACT

For formaldehyde, the C — O stretch potential of $^1(\pi, \pi^*)$ crosses all 1A_1 Rydberg potentials, such as $n, 3p_y, n, 3d_{yz}$, etc., thereby transferring the intensity of the unassigned $^1(\pi, \pi^*) \leftarrow \tilde{X}$ system to these Rydberg states. For thioformaldehyde, the situation is similar but a shift in the potentials allows for direct observation of $^1(\pi, \pi^*)$. In its $^1(\pi, \pi^*)$ state, H_2CO is planar, having a low barrier of about 0.2 eV toward the nonplanar $^1(\sigma, \pi^*)$ state. For H_2CS , the planar conformation of $^1(\pi, \pi^*)$ is a saddle point, with $^1(\sigma, \pi^*)$ being the global minimum on the $2^1A'$ surface. The triplet π, π^* states of H_2CO and H_2CS are nonplanar, having inversion barriers of 0.1 and 0.05 eV, respectively. For both H_2CO and H_2CS , the π, π^* configuration also crosses the ground-state configuration, which explains predissociation and radiationless transitions of some Rydberg states. © 1996 John Wiley & Sons, Inc.

Introduction

In the absorption spectrum of formaldehyde, the electric dipole forbidden transition $^1A_2(n, \pi^*) \leftarrow \tilde{X}^1A_1$ is observed and well studied, whereas the allowed transition $^1(\pi, \pi^*) \leftarrow \tilde{X}^1A_1$, despite being predicted to be very intense, has so far escaped all attempts at detection. The problem of the "missing" $^1(\pi, \pi^*)$ state also plagues many other aldehyde and ketones. Consequently, Robin, a prominent reviewer in the field of higher excited states, wrote that "aldehydes and ketones are a most perplexing chromophoric group" [11].

For a long time, it was believed that $^1(\pi, \pi^*)$ had a vertical excitation energy in excess of the first ionization potential (IP) of 10.8887 eV [2] and, therefore, is not observed. For example, Langhoff et al. [3] predicted $^1(\pi, \pi^*)$ to be near 11.2 eV.

The absorption spectrum in the vacuum ultraviolet (VUV) region of formaldehyde was first studied by Price [4]. Currently, all medium and strong bands in the VUV spectrum of H_2CO are assigned to Rydberg transitions. The latest assignments by Brint et al. [5] identified $n \rightarrow s, p, d, f$ -Rydberg transitions up to 5s, 12p, 12d, and 9f, converging to the first IP. However, in many cases, the intensities or quantum defects do not conform to expectations for Rydberg transitions. For example, the

intensity of $n, 4p$ is higher than that of $n, 3p$, and the quantum defect of $n, 3d$ is 0.4, whereas it is expected to be ≤ 0.1 . Further, for $n > 4$, the np , nd , and nf transitions have similar intensities, contrary to their normal behavior [1, 5]. Although the source of the Rydberg anomalies is usually attributed to Rydberg–valence interactions, the nature of the perturbing valence state has never been positively identified.

In contrast to the missing singlet $\pi \rightarrow \pi^*$ system, the triplet $\pi \rightarrow \pi^*$ system of H_2CO has been observed by electron impact studies ([6] and references therein). It should also be noted that the absorption spectrum of thioformaldehyde, whose electronic spectrum is expected to be similar to that of formaldehyde, shows a progression of bands, lying between $n \rightarrow 4s$ and $n \rightarrow 4p$, that were assigned to $^1(\pi, \pi^*)$.

Obviously, it is of significant interest to investigate theoretically the reasons for the strange behavior of the π, π^* state. In a series of multireference (MR) configuration interaction (CI) studies performed over the last few years, potential energy curves for the C — O stretch and the out-of-plane motion were obtained for H_2CO [7–11] and H_2CS [12–15]. Using more extended basis sets and large CI expansions, the vertical excitation energy of the $^1(\pi, \pi^*)$ state of H_2CO is calculated to be 9.6 eV [8]. It is important to include the doubly excited configuration n^0, π^{*2} in the set of reference configurations. From the calculated potential energies, vibronic energy levels and oscillator strengths were evaluated [8, 13]. The results, as they concern the π, π^* state of H_2CO and H_2CS , are most interesting and, in our opinion, explain why $^1(\pi, \pi^*)$ had previously not been assigned in the absorption spectrum of H_2CO .

Methods

Ab initio MR–CI calculations were performed using the MRD–CI programs [16]. A $(10s6p/5s4p)$ basis set for C and O, $(12s9p/5s4p)$ for S, with additional polarization functions and s, p, d Rydberg functions on C and O (C and S for H_2CS) is used. The hydrogen basis is $(5s/3s)$ with a p polarization function. Details are given in [8, 10, 13, 14]. In their ground states, H_2CO and H_2CS are planar, having C_{2v} symmetry. For the out-of-plane motion, C_s symmetry was observed. The number of reference configurations varied between 40 and

60. They were selected such that all symmetry-adapted functions (SAF) with $c^2 > 0.001$ in the final wave function were part of the reference space, for the whole range of geometries covered by the calculations.

The Role of $^1(\pi, \pi^*)$ in the Absorption Spectrum of H_2CO

In Figure 1, the 1A_1 potential curves for the C — O stretch of H_2CO are shown. They are similar to the ones obtained in [8], but a lower configuration selection threshold ($4 \mu\text{Hartrees}$) was used. The other geometry parameters were held at experimental ground state (GS) values ($R_{\text{CH}} = 2.0796 a_0$ and $\phi(\text{HCH}) = 116.3^\circ$ [17]). It is seen that diabatically the $^1(\pi, \pi^*)$ state crosses all Rydberg potentials, also the higher ones not shown here. Even the apparent long-distance minimum of $^1(\pi, \pi^*)$, at $2.914 a_0$ is due to an avoided crossing of π, π^* with the GS configuration n^2 . At $3 a_0$, the 1A_1 wave function contains about 45% n^2 and 45% π, π^* , whereas 2^1A_1 has 40% n^2 and 45% π, π^* (see Fig. 2). (The percentage contribution was calculated from c_i^2 , where c_i is the coefficient of the respective SAF in the CI wave function. In the CI expansion, $^1(n, \pi^*)$ MOs were used. The given numbers change slightly, but not greatly, with the choice of MOs.) At the largest CO distance shown in Figure 2, $4 a_0$, the eventual dissociation to $\text{CH}_2 + \text{O}$ is not yet important. Open-shell configurations to describe the dissociation become dominant at larger distances than shown. The repulsive crossing of $^1(\pi, \pi^*)$ with all 1A_1 Rydberg states and the ground state leads to predissociation and radiationless transitions. According to Figure 1, the doubly excited $^1(n^0, \pi^{*2})$ state appears at about 10.2 eV, having a fairly shallow potential, and crossing π, π^* at small R and higher Rydberg states at larger R .

Figure 3 shows an enlarged version of the C — O stretch curves for 2^1A_1 to 4^1A_1 , including vibrational energy levels for each of the minima. It should be noted that all minima, except for $n, 3p_y$ and $n, 3d_{yz}$, are caused by avoided crossings with π, π^* . These potential wells are bounded by π, π^* on the left, and by a Rydberg configuration on the right. A notation such as $\pi, \pi^*/n, 3p_y$, used here to describe such potentials, should be obvious.

Assuming that all 1A_1 states are planar, and that the C — O stretch vibrations can be approximated

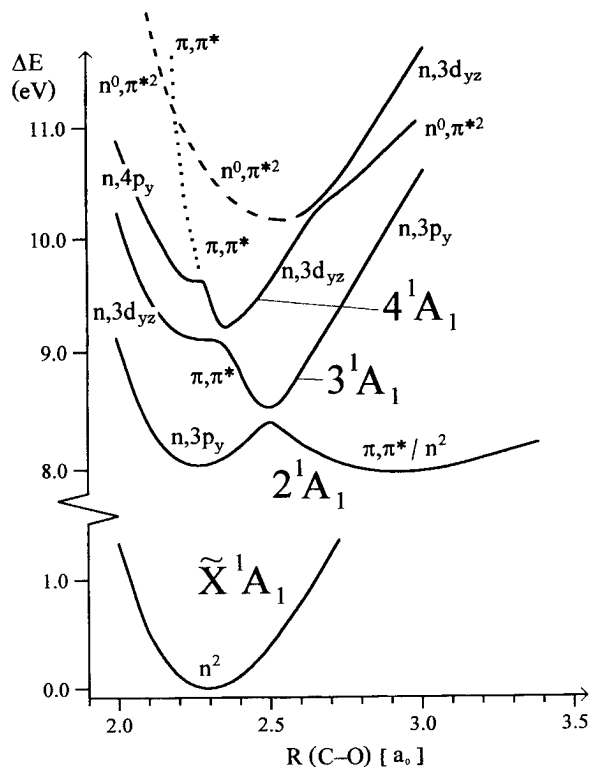


FIGURE 1. C — O stretch potentials for $1A_1$ states of H_2CO .

by the one-dimensional potentials given in Figure 3, the vibronic oscillator strengths were evaluated for each vibrational level, by first calculating the electric dipole transition moment as a function of R_{CO} and then combining it with the Franck-Condon (FC) factor.

In Table I, experimental values for energies and oscillator strengths are compared with calculated vertical values and with vibronic values evaluated for each vibrational level, as described above. For the 0-0 bands of the $n \rightarrow 3s$ and $n \rightarrow 3p$ transitions, the vertical numbers agree reasonably well with the experimental values. However, for the 0-0 bands of $n \rightarrow 3d_{yz}$ (8.88 eV), $n, 4s$ (9.26 eV), and higher states, the calculated vertical oscillator strengths are too small. Also, the 0-1 and 0-2 bands of Rydberg states have very low Franck-Condon factors, and the observed bands at 8.32, 9.04, and 9.18 eV could not be explained on the basis of vertical oscillator strengths.

In the last three columns of Table I, the calculated vibronic values are given. It is seen that vibronic energies can be matched with the energies of the observed bands to a maximum deviation of 0.24 eV, but mostly lying within 0.05 eV. Larger deviations may be indicative of the need for a non-Born-Oppenheimer treatment.

Except for the three lowest bands, the literature assignments, as given in Table I, had to be changed

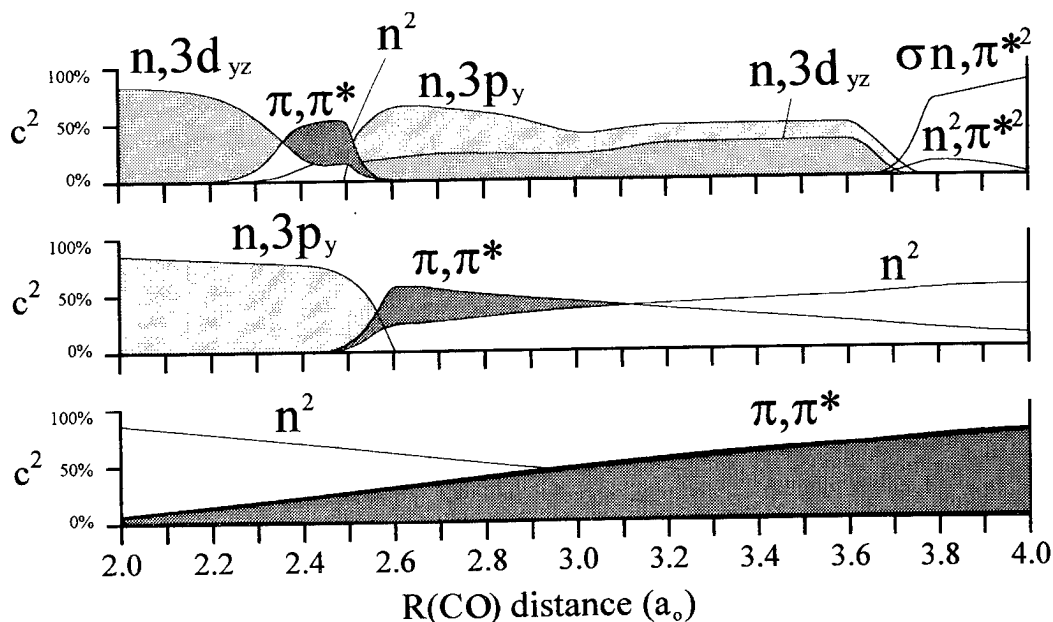


FIGURE 2. Contribution of various configurations to the wave functions 1^1A_1 to 3^1A_1 of H_2CO using $1(n, \pi^*)$ molecular orbitals.

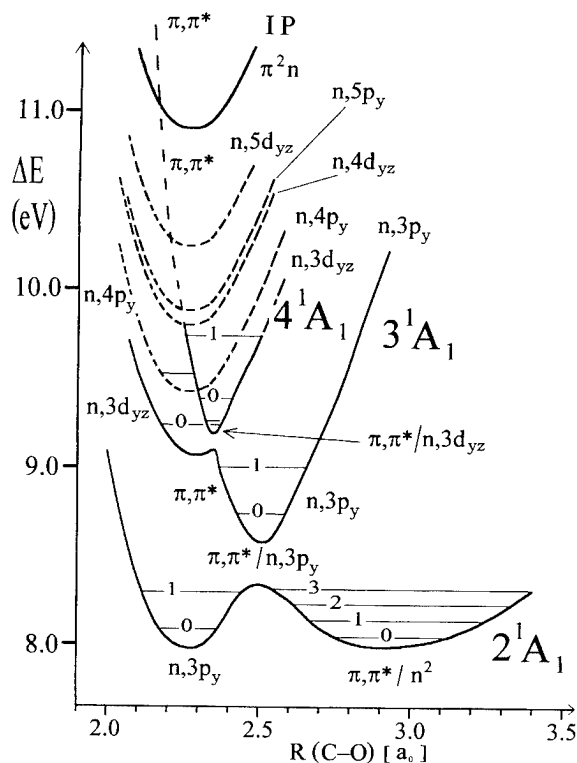


FIGURE 3. C—O stretch potentials for 2^1A_1 to 4^1A_1 states of H_2CO , showing vibrational energy as used in the calculations. Higher Rydberg potentials were estimated, and are shown as dashed lines.

to accommodate the new states that involve mixed $\pi, \pi^*/\text{Rydberg}$ potentials. For example, the peak observed at 9.04 eV was originally assigned to the 3_0^1 band of $n, 3d_{yz}$, where ν_3 is the symmetric CH_2 bending vibration. By itself, $n, 3d_{yz}$ has low intensity. This band is now associated with 2_0^1 of $\pi, \pi^*/n, 3p_y$, where ν_2 is the C—O stretch vibration. It clearly derives its intensity ($f_{\text{calc}} = 0.024$, $f_{\text{obs}} = 0.022$) from the π, π^* section of the potential.

Most of the calculated oscillator strengths are in surprisingly good agreement with the observed values. Exceptions are the 0_0^0 band of $n, 3s$, for which vibronic interaction with $\sigma, \pi^*/\pi, \pi^*$ may play a role, as outlined in [7]. The small calculated f -value for the 8.32 eV band may be due to the fact that both the $v = 3$ level of $\pi, \pi^*/n^2$ and the $v = 1$ level of $n, 3p_y$ lie close to the barrier in the 2^1A_1 potential, which was not taken into account in the calculations. The third exception is the peak at 9.26 eV, for which f_{calc} is too large. It is presumed that the rapidly increasing density of states in this high-energy region may allow for other possible interpretations of the observed bands.

Overall, the results of Table I show that the π, π^* state is the major intensity provider for transitions to Rydberg states higher than $n, 3p$. Since intensities of Rydberg transitions normally decrease with increasing quantum number (as n^{-3} [3]), the contribution of π, π^* to Rydberg transitions beyond the ones covered here, such as $n, 4d$ and $n, 5s$, etc., should be even more significant,

TABLE I

Comparison of observed values for energies ΔE (in eV) and oscillator strengths f with calculated vertical and adiabatic values for bands of H_2CO lying above 7 eV.^a

Experimental			Vertical		Vibronic		
ΔE	f	Assignment ^b	ΔE_{vert}	f_{vert}	ΔE	f_0^{v}	Assignment ^c
7.09	0.033	$0_0^0 n, 3s$	7.15	0.005	7.09	0.005	$0_0^0 n, 3s$
7.97	0.018	$0_0^0 n, 3p_z$	8.05	0.021	7.94	0.021	$0_0^0 n, 3p_z$
8.12	0.035	$0_0^0 n, 3p_y$	8.10	0.039	7.98	0.035	$0_0^0 n, 3p_y$
8.32	0.005	$2_0^1 n, 3p_y$	—	—	8.18	5×10^{-5}	$2_0^3 \pi, \pi^*/n^2 + 2_0^1 n, 3p_y$
8.88	0.014	$0_0^0 n, 3d_{yz}$	9.25	0.005	8.64	0.012	$0_0^0 \pi, \pi^*/n, 3p_y$
9.04	0.022	$3_0^1 n, 3d_{yz}$	—	—	8.90	0.024	$2_0^1 \pi, \pi^*/n, 3p_y$
9.18	~ 0.008	$3_0^2 n, 3d_{yz}$	—	—	9.16	0.013	$2_0^2 \pi/\pi^*/n, 3p_y + 0_0^0 n, 3d_{yz}$
9.26	~ 0.001	$0_0^0 n, 4s$	9.19	6×10^{-5}	9.27	0.049	$0_0^0 \pi, \pi^*/n, 3d_{yz}$
9.63	0.033	$0_0^0 n, 4p_y$	9.41	9×10^{-5}	9.63	0.027	$2_0^1 \pi, \pi^*/n, 3d_{yz}$
		$0_0^0 n, 4p_z$	9.47	9×10^{-4}			

^aData taken from [8, 11] and experimental references therein, except for vertical oscillator strengths.

^bLiterature assignment where ν_2 is CO stretch and ν_3 is CH_2 symmetric bend.

^cNew assignments based in part on $\pi, \pi^*/\text{Rydberg}$ potentials.

explaining the relatively high intensity observed for higher Rydberg states.

For other vibrational modes, the changes in geometry between the GS and excited Rydberg states are usually small (as tested in full geometry optimizations [10]), and, therefore, the 0-0 transition is expected to contain most of their intensity. Complications due to π, π^* , as encountered for the C—O stretch, are not likely.

Other symmetry species, such as 1B_1 ($n, 3d_{xy}; \dots$) and 1B_2 ($n, 3s; n, 3p_z; n, 3d_{x^2-y^2}; n, 3d_{z^2}; \dots$) are not affected by direct coupling with π, π^* . Therefore, C—O stretch bands of higher Rydberg states not belonging to the A_1 symmetry species cannot receive intensity from π, π^* directly and should therefore have much lower oscillator strengths than those of the 1A_1 transitions.

This is borne out by the vertical oscillator strengths given in Table I for $n, 4s$ and $n, 4p$ ($\sim 10^{-4}$). The calculated (vertical) oscillator strengths for $n, 3d_{x^2-y^2}$, $n, 3d_{z^2}$, and $n, 3d_{xy}$ are 0.001, 0.005, and 3×10^{-5} , respectively. Using T_e values of 9.12, 9.06, and 9.30 eV [8], respectively, these 3d-Rydberg transitions may be hidden in the more intense bands observed at 9.04, 9.18, and 9.26 eV.

The Geometry of the $^1(\pi, \pi^*)$ State of H_2CO

In Figure 4, the out-of-plane potentials are shown for the $2^1A'$ and $3^1A'$ states of H_2CO at $R_{CO} = 2.914 a_0$, corresponding to the $\pi, \pi^*/n^2$ minimum of 2^1A_1 (Fig. 1). R_{CH} and $\phi(HCH)$ were kept at the GS values. It is seen that $\pi, \pi^*/n^2$, at that distance about an equal mix of π, π^* and n^2 , is planar, although there is only a small barrier of about 0.2 eV toward the nonplanar σ, π^* . In all out-of-plane conformations, π, π^* mixes with σ, π^* , and for $\theta = 42.1^\circ$ and $R_{CO} = 2.89 a_0$ (the minimum of σ, π^*), the $2^1A'$ wave function is 44% σ, π^* , 32% π, π^* , and 11% n^2 .

Contour plots of $2^1A'$ are shown in Figure 5, and 3-dimensional plots, in Figure 6. The local π, π^* minimum is confined to a small range of coordinates, whereas $n, 3p_y$ is more extended; in comparison, the global σ, π^* minimum covers a wide range of geometries. Optimized geometries and adiabatic excitation energies for $^1(\pi, \pi^*)$, $^1(\sigma, \pi^*)$, and $^1(n, 3p_y)$, all lying on the $2^1A'$ surface, are

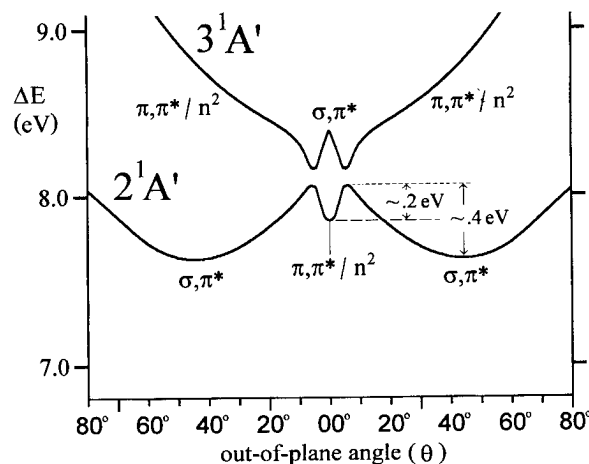


FIGURE 4. Out-of-plane potentials for $2^1A'$ and $3^1A'$ of H_2CO , at $R_{CO} = 2.914 a_0$.

given in Table II. The σ, π^* minimum lies about 0.35 eV below the π, π^* minimum.

The low barrier of π, π^* toward σ, π^* implies that the higher vibrational levels of the $\pi, \pi^*/n^2$ minimum in Figure 3 are not bound by $\pi, \pi^*/n^2$ but only by σ, π^* . Therefore, for such higher levels, the C—O mode may mix with the out-of-plane mode.

The $^1(\pi, \pi^*)$ State of H_2CS

In Figure 7, the C—S stretch potentials of the 1A_1 states of H_2CS are given. The R_{CH} distance and $\phi(HCH)$ angles were kept at the experimental values of $2.0645 a_0$ and 116.87° [18]. As in the case of H_2CO , π, π^* crosses all Rydberg states. However, there is an important difference. The crossing of the lowest A_1 Rydberg state $n, 4p_y$ occurs near its minimum rather than at larger R , as was the case in H_2CO . Therefore, the potential well for $n, 4p_y$ has effectively disappeared. The left-side turning points for the vibrational levels of the π, π^* potential move closer to the GS equilibrium distance, making the Franck-Condon factors for the electronic transition to π, π^* more favorable.

As for H_2CO , the 2^1A_1 wave function has an increasing contribution from n^2 as R_{CS} increases. At $3.85 a_0$, 2^1A_1 is 37% π, π^* and 42% n^2 , whereas 1^1A_1 is 52% π, π^* and 36% n^2 . The participation of the major configurations in the wave function is very similar to the case of H_2CO which was shown in Figure 2. Figure 7 also indicates that the doubly excited state n^0, π^{*2} has dropped below $n, 3p_z$,

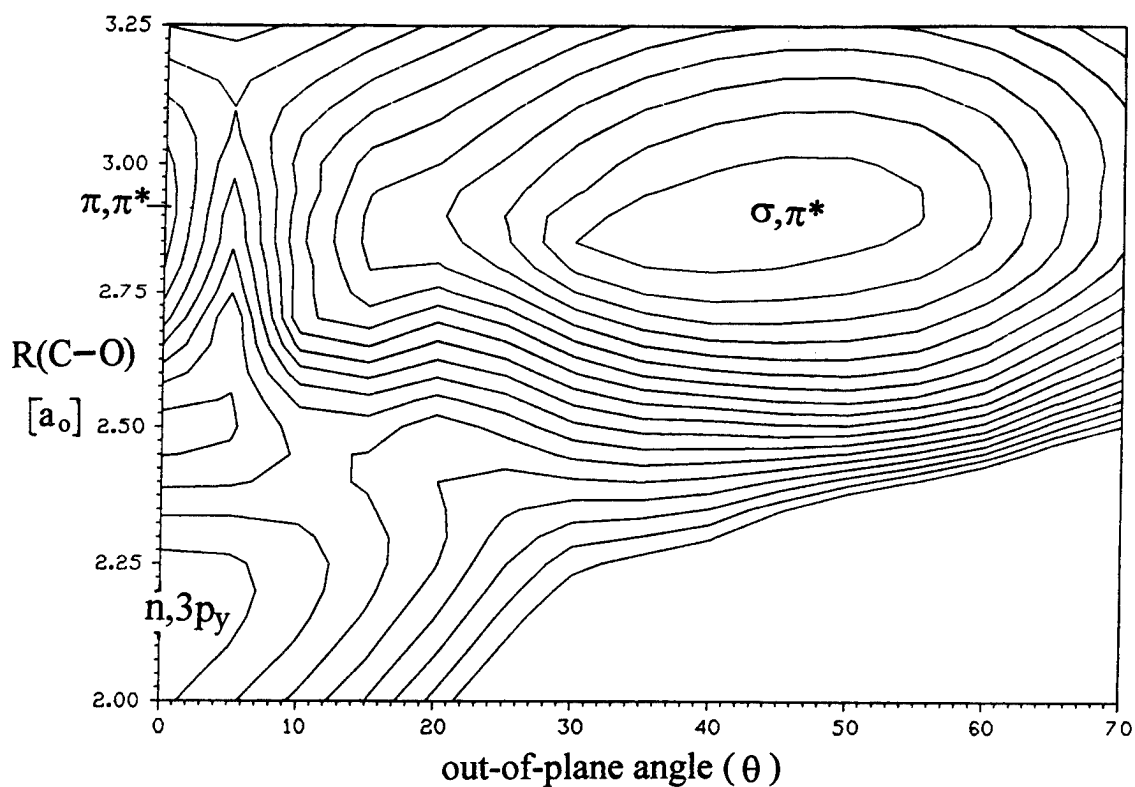


FIGURE 5. Contour plots for the $2^1A'$ state of H_2CO . R_{CO} distance in a_0 and angle θ in degrees. The outermost contour is 8.5 eV, and the innermost is 7.65 eV.

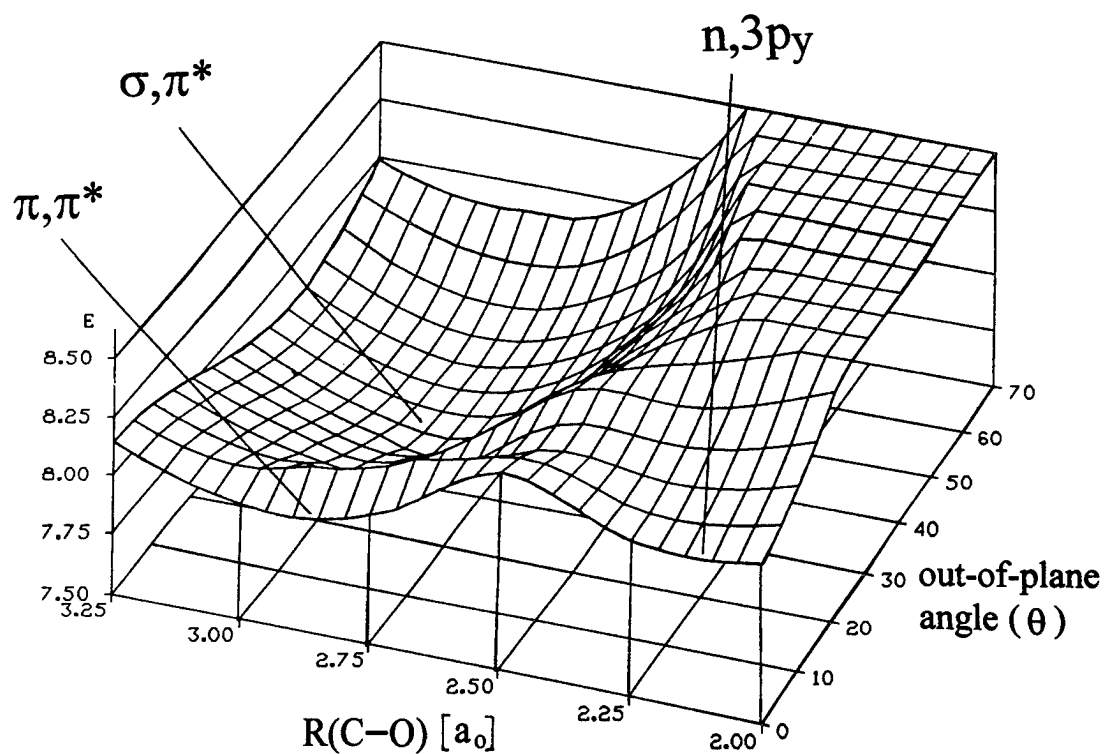


FIGURE 6. Three-dimensional plot of $2^1A'$ potential surface of H_2CO . Energies in eV relative to the ground state, R_{CO} distance in a_0 and angle θ in degrees.

TABLE II
Calculated and observed bands for H_2CO and optimized geometries for selected states of H_2CO .^a

ΔE calcd. (exptl.)	ΔE_{vert}	$f_0^{\nu'}$ calcd. (exptl.)	f_{vert}	Assignment ^a
7.09 (7.09)	7.15 {7.30}	0.005 (0.033)	0.005 {0.006}	$0_0^0 n, 3s$
7.94 (7.97)	8.05 {8.09}	0.021 (0.018)	0.021 {0.023}	$0_0^0 n, 3p_z$
7.98 (8.12)	8.10 {8.12}	0.035 (0.035)	0.039 {0.041}	$0_0^0 n, 3p_y$
8.15 (8.37)	8.32 {8.32}	— (—)	—	$0_0^0 n, 3p_x$
8.18 (8.32)	— {7.30}	5×10^{-5} (5×10^{-3})	—	$2_0^1 n, 3p_y \rightarrow$ $2_0^3 \pi, \pi^* / n^2 + 2_0^1 n, 3p_y$
8.64 (8.88)		0.012 (0.014)		$0_0^0 n, 3d_{yz} \rightarrow$ $0_0^0 \pi, \pi^* / n, 3p_y$
8.90 (9.04)	—	0.024 (0.022)	—	$3_0^1 n, 3d_{yz} \rightarrow$ $2_0^1 \pi, \pi^* / n, 3p_y$
9.16 (9.18)		0.013 (~ 0.008)		$3_0^2 n, 3d_{yz} \rightarrow$ $2_0^2 \pi, \pi^* / n, 3p_y + 0_0^0 n, 3d_{yz}$
9.18	9.25 {9.24}		5×10^{-3} { 3×10^{-3} }	— $n, 3d_{yz}$
9.10	9.80 {9.13}		1×10^{-3} { 6×10^{-3} }	— $n, 3d_{x^2-y^2}$
9.06	9.37 {9.31}		5×10^{-3} { 1×10^{-3} }	— $n, 3d_{z^2}$
9.17	9.40 {9.31}		—	— $n, 3d_{xz}$
9.30	9.34 {9.23}		3×10^{-5} { 3×10^{-4} }	— $n, 3d_{xy}$
9.19		9×10^{-5}		— $n, 4s$
9.27 (9.26)		0.049 (~ 10^{-3})		$0_0^0 n, 4s \rightarrow$ $0_0^0 \pi, \pi^* / n, 3d_{yz}$
9.41		9×10^{-5}		— $n, 4p_y$
9.47		5×10^{-4}		— $n, 4p_z$
9.63 (9.63)		0.027 (0.033)		$0_0^0 n, 4p \rightarrow$ $2_0^1 \pi, \pi^* / n, 3d_{yz}$

Optimized geometries and T_e for selected states of H_2CO ^b

State	Configuration	$R_e(\text{CO})$ (a_0)	$\theta(\text{OOP})$ (degrees)	$\phi(\text{HCH})$ (degrees)	$R_e(\text{CH})$ (a_0)	T_e (eV)
2^1A_1	π, π^*	2.914	0.0	120.8	2.113	7.95
$2^1A'$	σ, π^*	2.890	42.1	115.1	2.040	7.59
2^1A_1	$n, 3p_y$	2.266	0.0	123.3	—	7.89
$1^3A'$	π, π^*	2.789	38.1	119.9	2.032	4.43
$2^3A'$	σ, π^*	2.750	35.5	133.5	2.060	7.15
2^3A_1	$n, 3p_y$	2.256	0.0	—	—	~ 7.89

^a ν_2 is CO stretch and ν_3 is CH_2 symmetric bend.^bOptimized geometries obtained from [10] for the singlets and [9] for the triplets.

interfering with the π, π^* and $n, 3d_{yz}$ potentials at smaller R and with $n, 4p_y$ at larger R .

In Figure 8, the out-of-plane potential is shown for the $2^1A'$ state of H_2CS , at both $R_{\text{CS}} = 3.436 a_0$ and $R_{\text{CS}} = 3.850 a_0$. The latter distance corresponds to the C_{2v} minimum of π, π^* . At $3.436 a_0$, π, π^* has a minimum with a low barrier toward σ, π^* . However, at the π, π^* equilibrium distance of $3.850 a_0$, $2^1A'$ has a slight maximum at $\theta = 0^\circ$. While π, π^* may still be called planar (the

adiabatic π, π^* potential is indicated by the dashed curve), the planar minimum is a *saddle* point in the 3-dimensional potential surface including the out-of-plane angle, rather than a local minimum.

In Table III, the optimized geometries of the $^1(\pi, \pi^*)$, $^1(\sigma, \pi^*)$, and $^1(n, 4p_y)$ states, all lying on the $2^1A'$ surface, are given, together with T_e values. It should be noted that the minimum of σ, π^* lies only 0.07 eV below that of π, π^* . Therefore, π, π^* (and σ, π^*) have a shallow potential both

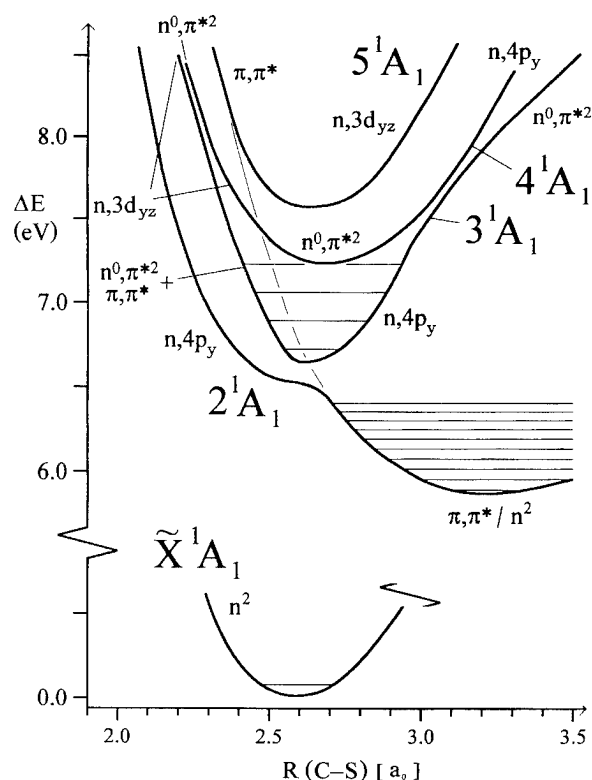


FIGURE 7. C — S stretch potentials for 1A_1 states of H_2CS .

for the C — S stretch and the out-of-plane angle, constituting a shallow potential over two dimensions rather than just one. The implications for spectroscopy should be rather interesting.

As mentioned in the Introduction, the π, π^* spectrum of H_2CS is known, and the observed bands have been interpreted as belonging to the C — S stretch mode ν_3 . For an out-of-plane angle of 36.2° , corresponding to the optimized value of $2^1A'$, the C — S potential is virtually parallel to the C — S potential for planar H_2CS (see dashed curve in Fig. 9). Therefore, the C — S stretch vibrational energies and vibronic oscillator strengths calculated in [13] for the supposedly planar π, π^* state, and reproduced in Table IV, retain some validity, although all energies should be corrected by the out-of-plane stabilization energy.

If the calculated energies are matched with nearest experimental values, as done in Table IV, then the problem arises that calculated oscillator strengths for the low-lying bands are too small to explain their observation. Therefore, a shift of the calculated energies toward the reported band origin at 5.54 eV is necessary. Also, a case has been

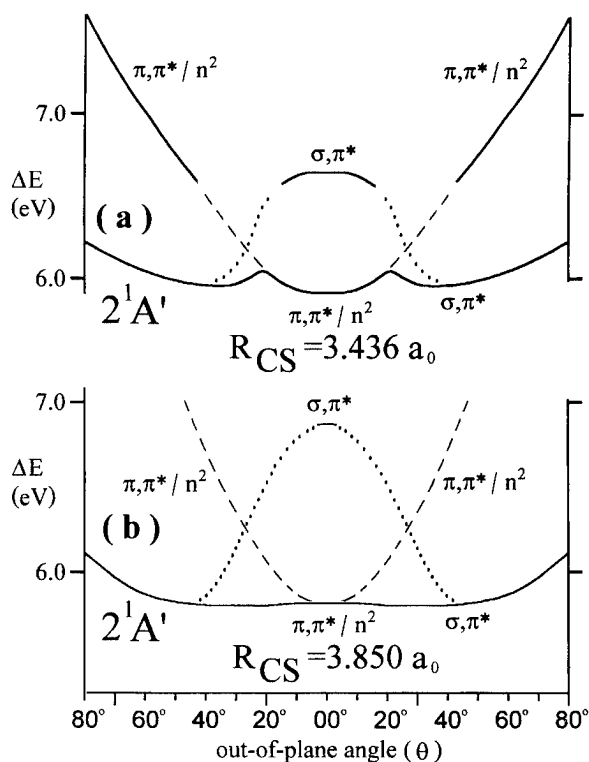


FIGURE 8. Out-of-plane potentials for $2^1A'$ state of H_2CS , at $R_{CS} = 3.436 a_0$ and at $3.850 a_0$.

made in [13] that hot bands, starting from $v'' = 1$ of the GS, might play a role. Since our calculated vibrational frequency of 473 cm^{-1} lies near the experimental value of 476 cm^{-1} , it should be possible, by proper choice of the origin and inclusion of hot bands, to match the experimentally observed spectrum quite closely.

TABLE III
Optimized geometries and T_e for selected states of H_2CS .^{a, b}

State	Configuration	$R_e(\text{CO})$ (a_0)	$\theta(\text{OOP})$ (degrees)	$\phi(\text{HCH})$ (degrees)	T_e (eV)
2^1A_1	π, π^*	3.850	0.0	118.5	5.85
$2^1A'$	σ, π^*	3.672	36.2	112.5	5.78
2^1A_1	$n, 4p_y$	3.155	0.0	~ 122	6.63
$1^3A'$	π, π^*	3.483	28	119.8	2.70
$2^3A'$	σ, π^*	3.553	56	131.5	5.52
2^3A_1	$n, 4p_y$	3.024	0.0	120.9	6.49

^aOptimized geometries obtained from [14] for the singlets and [15] for the triplets.

^b $R_{(\text{CH})}$ bond length was held constant at the GS equilibrium distance of $2.076 a_0$.

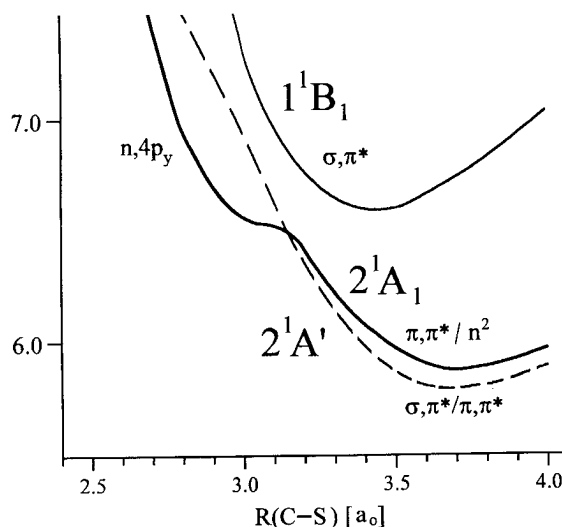


FIGURE 9. C — S stretch potentials of H_2CS showing that the potential of $\sigma, \pi^*/\pi, \pi^*$ at $\theta = 36.2^\circ$ (dashed curve) is nearly parallel to the $\pi, \pi^*/n^2$ potential at $\theta = 0.0^\circ$.

In the same article [13], calculated vibrational energies and oscillator strengths are given both for the $\pi, \pi^*/n, 4p_y$ adiabatic potential, similar to the $\pi, \pi^*/\text{Rydberg}$ states discussed earlier for H_2CO , and for the *diabatic* $n, 4p_y$ potential. In both cases, the calculated energy for the 0-0 band (6.65 eV adiabatic, 6.56 eV diabatic) agrees well with the observed origin of the $n \rightarrow 4p_y$ system at 6.60 eV [20]. However, in the adiabatic case, two addi-

TABLE IV
Vibronic transition energies $\Delta E_0^{v'}$ (in eV) and oscillator lengths $f_0^{v'}$ for the $2^1A_1 (\pi, \pi^*) \leftarrow \tilde{X}$ system in H_2CS .

v'	$\Delta E_0^{v'}$ calcd. ^a	$\Delta E_0^{v'}$ exptl. ^b	$f_0^{v'}$ calcd. ^a
0	5.821	—	4×10^{-7}
1	5.879	5.876	4×10^{-6}
2	5.949	5.927	2×10^{-5}
3	6.006	5.981	7×10^{-5}
4	6.065	6.036	2×10^{-4}
5	6.122	6.111	5×10^{-4}
6	6.177	6.138	9×10^{-4}
7	6.231	6.193	0.001
8	6.282	6.243	0.002
9	6.331	6.297	0.003

^aValues from [13], assuming planar geometry.

^bEstimated energies of band maxima from the spectrum of Moule et al. [19].

tional strong bands, at 6.82 (3_0^1) and 6.99 eV (3_0^2), are predicted, whereas in the diabatic case, higher bands have very low oscillator strengths. Unfortunately, the spectrum above 6.6 eV is poorly resolved, and, therefore, it cannot yet be determined which potential, diabatic or adiabatic, approaches reality more closely. Our experience with H_2CO would give a preference to the adiabatic results.

For H_2CS , spectra resulting from higher $\pi, \pi^*/\text{Rydberg}$ potentials have not been investigated. A complication arises here due to the doubly excited n^0, π^{*2} state, whose C — S potential lies, as was mentioned earlier, between the two lowest 1A_1 Rydberg states and crosses them as well as π, π^* .

The Triplet π, π^* States of H_2CO and H_2CS

In Figure 10, the 3A_1 potential curves for the C — O stretch of H_2CO are shown. It is seen that the $^3(\pi, \pi^*)$ potential lies well below the Rydberg

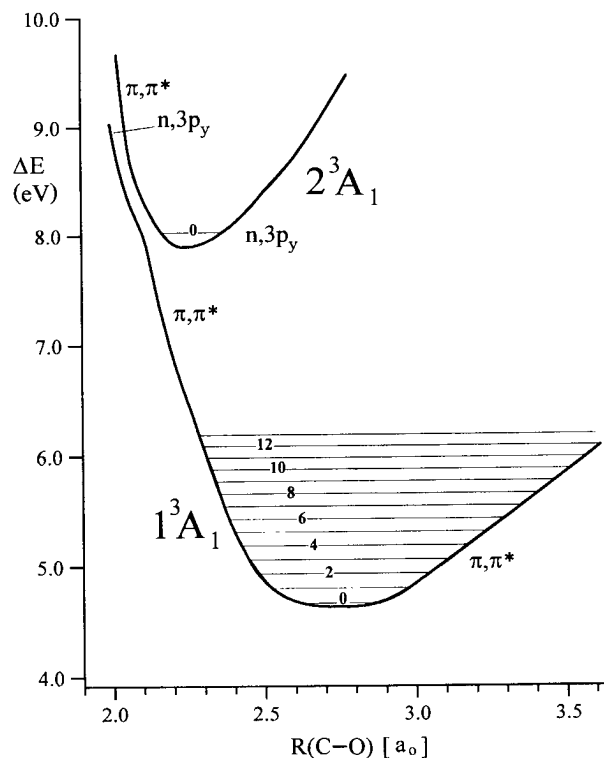


FIGURE 10. C — O stretch potentials of H_2CS for 3A_1 states of H_2CO , showing the location of π, π^* relative to $n, 3p_y$.

states, and the triplet $\pi \rightarrow \pi^*$ system should therefore be free of the Rydberg mixing which plagues its singlet counterpart. An electron-impact study by Taylor et al. [6] provided vibronic energies and intensities with which our calculated energies and Franck-Condon factors (based on the potential from Fig. 10) agree closely.

Contrary to the singlet π, π^* state, $^3(\pi, \pi^*)$ is nonplanar, as shown in the out-of-plane potentials in Figure 11. The calculated inversion barrier is 0.1 eV. The reason for the singlet being planar, and the triplet nonplanar, arises from the mixing of π, π^* with the closed-shell configuration n^2 in the singlet case, which is not possible for the triplet. Obviously, n^2 prefers planarity, whereas π, π^* , in conformity with the Mulliken-Walsh rules, prefers a nonplanar conformation. The optimized geometries and T_e 's of $^3(\pi, \pi^*)$, $^3(\sigma, \pi^*)$, and $^3(n, 3p_y)$ are included in Table II. In contrast to the singlet case, σ, π^* lies well above π, π^* , and, therefore, mixing between these configurations is negligible.

The situation for the triplet π, π^* of H_2CS is similar to that of H_2CO . In the planar case, $1^3A_1(\pi, \pi^*)$ lies much lower than the Rydberg states, and $^3(\pi, \pi^*)$ is nonplanar with $\theta = 28^\circ$, having an inversion barrier of 0.05 eV [14]. Its optimized geometry and T_e , as well as values for $^3(\sigma, \pi^*)$ and $^3(n, 4p_y)$, are given in Table III.

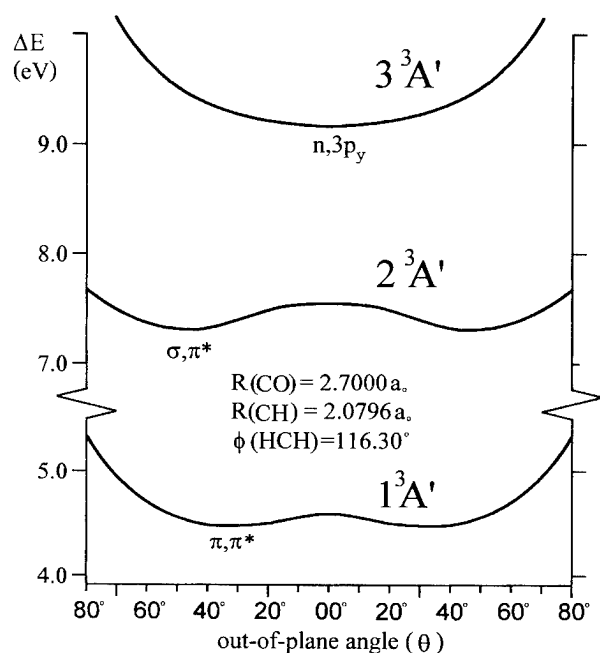


FIGURE 11. Out-of-plane potentials for $^3A'$ states of H_2CO , at $R_{\text{CO}} = 2.70 \text{ a}_0$.

Summary and Conclusion

In the absorption spectrum of formaldehyde, the $^1(\pi, \pi^*) \leftarrow \tilde{X}$ system is not seen directly, since the C — O stretch potential of π, π^* is repulsive and crosses all 1A_1 Rydberg potentials (as well as the ground-state potential). As a consequence, a series of avoided crossing minima are found which are bound on the left (smaller R_{CO}) by a section of the π, π^* potential, and on the right, by a Rydberg potential. Due to the fact that π, π^* and n , Rydberg states differ by a double excitation, their interaction is weak, as seen in the small energy difference between the states at the point of the avoided crossing, and usually the configuration change is very abrupt.

Due to such mixed $\pi, \pi^*/$ Rydberg potentials, the high intensity of the π, π^* transition is transferred to Rydberg states within the same symmetry species, making them appear much more intense than they ought to be, and also shifting their positions in unexpected ways, resulting in unusual quantum defects. Using the C — O stretch mode, all strong and medium peaks of the absorption spectrum of H_2CO above 8 eV could, at least in principle, be explained in this way. Many details still need to be sorted out, such as non-Born-Oppenheimer interactions, which should be particularly important near the avoided crossings. The further crossing of π, π^* into the GS may explain the observed predissociation of Rydberg bands.

For thioformaldehyde, as for H_2CO , the $^1(\pi, \pi^*)$ potential crosses all Rydberg potentials as well as the ground-state potential. Since the lowest 1A_1 Rydberg state is crossed near its minimum the π, π^* system has higher Franck-Condon factors than in the case of H_2CO and becomes directly observable.

Complications are introduced by the out-of-plane motion. While $^1(\pi, \pi^*)$ of H_2CO has a local minimum for the planar conformation, there is only a low barrier of about 0.2 eV toward the nonplanar global $^1(\sigma, \pi^*)$ minimum, lying 0.35 eV below $^1(\pi, \pi^*)$. For H_2CS , the $^1(\pi, \pi^*)$ minimum that is seen in the R_{CS} potential curves for planar geometry becomes a saddle point when the out-of-plane motion is also taken into account. However, the $^1(\sigma, \pi^*)$ minimum lies only about 0.1 eV below the π, π^* minimum. Therefore, the observed " π, π^* bands" of H_2CS should better be called σ, π^* bands, according to the predominant

configuration of the global minimum. Due to the small energy difference between π, π^* and σ, π^* , and the fact that the C — S potential at the out-of-plane angle $\theta = 36.2^\circ$, corresponding to the optimized value for σ, π^* , is nearly parallel to that at $\theta = 0^\circ$, the distinction between $^1(\sigma, \pi^*)$ and $^1(\pi, \pi^*)$ for the C — S stretch is perhaps not so important. The very shallow potential of $2^1A'$ over two internal coordinates is expected to introduce some interesting features into the spectrum.

For the triplet π, π^* states of both H_2CO and H_2CS , the R_{CO} (R_{CS}) potential curves lie well below the 3A_1 Rydberg potentials. Therefore, the $^3(\pi, \pi^*)$ spectra should be observable and have, indeed, been seen for H_2CO . For both molecules, $^3(\pi, \pi^*)$ is nonplanar, with energy lowerings from the planar to the nonplanar conformation of 0.17 eV for H_2CO , and 0.07 eV for H_2CS . Again, one deals here with fairly shallow potentials.

For alkylated carbonyl compounds, such as acetaldehyde and acetone, as well as for many larger systems, the $^1(\pi, \pi^*)$ transition has also not been assigned, although, as in H_2CO , it may have been observed indirectly. Recent calculations on acetone [21] give R_{CO} potential curves very similar to those of H_2CO . On the other hand, substitutions of hydrogens by halogens raise the energy of Rydberg states relative to π, π^* , due to the stabilization of the n_0 orbital interacting with halogen lone pairs. According to calculations performed in this laboratory [22], the $^1(\pi, \pi^*)$ potentials of F_2CO , Cl_2CO , and Cl_2CS lie well below the Rydberg potentials.

In summary, the fact that the $^1(\pi, \pi^*)$ state has not been observed directly in the spectrum of formaldehyde and alkylated carbonyl compounds can be explained by the accidental and somewhat unfortunate positioning of the $^1(\pi, \pi^*)$ R_{CO} -potential relative to the 1A_1 Rydberg potentials. As a consequence, $^1(\pi, \pi^*)$ transfers its intensity to the Rydberg states, providing them with unusually high oscillator strengths and also changing the vibrational energy levels.

ACKNOWLEDGMENTS

This work was supported by the Natural Sciences and Engineering Research Council (NSERC)

of Canada. We are grateful to Dr. P. Bruna for his contributions to the understanding of H_2CO and H_2CS and for many helpful discussions.

References

1. M. B. Robin, *Higher Excited States of Polyatomic Molecules* (Academic Press, New York, 1974), Vol. 2.
2. B. Niu, D. A. Shirley, Y. Bai, and E. Daymo, *Chem. Phys. Lett.* **201**, 212 (1993).
3. S. R. Langhoff, S. T. Elbert, C. F. Jackels, and E. R. Davidson, *Chem. Phys. Lett.* **29**, 247 (1974).
4. W. C. Price, *J. Chem. Phys.* **3**, 256 (1935).
5. P. Brint, J. P. Connerade, C. Mayhew, and K. Sommer, *J. Chem. Soc., Faraday Trans. 2* **81**, 1643 (1985).
6. S. Taylor, D. G. Wilden, and J. Comer, *J. Chem. Phys.* **70**, 291 (1982).
7. M. R. J. Hachey, P. J. Bruna, and F. Grein, *J. Chem. Soc., Faraday Trans.* **90**, 683 (1994).
8. M. R. J. Hachey, P. J. Bruna, and F. Grein, *J. Phys. Chem.* **99**, 8050 (1995).
9. P. J. Bruna, M. R. J. Hachey, and F. Grein, *J. Phys. Chem.* **99**, 16576 (1995).
10. M. R. J. Hachey, P. J. Bruna, and F. Grein, *J. Mol. Spectrosc.* **176**, 375 (1996).
11. M. R. J. Hachey and F. Grein, *Chem. Phys. Lett.* **256**, 179 (1996).
12. M. R. J. Hachey, F. Grein, and R. P. Steer, *Chem. Phys. Lett.* **183**, 204 (1991).
13. M. R. J. Hachey and F. Grein, *Can. J. Phys.* **73**, 18 (1995).
14. M. R. J. Hachey and F. Grein, *J. Mol. Spectrosc.* **172**, 384 (1995).
15. M. R. J. Hachey and F. Grein, *Chem. Phys.* **197**, 61 (1995).
16. R. J. Buenker, S. D. Peyerimhoff, and W. Butscher, *Mol. Phys.* **35**, 771 (1978); R. J. Buenker, *Int. J. Quantum Chem.* **29**, 435 (1986); D. B. Knowles, J. R. Álvarez, G. Hirsch, and R. J. Buenker, *J. Chem. Phys.* **92**, 585 (1990), and references therein.
17. J. L. Duncan, *Mol. Phys.* **28**, 1177 (1974).
18. D. R. Johnson, F. X. Powell, and W. H. Kirchhoff, *J. Mol. Spectrosc.* **39**, 136 (1971).
19. C. R. Drury, J. Y. K. Lai, and D. C. Moule, *Chem. Phys. Lett.* **87**, 520 (1982).
20. C. R. Drury and D. C. Moule, *J. Mol. Spectrosc.* **92**, 469 (1982).
21. M. Merchán, B. O. Roos, R. McDiarmid, and X. Xing, *J. Chem. Phys.* **104**, 1791 (1996).
22. M. R. J. Hachey and F. Grein, to be submitted.

SCMEH-MO Calculations on Lanthanide Systems. III. $\text{Ln}(\text{CO})_6$, $\text{Ln}(\text{OC})_6$ ($\text{Ln} = \text{Nd}, \text{Sm}$)

EDWARD A. BOUDREAUX

Department of Chemistry, University of New Orleans, New Orleans, Louisiana 70148

Received March 27, 1996; accepted July 29, 1996

ABSTRACT

The SCMEH-MO method with average relativistic and spin-orbit effects has recently been applied to study the electronic structure and bonding in samarium pentamethylcyclopentadienyls. In this report the same approach has been utilized in studying the electronic structures of Nd and Sm hexacarbonyls. In contrast to the stable transition metal *d*-block carbonyls, these lanthanide carbonyls are found to be quite unstable. These findings are based on calculated electronic structures and bond energies. © 1996 John Wiley & Sons, Inc.

Introduction

Over two decades ago the preparation of several lanthanide carbonyls were reported in Ar matrices at 10 K [1, 2]. The infrared (IR) spectra implied the presence of several $\text{Nd}(\text{CO})_x$ species, with $\text{Nd}(\text{CO})_6$ as the primary product. A couple of years prior to this the preparation of $\text{U}(\text{CO})_6$ was reported under similar conditions [3].

While the ground-state electron configuration of Nd is $4f^4 6s^2$, that of U is $5f^3 6d^1 7s^2$. Both have six valence electrons to afford an effective atomic number, EAN = 18, counting two electrons from each of the six CO ligands. Traditionally the EAN rule for *d*-block transition metals is well established for monomolecular carbonyls, so that those

not obeying the 18 EAN rule are unstable. But the electrons in *4f* orbitals of lanthanides are much more contracted than those of transition metal *d* orbitals, hence the former are restricted from effective orbital overlap. This is the reason that bonding in lanthanide compounds is invariably ionic. Thus, the formation of $\text{Nd}(\text{CO})_6$ and any of the other lanthanide carbonyls is quite surprising in light of the fact that ionic bonding is precluded for such molecules.

Although the production of $\text{Sm}(\text{CO})_6$ was not reported, it is interesting to consider this molecule, since Sm having a $4f^6 6s^2$ configuration would be an atypical hexacarbonyl with an EAN = 20.

Very recently, full relativistic DV- $X\alpha$ calculations were reported on several $\text{M}(\text{CO})_6$ carbonyls including $\text{U}(\text{CO})_6$ [4]. It was found that the highest molecular orbitals (MOs) consisted of a manifold

of relativistic levels involving an admixture of U 5*f* and 6*d* orbitals. But it was not reported whether these were open or closed shells, or a combination of both.

This work reports calculations on the systems Ln(CO)₆ and Ln(OC)₆, Ln = Nd, Sm, utilizing the SC-MEH-MO method with average relativistic and spin-orbit effects included [5]. Since it has been indicated that the M-OC bonding mode may be a preferred intermediate in the mechanisms of some carbonyl insertion reactions [6, 7], thus the Ln(OC)₆ ligation mode was included in this study.

Pertinent MO data obtained from these calculations are presented in Table I-IV. Calculated bond energies are presented in Table V.

Method of Computation

Details of the SC-MEH-MO method have already been described extensively elsewhere and have been successfully applied for some 30 plus years [5, 8].

The AO basis functions and associated orbital quantities essential for calculating STO overlaps, diagonal elements of the SCC Hamiltonian, electron repulsion, and spin-orbit parameters, were obtained from the HF-SCF quasirelativistic program provided by Klobukowski [9]. Since the SC-MEH-MO method employs a charge-dependent quadratic relation for the SCC Hamiltonian and the allowance for Ln negative charge would appear to be important [8], some reasonable means for obtaining the proper charge-dependent orbital energies of all valence and virtual Ln⁻ levels had to be derived. The difficulty is that our HF-SCF AO program does not converge for Ln⁻ cases. A density functional theory (DFT) routine developed by Perdew does calculate electron affinities for some Ln⁻ in their 5*d*¹ (5*d*² for Gd) configurations, but not for Sm and other lanthanides higher than Gd [10]. No stable 4*f*^{*n*+1} or 6*p*¹ configurations of Ln⁻ were computable in any case. Thus a graphical extrapolation procedure was applied to all calculated and spectroscopic data available for 5*s*, 5*p*, 4*f*, 5*d*, 6*s*, and 6*p* orbital energies in the charge

TABLE I
Pertinent MO parameters for Nd(CO)₆.^a

MO symmetry Type ^b	Elec. Occ. ^c	<i>E</i> (eV) ^d	Percent AO character (≥ 0.5)						
			5 <i>s</i>	5 <i>p</i>	4 <i>f</i>	5 <i>d</i>	6 <i>s</i>	6 <i>p</i>	CO
<i>t</i> _{2<i>g</i>}	0	-5.519				68.1			31.9
<i>t</i> _{1<i>u</i>}	0	-9.313							100
<i>t</i> _{1<i>u</i>}	0	-9.648			4.8			3.6	91.6
<i>t</i> _{2<i>u</i>}	0	-9.871			5.8				94.2
<i>t</i> _{1<i>u</i>}	0	-10.421			93.2			1.7	5.1
<i>t</i> _{2<i>u</i>}	0	-10.559			84.2				5.8
<i>a</i> _{2<i>u</i>}	0	-11.078			100				
<i>t</i> _{2<i>g</i>}	6	-12.016				27.8			72.2
<i>t</i> _{2<i>g</i>}	6	-12.289		2.0	1.9			20.1	76.0
<i>a</i> _{1<i>g</i>}	2	-13.486	0.7				15.6		83.7
<i>e</i> _{<i>g</i>}	4	-14.026				15.6			84.4
<i>t</i> _{1<i>u</i>}	6	-14.944						1.1	98.9
<i>t</i> _{2<i>g</i>}	6	-15.290				4.2			95.8
<i>t</i> _{1<i>u</i>}	6	-24.705		8.8				6.4	84.8
<i>a</i> _{1<i>g</i>}	2	-28.125	2.3				16.4		81.3
<i>e</i> _{<i>g</i>}	4	-29.164				1.1			98.9
<i>t</i> _{1<i>u</i>}	6	-42.873		16.3				2.5	81.2
<i>a</i> _{1<i>g</i>}	2	-45.153	1.0				4.7		94.3
<i>e</i> _{<i>g</i>}	4	-45.900				1.3			98.7
<i>t</i> _{1<i>u</i>}	6	-53.098		65.7					34.3
<i>a</i> _{1<i>g</i>}	2	-81.454	89.7						10.3

^a Populations: Nd = 5*s*^{1.9}, 5*p*^{5.6}, 4*f*^{2.0}, 5*d*^{2.4}, 6*s*^{0.8}, 6*p*^{1.8}. Atom charges: Nd = -0.421; C = 0.303; O = -0.233.

^b O_h point group.

^c Two more filled CO orbitals of *t*_{1*u*} symmetry have been omitted.

^d Includes average relativistic and spin-orbit effects here and in Tables II-IV.

TABLE II
Pertinent MO parameters for Nd(OC)₆.^a

MO symmetry Type	Elec. Occ. ^b	E (eV)	Percent AO character (≥ 0.5)						CO
			5s	5p	4f	5d	6s	6p	
<i>t</i> _{2g}		-5.801				86.5			13.5
<i>t</i> _{1u}		-8.108			4.7				95.3
<i>t</i> _{2u}		-8.116			10.8				89.2
<i>t</i> _{1u}		-8.127							100
<i>t</i> _{1u}		-8.240			93.2			1.7	5.1
<i>t</i> _{2u}	1	-8.284			94.2				5.8
<i>t</i> _{2u}	3	-8.429				27.8			72.2
<i>t</i> _{2g}	2	-8.992			100				
<i>a</i> _{2u}	6	-12.040		1.6				11.0	87.4
<i>a</i> _{1g}	2	-12.373	0.5				12.5		87.0
<i>e</i> _g	4	-13.031				9.7			90.3
<i>t</i> _{1u}	6	-14.708						0.6	99.4
<i>t</i> _{2g}	6	-15.185				4.4			95.6
<i>t</i> _{1u}	6	-26.672		6.1					93.9
<i>a</i> _{1g}	2	-27.520	0.9				2.2		96.9
<i>e</i> _g	4	-28.500				3.3			96.7
<i>t</i> _{1u}	6	-39.855		38.3				2.4	59.3
<i>a</i> _{1g}	2	-45.138	1.7				4.3		94.0
<i>e</i> _g	4	-46.189				2.1			97.9
<i>t</i> _{1u}	6	-51.634		52.2					47.8
<i>a</i> _{1g}	2	-82.750	95.9						4.1

^a Populations: Nd = 5s^{2.0}, 5p^{5.9}, 4f^{1.8}, 5d^{1.2}, 6s^{0.4}, 6p^{0.9}. Atom charges: Nd = 1.84; O = -0.640; C = 0.334.

^b There are 31 fully occupied orbitals plus 4 unpaired electrons in 2 triply degenerate orbitals.

sequence Ln⁻, Ln⁰, Ln⁺ for Ln = Nd, Sm. Monatomic trends between quadratic curves were assumed to be transferable among like orbitals.

Initial calculations were carried out on Ln(CO)₆ for Ln = Nd, Sm in regular octahedral geometries, for successive variations of 0.03 increments in the Ln-CO bond distance range 2.30–2.60 Å. Each of these was a completely separate calculations with set atomic charges. The optimized bond distances was taken to be that for which a self-consistency in Löwdin populations and minimum total energy were attained. Convergence was impossible to achieve in any other way, and even with this procedure it was still a very difficult and time-consuming problem.

The Ln(OC)₆ calculations were carried out a fixed Ln-O bond distances taken to be some 2–3% shorter than the computationally optimized Ln-C distances. While there are no experimental data available to confirm these per se, there are some data showing M-OC bond distances falling in a range of 97–98% of M-CO bonds, for M = U, Th [6, 7]. In all cases the C-O bond distances were fixed at 1.41 Å.

Energies of Ln-CO and Ln-OC bonds were computed via a relationship successfully applied to HCo(CO)₄ and a variety of other molecular systems [8].

Results and Conclusions

All pertinent MO parameters for these two lanthanide hexacarbonyls in both carbonyl and oxonyl bonding conformations are presented in Tables I–IV. The computed optimized bond distances and bond energies are contained in Table V.

As noted in Table I, the Nd(CO)₆ highest occupied molecular orbital (HOMO) is a filled *t*_{2g} level lying 1 eV lower than the *a*_{2u} lowest unoccupied molecular orbital (LUMO). The HOMO is about 28% Nd 5d and 72% CO character. The LUMO is composed totally of the 4*f*_{xyz} orbital with the other 4*f* levels only some 0.4–0.6 eV above it.

The results for Nd(OC)₆ in Table II shows a quite different situation. The six Nd valence electrons are distributed over a filled *a*_{2u} orbital, plus three electrons in the *t*_{2g} and one in the *t*_{2u} level.

TABLE III
Pertinent MO parameters for Sm(CO)₆.^a

MO symmetry Type	Elec. Occ. ^b	<i>E</i> (eV)	Percent AO character (≥ 0.5)						
			5s	5p	4f	5d	6s	6p	CO
<i>t</i> _{1u}	0	-9.186							100
<i>t</i> _{1u}	0	-9.666			29.1			3.8	67.1
<i>t</i> _{2u}	0	-9.879			8.4				91.6
<i>t</i> _{1u}	0	-0.998			97.3			0.9	1.8
<i>t</i> _{2u}	0	-10.005			91.6				8.4
<i>a</i> _{2u}	2	-10.994			100				
<i>t</i> _{2g}	6	-11.962				25.8			74.2
<i>t</i> _{1u}	6	-12.294		1.9	0.6			16.0	75.4
<i>a</i> _{1g}	2	-13.386	0.7				16.0		83.3
<i>e</i> _g	4	-13.974				15.8			84.2
<i>t</i> _{1u}	6	-14.951						1.3	98.7
<i>t</i> _{2g}	6	-15.307				3.6			96.4
<i>t</i> _{1u}	6	-24.558		7.7				7.0	85.3
<i>a</i> _{1g}	2	-27.939	2.1				16.9		81.0
<i>e</i> _g	4	-29.080				9.3			90.7
<i>t</i> _{1u}	6	-43.151		11.9				2.8	85.3
<i>a</i> _{1g}	2	-45.088	0.8				4.7		94.5
<i>e</i> _g	4	-45.888				1.1			98.9
<i>t</i> _{1u}	6	-55.115		70.8					29.2
<i>a</i> _{1g}	2	-92.128	89.4						10.6

^a Populations: Sm = 5s^{1.9}, 5p^{5.6}, 4f^{3.7}, 5d^{2.3}, 6s^{0.8}, 6p^{2.0}. Atom charges: Sm = -0.204; C = 0.256; O = -0.222.

^b There are a total of 34 fully occupied orbitals.

The interval spacings of these levels are some 0.6 eV between *a*_{2u} and *t*_{2g} and 0.1 eV between *t*_{2g} and *t*_{2u}. There are also some vacant orbitals lying only 0.06–0.12 eV above the occupied ones. Thus the open-shell quintet ground state is amenable to extensive delocalization of electron density over both metal and ligands.

Sm(CO)₆ is shown in Table III to have a closed-shell *a*_{2u} ground state totally 4*f*_{xyz} in character and about 1 eV below the *t*_{2u} LUMO also of predominately 4*f* character. However, there are two other vacant levels within the very close proximity of 0.1–0.3 eV with predominately CO character.

Finally, Sm(OC)₆ has a spin nonet ground state with eight unpaired electrons distributed over a manifold of levels spanning a total of only 0.5 eV from lowest to highest occupied (see Table IV). These levels consist of an admixture of Sm 4*f* (with some 5*d*) and CO character. The LUMO also lies in the same energy range but is of totally CO character.

Notably in the case of Nd(CO)₆ there is a moderate net negative charge on Nd, which is about half that magnitude on Sm in Sm(CO)₆. This is in

keeping with the evidence indicating that the electron affinity of Nd, though a small positive value, should certainly be higher than that of Sm [10–13]. However, in both Nd(OC) and Sm(OC)₆ the net metal charges are both positive, with that of Nd 3.6 times higher than the Sm charge. This is in agreement with the evidence that M–OC bonds are more typically ionic than M–CO bonds [6, 7].

As shown in Table V, the calculated bond energies are found to be quite small for both the Ln(CO)₆ and Ln(OC)₆, but those for which Ln = Nd are a little higher than those of Sm. However, none of these are high enough to suggest any meaningful bond stability.

Apparently the low bond energies and close proximity of HOMO and LUMO levels provides a reasonable explanation for the instability of these molecules, and hence the reason for their fleeting existence in low-temperature noble-gas matrices. This study also shows that Ln(OC)₆ oxonyl bonding mode is less stable than the Ln(CO)₆ carbonyl bonding.

Further work is currently underway to complete an ab initio DFT calculation on Nd(CO)₆ and to continue SC-MEH-MO calculations on the remain-

TABLE IV
Pertinent MO parameters for $\text{Sm}(\text{OC})_6$.^a

MO symmetry Type	Elec. Occ. ^b	E (eV)	Percent AO character (≥ 0.5)						CO
			5s	5p	4f	5d	6s	6p	
t_{2g}	0	-5.745				84.0			16.0
t_{1u}	0	-7.908			99.5				0.5
t_{1u}	0	-8.368							99.7
t_{1u}	0	-8.379							100
t_{2u}	1	-8.394			1.1				98.9
t_{2u}	3	-8.482			98.9				1.1
t_{2g}	3	-8.647				11.1			88.9
a_{2u}	1	-8.925			100				
t_{1u}	6	-12.079		1.5				12.5	86.0
a_{1g}	2	-12.295					13.4		86.6
e_g	4	-13.128				10.6			89.4
t_{2g}	6	-15.201				4.7			95.3
e_g	4	-28.844				3.4			96.6
t_{1u}	6	-41.107		27.5				2.9	69.6
a_{1g}	2	-45.405	1.5				4.4		94.1
e_g	4	-46.573				2.1			97.9
t_{1u}	6	-54.401		63.8					36.2
a_{1g}	2	-89.869	96.0						4.0

^a Populations: $\text{Sm} = 5s^{2.0}, 5p^{5.9}, 4f^{5.0}, 5d^{1.3}, 6s^{0.4}, 6p^{1.0}$. Atom charges: $\text{Sm} = 0.510$; $\text{O} = -0.529$; $\text{C} = 0.444$.

^b There are a total of 30 fully occupied orbitals plus 4 singularly occupied orbitals (2 triply degenerate), providing 8 unpaired electrons.

TABLE V
Comparative bond energies and bond lengths.

Molecule	R(M-C) (Å)	R(M-O) (Å)	Average bond energy (kJ mol ⁻¹)
$\text{Nd}(\text{CO})_6$	2.40 ^a		61 ^a
$\text{Nd}(\text{OC})_6$		2.34 ^a	56 ^a
$\text{Sm}(\text{CO})_6$	2.37 ^a		49 ^a
$\text{Sm}(\text{OC})_6$		2.31 ^a	48 ^a
$\text{Cr}(\text{CO})_6$	1.91		108 ^b
$\text{Mo}(\text{CO})_6$	2.06		152 ^b
$\text{W}(\text{CO})_6$	2.06		179 ^b
$\text{U}(\text{CO})_6$	2.21		—

^a This work; optimized bond lengths.

^b From J. A. Connor, Topics Current Chem. **71**, 71 (1977).

ing $\text{Ln}(\text{CO})_6$ molecules for $\text{Ln} = \text{Ce}, \text{Pr}, \text{Eu}, \text{Gd}, \text{Tb}, \text{Dy}, \text{Ho}, \text{Er}, \text{Tm}, \text{Yb}, \text{and Lu}$.

ACKNOWLEDGMENTS

The provisions made available through the University of New Orleans Department of Chemistry and the Computer Research Center are gratefully acknowledged.

References

1. J. L. Slater, T. C. DeVore, and V. Calder, *Inorg. Chem.* **12**, 1918 (1973).
2. J. L. Slater, T. C. DeVore, and V. Calder, *Inorg. Chem.* **13**, 1808 (1974).
3. J. L. Slater, R. K. Sheline, K. C. Lin, and W. W. Weltner, Jr., *Chem. Phys.* **55**, 5129 (1971).
4. C. S. Nash and B. E. Bursten, *New J. Chem.* **19**, 669 (1995).
5. E. A. Boudreaux and E. Baxter, *Int. J. Quantum Chem.; Quantum Chem. Symp.* **29**, 605 (1995). E. A. Boudreaux, *Vibrational Spectra and Structure*, J. R. Durig, Ed. (Elsevier, Amsterdam, 1993), Vol. 20, pp. 189-238.
6. P. J. Fagan, J. M. Manriquez, S. H. Vollmer, C. S. Day, V. W. Day, and T. J. Marks, *J. Am. Chem. Soc.* **103**, 2206 (1981).
7. K. G. Moloy and T. J. Marks, *J. Am. Chem. Soc.* **106**, 7051 (1984).
8. E. A. Boudreaux, *Inorg. Chim. Acta* **82**, 183 (1984).
9. M. Klobukowski, *J. Comput. Chem.* **4**, 350 (1983). Private communication of computer program.
10. L. A. Cole and J. P. Perdew, *Phys. Rev. A* **25**, 1265 (1982).
11. R. J. Zollway, *J. Chem. Phys.* **50**, 4251 (1969).
12. L. Brewer, *J. Opt. Soc. Am.* **61**, 1101 and 1666 (1971).
13. S. G. Bratsch, *Chem. Phys. Lett.* **98**, 113 (1983).
14. J. C. Culberson, P. Kanappe, N. Rosch, and M. C. Zerner, *Theor. Chim. Acta* **71**, 21 (1987).

The Electronic g -Tensor of MgF: A Comparison of ROHF and MRD-CI Level Results

G. H. LUSHINGTON AND F. GREIN

Department of Chemistry, University of New Brunswick, B.S. #45222, Fredericton, N.B., E3B 6E2 Canada

Received February 25, 1996; revised manuscript received April 17, 1996; accepted April 22, 1996

ABSTRACT

Despite their importance in the characterization of molecular magnetism, electronic g -tensors have received rather little theoretical attention. In this work, however, the ground-state g -tensor of MgF is computed at both the ROHF and multireference CI levels. The calculations are expanded complete to second order in appropriate Breit-Pauli terms and the contributions of all important magnetically coupled excited states are accounted for. Both the CI- and ROHF-level Δg_{\parallel} -values (-59 and -55 ppm, respectively) are in agreement with experiment (-319 ± 500 ppm) within the range of experimental uncertainty. For Δg_{\perp} , however, the ROHF treatment yields a value (-659 ppm) in substantial disagreement with experiment (-1319 ± 500 ppm). Fortunately, this discrepancy is alleviated by CI level treatment ($\Delta g_{\perp} = -1447$ ppm). © 1996 John Wiley & Sons, Inc.

Introduction

When molecular radicals are subjected to an external magnetic field \mathbf{B} , their M_s levels become energetically nondegenerate. This energetic splitting, called the electronic Zeeman effect, is described by the relation

$$\Delta E = h\nu = -\boldsymbol{\mu} \cdot \mathbf{B}, \quad (1)$$

where $\boldsymbol{\mu}$ is the magnetic dipole moment of the radical.

Due to molecular anisotropy $\boldsymbol{\mu}$ is often directionally dependent. This dependence can be parametrized as follows:

$$\boldsymbol{\mu} = -\mu_B \mathbf{S} \cdot \mathbf{g}, \quad (2)$$

where \mathbf{g} is a second rank tensor called the electronic g -tensor; μ_B , the Bohr magneton; and \mathbf{S} , the molecule's spin angular momentum. Substituting Eq. (1) in (2), we get the following generalized expression for the Zeeman effect:

$$\Delta E = \mu_B \mathbf{S} \cdot \mathbf{g} \cdot \mathbf{B}. \quad (3)$$

Their relation to magnetic dipole moments makes g -tensors important as molecular parameters. Because of their computational complexity, however, very few ab initio studies have been done on these quantities.

In recent work [1-3], however, we performed several ROHF-level calculations of electronic g -tensors. These studies include the first-ever ab initio treatments complete to second order in Rayleigh-Schrödinger perturbation theory [2, 3] and also provide basis-set and gauge-dependence analysis [1, 2].

These ROHF-level calculations were able, for the first time, to reproduce general experimental trends with reasonable consistency. For many of the systems examined, however, sizable discrepancies were observed ($\sim 50\%$) between experiment and theory.

Except for small radicals with relatively few electrons [3], the most dominant contribution to the g -tensor usually comes from a second-order (sum-over-states) expansion wherein the ground state magnetically couples with the excited-state manifold. It is expected that electron correlation should play a major role in the treatment of such terms.

In this work, therefore, we compared and contrasted ROHF- and multireference CI-level g -tensor calculations for the $X^2\Sigma^+$ ($6\sigma^2 2\pi^4 7\sigma^1$) ground state of MgF.

Theory

The g -tensor expansion, complete to second order in appropriate Breit-Pauli operators, can be written as follows:

$$g^{ab} = g_e \delta^{ab} + \Delta g^{ab}, \quad (4)$$

where $g_e = 2.002319304386$ [4] is the free-electron g -factor, $a, b \in \{x, y, z\}$ are Cartesian coordinates, and

$$\begin{aligned} \Delta g^{ab} = & \Delta g_{RMC-SZ} \delta^{ab} + \Delta g_{GC-SZ}^{ab}(1e) \\ & + \Delta g_{GC-SZ}^{ab}(2e) + \Delta g_{2o}^{ab} \end{aligned} \quad (5)$$

is the g -shift. Expressions for all the above contributions are given elsewhere in regular [5] and spin-field reduced forms [1].

Most of the contributions to Eqs. (4) and (5) are obtained as expectation values of different

Breit-Pauli operators. The constant g_e , e.g., is obtained as the expectation value of the spin-Zee-man operator. Δg_{RMC-SZ} is obtained similarly as a relativistic mass correction to the spin-Zee-man operator, and $\Delta g_{GC-SZ}(1e)$ and $\Delta g_{GC-SZ}(2e)$ are one- and two-electron gauge corrections.

By contrast, Δg_{2o} comes from a second-order sum-over-states expansion:

$$2 \sum_n \frac{\langle \Psi_0 | H_{SO}(1e) + H_{SO}(2e) | \Psi_n \rangle \langle \Psi_n | H_{OZ} | \Psi_0 \rangle}{E_n - E_0}, \quad (6)$$

which describes the total magnetic coupling between the ground and excited states [5]. $H_{SO}(1e)$ and $H_{SO}(2e)$ are the one- and two-electron spin-orbit operators, H_{OZ} is the orbital-Zee-man operator and $E_n - E_0$ represents the vertical excitation energy of the excited state Ψ_n . More details of this are provided elsewhere [1, 5].

Computing Δg_{2o} at the Hartree-Fock level generally requires that the spin-orbit and orbital-Zee-man matrix elements and the vertical excitation energies be estimated in terms of the ground-state molecular orbitals. The resulting formula, given in previous work [1, 2], is computationally simple but yields rather approximate results.

Using correlated methods such as CI, it is possible to resolve the matrix elements and vertical excitation energies with much improved accuracy [6]. Such a treatment should thus yield more reliable results for Δg_{2o} .

CI treatment of the sum-over-states expansion is, however, much more computationally demanding. Fortunately, only states of certain symmetry species may contribute. In the case of MgF ($^2\Sigma^+$ ground state), only Π states may contribute to Δg_{\perp} ($= \Delta g^{xx}, \Delta g^{yy}$), while only Σ^- states are relevant for Δg_{\parallel} ($= \Delta g^{zz}$). As well, since H_{OZ} is not spin-dependent, the $\Delta S = 0$ selection rule holds firmly for g -tensor calculations. Finally, it should be mentioned that although the $\Sigma^+ \leftrightarrow \Sigma^-$ (Δg_{\parallel}) coupling is symmetry allowed, it is expected to be very weak [7]. While ROHF-level treatment gives a strictly zero second-order contribution to Δg_{\parallel} [8], CI calculations allow for (extremely small) nonzero shifts due to contributions from three open-shell $\pi \rightarrow \pi^*$ states.

CI methods have the disadvantage that the sum-over-states expansion must be truncated at some point and that the contribution of discarded terms is difficult to estimate. In this respect, methods which implicitly include *all* excited-state con-

tributions, such as propagator techniques, would be preferable. As yet, however, no methodology suitable for ab initio polarization propagator *g*-tensor calculations has been developed.

Computation

Both the ROHF and CI wave functions for MgF were generated using the MRD-CI package [9]. ROHF-level *g*-tensor calculations were performed with the GSTEPS suite of programs [1, 2, 10] (incorporating external integral routines [11, 12]), while CI level treatment was effected through a combination of the MRD-CI (with accompanying spin/orbit programs) and GSTEPS packages.

In this work, $\Delta g_{GC-SZ}(2e)$ is only computed at the Hartree-Fock level, due to inefficiency in our present code. Therefore, our best *g*-tensor results correspond to the sum of $\Delta g_{RMC-SZ} + \Delta g_{GC-SZ}(1e + \Delta g_{2o})$ computed at the CI level plus the ROHF value for $\Delta g_{GC-SZ}(2e)$. As $\Delta g_{GC-SZ}(2e)$ makes only a small contribution to the *g*-tensors of MgF (see Results), the corresponding correlation error is expected to be minimal.

Our calculations use the experimentally determined Mg-F bond distance ($R_{MgF} = 3.31$ bohr) [13]. As per convention, the molecule was specified to lie in the *z*-axis. The gauge origin was chosen to reside at the electronic charge centroid (see [2, 14]) as computed at the Hartree-Fock level. An estimate of the gauge dependence was obtained by computing the *g*-tensor with a gauge centered on the Mg nucleus.

The basis sets chosen are triple-zeta polarized Cartesian sets of Sadlej [15, 16] [(13s10p4d) \rightarrow [7s5p4d] for Mg; (10s6p4d) \rightarrow [5s3p4d] for F; *d* primitives left uncontracted].

While the basis-set criteria for *g*-tensor calculations have not been fully established, the Sadlej basis set is designed to treat both electric dipoles and polarizabilities at correlated levels [15] and may thus provide the flexibility necessary for computing our complete-to-second-order expansion [Eqs. (5) and (6)]. It is therefore seen as a good starting point for these calculations.

With four polarization primitives (of which two are diffuse) and a reasonable valence expansion, one would expect a decent description of both the ground and (valence) excited states. As well, the range of primitives from very compact to fairly

diffuse is appropriate for computing spin-dependent properties [17].

The most diffuse *s* and *p* functions on Mg are essentially equivalent to Rydberg functions. To ensure the resolution of lower-lying Rydberg states, however, additional 3*s* and 3*p* Rydberg functions ($\alpha_{3s} = 0.036$, $\alpha_{3p} = 0.029$) of Dunning and Hay [18] are included in the fluorine basis set. Our total description, therefore, amounts to 88 functions.

Details of the CI wave functions for the relevant magnetically coupled excited states are presented in Table I. The lowest three core orbitals (1*s*² on F and 1*s*²2*s*² on Mg) are frozen and the highest three virtual orbitals are discarded. While the generated CI expansions range in size up to 3.0 million symmetry-adapted functions (SAFs), the selection thresholds (0–2 μ Hartree) are set to retain only the most important 25,000 to 32,000 configurations. The Σc^2 values (sum of squares of the expansions coefficients of the reference configurations in the CI expansion) mostly range from 0.94 to 0.96, indicating that the states are consistently well described by the reference configurations [20]. The state energies reported correspond to approximate full CI energies as obtained by the generalized version [21] of Davidson's extrapolation technique [22].

In computing Δg_{2o} at the CI level, all valence states (and some low-lying Rydbergs) are treated in energetically increasing order until three consecutive states with minimal importance ($|\Delta g_{2o}^{ab}(\Psi_n)| < 1\%$ of Δg^{ab}) are encountered. At this point, all further contributions are assumed to be insignificant and the expansion is truncated. Only those states making appreciable ($> 1\%$) contributions are retained in Δg_{2o} . The discarded states, while not useful in computing Δg_{2o} , can provide a rough approximation to the error range of Δg_{2o} as follows:

$$\Delta(\Delta g_{2o}^{ab}) \approx 2 \times \sum_{\substack{\text{discarded} \\ \text{test} \\ \text{states}}} \Delta g_{2o}^{ab}(\Psi_n). \quad (7)$$

One should note two things about this formalism: (1) it tends to ignore most of the higher Rydberg states, and (2) the expansion may proceed beyond the molecule's ionization limit into the range of high-energy valence states. Both these conditions are reasonable since (1) the higher Rydberg states are generally much too diffuse to couple effectively with the ground state and (2) the high-energy valence states, although physically

TABLE I
CI wave function data for relevant states of MgF.

State	Leading Configuration	Σc^{2a}	E_{thr}^b	SAFs ^c	Vertical excitation energies (eV)		
					This work	Theoretical ^d	Exp. ^e
$X^2\Sigma^+$	$6\sigma^2 2\pi^4 7\sigma^1$	0.947	0.2	27925	—	—	—
$1^2\Sigma^-$	$2\pi \rightarrow 3\pi$	0.913	2.0	25630	8.7231		
$2^2\Sigma^-$	$2\pi \rightarrow 3\pi$	0.919	2.0	25630	10.1969		
$3^2\Sigma^-$	$2\pi \rightarrow 4\pi$	0.968	1.5	27268	20.0115		
$1^2\Pi$	$7\sigma \rightarrow 3\pi$	0.944	0.6	31160	3.4470	3.3	3.45
$2^2\Pi$	$7\sigma \rightarrow 4\pi$	0.943	0.6	31287	6.1359	6.2	6.73
$3^2\Pi$	$7\sigma \rightarrow 5\pi$	0.942	0.3	29125	7.0223		
$4^2\Pi$	$7\sigma \rightarrow 6\pi$	0.948	0.6	27592	8.5875		
$5^2\Pi$	$6\sigma \rightarrow 3\pi$	0.948	1.2	25637	8.7797		
$6^2\Pi$	$2\pi \rightarrow 7\sigma$	0.904	1.0	27684	10.9284		
$7^2\Pi$	$6\sigma \rightarrow 3\pi$	0.999	1.0	26649	19.7708		
$8^2\Pi$	$7\sigma \rightarrow 7\pi$	0.990	0.6	29601	20.2130		
$9^2\Pi$	$6\sigma \rightarrow 5\pi$	0.998	1.0	26142	20.6257		

^a Squares of CI expansion coefficients summed over reference configurations.^b Energy threshold (in μ Hartree) for retention of configurations in the CI expansion.^c No. of symmetry-adapted functions (i.e., configurations) included in the selected CI space.^d Obtained from [19].^e Obtained from [13].

unstable, may be computationally significant and have been found in some cases [10] to yield appreciable contributions to the g -tensor.

Results and Discussion

Table II provides details of states whose magnetic coupling contributes to Δg_{2o} . From this, one notices two things: (1) As expected [7, 8], there do not appear to be any significant second-order contributions to $\Delta g_{||}$, and (2) $(\Delta g_{2o})_{\perp}$ is apparently dominated by the first $^2\Pi$ state.

The $X^2\Sigma^+ \leftrightarrow 1^2\Pi$ coupling is especially favorable for two reasons: The state is low in energy and its singly occupied molecular orbital (SOMO), 3π , is located primarily on the Mg atom and thus can interact strongly with the ground-state SOMO (also on Mg). No other $^2\Pi$ states possess both such qualities; thus, $(\Delta g_{2o})_{\perp}$ is effectively a one-state expansion.

Table III gives the breakdown of different contributions to the ROHF and CI level g -tensors. In both cases, second-order terms dominate Δg_{\perp} , while first-order contributions determine $\Delta g_{||}$.

TABLE II
Magnetic coupling data for excited states contributing to Δg_{2o} of MgF; spin-orbit and orbital-Zeeman matrix elements, vertical excitation energies, and Δg_{2o} contribution given.^a

	$\langle H_{SO} \rangle$ $\times 10^{-4}$ (eV)	$\langle H_{OZ} \rangle^b$ $\times 10^{-4}$ (eV)	ΔE (eV)	$\Delta g_{2o}(\Psi_n)$ (ppm)
$\Delta g_{ }$				
$1^2\Sigma^-$	-13.4183	-2×10^{-7}	8.7231	0
$2^2\Sigma^-$	-20.5968	-1×10^{-8}	10.1969	0
$3^2\Sigma^-$	1.1201	4×10^{-5}	20.0115	0
Δg_{\perp}				
$1^2\Pi$	-16.2122	0.9053	3.4470	-1471
$2^2\Pi$	-7.9868	0.1918	6.1359	-86
$3^2\Pi$	-3.1030	-0.1603	7.0223	14
$4^2\Pi$	11.9253	-0.0423	8.5875	-20
$5^2\Pi$	1.2059	0.2568	8.7797	12
$6^2\Pi$	16.4946	0.2390	10.9284	125
$7^2\Pi$	-16.3599	0.0019	19.7708	1
$8^2\Pi$	1.0662	0.0617	20.2130	1
$9^2\Pi$	0.0786	0.0689	20.6257	0

^a Coupling is with respect to the $X^2\Sigma^+$ ground state.^b Assuming a field strength of 1 Tesla.

TABLE III
ROHF and CI level g -shifts for MgF showing
contributions from different terms
(all values in ppm).

		ROHF	CI	
Δg_{RMC-SZ}^a		-63	-68	
$\Delta g_{GC-SZ}(1e)$	Δg_{\perp}	144	150	
	Δg_{\parallel}	90	90	
$\Delta g_{GC-SZ}(2e)^b$	Δg_{\perp}	-103	-103	
	Δg_{\parallel}	-81	-81	
Δg_{2o}^c	Δg_{\perp}	-637	-1426	± 4
	Δg_{\parallel}	0	0	± 0
Total	Δg_{\perp}	-659	-1447	
	Δg_{\parallel}	-55	-59	
Exp. ^d	Δg_{\perp}		-1319	± 500
	Δg_{\parallel}		-319	± 500

^a Relativistic mass correction is isotropic.

^b Values for $\Delta g_{GC-SZ}(2e)$ are computed at the ROHF level.

^c States contributing only minimally to Δg_{2o} are omitted from the CI sum-over-states expansion. These states are used, however, in estimating the uncertainty for Δg_{2o} .

^d [23].

First-order terms are well described at the ROHF level; thus, there is little difference between the ROHF and CI g_{\parallel} -shifts. Correlation plays a very important role for Δg_{\perp} , however, in particular because of the failure of the ROHF treatment to adequately describe the $X^2\Sigma^+ \leftrightarrow 1^2\Pi$ interaction.

The matrix elements for the $X^2\Sigma^+ \leftrightarrow 1^2\Pi$ spin-orbit and orbital-Zeeman interactions are both substantially underestimated (-6.70×10^{-4} and 0.69×10^{-4} eV, respectively) at the ROHF level compared to the corresponding CI values (-16.21×10^{-4} and 0.91×10^{-4} eV). Additionally, the excitation energy determined by the ROHF treatment (5.22 eV) is more than 1.7 eV too large (CI: 3.45 eV). From all three factors, therefore, one sees why Δg_{\perp} is drastically underestimated (-659 ppm) at the ROHF level. The CI value (-1447 ppm), although possibly larger than the experimental value (-1319 ± 500 ppm, Ne/Ar matrix) is in much better agreement.

With regard to the g_{\parallel} shift, very little difference is observed when comparing CI (-59 ppm) and ROHF-level (-54 ppm) values. Both are well within the range of experimental error (-319 ± 500 ppm), although it is possible that they under-

estimate the magnitude of the negative shift. This would be consistent with other matrix isolation data on diatomic species. In the extreme case of CO^+ , e.g., the experimental Δg_{\parallel} value is -1419 ± 500 ppm [24], while the best theoretical estimate is -178 ppm [10]. The relatively large experimental $|\Delta g_{\parallel}|$ values may indicate matrix interactions which reduce the molecule's effective symmetry, thereby allowing spin-orbit coupling to occur along the bond axis [7]. It may therefore be somewhat inappropriate to compare our Δg_{\parallel} values with matrix isolation data.

Finally, while most aspects of the CI g -tensor treatment have yielded very encouraging results for MgF, we found the CI-level results to have a surprisingly large gauge dependence. The Δg_{\perp} value computed with the origin on the Mg atom (i.e., shifted by 1.34 bohr from the ECC) was substantially smaller (-1187 ppm), leading to a CI-level gauge dependence of 260 ppm/bohr (18.0% the size of Δg_{\perp}). This is in stark contrast to the CI-level results that we have obtained for other molecules [10]. For example, the CI-level gauge dependence of CO^+ has a value only 0.3% the size of Δg_{\perp} [10].

The ROHF-level gauge dependence for MgF is found to be only 8 ppm/bohr (1.2% of Δg_{\perp}). The discrepancy between this value and the CI-level gauge dependence is difficult to explain. While the larger CI value may be related to the truncation in the sum-over-states expansion, this is unlikely due to the rapid decline in importance of higher contributions (see Table II). Further study of this phenomenon may be in order.

In light of these gauge-dependence findings, we do stress that all our calculations are conducted with the center at the molecule's electronic charge centroid. This provides a nonarbitrary choice of gauge, which, in theory [14], should provide results in consistent proximity to the correct values.

Summary and Conclusions

Although our ROHF g -tensor calculations [1-3] are adequate to reproduce qualitative trends in experimental data, we found in this article that the extension of the method to correlated levels substantially improves agreement with experiment. In particular, the CI level Δg_{\perp} value for MgF differs by only 10% from the experimental value (well

within the error margin), while the discrepancy was 50% at the ROHF level. While first-order terms appear to be well described at the ROHF level, a reliable treatment of excitation energies and spin-orbit coupling requires correlation.

While this treatment is the most advanced yet applied to the g -tensor problem, we admit to some technical difficulties: First, we have not yet devised an efficient method for obtaining values for the $\Delta g_{GC-SZ}(2e)$ term at the CI level. Neglect of correlation in this term, however, is expected to introduce only minor errors, likely on the order of 20 ppm or less for most systems.

Second, our approach to computing $\Delta g_{2,0}$ at the CI level introduces a degree of uncertainty because of the truncation of the sum-over-states expansion. This is of little worry in the case of MgF, where $\Delta g_{2,0}$ is dominated by just one state ($1^2\Pi$), while other states contribute only 3% to Δg_{\perp} . One can envision systems, however, in which substantial difficulties would be encountered. A more effective way of treating such a perturbation expansion would be through the use of a spin-orbit-perturbed CI formalism, such as that proposed by Hess [25]. Unfortunately, no such program is yet available.

Nonetheless, MgF (and other such simple radicals) provide excellent examples of systems for which our CI-level g -tensor treatment is particularly successful. It is not certain whether such accurate calculations will be possible for all molecular radicals; however, this work represents an important step in the development of effective *ab initio* electronic g -tensor computation.

ACKNOWLEDGMENTS

This work was funded by the Natural Sciences and Engineering Research Council (NSERC) of Canada.

References

1. G. H. Lushington, P. Bündgen, and F. Grein, *Int. J. Quantum Chem.* **55**, 377 (1995).
2. G. H. Lushington and F. Grein, *Theor. Chim. Acta.* **93**, 259 (1996).
3. G. H. Lushington, P. J. Bruna, and F. Grein, *Z. Phys. D* **36**, 301 (1996).
4. E. R. Cohen and B. N. Taylor, *Rev. Mod. Phys.* **59**, 1121 (1987).
5. J. E. Harriman, *Theoretical Foundations of Electron Spin Resonance* (Academic Press, New York, 1978).
6. R. McWeeny and B. T. Sutcliffe, *Methods of Molecular Quantum Mechanics* (Academic Press, New York, 1976).
7. W. Weltner, *Magnetic Atoms and Molecules* (Dover, New York, 1983).
8. P. W. Atkins and M. C. R. Symons, *Structure of Inorganic Radicals* (Elsevier, New York, 1967).
9. R. J. Buenker, S. D. Peyerimhoff, and W. Butscher, *Mol. Phys.* **35**, 771 (1978); D. B. Knowles, J. R. Álvarez-Collado, G. Hirsch, and R. J. Buenker, *J. Chem. Phys.* **92**, 585 (1990), and references therein.
10. G. H. Lushington, PhD Thesis (University of New Brunswick, Fredericton, Canada, 1996).
11. P. Chandra and R. J. Buenker, *J. Chem. Phys.* **79**, 366 (1983); *Ibid.* **79**, 358 (1983); C. M. Marian, Doktorarbeit (University of Bonn, Bonn, Germany, 1981); B. A. Hess, Doktorarbeit (University of Bonn, Bonn, Germany, 1981).
12. J. D. Augspurger and C. E. Dykstra, *J. Comp. Chem.* **11**, 105 (1990).
13. K. P. Huber and G. Herzberg, *Molecular Spectra and Molecular Structure. Vol. 4: Constants of Diatomic Molecules* (Van Nostrand Reinhold, New York, 1979).
14. A. V. Luzanov, E. N. Babich, and V. V. Ivanov, *J. Mol. Struct. (Theochem)* **311**, 211 (1994).
15. A. J. Sadlej, *Coll. Czech. Chem. Commun.* **53**, 1995 (1988).
16. A. J. Sadlej, *J. Mol. Struct. (Theochem)* **234**, 147 (1991).
17. S. P. A. Sauer, I. Paidarová, and J. Oddershede, *Theor. Chim. Acta* **88**, 351 (1994).
18. T. H. Dunning and P. J. Hay, in *Modern Theoretical Chemistry*, H. F. Schaeffer III, Ed. (Plenum Press, New York, 1977), Vol. 3.
19. T. E. H. Walker and W. G. Richards, *J. Phys. B* **1**, 1061 (1968).
20. P. J. Bruna and S. D. Peyerimhoff, in *Ab Initio Methods in Quantum Chemistry*, K. P. Lawley, Ed. (Wiley, New York, 1987).
21. G. Hirsch, P. J. Bruna, S. D. Peyerimhoff, and R. J. Buenker, *Chem. Phys. Lett.* **52**, 442 (1977); P. J. Bruna, S. D. Peyerimhoff, and R. J. Buenker, *Chem. Phys. Lett.* **72**, 278 (1980).
22. S. R. Langhoff and E. R. Davidson, *Int. J. Quantum Chem.* **8**, 1516 (1974).
23. L. B. Knight, W. C. Easley, and W. Weltner, *J. Chem. Phys.* **54**, 322 (1971).
24. L. B. Knight and J. Steadman, *J. Chem. Phys.* **77**, 1750 (1982).
25. B. A. Hess, private communication.

Wave-Function Splitting Technique for Calculating Above-Threshold Ionization Electron Spectra

S. CHELKOWSKI AND A. D. BANDRAUK

Laboratoire de Chimie Théorique, Faculté des Sciences, Université de Sherbrooke, Sherbrooke, Québec, Canada J1K 2R1

Received March 29, 1996; revised manuscript received May 7, 1996; accepted May 8, 1996

ABSTRACT

In intense laser fields, atoms and molecules can absorb many more photons than required for ionization. This phenomenon is called above-threshold ionization (ATI) and it shows up in kinetic energy spectra of ionized electrons. The presence of very high energy photoelectrons necessitates the use of extremely large grids in numerical simulations based on the full time-dependent Schrödinger equation. We show that by using a wave function splitting scheme one can circumvent the problem of large grids and thus obtain accurate multiphoton photoelectron spectra. This scheme will be very useful in studies of ATI spectra generated by molecules in intense laser fields. We illustrate this method for a one-dimensional model of the H atom in intense laser fields. © 1996 John Wiley & Sons, Inc.

Introduction

The interaction of intense laser pulses (intensity $I > 10^{13}$ W/cm²) with atoms and molecules leads to many interesting multiphoton, non-perturbative phenomena such as high-order harmonic generation and above-threshold ionization (ATI). This has been an area of active research in the past decade [1–4]. One of the theoretical approaches to deal with this nonperturbative problem relies on exact numerical solutions of the time-dependent Schrödinger equation (TDSE) on

recently available powerful computers. So far, this approach has been successfully applied to one-electron atoms and molecules (or two 1-D electrons). Typically, in such numerical simulations, the initial wave function of the electron is well localized in space and later becomes spread over a huge distance. For a short, intense, 40 fs laser pulse, the front edge of the wave packet of the ionizing electron can be as far as 4000 bohr from the nucleus (for $I = 2 \times 10^{14}$ and $\lambda = 630$ nm) and continues to expand for longer times. Thus, to avoid reflections from the boundaries, prohibitively large boxes (grids with 32,000 points or more), in which the electron wave packet is fully

contained, should be used. The most common solution to this difficulty is to use much smaller boxes with absorbing boundary conditions. This approach allows one to calculate the ionization rates and harmonic generation spectra but it does not allow one to calculate the photoelectron spectra, since the external part of the wave function is thrown away. Also, in our recent numerical studies of competition between ionization and dissociation [5], the use of an absorber for the electron flux led to a considerable loss of information about the nuclear movement. In this article, we develop a technique which allows one to reconstruct the absorbed electron wave packet in momentum space and propagate it in time, analytically to any time after the pulse turn-off. Thus, with the help of this technique, one can calculate efficiently the photoelectron spectra after the turn-off of the pulse. A similar technique has been used earlier [6], for calculating kinetic energy spectra of photodissociation products, with the laser-molecule coupling neglected in the asymptotic region. Recently [7], this technique was generalized for nondecaying (for larger distances) dipole couplings (for dissociating molecules) and for the calculation of the ATI spectra from the TDSE in the Kramers-Henneberger (K-H) representation [8] for high-frequency laser fields. In these cases, the laser-induced quiver (ponderomotive) motion is small. In this article, we use the electric field representation (gauge) for near-infrared-visible frequencies, when quiver motions are large. In [8], the projections on exact eigenstates of hydrogen were performed. Here, we do not use the (K-H) frame and show that correct spectra can be obtained by projecting on plane waves in the asymptotic region instead of projecting on hydrogen asymptotic outgoing Coulomb waves. This technique will allow us to develop a rigorous theory of multiphoton electron spectroscopy based on ATI in molecules with the aim of developing a new tool for studying electron-molecule dynamics.

Description of the Wave-Function Splitting Algorithm

The dynamics of a hydrogen atom interacting with an intense, linearly polarized laser field is frequently described by the 1-D Schrödinger equation [2]:

$$i\hbar \frac{\partial \psi(z, t)}{\partial t} = \left(-\frac{1}{2} \frac{\partial^2}{\partial z^2} - \frac{1}{\sqrt{1+z^2}} + zE(t) \right) \psi(z, t), \quad (1)$$

where $E(t) = E_M \sin^2(\pi t/t_p) \sin(\omega t)$ and E_M is the maximum value of the electric field. This equation is usually discretized and solved numerically for $|z| < z_M$. For our test calculations, we chose the laser intensity $I = 2.2 \times 10^{14} \text{ W/cm}^2$, $\lambda = 630 \text{ nm}$, and $t_p = 20$ cycles (1 cycle = 2.17 fs) in order to compare with the results from [9]. The photoelectron spectra from this reference show a plateau extending up to $8U_p = 70 \text{ eV}$ with a slowly decaying tail up to 130 eV (70 photons absorbed), where $U_p = [eE_M/(2m\omega)]^2$ is the electron ponderomotive energy. Thus, the fastest electron has a speed $v_M = 2.3 \text{ au}$ and $t_p = 43 \text{ fs}$ can be as far as 4050 bohr. Typically, the integration step in space is $\delta z = 0.25 \text{ bohr}$, which means that the grids with over 32,000 grid points should be used for a 43 fs pulse. For n times longer pulses, n time greater grids should be used. This constitutes a serious difficulty, even for 1-D problems. Therefore, a fast algorithm for large z 's is very desirable. In particular, since the Coulomb forces are smooth and negligible for large z 's, larger interaction steps in space δz , as well as much larger steps in time, can be used.

Let us divide the total grid into three overlapping regions in space, in which different evolution algorithms will be used: the internal and two external (asymptotic, for positive and negative z 's) parts defined by

$$\text{internal: } |z| < z_{in} \quad \text{and external: } z_{ex} < |z| < z_M, \quad (2)$$

where $z_{in} - z_{ex} = z_0 > 0$ is the size of the overlap of both regions. In this overlapping (or "matching") region, the absorbing potential is introduced, which we have chosen in the following form:

$$V_{abs}(z) = iV_0 \left(\frac{z - z_{ex}}{z_0} \right)^2 \quad \text{for } z_{ex} < |z| < z_{in}. \quad (3)$$

The electron wave function $\psi(z, t)$ is split into internal ψ_{in} and external ψ_{ex} parts, by applying this absorbing potential in the overlapping region, at times $t = k\delta t$, where δt is much larger than the integration time dt ($dt = 0.03$ au, $\delta t = 150$ dt, in our simulations) with the help of the following formulas:

$$\psi(z, t) = \psi_{in}(z, t) + \psi_{ex}(z, t), \quad (4)$$

$$\psi_{in}(z, t) = f(z, \delta t)\psi(z, t), \quad (5)$$

$$\psi_{ex}(z, t) = (1 - f(z, \delta t))\psi(z, t), \quad (6)$$

where

$$f(z, \delta t) = \exp(-\delta t V_{abs}(z)) \quad \text{for } z_{ex} < |z| < z_{in}, \quad (7)$$

$$f(z, \delta t) = 1 \quad \text{for } |z| < z_{ex}, \quad (8)$$

and

$$f(z, \delta t) = 0 \quad \text{for } |z| > z_{in}. \quad (9)$$

Our calculation scheme relies on the assumption that in the asymptotic zone (defined by $|z| > z_{ex}$) the Coulomb potential can be neglected. This allows us to perform the time evolution exactly and over an arbitrary time interval by calculating first the wave function in the velocity gauge $\psi_v(z, t)$ with the help of the formula

$$\psi_v(z, t) = \exp(-i\Delta(t, 0)z)\psi(z, t), \quad (10)$$

where

$$\Delta(t_1, t_2) = -\int_{t_1}^{t_2} E(t) dt \quad (11)$$

is the electric field area over the interval t_1, t_2 . Next, we calculate the Fourier transform $\varphi_v(p, t)$ of $\psi_v(z, t)$, which evolves in time according to the equation

$$\varphi_v(p, t_2) = U(t_2, t_1)\varphi_v(p, t_1), \quad (12)$$

where

$$U(t_1, t_2) = \exp\left(-\frac{i}{2}\int_{t_1}^{t_2}(p^2 + 2\Delta(t, 0)p + \Delta^2(t, 0))dt\right). \quad (13)$$

In our algorithm, we perform the series of following operations at each time $t_k = k\delta t$:

- (i) The exact time evolution of ψ_{in} is evaluated in the internal zone ($|z| < z_{in}$) using the split-operator spectral method [10].
- (ii) The outgoing wave is eliminated from the internal zone with the help of Eq. (5).
- (iii) The splitting operation described by Eq. (6) is performed to provide the outgoing wave ψ_{ex} defined in the "matching zone," $z_{ex} < |z| < z_{in}$.
- (iv) The velocity gauge wave function ψ_v and its Fourier transform φ_v are calculated:

$$\varphi_v(p, t_k) = (2\pi)^{-\frac{1}{2}} \int_{z_{ex}}^{z_{in}} \exp(-ipz) \psi_v(z, t_k) dz. \quad (14)$$

- (v) The momentum wave function $\varphi_v(p, t_f)$ is calculated at some final time $t_f \geq t_p$ (at which the photoelectron spectra are to be calculated), using the formula

$$\varphi_v(p, t_f) = U(t_f, t_k)\varphi_v(p, t_k). \quad (15)$$

- (vi) The momentum wave function $\varphi_v(p, t_f)$ is added to $\varphi_v(p, t_f)$'s accumulated at previous steps.
- (vii) The loop ends here and calculation starts at step (i) with the integer k replaced by $k + 1$.

Results and Discussion

The most difficult part of the scheme presented here is the choice of the free parameters: V_{abs} , δt , z_{in} , and z_0 . Several obvious necessary (but not sufficient) physical conditions should be satisfied: First, the external zone ($|z| > z_{ex}$) in our scheme is the asymptotic region in which we neglect the Coulomb forces; therefore, we must require that at $z = z_{ex}$ the Coulomb force is much less than the electric force eE_M , i.e.:

$$\frac{e^2}{z_{ex}^2} \ll eE_M. \quad (16)$$

Second, our scheme is based on the assumption that the wave entering the "matching" zone (of length z_0) does not return back to the nucleus, as

TABLE I
Values of parameters (in atomic units) used in the wave-function splitting scheme.

U_p	α_0	dt	δt	dz	n_{in}	n_{ex}	V_{abs}
0.32	16.1	0.03	4.5	0.25	4196	3300	2

n_{in} is number of grid points in the internal zone ($|z| < z_{in}$) and n_{ex} is the number of grid points in the external zone, in momentum space with the momentum resolution $\Delta p = 2\pi/7168$ au.

well as that the wave exiting this zone does not return to it. This means that we should require that the classical ponderomotive radius α_0 is much smaller than the size of the internal box z_{in} and also smaller than the size of the matching "zone":

$$\alpha_0 \ll z_{in} \text{ and } \alpha_0 \ll z_0, \text{ where } \alpha_0 = \frac{eE}{m\omega^2}. \quad (17)$$

In addition, we must require that the matching should be redone after the time interval δt shorter than the time necessary to move for the fastest electron across the matching "zone." Assuming that the fastest electron has the energy $E_{max} = 8U_p$, we thus get

$$\delta t \ll \frac{z_0}{4\sqrt{mU_p}}. \quad (18)$$

Finally, the absorption should occur on the distance z_0 longer than de Broglie wavelength of the slowest electron. Assuming that the slowest electron has the energy $\hbar\omega$, we thus get

$$z_0 \gg \pi \sqrt{\frac{2}{(\hbar\omega)}}. \quad (19)$$

For the laser parameters chosen in this article, $I = 2.2 \times 10^{14}$ W/cm² and $\lambda = 630$ nm, the values of two relevant parameters are $\alpha_0 = 16.1$ bohr, $U_p = 0.32$ au = 8.7 eV, and $\omega = 0.7$ au. We have listed in Table I the values of all parameters which we used in our calculations and which satisfy all inequalities Eqs. (16)–(19). The spectra of electrons moving in the direction of positive z where calculated according the formula

$$\text{probability}(E) = |\varphi(p(E))|^2 \frac{m}{p(E)}, \quad (20)$$

where $p(E) = \sqrt{2mE}$. We display in Figure 1 the low-energy part of the calculated spectra, and in

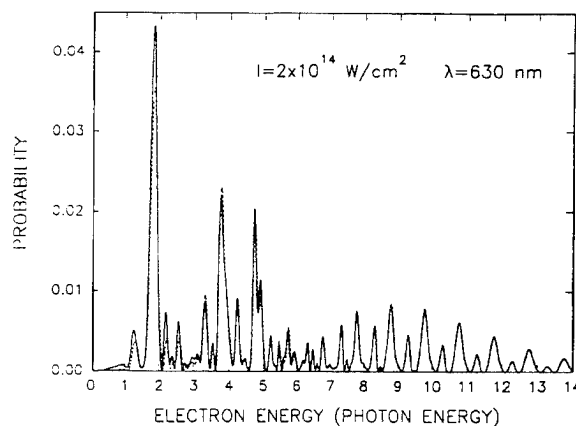


FIGURE 1. Low-energy part of the ATI photoelectron spectrum. The laser intensity $I = 2.2 \times 10^{14}$ W/cm² and the wavelength $\lambda = 630$ nm. Solid line: two-box calculation; dashed line: one-box calculation.

Figure 2, the entire spectrum, on the logarithmic scale. We also calculated, for comparison (dashed line), the photoelectron spectra using one large box defined by $|z| < 7000$ bohr. We note a slight disagreement between the heights (not positions) of several first photoelectron peaks. This disagreement becomes less when the spectra are calculated at later times, $t_f > t_p$ (with the laser turned-off for $t_f > t_p$), since, then, all slow electrons have enough time to leave the matching zone. The peaks for energies higher than 5ω , obtained from one-box and two-box calculations, overlap exactly and they agree well with previous calculations [8, 9], in which projections were done on exact Coulomb waves, while we performed projections on plane waves in the external zone, $|z| > z_{ex}$.

We are currently extending this method to include the nuclear motion as well, following the numerical procedure described in our previous work [5, 10]. We expect the ensuing multiphoton electron spectra to reveal the full electron–nuclear dynamics of molecules in strong laser fields.

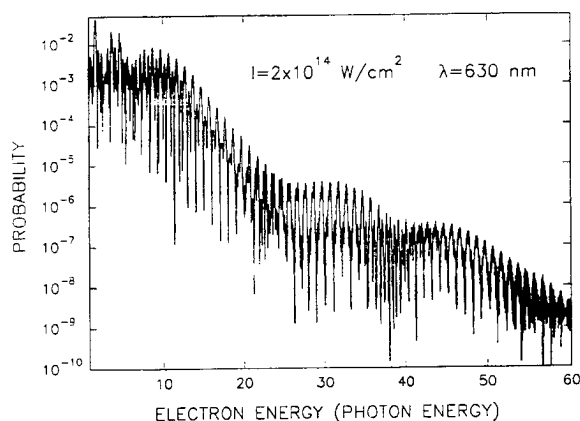


FIGURE 2. Entire ATI photoelectron spectrum. The laser intensity $I = 2.2 \times 10^{14} \text{ W/cm}^2$ and the wavelength $\lambda = 630 \text{ nm}$.

ACKNOWLEDGMENTS

The financial support from the Natural Sciences and Engineering Research Council of Canada is

gratefully acknowledged. We also acknowledge stimulating discussions with T. Zuo.

References

1. G. Mainfray and C. Manus, *Rep. Prog. Phys.* **54**, 1333 (1991).
2. J. H. Eberly, J. Javanainen, and K. Rzazewski, *Phys. Rep.* **204**, 331 (1991).
3. A. L'Huillier, K. J. Schafer, and K. C. Kulander, *J. Phys. B* **24**, 3315 (1991).
4. *Molecules in Laser Fields*, edited by A. D. Bandrauk (Marcel Dekker, New York, 1993).
5. S. Chelkowski, T. Zuo, O. Atabek, and A. D. Bandrauk, *Phys. Rev. A* **52**, 2977 (1995).
6. R. Heather and H. Metiu, *J. Chem. Phys.* **86**, 5009 (1987).
7. A. Keller, *Phys. Rev. A* **52**, 1450 (1995).
8. T. Millack, *Phys. Rev. A* **48**, 786 (1993).
9. G. G. Paulus, W. Nicklich, Huale Xu, P. Lambropoulos, and H. Walther, *Phys. Rev. Lett.* **72**, 2851 (1994).
10. S. Chelkowski, T. Zuo, and A. D. Bandrauk, *Phys. Rev. A* **46**, 5342 (1992).

Kernel Projector Matrices for Leu¹-Zervamicin

L. HUANG*

Laboratory for the Structure of Matter, Naval Research Laboratory, Washington, D.C. 20375-5341

L. MASSA

Hunter College and the Graduate Center of City University, New York, New York 10021-5024

J. KARLE[†]

*Laboratory for the Structure of Matter, Naval Research Laboratory, Washington, D.C. 20375-5341;
e-mail: williams@harker.nrl.navy.mil*

Received February 25, 1996; revised manuscript received March 21, 1996; accepted April 24, 1996

ABSTRACT

By performing ab initio calculations on fragments of leu¹-zervamicin, it is demonstrated that accurate wave functions can be obtained for this large structure by combining the results from the fragments. Input information consists of atomic coordinates as obtained, for example, from a crystal structure determination. The fragments are composed of a kernel of atoms surrounded by a chosen neighborhood of atoms. The entire molecule is divided into individual kernels and their neighborhoods are added for the individual fragment calculations on the basis of the distances of other atoms from the atoms in a kernel. The hydrated leu¹-zervamicin is composed of 295 atoms which could be handled in full by Gaussian 94. The results of the fragment calculations were combined to provide an electron density distribution for the molecule. This distribution was compared with one that represents the distribution obtained from a calculation on the entire molecule at once. The clear implication of this study is that it is feasible to perform ab initio calculations on structures by the use of fragments. The time involved increases essentially linearly with complexity. © 1996 John Wiley & Sons, Inc.

*Permanent address: Geo-Centers, Inc., 10903 Indian Head Highway, Fort Washington, Maryland 20744-4018.

[†]To whom correspondence should be addressed.

Introduction

In a previous article [1], an intimate connection was made between structure factor magnitudes obtained from X-ray diffraction data and those obtained from quantum mechanical models of electron density distributions. The objective has been to obtain wave functions consistent with crystallographic diffraction data for use in the calculation of various properties of a broad variety of substances. In our approach to the calculation of the quantum mechanical model, the electron density distribution in a crystal is defined in terms of a single determinant of orbitals. In the single-determinant approach, a main feature is the occurrence of a projector matrix in the quantum mechanical definition of the electron density distribution. The quantum mechanical model is matched to the experimental X-ray data by making adjustments to the elements of the projector matrix by use of the least-squares technique. The goal then is to obtain a projector matrix that provides a good fit to the X-ray data and is suitable for antisymmetric N -electron wave functions. Such a matrix is called N -representable [2-4]. Evidently, it is desirable to have a good-quality projector matrix for use in initiating the calculations.

A Hartree-Fock or density functional theory calculation produces a suitable projector matrix for initiating the desired calculations. In their present configuration, currently available computer programs can handle a polypeptide composed of several hundred atoms. When this type of capacity is not exceeded, there may be no reason to consider fragment calculations that can produce projector matrices in a stepwise fashion [1]. On the other hand, fragment calculations would certainly be indicated for molecules larger than the capacity of computers and computer programs. Fragment calculations performed on parallel computers may afford an advantage in speed that may be worth considering even when the capacity to make the calculation for the entire molecule at once exists.

Quantum mechanical calculations have been performed on molecular moieties for several purposes in a variety of ways. Some of these types of calculations have already been noted in our previous study [1]. They concerned the work of Yang and Lee [5, 6] who solved the Kohn-Sham [7] equations for partial structures and obtained a

representation of a full molecule by using spatial partition functions to weight a sum of partial structures, the calculations of Christofferson and co-workers [8-10] who solved the Schrödinger equation approximately for partial structures with the use of Hartree-Fock calculations and used the solutions as a source of molecular orbitals which could serve as a basis set of functions for solving the Schrödinger equation for the complete molecule, the approach of Bader and co-workers [11-14] who developed a method for splitting the known electron density of a molecule into densities for atomic groupings that have sharply defined borders, and the "lego" method of Walker and Mezey [15] who make a database of the electron densities of the various atomic groupings required for assembly to form the electron densities of larger molecules of interest.

Additional types of calculations are related to our fragment method, in that they all scale linearly with the number of atoms for essentially the same reasons. They are also similar to ours in that they use expansions in direct (coordinate) space with basis functions localized to one region of space. They are distinguished from one another according to whether the principal objects emphasized are density matrices or wave functions. Li, Nunes, and Vanderbilt [16, 17] obtain a variational density matrix, constrained to be idempotent with off-diagonal elements equal to zero, if they "connect" basis functions separated by a distance larger than a parametric "cutoff" distance. The method is applied in the context of tight-binding models of solids. In a closely related work Daw [18] obtains a variational sparse density matrix and applies this method to three examples, viz., a one-dimensional infinite chain, a semi-infinite chain, and a vacancy in a simple cubic lattice. Hernandez and Gillan [19] employ a density matrix method that relies closely upon that of references [16, 17] to calculate results for crystalline silicon systems.

Mauri, Galli, and Car [20, 21] obtain molecular orbitals by a Kohn-Sham related scheme, which uses basis orbitals defined in local regions of direct space. They apply their method to semiconducting systems and in particular show that it is useful for obtaining molecular dynamics simulations of silicon atoms in a diamond lattice configuration [20] and of liquid carbon at 5000 K [21]. Kim, Mauri, and Galli [22] address explicitly a multiple minimum problem of energy functionals based on localized basis orbitals and treat numerous examples concerning surfaces, bulk systems, and clusters.

Ordejon and co-workers [23], using a method similar to that of Mauri, Galli, and Car [20, 21], obtain results for a tight-binding model of silicon. This method is developed further in a more recent study [24], giving a detailed comparison of their work and that of Daw [18] and Li, Nunes, and Vanderbilt [16, 17]. Goedecker and Teter [25] describe a tight-binding total-energy and molecular dynamics algorithm that scales linearly with system size and is applicable with parallel computers.

Yang and Lee [26] generalize the "divide and conquer" density method [6] to one based on the density matrix. Their density matrix for a full molecule may be obtained from subsystem contributions in a manner consistent with Mulliken population analysis and incorporates zero elements in a way that is analogous to the definitions of our previous study [1] and that of Walker and Mezey [15]. They apply their method in a density functional context to 4-glycine, 8-glycine, and 12-glycine polypeptides.

A density functional/Wannier function formalism is given by Kohn [27] whose objective is similar to that of Lee and Yang [6] but "differs by the central role of the systematic construction of the generalized Wannier function."

In this study, we present purely quantum mechanical calculations. The only use of crystallography is to provide atomic coordinates. The purpose of the calculations is to illustrate how fragment calculations, using standard programs, can be used to obtain parts of projector matrices. These parts can be added together to form the projector matrix for a large molecule, and the calculations increase linearly with increase in the number of atoms in the structure. When the calculation is programmed for high-performance parallel computers, the increase in computing time should be very small. The details of the computation of the individual parts of the projector matrix from the fragments and how the parts are combined are discussed in detail. Once the projector matrix is completed, wave functions follow by standard methods of quantum mechanics.

All of the above methods emphasize that their computational difficulty increases linearly with the number of atoms in the system, in contrast to standard methods which scale with a higher power of that number.

The various aspects of the fragment calculations used in this study for the molecule of leu¹-zervamicin differ somewhat from the de-

scription in our previous work [1] and will be discussed in some detail.

Initial Considerations

The fragment calculations to be presented in this study are based on structural data, i.e., atomic positions, for the molecule leu¹-zervamicin, Ac-Leu-Ile-Gln-Iva-Ile-Thr-Aib-Leu-Aib-Hyp-Gln-Aib-Hyp-Aib-Pro-Phol (Aib: α -aminoisobutyric acid; Iva: isovaline, Hyp: 4-hydroxyproline; Phol: phenylalaninol) obtained from a crystal structure determination [28]. The formation of molecular orbitals follows the procedure presented in Ref. [1], with the necessary adjustments for the different peptide residues and solvents present.

A typical molecular orbital is

$$\phi_i = \sum_{j=1}^{835} C_{ij} \psi_j, \quad (1)$$

where the ψ_j are individual orbitals and the C_{ij} are the coefficients. The upper limit of the sum follows from 1S orbitals for each of the 160 hydrogen atoms and 1S, 2S, 2P_x, 2P_y, and 2P_z orbitals for each of the 135 other atoms, giving 835 total orbitals, ψ_j . The hydrated peptide has 1048 electrons and therefore 524 doubly occupied molecular orbitals and 311 unoccupied ones.

The electron density distribution ρ is

$$\rho = 2 \sum_{i=1}^{524} \phi_i \phi_i. \quad (2)$$

The two on the right side of Eq. (2) reflects the fact that the orbitals are doubly occupied. If the ψ_j form a column vector in Eq. (1), then so do the ϕ_i and

$$\rho = 2 \text{tr } \Phi \Phi^\dagger. \quad (3)$$

The trace includes only occupied molecular orbitals. We may write

$$\Phi = \mathbf{C} \Psi. \quad (4)$$

and from Eq. (3) it follows that

$$\rho = 2 \text{tr } \mathbf{C} \Psi \Psi^\dagger \mathbf{C}^\dagger = 2 \text{tr } \mathbf{C}^\dagger \mathbf{C} \Psi \Psi^\dagger. \quad (5)$$

The following definitions are made

$$\mathbf{S} = \int \Psi \Psi^\dagger dr, \quad (6)$$

where the integration is performed over the individual elements of the product matrix $\psi\psi^\dagger$,

$$\mathbf{R} = \mathbf{C}^\dagger \mathbf{C} \quad (7)$$

and

$$\mathbf{R}\mathbf{S} = \mathbf{P}_a, \quad (8)$$

where \mathbf{P}_a is a projector. The subscript a indicates that unless special steps are taken in forming the matrix ψ the projector matrix will not be symmetric. It can be shown that, as a consequence of the fact that the ϕ are composed of elements that are orthonormal,

$$\mathbf{P}_a^2 = \mathbf{P}_a \quad (9)$$

and

$$\text{tr } \mathbf{P}_a = N, \quad (10)$$

where N is the number of doubly occupied orbitals in the molecule of interest. Equation (9) is the projector property.

It is worthwhile to have a projector \mathbf{P}_s that is symmetric since it reduces, almost by a factor of 2, the number of elements in the projector that must be considered. From Eq. (8), it follows that

$$\mathbf{S}^{1/2} \mathbf{R} \mathbf{S} \mathbf{S}^{-1/2} = \mathbf{S}^{1/2} \mathbf{P}_a \mathbf{S}^{-1/2}. \quad (11)$$

This matrix product is a symmetric projector \mathbf{P}_s and may be written

$$\mathbf{P}_s = \mathbf{S}^{1/2} \mathbf{R} \mathbf{S}^{1/2}. \quad (12)$$

It follows from Eqs. (6)–(8) and (11) that the electron density can be written

$$\rho = 2 \text{tr } \mathbf{R} \psi \psi^\dagger = 2 \text{tr } \mathbf{P}_a \mathbf{S}^{-1} \psi \psi^\dagger \quad (13)$$

and

$$\rho = 2 \text{tr } \mathbf{P}_s \mathbf{S}^{-1/2} \psi \psi^\dagger \mathbf{S}^{-1/2}. \quad (14)$$

In view of Eqs. (4), (13), and (14), it is worthwhile to characterize \mathbf{C} and the molecular orbitals. The matrix \mathbf{C} has 524 rows and 835 columns.

$$\mathbf{C} = \begin{bmatrix} C_{1,1} & C_{1,2} & C_{1,3} & \cdots & C_{1,835} \\ C_{2,1} & C_{2,2} & C_{2,3} & \cdots & C_{2,835} \\ \vdots & & & & \\ C_{524,1} & C_{524,2} & C_{524,3} & \cdots & C_{524,835} \end{bmatrix} \quad (15)$$

\mathbf{C}^\dagger has 835 rows and 524 columns. The product $\mathbf{C}^\dagger \mathbf{C}$ produces a square matrix of dimension 835. If \mathbf{C} multiplies the column matrix of orbitals ψ , it

produces 524 molecular orbitals, each having 835 terms.

According to Eq. (3),

$$\int \rho \, dr = 2 \text{tr} \int \phi \phi^\dagger \, dr = 1048, \quad (16)$$

where the integral is taken over all three-dimensional space. According to Eqs. (5)–(10),

$$\text{tr } \mathbf{P}_a = 524. \quad (17)$$

Fragment Calculation: Example and Results

The purpose of the fragment calculations presented here is to obtain an ab initio projector matrix \mathbf{P} , when ab initio calculations of an entire molecule is either not feasible or considered to be too time-consuming. In our calculations, a fragment consists of an inner core, or "kernel," and a number of neighboring atoms called a "neighborhood." The molecule is divided into a suitable number of kernels, which, when recombined, form the complete molecule.

Since the coordinates of the structure of interest are available, it is readily possible to calculate which atoms would occur within a particular chosen distance from each of the atoms in a kernel. Such atoms would form the neighborhood. In order to effect a pairing of all electrons and an even number of electron pairs, it may be necessary to attach some hydrogen atoms to atoms belonging to the neighborhood or a moiety that is part of the molecule, or both. This can extend the outer limits of the fragment somewhat. It was used in the leu¹-zervamicin example to be described.

A rule employed in our procedure is that all atoms present must be a member of some kernel once and only once. With atomic positions held fixed, the electron density distribution in a fragment is computed. Such a calculation delivers contributions to an \mathbf{R} matrix and an \mathbf{S} matrix from which the portion that concerns the kernel is saved in the form of $\mathbf{P}_k = \mathbf{S}_k^{1/2} \mathbf{R}_k \mathbf{S}_k^{1/2}$ where the subscript k refers to a kernel matrix. The elements that are saved in a kernel projector matrix are described as follows. Those contributions to the \mathbf{P} matrix involving orbitals from a neighborhood atom and an atom in the kernel are saved at the

fractional value of one-half, in accordance with the above rule. If all neighborhood atoms occur only once as part of a kernel, another one-half value would be added to those contributions to the \mathbf{P} matrix already saved at one-half values, when the values associated with the adjoining kernels are calculated. Contributions from pairs of atoms, both in the same kernel, are saved with a coefficient of 1.

In our previous procedure [1], we saved the $\mathbf{R}_k(0)$ instead of the $\mathbf{P}_k(0)$ and obtained an $\mathbf{R}(0)$ matrix for the full molecule by combining all the $\mathbf{R}_k(0)$ for the various kernels. The $\mathbf{P}_a(0)$ matrix was then obtained by multiplying the $\mathbf{R}(0)$ matrix by $\mathbf{S}(0)$ according to Eq. (8). The \mathbf{P}_k are saved here instead and in symmetric form. The \mathbf{P}_k are very good kernel representations and lead to a full \mathbf{P}_s matrix that is a very good projector, an improvement on $\mathbf{P}_a(0)$. The symbol (0) implies a certain pattern of zeros that was special to the cyclic hexapeptide treated in our previous article [1]. For this hexapeptide, it was possible to obtain good results by defining the single adjacent peptide

residue on both sides of a kernel residue as a neighborhood. As a consequence of the denser packing of residues in leu¹-zervamicin, more residues were required to form the neighborhoods of each kernel.

The matrix \mathbf{S} , defined in Eq. (6), is a matrix representing the overlap integrals of pairs of orbitals. For pairs of orbitals belonging to atoms that are separated by large distances, the values of the overlap integrals will be close to zero. The behavior of \mathbf{S} is the reason why the fragment calculations can give accurate values for the elements of \mathbf{P} for the molecule as a whole.

The fragment calculations for the hydrated hexadecapeptide, leu¹-zervamicin, were performed by defining 19 kernels as the 16 peptide residues, two clusters of water molecules and a cluster of a water and an ethanol molecule. In this application, the neighborhoods were formed with atoms within 5 Å of the kernels plus some few additions to assure that all electrons were paired and the number of electron pairs was even. The kernels and their neighborhoods are listed in Table I. The num-

TABLE I
Composition of the 19 fragments, i.e. kernels and their corresponding neighborhoods, used in the calculation of the \mathbf{P} matrix for the hydrated hexadecapeptide, leu¹-zervamicin.^a

Kernel	Neighborhood	Kernel		Neighbors	
		No. of Atoms	No. of Basis	No. of Atoms	No. of Basis
1 (Ac-Leu)	2,3,4,5, H6a	27	69	99	275
2 (Ile)	1,3,4,5,6, H7a, Wb3	19	51	124	348
3 (Gln)	1,2,4,5,6,7, N8, H8a Wb2, Wa3, W4	17	53	147	403
4 (Iva)	1,2,3,5,6,7,8, H9a, Wb2	16	44	148	412
5 (Ile)	1,2,3,4,6,7,8,9, H10f	19	51	159	447
6 (Thr)	O1,2,3,4,5,7,8,9,10, Wb2, Wa3, Wb3	14	42	158	446
7 (Aib)	O2,3,4,5,6,8,9,10, H11e, H11h, Wb2, Wa3	13	37	153	441
9 (Leu)	O3,4,5,7,9,10,11,12	19	51	143	411
9 (Aib)	O4,5,6,7,8,10,11,12,13	13	37	164	465
10 (Hyp)	O5,6,7,8,9,11,12,13,14, Wa1, Wa2	15	47	142	414
11 (Gln)	O7,8,9,10,12,13,14,15, Wa1, Wa2	17	53	164	480
12 (Aib)	8,9,10,11,13,14,15, H16a, H16c, EtOH, Wa1	13	37	141	401
13 (Hyp)	9,10,11,12,14,15,16, EtOH, Wa1, Wa2, W8	15	47	142	410
14 (Aib)	10,11,12,13,15,16, Wa1, Wa2	13	37	117	345
15 (Pro)	11,12,13,14,16	14	42	143	411
16 (Phol)	O12,13,14,15, EtOH, W8	23	67	112	311
EtOH, W8	12,13,16	12	28	116	324
Wa1, Wa2	10,11,12,13,14	6	14	85	253
Wb2, Wa3, Wb3, W4	2,3,4,6,7	12	28	145	411

^a The individual numbers in the first column, associated with the 16 sequential peptide residues, imply the same corresponding residues in column 2. Other numbers in column 2 have letters with them, e.g., H for hydrogen, O for oxygen, N for nitrogen, and W for water. EtOH symbolizes ethanol. The structural aspects of these symbols are to be found in Ref. [28].

bers refer to the peptide residues in the sequence that was given above in the description of the chemical content of the leu¹-zervamicin molecule. The symbols in Table I correspond to those found in the crystal structure analysis [28]. The crystal structure analysis provided the atomic coordinates used in the calculations reported in this article and also afforded the information from which the selection of the associated solvent molecules was based. The last four columns of Table I show the number of atoms and the number of basis functions for each kernel and for each neighborhood.

The Hartree-Fock calculations for the entire hydrated leu¹-zervamicin molecule and for the separate fragment calculations were made by use of the Gaussian 94 program [29] employing the STO3g basis. The structure of the **R** matrix, obtained from the calculations, which is preliminary to obtaining the projector matrix by use of Eq. (12), is now presented in some detail. A schematic diagram of the entire **R** matrix, obtained from the fragment calculations, is shown in Figure 1. The horizontal rows are characterized in Table I. All of the squares in Figure 1 contain numerous elements of the **R** matrix which has a dimension of 835. The values of the elements in the dark blocks, obtained from the fragment calculations are entered in the dark blocks with a coefficient of 1. The values of the elements in the gray areas are formed from two fragment calculations, one in which one orbital is part of a kernel atom and the other is part of a neighborhood atom and a second calculation in which the roles of the same two orbitals are interchanged. Each such fragment calculation produces a value which is saved with a coefficient of one half. The two values are then added together to give values for the appropriate elements in the **R** matrix [1].

The number of elements for the **R** matrix represented in the various boxes in Figure 1 varies considerably and may be judged by examination of Table I with respect to the atomic composition of the kernels and also their neighborhoods. Nevertheless each row and each column of both **R** and **P** has a total of 835 elements. The occurrence of empty boxes in Figure 1 is a consequence of the limitation put on the extent of the neighborhoods. Estimates of the validity of the limitation can come from various comparisons, one of the most obvious being an inspection of corresponding elements in the full molecule calculation and the fragment calculation. There are a total of 697,225 elements in

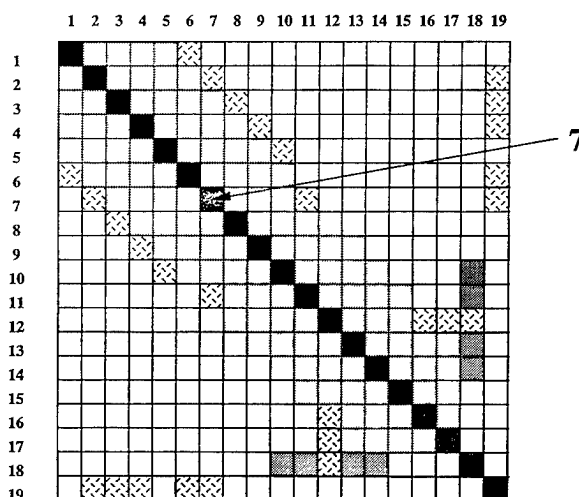


FIGURE 1. Schematic diagram of the **R** matrix obtained from the fragment calculations for hydrated leu¹-zervamicin. The numbers in the figure label the kernels as in Table I. The elements in the dark squares are composed of functions of the coefficients of pairs of orbitals associated with the atoms of the particular kernel. The elements in the gray squares and hatched squares are composed of functions of the coefficients of pairs of orbitals, one of which is associated with a kernel atom of the dark square in the same row and the other is associated with an atom of the labeled neighborhood. The contents of the dark square labeled by kernel 7 are shown in Figure 2 at higher resolution.

the matrix and 412,902 of them, i.e., 59.2%, have a zero value.

The numbers label the kernels as in Table I. The elements in the squares are functions solely of the coefficients of pairs of orbitals associated with the kernels that label the squares. The elements of the dark block-diagonal squares are functions of the coefficients of pairs of orbitals associated with kernel atoms. The gray squares in the same row as a dark square contain elements functions of the coefficients for pairs of orbitals, one of which is associated with a kernel atom and one with a neighborhood atom. The hatched squares contain elements that are functions of the coefficients of pairs of orbitals from only some of the neighborhood atoms represented by the hatched square and only some of the kernel atoms represented by the dark square in the same row.

Figure 2 is an enlargement of the dark block in Figure 1 which represents the elements of the **R** matrix formed from functions of the coefficients of the orbitals associated with the atoms comprising

kernel number 7. Those atoms label the individual squares that contain within them the elements of the **R** matrix that derive from the orbitals associated with the labeling atoms.

A further enlargement of the box labeled N7, N7 in Figure 2 is made in Figure 3. The specific orbitals associated with N7 label the squares that contain within them a single function of the coefficients of the corresponding orbitals. The numerical values of the functions in this calculation are given.

As mentioned above, as soon as a contribution to the **R** matrix was obtained from a fragment calculation, it was converted to the corresponding contribution to the **P** matrix by the use of Eq. (12) and stored. The sum of all such contributions forms the **P** matrix for the complete structure. Also noted previously was the fact that a consequence of the fragment calculations is that the values of the elements in the blank squares are replaced by zeros. The resulting **P** matrix has the same pattern of zeros as the **R** matrix, but the filled squares have more complicated functions of the orbital coefficients and do not follow the labeling of the rows and columns of Figure 1. Both **R** and **P** are symmetric.

FIGURE 2. Contents at higher resolution of the dark square in Figure 1 labeled by kernel 7. The elements in the squares are functions of the coefficients of the orbitals associated with the atoms that label the squares. The contents of the square labeled by N7 are shown in Figure 3 at orbital resolution.

	N7	1S	2S	2Px	2Py	2Pz
N7						
1S	1.0394	-.1470	.0044	.0013	-.0010	
2S	-.1470	.6247	-.0331	-.0105	-.0126	
2Px	.0044	-.0331	.4262	-.0953	-.0899	
2Py	.0013	-.0105	-.0953	.5837	.2245	
2Pz	-.0010	-.0126	-.0899	.2245	.6546	

FIGURE 3. Contents at orbital resolution of the square in Figure 2 labeled by N7. The elements in the squares are functions of the coefficients of the orbitals that label the squares. These rather complex functions of the coefficients have the values given in the squares.

Comparison of Electron Densities

Isodensity surfaces have been calculated by use of Eqs. (1) and (2) from the Hartree-Fock orbitals for the hydrated leu¹-zervamicin molecule. Use was made of the **P** matrix obtained at once for the full molecule and that obtained from the fragment calculations. The two sources gave electron densities that appeared to be quite similar. Therefore, a portion of the one obtained from the full molecule calculation, as a representative of both types of calculation, is illustrated in Figure 4, at an isodensity surface of $0.005 \text{ e}/\text{\AA}^3$. Confining the computed volume to a region of interest, as illustrated, saves time and memory when desirable or necessary. A ball-and-stick model of the structure is superimposed. In order to obtain a more quantitative insight into the similarity of both types of density calculation, a series of difference isodensity surfaces were calculated in which differences that did not exceed increasingly larger values were omitted. Evidently, this is a calculation that can determine and locate the largest differences between the electron densities.

The difference isodensity surfaces shown in Figures 5 and 6 were obtained from $P_F - P_K$ by use of Eq. (14), where the subscripts imply full molecule

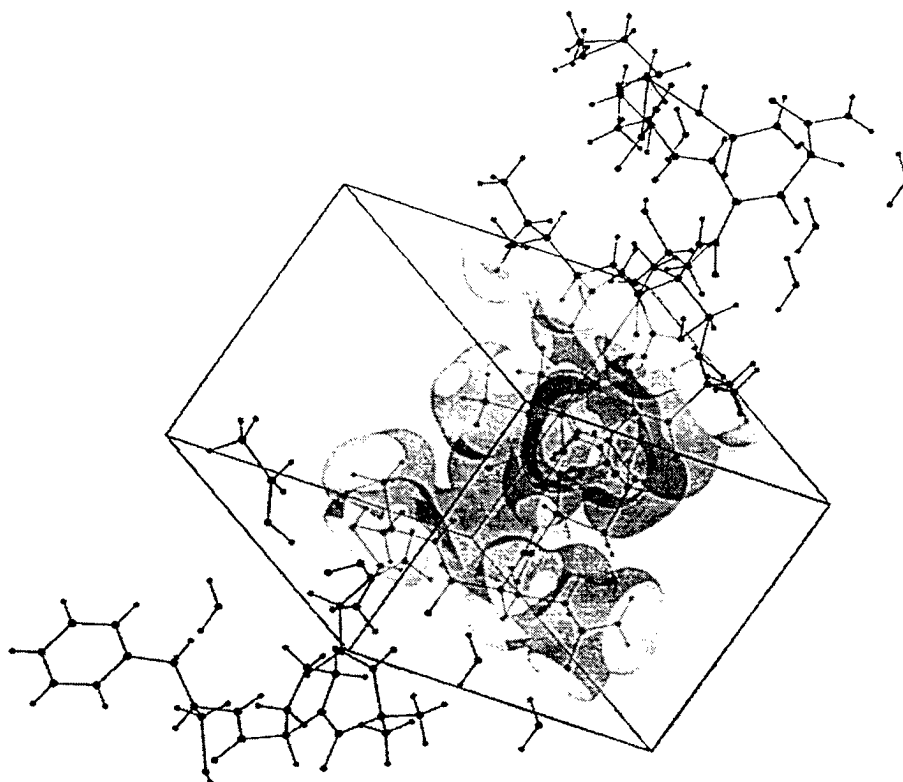


FIGURE 4. Isodensity surface of $0.005 \text{ e}/\text{\AA}^3$ within a selected volume for hydrated leu¹-zervamicin. This isodensity surface was obtained from a Hartree-Fock calculation performed on the entire hydrated molecule and the further use of Eqs. (1) and (2) applied to the resulting wave functions. A ball-and-stick model of the molecule is superimposed on the isodensity surface.

(F) and sum over kernel (K) matrices. A difference isodensity surface is shown at the values of $1.0 \times 10^{-3} \text{ e}/\text{\AA}^3$ in Figure 5, and $-1.2 \times 10^{-3} \text{ e}/\text{\AA}^3$ in Figure 6. Some small fuzzy regions are visible at which there are differences as large or larger than the values of the difference isodensities shown. The fuzzy regions should all disappear at slightly larger difference isodensities. Evidently, the fuzzy regions in Figures 5 and 6 are quite small and highly localized.

The difference studies shown in Figures 5 and 6 indicate that the electron density is well represented by the P matrix obtained from the fragment calculations. As has been noted, the method for developing a P matrix presented here differs from the one presented in our previous article [1]. The P matrix formed here is more accurate than that formed from the R matrix in the previous study. It was not necessary to employ the Clinton equations here to improve the projector quality. In fact, use of the Clinton equations left the good quality of the P matrix unchanged. Even greater accuracy

may accrue if more atoms were included in the neighborhoods of the kernels.

Concluding Remarks

With the use of the known structure of the molecule, leu¹-zervamicin, from a crystal structure analysis, it has been shown once again that it is feasible to make ab initio quantum mechanical calculations to good approximation for very large molecules. With the use of sequential computers, the computations increase only linearly with time. Were programs to become available for parallel computers, the time required for very large structures should increase even more slowly. The key to such computations is the fragment calculation wherein a molecule is divided into kernels and ab initio calculations are performed on each of the kernels and their corresponding neighborhoods of atoms. The theoretical basis for the fragment calculations suggests that the larger the neighborhood

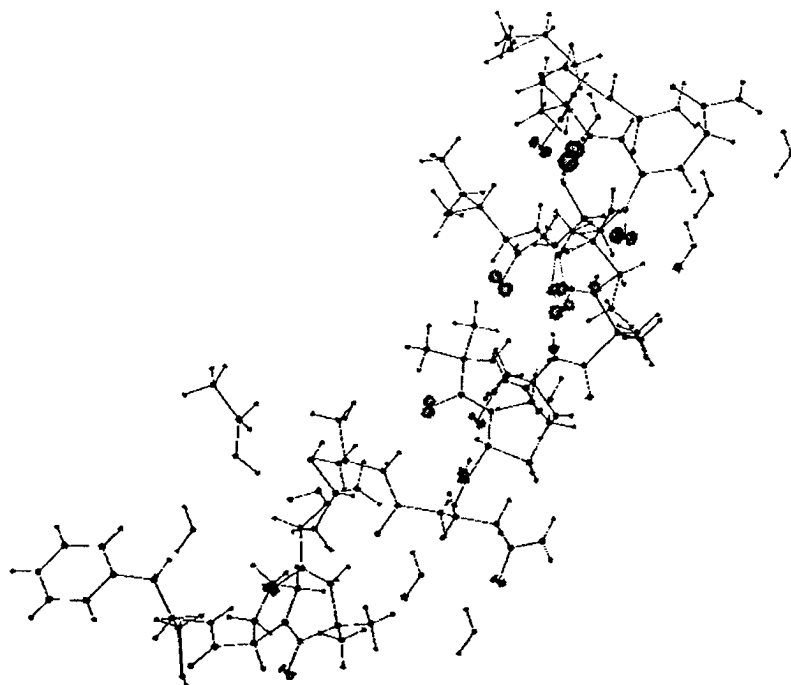


FIGURE 5. Difference isodensity surface of $1.0 \times 10^{-3} \text{ e}/\text{\AA}^3$ for the hydrated leu¹-zervamicin molecule. The difference isodensity surface was obtained from $\mathbf{P}_F - \mathbf{P}_K$. Small fuzzy regions represent the remaining difference. They involve a small molecular volume and are evidently small in magnitude.

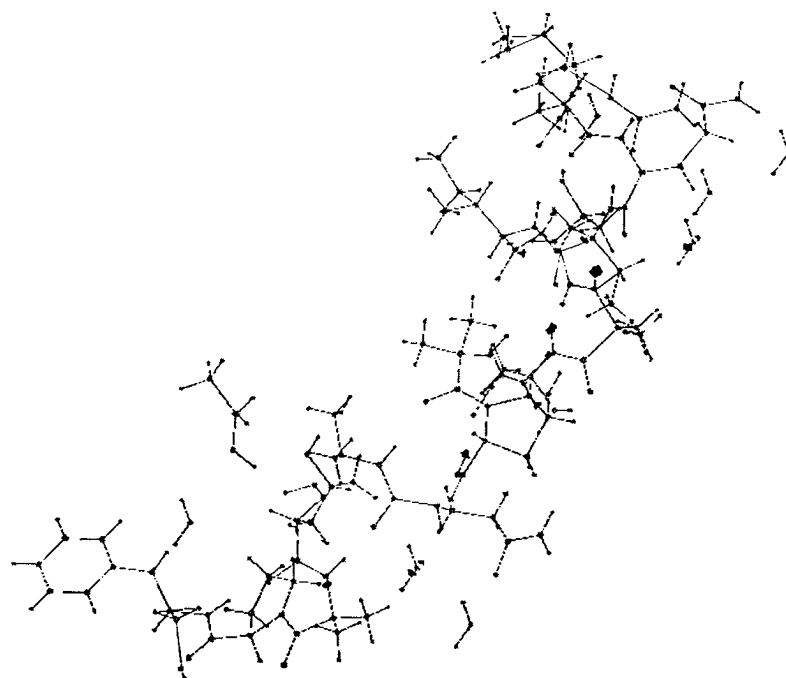


FIGURE 6. Difference isodensity surface of $-1.2 \times 10^{-3} \text{ e}/\text{\AA}^3$ for the hydrated leu¹-zervamicin molecule. The difference isodensity surface was obtained from $\mathbf{P}_F - \mathbf{P}_K$. Small fuzzy regions represent the remaining difference. They involve a small molecular volume and are evidently small in magnitude.

of a kernel, the greater the accuracy. The kernel matrices consisting of the results of interactions of the kernel orbitals with each other with a weight of one and the results of interactions of kernel orbitals and neighborhood orbitals with a weight of one-half, are additive and combine to form the desired matrix for the complete molecule. The procedure used here for the calculation of the kernel matrices resulted in a total matrix with good projector properties, namely, $\text{tr}(\mathbf{P}^2 - \mathbf{P})^2 = 8 \times 10^{-5}$.

The hexadecapeptide of this article was treated within the context of the ab initio Hartree-Fock approximation. However, the concept of extracting kernel matrices from fragments smaller than a full molecule would be applicable within the context of any method based on a molecular orbital representation, e.g., density functional theory.

The kernel-neighborhood fragment calculation affords the opportunity to make ab initio calculations for molecules whose complexity exceeds the capacity of available computer programs, particularly since the increase in computer time is essentially a linear function of the complexity. In addition, the fragment calculation may save time when employed as an alternative to a calculation made on a complex, full molecule.

The \mathbf{P} matrix obtained from fragment calculations may be used to derive molecular properties from the density matrix using the standard rules of quantum mechanics.

ACKNOWLEDGMENT

This research was supported in part by the Office of Naval Research and in part by Public Health Service Grant GM30902. One of us (L.M.) wishes to thank the U.S. Navy Summer Faculty Research Program administered by the American Society of Engineering Education for the opportunity to spend summers at NRL.

References

1. L. Massa, L. Huang, and J. Karle, *Int. J. Quantum Chem., Quantum Chem. Symp.* No. 29, 371 (1995).
2. P.-O. Löwdin, *Phys. Rev.* **97**, 1474 (1955).
3. R. McWeeney, *Rev. Mod. Phys.* **32**, 335 (1960).
4. A. J. Coleman, *Rev. Mod. Phys.* **35**, 668 (1963).
5. W. Yang, *Phys. Rev. Lett.* **66**, 1438 (1991).
6. C. Lee and W. Yang, *J. Chem. Phys.* **96**, 2408 (1992).
7. W. Kohn and L. J. Sham, *Phys. Rev. A* **140**, 1133 (1965).
8. R. E. Christoffersen and G. M. Maggiora, *Chem. Phys. Lett.* **3**, 419 (1969).
9. R. E. Christoffersen, L. L. Shipman, and G. M. Maggiora, *Int. J. Quantum Chem.* **5**, 143 (1971).
10. R. E. Christoffersen, D. Spangler, G. G. Hall, and G. M. Maggiora, *J. Am. Chem. Soc.* **95**, 8526 (1973).
11. R. F. W. Bader and T. T. Nguyen-Dang, *Adv. Quantum Chem.* **14**, 63 (1981).
12. R. F. W. Bader, *Acc. Chem. Res.* **18**, 9-15 (1985).
13. R. F. W. Bader, M. T. Carroll, J. Chessman, and C. Chang, *J. Am. Chem. Soc.* **109**, 7968 (1987).
14. R. F. W. Bader, *Atoms in Molecules—A Quantum Theory* (Oxford University Press, Oxford, 1990).
15. P. D. Walker and P. G. Mezey, *J. Am. Chem. Soc.* **115**, 12423 (1993).
16. X.P. Li, R. W. Nunes, and D. Vanderbilt, *Phys. Rev. B* **47**, 10891 (1993).
17. R. W. Nunes and D. Vanderbilt, *Phys. Rev. B* **50**, 17611 (1994).
18. M. S. Daw, *Phys. Rev. B* **47**, 10895 (1993).
19. E. Hernández and M. J. Gillan, *Phys. Rev. B* **51**, 10157 (1995).
20. F. Mauri, G. Galli, and R. Car, *Phys. Rev. B* **47**, 9973 (1993).
21. F. Mauri and G. Galli, *Phys. Rev. B* **50**, 4316 (1994).
22. J. Kim, F. Mauri, and G. Galli, *Phys. Rev. B* **52**, 1640 (1995).
23. P. Ordejón, D. A. Drabold, M. P. Grumbach, and R. M. Martin, *Phys. Rev. B* **48**, 14646 (1993).
24. P. Ordejón, D. Drabold, R. M. Martin, and M. P. Grumbach, *Phys. Rev. B* **51**, 1456 (1995).
25. S. Goedecker and M. Teter, *Phys. Rev. B* **51**, 9455 (1995).
26. W. Yang and T.-S. Lee, *J. Chem. Phys.* **103**, 5674 (1995).
27. W. Kohn, *Chem. Phys. Lett.* **208**, 167 (1993).
28. I. L. Karle, J. L. Flippen-Anderson, S. Agarwalla, and P. Balaram, *Biopolymers* **34**, 721 (1994).
29. M. J. Frisch, G. W. Trucks, H. B. Schlegel, P. M. W. Gill, B. G. Johnson, M. A. Robb, J. R. Cheeseman, T. Keith, G. A. Petersson, J. A. Montgomery, K. Raghavachari, M. A. Al-Laham, V. G. Zakrzewski, J. V. Ortiz, J. B. Foresman, J. Cioslowski, B. B. Stefanov, A. Nanayakkara, M. Challacombe, C. Y. Peng, P. Y. Ayala, W. Chen, M. W. Wong, J. L. Andres, E. S. Replogle, R. Gomperts, R. L. Martin, D. J. Fox, J. S. Binkley, D. J. Defrees, J. Baker, J. P. Stewart, M. Head-Gordon, C. Gonzalez, and J. A. Pople, *Gaussian 94*, Revision C.4, Gaussian Inc., Pittsburgh, PA, 1995.

Fission of Metal Clusters: A Comparison of Jellium Model Calculations and Shell Correction Method Calculations

HIROYASU KOIZUMI* and YUJI FUKUMOTO

Faculty of Science, Himeji Institute of Technology, Kamigori-cho, Ako-gun, Hyogo 678-12, Japan;
e-mail for H.K.: koizumi@sci.himeji-tech.ac.jp

Received February 24, 1996; revised manuscript received March 13, 1996; accepted March 18, 1996

ABSTRACT

We investigate the fission process $\text{Ag}_{23}^{2+} \rightarrow \text{Ag}_{12}^{+} + \text{Ag}_{11}^{+}$ in order to compare total energies that calculated by the shell correction method and jellium models. A cavity potential and a Woods-Saxon-type potential are used as the shell potential for the shell correction method, with which the single-particle energy levels are calculated. Shell corrections are obtained by using the Balian-Bloch formula and by smoothing the discrete energy levels in the shell potentials. The jellium model calculations are performed in the framework of the local spin density functional approximation. The conventional jellium model and stabilized jellium model are used. Although the qualitative agreement between the shell correction method calculations and the stabilized jellium calculations is very good, an improvement of the liquid drop energy will be necessary for the satisfactory quantitative agreement. © 1996 John Wiley & Sons, Inc.

1. Introduction

The concepts and methodologies used for atomic nuclei are very useful in studying metal clusters. The method of shell corrections is one of them [1–3]. In this method the cluster is first considered as a classical liquid drop, then quantum mechanical corrections are added. The scheme presented by the method of shell corrections, i.e., a classical description of a system with

quantum mechanical corrections, may be a promising method to deal with large systems where purely microscopic calculations are practically impossible but purely macroscopic theories overlook important details.

The most important quantum mechanical correction arises from the inhomogeneous distribution of single-particle energy levels in an effective potential such as the Hartree-Fock field. The effective potential is not known unless we calculate it, but we may be able to construct a model potential which mimics the effective potential very well. This model potential is called the shell potential.

* To whom correspondence should be addressed.

The single-particle energy levels are calculated with the shell potential and then the shell correction is obtained as the energy fluctuation caused by the inhomogeneous distribution of the discrete energy levels.

In order to obtain satisfactory results from shell correction calculations, we have to have a good shell potential. Actually the shell potential needs not to mimic the detail of the effective potential, but the energy level distribution near the highest occupied level or the Fermi level. In the previous calculations we used a cavity potential of a cluster shape as the shell potential. In the present work we also use a Woods-Saxon-type potential, which is commonly used in nuclear physics.

Once the single-particle energy levels are obtained, the next step is to calculate a smoothed density of states. For the cavity potential, there exists the formula by Balian and Block. But such a formula is not available for the Woods-Saxon potential. Therefore, we will calculate the smoothed density of states from the discrete density of states by employing the standard method in nuclear physics [4].

We also performed the jellium model calculations. We used two types of jellium models, the conventional jellium model, and the stabilized jellium model. The stabilized jellium model is a modification of the conventional jellium model so that the jellium is in mechanical equilibrium. This model is known to give much better results for surface energy of metals than the conventional one [5, 6].

II. Method

A. SHELL CORRECTION METHOD

In the shell correction method the metal cluster is first considered as a charged liquid drop. The energy of the liquid drop, E_{LD} , is given by

$$E_{LD} = E_{vol} + E_{surf} + E_{Coulomb}, \quad (2.1)$$

where the surface energy, E_{surf} , is a product of surface energy σ and surface area S , the Coulomb energy, $E_{Coulomb}$, is the Coulomb energy of the charged conductor, and the volume energy, E_{vol} , is the energy proportional to the number of the atoms in the cluster. The volume energy is omitted in the following discussion because we only consider the volume conserving deformations and fission.

The shape of the cluster is determined by a shape function. We used the following shape function, which is a modified version of the one used in nuclear fission [2]:

$$\rho_s(z) = s \left\{ \left[1 - (z/s)^2 \right] \left[(C^{-3} - B/5) + 2\alpha Bz/s + B(z/s)^2 \right] \right\}^{1/2}. \quad (2.2)$$

The shape of the cluster is given by $\rho_s(z) = \sqrt{x^2 + y^2} = \rho$. The modification is made so that the volume ratio of two fragments is constant along the fission line

$$BC^3 = \alpha^2 - \frac{1}{5}, \quad (2.3)$$

where the parameter α is determined by the volume ratio of the two fragments which contain N_1 atoms and N_2 atoms, respectively:

$$\frac{N_1}{N_2} = \frac{(\alpha - 1)^4(4 + \alpha)}{(\alpha + 1)^4(4 - \alpha)}. \quad (2.4)$$

Now we add the shell correction to the liquid drop energy as the quantum mechanical correction. The correction we take into account is the energy fluctuation from the average that arises from the inhomogeneous distribution of the valence electron levels.

The shell correction is given by

$$E_{shell} = \sum_{i=1}^{\infty} n_i \varepsilon_i - \int_{-\infty}^{\varepsilon_F} \varepsilon \Gamma(\varepsilon) d\varepsilon, \quad (2.5)$$

where ε_i and n_i are the energy and occupation number of the i th energy level in the shell potential, $\Gamma(\varepsilon)$ is a smoothed density of states, and ε_F is the Fermi energy associated with the smoothed density of states.

The standard formula to obtain the smoothed density of states from the discrete density of states of the shell potential, $g(\varepsilon) = \sum_i \delta(\varepsilon - \varepsilon_i)$, is [4]

$$\Gamma(\varepsilon) = \gamma^{-1} \sum_i f[(\varepsilon - \varepsilon_i)/\gamma], \quad (2.6)$$

where the smoothing function f is expressed using the Hermit polynomials H_k as

$$f(x) = \pi^{-1/2} \exp(-x^2) \sum_{k=0,2}^{2M} a_k H_k(x), \quad (2.7)$$

where

$$a_0 = 1, \quad a_k = -a_{k-2}/2 \quad \text{for } k \geq 2. \quad (2.8)$$

We use $2M = 6$ in the present work.

We try two types of shell potentials. One is a cavity potential in which free electrons move in the cavity of the cluster shape, and the other is a Woods-Saxson-type potential, which is commonly used in nuclear physics.

The Woods-Saxson potential is given by

$$V(\rho, z) = \frac{V_0}{1 + \exp[d(\rho, z)/d_0]}, \quad (2.9)$$

where

$$d(\rho, z) = \pm \sqrt{\rho^2 - \rho_s(z)^2}, \quad (2.10)$$

and the $+$ sign is taken if (ρ, z) is inside the cluster and the $-$ sign is taken if it is outside. The parameters V_0 and d_0 are set to $V_0 = -0.9(\text{a.u.})$, $d_0 = \pi r_{ws}$, where r_{ws} is the Wigner-Seitz radius [$r_{ws} = 3.02(\text{a.u.})$ for silver].

In addition to the smoothing formula [Eq. (2.6)], the Balian and Bloch formula [7] can be used for the smoothed density of states in the cavity potential

$$\Gamma_{BB}(\varepsilon) = \frac{m}{2\pi^2\hbar^2} \left[V\varepsilon - \frac{\pi S}{4} + \frac{1}{6k} \int dS \left(\frac{1}{R_1} + \frac{1}{R_2} \right) \right], \quad (2.11)$$

where

$$k = \sqrt{\frac{2m\varepsilon}{\hbar^2}}, \quad (2.12)$$

and S and V are surface area and volume of the cavity, respectively, and R_1 and R_2 are the main curvatures of radii of the surface. We used Eqs. (2.6) and (2.11) for the smoothed density of states for the cavity potential, while Eq. (2.6) is used for that for the Woods-Saxson potential.

B. JELLIUM MODEL

The jellium model has been shown to give satisfactory results for metal clusters [8, 9]. In this model valence electrons move in the positive ion cores which is approximated by a uniformly

charged background jellium. We solve the problem of valence electrons moving in the background jellium by employing the density functional method of Kohn and Sham [10]. The local-spin density functional by Vosko, Wilk, and Nusair [11] is used.

The eigenvalue problem of the Kohn-Sham equations are solved using the discrete valuable representation (DVR) [12-14]. In this representation the basis is coordinate points. A DVR basis $\{|x_\alpha\rangle, \alpha = 1, \dots, N\}$ is related to a finite basis representation (FBR) basis $\{|\phi_i\rangle, i = 1, \dots, N\}$ via a unitary transformation:

$$|x_\alpha\rangle = \sum_{i=1}^N U_{\alpha i} |\phi_i\rangle, \quad |\phi_i\rangle = \sum_{\alpha=1}^N U_{i\alpha}^\dagger |x_\alpha\rangle \quad (2.13)$$

where the unitary matrix U is given by

$$U = YS^{-1/2}, \quad (2.14)$$

$$Y_{\alpha i} = \langle x_\alpha | \phi_i \rangle, \quad S_{ij} = \sum_{\alpha=1}^N \langle \phi_i | x_\alpha \rangle \langle x_\alpha | \phi_j \rangle. \quad (2.15)$$

Because the shape function (2.2) has an axial symmetry, we use cylindrical coordinates assuming the axial symmetry of the Kohn-Sham orbitals. Then the angular momentum around the z axis, ν , becomes a good quantum number, and we solve two-dimensional eigenvalue problems for each ν . As the basis for the z coordinate we use

$$\langle z_\alpha | q_i \rangle = \sqrt{\frac{2}{z_{\max} - z_{\min}}} \sin q_i (z_\alpha - z_{\min}), \quad (2.16)$$

$$q_i = i\pi/(z_{\max} - z_{\min}), \quad i = 1, \dots, N_z$$

$$z_\alpha = z_{\min} + \alpha(z_{\max} - z_{\min})/N_z, \quad \alpha = 1, \dots, N_z,$$

where N_z is the number of grid points in the z coordinate, z_{\min} and z_{\max} are the minimum and the maximum of the grids, respectively.

Note that the vectors $\langle z | q_i \rangle$ are eigenvectors of the z component kinetic energy

$$-\frac{\partial^2}{\partial z^2} \langle z | q_i \rangle = q_i^2 \langle z | q_i \rangle. \quad (2.17)$$

As the basis for the ρ coordinate, we use the following two sets:

$$\langle \rho_{\alpha,0} | n, 0 \rangle = e^{-a_{\alpha,0}/2} \frac{\sqrt{a_{N_{\rho},0}}}{\rho_{\max}} L_n(a_{\alpha,0}), \quad (2.18)$$

$$\rho_{\alpha,0} = \rho_{\max} \sqrt{a_{\alpha,0}/a_{N_{\rho},0}}, \quad \alpha = 1, \dots, N_{\rho},$$

and

$$\langle \rho_{\alpha,1} | n, 1 \rangle = e^{-a_{\alpha,1}/2} \frac{\sqrt{a_{\alpha,1} a_{N_{\rho},1}}}{\rho_{\max} \sqrt{n+1}} L_n^1(a_{\alpha,1}), \quad (2.19)$$

$$\rho_{\alpha,1} = \rho_{\max} \sqrt{a_{\alpha,1}/a_{N_{\rho},1}}, \quad \alpha = 1, \dots, N_{\rho},$$

where N_{ρ} is the number of grid points in the ρ coordinate, ρ_{\max} is the maximum of the grids, L_n and L_n^1 are the Laguerre polynomials and the associated Laguerre polynomials, respectively, and $a_{\alpha,0}$ and $a_{\alpha,1}$ are their zeros, respectively. The reason we use two basis sets is that the behavior of wave functions at $\rho = 0$ is significantly different depending on whether the angular momentum around z axis is even or odd. Therefore changing grid points increases the accuracy of the calculated energy levels.

Note that the vectors $\langle \rho | n, \nu \rangle$ are eigenvectors of the two-dimensional harmonic oscillator

$$\begin{aligned} & \left[-\frac{1}{2} \frac{\partial^2}{\partial \rho^2} - \frac{1}{2\rho} \frac{\partial}{\partial \rho} + \frac{\nu^2}{2\rho^2} + \frac{a_{N_{\rho},\nu}}{2} \left(\frac{\rho}{\rho_{\max}} \right)^2 \right] \\ & \times \langle \rho | n, \nu \rangle \\ & = \frac{a_{N_{\rho},\nu}}{\rho_{\max}^2} (2n + \nu + 1) \langle \rho | n, \nu \rangle. \end{aligned} \quad (2.20)$$

The bases for z and ρ are combined to the total DVR basis, $\{|\rho_{\alpha,0}\rangle \otimes |z_{\beta}\rangle\}$ and $\{|\rho_{\alpha,1}\rangle \otimes |z_{\beta}\rangle\}$. The first set is used if the angular momentum around the z axis of the single-particle level is even, and the second set is used if it is odd. This distinction is important to obtain accurate single-particle energy levels.

In addition to the conventional jellium model, we try the stabilized jellium model. It has been pointed out that the normal jellium model is not in mechanical equilibrium if it is applied to metals other than sodium. Methods of improvement to take account mechanical equilibrium have been presented by Perdew et al. [5] and Shore et al. [6].

By following Shore we add

$$v_0 = e_{\text{jell}}(n) - \mu_{\text{jell}}(n) \quad (2.21)$$

to the chemical potential inside the jellium, where $e_{\text{jell}}(n)$ is the energy per electron in the uniform electron gas of density n and μ_{jell} is the chemical potential of the uniform electron gas.

Using

$$e_{\text{jell}}(n) = \frac{3}{10} (3\pi^2 n)^{2/3} + e_{\text{xc}}(n), \quad (2.22)$$

$$\mu_{\text{jell}}(n) = \frac{\partial}{\partial n} n e_{\text{jell}}(n), \quad (2.23)$$

and the local density functional of VWN [11], we obtain $v_0 = -0.024$ (a.u.) for silver [$n = 3/(4\pi r_{\text{ws}}^3)$, $r_{\text{ws}} = 3.02$ (a.u.)]. In the actual calculation the step function causes instability in the calculation. Therefore we broaden it by using the Woods-Saxon potential form (2.9) with $V_0 = v_0$, $d_0 = r_{\text{ws}}$.

III. Results and Discussion

We apply the jellium model and shell correction method calculations to the fission $\text{Ag}_{23}^{2+} \rightarrow \text{Ag}_{12}^{+} + \text{Ag}_{11}^{+}$. In Figure 1 shapes of the cluster at various values of parameters B and C are depicted. Parameter C describes elongation and B describes

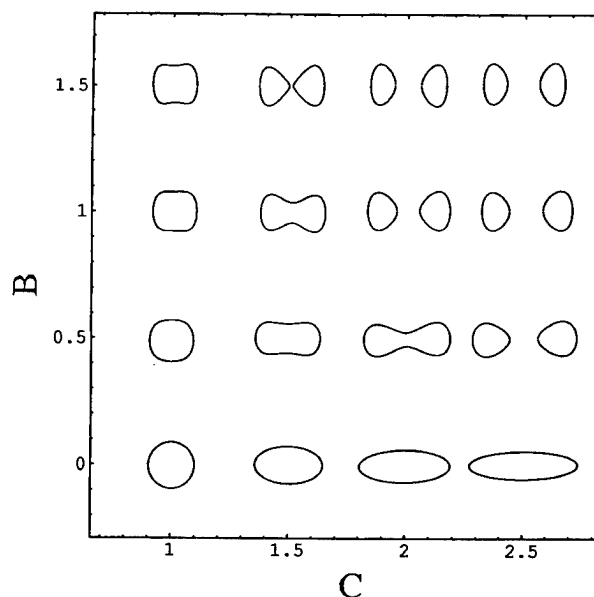


FIGURE 1. Shapes of the cluster at various values of B and C for $\text{Ag}_{23}^{2+} \rightarrow \text{Ag}_{12}^{+} + \text{Ag}_{11}^{+}$ ($\alpha = 0.0116$).

neck formation and scission. The liquid drop energy surface is shown in Figure 2. This surface is very smooth and does not have much structure. In Figure 3 the total energy surface obtained by the shell correction method is depicted. This surface is rich in structure due to the shell correction. There is a local minimum at $C = 1.5$, $B = 0.5$. A ridge appears around $B = 0.52$, $2 \leq C \leq 3$. There are two saddles for fission: One of them is around $C = 2.6$, $B = 0.25$ and the other is around $C = 1.5$, $B = 1.2$. Usually only one saddle dominates [2], but for this fission process, there are two comparable saddles for fission.

Now we compare total energies obtained by the shell correction method and the jellium models along two fission paths shown in Figure 2. These two paths pass near the two saddles for fission by the shell correction method estimate. The fragments are prolatelike along path 1, while the fragments are oblatelike along path 2. It is predicted that path 1 produces low-spin fragments, $\text{Ag}_{11}^+(S = 0)$ and $\text{Ag}_{12}^+(S = \frac{1}{2})$, while path 2 produces the high-spin fragments, $\text{Ag}_{11}^+(S = 1)$ and $\text{Ag}_{12}^+(S = \frac{3}{2})$ [15].

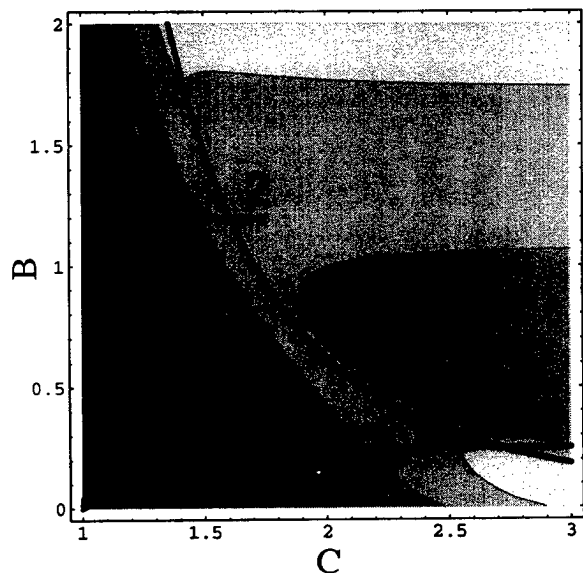


FIGURE 2. Contour plot of the liquid drop energy for $\text{Ag}_{23}^{2+} \rightarrow \text{Ag}_{12}^+ + \text{Ag}_{11}^+$. The zero of the energy is at $C = 1$, $B = 0$. The contours are from 1 to 4 eV with spacing of 1 eV. The gray levels of the shading run from black to white with increasing energy. The lines denoted by 1 and 2 are path 1, $B = 0.5(C - 1)$, $1 \leq C \leq 1.5$ and $B = 0.25$, $1.5 \leq C \leq 3$; and path 2, $B = 0.5(C - 1)$, $1 \leq C \leq 1.2$ and $B = 1.2$, $1.2 \leq C \leq 1.75$, respectively. The solid curve is the fission line.

The parameters for the jellium calculations are $z_{\text{max}} = 35.0(\text{a.u.})$, $z_{\text{min}} = -35.0(\text{a.u.})$, $\rho_{\text{max}} = 25.0(\text{a.u.})$, $N_z = 50$, and $N_p = 30$. The convergence problem of self-consistent calculation caused by near-degenerate levels are handled by broadening the occupation numbers using the finite temperature distribution. The temperature is set to 500 K. It is seen in the calculation that if we use a much higher temperature than 500 K, the energy barrier is reduced but it does not change much by raising the temperature up to 1000 K. Therefore the broadening by 500 K will not change the barrier significantly.

In Figure 4 the total energy and shell correction along path 1, $B = 0.5(C - 1)$, $1 \leq C \leq 1.5$; $B = 0.25$, $1.5 \leq C \leq 3$, are depicted. The cluster first elongates and then disintegrates along this path. Shell corrections are qualitatively the same irrespective of the method as is seen in the bottom figure of Figure 4. The abrupt jump at $C = 2.75$ seen in the shell correction energy by the Balian-Bloch formula is an artifact. This comes from the difference in the accuracy of the Balian-Bloch formula for a single cluster and for fragments. Because the number of atoms in the single cluster and its fragments are different, the

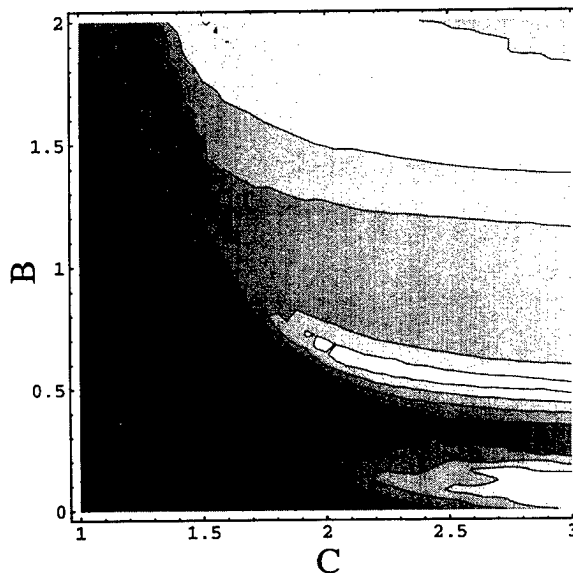


FIGURE 3. Contour plot of the total energy for $\text{Ag}_{23}^{2+} \rightarrow \text{Ag}_{12}^+ + \text{Ag}_{11}^+$. The shell correction is calculated with the cavity potential, $\gamma = 0.15(\text{a.u.})$. The zero of the energy is the liquid drop energy at $C = 1$, $B = 0$. The contours are from 0 to 6 eV with spacing of 1 eV. The gray levels of the shading run from black to white with increasing energy.

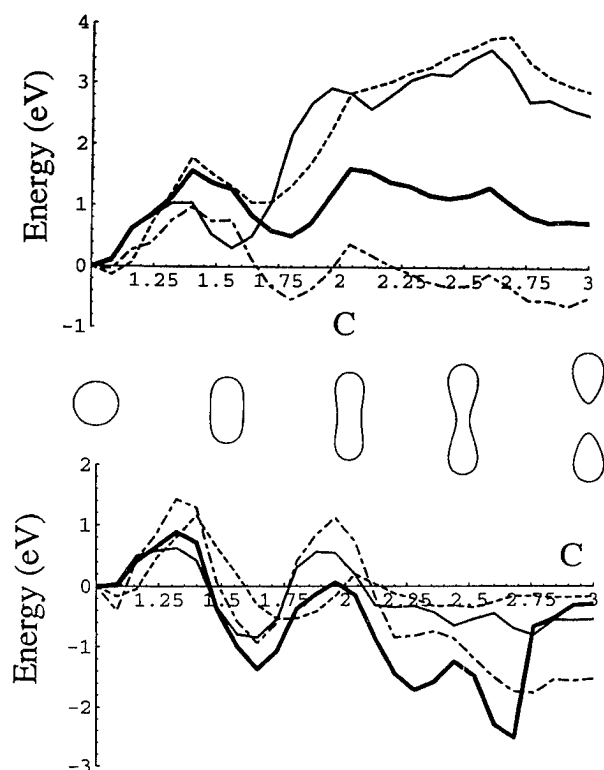


FIGURE 4. The total energy and shell correction along path 1. Top: Total energies by the shell correction method with the cavity potential, $\gamma = 0.15(\text{a.u.})$ (solid line), by the shell correction method with the Woods-Saxon potential, $\gamma = 0.15(\text{a.u.})$ (dotted line), by the stabilized jellium model (thick solid line), and by the normal jellium model (dash-dot line). Middle: The shape of the cluster at $C = 0, 1.5, 2, 2.5$, and 3 . Bottom: Shell corrections by the shell correction methods with the cavity potential, $\gamma = 0.15(\text{a.u.})$ (solid line), with the cavity potential, $\gamma = 0.35(\text{a.u.})$ (dash-dot line), with the Woods-Saxon potential, $\gamma = 0.15(\text{a.u.})$ (dotted line), and with the cavity potential using the Balian-Bloch formula (thick solid line).

accuracy of the Balian-Bloch formula is different. This difference will not be significant for larger clusters, but it causes a sudden jump of the shell correction for the cluster size considered here.

The smoothed density of states obtained by Eq. (2.6) does not have this problem. The smoothing parameter γ is of the order of typical spacing of energy levels. The error of the calculated shell correction may be minimized by finding γ that satisfies the stationary condition

$$\frac{\delta E_{\text{shell}}}{\delta \gamma} = 0. \quad (3.1)$$

We first tried to find the stationary γ for each cluster shape, but we could not find a stationary value for some shapes. Therefore we decided to keep using the constant γ value through a fission path, where the value is an average that satisfy the stationary condition near spherical shapes. We use two values for γ : $\gamma = 0.15(\text{a.u.})$ and $\gamma = 0.35(\text{a.u.})$, where the former is in the order of typical spacing of levels and the latter is almost the same as the energy difference between the ground level and the Fermi level. The shell correction obtained by using $\gamma = 0.35(\text{a.u.})$ is very similar to the one obtained by the Balian-Bloch formula, but it gives a higher threshold energy for fission than $\gamma = 0.15(\text{a.u.})$. It seems that $\gamma = 0.35(\text{a.u.})$ is too large and $\gamma = 0.15(\text{a.u.})$ is a better value.

A better shell potential may be the Woods-Saxon-type potential. This potential allows the spill-out of the electron wave functions. We use $\gamma = 0.15(\text{a.u.})$ as the smoothing parameter. Due to the spill-out, it is seen in the shell correction by the Woods-Saxon potential that the local minimum around $C = 1.7$ is shifted to a larger C compared with the cavity potential result. It is also seen that the oscillation of the shell correction along the fission path is somewhat reduced.

The total energy is compared in the top figure of Figure 4. The improvement made by the stabilized jellium is significant. The conventional jellium calculation predicts much less fission barrier than the stabilized jellium, although their qualitative features are the same. The total energies obtained by shell correction methods using the cavity potential and the Wood-Saxon potential give almost the same fission barrier.

The position of the local minimum around $C = 1.75$ by the jellium calculation is closer to the minimum position obtained by the Woods-Saxon potential calculation than to that obtained by the cavity potential calculation. Therefore the spill-out is necessary to predict the right shape for the local minimum.

The fission barrier obtained by the shell correction method is higher than that obtained by the stabilized jellium model. Because the shell corrections are not so different among the various methods, this difference is probably due to the inaccuracy in the model of calculating the liquid drop energy. The quantitative agreement between the stabilized jellium result and the shell correction results are very good for clusters with near spherical shapes, although the agreement is poor for those with large deformations.

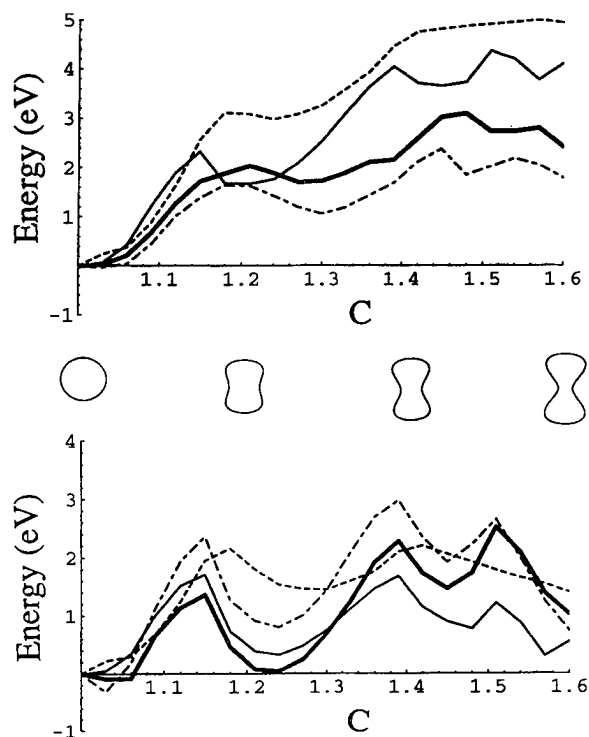


FIGURE 5. The total energy and shell correction along path 2. Top: Same as the top of Figure 4 but for the path 2. Middle: The shape of the cluster at $C = 0, 1.2, 1.4$, and 1.6 . Bottom: Same as the bottom of Figure 4 but for the path 2.

In Figure 5, the total energy and shell correction along path 2, $B = 6(C - 1)$, $1 \leq C \leq 1.2$; $B = 1.2$, $1.2 \leq C \leq 1.5$, are shown. The cluster forms the neck without substantial elongation along this path. The qualitative feature of the stabilized jel-

lium result and the shell correction method using the Woods-Saxson potential are the same.

In order to improve the quantitative prediction by the shell correction method, the model for calculating the liquid drop energy must be improved. But even with the present model, it is expected that the accuracy of the shell correction method estimate will increase as the size of the cluster increases since the cluster energy will approach to the bulk value as the cluster size increases.

References

1. M. Brack, J. Damgaard, A. S. Jensen, H. C. Pauli, V. M. Strutinsky, and C. Y. Wong, *Rev. Mod. Phys.* **44**, 320 (1972).
2. H. Koizumi, S. Sugano, and Y. Ishii, *Z. Phys. D* **28**, 223 (1993).
3. C. Yannouleas and U. Landman, *Phys. Rev. B* **48**, 8376 (1993).
4. S. M. Riemann, M. Brack, and K. Hansen, *Z. Phys. D* **28**, 235 (1993).
5. J. P. Perdew, H. Q. Tran, and E. D. Smith, *Phys. Rev. B* **42**, 11627 (1990).
6. H. B. Shore and J. H. Rose, *Phys. Rev. Lett.* **66**, 2519 (1991).
7. R. Balian and C. Bloch, *Ann. Phys. (N.Y.)* **60**, 401 (1970).
8. W. Ekardt, *Phys. Rev. B*, **29**, 1558 (1984).
9. D. E. Beck, *Solid State Comm.* **49**, 381 (1984).
10. W. Kohn and L. J. Sham, *Phys. Rev.* **140**, B 1133 (1965).
11. S. H. Vosko, L. Wilk, and M. Nusair, *Can. J. Phys.* **58**, 1200 (1980).
12. J. C. Light, I. P. Hamilton, and J. V. Lill, *J. Chem. Phys.* **82**, 1400 (1985).
13. Z. Bačić and J. C. Light, *Ann. Rev. Phys. Chem.* **40**, 469 (1989).
14. C. Leforestier, *J. Chem. Phys.* **94**, 6388 (1991).
15. H. Koizumi and S. Sugano, *Phys. Rev. A* **51**, R886 (1995).

Comparisons of the Theoretical Calculation of Nitrogen Clusters by Semiempirical MO Method

CHENG CHEN* AND KUANG-CHUNG SUN

Department of Applied Chemistry, Chung-Cheng Institute of Technology, Ta-Hsi, Taoyuan 33509, Taiwan, Republic of China; e-mail for C.C.: chenc@cc02.ccit.edu.tw

Received February 25, 1996; revised manuscript received May 21, 1996; accepted August 5, 1996

ABSTRACT

Various nitrogen clusters, N_x , are selected for the present theoretical study. The number of nitrogen atoms chosen in this work varies from $x = 8$ to $x = 32$. PM3, which is known as one of the best semiempirical methods, is selected for the self-consistent molecular orbital calculations. The geometrical optimization, vibrational frequencies, and thermochemical computations are all involved for various types of molecular nitrogen clusters. The results show that all N_x 's belong to the category of stable high-energy compounds. Comparison of average bond energy and delocalization energy of all cases reveals that $N_{20}(I_h \text{ symmetry})$ is the most stable molecule among all the nitrogen clusters studied. In addition, our results show five-membered rings are the most favored in the structures of nitrogen clusters (N_x). © 1996 John Wiley & Sons, Inc.

Introduction

In the period from 1990 to 1992, a hypothetical molecule N_8 having O_h symmetry was introduced and developed by Lauderdale et al. [1] and Engelke and Stine [2] using ab initio calculations. They proposed the cubane-type N_8 molecule to be a stable high-energy structure. Recently, N_{20} with I_h symmetry [3–6] and N_{28} with T_d symmetry [7] have been successfully developed and reported in the literature, with both ab initio as well as

semiempirical theoretical predictions. We have observed in the present study that I_h -type N_{20} and T_d -type N_{28} are both similar to the previously mentioned N_8 . All the molecules are more stable than nitrogen atoms and have higher energy than $N_2(g)$ molecules, thus belonging to the category of stable high-energy compounds. In order to examine the comparative stability among nitrogen clusters in general, we studied several N_x ($x = 8$ –32) structures. According to both experimental and theoretical results, the midsize clusters of the pure element with covalent bonds usually exist with highly symmetric structures. The well-known molecule buckminsterfullerene (C_{60}) is formed

*To whom correspondence should be addressed.

with I_h symmetry [8–10], and even the smallest fullerene cluster (C_{28}) with a 5A_2 open-shell ground state still belongs to the T_d point group [11]. Since both the nitrogen and carbon clusters are constructed with equivalent covalent bonds and the same kind of atoms, similar to the structures of carbon clusters, we select the highly symmetric structure for each N_x of nitrogen clusters. In addition to the behavior of symmetry, we should also pay attention to the structure of local rings in each cluster. When nitrogen atoms are forming a three-dimensional cluster, three equivalent single bonds are required for each atom. These three bonds are usually formed with the polarized sp^3 type or delocalized sp^3 type of structure. The favored bond angles of these bonds in each atom are usually more or less near to the tetrahedral angle (109°). The self-consistent field type optimized rings in the cluster of molecular orbital (MO) calculation are usually in favor of planar or near to the planar local ring structure due to the delocalization effect. In the planar regular polygonal rings, the inside bond angles of a triangle is 60° , of a square is 90° , of a five-membered ring is 108° , of a six-membered is 120° , of a seven-membered is 129° and of a eight-membered is 135° . If one compares these angles with the sp^3 type of angle as shown above, it is not difficult to find out that 108° of five-membered ring is the most suitable local structure for the nitrogen clusters. Consequently, for the planar or nearly planar rings, small rings with a size of 3 or 4 get the prominent negative bond angular deviation from the sp^3 angle ($\Delta\theta = 60^\circ - 109^\circ = -49^\circ$ for the size 3 and $\Delta\theta = 90^\circ - 109^\circ = -19^\circ$ for the size of 4); large rings with sizes of 7 or 8 get the prominent positive bond angular deviation from the sp^3 angle ($\Delta\theta = 135^\circ - 109^\circ = 26^\circ$ for the size of 8 and $\Delta\theta = 129^\circ - 109^\circ = 20^\circ$ for the size of 7). Both of these negative and positive deviation from sp^3 angle will cause the large angular strain for the single-bond-based nitrogen clusters. For nonplanar large rings with the sizes of 7 or 8 case, bond angle may be shrunk by changing dihedral angle. However, the symmetry of a three-dimensional system of clusters will be distorted, and the small rings of size 3 or 4 may occur, and the whole cluster will be less compact than the original regular polygonal system. The instability and another kind of angular strain may happen again due to nonplanar distortion of large rings. Therefore, for the single-bond-based three-dimensional nitrogen cluster in this work, we de-

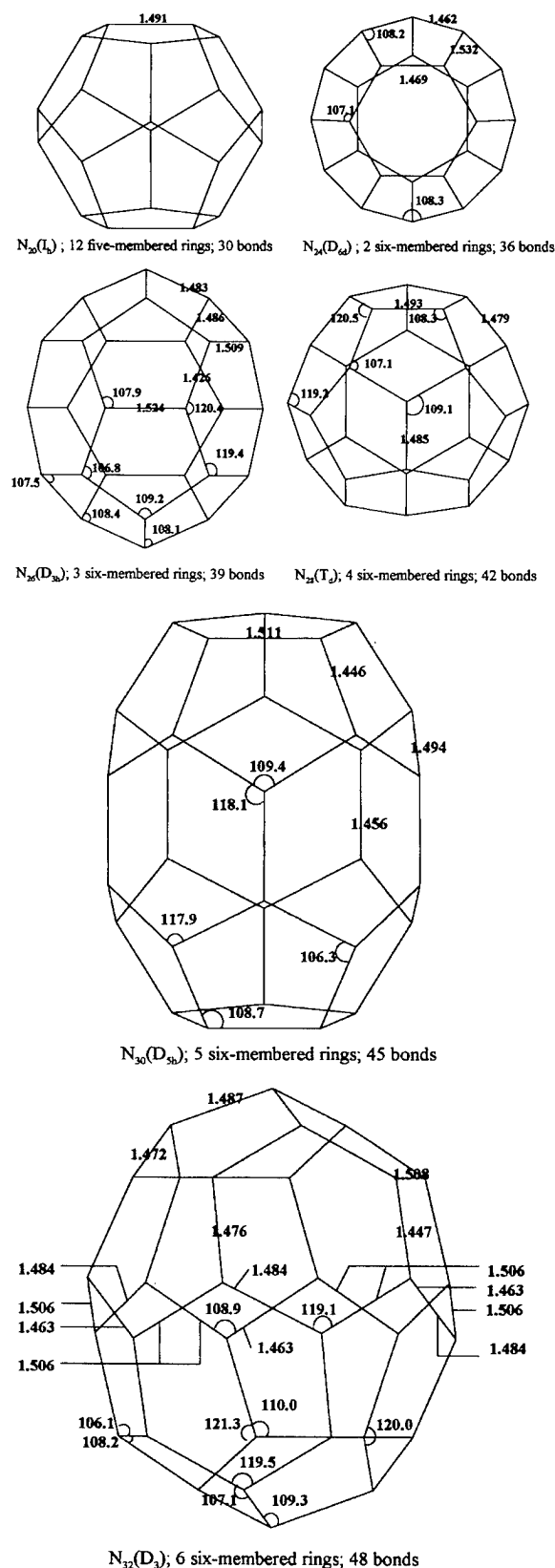


FIGURE 1. The geometry of N_x clusters (which consisted of five and six-membered rings for $x \geq 2$).

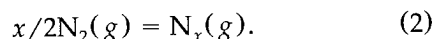
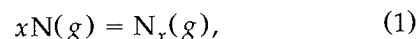
fined that both the negative and positive deviation of angles will be increasing angular strain and decreasing the stability of the cluster formation whenever the size of the ring is smaller or larger than 5. The introductory idea of this angular strain-type argument was first introduced by us in our former work of the semiempirical study of $N_{20}(I_h)$ [4]. If the above argument is true, the priority of our cluster structures assignment of this work are selected according to the following two principles. First of all, the five-membered rings are assigned as much as possible for the cluster in order to decreasing its angular strain. The second important principle is to assign the structure of clusters according to their highly symmetric property. Under these two principles of assignment, $N_{20}(I_h)$, $N_{24}(D_{4d})$, $N_{26}(D_{3h})$, $N_{28}(T_d)$, $N_{30}(D_{5h})$, and $N_{32}(D_3)$ as shown in Figure 1 and $N_8(O_h)$, $N_{10}(D_{3h})$, $N_{12}(D_{6h})$, $N_{14}(D_{3h})$, and $N_{16}(D_{4d})$ as shown in Figure 2 are selected for this work. In order to testify about stability and angular strain of various N_x 's with the same number of nitrogen atoms (x), we also select the high strained $N_{14}(D_{7h})$, $N_{16}(D_{8h})$, $N_{24}(O_h)$, $N_{28}(D_{7d})$, and $N_{32}(O_h)$ as shown in Figure 3 to compare them with the related less strained N_x ($x = 14, 16, 24, 28, 32$) of Figures 1 and 2. With this type of comparison, the real evidence of the angular strain of various sized localized rings in nitrogen clusters may be testified as shown in the following section.

The MO method used in this work is the PM3 method which is known to be one of the best semiempirical methods so far [12]. As shown in our previous study on N_{20} [6], the optimized structures, the calculated first ionization potentials, and thermochemical results of both the semiempirical PM3-MO as well as ab initio type 6-31G are all very close to each other. Consequently, we believe that using the semiempirical type PM3-MO method as an instrument for the theoretical study of nitrogen clusters will be very effective, efficient, and reliable in the present comparative analysis.

Calculation

The versions of PM3 in Gaussian 92 [13] and HyperChem [14] were both used in the present work. For various nitrogen clusters, different calculations of the same molecule by these two programs usually yield the identical results. The ver-

sion of PM3 in the Gaussian package was used since it provided better degeneracies for both MOs and vibrational frequencies in the cases of high symmetry point groups. The version of PM3 in HyperChem usually yielded the calculated binding enthalpy and enthalpy of formation directly for the following reactions:



For comparing the stability of the bonding behavior for each cluster, similar to the average bond energy calculations as reported earlier [3, 7], we calculated the average bond energies (BE) with enthalpy of atomization, i.e., a negative value of binding enthalpy divided by the number of bonds (n) in the molecule as

$$BE = \Delta H_a/n. \quad (3)$$

In addition to these quantities, the newly defined "delocalization energy" (DE) of a single bonded structure of $C_{24}N_4$ cluster [15] is also applied in this work:

$$DE = \Delta H_a - \sum_i n_i(\Delta H_{\text{bond}_i}), \quad (4)$$

where n_i and ΔH_{bond_i} are the number of bonds and bond energy of i th type of bond. For the N_x clusters in this work, all bonds are referenced to the N-N single bond

$$DE = \Delta H_a - n \Delta H_{\text{bond(N-N)}}, \quad (5)$$

where n is the number of N-N bonds in the cluster; $\Delta H_{\text{bond(N-N)}} = 163 \text{ kJ mol}^{-1}$ is assigned from a recent textbook of physical chemistry [16].

For the purpose of comparison between various N_x , the average delocalization energy of each bond can be easily evaluated as

$$\begin{aligned} DE/n &= \Delta H_a/n - \Delta H_{\text{bond(N-N)}} \\ &= BE - 163 \text{ kJ mol}^{-1}. \end{aligned} \quad (6)$$

The cluster type of molecules calculated in this work are all assumed to consist of nitrogen atoms. The size of the molecules assigned here lies in the range between 8 and 32 atoms. The assignment of cluster structures was according to the principle of less angular strain and their symmetric behavior of the assigned symmetry group. Hence we first con-

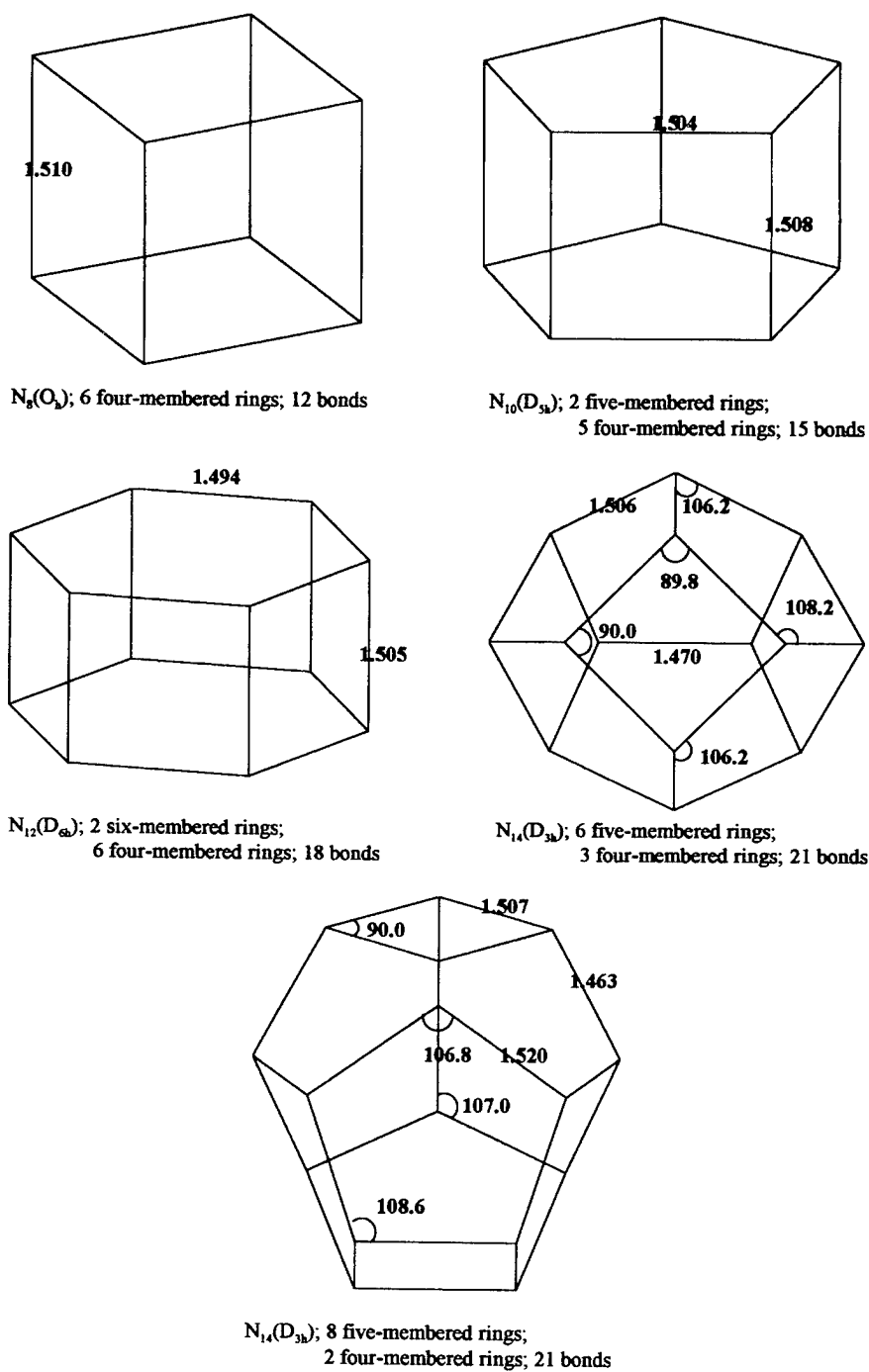


FIGURE 2. The geometry of N_x nitrogen clusters (which consisting of four, five or six-membered rings for $x < 20$).

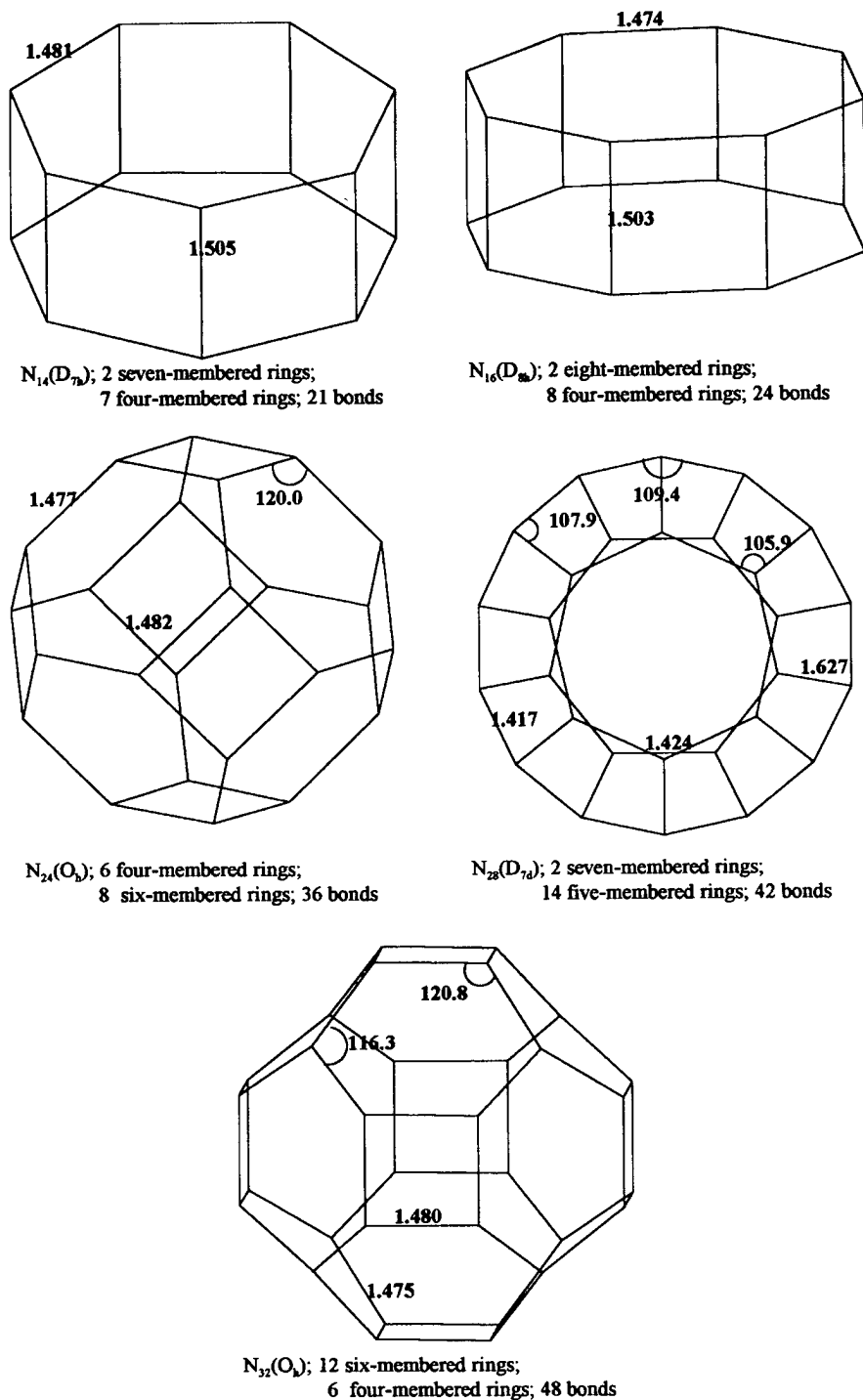


FIGURE 3. N_x clusters ($x = 14, 16, 24, 28, 32$) with comparative larger angular strain.

structed geometries consisting of five- and six-membered rings. The I_h type N_{20} is constructed with 12 regular five-membered rings. For $x > 20$, $N_{24}(D_{6d})$ has 2 six-membered rings, the $N_{26}(D_{3h})$ has 3 six-membered rings, the $N_{28}(T_d)$ has 4 six-membered rings, $N_{30}(D_{5h})$ has five six-membered rings, and $N_{32}(D_3)$ has 6 six-membered rings, in addition to 12 five-membered rings in each case, as shown in Figure 1. For cluster sizes less than 20, structures formed with four- and five-membered rings or four- and six-membered rings were chosen, including the cubane-like $N_8(O_h)$, $N_{10}(D_{5h})$, $N_{12}(D_{6h})$, $N_{14}(D_{3h})$ with 3 four-membered and 6 five-membered rings, and $N_{16}(D_{4d})$ with 2 four-membered and 8 five-membered rings as shown in Figure 2. In order to verify the principle of large angular strain in the cases of large (7 or 8) or small (3 or 4) sizes of rings, we also selected clusters with seven- or eight-membered rings, such as $N_{14}(D_{7h})$, $N_{16}(D_{8h})$, and $N_{29}(D_{7d})$ along with an analogous larger cluster with four-membered rings such as $N_{24}(O_h)$ and $N_{32}(O_h)$ as shown in Figure 3, for the purpose of comparison. Thus, a total of 16 nitrogen cluster structures (N_x , x varying from 8 to 32) have been evaluated in this work.

Both the geometry optimization and vibrational frequency calculations of all the clusters mentioned above were successfully computed. All the calculated ground-state electronic configurations are closed-shell singlets. $N_{16}(D_{8h})$ exhibited two imaginary vibrational frequencies and proved not to be a local minimum, whereas the vibrational frequencies of all the remaining 15 structures were found to be positive real values lying between 89 and 1108 cm^{-1} . Consequently, they are stable structures on their respective potential surfaces.

Result and Discussion

COMPARISON BETWEEN LESSER OR LARGER ANGULAR STRAIN N_x

In order to demonstrate the significant effect of angular strain on the N_x molecules, we initially selected N_{14} , N_{16} , N_{24} , N_{28} , and N_{32} consisting of comparably lesser angular strain structures of Figures 1 and 2 and compared them with the related five larger strain molecules, as shown in Figure 3. We selected the calculated result of the first ionization potentials, i.e., I_{1st} , the energy gap between the highest occupied molecular orbital (HOMO) and lowest unoccupied molecular orbital (LUMO), i.e., $\Delta\epsilon = \epsilon_{LUMO} - \epsilon_{HOMO}$ the average bond energies from Eq. (3), and heat of formations, in order to compare the stability of the five pairs of N_x ($x = 14, 16, 24, 28, 32$). The calculated values of PM3 are listed in Table I for comparison. From the results in this table we found that for N_x with identical x , I_{1st} , $\Delta\epsilon$, and BE of molecules having lesser strain are larger than the corresponding values of molecules having larger strain. The ΔH_f° of lesser strain cases is lower than the ΔH_f° of larger strain cases. All these results imply that nitrogen clusters consisting of five- or six-membered rings are favored over the structures which containing seven-, eight-, or four-membered rings.

COMPARISON OF THE MOST STABLE N_x ($x = 8$ TO 32)

After the geometrical optimization and vibration frequency calculations of various N_x in Fig-

TABLE I
Comparisons of the angular strain effect in N_x ($x = 14, 16, 24, 28, 32$).

N_x	Sym. Group	Geometric Structure	I_{1st} (eV)	$\Delta\epsilon$ (eV)	BE (kJ bond ⁻¹)	ΔH_f° (kJ mol ⁻¹)
N_{14}	D_{3h}	Fig. 2	13.15	10.15	195.09	2522.2
	D_{7h}	Fig. 3	12.40	9.32	175.57	2932.0
N_{16}	D_{4d}	Fig. 2	13.21	10.01	197.66	2820.9
	D_{8h}	Fig. 3	12.50	8.84	169.29	3501.6
N_{24}	D_{6d}	Fig. 1	12.95	8.90	199.23	4174.9
	O_h	Fig. 3	12.90	8.87	190.54	4487.6
N_{28}	T_d	Fig. 1	12.98	8.62	197.53	4942.0
	D_{7d}	Fig. 3	12.60	8.55	196.49	4985.4
N_{32}	D_3	Fig. 1	12.85	8.00	195.68	5737.0
	O_h	Fig. 3	12.73	7.51	188.34	6089.1

ures 1 and 2, all the calculated bond distances and angles are marked in the related figures and all the other results are list in Tables II and III.

I_{1st} and HOMO-LUMO Energy Gap

As shown in Figure 4 and Table II, the calculated first ionization potentials (I_{1st}) of various N_x are very close to each other; their I_{1st} are all close to 13 eV. The HOMO-LUMO energy gap ($\Delta\epsilon$) are decreased whenever the number of nitrogen (x) increased. The tendency of $\Delta\epsilon$ decreasing in more prominent for larger cluster whenever $x > 20$ than in the cases of smaller cluster ($x < 20$). If one

compares the observed $I_{1st} = 15.58$ eV and PM3 calculated HOMO-LUMO energy gap $\Delta\epsilon = 14.36$ eV of N_2 molecule, it is found that both I_{1st} and energy gap $\Delta\epsilon$ of various cluster molecules are all less than the related values of N_2 ; that means the large nitrogen clusters are more reactive than N_2 from the viewpoint of charge transfer processes.

Vibration Frequency Calculation

All the vibrational frequencies of these 11 nitrogen clusters are positive between 158 and 1108 cm^{-1} . The largest frequencies of them are all less than 1200 cm^{-1} due to a lack of stretching-type

TABLE II
Comparisons of the I_{1st} , energy gap ($\Delta\epsilon$), average bond energies (BE), delocalization energies (DE/n), and heat of formations ($\Delta H_f^\circ / nN_2$) in N_x ($x = 8$ to 32).

N_x	Symmetry Group	I_{1st} (eV)	$\Delta\epsilon$ (eV)	BE (kJ bond $^{-1}$)	DE/ n (kJ mol $^{-1}$) (n : No of N-N bonds)	$\Delta H_f^\circ / nN_2$ [kJ (N_2) $^{-1}$]
N_8	O_h	12.99	11.03	173.59	10.59	424.82
N_{10}	D_{5h}	13.33	11.18	183.22	20.23	395.91
N_{12}	D_{6h}	12.82	9.70	180.64	17.64	403.67
N_{14}	D_{3h}	13.15	10.15	195.09	32.09	360.32
N_{16}	D_{4d}	13.21	10.01	197.66	34.66	352.61
N_{20}	I_h	13.17	9.63	201.55	38.55	340.95
N_{24}	D_{6d}	12.95	8.90	199.22	36.23	347.91
N_{26}	D_{3h}	12.82	8.60	198.45	35.45	350.24
N_{28}	T_d	12.98	8.62	197.53	34.53	353.00
N_{30}	D_{5h}	12.79	8.28	197.47	34.47	353.16
N_{32}	D_3	12.85	7.96	195.68	32.68	358.56

TABLE III
Comparisons of the average bond lengths (in Å), the longest (or weakest) bond length (in Å), vibrational frequency ranges, and the difference between the highest frequency and the lowest frequency in N_x ($x = 8$ to 32).

N_x	Symmetry Group	Ave. Bond Length	Longest Bond Length	Vib. Freq. Range (cm $^{-1}$)	$\Delta\tilde{\nu}$ (cm $^{-1}$)
N_8	O_h	1.510	1.510	537 ~ 1108	571
N_{10}	D_{5h}	1.505	1.508	395 ~ 1019	624
N_{12}	D_{6h}	1.498	1.505	274 ~ 1003	729
N_{14}	D_{3h}	1.498	1.506	370 ~ 946	576
N_{16}	D_{4d}	1.497	1.520	251 ~ 965	714
N_{20}	I_h	1.491	1.491	356 ~ 947	591
N_{24}	D_{6d}	1.488	1.532	292 ~ 997	705
N_{26}	D_{3h}	1.485	1.524	273 ~ 1024	751
N_{28}	T_d	1.483	1.493	287 ~ 1000	713
N_{30}	D_{5h}	1.483	1.511	158 ~ 1093	935
N_{32}	D_3	1.480	1.506	228 ~ 1041	813

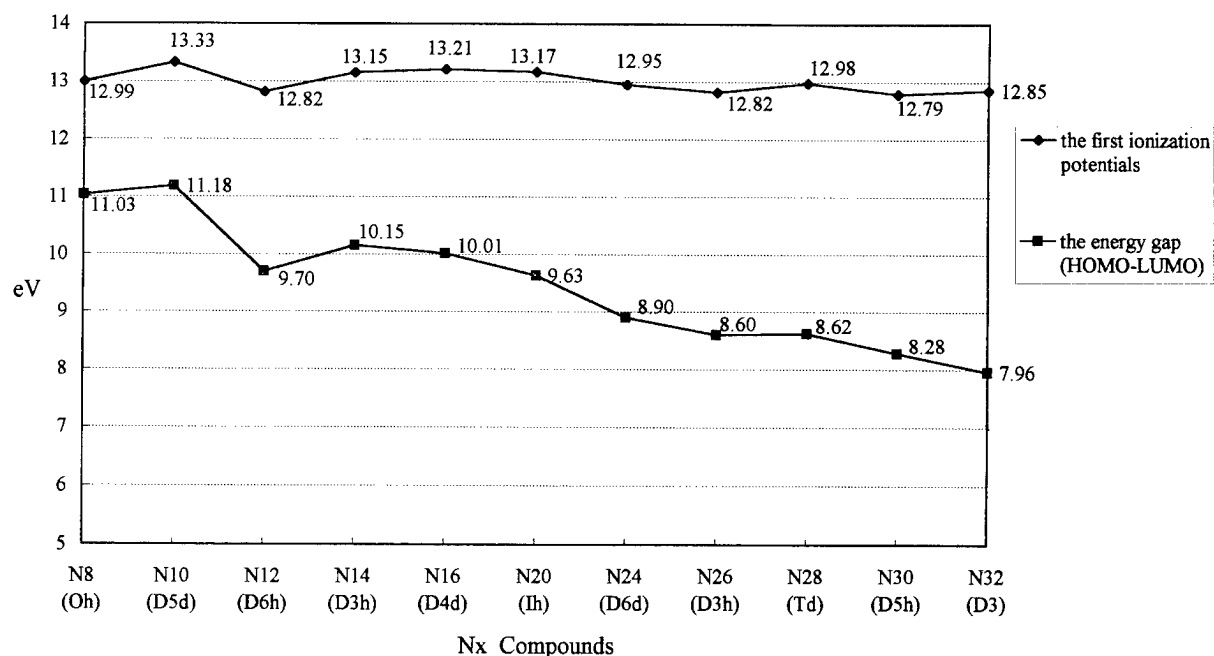


FIGURE 4. Comparisons of the first ionization potentials and the energy gap in N_x ($x = 8$ to 32).

vibrations of the special functional group. This skeleton vibrational frequencies of clusters are usually very small. The largest frequencies of various nitrogen clusters are more or less around 1000 cm^{-1} . For the sake of simplicity, only the range of frequencies and difference between largest and smallest frequencies, ($\Delta\nu = \Delta\nu_{\text{largest}} - \Delta\nu_{\text{smallest}}$) are collected and listed in Table III for comparison. From $\Delta\nu$'s of the various clusters, one may easily identify the clusters with comparable smaller $\Delta\nu$ (N_8 , N_{14} , and N_{20}), structures which are more compact or more symmetric than other clusters. The larger $\Delta\nu$ cases, such as the clusters of N_{30} and N_{32} , are relatively larger and more flexible than the other clusters. Both the anomalous large $\Delta\nu$ and small HOMO-LUMO gap of $N_{12}(D_{6h})$ show that the hexagonal type N_{12} is a less rigid and less stable nitrogen cluster compared to the pentagonal-type $N_{10}(D_{5h})$ cluster with five-membered rings.

Bond Distance

Most of the calculated bond distances shown in Figures 1 and 2 are less than the standard N-N single bond distance 1.45 \AA assigned by Pople and Beveridge [17]. In order to compare the geometri-

cal size, the average bond distance of each cluster is calculated:

$$(\bar{d})_{\text{ave.}} = \frac{\sum_i n_i d_i}{\sum_i n_i} \quad (7)$$

and listed in Table III and Figure 5. In Eq. (7) n_i and d_i are number and length of the i th type of bond. The range of average bond distance lies between 1.51 and 1.48 \AA . The larger cluster gives the shorter average distance due to delocalization effect of this single-bond-based system of larger cluster.

In the simplest sense, the bond will be strong when the bond distance is short. From the gross point of view, the larger cluster with shorter average bond length will be stronger and more difficult to break than the other smaller clusters. However, the bond breaking is not a gross problem, but it is a problem of local region or local bond. Therefore, the weakest bond or longest bond distance in each cluster should be selected for comparison. If one looks at Figure 5, the minimum in this curve belongs to the $N_{20}(I_h)$ cluster. This fact means that all bonds in the highly symmetric and five-membered ring systems are all equivalent and balanced

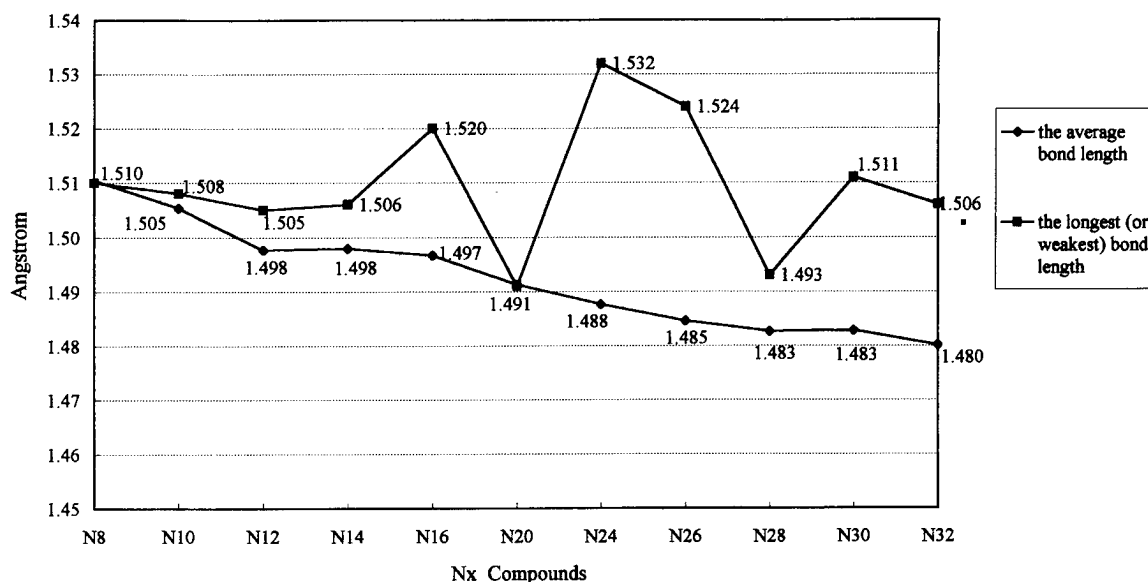


FIGURE 5. Comparisons of the average bond length and the longest bond length in N_x ($x = 8$ to 32).

local parts in the N_{20} cluster, and there is no weak point (or special long bond distance) like the other nonequivalent bond systems of the other clusters.

BE, (DE) / n , and ΔH_f / (no. of N_2)

The last and the most important problem is the comparison of the energy differences between $N_x(g)$ and $xN(g)$ or $N_x(g)$ and $x/2N_2(g)$. In addition to the average bond energy (BE) and average delocalization energy (DE/ n), we also calculate ΔH_f / (no. of N_2) for

$$N_2(g) = \left(\frac{1}{x/2} \right) N_x(g)$$

reaction in which

$$\Delta H_f / (\text{no. of } N_2) = \Delta H_f / (x/2). \quad (8)$$

These results are shown in Table II. Because DE/ n may be evaluated by Eq. (6) and which is calculated by BE-163 (kJ mol⁻¹). The reason we calculate DE/ n in this work is to show the delocalization effect related to N-N single bond. Although, in the bond distance calculation of the last paragraph, most calculated d_{N-N} 's are larger than the standard single-bond distance (1.45 Å), all the calculated DE and DE/ n are positive values for all clusters. This result shows that all the N-N bonds in various N_x clusters are stronger than the ordinary N-N single bond. If one compares the BE,

DE/ n , and ΔH_f / (no. of N_2) for all clusters, all the evidences prove that $N_{20}(I_h)$ is the most stable nitrogen cluster. If one compares the BE, DE/ n of the small clusters $N_8(O_h)$, $N_{10}(D_{5h})$, and $N_{12}(D_{6h})$, the most stable cluster among these three clusters is $N_{10}(D_{5h})$. The idea of angular strain of this work shown above is strongly supported by these results. The less angular strained five-membered rings is the fundamental unit for the stable nitrogen clusters formation.

Conclusion

From the above results we conclude:

1. For nitrogen clusters, five- and six-membered rings have less angular strain and are favored over four-, seven-, and eight-membered rings, just as expected for analogous carbon structures.
2. From both energy and largest bond distance comparisons, $N_{20}(I_h)$ is the most stable N_x cluster in this work.
3. From the energy viewpoint, $N_{10}(D_{5h})$ is the most stable structure among N_8 , N_{10} , and N_{12} , which is the additional evidence to show five-membered rings are preferred also in cases of small nitrogen clusters.
4. In the case of carbon clusters, such as graphite, C_{60} , and C_{70} , their six-membered

ring part is usually more important than the five-membered ring part. In this work, all the PM3 results show that the five-membered ring is the most favored fundamental structural unit in the nitrogen cluster molecules, which may be quite different from those of carbon clusters. The idea of smallest angular strain of the five-membered ring system is strongly verified by all the above-mentioned results of this work.

References

1. W. J. Lauderdale, J. F. Stanton, and R. J. Bartlett, *J. Phys. Chem.* **96**, 1173 (1992).
2. R. Engelke and J. R. Stine, *J. Phys. Chem.* **94**, 5689 (1990).
3. C. Chen, L-H. Lu, and Y. W. Yang, *J. Chung-Cheng Inst. Tech.* **20(2)**, 133 (1992).
4. (a) C. Chen, L-H. Lu, and Y. W. Yang, *J. Mol. Struct. (Theochem)* **253**, 1 (1992). (b) A. A. Bliznyuk, M. Shen, and H. F. Schaefer III, *Chem. Phys. Lett.* **198**, 249 (1992).
5. C. Chen, K-C. Sun, and L-H. Lu, *J. Chin Chem. Soc.* **40**, 199 (1993).
6. C. Chen and K-C. Sun, *J. Mol. Struct. (Theochem)* **340**, 143 (1995).
7. (a) K-C. Sun and C. Chen, *Chinese Chem. Soc., Taiwan (Chem.)* **53**, 255 (1995). (b) C. Chen and K-C. Sun, *J. Mol. Struct. (Theochem)* **362**, 181 (1996).
8. C. S. Yannoni, P. P. Bernier, D. S. Bethune, G. Meijer, and J. R. Salem, *J. Am. Chem. Soc.* **113**, 3190 (1991).
9. K. Hedberg, L. Hedberg, D. S. Bethune, C. A. Brown, H. C. Dorn, R. D. Johnson, and M. de Vries, *Science* **254**, 410 (1991).
10. S. Liu, Y. J. Lu, M. M. Kappes, and J. A. Ibers, *Science* **254**, 408 (1991).
11. T. Guo, R. E. Smalley, and Scuseria, *J. Chem. Phys.* **99**, 352 (1993).
12. J. J. P. Stewart, *J. Comp. Chem.* **11**, 543 (1990).
13. M. J. Frisch, G. W. Trucks, M. Head-Gordon, P. M. W. Gill, M. W. Wong, J. B. Foresman, B. G. Johnson, H. B. Schlegel, M. A. Robb, E. S. Replogle, R. Gomperts, J. L. Andres, K. Raghavachari, J. S. Binkley, C. Gonzalez, R. L. Martin, D. J. Fox, D. J. Defrees, J. Baker, J. J. P. Stewart, and J. A. Pople, *Gaussian 92, Revision E.3*, Gaussian, Inc., Pittsburgh, PA, 1992.
14. J. J. P. Stewart, *HyperChem*, Release 3, Autodesk, Inc. Sausalito, California, 1993.
15. K-C. Sun and C. Chen, *J. Mol. Struct. (Theochem)* **360**, 157 (1996).
16. P. W. Atkins, *Physical Chemistry*, 5th ed. (Oxford University Press, Oxford, U.K., 1994), p. 80.
17. J. A. Pople and D. L. Beveridge, *Approximate Molecular Orbital Theory* (McGraw-Hill, New York, 1970), p. 111.

Combined Effect of the Screening of a Donor Ion and the Conduction Band Nonparabolicity on the Binding Energy of a Donor at the Center of a Spherical Quantum Dot

A. M. ELABSY,^{1*} P. CSAVINSZKY^{2**}

¹Department of Physics, Faculty of Science, United Arab Emirates University, P.O. Box 17551, Al-Ain, United Arab Emirates

²Department of Physics and Astronomy, University of Maine, Orono, Maine 04469-5709

Received 2 February 1996; revised 12 February 1996; accepted 25 February 1996

ABSTRACT

We carried out variational model calculations for the assessment of the combined effect of the nonparabolicity of the electron effective mass and the screening of the donor ion by the valence electrons of GaAs for a donor placed at the center of a spherical quantum dot. We considered finite confining potentials between the GaAs QD and the surrounding Ga_{1-x}Al_xAs matrix. We found that the combined effect becomes more pronounced as the radius of the quantum dot decreases. © 1996 John Wiley & Sons, Inc. *Int J Quant Chem* 60: 507–510, 1996

Introduction

Reduced dimensional structures, such as a quantum well (QW), a quantum-well wire (QWW), or a quantum dot (QD), are man-made

*On leave from the Department of Physics, Faculty of Science, Mansoura University, Mansoura, Egypt

**We are deeply saddened by the loss of Peter Csavinszky, an author published in the *International Journal of Quantum Chemistry* for many many years and a continuous participant at the annual Sanibel Symposia.

Correspondence to: Dr. Kenneth R. Brownstein, Chair, Department of Physics and Astronomy, 5709 Bennett Hall, University of Maine, Orono, ME 04469-5709

structures that can be fabricated by chemical vapor deposition (CVD) [1, 2] and molecular-beam epitaxy (MBE) [3–5]. Donor atoms in these structures are expected to have different binding energies than have the same donor atoms in the bulk semiconductor.

Each of these reduced dimensional structures has received an extraordinary amount of attention in the literature. For this reason, we shall severely curtail the number of references in the present article and refer only to publications that we deem essential.

Much studied hetero structures are the following: the quasi-two-dimensional QW, such as a GaAs slab sandwiched between two semi-infinite

$\text{Ga}_{1-x}\text{Al}_x\text{As}$ blocks, the quasi one-dimensional QWW, such as a GaAs wire placed in an infinite $\text{Ga}_{1-x}\text{Al}_x\text{As}$ matrix, and the quasi zero-dimensional QD, such as a GaAs sphere placed in a $\text{Ga}_{1-x}\text{Al}_x\text{As}$ bulk.

The finding energy of a hydrogenic donor in a $\text{Ga}_{1-x}\text{Al}_x\text{As}/\text{GaAs}/\text{Ga}_{1-x}\text{Al}_x\text{As}$ QW was calculated by Bastard [6, 7], who applied a variational approach. The binding energy in a $\text{GaAs}/\text{Ga}_{1-x}\text{Al}_x\text{As}$ QWW of a circular cross section was calculated by Brown and Spector [8], also by a variational approach. The effect of changing the shape of the QWW was studied by Bryant [9]. The binding energy of a hydrogenic donor in the center of a $\text{GaAs}/\text{Ga}_{1-x}\text{Al}_x\text{As}$ QD was studied by Porras-Montenegro and Pérez-Merchancano [10], Zhu et al. [11], and Zhu [12]. The binding energy of an off-center donor in a spherical QD has also received the attention of Zhu and Chen [13, 14].

The screening of a donor ion by the valence electrons of GaAs in a $\text{Ga}_{1-x}\text{Al}_x\text{As}/\text{GaAs}/\text{Ga}_{1-x}\text{Al}_x\text{As}$ QW was considered by Csavinszky and Elabsy [15], who used an analytical screening function obtained by Resta [16]. The screening of a donor ion by the valence electrons of GaAs in a $\text{GaAs}/\text{Ga}_{1-x}\text{Al}_x\text{As}$ QWW of circular cross section was studied by Csavinszky and Oyoko [17, 18]. Recently, Elabsy and Csavinszky [19] considered the screening of a donor ion by the valence electrons of GaAs in a spherical $\text{GaAs}/\text{Ga}_{1-x}\text{Al}_x\text{As}$ QD.

In all the above calculations, the donor electron was described by a constant scalar effective mass. It is, however, known that the conduction band (CB) of GaAs deviates from the parabolic form. The effect of the nonparabolicity of the CB on the binding energy of a donor in a $\text{Ga}_{1-x}\text{Al}_x\text{As}/\text{GaAs}/\text{Ga}_{1-x}\text{Al}_x\text{As}$ QW was studied by Chaudhuri and Bajaj [20] who considered a finite confining potential. A similar calculation was performed by Csavinszky and Elabsy [21]. Both of these calculations made use of an energy-dependent effective mass for the calculation of the binding energies of hydrogenic donors placed in on-center [18] and off-center [19] positions in the $\text{Ga}_{1-x}\text{Al}_x\text{As}/\text{GaAs}/\text{Ga}_{1-x}\text{Al}_x\text{As}$ QW. Recently, the effect of the CB nonparabolicity on the binding energy of an on-center donor in a $\text{GaAs}/\text{Ga}_{1-x}\text{Al}_x\text{As}$ QD has been considered by Elabsy and Csavinszky [22].

In this article, we study the combined effect of screening and nonparabolicity on the binding energy of a donor located at the center of a spherical

$\text{Ga}_{1-x}\text{Al}_x\text{As}/\text{GaAs}$ QD. We consider a finite barrier confining potential. Our approach is a variational approach, and our units are atomic units (unit of energy is the Hartree, unit of length is the bohr).

Theory

In this section, we restrict ourselves to a very brief presentation of the theory of the combined effect of screening and the nonparabolicity of the electron effective mass.

The Hamiltonian, for a donor in the center of a spherical QD of radius R , is given by

$$H = -\frac{1}{2m_E^*}\nabla^2 - \frac{1}{\epsilon_l(r)r} + V_b(r). \quad (1)$$

In Eq. (1), m_E^* denotes the energy-dependent effective mass (hence, the subscript E) of Hrivnak [23], given by

$$m_E^* = m^{\Gamma} + \frac{E}{\gamma}. \quad (2)$$

In Eq. (2), m^{Γ} is the electron effective mass at the Γ -point, $m^{\Gamma} = 0.0665 m_0$, E is the electron energy expressed in eV units, and $\gamma = 9.41$ eV.

Also in Eq. (1), $\epsilon_l(r)$ denotes Resta's [16] screening function, obtained from a linearized differential equation (hence, the subscript l), and $V_b(r)$ is the confining potential given by

$$V_b(r) = \begin{cases} 0 & r \leq R \\ V_0 & r > R \end{cases}. \quad (3)$$

By assuming that 60% of the energy band gap discontinuity is related to the conduction band, Batey and Wright [24] obtained

$$V_0 = 0.60 \Delta E_g^{\Gamma}, \quad (4)$$

where ΔE_g^{Γ} is the difference in band gaps of $\text{Ga}_{1-x}\text{Al}_x\text{As}$ and GaAs at the Γ -point. This quantity is then

$$\Delta E_g^{\Gamma}(\text{eV}) = 1.247x, \quad x \leq 0.45. \quad (5)$$

Our variational trial function is of the form

$$\psi(r) = \begin{cases} \frac{N \sin(\zeta_{10} r)}{r} e^{-\lambda r} & r \leq R \\ N \frac{1}{r} \sin(\zeta_{10} R) e^{\chi_{10}(R-r)} e^{-\lambda r} & r \geq R \end{cases} \quad (6)$$

In Eq. (6), N is a normalization constant, given in [15], and λ is a variational parameter. Finally, the quantities χ_{10} and ζ_{10} are defined by

$$\chi_{10} = [2m^*(V_b - E_{10})]^{1/2} \quad (7)$$

and

$$\zeta_{10} = [2m^*E_{10}]^{1/2}. \quad (8)$$

The binding energy, $E_b(r)$, described by the Hamiltonian in Eq. (1), is defined as

$$E_b(R) = E_{10}(R) - \zeta_{\min}(R). \quad (9)$$

In Eq. (9), E_{10} is obtained by solving the transcendental equation of Porras-Montenegro and Pérez-Merchancano [10]. By extremalizing the expectation value of the energy, $\zeta(R)$, with respect to λ , one obtains $\zeta_{\min}(R)$.

The results of our variational calculations, for $x = 0.30$ and $x = 0.45$, are given in Figures 1–4.

Figure 1 shows the dependence of E_b on R for $x = 0.30$ calculated for a nonparabolic conduction

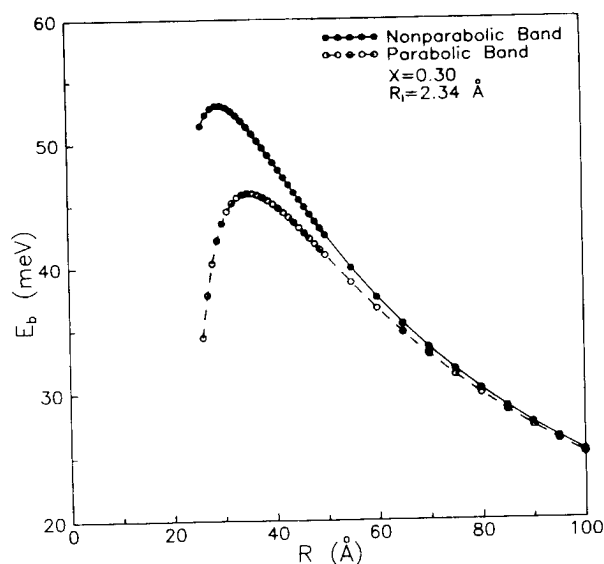


FIGURE 1. Dependence of E_b on the CB nonparabolicity (for $x = 0.30$) as a function of R .

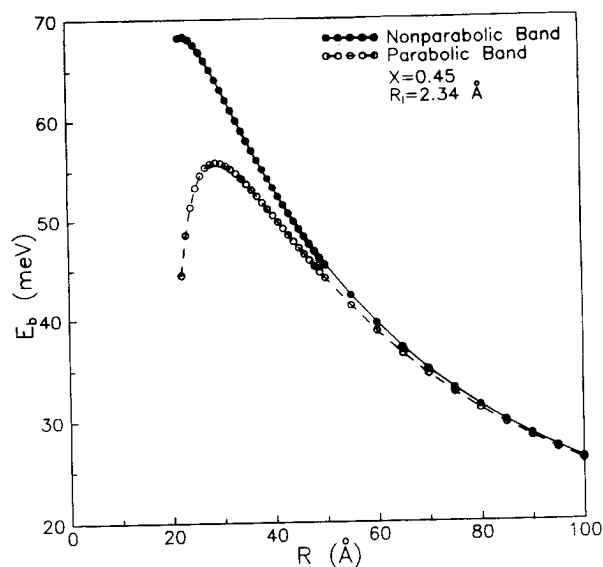


FIGURE 2. Dependence of E_b on the CB nonparabolicity (for $x = 0.45$) as a function of R .

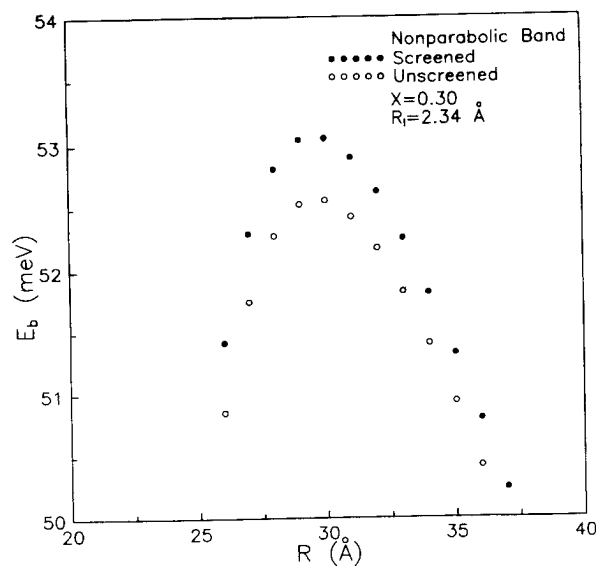


FIGURE 3. Dependence of E_b on R when the CB nonparabolicity is considered simultaneously with valence dielectric screening ($x = 0.30$).

band for a screened donor with the relevant data for a parabolic conduction band. It is noted here that while we have calculated E_b using atomic units the graphs are given in meV and Å, since these units are most often used for data presentation in the literature. Figure 2 is similar to Figure 1, except that it is obtained for $x = 0.45$.

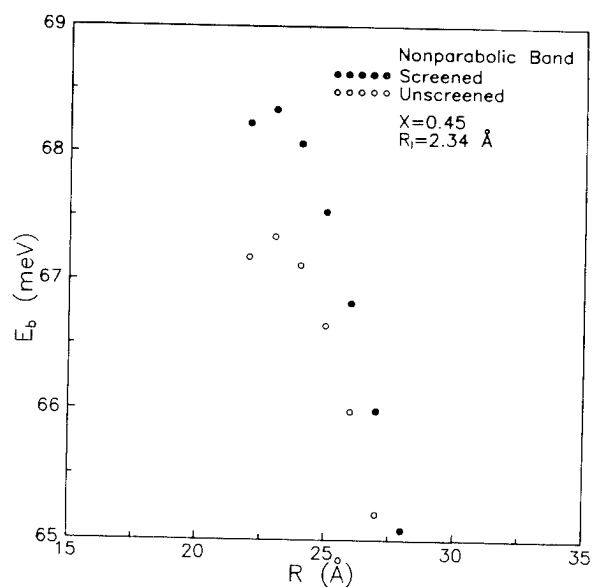


FIGURE 4. Dependence of E_b on R when the CB nonparabolicity is considered simultaneously with valence dielectric screening ($x = 0.45$).

Figure 3 compares E_b vs. R , calculated for a nonparabolic conduction band for both a screened and unscreened donor in a QD of aluminum fraction $x = 0.30$. Figure 4 is similar to Figure 3, except that it is obtained for $x = 0.45$. Finally, in Figures 1–4, the numerical value of the screening radius is also displayed.

Discussion

Both Figure 1 ($x = 0.30$) and Figure 2 ($x = 0.45$) show that the CB nonparabolicity of GaAs has a significant effect on the binding energy of a screened donor placed at the center of a spherical QD compared to that obtained using a parabolic CB of GaAs. It is also seen from Figures 1 and 2 that the effect increases as the radius of the QD decreases. It is further evident from the figures that the binding energy, both for the parabolic and for the nonparabolic cases, increases at first as the QD radius R decreases, reaches a maximum at a certain R value, and then starts decreasing as the

QD radius R decreases further. Figures 1 and 2 permit yet another observation: They show that the maxima in the binding energy do not occur at the same value of R for the parabolic and nonparabolic cases.

Figures 3 ($x = 0.30$) and 4 ($x = 0.45$) show the dependence of E_b on R when the conduction band nonparabolicity is considered together with both screening and nonscreening of a donor placed at the center of the QD. Consideration of screening enhances the binding energy E_b .

References

1. H. M. Manasevit, *J. Electrochem. Soc.* **118**, 647 (1971).
2. R. D. Dupuis and P. D. Dapkus, in *7th International Symposium on GaAs and Related Compounds*, St. Louis, 1978, C. M. Wolfe, Ed. (Institute of Physics, London, 1979) pp. 1–9.
3. A. Y. Cho, *J. Appl. Phys.* **42**, 2074 (1971).
4. E. H. C. Parker, *The Technology and Physics of Molecular Beam Epitaxy* (Plenum, New York, 1985).
5. J. Cibert, P. M. Petroff, G. J. Dolan, S. J. Pearton, A. C. Gossard, and J. J. English, *Appl. Phys. Lett.* **49**, 1275 (1986).
6. G. Bastard, *Phys. Rev. B* **24**, 4714 (1981).
7. G. Bastard, *Surf. Sci.* **113**, 165 (1982).
8. J. W. Brown and H. N. Spector, *J. Appl. Phys.* **59**, 1179 (1986).
9. G. W. Bryant, *Phys. Rev. B* **31**, 7812 (1985).
10. N. Porras-Montenegro and S. T. Pérez-Merchancano, *Phys. Rev. B* **46**, 9780 (1992).
11. J. L. Zhu, J. J. Xiong, and B. L. Gu, *Phys. Rev. B* **41**, 6001 (1990).
12. J. L. Zhu, *Phys. Rev. B* **39**, 8780 (1989).
13. J. L. Zhu and X. Chen, *J. Phys. Condens. Mat.* **6**, L123 (1994).
14. J. L. Zhu and X. Chen, *Phys. Rev. B* **50**, 4497 (1994).
15. P. Csavinszky and A. M. Elbasy, *Phys. Rev. B* **32**, 6498 (1985).
16. R. Resta, *Phys. Rev. B* **16**, 2717 (1977).
17. P. Csavinszky and H. Oyoko, *J. Math. Chem.* **9**, 197 (1992).
18. P. Csavinszky and H. Oyoko, *Phys. Rev. B* **43**, 9262 (1991).
19. A. M. Elbasy and P. Csavinszky, *Croat. Chem. Acta* **68**, 309 (1995).
20. S. Chaudhuri and K. K. Bajaj, *Phys. Rev. B* **29**, 1803 (1984).
21. P. Csavinszky and A. M. Elbasy, *Int. J. Quantum Chem., Quantum Chem. Symp.* **22**, 25 (1988).
22. A. M. Elbasy and P. Csavinszky, *J. Math. Chem.* **16**, 309 (1994).
23. L. Hrivnak, *J. Appl. Phys.* **71**, 4370 (1992).
24. J. Batey and S. L. Wright, *J. Appl. Phys.* **59**, 200 (1986).

International Journal of Quantum Chemistry

Quantum Chemistry Symposium

Author Index—Volume 30

Adams, W. H., 1279
Arteca, G. A., 1515

Baerends, E. J., 1375
Bandrauk, A. D., 1685
Baronavski, A. P., 1595
Bergson, G., 1215
Boegel, H., 1409
Boettger, J. C., 1345
Boudreaux, E. A., 1673
Brąjczewska, M., 1537
Brändas, E. J., 1217
Broo, A., 1331

Castro, M., 1351, 1419
Chelkowski, S., 1685
Chen, C., 1709
Chojnacki, H., 1385
Costa Cabral, B. J., 1651
Csavinszky, P., 1719

Dacosta, H. F. M., 1469
Das, G. P., 1499
Day Jr., O. W., 1623
Deleuze, M., 1505
Delhalle, J., 1487, 1505
Doerksen, R. J., 1633
Dolgounitcheva, O., 1241
Dudis, D. S., 1499

Eguiluz, A. G., 1457
Elabsy, A. M., 1719

Fiolhais, C., 1537
Flamant, I., 1487
Fripiat, J. G., 1487
Fukumoto, Y., 1701

Gardioli, P., 1429
Gorb, L. G., 1525
Grein, F., 1661, 1679
Gritsenko, O. V., 1375
Gross, E. K. U., 1393
Guo, H., 1479

Hachey, M. R. J., 1661
Hagmann, M. J., 1231
Harris, F. E., 1311
Heinonen, O., 1443
Huang, L., 1691

Ivanov, S., 1403
Iwata, S., 1319, 1607

Jain, J. L., 1257
Johnson, M. D., 1443
Jones, H. W., 1257

Karle, J., 1691
Kawabe, H., 1223, 1261
Kiribayashi, S., 1291
Kodama, K., 1261
Koizumi, H., 1701
Koures, V. G., 1311

Lee, S.-L., 1567
Leite, J. R., 1559
Levitina, T., 1217
Lino, A. T., 1559
Liu, L., 1479
Lowrey, A. H., 1595
Lubin, M. I., 1443
Lushington, G. H., 1679

March, N. H., 1549
Massa, L., 1691
McGill, R. A., 1595
Micha, D. A., 1469
Morrison, R. C., 1623

Nagao, H., 1223, 1261, 1291
Nagaoka, M., 1303
Nakano, M., 1261, 1291
Nguyen, U. N., 1615
Nip, A. M. L., 1549
Nishikawa, K., 1223, 1261

Öhrn, N. Y., 1213
Ortiz, J. V., 1241
Owrutsky, J. C., 1595

Perdew, J. P., 1537
Petersilka, M., 1393
Politzer, P., 1351

Rice, J. K., 1595
Rinaldi, D., 1525
Rincón, L., 1249
Rivail, J.-L., 1525
Runge, K., 1469

Sabin, J. R., 1213
Schulz, L., 1385
Scolfaro, L. M. R., 1559

Seminario, J. M., 1271, 1351
Shigemoto, I., 1291
Shigeta, Y., 1261, 1291
Slanina, Z., 1567
Sosa, R. M., 1429
Soscun M., H. J., 1351
Stefanovich, E. V., 1615
Stavrev, K. K., 1585, 1595
Steiner, M. M., 1325
Sun, K.-C., 1709
Sun, M.-L., 1567

Takahashi, E. K., 1559
Tamm, T., 1585, 1595
Ten-No, S., 1319
Thakkar, A. J., 1633
Thery, V., 1525
Tobisch, S., 1409
Tong, W., 1623
Truong, T. H., 1615
Tuszyński, J. A., 1549

van Leeuwen, R., 1375
Vieira, A., 1537

Watanabe, H., 1607
Wenzel, W., 1325
Wilson, K. G., 1325
Winkler, P., 1643

Xu, Z.-J., 1577

Yamada, S., 1291
Yamaguchi, K., 1261, 1291
Yamaki, D., 1291
Yamanaka, S., 1291
Yan, J.-M., 1577
Yeates, A. T., 1499

Zacarias, A. G., 1351
Zacarias, A., 1419
Zakrzewski, V. G., 1241
Zerner, M. C., 1213, 1585, 1595
Zhang, L., 1643
Zhu, C.-B., 1577
Ziesche, P., 1361

**Published Symposia of the
*International Journal of Quantum Chemistry***

- 1967** QUANTUM CHEMISTRY SYMPOSIUM NO. 1
(Proceedings of the International Symposium on Atomic, Molecular, and Solid-State Theory)
- 1968** QUANTUM CHEMISTRY SYMPOSIUM NO. 2
(Proceedings of the International Symposium on Atomic, Molecular, and Solid-State Theory and Quantum Biology)
- 1969** QUANTUM CHEMISTRY SYMPOSIUM NO. 3 PART 1
(Proceedings of the International Symposium on Atomic, Molecular, and Solid-State Theory and Quantum Biology)
- 1970** QUANTUM CHEMISTRY SYMPOSIUM NO. 3 PART 2
(Proceedings of the International Symposium on Atomic, Molecular, and Solid-State Theory and Quantum Biology)
- 1971** QUANTUM CHEMISTRY SYMPOSIUM NO. 4
(Proceedings of the International Symposium on Atomic, Molecular, and Solid-State Theory and Quantum Biology)
- 1971** QUANTUM CHEMISTRY SYMPOSIUM NO. 5
(Proceedings of the International Symposium on Atomic, Molecular, and Solid-State Theory and Quantum Biology)
- 1972** QUANTUM CHEMISTRY SYMPOSIUM NO. 6
(Proceedings of the International Symposium on Atomic, Molecular, and Solid-State Theory and Quantum Biology)
- 1973** QUANTUM CHEMISTRY SYMPOSIUM NO. 7
(Proceedings of the International Symposium on Atomic, Molecular, and Solid-State Theory and Quantum Biology)
- 1974** QUANTUM CHEMISTRY SYMPOSIUM NO. 8
(Proceedings of the International Symposium on Atomic, Molecular, and Solid-State Theory and Quantum Statistics)
QUANTUM BIOLOGY SYMPOSIUM NO. 1
(Proceedings of the International Symposium on Quantum Biology and Quantum Pharmacology)

- 1975** QUANTUM CHEMISTRY SYMPOSIUM NO. 9
(Proceedings of the International Symposium on Atomic, Molecular, and Solid-State Theory and Quantum Statistics)
QUANTUM BIOLOGY SYMPOSIUM NO. 2
(Proceedings of the International Symposium on Quantum Biology and Quantum Pharmacology)
- 1976** QUANTUM CHEMISTRY SYMPOSIUM NO. 10
(Proceedings of the International Symposium on Atomic, Molecular, and Solid-State Theory and Quantum Statistics)
QUANTUM BIOLOGY SYMPOSIUM NO. 3
(Proceedings of the International Symposium on Quantum Biology and Quantum Pharmacology)
- 1977** QUANTUM CHEMISTRY SYMPOSIUM NO. 11
(Proceedings of the International Symposium on Atomic, Molecular, and Solid-State Theory, Collision Phenomena, and Computational Methods)
QUANTUM BIOLOGY SYMPOSIUM NO. 4
(Proceedings of the International Symposium on Quantum Biology and Quantum Pharmacology)
- 1978** QUANTUM CHEMISTRY SYMPOSIUM NO. 12
(Proceedings of the International Symposium on Atomic, Molecular, and Solid-State Theory, Collision Phenomena and Computational Methods)
QUANTUM BIOLOGY SYMPOSIUM NO. 5
(Proceedings of the International Symposium on Quantum Biology and Quantum Pharmacology)
- 1979** QUANTUM CHEMISTRY SYMPOSIUM NO. 13
(Proceedings of the International Symposium on Atomic, Molecular, and Solid-State Theory, Collision Phenomena, Quantum Statistics, and Computational Methods)
QUANTUM BIOLOGY SYMPOSIUM NO. 6
(Proceedings of the International Symposium on Quantum Biology and Quantum Pharmacology)
- 1980** QUANTUM CHEMISTRY SYMPOSIUM NO. 14
(Proceedings of the International Symposium on Atomic, Molecular, and Solid-State Theory, Collision Phenomena, Quantum Statistics, and Computational Methods)
QUANTUM BIOLOGY SYMPOSIUM NO. 7
(Proceedings of the International Symposium on Quantum Biology and Quantum Pharmacology)

- 1981** QUANTUM CHEMISTRY SYMPOSIUM NO. 15
(Proceedings of the International Symposium on Atomic, Molecular, and Solid-State Theory, Collision Phenomena, and Computational Quantum Chemistry)
QUANTUM BIOLOGY SYMPOSIUM NO. 8
(Proceedings of the International Symposium on Quantum Biology and Quantum Pharmacology)
- 1982** QUANTUM CHEMISTRY SYMPOSIUM NO. 16
(Proceedings of the International Symposium on Quantum Chemistry, Theory of Condensed Matter, and Propagator Methods in the Quantum Theory of Matter)
QUANTUM BIOLOGY SYMPOSIUM NO. 9
(Proceedings of the International Symposium on Quantum Biology and Quantum Pharmacology)
- 1983** QUANTUM CHEMISTRY SYMPOSIUM NO. 17
(Proceedings of the International Symposium on Atomic, Molecular, and Solid-State Theory, Collision Phenomena and Computational Quantum Chemistry)
QUANTUM BIOLOGY SYMPOSIUM NO. 10
(Proceedings of the International Symposium on Quantum Biology and Quantum Pharmacology)
- 1984** QUANTUM CHEMISTRY SYMPOSIUM NO. 18
(Proceedings of the International Symposium on Atomic, Molecular, and Solid-State Theory, and Computational Quantum Chemistry)
QUANTUM BIOLOGY SYMPOSIUM NO. 11
(Proceedings of the International Symposium on Quantum Biology and Quantum Pharmacology)
- 1985** QUANTUM CHEMISTRY SYMPOSIUM NO. 19
(Proceedings of the International Symposium on Atomic, Molecular, and Solid-State Theory, Scattering Problems, Many Body Phenomena, and Computational Quantum Chemistry)
QUANTUM BIOLOGY SYMPOSIUM NO. 12
(Proceedings of the International Symposium on Quantum Biology and Quantum Pharmacology)
- 1986** QUANTUM CHEMISTRY SYMPOSIUM NO. 20
(Proceedings of the International Symposium on Atomic, Molecular, and Solid-State Theory, Scattering Problems, Many Body Phenomena, and Computational Quantum Chemistry)

- 1986** QUANTUM BIOLOGY SYMPOSIUM NO. 13
(Proceedings of the International Symposium on Quantum Biology and Quantum Pharmacology)
- 1987** QUANTUM CHEMISTRY SYMPOSIUM NO. 21
(Proceedings of the International Symposium on Quantum Chemistry, Solid-State Theory, and Computational Methods)
QUANTUM BIOLOGY SYMPOSIUM NO. 14
(Proceedings of the International Symposium on Quantum Biology and Quantum Pharmacology)
- 1988** QUANTUM CHEMISTRY SYMPOSIUM NO. 22
(Proceedings of the International Symposium on Quantum Chemistry, Solid-State Theory, and Computational Methods)
QUANTUM BIOLOGY SYMPOSIUM NO. 15
(Proceedings of the International Symposium on Quantum Biology and Quantum Pharmacology)
- 1989** QUANTUM CHEMISTRY SYMPOSIUM NO. 23
(Proceedings of the International Symposium on Quantum Chemistry, Solid-State Theory, and Molecular Dynamics)
QUANTUM BIOLOGY SYMPOSIUM NO. 16
(Proceedings of the International Symposium on Quantum Biology and Quantum Pharmacology)
- 1990** QUANTUM CHEMISTRY SYMPOSIUM NO. 24
(Proceedings of the International Symposium on Quantum Chemistry, Solid-State Physics, and Computational Methods)
QUANTUM BIOLOGY SYMPOSIUM NO. 17
(Proceedings of the International Symposium on Quantum Biology and Quantum Pharmacology)
- 1991** QUANTUM CHEMISTRY SYMPOSIUM NO. 25
(Proceedings of the International Symposium on Quantum Chemistry, Solid-State Physics, and Computational Methods)
QUANTUM BIOLOGY SYMPOSIUM NO. 18
(Proceedings of the International Symposium on Quantum Biology and Quantum Pharmacology)

- 1992** QUANTUM CHEMISTRY SYMPOSIUM NO. 26
(Proceedings of the International Symposium on Atomic, Molecular, and Condensed Matter Theory and Computational Methods)
QUANTUM BIOLOGY SYMPOSIUM NO. 19
(Proceedings of the International Symposium on the Application of Fundamental Theory to Problems of Biology and Pharmacology)
- 1993** QUANTUM CHEMISTRY SYMPOSIUM NO. 27
(Proceedings of the International Symposium on Atomic, Molecular, and Condensed Matter Theory and Computational Methods)
QUANTUM BIOLOGY SYMPOSIUM NO. 20
(Proceedings of the International Symposium on the Application of Fundamental Theory to Problems of Biology and Pharmacology)
- 1994** QUANTUM CHEMISTRY SYMPOSIUM NO. 28
(Proceedings of the International Symposium on Atomic, Molecular, and Condensed Matter Theory and Computational Methods)
QUANTUM BIOLOGY SYMPOSIUM NO. 21
(Proceedings of the International Symposium on the Application of Fundamental Theory to Problems of Biology and Pharmacology)
- 1995** QUANTUM CHEMISTRY SYMPOSIUM NO. 29
(Proceedings of the International Symposium on Atomic, Molecular, and Condensed Matter Theory and Computational Methods)
QUANTUM BIOLOGY SYMPOSIUM NO. 22
(Proceedings of the International Symposium on the Application of Fundamental Theory to Problems of Biology and Pharmacology)
- 1996** QUANTUM CHEMISTRY SYMPOSIUM NO. 30
(Proceedings of the International Symposium on Atomic, Molecular, and Condensed Matter Theory and Computational Methods)
QUANTUM BIOLOGY SYMPOSIUM NO. 23
(Proceedings of the International Symposium on the Application of Fundamental Theory to Problems of Biology and Pharmacology)

All of the above symposia can be individually purchased from the Subscription Department, John Wiley & Sons.

Diskette Submission Instructions

International Journal of Quantum Chemistry

Authors are strongly encouraged to deliver the final, accepted version of their manuscript on diskette.

- Storage medium. 5¼ or 3½ inch diskette in IBM MS-DOS, Windows, or Macintosh format.
- Software. Wordperfect® 5.1 (or later) is preferred. However, manuscripts prepared on any microcomputer wordprocessor are acceptable. [The use of desktop publishing software (Aldus Pagemaker®, QuarkXpress®, etc.) is discouraged. If you prepared your manuscript with such a program, export the text to a wordprocessing format.]
- Format. Keep the document as simple as possible. Refrain from any complex formatting. Do not use the footnote function of your word processor.
- Illustrations. Submission of electronic illustrations is encouraged, but not required. Submit illustrations on a separate diskette from the text. TIFF and EPS files or native application files are acceptable. For gray scale and color figure submissions please contact us for more detailed instructions. Illustration files may be submitted on SyQuest® 44 or 88 megabyte cartridges, which will be returned after publication.
- File name. Submit each article as a single file. Name each file with your last name (not to exceed 8 letters), followed by a period, plus the three letter extension QUA. If your last name exceeds eight letters it should be truncated to fit. For example, files prepared by author Hendrickson would be named; Hendrick.QUA. If you are using a Macintosh, maintain the MS-DOS file naming convention of eight letters, a period, and the three letter extension.
- Disk label. Label all diskettes with your name, the file name, and the wordprocessing program used.
- Paper copy. The diskette must be accompanied by hard copy printout. If the disk and paper copy differ, the paper copy will be considered the definitive version.

??? Questions ???

Sheila Kaminsky
Internet: SKaminsk@Wiley.com
Telephone: 212-850-6540
Fax: 212-850-6052



COPYRIGHT TRANSFER AGREEMENT

Date:

To:

Production/Contribution
ID# _____
Publisher/Editorial office use only

Re: Manuscript entitled _____
for publication in _____ (the "Contribution")
published by John Wiley & Sons, Inc. _____ (the "Journal")

Dear Contributor(s):

Thank you for submitting your Contribution for publication. In order to expedite the publishing process and enable the Publisher to disseminate your work to the fullest extent, we need to have the following copyright transfer agreement signed and returned to us as soon as possible. If the Contribution is not published in any edition of the Journal, this Agreement shall be null and void.

- A. The Contributor hereby transfers to John Wiley & Sons, Inc. (the "Publisher"), during the full term of copyright, the full and exclusive rights comprised in the copyright in and to the Contribution, including but not limited to the right to publish, republish, transmit, sell, distribute and otherwise use the Contribution and the material contained therein in electronic and print editions of the Journal and all derivative works therefrom throughout the world, in all languages and in all media of expression now known or later developed, and to license or permit others to do so.
- B. Notwithstanding the above, the Contributor retains all proprietary rights other than copyright, such as patent rights, in any process, procedure or article of manufacture described in the Contribution.
- C. The publisher grants back to the Contributor the following:
1. The right to make and distribute copies of all or part of the Contribution for the Contributor's use in teaching.
 2. The right to use, *after publication* in the Journal, all or part of the material from the Contribution in a book by the Contributor, or in a collection of the Contributor's work.
 3. The royalty-free right to make copies of the Contribution for internal distribution within the institution/company that employs the Contributor subject to the provisions of paragraph E below for a work-made-for hire.
 4. The right to use figures and tables from the Contribution, and up to 250 words of text, for any purpose.
 5. The right to make oral presentations of material from the Contribution.
- D. In the case of a Contribution prepared under U.S. Government contract or grant, the U.S. Government may reproduce, royalty-free, all or portions of the Contribution and may authorize others to do so, for official U.S. Government purposes only, *if the U.S. Government contract or grant so requires*.
- E. If the Contribution was written by the Contributor as a work-made-for-hire in the course of employment, the Contribution is owned by the company/employer which must sign this Agreement in the space provided below. In such case, the company/employer hereby transfers and assigns to the Publisher the full and exclusive rights in the Contribution specified in paragraph A above. In addition to the rights specified as retained in paragraph B above, the Publisher hereby licenses back to such company/employer, its subsidiaries and divisions, the royalty-free right to use and distribute the Contribution internally or for promotional and non-commercial purposes only. Copies so made shall not be available for re-sale but may be included by the company/employer as part of an information package for licensing purposes.
- F. The Contributor and the company/employer agree that any and all copies of the Contribution or any part thereof published under the terms of paragraphs C and E will include a notice of copyright in the Publisher's name and a citation to the Journal.
- G. The Contributor represents that the Contribution is the Contributor's original work. If the Contribution was prepared jointly, the Contributor agrees to inform the co-Contributors of the terms of this Agreement and to obtain their signature to this Agreement or their written permission to sign on their behalf. The Contribution is submitted only to this Journal and has not been published before. (If excerpts from copyrighted works are included, the Contributor will obtain written permission from the copyright owners and show credit to the sources in the Contribution.) The Contributor also warrants that the Contribution contains no libelous or unlawful statements, does not infringe on the rights of others, or contain material or instructions that might cause harm or injury.

Check one:

____ Contributor-owned work

____ Contributor's signature _____ Date _____

____ Typed or printed name and title _____

____ Co-contributor's signature _____ Date _____

____ Typed or printed name and title _____

____ Work-made-for-hire for Employer

____ Institution or company (Employer-for-Hire) _____ Date _____

____ U.S. Government work

____ Authorized signature of Employer _____

ATTACH ADDITIONAL SIGNATURE PAGE AS NECESSARY

Note to U.S. Government Employees

A Contribution prepared by a U.S. federal government employee as part of his/her official duties is called a "U.S. Government work," and is in the public domain in the United States. In such case, Paragraph A above applies only outside the United States. If the Contribution was not prepared as part of the employee's duties, it is not a U.S. Government work.

If the Contribution was prepared jointly, and any co-contributor is not a U.S. government employee, *the Contribution is not a U.S. Government work*. In such case, the co-contributor who is not a non-U.S. government employee should be delegated in writing by the other co-contributors to sign this Agreement on their behalf.

International Journal of Quantum Chemistry

Information for Contributors

1. Manuscripts should be submitted in triplicate and accompanied by an executed Copyright Transfer Form to the Editorial Office, International Journal of Quantum Chemistry, Quantum Chemistry Group, University of Uppsala, Box 518, S-75120 Uppsala, Sweden. Authors may also submit manuscripts to the Editorial Office, International Journal of Quantum Chemistry, Quantum Theory Project, 362 Williamson Hall, University of Florida, Gainesville, Florida 32611.

All other correspondence should be addressed to the Publisher, Professional, Reference, & Trade Group, John Wiley & Sons, Inc., 605 Third Ave., New York, NY 10158.

2. It is the preference of the Editors that papers be published in the English language. However, if the author desires that his paper be published in French or German, it is necessary that a particularly complete and comprehensive synopsis be furnished in English.

3. Manuscripts should be submitted in triplicate (one *original*, two carbon copies) typed *doubled spaced* throughout and on one side of each sheet only, on a *heavy* grade paper with margins of at least 2.5 cm on all sides. Copyright: No article can be published unless accompanied by a signed publication agreement, which serves as a transfer of copyright from author to publisher. A publication agreement may be obtained from the editor or the publisher. A copy of the publication agreement appears in most issues of the journal. Only original papers will be accepted and copyright in published papers will be vested in the publisher. It is the author's responsibility to obtain written permission to reproduce material that has appeared in another publication. A copy of that agreement, executed and signed by the author, is now required with each manuscript submission. (If the article is a "work made for hire," the agreement must be signed by the employer.)

4. A short synopsis (maximum length 200 words) is required. The synopsis should be a summary of the entire paper, not the conclusions alone. If the paper is written in French or German, a synopsis in English should also be prepared. The paper should be reasonably subdivided into sections and, if necessary, subsections.

5. A list of five key words or phrases for indexing must accompany each submission.

6. Authors are cautioned to type—wherever possible—all mathematical and chemical symbols, equations, and formulas. If these must be handwritten, please print clearly and leave ample space above and below for printer's marks; please use only ink. All Greek or unusual symbols should be identified in the margin the first time they are used. Please distinguish in the margins of the manuscript between capital and small letters of the alphabet wherever confusion may arise (e.g., k , K , κ). Please underline with a wavy line all vector quantities. Use fractional exponents to avoid root signs.

The nomenclature sponsored by the International Union of Pure and Applied Chemistry is requested for chemical compounds. Unit abbreviations should follow the practices of the American Institute of Physics. Chemical bonds should be correctly placed, and double bonds clearly indicated. Valence is to be indicated by superscript plus and minus signs.

7. The references should be numbered consecutively in the order of their appearance and should be complete, including authors' initials and—for unpublished lectures or symposia—the title of the paper, the date, and the name of the sponsoring society. Please compile references on a separate sheet at the end of the manuscript. Abbreviations of journal titles should conform to the *Bibliographic Guide for Editors & Authors* published by the American Chemical Society.

References should be limited to literature citations. Explanatory or supplementary material should be treated either as footnotes to text or appendices. Examples:

- [1] D.N. Zubarev, *Nonequilibrium Statistical Thermodynamics* (Consultants Bureau, Plenum, New York, 1974).
- [2] H. Adachi, M. Tsukada, and C. Satoko, *J. Phys. Soc. Jpn.* **45**, 875 (1978).
- [3] K. Fukui, T. Yonezawa, C. Nagata, H. Katou, A. Imamura, and K. Morokuma, in *Introduction to Quantum Chemistry* (Kagakudojin, Kyoto, 1963), Vol. I, p. 197.

8. A limited number of color figures that are of critical importance and that significantly enhance the presentation will be considered for publication at the publisher's expense. Color separations or

transparencies (negatives or positives) are optimal. Color slides are preferable to color prints. Any cropping of the color figure should be clearly indicated. Final decision on publication of color figures will be at the discretion of the Editor.

9. Each table should be supplied on a separate sheet (not interspersed with text). Please supply numbers and titles for all tables. All table columns should have an explanatory heading.
10. Please supply legends for all figures and compile these on a separate sheet.
11. Figures should be professionally prepared and submitted in a form suitable for reproduction (camera-ready copy). Computer-generated graphs are acceptable only if they have been printed with a good quality laser printer. Artwork is generally reduced so that the type in the figures is about 2.5 mm high. The maximum final size of figures for this journal is 16×21 cm after reduction. Good glossy photographs are required for halftone

reproductions. If in doubt about the preparation of illustrations suitable for reproduction, please consult the publisher at the address given in paragraph 1.

12. Senior authors will receive 50 reprints of their articles without charge. Additional reprints can be ordered and purchased by filling out the form enclosed with the proof.
13. The publisher will do everything possible to ensure prompt publication. It will therefore be appreciated if manuscripts and illustrations conform from the outset to the style of the journal. Contributors should use the *Style Manual* of the American Institute of Physics; papers will otherwise have to be returned to the author for revision.

Corrected proofs must be sent back to the publisher within two days to avoid the risk of the author's contribution having to be held over to a later issue.

Available on
STN International

Look no further than
your own computer terminal
to find the results of
worldwide polymer research
with . . .

**CHEMICAL JOURNALS
ONLINE**

**WILEY POLYMER JOURNALS
(CJ Wiley)**

now available as part of **CHEMICAL JOURNALS
ONLINE**, comprises three authoritative journals
published by John Wiley & Sons, Inc.:

JOURNAL OF APPLIED POLYMER SCIENCE

JOURNAL OF POLYMER SCIENCE

BIOPOLYMERS

With **CHEMICAL JOURNALS ONLINE**, you will have the capability to search and display original polymer research • vital experimental data • experimental procedures • new preparation techniques • literature citations • crossover to other chemical information including CAS Online.

Easily accessible and cost-effective, **CHEMICAL JOURNALS ONLINE** (which also includes journals from the Royal Society of Chemistry and the American Chemical Society) will enable you to obtain immediate results without even leaving your desk!

To find out more about how CJ Wiley — and the *entire* **CHEMICAL JOURNALS ONLINE** database — can work for you, call toll-free 800-227-5558. An American Chemical Society sales representative will be pleased to answer any questions you might have.

You can also write to the Marketing/Communications Department, American Chemical Society, 1155 Sixteenth Street, N.W., Washington, D. C. 20036.



The Computer-Powered
Full-Text Search System
From The American
Chemical Society

**CHEMICAL JOURNALS
ONLINE**

Physical Methods in Chemistry



Second Edition

Special Set Price \$1695 • Save Over 15%

Series Editors:

**Bryant W. Rossiter
& J.F. Hamilton**

both of Eastman Kodak Company

This well-respected series provides chemists in a wide range of industries and research with an appreciation for the potential and limitations of the many techniques used in evaluating and analyzing substances and materials. The volumes include coverage of theory and apparatus.

TO ORDER: You can order these and other Wiley titles through your bookseller or send your order direct to:

John Wiley & Sons, Inc. Attention: S. Schinder
605 Third Avenue New York, NY 10158-0012

or

Call toll free: **1-800-US-WILEY (1-800-879-4539)**
In Canada, call 1-800 263-1590.

Prices subject to change without notice and may be higher outside the U.S.

10-Volume Set

0-471-57086-9
\$1695

Vol. 1 Components of Scientific Instruments and Applications to Chemical Research

0-471-08034-9 1986
834pp. \$210

Vol. 2 Electrochemical Methods

0-471-08027-6 1986
904pp. \$210

Vol. 3A Determination of Chemical Composition and Molecular Structure

0-471-85401-1 1987
624pp. \$165

Vol. 3B Determination of Chemical Composition and Molecular Structure

0-471-85051-9 1989
971pp. \$190

Vol. 4 Microscopy

0-471-08026-8 1991
560pp. \$165

Vol. 5 Determination of Structural Features of Crystalline and Amorphous Solids

0-471-52509-X 1990
640pp. \$150

Vol. 6 Determination of Thermodynamic Properties

0-471-57087-7 1992
750pp. \$245

Vol. 7 Determination of Elastic and Mechanical Properties

0-471-53438-2 1991 \$110

Vol. 8 Determination of Electronic and Optical Property

0-471-54407-8 1993
400pp. \$150

Vol. 9A Investigations of Surfaces and Interfaces

0-471-54406-X 1992
528pp. \$140

Vol. 9B Investigations of Surfaces and Interfaces

0-471-54405-1 1993
750pp. \$250

Vol. 10 Supplement and Cumulative Index

0-471-57086-9 1993
ca.450pp. \$195



WILEY

Publishers Since 1807

ALGEBRAIC METHODS IN MOLECULAR & NUCLEAR STRUCTURE PHYSICS

by Alejandro Frank, Universidad
National Autónoma de México and
Pieter Van Isacker, University of Surrey,
England and Grand Accélérateur
National d'Ions Lourds, France

This book provides the basic technical background required in the applications of algebraic models in nuclear physics with an emphasis on group-theoretical techniques. The material is divided into three parts of increasing mathematical complexity. Part I is designed to familiarize the reader with concepts and terminology of group theory as well as with the basic features of boson-fermion systems. Part II is devoted to the study of molecular algebraic models and Part III deals with the interacting boson model of nuclear structure.

Contents:

Part I, *Schematic Models*: Identical Bosons • Non-identical Bosons • Bosons and Fermions • Supersymmetry and F Spin.

Part II, *Molecular Models*: Diatomic Molecules • Triatomic Molecules • Bose-Fermi Symmetries and Molecular Electronic Spectra.

Part III, *Nuclear Models*: The Interacting Boson Model • The Neutron-Proton Interacting Boson Model • The Interacting Boson-Fermion Model • Group Theory and the Algebraic Approach • The Unitary and Orthogonal Algebras • Dragt's Theorem

1994 • 488pp. • 0-471-52640-1 • \$64.95

ANGULAR MOMENTUM

An Illustrated Guide to Rotational Symmetries for Physical Systems
by William J. Thompson, University of North Carolina, Chapel Hill

Pedagogically consistent and self-contained, this extensively illustrated guide to rotational symmetries is an excellent learning aid for students of physics, chemistry, and mathematics, as well as a valuable resource for researchers in the physical sciences and applied mathematics. Includes *Mathematica* software that allows you to create vivid images of rotational symmetries.

Contents: The Computer Interface • Symmetry in Physical Systems • Mathematical and Quantal Preliminaries • Rotational Invariance and Angular Momentum • Angular Momentum Eigenstates • Angular Momentum in Quantum Systems • Finite Rotations of Angular Momentum Eigenstates • Combining Two Angular Momentum Eigenstates • Irreducible Spherical Tensors and Spin • Recombining Several Angular Momentum Eigenstates

1994 • 461pp. • 0-471-55264-X • \$64.95

PRINCIPLES OF SYMMETRY, DYNAMICS, AND SPECTROSCOPY

by William G. Harter, University of Arkansas, Fayetteville

This book is designed to explain the applications of group theory and symmetry analysis to physics by using a novel physical approach. Prof. Harter breaks down the complex mathematics of group theory representation by first introducing the simplest physical problem to show and prove each mathematical concept. These important mathematical quantities are discussed and derived after their need is demonstrated by a physical problem. This approach enables the reader to tackle more complex problems by synthesizing simpler mathematical concepts. This book is a valuable contribution to the rapidly growing field of laser spectroscopy.

Contents: A Review of Matrix Algebra and Quantum Mechanics • Basic Theory and Applications of Symmetry Representations (Abelian Symmetry Groups) • Basic Theory and Applications of Symmetry Representations (Non-Abelian Symmetry Groups) • Theory and Applications of Higher Finite Symmetry and Induced Representations • Representations of Continuous Rotation Groups and Applications • Theory and Applications of Symmetry Representation Products (Finite Groups) • Theory and Application of Symmetry Representation Products (Continuous Rotation Groups) • Symmetry Analysis for Semiclassical and Quantum Mechanics: Dynamics with High Quanta

1993 • 846pp. • 0-471-05020-2 • \$125.00

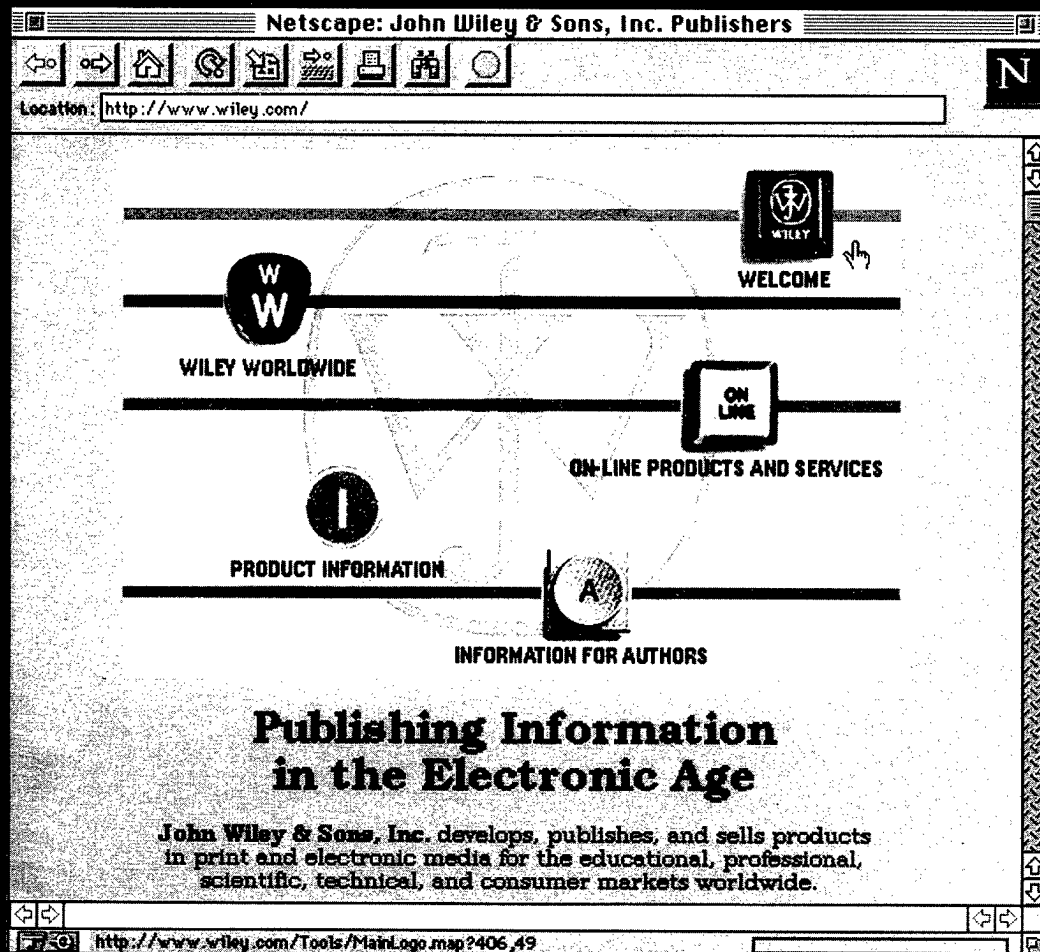
JOHN WILEY & SONS, INC.

605 THIRD AVENUE, NEW YORK, NY 10158-0012

To order by phone: (800) 879-4539; To order by fax: (201) 302-2300; Other inquiries (212) 850-6418

Prices subject to change and may be slightly higher outside U.S.A.

We're Online!



Stop by our new location on the Internet.

You can find us at

<http://www.wiley.com>

Drop in and explore. Get the very latest information on new books, journals, and other publications along with special promotions and publicity. Discover a variety of online services, including online journals. Download a sample chapter or software. And much more.

Join us *online* today!

 **WILEY**



0161-3642(1996)60:7;1-3